EXPERIMENTAL STUDY ON KINEMATICS AND DYNAMICS OF BREAKING WAVES IN DEEP WATER

A Dissertation

by

HO JOON LIM

Submitted to the Office of Graduate Studies of
Texas A&M University
in partial fulfillment of the requirements for the degree of

DOCTOR OF PHILOSOPHY

August 2010

Major Subject: Ocean Engineering

EXPERIMENTAL STUDY ON KINEMATICS AND DYNAMICS OF BREAKING WAVES IN DEEP WATER

A Dissertation

by

HO JOON LIM

Submitted to the Office of Graduate Studies of
Texas A&M University
in partial fulfillment of the requirements for the degree of

DOCTOR OF PHILOSOPHY

Approved by:

Chair of Committee,	Kuang-An Chang
Committee Members,	Hamn-Ching Chen
	Robert E. Randall
	Chin B. Su
Head of Department,	John Niedzwecki

August 2010

Major Subject: Ocean Engineering

ABSTRACT

Experimental Study on Kinematics and Dynamics of Breaking Waves in Deep Water.

(August 2010)

Ho Joon Lim, B.S.; M.S., Inha University

Chair of Advisory Committee: Dr. Kuang-An Chang

A new measurement technique called fiber optic reflectometer (FOR) was developed to investigate multiphase flows. The principle and setup of the FOR technique were introduced and applied to various experiments. Based on the coherently mixed signal between the Fresnel reflection off the fiber-liquid interface and the scattered signal off the object, such as a gas bubble, and a solid particle, this single probe technique is capable of simultaneously measuring the velocity of the object with a high accuracy and the phase of the fluid. In addition, bubble diameter, velocity, and void fraction were measured directly.

By means of a simple modification of the FOR technique, solute concentration and refractive index change were measured with a greatly improved accuracy. This modified technique was used for measuring of a NaCl concentration in deionized water to validate a new normalization technique.

In the second part of this thesis, a plunging breaking wave in deep water has been studied. Using the wave focusing method, a strong plunging breaker was generated with accuracy in the deep water condition in a two-dimensional wave tank. It was possible to describe the breaking process in detail using a high speed camera with a frame rate of

500 or 1000 *fps*.

Four kinds of experimental techniques were employed or developed to investigate the plunging breaker. Bubble image velocimetry (BIV) and particle image velocimetry (PIV) were used to measure the velocity fields. The velocity fields of the highly aerated region were obtained from the BIV measurements. In addition, the modified PIV technique is capable of measuring the velocities in the entire flow field including the aerated region. Mean and turbulent properties were obtained by the ensemble average. The mean velocity, mean vorticity, and mean kinetic energy were examined over the entire flow field. In addition, the Reynolds stresses and turbulent kinetic energy were calculated with high temporal and spatial resolutions. Free surface elevation was obtained from wave gauge measurements. BIV and PIV images were also used to obtain the free surface elevation and the boundary of the aerated region for more accurate results.

The FOR technique was used to obtain the void ratio at each splash-up region. Compressibility of the plunging breaker was considered. Mass flux, momentum flux, kinetic energy, and Reynolds stresses at each FOR station were recalculated using the void ratio obtained from the FOR measurements. All terms at the first splash-up region were highly overestimated more than 100% unless the void ratio was applied to the calculation of fluxes and energies. Compared with the fully developed first splash-up region, the overestimation at the second and third splash-up was less significant. However, most terms were overestimated by 20~30% when the void ratio was not considered.

DEDICATION

This dissertation is dedicated,

with love and respect,

to my wife, two sons, parents and parents-in-law .

ACKNOWLEDGEMENTS

I would like to first thank my advisor, Dr. Kuang-An Chang, for his guidance and advice. This dissertation could not have been completed without his insight, experience and comments. I also deeply appreciate his continuous encouragement from the beginning of the study.

I thank Dr. Chin B. Su for his kind help and advice. His insight and teaching have always helped me to open up to different fields of study. I would like thank the rest of my committee, Dr. Robert E. Randall and Dr. Hamn-Ching Chen, for their guidance and advice throughout the study.

Thanks to my research mates, Dr. Kwang-Hyo Jung, Dr. Yong-Uk Ryu and Kusalika Ariyarathne, for their help, friendship and encouragement. I would like to thank Mr. John Reed for his help and advice in the laboratory. Thanks also to my officemates and friends in the department for their friendship and encouragement.

Lastly, I would like to express my special gratitude and love to my wife, two sons, parents and parents-in-law. This dissertation would not have been possible without their invaluable love, trust and support.

TABLE OF CONTENTS

Page

CHAPTER Page

CHAPTER Page

CHAPTER Page

LIST OF FIGURES

Page

Page

Page

Page

Page

Page

Page

Page

Page

Page

Page

Page

Page

Page

LIST OF TABLES

Page

CHAPTER I

INTRODUCTION

1.1 Background of Breaking Waves

Wave breaking in the ocean is one of the most extreme events of water waves and the understanding of wave breaking processes with qualitative and quantitative insight is important in the study of various fields such as coastal and offshore structure design, multiphase flow due to air entrainment, turbulence, energy dissipation, scalar mixing, and sediment transport in the surf zone. Many ocean and coastal engineers have been interested in the huge wave loads of extreme waves and their interaction with ocean structures, such as the stability and damage sustained by these structures due to significant impacts and associated overtopping greenwater. On the other hand, the physics, kinematics, and dynamics of breaking waves have been of great interest to many researchers for several decades. As diverse technologies such as high capacity, fast computers and high speed cameras are developing rapidly, many meaningful results have been reported using experimental and/or numerical methods. However, both experimental and computational research on breaking waves are still very challenging since breaking waves are nonlinear with multiphase and turbulent flows within the highly aerated region.

This dissertation follows the style and format of the Journal of Ocean Engineering.

Most studies have been completed using laboratory experiments and numerical models because it is extremely difficult to describe breaking waves analytically due to the nonlinear phenomenon. Real scale field measurements are also not appropriate to investigate the inside of the breaking process.

There exist many excellent reviews on breaking waves in deep water (Bonmarin, 1989; Banner and Peregrine, 1993) and in the surf zone (Peregrine, 1983; Basco, 1985; Battjes, 1988). Recently, Christensen *et al*. (2002) gave a review on recent advances in both numerical models and measurement techniques of breaking waves within the surf zone.

Numerical models of the surf zone have been developed using various approaches such as depth-integrated models, Boussinesq-type models, Reynolds averaged Navier-Stokes equations (RANS) solvers, and two- or three-dimensional large eddy simulators (LES) (e.g., Schaffer *et al*., 1993; Lin and Liu, 1998a, 1998b; Watanabe and Saeki, 1999; Christenen and Deigaard, 2001; Watanabe *et al*., 2005; Christensen, 2006; Lynett, 2006). However, limited success has been achieved due to the complexity of the splashing free surface in the turbulent bore region after wave impingement and the lack of experimental data to validate the calculations.

For the experimental approach, velocity measurements for the entire flow field of the breaking process, including the aerated region are essential to evaluate the turbulence structure induced by breaking waves. However, like that of numerical methods, experimental measurements have suffered from the difficulties associated with the presence of the highly aerated region. Reliable quantitative measurement techniques

were not available until the late 1970's. Most experiments on breaking waves have been based on qualitative data. Non-intrusive optical techniques for velocity measurements, such as laser Doppler velocimetry (LDV) and particle image velocimetry (PIV), have recently become available in the last three decades to obtain quantitative data. Although measurements of the aerated region were still unavailable, these techniques have been applied to numerous laboratory experiments with limited success. The LDV technique is usually capable of measuring the velocity field under the trough level with a high temporal resolution (e.g., Nadaoka *et al*., 1989; Ting and Kirby, 1994, 1995, 1996; Longo, 2003; Stansby and Feng, 2005; Shin and Cox, 2006). Currently, the relatively new PIV technique is perhaps the most robust and state-of-the-art technique among all the addressed experimental methods for determining of flow velocity (Perlin *et al*., 1996; Skyner, 1996; Chang and Liu, 1998, 1999, 2000; Melville *et al*., 2002; Govender *et al*., 2002a, 2002b, 2004; Cowen *et al*., 2003; Kimmoun and Branger, 2007; Drazen and Melville, 2009; Huang *et al*., 2009). This is due to its full field nature, and its recent advances in the improvement of the temporal and spatial resolutions. Valuable reviews on PIV can be found in Adrian *et al*. (1999), Raffel *et al*. (2001) and Adrian (2005).

Among the recent advances in breaking wave measurements using PIV, Chang and Liu (1998) measured the maximum velocity, associated acceleration, and vorticity of an overturning jet of a breaking wave. As a wave breaks and entrains air bubbles, the technique is then restricted to the region outside the aerated area. Despite some successes in measuring the properties of a breaking wave, the flow field and generated turbulence outside the aerated region could not be measured (Chang and Liu, 1999,

2000; Melville *et al*., 2002; Huang *et al*., 2009). In general, most measurements were limited to weak spilling breakers as well as under the trough level (LDV), outside the aerated region (PIV), or away from the breaking point, which is a relatively less important region.

Advances in understanding the flow structure inside the highly aerated region have rarely been reported. Few exceptions are perhaps the early work of Jansen (1986), the recent work of Govender (1999), Govender *et al*. (2002a, 2002b, 2004), Ryu *et al*. (2005), Stansby and Feng (2005) and Kimmoun and Branger (2007). Jansen measured particle trajectories within the aerated region of breaking waves using fluorescent tracers and ultraviolet light. Due to the nature of this method, the measurements suffered from poor spatial resolution. More comprehensive laboratory measurements for the surf zone were obtained by Govender *et al*., who used digital correlation image velocimetry (DCIV) technique with a strobed light sheet in order to illuminate the particles and the aerated region. This process is similar to PIV and is based on digital image acquisition and cross-correlation algorithms. Bubble structures in the images were used for correlation between consecutive images for velocity determination. Even though these measurements were promising, there were important velocity vectors missing near the wave crest where the maximum velocity occurs.

A new technique called bubble image velocimetry (BIV) was introduced by Ryu *et al*. (2005). They combined PIV and the shadowgraphy method to obtain the velocity of bubbles. In their technique, bubbles are used as tracers, and correlation between bubbles is calculated for velocity determination. No lasers are needed in this technique while the

measurement plane is defined by carefully controlling the depth of field. They measured the velocity fields of breaking waves impinging on a structure and associated overtopping greenwater. This technique is perhaps the first systematic method for measuring bubble (air-water mixture) velocity within the highly aerated region. Although the BIV measurements provide air-water mixture velocity fields with a high temporal and spatial resolution, velocity fields of the water phase, which is the outside of the aerated region, cannot be obtained by BIV. Therefore, other techniques, such as PIV, that are capable of measuring water particle velocities should be employed for measuring two phase flows.

Stansby and Feng (2005) used the LDV technique to measure weakly plunging breakers transforming into the bore region within the surf zone. Vorticity magnitude was compared with hydraulic jump value. They reported some similarities only during the initial stages of the breaking. They also obtained the terms in the depth-integrated RANS equation in order to evaluate the magnitudes of different effects. They found that the maximum horizontal velocity at the initial stage of the weakly plunging breakers were similar to that at the initial stage of gentle spilling breakers.

Recently, Kimmoun and Branger (2007) measured the entire velocity fields of spilling waves in the surf zone using the PIV technique. They also estimated the turbulence dissipation rate by examining the turbulent kinetic energy budget and the Kolmogorov length scale. Their results have provided better understanding of breaking waves in the surf zone.

Huang *et al*. (2009) measured turbulence and wave energy dissipation of spilling

breakers in the surf zone using PIV. Although the highly aerated region of the spilling breaker was not measured, they obtained turbulent kinetic energy, mean flow energy and total energy across the surf zone. The turbulence dissipation rate was also estimated using several different approaches.

Indeed, LDV and PIV are the most common techniques employed to measure flow velocities of breaking waves. Both techniques, which are noninvasive techniques, have some advantages and disadvantages in addition to the limitations of the traditional techniques as mentioned above. For example, the traditional PIV technique is the most reliable technique to obtain the velocity map within a spatial domain with a very high spatial resolution, while data sampling rate is usually about 10 Hz due to the limitation from a pulsed laser and a camera framing rate. The PIV method is very useful to obtain flow properties including the gradient terms, such as vorticity, and most terms in the turbulent kinetic energy budget. However, due to the low temporal resolution, it is not suitable in obtaining flow properties including the time derivative or the time-averaged values at an arbitrary point or station such as local acceleration and fluxes of mass, momentum, or energy. On the other hand, the LDV technique provides a velocity time series at a point with a high temporal resolution. It is useful to obtain time series of flow properties and time mean values at a point. However, it is not suitable for flows whose velocity gradient is important. It is extremely difficult to obtain an instantaneous velocity field. Indeed, advantages of the PIV method are disadvantages of the LDV method and vice versa.

Since breaking waves are multiphase flows including a highly aerated region, void

ratio measurement is required to investigate breaking waves, especially for plunging breakers. It is also essential to consider the compressibility during the breaking process in order to estimate wave energy dissipation. Compared with spilling waves, plunging waves have a much higher void ratio, especially at the first impingement and splash-up. Despite the importance of the void fraction as well as the velocity inside the aerated region, few quantitative measurements of void ratio exist. Intrusive probes have been commonly used to investigate various multiphase flows. In the measurement of general bubble flumes (air-water two phase flows), conductivity probes (e.g., Chanson, 1996; Chanson & Brattberg, 2000; Chanson, 2002) and fiber optic probes (e.g., Cartellier, 1992; Rinne and Loth, 1996; Barrau *et al*., 1999; Murzyn *et al*., 2005; Rensen and Roig, 2001; Kiambi *et al*., 2001; Chang *et al*., 2003; Juliá *et al*. 2005; Lim *et al*., 2008) have been successfully applied to diverse multiphase flows. In the case of void ratio measurements for breaking waves, intrusive techniques using acoustic, electric, and optical methods have also been applied to measure bubble size distributions and void ratio in field and laboratory experiments (e.g., Lamarre and Melville, 1991, 1992, 1994; Deane, 1997; Vagle and Farmer, 1998; Deane and Stokes, 2002; Cox and Shin, 2003; Hoque and Aoki, 2005; Blenkinsopp and Chaplin, 2007; Rojas and Loewen, 2007). It is widely accepted that intrusive probes are the most appropriate technique to measure the high concentration of air bubbles under breaking waves. Lamarre and Melville (1992) developed an impedance probe to measure the void ratio field in laboratory breaking waves. Deane (1997) reported the results of acoustic and optical measurements of breaking waves in the surf zone and obtained a total void ratio of 0.3 - 0.4. Cox and Shin

(2003) used an impedance void fraction meter to measure the void ratios in three different waves (spilling, plunging and spilling/plunging) in the surf zone, and maximum ensemble averaged void ratio were between 0.15 and 0.2. They presented the temporal variation of the void ratio above and below the still water level. The averaged void ratio in each case was self-similar, and was modeled with linear growth and exponential decay. Hoque and Aoki (2005) used a conductivity probe to obtain the void ratio under breaking waves in the surf zone. They reported that the void ratio distribution followed the analytical solution of the diffusion equation. The maximum void ratio at the still water level was 0.2 and 0.16 for plunging and spilling waves, respectively. Blenkinsopp and Chaplin (2007) also measured the void ratios of breaking waves in the laboratory using optical fiber probes. They used a submerged reef structure to generate different types of breaking waves (strong plunging, plunging and spilling/plunging). They found that integral properties of the void ratio fields have a remarkable similarity between characteristics in different breaker types.

Although recent reports on the highly aerated region have provided a much better understanding of the breaking wave (Govender *et al*, 2002a, 2002b, 2004; Kimmoun and Branger, 2007), research on plunging waves in deep water has not been reported. In addition, simultaneous measurements of both velocity and void ratio in the aerated region have not been reported. In the present study, strong plunging waves are investigated with high temporal and spatial resolutions using various experimental techniques. It is believed that this study will provide better insight into the nature of the plunging breaker in deep water without any effects from the bottom boundary or the

previous turbulence due to the repetitive breaking in the surf zone.

1.2 Objective and Scope of the Study

The first objective of the study is to develop appropriate measurement techniques or systems for the multiphase flow measurement. After validation of the new technique by measuring the velocity and fraction ratio of each phase in the multiphase flows, it will be employed to investigate the kinematics and dynamics of plunging breakers in deep water, which is the second objective of the study. In advance, a qualitative study is performed using a high speed camera with a high frame rate after generating a strong plunging wave in deep water using wave focusing methods (Skyner *et al*, 1990; Skyner 1996). Velocity fields, void ratio, and wave elevation are measured using traditional and newly developed measurement techniques such as PIV, BIV, and FOR. Since the traditional PIV technique does not work in the highly aerated region due to the air entrainments after wave impinging, which is crucial in this study, the BIV technique is employed for the velocity measurement in the aerated region while the PIV technique is used to obtain velocity fields outside the aerated region to cover the entire flow field and compare these values with the results from previous works. However, the velocity field in the aerated region could be obtained in this experiment using a modified PIV technique. The images of the aerated region have bubble structures with various intensities like images from the BIV measurement. It is possible that the bubble images from the PIV measurements could be obtained by using a weak continuous laser light, which allows the reflection of the light from bubbles to attenuate. Bubble velocity in the aerated region is obtained from the modified PIV method, and is validated by comparing with Stokes wave and

results from the BIV method. Several wave gauges are used to obtain wave elevation. In addition, the boundary of the aerated region and the free surface, including the aerated region, are obtained from the BIV and PIV images. A void ratio in the highly aerated region can be easily obtained by using the FOR technique, which can measure velocity and fraction ratio of all phases simultaneously in a multiphase flow at a given point.

1.3 Organization of the Dissertation

This dissertation is composed of two main parts. The first part is related to the FOR technique and follows the organization method of combining papers. The second part covers an experimental study on the plunging breaker, which is the main subject of the dissertation.

The modified FOR technique is introduced in Chapter II along with the measurements of solute concentration and refractive index change in the fluid. The FOR technique is introduced and validated through various measurements in multiphase flows in Chapter III. Chapter IV measures the bubble diameter, velocity, and void ratio using the FOR technique developed in Chapter III.

In the second part, the experimental setups and conditions for four kinds of measurement techniques to investigate plunging breakers are presented in Chapter V. The qualitative description of the breaking process can be seen in Chapter VI. Chapter VII uses the BIV and PIV images to detect the free surface and the boundary of the aerated region. The wave gauge measurements are also presented in this chapter. Chapter VIII shows the results from the BIV measurements. Chapters IX and X use the modified PIV technique to obtain the mean and turbulent quantities of the flow. Void

ratio measurements are presented in Chapter XI using the FOR technique developed and applied in Chapters III and IV. Results considering compressibility of the plunging breaker are also presented in this chapter. Conclusion and future work are presented in Chapter XII.

Appendixes A and B shows various results with additional figures obtained from the BIV and PIV measurements respectively.

Chapter II has been published in *Measurement Science and Technology* (Chang *et al*., 2002). Chapter III has been published in *Review of Scientific Instruments* (Chang *et al*., 2003). Chapter IV has been published in *Review of Scientific Instruments* (Lim *et al*., 2008). Part of Chapter XIII (8.2) has been published in *Measurement Science and Technology* (Ryu *et al*., 2005). Parts from Chapter V to Chapter XII are subject of a publication in preparation.

CHAPTER II

CONCENTRATION MEASUREMENTS: A FIBRE OPTIC FRESNEL RATIO METER FOR MEASUREMENTS OF SOLUTE CONCENTRATION AND REFRACTIVE INDEX CHANGE IN FLUIDS*

A new and simple normalization technique that greatly enhances the measurement resolution of conventional fibre-optic reflectometry based on Fresnel reflection from the tip of a fibre is used for demonstrating the feasibility of measuring solute concentrations and index changes in fluids to very high precision. The amplitude of pulses originating from reflection from the fibre-fluid interface is compared in real-time with the amplitude of reference pulses from a fibre-air interface such that errors caused by pulse amplitude fluctuations and slightly varying detector responses are corrected. Using solutions of sodium chloride and water, it is demonstrated that the technique is capable of measuring index changes of 2×10^{-5} corresponding to a NaCl concentration of 0.02%.

2.1 Introduction

The measurement of fluid concentration in real time has been of great interest to many engineering disciplines. In the study of fluid dynamics, not only is it important to

*Reprinted with permission from "A fibre optic Fresnel ratio meter for measurements of solute concentration and refractive index change in fluids" by Chang, Lim, and Su (2002). *Measurement Science and Technology*. DOI 10.1088/0957-0233/13/12/32, Copyright [2002] IOP Publishing

obtain concentration field precisely, it is often essential to obtain the concentration as a function of time and space in a dynamic problem. For example, the concentration measurement of a turbulent jet is important in the study of pollutant mixing and transport (Fischer *et al*., 1979). The problem is strongly temporally and spatially dependent and requires precise concentration data with high temporal and spatial resolutions. To preserve the flow characteristics a small probe is also necessary to minimize the disturbance caused by the introduction of the probe. This type of dynamic concentration measurement is often performed in a laboratory water flume under controlled environment and uses salt as the tracer. Whether pure NaCl–water mixture or real seawater is used is immaterial since both simulate the same dynamics of transport phenomena in an aqueous environment such as lake, river or ocean. However, with pure NaCl-water mixture or other passive tracer, fibre-optic techniques can be applied without contaminating the fibre tip while the relationship between refractive index and concentration is easy to establish and convert.

High-performance liquid chromatography (HPLC) using interferometric and flow-cell techniques (e.g., Woodruff and Yeung, 1982; Brandemburg, 1997; Wilson and Reed, 1993) for chemical analysis have extremely high resolution, but their constructions and geometries are cumbersome and inappropriate for the envisioned application mentioned above. A number of optical techniques, implemented with bulk optics, that may be appropriate for measuring the spatial and temporal dependence of NaCl concentration in the water tank have been reported. They measure the refraction angle as a function of liquid index (Krishna *et al*., 2000), and intensity change caused by Fresnel reflection

between a glass plate and a liquid (Fan and Longtin, 2000). By allowing an air-gap between two optical fibres, liquid solutions can be placed between the two fibres. Solute concentrations can then be determined from the transmitted signal spectra through the two fibres when the fluid to be measured fills the gap (Lin and Brown, 1993a; Lin and Brown, 1993b). Seawater salinity (Lin and Brown, 1993a) and electrolytes concentration (Lin and Brown, 1993b) have been measured by this technique.

Here, we introduce a new normalization technique that greatly enhances resolution when applied to conventional fibre optic reflectometry that is based on Fresnel reflection from the fibre tip. The overall technique provides accuracy, simplicity, near non-invasiveness because of the small dimension of the optical fibre, high spatial resolution of less than 10 μm and almost unlimited temporal resolution.

2.2 Principle and Experimental Setup

The idea of this technique is to measure the reflected optical power due to Fresnel reflection from the fibre-fluid interface. A change in the reflected optical power measures the change in the refractive index of the fluid. However, to increase measurement resolution, the reflected power is normalized by a similar reflected power from a reference fibre-air interface, with both reflected signal derived from the same optical source, and detected by a common detector. The normalization procedure corrects for fluctuations that are common to the signal and reference arms.

The idea mentioned above was implemented by the experimental setup shown in Fig. 2.1. A train of optical pulse, derived from a diode laser driven by a pulse generator, is launched into a standard telecommunications graded single-mode optical fibre (SMF-

28 fibre). The optical pulse is divided into two paths by a 2 × 2 single-mode fused fibre coupler with a nominal 50%:50% splitting ratio. The end of the signal fibre is immersed in the test fluid while the end of the reference fibre rests free in air. Returned pulses due to Fresnel reflections from both fibre ends are detected by a dc-coupled detector. The pulses are subsequently amplified and processed by a computer. The experiment is conducted in the pulse mode so that the reflected power from the signal and reference fibres can be temporally separated. Thus, the signal path consists of only a few metres of fibre while the reference path is a spool of long fibre. The length of the long fibre used is arbitrary as long as the returned signal and reference pulses can be temporally separated. The long fiber length is not a problem because the optical waveguide effect of the fibre remains intact independent of the fiber length, unless the fiber is excessively bent during the course of the experiment causing radiation loss.

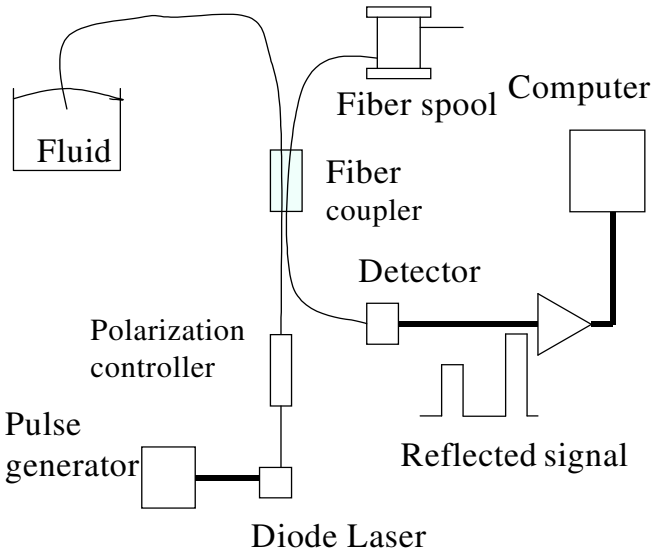

Fig. 2.1 The experimental setup for concentration measurements. The light source is a 1.3 μm wave length multi-longitudinal diode laser.

A pair of time-separated optical pulses reflected from the fibre-fluid and fibre-air interface is shown in Fig 2.2. It is important to note that both pulses are derived from a common optical pulse but delay in time by $2L/c$, where L is the length difference between the two optical paths and c is the speed of light in the fibre. This assures that any pulse amplitude fluctuation will not limit the measurement precision.

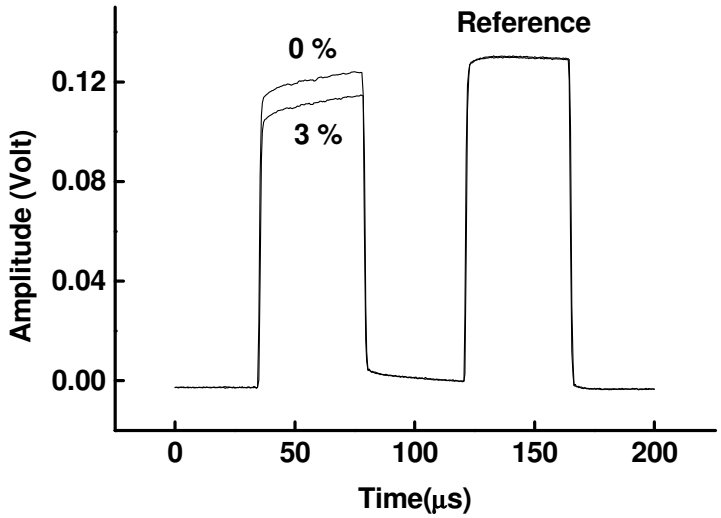

Fig. 2.2 Two typical pairs of reflectance pulses from the fluid-fibre and air-fibre interfaces for 0 and 3 % salt concentration.

The first pulse which represents the overlay of two reflected pulses from the fibre-fluid interface with two different NaCl concentrations of 0 and 0.03 g cm^{-3} (3% salt) shows the amplitude dependence on solute concentration. The second pulse is the reference pulse. It is noted that, unlike the second pulse, the first pulse does not have a flat top. This is due to the additional contribution originating from backscattered Rayleigh light from the reference pulse traveling in the long fibre. However, the

Rayleigh backscattered light does not affect the differential index measurement because its magnitude is proportional to the laser power which is corrected by this normalization technique. The amplitude of each pulse is made almost equal by adjusting the splice loss while splicing the reference arm to the fibre coupler when the tip of the signal arm is immersed in pure water. This gives the reference value for the amplitude ratio. Any deviation from this ratio is indicative of an index change. However, any NaCl concentration can be taken as the reference ratio.

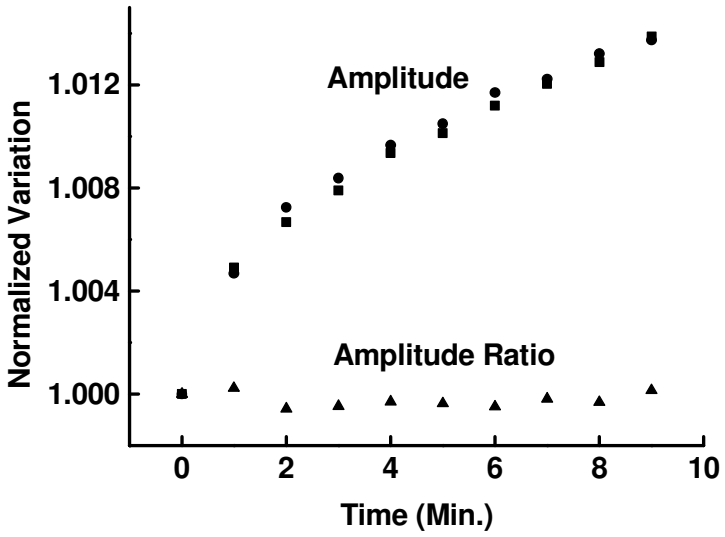

Fig. 2.3 Squares and circles show the drift of the signal and reference pulse amplitude normalized to the initial value. Triangles show the normalized amplitude ratio.

The quantity of interest is the amplitude ratio *R* between the signal and the reference pulse. By taking the ratio, drifts in laser optical power, potential non-polarization dependent temporal variations in the splitting ratio of the fibre coupler and,

to a good degree, the drift in the detector response can be normalized out. To demonstrate the merit of our ratio technique, we measured the amplitude and their ratio immediately after the system was switched on. Fig. 2.3 shows the plot of the amplitude of the individual signal and reference pulse and the amplitude ratio R as a function of time upon the turn-on of the system. It is noted that the ratio R stays relatively constant despite the drift in the individual amplitude. By taking the ratio, it is shown that our method is effective in correcting the drift.

One issue is the somewhat polarization dependent loss of the fibre coupler as the fibre used are standard telecommunication fibre which are birefringent in nature. Therefore, the polarization state of the returned pulse cannot be maintained indefinitely in a routine environment, causing the relative polarization between the signal and reference pulse to vary in time. The polarization effect is the drawback of this technique. This effect, which causes the amplitude ratio R to drift slightly in time, can be simulated by adjusting the polarization controller shown in Fig. 2.1. The data shown in Fig. 2.3 indicates a slightly varying amplitude ratio R due to the polarization effect. This effect, according to Eq. (2.1) given below, limits the index resolution to better than 2×10^{-5} in the present experiment.

The formula used in this experiment for calculating the concentration dependent refractive index change is given below. Taking the derivative of the Fresnel reflection formula for normal incidence (Born and Wolf, 1965) with respect to the refractive index of the solution, one obtains the change in the amplitude ratio δR due to a change in the refractive index δn of the solution.

$$\frac{\delta R(C)}{R(C)} = -\left(\frac{4n_f}{n_f^2 - n^2(C)} \right) \delta n(C) \tag{2.1}$$

where n_f is the refractive index of the fibre and $n(C)$ is the refractive index of the solution at a solute concentration of C. Writing $R(C) = R(0) + \delta R(0)$, and using Eq. (2.1) for $\delta R(0)$, one obtains,

$$1 - \frac{R(C)}{R(0)} = \left(\frac{4n_f}{n_f^2 - n^2(0)} \right) \frac{dn}{dC} \delta C \tag{2.2}$$

where $n(0)$ is the refractive index of pure water and $R(0)$ is the ratio at zero concentration. Eq. (2.2) is used for analyzing the data.

2.3 Results

Two separate sets of data were taken on different days. One set of data was taken for NaCl concentration ranging from 1×10^{-3} to 6×10^{-2} $g\text{cm}^{-3}$. The other set was taken for concentration varying from 2×10^{-4} to 1×10^{-3} $g\text{cm}^{-3}$. The data for the lower concentration set was taken within 5 min to minimize temperature and polarization effects, since the refractive index of water is a fairly strong function of temperature (Yunus, 1992). The higher concentration set was taken within 2.5h. Each set of data for $R(C)$ was normalized by $R(0)$ measured once at the beginning of each data set.

Errors due to temperature effects are calculated from the formula,

$$\frac{1}{R(C)} \frac{dR(C)}{dT} = \frac{4}{n_f^2 - n^2} \left(n \frac{dn_f}{dT} - n_f \frac{dn}{dT} \right) \tag{2.3}$$

obtained by taking the derivative of the Fresnel reflection formula (Born and Wolf, 1965) with respect to temperature, where n are evaluated at concentration C. For low

concentration, as is the case here, we merely use the temperature coefficient of pure water and approximate $\frac{1}{R(C)}\frac{dR(C)}{dT}$ by $\frac{d(R(C)/R(0))}{dT}$. For pure water, n = 1.33, $dn/dT = 9 \times 10^{-5}$ °C^{-1}, and for the fibre, n_f = 1.45, $dn_f/dT = 1 \times 10^{-5}$ °C^{-1}. From the temperature coefficients, the calculated error in the ratio $R(C)/R(0)$ is 1.4×10^{-3} per degree due mainly to the temperature coefficient of water. The corresponding error in determining the index change is about 8×10^{-5} per degree. However, within the 5 min measurement time the temperature is constant to about 0.1 °C, the resolution of the thermal couple used in the temperature measurement. Thus, the corresponding index resolution limited by temperature effects is about 8×10^{-6} for 0.1 °C stability.

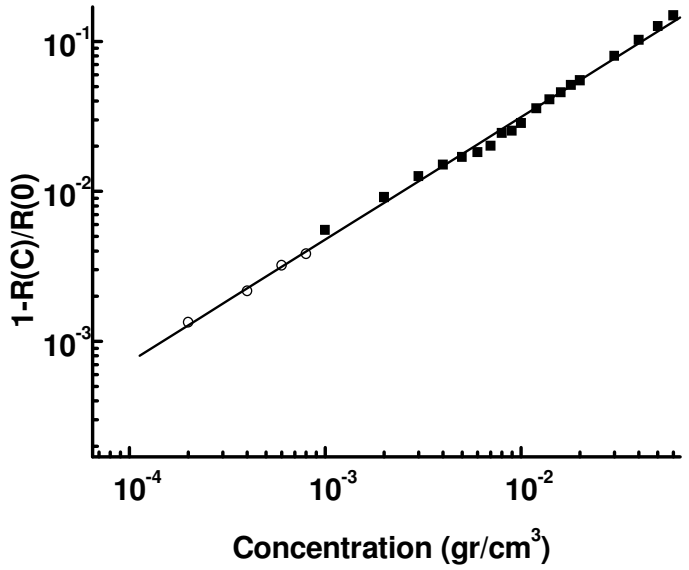

Fig. 2.4 A plot of {1 - $R(C)/R(0)$} versus concentration C on a log scale. The open circles are low concentration data taken on a different day.

The measured data are plotted in Fig. 2.4 as {1 - $R(C)/R(0)$} versus C in log scale to better shown the data at very low concentration and its connectivity to the higher concentration data. We use Eq. (2.2) to calculate dn/dC from the measured data. Using a value of n_f = 1.45 for the fibre and $n(0)$ = 1.33 for water, we found that dn/dC = 0.13 g^{-1} cm^3 in good agreement with a value of 0.12 g^{-1} cm^3 from Wilson and Reed (1993). From Fig. 2.4 it is observed that the resolution of the present technique is about 2 $\times$ 10^{-4} g cm^{-3} of the NaCl concentration. This corresponds to an index resolution of 2 $\times$ 10^{-5}. This resolution is about a factor of five better than the best bulk-optic technique (Krishna *et al*., 2000; Fan and Longtin, 2000).

2.4 Conclusion

We have introduced a new normalization technique that greatly enhances resolution of concentration and refractive index measurements when applied to conventional fibre optic reflectometry based on Fresnel reflection from the fibre tip. The technique was used for demonstrating measurement of NaCl concentration in water. The technique gives a refractive index measurement resolution of about 2 $\times$ 10^{-5} and salt concentration resolution of about 2 $\times$ 10^{-4} $g cm^{-3}$ limited by temperature and polarization effects. This ratio-meter should be appropriate for various measurements, in particular for measurements of the spatially and temporally dependent concentration field in an environment such as a water tank.

CHAPTER III

VELOCITY AND FRACTION RATIO MEASUREMENTS: FIBER OPTIC REFLECTOMETER FOR VELOCITY AND FRACTION RATIO MEASUREMENTS IN MULTIPHASE FLOWS*

A technique based on the coherent mixing of scattered signal with Fresnel reflection signal from the tip of an optical fiber is used to demonstrate the feasibility of measuring the velocity and fraction ratio of solid particles and gas bubbles or liquid droplets in a liquid or gas flow. If the liquid or gas flow is seeded with small neutrally buoyant particles, the technique is then capable of measuring the velocity as well as the fraction ratio of all three phases of the flow at a given point. The method is briefly described as follows. An optical signal derived from a diode laser driven by a constant current is launched into a single-mode optical fiber and transmitted, through a fiber coupler, to the signal fiber inserted into the test fluid. The diode laser used is a multilongitudinal mode device that has a low coherence length of about 200 μm. The coherently mixed signal propagates back to the signal fiber, through the fiber coupler, and detected by a detector. By analyzing the signal, the velocity and fraction ratio of each phase can be obtained. Using water seeded with small solid particles and air

*Reprinted with permission from "Fiber optic reflectometer for velocity and fraction ratio measurements in multiphase flows" by Chang, Lim, and Su (2003). *Review of Scientific Instruments*, DOI 10.1063/1.1578152, Copyright [2003] American Institute of Physics

bubbles, it is demonstrated that the technique is capable of measuring the velocity in the direction parallel to the fiber. Since the only intrusion to the fluid is the tiny fiber probe (a dimension of 125 μm in diameter), the disturbance to most fluid flows is negligible, therefore, the technique is nearly non-intrusive.

3.1 Introduction

The measurements of velocity, particle density (or particle number), and fraction ratio of all phases in a multiphase flow have been of great interest to engineers and scientists in the fluid mechanics and related community. In many fluid dynamics problems, not only is it important to obtain the velocity field of the flow, it is often essential to obtain the velocity and fraction ratio of one or more phases such as solid particles and gas bubbles in a liquid flow, or liquid droplets and solid particles in a gas flow. For example, the understanding of velocity and void fraction under breaking waves is important in the study of scalar mixing, air entrainment, energy dissipation, and sediment transport in the surf zone and ocean. Nevertheless, reports on the velocity and fraction ratio measurements of two or three phases have been rare. This is mainly due to the inability of measuring velocity and fraction ratio of one or more phases in the multiphase flow using existing techniques. Although some bulky devices were able to obtain velocity or void fraction information in liquid–gas flows (but rarely both) for one phase in the field, issues in data precision and uncertainty were frequently raised due to the deployment of the bulky invasive devices while careful data interpretation was often needed. The problem becomes especially severe in the laboratory because of its relatively small scale. It is common that many of the physical phenomena not only are

strongly temporal and spatial dependent but also require precise velocity and phase information with high temporal and spatial resolutions. To preserve the flow characteristics, a small probe with good resolution and accuracy is necessary to minimize the disturbance caused by the introduction of the probe while providing useful information of the flow.

Traditional nonintrusive optical methods for velocity determination, such as the particle image velocimetry (PIV) and the laser Doppler velocimetry (LDV) techniques, have had great difficulties when applied to the study of multiphase flows. Noise due to the scattering of light from air bubbles or attenuation of light in solid particles, especially when the concentration is high, often gives questionable or invalid data. This can be seen from the seven papers published in the multiphase flow section in the 1999 International PIV Workshop (Adrian *et al*., 1999), and the velocity measurements under breaking waves (e.g., Chang and Liu, 1999; Chang and Liu, 2000). Other traditional intrusive techniques such as acoustic Doppler velocimetry and thermal anemometers are capable of measuring the velocity of only one phase and may significantly disturb the flow resulting in frequent unreliable noisy data, especially on the laboratory scale.

Intrusive probes using conductivity have been successfully applied for measuring the void fraction of gas–liquid flows (e.g., Chanson, 1996), and by using multiple probes with cross correlation of the signals, the velocity of the gas bubbles (but not the liquid). More recently, intrusive miniaturized probes using optical fibers have been employed in the measurement of local void fraction using refractive index change at the tip of the fibers. Similar to the conductivity probes, if multiple fibers with a small distance

between the fibers are used, the velocity can be obtained through cross correlation of the bubble signal. With the velocity information, the bubble chord length can subsequently be obtained. If the bubbles are small so their shape is either spherical or ellipsoidal (typically less than 9 mm in diameter), the mean bubble diameter and interfacial area can be calculated through the bubble size probability density function. Less disturbance is caused by the optical fiber due to its small dimensions [125 μm in diameter, compared with the conductivity probes of O(1 mm) or larger]. Reports in various applications using optical fiber probes in gas–liquid flows can be found in Rinne and Loth (1996), Barrau *et al*. (1999), Kiambi *et al*. (2001), and Rensen and Roig (2001), while reports on gas–solid flows can be found in Cavalier *et al*. (1989) and Herbert *et al*. (1994) Other techniques using acoustics for bubble sizing and velocity measurements (e.g., Vagle and Farmer, 1998) in general, require relatively large dimensions for the instrument and create greater disturbance. They may be suitable for *in situ* or large-scale laboratory experiments but are outside the scope of this study and will not be discussed here.

It should be pointed out that some intrusive phase detection probes, based on refractive index or electrical conductivity changes, have been used in gas bubble velocity and void fraction measurements with certain degrees of success. However, hurdles remain in the interpretation of the data and in the measurements of the solid particles and liquid velocities (Chanson, 2002). Disturbance caused by methods employing larger dimension probes is also a big concern to the accuracy of the experimental data. At least for now, it seems that the miniaturized optic fiber probe is in a better position due to its small dimensions and relatively low cost. Overall, measurements of all three phases (gas,

solid, and liquid) in multiphase flows are still rare, no matter what techniques have been chosen.

In this article, a technique based on signal mixing of scattered light from air bubbles or solid particles and reference light from Fresnel reflection off the fiber end face is employed. This technique, using multimode fiber, is first reported by Dyott (1978) for studying Brownian motion, and subsequently for LDV by Nishihara *et al.* (1984) using single-mode fiber. Similar techniques but with variable reference signal strength obtained from wavelength-dependent reflection off fiber Bragg grating have been reported by Byrne *et al*. (2001) Low-coherence techniques for Doppler velocimetry using either multimode laser diodes (Meggitt *et al*., 1990) or light-emitting diodes (Ning *et al*., 1992) have also been reported.

The fiber technique provides simplicity, near noninvasiveness because of its small dimension of the optical fiber (typical diameter approximately 125 μm with protective buffer coating removed), high spatial resolution (typically less than 10 μm), and high temporal resolution (typically less than 50 μs). The technique is capable of measuring the velocities and fraction ratio of seeded particles and gas bubbles in a liquid flow, and the velocity and fraction ratio of liquid droplets and solid particles in a gas flow. To prove the technique, a constant head free liquid jet is used to validate the velocity measurement while a liquid column filled with bubbles is used to validate the void fraction measurement.

3.2 Principle and Experimental Apparatus

For the fraction ratio study, measured quantities are the reflected optical power due

to Fresnel reflections off the fiber-fluid interface at the fiber tip. For the velocity measurement, the measured quantity is the coherent beat-signal between the Fresnel reflection off the fiber-fluid interface and the scattered signal off the gas bubbles, solid particles, or liquid droplets.

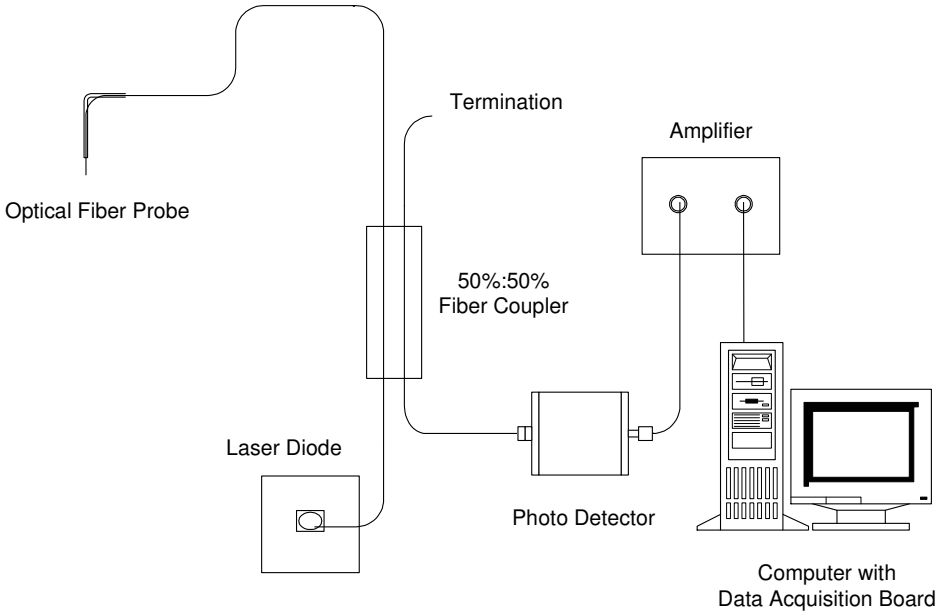

Fig. 3.1 The experimental apparatus.

The experimental setup is shown in Fig. 3.1. The source laser is a 1.3 μm wavelength multilongitudinal mode diode laser with short coherence length. This wavelength is used because components such as couplers and fibers are cost effective, readily available, and single mode at this wavelength, although 1.5 μm wavelength diode laser could also be used. Continuous-wave optical signal from the diode laser is launched into a standard telecommunications graded single-mode optical fiber (SMF-28 fiber). The fiber core diameter is about 8 μm and the overall fiber diameter with the

protective coating removed is 125 μm. Although the robustness of the fiber tip is compromised because the buffer coating is removed at the tip, it does not hinder the experiment since the fiber tip is simply dipped in the fluid with no additional lensing components. The light diverges from the fiber end. For the void fraction measurement, signal counts occur only when an air bubble comes in contact with the fiber tip, while for the velocity measurement, it is the period of oscillation that is of interest. In both cases, the signal magnitude is immaterial as long as the signal is observable. Therefore, the diverging light is tolerable. In this light, it is noted that whether the source has a long or short coherence length is also immaterial. However, the size of the particles is not measurable by this technique but we can measure the number of particles. The optical waves are divided into two paths by a 2 × 2 single-mode fused fiber coupler with a nominal 50%:50% splitting ratio. The *signal* fiber end face is cleaved at normal angle while the end of the other fiber is slanted and rests free in air with essentially zero reflection from the fiber–air interface. The returned signal from the signal fiber is detected by a dc-coupled detector. The signal is subsequently acquired by a data acquisition board and processed by a computer. Assuming no energy losses, the formula for Fresnel reflectivity can be written as

$$p = p_0 \alpha_1 \alpha_2 \left(\frac{n - n_f}{n + n_f} \right)^2 \tag{3.1}$$

where p is the detected power (signal), p_0 is the laser power ($p_0 \approx 1$ mW), α is the splitting ratio of the fiber coupler ($\alpha = 0.5$), n is the refractive index of the tested fluid, and n_f is the refractive index of the fiber ($n_f = 1.44$). In a water flow with air bubbles,

the refractive index n =1.0 for air and n = 1.33 for water. According to Eq. (3.1) and using parameters given herein, the power change when the fiber tip encountered an air bubble is about 7.6 μW, which is easily measurable (a few volts: see Fig. 3.3). For a 15 μm size solid particle, the signal level is experimentally determined to be about 0.15 V (see Fig. 3.6).

Although the determination of phases is obvious using Eq. (3.1), the determination of velocity is not. Most existing studies used multiple fibers and cross-correlation to obtain velocity information in the flow of gas bubbles in a liquid or solid particles in a liquid or gas. One exception is in Cartellier (1992), who employed a single fiber to measure the velocity of gas bubbles by examining the signal rising time (phase change from liquid to gas) and subsequently complicated signal processing. This is because the duration required for the optical signal to rise is a function of several interfacial parameters, including the bubble velocity and curvature. Although in Cartellier's work (Cartellier, 1992), the result in the bubble size measurement is very good (error is about 2%), the error in the bubble velocity measurement is quite big (about 20%). As stated in Cartellier's paper (Cartellier, 1992), an interesting but not understood phenomenon occurred in all the measurements. Namely, a low amplitude peak just prior to the strong rise in the optical signal always appears. In this article, we show that, by sampling at high frequency, this initial low amplitude peak actually consists of a train of oscillatory waves. We assume that the waves are caused by the coherent beat between the Fresnel reflection off the fiber–liquid interface and the scattered signal off the gas bubble or the solid particle. We used this new information to determine the velocity of bubbles and

solid particles in a liquid flow. We also assume that a similar wave train occurs in the gas flow seeded with liquid droplets and solid particles. The oscillation wave train is indeed equivalent to the Doppler fringes in LDV. Note that only the velocity component parallel to the fiber axis is measured. Multiple fiber probes are needed if other velocity components are to be measured.

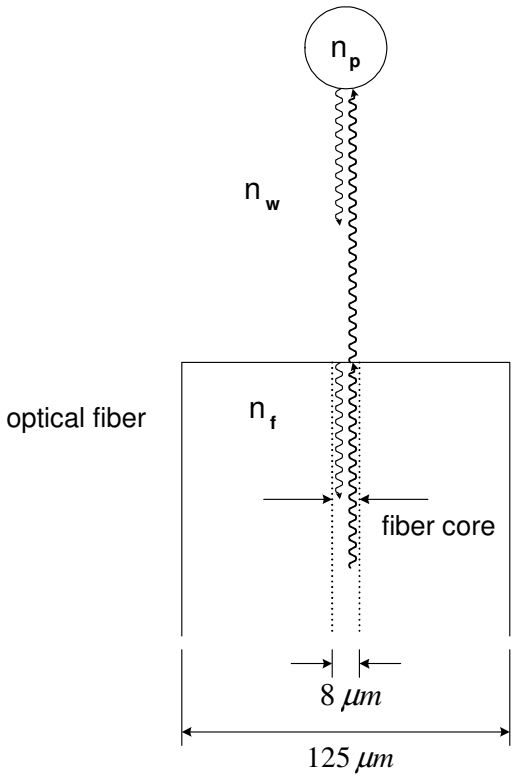

Fig. 3.2 Sketch of a particle in front of the fiber tip.

Fig. 3.2 clarifies the following discussion. The multi-longitudinal mode diode laser used in this experiment has a coherence length of about 200 μm. Objects (e.g., solid particles in a liquid or gas flow, gas bubbles in a liquid flow, or liquid droplets in a gas flow) within such a distance in front of the flat-cut fiber tip scatter the light back to the

fiber and coherently beat with the optical signal reflected off the fiber-fluid interface. Outside the coherence length the oscillation amplitude is reduced. As the object moves, a time-dependent interference wave will be observed. The period of the oscillatory waves gives the velocity of the object in the direction normal to the fiber end face (or parallel to the fiber). According to the Fresnel formula, the electric field reflectivity is given by $(n_2-n_1)/(n_2+n_1)$ for light propagating in a medium with an index n_1 into a medium with an index n_2. If $n_1 > n_2$, the field reflectivity is negative representing a π phase shift of the reflected field. If $n_1 < n_2$, the phase shift is zero. Thus, the reflected field E_a at the fiber-fluid interface and the scattered field E_b from the fluid-object interface can be expressed as

$$E_a = b_a e^{i\phi_a} \quad , \quad E_b = b_b e^{i(\phi_b+\psi)} \tag{3.2}$$

where b_a and b_b describe the amount of light coupled back into the fiber from the two interfaces, and ϕ_a or ϕ_b is either zero or π. ψ describes the round-trip phase shift of the field propagating between the fiber-fluid interface and the fluid-object interface, and is given by

$$\psi = \frac{4\pi}{\lambda} n_w \Delta d \tag{3.3}$$

where λ is the laser wavelength, n_w is the refractive index of the fluid, and Δd is the wavelength of the oscillatory returned signal. The total returned power P due to E_a and E_b is $P = |E_a+E_b|^2$. From Eq. (3.2), P can be expressed as,

$$P = b_a^2 + b_b^2 + 2b_a b_b \cos(\delta + \psi) \tag{3.4}$$

where the last term is the coherent-beating term which produces the oscillatory waves. δ

is zero if the two interfaces produce the same phase shift, and π if the phase shift is opposite. The period of the oscillation is derived by the condition $\psi = 2\pi$. From Eq. (3.3), the distance Δd that the object has to travel for one complete oscillation cycle is

$$\Delta d = \frac{\lambda}{2n_w} \tag{3.5}$$

By measuring the period of the oscillation, T, the velocity of the object can be calculated from

$$u = \frac{\Delta d}{T} \tag{3.6}$$

where u is the velocity of the object in the direction parallel to the fiber. Note that Eq. (3.6) does not provide the information on whether the object is approaching or moving away from the fiber tip. This means that there exists a directional ambiguity. Therefore this technique can only be used in unidirectional flows unless applying cross-correlation with signals taken from multiple fibers (e.g., Cavalier *et al.* 1989, Rinne and Loth 1996, Barrau *et al.* 1999, Rensen and Roig 2001, Kiambi *et al.* 2001) is used to resolve the flow direction. Moreover, Eq. (3.6) only provides velocity information in one direction (parallel to the fiber). Additional fiber probes may be needed if more than one velocity component is to be obtained.

Although the fiber probe has a very small dimension, errors could still be significant unless cares are taken. Possible errors come mainly from two sources: the presence of the fiber tends to slow down the flow in the vicinity of the fiber, and small particles passing the fiber tip at an angle to the fiber orientation. Both errors will be demonstrated and minimized with a remedy strategy. Signal processing and results will be given in the next section.

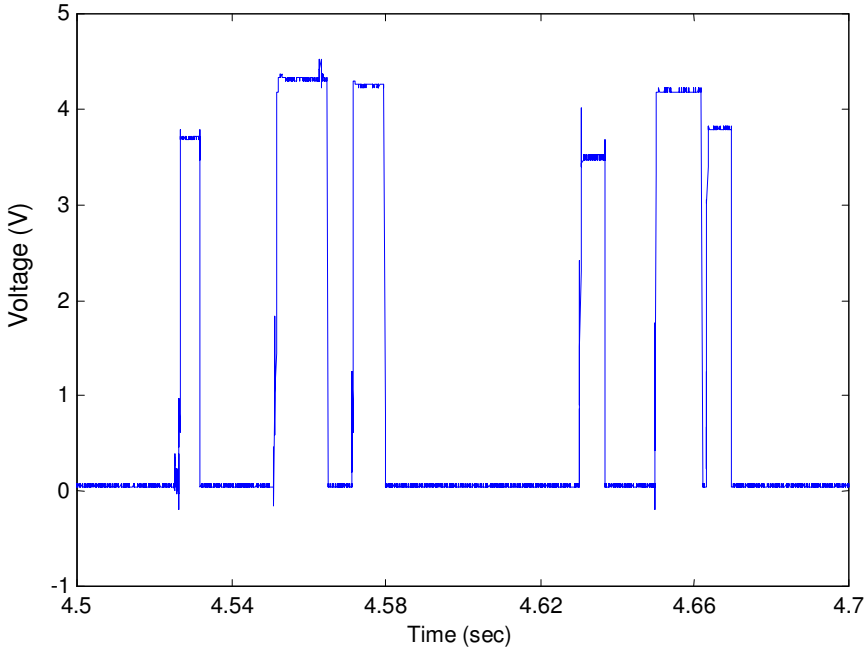

(a)

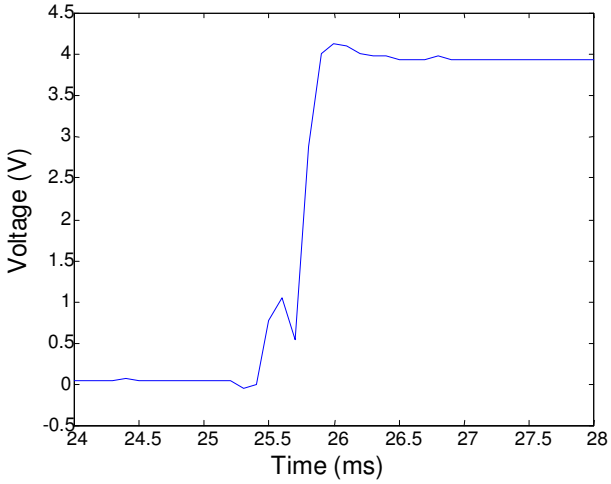

(b)

Fig. 3.3 Low sampling rate (10 *k*Hz) of a bubble signal: (a) raw signal and (b) detail of rising front.

A proof of concept experiment is first conducted using a flow with water and air bubbles. Fig. 3.3(a) shows a portion of the typical raw signal with a sampling rate of 10 kHz, while Fig. 3.3(b) shows the detail of the signal at the rising front. A low amplitude signal in front of the rising front similar to that reported in Cartellier (1992) is clearly seen in Fig. 3.3(b).

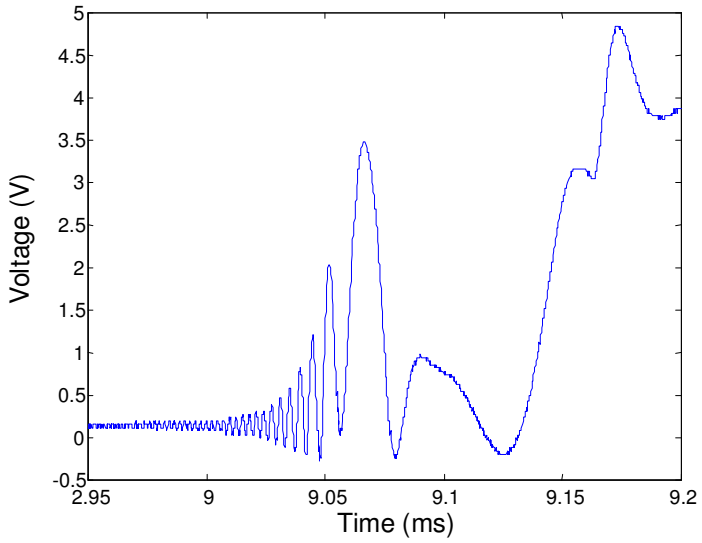

Fig. 3.4 High sampling rate (10 MHz) of the rising front of a bubble signal.

Fig. 3.4 shows the rising front of a similar case with the signal taken at a much higher sampling rate of 10 MHz. The oscillatory fluctuations are clearly evident. The feature of the low amplitude hump in Fig. 3.3(b) is indeed the envelope of the high-frequency waves, as described in Eq. (3.4) and shown in Fig. 3.4. This phenomenon also appears when a solid particle is encountered (Fig. 3.6). This demonstrates the assumption that the waves are caused by the coherent beat between the Fresnel reflection

off the fiber-liquid interface and the scattered signal off the gas bubble or the solid particle may be correct. Therefore, the velocity in the direction parallel to the fiber axis of the object could be calculated using Eq. (3.6). Once the oscillating period T in Eq. (3.6) is obtained, velocity can be easily computed, provided the wavelength of the light source (λ) and the refractive index of the fluid (n_w) are known [so that Δd can be obtained using Eq. (3.5). To find T the power spectral of the oscillating signal is first computed to locate the peak frequency. Curve fitting using a four-point cubic-spline method in the vicinity of the peak frequency is subsequently applied to interpolate the peak of the spectral for better accuracy.

Two sets of experiments are conducted to validate the technique for velocity and fraction ratio measurements. The first set of experiment is to measure the solid particle velocity and the second set of experiment is to measure the bubble void fraction.

3.3 Validation of Velocity Measurement

A free water jet seeded with spherical polystyrene particles (mean diameter 15 μm) coming out from a constant head reservoir into air is used to validate the velocity measurement. The particles are neutrally buoyant and very small, indicating that the measured particle velocity is indeed the fluid velocity. The inner diameter of the jet orifice is 4.5 mm with its flow rate regulated by a valve. The jet mean velocity is calculated through weighting the outflow. The optical fiber sensor is located right at the jet exit and is set at four different angles (parallel, normal, 35° and 60°) to the jet direction (horizontal) to test the feasibility of the technique. Fig. 3.5 sketches the setup of the jet and the optical fiber. The jet velocity is varied from 0.63 m/s to 0.78 m/s (the

nozzle based jet Reynolds number is between 2,800 and 3,500). The experiments were run multiple times for each combination of jet velocity and fiber angle with data taken near the center of the jet. Using Eq. (3.6) the velocity component in the direction parallel to the optical fiber is calculated.

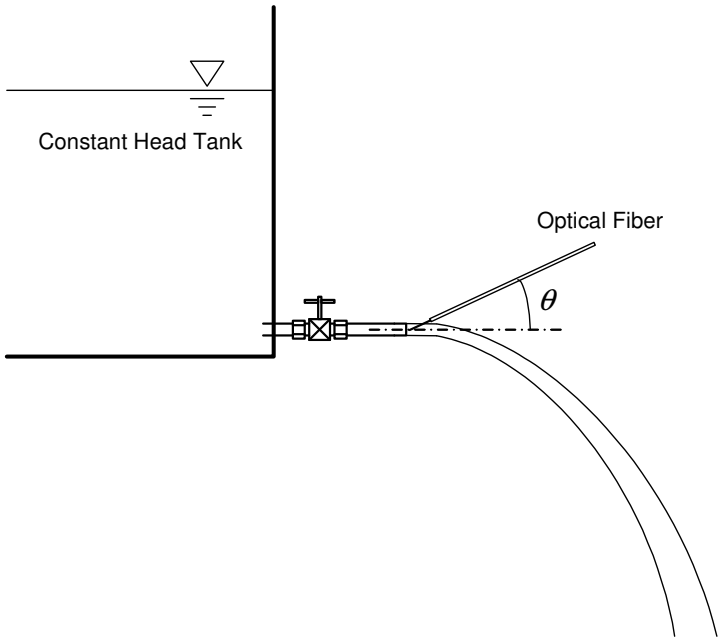

Fig. 3.5 Sketch of the setup and velocity measurement of the free jet.

Fig. 3.6(a) shows a typical signal of the particle-seeded flow sampled at 10 MHz. The experimental condition in Fig. 3.6 is that the jet velocity is 0.78 m/s while the fiber probe is parallel to the flow. The data, if expanded, indicate that the period of the waves becomes longer at the end of the signal, compared to that at the beginning of the signal, suggesting a decrease in velocity when the particle approaches the fiber. This is consistent with the fact that the velocity of the particle must decrease and inevitably

changes its direction slightly due to the presence of the fiber and the stagnation point at the fiber tip. This means that one could underestimate the particle (and thus the fluid) velocity when the particle is too close to the fiber.

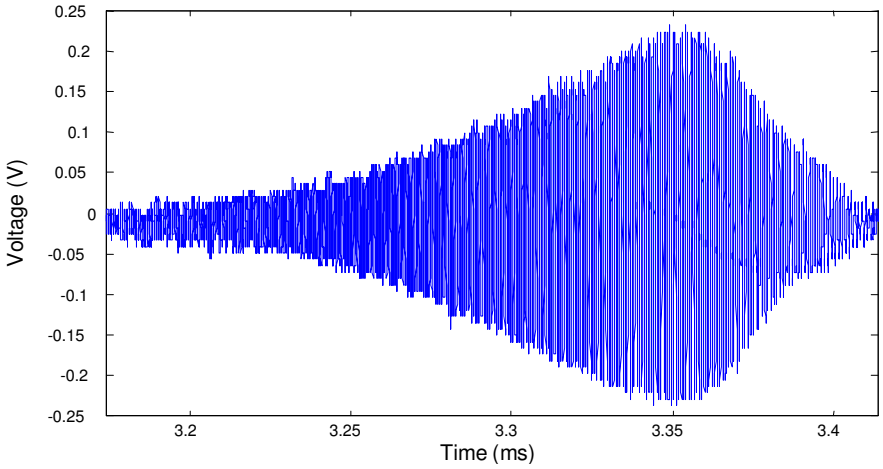

(a)

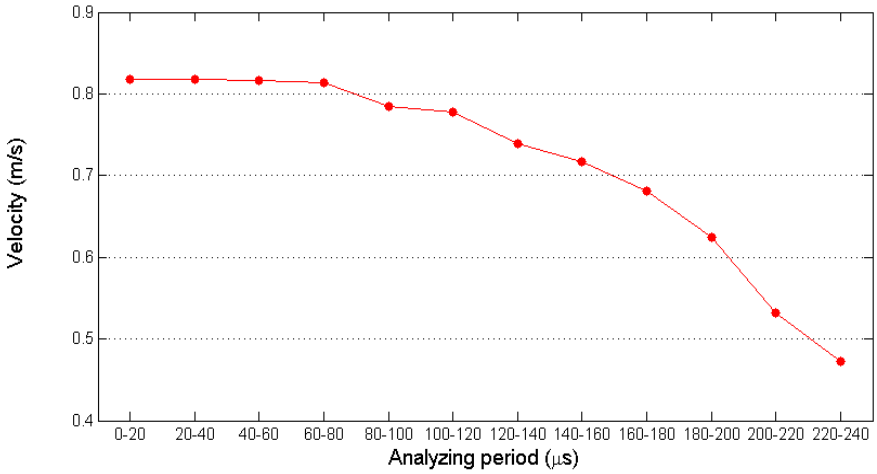

(b)

Fig. 3.6 (a) Signal of a particle. (b) Corresponding velocity calculated using every 20 μs of the signal.

Fig. 3.6(b) shows the measured velocity calculated from each 20 ms interval of the signal in Fig. 3.6(a), indicating the decrease of the particle velocity when it is close to the fiber tip. Therefore, the later part of the oscillatory signal is not as useful due to the interference of the fiber. Roughly speaking, using the first one-quarter of the signal proves to be reliable for the present tests. For other flow conditions, the same analysis can be performed to identify the useful portion of the signal. It is noted that the total time span in Figs. 3.6(a) and 3.6(b) is 240 μs. Within this time span, the total number of oscillations is 360 which corresponds to a span length of 175 μm, according to Eq. (3.5). Thus, Fig. 3.6(b) indicates that, for a distance of about 125 μm away from the fiber tip, the velocity is not affected by the presence of the fiber. Note that 125 μm is equal to the fiber diameter and within the coherent length of the laser employed. The length between 125 μm and 175 μm from the fiber end face, which is 50 μm, multiplied by the beam diameter of about 30 μm (corresponding to a beam divergent angle of 11°) can be considered as the maximum measurement volume of the technique, as not all scattered light from within this volume couples back into the fiber.

The measured velocity using the optical fiber technique is compared with the *mean* velocity measured by the weight of the water coming out of the nozzle. The comparison is shown in Fig. 3.7. Very good agreement is obtained. Note that the velocity in Fig. 3.7 only represents the velocity component parallel to the fiber probe, not the jet speed. The consistently slightly higher velocity using the fiber technique could be due to the fact that the velocity at the center of the jet is slightly higher than the mean velocity. It should be pointed out that when $\theta = 90°$ (fiber orientation is normal to the flow), the

measured velocity is nonzero. This is an intrinsic nature of the technique - the distance between the particle surface and the fiber tip varies as the particle passing the fiber even if at the normal angle. The approximately 0.02 m/s (about 3% of the mean jet speed) measured velocity can be treated as an inherent error of the technique. The technique has a very high repeatability in velocity measurement - the standard deviation of the repeated measurements is between 0.01 m/s and 0.02 m/s which is relative small (less then 2%) compared with the measured mean velocity. From the comparison, it is evident that the proposed technique is capable of measuring velocity with a reasonable high accuracy.

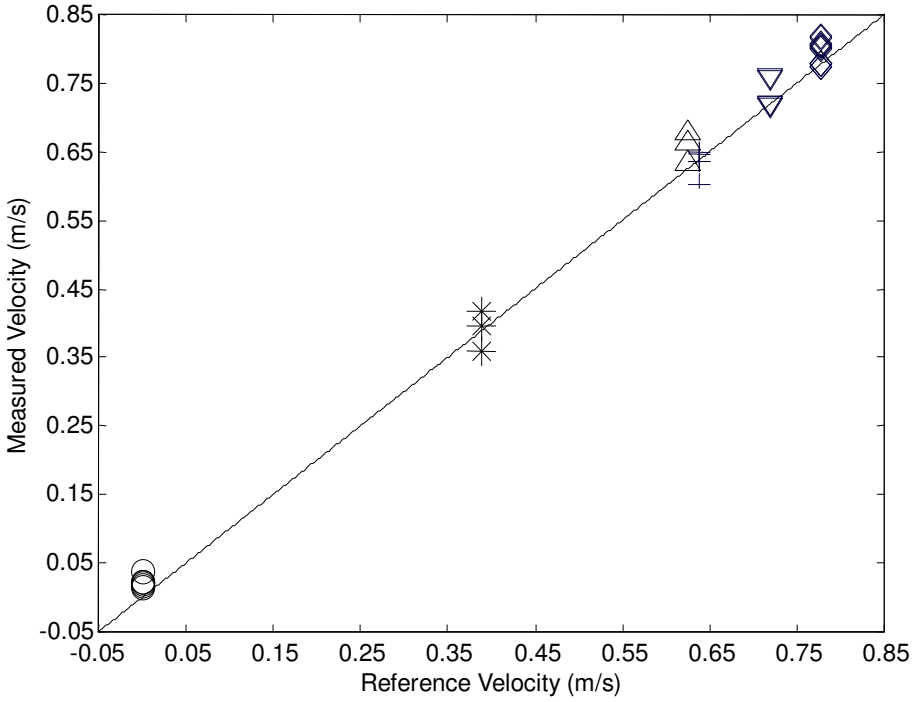

Fig. 3.7 Comparison of particle velocity measurements. O, θ = 90 degree; *, θ = 60 degree; +, θ = 35 degree; Δ, θ = 0 degree, u = 0.63 m/s; ∇, θ = 0 degree, u = 0.72 m/s; ◊, θ = 0 degree, u = 0.78 m/s. Note that the jet exit velocity u = 0.78 m/s in all the cases except in the θ = 0 degree cases.

3.4 Validation of Fraction Ratio Measurement

Due to the change in refractive index, the phase of the flow at the measurement point (the fiber tip) can be easily identified, allowing the measurement of the fraction ratio of each phase. To validate the technique, a bubbling water column is used. Fig. 3.8 sketches the setup of the experiment. A transparent long vertical pipe with an inner diameter of 4.15 cm and a height of 117 cm filled with water was used to observe the change of the free surface elevation with and without air bubbles. A bubble generator with a valve to control the bubble rate is used to generate air bubbles. The generated bubbles come out from a porous air stone located near the bottom of the pipe. The height h is the original water level, measured from the air stone, before the bubble generator is turned on, while the height h_b is the increased water level after the bubble generator is turned on. The fiber optic probe is inserted vertically downward as depicted in Fig. 3.8.

Three sets of void fraction tests with different combinations of h and h_b are conducted: (h, h_b) = (0.934, 0.143) m, (h, h_b) = (0.980, 0.101) m, and (h, h_b) = (1.029, 0.055) m. The measurement duration is kept constant at 52 s with a fixed sampling rate of 20 kHz for each test. The fiber optic probe is located at 8 cm below the mean free surface (after the bubble generator is turned on) in all the cases. Note that the observed *global* void fraction is calculated using $h_b/(h+h_b)$, which is different from the void fraction at the measurement point (hereafter called the *local* void fraction) of the optical fiber due to the compressibility of the air. The ideal gas law with the assumption of hydrostatic pressure is applied to backcalculate the local void fraction at the measurement point from the global void fraction for comparison with the measurements.

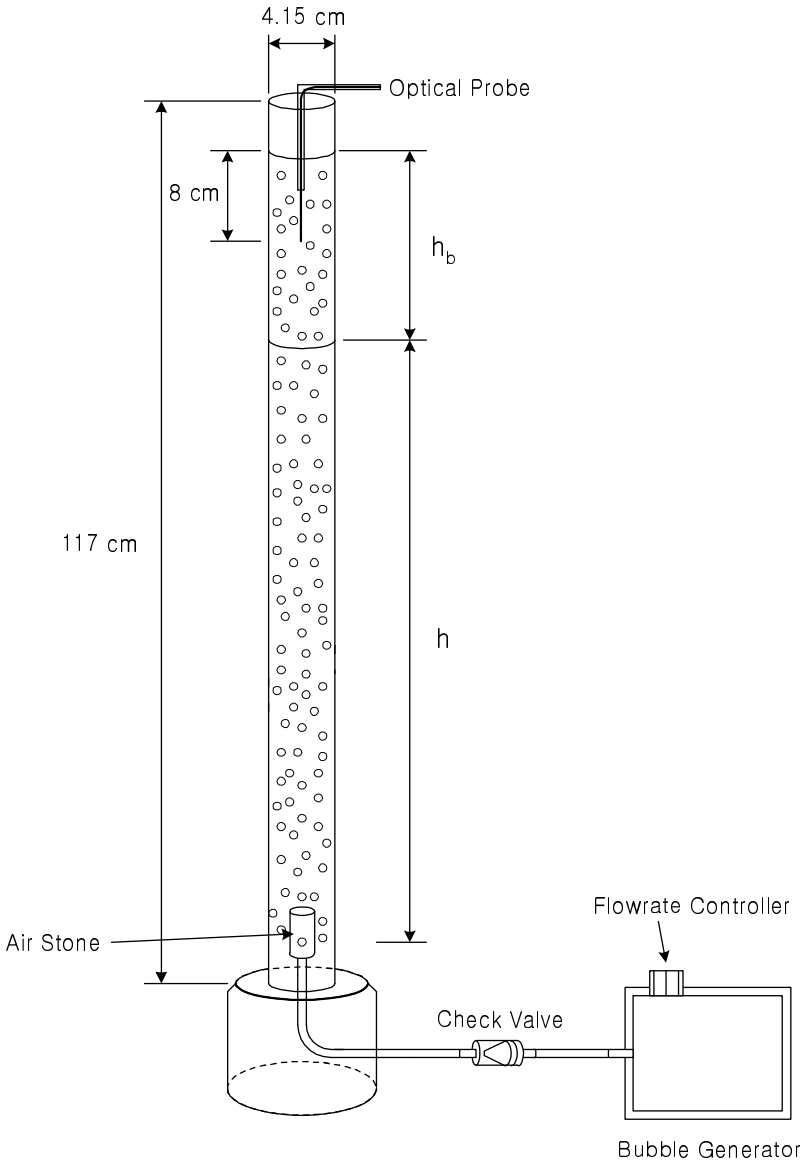

Fig. 3.8 Experimental setup for the void ratio measurement.

Fig. 3.9 shows the global void fraction, the local void fraction converted from the observed global void fraction using ideal gas law, and the measured void fraction using optical fiber for the case of (h, h_b) = (0.934, 0.143) m. Although the six data points taken

by the optical fiber are very consistent, their values are all lower by approximately 1% from the *true* local void fraction. This is due to the fact that the fiber end face needs a short period of time to dry out when it encounters an air bubble (water tends to collect at the fiber surface rather than at the end face due to surface tension). This duration is estimated to be 0.71 ms, calculated by shifting the optical fiber measurement up (about 1%) to match the local void fraction with the known number of bubbles (mean is 760) and mean velocity of bubbles (0.170 m/s) measured using the present technique. In other word the measured void fraction using optical fiber needs to be corrected by adding the short duration for each bubble encounter.

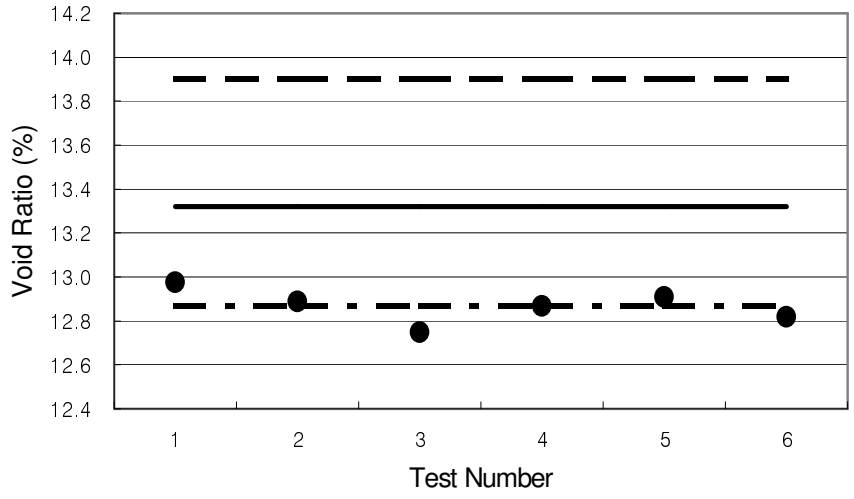

Fig. 3.9 Correction of the void fraction measurements for the case of (h, h_b) = (0.934, 0.143) m. ——, observed global void ratio; – –, local void ratio at the measurement point using the ideal gas law from the global void ratio; •, measured void ratio using optical fiber without correction; – · –, mean measured void ratio without correction.

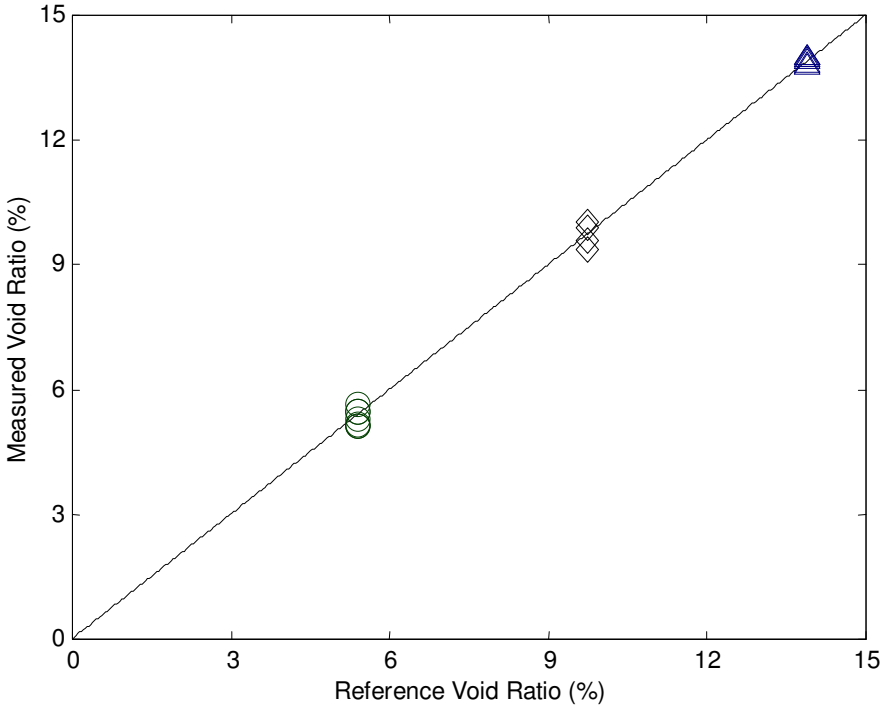

Fig. 3.10 Comparison of void fraction measurements. O, (h, h_b) = (0.934, 0.143) m; ◊, (h, h_b) = (0.980, 0.101) m; Δ, (h, h_b) = (1.029, 0.055) m.

With the correction, Fig. 3.10 shows the comparison of the local void fraction measurements from the three sets of experiments (a total of 17 tests). Very good agreement is obtained. The root-mean-square error in the void fraction measurement is 0.19%. From the comparison, it is evident that the present technique is capable of measuring the void fraction with a high accuracy. Since the technique is also capable of measuring the bubble velocity, the distribution of the bubble chord length can also be obtained through the measured duration of each void (bubble encounter) with its corresponding velocity. The measured distribution of bubble chord length for the case of (h, h_b) = (0.934,0.143) m is demonstrated in Fig. 3.11. The technique has indeed been

tested using a liquid flow seeded with air bubbles and solid particles. As expected, the technique is able to measure both the bubble and particle velocities. The resulting signal is basically the mix of those in Figs. 3.3(a) and 3.6(a). A preliminary experiment on liquid spray into the air was also attempted. The oscillation is not completely resolvable because the speed of the available data acquisition board is insufficient to resolve the high spray velocity. Since the real velocities of these tests are not available, they are not presented in the validation sections.

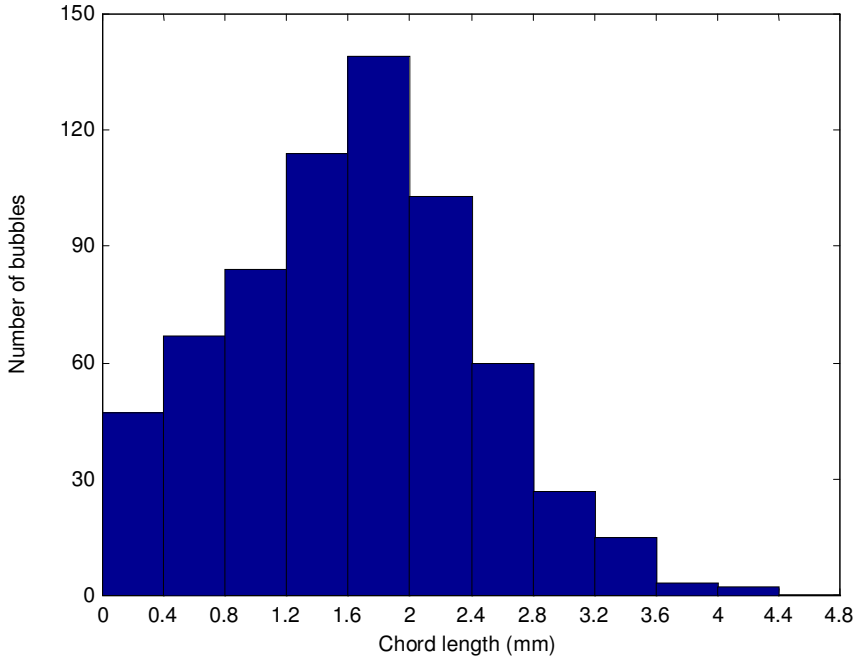

Fig. 3.11 Measured distribution of the bubble chord length for the case of (h, h_b) = (0.934, 0.143) m.

3.5 Conclusion

In conclusion, the technique for the measurements of the fluid velocity of a liquid–solid flow and the void fraction of a liquid–gas flow is present and validated. Based on the coherent beat signal between the Fresnel reflection off the fiber–liquid interface and the scattered signal off the object (gas bubble or solid particle), the technique is capable of measuring the velocity of the object in the direction parallel to the fiber with a high accuracy. In addition, based on the change in refractive index from the fiber–fluid interface, the phase of the fluid at the measurement point can be easily distinguished, allowing the measurement of the fraction ratio of each phase, including the number of solid particles and the void fraction of gas.

CHAPTER IV

BUBBLE SIZE MEASUREMENTS: BUBBLE VELOCITY, DIAMETER, AND VOID FRACTION MEASUREMENTS IN A MULTIPHASE FLOW USING FIBER OPTIC REFLECTOMETER*

A fiber optic reflectometer (FOR) technique featuring a single fiber probe is investigated for its feasibility of measuring the bubble velocity, diameter, and void fraction in a multiphase flow. The method is based on the interference of the scattered signal from the bubble surface with the Fresnel reflection signal from the tip of the optical fiber. Void fraction is obtained with a high accuracy if an appropriate correction is applied to compensate the underestimated measurement value. Velocity information is accurately obtained from the reflected signals before the fiber tip touches the bubble surface so that several factors affecting the traditional dual-tip probes such as blinding, crawling, and drifting effects due to the interaction between the probe and bubbles can be prevented. The coherent signals reflected from both the front and rear ends of a bubble can provide velocity information. Deceleration of rising bubbles and particles due to the presence of the fiber probe are observed when they are very close to the fiber

*Reprinted with permission from "Bubble velocity, diameter, and void fraction measurements in a multiphase flow using fiber optic reflecometer" by Lim, Chang, Su and Chen (2008). *Review of Scientific Instruments*, DOI 10.1063/1.3053271, Copyright [2008] American Institute of Physics

tip. With the residence time obtained, the bubble chord length can be determined by analyzing the coherent signal for velocity determination before the deceleration starts. The bubble diameters are directly obtained from analyzing the signals of the bubbles that contain velocity information. The chord lengths of these bubbles measured by FOR represent the bubble diameters when the bubble shape is spherical, or represent the minor axes when the bubble shape is ellipsoidal. The velocity and size of bubbles obtained from the FOR measurements are compared with those obtained simultaneously using a high speed camera.

4.1 Introduction

Bubble characteristics such as the velocity, size, and void fraction in multiphase flows have been of great interest to many researchers for several decades. Most studies have been conducted using laboratory experiments with various optical techniques. Traditional nonintrusive techniques such as laser Doppler velocimetry and particle image velocimetry (PIV) have been successfully used to measure the liquid velocity in gas-liquid flows by tracking or correlating tiny seeding solid particles. However, measurements become questionable or invalid due to noise caused by the scattering of light from gas bubbles or attenuation of light by solid particles when applied to multiphase flows. Certain success has been achieved by using PIV and its derivatives with advanced approaches such as using multiple cameras and various image processing methods to obtain velocity of each phase (e.g., Lindken *et al*., 1999; Deen *et al*., 2002; Seol *et al*., 2007; Ryu *et al*., 2005; Bröder and Sommerfeld, 2007; Kashima *et al*., 2006). However, hurdles remain due to the presence of the dispersed phase especially with a

high concentration of bubbles, while in most cases only velocities of a single phase were measured.

As for intrusive probes, conductivity probes (e.g., Chanson, 1996; Chanson & Brattberg, 2000; Chanson, 2002) and fiber optic probes have been successfully applied to multiphase flows. Various intrusive fiber optic probes with a single tip, double tips, or quadruple tips have commonly been used for the measurements of multiphase flows due to its simplicity, high temporal resolution, and high spatial resolution compared with some conductivity probes. Diverse applications using single or double fiber optic probes in liquid-gas flows can be found in Cartellier (1992), Rinne and Loth (1996), Barrau *et al*. (1999), Murzyn *et al*. (2005), Rensen and Roig (2001), Kiambi *et al*. (2001), and Rojas and Loewen (2007). In addition, applications in gas-solid flows can be found in Cavalier *et al*. (1989) and Hervert *et al*. (1994). A four-point fiber optic probe was also used to measure the bubble size and velocity by Guet *et al*. (2003) and Luther *et al*. (2004). In most fiber optic techniques, the local void fraction is obtained by a single fiber probe, the first probe in a dual tip probe, or the central tip in the four-point probe that uses the reflected power change due to the refractive index change at the fiber tip. Similar to the conductivity probes, dual fiber probes feature a small distance between the fiber tips that are employed to obtain the velocity information through cross correlating the bubble signals. It has also been reported that bubble velocities can be obtained using a single fiber probe by analyzing the latency length (e.g., Cartellier, 1992; Barrau *et al*., 1999; Cartellier and Barrau, 1998; and Juliá *et al*., 2005). Moreover, bubble velocities can also be obtained by analyzing the coherently mixed signals from light scattered off

the bubble surface and Fresnel reflection from the tip of the single fiber in the fiber optic reflectometer (FOR) system, as introduced by Chang *et al.* (2003, 2004). The FOR technique is capable of measuring the velocities and fraction ratio of liquid (by measuring the tiny seeded particles) and gas bubbles in a gas-liquid flow. It is also capable of measuring the velocities and concentration of liquid droplets or solid particles in a gas-liquid or a gas-solid flow. The drawback is that a very high sampling rate is needed if a high velocity is to be measured (Chang *et al*., 2004). A similar measurement technique using the same principle as the FOR technique can be found in Wedin *et al*., (2003). They obtained velocities of micro-bubbles that behave similar to solid spheres seeded in water. The electrochemically generated micro bubbles have a diameter that is small enough to prevent them from being pierced through by the optical fiber probe. The present study mainly focusing on large bubbles may be considered as a complementary work of Wedin *et al.* (2003).

Information of the bubble size and its distribution is important in the study of gas-liquid flows. The bubble size, aspect ratio, and origin as well as bubble and liquid velocity fields have been obtained using various imaging techniques such as backlighting (e.g., Rye *et al*., 2005) and advanced PIV (e.g., Lindken *et al*., 1999; Deen *et al*., 2002; Seol *et al*., 2007) with appropriate post processing methods applied to the acquired images. Kawaguchi *et al*. (2002) used an interferometric laser imaging for droplet sizing (ILIDS) technique to measure the size of droplets and bubbles. The ILIDS technique measures the diameter of spherical transparent particles or spherical bubbles by examining the fringe pattern generated by the reflected laser light and the scattered

laser light from the objects. One or two laser light sheets and a charge coupled device (CCD) camera are required with predetermined angles for an accurate measurement. Unlike the ILIDS technique that uses the interference image in the non focal plane, Dehaeck *et al*. (2005) employed a glare point velocimetry and sizing (GPVS) technique which uses two glare points of reflected laser light and refracted laser light in the focal plane to obtain the size of spherical bubbles. The ILIDS and GPVS techniques provide accurate size measurements of droplets or bubbles. However, the experimental setup and analysis algorism are rather complicated, such as deciding the angles of laser light sheets and the camera, and the objects must be spherical.

Although using imaging methods seems to be easier and more accurate in bubble size measurements in comparison to the use of optical fiber probes (such as those mentioned above), imaging methods are restricted to the multiphase flows with a relatively low void fraction. Also there must be no obstructions between the target bubbles and the cameras if imaging methods are to be used. Employment of intrusive optical fiber or conductivity probes is necessary to obtain bubble size, velocity, and void fraction in the flows with a high void fraction such as breaking waves (e.g., Ryu *et al*., 2005; Rensen and Roig, 2001) and hydraulic jumps (e.g., Chanson and Brattberg, 2000; Murzyn *et al*., 2005), or having difficulty for optical access. Double optical fiber or double conductivity probes are frequently used to estimate the size of bubble (e.g., Chanson and Brattberg, 2000; Chanson, 2002; Cartellier, 1992; Rinne and Loth, 1996; Barrau *et al*, 1999; Murzyn *et al*., 2005; Rensen and Roig, 2001; Kiambi *et al*., 2001) because the velocity information, obtained from cross-correlating the signals, is

necessary in obtaining the chord length of each bubble (by multiplying the residence time of bubble). Since most dual-probe techniques, either conductivity or optical base, are not capable of measuring the bubble diameter directly, the mean bubble diameter or the bubble size distribution are indirectly estimated from the mean chord length or chord length distribution. The air-water interfacial area is then obtained from the estimated bubble diameter and local void fraction. Nevertheless, this approach works only if the bubble size distribution is either uniform or within a narrow band. Otherwise only the bubble chord length distribution is obtained rather than the bubble diameter.

The objective of this study is to measure the diameter of bubbles directly in a bubbly flow using the FOR technique developed by Chang *et al*. (2003). It is found that an individual bubble size can be directly obtained using the FOR technique if the corresponding bubble contains velocity information. More detailed explanation is presented in Section 4.5. In order to validate the results obtained using the FOR technique, images taken using a high speed camera were used to measure the bubble velocity and diameter simultaneously with the FOR probe.

4.2 Principle and Experimental Condition

The FOR technique featuring a single fiber optic probe allows simultaneous measurements of bubble velocity, bubble diameter, void fraction as well as acceleration. Especially, the technique is capable of measuring velocities and fraction ratio of all phases in a multiphase flow at a given point. The apparatus of FOR is shown in Fig. 4.1. The technique can be briefly described as follow: A continuous-wave optical signal, derived from a multi-longitudinal mode diode laser (wavelength 1.3 μm, power level 1

mW) driven by a constant current (30 mA), is launched into a standard telecommunication graded single-mode optical fiber (SMF-28 fiber). The fiber core diameter is about 8 μm and the overall fiber diameter with the protective coating removed is 125 μm. The fiber refractive index is 1.44 at the 1.3 μm wavelength. The optical waves are divided into two paths by a 2×2 single-mode fused fiber coupler with a nominal 50%:50% splitting ratio. The signal fiber end-face is cleaved at normal angle while the end of the other fiber is slanted and rests free in air with essentially zero reflection from the fiber-air interface. The coupled reflected (by fiber end face) and returned (by scattering outside the fiber) signal is detected by a dc-coupled detector. The detected signal is subsequently acquired by a data acquisition board and processed by a computer.

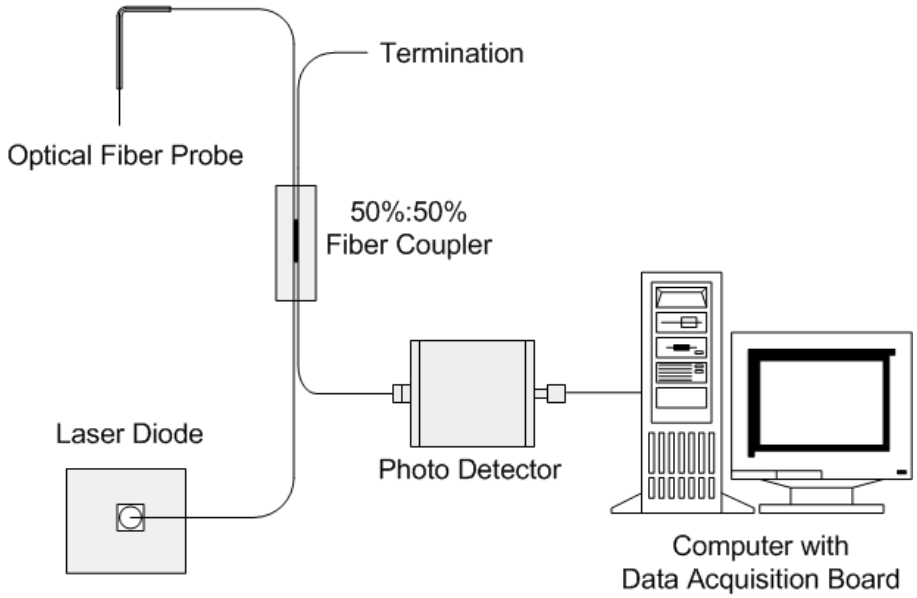

Fig. 4.1 Apparatus of the FOR system.

The amplitude of the received signal represents the reflected optical power due to Fresnel reflections off the fiber-fluid interface at the fiber tip. Assuming no energy losses, the power of the light reflected from the fiber-fluid interface using Fresnel reflectivity can be written as

$$P_1 = P_0 \alpha_1 \alpha_2 \left(\frac{n - n_f}{n + n_f} \right)^2 \tag{4.1}$$

where P_1 is the detected power of the light reflected from the fiber-fluid interface, P_0 the laser power, α_1 and α_2 the splitting ratio of the fiber coupler ($\alpha = \alpha_1 = \alpha_2 = 0.5$ in the experiment), n the refractive index of the fluid, and n_f the refractive index of the fiber ($n_f = 1.44$ in the experiment). In a water flow with air bubbles and solid particles, the refractive index is $n = 1.0$ for air and $n = 1.33$ for water. The power change due to the fiber tip encountering an air bubble is very large and can be easily measured, while the power change due to the fiber tip encountering a solid particle can also be easily detected and is distinguishable from the encounters of air and water.

Although the determination of phases is obvious based on Eq. (4.1), the determination of velocity is not. The diode laser used in the experiment has a coherence length of about 300 μm. An object (e.g., a solid particle in a liquid or gas flow, a gas bubble in a liquid flow, or a liquid droplet in a gas flow) within such a distance in front of the flat-cut fiber tip scatters the light back into the fiber. The light coherently beats with the optical signal reflected off the fiber-fluid interface. Outside the coherence length the oscillation amplitude is reduced rapidly. As the object moves, a time-dependent interference wave train is observed. The period of the oscillatory waves gives

the continuous velocity information of the object in the direction normal to the fiber end face (i.e., parallel to the fiber axis). According to the Fresnel formula, the electric field reflectivity is proportional to $(n_2\text{-}n_1)/(n_2+n_1)$ for light propagating in a medium with a refractive index n_1 into a medium with an index n_2. If $n_1 > n_2$ the field reflectivity is negative representing a π phase shift of the reflected field. If $n_1 < n_2$ the phase shift is zero. Thus, the reflected field E_a at the fiber-fluid interface and the scattered field E_b from the fluid-object interface can be expressed as

$$E_a = b_a e^{i\phi_a} \quad , \quad E_b = b_b e^{i(\phi_b+\psi)} \tag{4.2}$$

where b_a and b_b describe the amount of light coupled back into the fiber from the two interfaces, and ϕ_a or ϕ_b is either zero or π. ψ denotes the round-trip phase shift of the field propagating between the fiber-fluid interface and the fluid-object interface, and is given by

$$\psi = \frac{4\pi}{\lambda} n_w \Delta d \tag{4.3}$$

where λ is the laser wavelength, n_w is the refractive index of the fluid, and Δd is the corresponding distance that the object travels to create such a phase shift. The total returned power P due to E_a and E_b is $P = |E_a+E_b|^2$. From Eq. (4.2), P can be expressed as

$$P = b_a^2 + b_b^2 + 2b_a b_b \cos(\delta + \psi) \tag{4.4}$$

where the last term is the coherent-beating term which produces the oscillatory waves. δ is zero if the two interfaces produce the same phase shift, and π otherwise. The period of the oscillation is derived by the condition $\psi = 2\pi$. From Eq. (4.3), the distance Δd that

the object needs to travel for completing one oscillation cycle is

$$\Delta d = \frac{\lambda}{2n_w} \tag{4.5}$$

By measuring the period of the oscillation, T, the velocity of the object, u, can be calculated as

$$u = \frac{\Delta d}{T} \tag{4.6}$$

Since Δd is 0.492 μm in the current setup when the fluid is water, a high sampling rate is required in order to detect the high frequency signal of the coherent-beating light. The minimum sampling rate required based on the Nyquist frequency is approximately $4|u|$ MHz with u in m/s (Chang *et al*., 2004).

For an air bubble in water, the velocity information can be obtained from the front signal before the fiber tip touches the bubble's frontal water-air interface. In this way the blinding, crawling, and drifting effects (Barrau *et al*, 1999; Julia *et al*., 2005) due to the interaction between the probe and the bubble can be avoided. In addition, the velocity of bubble may also be obtained from the rear interface signal before the fiber tip, when inside the bubble, reaches the rear air-water interface and returns back into the water. Note that in such a case Δd calculated based on Eq. (4.5) equals 0.655 μm in the experiment because the bubble interior is filled with air. Note that the acceleration of bubbles can also be obtained since the velocity changes can be continuously monitored with a high temporal resolution (approximately 2 μs in the present study) based on the oscillatory signal within the coherence length of the laser.

Fig. 4.2 shows the sketch of a bubble in front of a FOR fiber tip. The optical signal emerging from the fiber diverges at an angle of 10° and may be reflected back from the

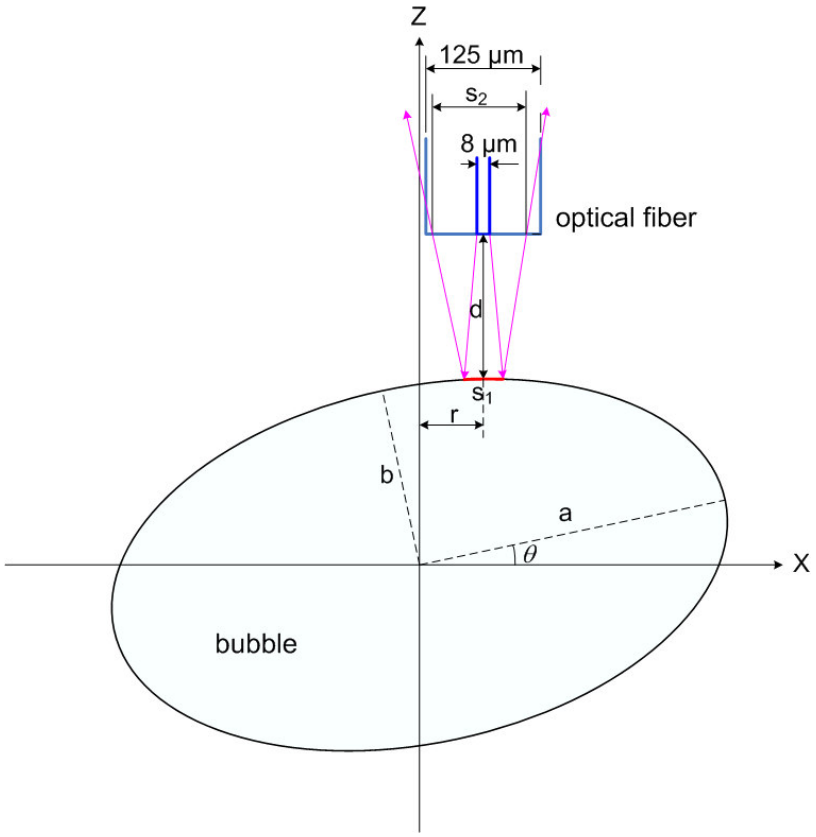

Fig. 4.2 Sketch of a bubble in front of the fiber tip.

bubble surface. Not all the reflected light from the bubble couples back into the fiber. The cross section of the reflected light at the fiber end face is denoted as s_2 and the location on the surface of the bubble illuminated by the light beam is denoted as s_1. The percentage of the reflected light that couples back into the fiber depends on the surface angle at s_1 and the distance between the fiber tip and the surface of the bubble. The returned power can be described as

$$P_2 = \beta P_0 \tag{4.7}$$

where P_2 is the power reflected from the bubble and returned back into the fiber and β is the ratio of the returned power into the fiber core to the reflected power at the surface s_2.

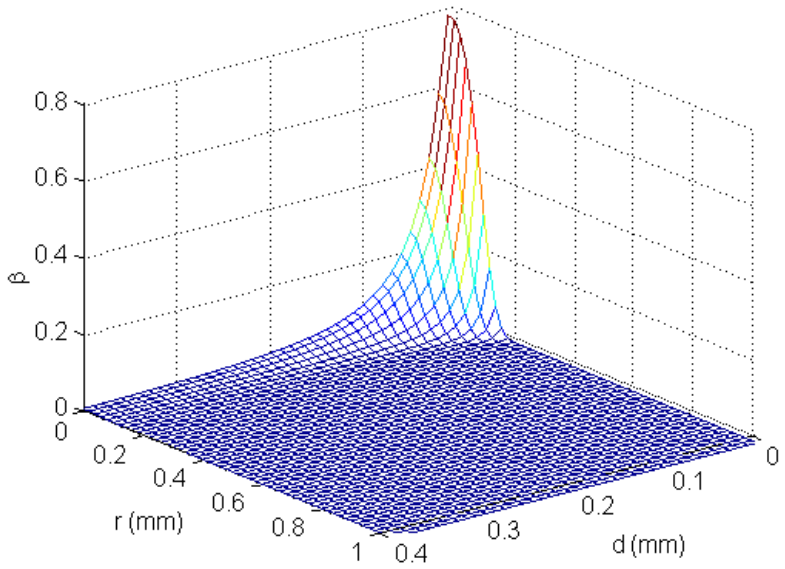

(a)

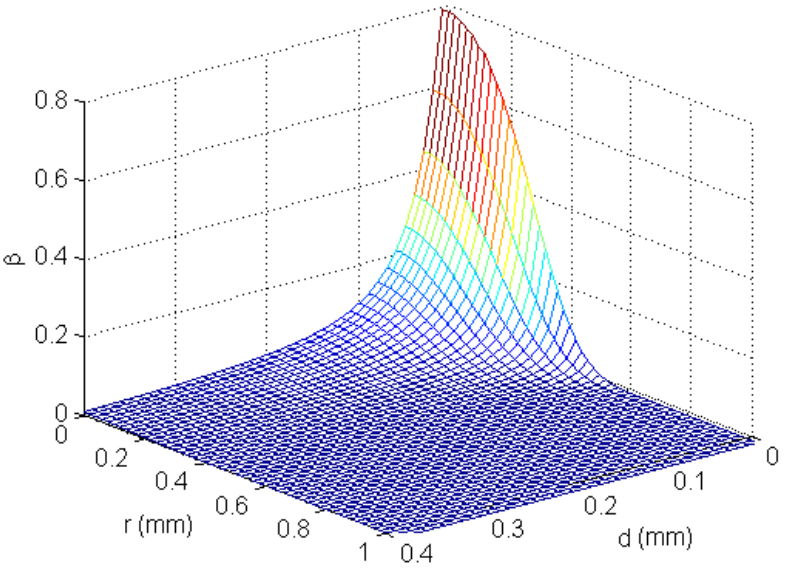

(b)

Fig. 4.3 Percentage of returned power of light back into the fiber. (a) spherical bubble with a diameter of 4 mm (*a* = *b* = 2 mm) and (b) ellipsoidal bubble with *a* = 2 mm and *b* = 1 mm.

The surface angle of the bubble at s_1 is a function of *r, a, b,* and θ, thus β can be described as

$$\beta = f(d, r, a, b, \theta) \tag{4.8}$$

where d is the distance between the fiber tip and the bubble surface, r is the location of the center of the fiber in the x direction, a is one-half of the major axis of the bubble, b is one-half of the minor axis, and θ is the slant angle of the bubble.

Fig. 4.3 shows an example of the percentage of returned power for different r and d when the shape of the bubble is a sphere with a diameter of 4 mm (i.e., $a = b = 2$ mm) [Fig. 4.3(a)], and an ellipsoid with $a = 2$ mm and $b = 1$ mm [Fig. 4.3(b)]. We assume that the spatial distribution of the light beam follows a Gaussian distribution. As expected, the smaller the values of r and d, the greater the power P_2. The figure also indicates that only within a short distance of r and d enough light power is reflected back into the fiber from the bubble surface. The threshold value of β depends on the sensitivity of the photo detector used. The result implies that the velocity of bubble can be obtained only if the fiber is located near the center of the bubble during the encounter. Otherwise the optical signal provides only the residence time of the bubble but, owing to lack of the reflected signal from the bubble surface, not velocity information of the bubble.

The total returned power, P_r, from the fiber-water interface and water-bubble interface that produces the coherent beating oscillatory waves can be expressed as

$$P_r = 2\sqrt{P_1 P_2} = 2\alpha\left(\frac{n - n_f}{n + n_f}\right)\sqrt{\beta} P_0 \tag{4.9}$$

The power P_r can be converted to a voltage V_r by

$$V_r = cP_r \tag{4.10}$$

where c is 4×10^4 V/mW for the detector-amplifier module used in this experiment.

For the case of a solid particle seeded in water, the optical signal coming out from the fiber tip and scattering from the particle surface has very high probability of being reflected back into the fiber if the size of the particle is very small (i.e., comparable with the size of the fiber core). This is because the smaller the object, the wider the angle for light scattering from the object. This indeed is the typical way to measure the fluid velocity by indirectly measuring the tiny seeding particles moving with the fluid. Moreover, the light scattering from the particle surface is in general non-directional because of the relatively rough particle surface. Therefore, velocity information can be obtained from almost all solid particles the probe encountered, as experienced in Chang *et al*. (2003). On the contrary, the velocity information for bubbles can be obtained from only a fraction of bubbles among all the bubbles encountered because the bubble surfaces are mirror-like so the directional reflection depends on Eqs. (4.7) and (4.8). Accordingly, reflected light from a larger bubble can return back to the fiber only when the angle of surface at s_1 is nearly normal to the fiber end surface. The ratio between the number of bubbles with velocity information and all the encountered bubbles can be estimated from

$$\gamma = \frac{A_i}{A_o} \tag{4.11}$$

where A_o is the projected area of the object (i.e., bubble) and A_i is the projected area on the surface of the object where the reflected light can couple back into the fiber under

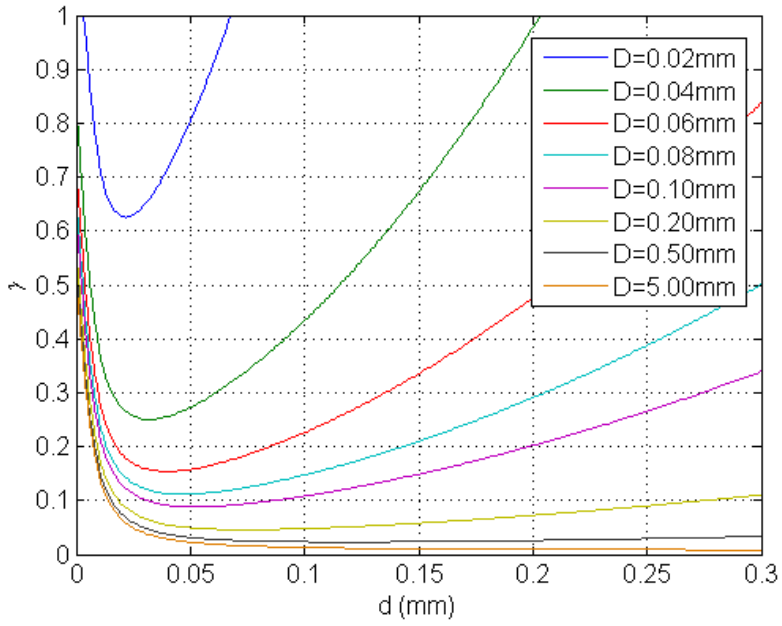

(a)

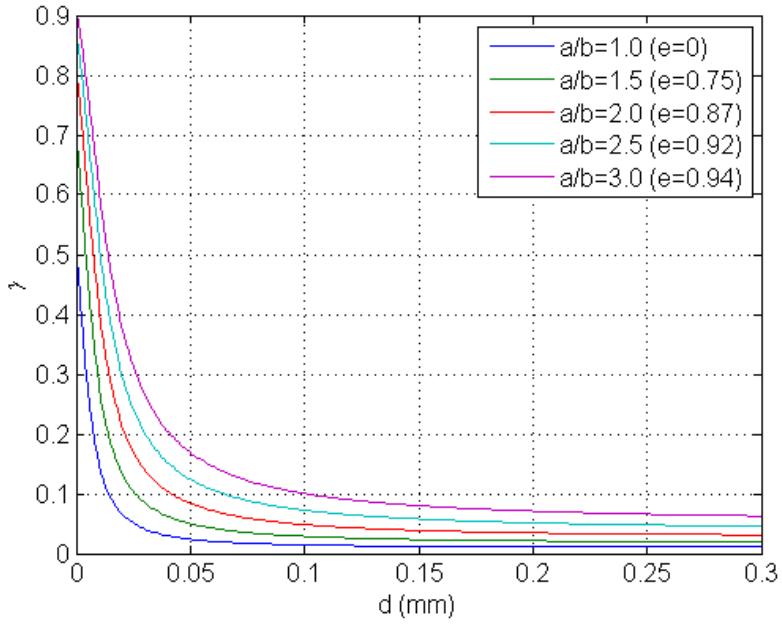

(b)

Fig. 4.4 Ratio for the number of bubbles providing velocity information to all detected bubbles: (a) spherical bubbles with various diameters and (b) ellipsoidal bubbles with various eccentricities and b = 1 mm.

the condition of $\beta > 0$. Therefore, the bubble signal will provide velocity information only if the projected location of the fiber probe is within A_i. The ratio γ depends mainly on the bubble size and shape (eccentricity) if the coherently mixed signal is detectable (i.e., $\beta > 0$). Fig. 4.4(a) shows the ratio γ versus d for various bubble diameters, D, when the bubble shape is spherical. As expected, the smaller the bubble, the higher the value of γ because of the wider angle of light scattering. Fig. 4.4(b) shows γ versus d for various bubble shapes (range of the eccentricity e = 0 ~ 0.94) when b is fixed at 1 mm. Note that the eccentricity is defined as $e = \sqrt{a^2 - b^2} / a$. The more ellipsoidal the bubble is, the higher the value of γ because of a flatter surface.

Although using the FOR technique velocity information cannot be obtained from all the bubbles encountered, the diameter of certain bubbles can be directly obtained for those bubbles containing velocity information. We assume the spiral movement of a bubble is small during the short encounter by the FOR probe. If the fiber tip pierces near the center of the bubble, the contact will be nearly normal angle (i.e., a short r in Fig. 4.2) and therefore light will reflect back to the fiber and enable the velocity determination. In such a case, the chord length obtained by the FOR probe is indeed the diameter or the minor axis of the bubble of spherical or ellipsoidal shape, respectively.

In order to validate the FOR technique for bubble diameter measurements, the chord length of each bubble obtained from the FOR measurements was compared with the diameter obtained from the images captured by a high speed camera. The experiment was performed in a rectangular water tank filled with distilled water.

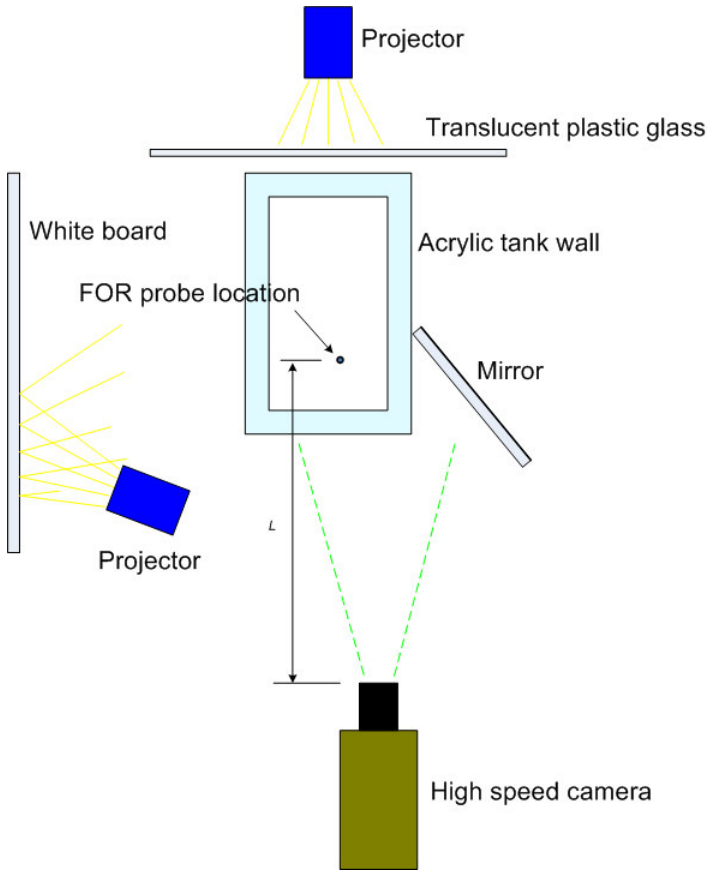

Fig. 4.5 Experimental setup with FOR probe and high speed camera.

Fig. 4.5 shows the setup of the experiment. The tank is 25 mm long, 45 mm wide, and 600 mm high and made of transparent acrylic plates with a thickness of 5 mm. The equivalent diameter, d_e, which provides the same pressure loss as the rectangular tank used in the experiments is 36.3 mm. Using such a small cross section is to ensure that the air bubbles are evenly distributed after a certain distance from the bubble source. Air bubbles emanated from a porous air stone located near the bottom of the tank. A flow meter and valve were used to control the air flow rates. A high speed video camera located in front of the tank was used to take bubble images. Through a mirror mounted at

a 45°, the same camera was able to capture images of bubbles from both the front and the 90° side. The images provide the front view and side view so the sizes of bubbles and the locations in contact with the FOR probe can be revealed and recorded. The synchronous experiments were performed with bubbles having a 1.86 mm minor axis and a 2.91 mm major axis. The diameter variations range between 1.30 mm and 3.06 mm in the minor axis and between 1.38 mm and 4.91 mm in the major axis. The equivalent diameter of bubbles, D_e, is 2.4 mm. The Weber number, Bond number, Reynolds number, and Capillary number are 1.20, 0.28, 355, and 586, respectively. The equivalent radius of bubbles was used as the characteristic length in the above characteristic numbers. The ratio of the equivalent bubble diameter to the equivalent tank diameter, D_e/d_e, is 0.07 and is never lower than 0.03 in the present study. The bubble void ratio was found evenly distributed across the small tank.

4.3 Validation of Void Fraction Measurement

In the experimental setup in Fig. 4.5, the original water level, h, in the tank before turning on the bubble generator was maintained at 470 mm throughout the experiment. After bubble generation, the water depth increment is denoted as h_b. For void fraction measurement, a total of six different air flow rates of 0.49, 0.62, 0.75, 0.94, 1.54, and 1.97 *l*/min for bubble generation were used to obtain a void fraction corresponding to h_b = 3.0, 6.0, 12.0, 16.0, 35.0, and 55.0 mm. The optical fiber probe was located at 390 mm from the bottom of the tank in all the test cases (i.e., 80 mm below the original water level before bubble generation). The measurement duration was kept constant at 100 s with a fixed sampling rate of 10 kHz. The observed *global* void fraction, defined as

$h_b/(h+h_b)$, is different from the *local* void fraction at the measurement point of the FOR probe due to the compressibility of air. Ideal gas law with an assumption of hydrostatic pressure was applied to calculate the *local* void fraction at the measurement point from the observed global void fraction for comparison with the FOR measurements. The range of local void fraction tested is between 0% and 12%.

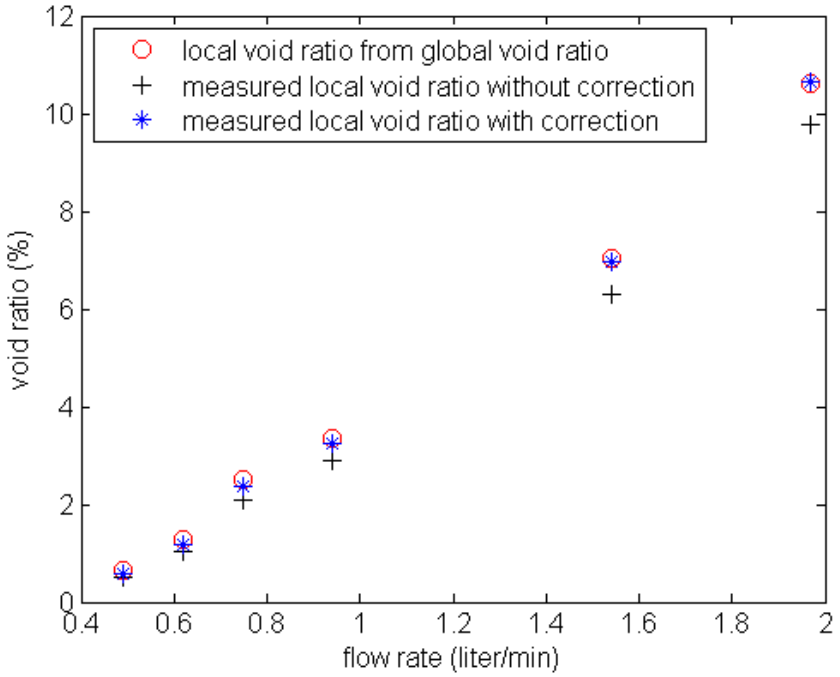

Fig. 4.6 Comparison of void fraction: o, local void fraction corrected using ideal gas law based on the global void fraction measurement; +, measured void fraction using FOR without correction; *, measured void fraction using FOR with correction.

The FOR technique measures velocities using the reflected signal before the fiber tip touches the object (i.e., the surface of a bubble in the tests). Therefore, the crawling, blinding, and drifting effects induced by a piercing event do not affect the velocity

measurements. However, the piercing effect should be considered in the bubble residence time (and therefore chord length and void ratio) measurement since it requires the probe to penetrate through bubbles. Many researchers such as Juliá *et al*., (2005) have reported an underestimation of the residence time due to the partial blinding effect, large-scale deformation, and additional drifting effect in the outer region of bubbles. Similar results and correction due to the piercing effect were reported by Chang *et al*. (2003). In the study the residence time of air bubbles was found to be underestimated, when measured using the FOR system, and a short duration of 0.71 ms for each bubble encounter was added to correct the problem.

Since the same FOR system was used in the present study, the same corrective time of 0.71 ms was added to the residence time for each bubble encounter. Fig. 4.6 shows the comparison among the local void fractions [back calculated using ideal gas law from the measured global void fraction of $h_b/(h+h_b)$], the measured void fraction using the FOR system without correction, and the measured void fraction corrected by adding the corrective time to each bubble encounter. Very good agreement was obtained between the void fractions, and the correction for the piecing effect is correct and necessary. The root-mean-square (r.m.s.) error in the void fraction measurement is 0.09%. It is evident that the FOR technique is capable of measuring the void fraction with a high accuracy.

4.4 Bubble Velocity Measurement

For the velocity measurement, the optical fiber probe was located at 390 mm above the tank bottom throughout the experiment (i.e., the same as in the void fraction

measurements). The air flow rate was maintained at 0.62 - 0.75 *l*/min. The measurement duration was kept constant at 4 s with a fixed sampling rate of 10 MHz. An imaging technique was used to validate the measurements of bubble velocity and bubble size taken using the FOR method. The imaging technique is similar to that in the bubble image velocimetry technique (Ryu *et al*., 2005) with the use of backlighting. The images were captured by a high speed camera mounted on a three-dimensional traverse. The camera framing rate was set at 500 Hz and the aperture was set at f/4.0. The field of view was 50×50 mm^2, resulting in an image resolution of 0.0493 mm/pixel for 1024×1024 pixels. The FOR system and the high speed camera were synchronized so data acquired from individual bubbles can be directly compared.

A total of 130 sets of measurements corresponding to a total measurement time of 520 s were performed using the FOR technique and the imaging method simultaneously. It results in a total of 1517 bubbles being detected by the FOR probe. The size of bubbles was found between 1.38 and 4.91 mm in the major axis. Note that the bubble size is much greater than the diameter of the fiber core of 8 μm and the diameter of the fiber of 125 μm. The average local void ratio is 1.64% and the bubble frequency is 2.92 s^{-1}. Although the void fraction of each bubble can be easily obtained, only a small percentage of bubbles provide velocity information. Note that in the FOR technique, the bubble velocity is obtained by analyzing the signal during the period when the distance between the fiber tip and the bubble is between 100 μm and 300 μm.

The oscillatory waves providing velocity information can be obtained when the angle between the fiber tip and bubble surface is nearly normal (or with a small *r* as

plotted in Fig. 4.3). Although all the bubbles passing through the fiber tip were detected, the oscillatory signals were not produced from all the detected bubbles. Among the bubbles, only 31 provide good oscillatory front signals (right before the fiber tip in contact with the front surface of bubble) for velocity determination, while only 34 provide good rear signals (right before the fiber tip in contact with the rear surface of the bubble and leaving the bubble). Based on the front signals, the number of bubbles containing velocity information is therefore only about 2% of the total number of bubbles. The ratio is similar to the ratio γ calculated based on Eq. (4.11) and plotted in Fig. 4.4. The value of γ based on the probability of bubbles containing velocity information is between 0.017 and 0.026 within the range of the laser coherent length when the eccentricity of bubbles is 0.75. If tiny neutrally buoyant particles are seeded in the water for water velocity determination, nearly 100% of the detected signals (i.e., particle encounters) provides velocity information, as shown in Fig. 4.4(a), because the mean diameter of the particles is usually very small [$O(10\ \mu\text{m})$] in addition to the rougher surface of the particles. This was found true in the study of Chang *et al*. (2003).

Fig. 4.7 shows sample FOR signals of bubbles and the corresponding video images. The left images are the front view images (with the camera looking at a 0° angle) and the right images are the side view ones (with the camera looking at a 90° angle through a mirror). Both images were analyzed to obtain the bubble size and its relative position to the FOR probe. Cartellier and co-workers (Cartellier, 1992; Barrau *et al*., 1999; Cartellier and Barrau, 1998) reported that a low amplitude peak prior to the strong rise of

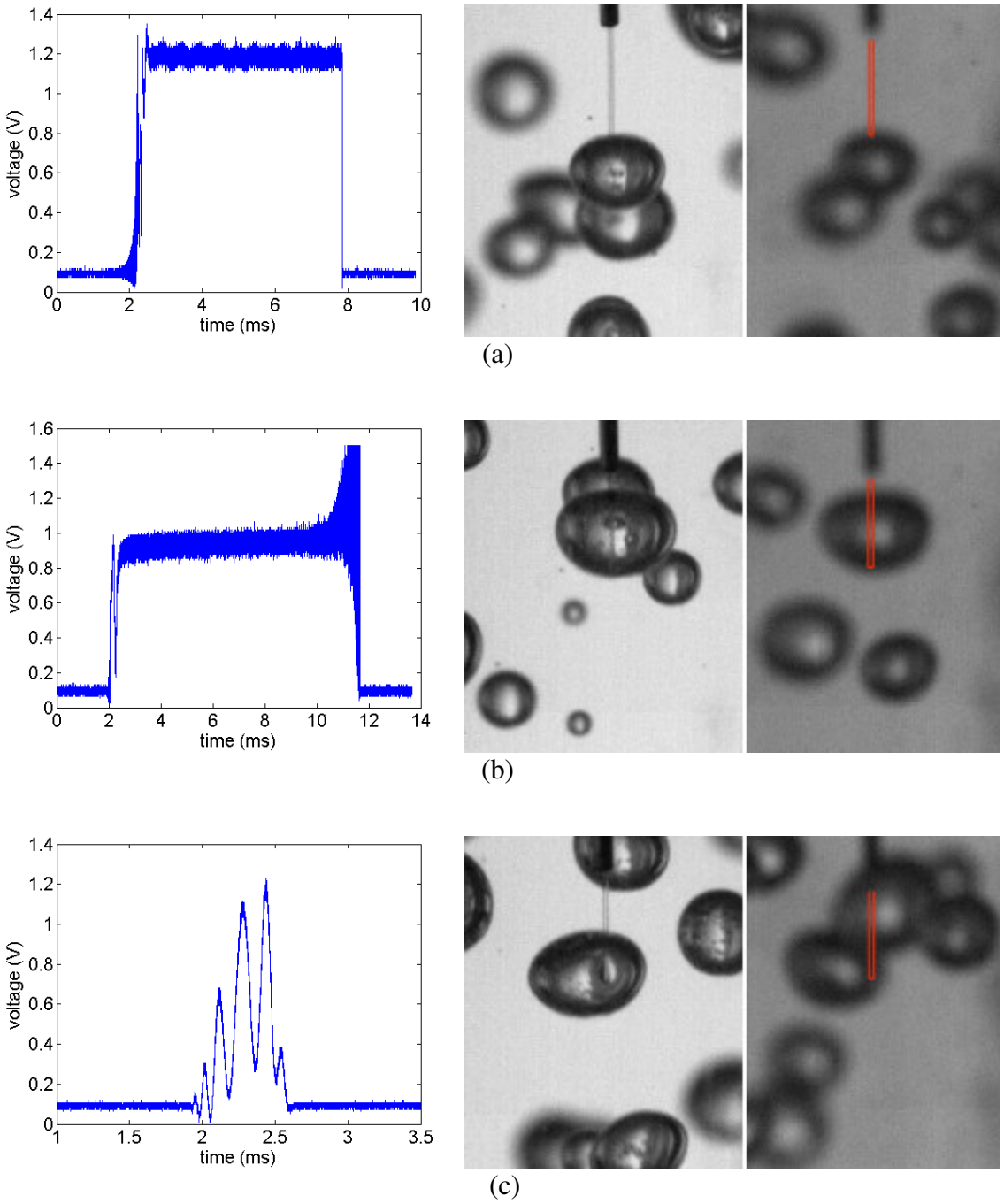

Fig. 4.7 Sample bubble signal: (a) FOR signal taken at the front interface and corresponding image and velocity information. (b) FOR signal taken at the rear interface and corresponding image and velocity information. (c) FOR signal and image when the probe is in contact with the bubble edge.

the optical signal appears when the angle between the fiber and bubble surface is nearly normal. It was found by Chang *et al*. (2003) that the low amplitude peak indeed consists of a train of oscillatory waves generated by the coherent mixing between the Fresnel reflection off the fiber-liquid interface and the scattered signal off the gas bubble [corresponding to Fig. 4.7(a)]. This phenomenon also appears when the probe encounters solid particles and liquid droplets. In addition, the oscillatory waves are also found right before the fiber tip exits bubbles with a nearly perpendicular angle [corresponding to Fig. 4.7(b)]. On the other hand, Fig. 4.7(c) shows the case when the probe tip penetrates the side of a bubble. The signal increases with low frequency fluctuations at the front water-air interface and then suddenly decreases at the rear air-water interface. These increase and decrease in signal with relatively low frequency fluctuations can always be seen at the interfaces for such an encounter. While the bell shape signal can be detected at a low sampling rate, a high sampling rate is needed to resolve the oscillation.

Figs. 4.8-4.10 provide detailed description of the FOR signals taken at a high sampling rate of 10 MHz. Fig. 4.8 shows the front signal between 1.7 and 2.7 ms in Fig. 4.7(a). A constant signal of 0.1 V is detected when the probe is in water and outside the coherent length of the laser. As the bubble approaches the probe, the coherently mixed signal appears in the interval between points A and C (i.e., the bubble is within the coherent length). Accordingly, the distance between the fiber tip and the bubble is about 100 - 300 μm, depending on the power of the return signals. The amplitude of the high frequency oscillatory waves continues to increase until the fiber tip reaches the

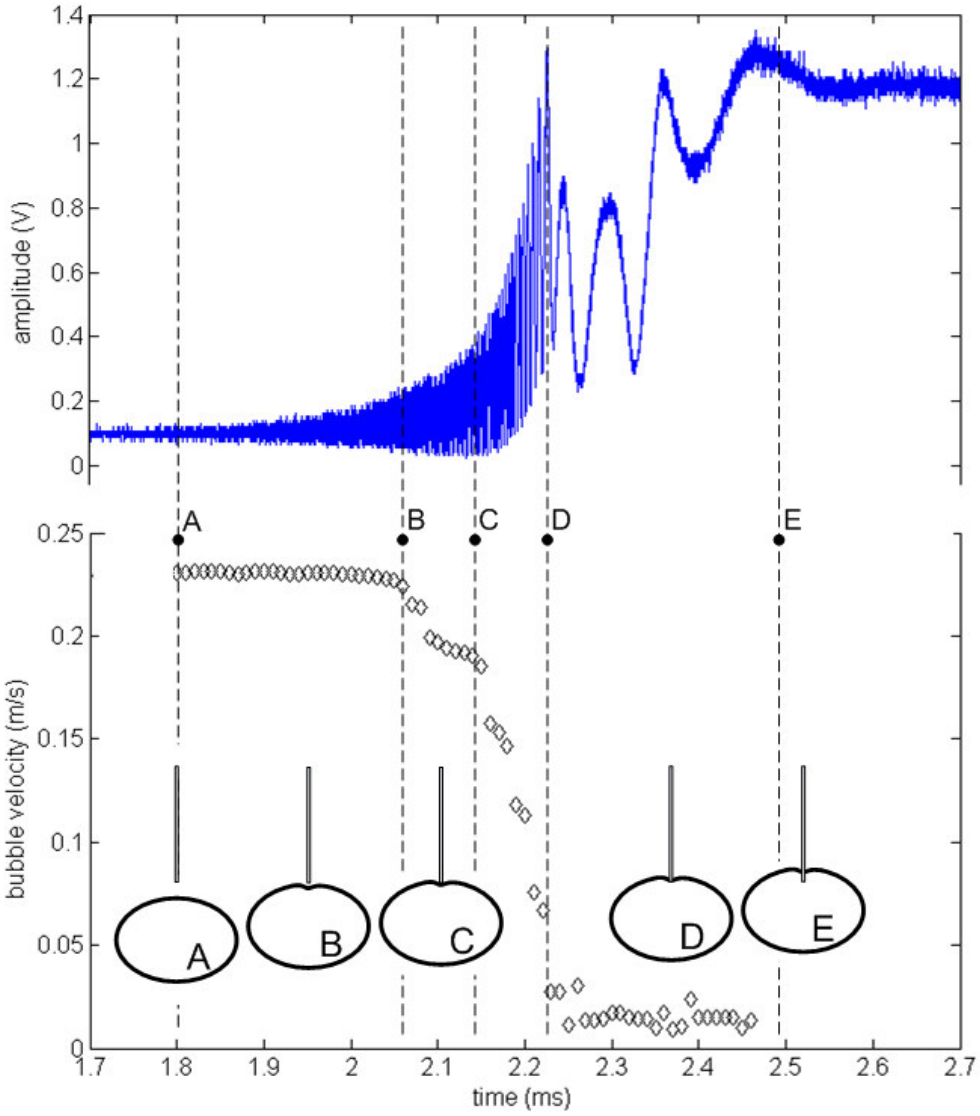

Fig. 4.8 Analysis of bubble front signal and velocity.

water-air interface (point C). The signal then rises sharply with relatively low frequency oscillations when the fiber reaches the interface (point C) and lasts until the fiber penetrates the bubble (point D). Subsequently, signal fluctuations between points D and E right after the piercing event are observed, representing the drying off of the fiber tip

during the interval. After that, the signal maintains a constant high voltage indicating the fiber tip is dry and in air. Note that point C representing the instance when the bubble touches the fiber end has the minimum voltage.

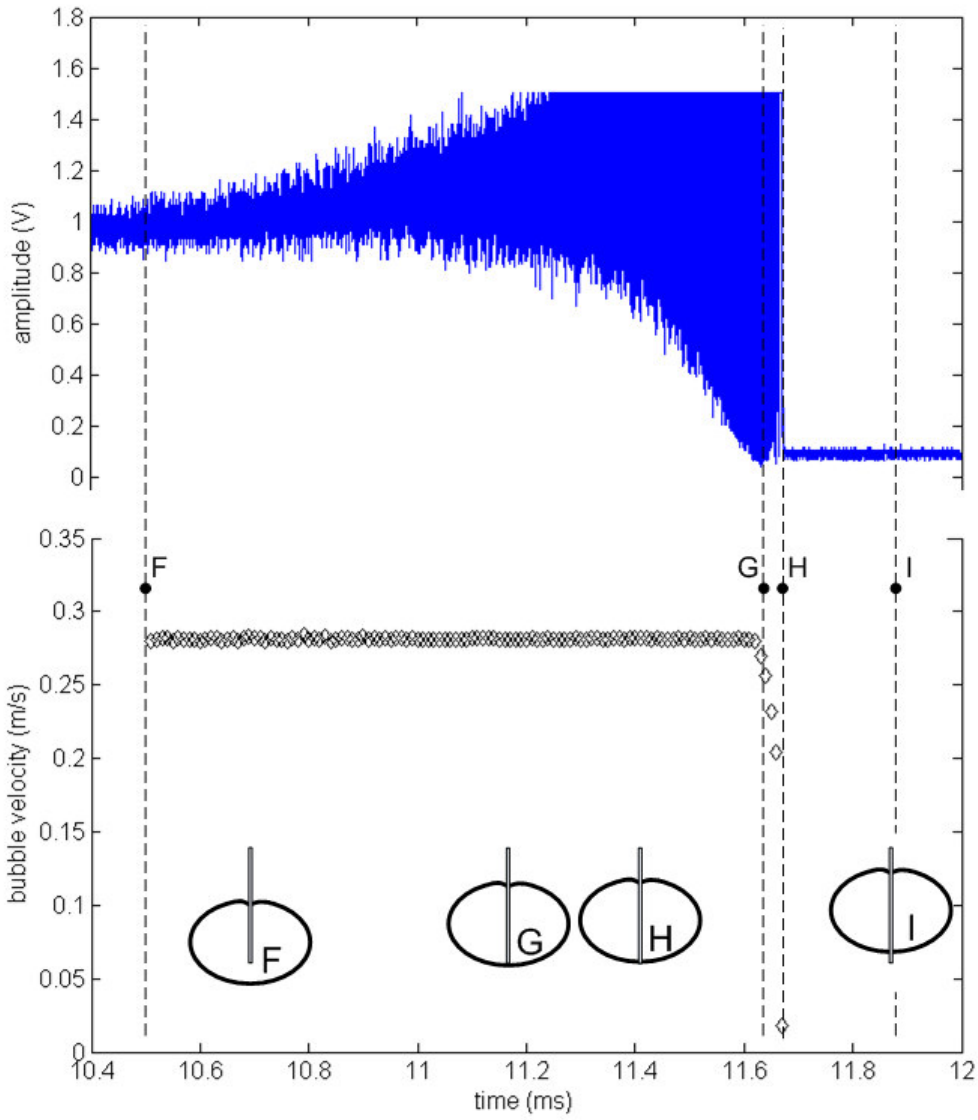

Fig. 4.9 Analysis of bubble rear signal and velocity.

Although the coherently mixed signal appears in the interval between points A and C in Fig. 4.8, only the coherent signal between points A and B is useful for obtaining the bubble velocity. The signal is analyzed by spectral analysis for velocity determination using Eq. (4.6). The power spectral of the signal over each short interval of 20 μs is first computed to find the peak frequency. Curve fitting with a 3-point or 4-point cubic-spline method is then applied to locate the peak of the spectral for a better accuracy. Fig. 4.8 shows the variation of the bubble velocity within the coherent length before the bubble touches the fiber tip. The bubble velocity is almost constant in the interval between A and B. A deceleration of about 30g to 50g occurs beyond point B due to the interaction between the fiber tip and the bubble, with g being the gravitational acceleration. A similar deceleration was also observed in the velocity measurement of solid particles due to the presence of the fiber (Chang *et al*., 2003).

When the fiber tip is inside the bubble, the coherent-beat signal is also observed before the fiber tip reaches the rear end of the air-water interface and back to the water if the fiber tip and the air-water interface are nearly perpendicular. Fig. 4.9 shows the rear signal between 10.4 and 12 ms in Fig. 4.7(b). A constant voltage signal of approximately 1 V, representing the fiber tip is inside the air bubble, is detected outside the coherence length before point F. The coherently mixed signal with a high oscillatory frequency appears in the interval between points F and G. The amplitude of the coherent-beat signal increases continuously until the fiber tip reaches the rear air-water interface (point G) and then decreases dramatically with low frequency oscillations after the fiber reaches the interface. Finally, the fiber exits the bubble (point H) and the signal returns

to a constant voltage of 0.1 V, representing the fiber tip is in water. Unlike the front signal, there is no deceleration (as between points B and C in Fig. 4.8) when the probe is exiting the bubble. The period of oscillatory waves is obtained by applying spectral analysis over the interval from points F to G. Noted that Δd is 0.655 μm in such case since the fluid is air (Δd = 0.492 μm if the fluid is water).

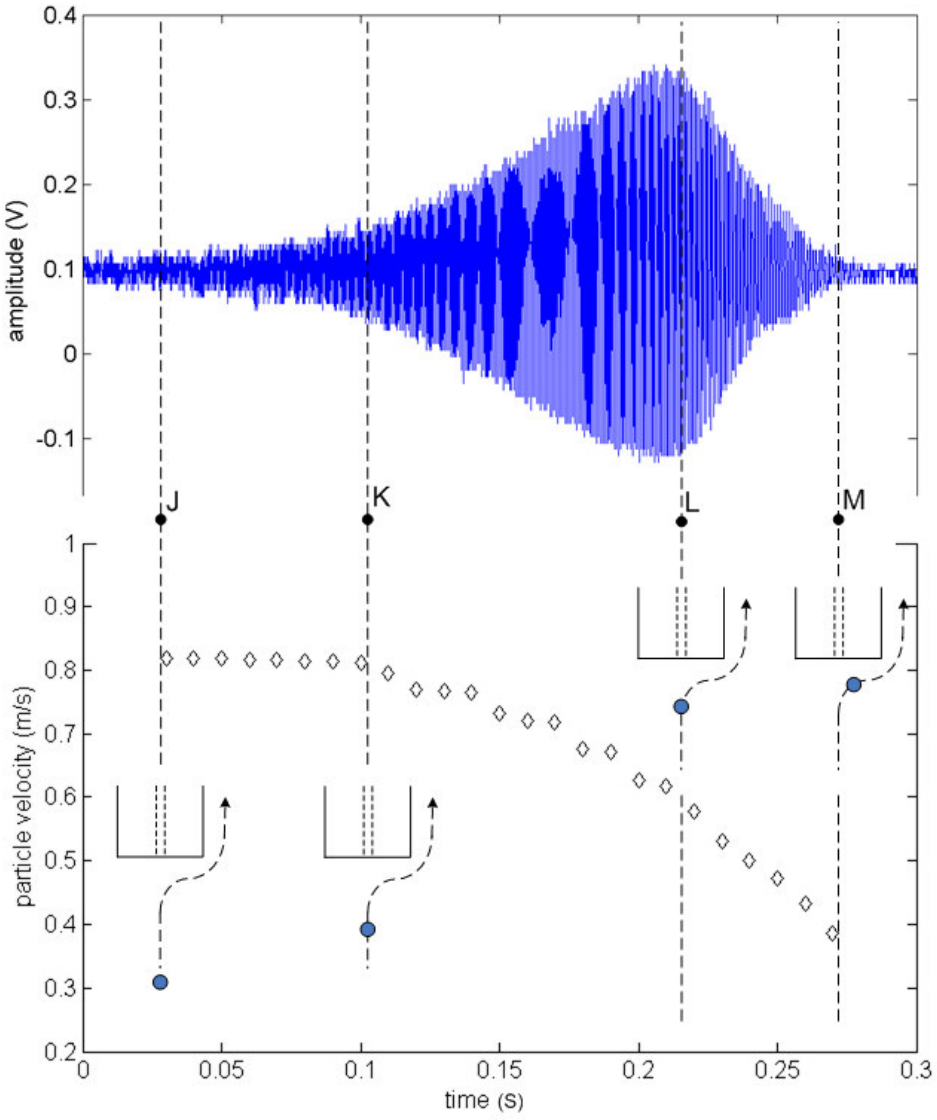

Fig. 4.10 Analysis of small particle signal and velocity.

Fig. 4.10 shows a typical signal from a small particle with a mean diameter of 15 μm seeded in water as presented in Chang *et al*. (2003). The coherently mixed signal is observed in the interval between points J and M when the particle is passing the fiber tip. Similar signals can be found for micro bubbles in Wedin *et al.* (2003) if the bubbles are small enough to prevent them from being pierced through by the fiber and thus behave similar to solid spheres. As the particle approaches the probe, the coherently mixed signal appears from point J. The amplitude of the high frequency oscillation continues to increase until the particle begins to change its path at point L due to the presence of the fiber tip. The deceleration of particle starts at point K due to the viscous effect of being close to the fiber tip (with a distance about the diameter of the fiber). Therefore, only the coherent signal between points J and K is useful for obtaining the particle velocity because it is not affected by the presence of the fiber. Subsequently, a deceleration (in the direction of the fiber axis) is also observed between points L and M after the particle starts to change its direction.

The measured velocity of individual bubble using the FOR technique is compared with the velocity measured using the high speed camera. The bubble velocity obtained using the FOR technique is the velocity of the front water-air interface. Therefore, the bubble velocity from a high speed camera was calculated by tracking the trajectory of the upper water-air interface during a time interval of 10 ms right before the bubble touched the fiber tip to avoid uncertainties caused by the presence of the fiber. Since the spatial resolution is 1 pixel in an image over an average displacement of 50 pixels, the uncertainty for velocity measurements using the high speed camera is about 0.01 m/s.

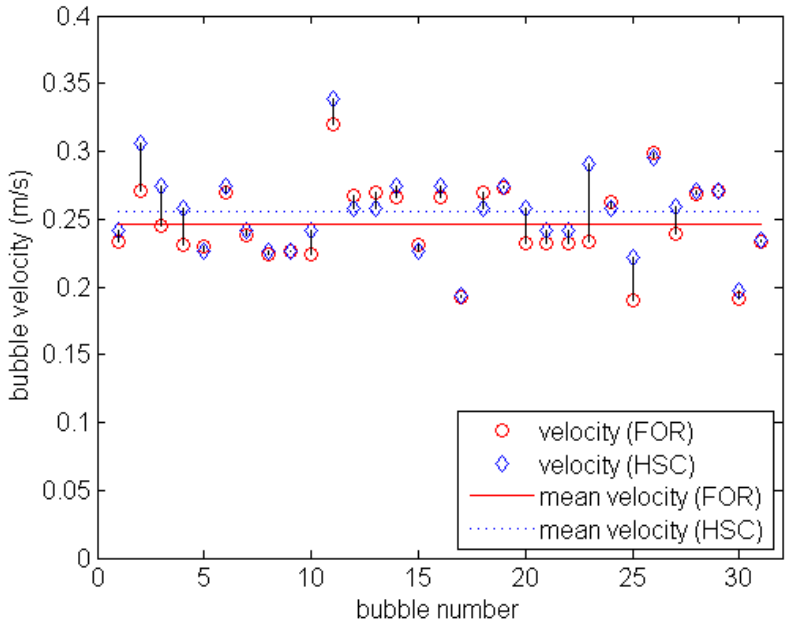

(a)

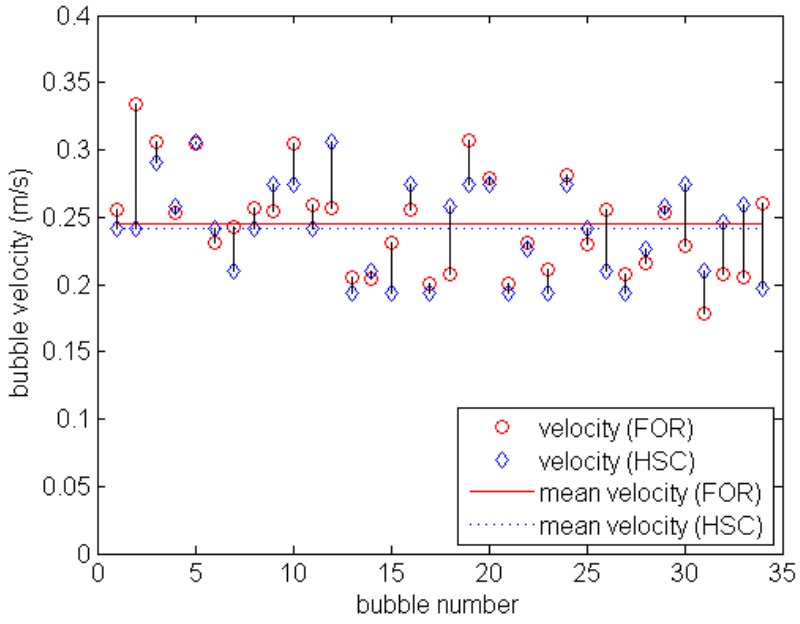

(b)

Fig. 4.11 Comparison of bubble velocity measurements: (a) Velocities based on the front signal. (b) Velocities based on the rear signal.

Fig. 4.11(a) and Fig. 4.11(b) show the comparisons of velocities obtained from the front signal and rear signal, respectively, using the FOR technique and the high speed camera. The bubble velocity is in the range of 0.19 - 0.32 m/s. The r.m.s. error in the velocity measurements is 0.017 m/s for the front signal and 0.031 m/s for the rear signal. The error from the rear signal is slightly greater. The velocity obtained using the high speed camera is prior to the contact of bubbles and the fiber tip. Therefore a higher uncertainty may be caused by the existence of the fiber and the deformation as well as acceleration/deceleration of the bubbles. It is worth pointing out that if the velocity of bubbles is obtained using the signal before the fiber tip reaches the bubble front surface, such as that in Fig. 4.11(a), the effects due to the interaction between the probe and the bubbles such as blinding, crawling, and drifting can be avoided.

4.5 Bubble Size Estimation

In the FOR measurements, the diameter of individual bubble can be obtained from the bubbles containing velocity information by multiplying the velocity to the corresponding residence time. In the residence time measurement for bubble size estimation, care needs to be taken on choosing the starting point in the signal to present the encounter of the bubble front interface. The residence time of the bubble was calculated from point C in Fig. 4.8. Point C represents the instance when the bubble touches the fiber end. A minimum voltage would be recorded at this instance due to continuous increase in the oscillation amplitude as the bubble approaches the probe while the mean signal either remains constant or increases gradually. After the instance at point C, the mean signal shoots up rapidly because the bubble interface is no longer

approaching the probe but touched the probe so the reflected signal changes from low (in water) to high (in air).

With an available velocity measured, it implies that the fiber tip enters and/or exits the bubble near the center of the bubble and the angle between the fiber axis and the bubble surface is close to normal. Although the bubble trajectories are neither straight nor constant, the spiral movement of bubbles is small during such a short interval. Accordingly, we assume that the spiral movement is insignificant during such a short piercing event; the chord length obtained indeed represents the diameter of the bubble when the bubble is spherical or the minor axis when the bubble is ellipsoidal. In reality the optical fiber probe does not always pass through the center of bubbles within the effective projecting area A_i in Eq. (4.11) to provide the bubble velocity and size information. However, whenever a bubble provides a high frequency oscillatory signal as shown in Fig. 4.8, it indicates the fiber end penetrates near the center of the bubble and the bubble path is nearly straight during the piercing event.

In the present study, there are two criteria for finding bubble signals that determine the bubble velocity and the bubble diameter. First, the bubble piercing location should be close to the center of bubble. For example, the piercing location should be inside the area A_i in Eq. (4.11). This way the coherently mixed signal with high oscillation frequencies can be observed within the coherent length right before the piercing. Second, the bubble path should be almost straight during the piercing event. As shown in Fig. 4.8, the interval between points A and B with a constant velocity should be long enough. The minimum time for the interval $\overline{\text{AB}}$ was set as 100 μs in the present study and the

interval $\overline{AB}$ must be longer than the interval $\overline{BC}$. If satisfying the above two criteria, bubble velocities and diameters can be easily found through data analysis. The signal in Fig. 4.8 certainly satisfies the two criteria. The coherently mixed signal with high frequencies in the interval between points A and D ensures that the fiber probe was piercing through the bubble center. In addition, the long interval between points A and B ($\overline{AB} \approx 260\ \mu s > 100\ \mu s$) before deceleration ensures a straight bubble path in this duration. Note that the entire interval of the interfered signal before the bubble touches the fiber end is $\overline{AC} \approx 340\ \mu s$. The velocity and the maximum chord length (i.e., the diameter) of the bubble are thus measured. Based on the principle, the technique can be applied to a broad bubbles size distribution.

Fig. 4.12 shows the comparisons of the FOR measured chord length distributions between all detected bubbles (a total of 1517 bubbles) and bubbles containing velocity information (a total of 65 bubbles). Fig. 4.12(a) shows the chord length distribution of all detected bubbles. Since only a fraction of the bubbles containing velocities, the chord length is calculated based on the measured residence time multiplied by the mean bubble velocity of 0.245 m/s measured using the FOR system as shown in Fig. 4.11(a). The measured local void ratio is 1.64% and the mean bubble frequency is 2.92 s^{-1}. Accordingly, the mean chord length, equal to the void fraction times the velocity and divided by the bubble frequency, is 1.37 mm. On the other hand, the chord length distribution of bubbles containing velocity information is shown in Fig. 4.12(b). The maximum chord length (bubble diameter) of each bubble (a total of 65 bubbles) shown in the figure is directly obtained by the FOR technique and represents the diameter of the

corresponding bubble. The mean diameter is 1.82 mm that is much greater than the average chord length of 1.37 mm.

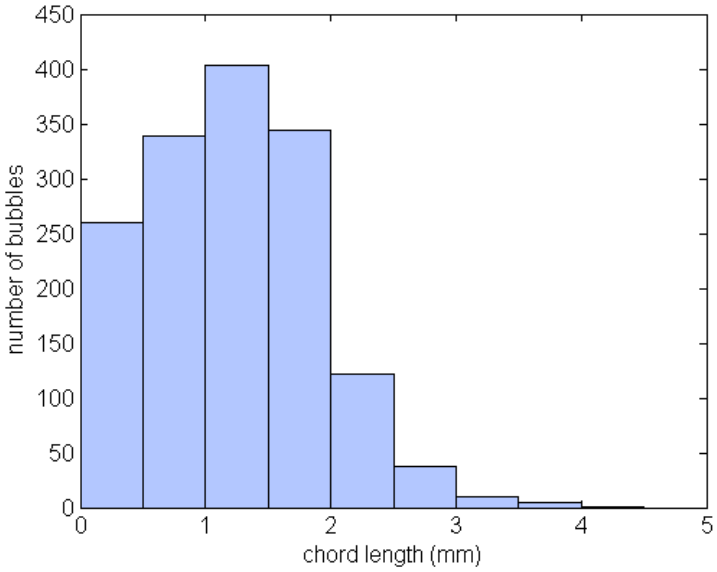

(a)

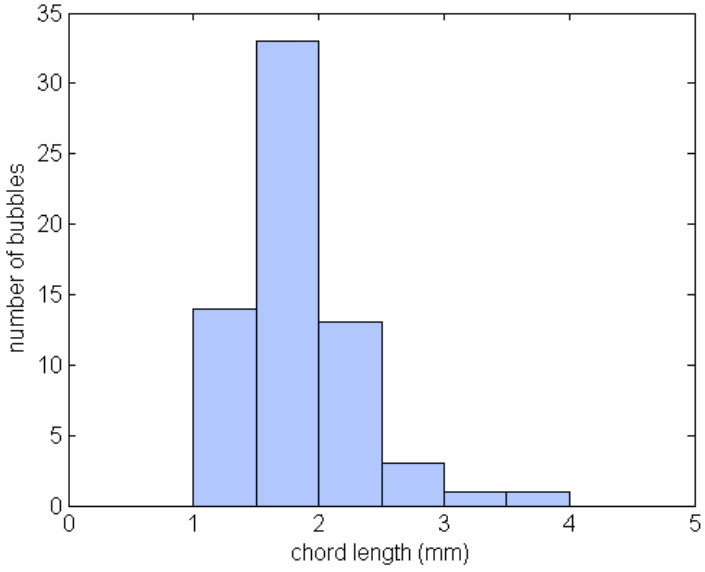

(b)

Fig. 4.12 Comparison of chord length distributions: (a) Chord length distribution of all bubbles. (b) Chord length distribution of bubbles containing velocity information.

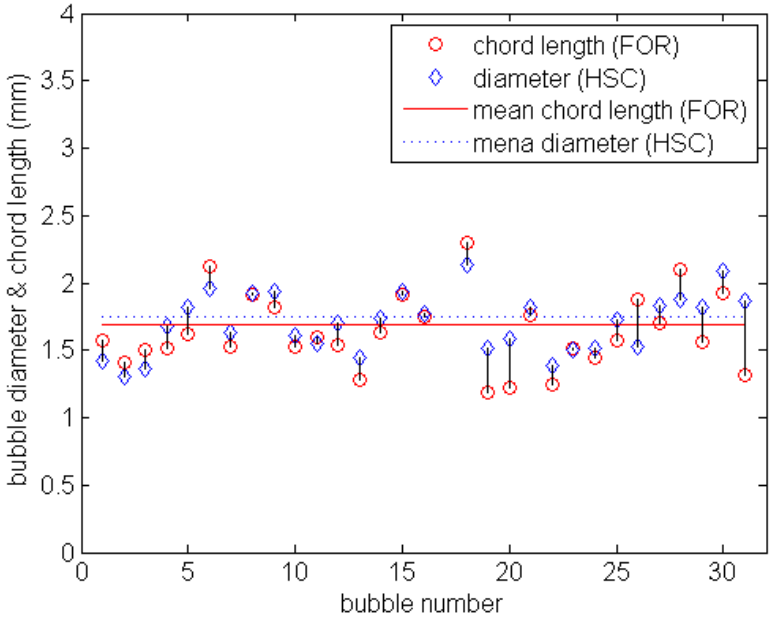

(a)

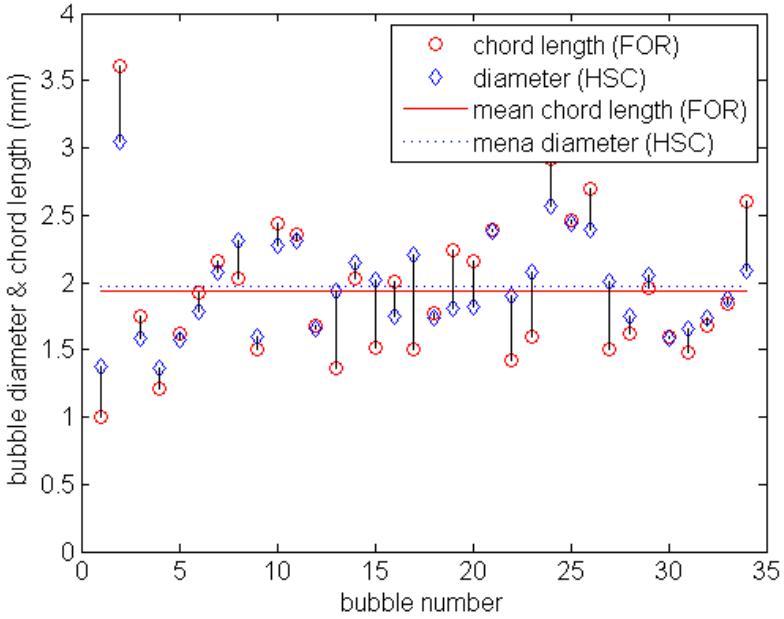

(b)

Fig. 4.13 Comparison of bubble diameters: (a) Diameters based on the front signal. (b) Diameters based on the rear signal.

Images obtained using the high speed camera are used to validate the bubble size measurement taken using the FOR technique. The bubble size is measured based on both the front image and the side image (from the side mirror in Fig. 4.5). The resolution of the images is 0.0493 mm/pixel. The major axis and minor axis of each bubble are obtained by averaging the results based on the front image and side image, even though the difference is very small. The size of bubbles varies in the range of 1.30 - 3.06 mm for the minor axis and 1.38 - 4.91 mm for the major axis. The mean minor axis is 1.86 mm and the mean major axis is 2.91 mm. The range of eccentricity of bubbles is between 0.0 and 0.92 with a mean eccentricity of 0.77.

Fig. 4.13(a) and Fig. 4.13(b) show the comparisons of bubble size between the high speed camera measurement and the FOR measurement obtained using the front signal and the rear signal, respectively. Based on the FOR measurement, the size of bubbles varies in the range of 1.00 - 3.60 mm with a mean diameter of 1.82 mm. The mean bubble diameter is 1.69 mm based on the front signal, and 1.93 mm based on the rear signal. The r.m.s. error in the bubble diameter measurement is 0.20 mm if using the front signal, and 0.31 mm if using the rear signal when compared with the high speed camera measurement. The error is consistent with that in the velocity measurements; using the front signal results in a better accuracy in comparison to using the rear signal. Fig. 4.14(a) and Fig. 4.14(b) show the normalized bubble diameter measurement using FOR based on the front signal and rear signal, respectively. The diameter of each bubble obtained using the FOR measurement is normalized by the diameter of the corresponding bubble obtained using the high speed camera. The mean chord length

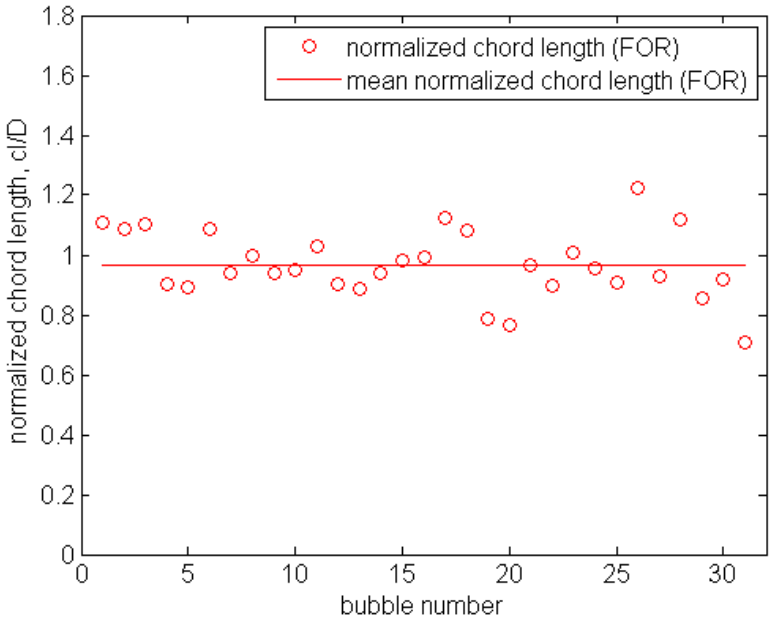

(a)

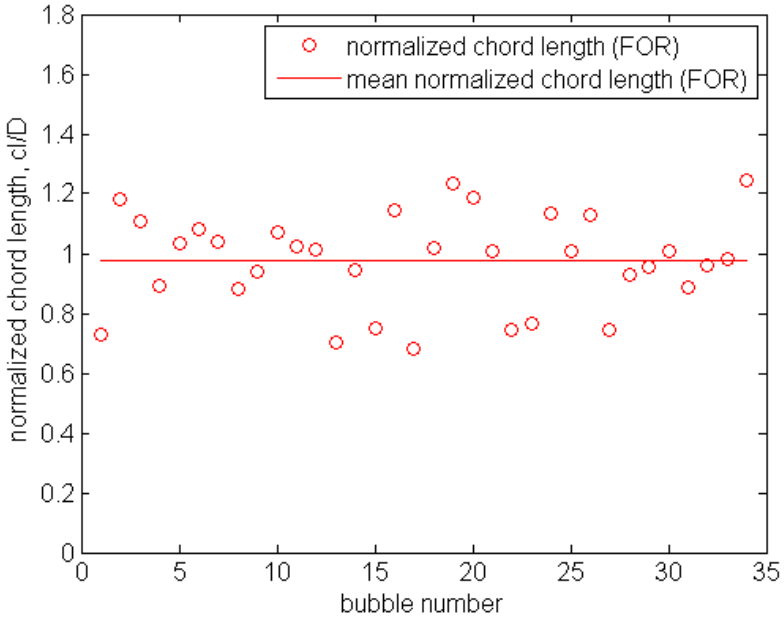

(b)

Fig. 4.14 Comparison of normalized bubble diameters: (a) Diameters obtained based on the front signal. (b) Diameters obtained based on the rear signal.

obtained using FOR is 97% of that obtained using the high speed camera. The r.m.s. error is 11.4% based on the front signal, and 15.7% based on the rear signal. Overall, the bubble diameter obtained using the FOR technique is in good agreement with that obtained using the imaging method. This indicates the bubble diameter measurement using FOR is reasonably accurate, especially using the front signal, even though the number of bubbles with diameter measurements (and therefore velocities measurements) is quite small for such bubble size. Multiple probes may be needed to increase the number of bubbles with valid velocity and size measurements.

There exist many advantages for the FOR technique in bubble velocity and size measurements. Conventional intrusive techniques based on fiber optic or conductivity probes require a piercing event to obtain the bubble velocity. The FOR technique measures bubble velocity using signal taken before the fiber tip in contact with the bubble surface therefore the detrimental effect due to the bubble-fiber interaction can be minimized, if not eliminated. This way measurement errors caused by the intrusiveness of the probes can be significantly reduced. Similar to gas bubbles, velocities of solid particles and water droplets in various multiphase flows can also be obtained. On the contrary, a piercing event is required for velocity measurements using conventional multi-probe methods. Velocity measurements for solid particles and water droplets may not be feasible if conventional methods are used. In addition, the FOR technique may potentially be used for acceleration measurement by acquiring continuous velocity information of an object due to its high temporal resolution. An example can be found in Fig. 4.8. The measured acceleration is Lagrangian since the technique records the motion

of an individual object.

The FOR technique may not provide any advantages in bubble size determination if the size of bubbles is close to uniform. However, the technique does provide a way to measure the size of bubbles if the bubble size is random or has a broad range of size distribution. Note that the FOR technique is not capable of measuring the slant angle, θ, of bubbles therefore the measured bubble diameter may post a large error if the slant angle is large and the shape of bubble is ellipsoidal.

4.6 Conclusion

In conclusion, the FOR technique is capable of measuring the bubble velocity, diameter, and void fraction in multiphase flows. The measured velocities have a high spatial and temporal resolution and are taken prior to the contact with bubbles. The velocity measurements are therefore considered as nearly nonintrusive. Even though not all the bubbles return coherently mixed signals that provide velocity information, for those that do provide velocity information their diameters can be obtained. The FOR technique would have a higher successful rate in velocity measurement if smaller bubbles were used. As shown in Fig. 4.4(a), the detection rate γ for velocity measurement increases dramatically as the size of bubbles or particles become smaller. The FOR probe that directly measures bubble diameters is one of very few techniques that are capable of measuring bubble diameter, velocity, and void fraction directly. The technique is especially useful for the bubbles having a wide range of sizes.

CHAPTER V

BREAKING WAVES IN DEEP WATER: EXPERIMENTAL TECHNIQUES AND CONDITIONS

5.1 Introduction

This chapter will present and discuss the experimental techniques and conditions used to study wave breaking in deep water. From this chapter, an experimental study on wave breaking in deep water is the main topic of this dissertation and will be presented and discussed. The measurement and data analysis of breaking waves is challenging because of the characteristics of the flow which is nonlinear, turbulent and multiphase due to air entrainment. As shown in previous Chapters II - IV, the FOR system and technique were developed and applied to measure multiphase flows (Chang *et al*., 2002, 2003, 2004; Lim *et al*., 2008). The FOR technique has been applied to breaking waves to measure water particle velocity, bubble velocity and void ratio simultaneously. However, the FOR technique might not be suitable to measure bubble velocity field of breaking waves. As mentioned in Chapter IV, the detection rate of bubbles which provide velocity information is too low in the FOR measurement. In addition, the technique is based on point measurements, such as laser Doppler velocimetry (LDV) which measures the time series of water particle velocity at a point. In spite of some demerits for the velocity measurement of breaking waves. The FOR technique is a very reliable technique to measure the void ratio in multiphase flows, especially when the void ratio is very high

such that images techniques can not be used. The FOR technique was used to obtain the void ratio of the breaking waves. The bubble image velocimetry (BIV) technique (Ryu *et al*., 2005) was employed to obtain the velocity field of highly aerated region of breaking waves. The BIV technique is capable of measuring air-water mixture velocity of the aerated region with very good agreement whereas the traditional PIV technique can not measure in this region. The drawback of the BIV technique is that it cannot measure water velocity outside of the aerated region. PIV was used to obtain velocity outside of the aerated region. However, it was possible to measure velocity fields for the entire flow including the highly aerated region by modifying the experimental conditions of the traditional PIV technique. Since the frame rate used in the BIV measurements was 500 frames per second (*fps*) with a high speed camera, the identical high speed camera was used in the PIV measurements to increase temporal resolution of image data. In addition, a continuous laser was used to generate a continuous light sheet to obtain high temporal resolution of 500 *fps* unlike traditional PIV measurements.

The generation of breaking waves in deep water with a constant water depth is presented in this chapter, in addition to the description of the experimental techniques and conditions. Combination and synchronization of various experimental techniques were required to investigate breaking waves in deep water, which is one of most complex flows because it is nonlinear, multiphase and turbulent.

The experiments on wave breaking were performed in a two-dimensional glass-walled wave tank, which is 35 m long, 0.91 m wide, and 1.2 m deep equipped with a flap-type wavemaker. A 1:5.5 sloping beach with a horsehair layer is located at the far

end of the tank to absorb the wave energy and reduce reflection. The water depth was maintained at 0.80 m throughout the experiments to generate breaking waves in deep water. After generating strong breakers with good repeatability, four kinds of experimental techniques were employed to measure various quantities.

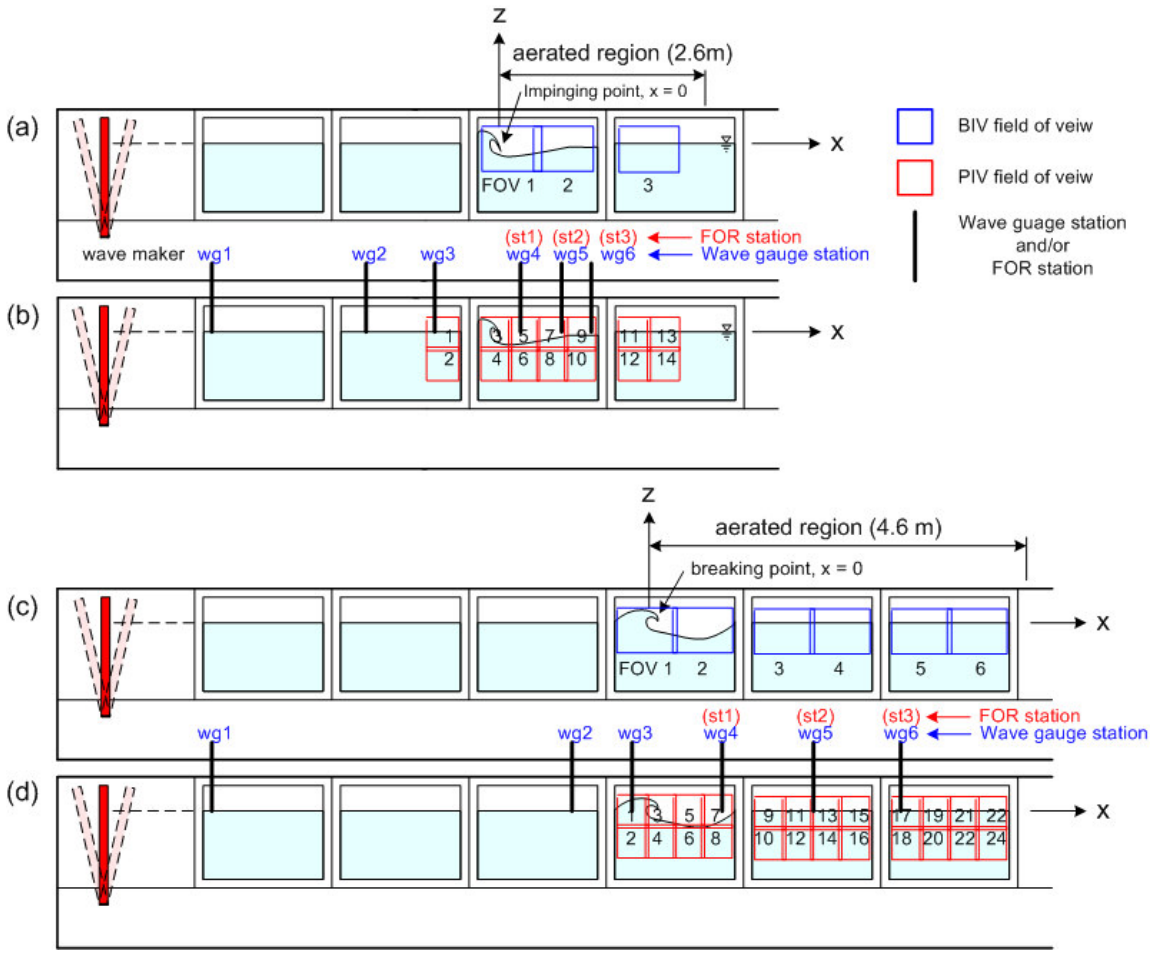

Fig. 5.1 Sketch of the location of each measurement: (a) BIV for plunging breakers (b) PIV, wave gauge, and FOR stations for plunging breakers (c) BIV for spilling breakers (d) PIV, wave gauge, and FOR stations for spilling breakers.

Detailed information of all the experiments used in this study is sketched in Fig. 5.1. The wave elevation was measured using six wave gauges which are double-wired resistant type. The bubble image velocimetry (BIV) technique was used to measure a velocity field of aerated region in the breaking waves. In addition, the modified particle image velocimetry (PIV) technique was used to investigate the entire flow field including the pre-breaking region and highly aerated region. Finally, the FOR technique mentioned in Chapters III and IV was used to measure a void ratio at three stations which are located at each splash-up region. As shown in Fig. 5.1, two coordinate systems were used for plunging and spilling breaking waves respectively. The breaking point in a plunging breaker is defined as the point at which a wave impinges on the front wave surface near the still water level.

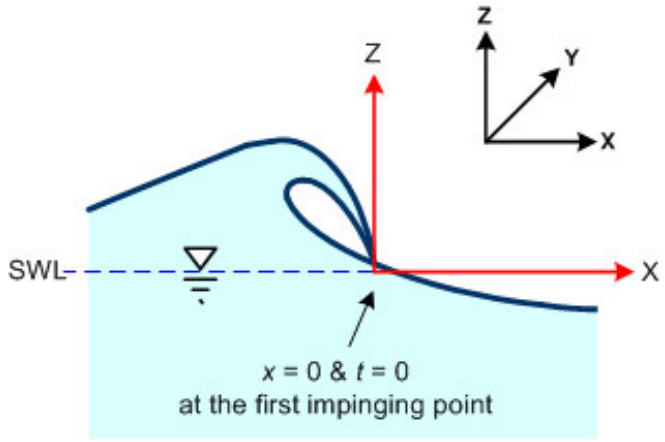

Fig. 5.2 Coordinate system for the plunging breaker.

In the rectangular coordinate system shown in Fig. 5.2, $x = 0$ and $t = 0$ are at the breaking point of each wave and $z = 0$ at the stationary water level. Although the

measurement is two-dimensional, it is worthwhile to note the y direction, such that positive vorticity is clockwise and negative vorticity is counterclockwise. Note that the results for a spilling breaker will not be included in this dissertation. All the measurements used for a plunging breaker were applied to a spilling breaker with same manners as shown in Fig. 5.1. However, data analysis for the spilling breaker has not been finished due to huge data size more than 15 TB. The spilling breaker will be mentioned only in this chapter regarding the experimental setups.

5.2 Generation of a Breaking Wave

Both plunging and spilling waves were generated for constant water depth by a method similar to that described in Skyner *et al*. (1990). In this method, wave focusing technique was used to generate the desired plunging and spilling breaking waves in deep water. Fig. 5.3 shows an overturning moment of a plunging breaker generated in the two-dimensional wave tank. The wave train consists of 13 waves with various wavelengths and amplitudes that can be controlled to obtain the desired waves. As shown in Fig. 5.4, the shortest and smallest wave is in front and then waves became longer and bigger. A long wave propagates faster and it will catch up to the front shorter waves. Eventually, both plunging and spilling waves broke at a desired location with good repeatability. The wave steepness, H/L, of plunging and spilling waves generated are 0.19 and 0.15 respectively (see Table 5.1) where H is the wave height and L is the wavelength of the primary wave. In shallow water measurements, waves will break continuously depending on the incident wave properties from deep water and the geometry of the shore. For example, individual waves break when $H > 0.8h$ where h is

the water depth. On the contrary, there is only one breaking event as sending the wave train with a wavemaker. It was require to wait about 15 minutes until water become calm between tests. Therefore, enough measurement time for turbulence properties can be limited. At least 20 tests were performed at the same condition for all the measurements (wave gauge, BIV, PIV and FOR). Repeatability of wave generation is very good in the focusing method. It can be considered as steady waves.

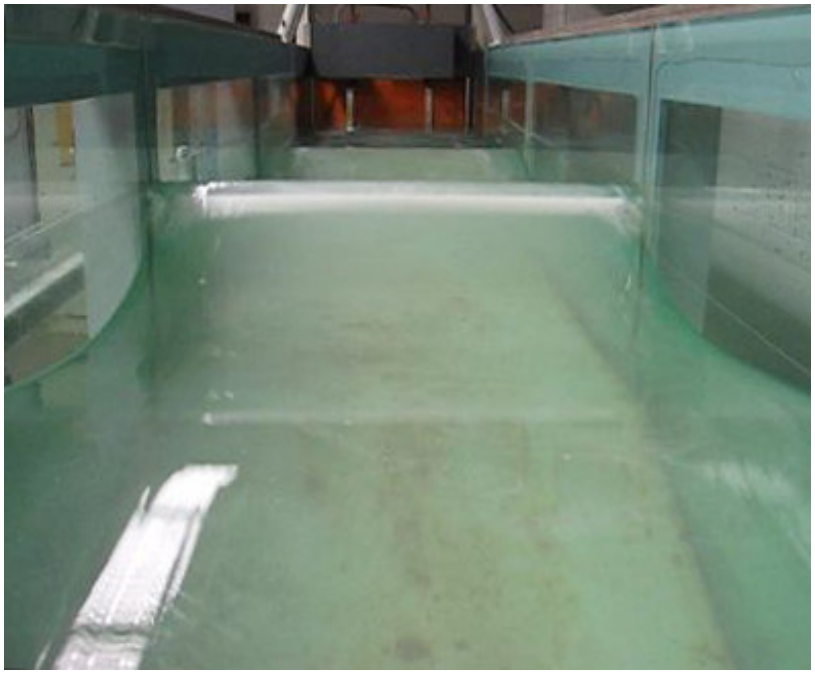

Fig. 5.3 Generation of a plunging wave in a 2D wave tank.

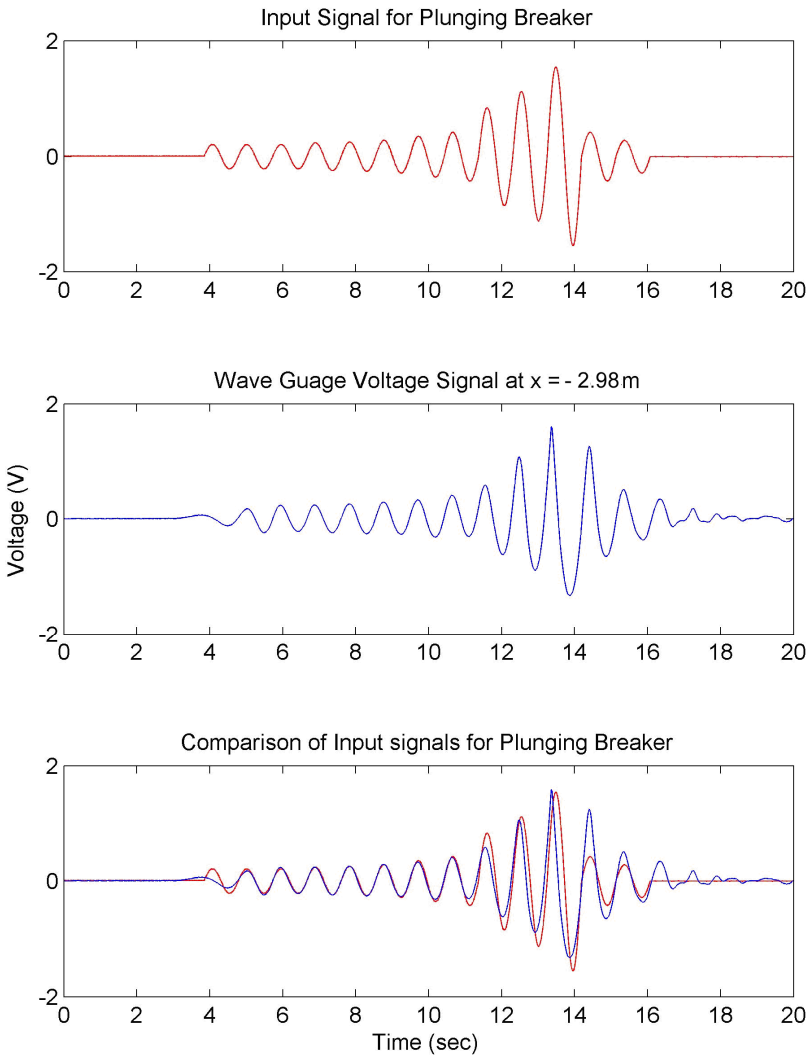

Fig. 5.4 Input signal to generate a plunging breaker and wave elevation at x = -2.98 m (WG1).

Table 5.1
Breaking wave properties for a primary wave

	Plunging Breaker	Spilling Breaker
Wave height, H	0.204 m	0.265 m
Wave period, T	0.83 s	1.09 s
Wave length, L	1.08 m	1.84 m
Phase speed. C	1.3 m/s	1.68 m/s

5.3 Wave Gauge Setup and Conditions

The wave elevation was measured using six wave gauges located at various location as shown in Fig. 5.1 and 5.5. Fig. 5.5 shows the first three windows that are closest from the wavemaker in the two-dimensional wave flume. The detail description about the locations can be seen in Table 5.2. The first wave gauge (WG1) is located near the wavemaker so the wave elevation shape is similar to the input wave signal. The second wave gauge (WG2) is located just before the wave deformation so its shape is symmetric. The third wave gauge (WG3) is located just before wave face becomes vertical. The wave gauges 4, 5 and 6 (WG4, WG5 and WG6) are located at the middle of each splash-up region as shown in Fig. 5.6. In addition, the void ratio measurements were performed at those three station for each splash-up region with the measurement results presented in Chapter VII.

Fig. 5.5 Measurement locations of six wave gauges.

Table 5.2
Measurement locations of six wave gauges

	Location (m)	Description
Wave gauge 1 (WG1)	x = -2.98 (1.30 from WM)	Elevation similar to the input wave
Wave gauge 2 (WG2)	x = -1.31 (2.97 from WM)	Just before skewed to the left (before deformation)
Wave gauge 3 (WG3)	x = -0.57 (3.71 from WM)	Just before wave face become vertical (at x = - 0.42 m)
Wave gauge 4 (WG4) FOR station 1 (FOR1)	x = 0.43 (4.71 from WM)	Middle of the fully developed 1st splash-up
Wave gauge 5 (WG5) FOR station 2 (FOR2)	x = 0.88 (5.16 from WM)	Middle of the fully developed 2nd splash-up
Wave gauge 6 (WG6) FOR station 3 (FOR3)	x = 1.20 (5.48 from WM)	Middle of the fully developed 3rd splash-up

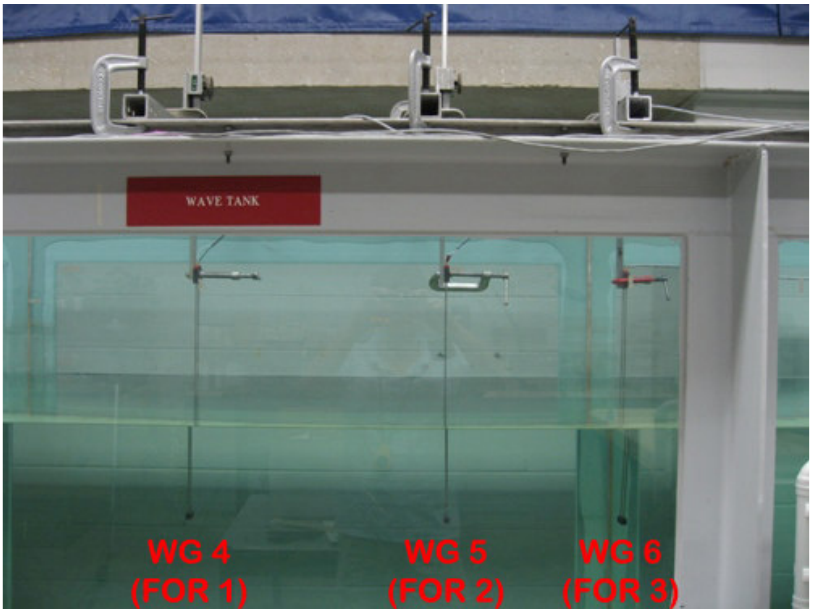

Fig. 5.6 Wave gauges 4, 5, and 6 (WG4, WG5, and WG6) corresponding to FOR station 1, 2, and 3 (FOR1, FOR2 and FOR3) respectively.

Since breaking waves are highly turbulent flows, 20 measurements for each station were carried out in order to obtain mean and r.m.s. elevations.

5.4 Bubble Image Velocimetry (BIV) Setup and Conditions

The BIV technique was used to obtain the velocity field in the aerated region after the wave impinges on its front surface. The images were captured by a high speed camera mounted with a Nikon 105 mm micro focal lens. The high speed camera has a resolution of 1024×1024 pixels and a 8 bit dynamic range. The camera's frame rate was set at 500 *fps* and the aperture was set at f/1.8 throughout the experiments. Regular 600 W light bulbs with reflecting mounts were used to illuminate the flow. No lasers are needed in this measurement.

The apparatus of BIV is shown in Fig. 5.7. The depth of field (DOF) for the captured images is 0.21 m with the camera located at 4.7 m in front of the center of the DOF, resulting in an uncertainty of 2.2% in the acquired images for later velocity determination. The principle and validation of the BIV technique are described in details by Ryu *et al.* (2005).

The time interval between the recorded images is 2.0 ms that is equal to the time separation between the consecutive frames captured by the high speed camera. The images with a resolution of 0.65 mm/pixel were processed using commercial software from LaVision, Inc. The velocity fields were calculated using an adaptive multi-pass algorithm with an initial interrogation window size of 32×32 pixels and a final window size of 16×16 pixels with a 50 % overlap. Therefore, the final resolution of the velocity vector map is 8×8 pixels corresponding to 5.26×5.26 mm^2. It should be pointed out that

temporal resolution is 10 ms. The experiments were repeated at least 20 times with the same test condition at each FOV. The mean and fluctuating velocities were calculated from the ensemble average of the 20 instantaneous velocity fields.

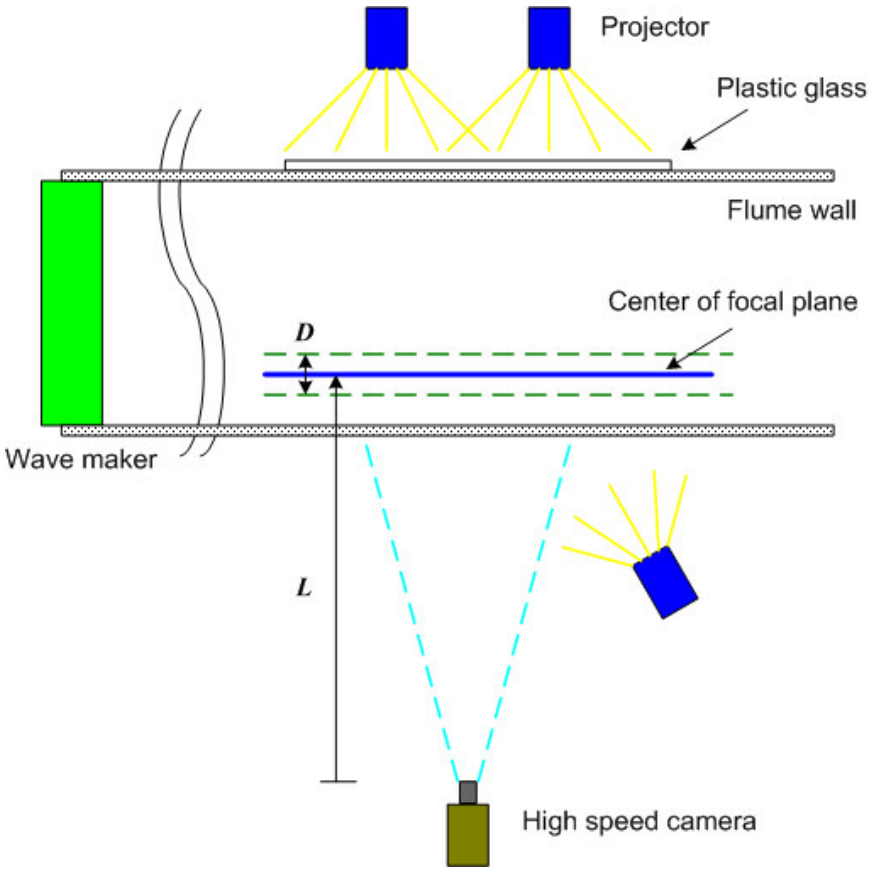

Fig. 5.7 Apparatus for the BIV system.

In the BIV measurements, 3 and 6 fields of view (FOV) were used to cover the entire aerated region of both plunging and spilling waves respectively as shown in Fig. 5.1. The sizes of fields of view are fixed as 0.66×0.495 m^2 in the BIV measurements. There was an overlap region of 84 mm between FOV1 and FOV2 and a gap of 270 mm

between FOV2 and FOV3 due to a steel column at the glass wall of the wave tank. The three fields of view cover the entire aerated region for both types of breaking waves with sufficient spatial and temporal resolutions.

In addition to the velocity field in the aerated region, raw images taken in the BIV measurement are used to obtain the free surface information including the aerated region and the boundary of the aerated region since resistive wave gauges used in the study can measure only water portion of waves. The results of the free surface estimation and detection of the aerated region obtained from the BIV measurements are presented in Chapter VII with results from the wave gauge measurement. Mean and turbulence quantities obtained from the BIV measurement are presented in Chapter VIII.

5.5 Particle Image Velocimetry (PIV) Setup and Conditions

The PIV technique was originally employed to measure only the velocity field outside the aerated region and under the trough level up to z = - 0.51 m after obtaining air-water mixture velocity of the aerated region by using BIV. However, it was found that the air-water mixture velocity field inside the aerated region could be obtained by using a weak continuous laser and moving the light sheet location as close as 20 cm from the front wall of the wave flume. Unlike traditional PIV measurements generally using the pulsed laser to generate a light sheet, application of a continuous Argon-Ion laser for the light source was attempted to obtain high frequency images with the identical high speed camera used in the BIV measurements. This is required because the velocity magnitude is large and the velocity gradient is high, especially at the first splash-up process followed by the first impingement of an overturning water jet. The

camera frame rate was set at 500 *fps,* the same as the BIV measurements and the aperture was set at f/1.4 with a 50 mm focal lens throughout the experiments. The exposure time was set at 100 μs which is short enough to prevent images of the seeded particles from skidding. Two cylindrical concave lenses were used for the light sheet optics to generate the wide light sheet. The seeding particles had a mean diameter of 56 μm and a specific weight of 1.02. The sketch and pictures of the setup for the PIV system are shown in Fig. 5.8 and Fig. 5.9.

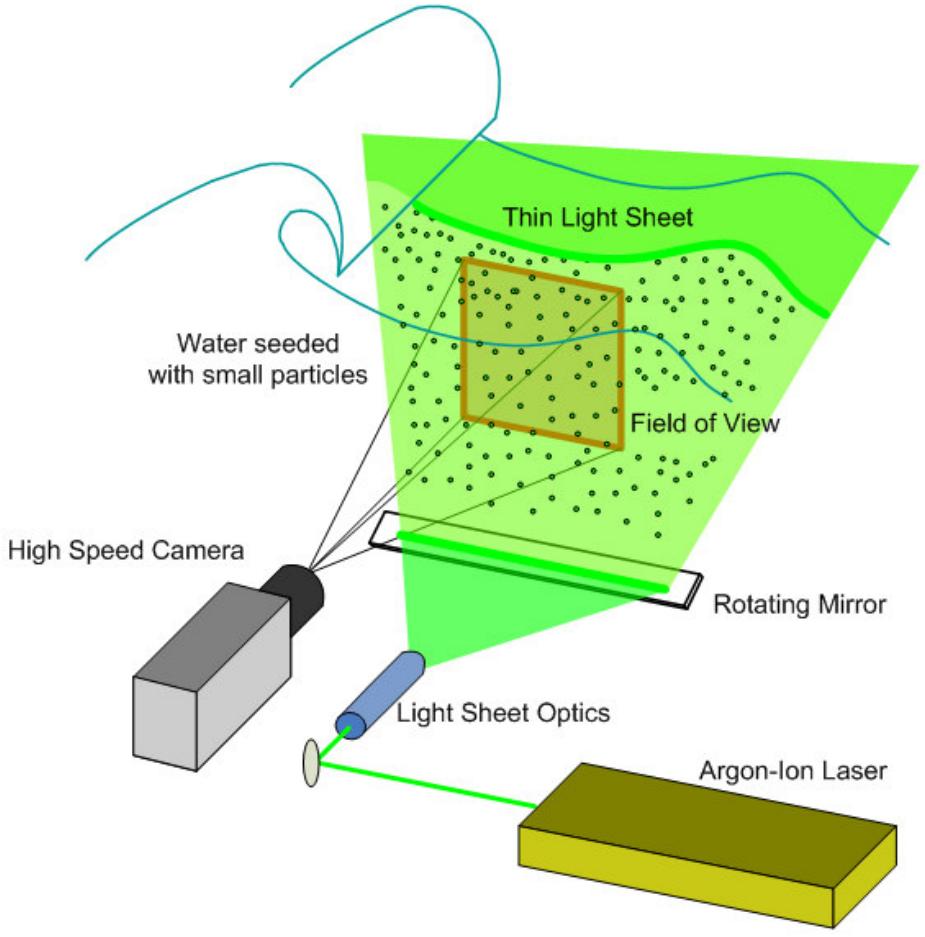

Fig. 5.8 Apparatus for the PIV system.

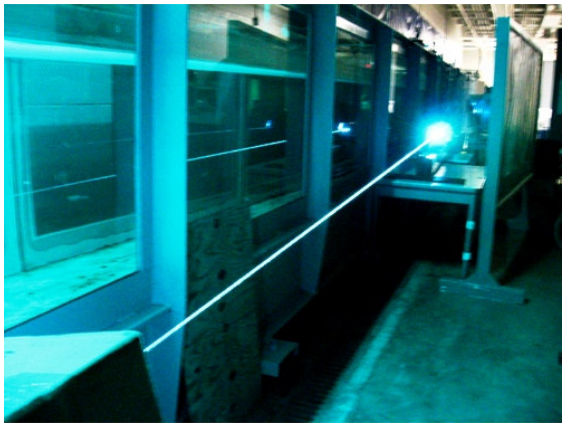

(a) continuous Argon-Ion laser

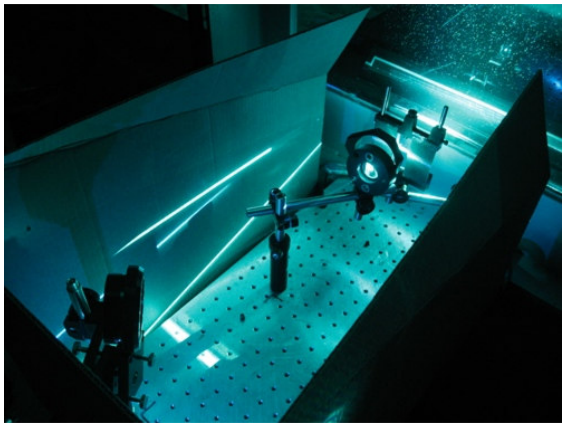

(b) light sheet optics

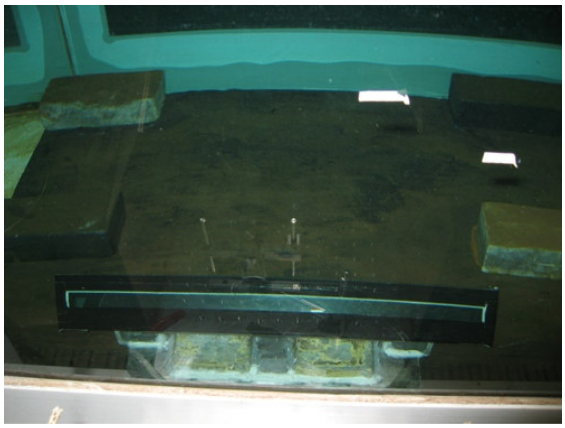

(c) rotating mirror at the bottom

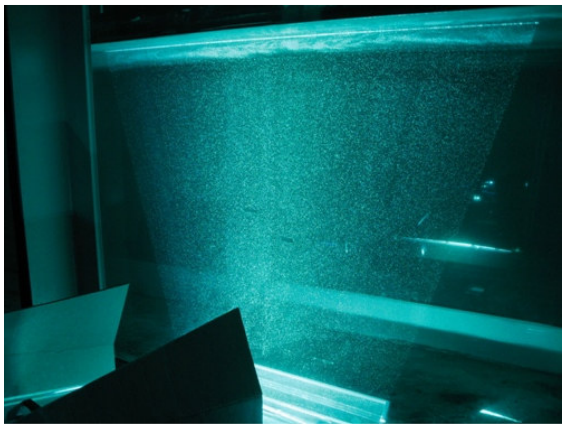

(d) wide light sheet generated

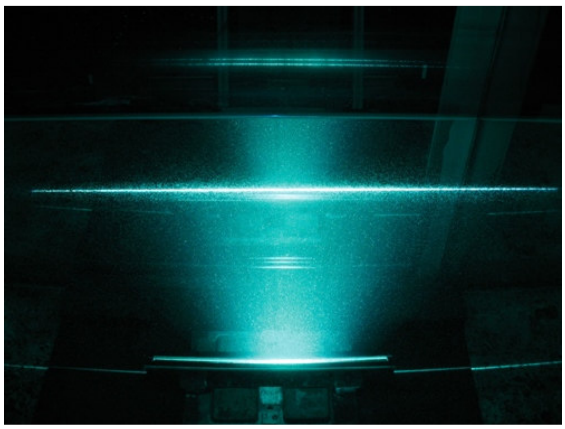

(e) with different view angle

(f) high speed camera and 3D traverse

Fig. 5.9 Pictures for the PIV measurement.

Fourteen and 24 fields of view were used to cover the entire flow field of both types of breaking waves including the aerated region in the PIV measurements. Note that the bottom located at z = - 0.80 m and a rotating mirror was equipped on the bottom. The sizes of the fields of view are fixed as 0.37×0.37 m^2 in these measurements. The location of each field of view can be seen in Fig. 5.1.

The velocity fields were calculated using an adaptive multi-pass algorithm with an initial interrogation window size of 64×64 pixels and a final window size of 32×32 pixels with a 50% overlap. Therefore, the resolution of the velocity vector is 16×16 pixels corresponding to 5.78×5.78 mm^2. Resolution of captured images is approximately 0.36 mm/pixel. The experiments were repeated 20 times with the same test condition at each FOV. It should be pointed out that temporal resolution of the PIV measurement is 2 ms. The mean and turbulence velocities were calculated from the ensemble average of the 20 instantaneous velocity fields in the same manner as BIV. Note that there are overlaps of 20 mm between adjacent fields of view. The fields of view using the mosaic concept cover the entire flow fields of both types of breaking waves with sufficient spatial and temporal resolutions.

5.6 Fiber Optic Reflectometer (FOR) Setup and Conditions

The Fiber optic reflectometer (FOR) technique was used to obtain the void ratio in the aerated region of both types of breaking waves. This technique based on the coherent mixing of scattered signal with Fresnel reflection signal from the tip of an optical fiber is capable of measuring the velocities and fraction ratio of all phases of the flow at a given point. Not only does FOR work in multiphase flows, it also provides simplicity and near

noninvasiveness because of its small dimension of the optical fiber (typical diameter 125 μm), high spatial resolution (typically less than 10 μm), and high temporal resolution (typically less than 50 μs).

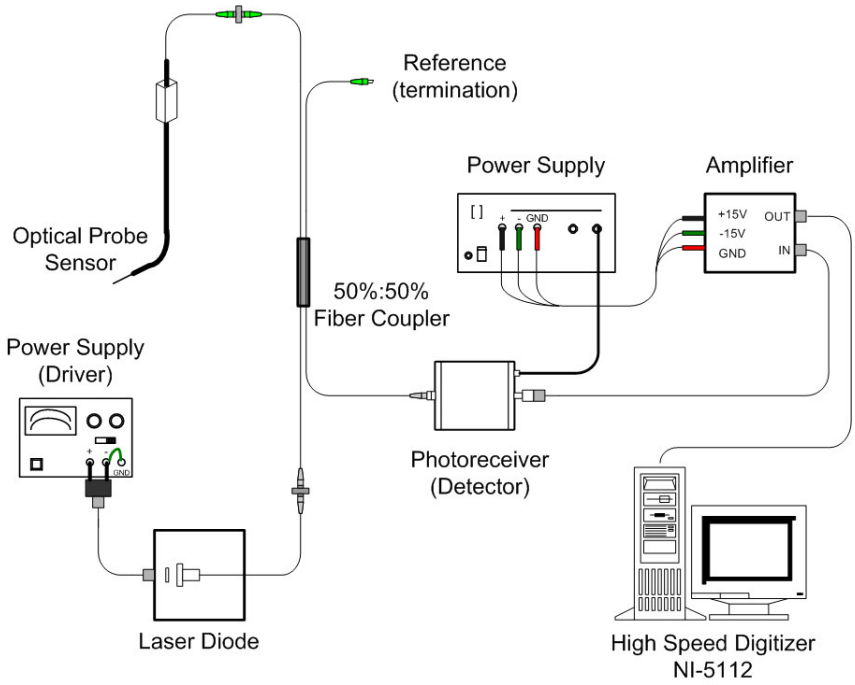

Fig. 5.10 Apparatus of the FOR system.

The apparatus of the FOR system is shown in Fig. 5.10 and is briefly described as follow: a continuous optical signal derived from a laser diode which is driven by a constant current is launched into a single-mode optical fiber and transmitted through a fiber coupler to the signal fiber inserted in the aerated region of the breaking waves. The coherently-mixed signal propagates back to the signal fiber through the fiber coupler which is then detected by a photoreceiver and acquired by a high-speed digitizer housed in a computer. By analyzing the signal, the velocity and fraction ratio of each phase can

be obtained. The principle, validation and application of the FOR technique are described in details in Chapters II, III and IV. Fig. 5.11 shows pictures for the void ratio measurements of the plunging breaker in the flume.

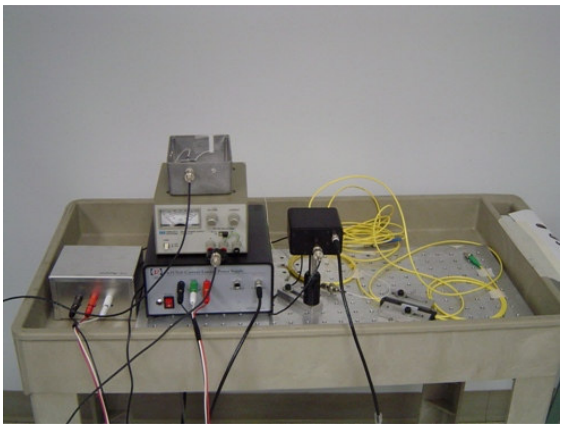

(a) FOR system

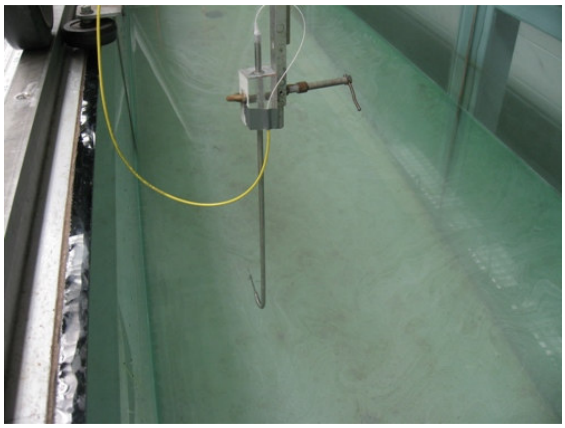

(b) optical sensor probe

(c) towing carriage

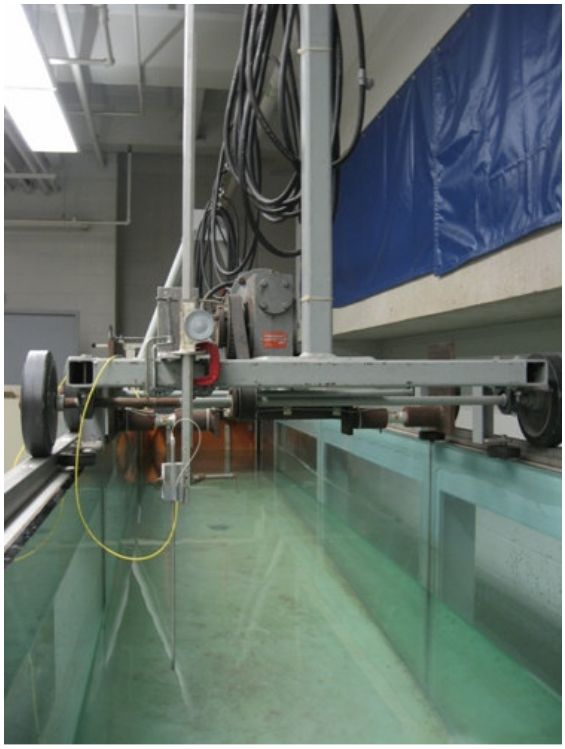

(d) probe with a towing carriage

Fig. 5.11 Pictures for the FOR measurements.

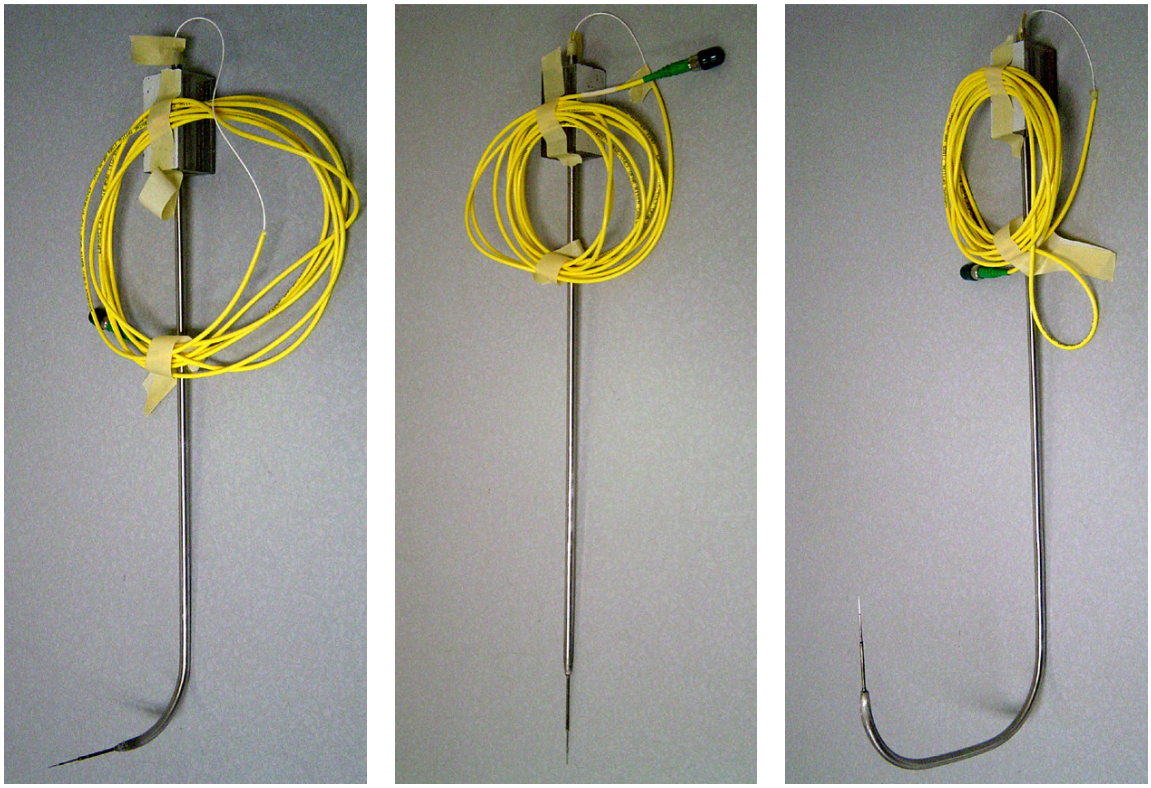

(a) u or -u probe (b) w probe (c) -w probe

Fig. 5.12 FOR measurement probes.

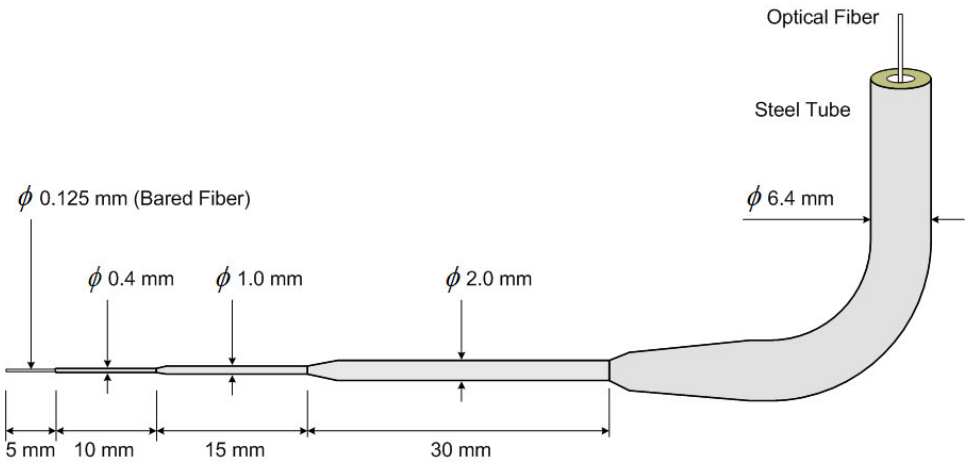

Fig. 5.13 Dimension of the FOR probe.

The locations of three measurement stations are shown in Fig. 5.1 and described in Table 5.2. The three stations are located in the middle of each splash-up region where they are fully developed.

Various probes depending on the measurement type of application are shown in Fig. 5.12. The probe shown in Fig. 5.12(a) was used in the void ration measurement. Fig. 5.13 shows the dimension of the FOR probe used in the void ratio measurements.

CHAPTER VI

QUALITATIVE DESCRIPTION OF WAVE BREAKING PROCESS

6.1 Introduction

Detailed description of the breaking wave process is presented in this chapter while quantitative results are presented beginning in Chapter VII. In addition to the quantitative measurements of breaking waves, it is also helpful to understand the breaking process by detailed qualitative description. It was possible to describe the breaking process of a strong plunging breaker due to various imaging techniques with a high speed camera. Diverse sizes of field of views, 1.20×0.60 m^2, 0.67×0.67 m^2, 0.37×0.37 m^2, and 0.20×0.20 m^2, were used to observe the breaking process. The camera frame rates used were 500 or 1000 *fps*. A large field of view was used for observation of the entire flow field while a small field of view is used to observe more detailed process such as wave impingements and splash-ups. Detailed description for each process of a plunging breaker can be shown in the next sections.

6.2 Qualitative Description of Wave Breaking Process

Although the origins of wave breaking in deep water and in the surf zone are different, the initial stage of wave breaking such as overturning of wave crests, first impingement and first splash-up of a plunging breaker are similar.

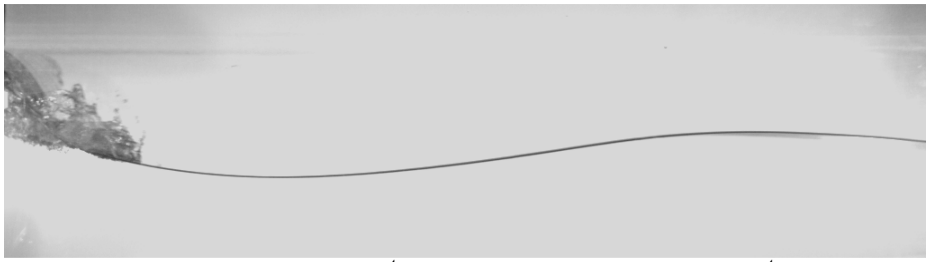

(a) t = 0.03 s (beginning of the 1st splash-up followed by the 1st impingement)

(b) t = 0.11 s (a small local crest between the two clockwise rollers)

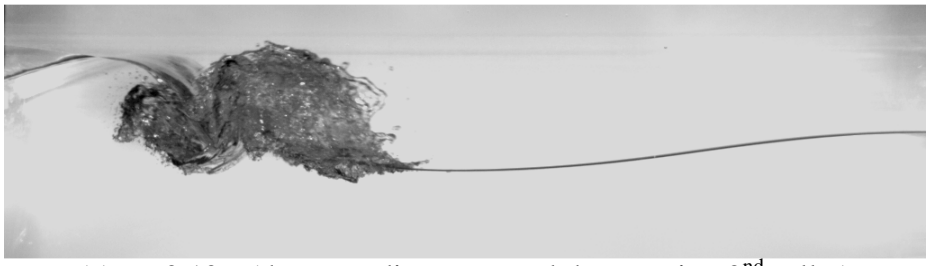

(c) t = 0.19 s (the ascending crest and the growing 2nd roller)

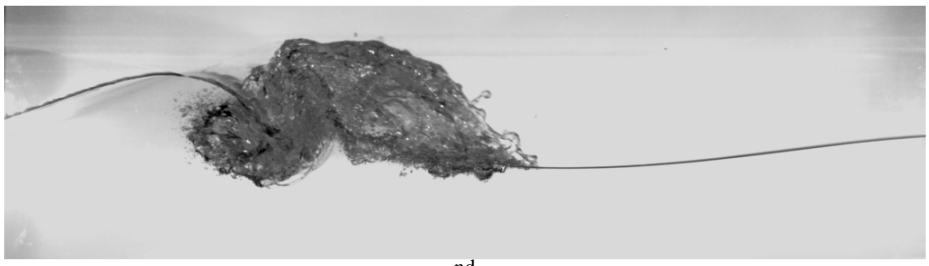

(d) t = 0.27 s (the fully developed 2nd roller & water spray impingement)

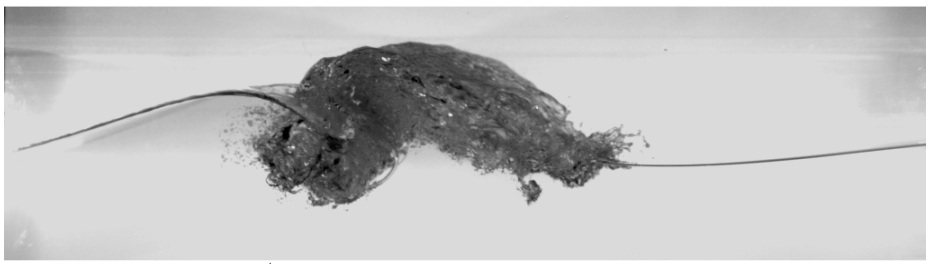

(e) t = 0.35 s (the 1st backward impingement from the ascending crest)

Fig. 6.1 Images of the wave breaking process in a plunging breaker.

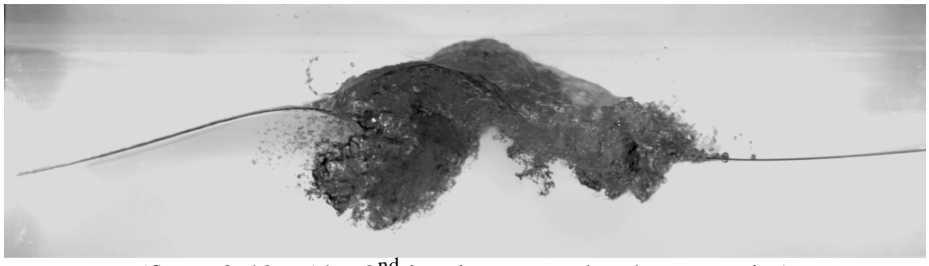

(f) t = 0.43 s (the 2nd impingement by the water jet)

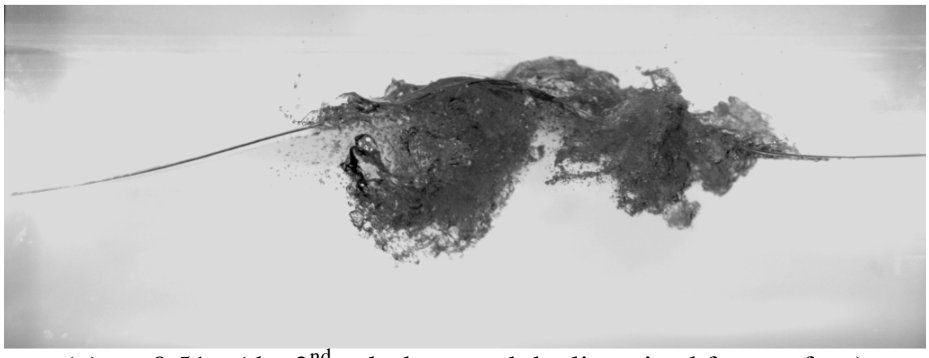

(g) t = 0.51 s (the 2nd splash-up and the linearized free surface)

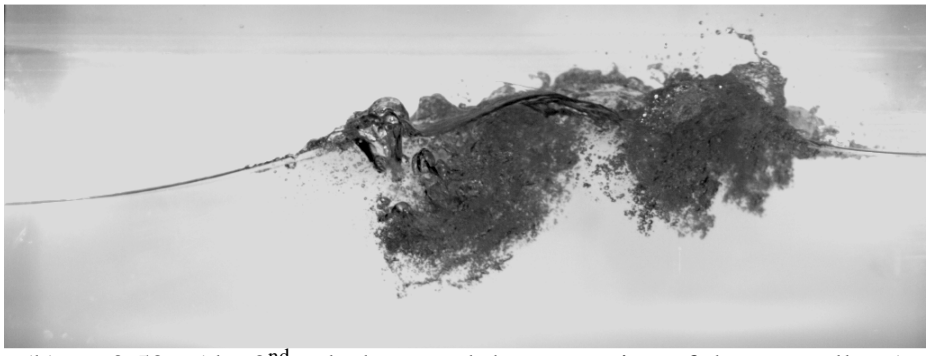

(h) t = 0.59 s (the 2nd splash-up and the separation of the two rollers)

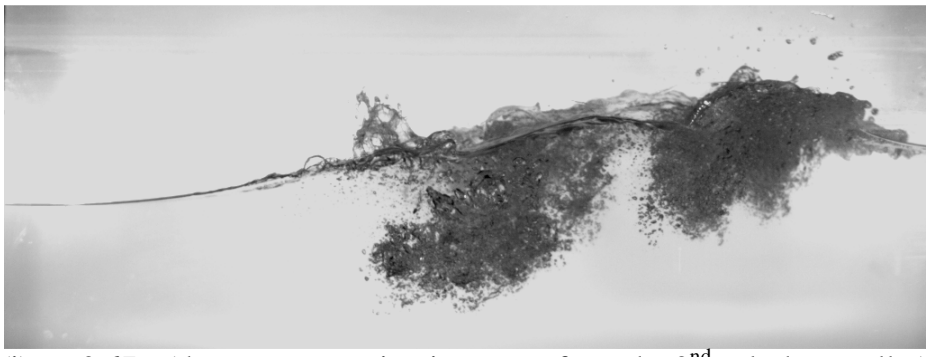

(i) t = 0.67 s (the water spray impingement from the 2nd splash-up roller)

Fig. 6.1 (Continued).

(j) t = 0.75 s (the 3rd splash-up which cannot be clearly seen here)

(k) t = 0.83 s (one wave period after the 1st impingement)

(l) t = 0.91 s (floating large bubbles caused by the 1st impingement)

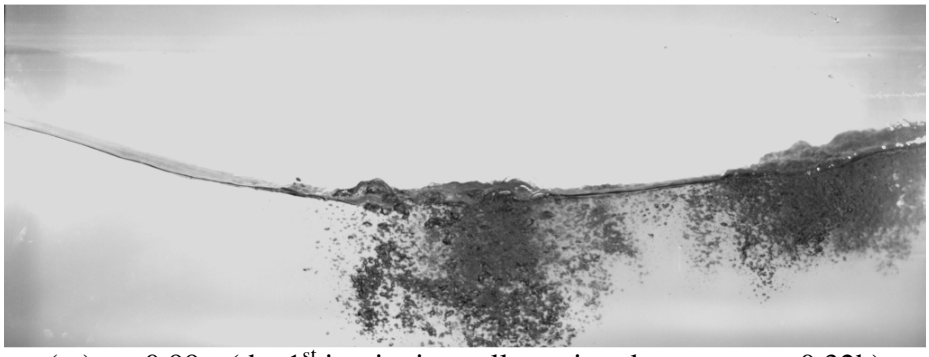

(m) t = 0.99 s (the 1st impinging roller going down to z = - 0.32h)

Fig. 6.1 (Continued).

(n) t = 1.19 s

(o) t = 1.39 s

(p) t = 1.79 s

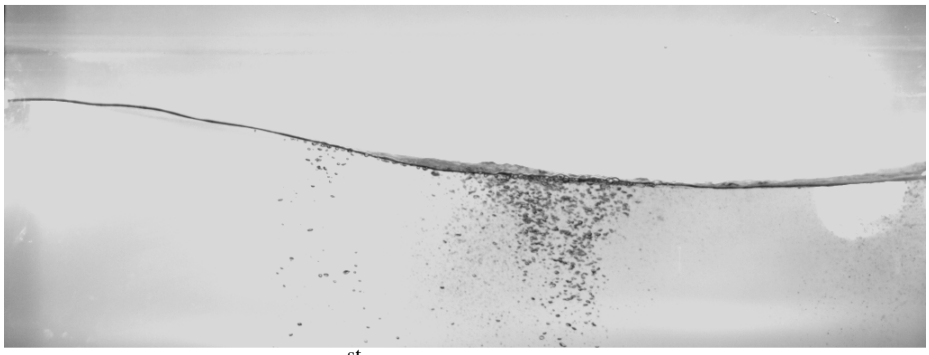

(q) t = 2.19 s (bubbles from the 1st roller disappear about t = 3 s which is about 3.6T)

Fig. 6.1 (Continued).

In shallow water, decreasing water depth and bottom friction make waves larger with more steepness (e.g. shoaling waves) and increased velocity of the wave crest overturning into front surface of the waves. On the other hand, in deep water with a constant water depth, waves sometimes become very big due to focusing of waves with various frequencies generated by wind or currents. A strong plunging breaker investigated in this study has several stages in the breaking process which are distinguishable by observing the breaking process. In addition, by using some quantitative information such as velocity and vorticity of the entire flow field provides better understanding of the process. Fig. 6.1 shows the breaking process. The original pictures were taken using a high speed camera with a frame rate of 500 *fps* and covered the third window of the wave tank corresponding to eight fields of view (FOV 3 to FOV 10) in the PIV measurement as shown in Fig. 5.1. A total of three impingements and three splash-ups of air-water mixture were observed as shown in Fig. 6.2. During this process, wave period and wavelength are decreased gradually.

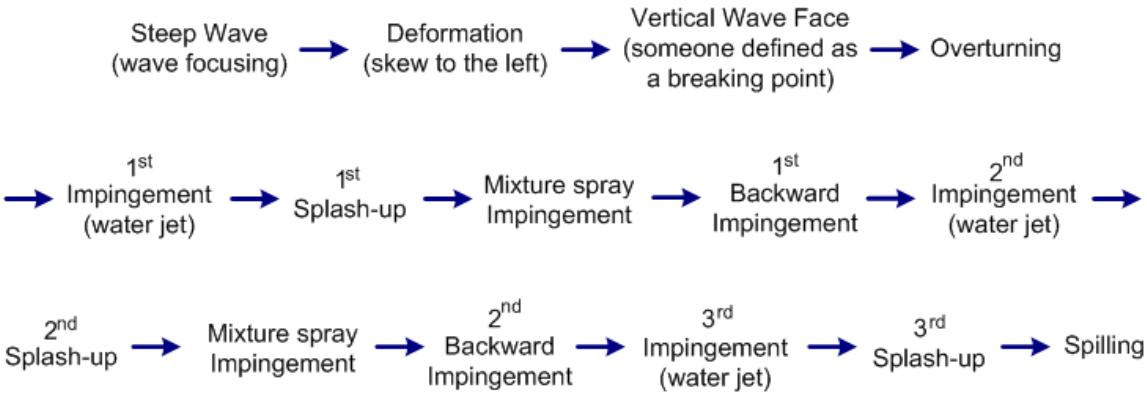

Fig. 6.2 Breaking process of a plunging breaker.

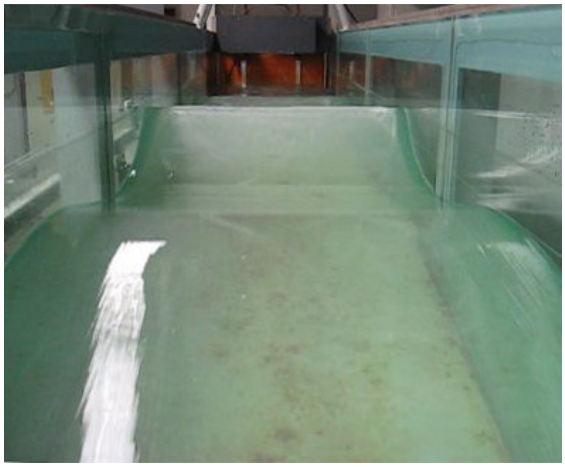

(a) wave deformation

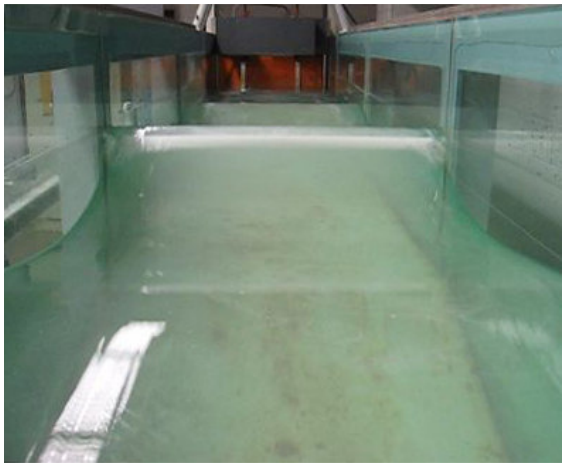

(b) overturning jet

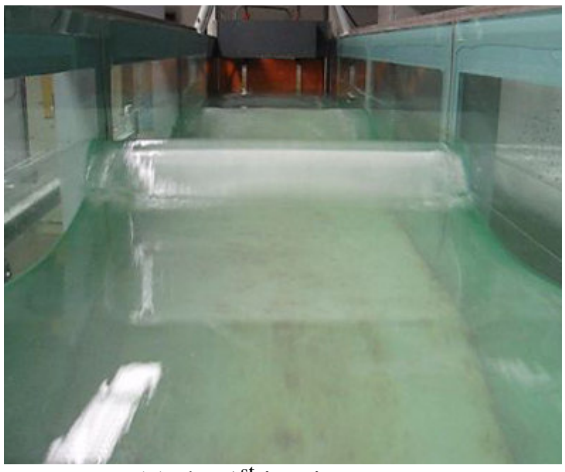

(c) the 1st impingement

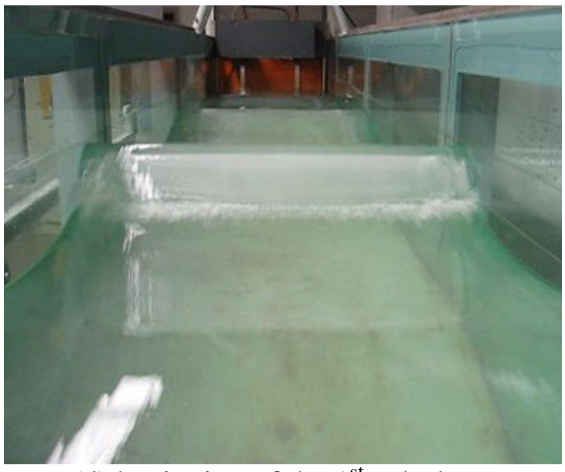

(d) beginning of the 1st splash-up

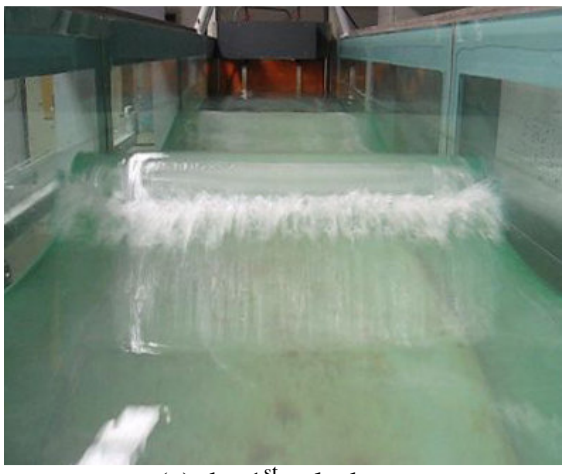

(e) the 1st splash-up

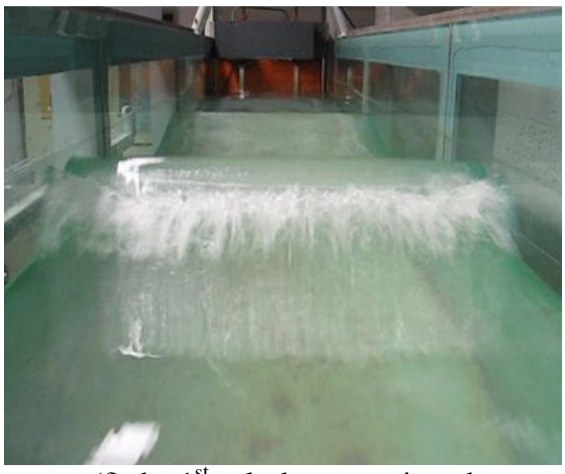

(f) the 1st splash-up continued

Fig. 6.3 Front view of a plunging wave in a 2D wave tank.

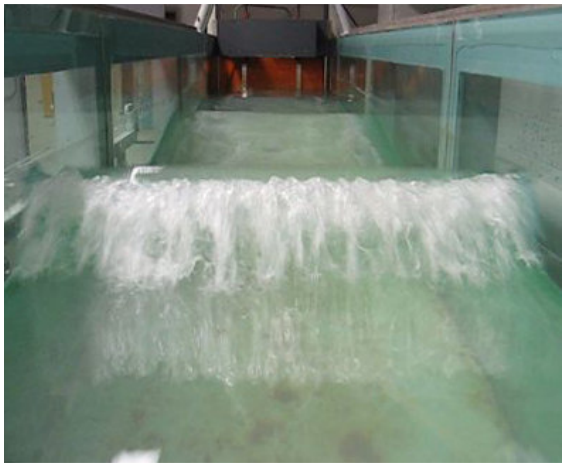

(g) the mixture spray impingement

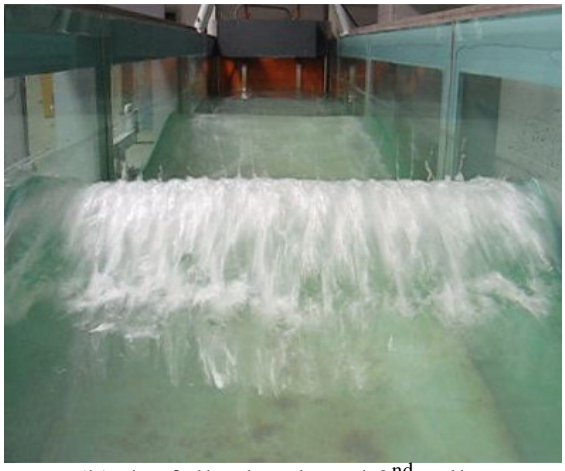

(h) the fully developed 2nd roller

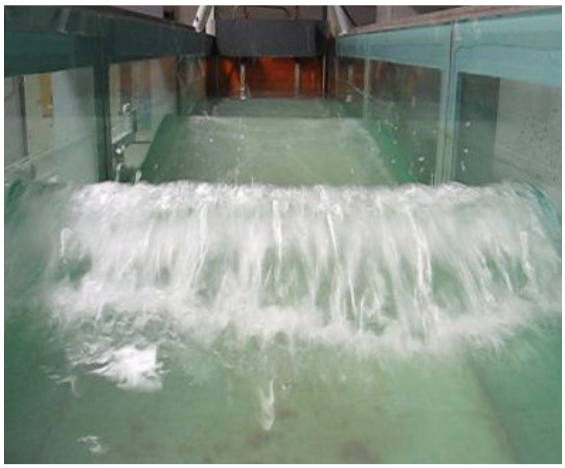

(i) the mixture spray impinging continued

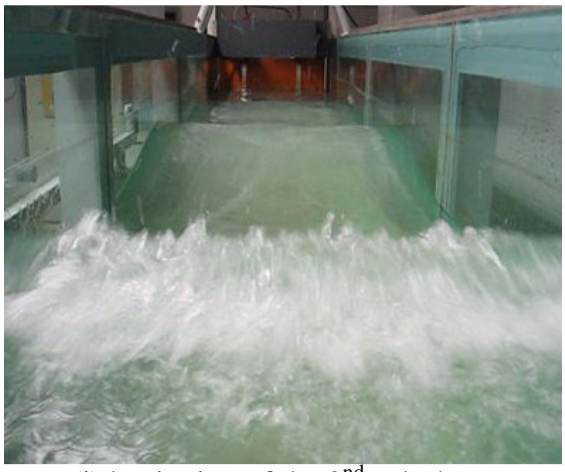

(j) beginning of the 2nd splash-up

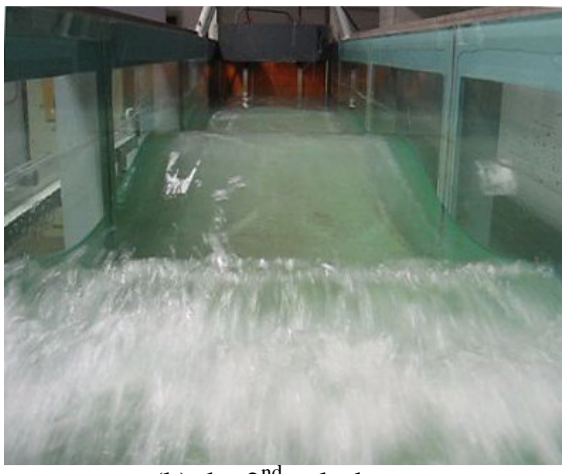

(k) the 2nd splash-up

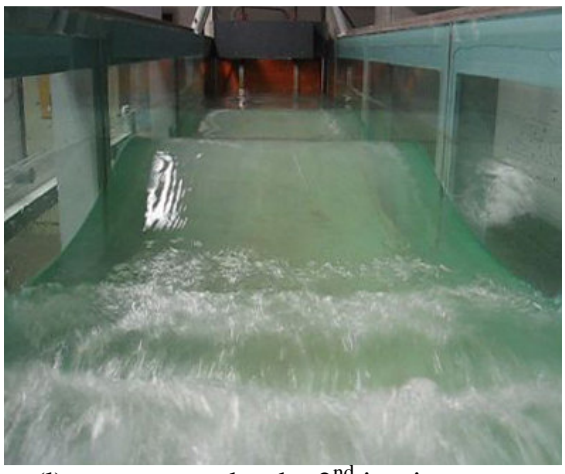

(l) a wave scar by the 2nd impingement

Fig. 6.3 (Continued).

Fig. 6.3 shows the front views of the breaking process of the plunging breaker generated in the two-dimensional wave tank in the department of Civil Engineering at Texas A&M University. The images were captured by a portable digital camera. More details on each process are discussed in the following sections.

6.2.1 Deformation of Wave

A wave becomes very steep but symmetric in shape as a front wave, which is smaller and shorter, is overcome by a bigger and longer wave. The primary wave starts to deform its own shape shortly so the shape of the wave is not symmetric any more but skewed to the left. Note that wave direction in the measurement is from the left to the right. The front face of the wave crest becomes vertical as the wave crest velocity which is faster than the wave phase speed is increased. It is possible that large upward momentum from near the trough level is transferred to the horizontal momentum of the crest. The wave has large energy before breaking its shape.

Fig. 6.4 shows the deformation and overturning process of a plunging breaker. As shown in Fig. 6.4(b), the wave front face becomes vertical, which is defined as a breaking point by some researchers. Location and time for this instance are x = - 0.42 m and t = - 0.2 s as x = 0 and t = 0 at the first impingement point. The first impingement point is defined as the breaking point in the present study. Overturning of the crest can be seen in Fig. 6.4(c) and (d). The pictures are instantaneous PIV images in PIV FOV1 which are taken at 500 fps with a high speed camera.

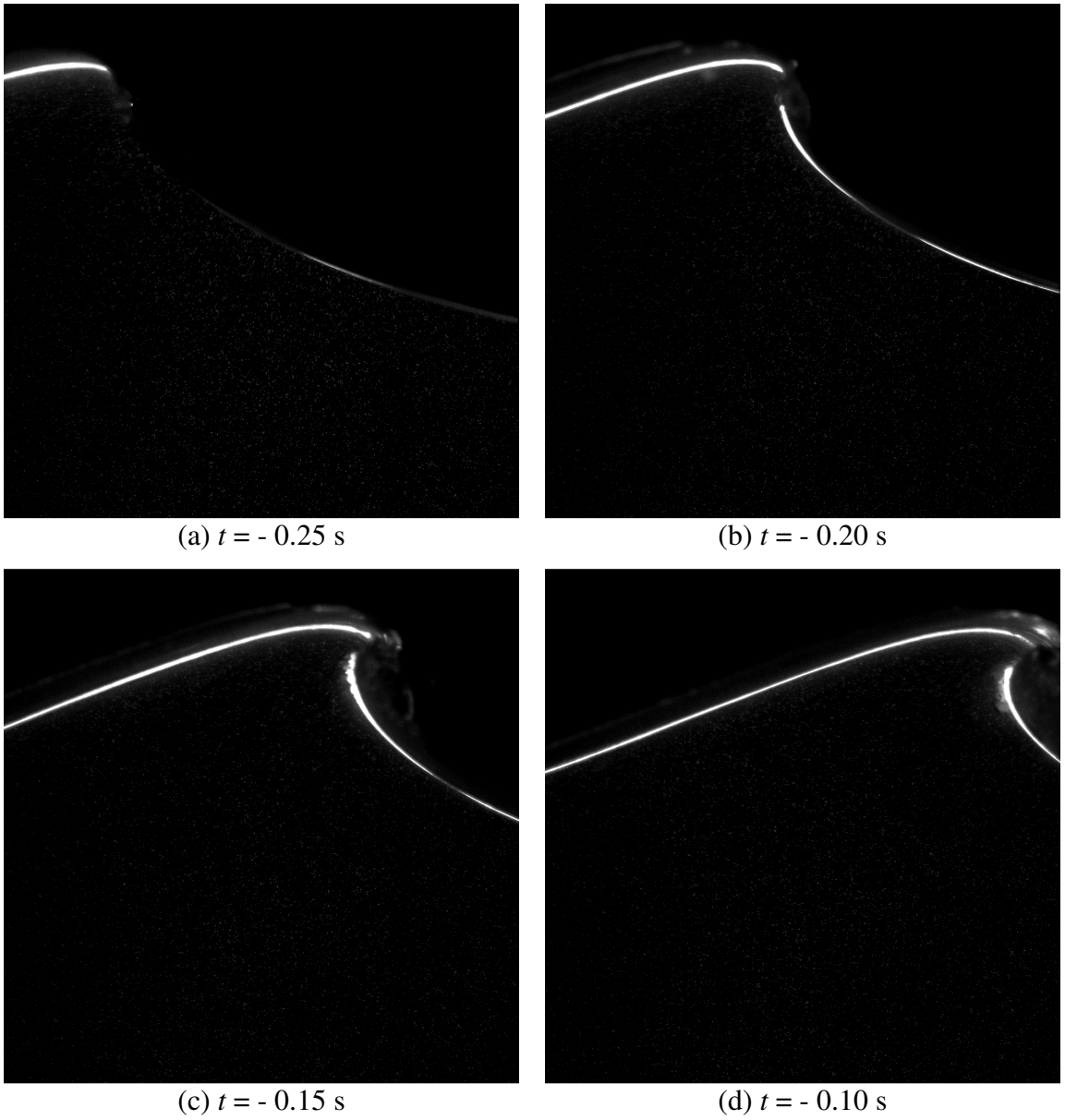

(a) t = - 0.25 s (b) t = - 0.20 s

(c) t = - 0.15 s (d) t = - 0.10 s

Fig. 6.4 Wave deformation and overturning.

6.2.2 The First Impingement and the First Splash-up

Overturning and impinging processes can be clearly seen in Fig. 6.5. The process from the overturning to the first impingement cannot be seen with one field of view due to a steel column whose width is about 0.15 m (every 1.54 m at the glass wall of the

wave tank in our laboratory as shown in Fig. 5.1 and Fig. 5.5). The location of the breaking point was moved to the right about 0.3 m with almost identical shape to observe the overturning and impinging processes continuously in a field of view.

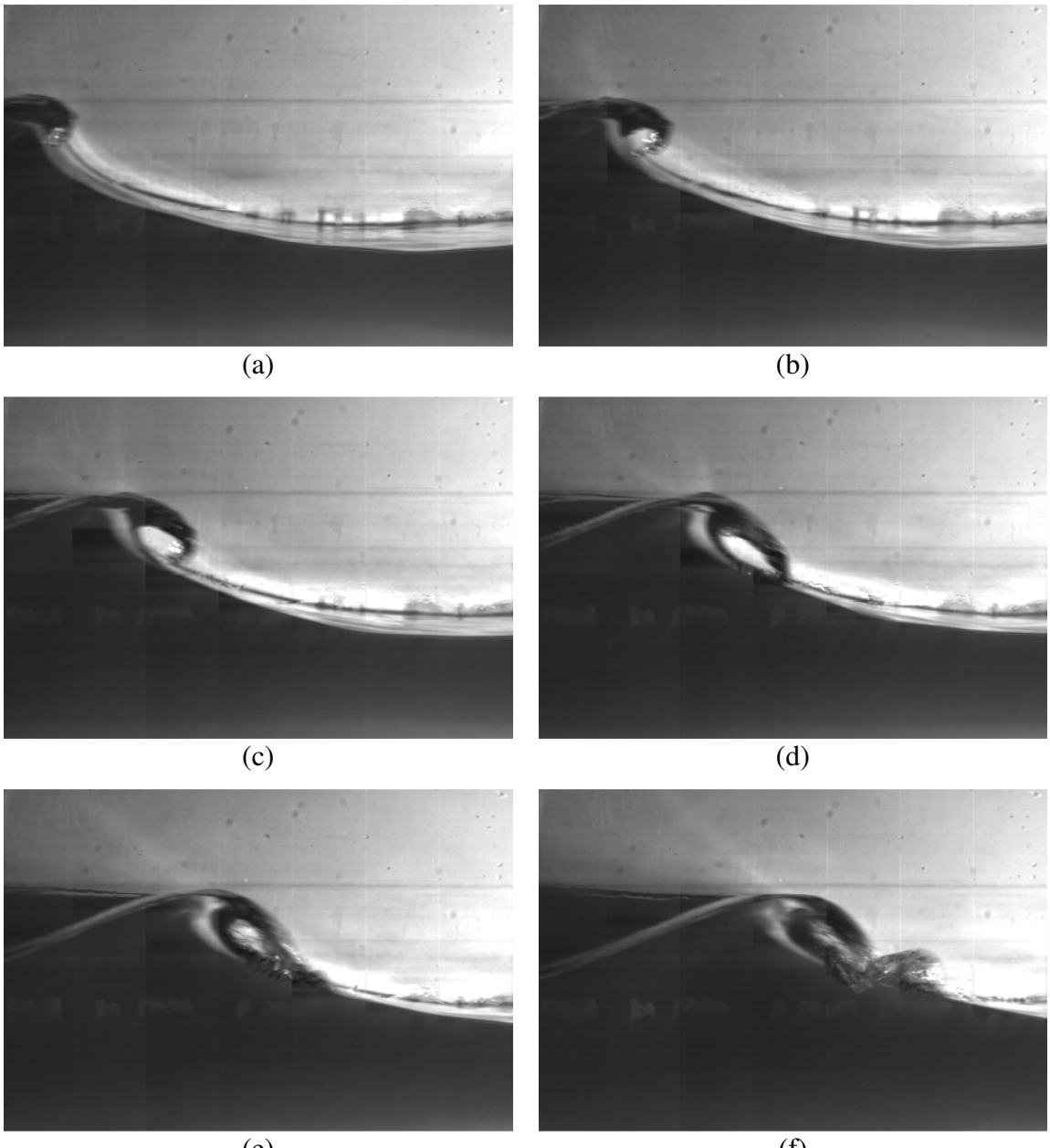

(a) (b) (c) (d) (e) (f)

Fig. 6.5 Overturning and the first impingement.

It is possible to move the location of the breaking point by controlling the frequencies and amplitudes of the input waves. This wave shows a beautiful curl of a overturning jet. The air pocket inside the curl is entrained into the first roller. It should be pointed out that all the entrained air is penetrated under the free surface without any rebound during the process of the first impingement and splash-up, disappearing within four wave cycles. Fig. 6.5(e) and (f) show the first impinging moment and the beginning of the first splash-up respectively. The first roller and the first splash-up (the second roller) are generated due to the strong first impingement which has a large momentum because its phase is mainly water with a large velocity about 1.5C, where C is the wave phase speed. A new wave crest is generated by the first impingement as shown in Fig. 6.6. This wave plays an important role for the second impingement that will be discussed in the next section. It is more interesting to observe the process after the first splash-up followed by the first impingement. Fig. 6.6(a) shows the beginning of the first splash-up. The impinging jet penetrates the front wave surface rather than rebounds of the impinging jet. When the overturning water jet hits a front water surface with large momentum, the front surface is broken and pushed up immediately with a small crest [Fig. 6.6(a)]. It is considered that the pushed-up water whose original momentum proceeds forward and upward is accelerated and explodes vertically due to mass conservation and momentum transferred from impinging jet. The size of small crest and the second roller are increased more and more because the impinging roller provides a forward and downward momentum continuously as shown in Fig. 6.6(b) and (c).

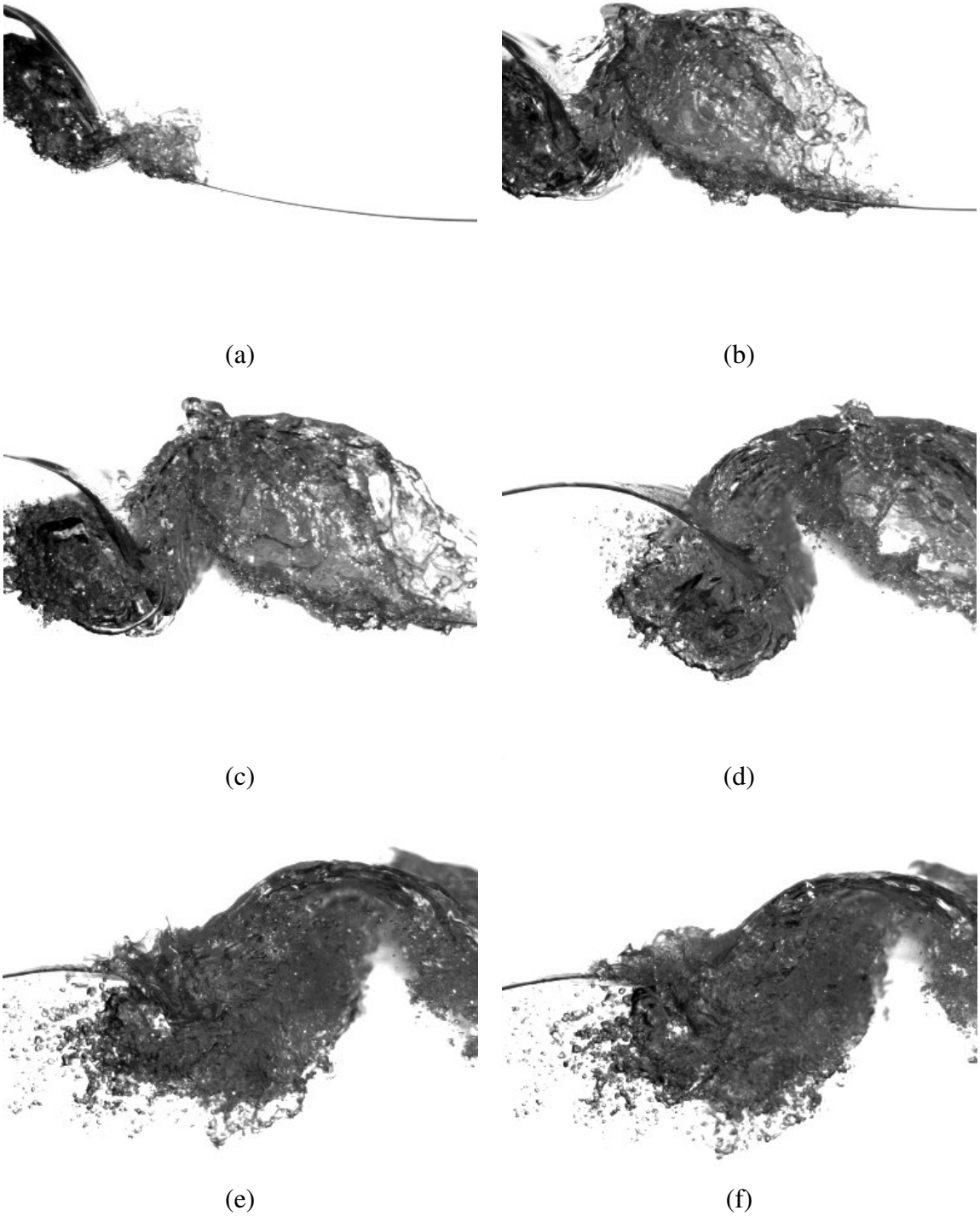

(a) (b)

(c) (d)

(e) (f)

Fig. 6.6 The first splash-up followed by the first impingement.

Two large rollers having clockwise rotation are separated by the new ascending water crest. The air-water mixture in the rear side of the new crest (vertical water column) has a counterclockwise vorticity while the air-water mixture in the front side of the new crest has a clockwise vorticity. The free surface elevation at the first splash-up (the second roller) is slightly lower than that at the first impingement. As the upward momentum of the ascending water crest weakens (although it still has horizontal momentum), the new water crest becomes obliquely ascending toward the rear wave. This is because the first roller provides more momentum to the lower side of the new wave as shown in Fig. 6.6(d). The air-water mixture in the rear part of the new crest begins falling down due to the loss of its kinetic energy causing the first backward impingement onto the first impinging roller and overtopping on the rear wave which is an original primary wave. This backward impinging process can be seen in Fig. 6.6(e) and (f). A water jet is observed due to the high pressure between the impinging roller and the backward impinging part of the newly ascending crest as shown in Fig. 6.7. This occurs because the velocity of the impinging roller is higher than that of the upper part of the ascending water. It should be pointed out that the first roller having a forward and downward momentum provides the new local crest with horizontal momentum at this moment, so the obliquely ascending crest becomes symmetric and a new primary wave as shown in Fig. 6.6 (d), (e) and (f). The two large rollers are separated by the new primary wave. Additional description with sketches for the first process can be seen in Fig. 6.8. The new primary wave impinges (the second impingement) and causes the second splash-up. It will be discussed in the next section in detail.

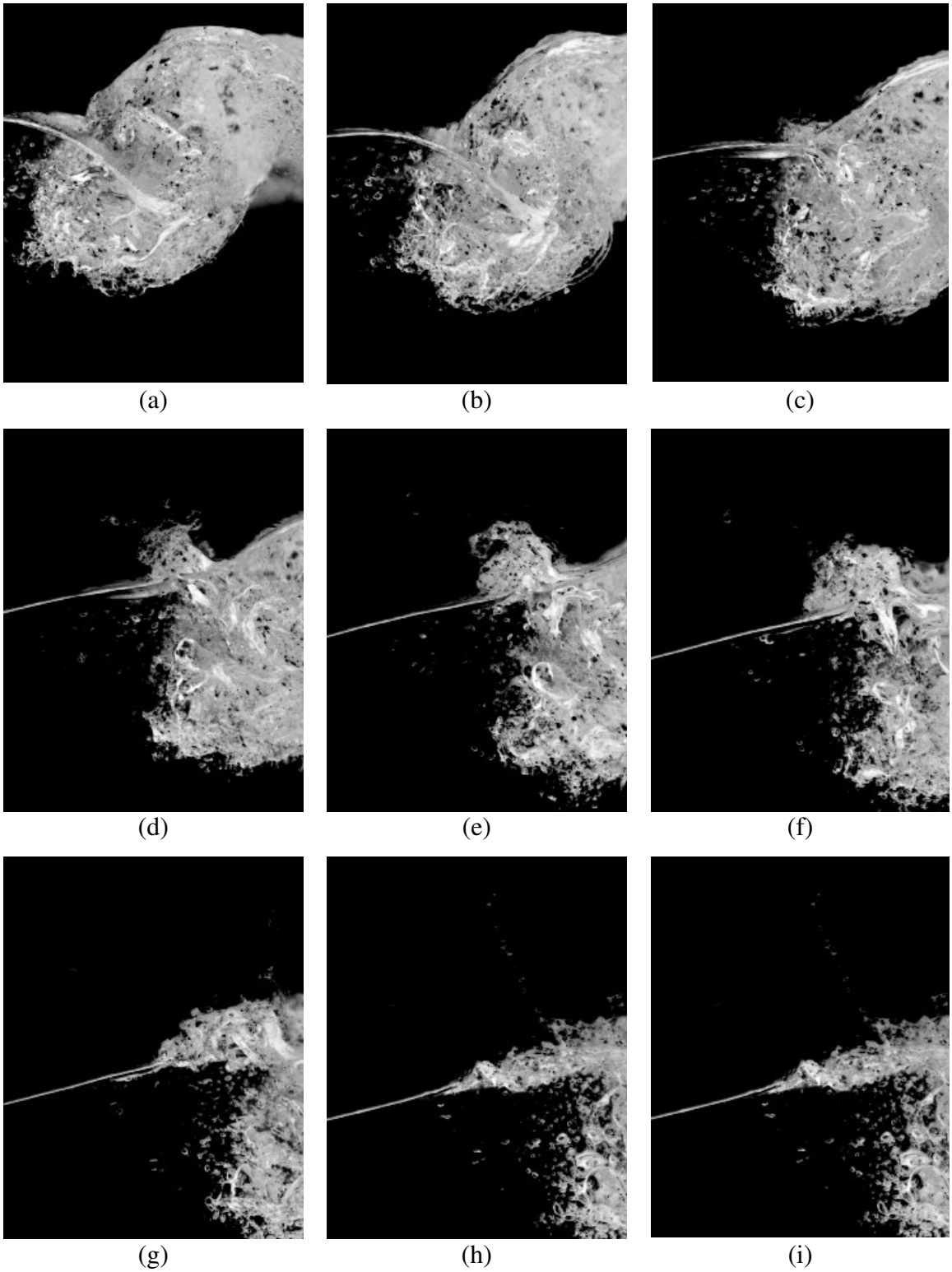

Fig. 6.7 The first backward impingement and water jet.

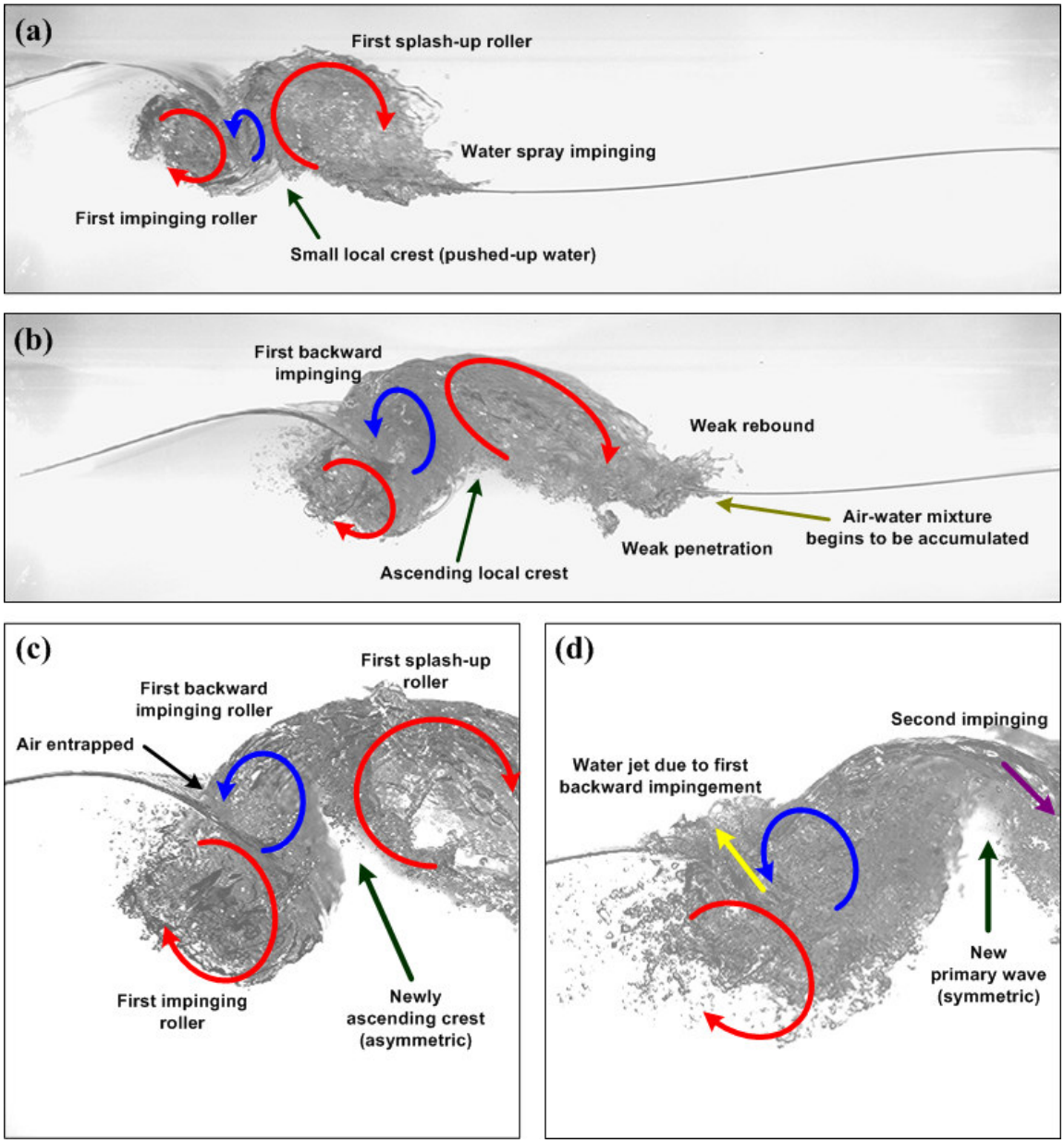

Fig. 6.8 Cartoons for the first process.

6.2.3 The Second Impingement and the Second Splash-up

The process of the second splash-up followed by the second impingement is different from the process of the first splash-up discussed in the previous section. The

air-water mixture spray caused by the first impingement is continuously impinged on the front trough region during the process of the first splash-up. The first splash-up starts immediately at the first impingement due to the large momentum of water jet. On the contrary, the mixture spray impingement from the first splash-up roller does not cause the splash-up immediately. It is believed that the difference is a combination of two possible reasons. First, the second impingement does not have enough momentum to generate another splash-up because the mixture density is very low (very high void ratio) although the mixture velocity is high. Second, the mixture spray impinges on the trough region which does not have a upward and forward momentum. Note the vertical location of each impinging point is always above the still water level ($z > 0$). At the second impingement, the part of the mixture spray penetrates the wave surface slightly near the trough or rebounds very slightly as shown in Fig. 6.9(a) and Fig. 6.9(b). Due to this phenomenon, most mixture spray from the first splash-up is accumulated on that location without any splash-up process as shown in Fig. 6.9(c). At first the accumulated mixture was just a small size eddy. However, the volume of the accumulated mixture, turbulence intensity and vorticity are increased. At the end of the mixture spray impingement, the new primary wave which is formed in the first impingement plunges on the location of the accumulated mixture with large momentum (main phase of flow is water). The wavelength and wave period are decreased more and more. Additional sketches for the second process can be also seen in Fig. 6.10.

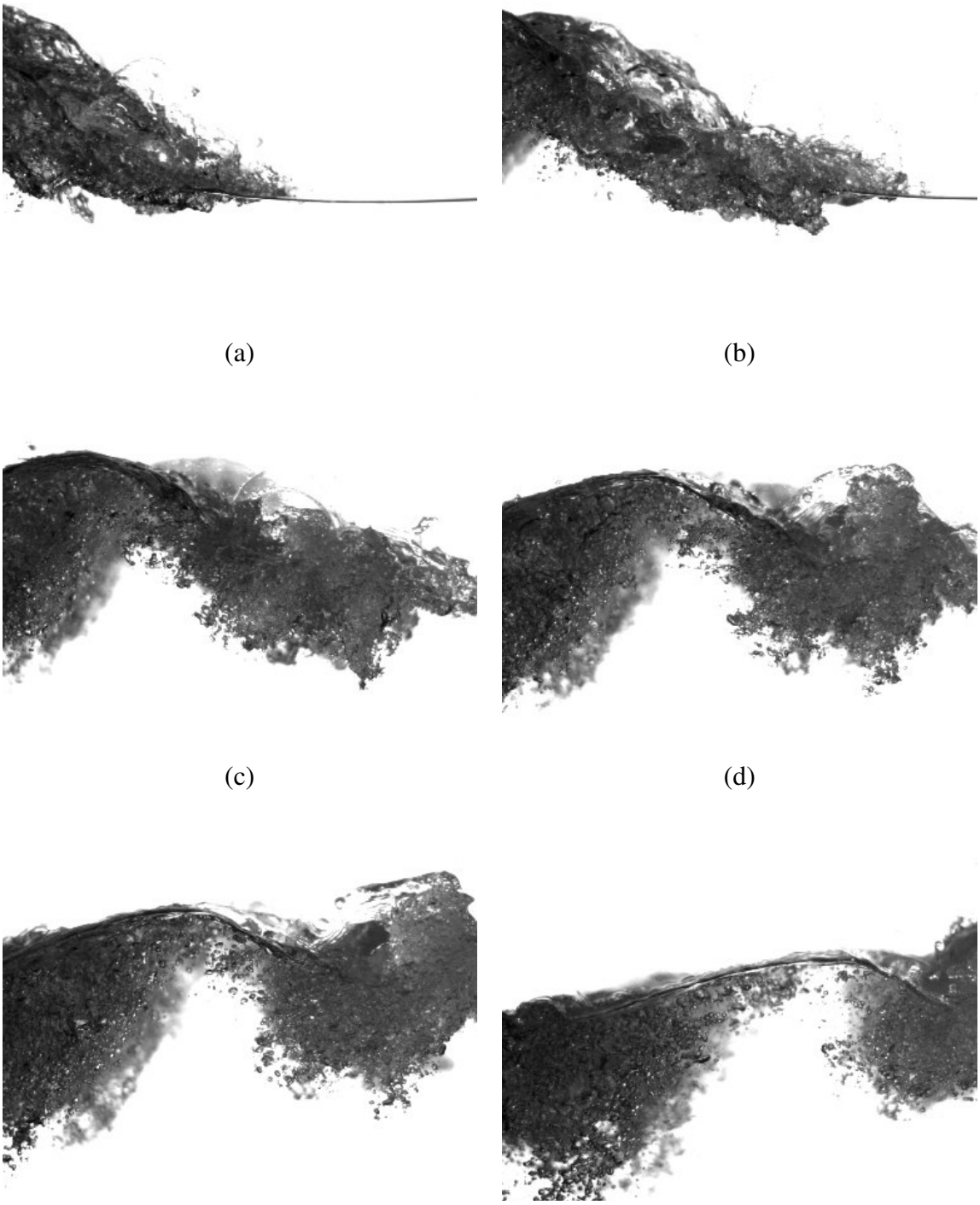

(a) (b)

(c) (d)

(e) (f)

Fig. 6.9 The second splash-up followed by the second impingement.

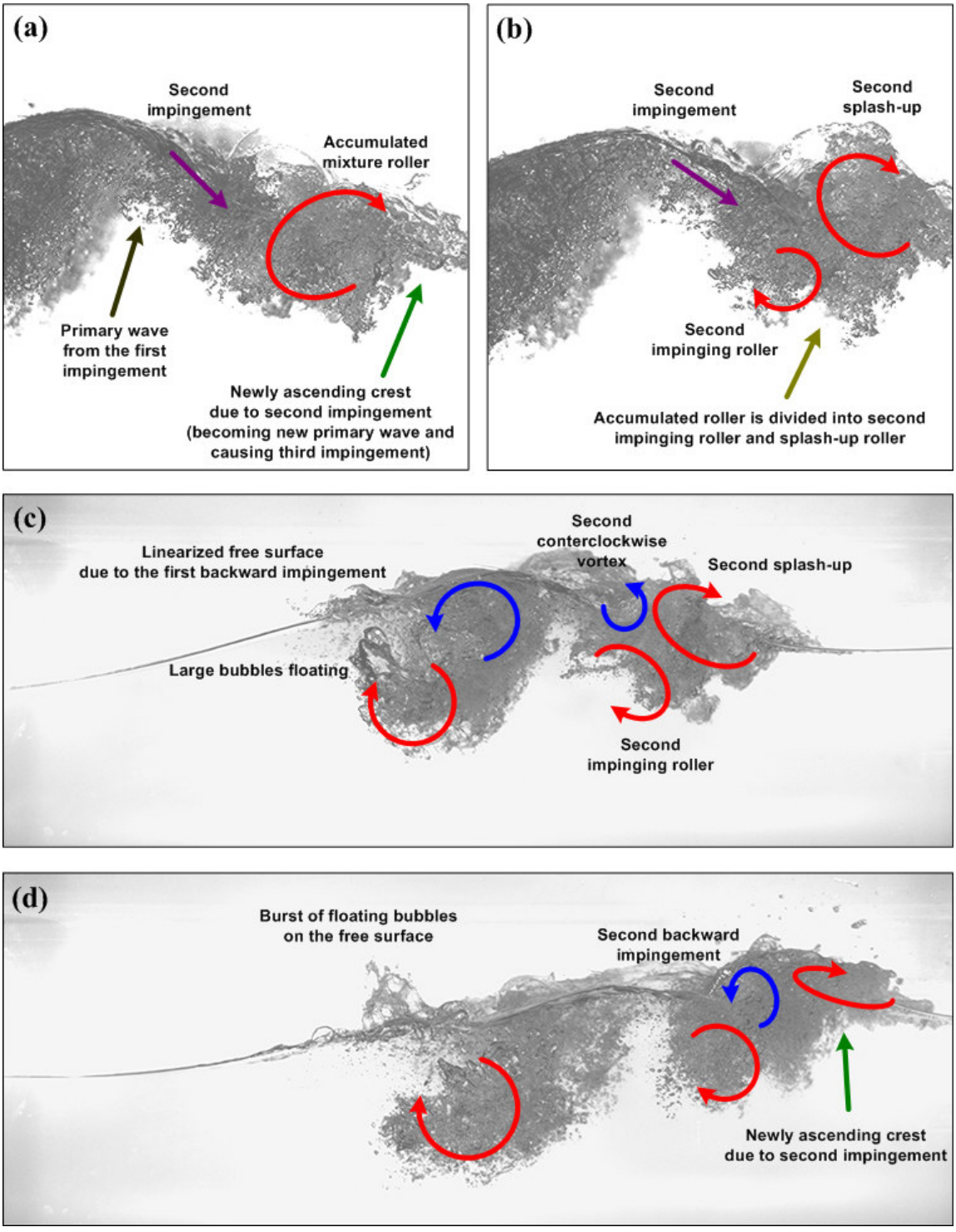

Fig. 6.10 Cartoons for the second process.

Fig. 6.9(c) shows the beginning of the second impingement by the water jet from the new primary wave. The second splash-up occurs immediately after the second impingement by water jet from the new primary wave as shown in Fig. 6.9(d). The accumulated mixture roller is divided into two parts due to the second impingement. The upper part of the mixture roller is splashed up (by the pushed up water below the mixture roller) with significantly increased velocity due to its low density while the lower part of the mixture remains similar to the first impinging roller. Fig. 6.9(d)-(f) show the second splash-up.

6.2.4 The Third Impingement and the Third Splash-up

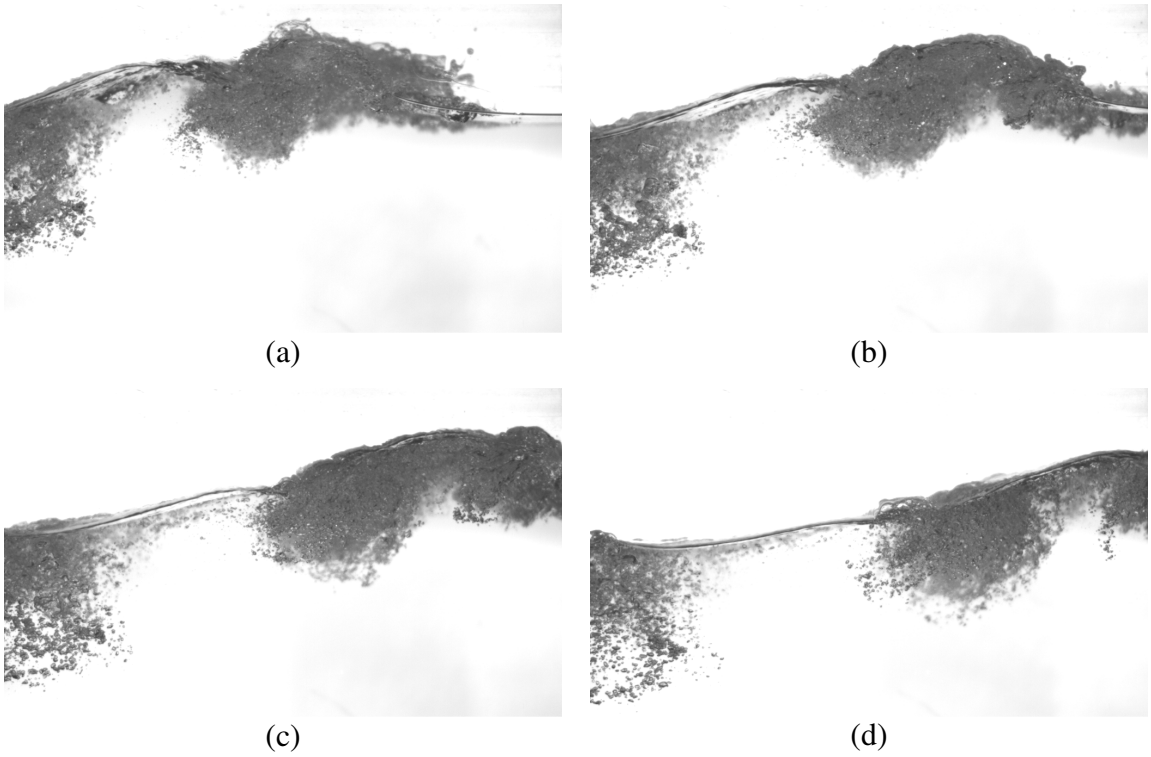

Fig. 6.11 The third impingement followed by the second splash-up.

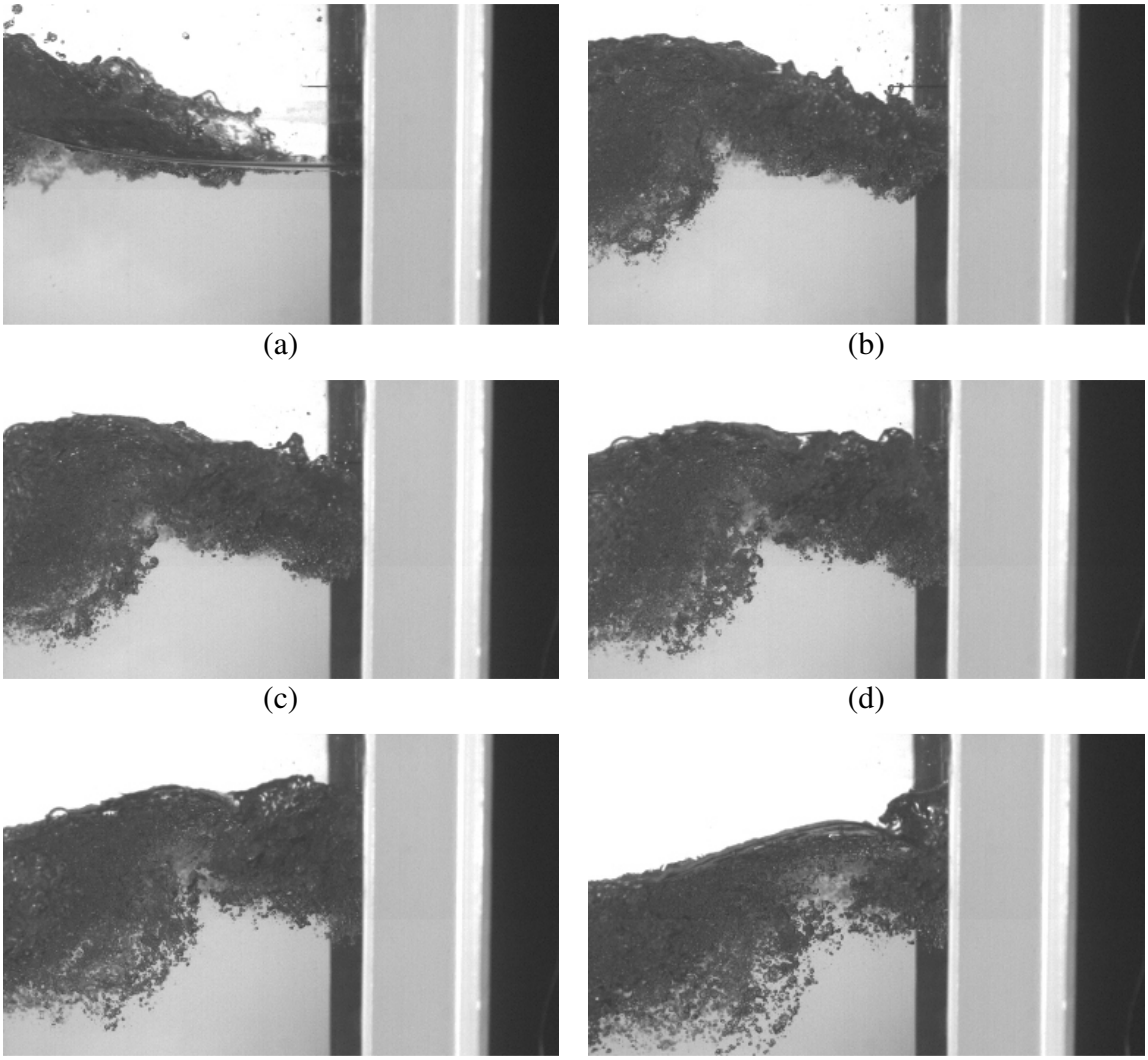

Fig. 6.12 The third splash-up followed by the third impingement.

The formation and process of the third impingement and splash-up are very similar to those of the second impingement and splash-up. Major difference is their scale. The scales of the strength and time at the third impingement and splash-up are much smaller. The size of the eddy is smaller due to the energy cascade. Fig. 6.11(a) and Fig. 6.12(a)

and (b) show the mixture impingement on the trough region and Fig. 6.11(b) and Fig. 6.12(c) and (d) show the third impingement causing the third splash-up. The third splash-up can be seen in Fig. 6.11(c) and Fig. 6.12(e)-(g). It was observed that the third process was a transition between a plunging and spilling wave. The small probe is an optical fiber sensor of the FOR system used to measure the void ratio at the third splash-up region.

6.2.5 Spilling Wave Phases

The significant turbulent motion is decreased rapidly just after the third splash-up process. There is a tiny forth impinging and splash-up whose process is very similar to a weak spilling wave. Fig. 6.13 shows the propagation of small eddies which have a low void ratio with the location of field of view corresponding to the PIV FOV11-14 shown in Fig. 5.1. The mixture velocity is similar to the water particle velocity. The size of the small eddies becomes much smaller. The turbulent bore region remains until about 1.65 s which is twice as long as the period of the primary wave in the pre-breaking region. Note that there are still bubbles and turbulence by the first impingement near the location of $x = 0.5L$ and it remains until about four times the wave period. Although this region is less important, it is good to know the total time and length of the breaking process. The total time of the breaking process is about double the wave period of the primary wave. Also, the total distance of the breaking process is also double the wavelength of the primary wave. An approximate time and location of the breaking process is presented in the next section.

(a) t = 1.02 s

(b) t = 1.12 s

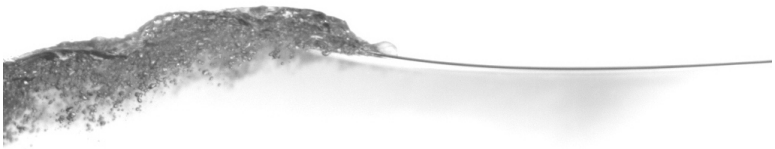

(c) t = 1.22 s

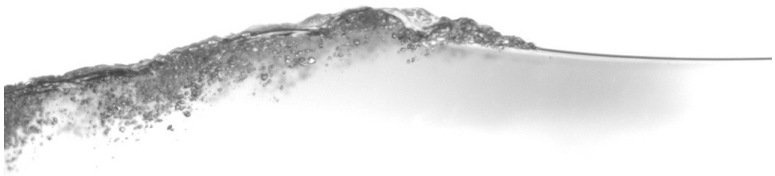

(d) t = 1.32 s

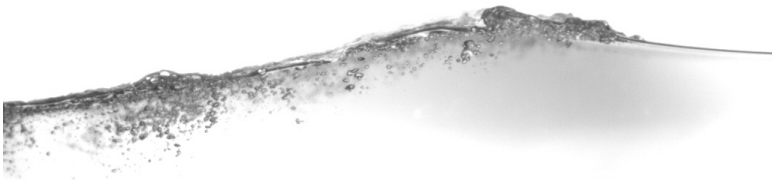

(e) t = 1.42 s

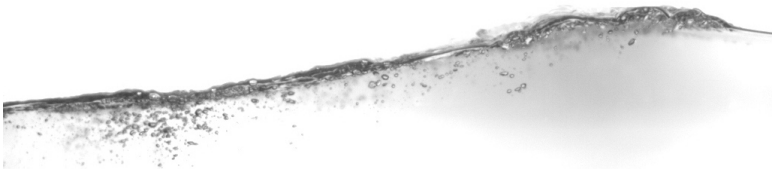

(e) t = 1.52 s

Fig. 6.13 Spilling wave ($x > L$).

6.3 Time and Location of the Breaking Process

Information on time and location of the breaking process was estimated briefly as shown in Table 6.1 and Table 6.2. In some cases, time or location of the process cannot be defined exactly. However this information may provide a brief insight for understanding the breaking process. In addition, it will be useful for the analysis and understanding of the quantitative results. More detailed discussion about each process is presented with various quantitative results beginning in Chapter VII.

Table 6.1
Time information for the breaking process

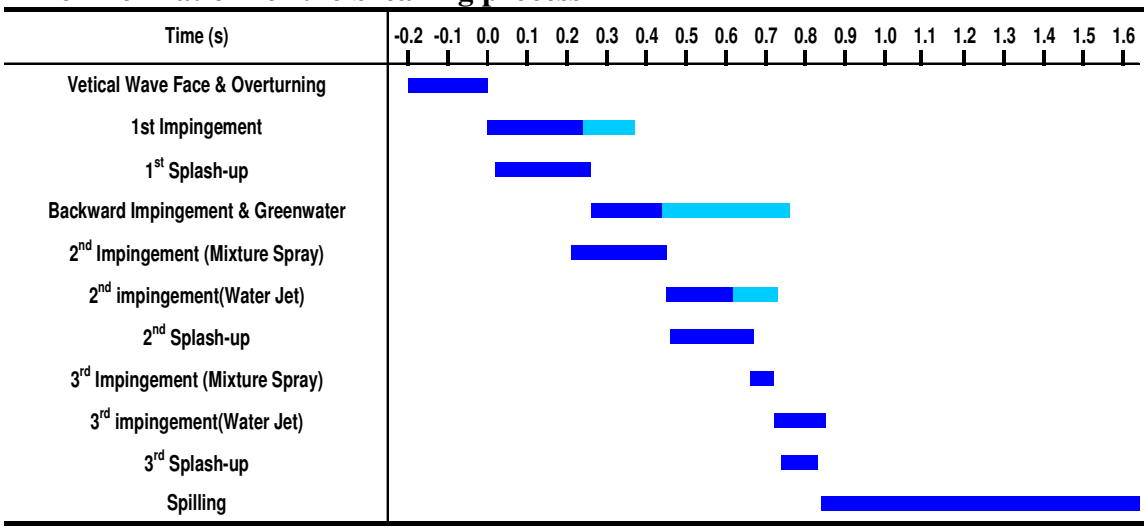

Table 6.2
Location of the breaking process

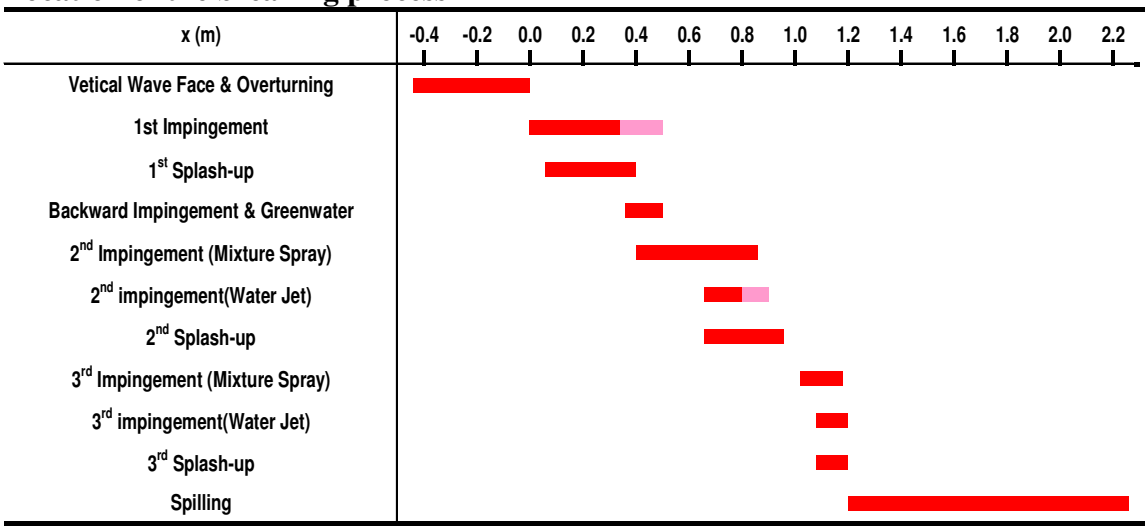

CHAPTER VII

DETECTION OF THE FREE SURFACE AND AERATED REGION

7.1 Introduction

In addition to the qualitative description, measurements of the free surface elevation are essential. Moreover, a boundary of an aerated region should be detected because a void ratio and a density variation should be considered since breaking waves are two phase flows. The void ratio inside the aerated region is quite high and it cannot be neglected. Accurate measurements for the free surface and the boundary of the aerated region are required to obtain other quantitative results such as, mass flux, kinetic energy, and potential energy. The free surface measurements using a common wave gauge are relatively easy. It provides a time series at a measurement station. However, the results are only the water portion of the waves since a resistance wave gauge is used in the measurement. Breaking waves, especially plunging waves, have a large void ratio due to air entrainment during the process of the strong impinging and splash-up. The aerated region in a plunging breaker is much deeper than that of a spilling breaker while the distance in a plunging breaker is shorter than that of a spilling breaker.

Although the wave elevation obtained from wave gauge measurements provides only the water portion of the wave, one advantage is that a time series of the depth-averaged void ratio can be obtained at a measurement station if the real free surface elevation is obtained, as shown Eq. (7.1):

$$\alpha_{da}(x,t) = \frac{\eta_{wg}(x,t) + h}{\eta(x,t) + h} \tag{7.1}$$

where α_{da} is the depth-averaged void ratio, η_{wg} is the wave elevation from the wave gauge measurement, η is the wave elevation including the aerated region, and h is the water depth. To obtain the elevation η and the boundary of the aerated region, raw images taken from the BIV measurements are used. Wave elevation results obtained from the wave gauge measurements and the imaging method are presented in the next section.

7.2 Wave Elevation from Wave Gauge Measurement

Fig. 7.1 shows wave elevation results measured at six different locations using wave gauges. A detailed location of each wave gauge position is given in Fig. 5.1 and Table 5.2. A total of 20 repeated measurements were carried out at each location to obtain mean and root-mean-square (r.m.s.) elevation since breaking waves are considered highly turbulent flows. All 20 measurements at each location are shown in Fig. 7.1. Also, overlapped 20 elevations for the primary wave are presented in Fig. 7.2. As shown in Fig. 5.1 and Table 5.2, wave gauges 1, 2, and 3 were located before the first impinging point, and their overlapped elevations verify repeatability. On the other hand, wave gauges 4, 5, and 6 were located beyond the first impinging point. Three wave gauges were located at the middle of the first splash-up, the second splash-up and the third splash-up, respectively. Therefore, fluctuating elevations can be observed in the results for those three wave gauges.

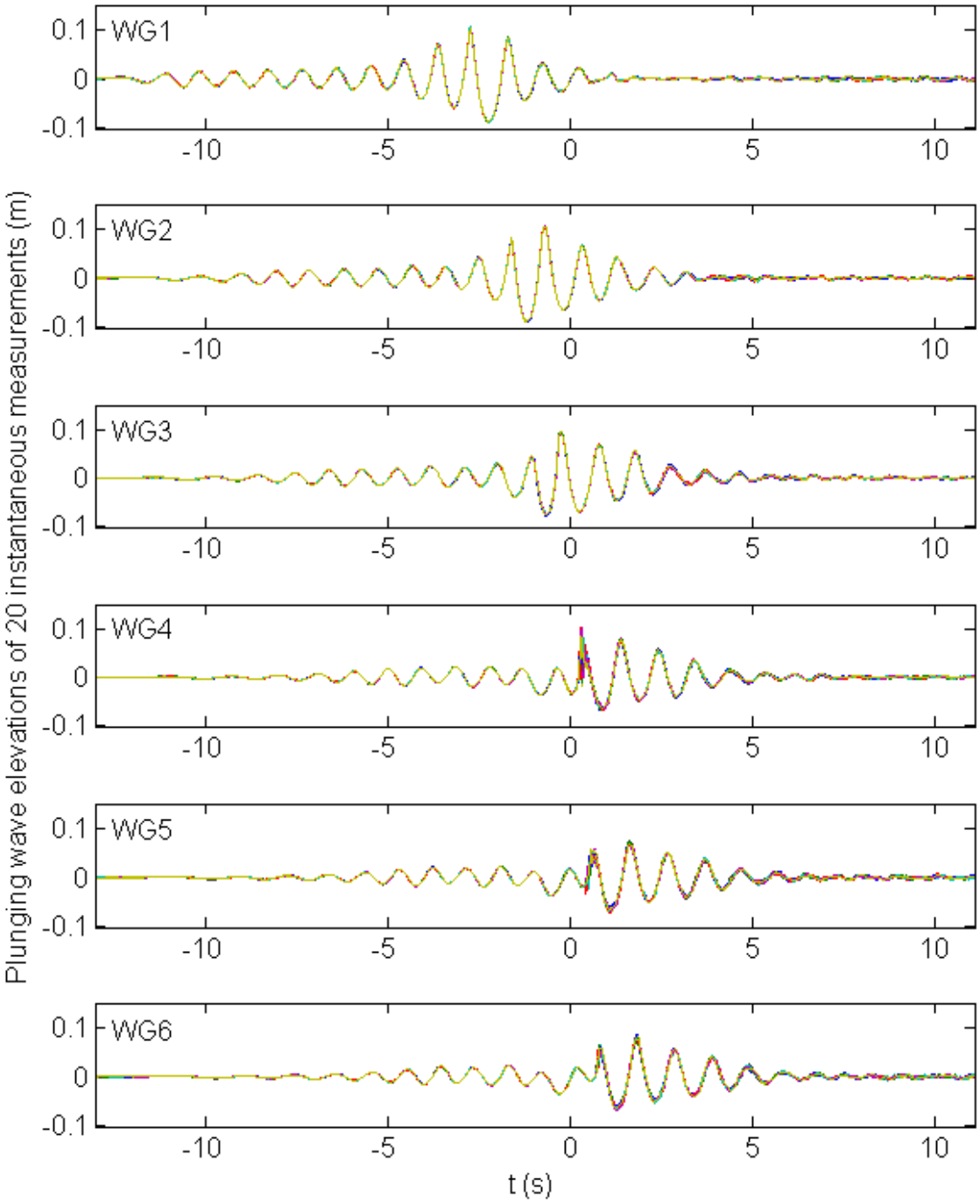

Fig. 7.1 Overlap of 20 wave gauge measurements.

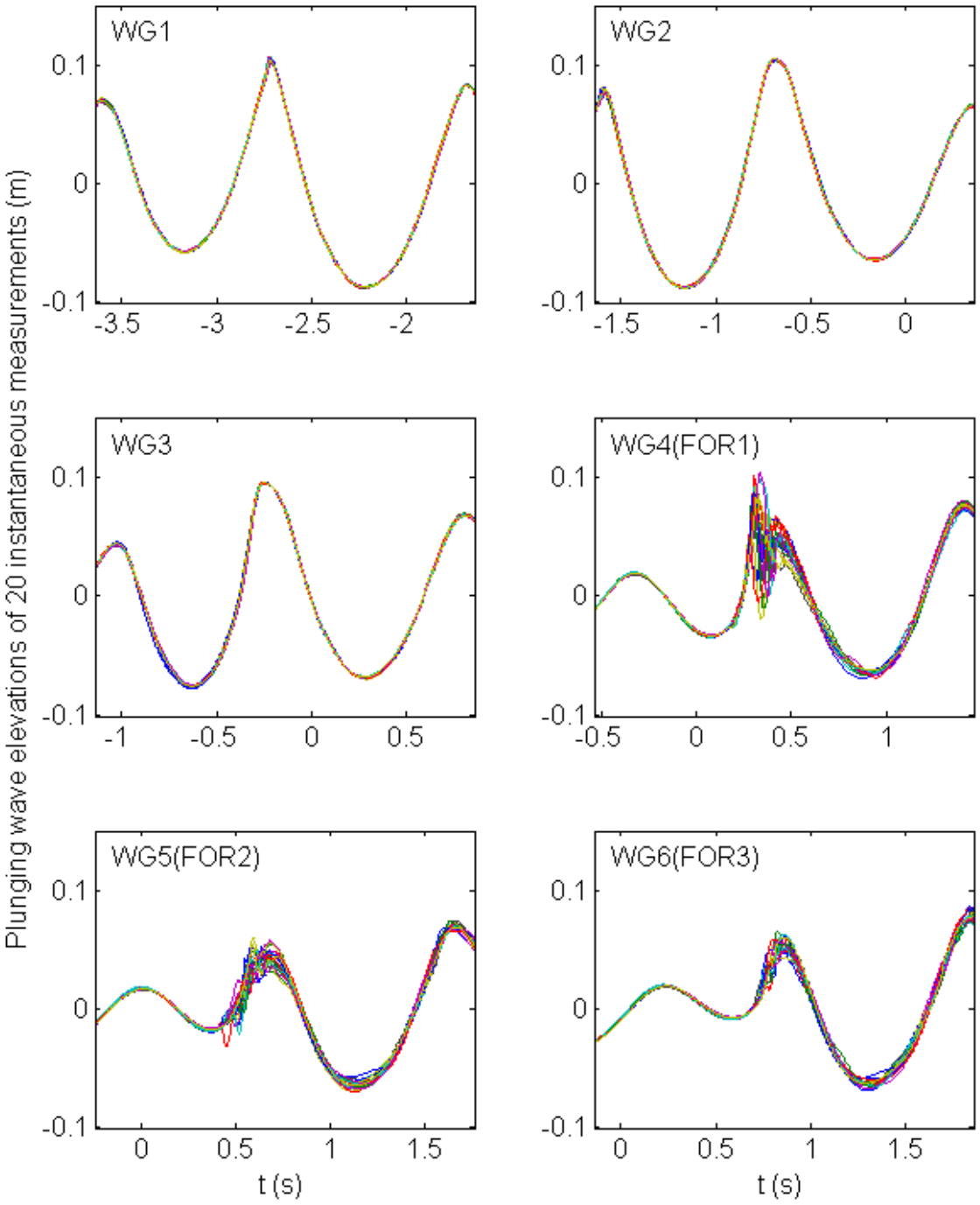

Fig. 7.2 Overlap of 20 wave gauge measurements (primary wave).

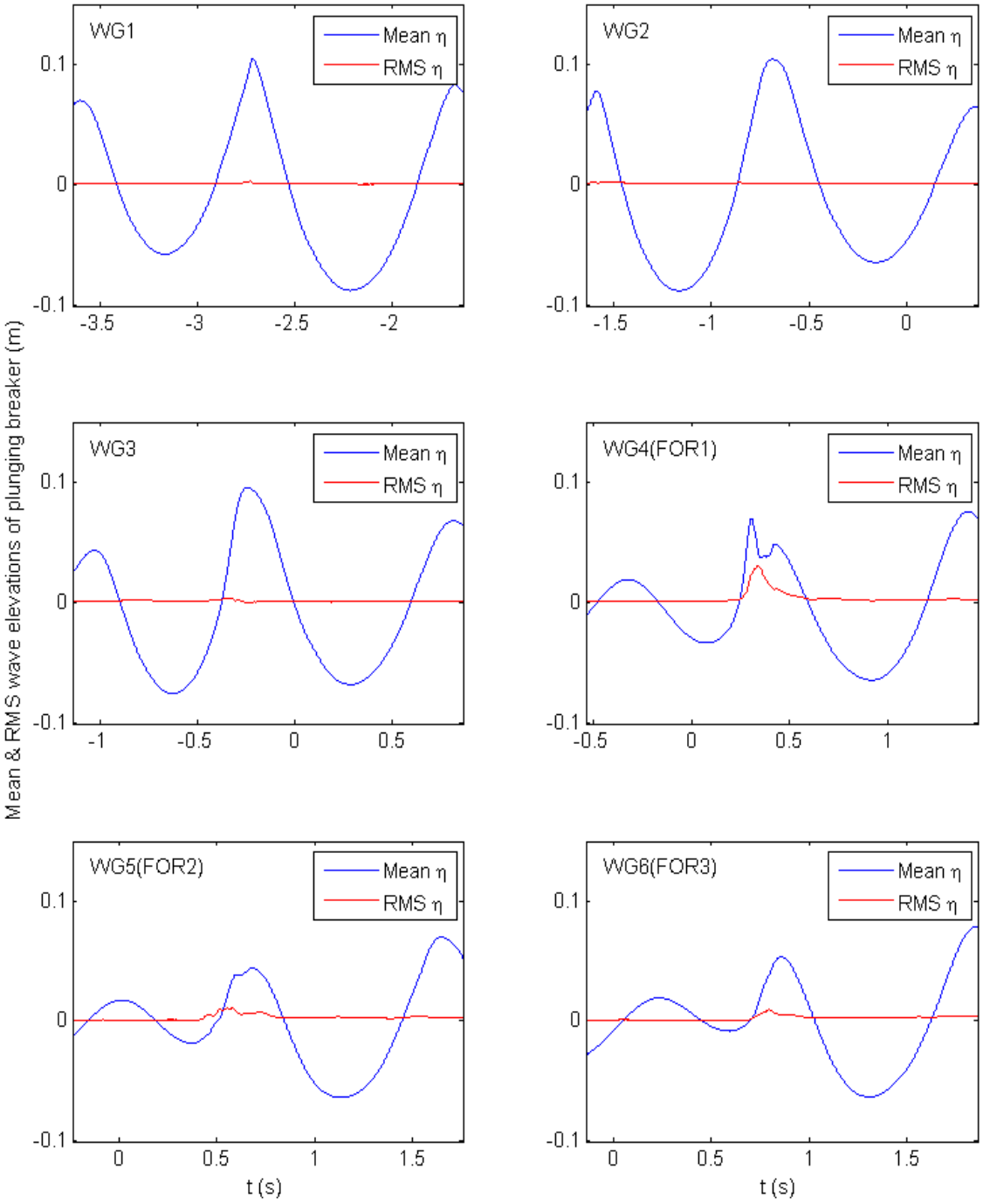

Fig. 7.3 Mean and r.m.s. wave elevation.

Fig. 7.3 shows the mean and root-mean-square elevation, and the detailed values are provided in Table 7.1. The r.m.s. elevations before the first impingement are very low. Maximum r.m.s. values are between 2 and 3 mm where average values of the r.m.s. elevations at each location are less than 1 mm. At the location of the three main splash-up regions, the r.m.s. values are still very low until a highly aerated roller reaches the wave gauges. There are small fluctuations after the primary wave has passed gauges 4, 5 and 6, because of remaining turbulence from these rollers. Additional discussion of wave elevation obtained from BIV images is presented in the next section.

Table 7.1
R.M.S. elevation of six wave gauges

	Location (m)	Maximum η_{rms}	Mean η_{rms}
Wave gauge 1 (WG1)	x = -2.98 (1.30 from WM)	3.18 mm	0.71 mm
Wave gauge 2 (WG2)	x = -1.31 (2.97 from WM)	2.38 mm	0.65 mm
Wave gauge 3 (WG3)	x = -0.57 (3.71 from WM)	3.34 mm	0.67 mm
Wave gauge 4 (WG4) FOR station 1 (FOR1)	x = 0.43 (4.71 from WM)	30.77 mm	0.90 mm
Wave gauge 5 (WG5) FOR station 2 (FOR2)	x = 0.88 (5.16 from WM)	10.48 mm	0.96 mm
Wave gauge 6 (WG6) FOR station 3 (FOR3)	x = 1.20 (5.48 from WM)	9.29 mm	0.95 mm

7.3 Imaging Method for the Free Surface and Aerated Region

Free surface information for the entire flow including the highly aerated region is required, as mentioned in Section 7.1. However, the resistance wave gauges used in the experiments are not able to measure the wave elevations including the aerated region. Since BIV and PIV are based on imaging techniques, these methods can be applied to obtain images that can be used to measure the wave elevation.

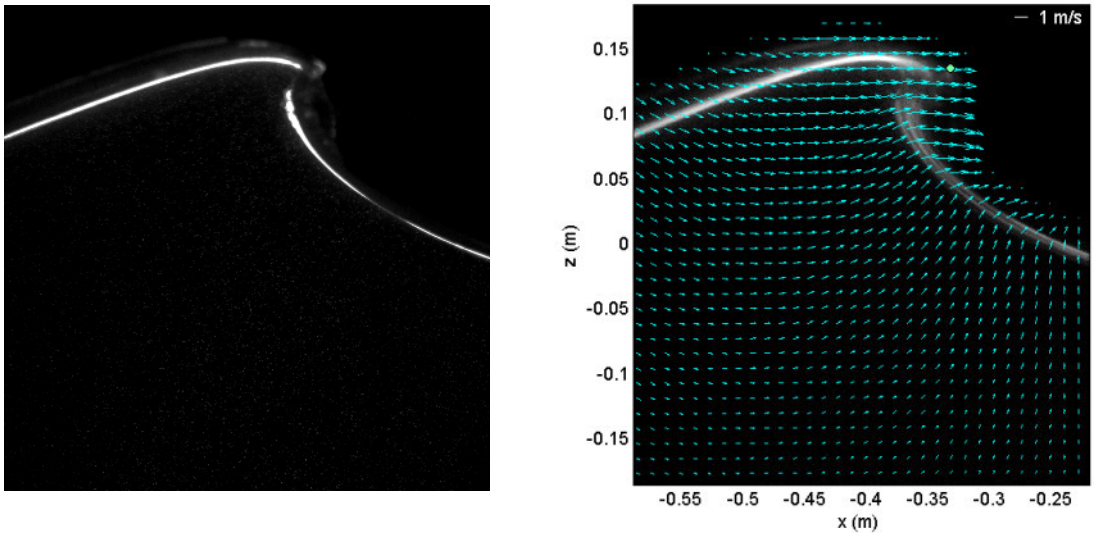

(a) instantaneous PIV image (b) velocity map without masking

Fig. 7.4 Example of mirror images in PIV images.

A masking process is required in the BIV and PIV analysis to obtain an accurate velocity map. Careful attention is needed for the free surface and the boundary of the aerated region during the masking process. For example, as shown in Fig. 7.4(b), there are velocity vectors over free surface in the PIV measurements. Free surface image between a light sheet and a front wall of the wave tank appears due to the camera angle

as shown in Fig. 7.4(a). Since digital cross-correlation algorithms employed in PIV and BIV use gray scale intensities of particles or air-water mixtures, an undesirable region over the free surface also has velocity information as shown in Fig. 7.4(b), and this should be removed in the correct manner.

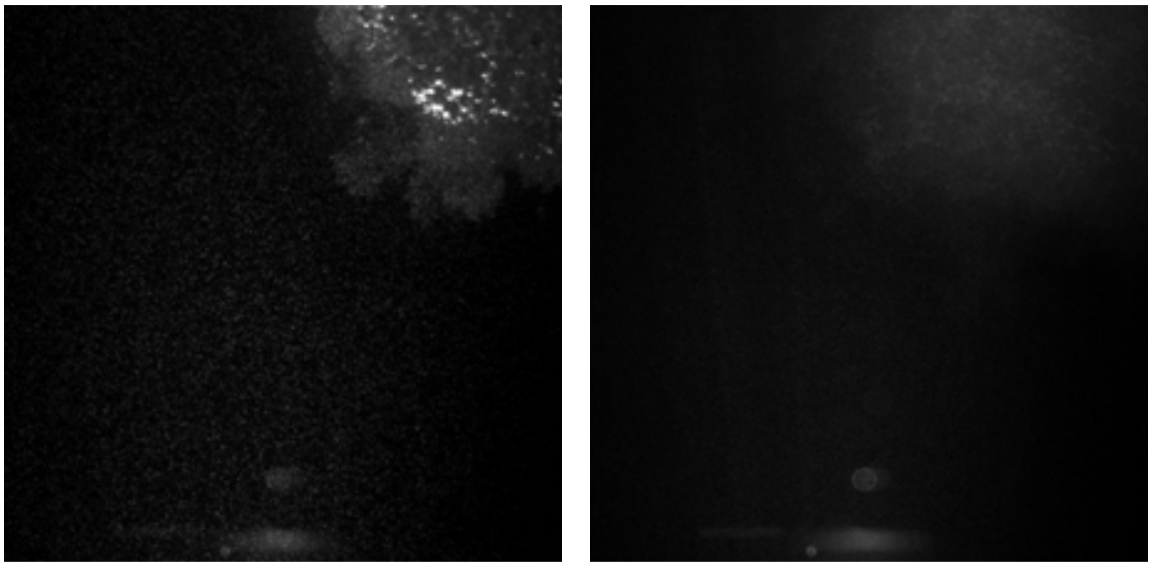

(a) instantaneous image (b) mean image

Fig. 7.5 Example of PIV images.

The other region requiring attention is the boundary of the air-water mixture. As shown in Fig. 7.5(a), more particles gather around the boundary of the aerated region when each impinging roller moves under the free surface. As shown in Fig. 7.5(b), it is difficult to distinguish between the particles and the aerated region using an averaging image due to the similar intensities of the particles and the bubbles in the aerated boundary that has a low void ratio. It is necessary to determine the boundary of the aerated region especially if a void ratio is to be obtained using the intensity information

of the images. For example, the void ratio outside the aerated region should be zero. Otherwise, the void ratio near the boundary will be overestimated due to gathered particles. The detailed masking process is given in the next section.

7.3.1 Detection of the Free Surface and Aerated Region Using BIV Images

Fig. 7.6(a) shows an instantaneous image of a BIV measurement at t = 0.39 s. In this phase, the first splash-up process followed by the first impingement continues and the first backward impingement causing counterclockwise vorticity is observed. An averaging image of 20 instantaneous images is shown in Fig. 7.6(b). Note that the gray scale of the mean image was inverted because using this image is more convenient to obtain images for masking. As shown in Fig. 7.6(b), inverted images after averaging were used to obtain various mask images as well as void ratios.

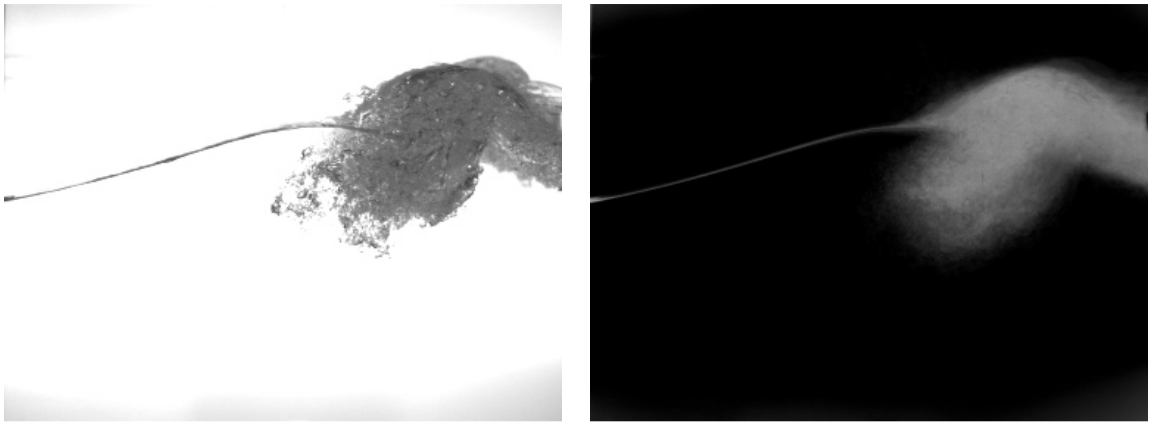

(a) instantaneous image (BIV) (b) inverted color and mean image (BIV)

Fig. 7.6 Instantaneous and averaged BIV images.

Fig. 7.7 shows the velocity and vorticity before applying the mask process. Undesirable values in both the velocity and vorticity measurements are observed in the

BIV measurements. Values outside the field of view, near the free surface, and above the aerated region should be removed to obtain precise quantities. In addition, the large negative vorticity over the free surface, especially over the aerated region, should be removed and it is good to validate the masking process.

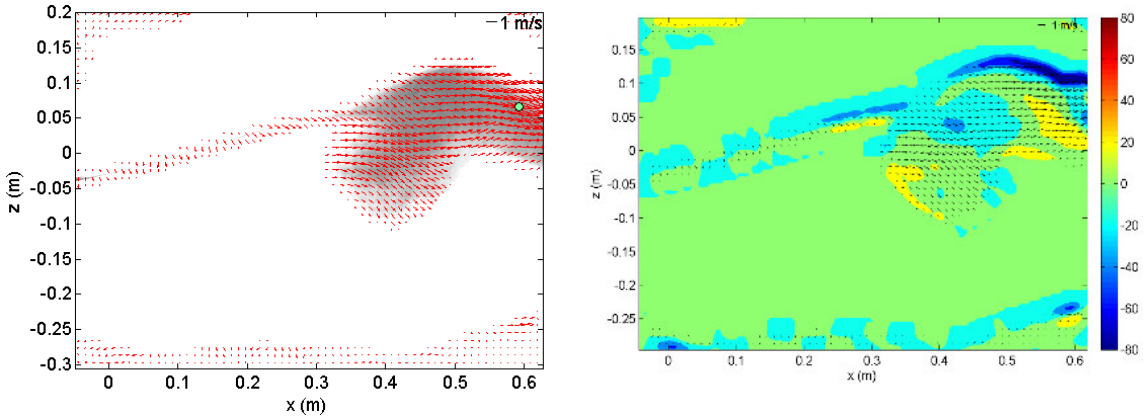

(a) velocity without masking (b) vorticity without masking

Fig. 7.7 Velocity and vorticity without masking (BIV).

In order to avoid overestimation near the free surface and errors near the boundary of the aerated region, it is crucial to obtain correct mask images. However, obtaining correct masking is challenging and time consuming, especially when there is an aerated region at a phase. In general, the intensity gradient variation near the free surface is useful to decide suitable threshold values and the free surface is easily determined from both BIV and PIV images. The challenging problem occurs at the aerated region. The free surface over the aerated region is obtained from the intensity gradient, and is usually overestimated due to the camera angle. Moreover, obtaining the boundary of the aerated region is more challenging than obtaining the free surface. Since no laser is required and

no particles are seeded in the BIV measurements, errors due to a laser light sheet and seeded particles are eliminated. In addition, overestimation of the free surface over the aerated region due to the camera angle is smaller in the BIV measurements because a 105 mm focal lens was used in the BIV measurements while a 50 mm lens was used in PIV measurements, which allowed for a closer distance to the depth of field. Note that although error due to image resolution is larger in the BIV measurements it is still not significant. For this reason, images for various masking were obtained from the BIV images manually even though it is very time consuming.

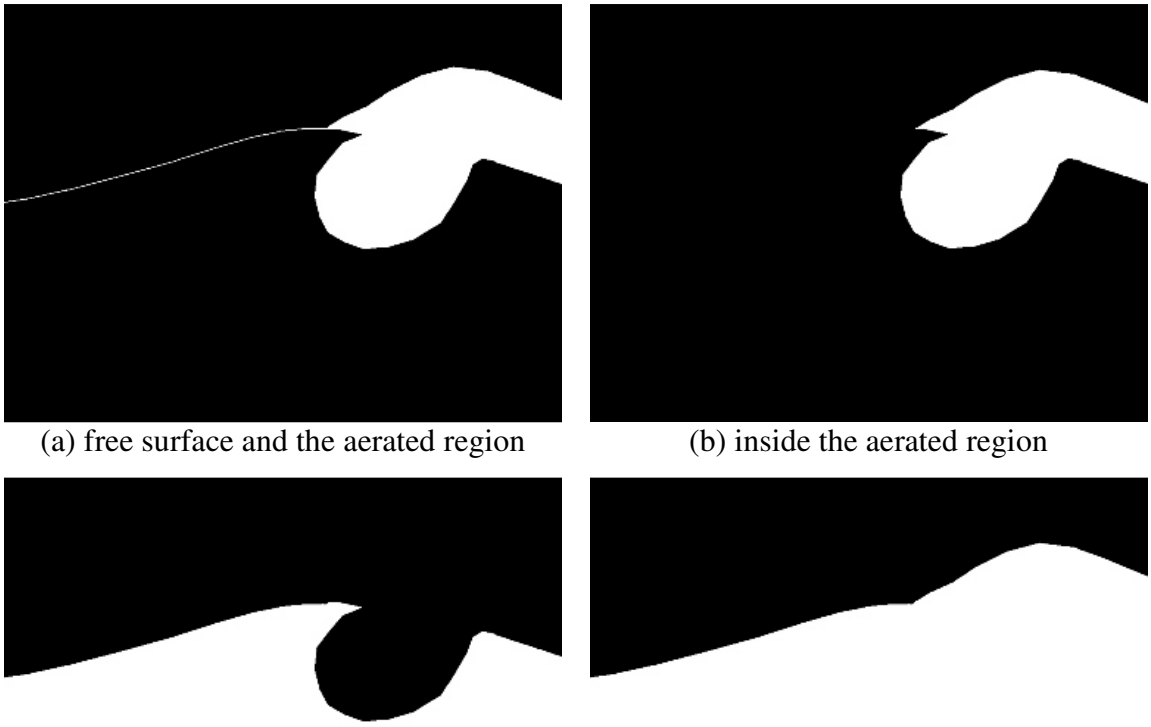

(a) free surface and the aerated region (b) inside the aerated region

(c) outside the aerated region (d) under the free surface

Fig. 7.8 Various BIV mask images.

Fig. 7.8 shows various mask images obtained from the BIV images. The image shown in Fig. 7.8(a) is manually obtained from the mean image shown in Fig. 7.6(b). The free surface and the boundary of the aerated region can be obtained from the image. The three images shown in Fig. 7.8(b)-(d) are obtained from Fig. 7.8(a) using Matlab and they are the mask images for inside of the aerated region, outside of the aerated region, and below the free surface, respectively. Only Fig. 7.8(b) is used to obtain the air-water velocity field inside the aerated region since BIV can measure the velocity of an air-water mixture only. The other two images shown in Fig. 7.8(c) and (d) are generated for the PIV analysis.

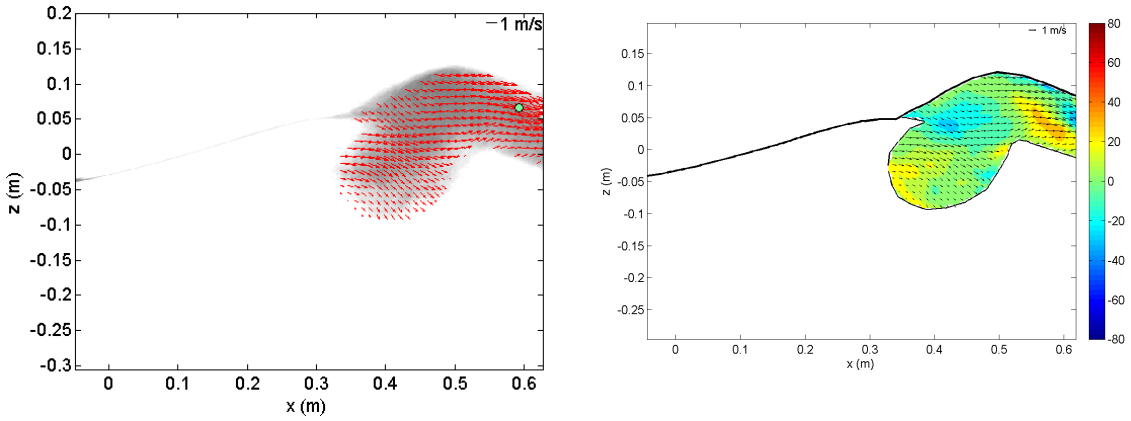

(a) velocity after masking (b) vorticity after masking

Fig. 7.9 Mean velocity and vorticity after applying a mask image (BIV).

Fig. 7.9 shows velocity and vorticity after applying the mask image of Fig. 7.8(b) to the images shown in Fig. 7.7. A green circle represents the location of maximum velocity in the phase. It is seen that the large negative vorticity over the free surface shown in Fig. 7.7(b) is removed by masking. Note that the negative vorticity around x =

0.4 m represents the first backward impingement due to the first splash-up. Fig. 7.10 shows the free surface and the boundary of the aerated region. Temporal resolution in the BIV and PIV measurements is 10 *m*s, although images were taken at 500 *fps*. Therefore, high resolution time series of wave elevation were obtained for the entire flows.

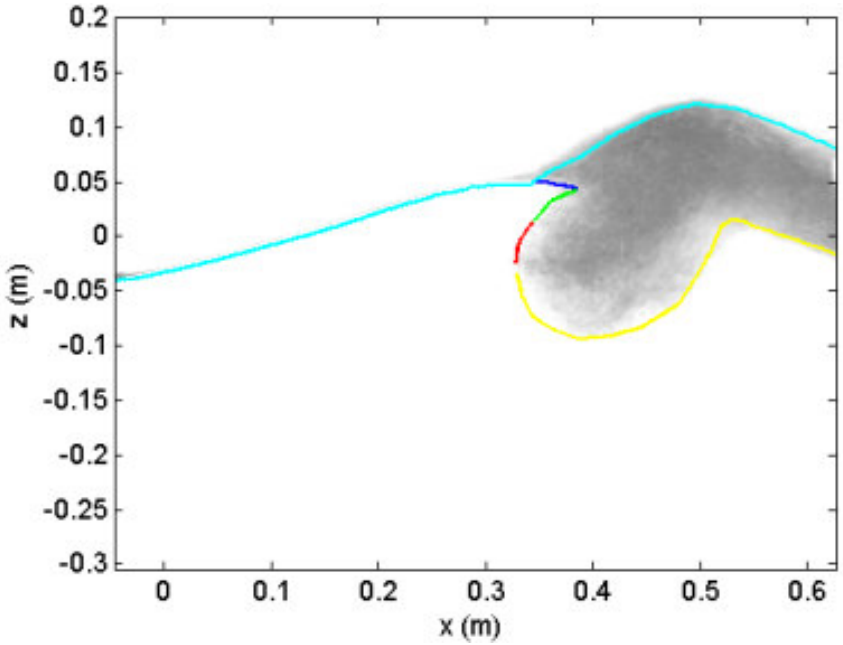

Fig. 7.10 Free surface and boundary of aerated region from BIV image.

7.3.2 Application to PIV Analysis

Since obtaining mask images from the BIV images is relatively ease and accurate, the mask images from the BIV images were applied to the PIV images. It is essential to adjust for spatial and temporal synchronization. Although all the experiments were not performed at the same time, the triggering signals for all experimental techniques, such as wave gauges, BIV, PIV, and FOR, were synchronized with the triggering of the

wavemaker. Therefore, spatial and temporal information for all experiments were obtained and synchronized as shown in Fig. 7.11. The background image represents an example of the free surface and the aerated region at t = 1.17 s obtained from the BIV images. Various mask images for the PIV measurements matched to the image shown in Fig. 7.11 with a time difference of 10 ms. Since the PIV measurements cover a larger area than the BIV measurements, some areas such as PIV FOV01, left side of PIV FOV03, right side of PIV FOV09 and left side of PIV FOV11 do not contain BIV images, thus PIV images were used to mask for these specific areas.

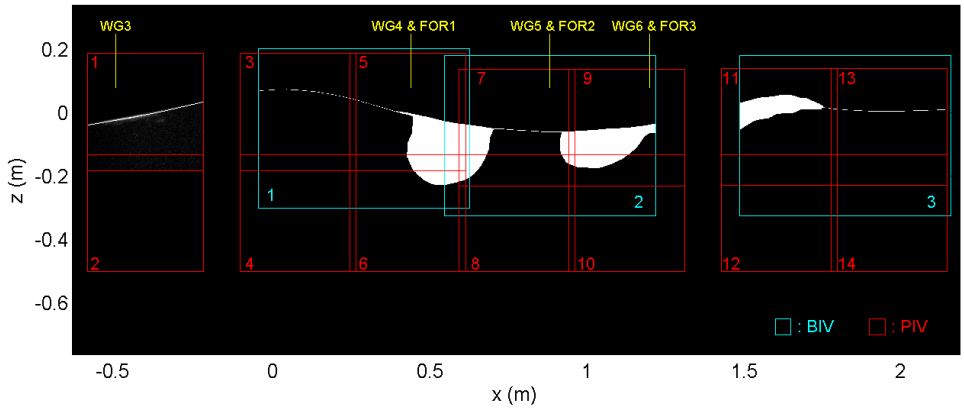

Fig. 7.11 Wave elevation and boundary of aerated region from BIV image.

Fig. 7.12 shows an example of various PIV mask images obtained from the BIV image. Fig. 7.12(a) shows an averaging image of 20 instantaneous PIV images at PIV FOV05 at t = 0.41 s. Fig. 7.12(b)-(d) represent PIV mask images for inside of the aerated region, outside of the aerated region, and below the free surface respectively.

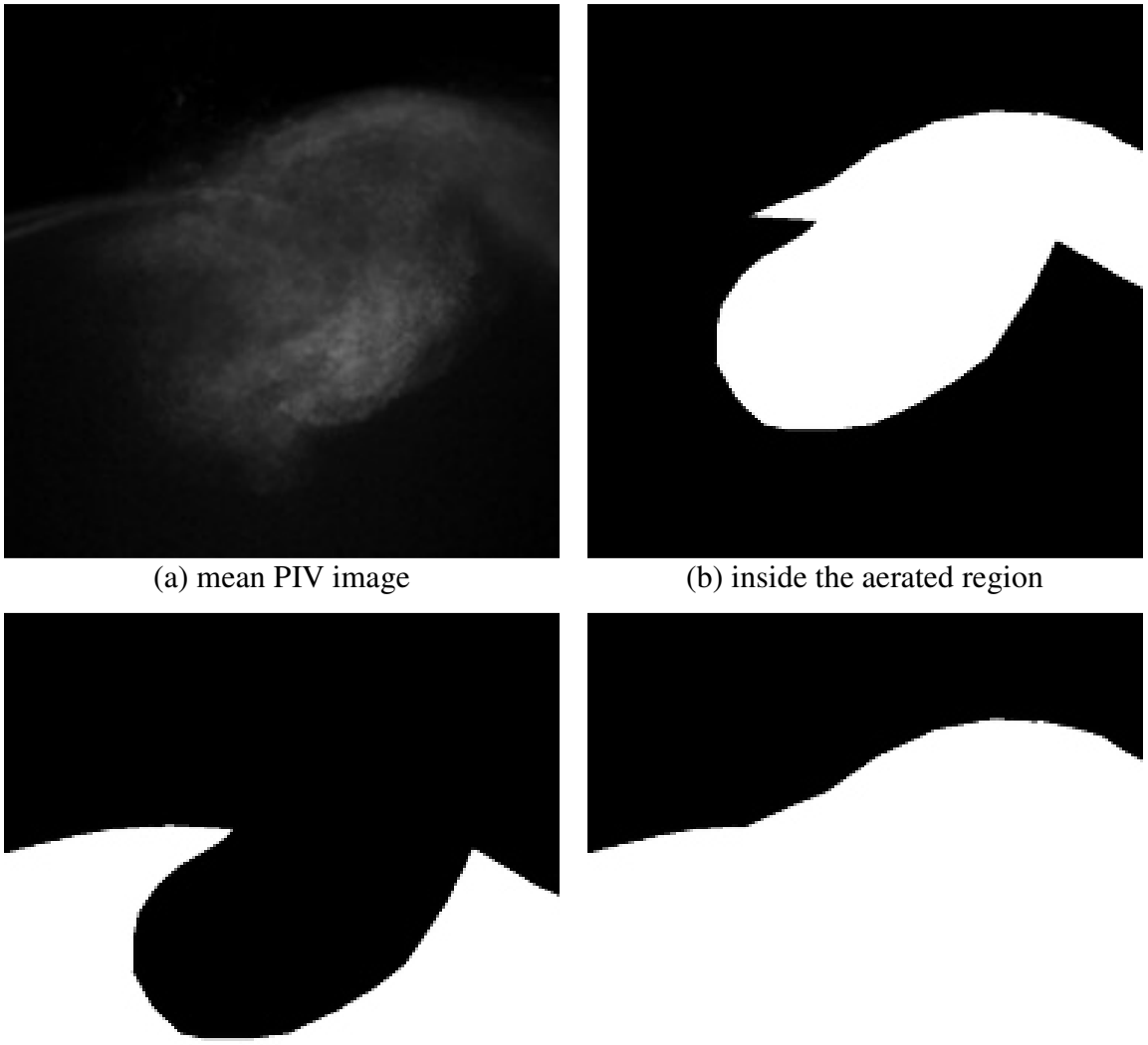

(a) mean PIV image (b) inside the aerated region

(c) outside the aerated region (d) under the free surface

Fig. 7.12 Various PIV masking images.

Fig. 7.13(a) shows a velocity field before applying a mask image, and Fig. 7.13(b)-(d) show a velocity map after applying various mask images inside the aerated region, outside the aerated region, and for the entire flow, respectively. Note that the velocity map obtained from the traditional PIV measurement is like Fig. 7.13(c).

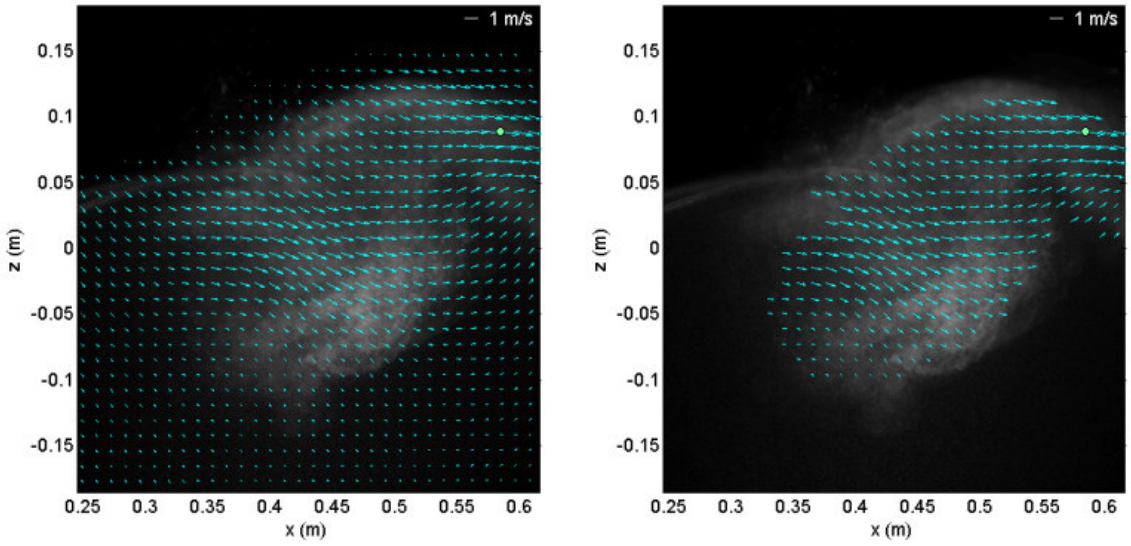

(a) velocity without masking (b) velocity inside the aerated region

(c) velocity outside the aerated region (d) velocity under the free surface

Fig. 7.13 Velocity with various masks (PIV).

Fig. 7.14 (a) shows a vorticity contour before applying a mask image, and Fig. 7.14(b)-(d) show vorticity after applying various mask images inside the aerated region, outside the aerated region, and for the entire flow, respectively.

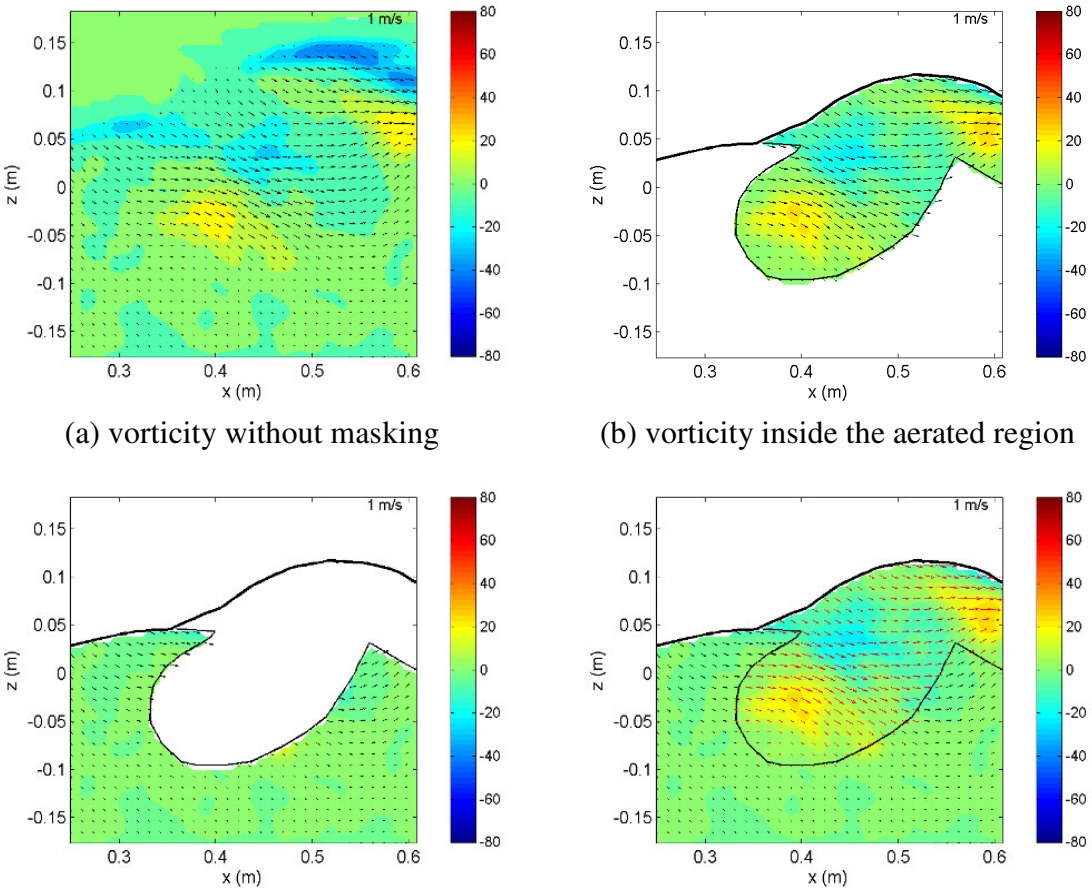

(a) vorticity without masking

(b) vorticity inside the aerated region

(c) vorticity outside the aerated region

(d) vorticity under the free surface

Fig. 7.14 Vorticity with various masks (PIV).

The free surface and the boundary of the aerated region can be seen in Fig. 7.15. All information for the locations of the free surface and the boundary were saved in Bitmap and ASCII formats. Spatial resolution of the free surface information is the same as the image resolution, which is 0.3613 mm/pixel. Wave elevation data were collected every 5.78 mm and were obtained with a time difference of 10 ms since the final spatial and temporal resolutions of the PIV data are 5.78 mm and 10 ms, respectively.

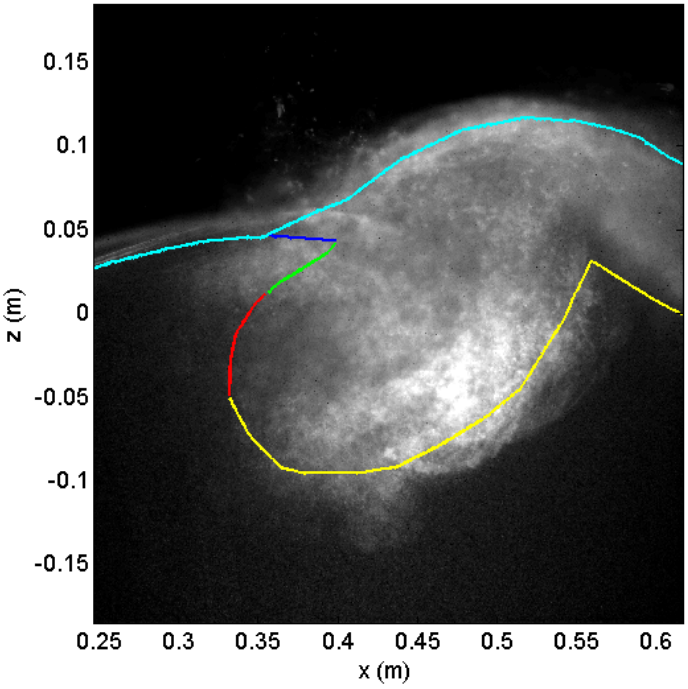

Fig. 7.15 Free surface and boundary of aerated region from PIV images.

Fig. 7.16 shows the water level envelops and their normalized values by primary wave height. Note that the horizontal distance from the breaking point is normalized by wave length of the primary wave. When a primary wave passes through every station with dx = 5.78 mm and dt = 0.01 s, local maximum (red), minimum (blue), and mean (green) water levels are given in the figure, and local wave height was obtained by subtracting a local minimum water level from a maximum water level at every station. Important locations such as impinging points and fully developed splash-up regions, which are measurement stations for both wave gauges and FOR, are provided in Fig. 7.16(a). Local maximum elevation is found at each fully developed splash-up region, and local minimum elevation is found at the location between each impingement and splash-up.

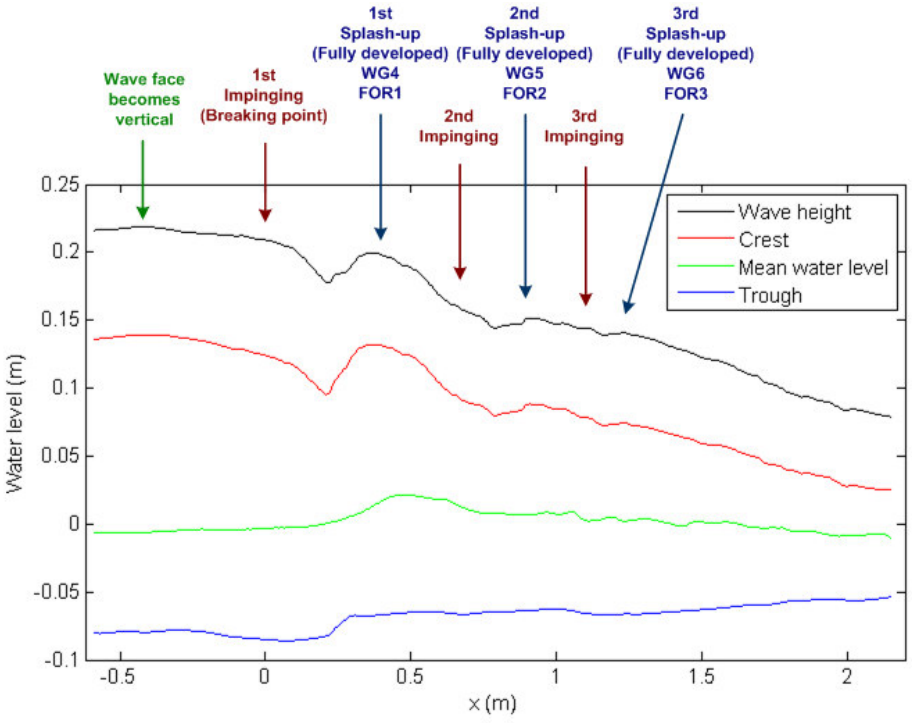

(a)

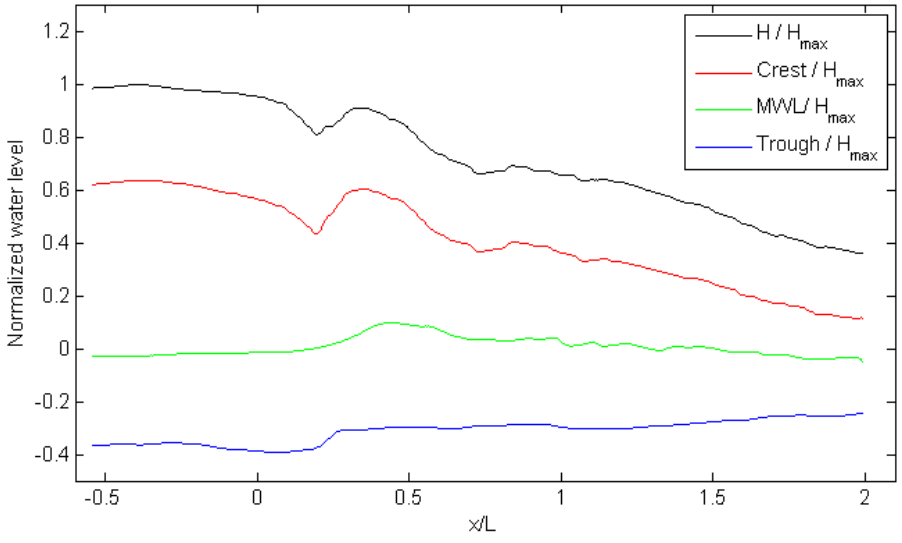

(b)

Fig. 7.16 Water level envelop from BIV and PIV images.

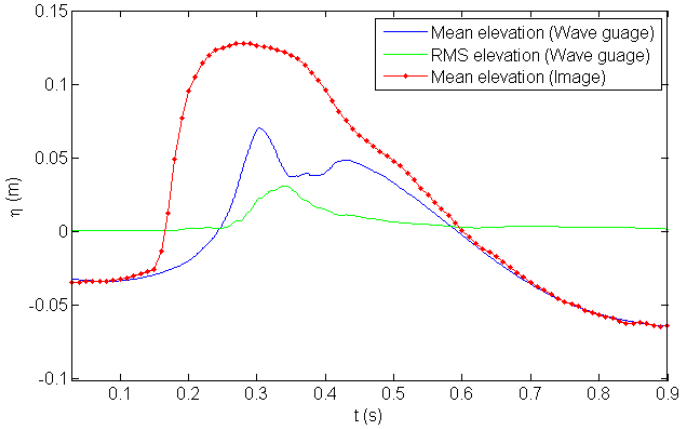

(a) WG4(FOR1) station (fully developed 1st splash-up)

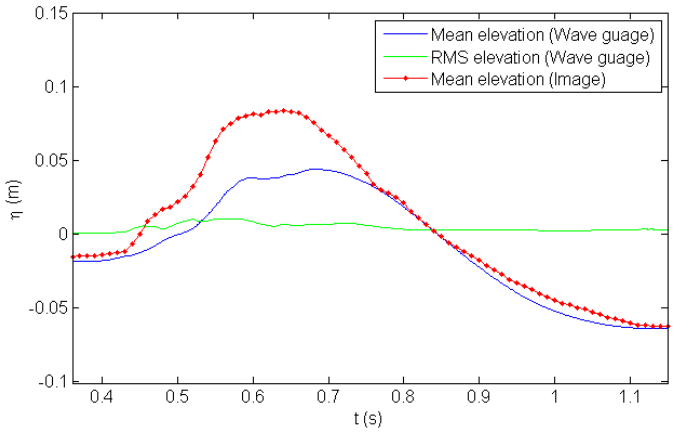

(b) WG5(FOR2) (fully developed 2nd splash-up)

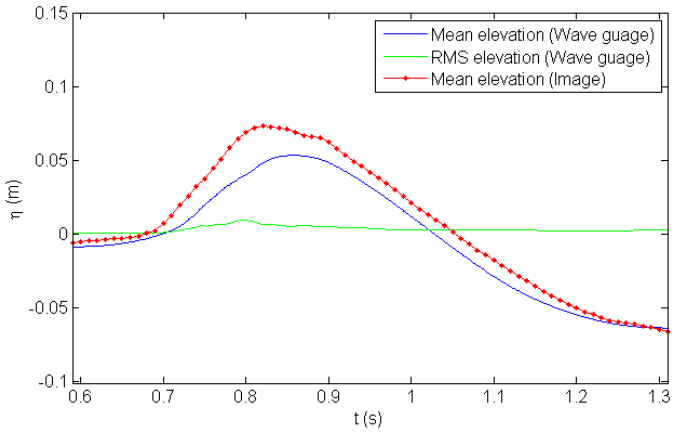

(c) WG6(FOR3) (fully developed 3rd splash-up)

Fig. 7.17 Comparison of wave elevation from wave gauges and images.

There are three stations to measure wave elevation and void ratio after the first impingement as shown in Table 7.1 and Fig. 7.11. Wave elevation results obtained from the BIV images at each station are compared with those obtained from wave gauges as shown in Fig. 7.17. The difference between the two results is largest at the WG4 (FOR1) station, whose location corresponds to the fully developed first splash-up region [Fig. 7.17(a)]. This is because the maximum void ratio is in the first splash-up region. The difference decreases gradually, and the difference at the WG6 (FOR3) station, whose location corresponds to the fully developed third splash-up region [Fig. 7.17(c)], is small but widely distributed. Detailed results of the void ratio measurement will be presented in Chapter XI.

CHAPTER VIII

AERATED REGION IN A PLUNGING BREAKER: BIV MEASUREMENT

8.1 Introduction

Results obtained from the BIV measurements are presented in this chapter. Velocity fields of the highly aerated region in breaking waves are obtained using the BIV technique. Imaging techniques is one of the reliable techniques to obtain a velocity and fraction ratio of each phase in the measurement of multiphase flows, for example, water and air bubble in two-phase bubbly flows. However, there is great difficulty when phase decomposition is required in multiphase flows with high void ratio. In such cases, an intrusive sensing technique such as FOR should be employed. Although it is impossible to decompose the air and water phases using BIV, the BIV technique is capable of measuring air-water mixture velocity of the aerated region with high precision. Therefore, the BIV method is indeed suitable for bubbly flow measurements. In addition, BIV can be a supplementary technique where the PIV method does not work properly.

Validation of the BIV technique was carried out by comparing results with the FOR technique. The validation part is provided in Section 8.2. A brief description of the BIV data analysis procedure is presented in Section 8.3. Section 8.4 shows the instantaneous velocity measurement by comparing with mean velocity fields. The flow structure only in the aerated region is discussed due to the limitation of the BIV technique. Velocity

measurements of the water phase in breaking wave are also essential to analyze the entire flow filed. Since the modified PIV technique used in this study is capable of measuring the entire flow fields including highly aerated regions as well as water particle velocity, results obtained from the BIV measurements are briefly introduced in this chapter for the comparison and validation of the results obtained from the PIV measurements. More detailed analysis with mean and turbulent quantities of the strong plunging breaker are presented in Chapters IX and X respectively.

8.2 Validation of the BIV Method*

The validation of BIV was performed in two ways: first to compare the velocity measured using the BIV technique with that measured using the fiber optic reflectometer (FOR) technique; second to check the effect of the blurry images out of the DOF in the BIV velocity measurement. A bubble plume in a water tank was used in the validation.

A two-phase quasi-steady bubbly flow in a vertical narrow tank was measured using both the BIV technique and the FOR technique. The objective of this experiment is to validate the BIV method by comparing the results obtained from these two methods. The FOR technique is capable of measuring the velocity time history of both water (seeded with small particles) and air bubbles at a given point in a multi-phase flow. Details of FOR are given by Chang *et al* (2003).

---

*Reprinted with permission from part of "Use of bubble image velocimetry for measurement of plunging wave impinging on structure and associated greenwater" by Ryu, Chang and Lim (2005). *Measurement Science and Technology*, DOI 10.1088/0957-0233/16/10/009, Copyright [2005] IOP Publishing

The vertical narrow tank used in the validation has a length of 0.4 m, a width of 0.4 m and a height of 0.8 m. Water was filled to a depth of 0.7 m in the tank. An air diffuser generating air bubbles was located at the bottom of the tank.

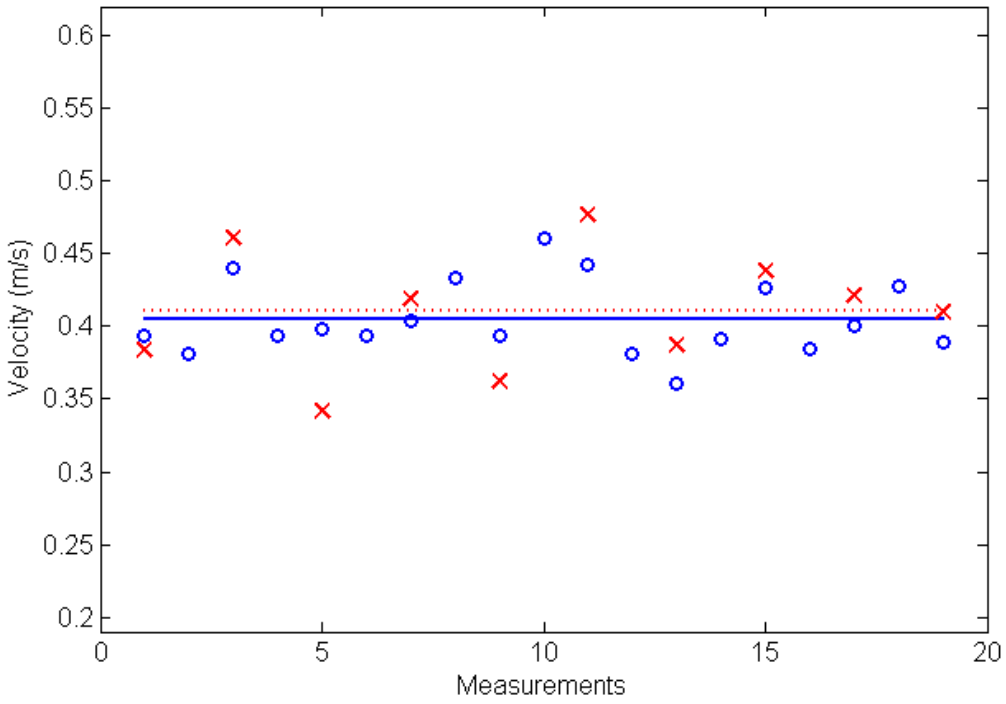

Fig. 8.1 Comparison of velocities by BIV and FOR measurements: 'o', BIV instantaneous velocities; '×', FOR instantaneous velocities; solid line, BIV mean velocity; dotted line, FOR mean velocity.

A bubble plume was formed in the tank with a diameter approximately 0.11m at the measurement section. The BIV method was used to measure the velocity of the bubble plume with a FOV of 12.6 cm×12.6 cm. Subsequently, the FOR technique was employed to measure the velocity at x_b = 0 and z_b = 45 cm, located in the region of the

BIV FOV with $x_b = 0$ and $z_b = 0$ being the centre of the air diffuser. The void fraction was 4% with the average size of a bubble equal to 3 mm at the FOR measurement point, obtained by FOR.

Fig. 8.1 shows the measured bubble velocities using both the BIV and FOR methods at the point where the FOR probe was located. The mean velocities were obtained using 20 and 10 instantaneous velocities in the BIV and the FOR measurements, respectively. The comparison of the mean velocities shows very good agreement with a relative error about 1% (approximately 4 mm s^{-1}). The scattering of the instantaneous velocities may be due to the turbulent nature of the flow.

In theory the blurred images contributed from bubbles outside the DOF are expected to have insignificant influence in the correlation for velocity determination because the intensity of the bubbles is much weaker (and spread wider) than that of the well-focused bubbles inside the DOF. Since typical BIV measurements are performed in highly aerated bubbly flows, the captured images are indeed the sharp images inside the DOF superimposed with blurry images outside the DOF. In order to investigate the blurry image effect on the BIV accuracy, the velocity obtained from clear bubble images was compared with that obtained from artificially superimposed blurry bubble images. One set focused at the centre of the bubble plume so the bubble images are sharp and clear, while another set focused 15 cm behind the centre of the plume therefore the bubble images are blurred and out of focus. Both sets of original images were processed with velocities obtained.

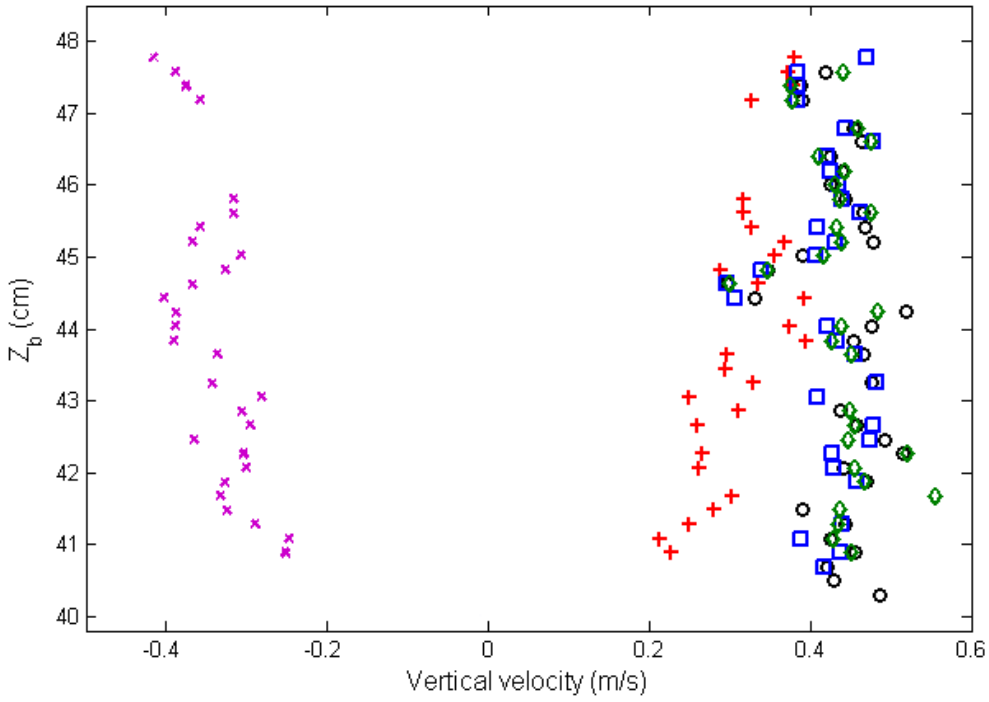

Fig. 8.2 Velocity distribution along the centreline of the bubble plume obtained from: clear images (o), blurry images (+), upside-down blurry images (×), superimposed clear and blurry images (□), superimposed clear and flipped blurry images (◊).

Clear and blurry images were then artificially added in two ways. Firstly, the blurry images were added to the clear images directly. Secondly, the blurry images were vertically flipped and then added to the clear images. Fig. 8.2 shows the instantaneous vertical velocity distribution obtained along the centerline of the bubble plume from the clear images, blurry images, vertically flipped blurry images, the superposition of the clear images and blurry images, and the superposition of the clear images and vertically flipped blurry images. The figure shows that both the velocities obtained from the clear–

blurry superimposed images are very close to that from the clear images. Therefore, the blurry and out of focus bubble images have little effect on the accuracy of the BIV velocity measurement.

8.3 BIV Data Analysis Procedure

In addition to the BIV experimental set up and conditions presented in Chapter V, BIV data analysis procedure is briefly described in this section. Description is limited to the plunging breaker, since only results obtained from the plunging breaker measurements are presented in this thesis. As shown in Fig. 5.1, Three fields of view (FOV) were chosen to cover the entire plunging wave after the first impingement. As discussed in Section 8.1, BIV cannot measure velocity fields outside the aerated region. Therefore, the pre-breaking region before the first impingement was measured using the PIV methods that is presented in Chapters IX and X.

The BIV image process is briefly described in Fig. 8.3. BIV images were taken for 4 s with a frame rate of 500 *fps*. A total of 121620 images (2027 images/measurement × 20 measurement/FOV × 3 FOVs) were obtained for the plunging breaker in the BIV measurements. Note that the number of images for a spilling breaker are 243240. By means of several preliminary tests, the time difference *dt* between two coupled images for velocity calculation with cross-correlation algorithms were carefully determined to reduce errors caused by inappropriate *dt*. Two or 4 ms were used depending on the flow velocity.

An outline chart for the procedure of the BIV measurement and data analysis is shown in Fig. 8.4. Matlab software was used for most image process and data analysis

and a commercial software DaVis was used for the velocity calculation of each instantaneous measurements. Mask images obtained from the BIV images are also used for the PIV analysis as discussed in Chapter VII.

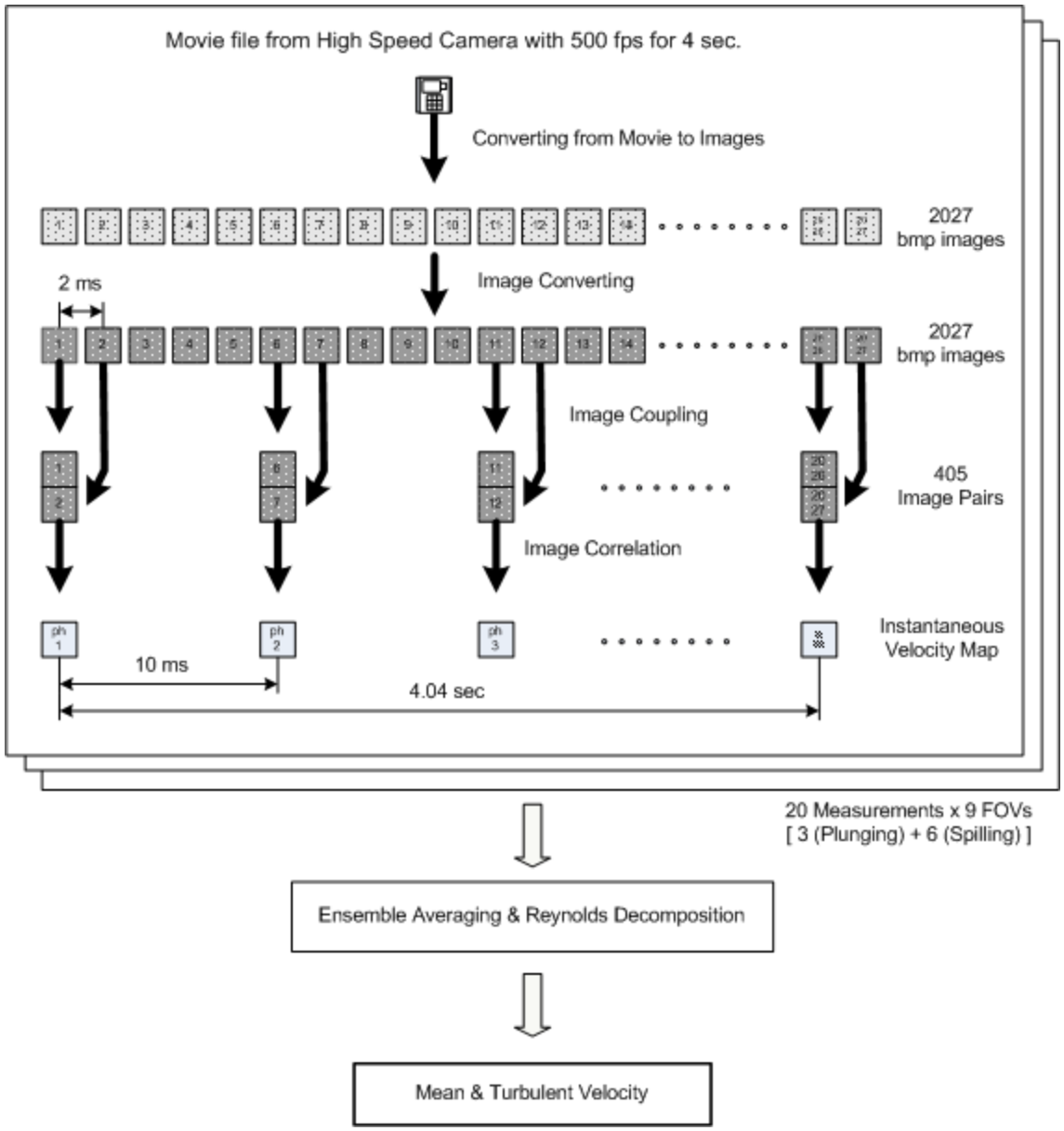

Fig. 8.3 BIV image processing.

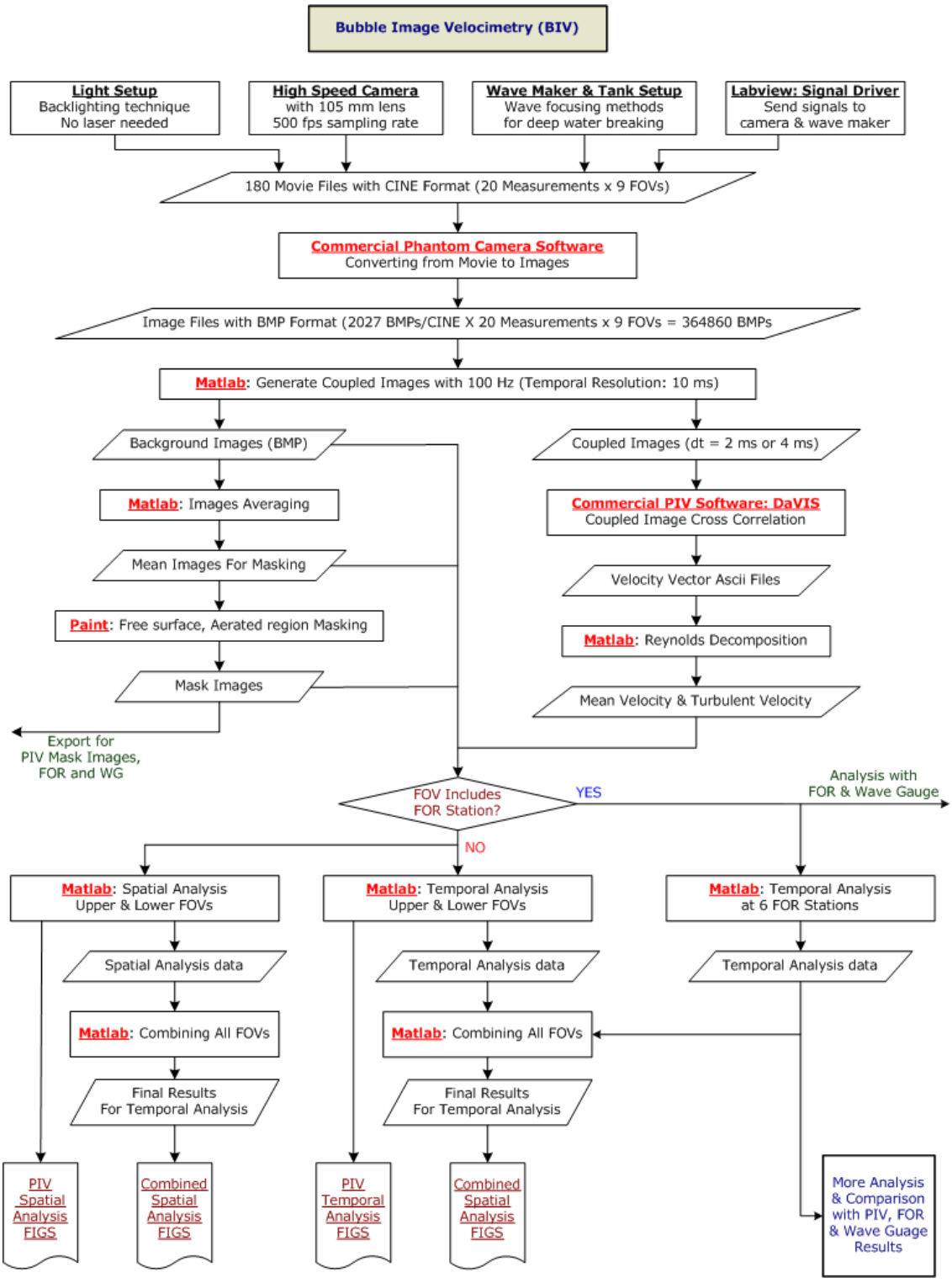

Fig. 8.4 BIV experiment and data analysis procedure.

8.4 Instantaneous Velocity Fields

This section will also provide more information and validation of the instantaneous velocity measurement by comparing with the mean velocity fields at several phases.

Fig. 8.5 shows the combined BIV fields of view (FOV). The number of points for each FOV is 128 × 96. The empty region between x = -0.6 and -0.1 m represents the pre-breaking region where the wave begins overturning. The velocity field for the pre-braking region was obtained using the PIV measurement since BIV can measure the aerated region only without any modification. Another empty space can be seen between x = 1.22 m and 1.49 m due to a steel column of the wave tank. However the PIV measurements covered a wider region and will be discussed in Chapter IX.

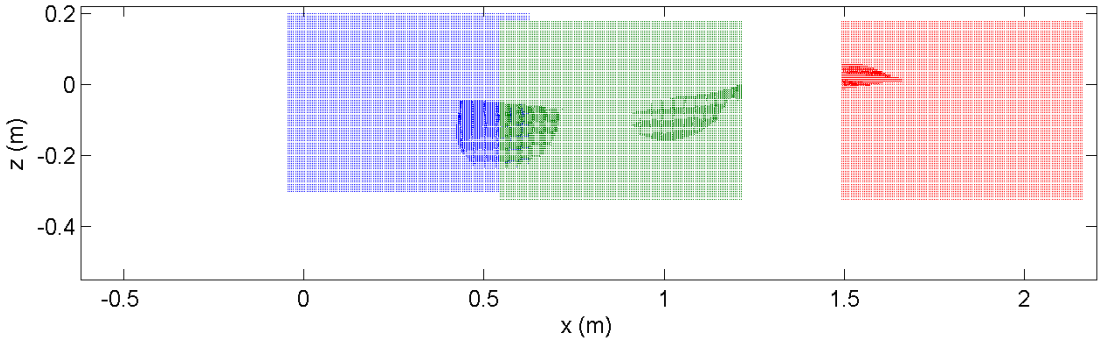

Fig. 8.5 Example of combined FOVs.

Fig. 8.6 shows examples of instantaneous and mean velocity fields at several phases obtained from BIV FOV1 and FOV2. Instantaneous velocity fields can be seen in figures in the left side with a cyan color while the right side figures with a red color represent mean velocity fields at the corresponding phases respectively.

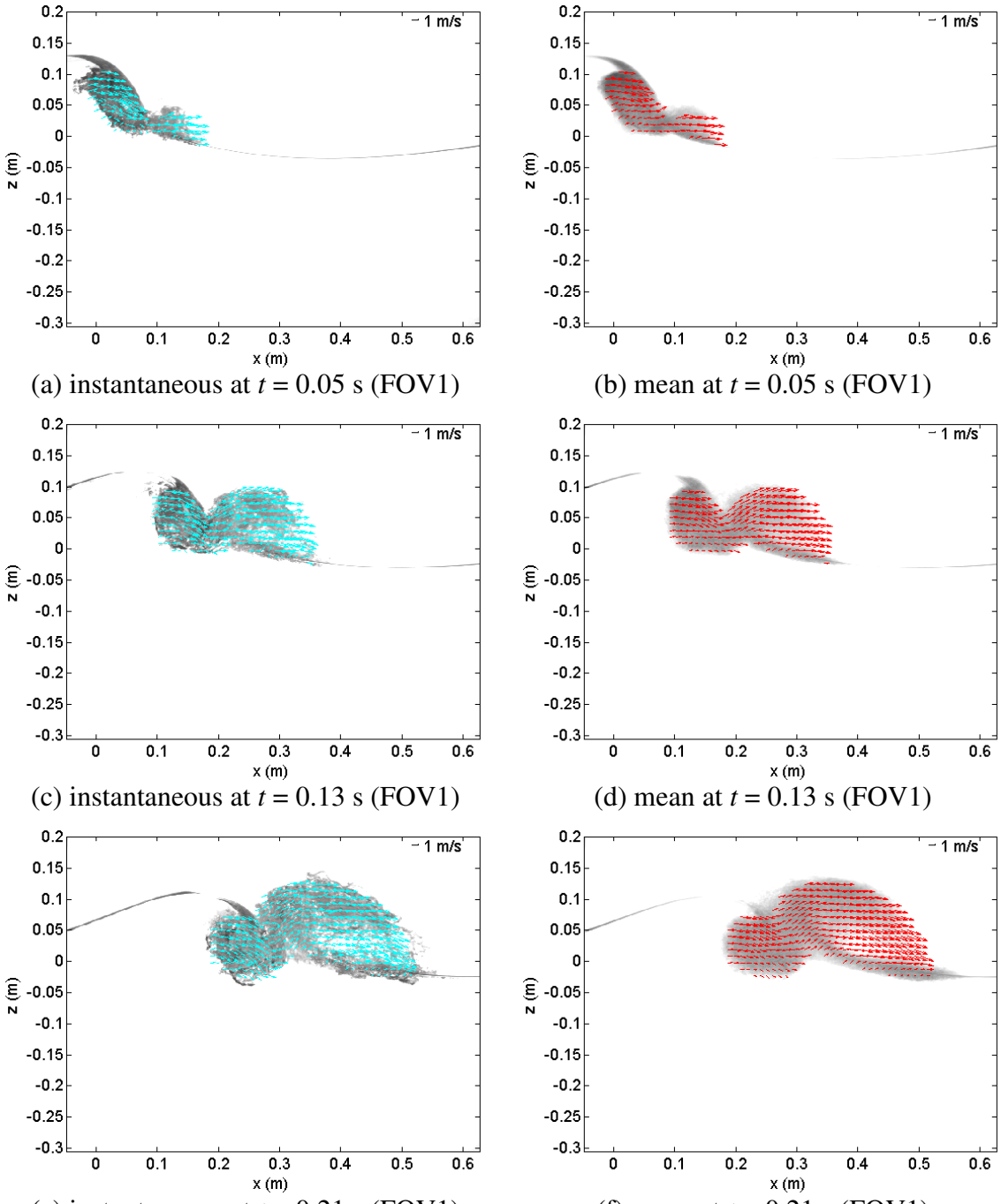

(a) instantaneous at t = 0.05 s (FOV1)

(b) mean at t = 0.05 s (FOV1)

(c) instantaneous at t = 0.13 s (FOV1)

(d) mean at t = 0.13 s (FOV1)

(e) instantaneous at t = 0.21 s (FOV1)

(f) mean at t = 0.21 s (FOV1)

Fig. 8.6 Examples of instantaneous and mean velocity fields.

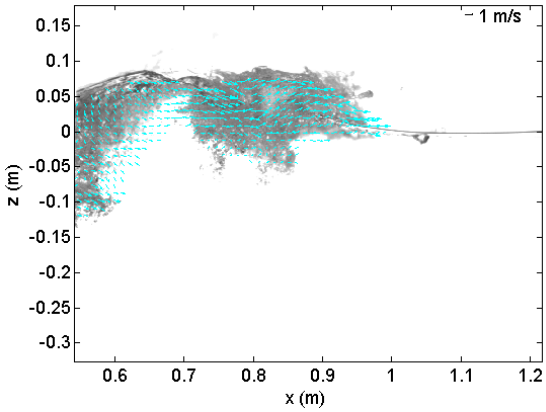

(g) instantaneous at t = 0.56 s (FOV2)

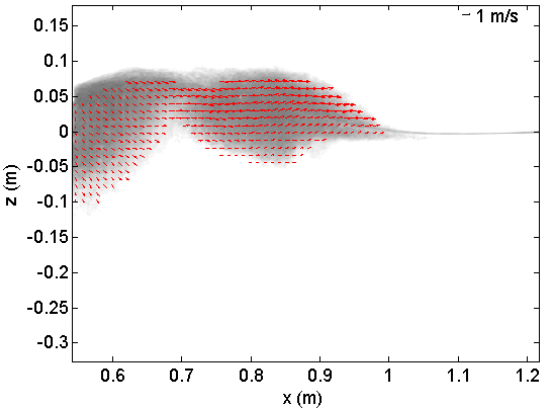

(h) mean at t = 0.56 s (FOV2)

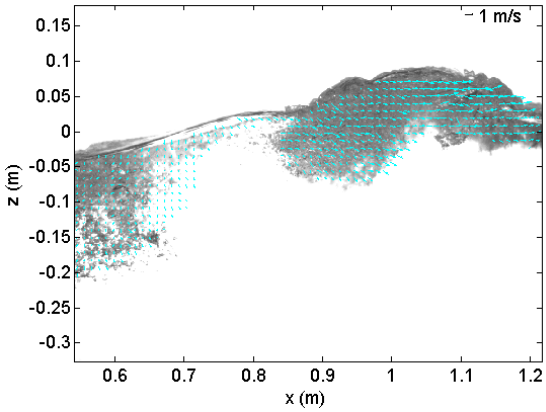

(i) instantaneous at t = 0.76 s (FOV2)

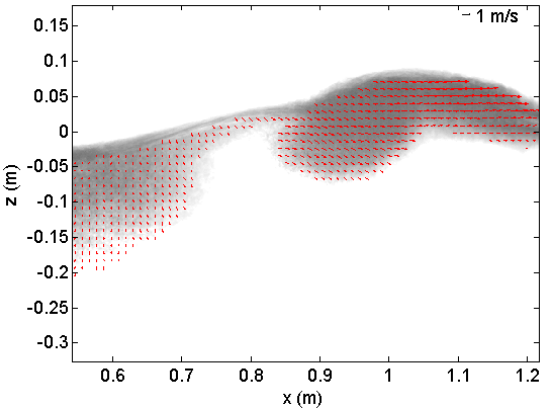

(j) mean at t = 0.76 s (FOV2)

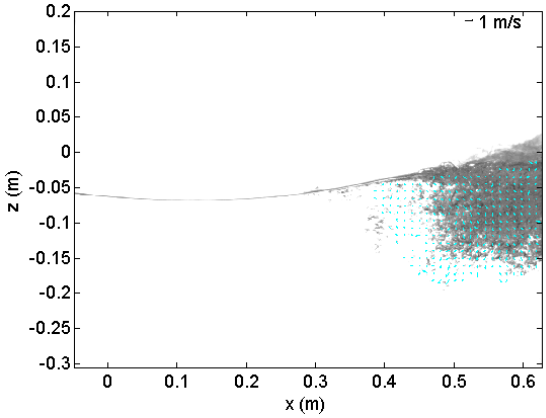

(k) instantaneous at t = 0.71 s (FOV1)

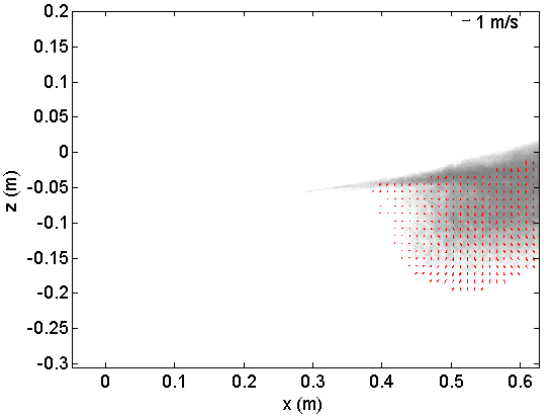

(l) mean at t = 0.71 s (FOV1)

Fig. 8.6 (Continued).

In Fig. 8.6, one of 20 instantaneous background images was overlapped with the other instantaneous velocity vectors for comparison while an averaged image of 20 instantaneous images was overlapped with the mean velocity vectors. Empty velocity vectors in the instantaneous velocity fields are rarely found and the plunging breaker has great repeatability.

8.5 Results from the BIV Measurements

Although numerous data was obtained from the BIV measurements, detailed results will not be presented in the main part of this dissertation. The BIV measurement results can be seen in appendix A. The time difference between presented figures is 0.05 s. Note that time resolution of original data is 0.01s. Table 8.1 shows the list for the BIV measurement results presented in appendix A.

BIV is indeed a reliable technique to measure velocity fields of the highly aerated region. However, it is essential to measure the velocity fields outside the aerated region to investigate the entire flow in the plunging breaker. Since the modified PIV technique used in this study is capable of measuring velocities of the entire flow field including the highly aerated region, most quantitative results are presented using the PIV analysis. Results from the PIV measurements can be seen in Chapters IX and X.

BIV results were mainly used to validate PIV results for the aerated region. In addition, for better comparison, various mask images for the PIV analysis were obtained from the BIV images to reduced errors caused by seeding particles as discussed in Chapter VII. The images taken using the BIV technique are also very helpful to describe flow structure of the breaking wave as shown in Chapter VI.

Table 8.1
List of the BIV measurement results in Appendix A

Figure Number	Description
Fig. A.1	Mean Velocity Map ($\sqrt{U^2+W^2}$)
Fig. A.2	Normalized Horizontal Velocity (U/C)
Fig. A.3	Normalized Vertical Velocity (W/C)
Fig. A.4	Normalized Mean Vorticity ($\Omega H/C$)
Fig. A.5	Normalized Mean Kinetic Energy (K/C^2)
Fig. A.6	Normalized Turbulent Kinetic Energy (k/C^2)
Fig. A.7	Normalized Horizontal Turbulence Intensity ($\sqrt{u'^2}/C$)
Fig. A.8	Normalized Vertical Turbulence Intensity ($\sqrt{w'^2}/C$)
Fig. A.9	Normalized Reynolds Stress ($-u'w'/C^2$)
Fig. A.10	Normalized Turbulent Kinetic Energy Transport by U (kU/C^3)
Fig. A.11	Normalized Turbulent Kinetic Energy Transport by W (kW/C^3)
Fig. A.12	Mean Void Ratio Before Calibration (α)
Fig. A.13	Relative Velocity ($U-C, W$)
Fig. A.14	Normalized Horizontal Local Acceleration ($\frac{\partial U}{\partial t}\Big/g$)
Fig. A.15	Normalized Vertical Local Acceleration ($\frac{\partial W}{\partial t}\Big/g$)
Fig. A.16	Normalized Horizontal Convective Acceleration ($\left(U\frac{\partial U}{\partial x}+W\frac{\partial U}{\partial z}\right)\Big/g$)
Fig. A.17	Normalized Vertical Convective Acceleration ($\left(U\frac{\partial W}{\partial x}+W\frac{\partial W}{\partial z}\right)\Big/g$)
Fig. A.18	Normalized Horizontal Total Acceleration ($\left(\frac{\partial U}{\partial t}+U\frac{\partial U}{\partial x}+W\frac{\partial U}{\partial z}\right)\Big/g$)
Fig. A.19	Normalized Vertical Total Acceleration ($\left(\frac{\partial W}{\partial t}+U\frac{\partial W}{\partial x}+W\frac{\partial W}{\partial z}\right)\Big/g$)

CHAPTER IX

MEAN QUANTITIES IN A PLUNGING BREAKER USING PIV

9.1 Introduction

The particle image velocimetry (PIV) technique was employed to measure the entire flow field. By modifying the traditional PIV system, a velocity field of the entire flow field including the highly aerated region was obtained with very high temporal and spatial resolution. Recently, laser Doppler velocimetry (LDV) and PIV have been mostly employed to measure flow velocities. Both techniques have some advantages and disadvantages. For example, the traditional PIV technique is the most reliable technique to obtain velocity maps in the spatial domain with very high spatial resolution; however, because the data sampling rate is about 10 Hz due to the limitation from a pulsed laser and a camera frame rate, there is lower temporal resolution.

The PIV method is very useful to obtain flow properties including the gradient terms such as vorticity and convective acceleration. However, due to the low temporal resolution it is not suitable to obtain flow properties including the time derivative or time-averaged values at an arbitrary point or station, such as local acceleration and fluxes of mass, momentum or energy.

On the other hand, the LDV technique provides time series of velocity at a point with high temporal resolution but it is a point measurement. It is useful to obtain time series of flow properties and time mean values. However, it is not suitable for flows

whose velocity gradient is important. Indeed, advantages of the PIV method are disadvantages of the LDV method and vice versa. The appropriate technique should be chosen depending on flow characteristics.

It is considered that the PIV technique is most reliable technique for the breaking wave measurements. However, there are two main concerns to be figured out in the PIV measurements. First, the traditional PIV has very low temporal resolution. Second, the technique cannot measure the inside of the aerated region although it is not a problem of PIV only. To investigate breaking waves experimentally, it is highly required to employ a proper measurement technique providing very high spatial and temporal resolution. In the present study, the spatial and temporal resolutions of the final data in the PIV measurements are 5.78 mm and 10 ms, respectively. Note that the resolutions in the BIV measurements are 5.26 mm and 10 ms. It was possible to use such very high resolutions due to use of a high speed camera and a continuous Argon-Ion laser to generate a light sheet without interruption. Originally, the PIV was employed to measure only the outside of the aerated region where BIV cannot measure as shown in Chapter VIII and Appendix A. During the preliminary test of the PIV measurement, it was found that the velocity field of the aerated region can be obtained using the modified PIV technique. This is because the power of the continuous laser is much less than the power of the pulsed laser used in the traditional technique such as a Nd:YAG laser. Various intensities due to air-water mixture in the aerated region were found. It is very similar to the images from the BIV measurements. In addition, weak laser power does not effect the quality of the velocity field for the outside of the aerated region.

Mean flow characteristics of the plunging breaking waves are presented in this chapter and turbulent characteristics will be discussed in Chapter X. Procedure of data analysis and validation of the PIV measurement are given in Section 9.2 and 9.3 respectively. Spatial analysis and temporal analysis of velocity, vorticity and mean kinetic energy can be seen in Section 9.4, 9.5 and 9.6 respectively.

9.2 PIV Data Analysis Procedure

Since the detailed experimental setup and conditions can be seen in Chapter V, The PIV data analysis procedure is briefly described here. A total of 14 fields of view (FOV) were chosen to cover the entire plunging wave as shown in Fig. 5.1. To obtain mean and turbulent properties, 20 measurements were repeated with the same condition for every 14 FOV. Fig. 9.1 shows the PIV image processing. Images were taken for 4 s with a frame rate of 500 *fps*. A total of 567560 images (2027 images/measurement × 20 measurements/FOV × 14 FOVs) were obtained for the plunging breaker in the PIV measurements. Note that the number of images for a spilling breaker is 972960. By means of a preliminary test and BIV results, the time difference *dt* between two coupled images for velocity calculation with cross-correlation algorithms were carefully chosen to decrease errors caused by *dt*. 2 ms or 4 ms of *dt* were used depending on the flow velocity. Due to the large amount of image data, temporal resolution for data analysis was decided as 10 ms. Although the data sampling rate was reduced from 500 Hz to 100 Hz, it is about 10 times better than the sampling rate of the traditional PIV measurements.

Fig. 9.2 shows an outline chart for the procedure of the PIV experiment and data analysis. Only the essential process is shown in the figure. It was necessary for the huge

data set and their repetitive analysis. With the exception of DaVis which is a commercial software was used for the velocity calculation of instantaneous measurements, Matlab software was used for most of the image processing and data analysis.

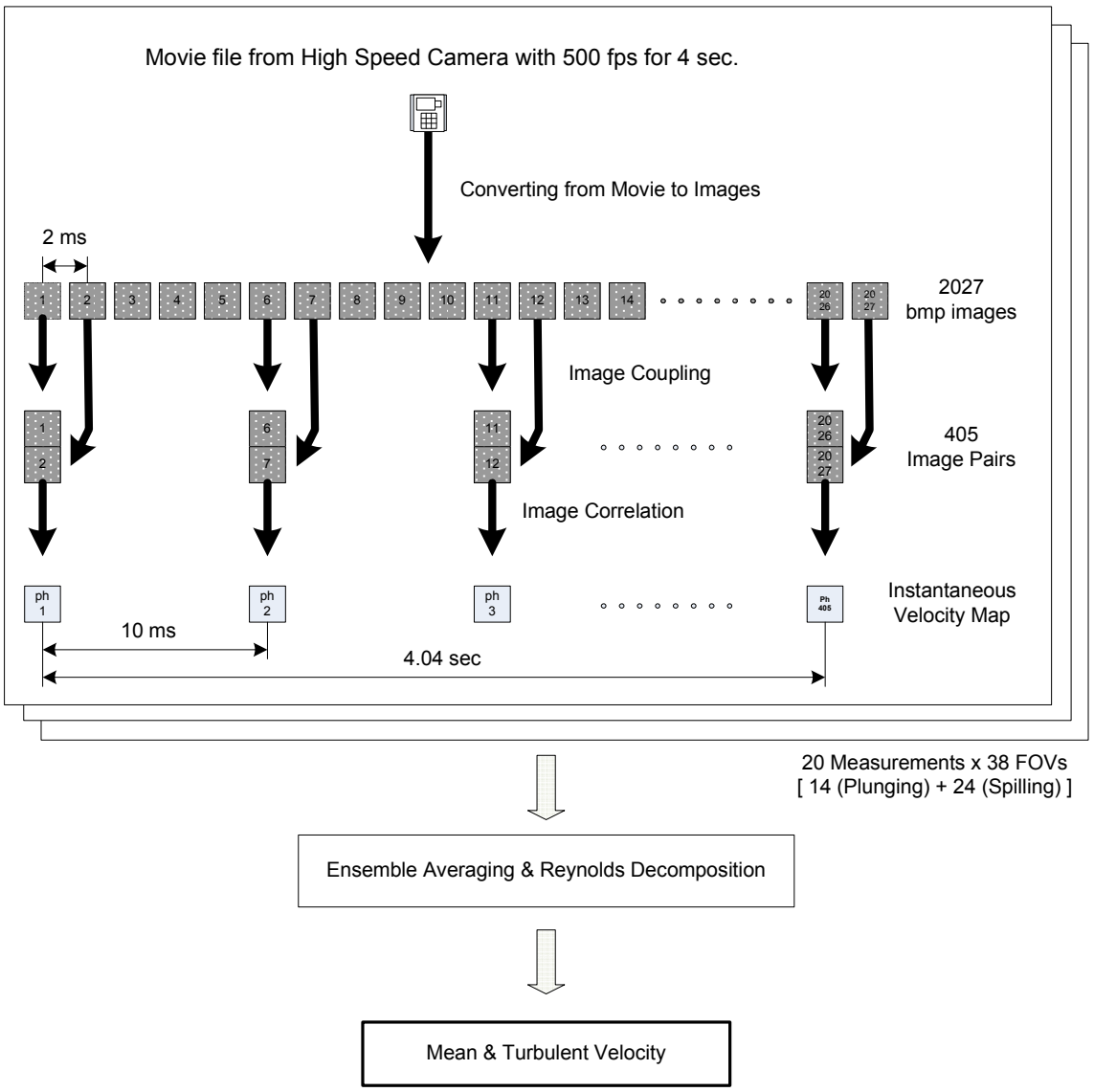

Fig. 9.1 PIV image processing.

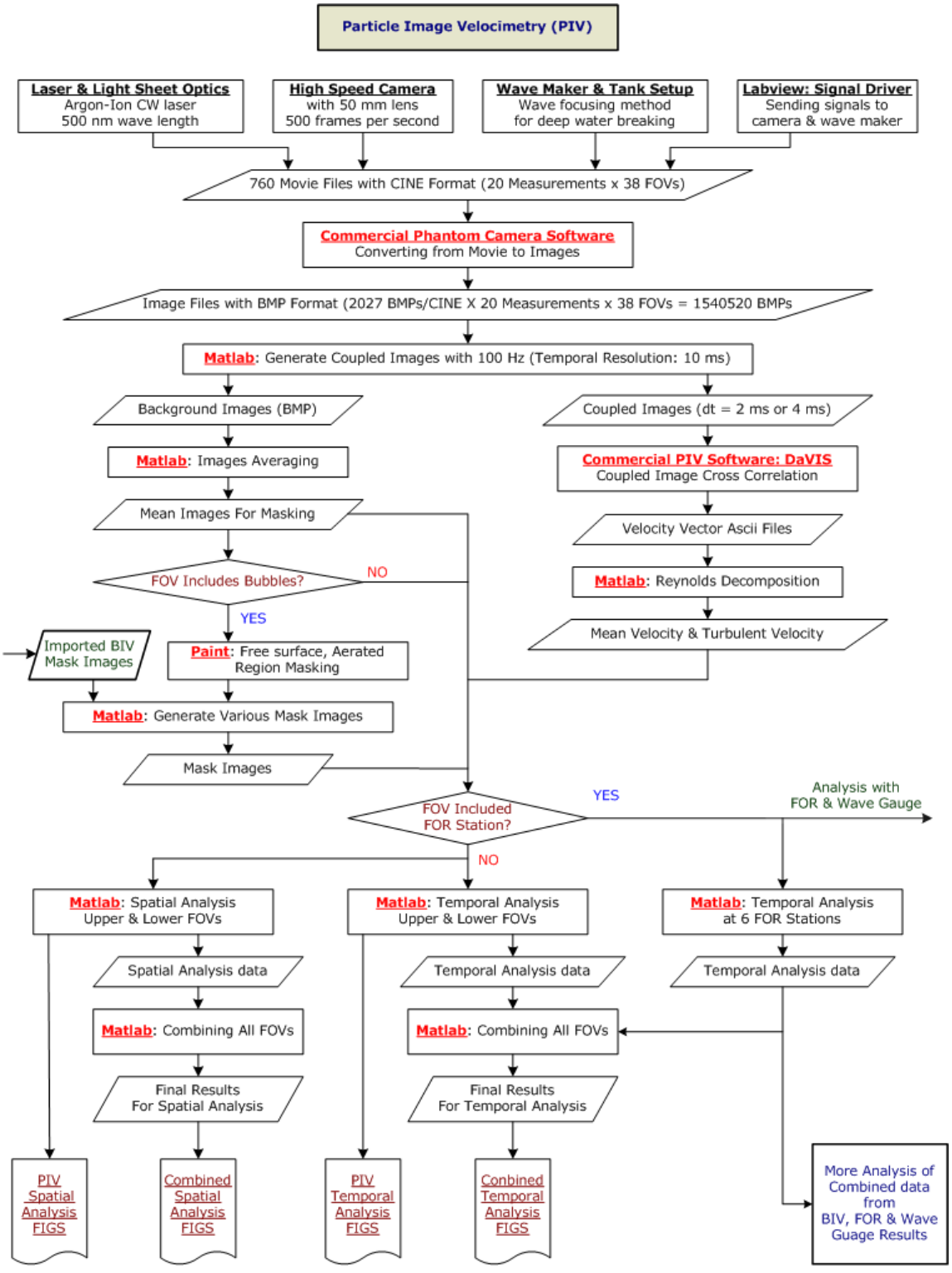

Fig. 9.2 PIV experiment and data analysis procedure.

9.3 Validation of PIV Measurements

It is necessary to validate the velocity obtained from the PIV measurements. It is required to check all the experimental conditions although the PIV technique is a well-known technique. Water particle velocities obtained from the PIV measurements before breaking were compared with those obtained from Stokes 5th order wave. It is impossible to validate velocities of the inside aerated region with theory. However, the velocities from the PIV measurements will be compared with results from BIV which is validated as shown in Chapter VIII. Since the wave focusing method was used unlike surf zone breaking waves and the location of the breaking point was very close to the wavemaker, it was difficult to find a regular wave to compare the wave theory. The only FOV before the first impinging point is FOV1, the closest FOV to the wavemaker. However, a primary wave has already deformed its shape, so it was determined to find the closest time when its properties are very similar to Stokes 5th order waves.

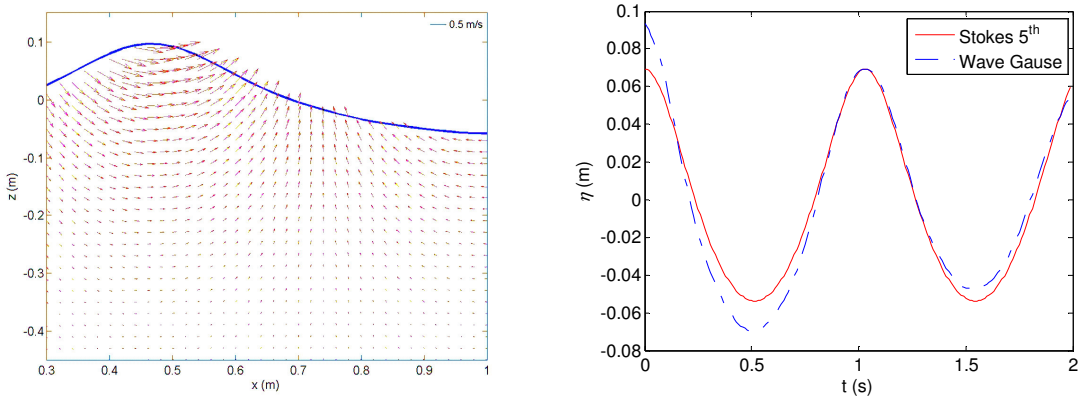

(a) velocity map of Stokes 5th wave (b) wave elevation

Fig. 9.3 Example of Stokes 5th wave and comparison of wave elevation.

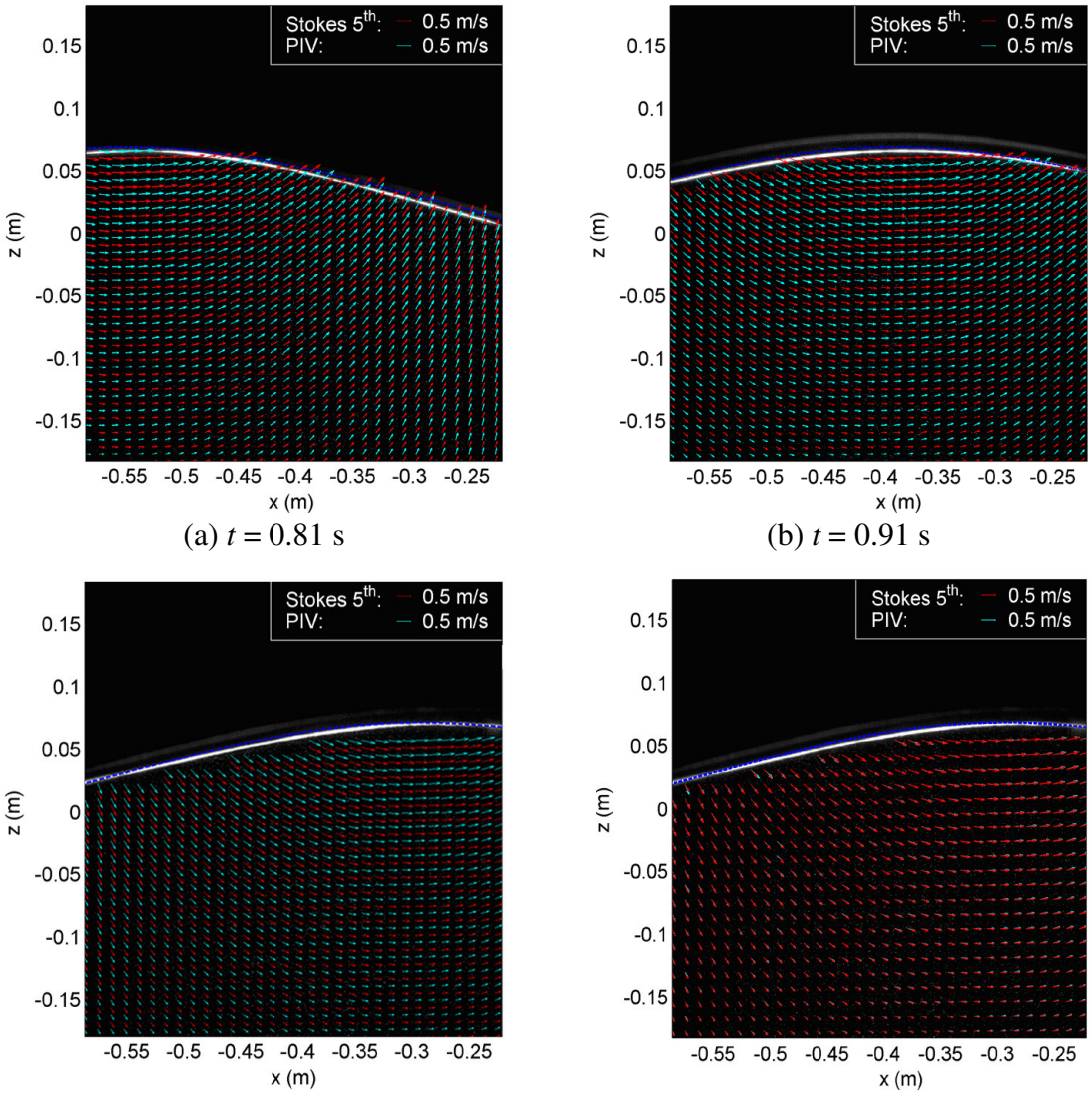

(a) $t = 0.81$ s (b) $t = 0.91$ s

(c) $t = 0.96$ s (d) $t = 0.96$ s

Fig. 9.4 Comparison of PIV velocity with Stokes 5th (PIV FOV1).

Fig. 9.3(a) shows an example of generated Stokes waves. By controlling wave properties of the generated Stokes wave, it was found that the instance shown in Fig. 9.3(b) was the best condition for the comparison although there was a difference near the trough. Therefore, the velocities near the crest were compared as shown in Fig. 9.4. The location is the first FOV (FOV1) in the PIV measurements and the time is around 0.9 s

after the primary wave passed the FOV1. Mean absolute error is about 0.004 m/s in horizontal velocity and 0.002 m/s in vertical velocity, where the absolute error is defined as $\left|U_{Stokes5^{th}} - U_{PIV}\right|$. Mean relative error is approximately 1.8% in horizontal velocity and 5.9% in vertical velocity, where the absolute error is defined as $\left|U_{Stokes5^{th}} - U_{PIV}\right| \Big/ U_{Stokes5^{th}}$.

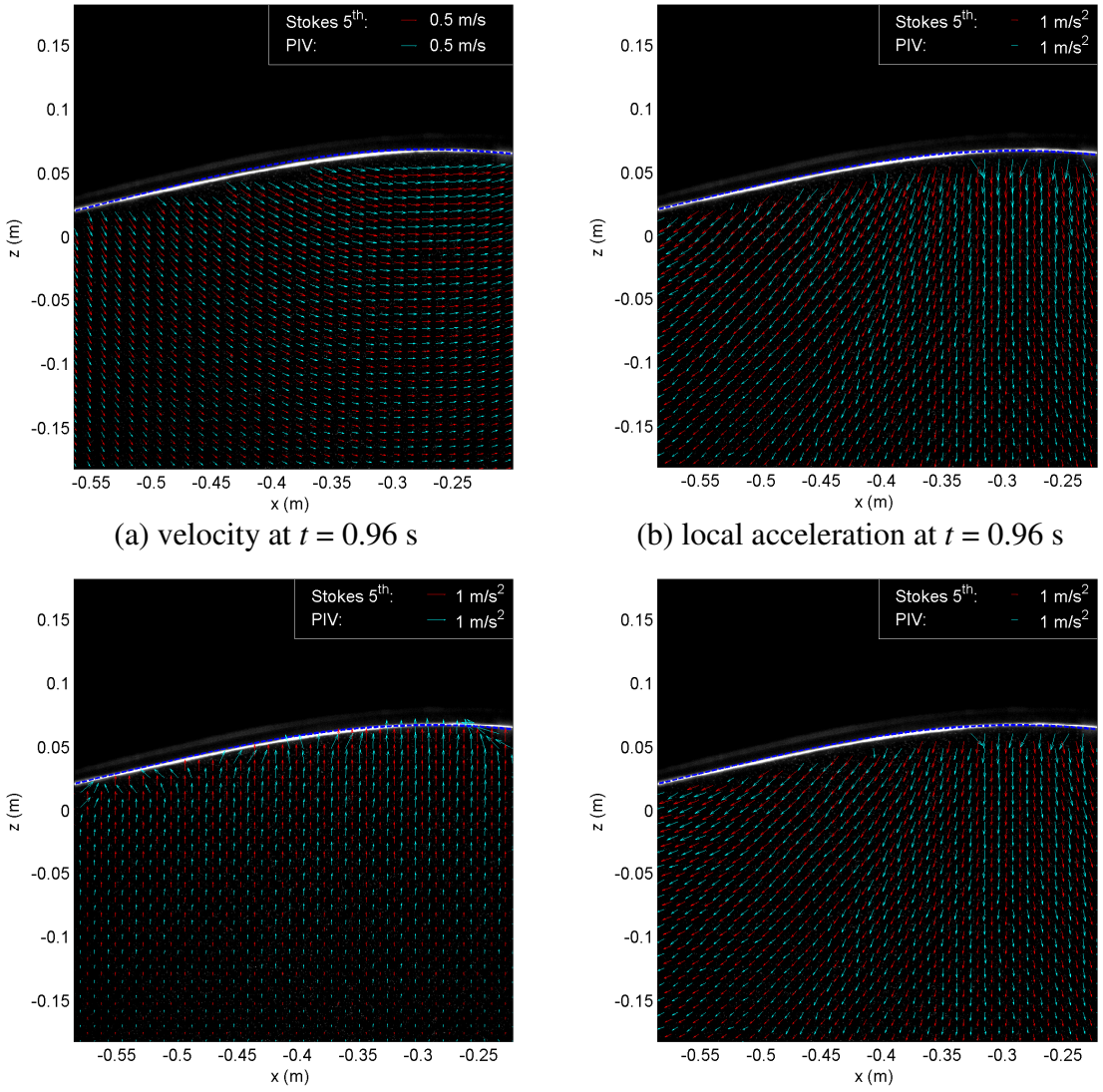

(a) velocity at t = 0.96 s

(b) local acceleration at t = 0.96 s

(c) convective acceleration at t = 0.96 s

(d) total acceleration at t = 0.96 s

Fig. 9.5 Example of acceleration measurement using PIV.

Fig. 9.5 shows examples of acceleration fields obtained from the PIV measurements. Local acceleration as well as convective acceleration can be obtained due to high temporal resolution.

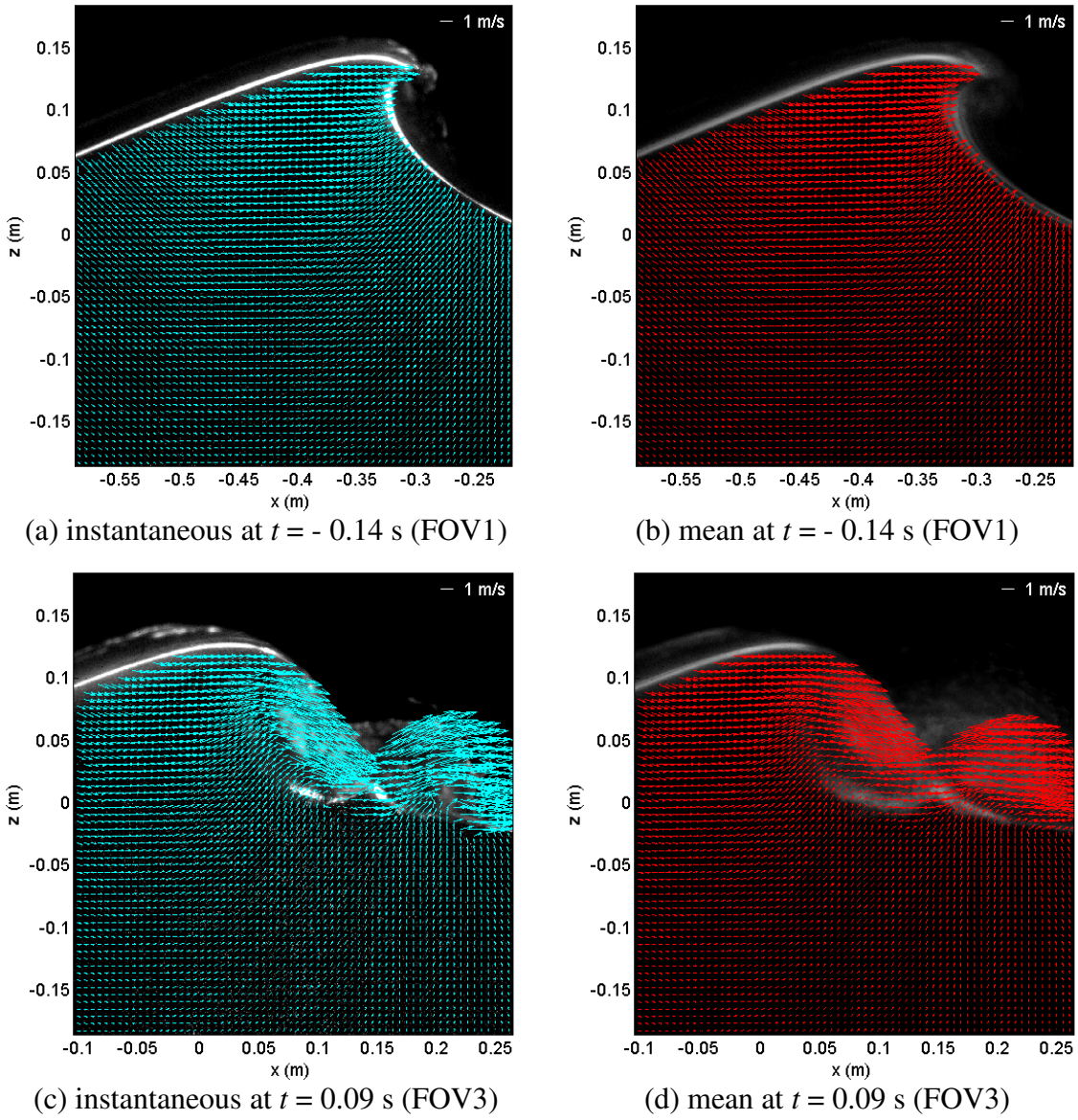

(a) instantaneous at t = - 0.14 s (FOV1)

(b) mean at t = - 0.14 s (FOV1)

(c) instantaneous at t = 0.09 s (FOV3)

(d) mean at t = 0.09 s (FOV3)

Fig. 9.6 Example of instantaneous (cyan) and mean (red) velocity fields.

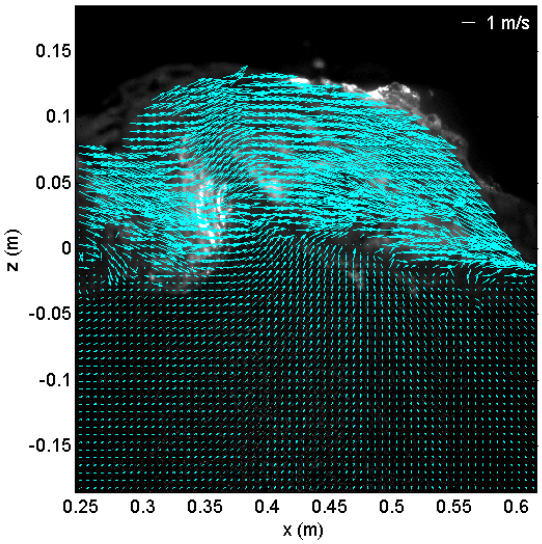

(e) instantaneous at t = 0.25 s (FOV5)

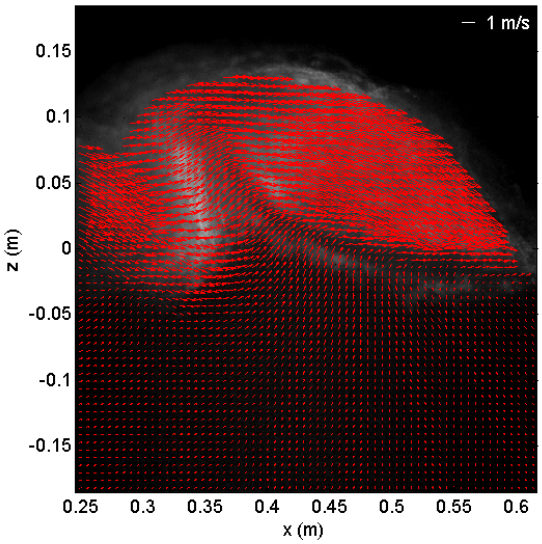

(f) mean at t = 0.25 s (FOV5)

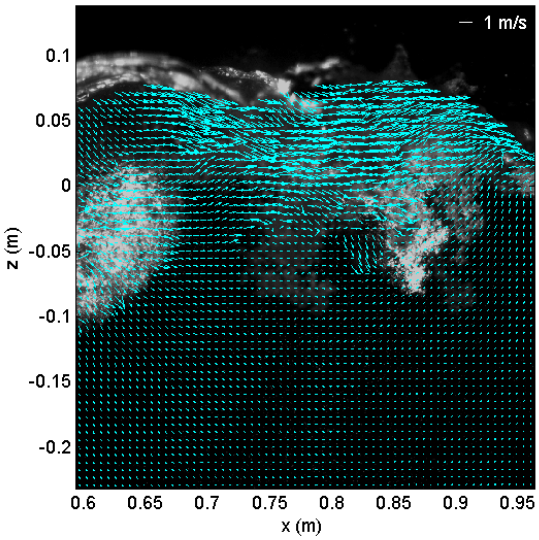

(g) instantaneous at t = 0.56 s (FOV7)

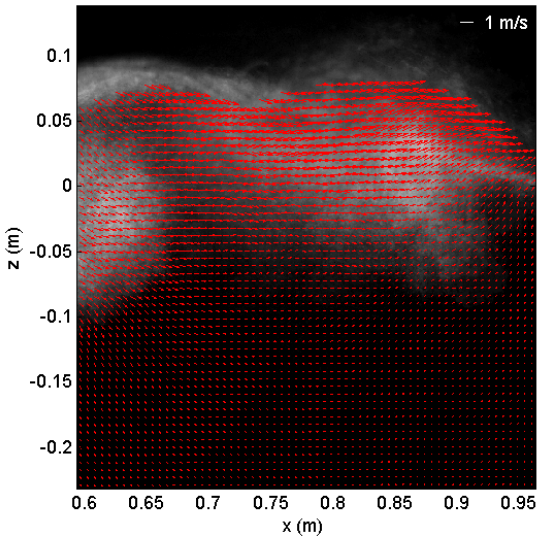

(h) mean at t = 0.56 s (FOV7)

Fig. 9.6 (Continued).

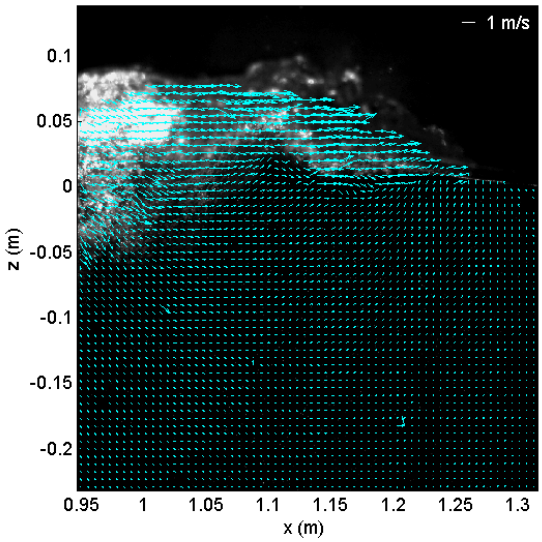

(i) instantaneous at t = 0.76 s (FOV9)

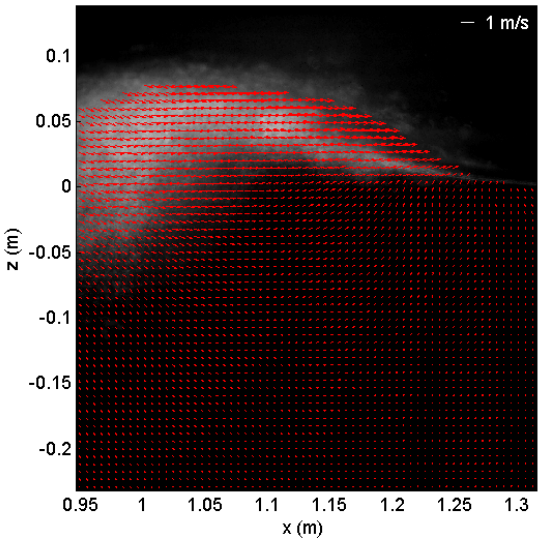

(j) mean at t = 0.76 s (FOV9)

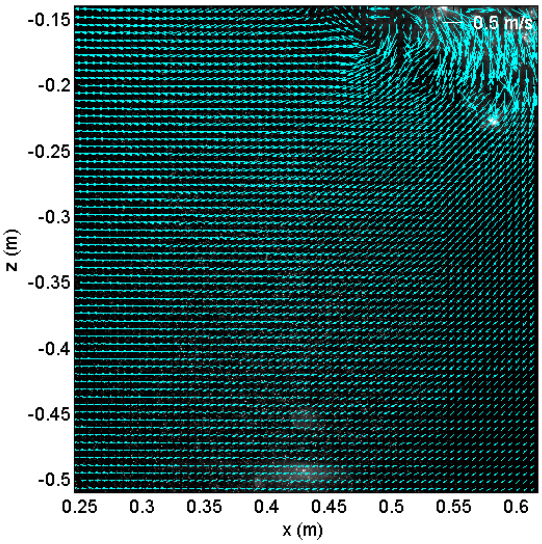

(k) instantaneous at t = 0.75 s (FOV6)

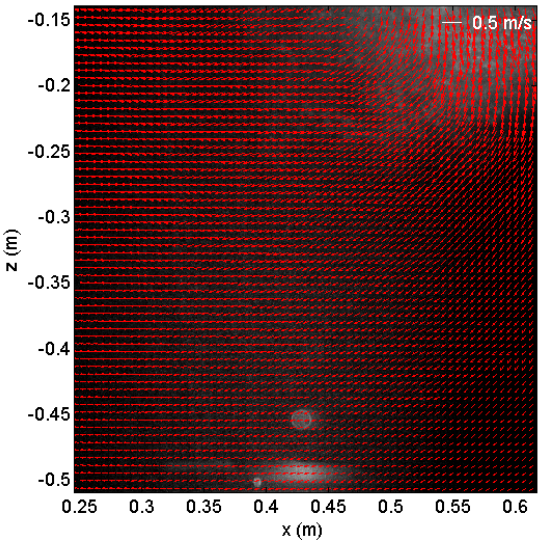

(l) mean at t = 0.75 s (FOV6)

Fig. 9.6 (Continued).

Fig. 9.6 shows examples of instantaneous and mean velocity fields at important moments, such as the first and second splash-ups. One of the instantaneous velocity fields can be seen on the left side with a cyan color and right side figures with a red color represent mean velocity fields at the corresponding phases. Fig. 9.6(a) and (b) show one

of the instantaneous velocity fields and a corresponding mean velocity field when the wave begins overturning. Fig. 9.6(c), (e) and (g) show the first impingement and splash-up, the first splash-up and mixture spray impingement, and the second impingement and splash-up. Fig. 9.6(k) shows the first roller in FOV6 which is one of the lower FOVs. Note that an even number of FOV represents FOVs at upper rows including free surface and an odd number FOV represents FOVs at lower rows as shown in Fig. 7.11.

Empty velocity vectors in the instantaneous velocity fields are rarely found even in the highly aerated region and the plunging breaker has great repeatability as shown in Fig. 9.6. Owing to good quality of the instantaneous velocity fields, it was not necessary to apply any kind of post processing to the instantaneous velocity fields shown in the figure. This is suggested to obtain more accurate quantities such as mean velocity and vorticity where their gradients are high.

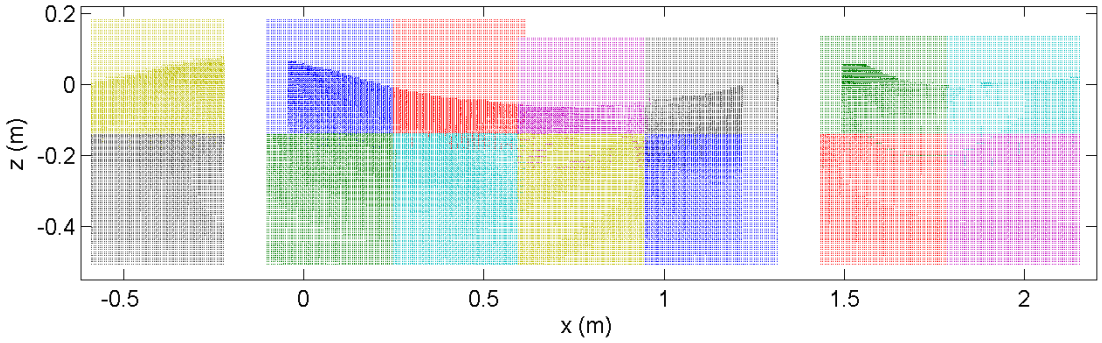

Fig. 9.7 Example of combining 14 PIV FOVs.

Fig. 9.7 shows the combined PIV FOVs. The number of grids for each FOV is 64 × 64 and the individual FOV is displayed with a different color. Two empty columns are caused by two steel columns of the wave tank.

Velocity data validation for the overlapped region of several FOVs is also necessary to avoid errors coming from the boundary of the FOV. Figs. 9.8 and 9.9 show examples of velocity vectors at the overlapped region of four FOVs. Except four corners, velocity vectors displayed show the overlapped vectors from two or four FOVs (middle). Figs. 9.8 and 9.9 show the overlapped regions of FOV3 to FOV6 and FOV5 to FOV8 respectively. They have good agreement at the region as shown in figures.

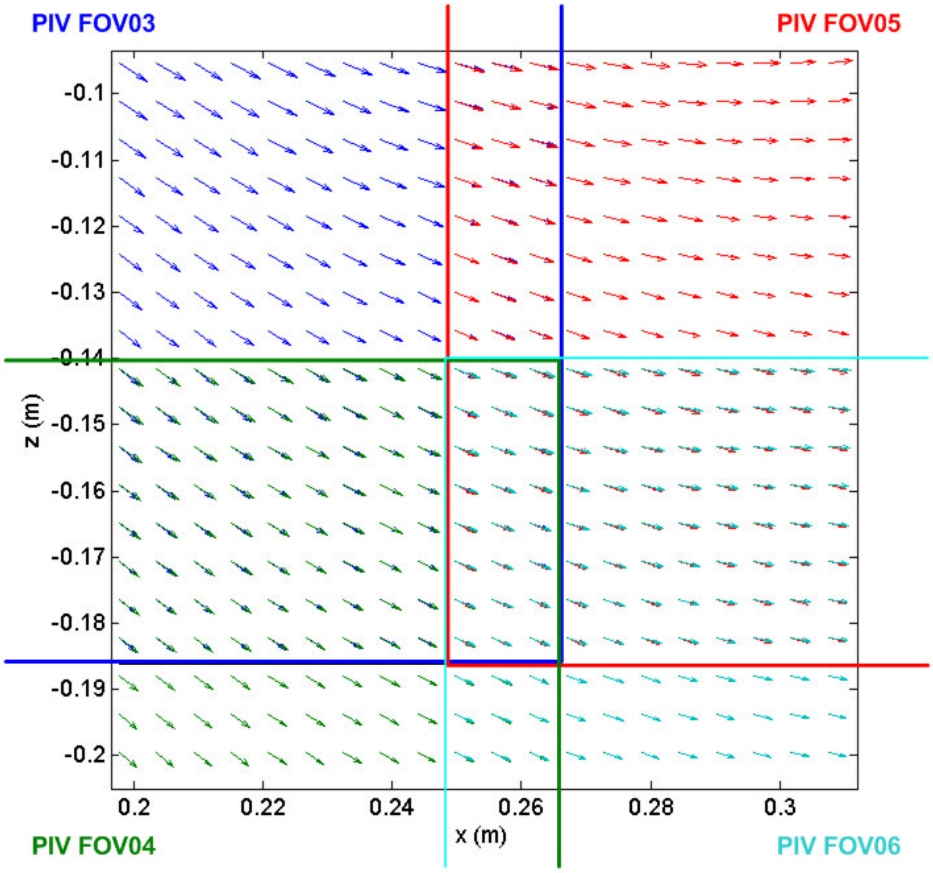

Fig. 9.8 Example of velocity fields at the overlap region (FOV3-6).

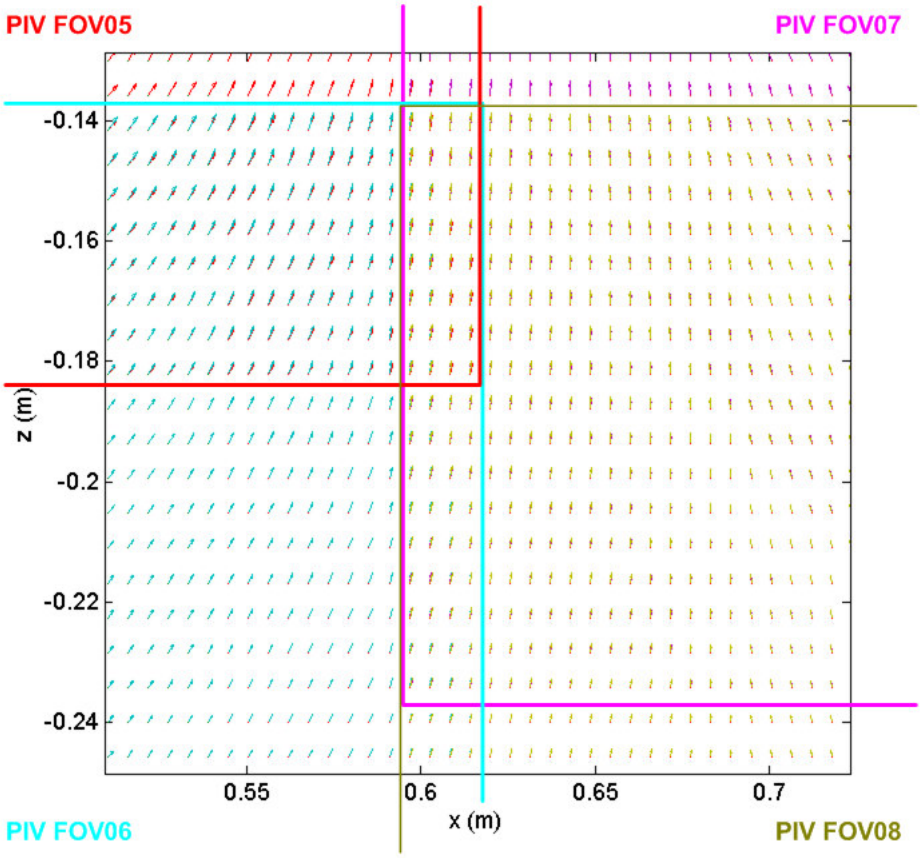

Fig. 9.9 Example of velocity fields at the overlap region (FOV5-8).

9.4 Mean Velocity

Mean and turbulent velocity fields were obtained by the ensemble average of 20 instantaneous velocity fields shown in Eqs. (9.1) and (9.2).

$$U(x,z,t)=\frac{1}{N}\sum_{i=1}^{N}u_i(x,z,t) \tag{9.1}$$

where U and u_i are the mean and instantaneous velocity and N is the total number of experiments. Therefore, fluctuating velocity for each instantaneous velocity can be obtained from

$$u_i'(x,z,t)=u_i(x,z,t)-U(x,z,t) \tag{9.2}$$

For convenience, the root mean square of u_i' is denoted by u' shown in Eq. (9.3).

$$u' = \sqrt{\overline{u_i'^2}}\,, \quad w' = \sqrt{\overline{w_i'^2}} \tag{9.3}$$

9.4.1 Spatial Analysis of Mean Flow Velocity

Spatial analysis results are presented in this section. The spatial analyses for mean flow were performed with high temporal resolution of 10 ms. The total number of FOVs is 14 as shown in Fig. 9.10. 14 red windows represent FOVs in the PIV measurements. Due to the large amount of data, results for important wave phases are discussed with some figures from an individual FOV for detailed discussion. For example, wave deformation and the first impingement are seen in PIV FOV1 and FOV3 respectively. The second and third impingements are seen in FOV7 and FOV9. Every fully developed splash-up processes are seen in FOV5, 7 and 9. Spilling waves after the third splash-up can be seen in FOV11 and FOV13. More results from combined FOVs with a mosaic method can be seen in Appendix B.

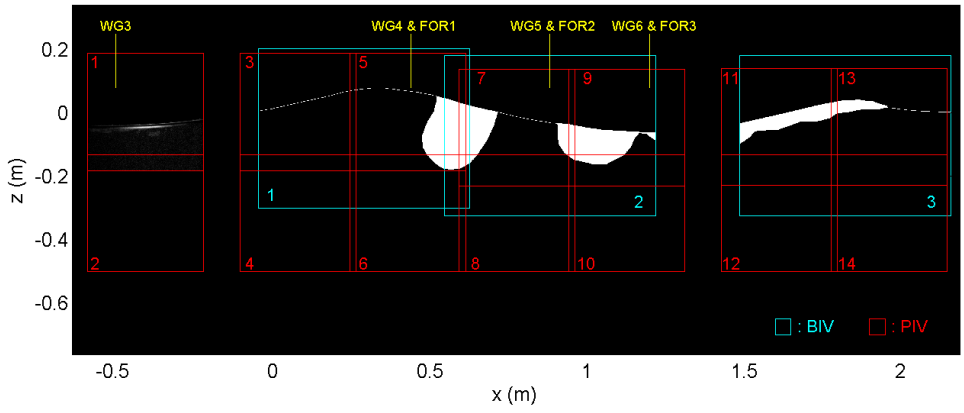

Fig. 9.10 Location of fields of view (FOV) in the PIV measurements (red).

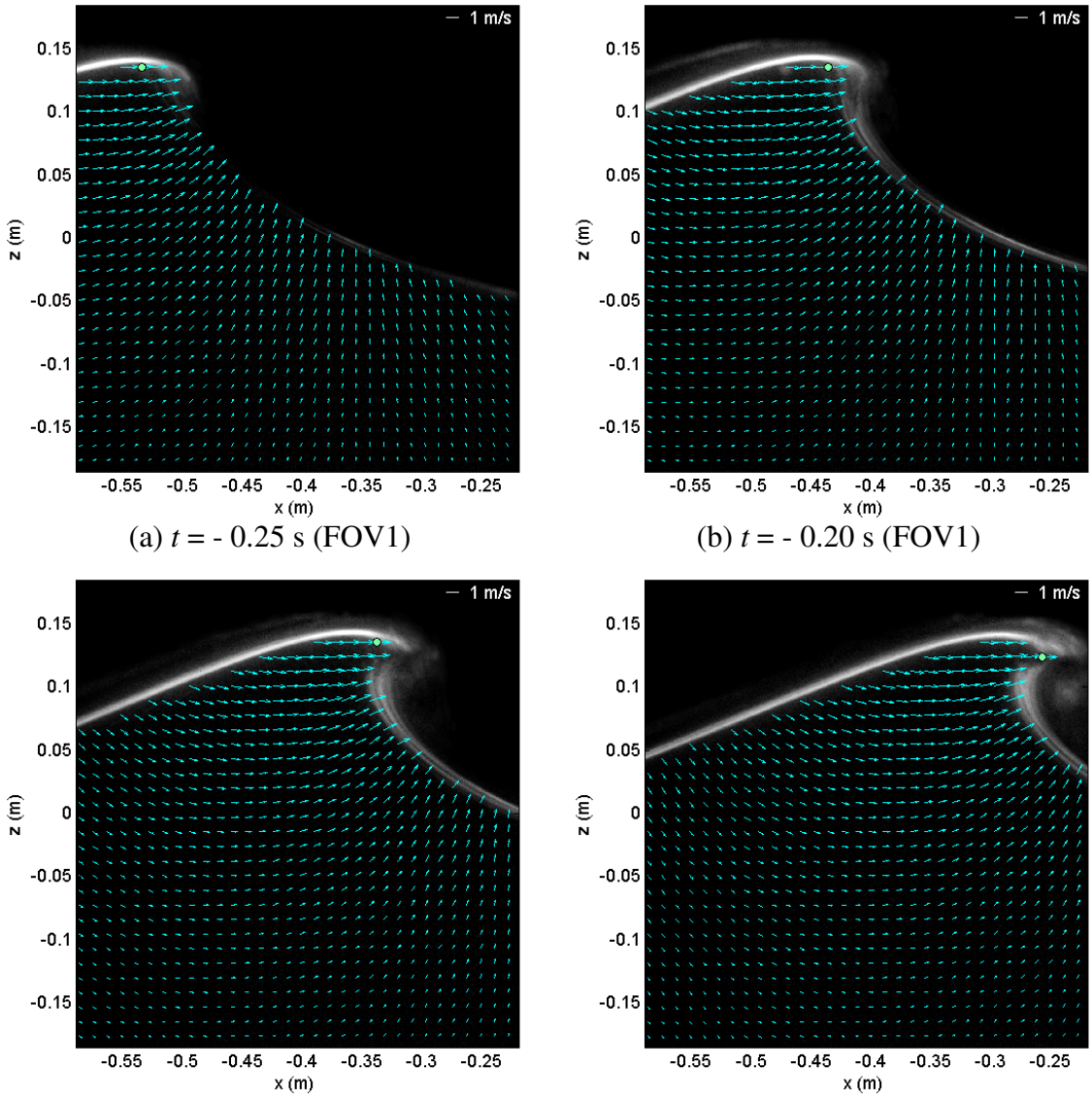

(a) t = - 0.25 s (FOV1)

(b) t = - 0.20 s (FOV1)

(c) t = - 0.15 s (FOV1)

(d) t = - 0.10 s (FOV1)

Fig. 9.11 Mean velocity in the pre-impinging region (FOV1).

Mean velocity fields for the overturning moment are shown in Fig. 9.11. Note that a green circle in Fig. 9.11 represents the location of maximum speed. For a better view, every other velocity vectors are presented in both x and z directions. The wave face

becomes vertical at x = - 0.42 m and t = - 0.2 s. Maximum velocity occurs at the crest and its magnitude is about 1.4C. Note that C is the wave phase speed and its magnitude is 1.3 m/s. Large upward momentum with maximum upward velocity more than 0.5C is transported to large horizontal momentum and the horizontal velocity at the crest is linearly increased during the overturning process as shown in Fig. 9.12.

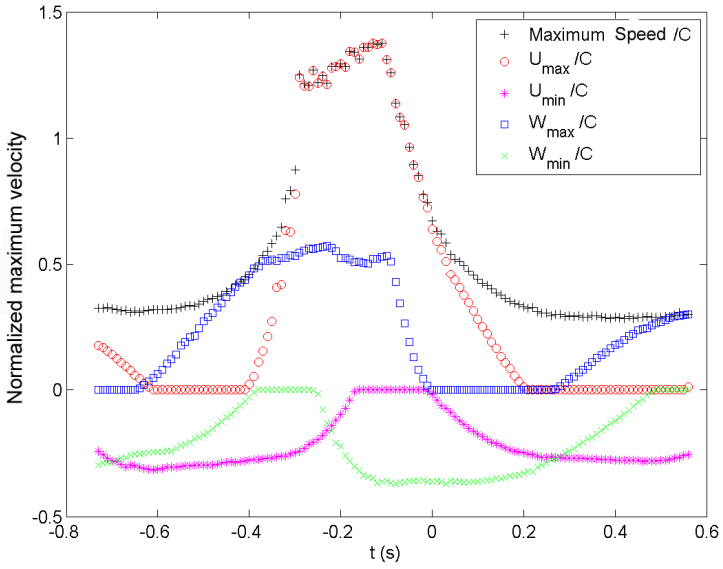

Fig. 9.12 Maximum velocity at FOV1.

Fig. 9.13 shows the beginning of the first splash-up process followed by the first impingement at FOV3. The velocity field at the overturning moment can be seen in Fig. 9.13(a). At this moment, the maximum horizontal and downward velocities of the overturning jet are about 1.5C and 0.6C and the velocities of the jet are gradually increased to 1.68C and 0.71C until the first impinging moment [Fig. 9.13(b)]. Fig. 9.14 shows maximum velocity variation in time at FOV3. Location of the maximum velocity

is moved from the impinging jet to the splash-up from t = 0.03 s. Maximum horizontal velocity in the entire breaking process occurs at the beginning of the first splash-up at t = 0.05 s and its magnitude is about 2.14C [Fig. 9.13(d)].

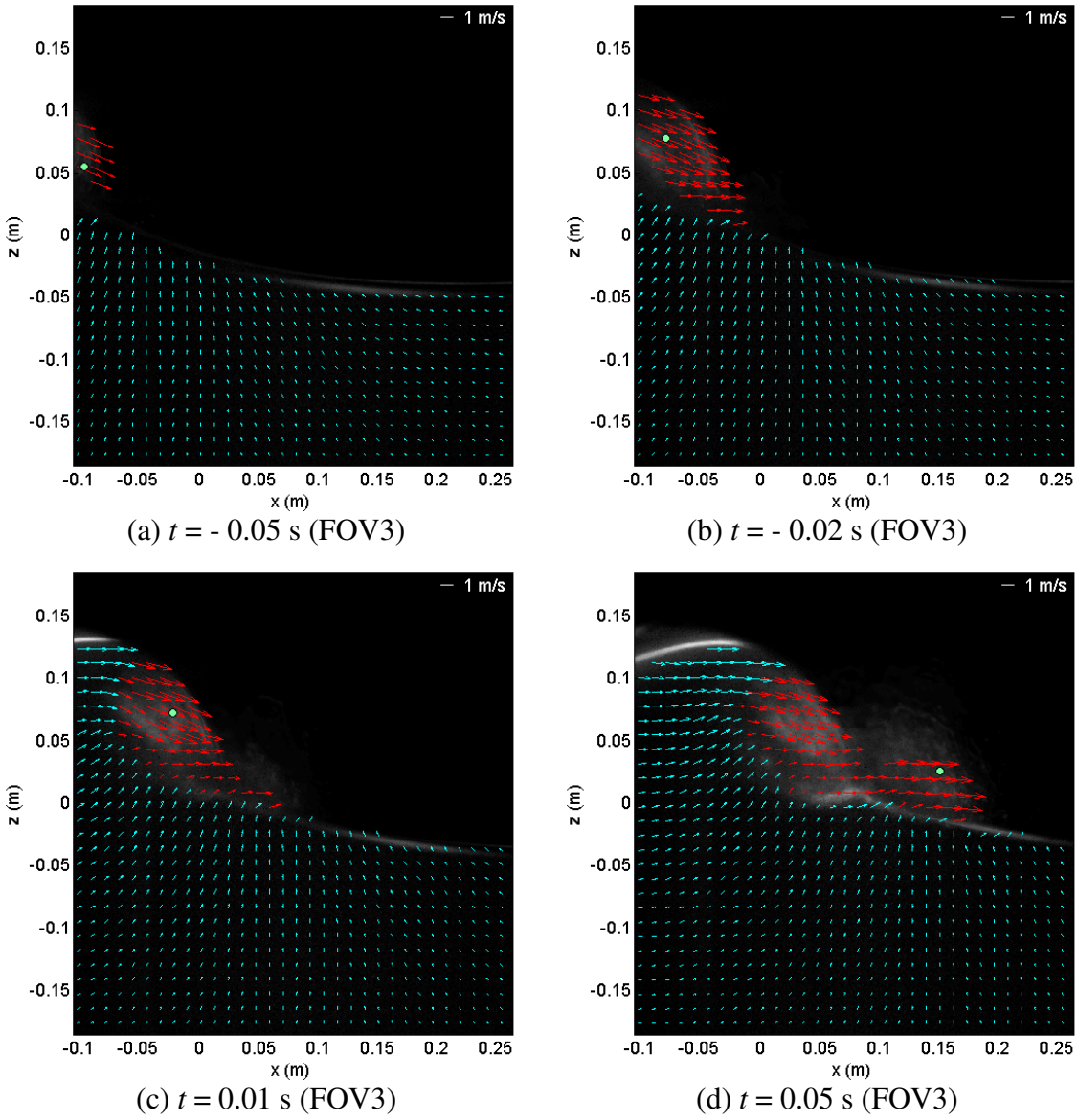

(a) t = - 0.05 s (FOV3)

(b) t = - 0.02 s (FOV3)

(c) t = 0.01 s (FOV3)

(d) t = 0.05 s (FOV3)

Fig. 9.13 Velocity at the first impingement and beginning of the first splash-up (FOV3).

Fig. 9.13(d) shows the moment when the maximum velocity occurs through the entire breaking process. As discussed in Chapter VI, a new local crest of water wave is generated between two large rollers due to the impinging jet, which can be seen at x = 0.08 m in Fig. 9.13(d). This small water crest is moving in front of the impinging first roller and its height is increased as the energy of the impinging jet is decreased gradually. As mentioned in Chapter VI, the impinging jet is rarely reflected to the splash-up. Most of the water structure of the jet penetrates into the front wave surface continuously with a clockwise rolling motion. Large downstream and downward momentum of the impinging jet begins to transfer to the ascending new water crest, which is causing the first splash-up and the second impingement later.

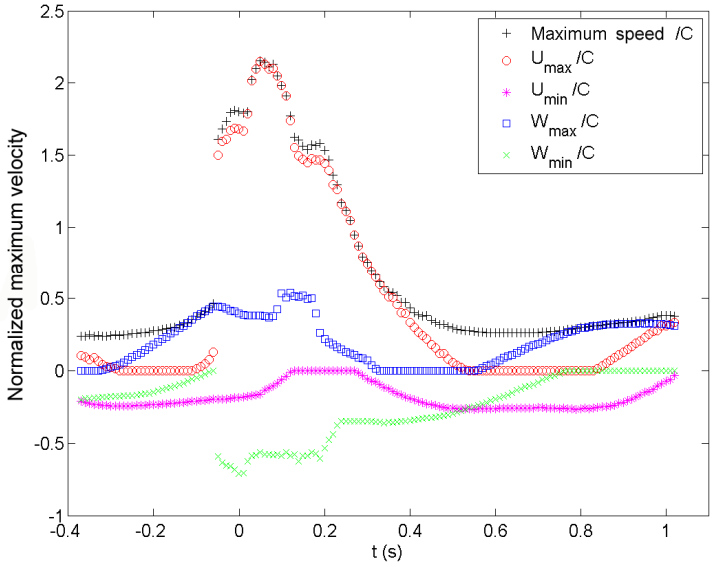

Fig. 9.14 Maximum velocity at FOV3.

It is difficult to observe the clockwise roller motion in normal velocity fields such as Fig. 9.13 due to large horizontal velocity of flow. Relative velocity fields are obtained

by means of subtracting the phase speed from the horizontal velocity. Two roller motions can be seen in Fig. 9.15. Horizontal velocity near the wave crest of the impinging jet is very close to the phase speed as shown in Fig. 9.15.

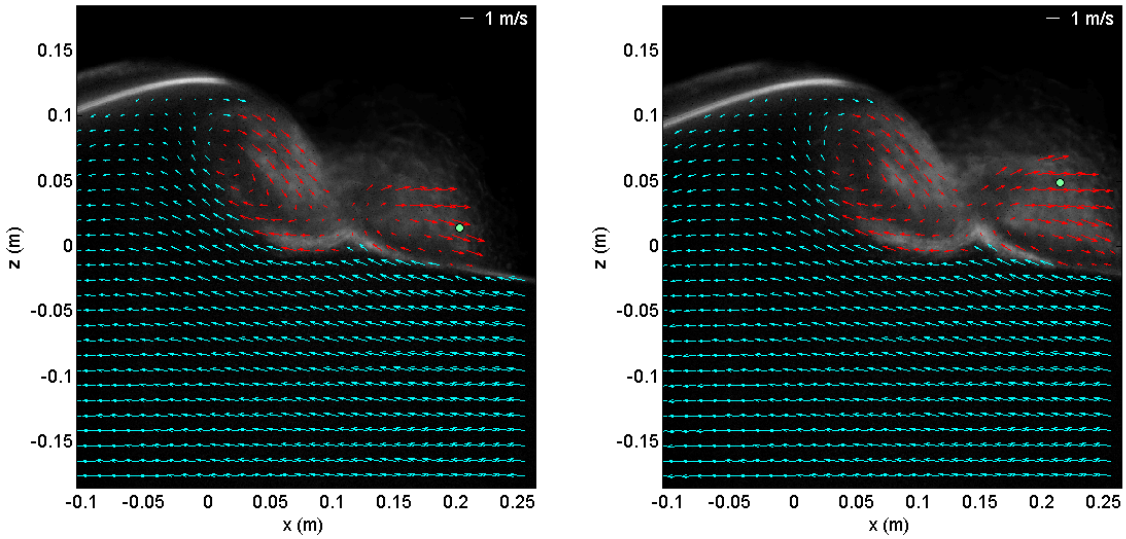

(a) t = 0.07 s (FOV3) (b) t = 0.09 s (FOV3)

Fig. 9.15 Relative velocity by moving frame with *C* (*U*-*C*) (FOV3).

Fig. 9.16 shows velocity fields at the first splash-up process followed by the first impingement. There is a first backward impingement onto the first impinging roller due to the ascending crest as shown in Fig. 9.17 and the first backward impingement will be discussed later. One of most important processes in this moment and region is the newly ascending water crest caused by the impinging jet. The impinging first roller is continuously providing large momentum to the ascending crest. The ascending crest is accelerated with large kinetic energy in an upward direction. The surface of the ascending crest becomes turbulence and the upper part of the crest is splashed up with

the form of water spray. The size of the second roller in the first splash-up region is gradually increased although the velocity of the splash-up decreases gradually as shown in Fig. 9.18. Air-water mixture spray with maximum velocity caused by the first splash-up impinges onto the front trough continuously.

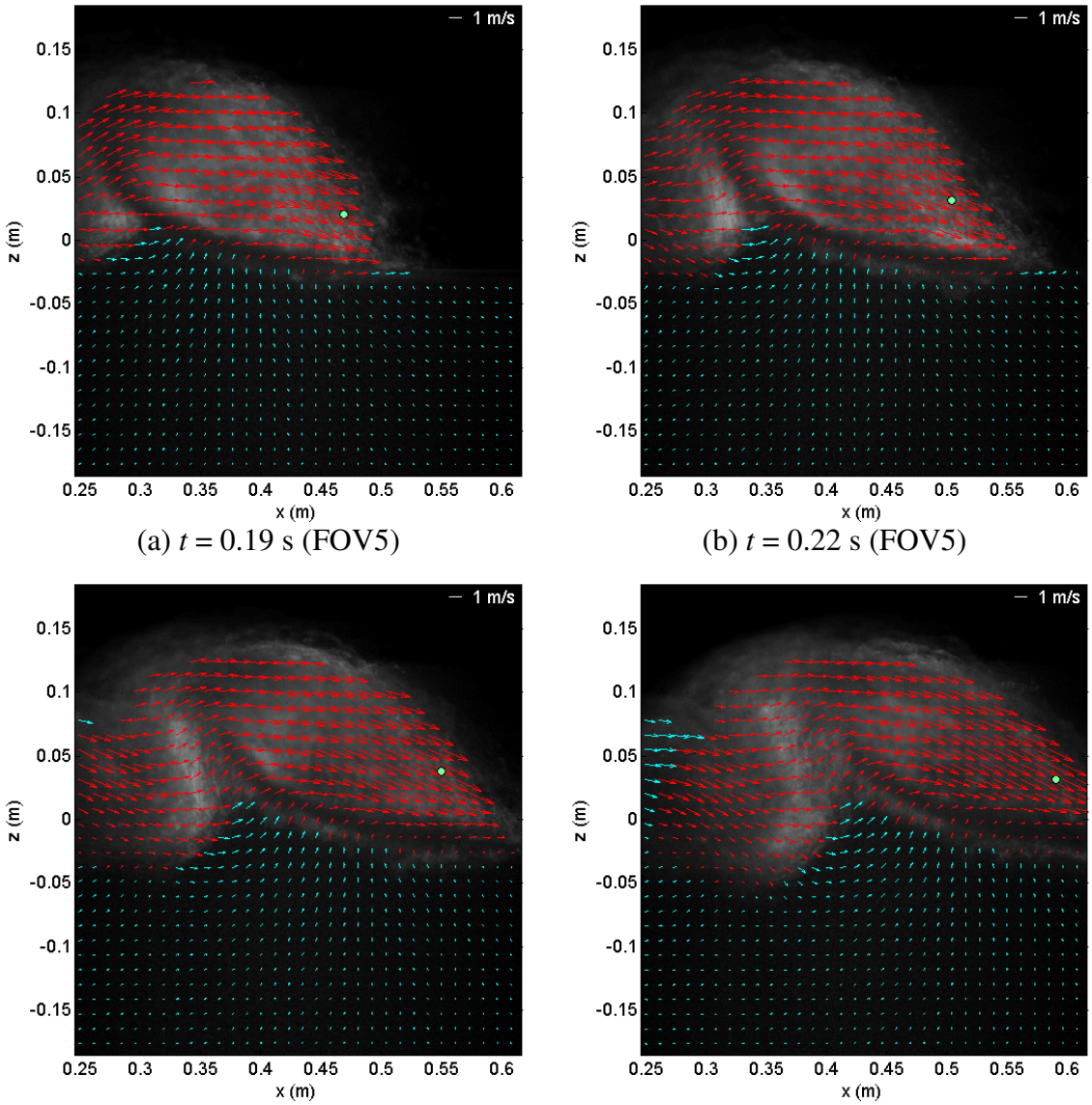

(a) t = 0.19 s (FOV5) (b) t = 0.22 s (FOV5)

(c) t = 0.25 s (FOV5) (d) t = 0.28 s (FOV5)

Fig. 9.16 Velocity at the first splash-up and first backward impingement (FOV5).

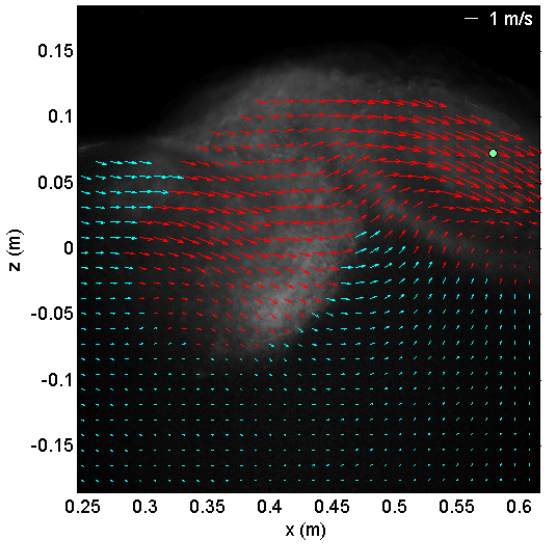

(e) $t = 0.33$ s (FOV5)

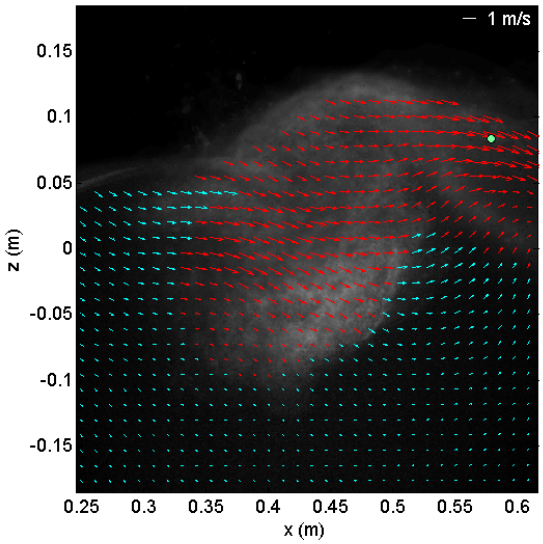

(f) $t = 0.38$ s (FOV5)

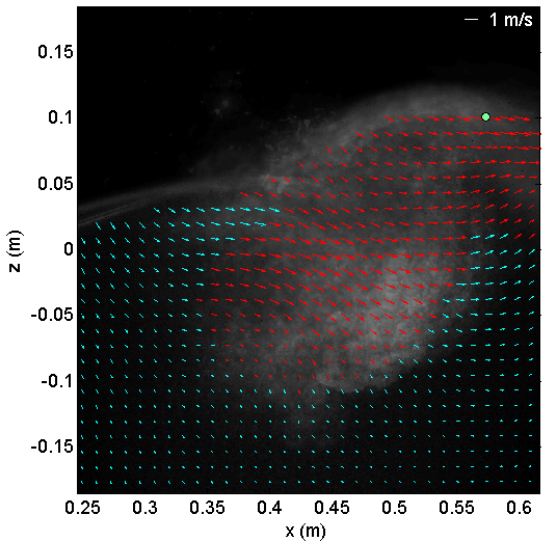

(g) $t = 0.43$ s (FOV5)

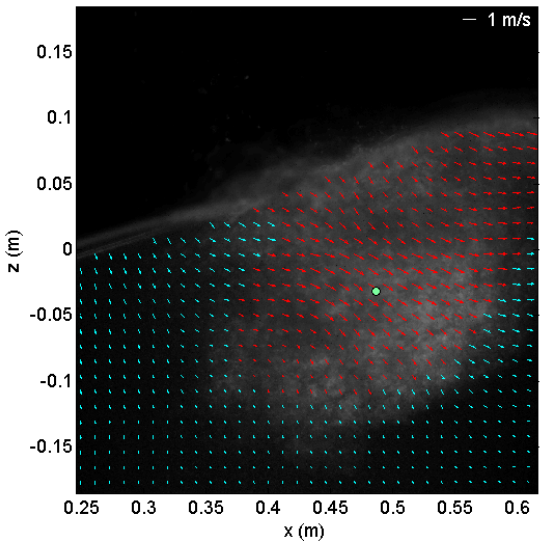

(h) $t = 0.48$ s (FOV5)

Fig. 9.16 (Continued).

It is easier to observe the first backward impingement causing negative vorticity (counterclockwise) as well as two large eddies using Fig. 9.17. In addition, the ascending crest can be seen more clearly as shown in Fig. 9.17. The ascending water crest is growing more and more and its upper part is moving with similar speed to the wave

celerity in the downstream direction and more than 0.5C in the upward direction. As mentioned in Chapter VI, the upper part of the ascending crest loses its kinetic energy when the ascending crest reaches around z = 0.1 m. Therefore, the upper and left part of the crest begins the first backward impinging onto the first roller [Fig. 9.17(c) and (d)].

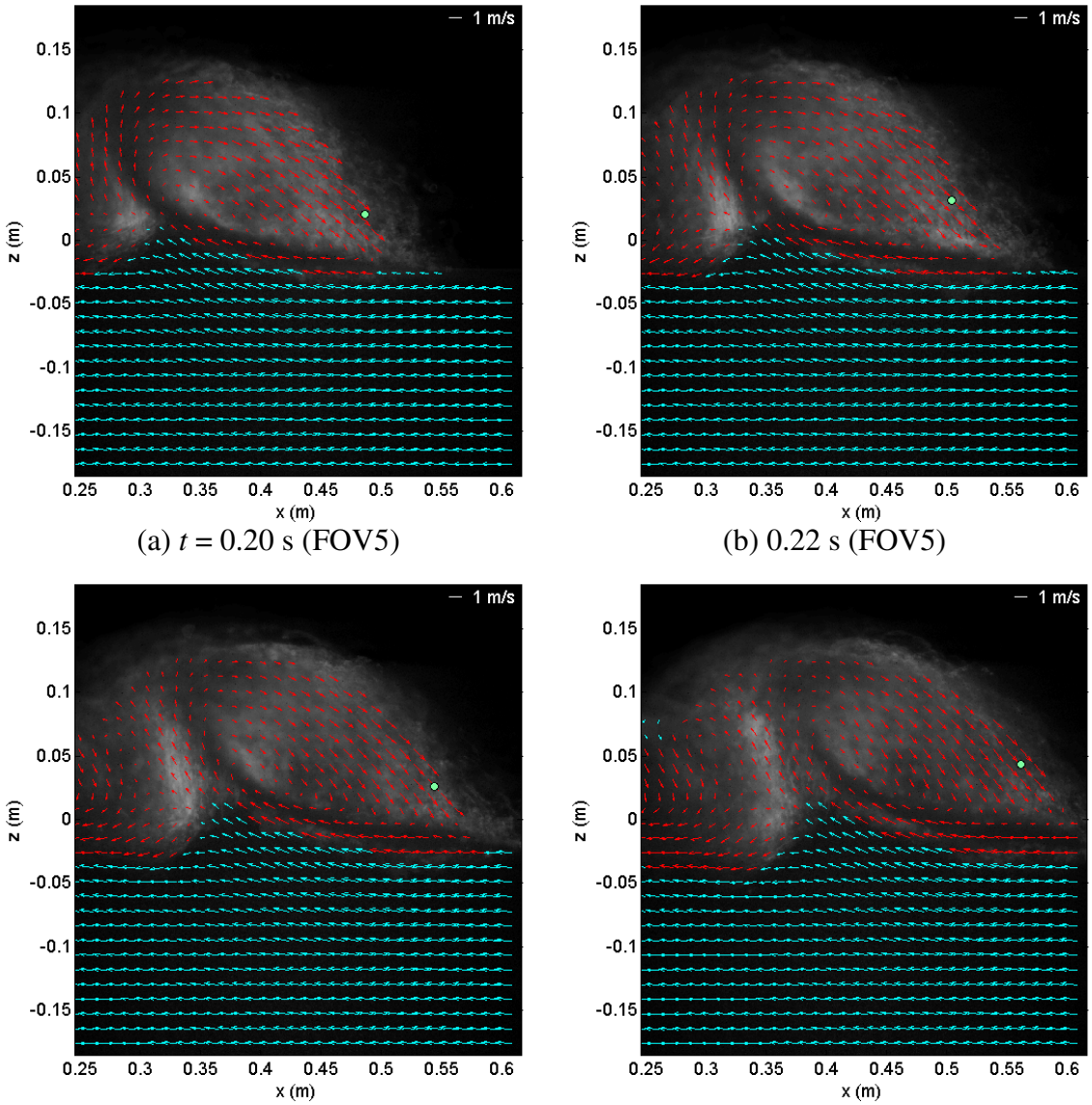

(a) t = 0.20 s (FOV5) (b) 0.22 s (FOV5)

(c) 0.24 s (FOV5) (d) t = 0.26 s (FOV5)

Fig. 9.17 Relative velocity at the two rollers and first backward impingement.

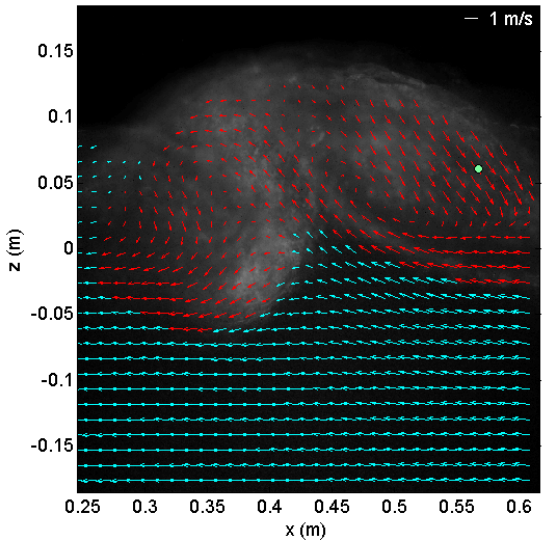

(e) t = 0.30 s (FOV5)

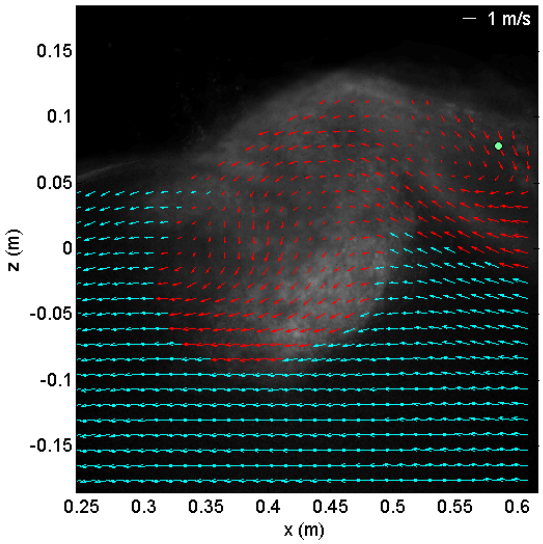

(f) t = 0.37 s (FOV5)

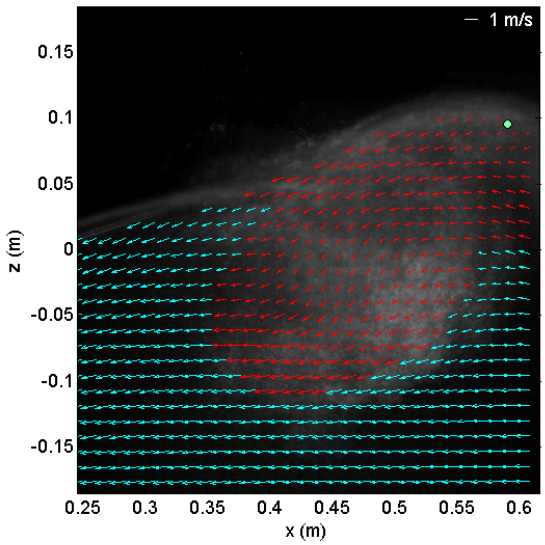

(g) t = 0.45 s (FOV5)

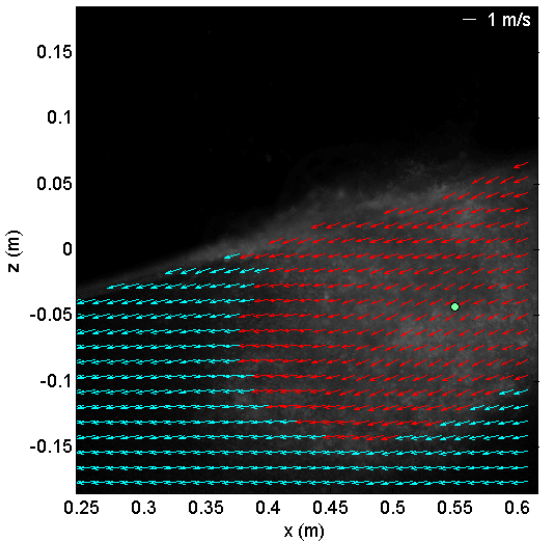

(h) t = 0.56 s (FOV5)

Fig. 9.17 (Continued).

The first backward impingement which starts at around t = 0.25 s, continues onto the first roller and another turbulence is generated due to the mixing between the first roller (clockwise) and the first backward impingement (counterclockwise). While the upper and left part of the ascending crest impinges backward, the obliquely ascending

crest changes its shape to be symmetric and becomes a new primary wave, which is causing the second impingement.

Fig. 9.18 shows maximum velocity variation in time at FOV5. Maximum upward velocity higher than 0.5*C* continued from the beginning of the first splash-up due to the ascending crest and the maximum downward velocity in the entire breaking process occurs due to the water spray impingement and its magnitude is about 0.78*C*. Note that the maximum downward velocity at the first impingement is approximately 0.71*C*. However, downward momentum at the first impingement is larger than that at the water spray impingement due to the high void ratio of the water spray. Fig. 9.19 represents vertical velocity contours. Note that 8 FOVs (FOV1 to FOV8) are combined. It will provide better understanding for the process of the first splash-up caused by the first impingement. In addition, the obliquely ascending crest and the first backward impingement can be seen from Fig. 9.19.

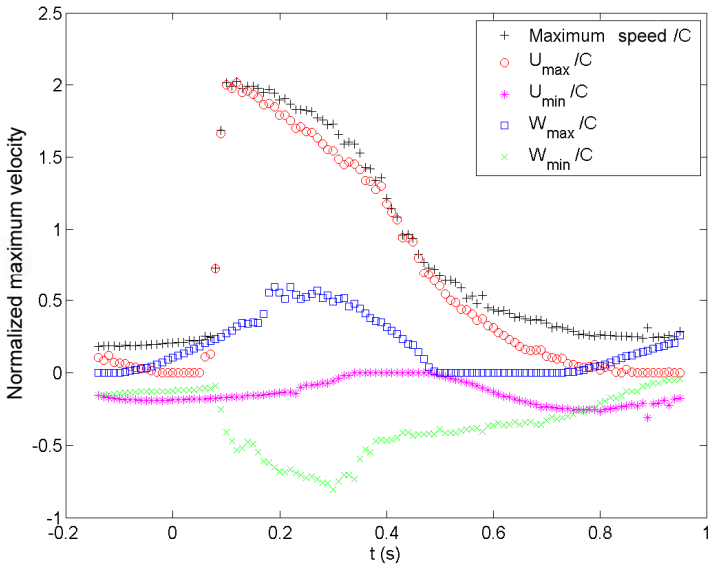

Fig. 9.18 Maximum velocity at FOV5.

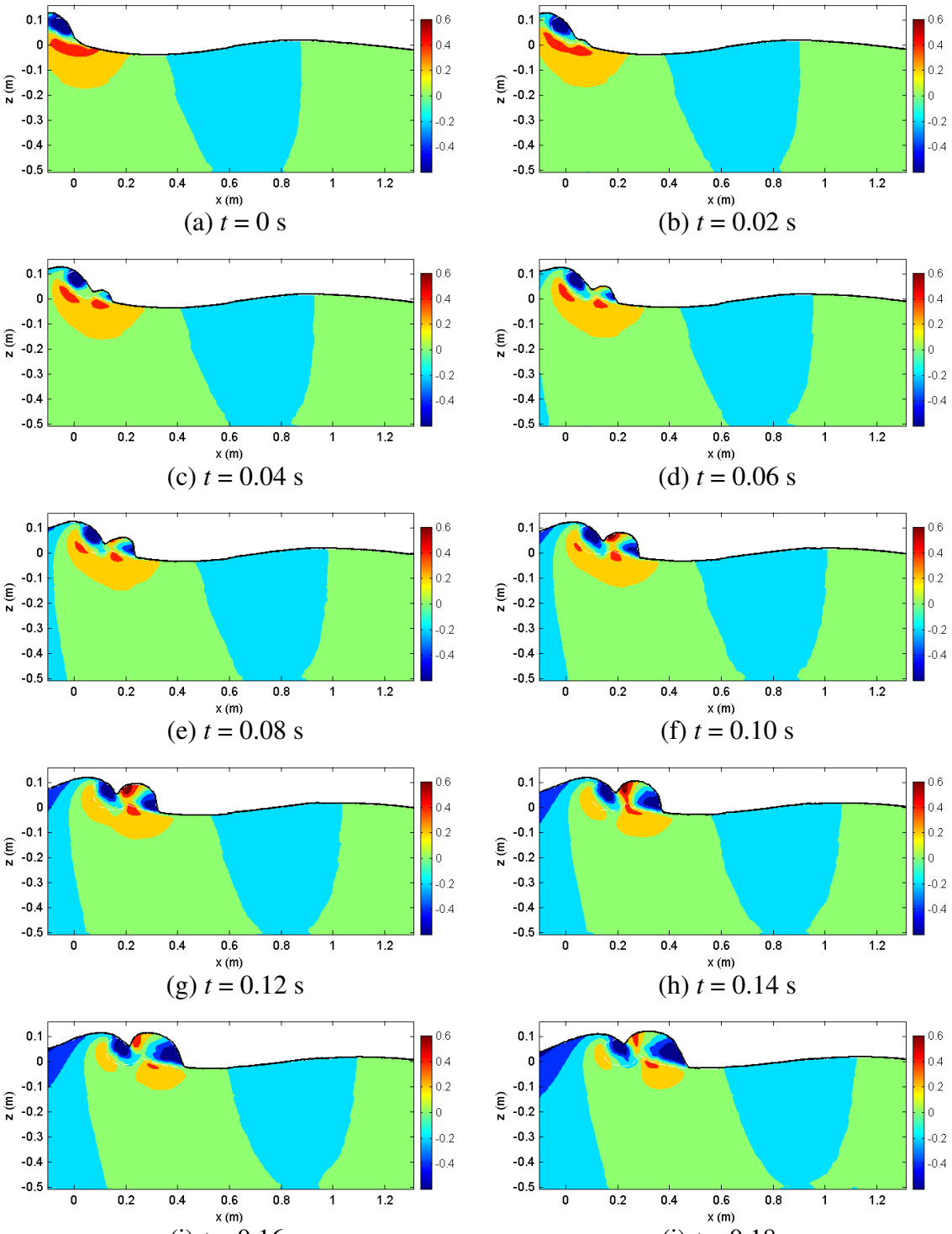

(a) $t = 0$ s (b) $t = 0.02$ s

(c) $t = 0.04$ s (d) $t = 0.06$ s

(e) $t = 0.08$ s (f) $t = 0.10$ s

(g) $t = 0.12$ s (h) $t = 0.14$ s

(i) $t = 0.16$ s (j) $t = 0.18$ s

Fig. 9.19 Vertical velocity contours at the first impingement and splash-up (unit: m/s).

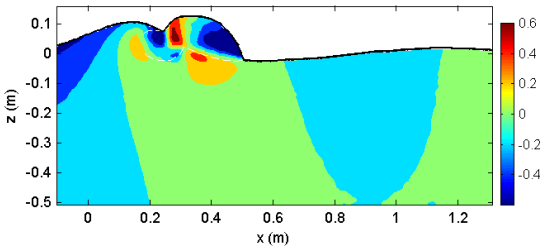

(k) t = 0.20 s

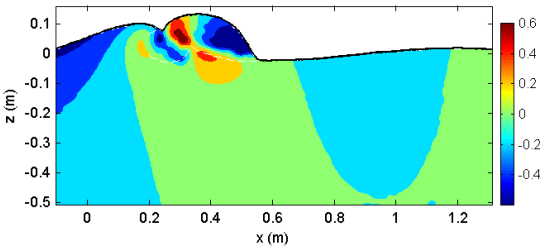

(l) t = 0.22 s

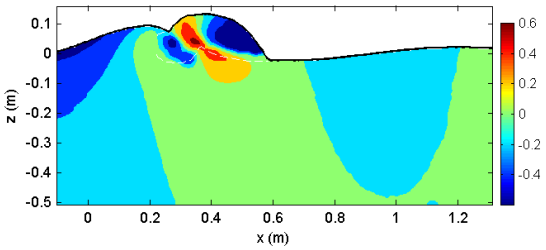

(m) t = 0.24 s

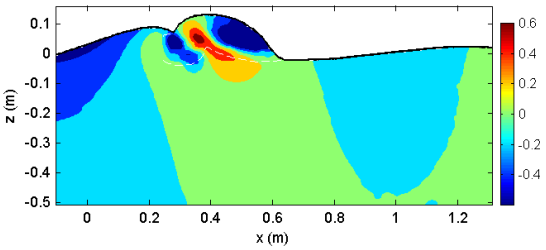

(n) t = 0.26 s

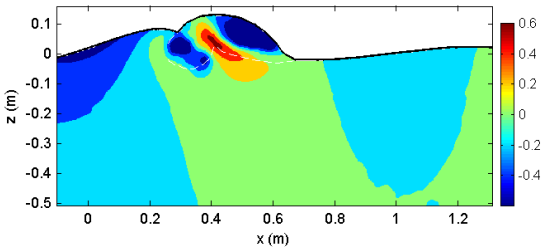

(o) t = 0.28 s

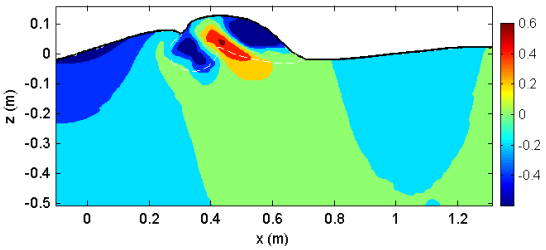

(p) t = 0.30 s

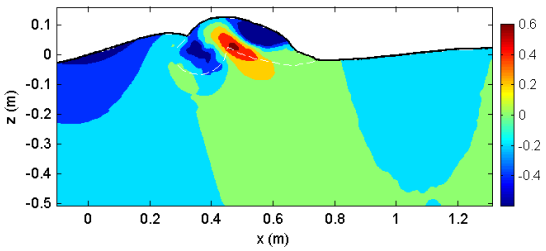

(q) t = 0.32 s

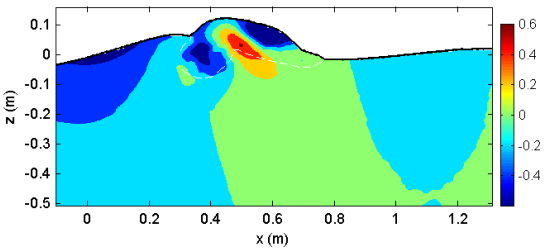

(r) t = 0.34 s

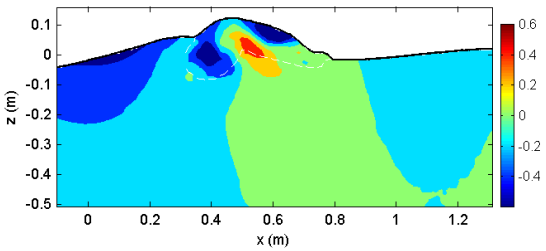

(s) t = 0.36 s

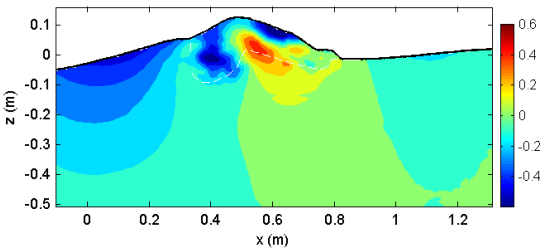

(t) t = 0.38 s

Fig. 9.19 (Continued).

The second impingement and splash-up processes are also very interesting. Fig. 9.20 shows velocity fields for the second impingement and splash-up at FOV7. In addition, vertical velocity contours can be seen in Fig. 9.23. Air-water mixture spray caused by the first splash-up impinges onto the front trough without any splash-up process as shown in Fig. 9.20(a) and (b).

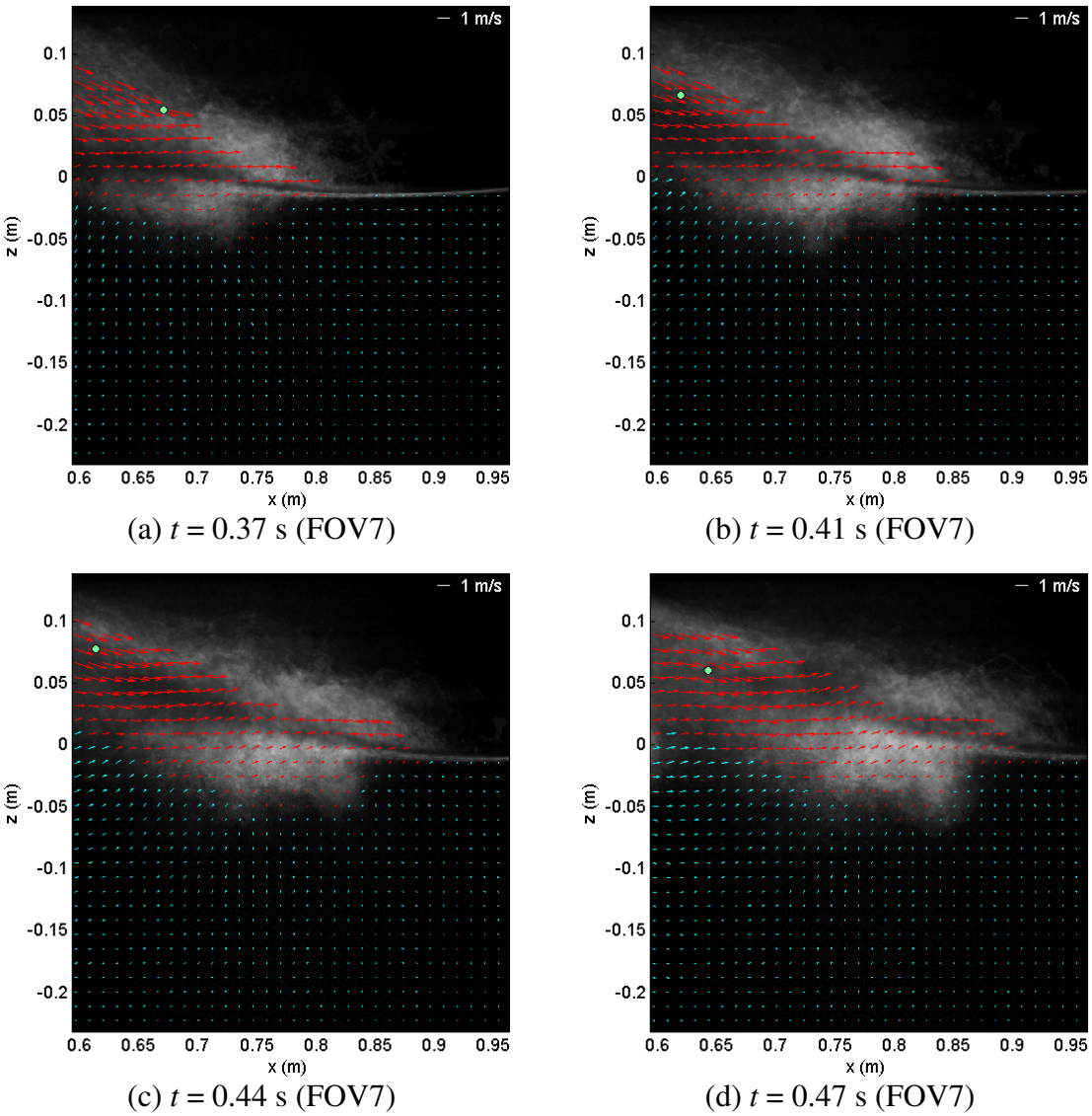

(a) $t = 0.37$ s (FOV7)

(b) $t = 0.41$ s (FOV7)

(c) $t = 0.44$ s (FOV7)

(d) $t = 0.47$ s (FOV7)

Fig. 9.20 Velocity at the second impingement and splash-up (FOV7).

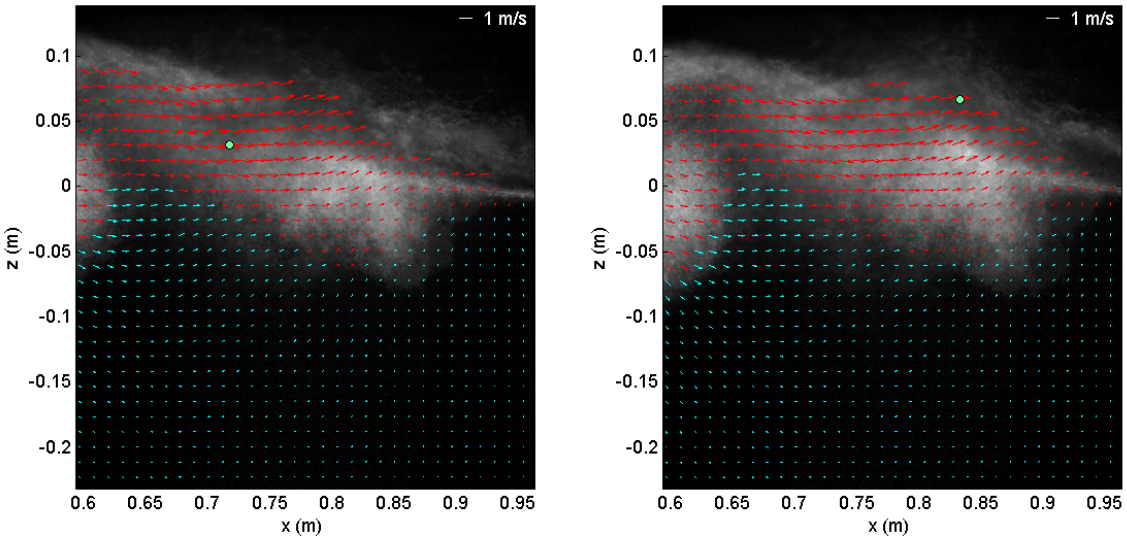

(e) $t = 0.50$ s (FOV7)

(f) $t = 0.53$ s (FOV7)

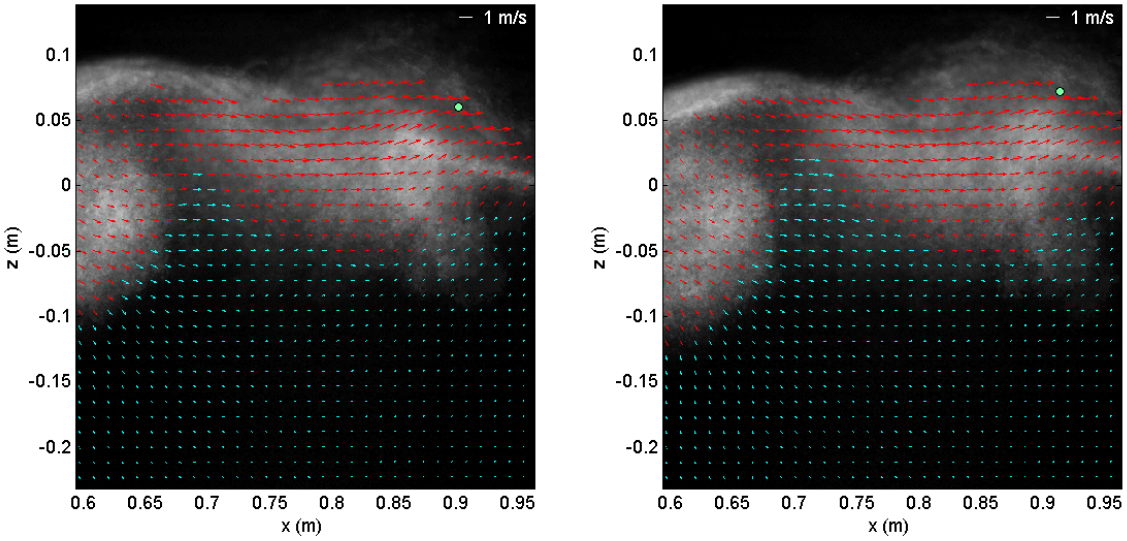

(g) $t = 0.56$ s (FOV7)

(h) $t = 0.59$ s (FOV7)

Fig. 9.20 (Continued).

Only a small part of the mixture spray rebounds slightly or penetrates the wave surface near the trough. Most mixture spray caused by the first splash-up is accumulated on the trough region around $x = 0.7$ to 0.8 m without significant horizontal momentum of the impinging mixture spray. Therefore, the accumulated mixture volume is increased

and turbulence is increased due to the mixing between the impinging spray and clockwise roller motion of the accumulated mixture. Finally, the new primary wave formed from the ascending crest, which is caused by the first splash-up, impinges onto the accumulated mixture with large momentum [Fig. 9.20(c)-(e)].

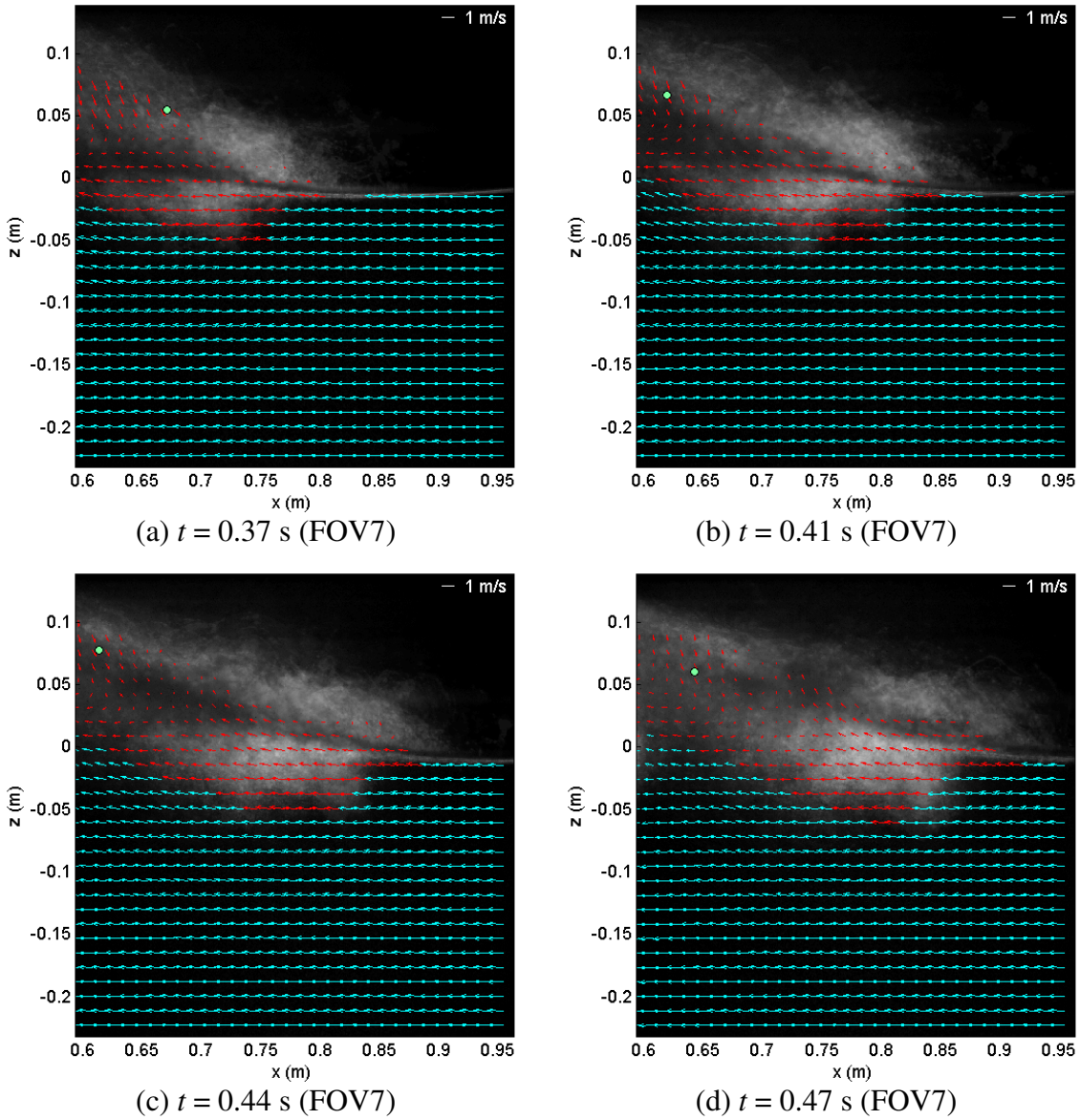

(a) t = 0.37 s (FOV7)

(b) t = 0.41 s (FOV7)

(c) t = 0.44 s (FOV7)

(d) t = 0.47 s (FOV7)

Fig. 9.21 Relative velocity at the second impingement and splash-up (FOV7).

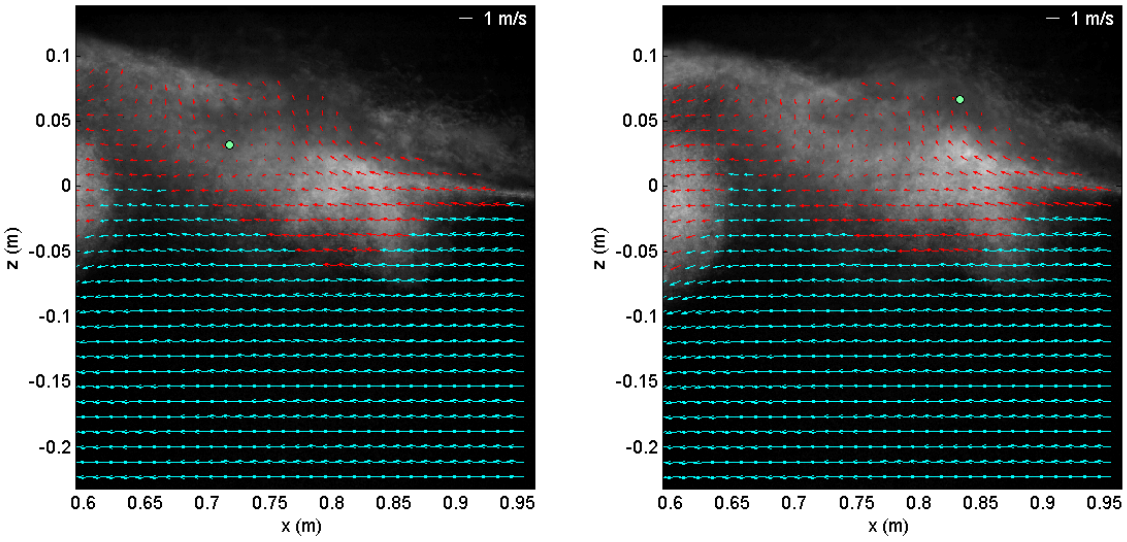

(e) $t = 0.50$ s (FOV7) (f) $t = 0.53$ s (FOV7)

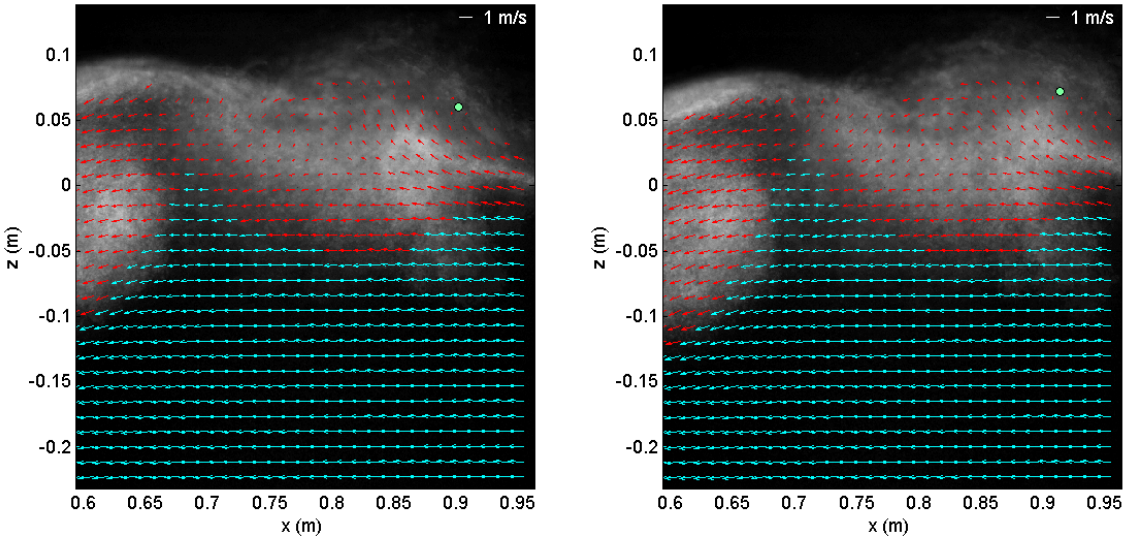

(g) $t = 0.56$ s (FOV7) (h) $t = 0.59$ s (FOV7)

Fig. 9.21 (Continued).

Fig. 9.20(e)-(h) shows the process of the second splash-up. By the second impingement of the new primary wave, the clockwise roller motion of the accumulated mixture is accelerated. The upper portion of the accumulated mixture is splashed up with acceleration while the bottom of the mixture penetrates downward with the impinging

water. Indeed, the largest second roller caused by the first splash-up is gathered around x = 0.7-0.8 m and then it is divided into two parts by the second impingement.

Fig. 9.21 shows relative velocity fields with moving frame at FOV7. As shown in Fig. 9.20 and Fig. 9.21, maximum velocity occurs at the region of the water spray jet or impinging jet rather than the accumulated mixture until the second splash-up. A small water crest at x = 0.9 m shown in Fig. 9.19(g) and Fig. 9.20(g) becomes another new primary wave and it will cause the third impingement later. The previous primary wave causing the second impingement divides two rollers and the nonlinear free surface due to the second impingement is linearized around t = 0.83 s after one period wave cycle (Fig. 9.22). Note that the nonlinear free surface due to the first impingement is linearized at t = 0.51 s. Each backward impingement contributes to the linearization of the free surface by filling up scars that were formed due to each impinging process.

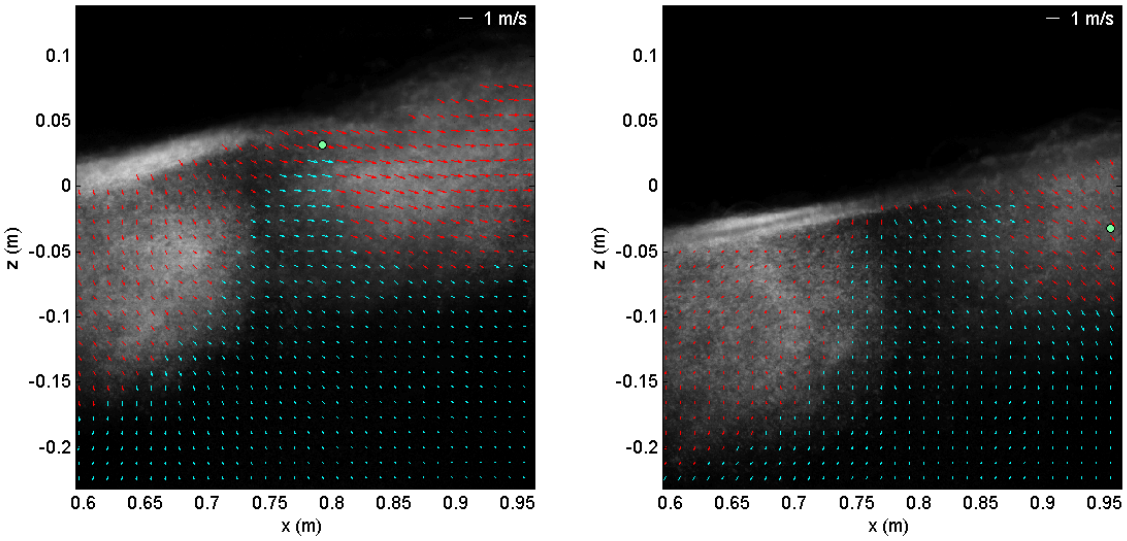

(a) t = 0.69 s (FOV7) (b) t = 0.83 s (FOV7)

Fig. 9.22 Roller separation and linearized free surface (FOV7).

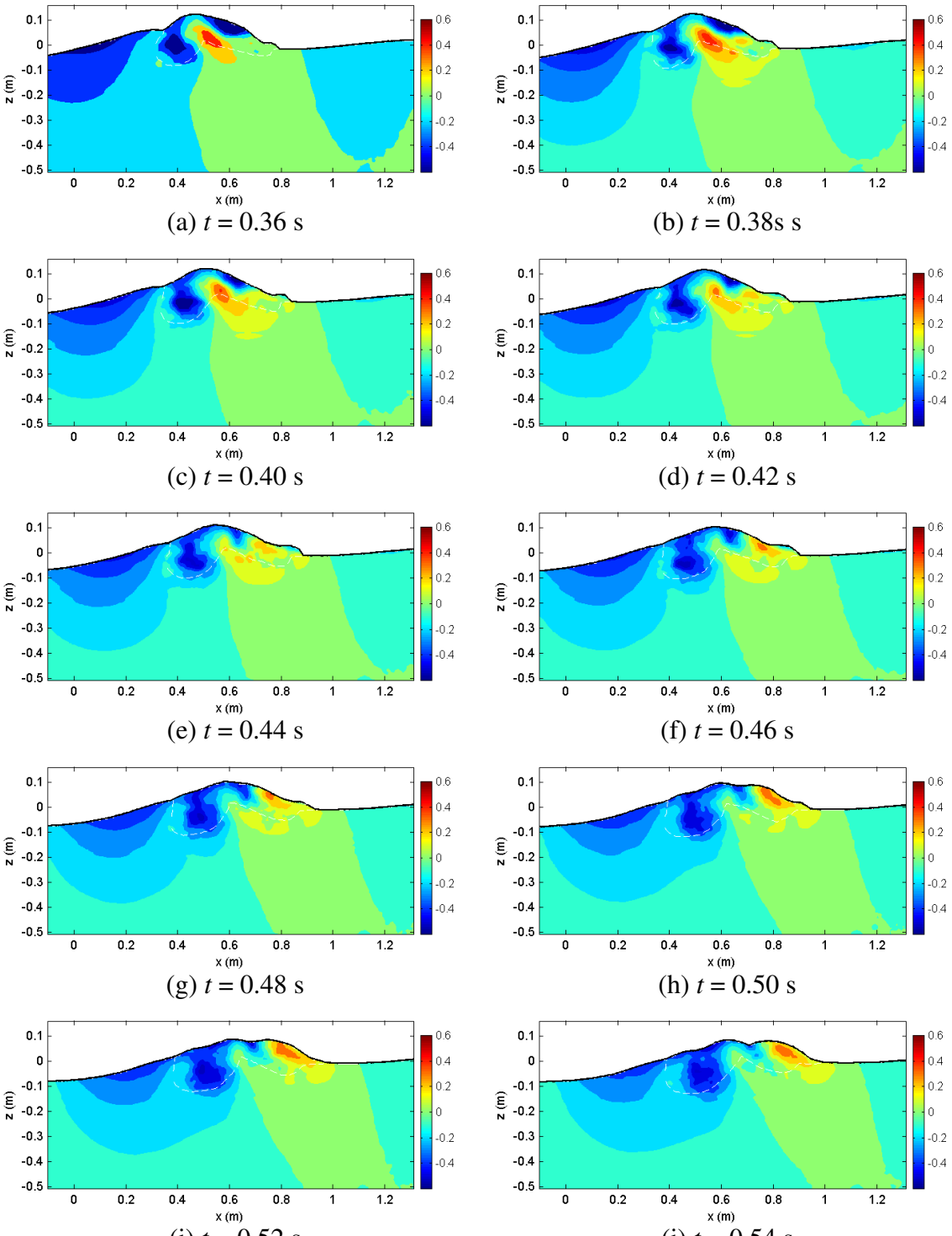

(a) t = 0.36 s (b) t = 0.38s s

(c) t = 0.40 s (d) t = 0.42 s

(e) t = 0.44 s (f) t = 0.46 s

(g) t = 0.48 s (h) t = 0.50 s

(i) t = 0.52 s (j) t = 0.54 s

Fig. 9.23 Vertical velocity contours at the second impingement and splash-up (unit: m/s).

Time and location differences between the second and third impingements are much shorter than that between the first and second impingement as shown in Table 6.1 and Table 6.2. It is believed that it is caused by decreased wavelength and wave period in the generation process of the new primary wave at each impingement.

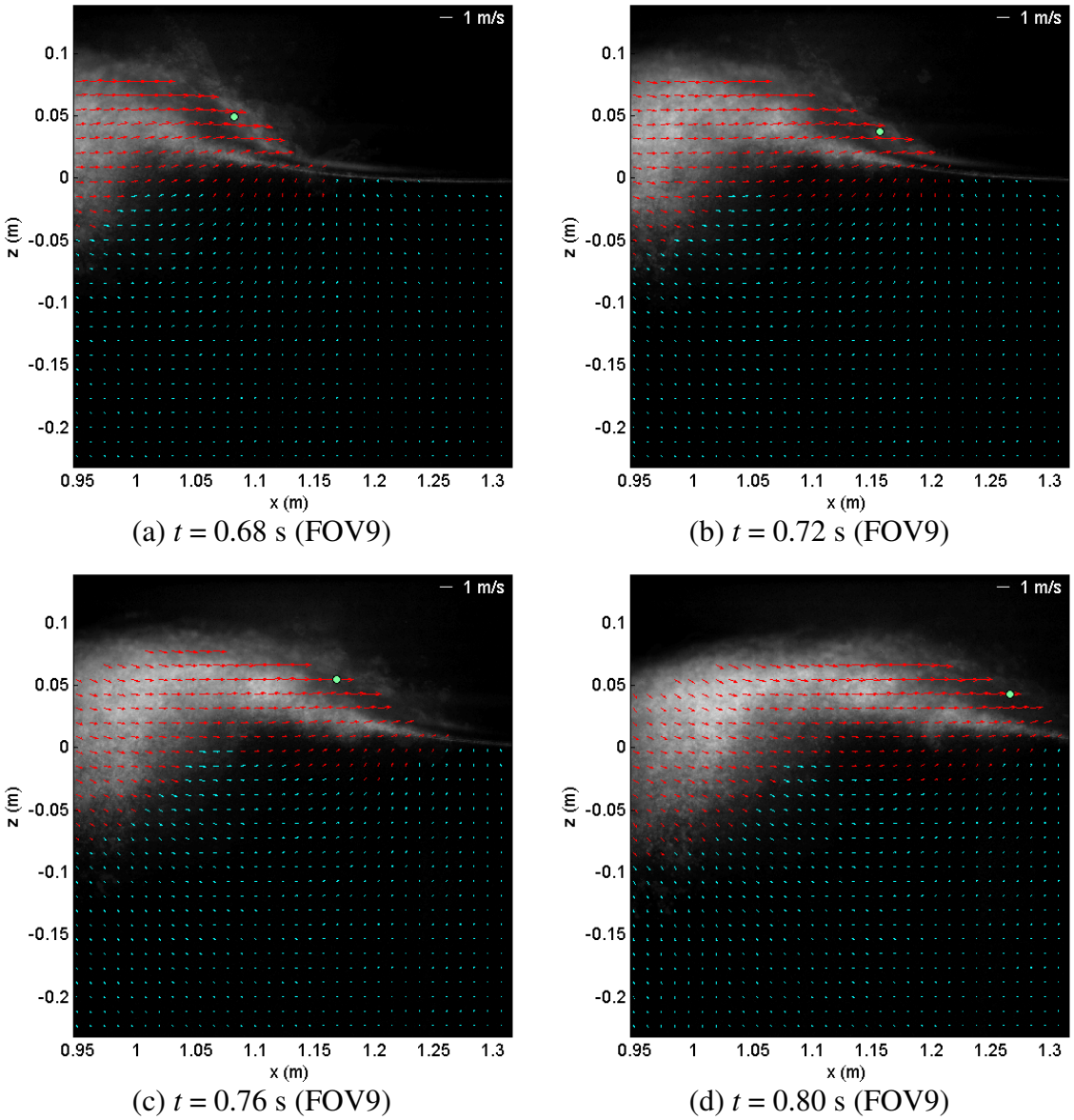

(a) t = 0.68 s (FOV9)

(b) t = 0.72 s (FOV9)

(c) t = 0.76 s (FOV9)

(d) t = 0.80 s (FOV9)

Fig. 9.24 Velocity at the third impingement and splash-up.

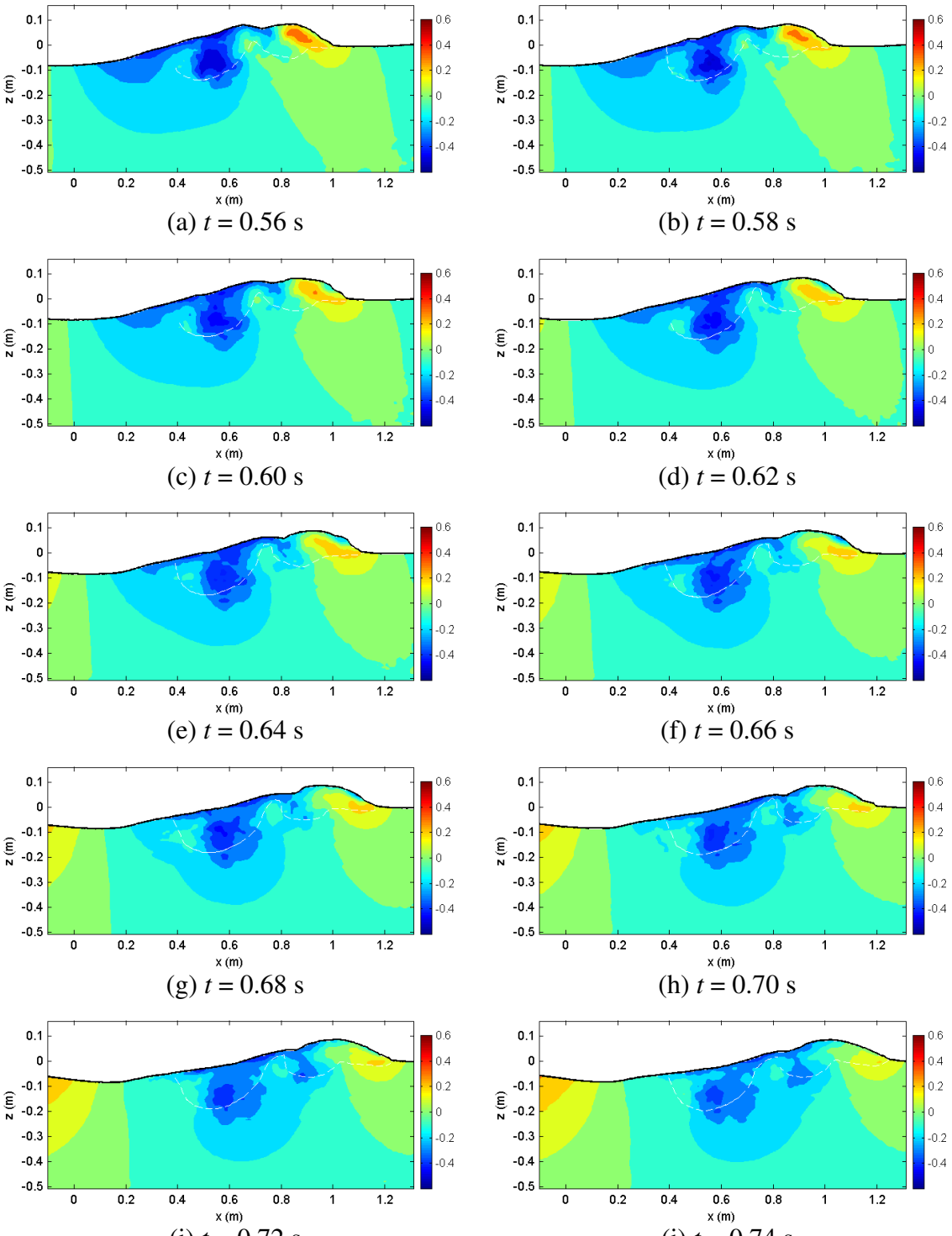

(a) $t = 0.56$ s (b) $t = 0.58$ s

(c) $t = 0.60$ s (d) $t = 0.62$ s

(e) $t = 0.64$ s (f) $t = 0.66$ s

(g) $t = 0.68$ s (h) $t = 0.70$ s

(i) $t = 0.72$ s (j) $t = 0.74$ s

Fig. 9.25 Vertical velocity contours at the third impingement and splash-up.

Fig. 9.24 shows the third impingement and splash-up. Fig. 9.25 shows the continued second splash-up and the third splash-up followed by the third impingement. Compared with the second water spray impingements caused by the first splash-up, the third impingement followed by water spray impinging has small downward momentum. Therefore, the scale of the third impingement is very small and the process is very similar to the breaking process of spilling breakers. The maximum velocity is still slightly higher than the wave phase speed as shown in Fig. 9.26.

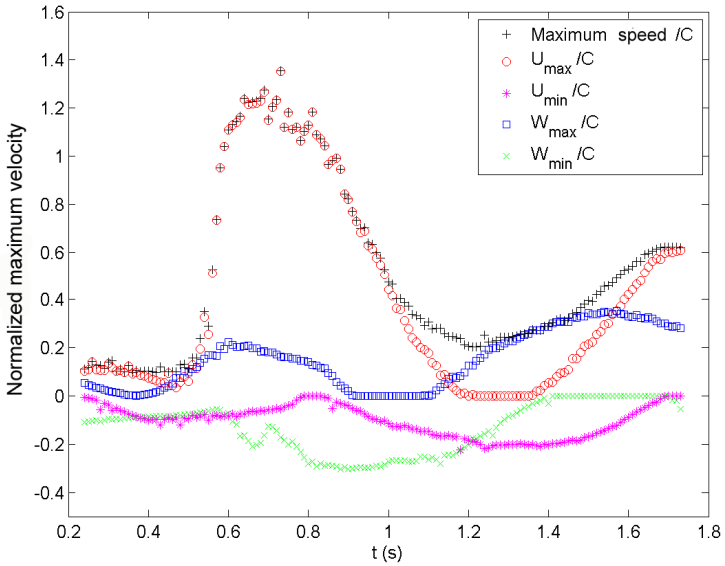

Fig. 9.26 Maximum velocity at FOV9.

Fig. 9.27 shows the first roller generated by the first impingement. For a better view, the size of the vector is increased and every other five vectors in the x direction are displayed. This roller penetrated into deep water about 0.32h, where h is the water depth. After the first impingement and the first backward impingement, the first roller loses kinetic energy rapidly. Then the nonlinear free surface caused by the first impingement

is linearized by the backward impingement at t = 0.51 s [Fig. 6.1(g)]. In this process, the mixing of the first roller and the backward impingement produces turbulent kinetic energy and then the turbulence diffusion process occurs. Detailed discussion about turbulence is presented in Chapter X.

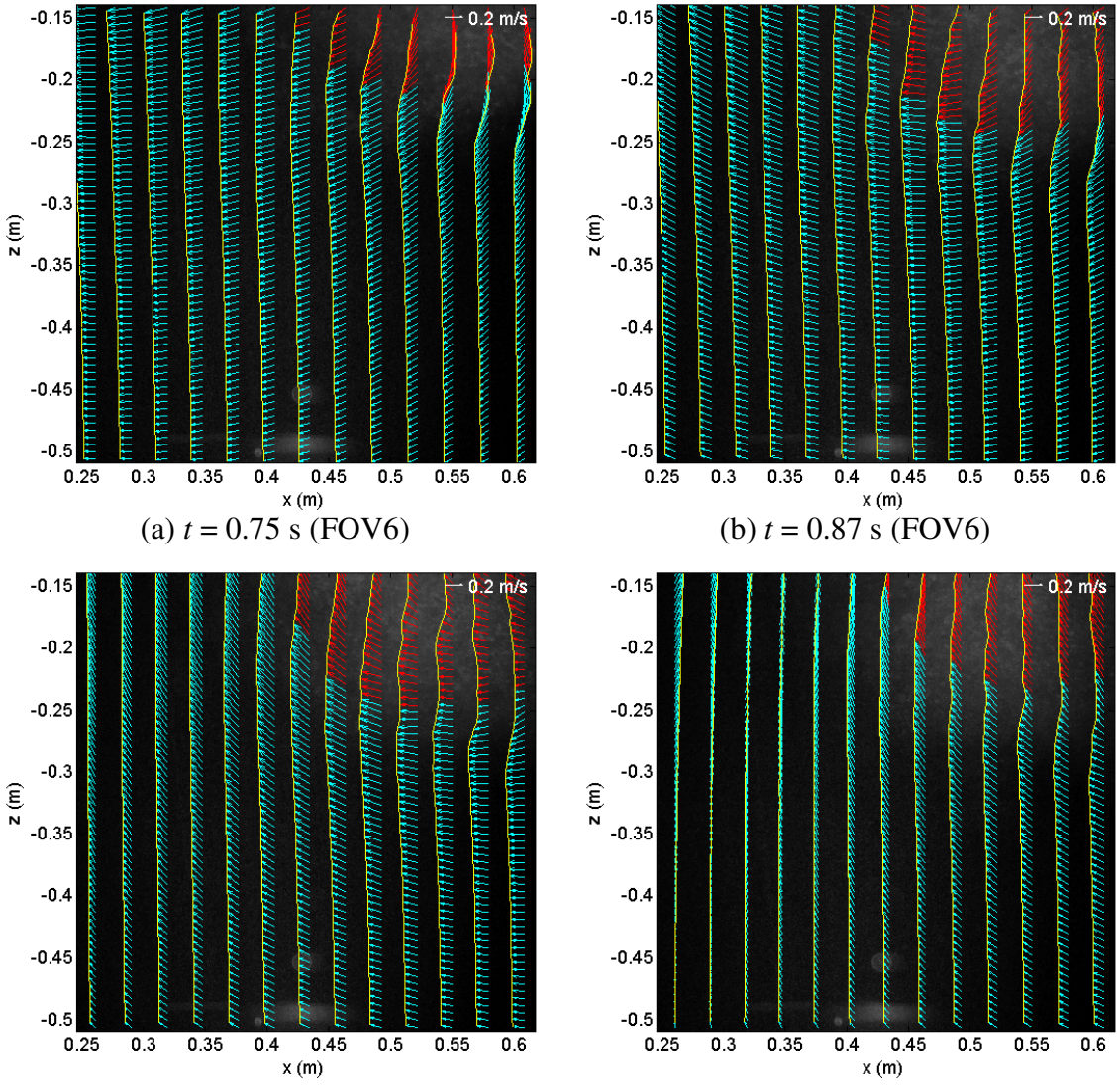

(a) t = 0.75 s (FOV6) (b) t = 0.87 s (FOV6)

(c) t = 0.99 s (FOV6) (d) t = 1.11 s (FOV6)

Fig. 9.27 The first roller at the bottom FOV (FOV6).

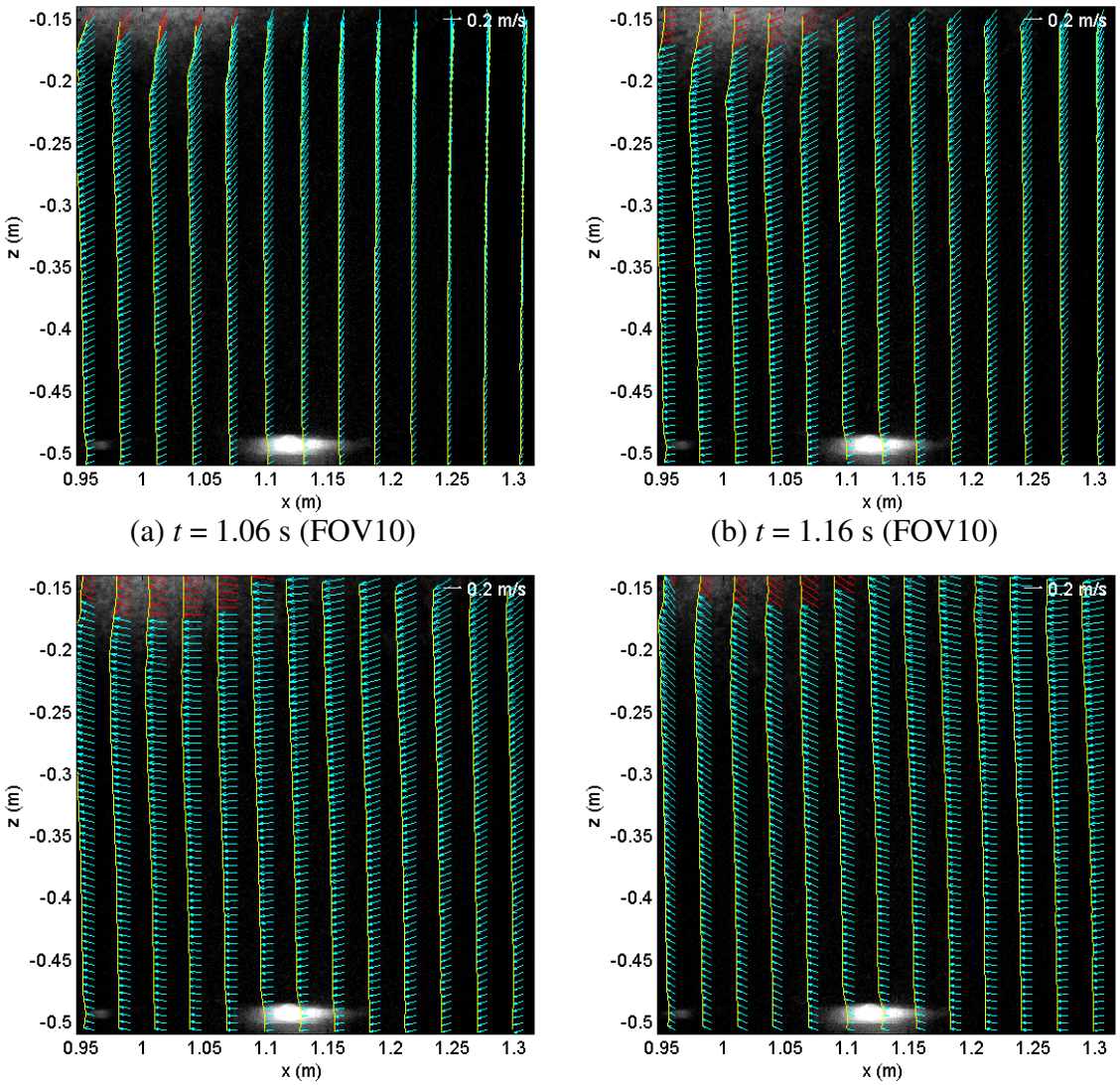

(a) t = 1.06 s (FOV10)

(b) t = 1.16 s (FOV10)

(c) t = 1.26 s (FOV10)

(d) t = 1.36 s (FOV10)

Fig. 9.28 The second roller at the bottom FOV (FOV10).

In addition, there is interference between mean flow and buoyancy of large bubbles, which is one of source for turbulence. Larger air bubbles, which are entrained in the process of the first impingement and the first backward impingement, begin floating then burst on the free surface from t = 0.51 to t = 1.00 s [Fig. 6.1(g)-(m)]. On the other hand,

small size bubbles, which do not have enough buoyancy, begin following the mean flow motion gradually losing their turbulent kinetic energy. Depending on the location and size of bubbles, they are slowly floating on the free surface following the mean flow motion. Finally, all the bubbles float and disappear around t = 3 s which is 3.6T.

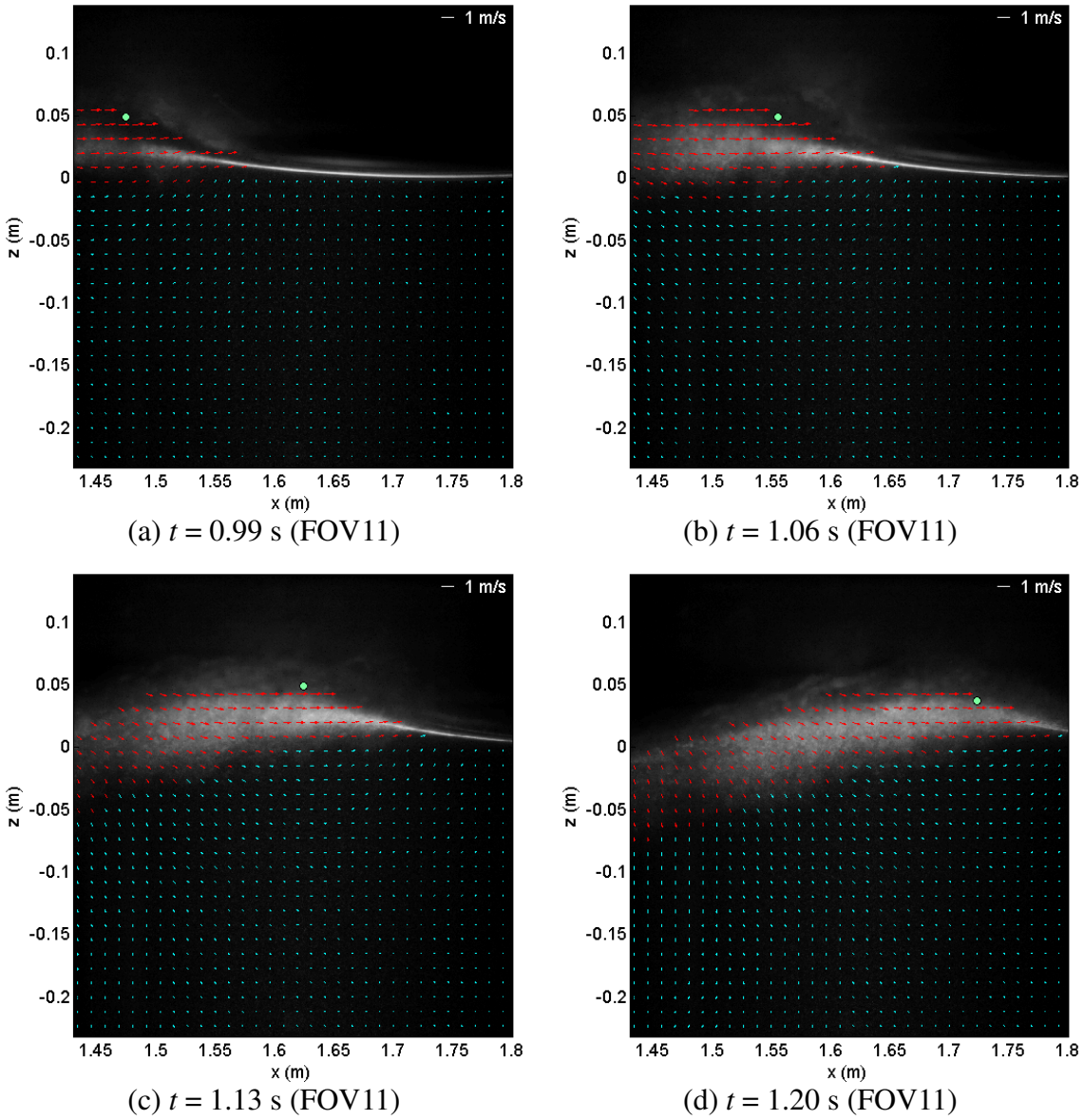

(a) t = 0.99 s (FOV11) (b) t = 1.06 s (FOV11)

(c) t = 1.13 s (FOV11) (d) t = 1.20 s (FOV11)

Fig. 9.29 Velocity at the spilling wave region (FOV11).

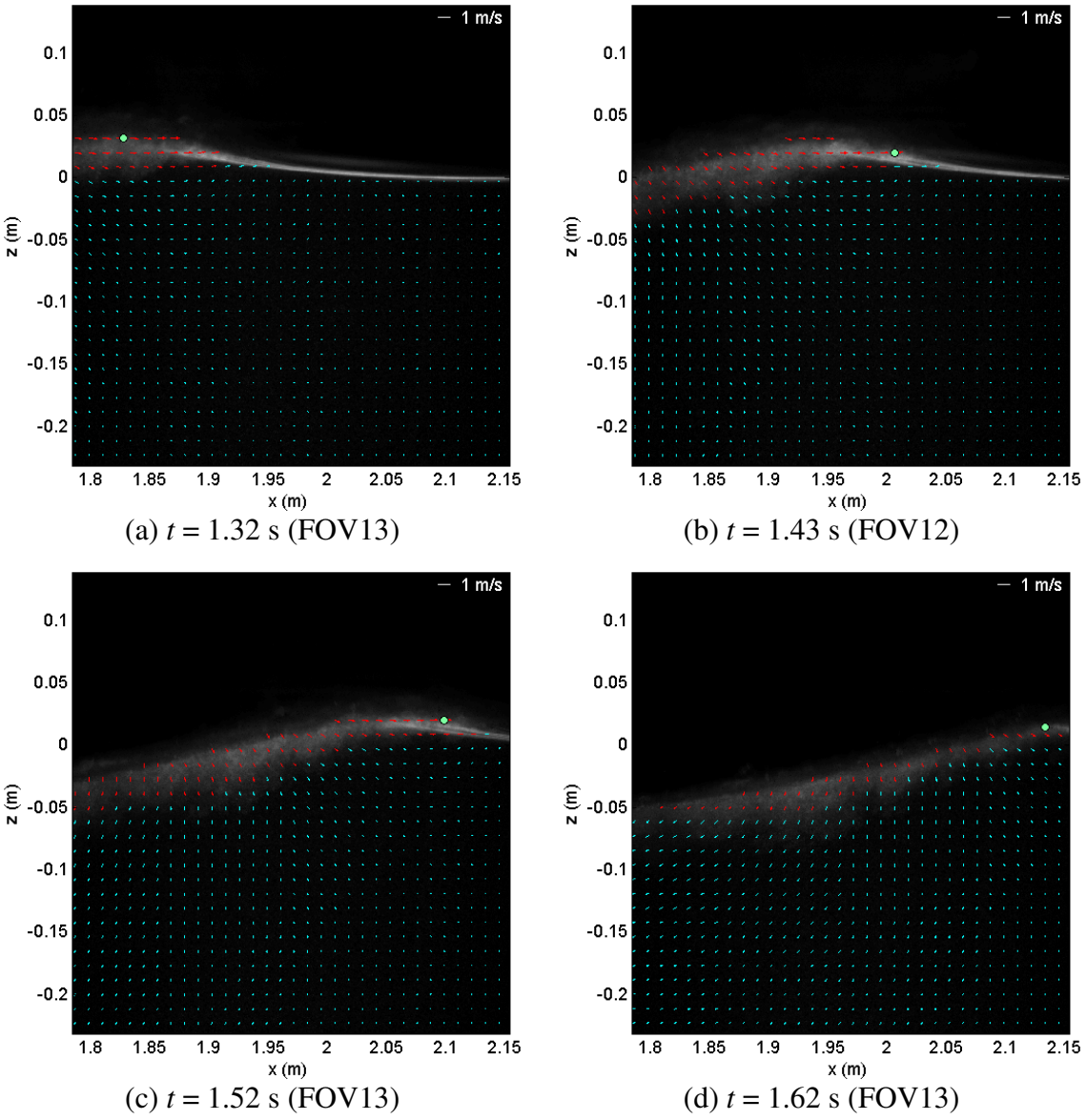

(a) t = 1.32 s (FOV13) (b) t = 1.43 s (FOV12)

(c) t = 1.52 s (FOV13) (d) t = 1.62 s (FOV13)

Fig. 9.30 Velocity at the spilling wave region (FOV13).

Fig. 9.28 shows that the second roller penetrates into deep water up to about 0.22h. Its size and momentum are smaller than those of the first roller because part of the second roller is splashed up in the process of the second impingement. The distance between the two rollers is about 0.45L, where L is the wavelength of the primary wave.

Fig. 9.29 and Fig. 9.30 show velocity fields for spilling waves after the third splash-up at FOV11 and FOV13 respectively. Note that the FOV13 is the last FOV in the upper row. The maximum velocity is rapidly decreased after the third splash-up. For example, the maximum velocity at the crest is decreased from 0.8*C* to 0.6*C* at FOV11 and 0.6*C* to 0.4*C* at FOV13. Due to the significant decrease of the velocity after the third splash-up, mean travel velocity of the breaking wave is very close to the wave phase speed. The breaking wave travels about 2.13 m in 1.62 s as shown in Fig. 9.30(d). Therefore, mean travel speed of the plunging breaker is about 1.31 m/s which is very close to the phase speed of the initial primary wave, which is 1.3 m/s.

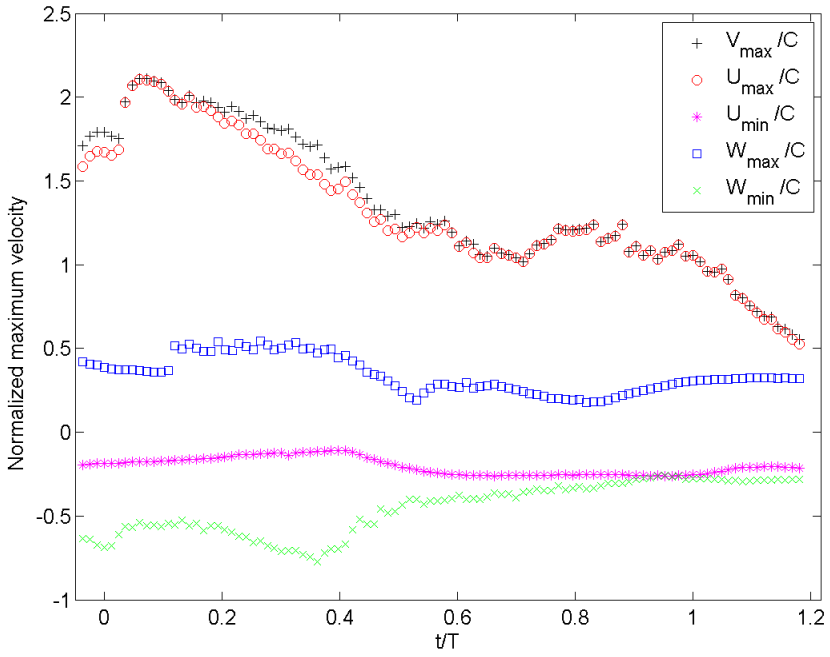

Fig. 9.31 Normalized maximum velocity.

Fig. 9.31 shows the maximum velocity variation in time at the combined FOVs (FOV3-FOV10) which includes all important breaking processes in one window between two steel columns of the wave tank. Maximum horizontal velocity variation is almost accord with maximum velocity except during the first impingement and the second impingement followed by water spray impinging. Local maximum velocities occur at each splash-up process. Maximum horizontal velocity occurs at t = 0.05 s (0.06T) at the beginning the first splash-up and the magnitude is about 2.14C. Maximum upward velocity is about 0.55C near the newly ascending crest during the first splash-up and maximum downward velocity in the entire flow is about 0.78C at t = 0.3 s (0.36T) during the water spray impinging process caused by the first splash-up. The local maximum occurs at the first impingement at t = 0 and the magnitude is about 0.71C. Maximum velocity is decreased gradually and becomes smaller than the wave phase speed after one wave period.

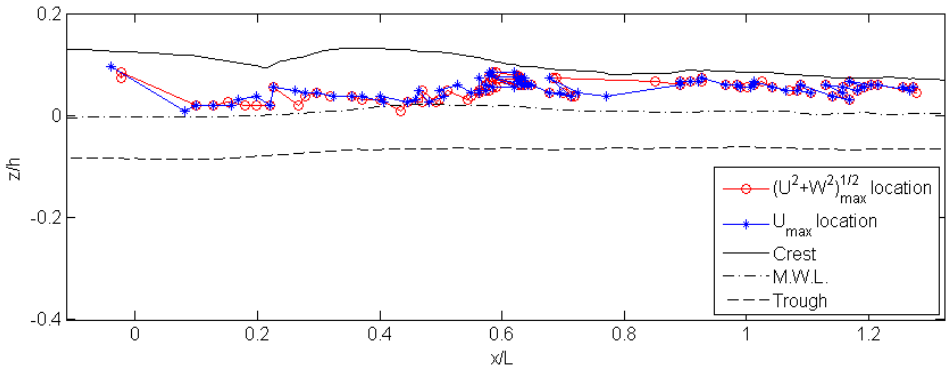

Fig. 9.32 Location of maximum velocity and horizontal velocity.

Fig. 9.32 and Fig. 9.33 show the location of the maximum velocity in the horizontal and vertical direction respectively. The time difference between markers is 0.01 s. Location of maximum horizontal velocity does not change much around $x = 0.6L$ due to accumulated mixture spray without significant horizontal motion. However, it is accelerated due to the second impingement of the water jet. The location of horizontal velocity follows the order of each process. That is, the first impinging jet, the first splash-up, water spray impinging, the second impinging jet, the second splash-up and so on.

The location of upward maximum velocity is under the overturning jet, providing upward momentum continuously before the first impingement. After the first impingement, the maximum location follows the newly generated ascending crest, the second splash-up and the new crest causing the third impinging. In case of downward maximum velocity, the location follows the first impinging jet, water spray from the first splash-up, the second impinging jet, the first roller penetrating into deep water, the second roller penetrating into water and then the third impingement.

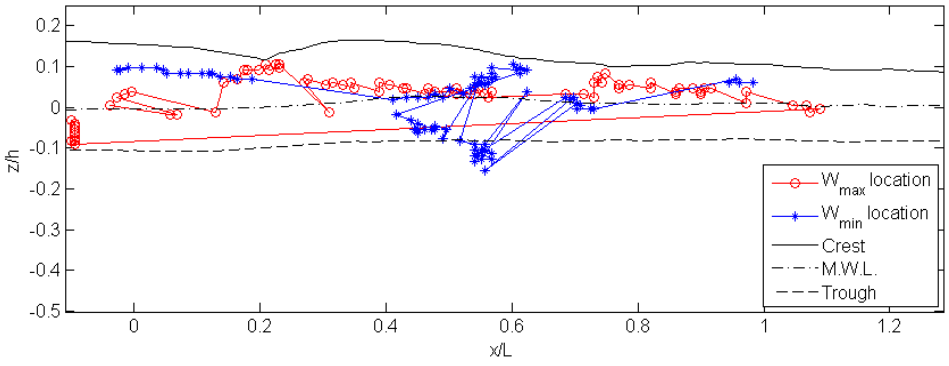

Fig. 9.33 Location of maximum vertical velocity.

Three lines shown in Fig. 9.32 and Fig. 9.33 represent envelopes of crest, mean water level and trough respectively. There are a total of 475 stations in the x direction with dx = 5.78 mm. Trough envelope, which is the minimum wave elevation, always occurs at the rear of the wave from the beginning of the breaking process. In the initial stage of the plunging breaker, The elevation of the front and rear troughs of the breaking wave becomes very close and trough in front of the primary wave is gradually increased from around x = - 0.4L where the wave face becomes vertical. As shown in Fig. 9.34, the elevation difference between two troughs is increased and the elevation of the front tough becomes close to still water level. Moreover, it is higher than mean water level from x = 1.5L.

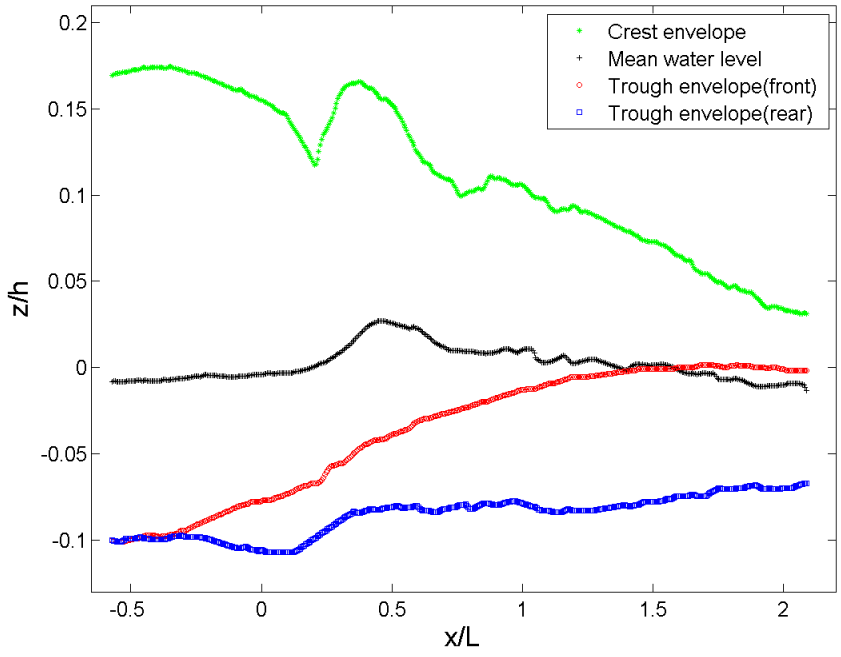

Fig. 9.34 Increase of the front trough level.

9.4.2 Temporal Analysis of Mean Velocity

In the previous section, spatial analyses of the strong plunging breaker were presented with detail descriptions of each impinging and splash-up process. Temporal analysis is also essential to investigate transport of mass, momentum and energy. Breaking waves have remarkable variation in both time and space, especially in the plunging breaker as shown in previous section. In the present study, one of great advantages is to obtain time-averaged values with more accuracy owing to the high temporal resolution in addition to the high spatial resolution.

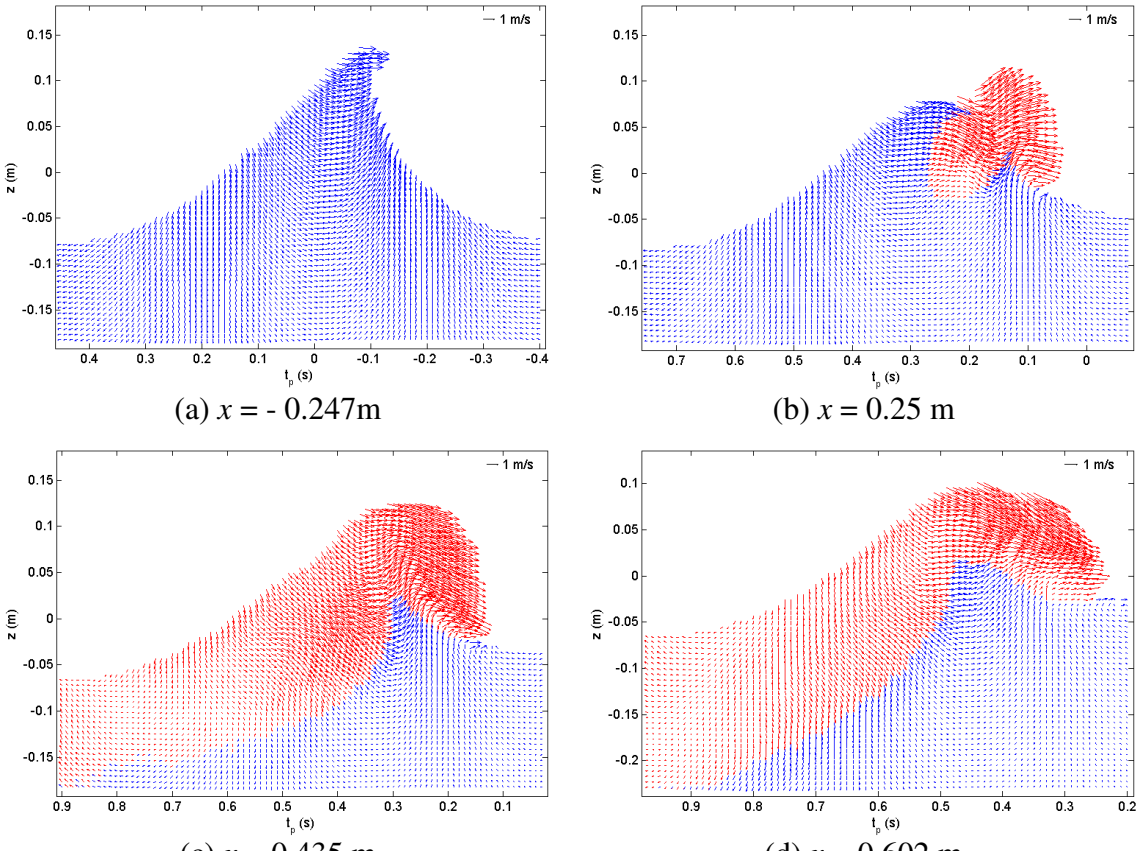

(a) x = - 0.247m (b) x = 0.25 m

(c) x = 0.435 m (d) x = 0.602 m

Fig. 9.35 Velocity time series at a station (red vectors: inside the aerated region and blue vectors: outside the aerated region).

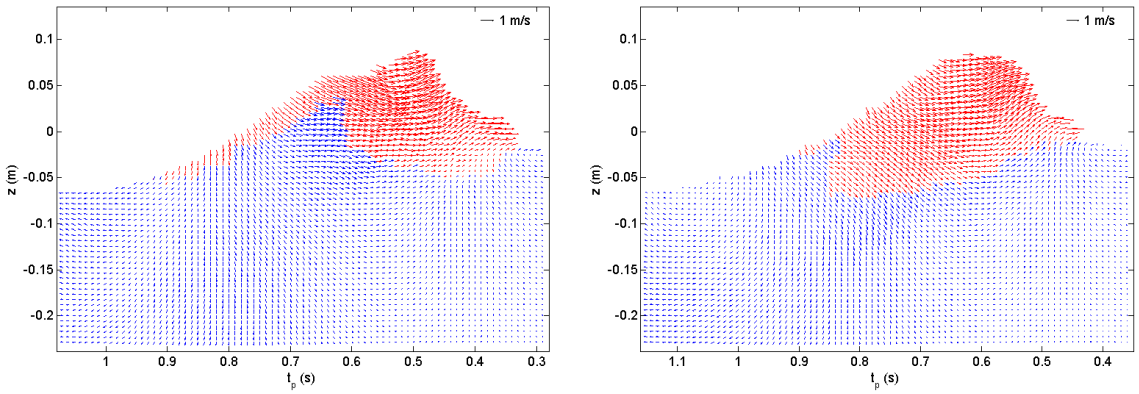

(e) x = 0.758 m (f) x = 0.886 m

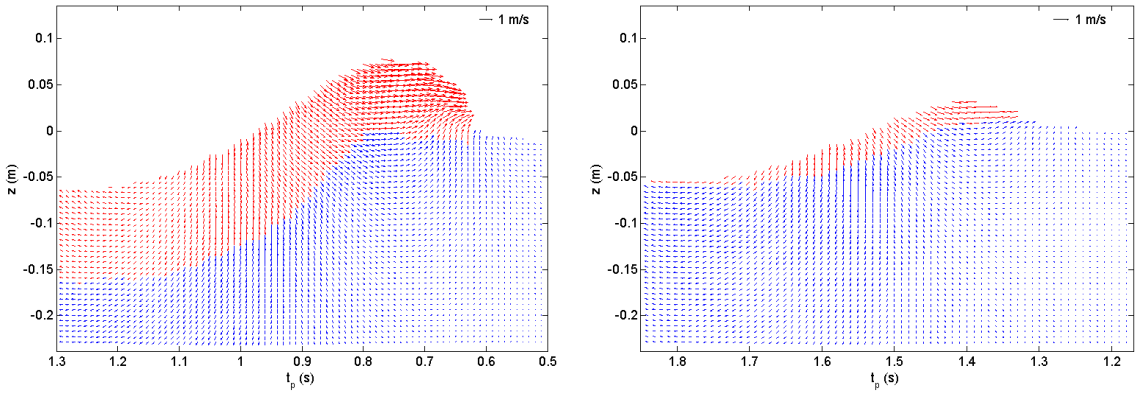

(g) x = 1.082 m (h) x = 1.938 m

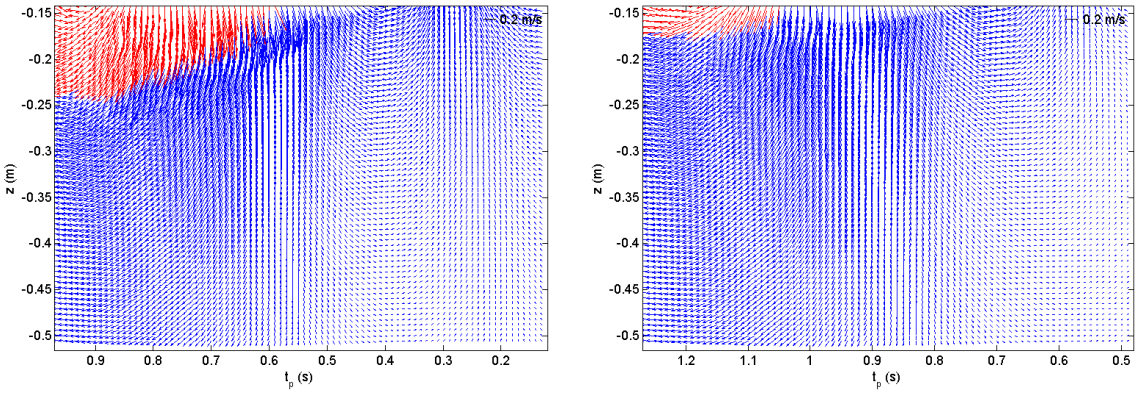

(i) x = 0.556 m (j) x = 1.053 m

Fig. 9.35 (Continued).

Fig. 9.35 shows the time series of velocity passing through a vertical station. Some examples of the results for several important vertical stations mentioned in previous

sections are presented among the total of 475 stations for the entire flow regime. Fig. 9.35(a) shows velocity time series at x = - 0.247 m where the crest is overturning after the wave face becomes vertical. Fig. 9.35(b) and (c) represent velocity variation at the beginning of the first splash-up and at the fully developed first splash-up. Note that velocity vectors in the aerated region are plotted in a red color and water particle velocities are plotted with a blue color. Fig. 9.35(d)-(f) represent velocity time series at the locations of the second impingement, the beginning of the second splash-up and the fully developed second splash-up. Fig. 9.35(g) and (h) show the velocities at the location of the beginning of the third splash-up and the spilling wave far away from the breaking point. Fig. 9.35(i) and (j) show examples of results for the first and second rollers penetrating to deep water, which were obtained from the lower FOVs (FOV6 and 10).

The velocity time series for all 475 stations provides insight into the breaking process with results from the spatial analysis. For example, there are small valleys of elevation between upward velocities due to the splash-up and downward velocities due to the impingement around the location of the beginning of each splash-up as shown in Fig. 9.35(b), (e) and (g) [t = 0.2 s in Fig. 9.35(b), t = 0.55 s Fig. 9.35(e) and t = 0.75 s in Fig. 9.35(g)]. The magnitude of the velocity for the first impinging and splash-up process is significant. In addition, the magnitude for the second splash-up is also remarkable. This is because the fluid of the second splash-up is an air-water mixture. Therefore, momentum at the second splash-up is overestimated although velocity is very high. On the other hand, compared with the first and second processes, it is difficult to observe the valley between the third impingement and the third splash-up. Horizontal

momentum is dominant in the third splash-up process as discussed in the previous section. Since impinging waves have lost their potential energy continuously during the impinging process, The elevation of waves passing the locations has local minimum values. This will be discussed in detail later. Another example is the location of the second impingement. The difference between the first and the second impingement is where the impinging water jet touches. The first overturning water jet impinges onto the front water surface over still water level and the front water is pushed up. On the other hand, the second impinging water is followed by the water spray impinging and impinges onto the lower part of accumulated air-water mixture. Thus, velocity direction near the location of the second impingement is downward and there is also a valley between the water spray impingement and the water impingement around t = 0.4 s as shown in Fig. 9.35(d).

The time interval to calculate time-averaged values between two troughs which are front and rear troughs of the progressing breaker and the time interval between two troughs is defined as a local wave period at a station. It was found that wave period changed in location. It is decreased gradually as the breaker travels with local maxima and minima as shown in Fig. 9.36. Fig. 9.36 shows the local wave periods at all 475 stations with dx = 5.78 mm. The local periods are normalized by the period of the initial primary wave just before the wave face becomes vertical. The wave period at the location where the breaking process is almost finished is about 0.7T. Therefore, it is necessary to obtain time information of two troughs for all vertical stations to obtain more accurate time-averaged values.

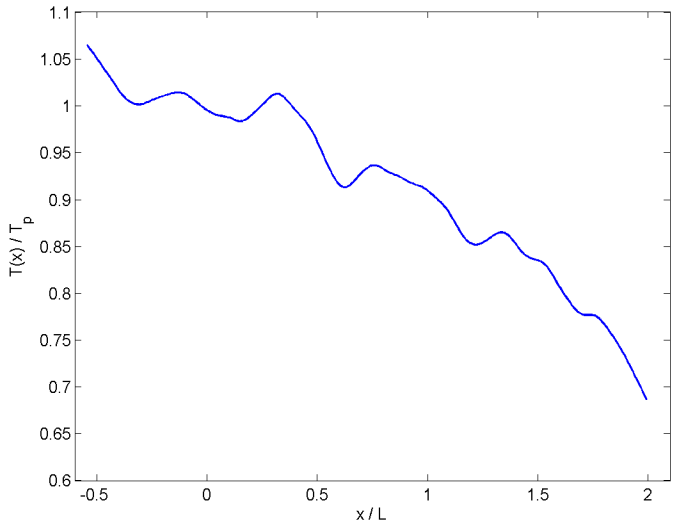

Fig. 9.36 Decrease of a local wave period.

Eqs. (9.4) and (9.5) show the calculation of wave-averaged and period-averaged quantities using the time series results shown in Fig. 9.35. Only wetted region is considered in the calculation of wave-averaged values while period-averaged values are obtained from the summation of quantities divided by the corresponding local wave period. Therefore, averaged values under the trough level are identical from both calculations.

$$U_{wa}(x,z) = \frac{\int_{t_{tr}(x)}^{t_{tr}(x)+T(x)} \delta(x,z,t)U(x,z,t)dt}{\int_{t_{tr}(x)}^{t_{tr}(x)+T(x)} \delta(x,z,t)dt} \tag{9.4}$$

$$U_{pa}(x,z) = \frac{\int_{t_{tr}(x)}^{t_{tr}(x)+T(x)} \delta(x,z,t)U(x,z,t)dt}{\int_{t_{tr}(x)}^{t_{tr}(x)+T(x)} dt} \tag{9.5}$$

where, $t_{tr}(x)$ is the local time when the front trough reaches the station and $T(x)$ is the local wave period. $\delta(x,z,t)=1$ in water under the free surface and $\delta(x,z,t)=0$ in air above the free surface. The time resolution dt is 0.01 s.

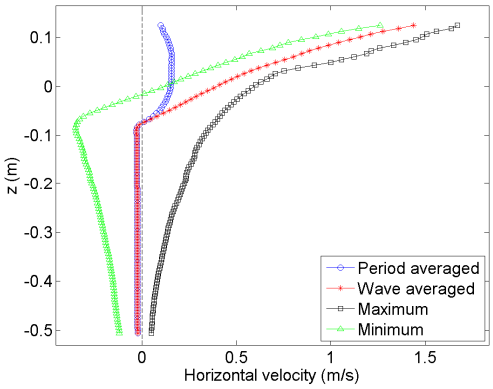

(a1) U at x = - 0.247m

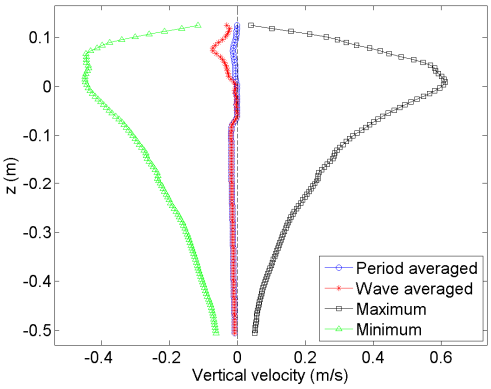

(a2) W at x = - 0.247 m

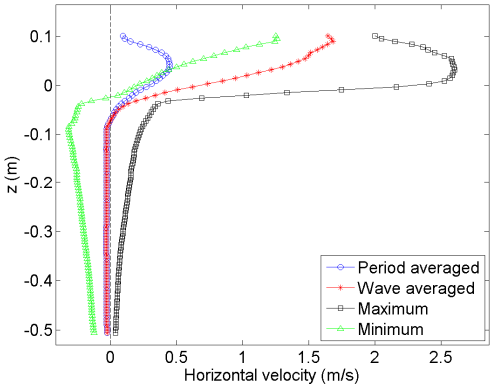

(b1) U at x = 0.250 m

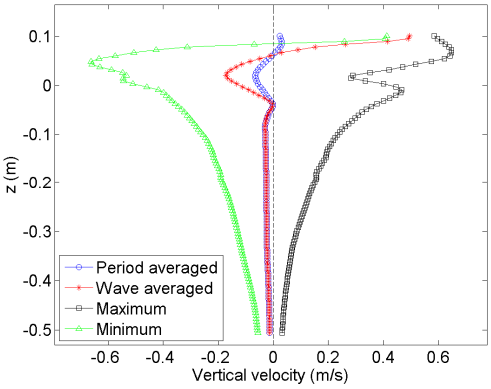

(b2) W at x = 0.250 m

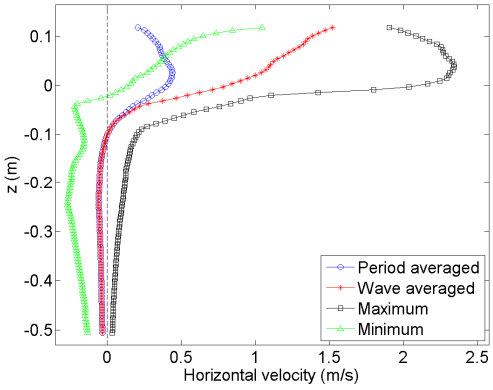

(c1) U at x = 0.435 m

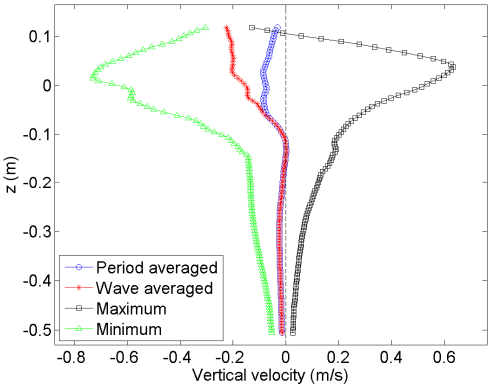

(c2) W at x = 0.435 m

Fig. 9.37 Time-averaged, maximum, and minimum velocity (unit: m/s).

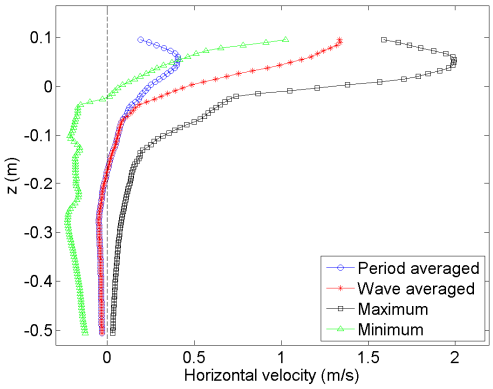

(d1) U at x = 0.602 m

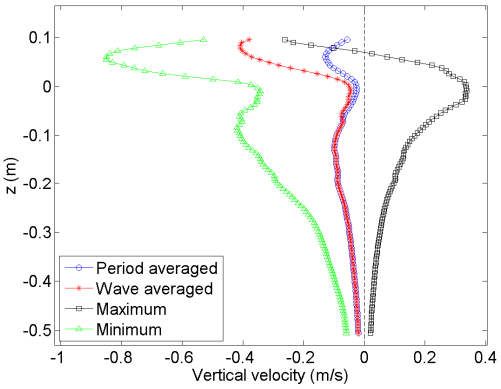

(d2) W at x = 0.602 m

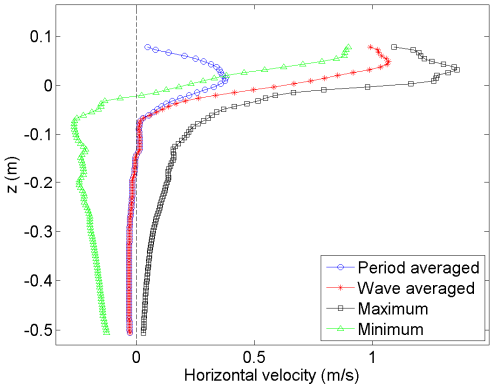

(e1) U at x = 0.758 m

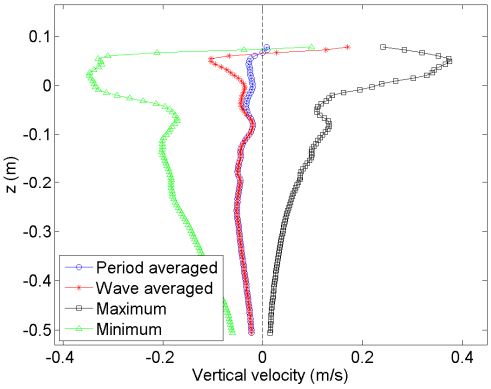

(e2) W at x = 0.758 m

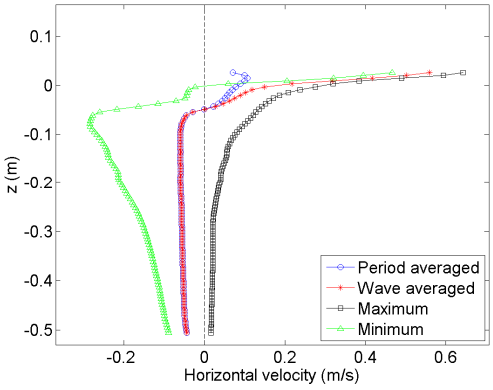

(f1) U at x = 1.938 m

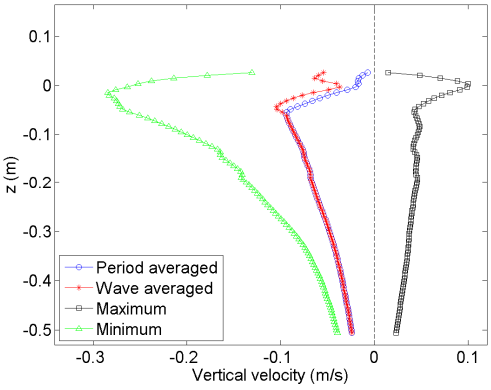

(f2) W at x = 1.938 m

Fig. 9.37 (Continued).

Fig. 9.37 shows vertical profiles of the wave-averaged and period-averaged velocities. In addition, vertical profiles of the maximum and minimum velocities at some stations mentioned in Fig. 9.35. Figures on the left side that are labeled as 1 (e.g., (a1)), represent vertical profiles of horizontal velocities while figures on the right side that are labeled as 2 (e.g., (a2)), represent vertical profiles of vertical velocities at the same location. Fig. 9.38 and Fig. 9.39 show the comparison of results with different locations which are $x < L$ for horizontal and vertical velocities respectively.

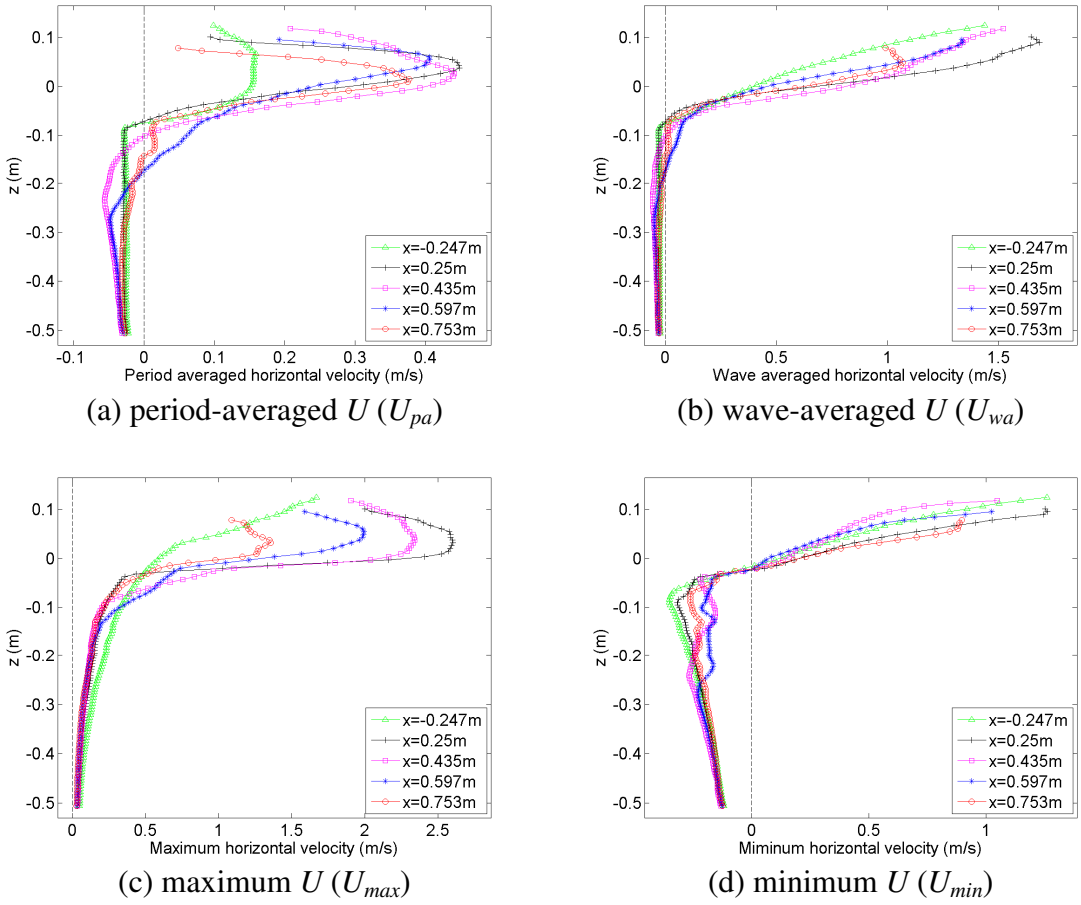

(a) period-averaged U (U_{pa})

(b) wave-averaged U (U_{wa})

(c) maximum U (U_{max})

(d) minimum U (U_{min})

Fig. 9.38 Time-averaged horizontal velocity at $x < L$ (unit: m/s).

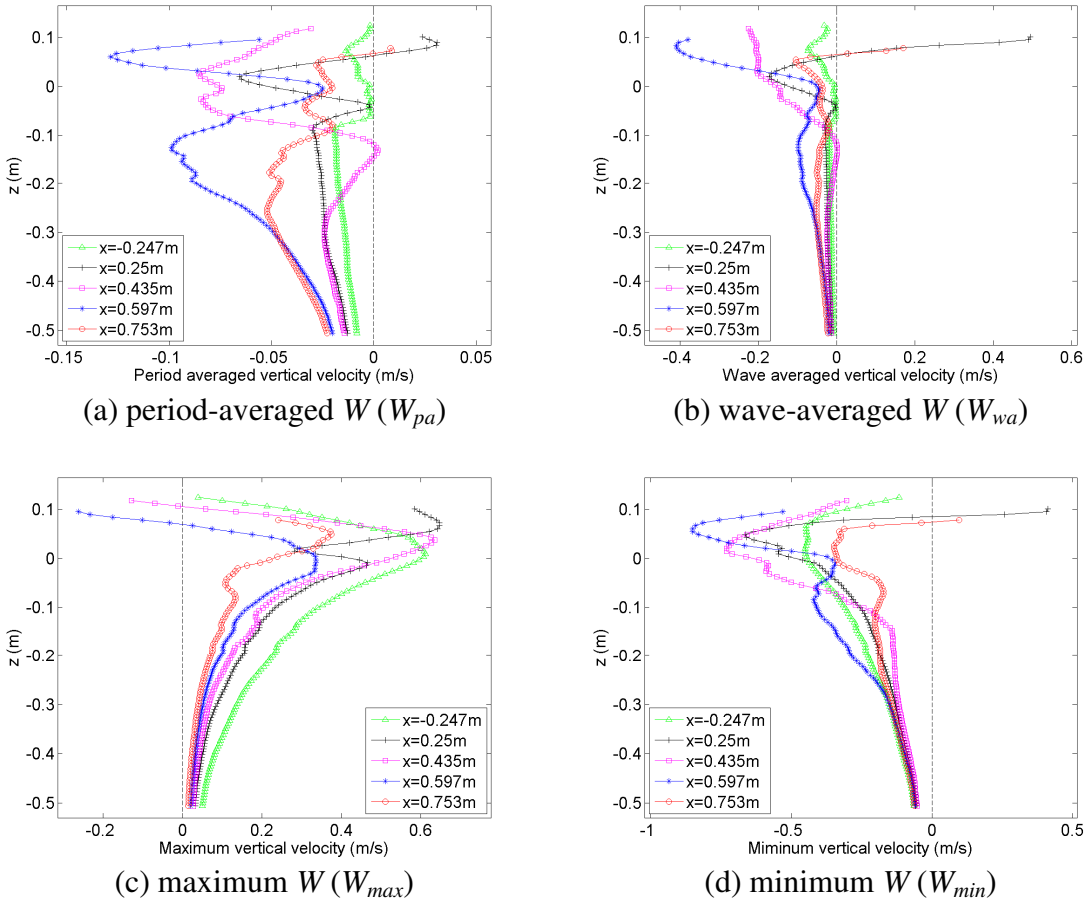

(a) period-averaged W (W_{pa}) (b) wave-averaged W (W_{wa})

(c) maximum W (W_{max}) (d) minimum W (W_{min})

Fig. 9.39 Time-averaged vertical velocity at $x < L$ (unit: m/s).

Fig. 9.40 and Fig. 9.41 show the comparison of results with different locations which are $x > L$ (spilling wave region) for horizontal and vertical velocities respectively. The results shown in Fig. 9.37 to Fig. 9.41 were obtained by combining upper and lower FOVs. Velocities for the overlapped region between two FOVs were obtained by averaging.

Variation of the time-averaged horizontal velocity profiles is not significant after the first impingement as shown in Fig. 9.38(a) and (b). Note that the velocity profile

presented with green squares is before the first impinging point. Some discrepancy under the trough level is due to the two rollers penetrating into deep water and is dependent on the location of the station. For example, the first roller caused by the first impingement passes through x = 0.597 m as shown in Fig. 9.38(a), that makes more positive transport between z = - 0.3 m and z = - 0.1 m. In the case of the spilling region where $x > L$, the second roller caused by the second impingement passes through x = 1.076 m as shown in Fig. 9.40(a).

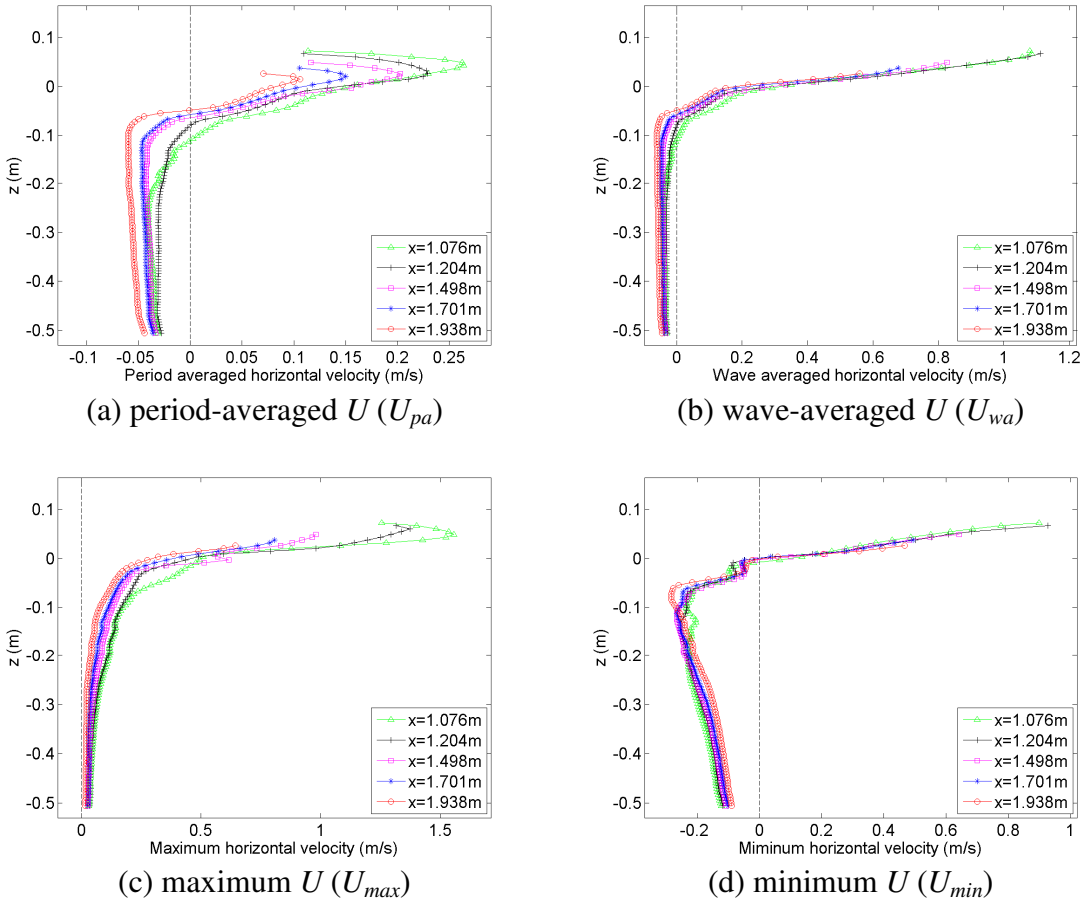

(a) period-averaged U (U_{pa}) (b) wave-averaged U (U_{wa})

(c) maximum U (U_{max}) (d) minimum U (U_{min})

Fig. 9.40 Time-averaged horizontal velocity at $x > L$ (unit: m/s).

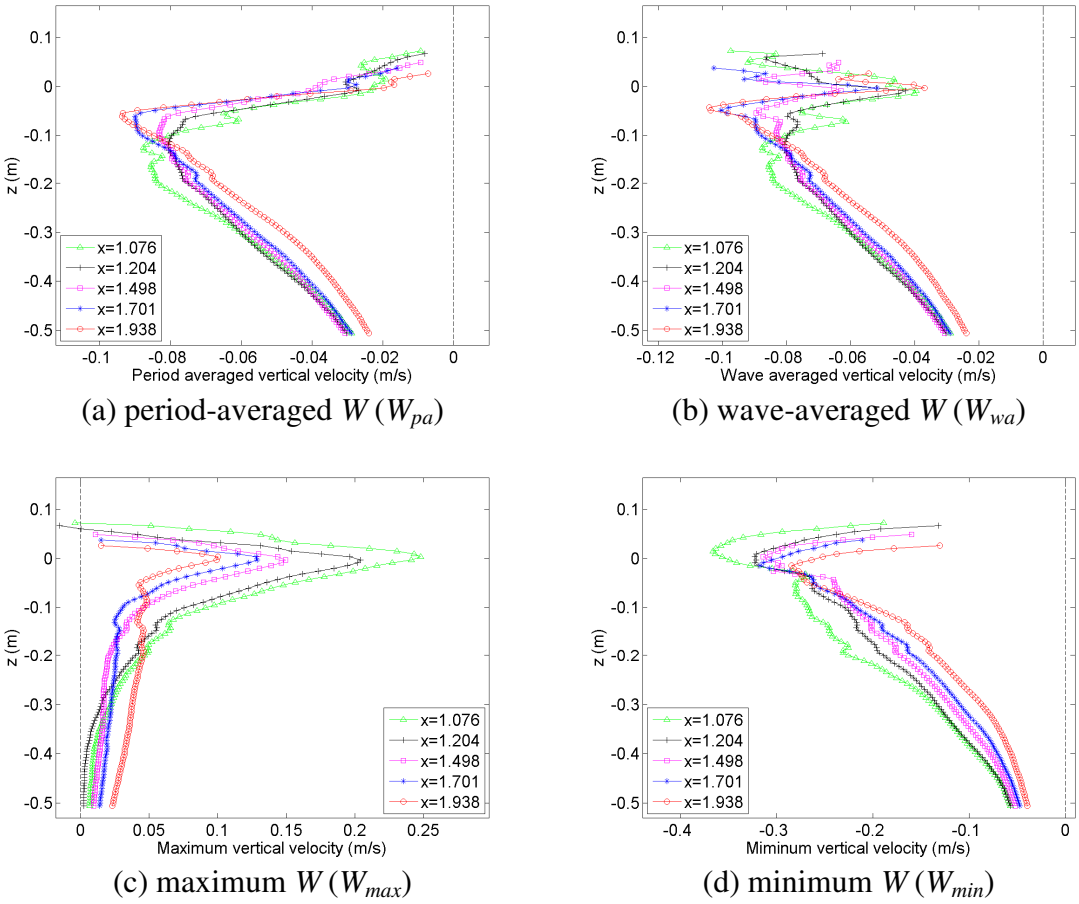

(a) period-averaged W (W_{pa}) (b) wave-averaged W (W_{wa})

(c) maximum W (W_{max}) (d) minimum W (W_{min})

Fig. 9.41 Time-averaged vertical velocity at $x > L$ (unit: m/s).

It can be clearly seen that variation of the vertical velocity profiles at $x < L$, where the first and second impingements occur, is very large [Fig. 9.39(a) and (b)] while variation of the vertical velocity profile at $x > L$, which is the spilling wave region from the third impingement, is much smaller [Fig. 9.41(a) and (b)].

One of the interesting profiles of the period-averaged vertical velocity occurs at the location between the developed first splash-up and the second impingement. An example can be seen from W_{pa} at x = 0.597m (blue) in Fig. 9.39(a). Two large negative averaged

profiles represent water spray impingement caused by the first splash-up and downward momentum of the wave rear face ($z > 0$), and penetrating first roller into deep water ($z < 0$) respectively. Therefore, downward momentum is dominant at this location except near the still water level. This is due to the newly ascending crest caused by the first impingement. The new ascending crest provides large upward momentum causing the first splash-up continuously as the crest is growing. Large downward momentum from the water spray impingement and the first roller penetration is compensated by the large upward momentum from the ascending crest around $z = 0$. As the impinging water jet pushes up front surface water, the large downward momentum of the first impinging jet is continuously transferred to the upward momentum of the ascending water crest and the ascending crest causes the first splash-up.

Since the PIV measurements were performed to cover the entire breaking wave, time series and time-averaged values can be obtained for all 475 stations and are shown in Fig. 9.35 to Fig. 9.41. Fig. 9.42(a) and (b) show the wave-averaged horizontal velocity and the period-averaged horizontal velocity at each point with $dx = dz = 5.78$ mm. Fig. 9.42(c) and (d) represent the maximum and minimum horizontal velocity at each point. The number of points is 55100 (475×116) and the time resolution in the calculation for the time averaging is 10 ms. Fig. 9.43(a) and (b) show the wave-averaged and period-averaged vertical velocity at each point. Fig. 9.43(c) and (d) represent the maximum and minimum vertical velocity at each point. The x and z components were normalized by constant water depth ($h = 0.8$ m) and wavelength of the primary wave ($L = 1.08$ m). All velocities presented were normalized by the wave phase speed ($C = 1.3$ m/s).

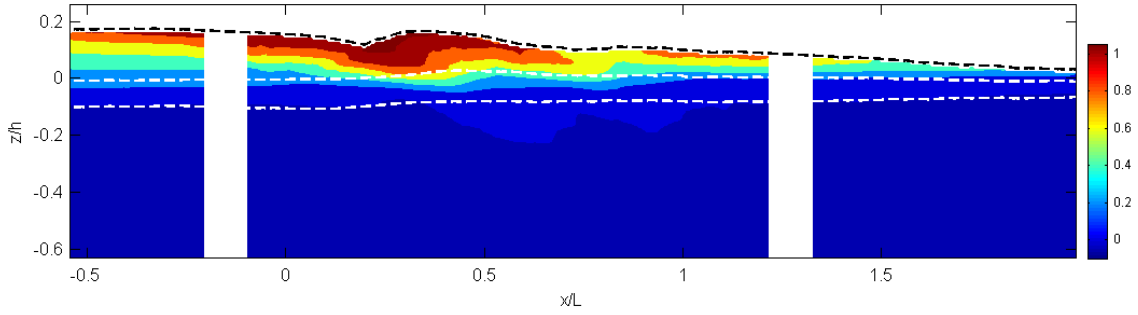

(a) wave-averaged U (U_{wa}/C)

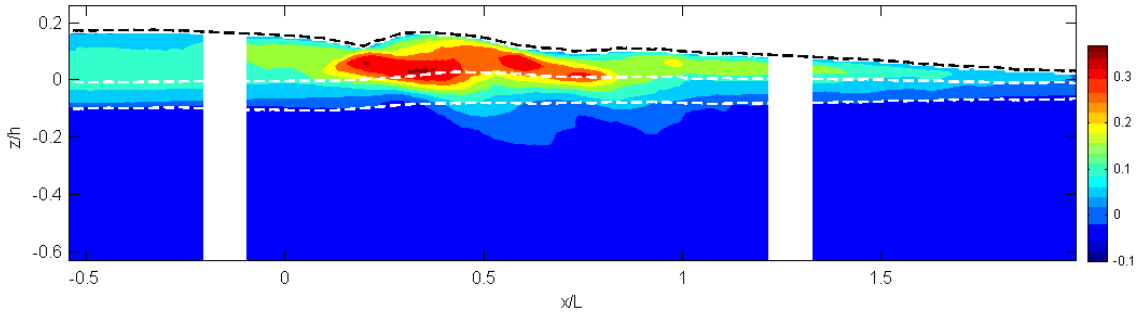

(b) period-averaged U (U_{pa}/C)

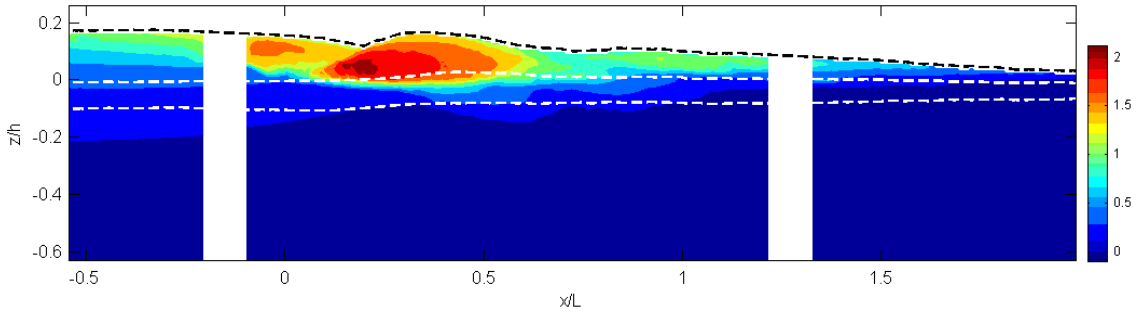

(c) maximum U (U_{max}/C)

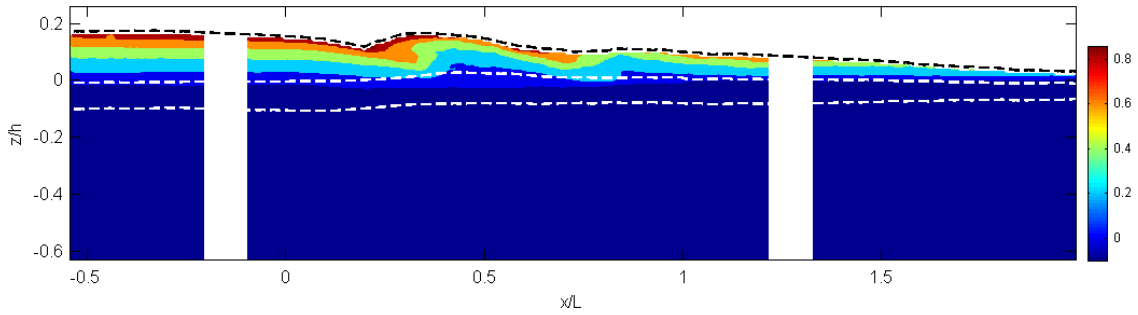

(d) minimum U (U_{min}/C)

Fig. 9.42 Normalized time-averaged, maximum, and minimum horizontal velocity.

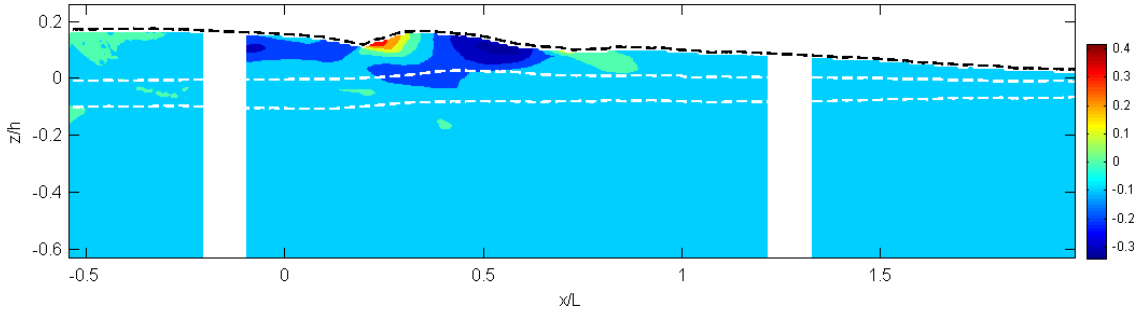

(a) wave-averaged W (W_{wa}/C)

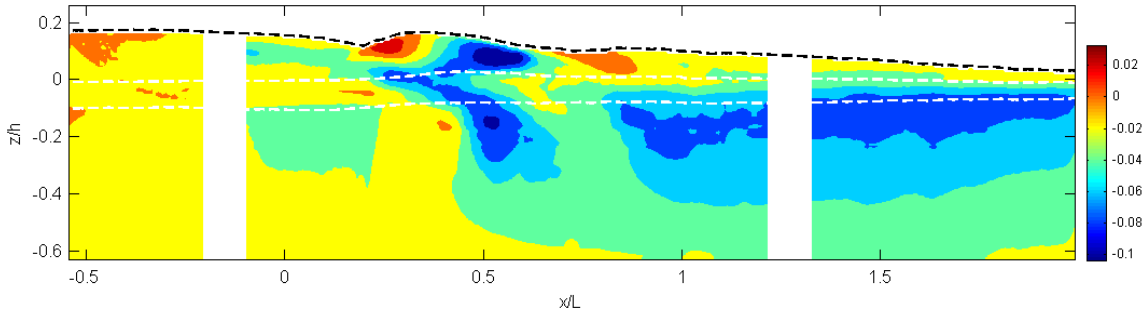

(b) period-averaged W (W_{pa}/C)

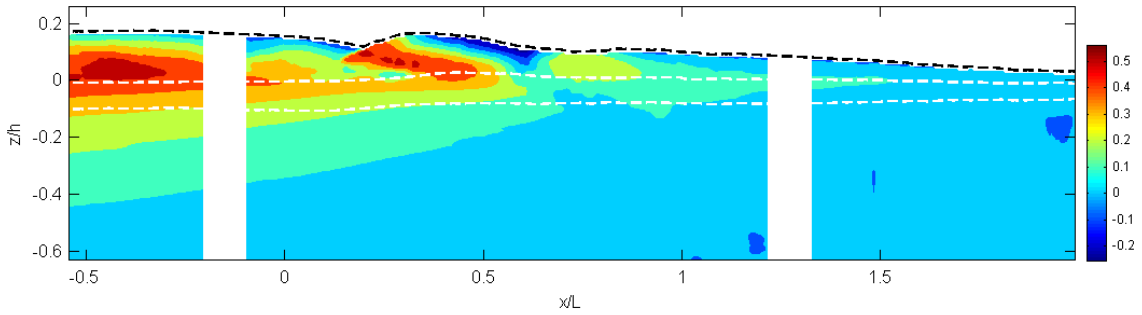

(c) maximum W (W_{max}/C)

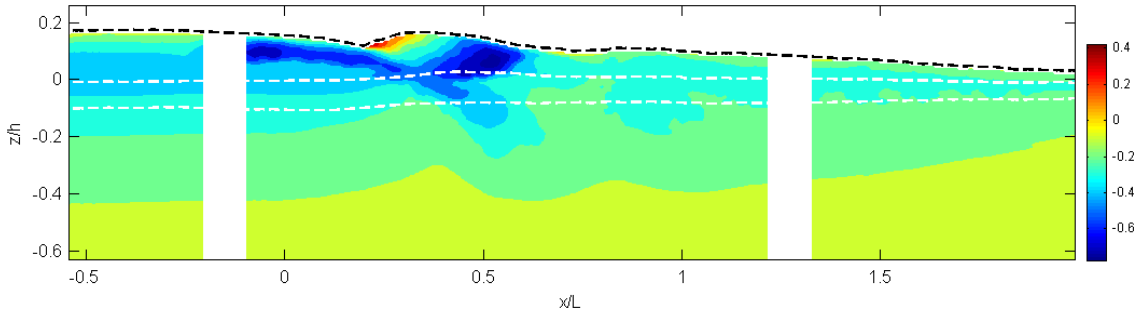

(d) minimum W (W_{min}/C)

Fig. 9.43 Normalized time-averaged, maximum, and minimum vertical velocity.

As shown in Fig. 9.42(a), it is clearly seen that the wave-averaged horizontal velocity has the maximum near crest level and the maximum in the entire flow occurs at around x = 0.25 m, where the full-scale first splash-up begins. In addition, the wave and period-averaged vertical velocities have their maximum at this location as shown in Fig. 9.43(a) and (b). The wave-averaged horizontal velocity is gradually decreased during the first splash-up process and is increased again because the upward momentum of the second splash-up is transported to horizontal momentum.

Period-averaged horizontal velocity has maximum values at x = 0.2 m to 0.45 m, as shown in Fig. 9.42(b), because the first roller caused by the overturning jet and the newly ascending crest causing the first splash-up passes through that location with large horizontal momentum. The horizontal momentum is transported in sequence of each impingement and splash-up process. As shown in Fig. 9.42(c), maximum horizontal velocity in the entire flow occurs around $x = 0.2L$ at $t = 0.06T$ corresponding to the beginning of the first splash up. Also the maximum upward velocity occurs at this location as shown in Fig. 9.43(c). It is interesting that the maximum upward velocity in the pre-impinging region (PIV FOV1), about z = - 0.1m to 0.1 m, is very high and is very close to the upward vertical velocity at the fist splash-up as shown in Fig. 9.43(c). Despite similar magnitude of the maximum upward velocity with the first splash-up shown in Fig. 9.43(c), the time-averaged value in the pre-impinging region is much lower than that in the first splash-up region. This is due to compensation by downward velocity in a wave cycle while upward motion is dominant in the first splash-up region as shown in Fig. 9.43. If flow density is considered, upward momentum will reach the

maximum at the pre-impinging region and at the ascending crest. This large upward momentum causes wave deformation and the overturning jet by transferring momentum to the wave crest of the primary wave.

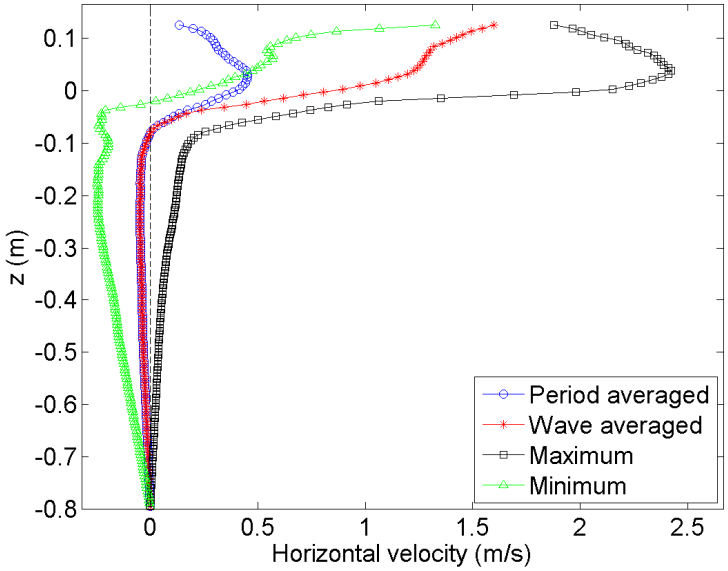

Fig. 9.44 Example of full depth extension of horizontal velocity.

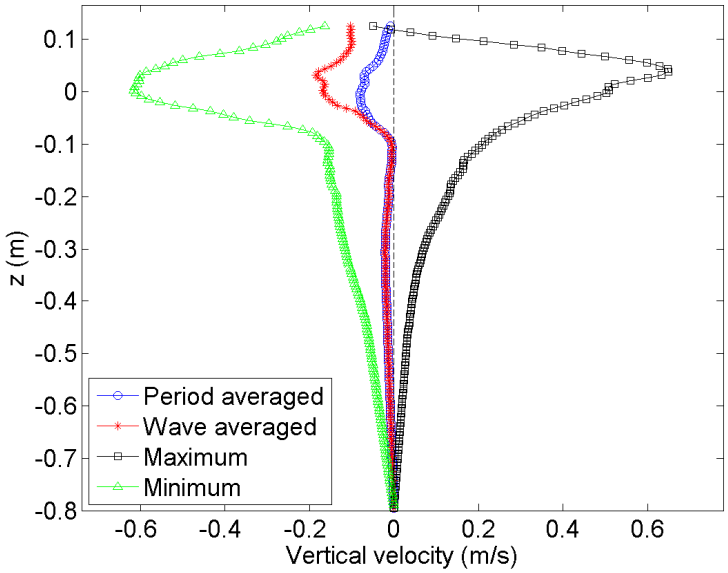

Fig. 9.45 Example of full depth extension of vertical velocity.

To obtain fluxes such as mass flux and momentum flux, it is necessary to expand the time-averaged values down to the bottom of the wave tank. However, the lowest measurement point in the PIV measurements is z = - 0.51m. With the assumption that both horizontal and vertical velocities are zero at the bottom, Velocity profiles between z = - 0.51 m and - 0.8 m were obtained using linear interpolation. Fig. 9.44 and Fig. 9.45 show examples of the full depth extension of velocity profiles at x = 0.435 m.

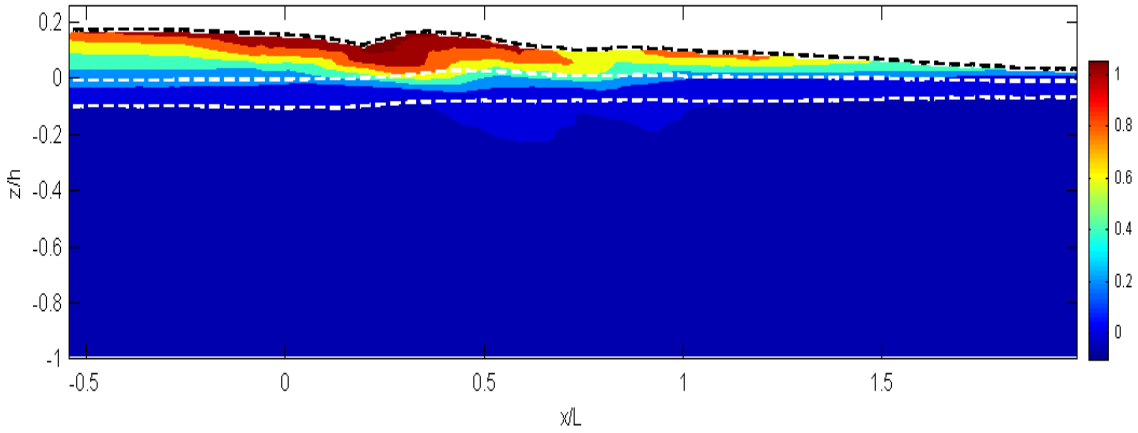

(a) full depth wave-averaged U (U_{wa}/C)

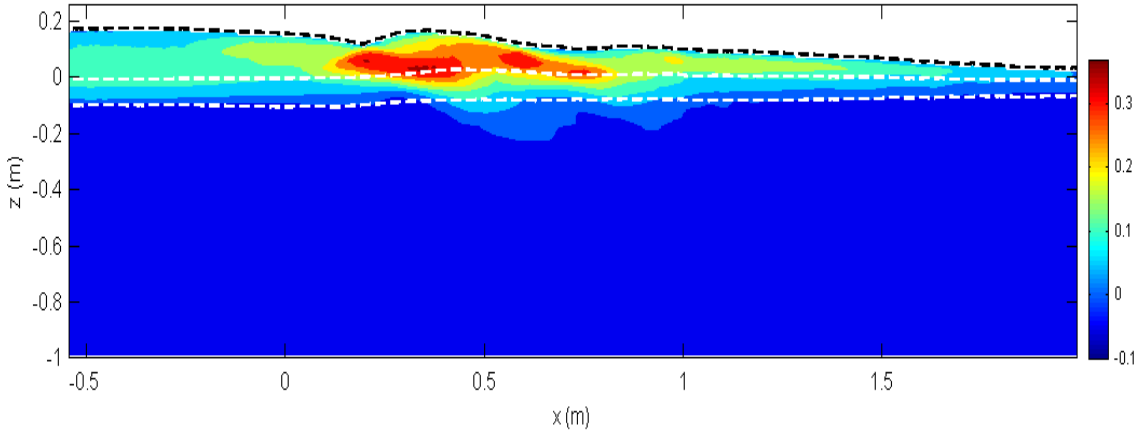

(b) full depth period-averaged U (U_{pa}/C)

Fig. 9.46 Full depth extension of time-averaged horizontal velocity (U/C).

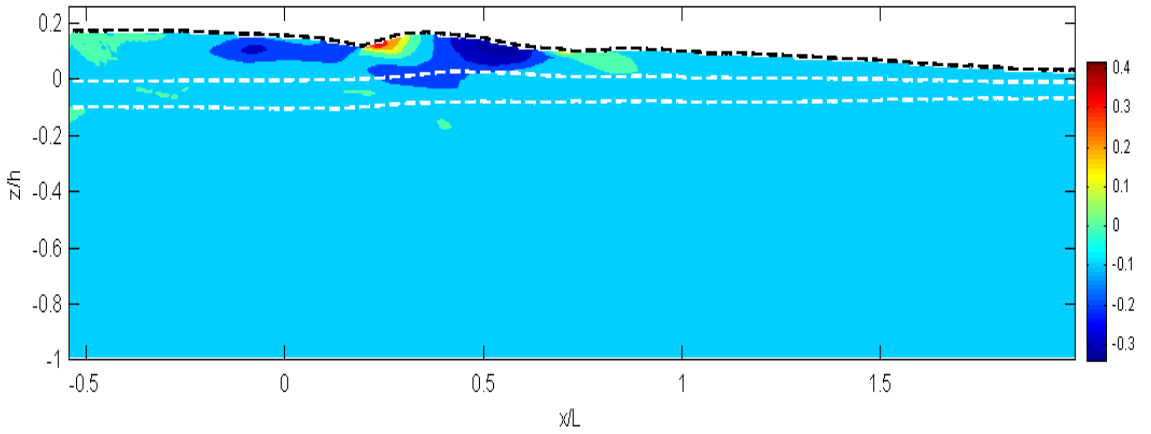

(a) full depth wave-averaged W (W_{wa}/C)

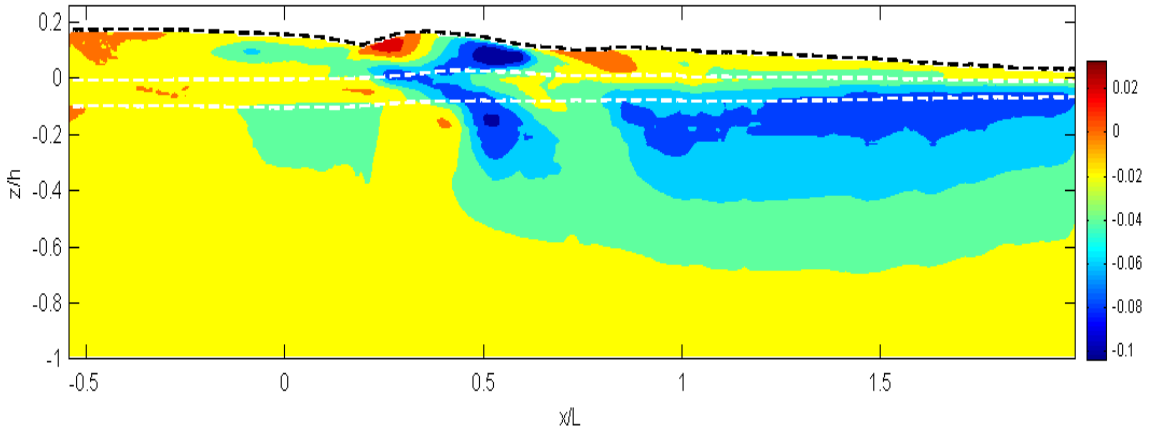

(b) full depth period-averaged W (W_{pa}/C)

Fig. 9.47 Full depth extension of time-averaged vertical velocity (W/C).

Fig. 9.46 and Fig. 9.47 show the time-averaged velocities applying the full depth extension for every station. In addition, the empty profiles shown in Fig. 9.42 and Fig. 9.43, which were due to two steel columns were filled by means of the linear interpolation for each row horizontally.

Fig. 9.48 shows normalized maximum velocity at each station. It is similar to the maximum velocity variation in time obtained from spatial analysis as shown in Fig. 9.31.

This is because most maximum velocity occurs at the front toe of the plunging breaker. However, there is discrepancy during the beginning of the splash-up process followed by the impingement, especially at the second process. When the splash-up begins, the maximum velocity occurs at the impinging jet rather than the splash-up. For example, during the second process, maximum velocity occurs at the region of the second water jet impingement followed by the water spray impingement as shown in Fig. 9.32. Fig. 9.48 and Fig. 9.31 will provide the location and time information of the maximum horizontal and vertical velocities.

Small decrement of the maximum horizontal velocity is found between each impingement and splash-up. In the case of the first process, the time and distance of the decrement is very small. However, in the second process, the decrement is remarkable at the location between $x = 0.55L$ and $0.75L$. This is because the accumulated roller caused by the water spray impingement moves slowly with roller motion above the trough. The maximum horizontal velocity of the accumulated roller is close to the wave phase speed and is suddenly increased due to the full-scale second splash-up.

The local maximum downward velocity occurs at each impinging location and the downward momentum is transferred to the horizontal and upward momentum of the front waves. The local maximum upward velocity occurs at the location of the wave face becoming vertical, the first splash-up and the second splash-up. From the location after one wavelength, both horizontal and vertical maximum velocities are linearly decreased without significant fluctuations.

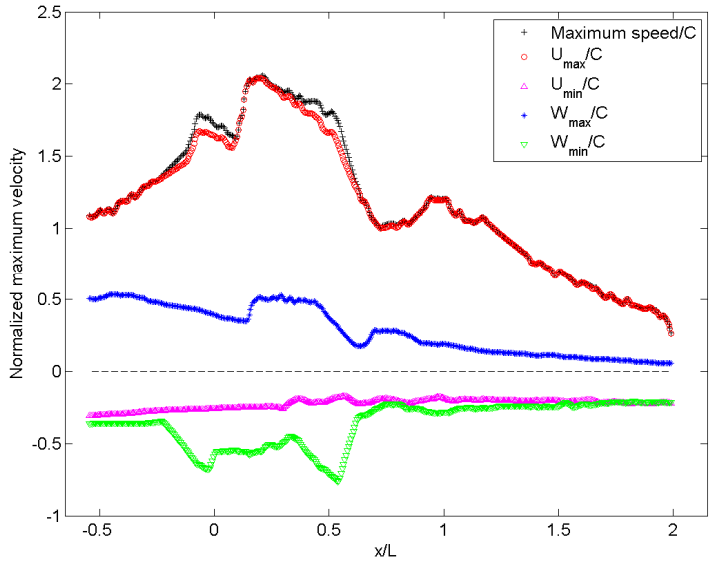

Fig. 9.48 Normalized maximum velocity at each station.

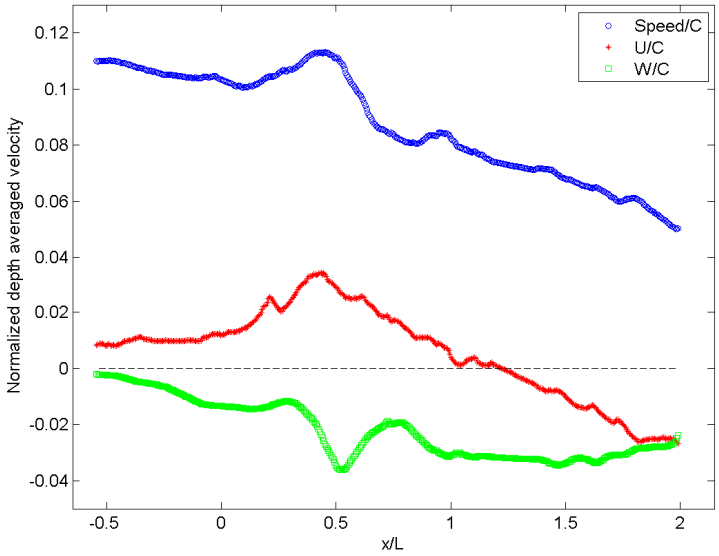

Fig. 9.49 Depth-averaged time mean velocity.

Fig. 9.49 shows depth-averaged time mean velocities normalized by the wave phase speed. The depth-averaged time mean horizontal velocity $\overline{U_{da}}$ at every station was

obtained by means of averaging the period-averaged horizontal velocity (U_{pa}). The depth-averaged time mean velocity can be obtained from Eq. (9.6).

$$\overline{U_{da}(x)} = \frac{\int_{-h}^{\eta(x)} U_{pa}(x,z)dz}{\int_{-h}^{\eta(x)} dz} \tag{9.6}$$

where,

$$U_{pa}(x,z) = \int_{t_{tr}(x)}^{t_{tr}(x)+T(x)} \delta(x,z,t)U(x,z,t)dt \Big/ \int_{t_{tr}(x)}^{t_{tr}(x)+T(x)} dt \tag{9.7}$$

Without considering a void ratio of the plunging breaker, volume flux (VF) and mass flux (MF) at each station can be obtained from U_{pa} or $\overline{U_{da}}$.

$$VF(x) = \int_{-h}^{\eta(x)} U_{pa}(x,z)dz = \overline{U_{da}(x)} \int_{-h}^{\eta(x)} dz \tag{9.8}$$

$$MF(x) = \rho_w \int_{-h}^{\eta(x)} U_{pa}(x,z)dz = \rho_w VF(x) \tag{9.9}$$

where, ρ_w is the water density.

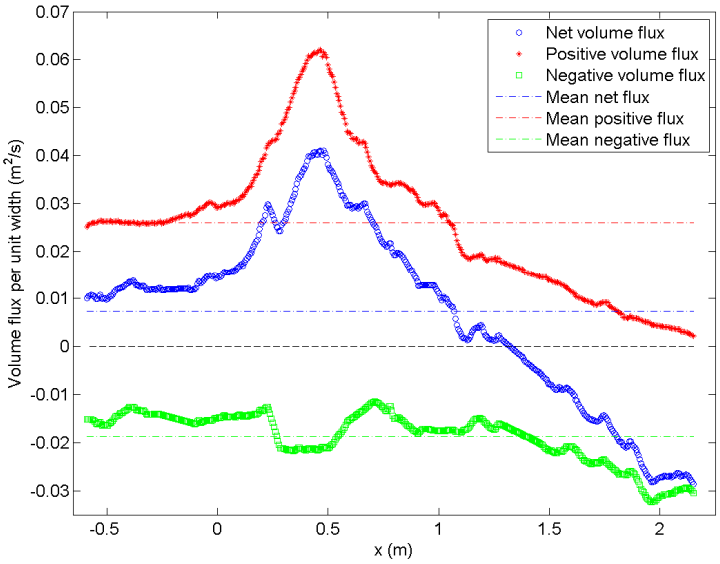

Fig. 9.50 Volume flux without considering void ratio.

Fig. 9.50 shows volume fluxes per unit width at all 475 stations and mean volume flux for the entire flow. The volume flux (*VF*) was obtained from Eq. (9.8) and was calculated without considering the void ratio effect. Red and green markers show the positive flux and the negative flux at each station respectively. Net flux at each station is plotted with blue circles. Red and green dashed lines represent positive and negative mean flux for all stations and their values are 0.0260 m^2/s and -0.0187 m^2/s respectively. The blue dashed line represents mean net flux of the entire station and the magnitude is 0.0074 m^2/s.

As shown in Fig. 9.50, huge positive fluxes are observed between $x = 0$ and $x = L$ where the void ratio cannot be negligible. It is believed that the positive flux is overestimated because the void ratio is not considered in the results. In addition, net flux is also positive before the first impinging point where the void ratio is zero. That means mass flux is not zero but positive regardless of the void ratio when wave deformation begins in the pre-impinging region. Although it is overestimated in the region where the void ratio is not zero, net flux starts decreasing linearly from around $x = 0.5L$ and becomes close to zero at $x = L$. From the spilling wave region ($x > L$), net flux changes to negative and the magnitude of the negative flux is increased more and more as shown in Fig. 9.50.

All other quantities, such as mean and turbulent kinetic energy, Reynolds stress, and momentum flux should be corrected by applying the void ratio. With more detailed discussion about the void ratio measurements, results applying the compressibility of the plunging breaker will be presented in Chapter XI.

9.5 Mean Vorticity

Compared with the LDV measurements, one of great advantages in the PIV measurements is that the vorticity in a control volume can be easily obtained with high spatial resolution. Since the generated plunging wave and the PIV measurement performed in this study are two-dimensional, three-dimensional vorticity, such as vortex stretching, can not be obtained. However, compared with a spilling wave, large horizontal eddies are more dominant in a plunging breaker and obliquely descending three-dimensional eddies which are important in spilling waves are not significant in plunging waves.

Mean vorticity was calculated from Eq. (9.10)

$$\Omega = \frac{\partial U}{\partial z} - \frac{\partial W}{\partial x} \tag{9.10}$$

As shown in Fig. 5.2, clockwise rotation is to be positive according to the coordinate system used in the present study.

9.5.1 Spatial Analysis of Mean Vorticity

Results on the spatial analysis of mean vorticity fields are provided in this section. Fig. 9.51 shows the vorticity field variation measured at FOV3 during the first impingement and the beginning of the first splash-up. From the first impingement, high vorticity is generated in the region of the first splash-up due to large shear flow between the splash-up and water body. In addition, there is large clockwise (positive) vortex in the first impinging roller. Maximum positive vorticity occurs around t = 0.05 s as shown in Fig. 9.52. Note that the maximum horizontal velocity occurs at the same time.

However, the location of the generated vortices is near the bottom boundary of the aerated region. A small negative (counterclockwise) vortex is observed in the front face of the impinging roller. It is considered that downward velocity of the impinging roller close to the splash-up region is smaller than that of the crest region due to the newly ascending water crest between two rollers. In addition, the ascending water crest causes a negative vortex later.

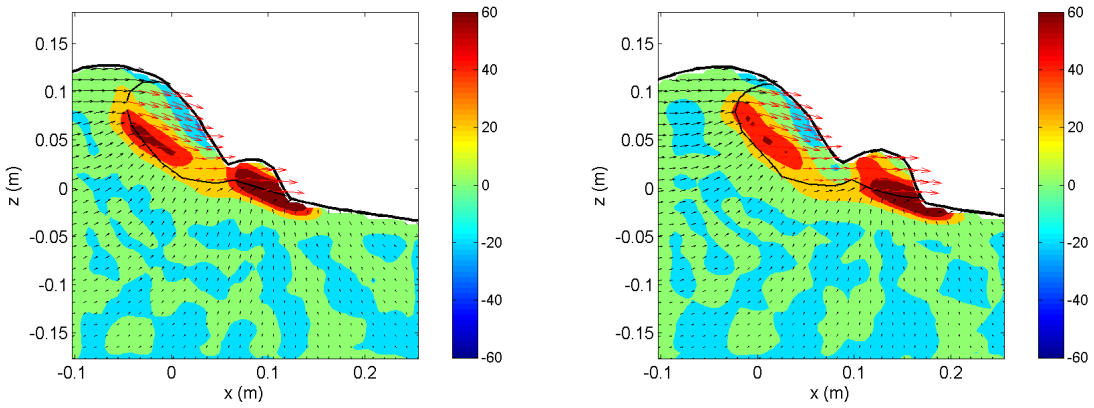

(a) t = 0.03 s (FOV3)

(b) t = 0.05 s (FOV3)

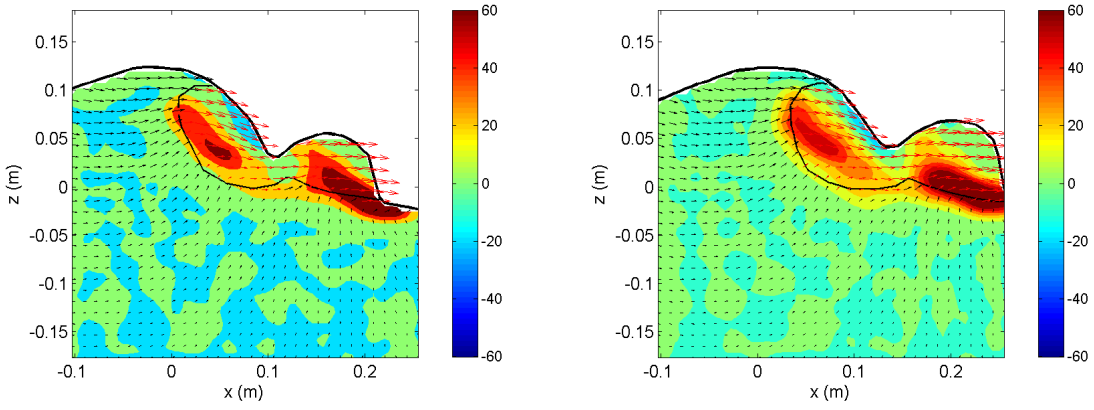

(c) t = 0.07 s (FOV3)

(d) t = 0.09 s (FOV3)

Fig. 9.51 Vorticity at the beginning of the first splash-up (FOV3) (unit: s^{-1}).

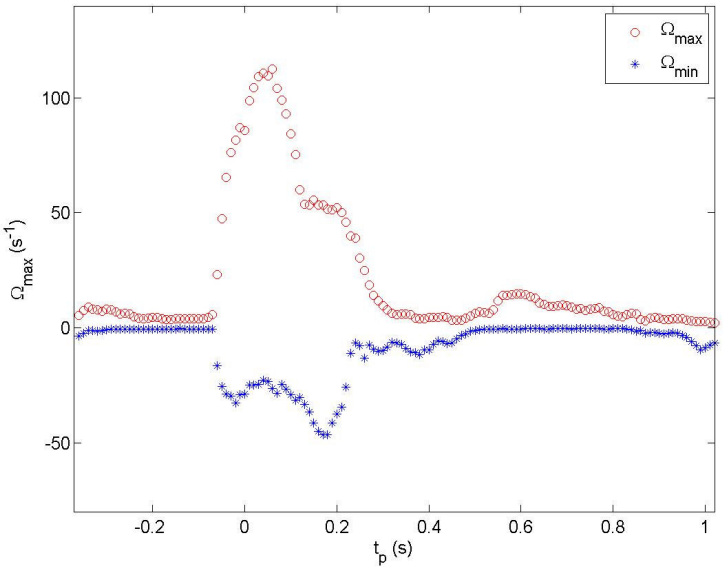

Fig. 9.52 Maximum vorticity at the beginning of the first splash-up (FOV3).

Fig. 9.53 shows the negative vorticity due to the new ascending crest. Note that black lines represent the free surface and the boundary of the aerated region. Velocity vectors in the aerated region are plotted in a red color. Although the first backward impingement begins at around t = 0.25 s when the ascending crest loses kinetic energy at the upper part, the negative vortex occurs due to reverse shear flow between the first roller and the ascending crest. The location of the negative vortex is always higher than the positive vortex. At the initial stages, the location of the negative vortex is slightly higher than that of the positive vortex in the first roller. The positive vortex is transported in a downward and downstream direction with speed higher than the wave phase speed, while the negative vortex is transported in an upward direction due to the ascending water crest and in a downstream direction with speed less than the first roller. Therefore, the location of the negative vortex becomes above the positive vortex as

shown in Fig. 9.53 and Fig. 9.54. The first backward impingement starts around t = 0.25 s and the maximum negative vorticity occurs at this moment. An interesting result is found between t = 0.19 and 0.24 s before the first impingement. During that time (about 0.05s), the negative vorticity becomes weaker. It is considered that kinetic energy of the upper and left part of the fully-grown ascending crest is converted into potential energy at that moment. It will be discussed in detail later.

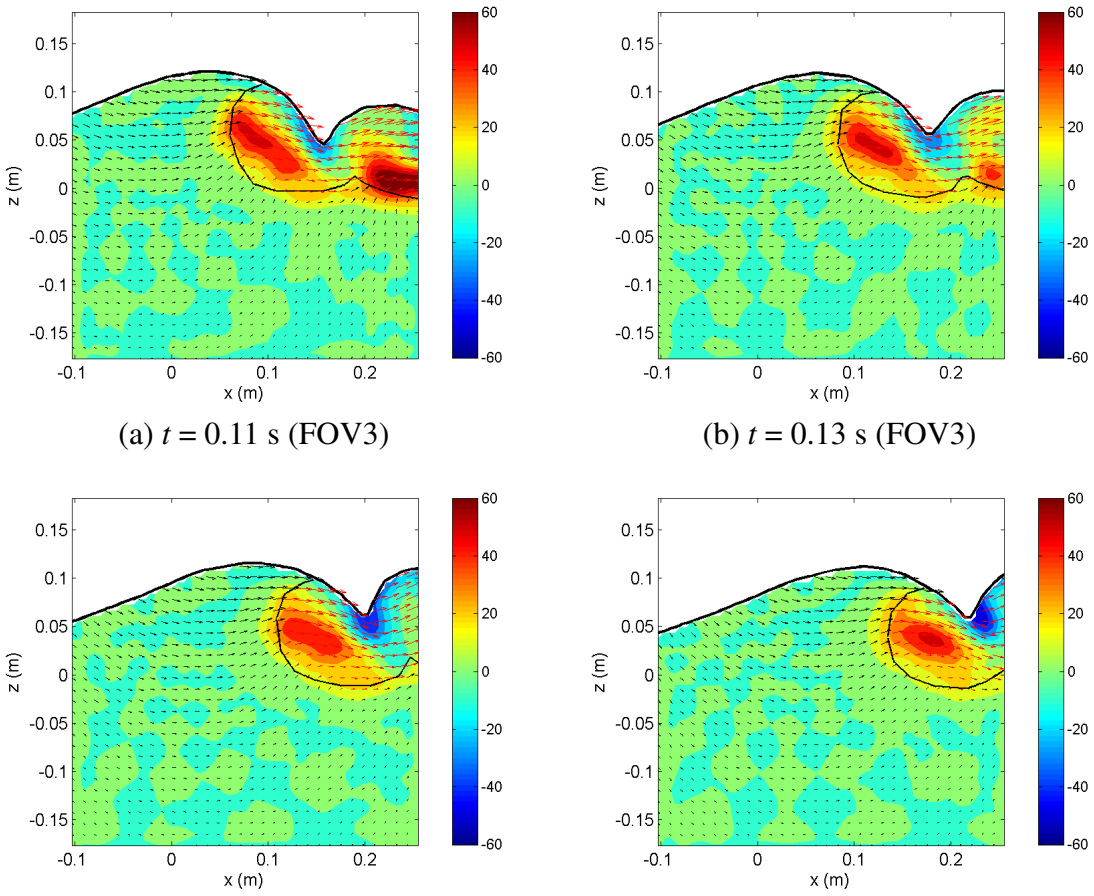

(a) t = 0.11 s (FOV3)

(b) t = 0.13 s (FOV3)

(c) t = 0.15 s (FOV3)

(d) t = 0.17 s (FOV3)

Fig. 9.53 Negative vorticity due to the new ascending crest (FOV3) (unit: s^{-1}).

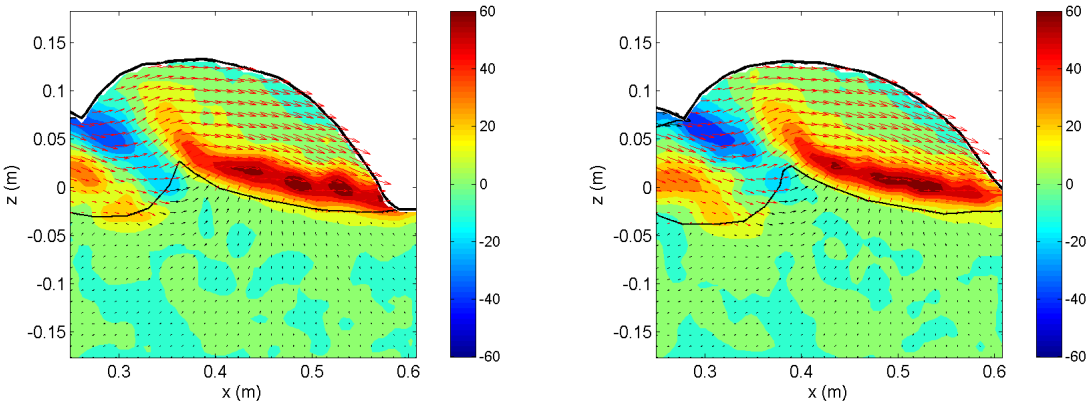

(a) t = 0.24 s (FOV5)

(b) t = 0.26 s (FOV5)

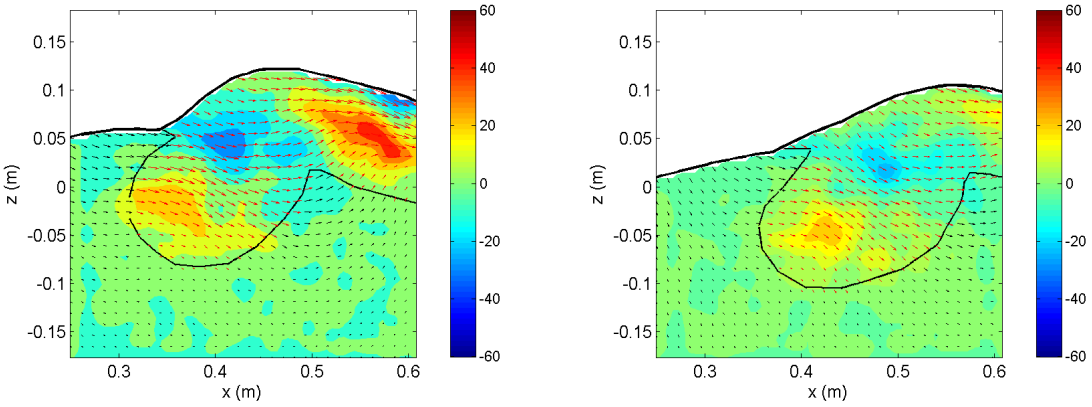

(c) t = 0.36 s (FOV5)

(d) t = 0.45 s

Fig. 9.54 Vorticity at the first splash-up and the backward impingement (FOV5) (unit: s^{-1}).

On the other hand, the positive vortex in the second roller caused by the first splash-up can be seen in Fig. 9.54(a) and (b) and the location of the maximum vorticity is above of the bottom boundary of the aerated region, which is the front face of the new primary wave.

Fig. 9.55 shows vorticity at the combined FOVs and vorticity transport due to the first splash-up roller and the backward impingement can be seen. Also vorticity at the accumulated mixture due to water spray can be seen.

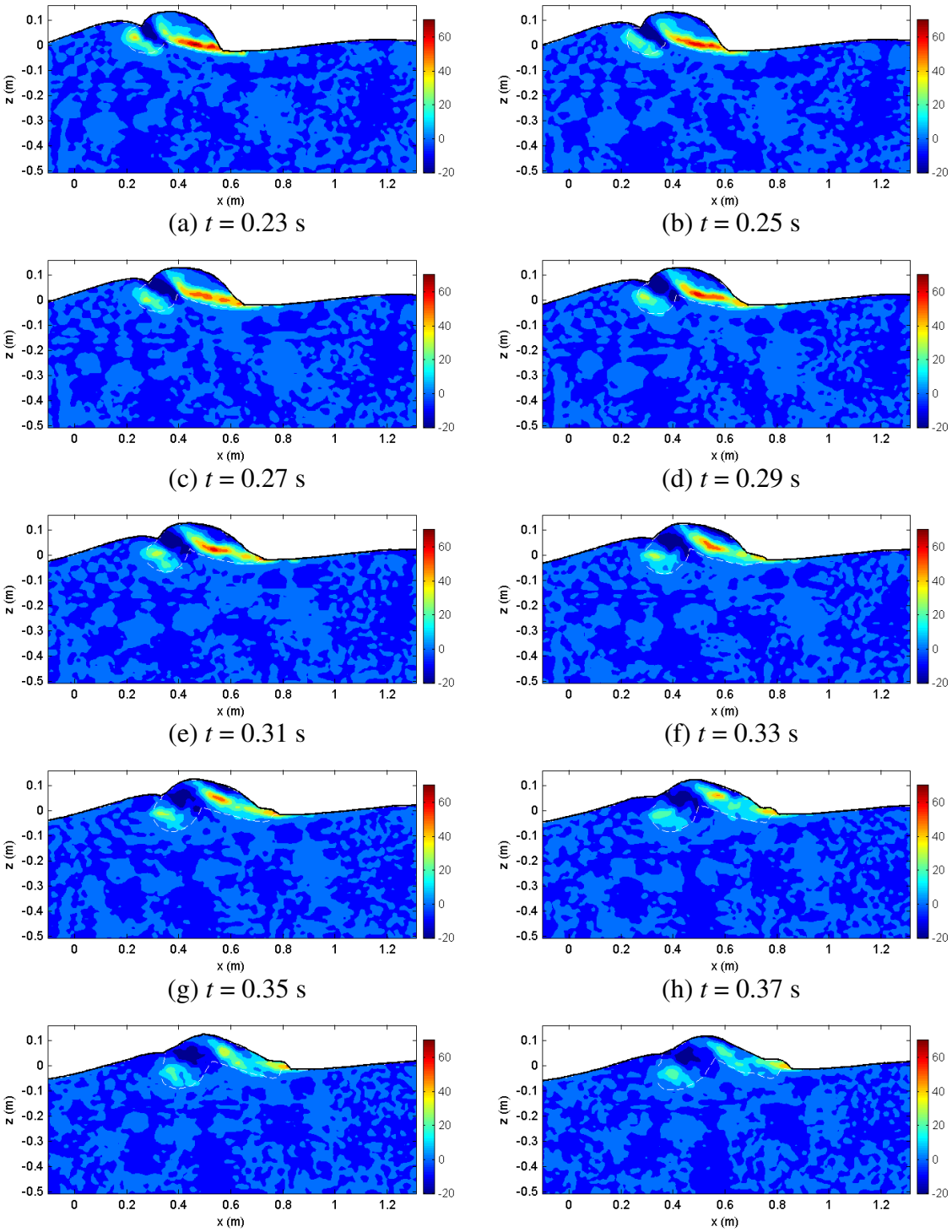

(a) t = 0.23 s (b) t = 0.25 s

(c) t = 0.27 s (d) t = 0.29 s

(e) t = 0.31 s (f) t = 0.33 s

(g) t = 0.35 s (h) t = 0.37 s

(i) t = 0.39 s (j) t = 0.41 s

Fig. 9.55 Vorticity at the first splash-up and first backward impingement (unit: s^{-1}).

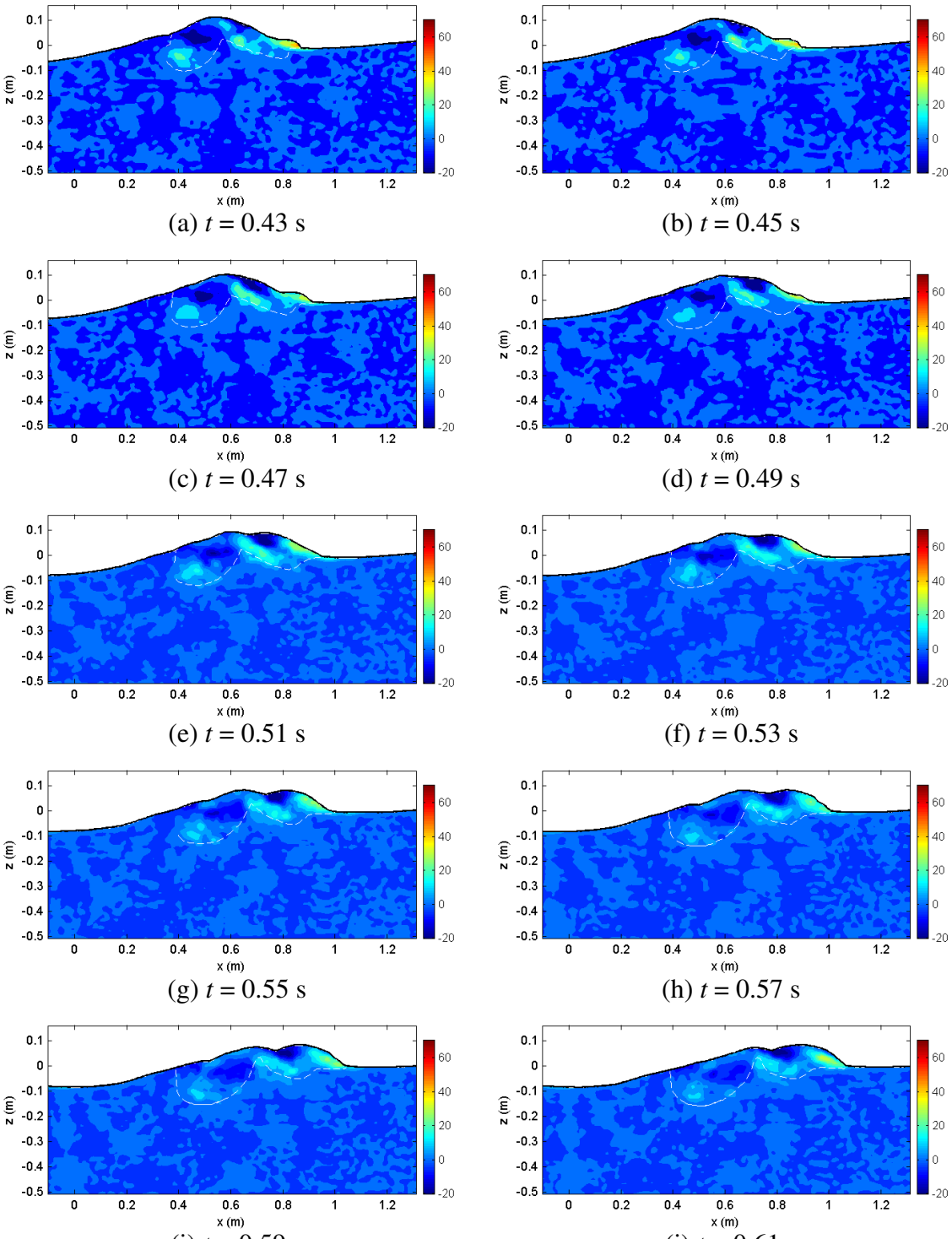

(a) t = 0.43 s (b) t = 0.45 s

(c) t = 0.47 s (d) t = 0.49 s

(e) t = 0.51 s (f) t = 0.53 s

(g) t = 0.55 s (h) t = 0.57 s

(i) t = 0.59 s (j) t = 0.61 s

Fig. 9.56 Vorticity at the second impingement and splash-up (unit: s^{-1}).

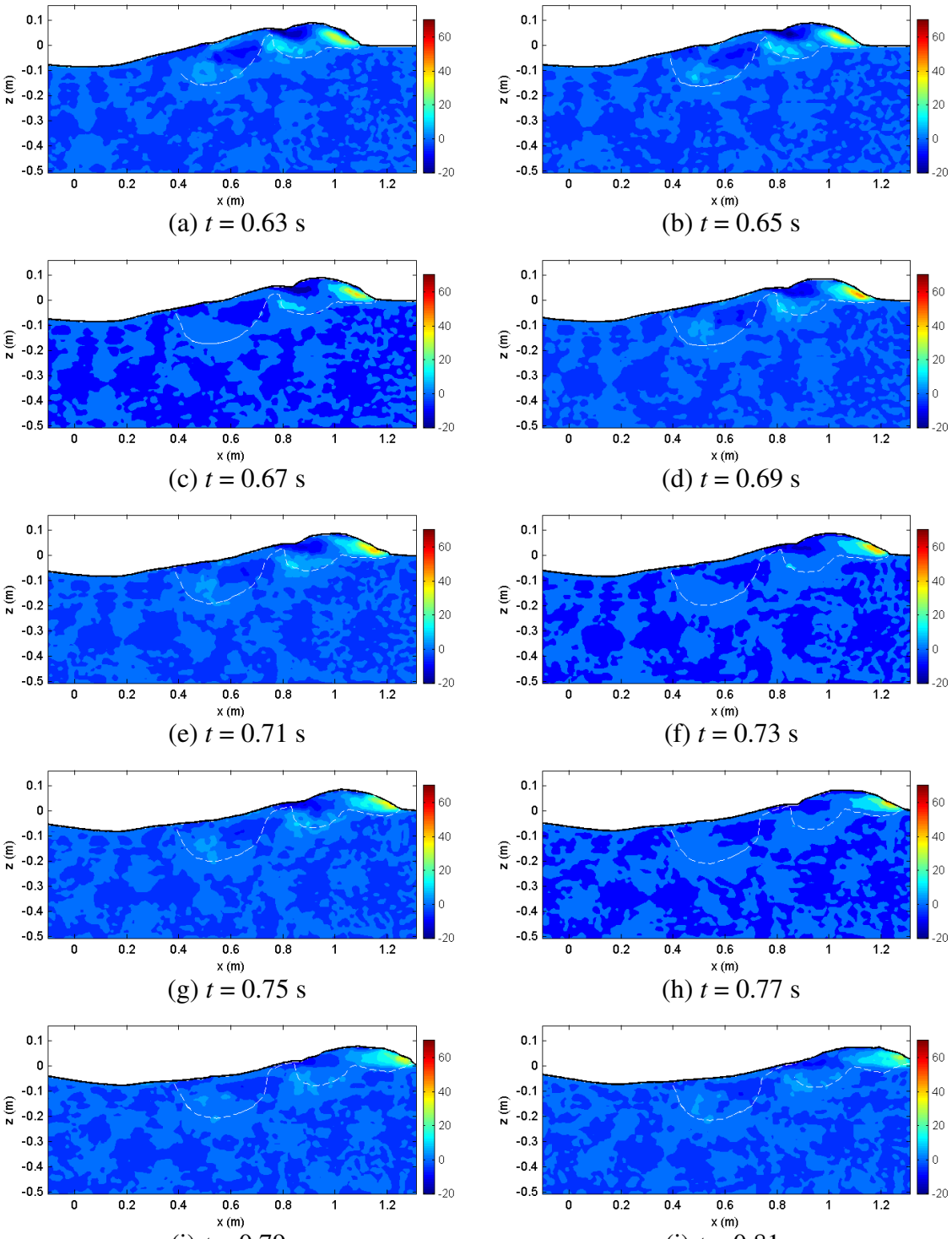

(a) t = 0.63 s (b) t = 0.65 s

(c) t = 0.67 s (d) t = 0.69 s

(e) t = 0.71 s (f) t = 0.73 s

(g) t = 0.75 s (h) t = 0.77 s

(i) t = 0.79 s (j) t = 0.81 s

Fig. 9.57 Vorticity at the third impingement and splash-up (unit: s^{-1}).

The negative vortex due to the ascending crest and the first backward impingement can be seen in Fig. 9.55. The scar on the wave surface between two rollers caused by the first impingement is filled up by the backward impingement, and the free surface is linearized at t = 0.51 s. This process can be seen in Fig. 9.55 and Fig. 9.56(a)-(e). The positive vortex at the toe of the first splash-up is weaker and weaker due to the growing air-water mixture as shown in Fig. 9.55(d)-(j). Although the motion of the accumulated mixture is clockwise, the speed is very slow and its size is increased due to more accumulation from the water spray. In this process, small size water droplets rebound slightly and large size droplets penetrate into water. However both are not significant as discussed in the previous section. Most water spray is accumulated without large horizontal momentum. The positive vorticity of the right side of the accumulated mixture roller is due to the small rebound of water spray.

Vorticity at the second impingement and splash-up can be seen in Fig. 9.56. The negative vortex between the second impingement and splash-up is also generated due to the second splash-up of the large volume of the accumulated roller. Fig. 9.57 shows vorticity at the third impingement and splash-up process. Although it is difficult to observe the third impingement from the figure, the third splash-up followed by the third impingement can be seen in Fig. 9.57(c)-(e). Small negative vorticity can be found between two areas of positive vorticity. Another scar caused by the second impingement is filled up by the second backward impingement and the free surface of the rear wave is linearized at t = 0.83 s, which is the period of the initial primary wave; this process can be observed in Fig. 9.57. Although the third scar caused by the third impingement can

not be seen in Fig. 9.57, the free surface is linearized around t = 0.97 s.

Fig. 9.58 shows the maximum positive and negative vorticity variation in time at FOV3 to FOV10 including all three processes of the impingement and splash-up. Vorticity is normalized by the wave height and phase speed of the primary wave. The maximum positive vorticity in the entire flow occurs around t = 0.06 s at the bottom of the aerated region for the beginning of the first splash-up. It is decreased gradually and then begins increasing when the second splash-up is developed.

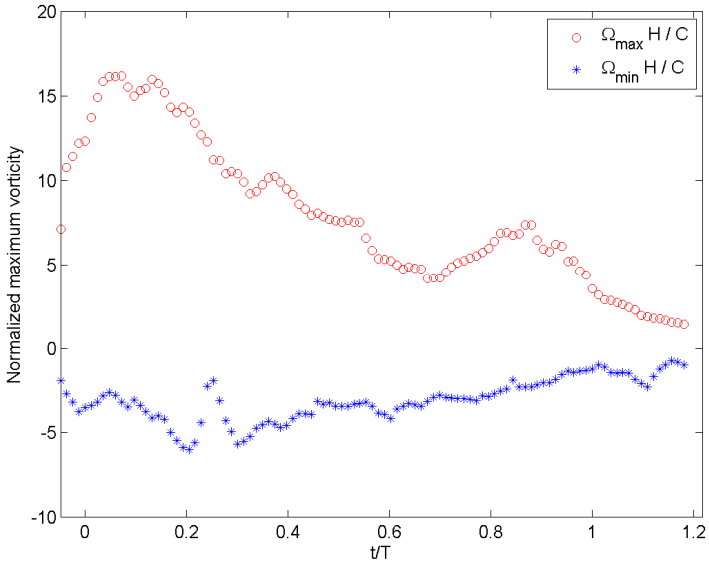

Fig. 9.58 Maximum vorticity normalized by *C* and *H*.

In the case of negative vorticity, the maximum counterclockwise vorticity has two similar local maxima around $t = 0.2T$ and $t = 0.28T$. As discussed before, there is sudden decrease of the negative vorticity between two moments. That time represents the moment of the first backward impingement. The newly ascending crest reaches the peak with large upward momentum around t = 0.2 s. The top potion of the ascending crest is

losing kinetic energy and is converting to potential energy. Finally, it falls down onto the first impinging roller. The negative vorticity is decreased for a while when the ascending crest stays at the peak elevation for about 0.05 s.

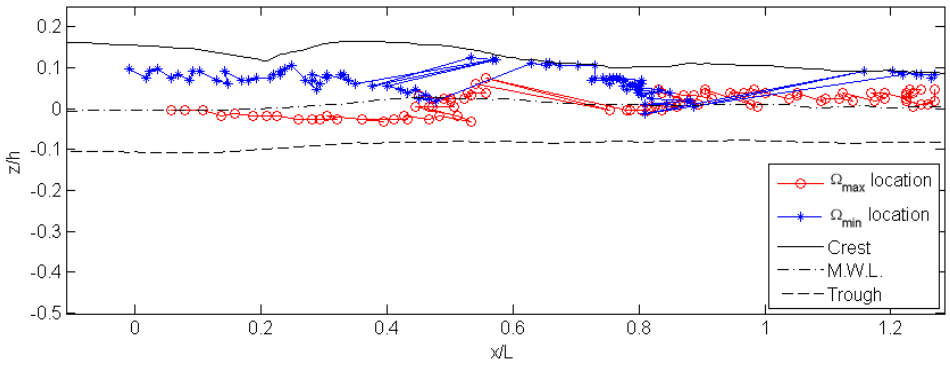

Fig. 9.59 Location of maximum vorticity.

Fig. 9.59 shows the location where the maximum vorticity occurs. The time difference between two markers is 0.01 s. The location of negative vorticity is always higher than the location of positive vorticity as shown in the previous results. The location of the maximum positive vorticity is usually near the toe of each splash-up and water spray in front surface. The maximum positive vorticity in the entire flow occurs around mean water level. During the first splash-up, the location is slightly lower than mean water level while the location after the second splash-up is slightly higher than mean water level. This is clearly expected because the front trough elevation is increased from -0.1 m at $x = -0.5L$ to zero at $x = 1.5L$ as shown in Fig. 9.34.

It can be clearly seen that two positive and negative vortices meet each other due to the backward impingement. The first one can be seen around $x = 0.5L$ and the second one can seen around $x = 0.85L$.

9.5.2 Temporal Analysis of Mean Vorticity

Temporal analysis for the vorticity measurement is presented in this section and is conducted in a similar manner as Section 9.4.2, which presented temporal analysis of mean velocity fields.

Fig. 9.60 shows the time series of vorticity passing through a vertical station. Some examples of the results for several stations are presented before showing the results for all 475 stations. This is a good way to understand flow structures. If negative values of the flow characteristic are important such as Reynolds stress and vorticity, the negative quantities can be offset by positive quantities.

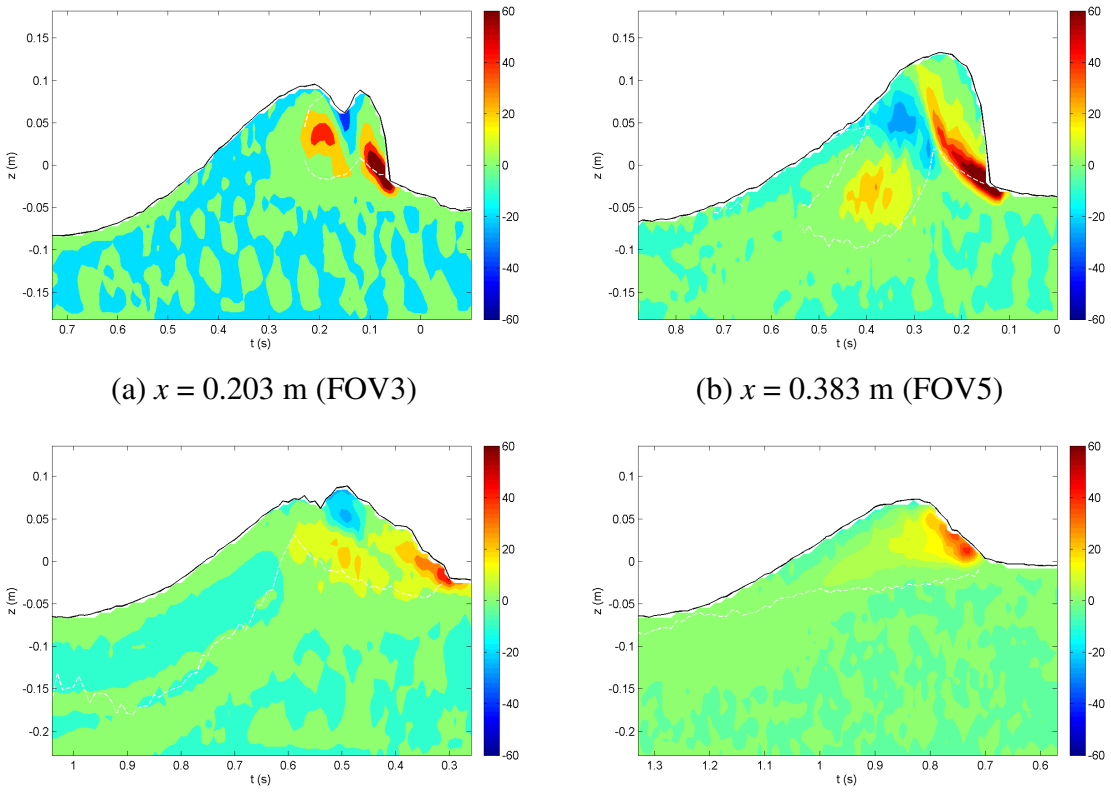

(a) x = 0.203 m (FOV3)

(b) x = 0.383 m (FOV5)

(c) x = 0.701 m (FOV7)

(d) x = 1.204 m (FOV9)

Fig. 9.60 Vorticity time series at a station (unit: s^{-1}).

The negative vorticity due to the ascending crest can be seen between two positive rollers in Fig. 9.60(a). The negative vorticity shown in Fig. 9.60(b) is caused by the first backward impingement. The second impingement and splash-up can be seen in Fig. 9.60(c) and Fig. 9.60(d) represents the fully developed third splash-up passing through the station.

Wave-averaged and period-averaged vorticities were calculated from Eqs. (9.4) and (9.5) respectively after combining upper and lower FOVs. Fig. 9.61 and Fig. 9.62 show vertical profiles of time-averaged vorticity and maximum vorticity at the same four stations shown in Fig. 9.60.

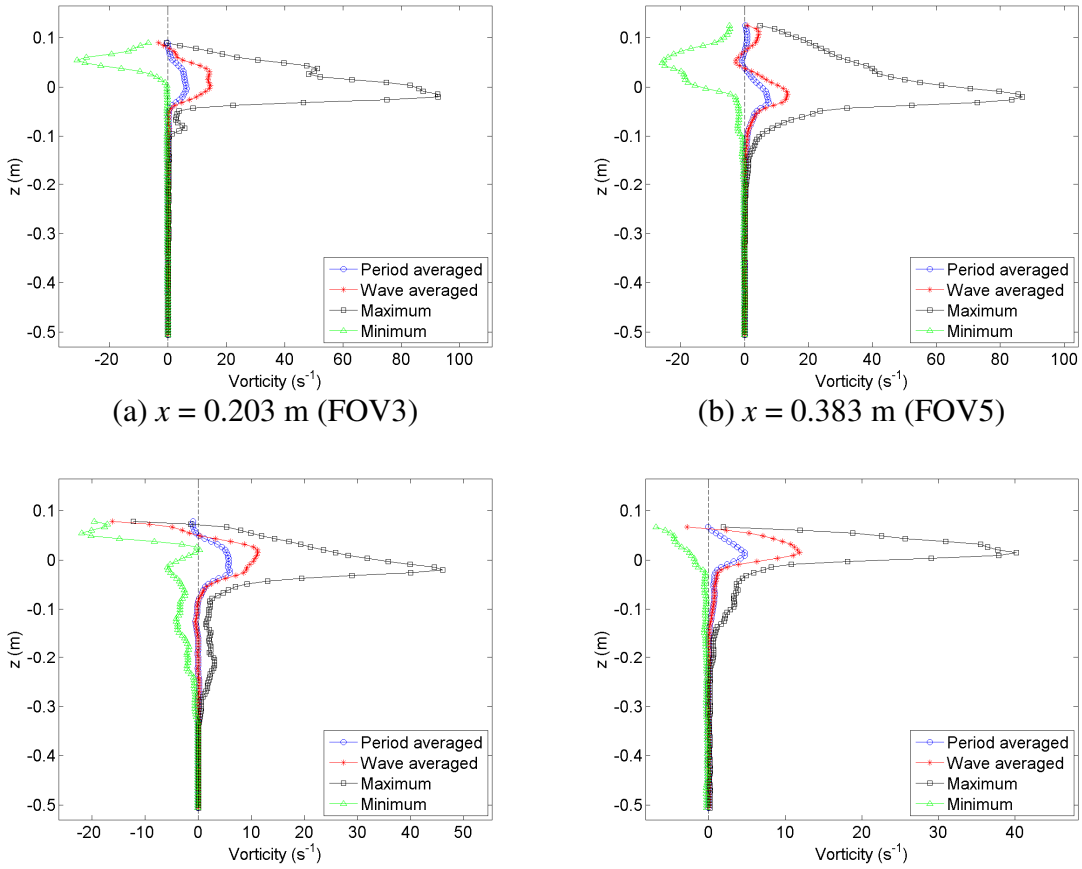

(a) x = 0.203 m (FOV3)

(b) x = 0.383 m (FOV5)

(c) x = 0.701 m (FOV7)

(d) x = 1.204 m (FOV9)

Fig. 9.61 Time-averaged, maximum, and minimum vorticity (unit: s^{-1}).

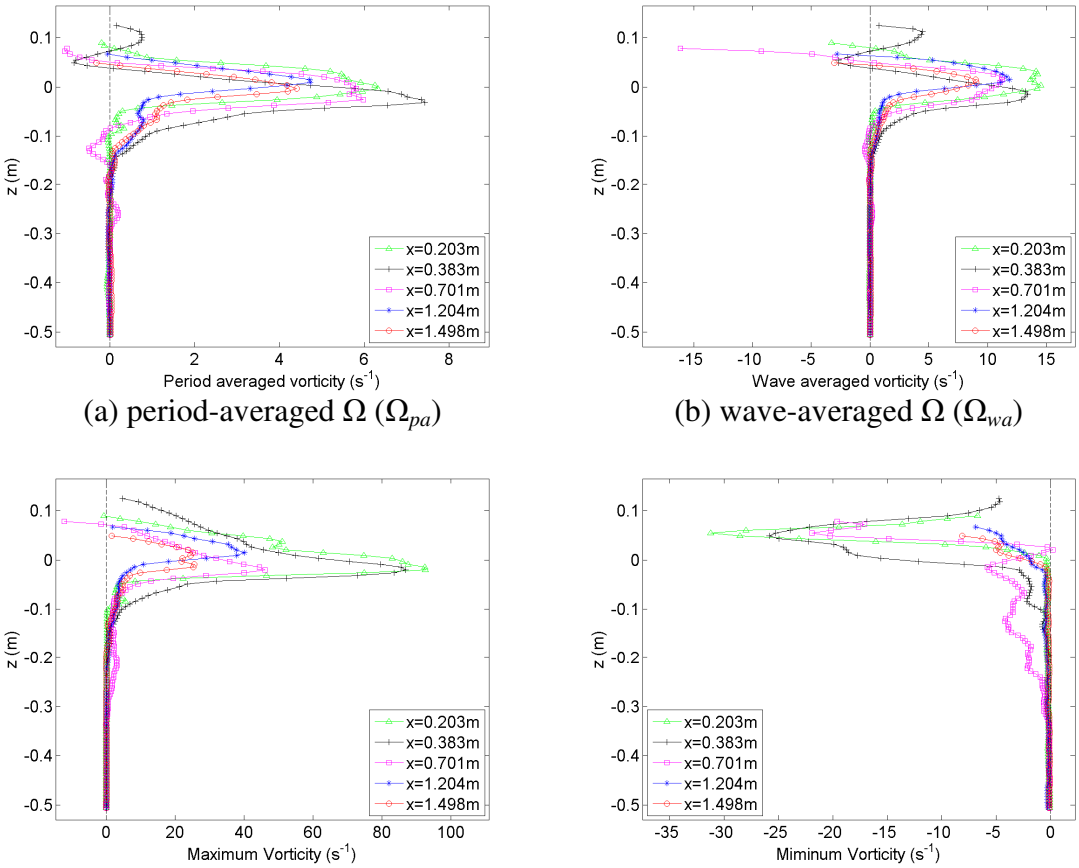

(a) period-averaged Ω (Ω_{pa}) (b) wave-averaged Ω (Ω_{wa})

(c) maximum Ω (Ω_{max}) (d) minimum Ω (Ω_{min})

Fig. 9.62 Comparison of the time-averaged, maximum, and minimum vorticity (unit: s^{-1}).

As mentioned in Section 9.4.2, the time series and time-averaged vorticity shown in Fig. 9.60 to Fig. 9.62 were obtained for all 475 stations covering the entire flow field.

Fig. 9.63(a) and (b) show the wave-averaged and period-averaged vorticities respectively. The maximum and minimum vorticities can be seen in Fig. 9.63(c) and (d) respectively. The maximum positive and negative vorticities shown in Fig. 9.63(c) and (d) are helpful to see vorticity offset by time averaging.

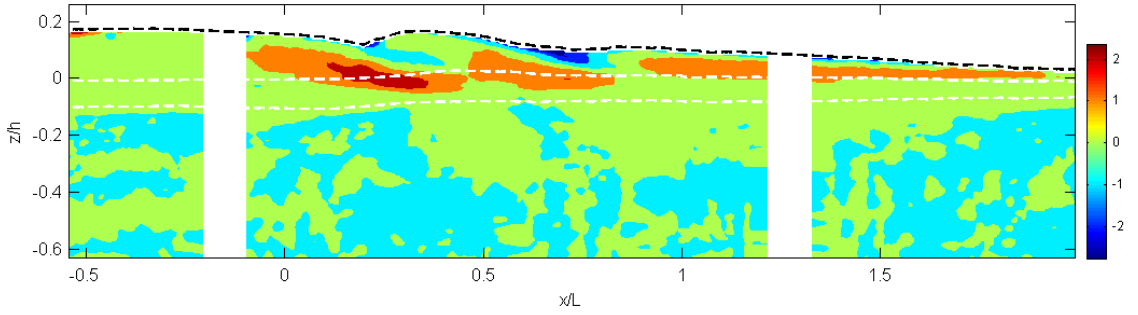

(a) wave-averaged Ω ($\Omega_{wa}H/C$)

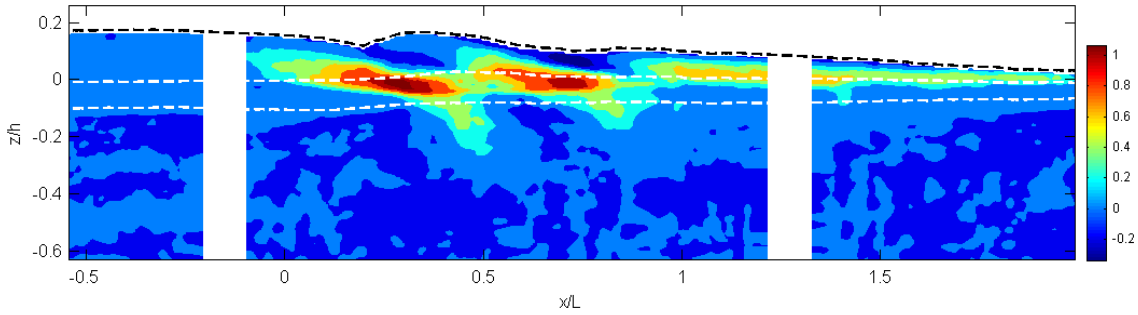

(b) period-averaged Ω ($\Omega_{pa}H/C$)

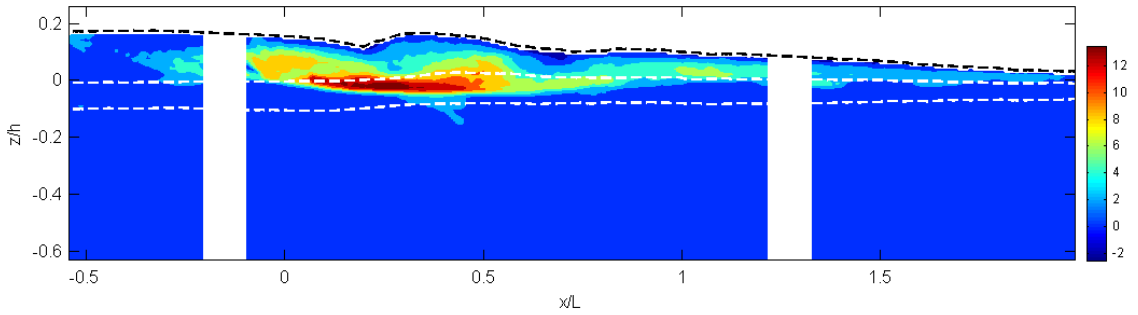

(c) maximum Ω ($\Omega_{max}H/C$)

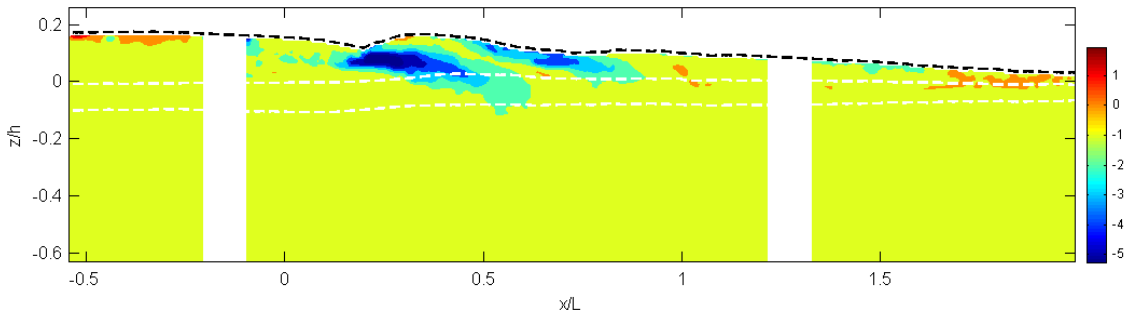

(d) minimum Ω ($\Omega_{min}H/C$)

Fig. 9.63 Normalized time-averaged, maximum and minimum vorticity ($\Omega H/C$).

Two positive vortices are generated due to the first impingement as shown in Fig. 9.51(a). One is generated in the first impinging roller and the other is at the toe of the second roller. The transport of two vorticities can be seen between $x = 0$ to $0.5L$. Actually, vorticity in the second roller is transported to the next process continuously while vorticity in the first roller penetrates into deep water and disappears. The path of the two vortices is very similar to each other at the initial stage. However, the vorticity in the first horizontal roller is transported downward slowly and the first roller penetrates into deep water while the vorticity in the left part of the second horizontal roller is transported upward due to the ascending new water crest (Fig. 9.54). The positive vorticity above the mean water level in the second roller is offset by the negative vorticity of the ascending crest and the first backward impingement. The effective horizontal range of the first negative vorticity is between $0.2L$ and $0.5L$ as shown in Fig. 9.63(d) and the negative vorticity has more strength above the mean water level. Positive vorticity above the mean water level near $x = 0.45L$ is not from the new roller but the second roller. Positive transport between $x = 0.45L$ and $x = 0.9L$ is due to the second impingement and the second splash-up. Similar phenomenon also happens between the second and third process around $x = 0.6$ - $0.8L$ as shown in Fig. 9.63. Fig. 9.64 shows the time-averaged and maximum vorticity strength, where mean vorticity strength is defined as $\sqrt{\Omega^2}$.

In summary, positive vorticity is actually transported continuously with the repetitive process of each impingement and splash-up. However, positive vorticity of the right side of the new ascending crest is always offset by the negative vorticity of the left

side of the new crest because their vertical location is very close. It is also helpful to see Fig. 9.59 which represents the location of the maximum and minimum vorticity. From the third impingement ($x > L$), vorticity is transported above the mean water level as the size of the eddies decreases. It is very similar to the spilling wave.

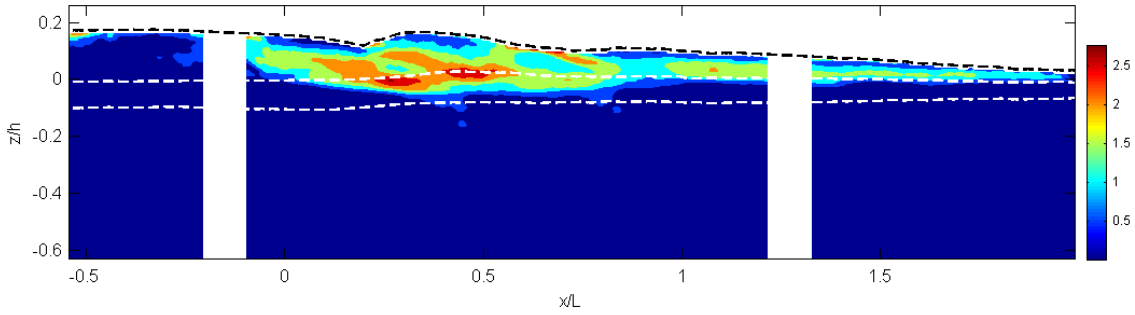

(a) wave-averaged ($\sqrt{\Omega^2} \cdot H/C$)

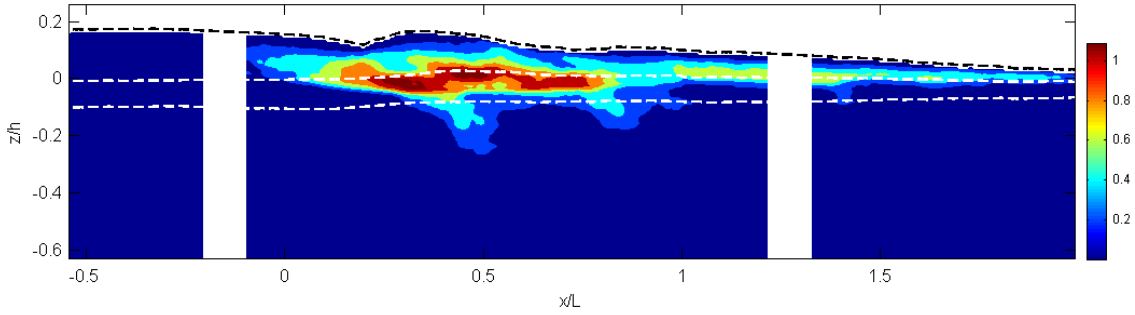

(b) period-averaged ($\sqrt{\Omega^2} \cdot H/C$)

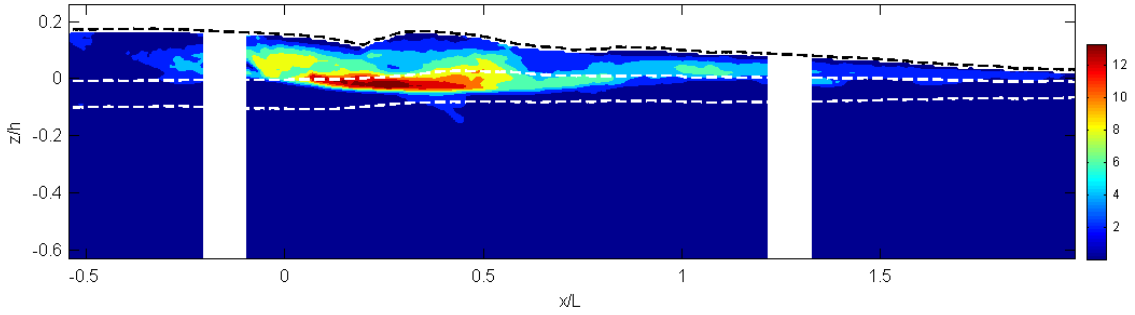

(c) maximum ($\sqrt{\Omega^2} \cdot H/C$)

Fig. 9.64 Time-averaged, maximum and minimum vorticity strength ($\sqrt{\Omega^2} \cdot H/C$).

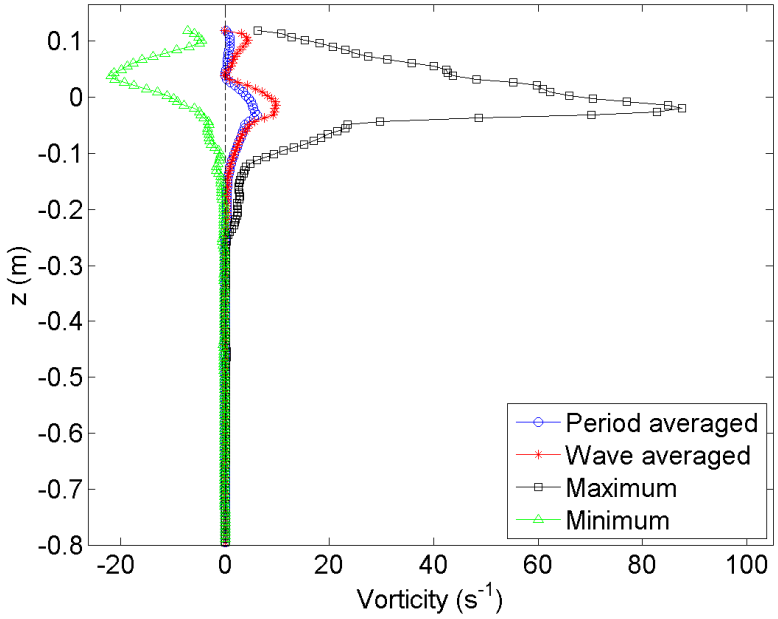

Fig. 9.65 Example of full depth extension of vorticity (x = 0.435 m).

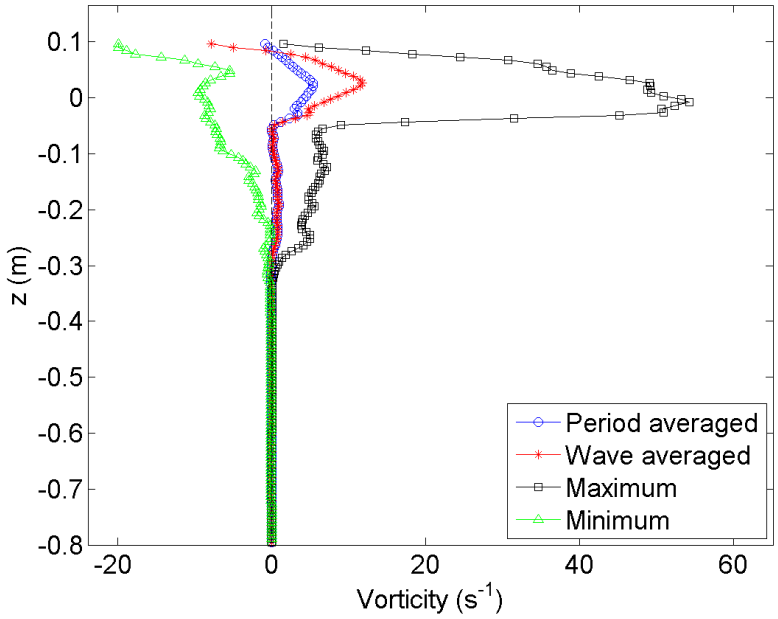

Fig. 9.66 Example of full depth extension of vorticity (x = 0.597 m).

Fig. 9.65 and Fig. 9.66 show examples of the full depth extension to obtain a depth-averaged value.

Normalized maximum positive and negative vorticities at every vertical station can be seen in Fig. 9.67. The maximum vorticity is normalized by the maximum wave height and the phase speed. The horizontal locations of the maximum positive and negative vorticities are very close to each other. However, the time of the maximum vorticity is different as shown in Fig. 9.58. Positive maximum vorticity occurs around $t = 0.06T$ at the first splash-up region and negative maximum vorticity occurs at $0.2T$ on the left side of the ascending crest during the first backward impinging process. Sudden decrement, as found in the maximum velocity at a station (Fig. 9.48), around $x = 0.8L$ is due to small roller motion of the accumulated mixture before the second splash-up.

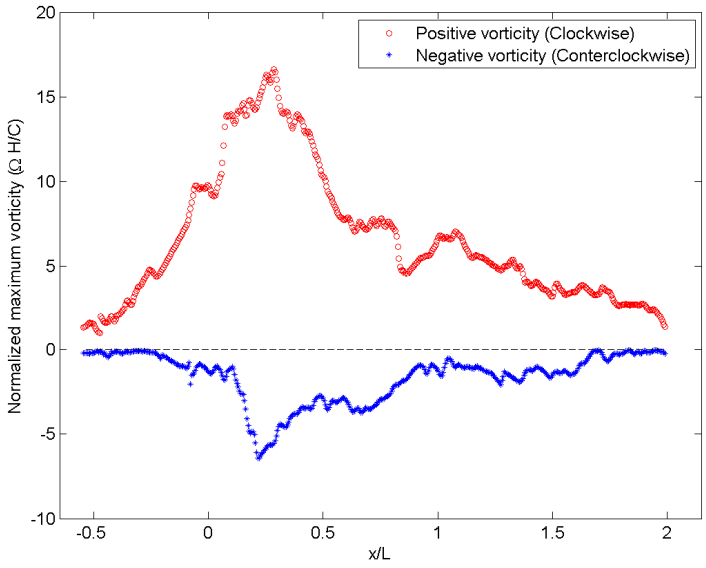

Fig. 9.67 Normalized maximum vorticity at each station.

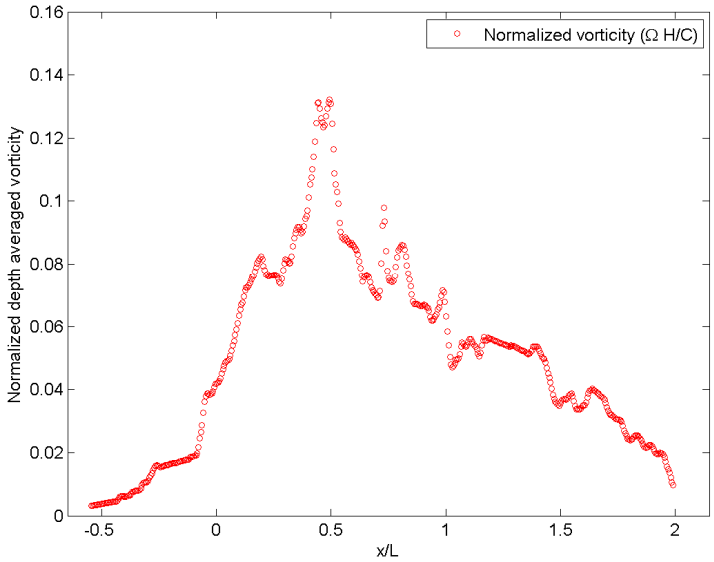

Fig. 9.68 Depth-averaged time mean vorticity.

Fig. 9.68 shows depth-averaged time mean vorticity normalized by the maximum wave height and the wave phase speed. The location of the maximum vorticity is around $x = 0.5L$ similar to the location of the maximum horizontal velocity ($\overline{U_{da}}$) as shown in Fig. 9.49.

9.6 Mean Kinetic Energy

Mean kinetic energy was obtained from the mean horizontal and vertical velocity as shown in Eq. (9.11).

$$K = \frac{1}{2}\left(U^2 + W^2\right) \tag{9.11}$$

9.6.1 Spatial Analysis of Mean Kinetic Energy

Spatial analysis results are presented in this section. Fig. 9.69 shows mean kinetic energy contours at the overturning moment at FOV1.

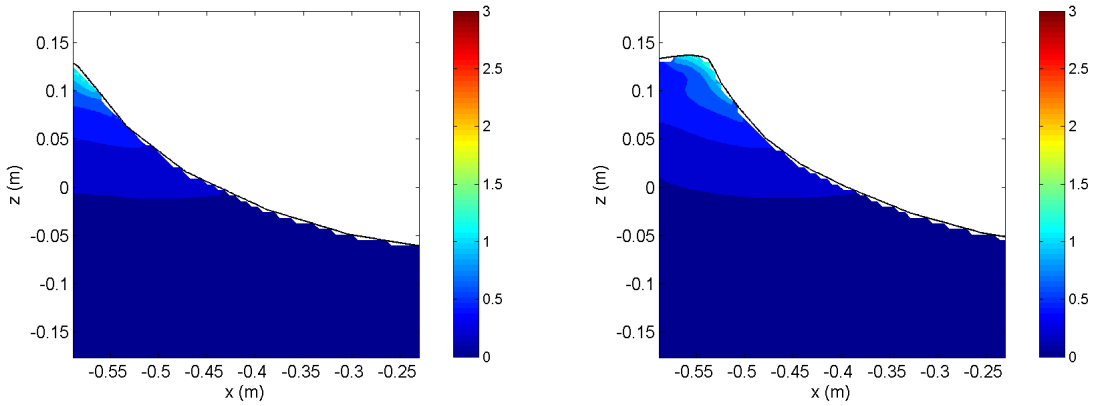

(a) t = -0.29 s (FOV1)

(b) t = -0.26 s (FOV1)

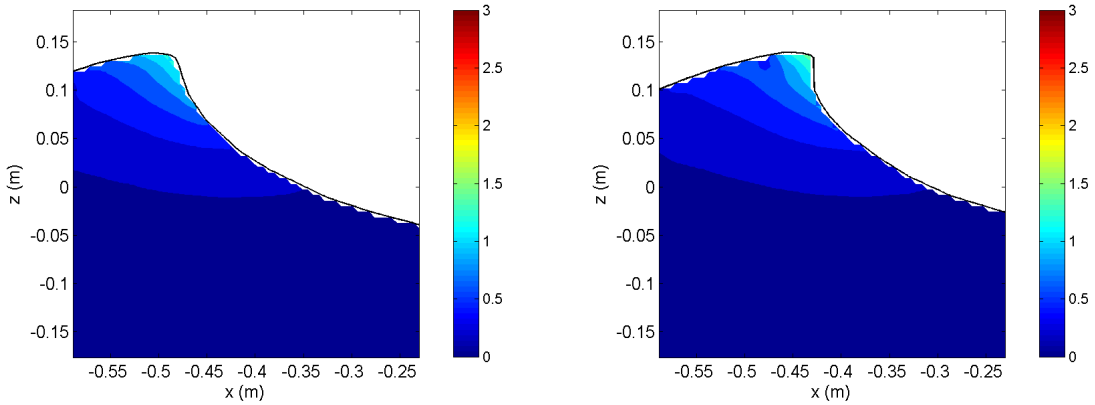

(c) t = -0.23 s (FOV1)

(d) t = -0.20 s (FOV1)

Fig. 9.69 Mean kinetic energy at the overturning jet (unit: m^2/s^2).

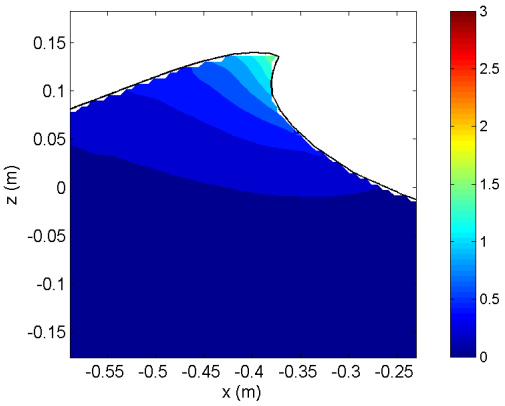

(e) t = -0.17 s (FOV1)

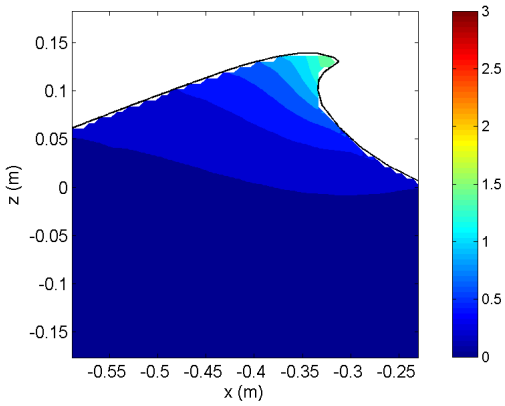

(f) t = -0.14 s (FOV1)

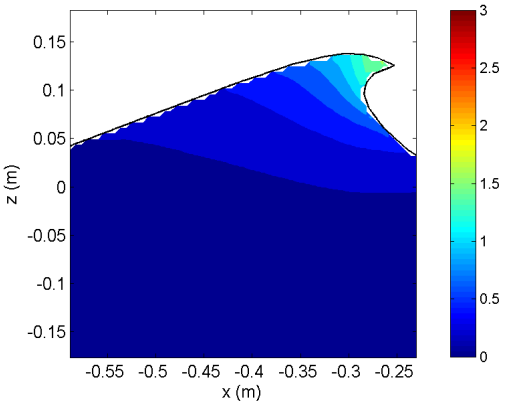

(g) t = -0.11 s (FOV1)

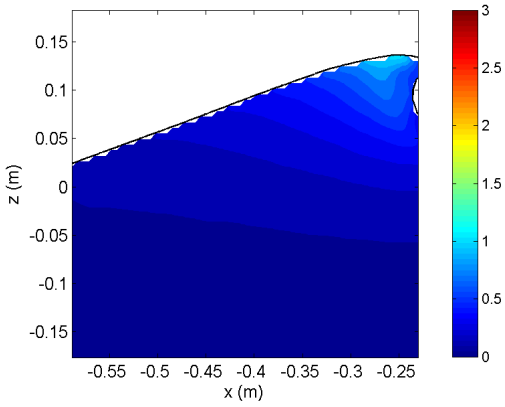

(h) t = -0.08 s (FOV1)

Fig. 9.69 (Continued).

The time difference between figures is 0.03 s. Shown in Fig. 9.69(g), maximum mean kinetic energy occurs at the tip of the overturning jet before the first impingement and the magnitude is about C^2 at t = - 0.11 s.

In Fig. 9.70 to Fig. 9.72, mean kinetic energy variation in time at the combined FOV can be seen with a time difference of 0.02 s. Fig. 9.70 shows contours at the first splash-up followed by the first impingement. Fig. 9.71 and Fig. 9.72 show the second and third processes respectively.

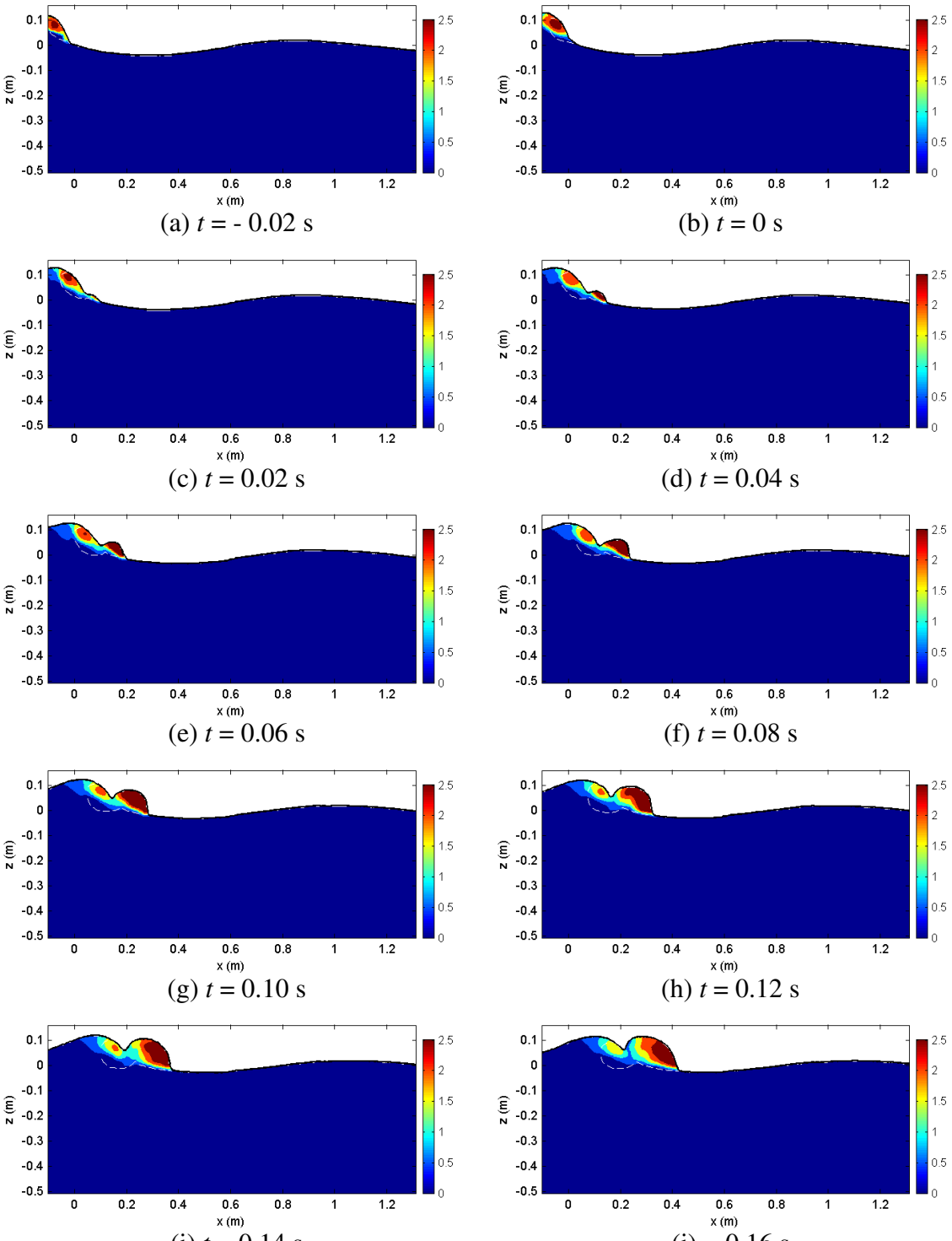

(a) t = - 0.02 s (b) t = 0 s

(c) t = 0.02 s (d) t = 0.04 s

(e) t = 0.06 s (f) t = 0.08 s

(g) t = 0.10 s (h) t = 0.12 s

(i) t = 0.14 s (j) = 0.16 s

Fig. 9.70 Mean kinetic energy at the first splash-up followed by the first impingement and water spray (unit: m^2/s^2).

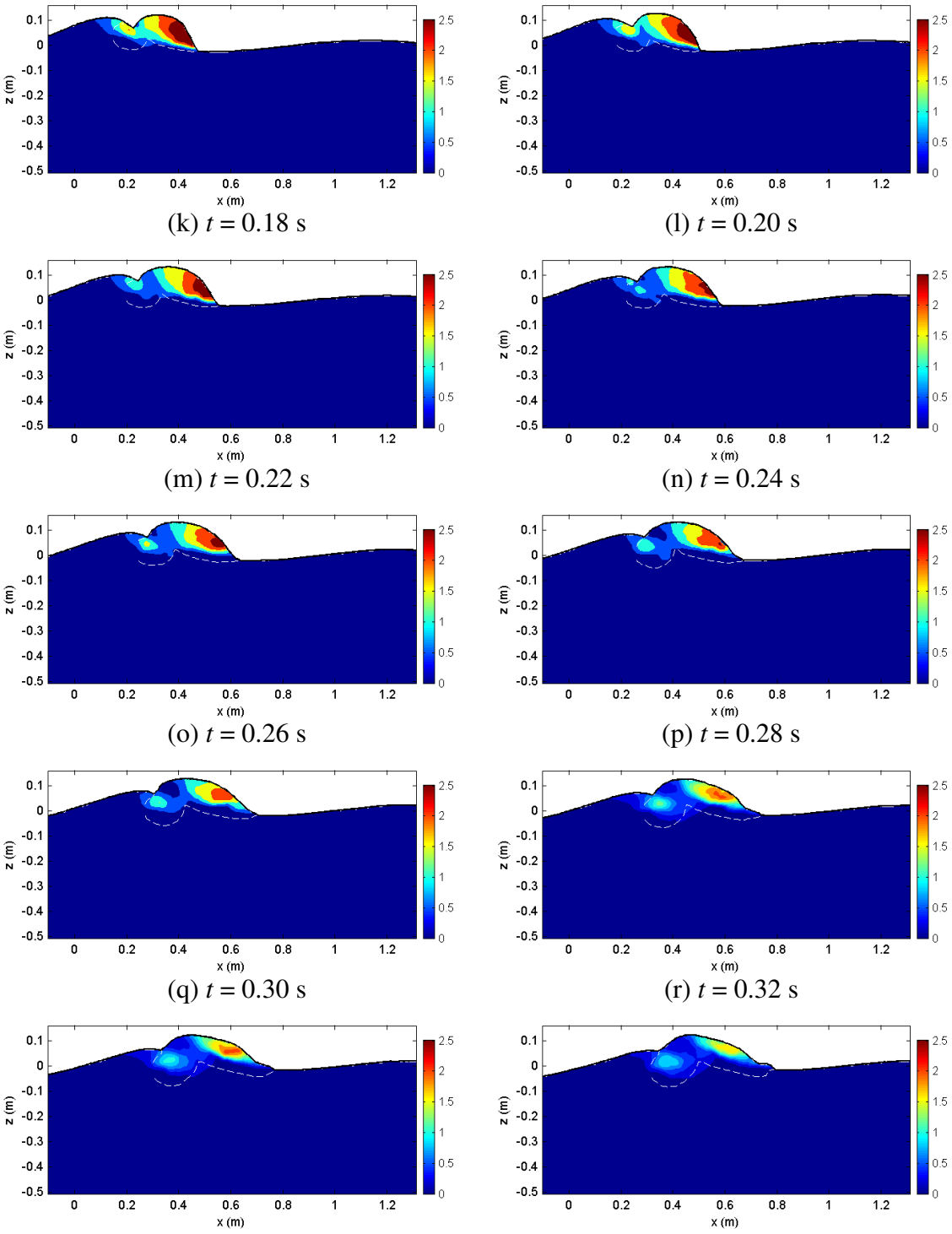

(k) t = 0.18 s (l) t = 0.20 s

(m) t = 0.22 s (n) t = 0.24 s

(o) t = 0.26 s (p) t = 0.28 s

(q) t = 0.30 s (r) t = 0.32 s

(s) t = 0.34 s (t) = 0.36 s

Fig. 9.70 (Continued).

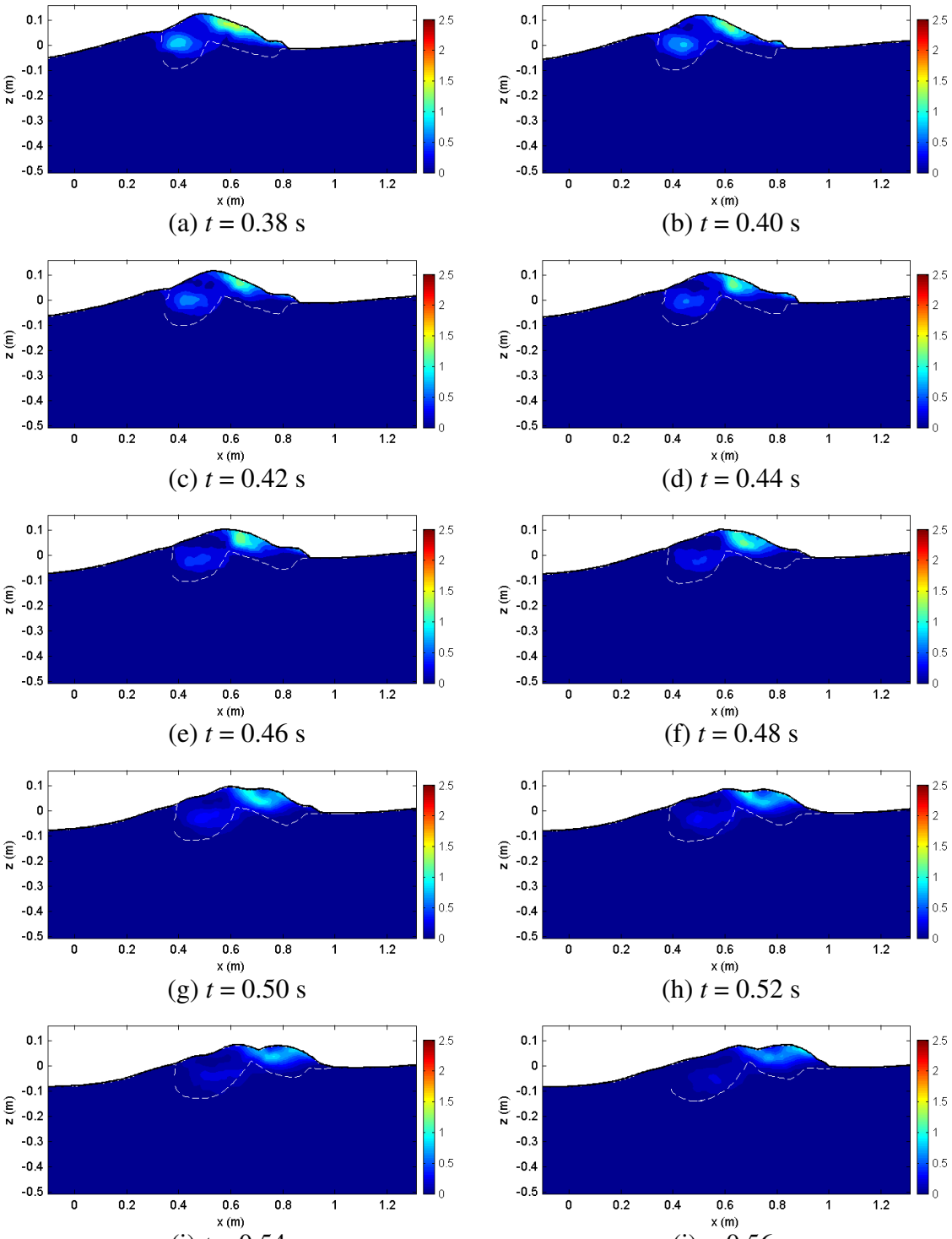

(a) t = 0.38 s (b) t = 0.40 s

(c) t = 0.42 s (d) t = 0.44 s

(e) t = 0.46 s (f) t = 0.48 s

(g) t = 0.50 s (h) t = 0.52 s

(i) t = 0.54 s (j) = 0.56 s

Fig. 9.71 Mean kinetic energy at the second impingement and splash-up (unit: m^2/s^2).

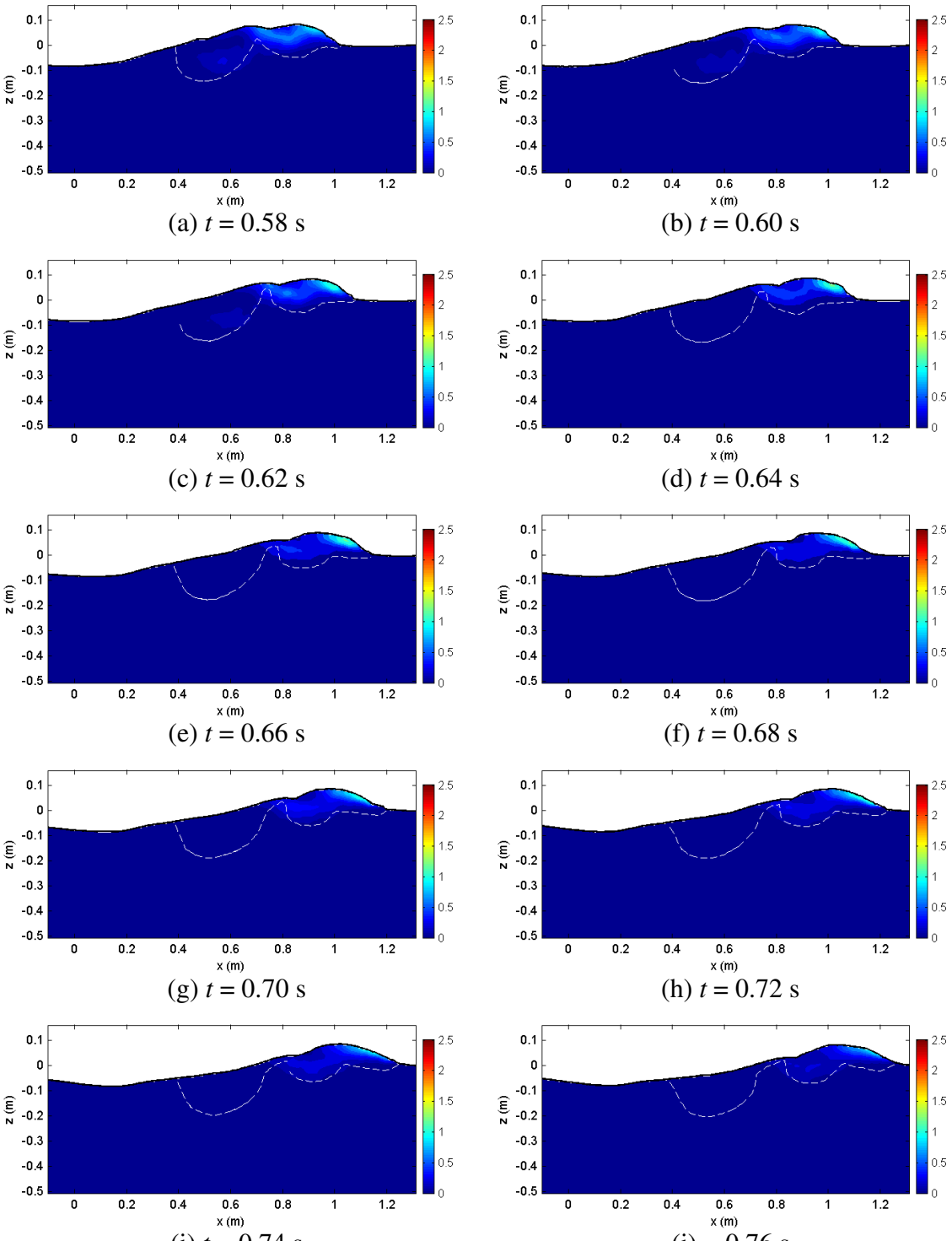

(a) t = 0.58 s (b) t = 0.60 s

(c) t = 0.62 s (d) t = 0.64 s

(e) t = 0.66 s (f) t = 0.68 s

(g) t = 0.70 s (h) t = 0.72 s

(i) t = 0.74 s (j) = 0.76 s

Fig. 9.72 Mean kinetic energy at the third impingement and splash-up followed by the second splash-up (unit: m^2/s^2).

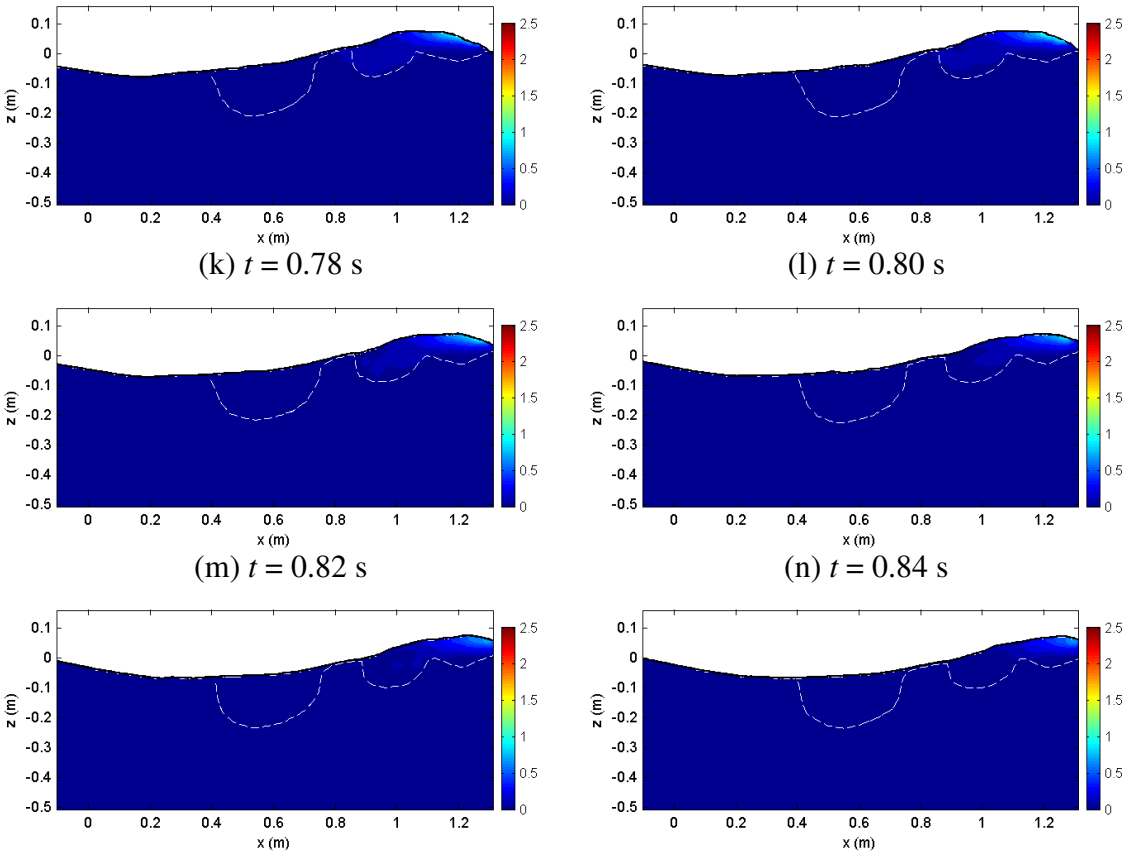

(k) t = 0.78 s (l) t = 0.80 s

(m) t = 0.82 s (n) t = 0.84 s

(o) t = 0.86 s (p) t = 0.88 s

Fig. 9.72 (Continued).

It is clearly seen that mean kinetic energy is transported and dissipated in the entire flow including the aerated region. In Fig. 9.70, kinetic energy in the impinging jet is transported to the first splash-up. Maximum mean kinetic energy during the first impingement is about $1.64C^2$ and occurs at t = 0.01 s [Fig. 9.70(b) and (c)]. Maximum kinetic energy during the first splash-up is about $2.31C^2$ and occurs at the beginning of the first splash-up at t = 0.05 s [Fig. 9.70(d) and (e)]; it is also the maximum in the entire flow. The ascending crest between the two rollers and the first impingement process can be seen in Fig. 9.70(k)-(t), It is clearly seen that the left part of the ascending water crest

is losing its kinetic energy [Fig. 9.70(m)-(q)]. Potential energy converted from kinetic energy begins converting to kinetic energy again as the ascending crest falls down onto the first roller, which is the first backward impingement [Fig. 9.70(q)-(t)]. During the first impingement process, the first roller, which is the source of the energy, is continuously providing energy to the second roller. The second roller is losing kinetic energy after the splash-up roller is fully developed [Fig. 9.70(m)-(t)]. The kinetic energy from the water spray is also decreased due to the growing air-water mixture roller as shown in Fig. 9.70(q)-(t) and Fig. 9.71(a)-(c). The maximum of the decreased kinetic energy reaches C^2 around $t = 0.37$ s [Fig. 9.70(t)].

Fig. 9.71 shows kinetic energy at the second impingement and the second splash-up. Small kinetic energy at the accumulated mixture can be seen in Fig. 9.71(a)-(c). After the water spray impingement onto the mixture [Fig. 9.70(r)-(t) and Fig. 9.71(a)-(c)], the new ascending crest impinges onto the mixture which is the second impingement [Fig. 9.71(d)-(f)]. Kinetic energy at the second splash-up process can be seen in Fig. 9.71(f)-(j) and Fig. 9.72(a)-(c). Kinetic energy is increased within a short period of time during the second splash-up and then is decreased again. It is observed that the starting time of the second splash-up is slightly earlier than the time when the nonlinear free surface due to the first impingement is linearlized by the first backward impingement.

Fig. 9.72 shows the kinetic energy during the third splash-up followed by the third impingement. Compared with the water spray impingement caused by the first splash-up, water spray due to the second splash-up has small downward momentum. In addition, the elevation of the front trough is increased and is close to still water level. Therefore,

the scale of the third process is very small and occurs shortly after the second process. Kinetic energy is slightly increased and then decreased during the process.

Fig. 9.73 shows the maximum kinetic energy variation in time at the control volume of the combined FOVs (FOV3-FOV10). The maximum kinetic energy was normalized by C^2. In addition, horizontal and vertical maximum kinetic energies are presented in the figure. Although the maximum kinetic energy in the vertical component is very small, vertical energy contributes to the period-averaged kinetic energy especially at the pre-breaking region. It will be discussed in next section with temporal analysis results.

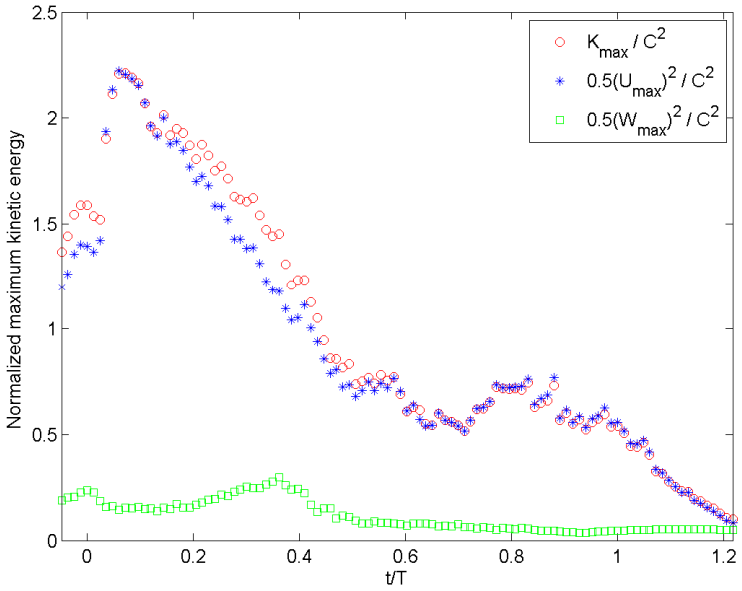

Fig. 9.73 Normalized maximum kinetic energy.

The location variation in time where the maximum mean kinetic occurs can be seen in Fig. 9.32. The location is definitely the same as the location of the maximum velocity. This was already discussed in Section 9.4.2.

9.6.2 Temporal Analysis of Mean Kinetic Energy

Temporal analysis of mean kinetic energy is presented in this section. Wave-averaged and period-averaged mean kinetic energies were obtained from Eqs. (9.4) and (9.5).

Fig. 9.74 shows vertical profiles of period-averaged, wave-averaged, maximum, and minimum mean kinetic energy at different locations. Mean kinetic energy profiles before the first impingement can be seen in Fig. 9.74(a). It is the maximum near the location shown in Fig. 9.74(b). Fig. 9.74(c), (e) and (f) show the profiles at each splash-up region where the splash-up is fully developed. Those three locations are close to the location of the FOR measurement stations. Fig. 9.74 provides information at a station while Fig. 9.75 provides a better comparison of each result at different location. Fig. 9.75(a) and (b) show vertical profiles of period-averaged and wave-averaged kinetic energy and Fig. 9.75(c) and (d) show vertical profiles of maximum and minimum mean kinetic energy.

As shown in Fig. 9.75(c), period-averaged kinetic energy above the trough level in the pre-impinging region is much smaller than the kinetic energy in the first splash-up region (x = 0.227 m and 0.429 m). However, period-averaged kinetic energy below the trough level in the pre-impinging region is much larger than the kinetic energy at any other location after the first impingement as shown in Fig. 9.75(a). Note that the station at x = - 0.571 m (green triangle) is the only station located before the first impingement. On the other hand, period-averaged kinetic energy above the trough level (x = 0.227 m and 0.429 m) is much larger in the first splash-up region than any other location.

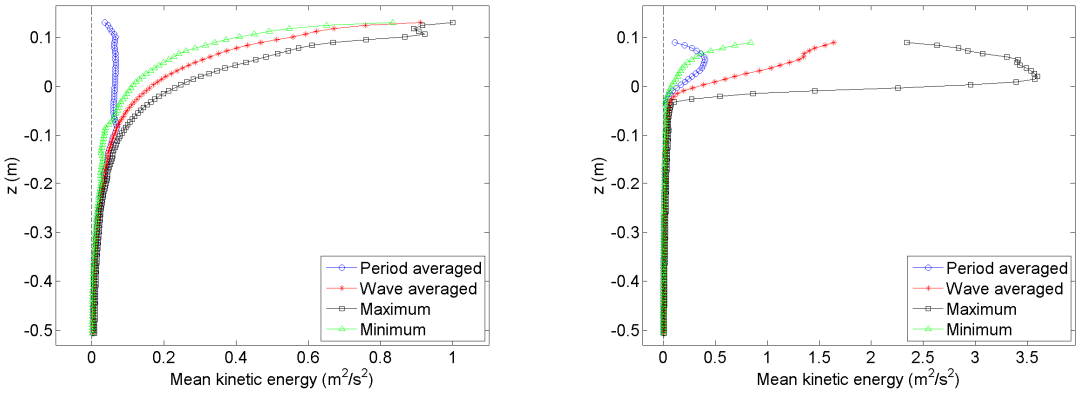

(a) x = - 0.571 m (b) x = 0.227 m

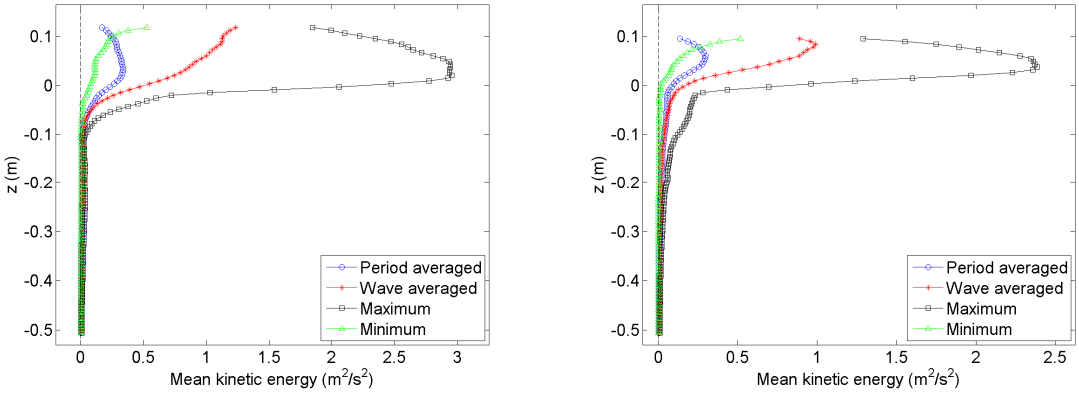

(c) x = 0.429 m (d) x = 0.597 m

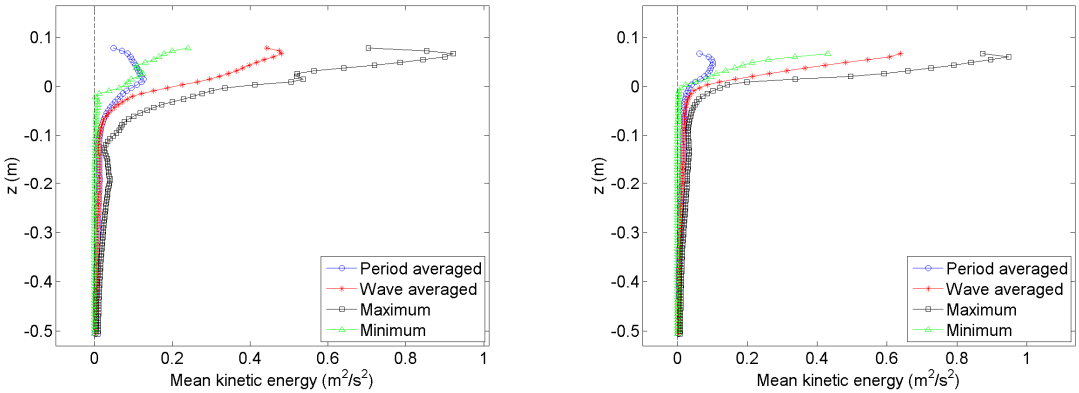

(e) x = 0.880 m (f) x = 1.204 m

Fig. 9.74 Time-averaged and maximum mean kinetic energy (unit: m^2/s^2).

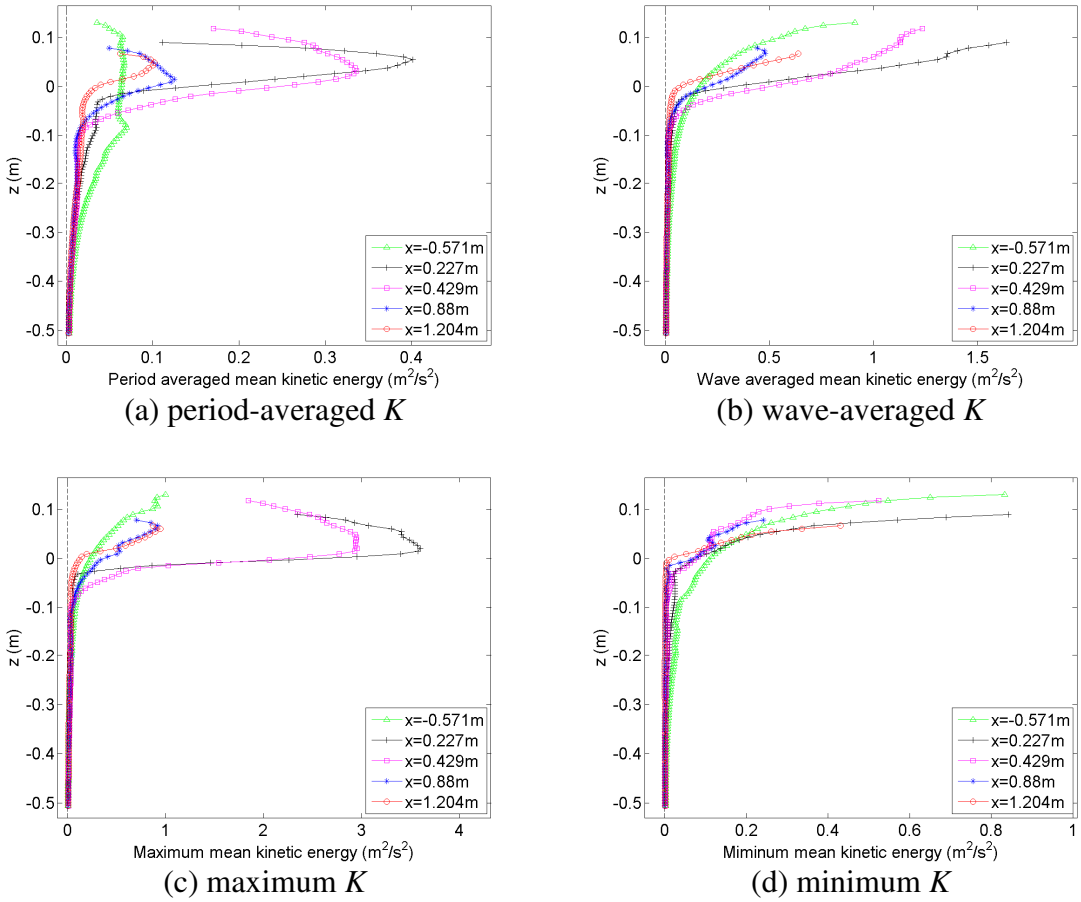

(a) period-averaged K (b) wave-averaged K

(c) maximum K (d) minimum K

Fig. 9.75 Comparison of time-averaged and maximum mean kinetic energy (unit: m^2/s^2).

The magnitude must be overestimated in the aerated region because the mixture density was not considered in this section. It is expected that the region of the first splash-up has the highest void ratio in the entire breaking process. This kind of overestimation occurs at the second and third splash-up process; although the overestimation is decreased as void ratio is decreased.

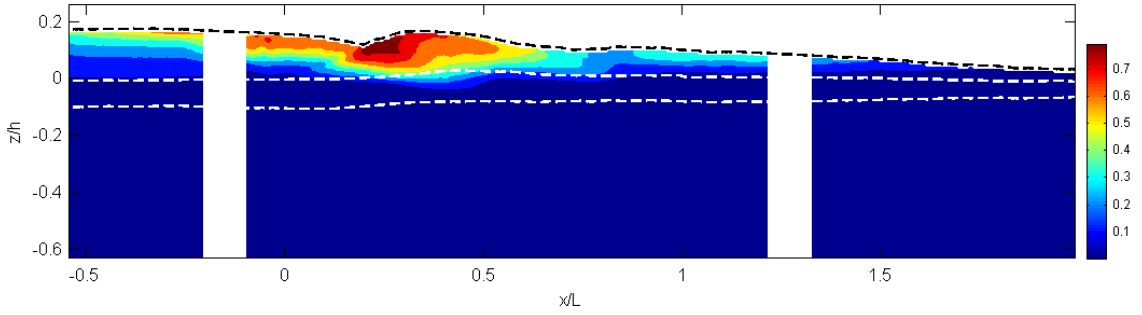

(a) wave-averaged K (K_{wa} /C^2)

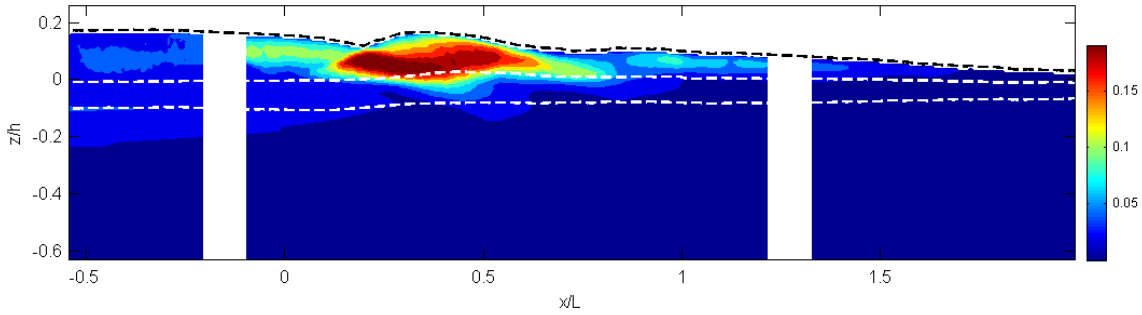

(b) period-averaged K (K_{pa} /C^2)

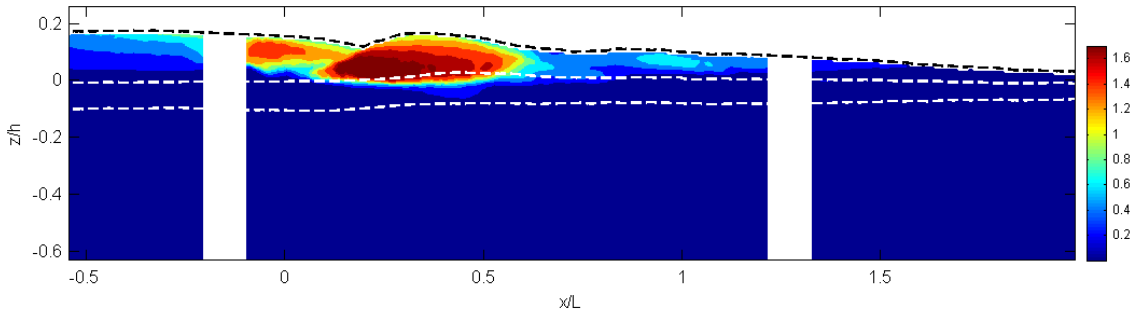

(c) maximum K (K_{max} /C^2)

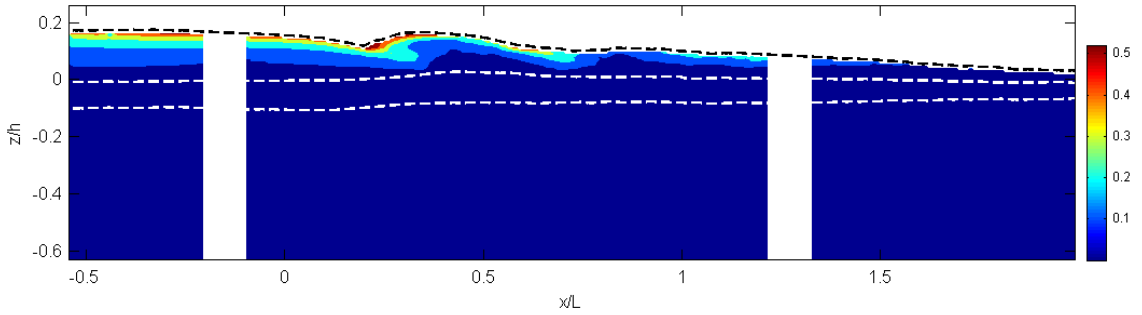

(d) minimum K (K_{min} /C^2)

Fig. 9.76 Normalized time-averaged and maximum mean kinetic energy (K/C^2).

Fig. 9.76 shows mean kinetic energy for the entire station and is normalized by C^2. Fig. 9.76(a) and (b) show the normalized wave-averaged and period-averaged mean kinetic energies. Fig. 9.76(c) and (d) show the normalized maximum and minimum kinetic energies at a point in the entire flow. Although vertical motion of the plunging breaker is much bigger than that of the spilling breaker, horizontal motion is dominant in the plunging breaker. Therefore, the contour for the period-averaged kinetic energy as shown in Fig. 9.76(b) is very similar to the contour for the period-averaged horizontal velocity [Fig. 9.42(b)] especially at the crest of the region after the impingement. However, there is a significant difference between period-averaged values of mean kinetic energy and horizontal velocity at the region where vertical motion is significant, such as the pre-breaking region which represents the region before the first impinging point. As shown in Fig. 9.76(b), mean kinetic energy is widely distributed throughout the water depth between x = -0.55L and 0.2L. The mean kinetic energy profile at the pre-breaking region can be also seen in Fig. 9.74(a) and Fig. 9.75(a). This is caused by huge upward and downward momentum during the wave cycle at the pre-breaking region, as discussed in Section 9.4.2.

Normalized maximum mean kinetic energy at each station is given in Fig. 9.77. Normalized maximum turbulent kinetic energy is also plotted for the comparison but it will be discussed in the next chapter. Maximum kinetic energy is increased close to the first impinging point (x = 0) and there is sudden decrement around the impinging point. It is increased where the first splash-up is developed and is decreased again gradually until x = 0.5L. It is found that remarkable decrement exists between x = 0.5L and 0.7L.

This is due to the accumulated roller caused by water spray impingement. The roller moves slowly without significant kinetic energy and the volume of the accumulated roller is increased. The kinetic energy begins increasing due to the second splash-up followed by the second impingement. A local maximum occurs about $x = 0.9L$ due to the fully developed second splash-up. Another local maximum occurs around $x = 1.2L$ due to the third splash-up.

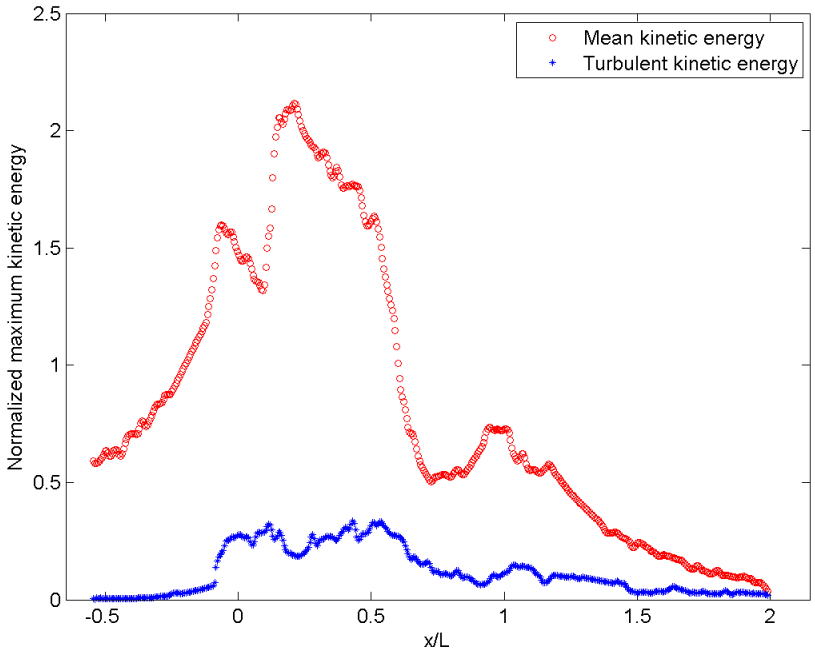

Fig. 9.77 Normalized maximum kinetic energy at each station.

A local maximum of the mean kinetic energy occurs at every splash-up process. However, there is a small delay in time and location because the splash-up process requires some time to be developed by continuously receiving energy. For example, the first splash-up is caused by the impinging water jet and it starts immediately at $x = 0$ and

t = 0; however, the location and time of the maximum kinetic energy for the splash-up are $x = 0.22L$ and t = 0.05 s. It is also interesting that the maximum mean kinetic energy is decreased around the location and time of each impingement during the impinging process. Fig. 9.73 and Fig. 9.77 show the maximum mean kinetic energy variation as function of time and location.

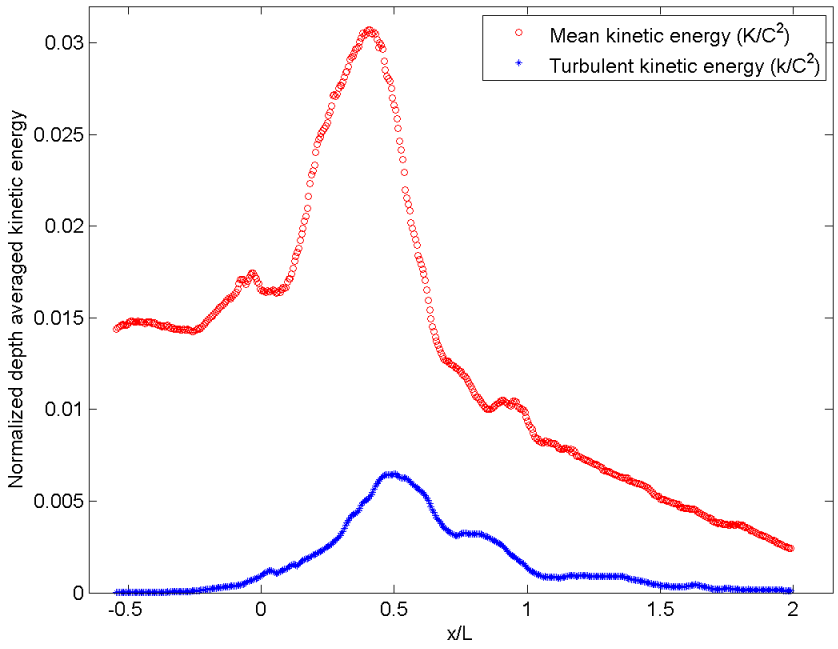

Fig. 9.78 Depth-averaged time mean kinetic energy normalized by C^2.

Another interesting result can be seen in Fig. 9.78 which shows the depth-averaged values of the period-averaged mean kinetic energy at all 475 stations. Result for turbulent kinetic energy is also plotted only for comparison. The primary wave in the pre-impinging region has large kinetic energy as well as large potential energy. Kinetic energy begins decreasing slightly just after the location where the wave face of the

primary wave becomes vertical. Note that the wave face becomes vertical at x = - 0.4L and x = 0 at the first impinging point. The kinetic energy is slightly decreased until x = - 0.25L and then begins increasing. The location of the maximum is about 0.4L. Another sudden decrement exists between x = 0.4L and 0.7L. There is small increment due to the second and third splash-up between x = 0.7L and L and then the kinetic energy is linearly decreased until the end of the plunging waves.

Large kinetic energy in the region exists between x = - 0.25L and 0.6L, although kinetic energy in the region must be overestimated because the density is not considered. It is due to two large rollers. One is the first roller caused by the first impingement and the other is the second roller representing the first splash-up. Both rollers are passing through the location with large momentum. Note that the kinetic energy considering the void ratio is presented in Chapter XI. Kinetic energy as well as potential energy of the impinging water may be converted to large kinetic energy of the splash-up during the first impingement and splash-up process. In addition, the first roller is continuously transported with its kinetic energy.

More discussion will be presented in detail with turbulent kinetic energy in Section 10.4.2 and with consideration of compressibility in Section 11.4.

CHAPTER X

TURBULENCE IN A PLUNGING BREAKER

10.1 Introduction

This chapter is another part from the PIV measurements. Results from the mean flow analysis such as mean velocity, mean vorticity and mean kinetic energy are presented in Chapter IX. The PIV measurement technique is described in Chapter V and Section 9.1. The PIV data analysis procedure using turbulent velocities and validation of the PIV measurements are presented in Section 9.2 and 9.3. The location of the 14 fields of view (FOV) in the PIV measurements can be seen in Fig. 5.1 and Fig. 9.10.

Analysis of the turbulence properties in the plunging breaker are presented in this chapter. Spatial and temporal analysis of the turbulence intensity, Reynolds stresses and turbulent kinetic energy are discussed in Sections 10.2, 10.3 and 10.4 respectively, in a similar manner shown in Chapter IX.

10.2 Turbulence Intensity

Mean and turbulent velocity fields were obtained using the ensemble average of 20 instantaneous measurements. Equations used in the calculation are given in Section 9.4 [Eqs. (9.1) – (9.3)]. For convenience, the root mean square value of $u_i'(x,z,t)$ and $w_i'(x,z,t)$ will be denoted by u' (horizontal turbulence intensity) and w' (vertical turbulence intensity) as shown in Eq. (10.1). In the present study, turbulence intensity is

defined as

$$I = \sqrt{\left\langle u_i'^2 \right\rangle + \left\langle w_i'^2 \right\rangle} = \sqrt{u'^2 + w'^2}, \quad I_x = \sqrt{\left\langle u_i'^2 \right\rangle} = u', \quad I_z = \sqrt{\left\langle w_i'^2 \right\rangle} = w' \tag{10.1}$$

where, $\langle\ \rangle$ denotes the ensemble averaging. The squares of the horizontal and vertical normal Reynolds stresses are defined as the horizontal and vertical turbulent intensities as shown in Eq. (10.1). Results from the spatial and temporal analysis are presented in Section 10.2.1 and 10.2.2.

10.2.1 Spatial Analysis of Turbulence Intensity

Spatial analysis of the turbulence intensity is presented in this section. The horizontal and vertical turbulence intensity will be discussed. In addition, the turbulence intensity defined in Eq. (10.1) will also be presented.

The turbulent kinetic energy k is defined in Eq. (10.2)

$$k = \frac{1.33}{2}\left(\left\langle u_i'^2 \right\rangle + \left\langle w_i'^2 \right\rangle\right) = \frac{1.33}{2} I^2 \tag{10.2}$$

where I is the turbulence intensity. Therefore, more discussion on the horizontal and vertical turbulence intensities will be presented.

Fig. 10.1 shows the turbulence intensities at the beginning of the first splash-up followed by the first impingement. Horizontal and vertical turbulence intensities at t = 0.05 s and 0.08 s are shown in Fig. 10.1(a) and (b) and turbulence intensity (I) can be seen in Fig. 10.1(c). Note that numbers 1 and 2 in parentheses represent horizontal and vertical intensities respectively and the letters represents different phases or time. In the beginning of the first impingement, the turbulence is generated near the impinging region. Note that the black lines represent the boundary of the aerated region.

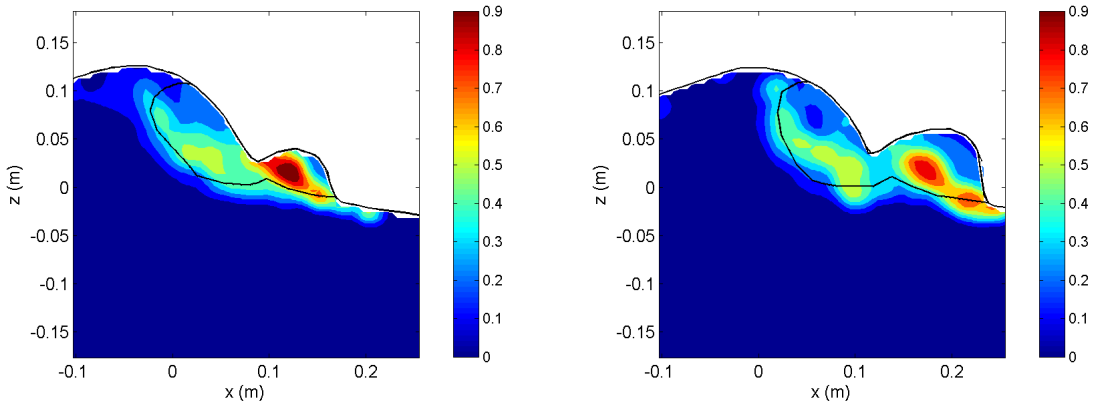

(a1) t = 0.05 s (u')

(b1) t = 0.08 s (u')

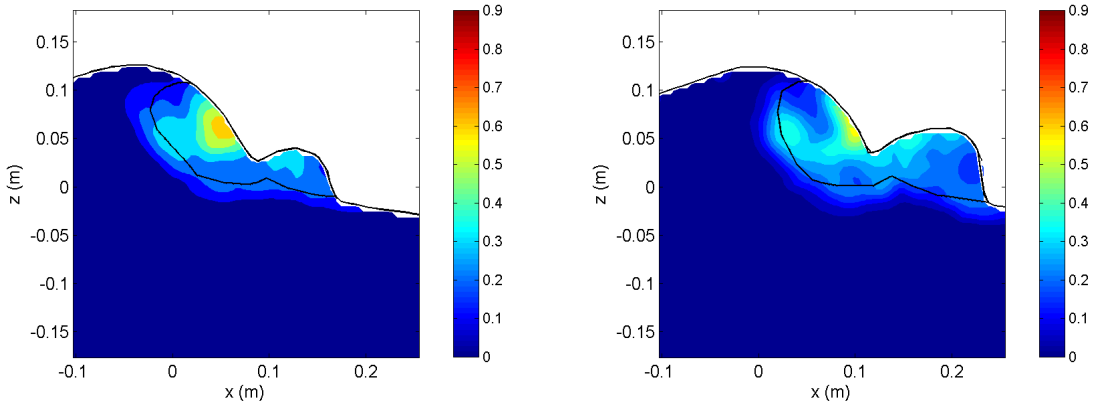

(a2) t = 0.05 s (w')

(b2) t = 0.08 s (w')

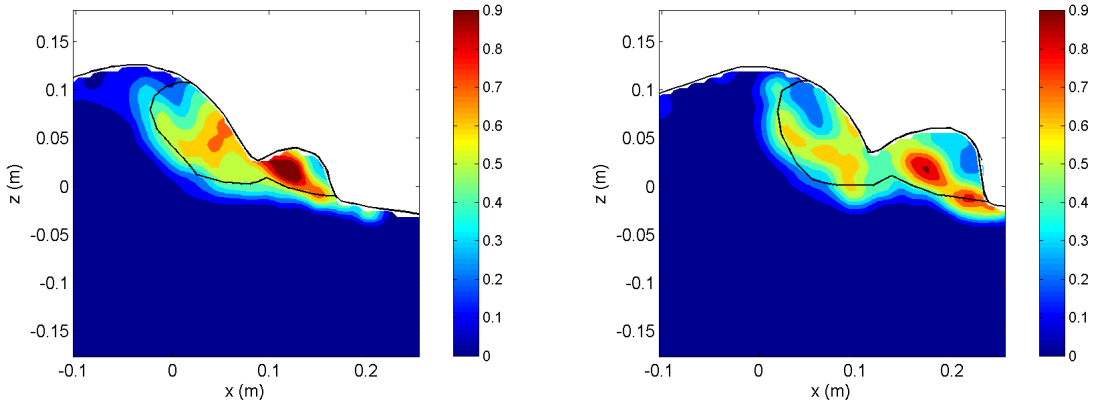

(a3) t = 0.05 s (I)

(b3) t = 0.08 s (I)

Fig. 10.1 Turbulence intensity at the beginning of the first splash-up (unit: m/s).

When the overturning water jet impinges onto the front wave surface with large momentum, the front water is pushed up and then the front water losing surface tension is split up in the form of water spray. As presented in Chapter IX, maximum velocity occurs at t = 0.05 s. The turbulence intensity also has a maximum value at the same time in both the horizontal and vertical components. The generated turbulence is continuously maintained at a similar level until the second impingement although the maximum velocity is gradually decreased after t = 0.05s. As shown in Fig. 10.1, the horizontal turbulent stress is generated in the shear region between the newly ascending crest and the first splash-up. This horizontal turbulence is transported downstream like vorticity. The turbulent normal stress in the vertical direction is generated near the impinging point due to the shear between the impinging jet and the ascending crest that has a large upward momentum. The maximum vertical turbulence occurs at this region and is maintained until the backward impingement starts. The turbulence intensity (I) in the two rollers is given in Fig. 10.1(a3) and (b3), since the dominant locations of the initially generated turbulence in the horizontal and vertical directions are slightly different.

Fig. 10.2 shows the horizontal and vertical turbulence velocities from the beginning of the first splash-up. Figures in the left side denoted as a number 1 in parentheses represent the horizontal turbulence intensities while figures in the right side denoted as a number 2 in parentheses represent the vertical turbulence intensities. Figures in a row denoted by the same letter in parentheses represent the horizontal and vertical intensities at the same time. Turbulence intensity (I) considering both directions are defined in Eq. (10.1) and shown in Fig. 10.3.

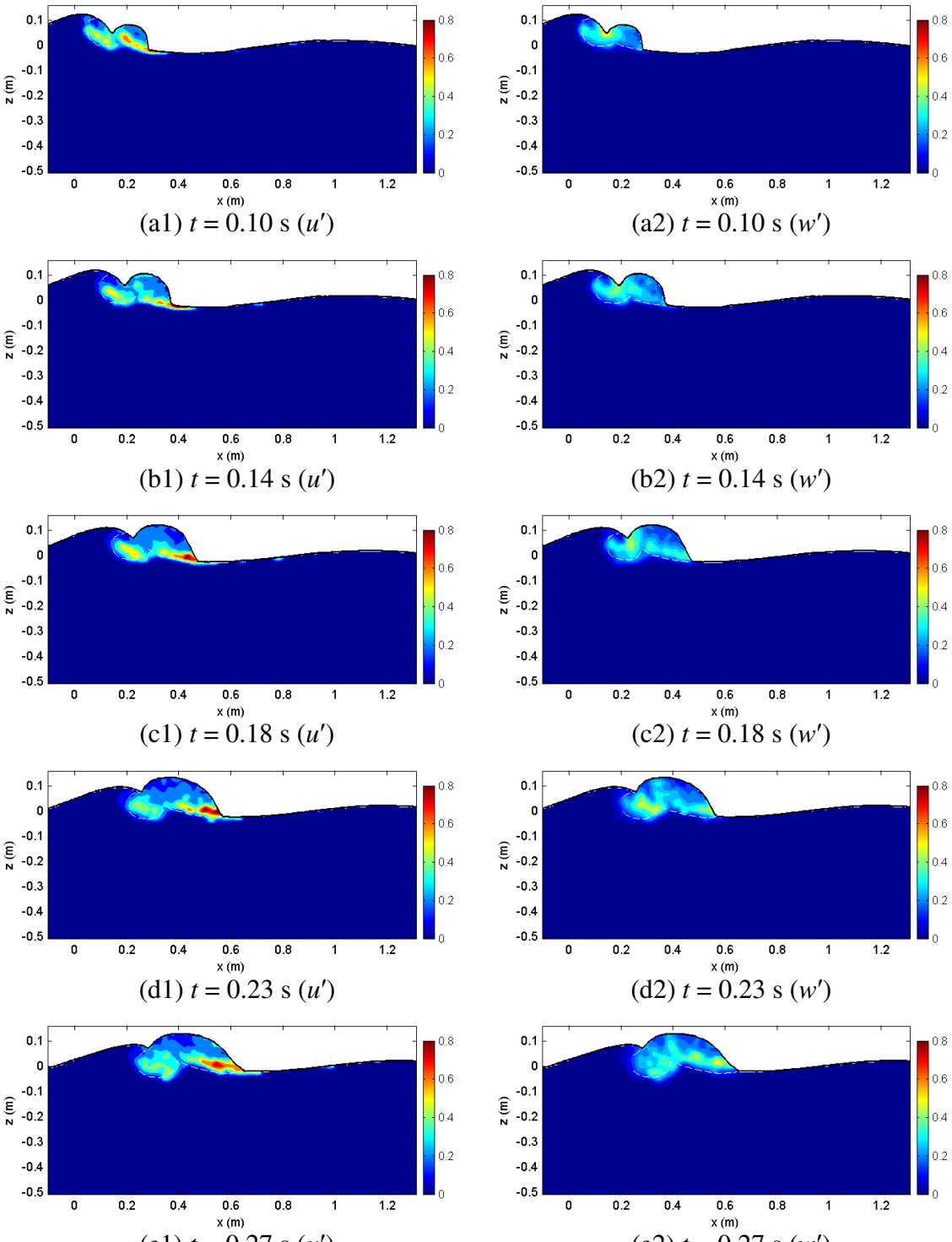

(a1) t = 0.10 s (u') (a2) t = 0.10 s (w')

(b1) t = 0.14 s (u') (b2) t = 0.14 s (w')

(c1) t = 0.18 s (u') (c2) t = 0.18 s (w')

(d1) t = 0.23 s (u') (d2) t = 0.23 s (w')

(e1) t = 0.27 s (u') (e2) t = 0.27 s (w')

Fig. 10.2 Horizontal and vertical turbulence intensities (unit: m/s).

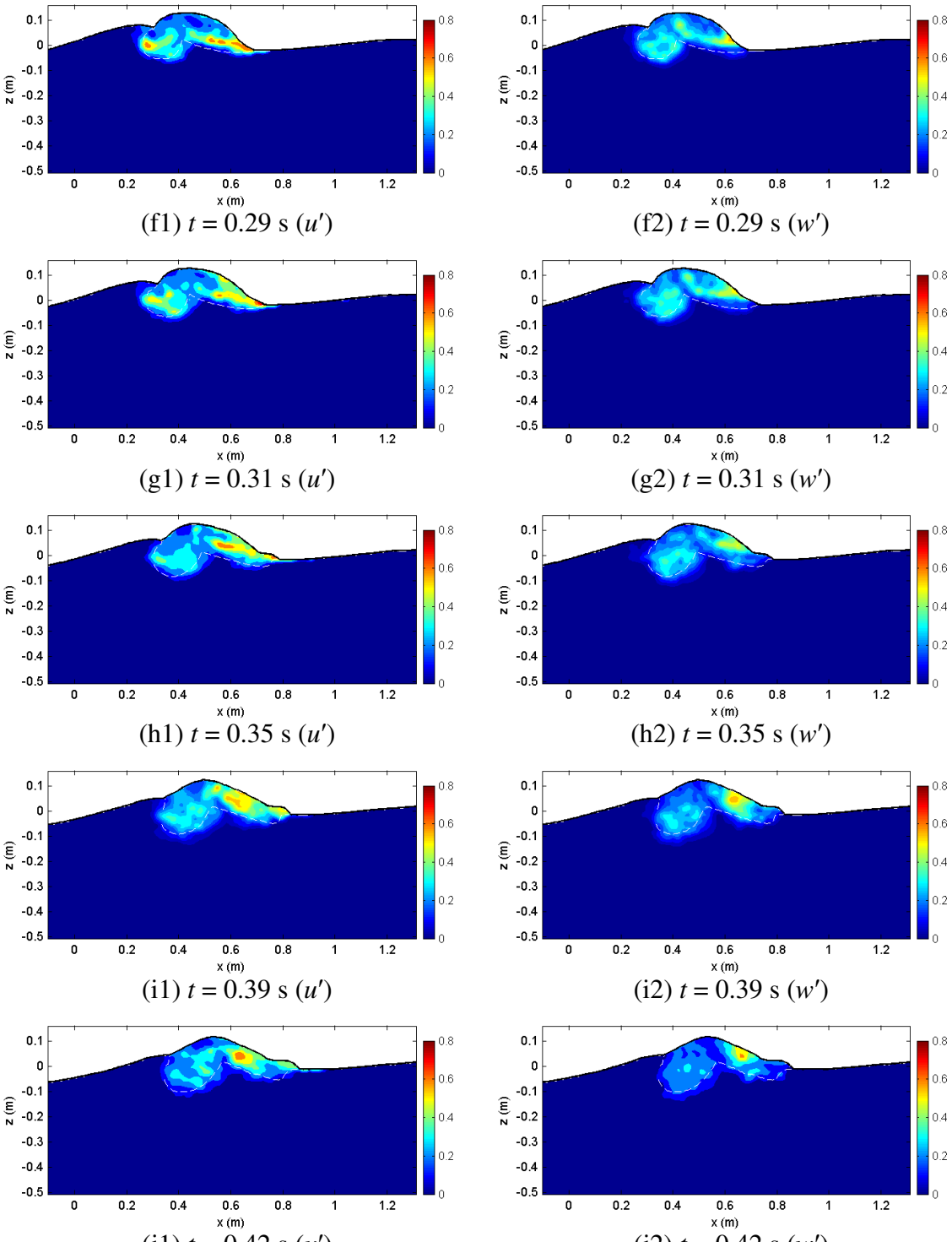

(f1) t = 0.29 s (u')

(f2) t = 0.29 s (w')

(g1) t = 0.31 s (u')

(g2) t = 0.31 s (w')

(h1) t = 0.35 s (u')

(h2) t = 0.35 s (w')

(i1) t = 0.39 s (u')

(i2) t = 0.39 s (w')

(j1) t = 0.42 s (u')

(j2) t = 0.42 s (w')

Fig. 10.2 (Continued).

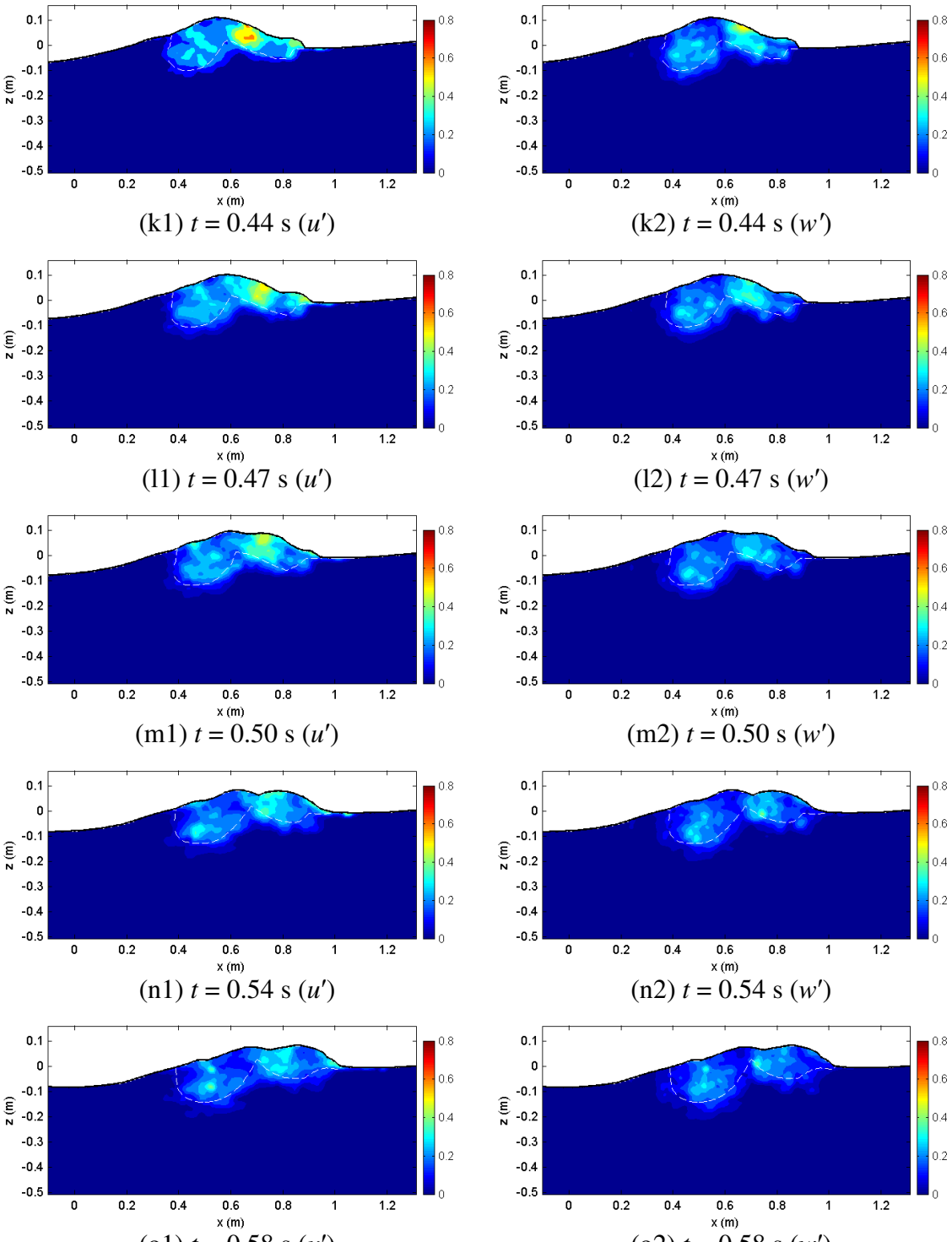

(k1) t = 0.44 s (u') (k2) t = 0.44 s (w')

(l1) t = 0.47 s (u') (l2) t = 0.47 s (w')

(m1) t = 0.50 s (u') (m2) t = 0.50 s (w')

(n1) t = 0.54 s (u') (n2) t = 0.54 s (w')

(o1) t = 0.58 s (u') (o2) t = 0.58 s (w')

Fig. 10.2 (Continued).

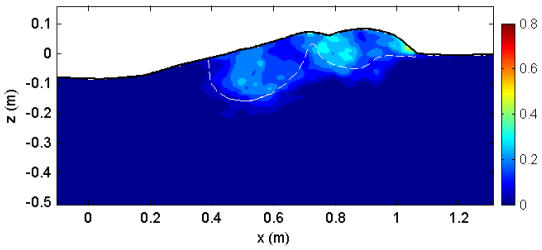

(p1) t = 0.61 s (u')

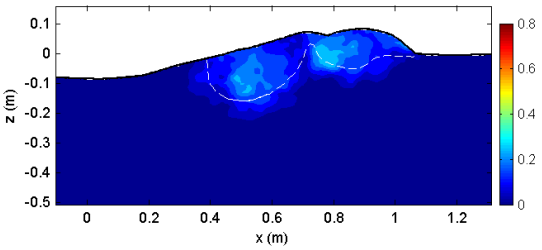

(p2) t = 0.61 s (w')

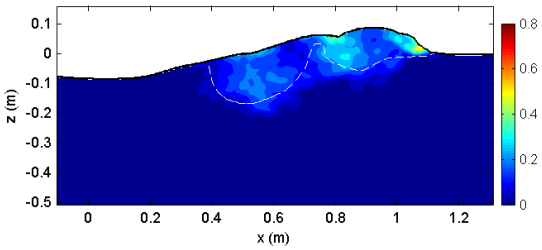

(q1) t = 0.64 s (u')

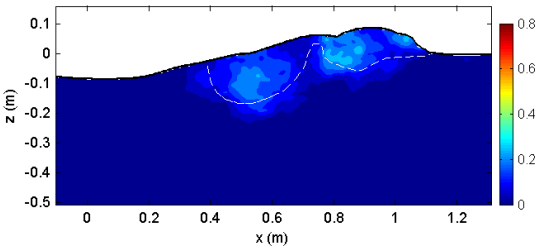

(q2) t = 0.64 s (w')

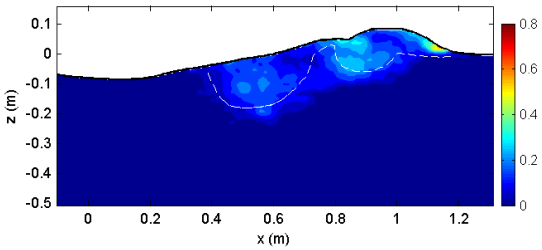

(r1) t = 0.69 s (u')

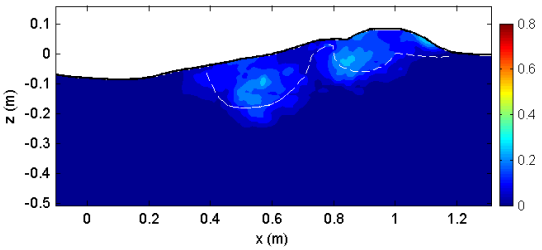

(r2) t = 0.69 s (w')

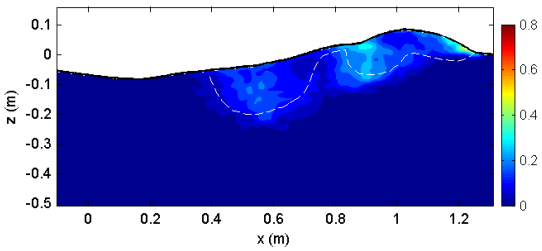

(s1) t = 0.75 s (u')

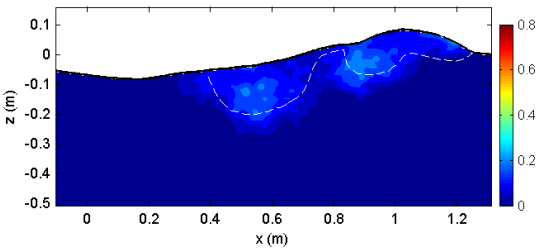

(s2) t = 0.75 s (w')

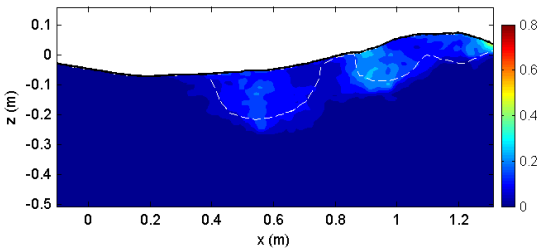

(t1) t = 0.82 s (u')

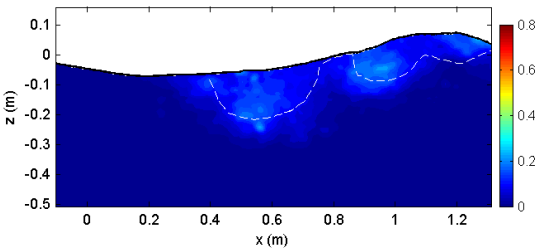

(t2) t = 0.82 s (w')

Fig. 10.2 (Continued).

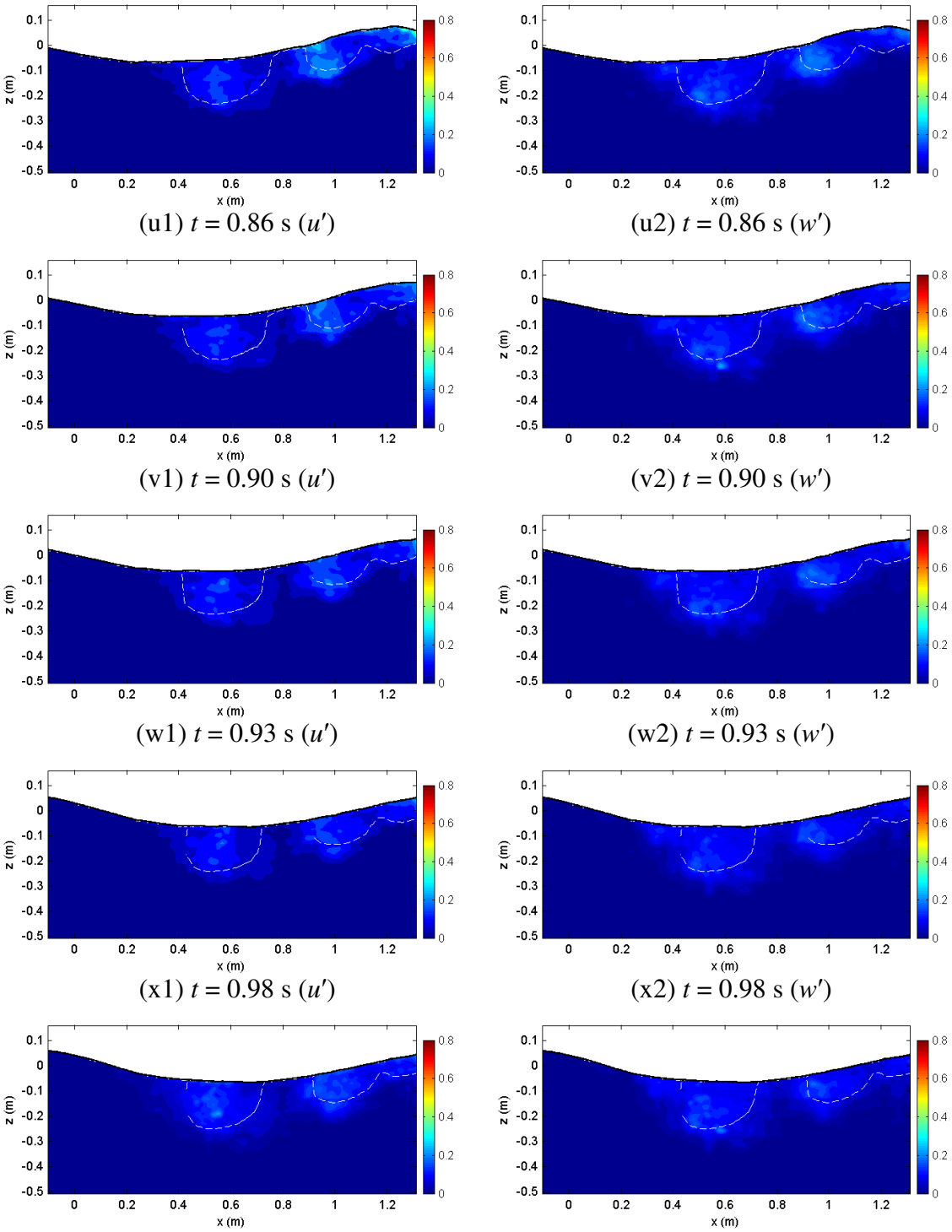

(u1) t = 0.86 s (u') (u2) t = 0.86 s (w')

(v1) t = 0.90 s (u') (v2) t = 0.90 s (w')

(w1) t = 0.93 s (u') (w2) t = 0.93 s (w')

(x1) t = 0.98 s (u') (x2) t = 0.98 s (w')

(y1) t = 1.00 s (u') (y2) t = 1.00 s (w')

Fig. 10.2 (Continued).

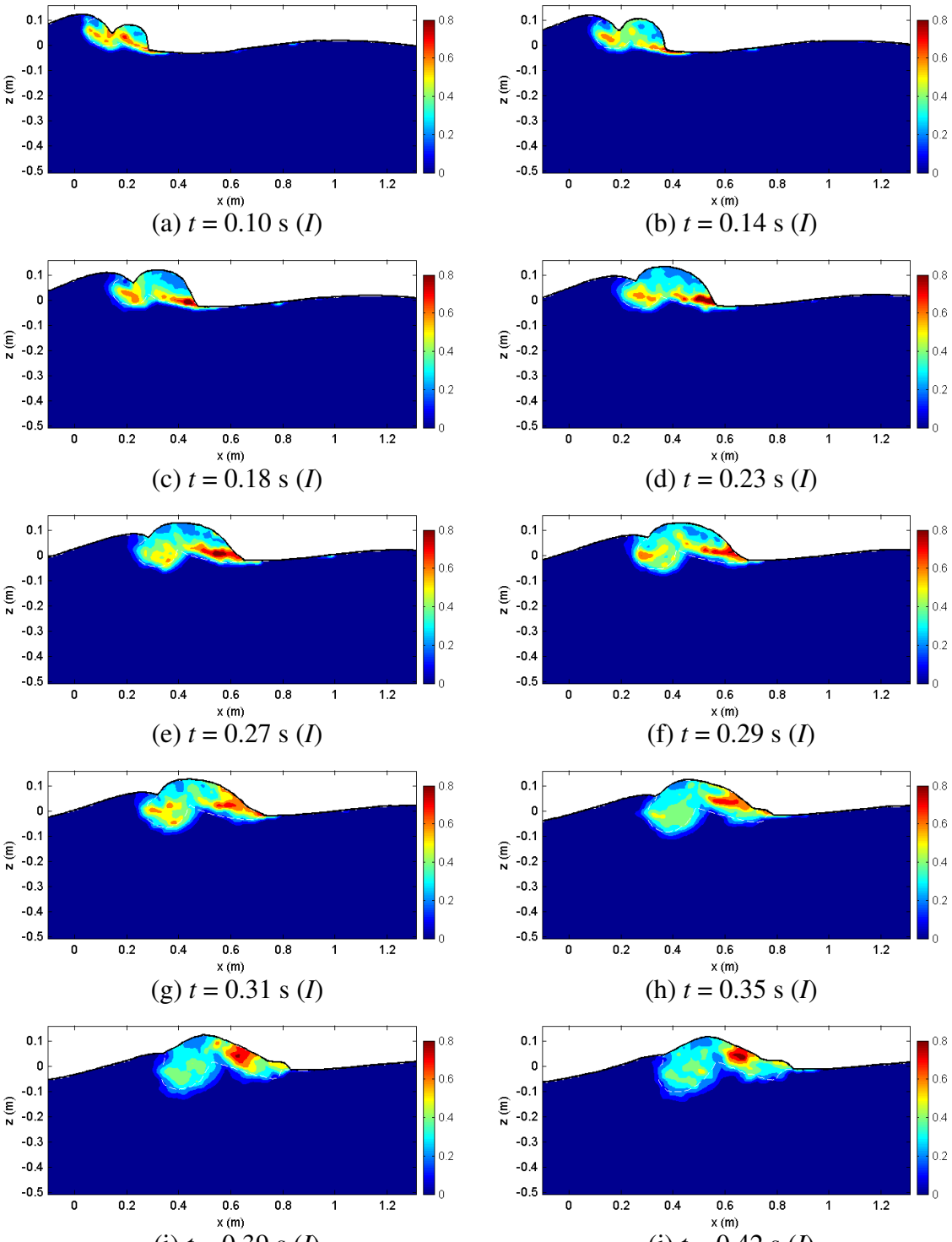

(a) t = 0.10 s (I)
(b) t = 0.14 s (I)
(c) t = 0.18 s (I)
(d) t = 0.23 s (I)
(e) t = 0.27 s (I)
(f) t = 0.29 s (I)
(g) t = 0.31 s (I)
(h) t = 0.35 s (I)
(i) t = 0.39 s (I)
(j) t = 0.42 s (I)

Fig. 10.3 Turbulence Intensity (I) (unit: m/s).

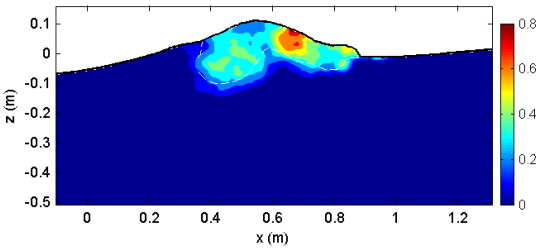

(k) t = 0.44 s (I)

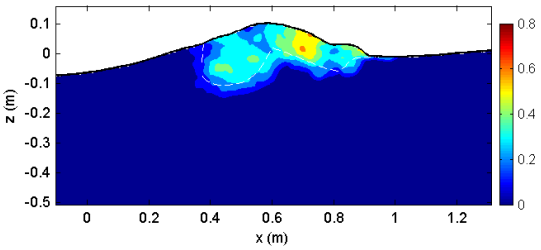

(l) t = 0.47 s (I)

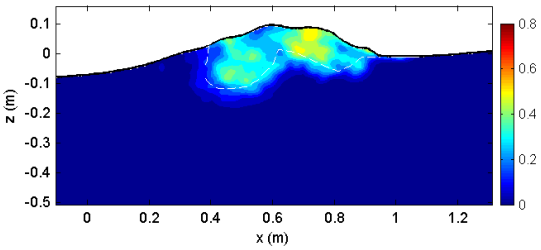

(m) t = 0.50 s (I)

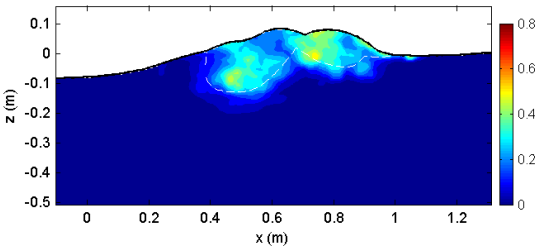

(n) t = 0.54 s (I)

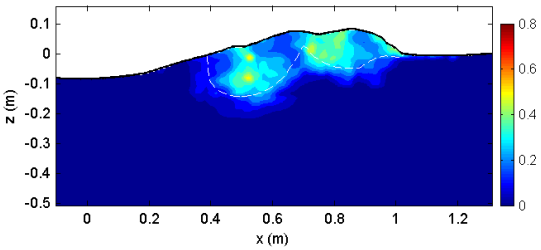

(o) t = 0.58 s (I)

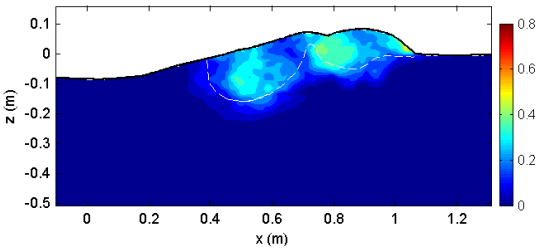

(p) t = 0.61 s (I)

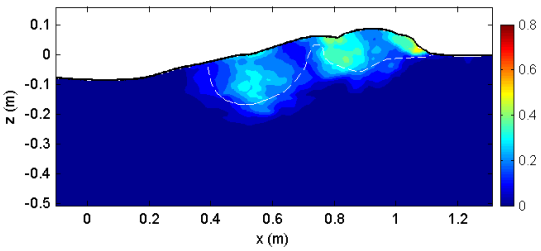

(q) t = 0.64 s (I)

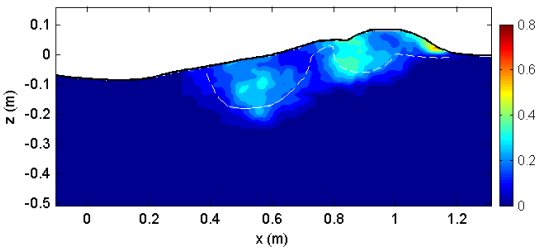

(r) t = 0.69 s (I)

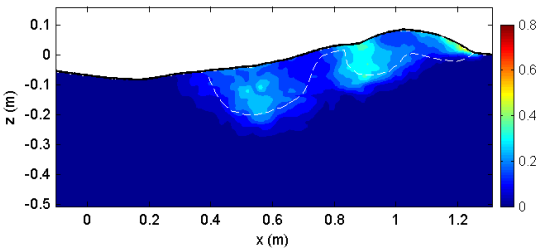

(s) t = 0.75 s (I)

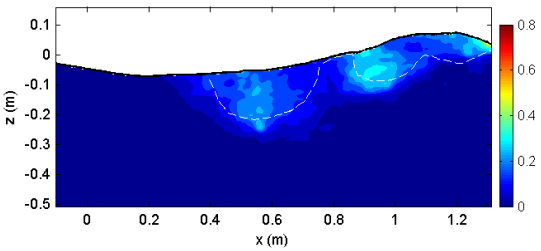

(t) t = 0.82 s (I)

Fig. 10.3 (Continued).

As shown in Fig. 10.1 and Fig. 10.2, horizontal turbulence occurs near the bottom boundary of the aerated region because shear flow is generated due to high velocity in the splash-up region between the water spray and the ascending crest. Note that the white dashed lines represent the boundary of the aerated region. The dominant location of the horizontal intensity is very similar to that of the positive clockwise vorticity as shown in Fig. 9.54 and Fig. 9.55 since vorticity is one of the sources for turbulence. On the other hand, the vertical stress occurs near the ascending crest. There is a shear flow in the left side of the ascending crest with negative vorticity due to the impinging jet and the rising crest. Therefore, the maximum vertical intensity occurs in the same region where the negative vorticity occurs [Fig. 10.2(a)-(c)]. The dominant location of the turbulence in the vertical direction is higher than the horizontal turbulence at the initial stage. Indeed, horizontal and vertical turbulence intensities are very similar to the positive and negative vorticities respectively.

As the first splash-up is developed by continuously transferred momentum from the first impinging roller, the horizontal intensity in the first roller is gradually decreased until the first backward impingement and the maximum intensity occurs at the toe of the water spray caused by the first splash-up. In this process, the vertical intensity is spread to the first roller and the second roller. Vertical intensity in the first roller is increased due to the first backward impingement and the vertical intensity in the toe of the first splash-up is also increased.

As shown in Fig. 10.2(d2) and (e2), a similar decrease of the vertical intensity is found just before the first backward impingement as discussed in the vorticity

measurements. The negative vorticity due to the counterclockwise vortex at the left side of the ascending crest is suddenly decreased when the ascending crest stays at the peak elevation before falling down onto the first impinging roller.

During the first splash-up process, the toe of the second roller (the first splash-up roller) has maximum intensities. The location is near the bottom boundary of the second roller, which is above the front face of the new crest [Fig. 10.2(a)-(f)]. Then, the turbulence is spread upward due to the accumulated roller caused by the water spray impinging onto the front trough region [Fig. 10.2(f)-(j)]. The size of the accumulated roller is increased due to the continuous impingement from the water spray and the roller moves slowly following the bottom water wave with clockwise rotation.

After the water spray impingement, there is the second impingement by the new primary wave. The new water wave impinges onto the accumulated mixture roller. In this process, high turbulence is produced near the mixture (especially at the upper and left side of the mixture). The mixture roller is totally originated from the second roller (the first splash-up roller). Due to the second impingement, the bottom part of the mixture roller travels with the second jet penetrating into the water like the first roller while the upper part is pushed up by the impingement and causes the second splash-up which is continuously generating turbulence. Vertical turbulence intensity is increased during the processes of the water spray impingement and the second water impingement. Both the horizontal and vertical intensities begin decreasing at the second splash-up.

During the third impingement, the horizontal intensity is increased again while the vertical intensity is still decreasing gradually after the second splash-up. It is because

there is no significant vertical fluctuation from the third process.

Fig. 10.4 shows the location of each maximum intensity. The time difference between markers is 0.02 s. The location of the turbulence intensity (I) is very close to the location of the maximum horizontal intensity. The location of the maximum vertical intensity is above the location of the horizontal intensity. The maximum horizontal intensity occurs near the bottom boundary of the aerated region while the maximum vertical intensity occurs near the ascending crest until the first splash-up is fully developed. From the time when the first splash-up is fully developed, both horizontal and vertical intensities occurs at the toe of the second roller (first splash-up roller) and the maximum locations have moved to the accumulated mixture roller. After the second splash-up, the location of the horizontal intensity follows the toe of the turbulent bore region. There is continuous shear between the roller in the bore region and the water body. Significant vertical fluctuation is not found from the third impingement. Therefore, the location of the maximum vertical intensity does not follow the bore crest. The location fluctuates between two rollers under the trough level and the bore crest.

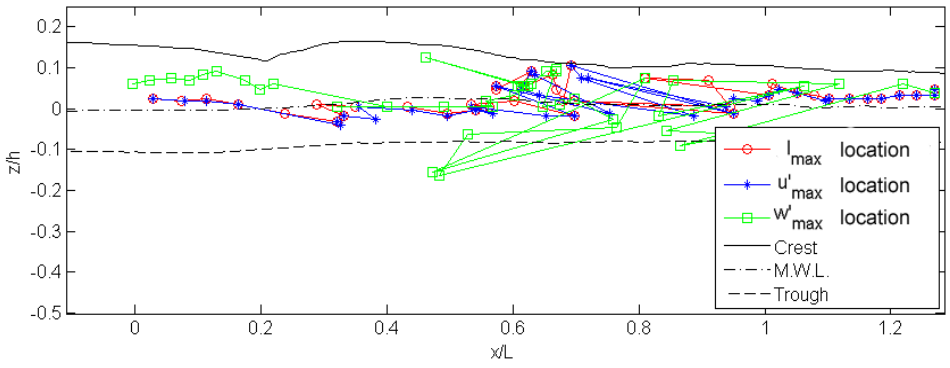

Fig. 10.4 Location of the maximum turbulence intensity.

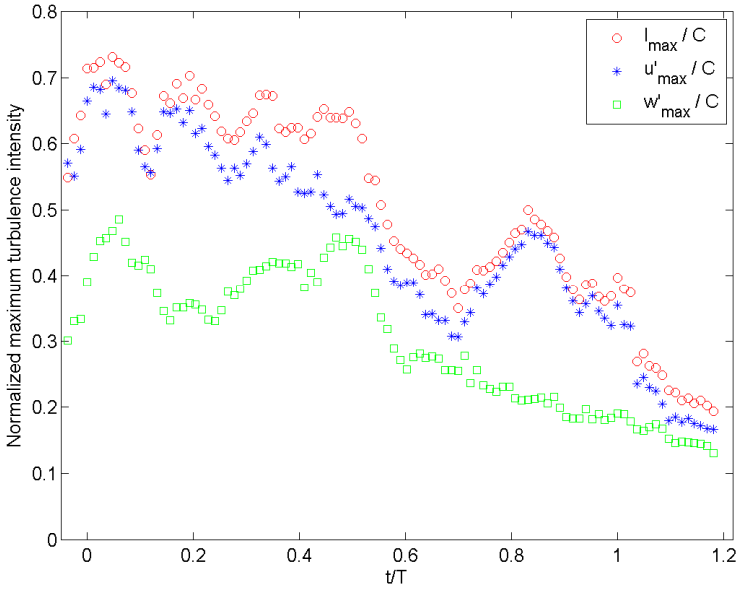

Fig. 10.5 Normalized maximum turbulence intensity (normalized by *C*).

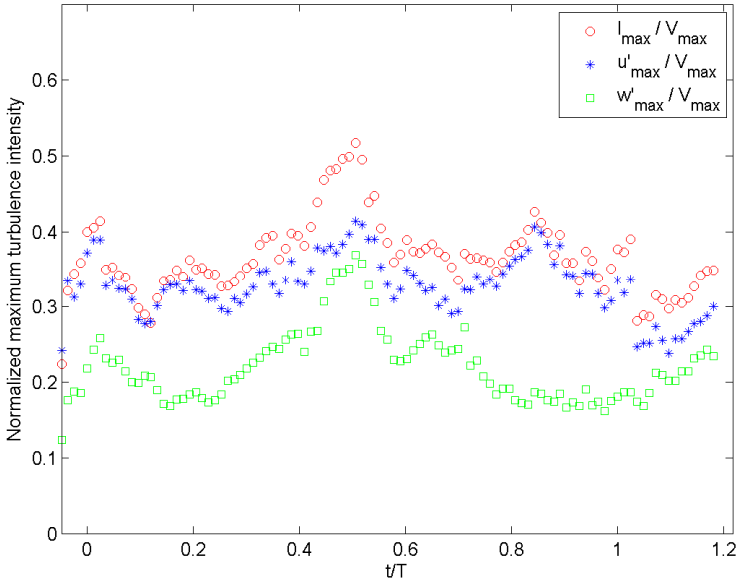

Fig. 10.6 Normalized maximum turbulence intensity (normalized by maximum speed, V_{max}).

Fig. 10.5 and Fig. 10.6 show the maximum intensity variation in time and was normalized by the wave phase speed (C = 1.3 m/s) and the maximum speed ($V_{max}(t)$) at each corresponding time as shown in Fig. 9.31. Both horizontal and vertical intensities have the maxima around t = 0.05 s at the beginning of the first splash-up. The maximum magnitudes in both direction are approximately 0.69C (0.39V_{max}) and 0.49C (0.26V_{max}) respectively. The maximum horizontal intensity is gradually decreased from that time while the maximum vertical intensity is suddenly decreased because the vertical shear between the downward impinging roller and the upward ascending crest is decreased as the ascending crest rises to the peak elevation around t = 0.2 s. Then, the vertical intensity begins increasing again due to the accumulated mixture caused by the water spray impingement. The vertical intensity has a local maximum at the second impingement and the magnitude is approximately 0.45C (0.35V_{max}). The absolute vertical intensity at the second impingement is slightly smaller than that at the first impingement (Fig. 10.5). However, the vertical intensity at the second impingement is higher than that at the first impingement when compared to the maximum speed at the corresponding time (Fig. 10.6).

Fig. 10.7 and Fig. 10.8 show the comparison of the time difference for the maximum mean velocity and turbulent velocity in each direction, respectively. In the case of the horizontal mean and turbulent velocities, there is no significant variation in time and the trends are very similar to each other (Fig. 10.7). It was also expected that the maximum vertical turbulence intensity variation in time has a similar pattern with the maximum downward mean velocity because the maximum vertical turbulence occurs at

the first and second impingement. In the case of vertical mean and turbulent velocities, trends are very similar to each other but there is a small time delay between the mean and turbulent flows (Fig. 10.8). The maximum downward velocity occurs at the impinging moment. However, the maximum vertical intensity occurs at a later time. For example, the maximum downward mean and turbulent velocities at the first impingement occur at t = 0 s and t = 0.05 s as shown in Fig. 10.8. Moreover, the time delay at the second impingement is longer because the maximum downward velocity at the second impingement occurs at the water spray impingement but the second splash-up is caused by the water impingement from the new crest.

After the second splash-up, the maximum vertical intensity is linearly decreased while the horizontal intensity has a local maximum during the third process as shown in Fig. 10.5 to Fig. 10.8.

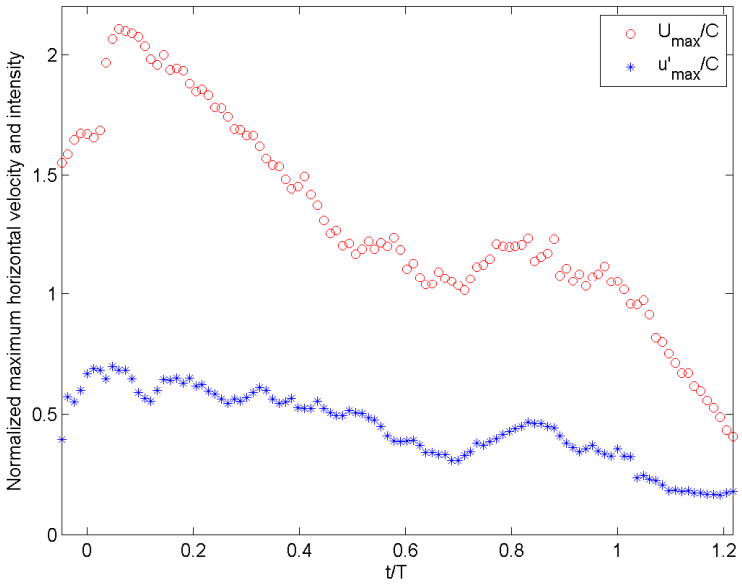

Fig. 10.7 Comparison of maximum U (U_{max}) and u' (u'_{max}).

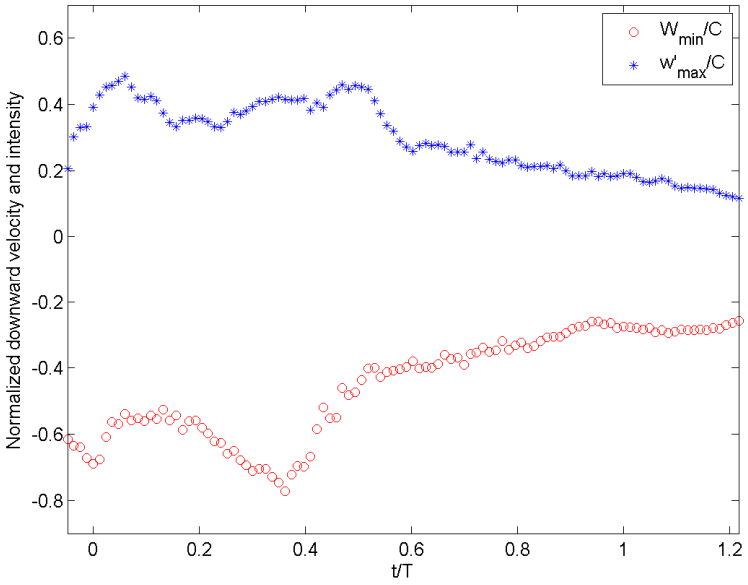

Fig. 10.8 Comparison of maximum W (W_{max}) and w' (w'_{max}).

10.2.2 Temporal Analysis of Turbulence Intensity

Temporal analysis for the turbulent velocity measurement is presented in this section in a similar manner as temporal analysis of the mean flow presented in Chapter IX.

Fig. 10.9 shows the time series of the horizontal and vertical turbulence intensities at several stations. As shown in Fig. 10.2, figures in the left side denoted as a number 1 in parentheses represent the horizontal turbulence intensities while figures in the right side denoted as a number 2 in parentheses represent the vertical turbulence intensities. Figures in a same row denoted as the same letter in parentheses represent the horizontal and vertical intensities at the same station, respectively. Fig. 10.10 shows the turbulence intensity (I) at the same stations shown in Fig. 10.9.

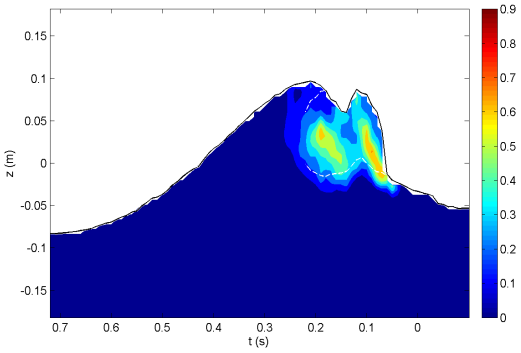

(a1) x = 0.198 m (u')

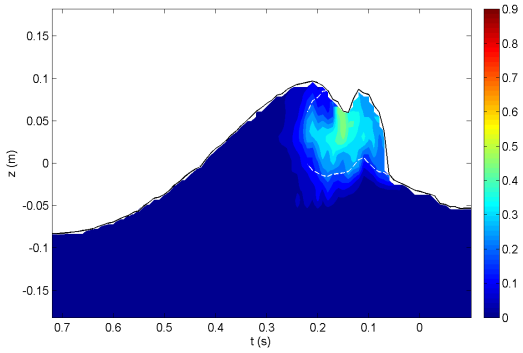

(a2) x = 0.198 m (w')

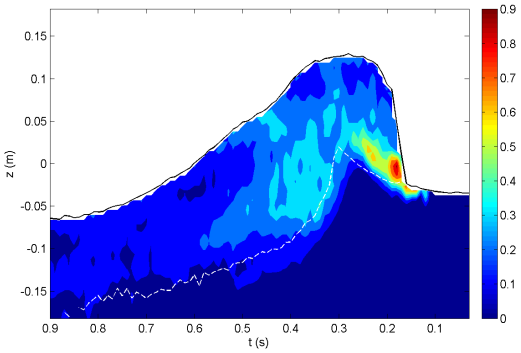

(b1) x = 0.435 m (u')

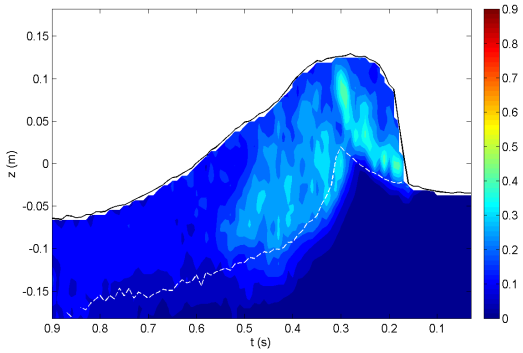

(b2) x = 0.435 m (w')

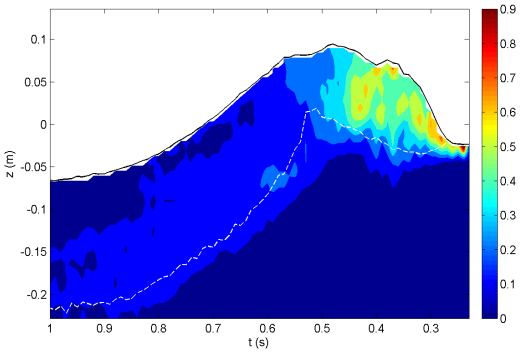

(c1) x = 0.649 m (u')

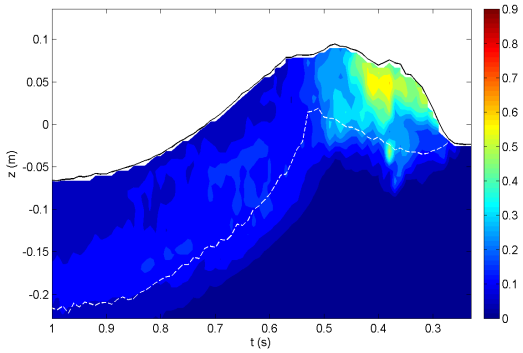

(c2) x = 0.649 m (w')

Fig. 10.9 Time series of horizontal and vertical intensities at a station (unit: m/s).

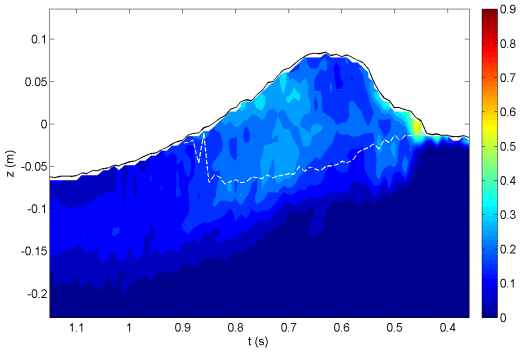

(d1) x = 0.880 m (u')

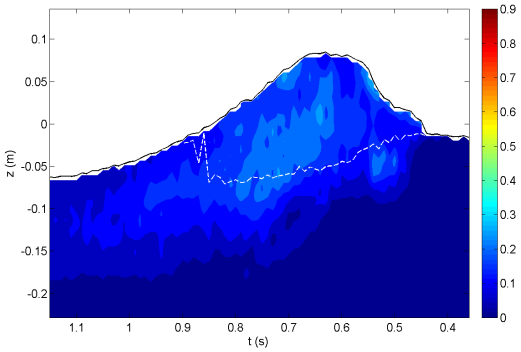

(d2) x = 0.880 m (w')

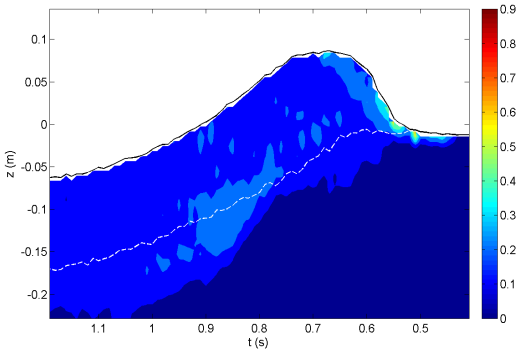

(e1) x = 0.967 m (u')

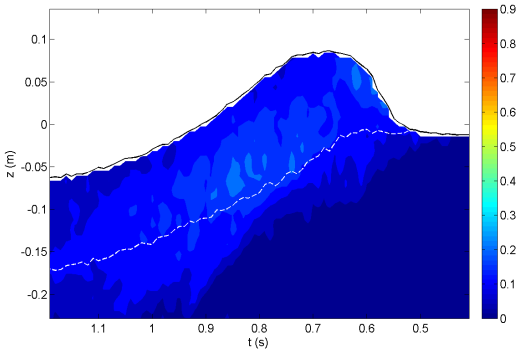

(e2) x = 0.967 m (w')

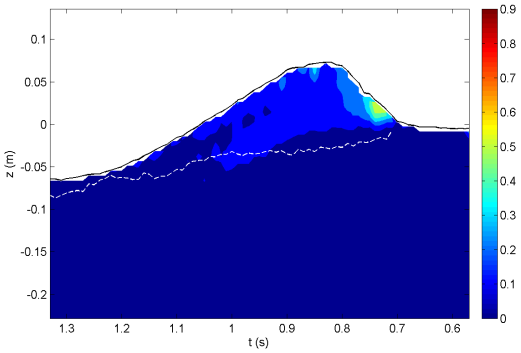

(f1) x = 1.204 m (u')

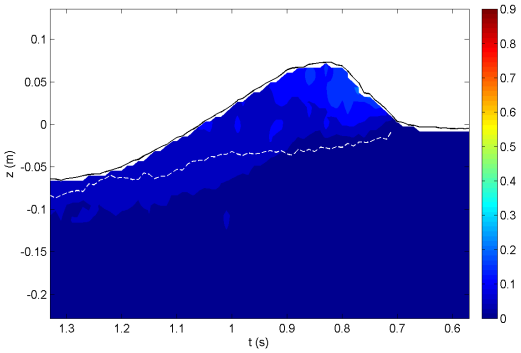

(f2) x = 1.204 m (w')

Fig. 10.9 (Continued).

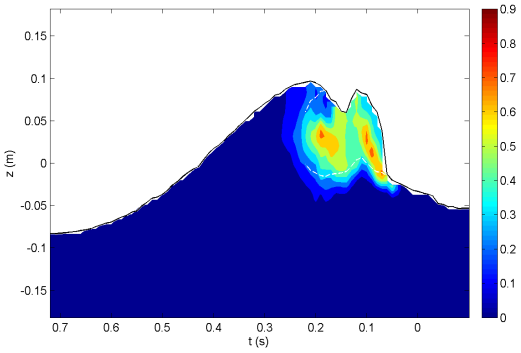

(a) x = 0.198 m (I)

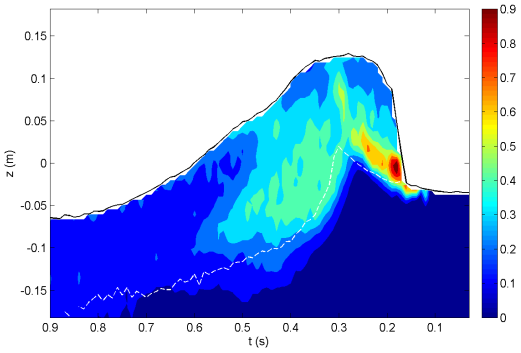

(b) x = 0.435 m (I)

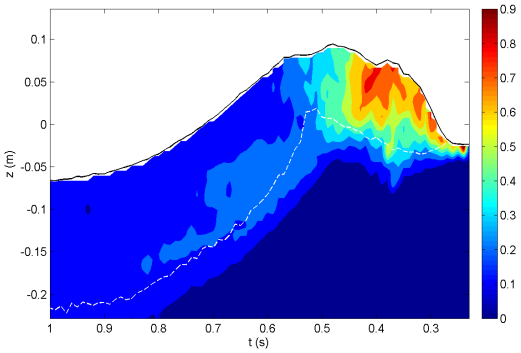

(c) x = 0.649 m (I)

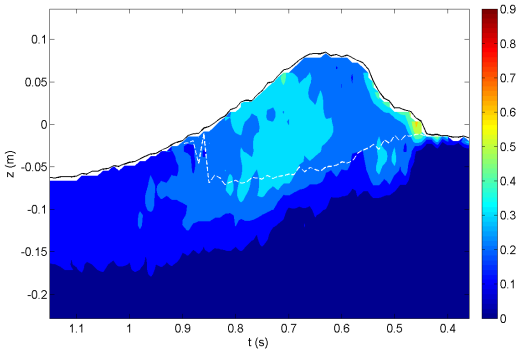

(d) x = 0.880 m (I)

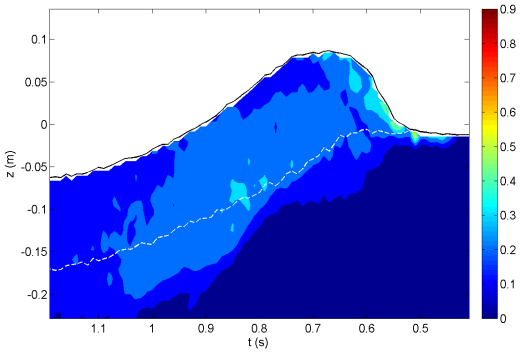

(e) x = 0.967 m (I)

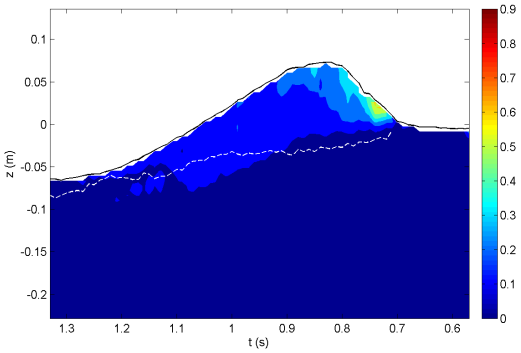

(f) x = 1.204 m (I)

Fig. 10.10 Time series of turbulence intensity (I) at a station (unit: m/s).

The location of the station shown in Fig. 10.9(a) and Fig. 10.10(a) is near the beginning of the first splash-up. It can be seen that the horizontal turbulence is generated near the bottom boundary of the aerated region in two rollers, which is near the mean water level while the vertical turbulence occurs near the ascending crest, which is slightly above the mean water level. Fig. 10.11 shows the wave- and period-averaged intensities in horizontal and vertical directions. Comparison of the maximum and minimum intensities at each station can be seen in Fig. 10.12. Time-averaged, maximum and minimum turbulence intensities (I) can be seen in Fig. 10.13. A station shown in Fig. 10.9(b) and Fig. 10.10(b) is located near the region of the fully developed first splash-up. The first roller passes below the still water level of the station after the fully developed second roller passing. Two stations in Fig. 10.10(d) and (f) are located near the region of the fully developed second and third splash-up respectively. Each impinging roller passes through the location where each fully developed splash-up passes. For example, when the second splash-up is fully developed, the maximum crest of the second splash-up passes through the station (x = 0.880 m) and then the impinging roller causing the second splash-up passes through the below of the station. The two other stations shown in Fig. 10.10(c) and (e) are located where the impinging rollers stays in deep water as their motions follow water particle motion after losing their large horizontal momentum. A detailed location of impinging roller under the trough level can be seen in Fig. 10.2. Note that white dashed lines in Fig. 10.2 represent the boundary of the aerated region.

As shown in Fig. 10.11(a) and Fig. 10.12(a), the period-averaged intensities at x = 0.198 m is much lower than those at x = 0.435 m and 0.649 m due to the low turbulence

in the water under the rear face of the impinging roller although the maximum intensities are close to each other. At the three stations (x = 0.435 m, 0.649 m and 0.88 m), the period-averaged intensities has similar levels to one another in both the horizontal and vertical directions. It can be clearly seen that the turbulence intensity is reduced at the third splash-up region (x = 1.204 m) especially for the vertical intensity as shown in Fig. 10.11(a) and Fig. 10.13(b) compared with the first splash-up (x = 0.435 m) and the second splash-up (x = 0.880 m).

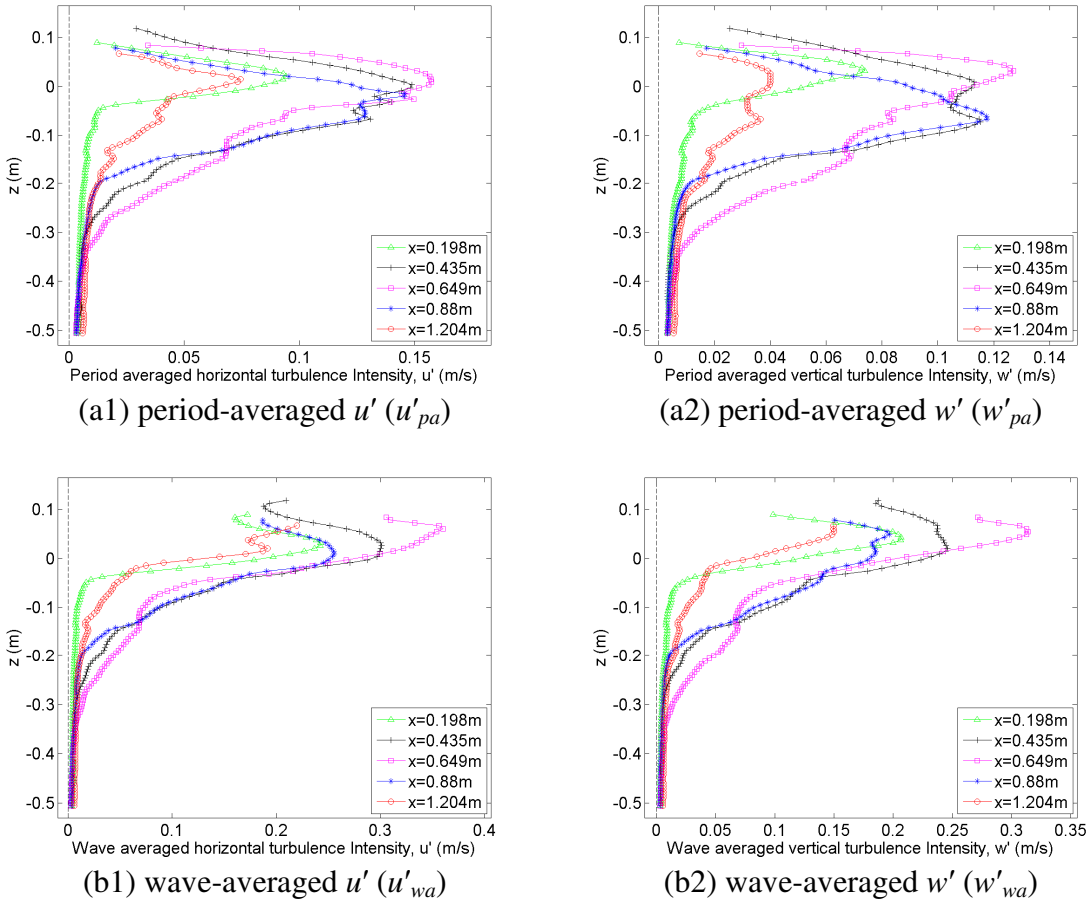

(a1) period-averaged u' (u'_{pa}) (a2) period-averaged w' (w'_{pa})

(b1) wave-averaged u' (u'_{wa}) (b2) wave-averaged w' (w'_{wa})

Fig. 10.11 Comparison of time-averaged horizontal and vertical intensities (unit: m/s).

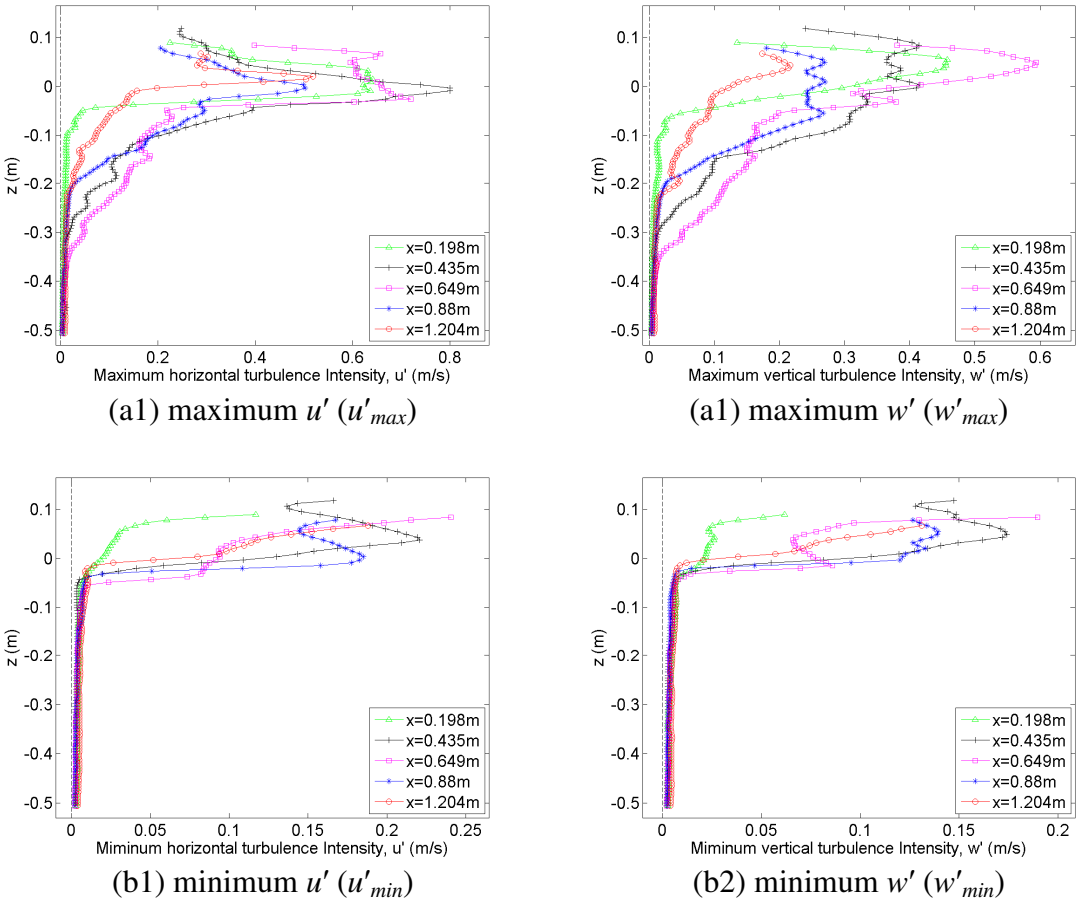

(a1) maximum u' (u'_{max})

(a1) maximum w' (w'_{max})

(b1) minimum u' (u'_{min})

(b2) minimum w' (w'_{min})

Fig. 10.12 Comparison of maximum and minimum horizontal and vertical intensities (unit: m/s).

Fig. 10.14 shows the time-averaged, maximum and minimum horizontal intensities (u') normalized by the wave phase speed. As mentioned in Chapter IX, the PIV measurements were performed to cover the entire breaking waves. Therefore, time series and time-averaged values at every point shown from Fig. 10.9 to Fig. 10.13 can be obtained for all 475 stations. Spatial resolution of the contours is 5.78 mm in both direction. Temporal resolution in calculation of time-averaged quantities is 0.01 s.

Fig. 10.15 shows the time-averaged, maximum and minimum vertical intensities

(w') normalized by C and the time-averaged, maximum and minimum turbulence intensities (I) normalized by C can be seen in Fig. 10.16.

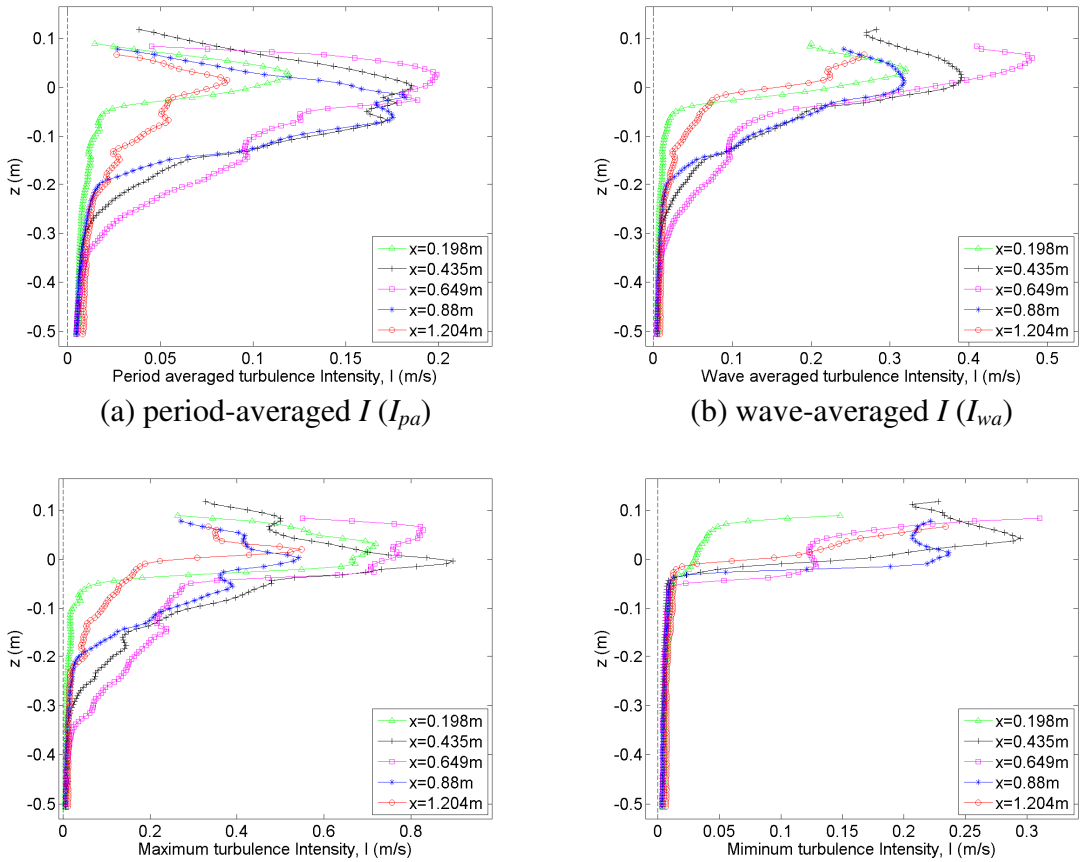

(a) period-averaged I (I_{pa})

(b) wave-averaged I (I_{wa})

(c) maximum I (I_{max})

(d) minimum I (I_{min})

Fig. 10.13 Time-averaged, maximum and minimum turbulence intensity (I) (unit: m/s).

As shown in Fig. 10.14, the period-averaged horizontal intensity is very high at the region between $x = 0.2L$ and $x = 0.8L$. The region covers the fully developed first splash-up to the second splash-up. However, the maximum intensities between $x = 0.6L$ and $0.8L$ are not high when compared with intensities in the region between $x = 0$ and $0.6L$.

This is because the most phases of the wave passing though the region during the one wave period have high intensities although there is not a significantly high level of the intensity. This is explained that the second splash-up of the accumulated roller passes the region and then the second impinging roller passes later. It can be seen from the vertical intensity in Fig. 10.15. Therefore, turbulence intensity (I) has a similar pattern as shown in Fig. 10.16. It can also be presented in Fig. 10.13(a). The period-averaged intensity at x = 0.88 m ($x = 0.81L$) is one of the stations in the region that is very close to the period-averaged intensities at x = 0.435 m and x = 0.649 m where the turbulence is very high in the entire flow. However, maximum intensity at x = 0.88 m is much lower and the minimum intensity is close when compared with the maximum and minimum intensities at x = 0.435 m and x = 0.649 m. On the contrary, the period-averaged intensity between x = 0 and $0.2L$ is not high although the maximum intensity is very high as shown in Fig. 10.14(b) and (c). This is due to the low turbulence in water under the rear face of the impinging roller as mentioned before. It is also seen in Fig. 10.13(c) and (d).

The region that turbulence flow with very high intensity passes in a wave cycle is near $x = 0.5L$ ($0.4L$ to $0.6L$) as shown in Fig. 10.14(b), Fig. 10.15(b) and Fig. 10.16(b). High intensity is widely distributed in the vertical direction up to $0.3h$. At first, water spray from the fully developed first splash-up impinges onto the region continuously and the first impinging roller followed by the ascending crest passes between the mean water level and the trough level. There is also the first backward impingement onto the first roller and the roller stays at the region following the orbital motion of the water wave. These processes create high intensity at the region continuously.

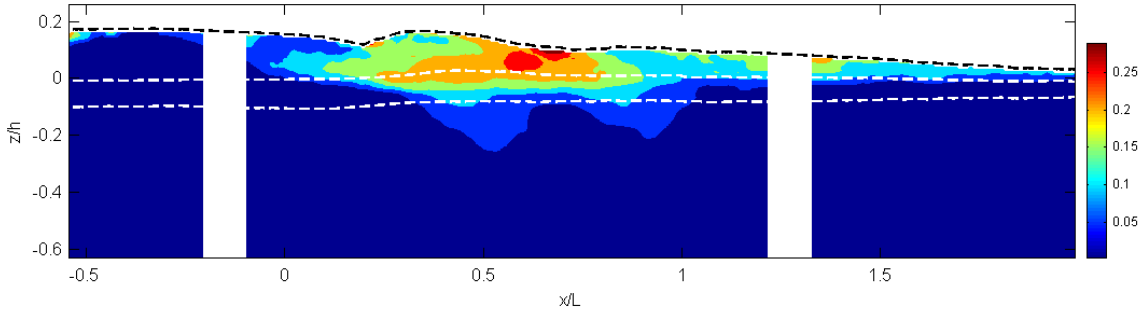

(a) wave-averaged u' (u'_{wa}/C)

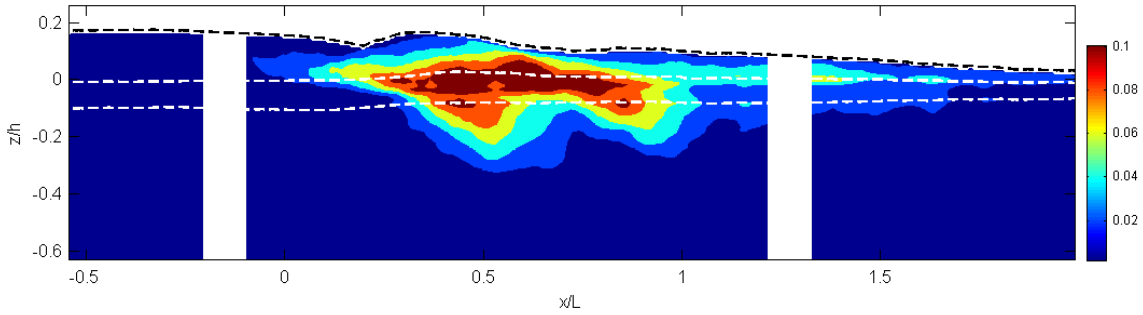

(b) period-averaged u' (u'_{pa}/C)

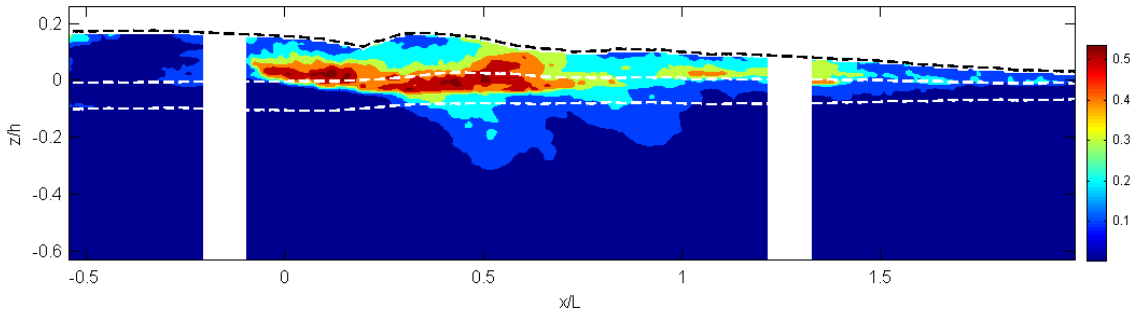

(c) maximum u' (u'_{max}/C)

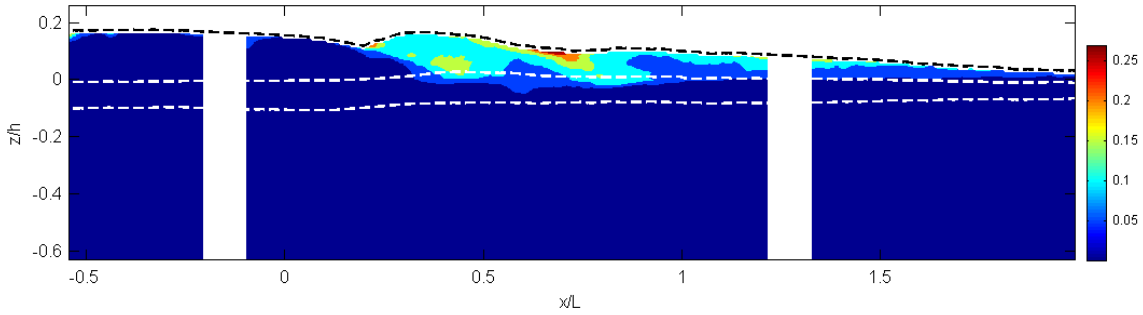

(d) minimum u' (u'_{min}/C)

Fig. 10.14 Normalized time-averaged, maximum and minimum u' (u'/C).

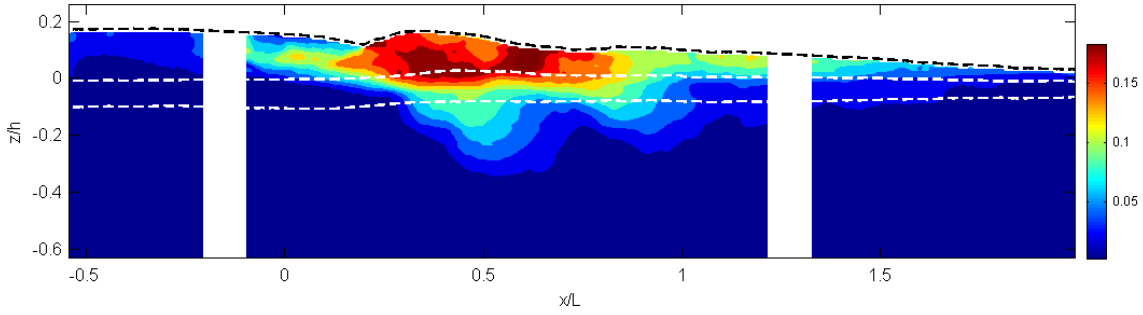

(a) wave-averaged w' (w'_{wa}/C)

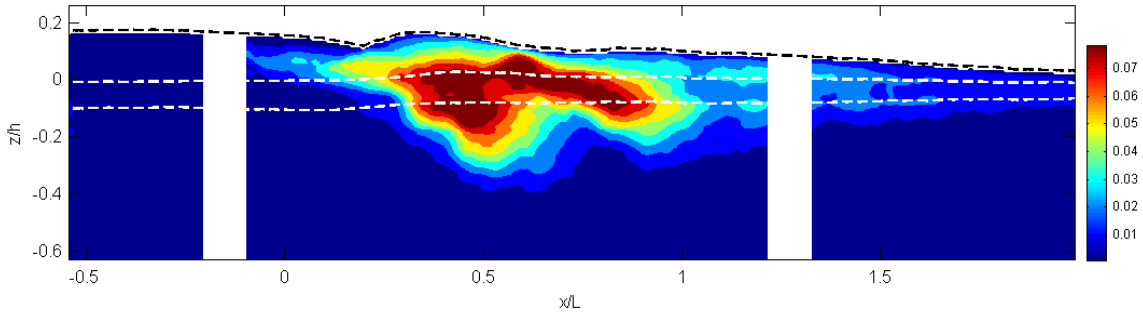

(b) period-averaged w' (w'_{pa}/C)

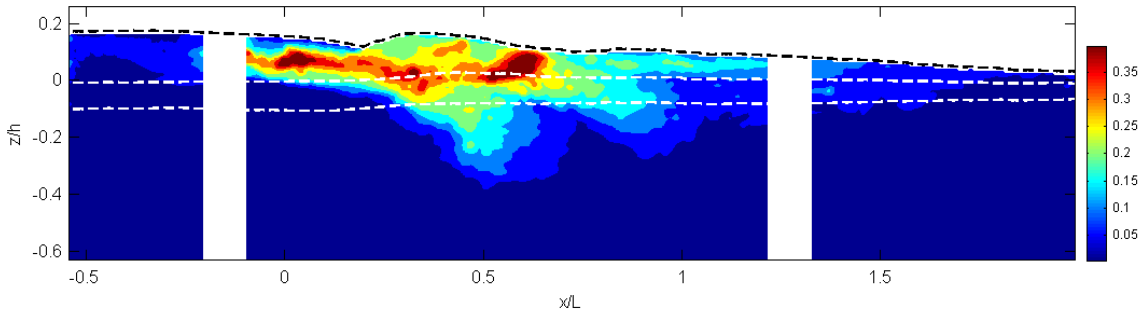

(c) maximum w' (w'_{max}/C)

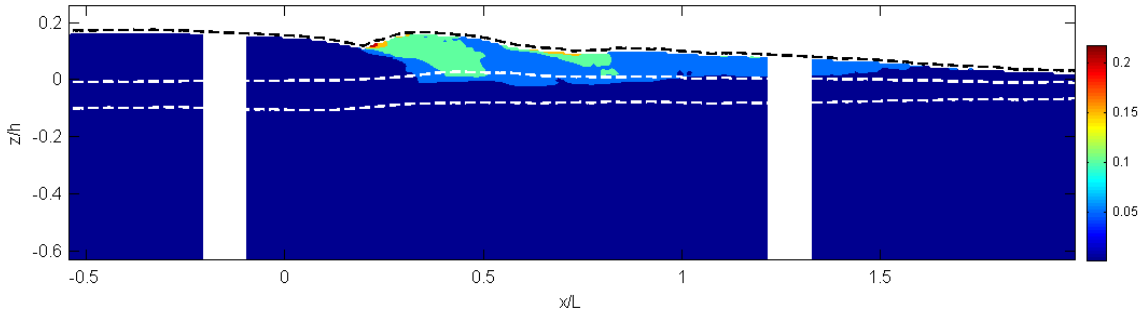

(d) minimum w' (w'_{min}/C)

Fig. 10.15 Normalized time-averaged, maximum and minimum w' (w'/C).

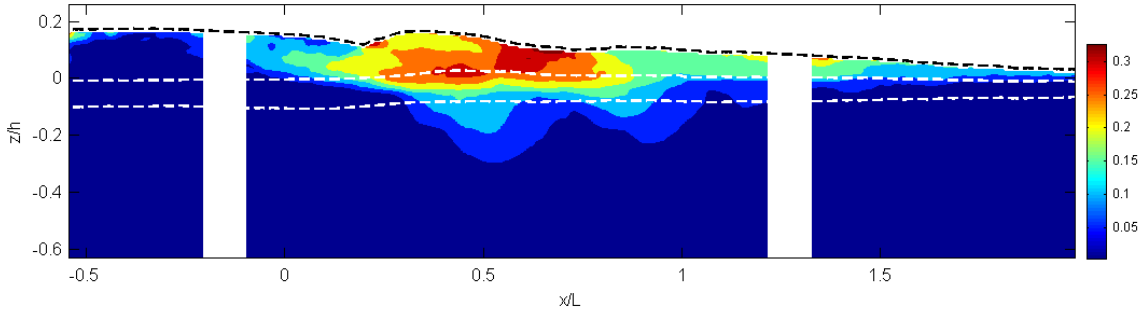

(a) wave-averaged I (I_{wa}/C)

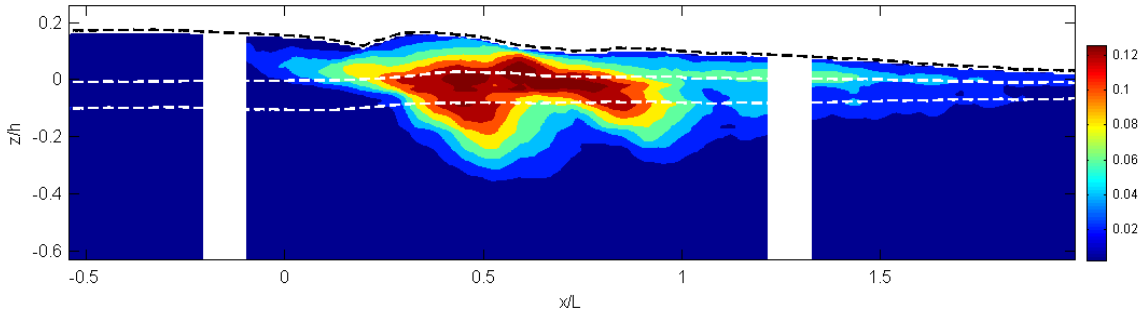

(b) period-averaged I (I_{pa} /C)

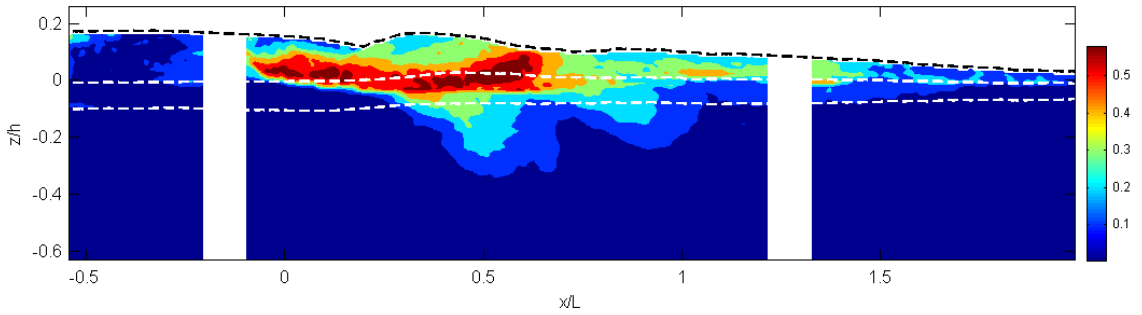

(c) maximum I (I_{max} /C)

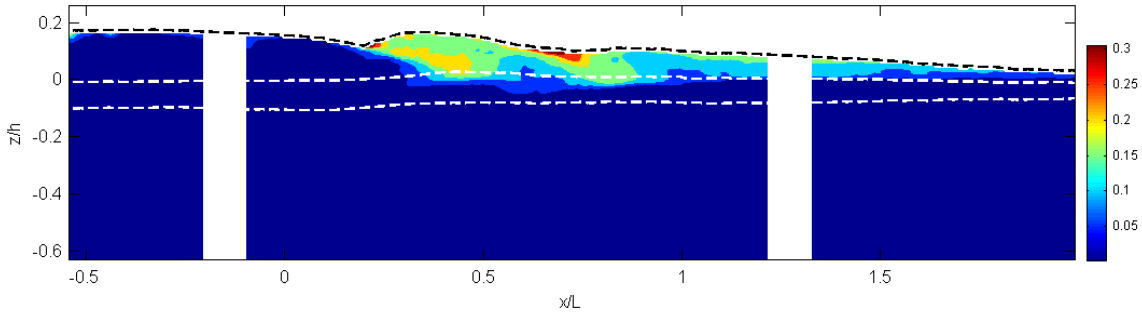

(d) minimum I (I_{min} /C)

Fig. 10.16 Normalized time-averaged, maximum and minimum intensity (*I*/*C*).

One of the most interesting regions is between $x = 0.55L$ and $0.7L$. As discussed in Chapter IX, the second impingement occurs at this region. The crest at this region has a high intensity although the region below the trough at this location has a low period-averaged intensity. High intensity near the crest is caused by the second impingement followed by the water spray impinging. As water spray impinges onto the front trough, the size of the accumulated roller is increased. Turbulent water spray impinges continuously onto the growing accumulated roller. During this process, both horizontal and vertical turbulence intensities are very high especially at the left and top side of the accumulated roller. Followed by the water spray impingement, the new water wave from the ascending crest impinges onto the accumulated roller. Shear stress occurs and is caused by the impinging roller and the splash-up of the accumulated roller. Although the momentum of the second impingement is smaller than that of the first impingement, the accumulated roller is pushed up vertically due to its low density. The underneath of the this location, the turbulence intensity under the trough level is very low compared with high intensities around $x = 0.5L$ (first impinging roller) and $x = 0.9L$ (Second impinging roller). This is because the first impinging roller cannot reach this location and the impinging roller after the second impingement near crest passes horizontally near the mean water level due to large horizontal momentum. Therefore, below each impinging point does not have the high turbulence intensity as shown in Fig. 10.16. Note that three impinging locations for each process are approximately $x = 0$, $0.6L$ and $1.05L$ respectively.

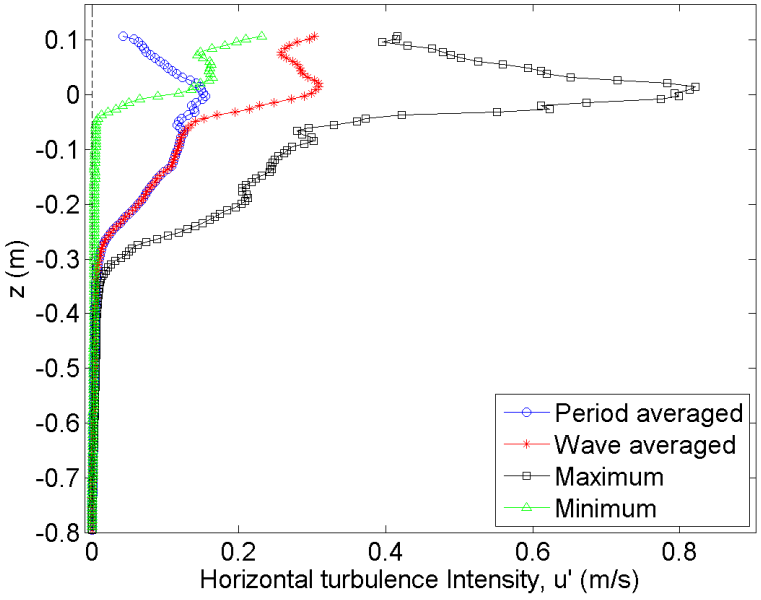

Fig. 10.17 Example of full depth extension of u' (x = 0.539 m).

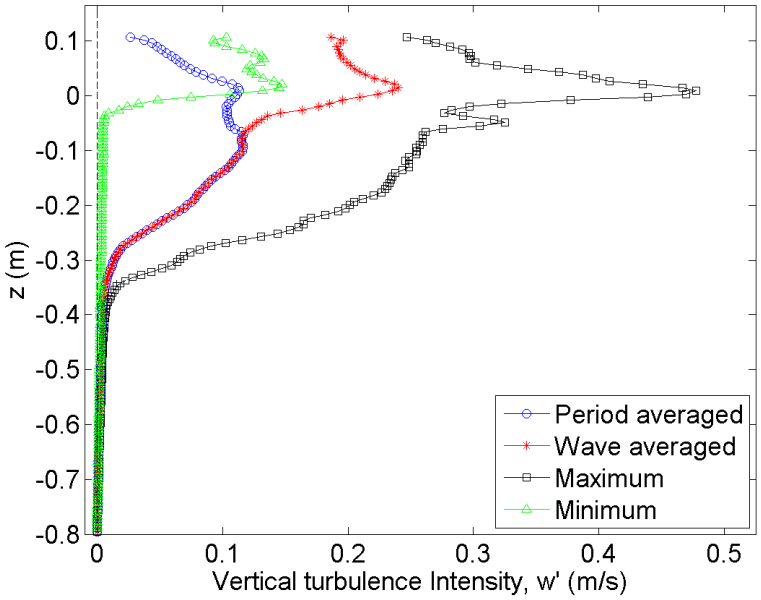

Fig. 10.18 Example of full depth extension of w' (x = 0.539 m).

To obtain the depth-integrated or depth-averaged quantities, it is necessary to extend measurement quantities up to the bottom (x = - 0.8 m). Fig. 10.17 and Fig. 10.18 show examples of the extended results for horizontal and vertical intensities at x = 0.539 m which is one of the highest turbulence region. Intensity profiles between z = - 0.51 m and – 0.8 m were obtained using linear interpolation with the same measurement grid size. Both intensities are close to zero at z = - 0.4 m although the intensities are most widely distributed at the location.

Fig. 10.19 shows the maximum intensities at each station with the magnitude normalized by the wave phase speed. Both intensities have local maximum intensities at the locations of the first (x = 0) and second (x = 0.6L) impinging locations while only the horizontal intensity has a local maximum at the third impingement (x = 1.05L) as discussed in previous section.

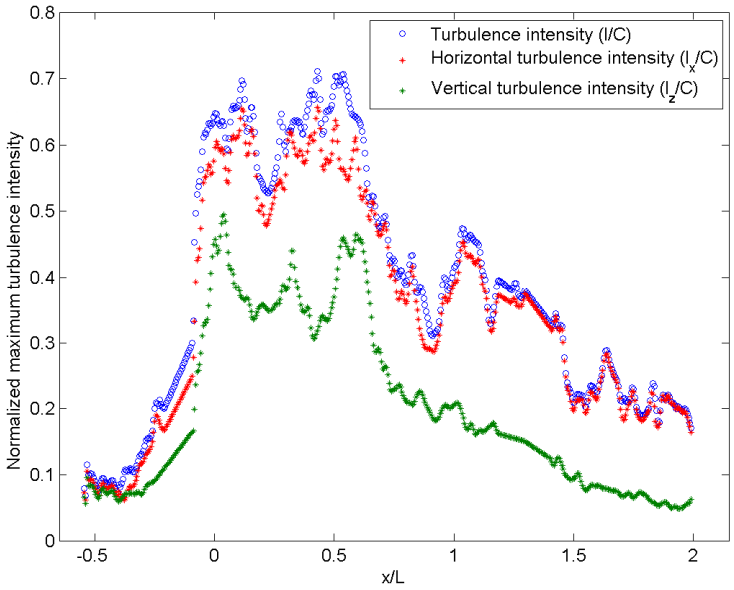

Fig. 10.19 Normalized maximum intensities at each station (normalized by *C*).

Fig. 10.20 shows the depth-averaged time mean intensity which is obtained from Eq. (9.6). Unlike the maximum intensities at each station, the horizontal intensity is less dominant in the depth-averaged values between $x = 0$ and $x = 0.45L$. The ratio of the depth-averaged vertical intensity to the horizontal intensity is about 85-97% between $x = 0$ and $0.5L$, while the ratio is about 70~85% between $x = 0.5$ and $x = 2L$

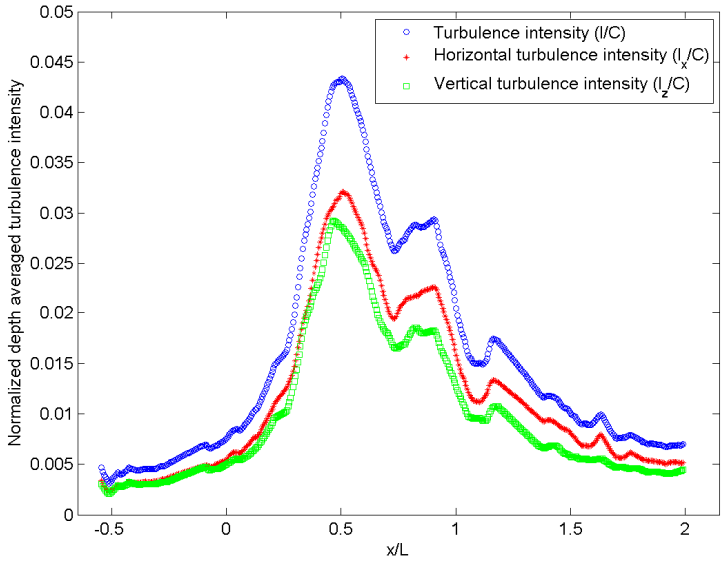

Fig. 10.20 Depth-averaged time mean intensity (normalized by *C*).

10.3 Reynolds Stress

The Reynolds shear stress is defined as $\langle -u_i' w_i' \rangle$ where $\langle\ \rangle$ denotes the ensemble averaging and it will be omitted with the subscript for simplicity. Spatial and temporal analysis results are presented in Sections 10.3.1 and 10.3.2 respectively.

10.3.1 Spatial Analysis of Reynolds Stress

The Reynolds stresses are positive in the entire flow field except at the beginning of the first and the second splash-up. Fig. 10.21 shows the Reynolds stress during the beginning of the first splash-up followed by the first impingement. At the beginning of the first splash-up, positive shear stress can be seen at the first impinging roller and small water spray impingement at the first splash-up. The maximum shear stress occurs at the impinging roller near the impinging point until the first splash-up and the positive stress occurs near the region of water spray impinging from the first splash-up. However, it is a small scale before fully developed.

The negative stress occurs at the splash-up as shown in Fig. 10.21 and Fig. 10.22. The negative stress due to upward momentum flux weakens when the first splash-up is fully developed. The size of the second roller caused by the first splash-up is gradually increased as elevation of the newly ascending water crest becomes higher. The ascending crest reaches a peak with a large upward momentum around t = 0.2 s. The top portion of the ascending crest loses its kinetic energy. Therefore, the left part falls down onto the first roller, which is the first backward impingement, and the large upward momentum contributing to the second roller weakens.

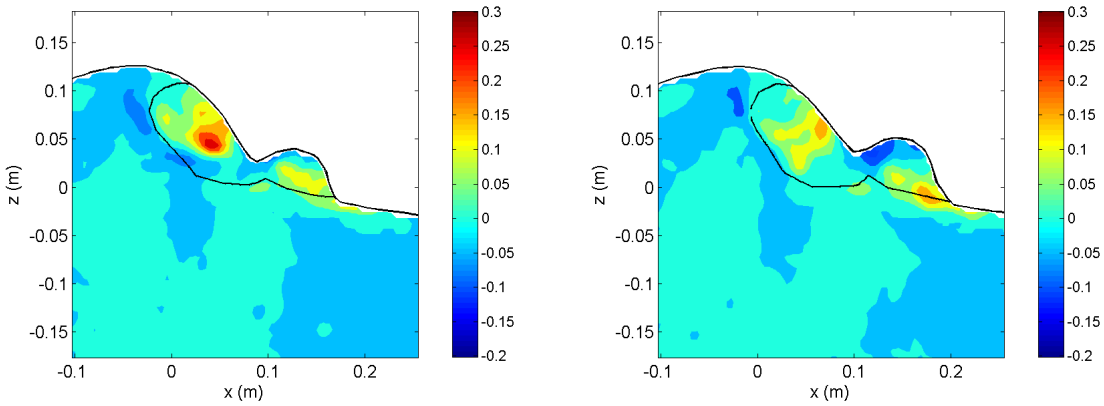

(a) t = 0.05 s (b) t = 0.06 s

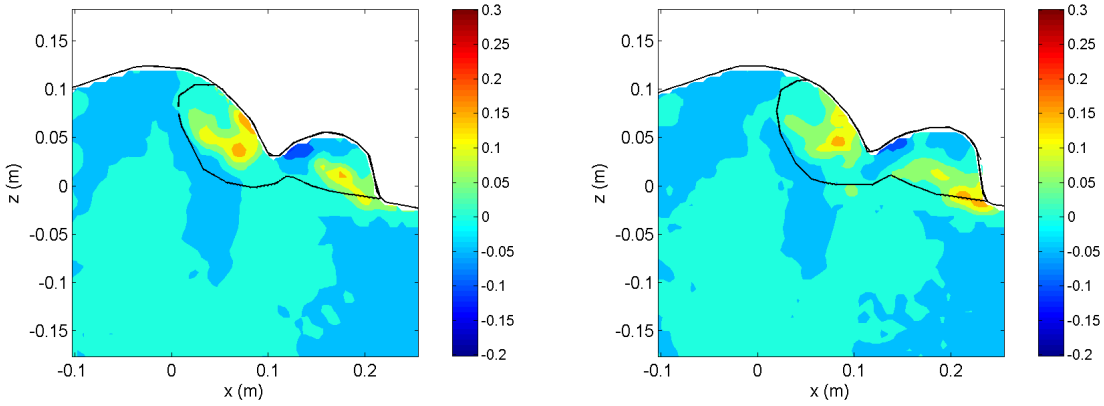

(c) t = 0.07 s (d) t = 0.08 s

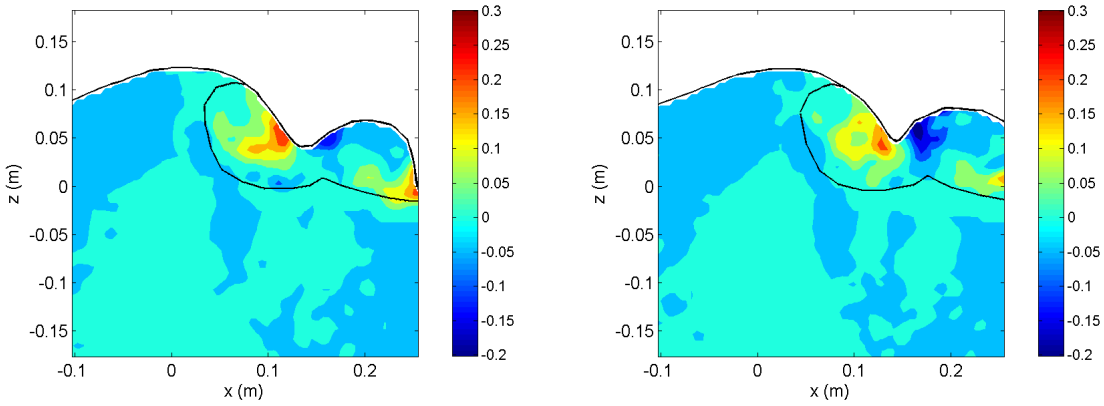

(e) t = 0.09 s (f) t = 0.10 s

Fig. 10.21 Reynolds stress at the beginning of the first splash-up (unit: m^2/s^2).

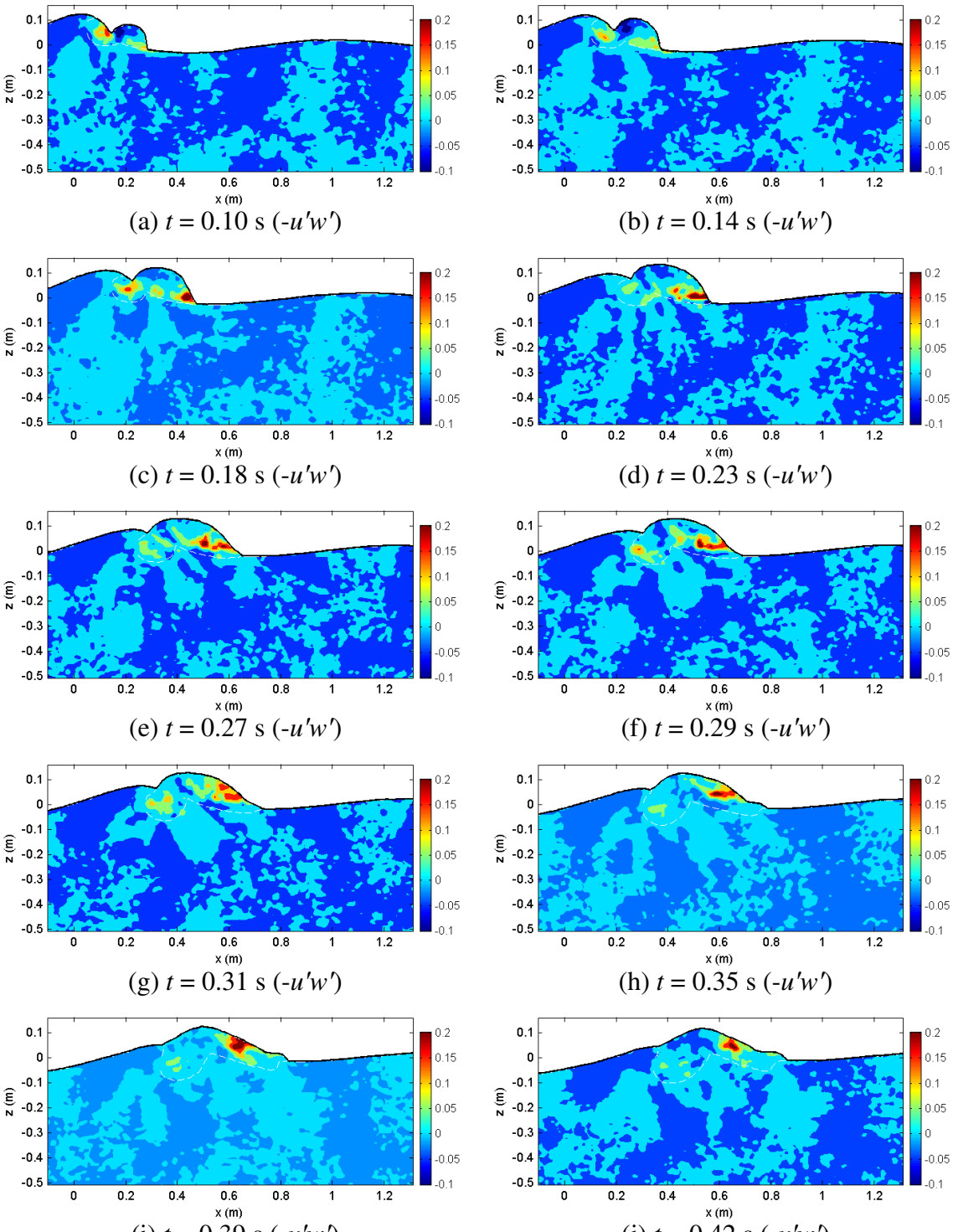

(a) t = 0.10 s ($-u'w'$)

(b) t = 0.14 s ($-u'w'$)

(c) t = 0.18 s ($-u'w'$)

(d) t = 0.23 s ($-u'w'$)

(e) t = 0.27 s ($-u'w'$)

(f) t = 0.29 s ($-u'w'$)

(g) t = 0.31 s ($-u'w'$)

(h) t = 0.35 s ($-u'w'$)

(i) t = 0.39 s ($-u'w'$)

(j) t = 0.42 s ($-u'w'$)

Fig. 10.22 Reynolds stress from the first splash-up (unit: m^2/s^2).

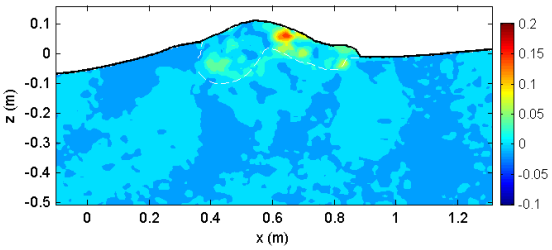

(k) t = 0.44 s (-$u'w'$)

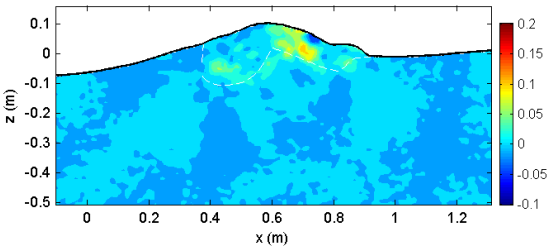

(l) t = 0.47 s (-$u'w'$)

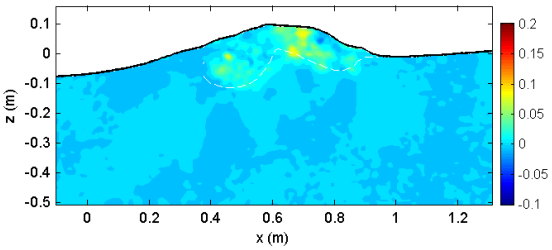

(m) t = 0.49 s (-$u'w'$)

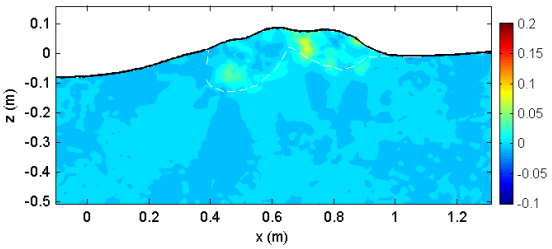

(n) t = 0.53 s (-$u'w'$)

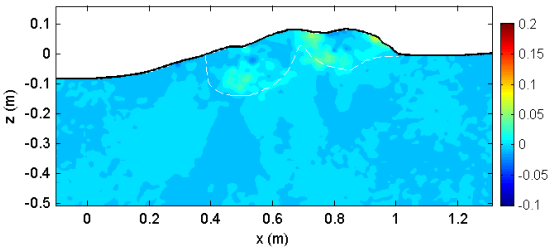

(o) t = 0.57 s (-$u'w'$)

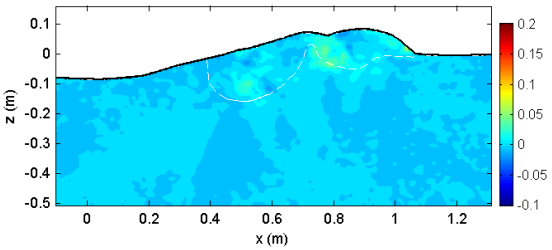

(p) t = 0.61 s (-$u'w'$)

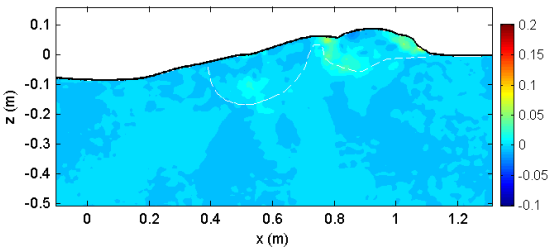

(q) t = 0.64 s (-$u'w'$)

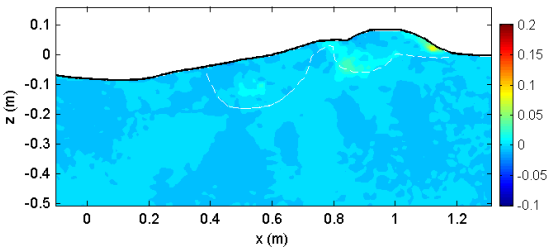

(r) t = 0.69 s (-$u'w'$)

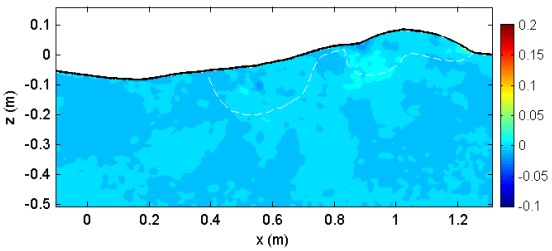

(s) t = 0.75 s (-$u'w'$)

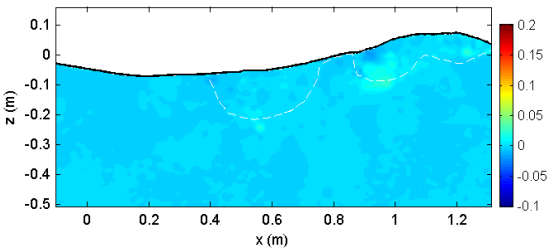

(t) t = 0.82 s (-$u'w'$)

Fig. 10.22 (Continued).

As shown Fig. 10.22(c)-(f), as the momentum of the first roller is gradually decreased, high positive stress occurs at the water spray impinging location due to the downward turbulence momentum of the water spray impingement from the fully developed first splash-up. Due to the continuous water spray impingement onto the front trough, the accumulated mixture roller occurs near x = 0.6 m and its size is gradually increased without significant horizontal momentum. The water spray impinges onto the accumulated roller continuously. Therefore, the positive Reynolds stress occurs at the water spray impinging region for a long time. This can be seen in Fig. 10.22(e)-(n). The maximum stress can be seen between x = 0.6 and 0.8 m for about 0.2 s. The location of the maximum stress becomes higher due to the increased size of the accumulated roller. There is a second impingement by the new ascending crest at the end of the water spray impingement [Fig. 10.22(j) and (k)]. A negative stress can also be seen at the second splash-up process as shown in Fig. 10.22(l) and (m). As shown in Fig. 10.22(l)-(t), after the second splash-up, the Reynolds stress is suddenly decreased.

Fig. 10.23 shows the maximum positive and negative Reynolds stress and the magnitude normalized by C^2. Three local maxima are found for the positive Reynolds stresses. The first maximum occurs at the first impingement during the beginning of the first splash-up process, and the second maximum occurs at the water spray impingement from the fully developed first splash-up around $t = 0.3T$. The positive Reynolds stress has the maximum value during this process for the entire flow. The third local positive maximum occurs at the second impinging onto the accumulated roller around $t = 0.47T$. The negative maximum stress occurs at the splash-up water just before the first splash-

up is fully developed.

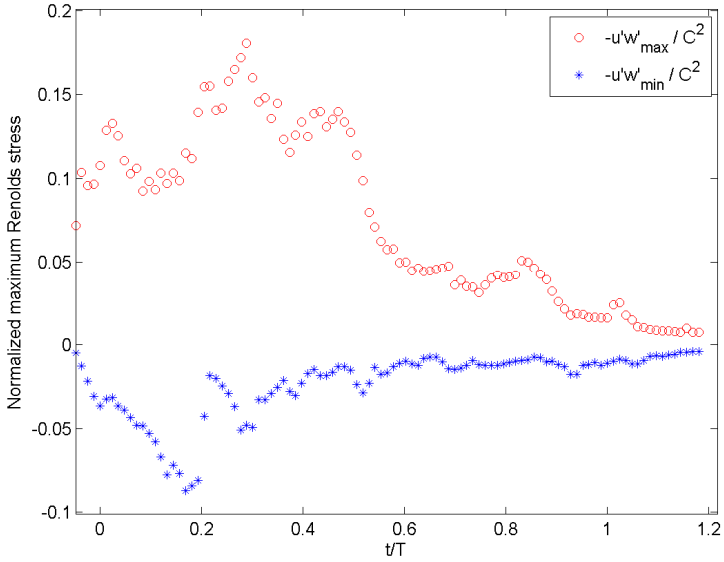

Fig. 10.23 Normalized maximum Reynolds stress (normalized by C^2).

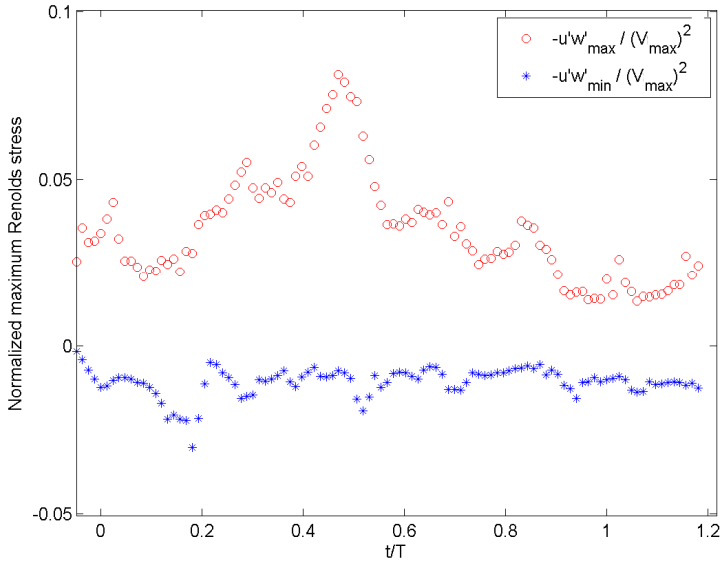

Fig. 10.24 Normalized maximum Reynolds stress (normalized by V_{max}^2).

Fig. 10.24 shows the maximum positive and negative Reynolds stress which was normalized by the square of the maximum speed at each phase. When compared with results from Fig. 10.23, the maximum positive Reynolds stress occurs at the second impingement at about $t = 0.47T$. This is because the maximum speed at the second impingement is much lower than that at the first impingement and the first splash-up. Local maximum negative stress can be seen around $t = 0.52T$, representing the second splash-up followed by the second impingement.

10.3.2 Temporal Analysis of Reynolds Stress

Temporal analysis for the Reynolds stress is presented in this section. Fig. 10.25 shows the time series of the Reynolds stress at a station. The locations of the six stations are identical as presented in Section 10.2.2. Fig. 10.26 shows the time-averaged and maximum Reynolds stresses at a station, which is presented in Fig. 10.25. Fig. 10.27 shows the comparison of the time-averaged and maximum stresses at several stations. The location of the station in Fig. 10.25(a) and Fig. 10.26(a) is near the beginning of the first splash-up. Weak positive stress can be seen at the weak water spray impinging before the first splash-up is fully developed. High positive stress is generated in the first roller. Negative stress is generated in the splash-up region as shown in Fig. 10.27(d). Positive stress is increased due to large horizontal and downward momentum of the water spray from the developed second roller. On the other hand, the stress in the first impinging roller is decreased when waves passes through the station located at $x = 0.435$ m and the negative stress is very weak as shown in Fig. 10.25(b) and Fig. 10.26(b) .

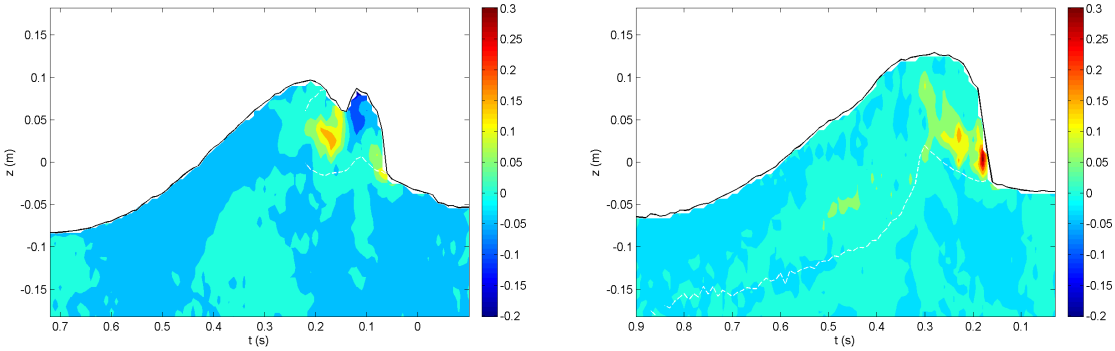

(a) x = 0.198 m (-$u'w'$)

(b) x = 0.435 m (-$u'w'$)

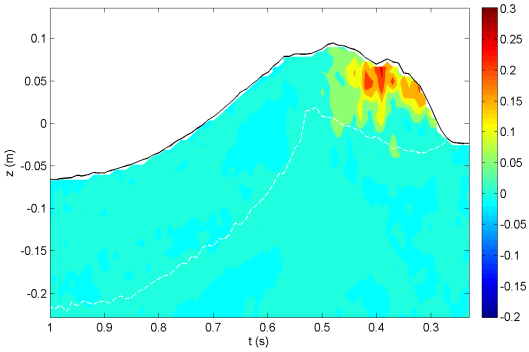

(c) x = 0.649 m (-$u'w'$)

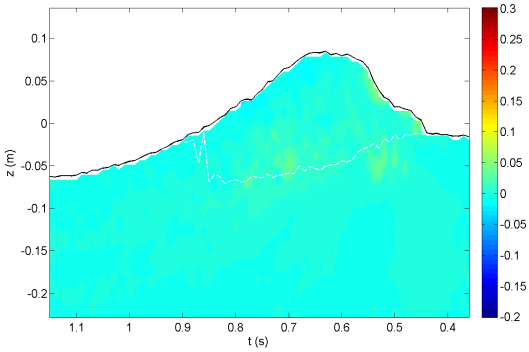

(d) x = 0.880 m (-$u'w'$)

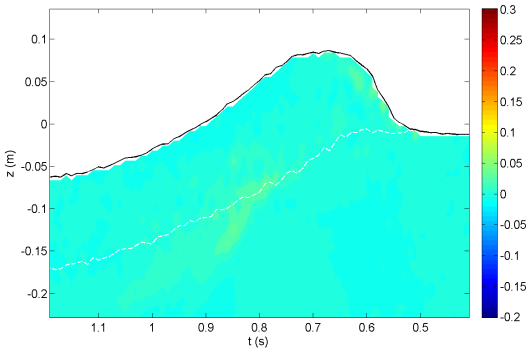

(e) x = 0.967 m (-$u'w'$)

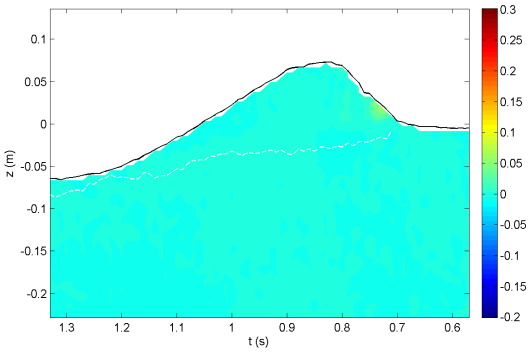

(f) x = 1.204 m (-$u'w'$)

Fig. 10.25 Time series of Reynolds stress at a station (unit: m^2/s^2).

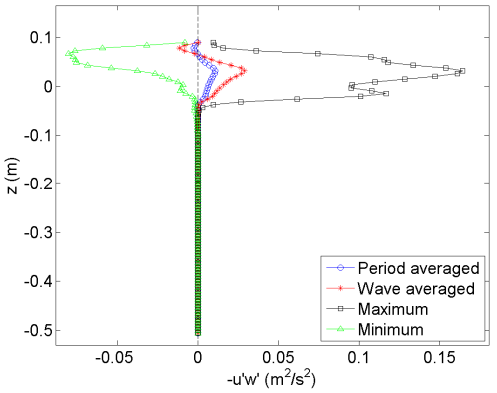

(a) x = 0.198 m

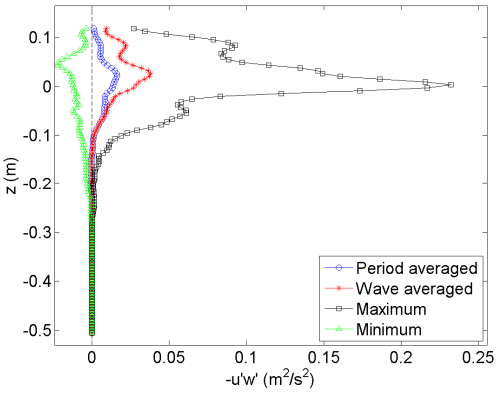

(b) x = 0.435 m

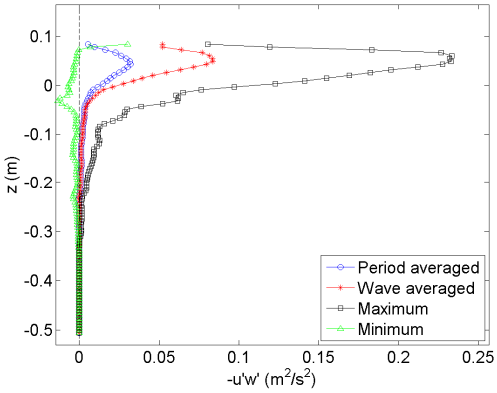

(c) x = 0.649 m

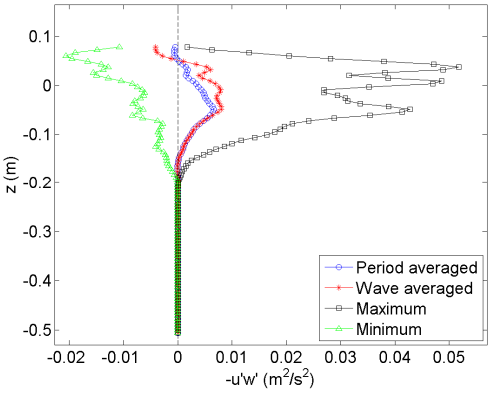

(d) x = 0.880 m

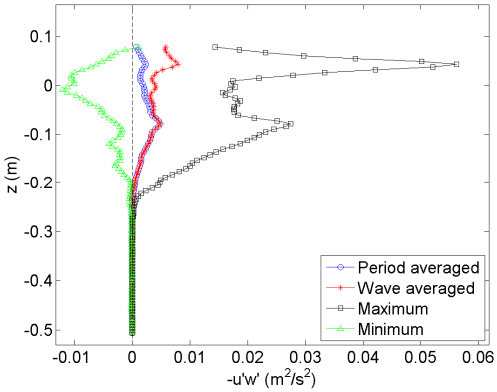

(e) x = 0.967 m

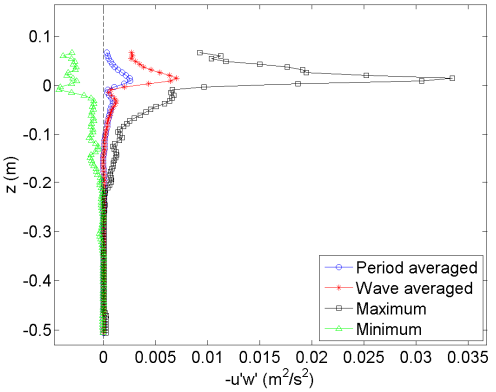

(f) x = 1.204 m

Fig. 10.26 Time-averaged, maximum, and minimum $-u'w'$ at a station (unit: m^2/s^2).

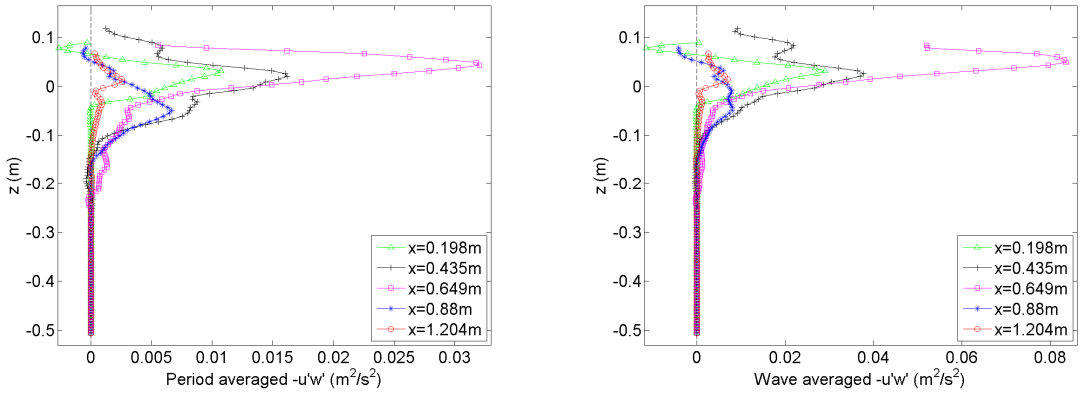

(a) period-averaged $-u'w'$ (b) wave-averaged $-u'w'$

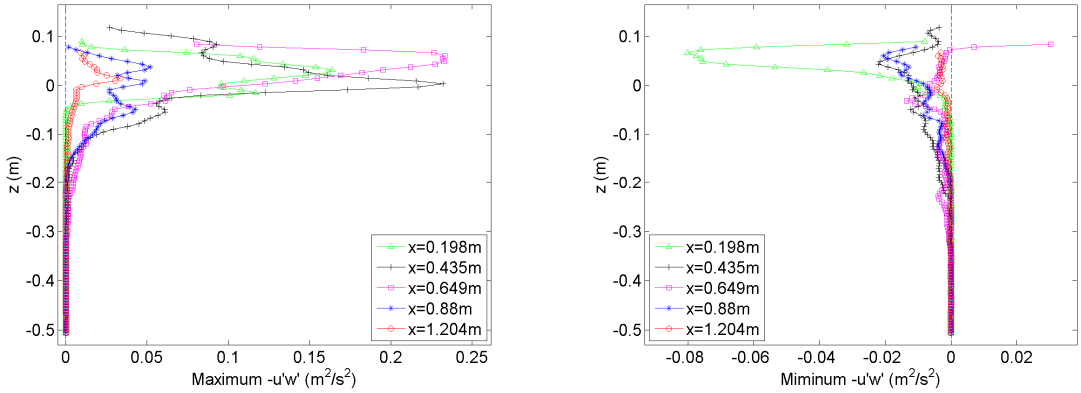

(c) maximum $-u'w'$ (d) minimum $-u'w'$

Fig. 10.27 Comparison of time-averaged, maximum, and minimum $-u'w'$ at a station (unit: m^2/s^2).

As shown in Fig. 10.25(c), Fig. 10.26(c) and Fig. 10.27, large positive stress passes through the station located at x = 0.649 m. The second impingement followed by a continuous water spray impingement occurs near the station. Although the maximum positive stress is similar to the maximum at x = 0.435 m, the period-averaged stress is much higher than the other region as shown in Fig. 10.27. The Reynolds stress is suddenly decreased just after the beginning of the second splash-up. The station at x = 0.88 m where the fully developed second splash-up passes has a low Reynolds stress as

shown in Fig. 10.27(a). In addition, a much smaller stress is generated at x = 1.204 m where the fully developed third splash-up passes.

Fig. 10.28 shows the normalized time-averaged and maximum Reynolds stresses at each point in the entire flow field. The Reynolds stresses were normalized by C^2. It is clearly seen from the wave-averaged Reynolds stress that the negative stress occurs due to the first splash-up and the positive stress is dominant through a wave cycle between x = 0.5L and 0.6L due to the water spray impingement and the second impingement. In addition, the period-averaged Reynolds stress has a maximum value near this region.

As shown in Fig. 10.28, most shear stresses are generated above the trough level, with much lower stresses under the trough level. Compared with other regions, much higher positive stresses are generated between x = 0.5L and 0.6L due to the continuous impingement of water spray. As discussed in 10.3.1, when the primary wave passes through this location, high Reynolds stress are generated above the mean water level through a local wave period [Fig. 10.22(e)-(n)].

Fig. 10.29 shows an example of the full depth extension of the period-averaged Reynolds stress for a station. It is required to obtain depth-integrated or depth-averaged Reynolds stress as shown in Fig. 10.31. Like other measurement quantities, the Reynolds stresses are almost zero between z = - 0.4 m and - 0.8m (bottom). Therefore, the Reynolds stresses from z = - 0.51 m to - 0.8 m were obtained using linear interpolation.

The maximum Reynolds stresses at each station can be seen in Fig. 10.30. The positive and negative maximum stresses occur around x = 0.5L and x = -0.25L. Note that the stresses were normalized by C^2.

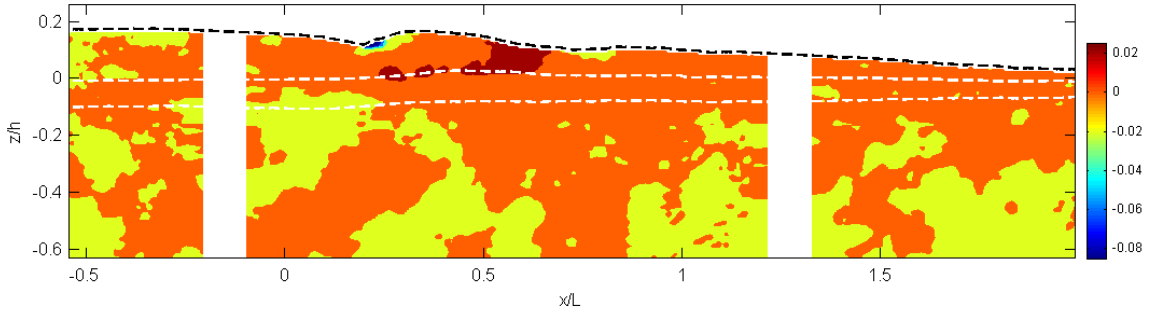

(a) wave-averaged $-u'w'$ ($-u'w'/C^2$)

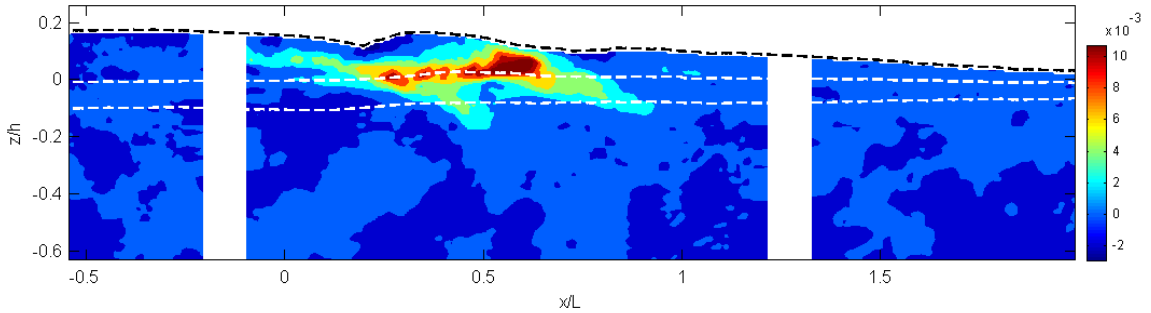

(b) period-averaged $-u'w'$ ($-u'w'/C^2$)

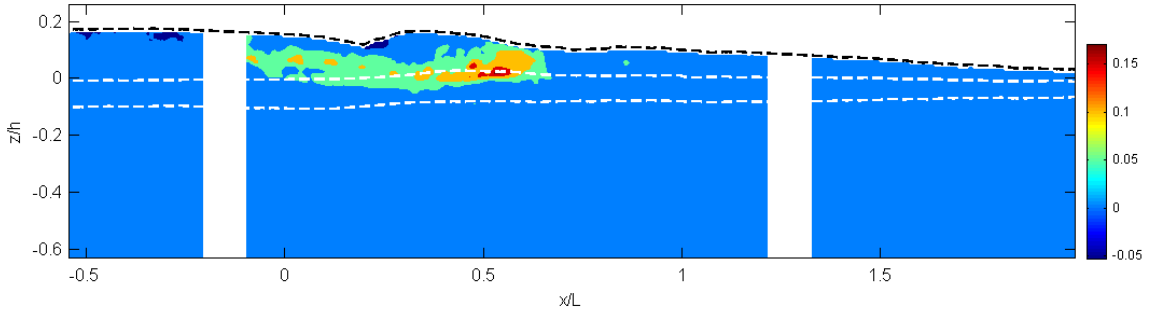

(c) maximum $-u'w'$ ($-u'w'/C^2$)

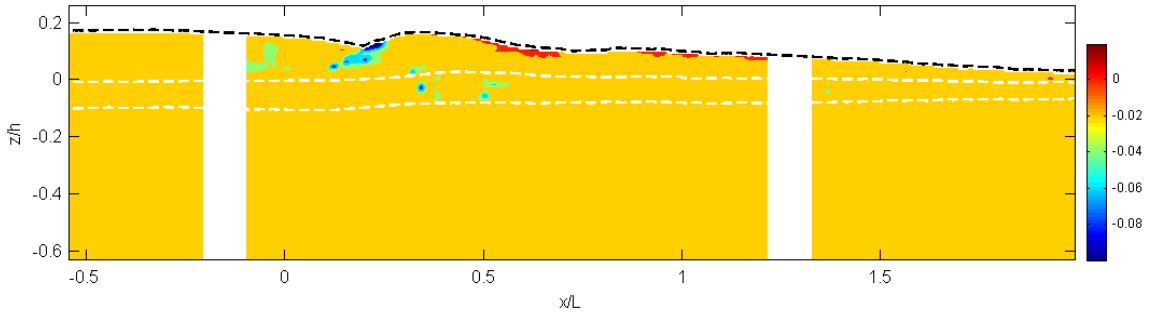

(d) minimum $-u'w'$ ($-u'w'/C^2$)

Fig. 10.28 Normalized time-averaged and maximum Reynolds stress ($-u'w'/C^2$).

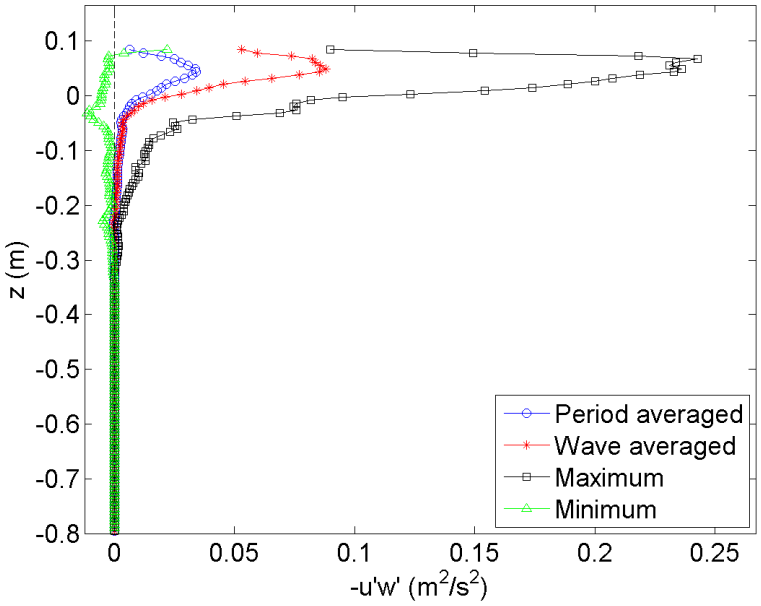

Fig. 10.29 Example of full depth extension of Reynolds stress (unit: m^2/s^2).

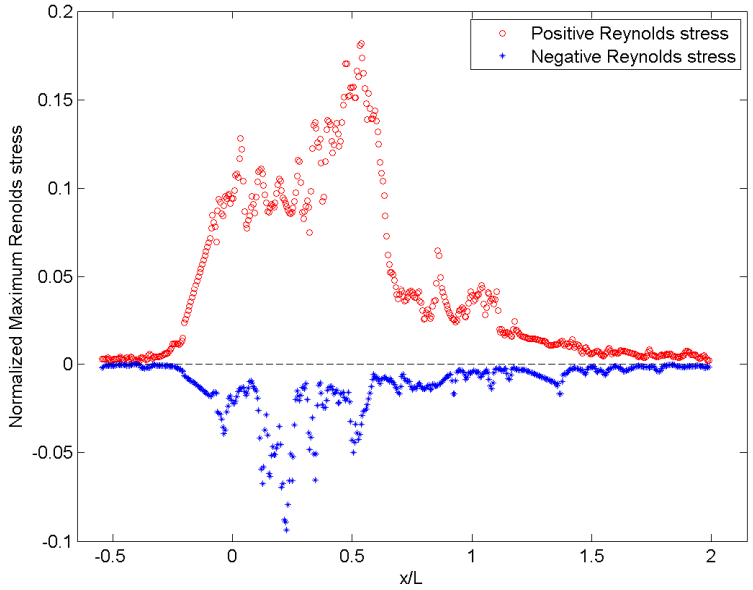

Fig. 10.30 Normalized maximum positive negative Reynolds stress ($-u'w'/C^2$).

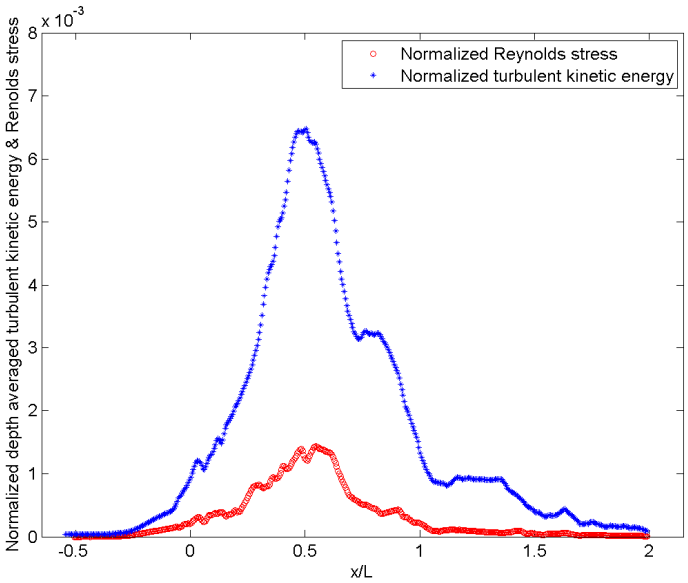

Fig. 10.31 Depth-averaged Reynolds stress and turbulent kinetic energy (normalized by C^2).

The depth-averaged time mean Reynolds stress (red circles) has the maximum near $x = 0.55L$ and the depth-averaged time mean kinetic energy (blue asterisks) is also presented for comparison.

10.4 Turbulent Kinetic Energy

As discussed in Section 10.2, fluctuating horizontal velocity mainly occurs at the bottom boundary of the aerated region where shear stresses occur between high speed roller and water under the trough region of water wave. High fluctuating velocity in the vertical direction occurs at between two rollers (one is the impinging roller and the other is the splash-up roller) due to the vertical shear. Turbulent kinetic energy is determined by the intensities of the turbulent velocities in both direction as shown in Eq. (10.2).

10.4.1 Spatial Analysis of Turbulent Kinetic Energy

Turbulent kinetic energy at the beginning of the splash-up followed by the first impingement can be shown in Fig. 10.32. Significant turbulent kinetic energy is generated near the ascending crest. The front water is pushed up and the newly ascending water crest, which will cause the second impingement later, is generated when the overturning water jet impinges onto the front water. The surface of the ascending crest is splashed up with the form of the water spray and causes the turbulence.

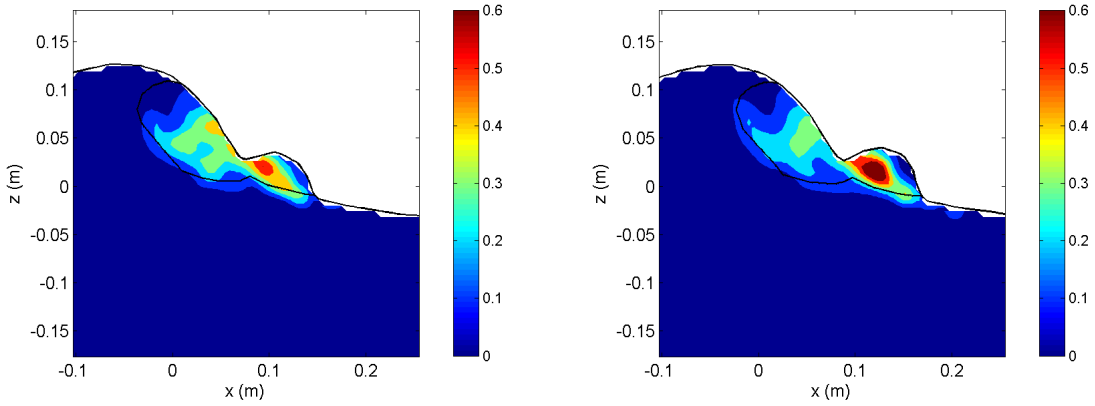

(a) t = 0.04 s (k) (b) t = 0.05 s (k)

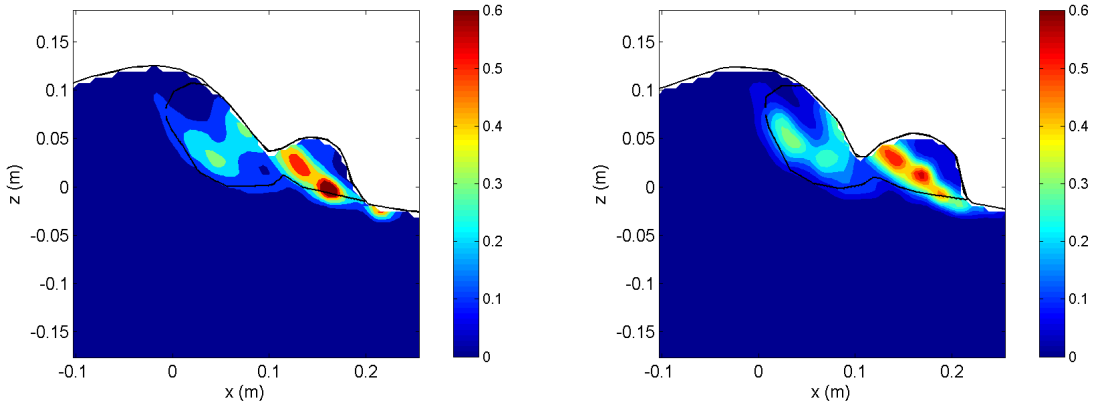

(c) t = 0.06 s (k) (d) t = 0.07 s (k)

Fig. 10.32 Turbulent kinetic energy at the beginning of the first splash-up (unit: m^2/s^2).

Another dominant location where turbulent kinetic energy is generated is between the impinging jet and the left side of the ascending crest. Vertical fluctuation is more dominant in this region. Fig. 10.33 shows the turbulent kinetic energy variation in time. As shown in Fig. 10.32 and Fig. 10.33, most turbulence is generated near the bottom boundary of the aerated region. The turbulent energy has received energy from the continuously generated shear flows between the aerated region and the water surface below the aerated region. The dominant location where the turbulent kinetic energy is generated by horizontal and vertical fluctuation is slightly different from each other as shown in Fig. 10.2. As the second roller which is the first splash-up roller is gradually developed by obtaining energy from the impinging roller, significant turbulent kinetic energy is generated at the impinging water spray region while turbulence energy is gradually dissipated in the first impinging roller. The dominant locations of the generated turbulence in both directions are close to each other. This can be seen in Fig. 10.32 and Fig. 10.33(a)-(e). Turbulent kinetic energy is generated near the toe of the second roller. Note that white dashed lines represent the boundary of the aerated region. Fig. 10.33(f)-(j) shows the turbulent kinetic energy at the process of the increment of the accumulated roller by the continuous water spray impingement. The dominant location of the turbulent kinetic energy is moved upward due to the presence of the accumulated roller. The turbulent kinetic energy is continuously generated between the impinging spray and the accumulated roller whose size and internal energy is slowly increased. During this process, mean kinetic energy is continuously decreased as shown in Fig. 9.70 and Fig. 9.71

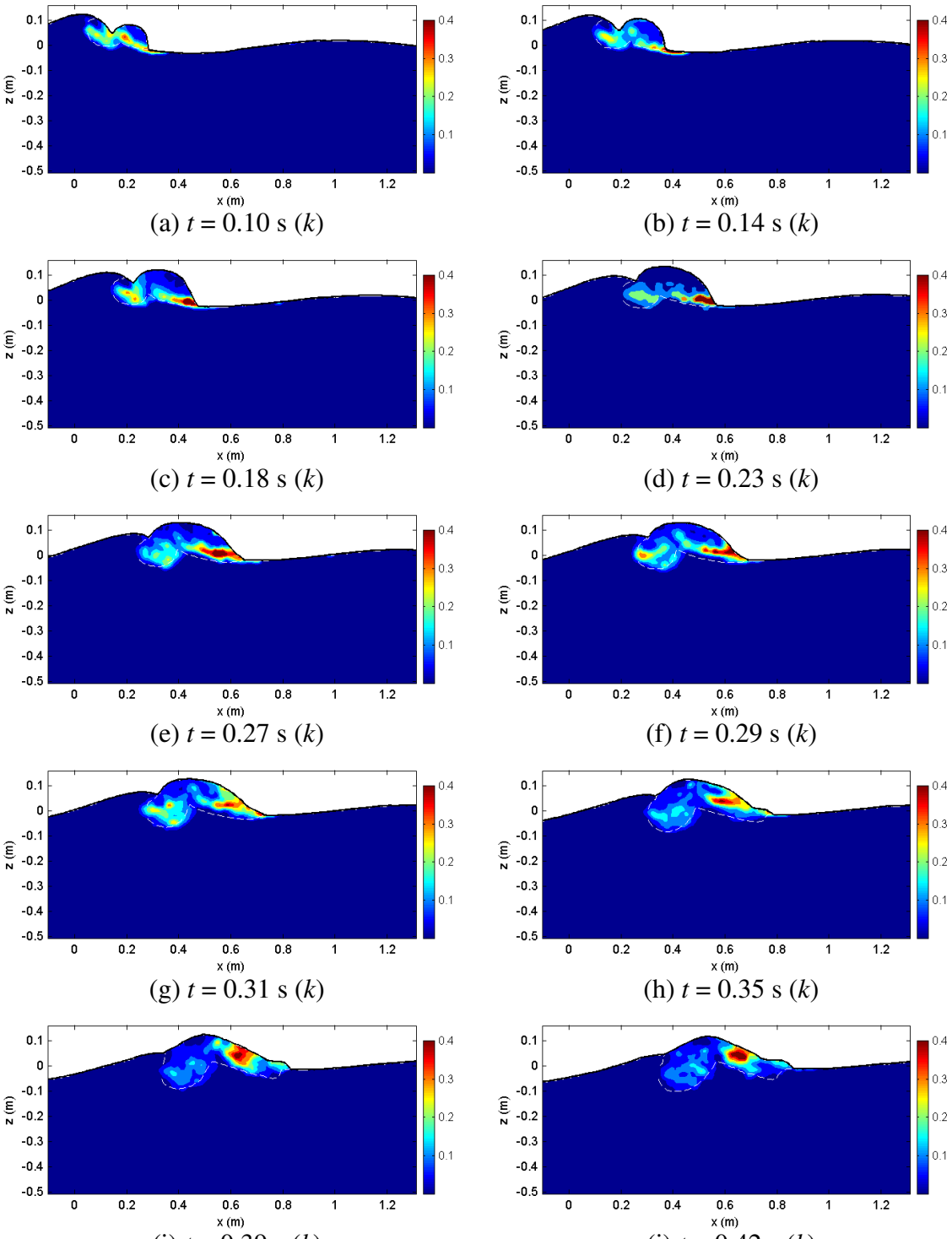

(a) $t = 0.10$ s (k)

(b) $t = 0.14$ s (k)

(c) $t = 0.18$ s (k)

(d) $t = 0.23$ s (k)

(e) $t = 0.27$ s (k)

(f) $t = 0.29$ s (k)

(g) $t = 0.31$ s (k)

(h) $t = 0.35$ s (k)

(i) $t = 0.39$ s (k)

(j) $t = 0.42$ s (k)

Fig. 10.33 Turbulent kinetic energy from the first splash-up (unit: m^2/s^2).

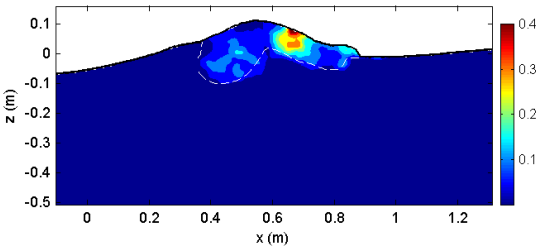

(k) t = 0.44 s (k)

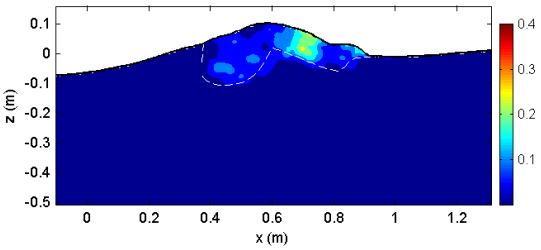

(l) t = 0.47 s (k)

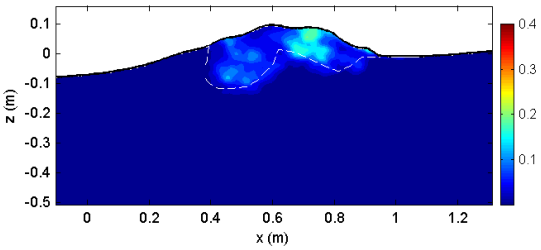

(m) t = 0.50 s (k)

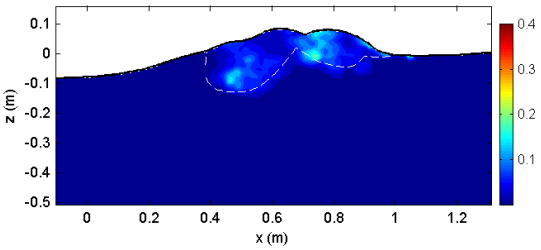

(n) t = 0.54 s (k)

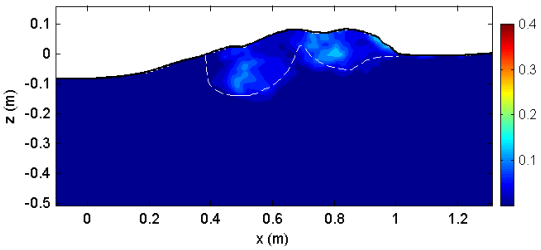

(o) t = 0.57 s (k)

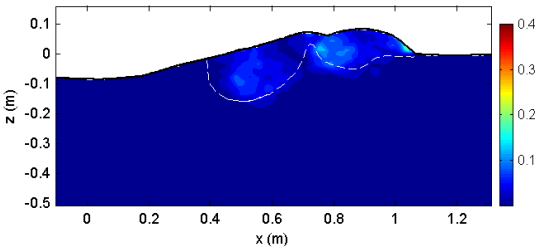

(p) t = 0.61 s (k)

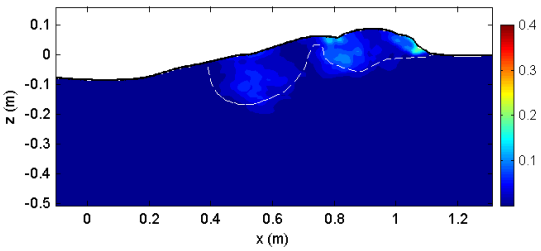

(q) t = 0.64 s (k)

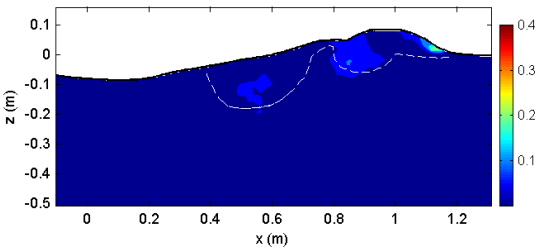

(r) t = 0.69 s (k)

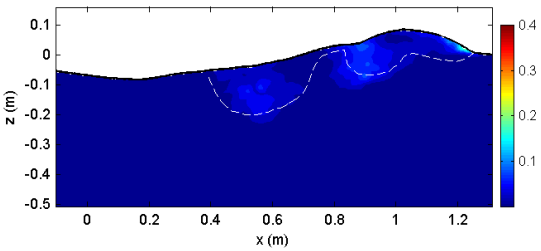

(s) t = 0.75 s (k)

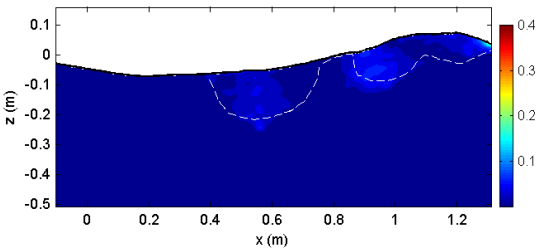

(t) t = 0.82 s (k)

Fig. 10.33 (Continued).

Fig. 10.33(j) and (k) show the turbulent kinetic energy at the moment of the second impingement by the new primary wave crest. The accumulated roller can be seen between $x = 0.7$ and $x = 0.8$ m and the roller itself does not have large kinetic energy. Fig. 10.33(l) and (m) show the turbulent kinetic energy at the beginning of the second splash-up. The left and top part of the accumulated roller is splashed up because the newly ascending crest is pushed up by the impinging jet and then it pushes up the above accumulated roller. This can be seen in Fig. 6.1(f)-(h). However, turbulent kinetic energy is not significant and is decreased when compared with that of the impinging process. From the beginning of the second splash-up, turbulent kinetic energy is gradually decreased except for a very small peak during the third impingement. Fig. 10.33(p)-(t) shows the turbulent kinetic energy at the third impingement and splash-up process.

Fig. 10.34 shows the normalized maximum turbulent kinetic energy variation in time and the magnitude normalized by C^2. This is presented with the maximum mean kinetic energy for better comparison. In addition, Fig. 10.35 shows the corresponding location when the kinetic energy has a maximum for each phase and the location for the maximum mean kinetic energy. The maximum turbulent kinetic energy is maintained with a small decrease until the second impingement, while the maximum mean kinetic energy is significantly decreased. Moreover, the decrease is continued during the second splash-up process around $t = 0.55T$, while the mean kinetic energy has a local maximum at the process. A more detailed variation can be seen in Fig. 10.5 that presents the maximum turbulence intensity in Section 10.2.1. The only difference is the magnitude scale since turbulent kinetic energy was defined as $k = \frac{1.33}{2} I^2$ in this study as shown in

Eq. (10.2).

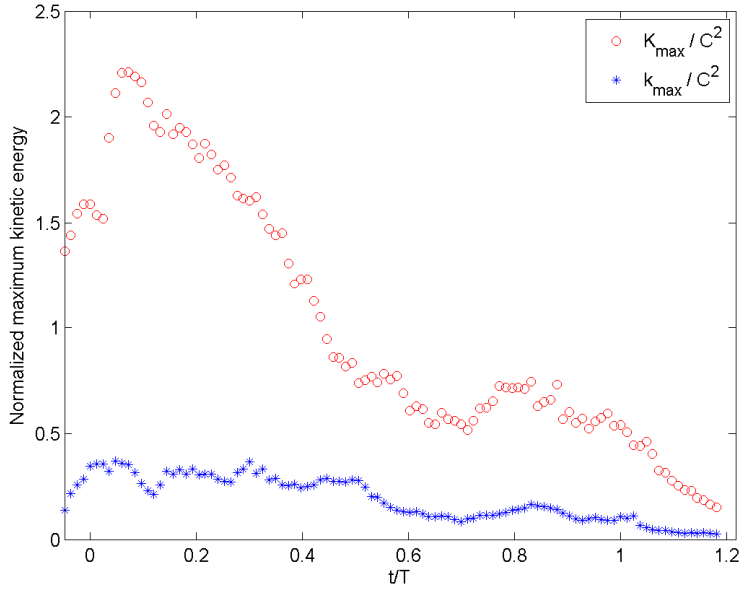

Fig. 10.34 Normalized maximum turbulent kinetic energy (with *K*).

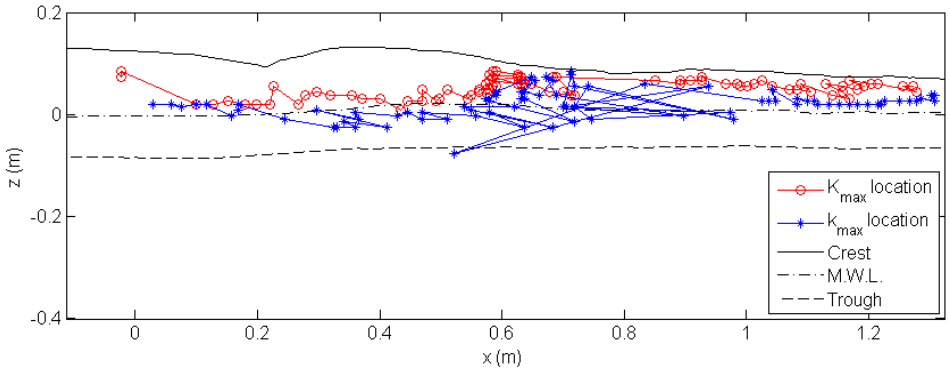

Fig. 10.35 Location of maximum kinetic energy.

As shown in Fig. 10.35, the location for the maximum turbulent kinetic energy is slightly lower than those for the mean kinetic energy. Note that the time difference

between makers is 0.01 s. The maximum mean kinetic energy always occurs above the mean water level. Most locations for the mean kinetic energy are near the crest. However, the maximum mean kinetic energy occurs near the mean water level during the first splash-up process. This is because the location of the maximum occurs near the toe of the second roller where the water spray impinges onto the trough region of the front wave. For the same reason, the maximum turbulent kinetic energy occurs between the mean water level and the trough level during the first splash-up. Since turbulent kinetic energy is significantly decreased after the second impingement, the location of turbulent kinetic energy is fluctuating between the impinged first roller and progressing roller.

The maximum values of the correlation between kinetic energy and mean flow that represents the transport of turbulent kinetic energy by mean flow can be seen in Fig. 10.36 and Fig. 10.37 with the magnitudes normalized by C^3. Each figure represents kinetic energy transport by the horizontal and vertical mean flow, respectively. Since the positive horizontal momentum is dominant, the trend of the maximum kU is close to that of the maximum horizontal velocity as shown in Fig. 9.31 but with fluctuating value due to turbulent kinetic energy. The minimum kU is very close to zero. In addition, the maximum and minimum kW have a similar trend with the maximum and minimum vertical mean velocity as shown in Fig. 9.31.

Fig. 10.38 and Fig. 10.39 show the location of the maximum and minimum of kU and kW. The time difference between two markers is 0.01 s. In the case of the maximum locations, the location for the maximum kU is closer to the maximum k location at $x <$

0.6L and is closer to the maximum U at $x > 0.6L$. On the other hand, the locations for the maximum and minimum kW are closer to the maximum and minimum W in the entire region. More discussion will be presented in 10.4.2, which provides results from temporal analysis of turbulent kinetic energy.

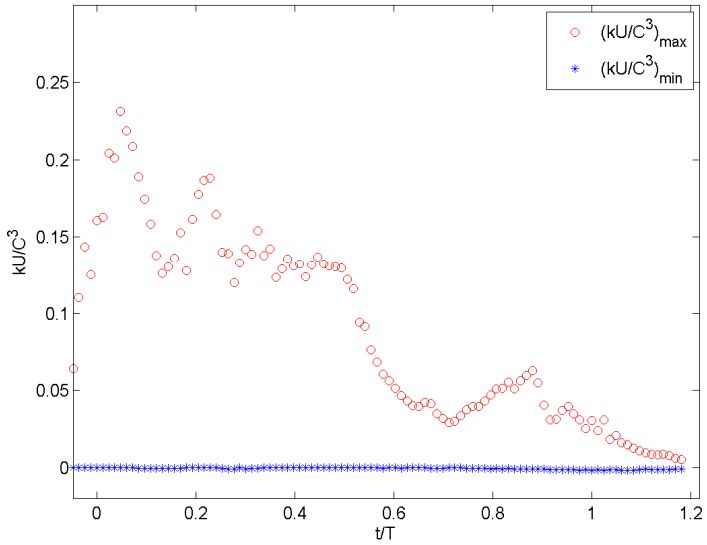

Fig. 10.36 Normalized maximum and minimum kU (kU/C^3).

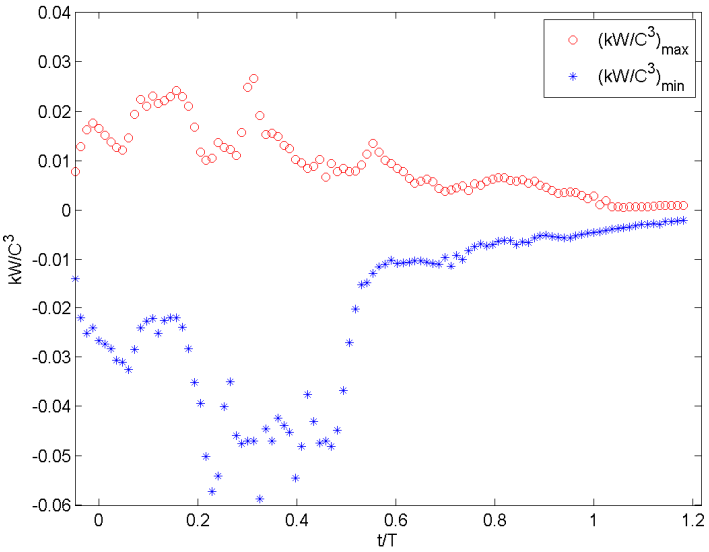

Fig. 10.37 Normalized maximum and minimum kW (kW/C^3).

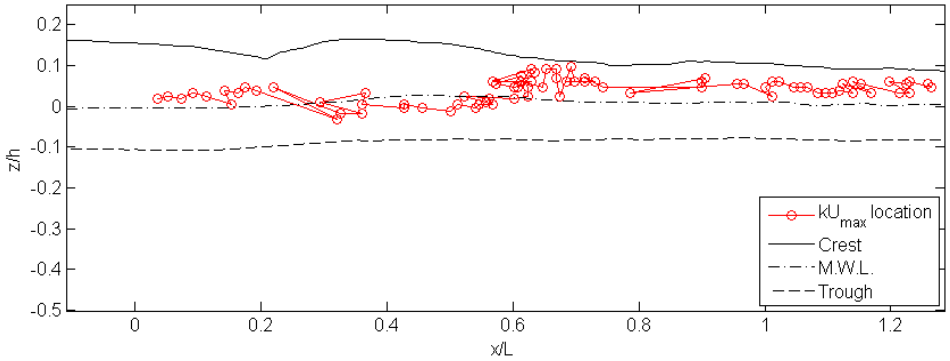

Fig. 10.38 Location of maximum *kU*.

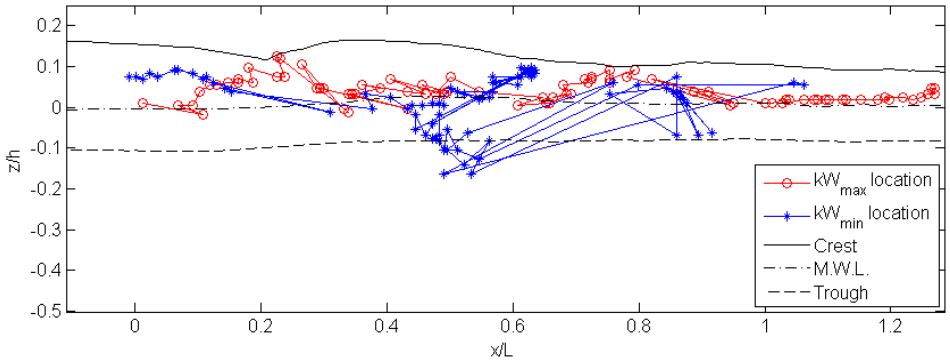

Fig. 10.39 Location of maximum *kW*.

10.4.2 Temporal Analysis of Turbulent Kinetic Energy

Temporal analysis for turbulent kinetic energy is presented in this section. Fig. 10.40 shows the time series of the turbulent kinetic energy at six stations. These six stations were chosen among 475 stations. The location of the stations are described in previous Sections 10.2.2 and 10.3.2.

Fig. 10.41 shows the time-averaged, maximum, and minimum turbulent kinetic energy at six stations and Fig. 10.42 shows the comparisons of each value.

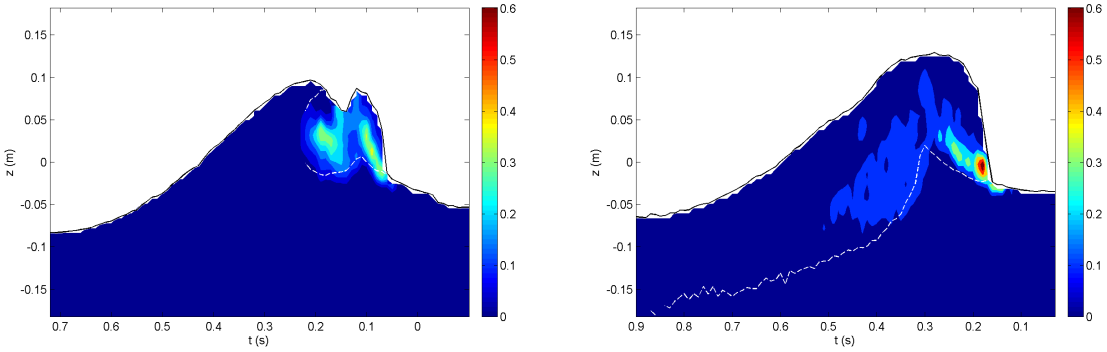

(a) x = 0.198 m (k)

(b) x = 0.435 m (k)

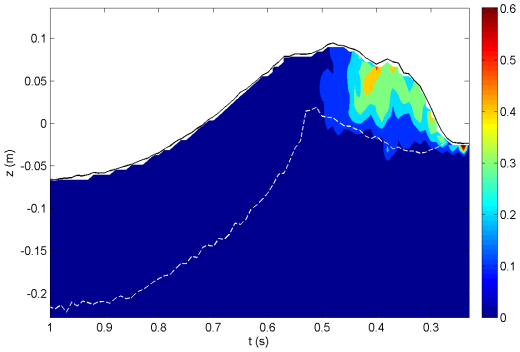

(c) x = 0.649 m (k)

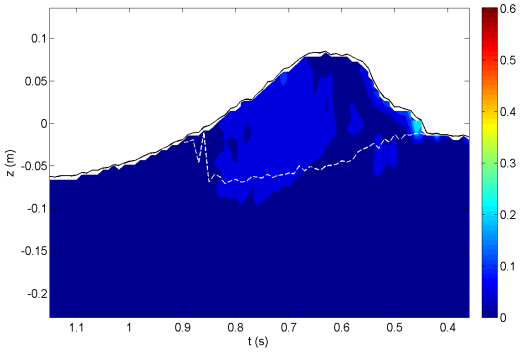

(d) x = 0.880 m (k)

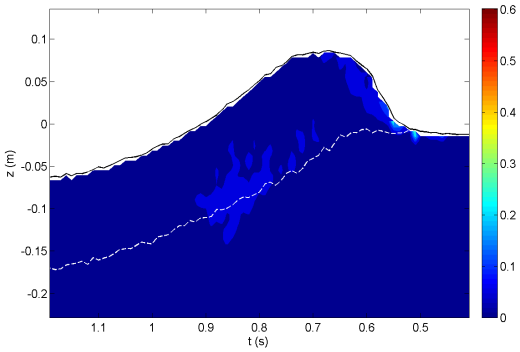

(e) x = 0.967 m (k)

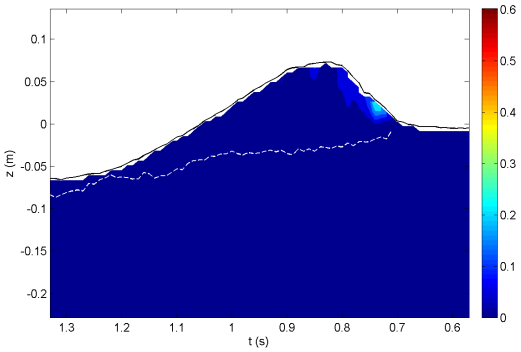

(f) x = 1.204 m (k)

Fig. 10.40 Time series of k at a station (unit: m^2/s^2).

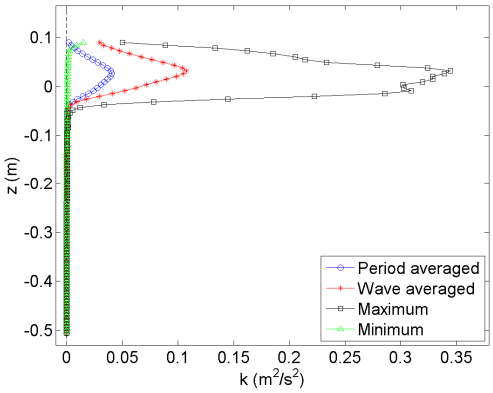

(a) x = 0.198 m

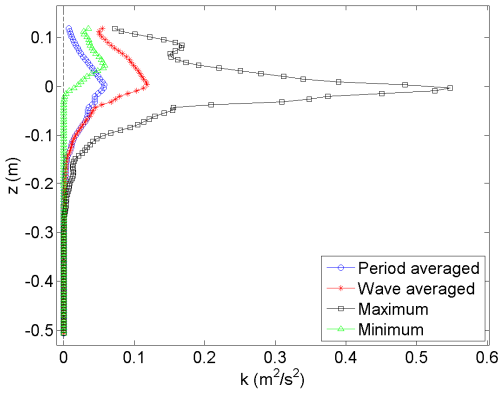

(b) x = 0.435 m

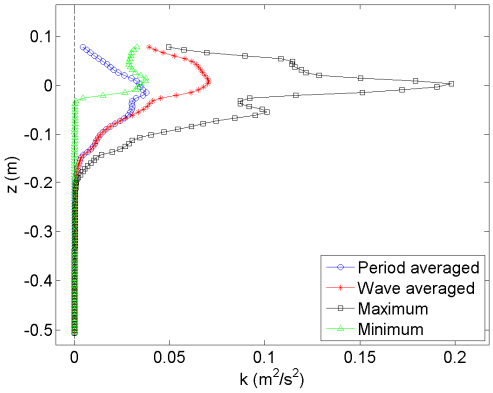

(c) x = 0.649 m

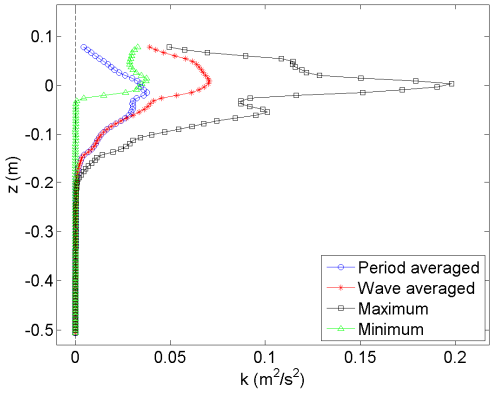

(d) x = 0.880 m

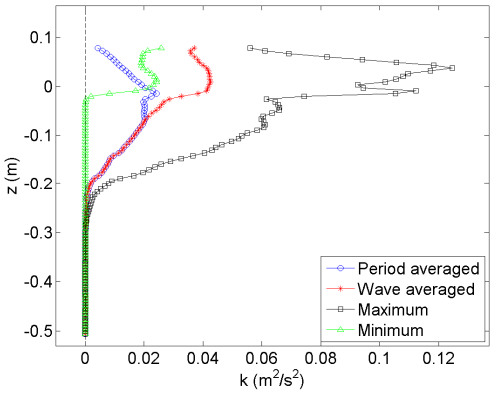

(e) x = 0.967 m

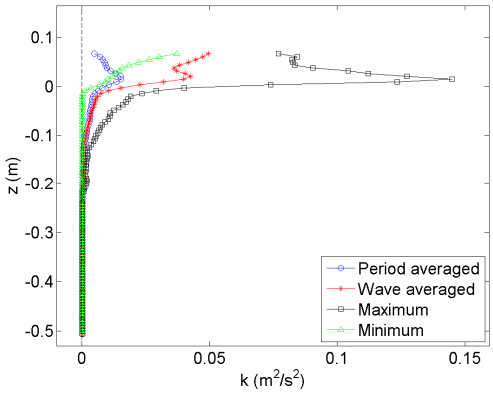

(f) x = 1.204 m

Fig. 10.41 Time-averaged, maximum, and minimum k (unit: m^2/s^2).

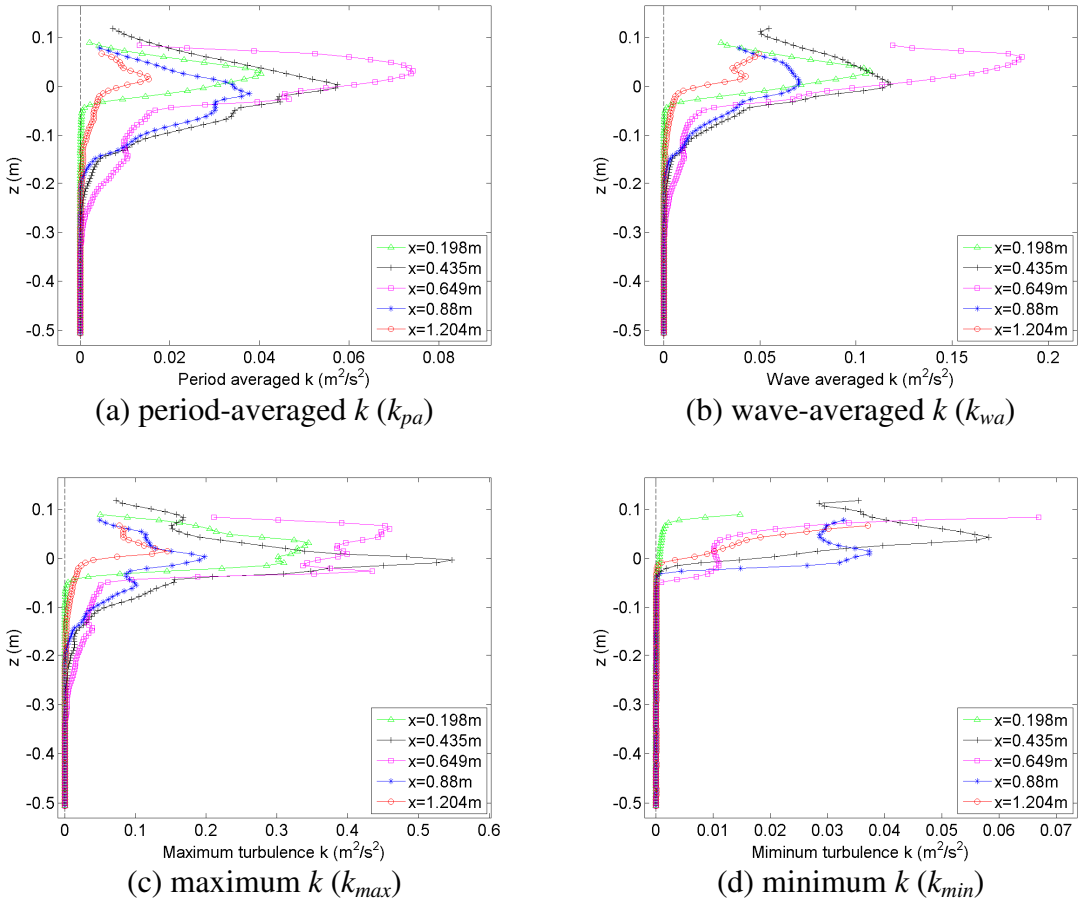

(a) period-averaged k (k_{pa}) (b) wave-averaged k (k_{wa})

(c) maximum k (k_{max}) (d) minimum k (k_{min})

Fig. 10.42 Comparison of time-averaged, maximum, and minimum k (unit: m^2/s^2).

As shown in Fig. 10.40(a) and Fig. 10.42(a), compared with the high maximum turbulent kinetic energy, the period-averaged value at the beginning of the first splash-up (x = 0.198 m) is much smaller than those at other stations located near the fully developed first splash-up (x = 0.435 m) and near the second impinging (x = 0.649 m). It can be seen in Fig. 10.42(d) that the minimum value at x = 0.198 m is much smaller than those from other stations due to the rear part of the impinging wave had a small turbulent kinetic energy. The turbulent kinetic energy has a maximum at the station located in x =

0.435 m. However, both the wave- and period-averaged turbulent kinetic energies have a maximum at x = 0.649 m. As discussed in Section 10.4.1, the turbulent kinetic energy suddenly decreases after the second impingement. As shown in Fig. 10.42, the maximum magnitude of the period-averaged values at the second splash-up (x = 0.88 m) is similar to that at the beginning of the first splash-up (x = 0.198 m) and the averaged turbulent kinetic energy at the third splash-up (x = 1.204 m) has a much smaller value. In Fig. 10.41, the wave-averaged (red) and period-averaged (blue) quantities must be identical below the trough level by the definition shown in Eqs. (9.4) and (9.5). Therefore, it is good to see how much turbulent kinetic energy is transported under the trough level.

Fig. 10.43 shows turbulent kinetic energy for all 475 stations with the magnitudes normalized by C^3. Fig. 10.43(a) and (b) show the wave-averaged and period-averaged turbulent kinetic energies while Fig. 10.43(c) and (d) show the maximum and minimum turbulent kinetic energies at each point. The number of points in each contour is 55100 (475 × 116) and the time resolution for the time averaging value is 0.01 s.

Both wave-averaged and period-averaged turbulent kinetic energies have the maximum near $x = 0.6L$, above the mean water level. As mentioned in Section 10.2.2, the period-averaged turbulent kinetic energy is high along the mean water level, approximately between $x = 0.2L$ and $0.8L$, while the maximum averaged turbulent kinetic energy occurs between x = 0 and $0.6L$. At the region between x = 0 and $0.2L$, the second roller for the first splash-up passes through the region before the second roller is fully developed and the first impinging roller passes. Although both rollers have high turbulent kinetic energy, it is compensated by low turbulent kinetic energy in the rear

water wave. It can be seen in Fig. 10.2 that the aerated first roller covers only the front wave from the crest while no aerated region in the rear wave. On the other hand, maximum turbulent kinetic energies between $x = 0.6L$ and $0.8L$ are low compared with those between $x = 0$ and $0.6L$. This is because the turbulent roller passes through the region in a wave period such as the second splash-up roller, the second impinging roller and the right side of the first impinging roller. A wide distribution of turbulent kinetic energy throughout the vertical station can be found near $x = 0.5L$ and $0.9L$ due to the first and second impinging rollers.

Fig. 10.44 shows the maximum turbulent kinetic energy at each station. In addition, the maximum mean kinetic energy was added in the figure for better comparison between mean and turbulent kinetic energies. Both maximum kinetic energies were normalized by C^2. The maximum turbulent kinetic energy generated from the first impingement is maintained with similar magnitude until about $x = 0.6L$ where the second impingement occurs and then the magnitude begins decreasing gradually until $x = 0.9L$. There is a local peak near $x = 1.05L$ where the third impingement occurs. On the other hand, the maximum mean kinetic energy suddenly decreases from $x = 0.52L$ and a local peak is also found in the region of the third process.

To obtain the depth-averaged or depth-integrated time mean values, linear interpolation was used to obtain the turbulent kinetic energy from the lowest measurement point ($z = - 0.51$ m) to the bottom ($z = - 0.8$ m) with the assumption that the turbulent kinetic energy is zero at the bottom. The assumption is reasonable because the turbulent kinetic energy is almost zero from $z = - 0.3h$ as shown in Fig. 10.43.

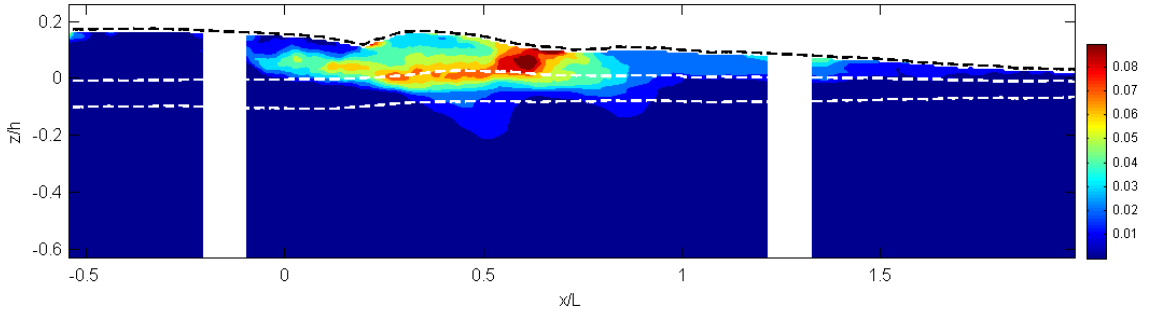

(a) wave-averaged k (k_{wa}/C^2)

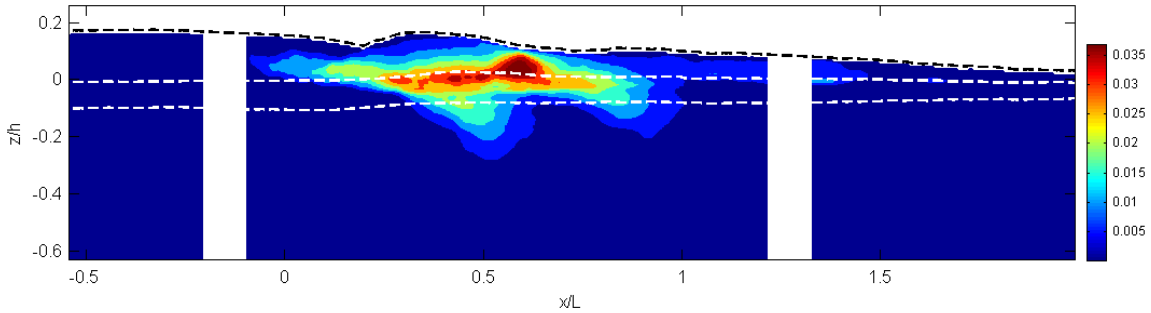

(b) period-averaged k (k_{pa}/C^2)

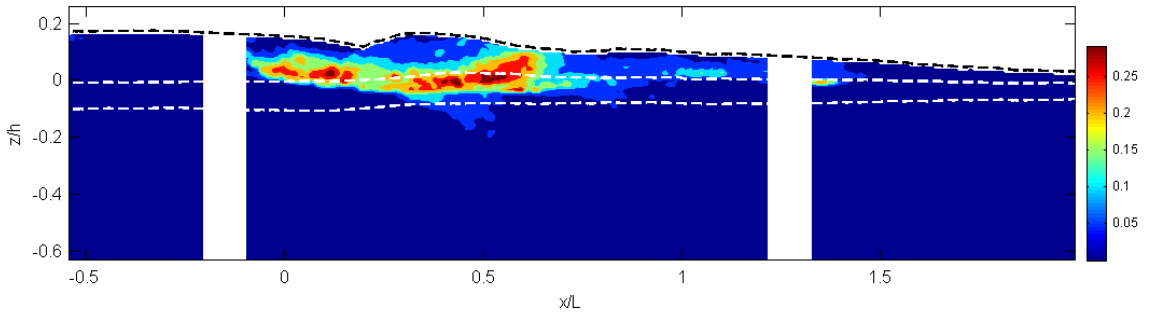

(c) maximum k (k_{max}/C^2)

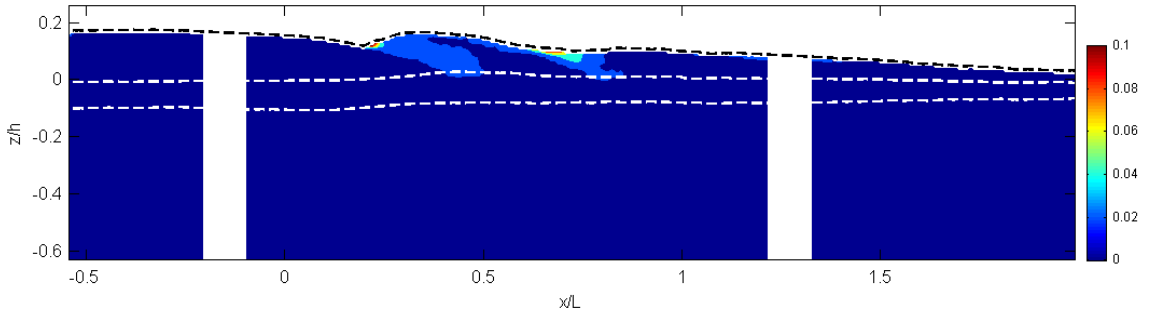

(d) minimum k (k_{min}/C^2)

Fig. 10.43 Normalized time-averaged, maximum, and minimum k (k/C^2).

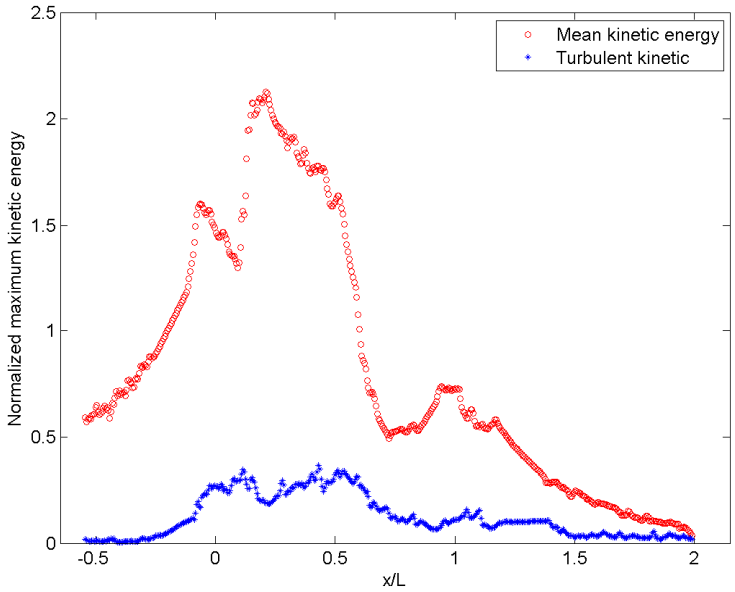

Fig. 10.44 Normalized maximum kinetic energy (normalized by C^2).

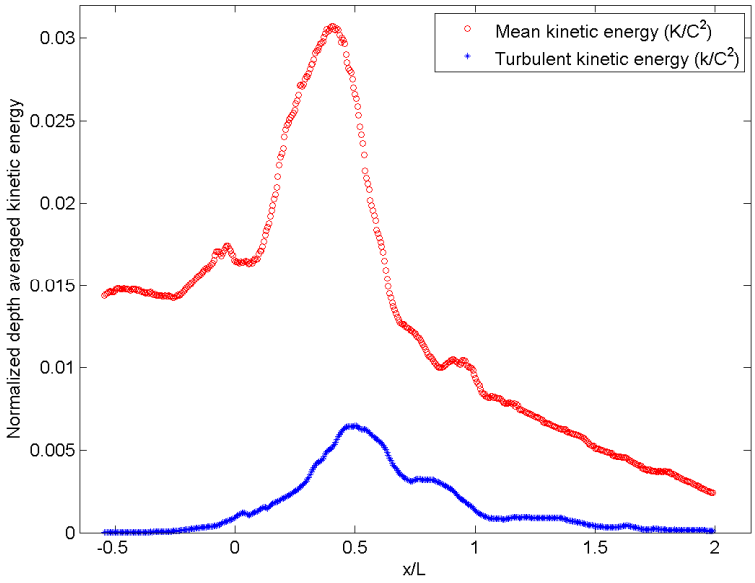

Fig. 10.45 Depth-averaged time mean kinetic energy (normalized by C^2).

Fig. 10.45 shows the depth-averaged and time mean kinetic energies, which were obtained using Eq. (9.6). The mean and turbulent kinetic energies suddenly increases from the first impingement. Both kinetic energies begin decreasing around $x = 0.5L$ (about $0.4L$ for the mean kinetic energy and $0.6L$ for the turbulent kinetic energy). A local maximum for turbulent kinetic energy is found around $x = 0.8L$ as seen in Fig. 10.43(b). The turbulent kinetic energy between $x = 0.5L$ and $0.8L$ is approximately 30% of the mean kinetic energy as shown in Fig. 10.46. Fig. 10.46 shows the ratio of the depth-averaged and period-averaged turbulent kinetic energy to the mean kinetic energy.

The magnitude of the aerated region from the impingement of the overturning jet must be overestimated due to excluding the void ratio (mixture density in the aerated region). This is especially important at the first splash-up roller (the second roller) whose void ratio is most significant in the entire breaking process. For example, without considering the void ratio, the mean kinetic energy at the fully developed first splash-up ($x = 0.42L$) is about twice as high as the mean kinetic energy before the first impingement as shown in Fig. 10.45.

The total kinetic energy was obtained by means of adding the mean kinetic energy to the turbulent kinetic energy, and is given in Fig. 10.47. The total kinetic energy at $x = 0.5L$ (near the first splash-up roller) is about 2.5 times higher than the total kinetic energy before the first impingement. Again, the magnitude of the kinetic energy in the aerated region, especially at the first splash-up, must be overestimated. It should decrease if the void ratio is applied to each point. More results and discussion including the void ratio are presented in Chapter XI.

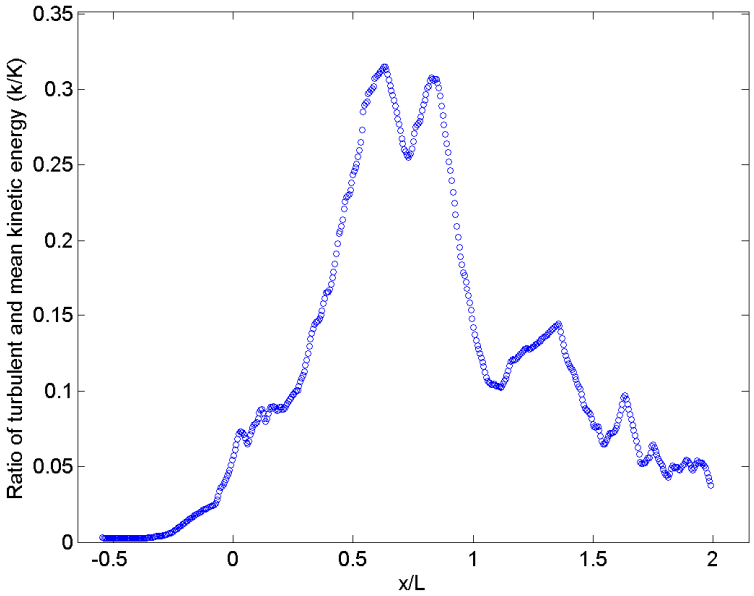

Fig. 10.46 Ratio of turbulent and mean kinetic energy ($\overline{k_{da}}/\overline{K_{da}}$).

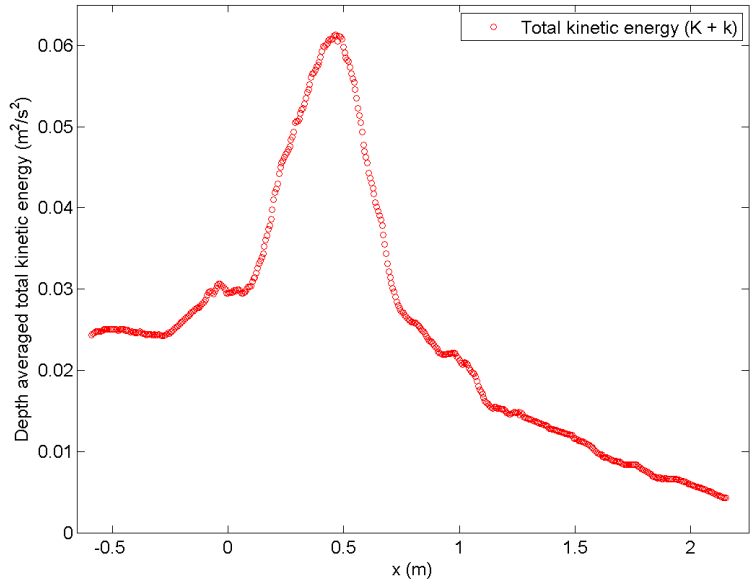

Fig. 10.47 Depth-averaged total kinetic energy ($\overline{K_{da}}+\overline{k_{da}}$).

Fig. 10.48 and Fig. 10.49 show the transport of turbulent kinetic energies by mean horizontal and vertical velocities where both wave-averaged and period-averaged magnitudes were normalized by C^3. As shown in Fig. 10.48, turbulent kinetic energy is transported near the mean water level by downstream mean flow during the first impingement and splash-up processes. After the first splash-up is fully developed, turbulent kinetic energy is transported between the crest and the mean water level due to the high horizontal momentum during the water spray impingement, the second impingement, and the second splash-up. There is a maximum transport of the turbulent kinetic energy around $x = 0.6L$ due to the continuous water spray impingement and the second impingement onto the accumulated roller.

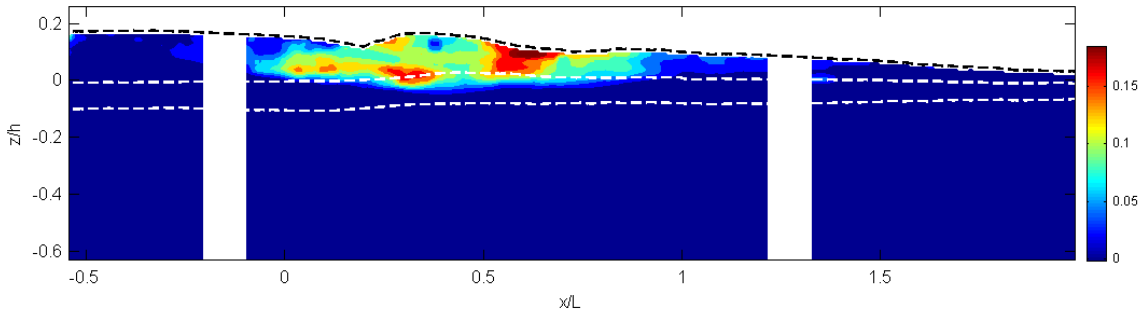

(a) wave-averaged kU (kU/C^3)

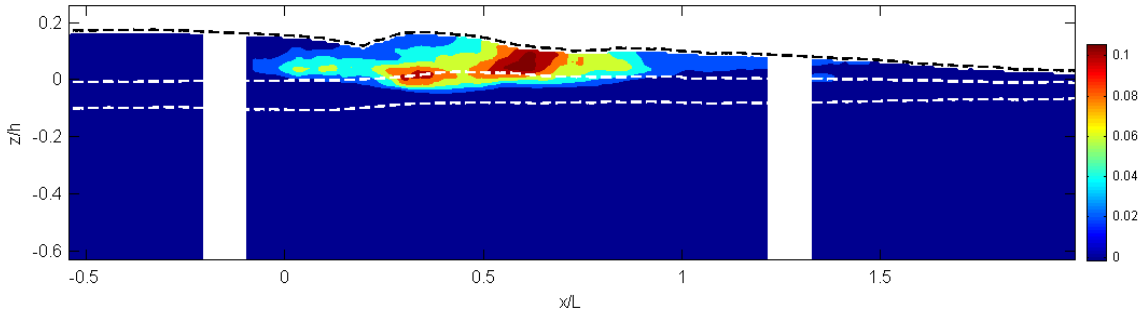

(b) period-averaged kU (kU/C^3)

Fig. 10.48 Normalized time-averaged kU/C^3.

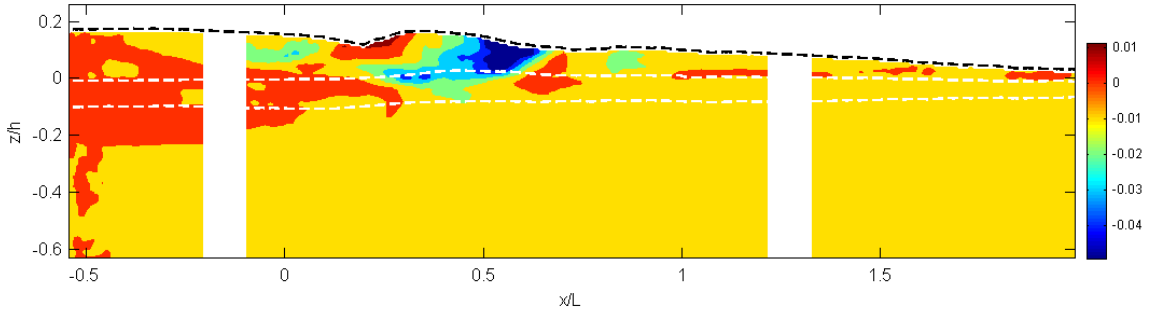

(a) wave-averaged kW (kW/C^3)

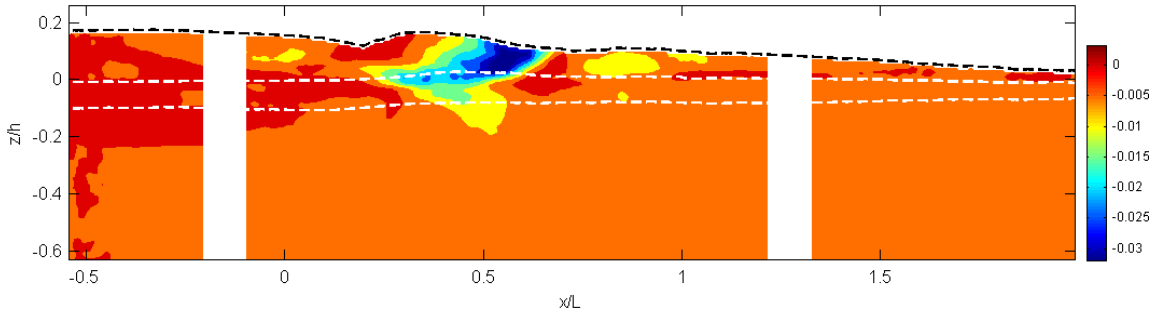

(b) period-averaged kW (kW/C^3)

Fig. 10.49 Normalized time-averaged kW/C^3.

As shown in Fig. 10.49, turbulent kinetic energy is mainly transported downward by a downward mean flow. Downward transport due to the first impinging roller is found under the mean water level between $x = 0.2L$ and $0.55L$. The maximum downward transport occurs around $x = 0.55L$ (above the mean water level) due to the continuous water spray and the second impingement. Indeed, in this region, high turbulent kinetic energy is transported downwards and in the downstream direction through the breaking process. This is the reason why the period-averaged Reynolds stress also has a high positive value in this region. Upward transport is also found although the magnitude is much smaller than the downward transport. Upward transport is found near the first and second splash-up region. In addition, it is found below the first roller because there

exists a large upward momentum below the impinging roller and the newly ascending crest although the turbulent kinetic energy in this region is small. It can be seen in Fig. 9.19 and Fig. 9.43.

CHAPTER XI

VOID RATIO AND COMPRESSIBILITY IN A PLUNGING BREAKER

11.1 Introduction

Since breaking waves are multiphase flows due to the highly aerated region, void ratio measurements are required to investigate breaking waves specifically for a strong breaker. Compared with a spilling wave, a plunging breaker has a much higher void ratio due to a repetitive processes of a splash-up followed by an impingement, especially at the first process.

Velocities obtained from the BIV and PIV measurements represent the velocities of the air-water mixture as discussed in Chapters VIII and IX. Most values such as kinetic energy, Reynolds stress, and mass flux are overestimated if the void ratio in the highly aerated region is not considered. Therefore, the mixture density considering the void ratio at each point should be applied to calculate most terms. It is found that there is a significant discrepancy when the void ratio is applied to the mean and turbulent properties. The effect of compressibility cannot be neglected since most values obtained will be substantially overestimated.

In this chapter, results of void ratio measurements using the FOR technique are presented in Section 11.2 and void ratio measurements using the BIV and PIV images are discussed in Section 11.3. Based on the results from the FOR measurements, updated

results considering compressibility are presented in the Section 11.4.

11.2 Void Ratio Measurements Using FOR

The FOR technique was used to obtain the void ratio of the highly aerated region in a plunging breaker. The experimental set up and conditions for the FOR measurements are presented in Section 5.6. Additionally, the principle and application of the FOR system are presented in Chapters III and IV.

There are three measurement stations as shown in Fig. 5.1 and Table 5.2. Each station was located in the region where each splash-up became fully developed. Fig. 11.1 shows three FOR measurement stations, which correspond to the locations of wave gauge stations 4, 5, and 6, respectively. Red dots shown in Fig. 11.1(a) represent measurement points, and the distance between points is 10 mm. Depending on the vertical range of the aerated region, the total number of measurement points was determined at each station. The total number of measurement points at each station is 19, 12 and 7, respectively. Twenty measurements were repeated at a point to obtain the mean void ratio. The vertical range at each station is z = - 0.06 m to 0.12 m, - 0.04 m to 0.07 m, and 0 to 0.06 m, respectively. The measurements at the location below the lowest point for each station were performed to verify that the void ratio was nearly zero at that position. It can be seen from the measurement points that the roller size and the depth of the aerated region decrease.

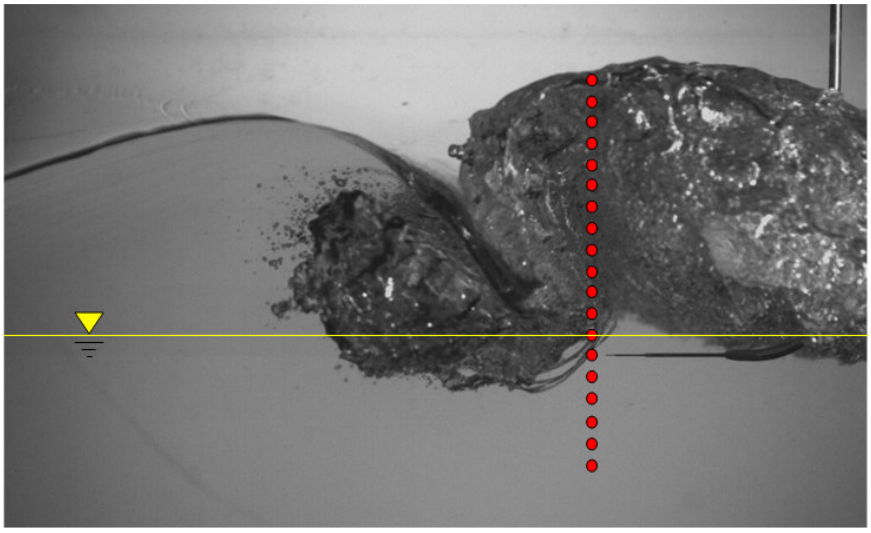

(a) FOR station 1 (FOR1)

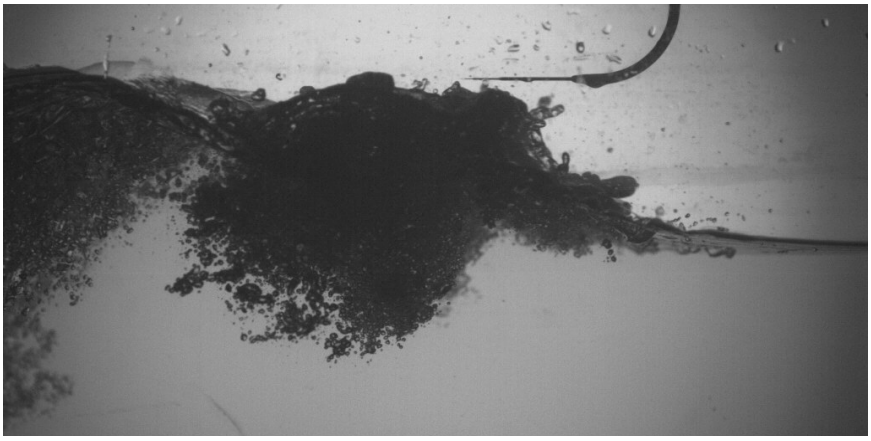

(b) FOR station 2 (FOR2)

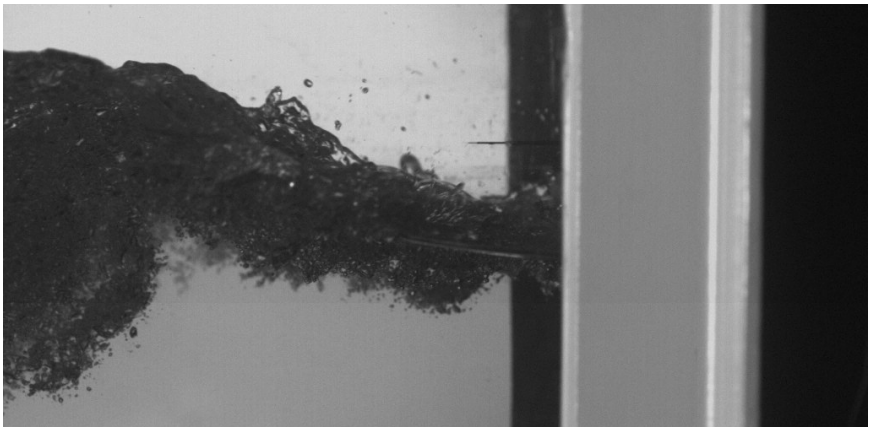

(c) FOR station 3 (FOR3)

Fig. 11.1 Three FOR stations.

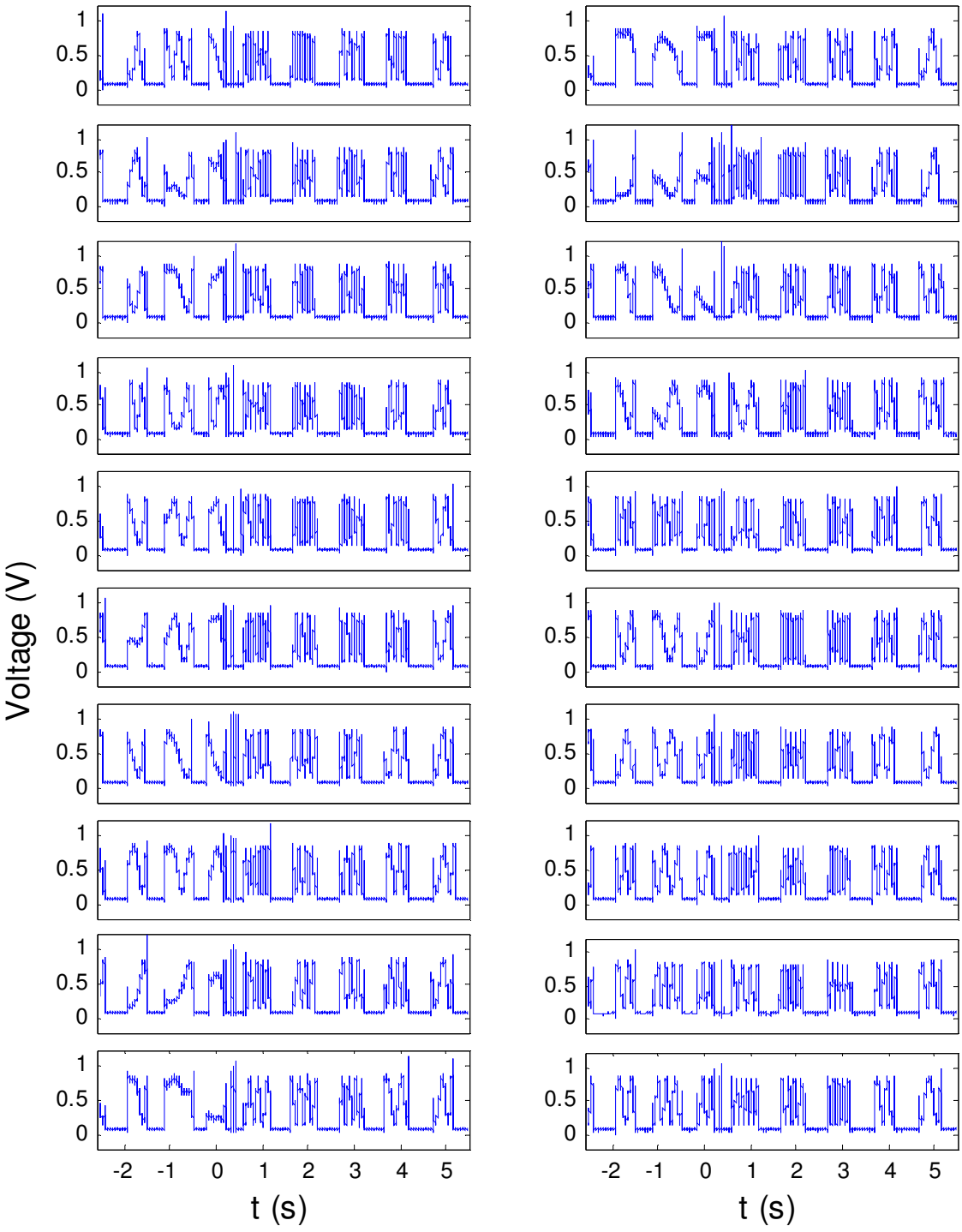

Fig. 11.2 20 instantaneous FOR signals at z = 0 m.

Fig. 11.2 shows examples of 20 instantaneous void ratio signals at $z = 0$ at station 1. A sampling rate of 100 kHz was used to obtain the void ratio at each point. Data was acquired for 8 s to check the repeatability of the plunging breaker although the longest period of the plunging breaker is less than 0.9 s. The repeatability was always checked in real time to reduce measurement errors in the turbulent properties. For example, the required time duration is approximately between $t = 0$ and 0.1 s at station 1 for the first splash-up (FOR1). The voltage signal variation for other time durations should be nearly identical if the plunging breaker has high repeatability.

In the signals obtained from the FOR measurements, high voltage signals represent air (above the free surface or air bubbles) while low voltage signals represent water (under the free surface). In addition, rising and falling signals represent water-air and air-water interfaces of a bubble, respectively. The general description of a FOR signal for a particle or an air bubble can be found in Fig. 4.8 to Fig. 4.10.

An example of a FOR signal in the plunging breaker measurements is presented in Fig. 11.3. The voltage signal was obtained at $z = 0.07$ m at FOR station 1. The most important phases such as the first splash-up roller, the first backward impingement, the first impinging roller, and the newly ascending water crest, have passed through at that point. Therefore, it is necessary to explain the signal shape by identifying the structure of the first splash-up followed by the first impingement in the plunging breaker.

Flat signals around 0.08 V represent that the fiber sensor tip is in the water at the corresponding time (around 0.3s and 0.4s), and signals around 1.0 V represent air (between 0 s and 0.21 s). However, high voltages representing air do not always

maintain 1.0 V depending on the flow situation because the fiber tip does not dry immediately. The signal fluctuates within a higher voltage range during the drying time (around t = 0.25 s and 0.35 s). The voltage difference between water and air is highly distinguishable even though the air signal fluctuates due to the fast variation of the flow phases. The rising and falling signals, representing the interface of two phases, result from air bubbles. As a result, the threshold value to decompose two phases approaches the voltage representing pure water in order to avoid underestimation of the void ratio (Lim *et al*, 2008). 0.11 V was used for the threshold voltage, which is slightly above the maximum noise level of the water signal.

In Fig. 11.3, the voltage amplitude is about 1.0 V before the first splash-up roller (the second roller) touches the end of the fiber probe tip. The impinging water spray touches the fiber tip around 0.212 s, and then the air pocket inside the fully developed splash-up passes through the fiber between 0.228 s and 0.277 s. The newly ascending water crest passes between t = 0.277 s and 0.309 s, and the amplitude is representative of water at 0.08 V. The signal for the mixture at the left side of the ascending crest is between 0.309 s and 0.326 s with a high void ratio corresponding to the continuous backward impingement. Another long air signal is found between 0.309 s and 0.379 s, which corresponds the air between the ascending crest and the first roller. Finally, the crest part of the original primary wave including the first impinging roller passes between 0.379 s and 0.42 s. Air bubble signals from the first roller are found in the first half while the second half represents the water crest of the original primary wave. After the wave passes through the tip, an air signal from above the free surface can be seen at t

= 0.42 s.

As discussed in Chapter IV, bubble chord length or diameter can be obtained by multiplying velocity and bubble time duration. Since velocity fields for the entire flow were obtained by PIV measurements, the bubble chord length can be obtained although the size obtained from this method does not represent the diameter of the bubbles. Note that the chord length only represents bubble diameter if the bubble velocity was obtained from FOR measurements.

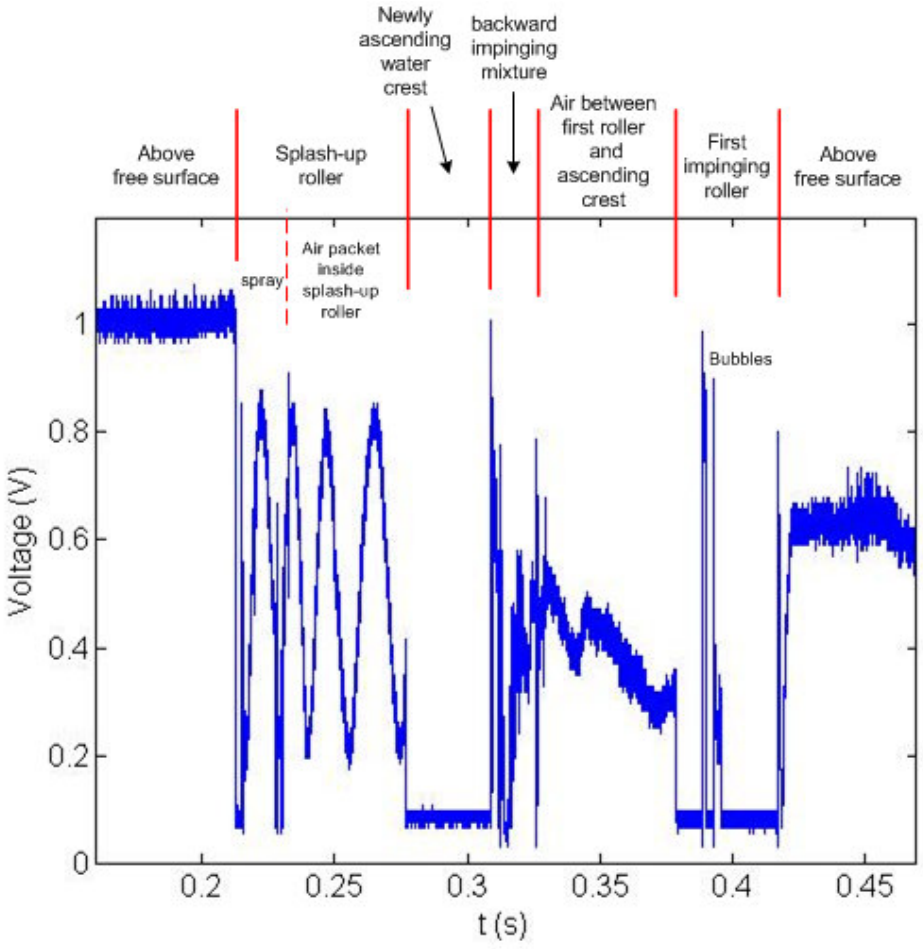

Fig. 11.3 Instantaneous signal at z = 0.07 m and signal description (FOR station 1).

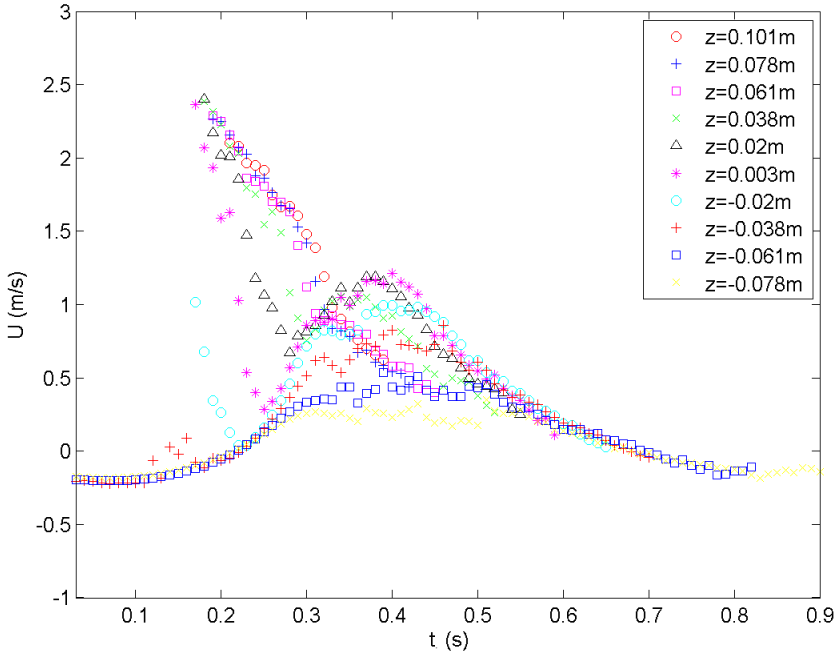

Fig. 11.4 Horizontal velocity time series at points (FOR station 1).

The exact size or volume of an air pocket in the first impingement or in the first splash-up can be estimated if the vertical measurement points at the station cover the size of the air pocket tube. For example, the signal duration for the air pocket in the splash-up roller is about 0.05 s (0.277 – 0.228 s) and the mean velocity is around 1.75 m/s as shown in Fig. 11.4. The horizontal size of the air pocket can be estimated as approximately 87.5 mm at z = 0.07 m at the first FOR station. Size and volume of the air pocket can be estimated with high accuracy since temporal resolution of the FOR technique is extremely high. In addition, the air pocket in the overturning jet in the first impingement can also be estimated. Although this estimation is out of scope of the present study it is a worthwhile research because all of the portions of the air pocket in the first roller penetrates into water without rebound. This means the void ratio in the

first roller is nearly the same as the void ratio in the impinging roller under water. However, a small decrease in the void ratio is present in the first roller due to large bubbles floating onto the free surface and a small increase is also present due to the backward impingement of the newly ascending crest.

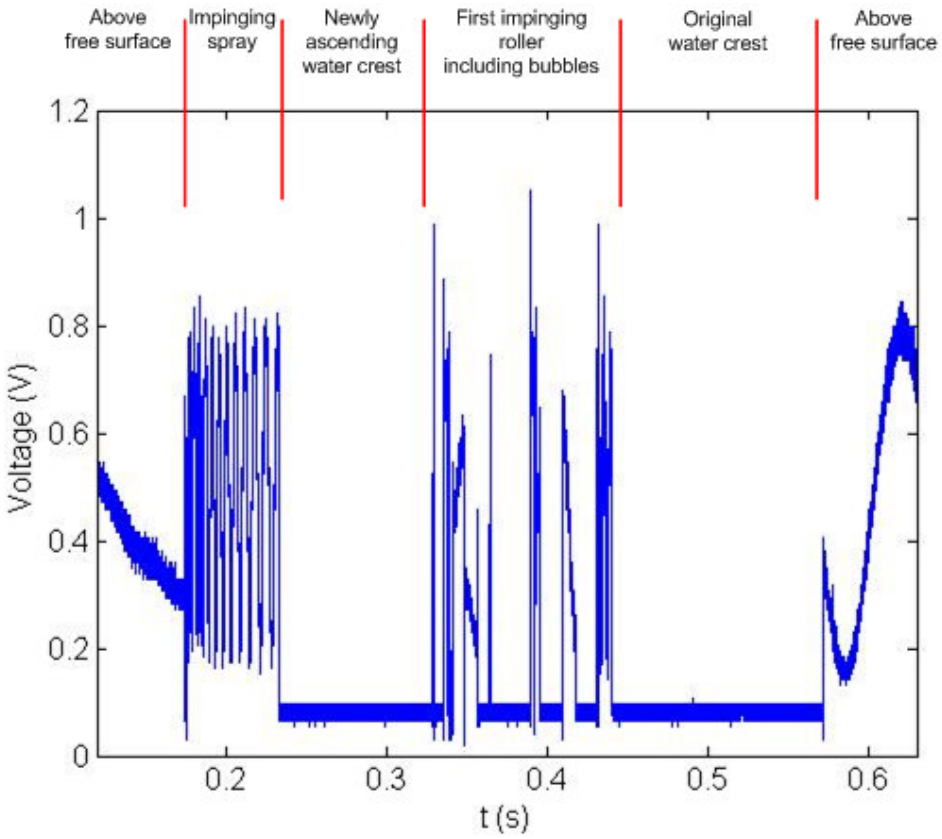

Fig. 11.5 Instantaneous signal at z = 0 m and signal description (FOR station 2).

Fig. 11.5 shows another example of a FOR signal at z = 0. Water spray from the first splash-up impinges near the still water level continuously around t = 0.2 s. The fluctuating signal represents the continuous spray impingement onto the interface

between the water and the aerated region. Air pockets are not found at the still water level. The newly ascending crest passes through the point. Next, the middle of the first roller including air bubbles passes through from 0.33 s and 0.44 s. Finally, the original primary wave passes about 0.57 s.

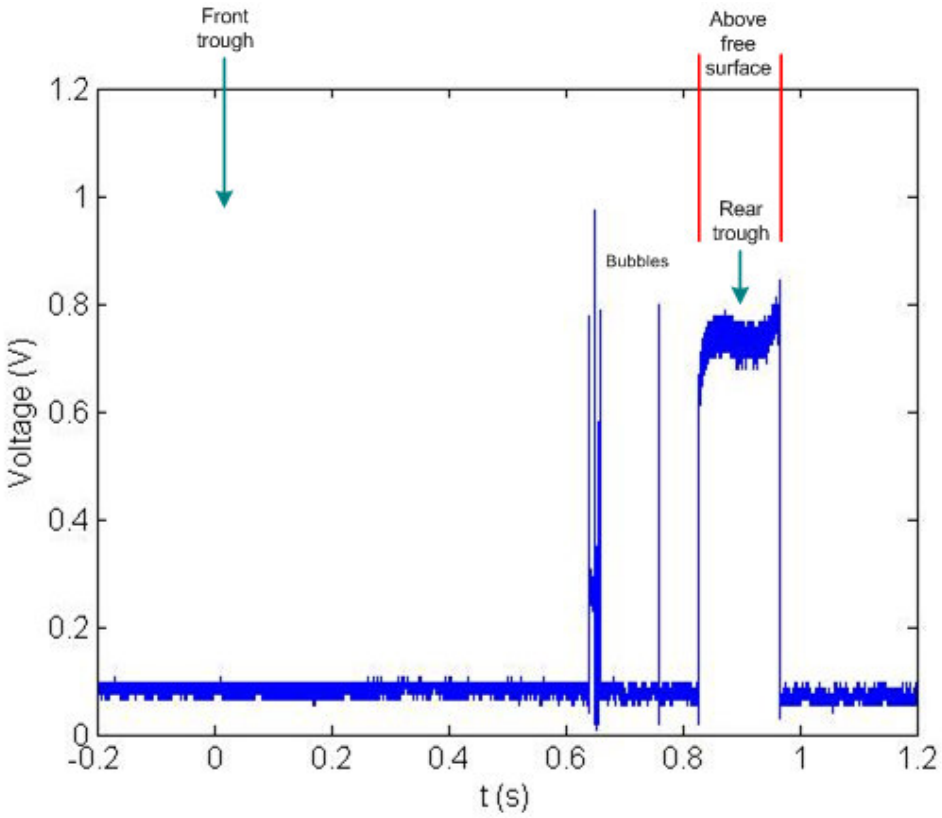

Fig. 11.6 Instantaneous signal at z = - 0.06 m and signal description (FOR station 3).

Fig. 11.6 shows a FOR signal at z = -0.06 m, which is close to the wave tough. Since the front trough is increased gradually during the breaking process as shown in Fig. 9.34, only the rear tough can be detected at this point. It is necessary to obtain the time information for the front trough to calculate the period-averaged void ratio. Free surface elevation obtained from the PIV images and the wave gauge measurements was used to

calculate the period-averaged void ratio. When the first splash-up roller passes FOR station 1, there are no bubbles under the second roller and air bubbles are rarely found at the spread first roller.

To obtain instantaneous void ratios for 20 measurements at each point, voltage amplitude representing water was set to zero while the amplitude of air was set to 1. Air above the free surface was set to the NaN (Not-A-Number) value in Matlab. Since sampling rate is 100 kHz, the averaged void ratio was obtained using every 1000 samples whose value were set to 0 (water) or 1 (air) previously. Therefore, the final temporal resolution of 100 Hz is identical with the final output data sampling rate in the BIV and PIV measurements. The vertical spatial resolution is 10 mm. Note that the spatial resolutions of the final vectors in the BIV and PIV measurements are 5.26 and 5.78 mm, respectively. After obtaining the instantaneous void ratio for every 0.01 s at each station, the phase-averaged mean and turbulent void ratios were calculated.

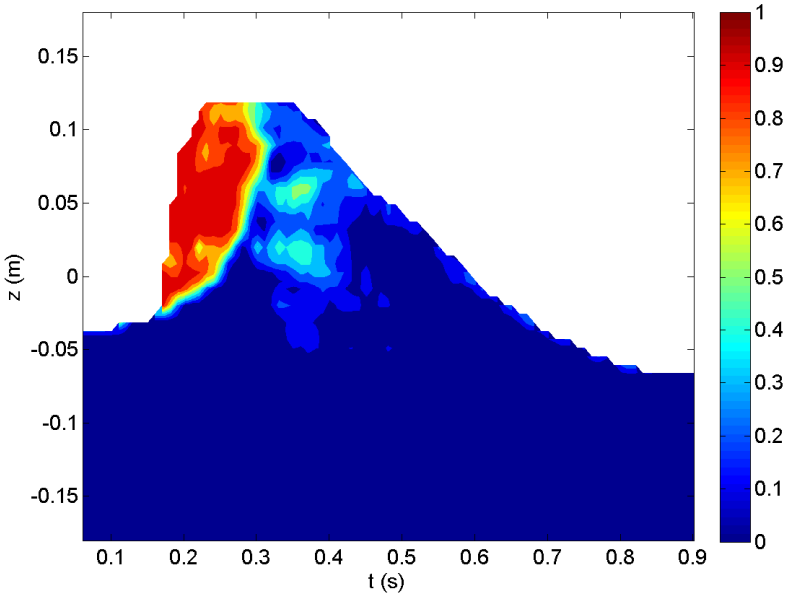

Fig. 11.7 Time series contour of void ratio at station 1 (FOR1).

The mean void ratio contour at FOR station 1 can be seen in Fig. 11.7. As expected, the first splash-up roller has a very high void ratio while the low void ratio at the ascending water crest can be observed around t = 0.3 s. The void ratio corresponding to the first impinging roller can be seen between 0.3 s and 0.45 s.

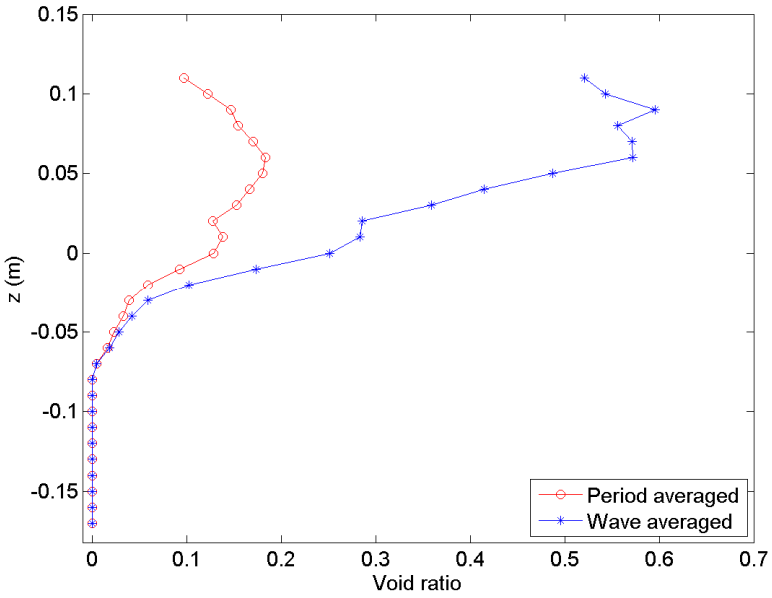

Fig. 11.8 Wave-averaged and period-averaged void ratios at station 1 (FOR1).

Wave-averaged and period-averaged void ratios were obtained using Eqs. (9.4) and (9.5), and these void ratios can be seen in Fig. 11.8. Wave-averaged and period-averaged void ratios are approximately 57% and 19% around z = 0.06 m, respectively. A time series of the depth-averaged void ratio can be seen in Fig. 11.9. The depth-averaged void ratio was calculated to the location z = - 0.18 m since there were no bubble below that location at the station 1. The maximum depth-averaged void ratio occurs at 0.21 s, representing the first splash-up roller, and is decreased due to the ascending water crest

around t = 0.3 s. A local maximum is found after the new water crest due to the mixture between the two rollers and the first impinging roller. As discussed in Chapter VII, a time series of the depth-averaged void ratio can be obtained using the difference between the free surface information obtained from the wave gauges and the image methods. The comparison of the results and more discussion are presented in Section 11.3.

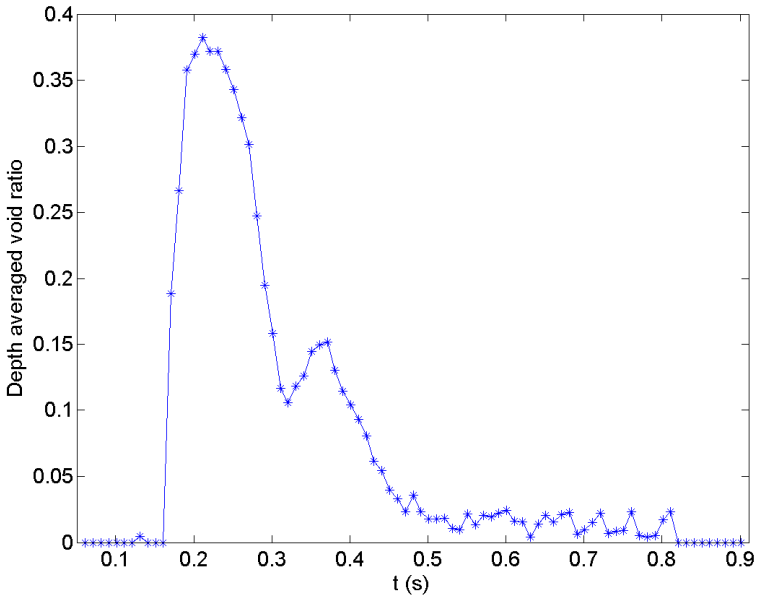

Fig. 11.9 Depth-averaged void ratio at station 1 (FOR1).

A time series contour of mean void ratio at FOR station 2 is shown in Fig. 11.10. The location of the second station corresponds to the second splash-up region. Fig. 11.11 shows the wave-averaged and period-averaged void ratios. The maximum wave-averaged void ratio is about 49% close to that of the first splash-up, and the maximum period-averaged void ratio is about 13% at z = 0.05 m. This is because the wetted duration near the crest of the second splash-up is shorter than that of the first splash-up.

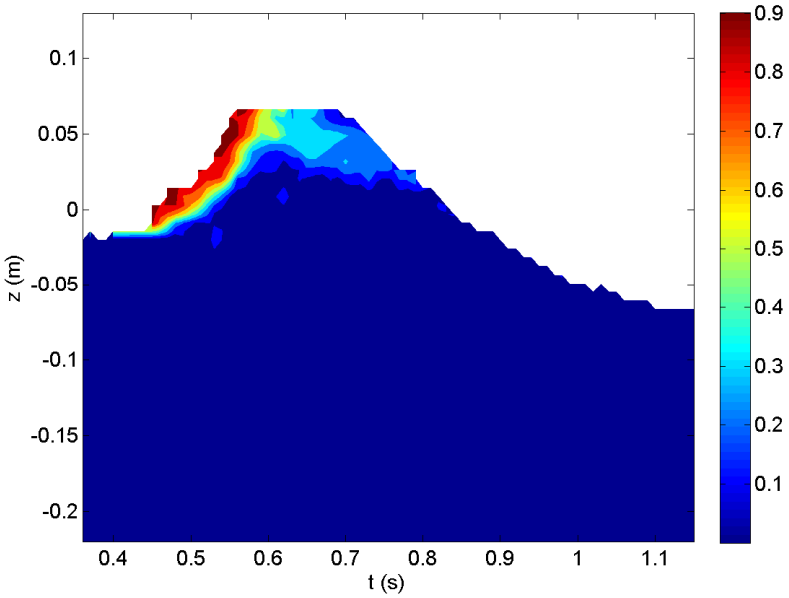

Fig. 11.10 Time series contour of void ratio at station 2 (FOR2).

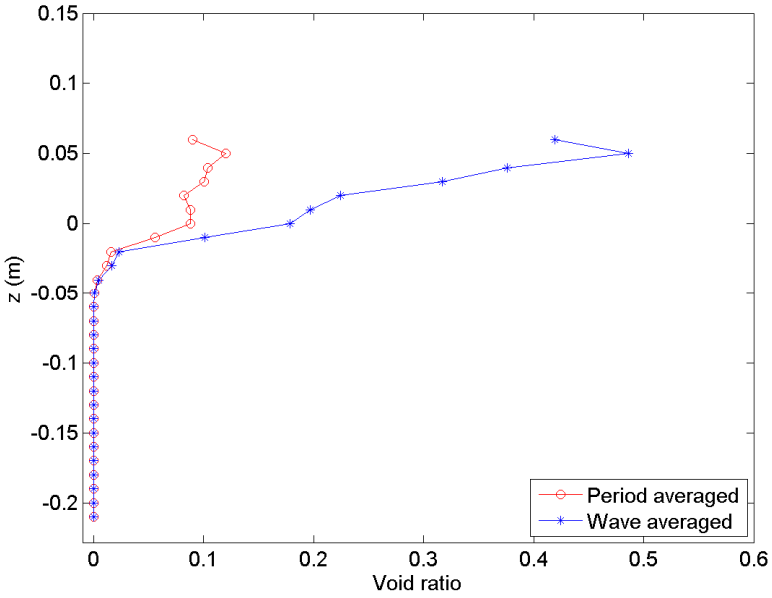

Fig. 11.11 Wave-averaged and period-averaged void ratios at station 2 (FOR2).

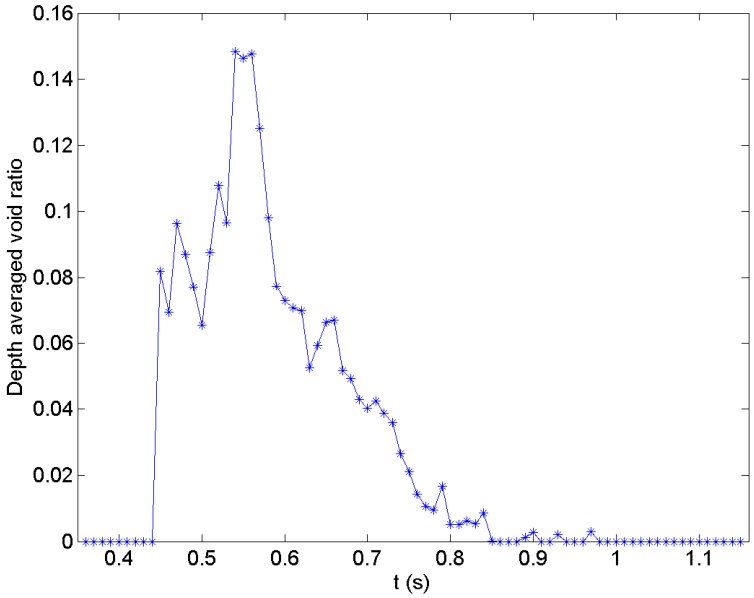

Fig. 11.12 Depth-averaged void ratio at station 3 (FOR3).

Fig. 11.12 shows the time series of the depth-averaged void ratio obtained by averaging the void ratios vertically up to z = -0.22 m. The maximum depth-averaged void ratio occurs at t = 0.54 s near the toe of the second splash-up, and a local maximum is found at t = 0.66 s due to the second impinging roller. A similar decrease observed in the first splash-up is found between the two rollers due to the new water crest caused by the second impingement although its scale is much smaller.

Fig. 11.13 shows the void ratio time series at the third station, which corresponds to the third splash-up region. Fig. 11.14 shows the wave-averaged and period-averaged void ratios and Fig. 11.15 shows the time series depth-averaged void ratio. The void ratio is significantly decreased compared with the first and second splash-up. The depth-averaged void ratio decrease due to the new water crest is not found at the third splash-up, since the breaking process at the third splash-up is similar to a spilling breaker.

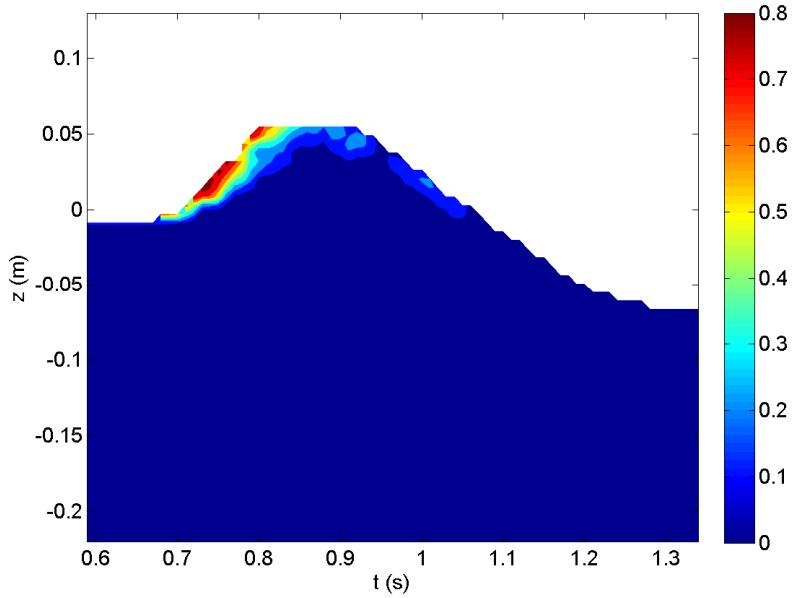

Fig. 11.13 Time series contour of void ratio at station 3 (FOR3).

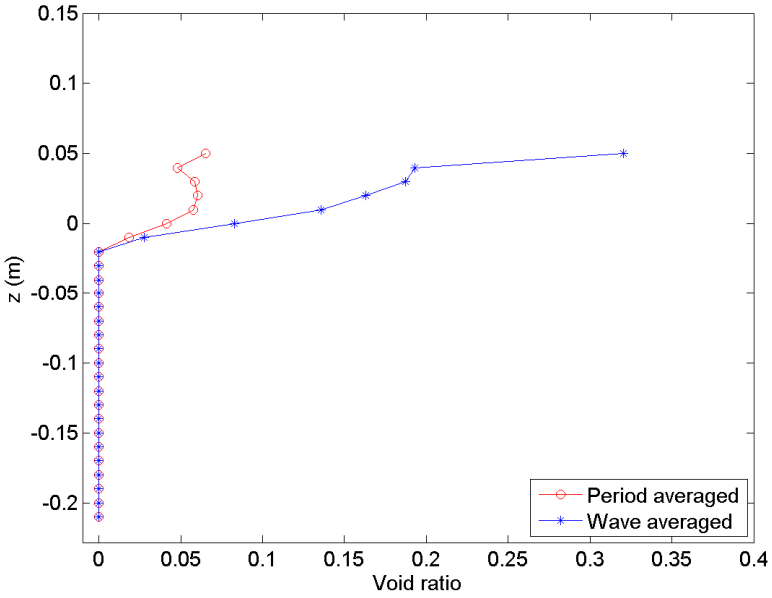

Fig. 11.14 Wave-averaged and period-averaged void ratios at station 3 (FOR3).

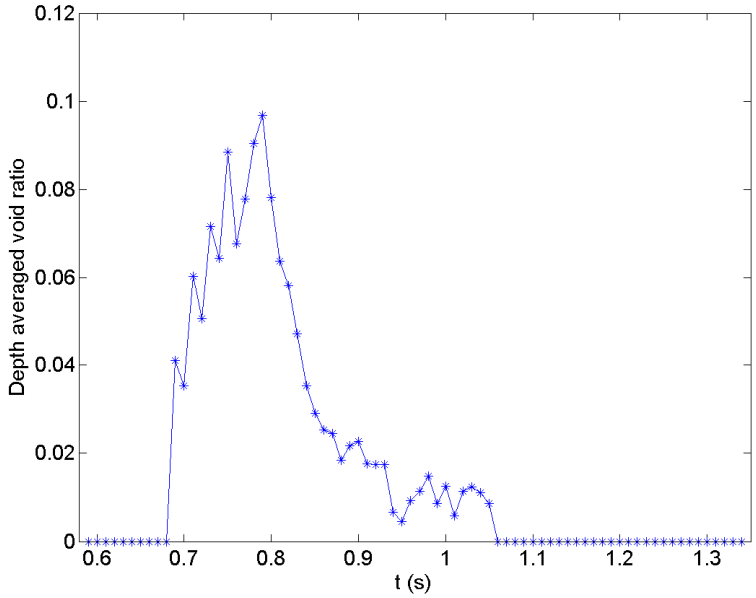

Fig. 11.15 Depth-averaged void ratio at station 3 (FOR3).

It is considered that the third process is a transition between a plunging and a spilling breaker. The depth-averaged void ratio decreases exponentially, similar to that of the void ratio in spilling waves (Cox and Shin, 2003).

The void ratio at station 1 covers the first impinging roller and the first splash-up. The void ratios from the two rollers are independent because the first splash-up is not from the impinging jet as discussed in Chapter VI. The void ratio at station 2 covers the second impinging roller and the second splash-up. Two rollers are produced from the first splash-up roller (second roller). The second roller becomes the accumulated roller, and then the accumulated roller is divided into the second impinging roller and the second splash-up roller by the second impingement of the newly ascending crest. This implies that the void ratio at the second splash-up should be very close to the void ratio at station 2. Therefore, the void ratio of the first impinging roller (overturning) can be

estimated by subtracting the void ratio at station 2 from the void ratio at station 1. In addition, the void ratio at station 3 should be close to the void ratio at the second splash-up roller. In the same manner, the void ratio of the second impinging roller can be estimated by subtracting the void ratio at station 3 from the void ratio at station 2.

As shown in Fig. 11.3, it is possible to describe the FOR signal in combination with the high speed camera and quantitative results from the BIV and PIV measurements.

11.3 Void Ratio Measurement Using Digital Images

Since both BIV and PIV techniques are based on the imaging techniques, the void ratio can be estimated using the image intensities of the aerated region. The high speed camera used in the BIV and PIV measurements has a dynamic range of 8-bits. Therefore, each image has 256 gray scales from 0 to 255 (black: 0 and white: 255). In the PIV images, water is black and air bubbles have higher intensities depending on their concentration. A higher concentration of bubbles (high void ratio) has a higher intensity (brighter). With this simple concept, the image intensity at each pixel was divided by 255 since the void ratios in water and air are 0 and 1 respectively. These image intensity data are the raw data and should be corrected or calibrated because the intensity of the laser light sheet is different at each location. For example, pixel intensity in the lower image is higher than in the upper image and is higher in the middle of the images than the left and right side.

In this section, preliminary results of the void ratios obtained from the BIV and PIV images before calibration or post processing are presented for comparison with the void ratios obtained from FOR measurements. It is crucial to understand the imaging

techniques required to obtain the void ratio, and more detailed research is required in the future.

11.3.1 Void Ratio Obtained From PIV Images

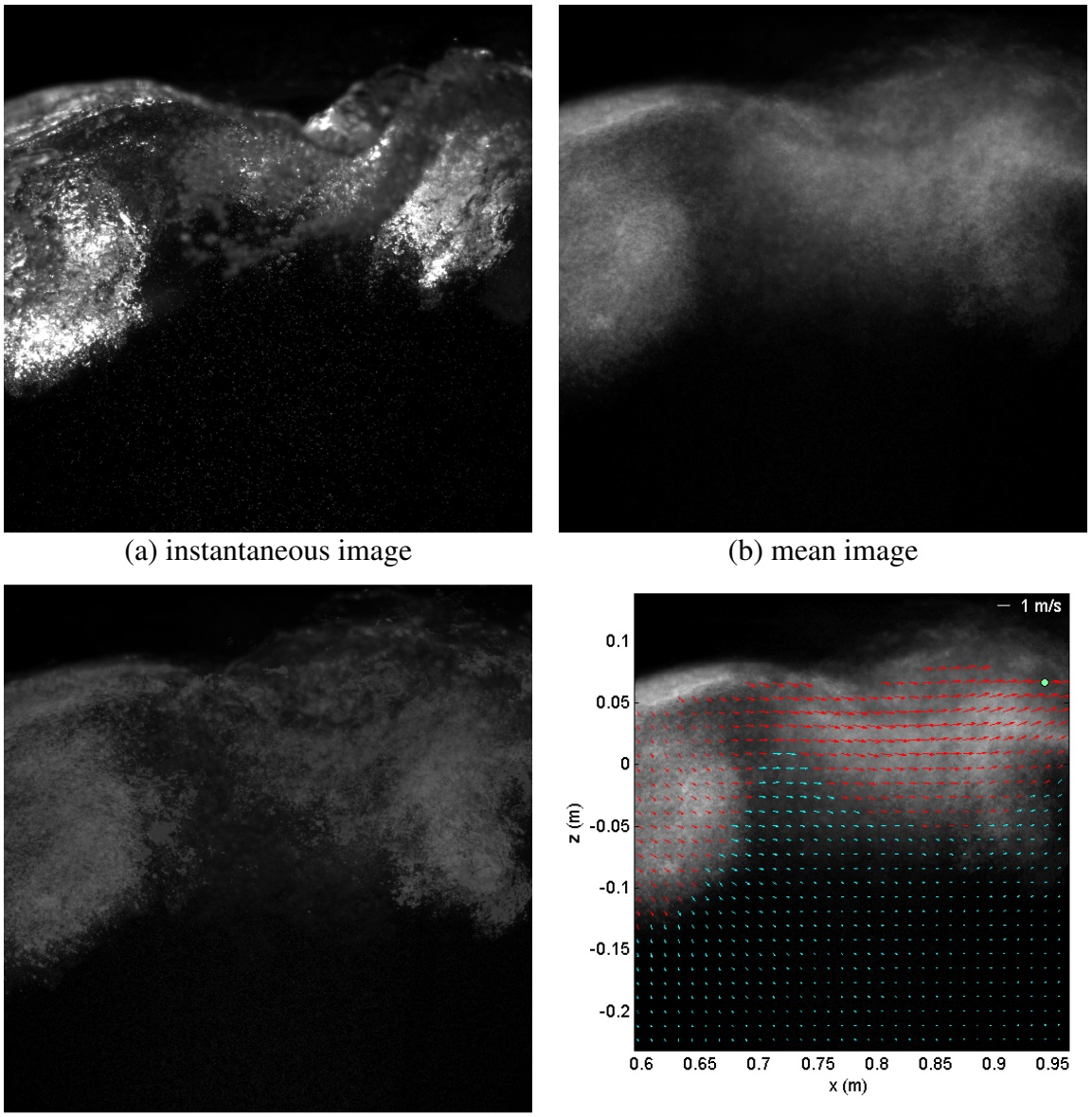

(a) instantaneous image (b) mean image

(c) r.m.s. image (d) velocity

Fig. 11.16 PIV image processing for void ratio at t = 0.60 s (FOV7).

Fig. 11.16(a) shows an instantaneous PIV image at t = 0.6 s during the second splash-up. Fig. 11.16(b) and (c) show the mean and r.m.s. images that were obtained from 20 instantaneous images. The mean and turbulent void ratios obtained from the PIV images can be seen in Fig. 11.17, respectively. As shown in Fig. 11.17, the void ratio of the impinging roller may be overestimated due to the high intensity caused by the laser light sheet. It is possible that the void ratio at a low concentration of bubbles are always overestimated when the imaging methods are employed. This is due not only to the laser light sheet but also the nature of imaging method. As shown in Fig. 11.16(d), bright images do not affect velocity fields because the mixture images in the aerated region have various intensities.

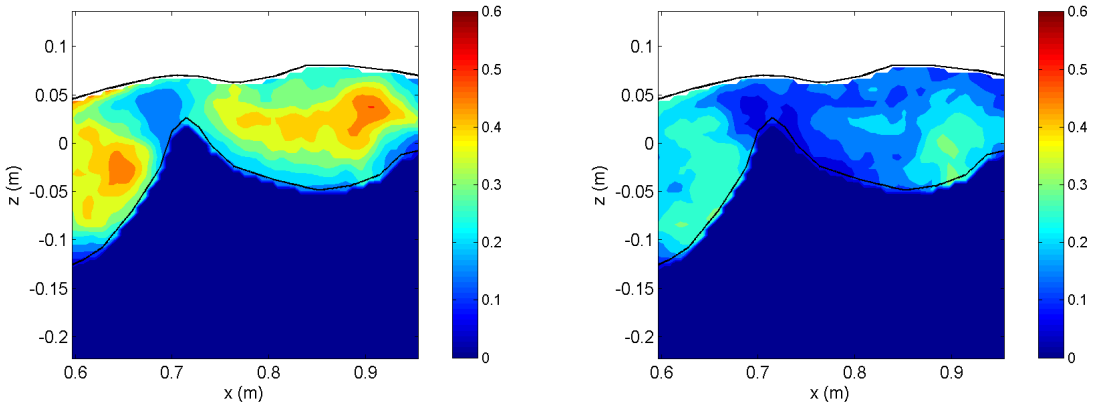

(a) void ratio (α) (b) fluctuating void ratio (α′)

Fig. 11.17 PIV void ratio at t = 0.60 s (FOV7).

Fig. 11.18 shows the void ratio time series obtained from the PIV measurements at station 1, while the results from the FOR measurement can be seen in Fig. 11.7. The comparison of time-averaged void ratios between FOR and PIV technique can be seen in

Fig. 11.19. The PIV void ratio near the crest (the splash-up roller) is lower than the FOR void ratio while the void ratio for the impinging roller using PIV is much higher than the FOR void ratio. Although void ratios from PIV must be calibrated, it appears that the PIV void ratio overestimates for the low void ratio regions and underestimates for the high void ratio regions.

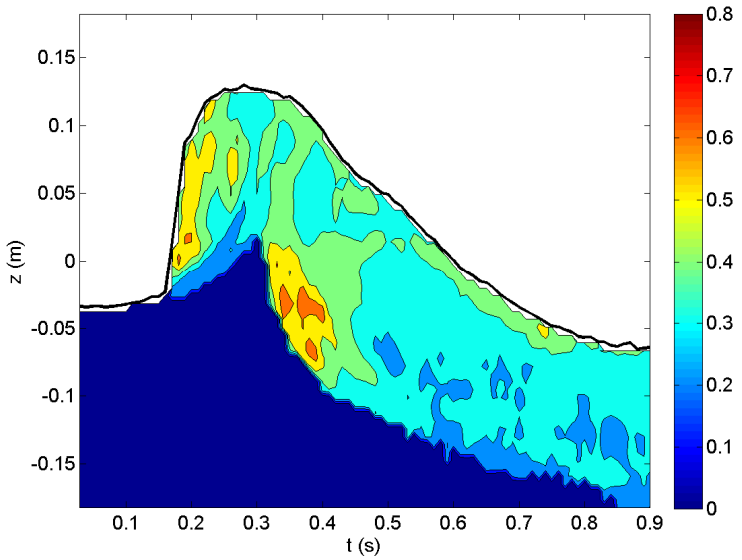

Fig. 11.18 Time series of void ratio at FOR station 1 (PIV).

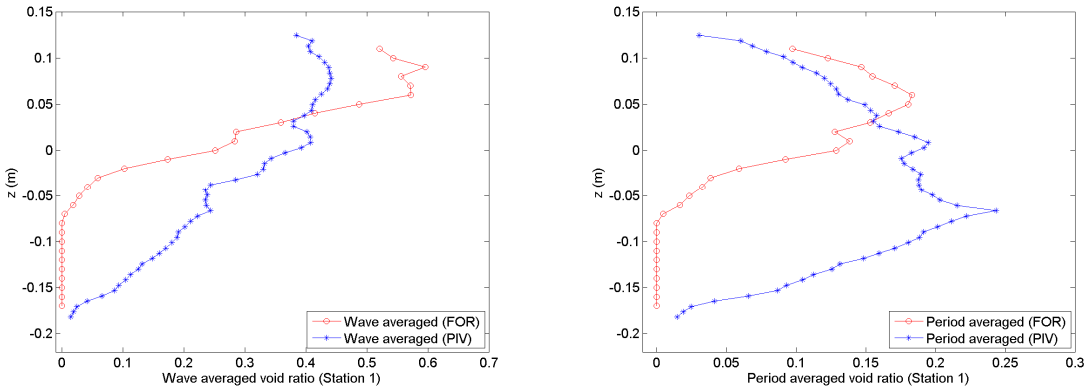

(a) wave-averaged α (b) period-averaged α

Fig. 11.19 Comparison of time-averaged void ratios at FOR station 1.

As discussed in Chapter VII, a time series of the depth-averaged void ratio can be obtained using the difference between the free surface information obtained from the wave gauges and the image methods as shown in Fig. 11.20. The depth-averaged void ratio was calculated up to the location z = - 0.18 m since there are no bubbles below that location at station 1. The comparison of three depth-averaged void ratios obtained from each measurement technique can be seen in Fig. 11.21. Results from the wave gauges and FOR measurements are similar while the PIV results are substantially different especially at the rear wave. Again, the PIV void ratio underestimates for the high void ratio region of the splash-up roller and overestimates for the low void ratio region of the impinging roller unless a calibration or correction is applied.

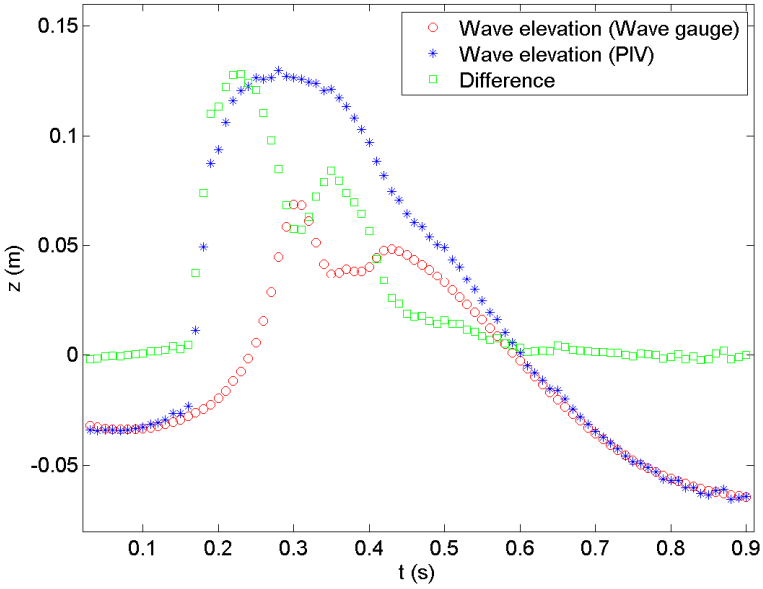

Fig. 11.20 Comparison of wave elevations at FOR station 1.

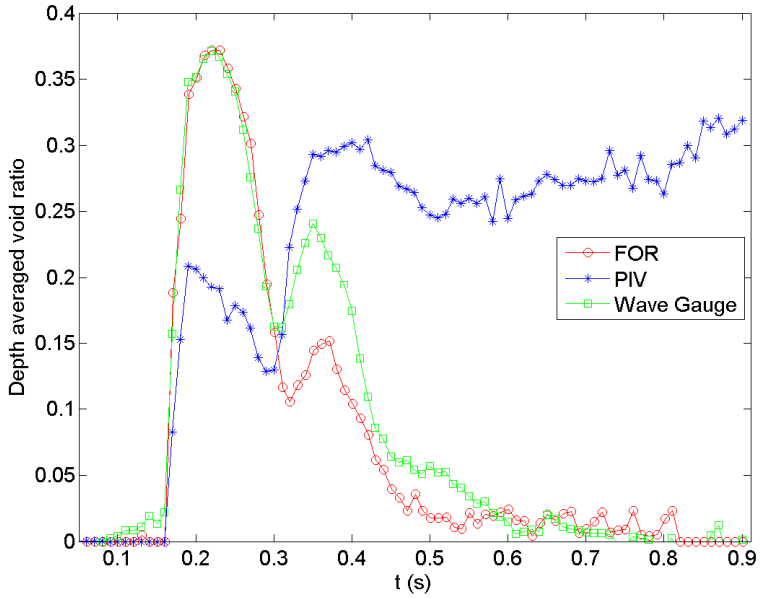

Fig. 11.21 Comparison of depth-averaged void ratios at FOR station 1.

Similar results are found at stations 2 and 3. The void ratios obtained at stations 2 and 3 from the PIV measurements are given in Fig. 11.22. The corresponding void ratios from FOR can be seen in Fig. 11.10 and Fig. 11.13.

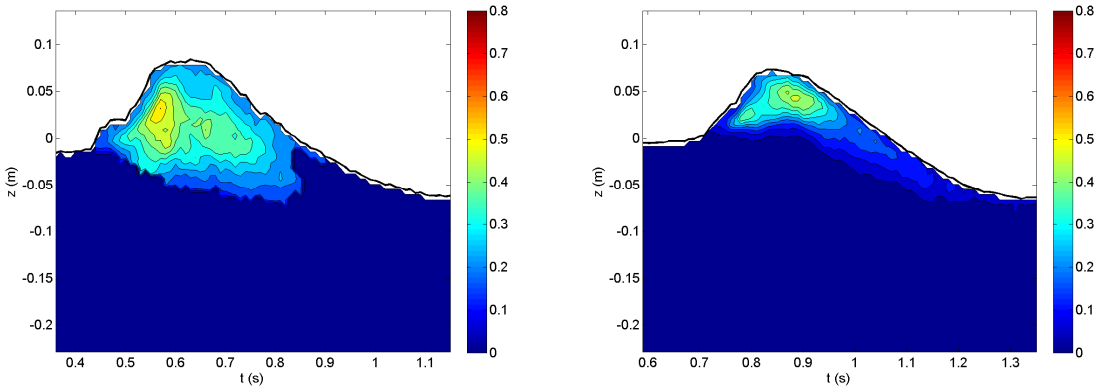

(a) void ratio (α) at station 2 (PIV) (b) void ratio (α) at station 3 (PIV)

Fig. 11.22 Time series of void ratios at FOR stations 2 and 3 (PIV).

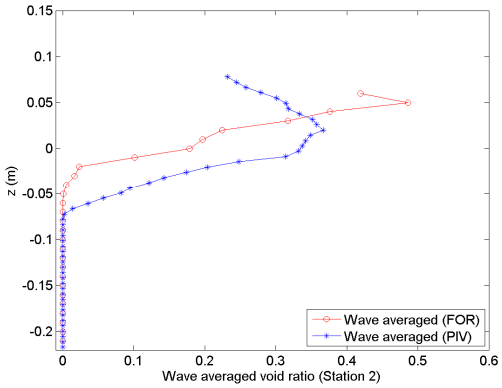

(a1) wave-averaged α (station 2)

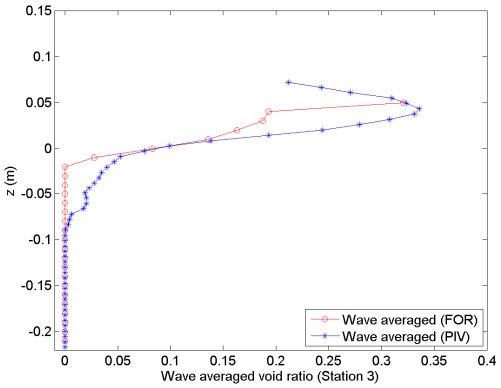

(b1) wave-averaged α (station 3)

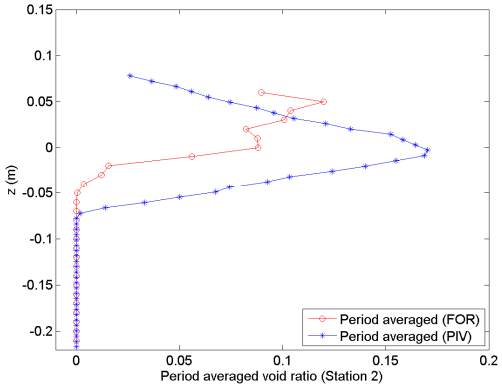

(a2) period-averaged α (station 2)

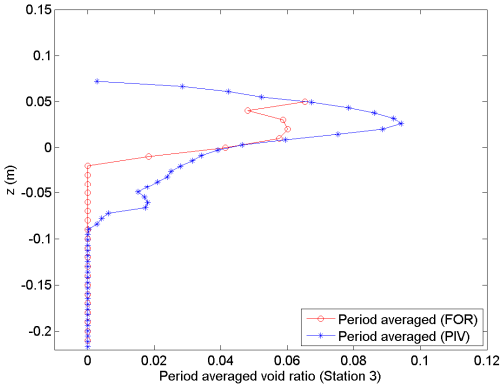

(b2) period-averaged α (station 3)

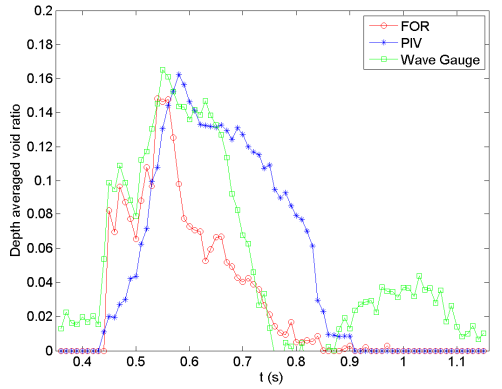

(a3) depth-averaged α (station 2)

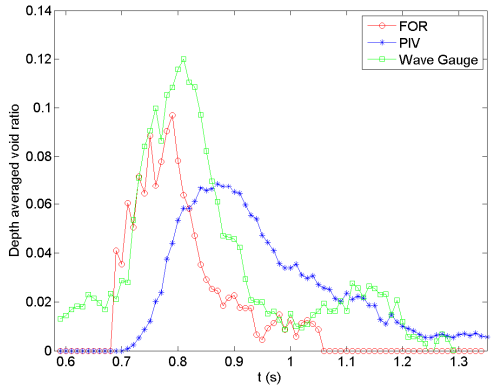

(b3) depth-averaged α (station 3)

Fig. 11.23 Comparison of void ratios at FOR stations 2 and 3.

Fig. 11.23 shows a comparison of the void ratios at stations 2 and 3. Note that numbers 1, 2 and 3 in parentheses represent wave-averaged, period-averaged and depth-averaged void ratio, respectively and a and b in parentheses represent stations 2 and 3.

11.3.2 Void Ratio Obtained From BIV Images

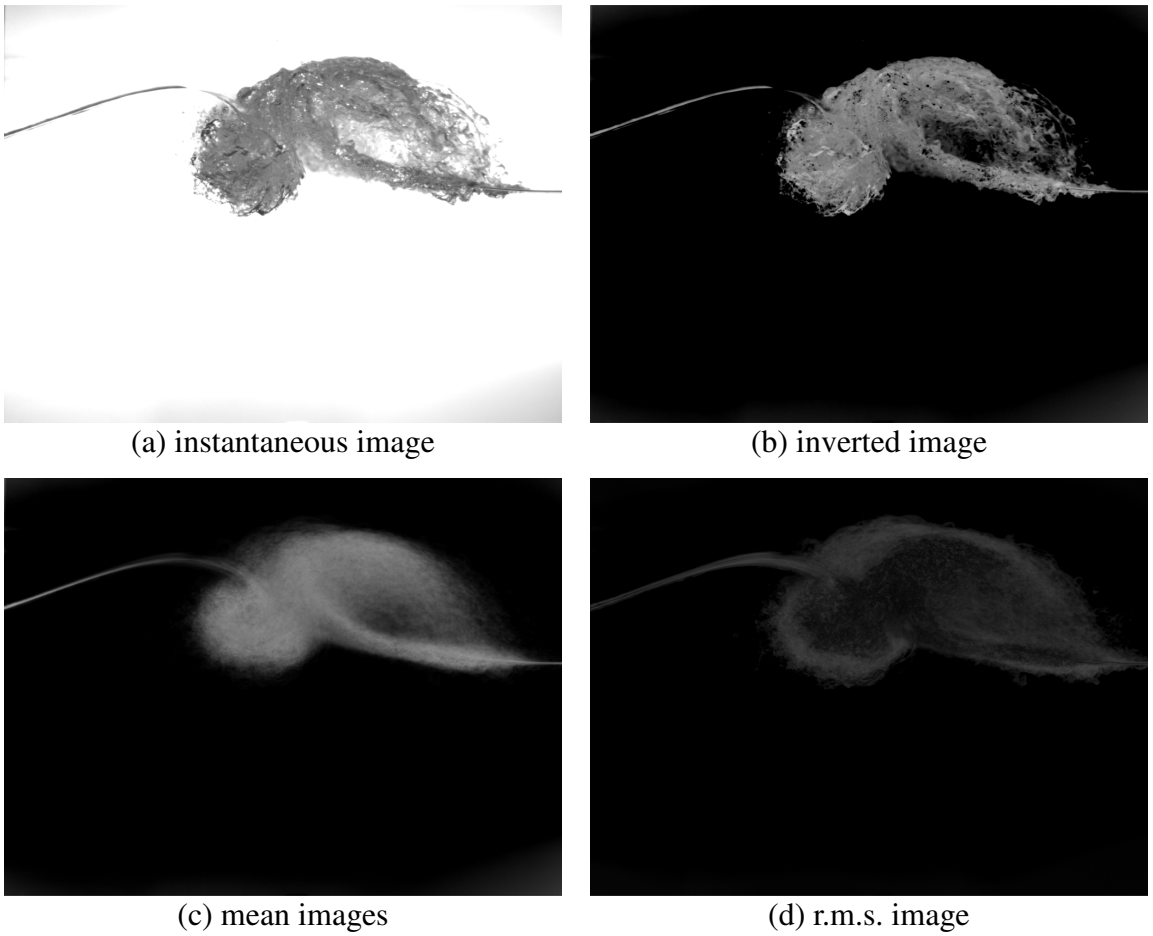

(a) instantaneous image (b) inverted image

(c) mean images (d) r.m.s. image

Fig. 11.24 BIV images for void ratio at t = 0.22 s.

The void ratio can be estimated from BIV images using a similar method to that discussed in Section 11.3.1. Intensities of an instantaneous raw image, as shown in Fig.

11.24(a), were inverted to force the water intensity to be zero [Fig. 11.24(b)]. Fig. 11.24(c) and (d) show the mean and r.m.s. images.

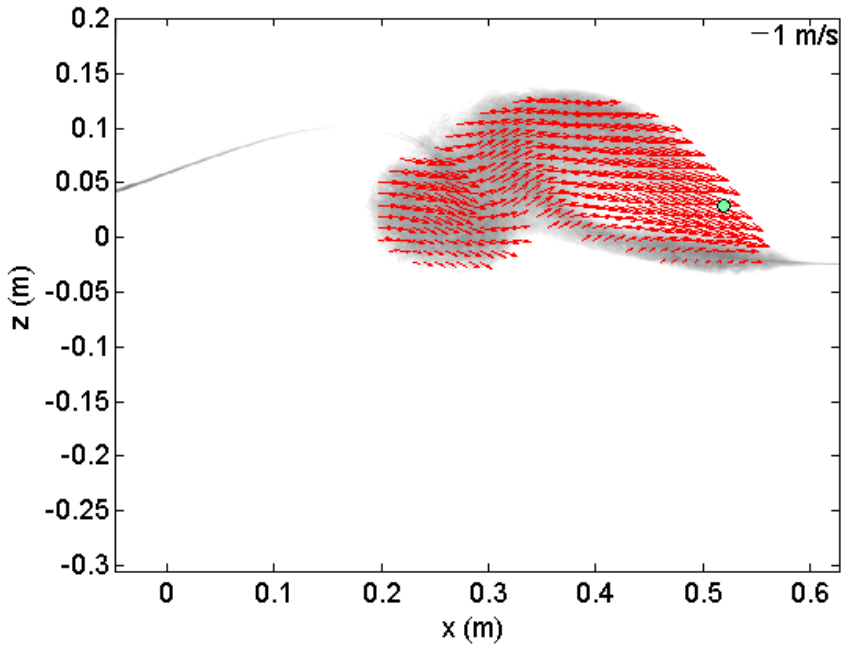

Fig. 11.25 BIV velocity field.

Velocity fields are reasonably obtained from the BIV technique as shown in Fig. 11.25. However, the void ratio for the air pocket in the first splash-up roller was underestimated. Mean and r.m.s. void ratios can be seen in Fig. 11.26. In the FOR measurements, the maximum void ratio occurs at the air pocket in the splash-up roller as discussed in Section 11.3.1. This is because the water and the air over the free surface (not air bubbles in water) have the same intensity, which is the nature of the BIV imaging technique. Since the plunging breaker has high repeatability, the air pocket shown in the instantaneous images can also be seen in the mean images.

Special care and attention is required when obtaining the void ratio from various imaging techniques. The FOR results can be useful in determining the weight function required for the correction of the void ratios obtained from the images. If the correction is reasonable, meaningful results considering the density variation for the entire flow field can be obtained using the imaging methods.

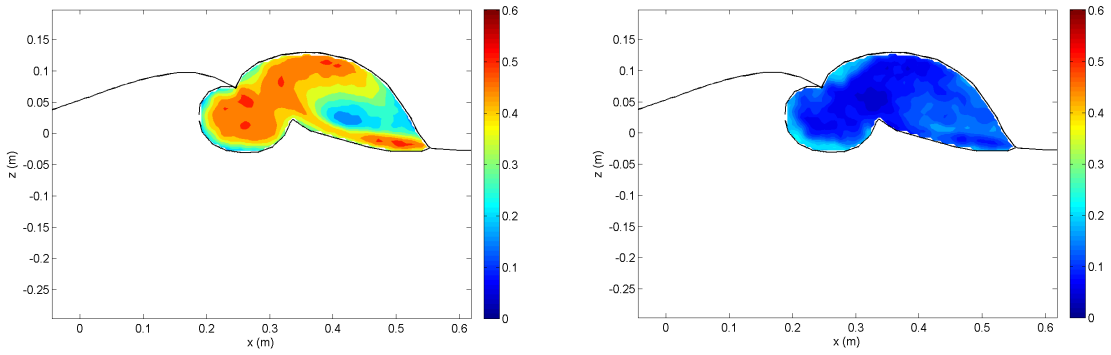

(a) mean void ratio (α) (b) fluctuating void ratio (α′)

Fig. 11.26 Mean and turbulent void ratios from BIV.

11.4 Results Considering Compressibility

The mass flux, momentum flux, mean and turbulent kinetic energy, and Reynolds stress at each FOR station are presented. Compressibility in the plunging breaker was considered, and based on the void ratio obtained from the FOR measurements.

In air-water two phase flows, mixture momentum per unit volume can be given by the following (Brennen, 2005):

$$\rho_m U_m = \rho_a U_a + \rho_w U_w \tag{11.1}$$

where, the subscript a, w, and m represent air, water, and air-water mixture respectively. It is difficult to decompose each phase in a highly aerated flow using the imaging technique such as BIV and PIV. Since the velocity fields of the aerated region of the plunging breaker obtained from the BIV and PIV measurements represent the velocities of the air-water mixture (U_m), the mixture density at each point is required. The mixture density can be obtained from Eq. (11.2).

$$\rho_m = \rho_a \alpha_a + \rho_w \alpha_w = \rho_a \alpha + \rho_w (1-\alpha) \tag{11.2}$$

where, α is a local void ratio at a point and $\alpha_a = \alpha$. Compared with the right side term, $\rho_w(1-\alpha)$, $\rho_a \alpha$ can be neglected. Therefore, the mixture density at each point can be rewritten as:

$$\rho_m(x,z,t) = \rho_w \left(1-\alpha(x,z,t)\right) \tag{11.3}$$

The volume flux (VF_α), mass flux (MF_α), and momentum flux (IF_α) applying the mixture density ρ_m can be obtained from Eqs. (11.4), (11.5), and (11.6) respectively.

$$VF_\alpha(x) = \int_{-h}^{\eta(x)} \int_{t_{tr}(x)}^{t_{tr}(x)+T(x)} \left(1-\alpha(x,z,t)\right) U(x,z,t)\, dtdz \tag{11.4}$$

$$MF_\alpha(x) = \int_{-h}^{\eta(x)} \int_{t_{tr}(x)}^{t_{tr}(x)+T(x)} \rho_m(x,z,t) U(x,z,t)\, dtdz = \rho_w \cdot VF_\alpha(x) \tag{11.5}$$

$$IF_\alpha(x) = \int_{-h}^{\eta(x)} \int_{t_{tr}(x)}^{t_{tr}(x)+T(x)} \rho_m(x,z,t) U(x,z,t)^2\, dtdz \tag{11.6}$$

where, $t_{tr}(x)$ is the local time when the front trough reaches the station and $T(x)$ is the local wave period.

The mixture density shown in Eq. (11.3) must be applied to all other quantities such as kinetic energy and Reynolds stress to obtain the depth-averaged or time-averaged values. For example, with consideration of the mixture density, the wave-averaged and

period-averaged values of the mean kinetic energy (K) are calculated using Eqs. (11.7) and (11.8) respectively.

$$K_{wa}(x,z) = \frac{\int_{t_{tr}(x)}^{t_{tr}(x)+T(x)} \delta(x,z,t)\rho_m(x,z,t)K(x,z,t)dt}{\int_{t_{tr}(x)}^{t_{tr}(x)+T(x)} \delta(x,z,t)dt} \tag{11.7}$$

$$K_{pa}(x,z) = \frac{\int_{t_{tr}(x)}^{t_{tr}(x)+T(x)} \delta(x,z,t)\rho_m(x,z,t)U(x,z,t)dt}{\int_{t_{tr}(x)}^{t_{tr}(x)+T(x)} dt} \tag{11.8}$$

where, $\delta(x,z,t) = 1$ in water under the free surface and $\delta(x,z,t) = 0$ in air above the free surface. The subscript *wa* and *pa* represent the wave-averaged and period-averaged values respectively. Note that K in the integral is the mean kinetic energy per unit mass rather than unit volume.

The depth-integrated and depth-averaged values of the mean kinetic energy (K) are also calculated using Eqs. (11.9) and (11.10) respectively.

$$K_{di}(x,t) = \int_{-h}^{\eta(x,t)} \rho_m(x,z,t)K(x,z,t)dz \tag{11.9}$$

$$K_{da}(x,t) = \frac{\int_{-h}^{\eta(x,t)} \rho_m(x,z,t)K(x,z,t)dz}{\int_{-h}^{\eta(x,t)} dz} \tag{11.10}$$

where, the subscript *di* and *da* represent the depth-integrated and the depth-averaged.

Fig. 11.27 shows the horizontal velocity contour at each station. Numbers 1-3 in parentheses represent the FOR stations and a and b in parentheses represent horizontal velocity without and with consideration of the void ratio. As shown in Fig. 11.27(a1), the maximum horizontal velocity (U) occurs at the impinging water spray. However, the maximum is located at the ascending crest and the impinging roller rather than the splash-up roller when considering the void ratio [$(1-\alpha)U$ in Fig. 11.27(b1)]. This means

the positive mass flux and momentum flux at the splash-up will be highly overestimated if the void ratio is not considered. Similar phenomena at the second and third splash-up can be seen in Fig. 11.27. Indeed, the maximum magnitude of the horizontal momentum occurs at the ascending crest and the impinging roller in the region where each splash-up is fully developed. The transferring of high momentum from the impinging roller to the ascending crest subsequently causes the next impingement.

Fig. 11.28 shows the mean kinetic energy considering the void ratio at each station. As expected from Fig. 11.27, the mean kinetic energy is significant at the ascending crest and the impinging roller rather than at the splash-up roller when considering the void ratio. Fig. 11.29 also shows the comparison of the turbulent kinetic energy at each station. The turbulent kinetic energy without considering the void ratio has the maximum at the bottom boundary of the splash-up roller. The turbulent kinetic energy considering the void ratio is dominant at the impinging roller as well as the impinging spray. However, at the third splash-up, which is the transition process between the plunging and the spilling phases, the maximum turbulent kinetic energy still occurs near the splash-up roller. The void ratio at the third station is more widely distributed under the crest.

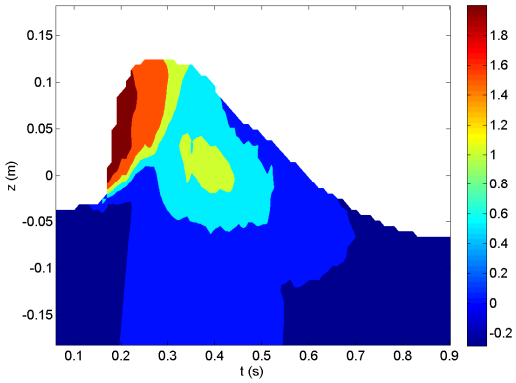

(a1) U (station 1)

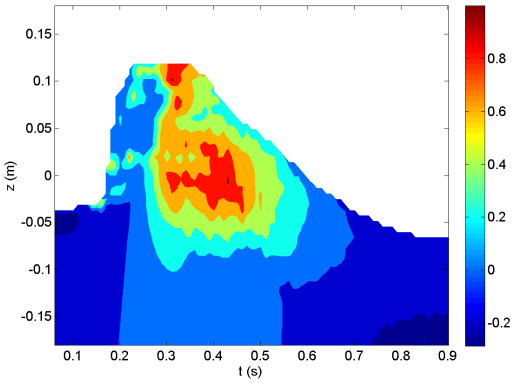

(b1) (1-α)U (station 1)

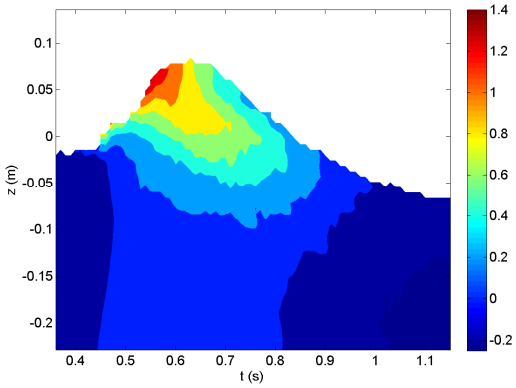

(a2) U (station 2)

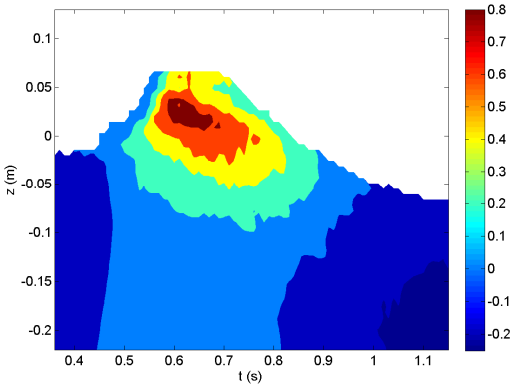

(b2) (1-α)U (station 2)

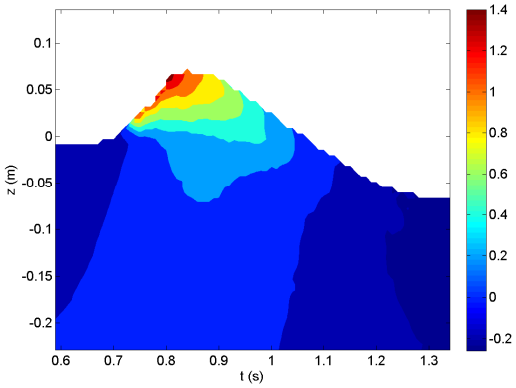

(a3) U (station 3)

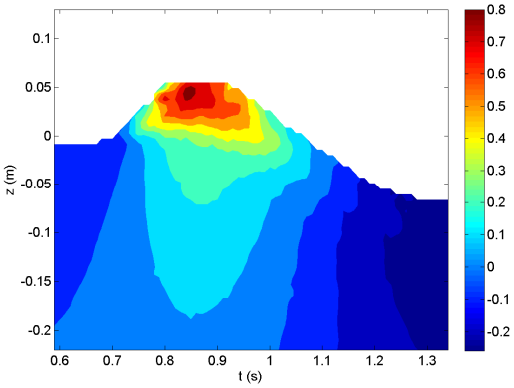

(b3) (1-α)U (station 3)

Fig. 11.27 Horizontal velocity considering void ratio (unit: m/s).

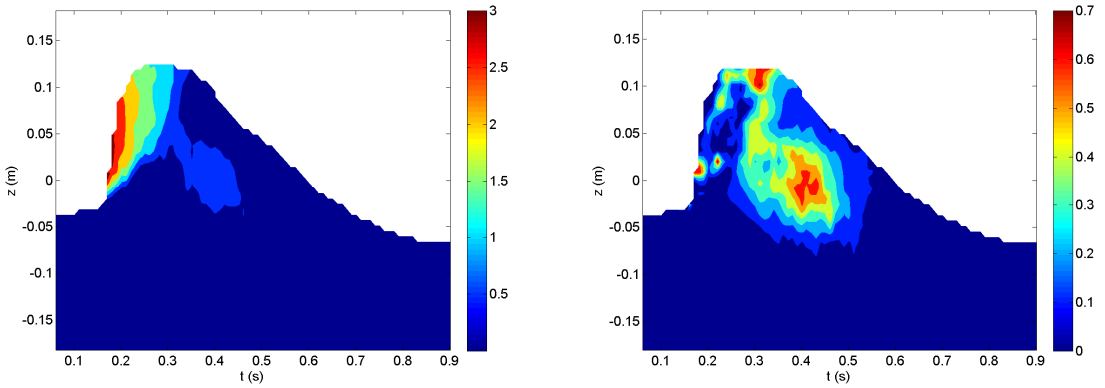

(a1) K (station 1)

(b1) (1-α)K (station 1)

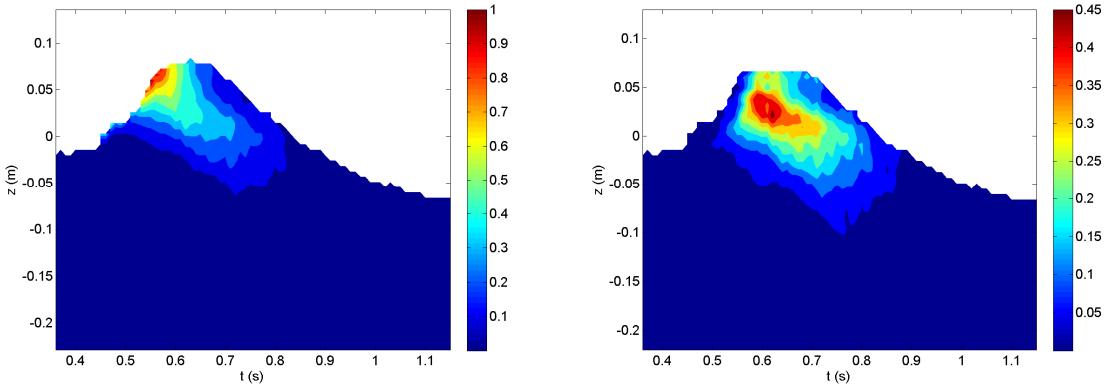

(a2) K (station 2)

(b2) (1-α)K (station 2)

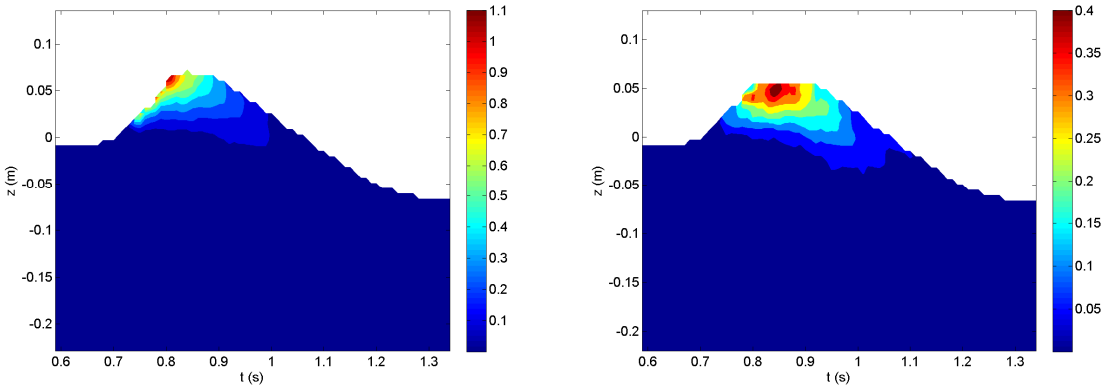

(a3) K (station 3)

(b3) (1-α)K (station 3)

Fig. 11.28 Mean kinetic energy considering void ratio (unit: m^2/s^2).

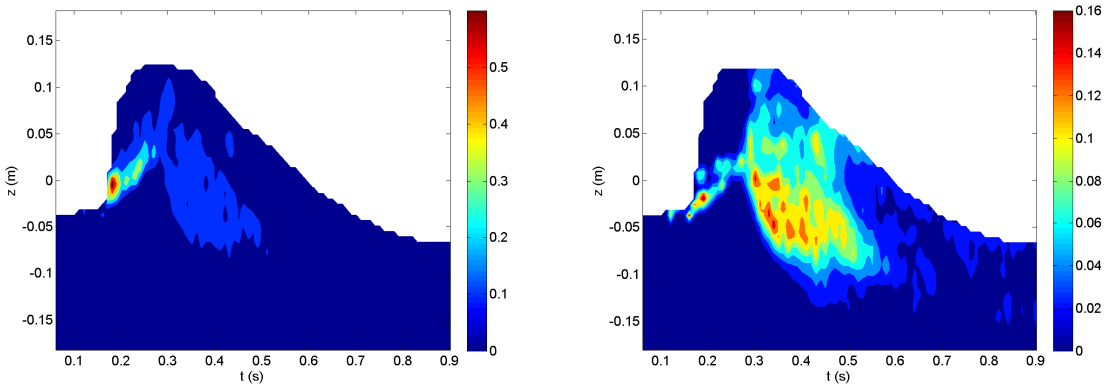

(a1) k (station 1)

(b1) (1-α)k (station 1)

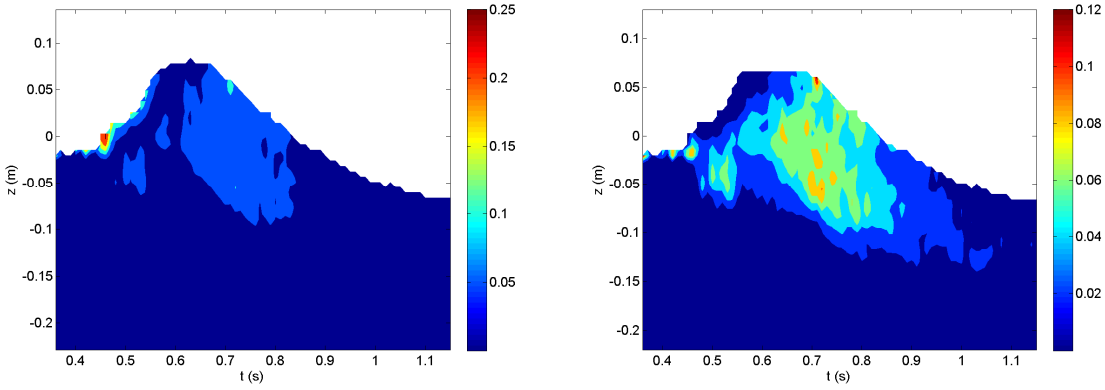

(a2) k (station 2)

(b2) k (station 2)

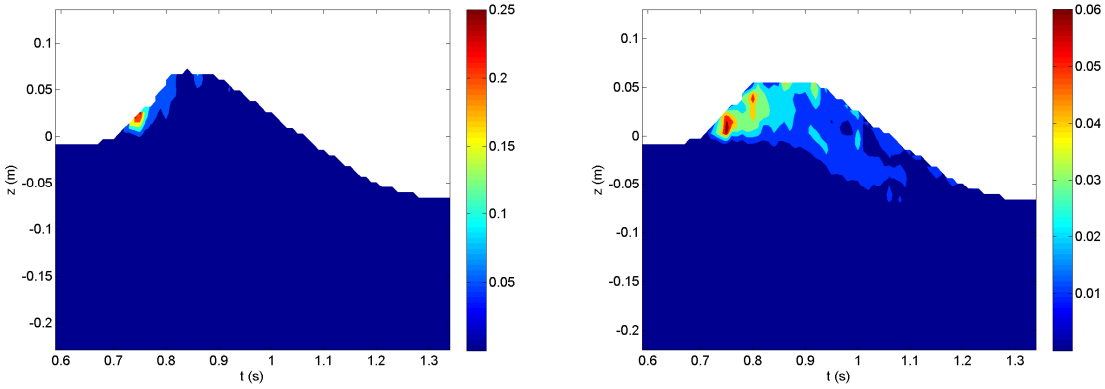

(a3) k (station 3)

(b3) k (station 3)

Fig. 11.29 Turbulent kinetic energy considering void ratio (unit: m^2/s^2).

In Fig. 11.30, the volume flux at each station considering the void ratio is compared with the volume flux excluding the void ratio. Note that the numbers 1-3 in parentheses represent the FOR measurement stations and a and b in parentheses represent the time series of the depth integrated horizontal velocities and the vertical profiles of the period-averaged horizontal velocities, respectively. Blue asterisks represent the depth-integrated (left panels) and period-averaged (right panels) horizontal velocities, respectively, while red circles represent the corresponding values when considering the void ratio. The dashed lines in the left panels represent the volume fluxes obtained by period averaging the depth integrated values while the dashed lines in the right panels represent the volume fluxes obtained by depth-integrating the period-averaged values. Fig. 11.31 to Fig. 11.33 are plotted in an identical manner.

Fig. 11.31 shows the comparison of the mass fluxes at each station. The mass flux was obtained by multiplying the water density (ρ = 1000 kg/m^3) by the volume flux shown in Fig. 11.30. There are large differences between the mass fluxes with and without the void ratio. For example, when considering the void ratio, net mass fluxes at the first and second splash-up are decreased by about 70% and 50%, respectively.

The comparison of the mean kinetic energy at each station can be seen in Fig. 11.32. In addition to the mass flux, large overestimation of the mean kinetic energy due to the high void ratio in the first splash-up roller can be seen in Fig. 11.32(a1). When considering the void ratio, the mean kinetic energy at the first splash-up is decreased about 55% while decreases at stations 2 and 3 are about 19.3% and 13.9% respectively.

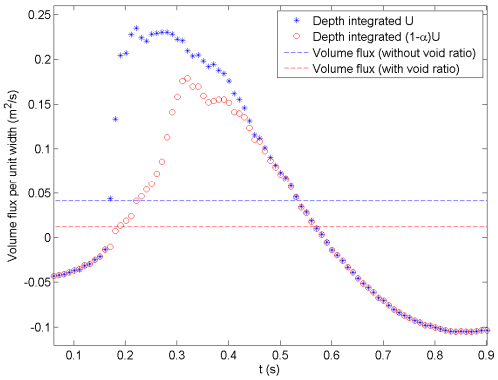

(a1) depth-integrated (1-α)*U* (station 1)

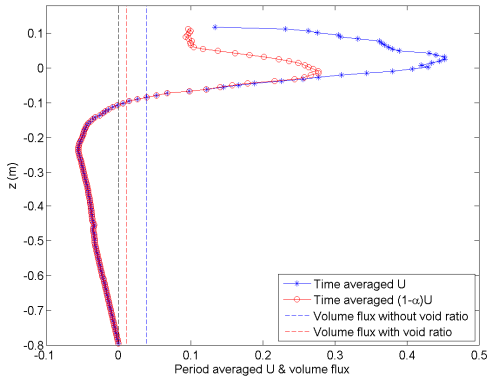

(b1) period-averaged (1-α)*U* (station 1)

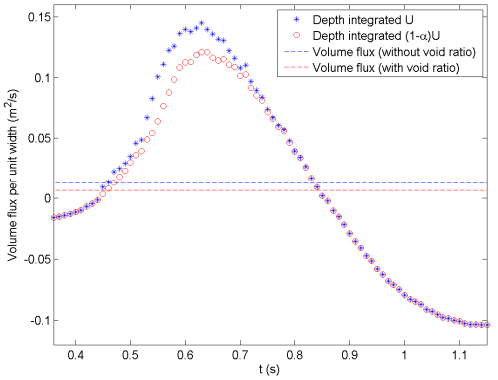

(a2) depth-integrated (1-α)*U* (station 2)

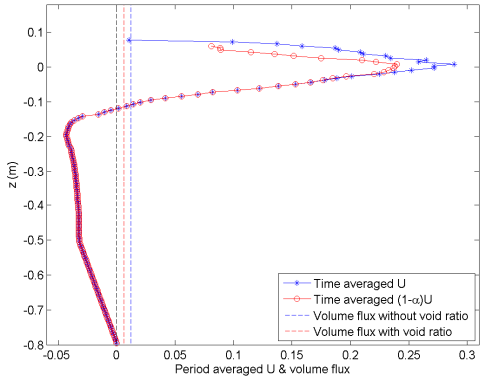

(b2) period-averaged (1-α)*U* (station 2)

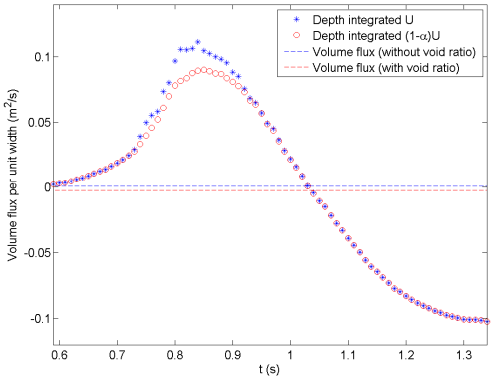

(a3) depth-integrated (1-α)*U* (station 3)

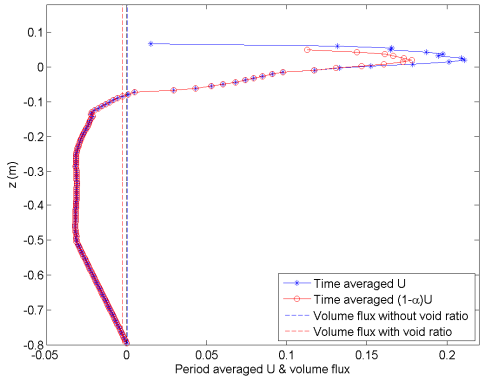

(b3) period-averaged (1-α)*U* (station 3)

Fig. 11.30 Volume flux considering void ratio.

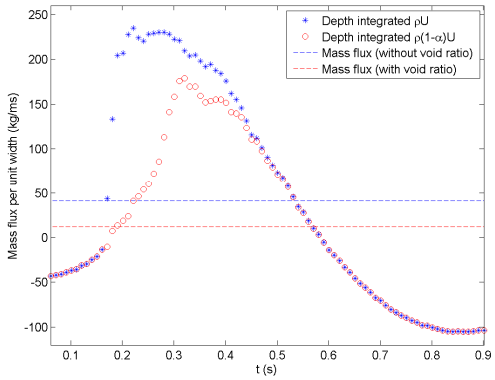

(a1) depth-integrated $\rho_w(1\text{-}\alpha)U$ (station 1)

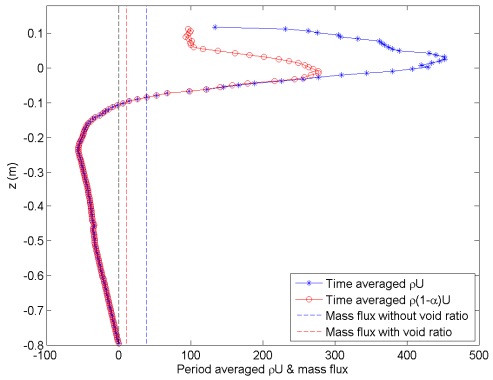

(b1) period-averaged ρ_w (1-α)U (station 1)

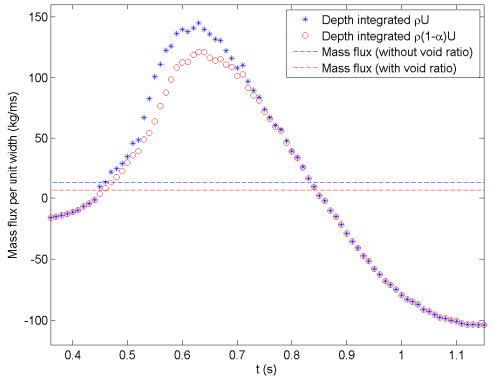

(a2) depth-integrated ρ_w (1-α)U (station 2)

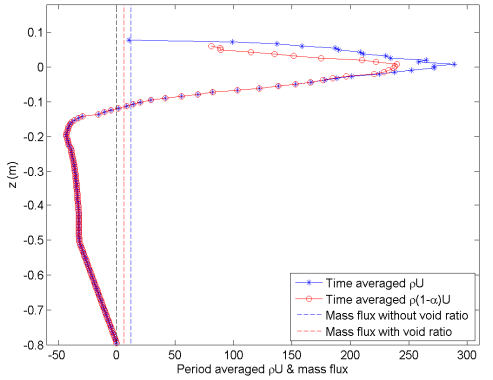

(b2) period-averaged ρ_w (1-α)U (station 2)

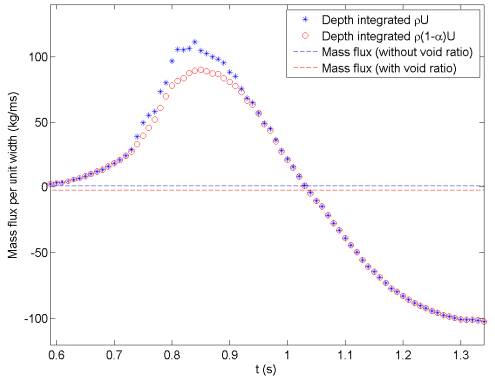

(a3) depth-integrated ρ_w (1-α)U (station 3)

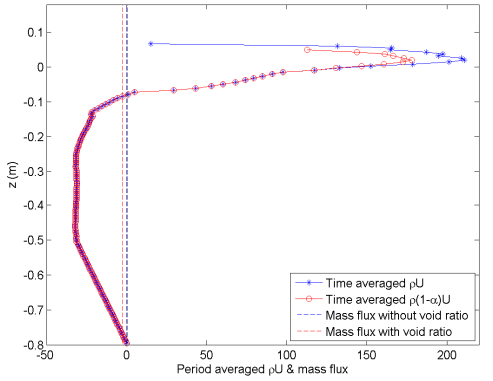

(b3) period-averaged ρ_w (1-α)U (station 3)

Fig. 11.31 Mass flux considering void ratio.

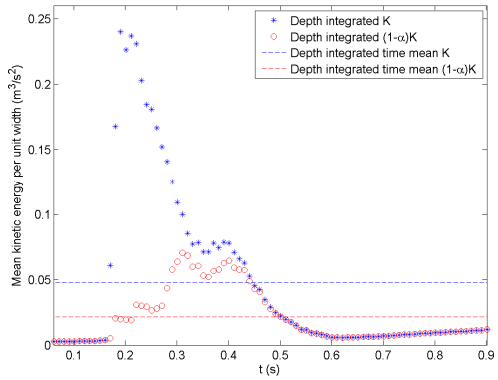

(a1) depth-integrated (1-α)*K* (station 1)

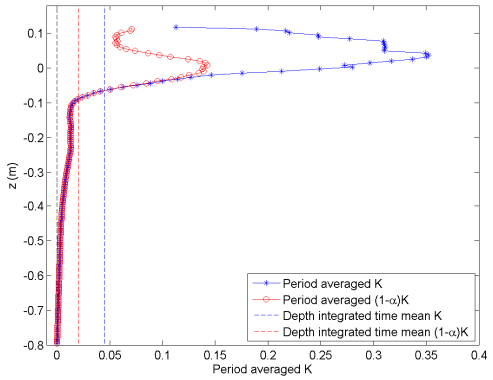

(b1) period-averaged (1-α)*K* (station 1)

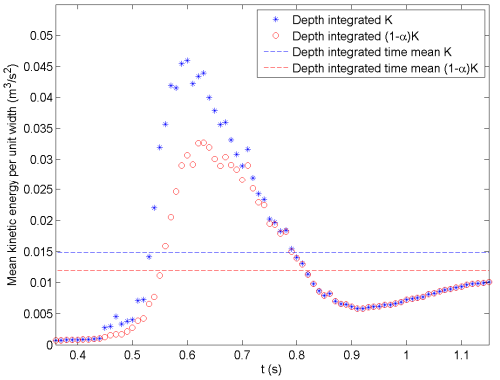

(a2) depth-integrated (1-α)*K* (station 2)

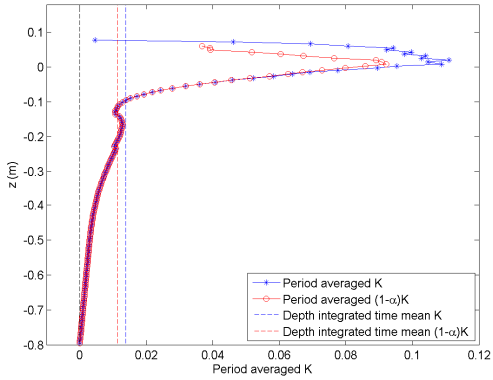

(b2) period-averaged (1-α)*K* (station 2)

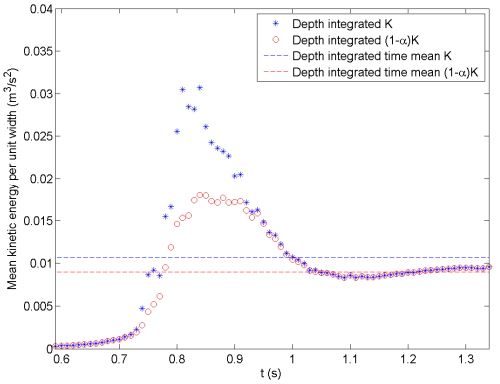

(a3) depth-integrated (1-α)*K* (station 3)

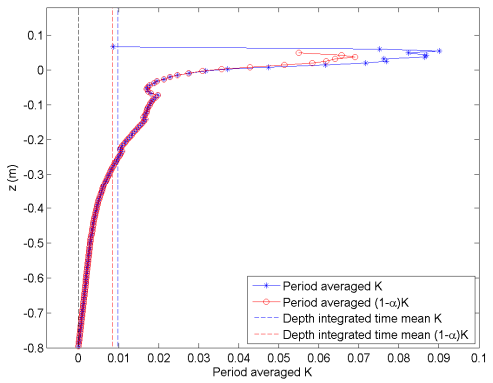

(b3) period-averaged (1-α)*K* (station 3)

Fig. 11.32 Mean kinetic energy variation in time and elevation with void ratio.

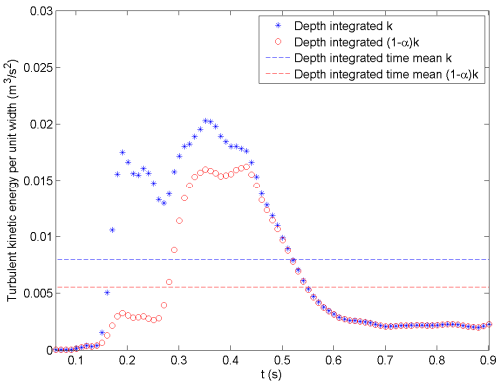

(a1) depth-integrated (1-α)*k* (station 1)

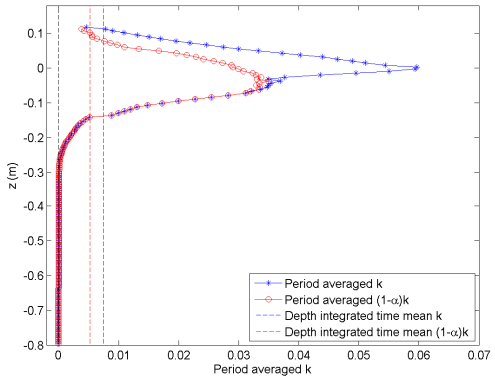

(b1) period-averaged (1-α)*k* (station 1)

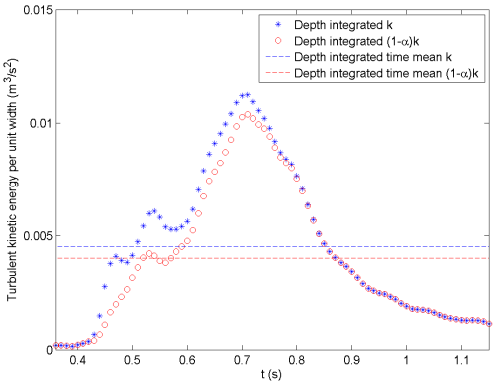

(a2) depth-integrated (1-α)*k* (station 1)

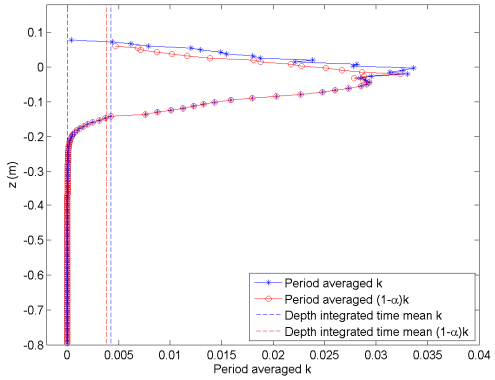

(b2) period-averaged (1-α)*k* (station 1)

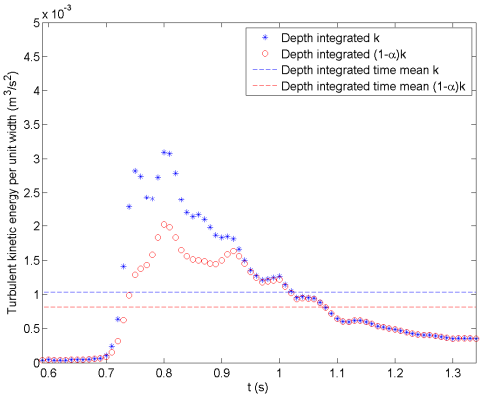

(a3) depth-integrated (1-α)*k* (station 1)

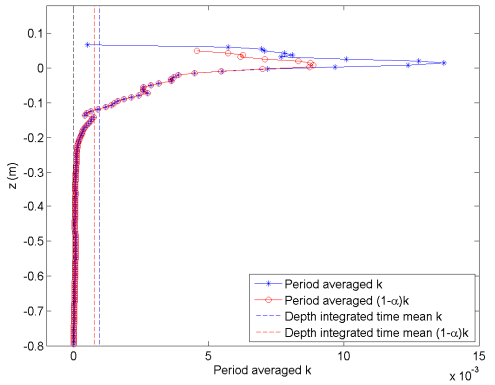

(b3) period-averaged (1-α)*k* (station 1)

Fig. 11.33 Turbulent kinetic energy variation in time and elevation with void ratio.

Fig. 11.33 shows the comparison of the turbulent kinetic energy at each station. When considering the void ratio, the turbulent kinetic energy at each station is decreased by about 30.8%, 11.1% and 23.9%, respectively.

Fig. 11.34 shows the mass flux comparison. Blue circles represent the mass fluxes at all 475 stations without considering the void ratio, and a blue dashed line represents the mean mass flux of all the stations. The four red asterisks represent the mass fluxes taking into account the void ratios. The three vertical dashed lines represent the three FOR stations. One station is chosen before the wave face becomes vertical, and the void ratio is zero at this station (x = - 0.41L). Compared with the mass flux at x = - 0.41L before breaking, the mass fluxes at the three FOR stations are reduced about 4.4%, 38.2% and 115%, respectively. It is expected that the initial net positive flux is slightly decreased through the first and second process. The net mass flux becomes negative at about $x = L$ and decreased linearly during the spilling wave phase ($x > L$).

The comparison of the momentum fluxes can be shown in Fig. 11.35. The momentum fluxes are decreased by about 59.8%, 22.4% and 21.7% at the three FOR stations, respectively, when considering the void ratio. Compared with the momentum fluxes at x = -0.41L, the momentum flux is increased about 51.3% at the first station while the fluxes at the second and third stations are reduced about 10.7% and 45.3% respectively.

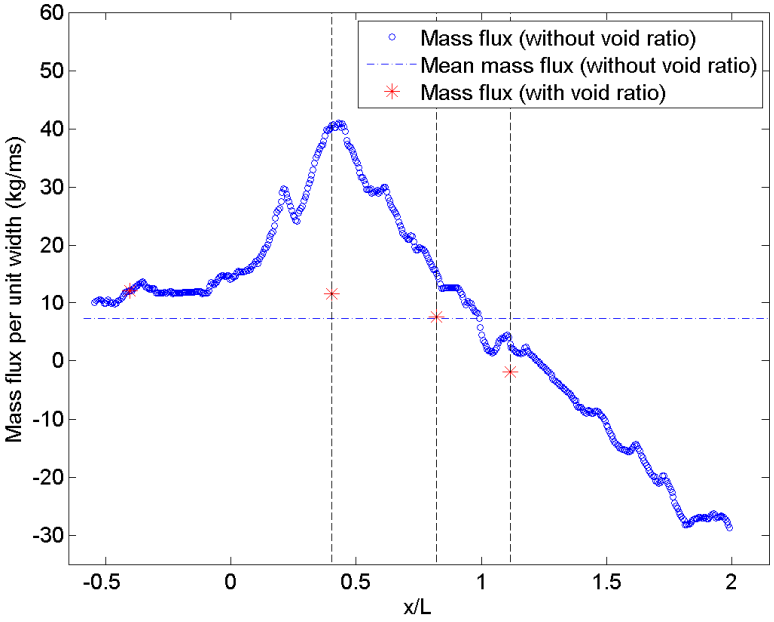

Fig. 11.34 Comparison of mass flux.

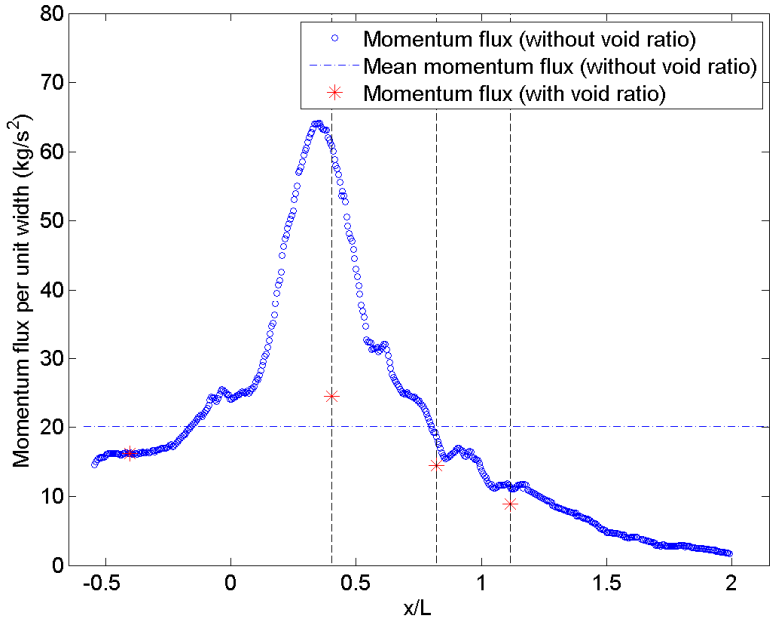

Fig. 11.35 Comparison of momentum flux.

Fig. 11.36 shows the comparison of the mean kinetic energy. The depth-averaged and period-averaged mean kinetic energies were normalized by C^2. Note that all the values represented in Fig. 11.36 to Fig. 11.41 are the depth-averaged and period-averaged values normalized by C^2. Compared with the mean kinetic energy at x = -0.41L, the mean kinetic energies at the three FOR stations are dissipated about 6%, 42% and 55.4% respectively. There is a large decrease during the second impingement process between FOR stations 1 and 2 as discussed in Chapter IX. On the other hand, turbulent kinetic energy is generated and increased significantly during the first impingement and splash-up process as shown in Fig. 11.37. It is dissipated very slightly during the second process and then decreases significantly after the second process.

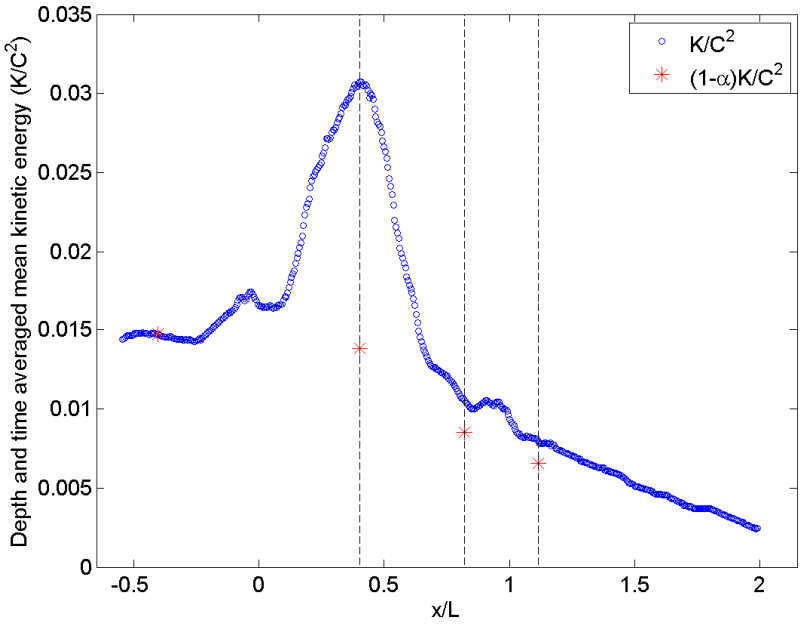

Fig. 11.36 Comparison of mean kinetic energy.

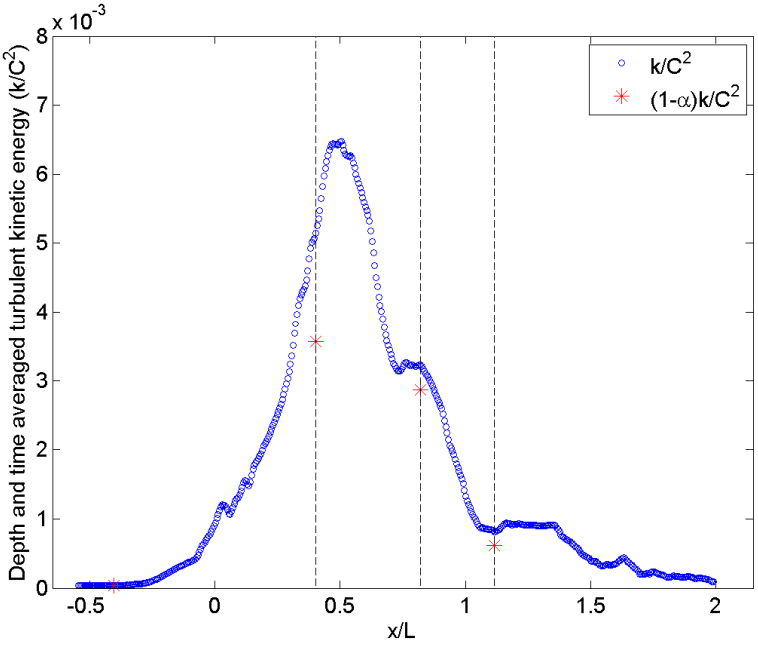

Fig. 11.37 Comparison of turbulent kinetic energy.

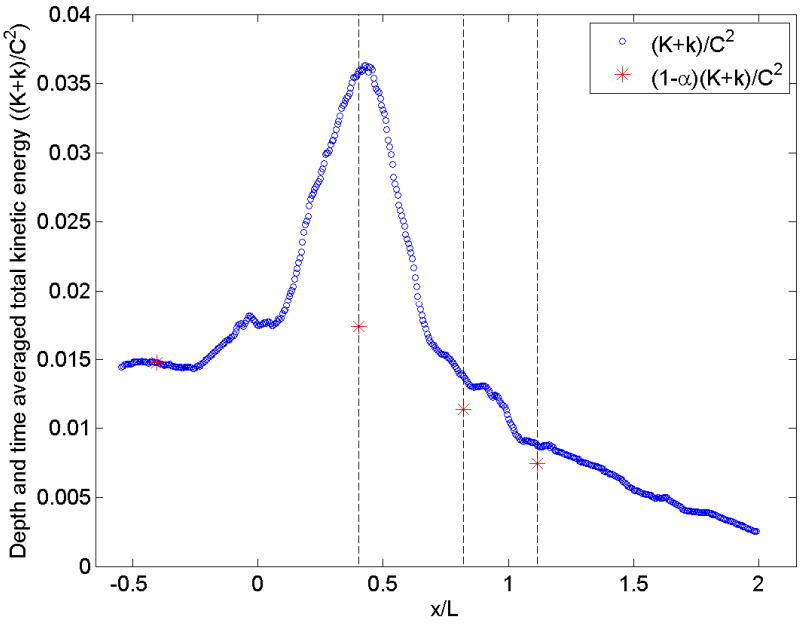

Fig. 11.38 Comparison of total kinetic energy.

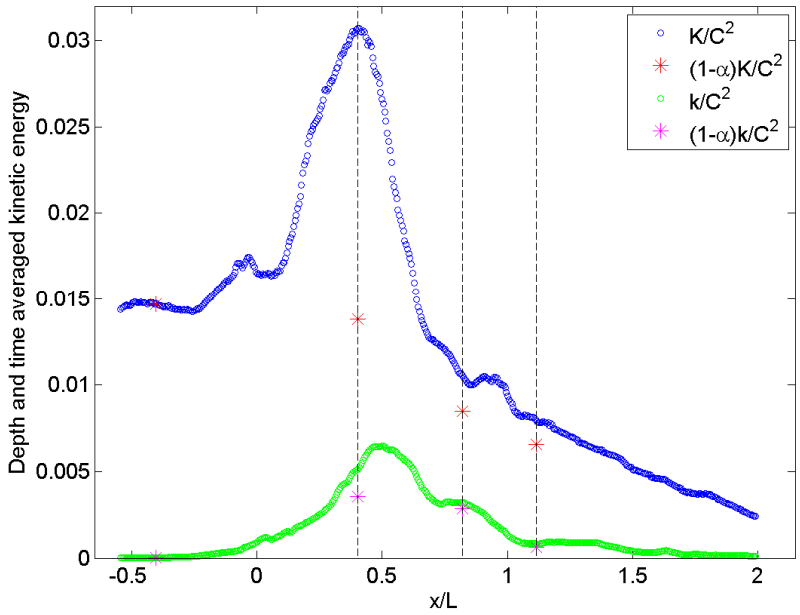

Fig. 11.39 Comparison of mean and turbulent kinetic energy.

As shown in Fig. 11.37, the turbulent kinetic energy is 4.14×10^{-5} close to zero at $x = -0.41L$. However, it increases significantly during the first process and the magnitude is 3.56×10^{-3} at the first splash-up ($x = 0.4L$). The turbulent kinetic energies at the second and third station are dissipated about 19.5% and 82.6% respectively, when compared with the turbulent kinetic energy at the first station.

Fig. 11.38 shows the normalized total kinetic energy. The total kinetic energies are decreased about 51.5%, 17.4% and 14.8% at the three FOR stations respectively, when considering the void ratio. Compared with the total kinetic energy at $x = -0.41L$, the total kinetic energy is increased about 17.8% due to the significant increase in the turbulent kinetic energy during the first process although the mean kinetic energy is decreased. The total kinetic energy at the second and third stations are dissipated by about 23% and

49.4% respectively, when compared with the total kinetic energy at x = -0.41L. It is estimated that about 85% of the total kinetic energy is dissipated at x = 2L. In addition, the mean kinetic energy is also dissipated by approximately 85% at x = 2L (Fig. 11.36).

Table 11.1
Ratio of turbulent and mean kinetic energy

	x = - 0.41L (pre-impingement)	x = 0.4L (1st splash-up)	x = 0.82L (2nd splash-up)	x = 1.11L (3rd splash-up)
$\overline{k_{da}} \Big/ \overline{K_{da}}$	0.28 %	16.74 %	30.59 %	10.23 %
$\overline{((1-\alpha)k)_{da}} \Big/ \overline{((1-\alpha)K)_{da}}$	0.28 %	25.74 %	33.70 %	9.44 %

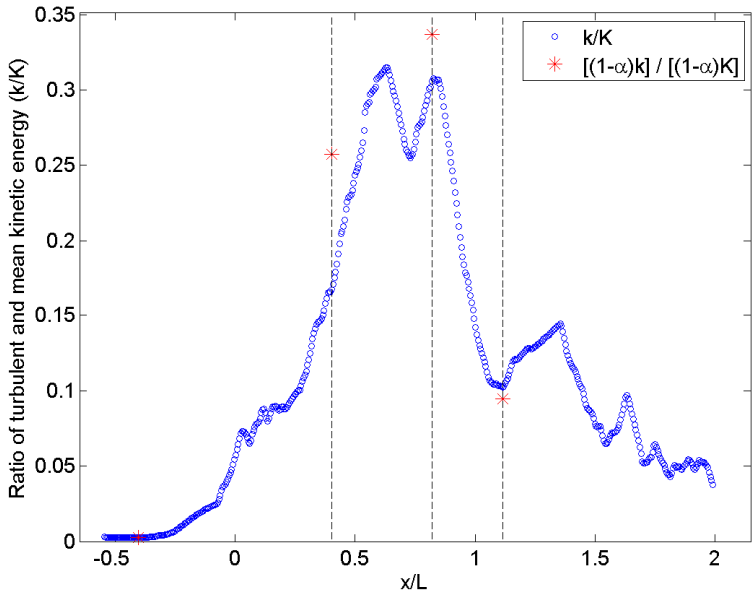

Fig. 11.40 Ratio of turbulent and mean kinetic energy.

The mean and turbulent kinetic energies can be seen in Fig. 11.39. The ratio of the turbulent kinetic energy to the mean kinetic energy was calculated as shown in Table 11.1 and Fig. 11.40. The ratios ($\overline{k_{da}}/\overline{K_{da}}$) at the four stations are approximately 0.28%, 16.74%, 30.59% and 10.23% when the void ratio is not considered. On the other hand, the ratios ($\overline{((1-\alpha)k)_{da}}\,/\,\overline{((1-\alpha)K)_{da}}$) become 0.28%, 25.74%, 33.70%, and 9.44% when the void ratio is applied to the kinetic energies.

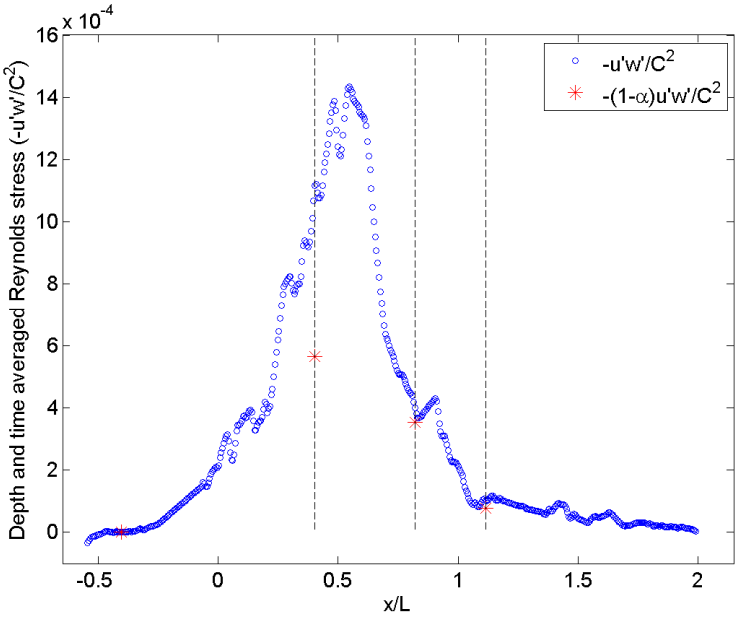

Fig. 11.41 Comparison of Reynolds stress.

Fig. 11.41 shows the comparison between Reynolds stresses. The Reynolds stress is significantly increased during the first impingement and splash-up. Compared with the Reynolds stress at the first splash-up, the Reynolds stresses at the second and third splash-up are decreased about 37.5% and 86.1% respectively.

As shown in the presented results, compressibility of the plunging breaker should not be ignored. All terms at the first splash-up are highly overestimated more than 100% unless the void ratio is applied to the calculation of fluxes and energies. For example, the mass flux per unit width at the first splash-up are 11.7 kg/ms with the void ratio and 40.6 kg/ms without the void ratio, respectively. Compared with the fully developed first splash-up region, the overestimation at the second and third splash-up is less significant. However, most terms at the second and third splash-up regions are overestimated about 20-30% when the void ratio is not considered. It is evident that the void ratio measurement is essential to investigate breaking waves, especially for plunging waves.

CHAPTER XII

CONCLUSION AND FUTURE WORK

12.1 Conclusion

Section 12.1.1 summarizes the results obtained from the FOR technique, which are mainly presented in Chapters II, III and IV, in the first part of this dissertation. Section 12.1.2 summarizes the results from the breaking wave measurements without applying the void ratio. The updated results considering compressibility of the plunging breaker are summarized in Section 12.1.3, based on the void ratio data obtained from the FOR measurements.

12.1.1 FOR Technique and Application

The FOR technique was developed to measure multiphase flows. Various experimental studies have been performed to validate the technique. Based on the coherent beat signal between the Fresnel reflection off the fiber-liquid interface and the scattered signal off the object such as a gas bubble or a solid particle, the technique is capable of measuring the velocity of the object with a high accuracy and the phases of the fluid simultaneously at the measurement point with a single fiber sensor. Therefore, the fraction ratio of each phase, including the number of solid particles and the void ratio of gas, can be easily estimated.

The bubble diameter as well as the velocity and void ratio can be measured using the FOR technique. It was verified that the low amplitude hump in front of the rising

bubble signal shown in the low sampling rate measurements was the envelope of the high frequency waves, which provides velocity information of the bubbles. Compared with the velocity measurement for the solid particles which have a very high detection rate for velocity information, not all bubbles return coherently mixed signals that provide velocity information. However, the diameters of the bubbles can be obtained for those that provide velocity information. The detection rate γ for the velocity measurement increases significantly as bubble size becomes smaller. The FOR technique with a single fiber probe is one of very few techniques that directly measure bubble diameter, velocity, and void fraction. Therefore, the technique is especially useful for bubbly flows that incorporate various size bubbles.

There exist many advantages for the FOR technique in bubble velocity and size measurements. Unlike conventional intrusive techniques based on fiber optic or conductivity probes that require a piercing event to obtain the bubble velocity, the FOR technique measure bubble velocity before the fiber tip comes in contact with the bubble surface. Therefore, the detrimental effect can be minimized if not eliminated whereby. Errors caused by the intrusiveness of the probes can be significantly reduced. Due to this characteristic, velocities of solid particles and water droplets can also be obtained, which is not feasible if conventional methods are used.

By simple modification of the FOR technique, solute concentration and refractive index change were measured with a greatly enhanced accuracy. The technique was used for measuring NaCl concentration in deionized water in order to validate the new normalization technique. In the concentration measurement, the technique provided a

refractive index resolution of 2×10^{-5} and a NaCl concentration resolution of approximately 2×10^{-4} $g\text{cm}^{-3}$. The technique is appropriate for various measurements, especially for measuring a spatially and temporally dependent concentration field in an environment, such as a water tank.

The developed FOR system was also used to validate the BIV technique and to obtain the void ratio of the plunging breaker.

12.1.2 Breaking Waves

Four kinds of experimental techniques were employed or developed to investigate strong plunging waves in deep water. The plunging breaker was generated in a deep water condition in a two-dimensional wave tank. The wave focusing method was employed to generate the strong plunging breaker at a desired location with high repeatability. BIV and PIV imaging techniques were used to measure the velocity and free surface elevation of the entire flow field including the highly aerated region. The void ratio was obtained from the FOR measurements. Wave elevation was obtained using resistance wave gauges. This section summarizes the experimental results of the plunging breaker in deep water, which are presented in Chapters V to XI.

In addition to quantitative measurements, it was possible to qualitatively describe the breaking process of the strong plunging breaker in detail by using a high speed camera with a high frame rate of 500 or 1000 *fps* with various sizes of field of view. The wave face becomes vertical at $x = -0.4L$ and $t = -0.24T$. Note that the breaking point in the present study was defined as the first impinging point, and the location and time at the first impinging point were set to $x = 0$ and $t = 0$. The front water is pushed up due to

the first impingement, and the pushed-up water rapidly ascends with large vertical momentum and causes the first splash-up. In this process, counterclockwise vorticity is also observed between the first impinging roller and the newly ascending water. As the new water crest reaches the peak elevation, the left and top portion of the crest impinge onto the first roller, which is the first backward impingement. Due to the first backward impingement, the first valley between the first and second roller is filled, and the free surface is linearized around $t = 0.61T$. This newly ascending water becomes the new primary wave and impinges onto the accumulated mixture which is the second impingement. The pushed up water caused by each impingement becomes the new primary wave crest and subsequently causes the next impingement.

The second impingement occurs around $t = 0.54T$ and $x = 0.65L$. The air-water mixture spray from the first splash-up roller impinges onto the front trough region continuously. The impinged spray is accumulated near the front trough and increases its size with slow roller motion. Originating from the newly ascending crest, the new primary water crest impinges onto the accumulated mixture roller. Then, the upper part of the mixture roller is splashed up (the second splash-up) due to the newly pushed up water below the mixture. The second valley caused by the second impingement is filled, and the free surface is linearized around $t = T$ by the second backward impingement.

The third splash-up followed by the third impingement is also caused by the new primary wave generated from the second impingement. The third impingement occurs around $t = 0.9T$ and $x = L$. The large vertical motions found in the first and second processes are not observed. An explanation is that the third process is the transition

region between the strong plunging region and the spilling wave region. The third valley caused by the third impingement is filled, and the free surface is linearized around t = 1.17T. A spilling wave region was observed after the third process.

The turbulent bore region of the primary wave crest eventually disappears around t = 2T and x = 2L. On the other hand, the first impinging roller goes into deep water until 0.32h and remains in deep water until about 3.6T. The distance between the first and second impinging point is about 0.65L. However, the distance between the two rollers is decreased at about 0.40-0.45L in deep water after impinging because the horizontal momentum of the first roller is much larger than that of the second roller.

In the initial stage of the plunging breaker, the elevations of the front and rear troughs are very close (about z = - 0.1h). The rear trough level is gradually increased and becomes about z = - 0.065h at x = 2L, while the front trough level is more rapidly increased and reaches the still water level (z = 0) at x = 1.5L. In addition, the wave period is gradually decreased during the breaking process and the local wave period becomes approximately 0.7T at x = 2L.

The BIV technique employed to measure the air-water mixture velocities in the highly aerated region. In addition, the modified PIV technique was used to investigate the entire flow field of the plunging breaker including the highly aerated region. The velocities in the aerated region can be measured by means of modifying the traditional PIV technique. Instead of using a high power pulsed laser, a continuous laser light sheet was used to illuminate the air-water mixture and the seeded particles. Images were taken by the high speed camera with a 500 *fps* to allow for a high temporal resolution. The

spatial resolutions of the present BIV and PIV data are 5.26 and 5.78 mm, respectively. Note that the wave height of the primary wave is 0.204 m. The temporal resolution of the presented data is 0.01 s in both measurements.

Mean velocities were obtained using the ensemble average of 20 instantaneous velocity fields. In the PIV measurements, the maximum horizontal velocity is about $1.25C$ when the wave face becomes vertical at $t = -0.24T$, and its magnitude is linearly increased until the first impingement. The maximum horizontal and downward vertical velocity at the first impingement occurs at $1.68C$ and $0.71C$, respectively. The maximum upward velocity for the entire process occurs at the first splash-up. However, it is also very high in the pre-impinging region between $z = -0.1h$ and $0.1h$, and its magnitude is close to that in the first splash-up. If density is considered, maximum upward momentum will occur at the pre-impinging region. The maximum horizontal velocity for the entire breaking process is $2.14C$ and occurs at the beginning of the first splash-up at $t = 0.06T$ after the location of the maximum speed moves from the impinging jet to the splash-up at $t = 0.036T$. After this moment, the maximum horizontal velocity is gradually decreased and becomes smaller than the wave phase speed at $t = T$ while the maximum downward velocity is gradually increased during the first splash-up. The maximum downward velocity in the entire flow is about $0.78C$ at $t = 0.36T$ in the water spray impinging process. Note that the maximum downward velocity at the first impingement is about $0.71C$. The maximum downward velocity is rapidly decreased immediately following the second impingement and is about $0.25C$ at the third impingement. It becomes about $0.2C$ in the spilling region.

Since PIV measurements were completed to cover the entire breaking wave, time-averaged values of the mean and turbulent properties were obtained from raw time series at every point all 475 station with $dx = dz = 5.8$ mm and $dt = 0.01$ s. In addition, the maximum and minimum values at every point were also obtained. Volume flux per unit width was calculated for every station. The averaged positive and negative flux for the entire stations are 0.0261 m^2/s and -0.0187 m^2/s respectively. Mean net flux is 0.0074 m^2/s. Even in the pre-impinging region, net flux is about 0.01m^2/s and there is a large positive flux between $x = 0$ and $x = L$ where the void ratio cannot be neglected. It should decrease if the mixture density is considered. Although it is overestimated in the aerated region, the net flux starts decreasing linearly from around $x = 0.6L$ and becomes close to zero at $x = L$. In addition, in the spilling wave region ($x > L$), the net flux changes to negative and becomes about - 0.03 m^2/s at $x = 2L$.

Due to the repetitive impingement and splash-up process in the strong breaker, large horizontal eddies can be observed and their vorticities were calculated. The location of the high positive (clockwise) vorticity is near the bottom boundary of the each roller, specifically at the toe of each splash-up roller due to the shear flow between the roller and the water wave below the roller. Negative (counterclockwise) vorticity was found between the impinging roller and the ascending crest during the impinging and splash-up process. The positive vorticity is transported near the mean water level through the flow field. During the first splash-up, the location is slightly lower than the mean water level while the location after the second impingement is slightly higher than the mean water level. This is because of the increasing front trough level. The location of

the maximum negative vorticity is usually above the maximum positive vorticity. Each negative vortex weakens and disappears after each backward impingement. The maximum positive vorticity occurs at $t = 0.06T$ in the second roller and the maximum negative vorticity is found at $t = 0.2T$ at the left side of the ascending crest

The maximum mean kinetic energy at $x = -0.5L$ is about $0.6C^2$ and is rapidly increased during the overturning process. The maximum mean kinetic energy reaches $1.64C^2$ at the first impingement. The maximum for the entire flow field is found at the beginning of the first splash-up and is about $2.31C^2$. The maximum energy decreases linearly with time while there is sudden decrease from $x = 0.55L$ in the spatial domain. The depth-averaged time mean value of the mean kinetic energy was obtained. The primary wave in the pre-impinging region has a large kinetic energy as well as a large potential energy. The mean kinetic energy decreases linearly except in the region corresponding to the first impingement, the first splash-up, and the second impingement ($x = -0.2L$ to $0.7L$). Although the kinetic energy in the region is overestimated if the mixture density is not considered, both the kinetic and potential energy of the impinging water must be converted to the kinetic energy of the splash-up.

Fluctuating velocities were obtained using the ensemble average of 20 instantaneous velocities. In addition, the ensemble averaged Reynolds stresses were obtained from the instantaneous turbulent velocities in both the horizontal and vertical directions. The horizontal turbulent normal stress is generated near the bottom boundary of each roller while the vertical normal stress is generated between the impinging roller and the ascending water crest. Since vorticity is one of the greatest sources for

turbulence generation, the generated location and transport of the horizontal and vertical normal stresses is very similar to those of the positive and negative vorticities. $\sqrt{\langle u'u' \rangle}$ and $\sqrt{\langle w'w' \rangle}$ have maximum magnitudes of $0.69C$ ($0.39V_{max}$) and $0.49C$ ($0.26V_{max}$) at the beginning of the first splash-up ($t = 0.06T$), respectively. $\sqrt{\langle w'w' \rangle}$ has a local maximum at the second impingement with a magnitude of $0.45C$ ($0.36V_{max}$). Only $\sqrt{\langle u'u' \rangle}$ has a local maximum in the third process due to the small vertical momentum fluctuation from the third process. The absolute vertical turbulence intensity at the second impingement is smaller than that at the first impingement while it is higher at the second impingement when normalized by the maximum speed at the corresponding time. The maximum $\sqrt{\langle u'u' \rangle}$ was maintained between 0.3-$0.4V_{max}$ while the maximum $\sqrt{\langle w'w' \rangle}$ was around 0.2-$0.25V_{max}$ except for the second impingement ($0.36V_{max}$). Unlike the maximum normal stresses at each station, the depth-averaged time mean $\sqrt{\langle u'u' \rangle}$ is less dominant between $x = 0$ and $0.45L$. Both depth-averaged time mean values have a maximum around $x = 0.5L$ due to the water spray impingement and the first impinging roller in deep water. The local maximum occurs during each process.

In addition to the Reynolds normal stresses, the ensemble averaged Reynolds shear stress was also obtained. The positive shear stress is more dominant than the negative shear stress in the entire flow except for the region corresponding to the beginning of the first and second splash-up processes. The negative stress due to the upward momentum flux at the beginning of the first splash-up becomes weak as the first splash-up becomes fully developed. The maximum positive shear stress in the entire flow occurs at the water spray impinging location due to a large downward momentum flux. Three local

maxima of the positive stress are found at the first impingement (0.03T), the water spray impingement (0.29T) and the second impingement (0.47T) while the maximum of the negative stress occurs at t = 0.17T. However, the maximum shear stress normalized by V_{max} has a maximum at the second impingement onto the accumulated roller. Although there are time differences between the two maxima (0.29T and 0.47T), the location is very close to each other (around 0.5L), which corresponds to the accumulated roller. In addition, the depth-averaged time mean Reynolds stresses are positive at all stations. The maximum occurs around x = 0.5 - 0.6L and is approximately $1.6\times 10^{-3}C^2$.

Turbulent kinetic energy is generated near the ascending crest at the beginning of the first splash-up. Significant turbulent kinetic energy is generated at the water spray impinging region while turbulence energy is gradually dissipated in the first impinging roller. The maximum turbulent kinetic energy is steady around $0.3C^2$ until the water spray impingement. Then, the maximum turbulent kinetic energy is rapidly decreased during the second impingement and splash-up process while the mean kinetic energy has a local peak at this time. There is a local maximum at the water spray impingement location resulting from the second splash-up. The locations for the turbulent kinetic energy are slightly lower than those for the mean kinetic energy. The depth-averaged time mean value of the turbulent kinetic energy is gradually increased until x = 0.5L and its magnitude is about $6.4 \times 10^{-3}C^2$. It begins decreasing from x = 0.6L while the mean kinetic energy begins decreasing from x = 0.4L. The turbulent kinetic energy between x = 0.5L and 0.8L is approximately 25 - 30% of the mean kinetic energy. It is found that the turbulent kinetic energy is continuously transported above the mean water level by

the mean horizontal flow during the first process. The maximum kinetic energy transport by U occurs around $x = 0.6L$ due to the continuous water spray impingement and the second impingement onto the accumulated roller. Downward transport due to the first impinging roller is found below the mean water level between $x = 0.25L$ and $0.5L$. The maximum downward transport occurs around $x = 0.55L$ due to the continuous water spray impingement and the second impingement. Upward transport is also found near the first and second splash-up region. Around $x = 0.5L$ to $0.65L$, the turbulent kinetic energy is continuously transported downward and downstream during the breaking process. Therefore, the Reynolds shear stress also has a large positive value in this region.

Using the FOR system, void ratio was measured at the three stations located in each splash-up region. In addition to the void ratio measurement, it was possible to describe the breaking process using the FOR signal since a high sampling rate of 100 kHz was used. It was found that depth-averaged void ratio at the first and second splash-up has two local maximum values. One represents the splash-up roller and the other represents the following impinging roller. It was also found that there is a local minimum void ratio between the two rollers. It represents the ascending water crest caused by each impingement, which is the most distinguishable characteristic of the plunging breaker from the spilling breaker. The maximum wave-averaged and period-averaged void ratios at $x = 0.4L$ (the middle of the fully developed first splash-up) are about 0.58 and 0.19 at z = 0.06 m, respectively. At the second station, these void ratios are about 0.49 and 0.13, respectively. The void ratio is significantly decreased at the third station. The maximum

wave-averaged and period-averaged void ratios are about 0.34 and 0.07 at z = 0.05 m, respectively. The void ratio obtained from the images was significantly overestimated below the still water level for the impinging roller. It is considered that this is due not only to the laser light sheet but also the nature of the imaging method, which overestimates the void ratio for a region with a low bubble concentration. Special care and correct validation are required when the void ratio is obtained from various imaging techniques.

12.1.3 Breaking Waves Considering Compressibility

Compressibility of the plunging breaker is considered. Mass flux, momentum flux, mean and turbulent kinetic energy, and Reynolds stresses at each FOR station were recalculated, based on the void ratio obtained from the FOR measurements. It was found that net mass fluxes at the first and second splash-up are decreased by about 70% and 50%, respectively, and momentum fluxes at the first and second splash-up are also decreased by about 60% and 22% when considering the void ratio. The mean and turbulent kinetic energies are significant at the ascending water crest and the impinging roller rather than the splash-up roller when applying the void ratio. All terms such as fluxes and kinetic energies at the first splash-up are highly overestimated (more than 100%) unless the void ratio is applied to the calculation of fluxes and energies. Compared with the fully developed first splash-up region, the overestimation at the second and third splash-up is less significant. However, most terms are overestimated by about 20~30% when the void ratio is not considered.

Compared with the mean kinetic energy of the pre-impinging region, the mean

kinetic energies at the three splash-up regions are dissipated about 6%, 42% and 55.4%. There is a large decrease during the second impingement process. In addition, the mean kinetic energy is dissipated by approximately 85% at $x = 2L$. The turbulent kinetic energy is $4.14 \times 10^{-5} C^2$ close to zero at $x = -0.41L$. However, it increases significantly during the first process and the magnitude is $3.56 \times 10^{-3} C^2$ at the first splash-up ($x = 0.4L$). The turbulent kinetic energies at the second and third station are dissipated by about 19.5% and 82.6% respectively, when compared with the turbulent kinetic energy at the first splash-up. The ratios of the turbulent kinetic energy and the mean kinetic energy at each splash-up are about 25.7%, 33.7%, and 9.4% when considering the void ratio. Compared with the total kinetic energy at the pre-breaking region, the total kinetic energy is increased by about 17.8% due to the significant increase of the turbulent kinetic energy during the first process although the mean kinetic energy is decreased. The total kinetic energy at the second and third stations are dissipated by about 23% and 49.4% respectively. It is estimated that about 85% of the total kinetic energy is dissipated at $x = 2L$. It is evident that the void ratio measurement is essential to investigate breaking waves, especially for plunging waves.

12.2 Future Work and Suggestions

Local acceleration as well as convective acceleration were able to be obtained due to the high spatial and temporal resolution. Acceleration data obtained from the BIV and PIV measurements can be seen in Appendixes A and B, respectively. However, this data should be validated although it is difficult to find results from other researchers. The inertia force of the plunging breaker will be estimated using the void ratio data from the

FOR measurements.

The turbulent kinetic energy transport equation will be examined. One of the important advantages in the present study is that the local rate of change of k, $\partial\langle k\rangle/\partial t$, can be easily obtained due to the high temporal resolution as compared with traditional PIV measurements. It is essential to examine the transport equation for the turbulent kinetic energy budget to describe more physics of the turbulent flow structure in the plunging breaker. Using the energy dissipation rate due to viscous stresses, Kolmogorov microscale, which is the smallest turbulence scale, can be estimated.

Since plunging breakers have a much more remarkable interaction between air and water than spilling breakers, it cannot be considered as incompressible flow. However, no research has yet been reported. The air-water mixture density varies in both time and space. Most values are likely overestimated and require correction with the void ratio measurement. Compressibility of the plunging breaker was carried out using the void ratio results obtained from FOR measurements. However, the number of measurement stations is limited to investigate the plunging breaker because the horizontal variation of a plunging breaker is also significant due to the repetitive impinging and splash-up process. As discussed in Chapter XI, the mixture density variation in time and space for the entire flow field can be estimated if the void ratios obtained from the imaging techniques are corrected with reasonable methods. The void ratio obtained from FOR measurements can be useful for the correction.

If it is possible to obtain the void ratio for the entire flow field using image techniques, another data set considering the mixture density can be obtained. Therefore,

it will be possible to compare the results without considering density effects for the entire flow filed. In addition, breaking wave force can be obtained using the acceleration data of the entire flow.

BIV and PIV measurements were performed to investigate spilling waves in deep water processing identical conditions as the plunging breaker measurements. In addition, void ratios were measured using the FOR technique. Therefore, it will beneficial to compare the plunging breaker results presented in this dissertation to the spilling breaker results after data analysis.

Since original images from the BIV and PIV measurements were taken at a frame rate of 500 *fps*, the temporal resolution of the final data can be improved up to 2 ms. This is necessary to obtain more accurate time-averaged or time derivative terms such as the local acceleration or the local rate of change of k.

REFERENCES

Adrian, R.J., 2005. Twenty years of particle image velocimetry. Experiments in Fluids 39, 159-169.

Adrian, R.J., Hassan, Y., Meinhart, C., ed. 1999. In: Proceedings of the 3rd International Workshops on PIV, 107-162, Santa Barbara, CA.

Banner, M.L., Peregrine, D. H., 1993. Wave breaking in deep water. Annual Review of Fluid Mechanics 25, 373-397.

Barrau, E., Rivière, N., Poupot, Ch., Cartellier, A., 1999. Single and double optical probes in air-water two-phase flows: real time signal processing and sensor performance. International Journal of Multiphase Flow 25, 229-256.

Basco, D.R., 1985. A qualitative description of wave breaking. Journal of Waterway, Port, Coastal and Ocean Engineering 111, 171-187

Battjes, J.A., 1988. Surf-zone dynamics. Annual Review of Fluid Mechanics 20, 257-293.

Blenkinsopp, C.E., Chaplin, J.R., 2007. Void fraction measurements in breaking waves. Proceedings of the Royal Society A 463, 3151-3170.

Bonmarin, P., 1989. Geometric properties of deep-water breaking waves. Journal of Fluid Mechanics 209, 405-433.

Born, M., Wolf, E., 1965. Principle of Optics. Pergamon, New York.

Brandemburg, A., 1997. Differential refractometry by an intergrated-optical Young interferometer. Sensors and Actuators B 39, 266-271.

Brennen, C.E., 2005. Fundamentals of Multiphase Flow. Cambridge University Press,

New York.

Bröder, D., Sommerfeld, M., 2007. Planar shadow image velocimetry for the analysis of the hydrodynamics in bubbly flow. Measurement Science and Technology 18, 2513-2528.

Byrne, G.D., James, S.W., Tatam, R.P., 2001. A Bragg grating based fibre optic reference beam laser Doppler anemometer. Measurement Science and Technology 12, 909-913.

Cartellier, A., 1992. Simutaneous void fraction measurement, bubble velocity, and size estimate using a single optical probe in gas-liquid two-phase flows. Review of Scientific Instruments 63, 5442-5453.

Cartellier, A., Barrau, E., 1998. Monofiber optical probes for gas detection and gas velocity measurements: conical probes. International Journal of Multiphase Flow 24, 1265-1294.

Cavalier, H., Thioye, M., Darrigo, R., 1989. Bubbling characterization in gas-solid fluidized beds using optical fiber probes and transitional analysis. Review of Scientific Instruments 60, 1312-1315.

Chang, K.-A., Liu, P.L.-F., 1998. Velocity, acceleration and vorticity under a breaking wave. Physics of Fluids 10, 327-329.

Chang, K.-A., Liu, P.L.-F., 1999. Experimental investigation of turbulence generated by breaking waves in water of intermediate depth. Physics of Fluids 11, 3390-3400.

Chang, K.-A., Liu, P.L.-F., 2000. Pseudo turbulence in PIV breaking-wave measurements. Experiments in Fluids 29, 331-338.

Chang, K.-A., Lim, H.-J., Su, C.B., 2002. A fiber optic Fresnel ratio meter for measurements of solute concentration and refractive index change in fluids. Measurement Science and Technology 13, 1962-1965.

Chang, K.-A., Lim, H.-J., Su, C.B., 2003. Fiber optic reflectometer for velocity and fraction ratio measurements in multiphase flows. Review of Scientific Instruments 74, 3559-3565.

Chang, K.-A., Lim, H.-J., Su, C.B., 2004. Reply to "Comment on 'Fiber optic reflectometer for velocity and fraction ratio measurements in multiphase flows.'" Review of Scientific Instruments 75, 286.

Chanson, H., 1996. Air Bubble Entrainment in Free-surface Turbulent Shear Flows. Academic, San Diego.

Chanson, H., 2002. Air-water flow measurements with intrusive, phase-detection probes. Can we improve their interpretation? Journal of Hydraulic Engineering, ASCE 128, 252-255.

Chanson, H., Brattberg, T., 2000. Experimental study of the air-water shear flow in a hydraulic jump. International Journal of Multiphase Flow 26, 583-607.

Christensen, E.D., 2006. Large eddy simulation of spilling and plunging breakers. Coastal Engineering 53, 463-485.

Christensen, E.D., Deigaard, R., 2001. Large eddy simulation of breaking waves. Coastal Engineering 42, 53-86.

Christensen, E.D., Walstra, D.-J., Emerat, N., 2002. Vertical variation of the flow across the surf zone. Coastal Engineering 45, 169-198.

Cowen, E.A., Sou, I.M, Liu, P.L.-F., Raubenheimer, B., 2003. Particle image velocimetry measurements within a laboratory-generated swash zone. Journal of Engineering Mechanics 129(10), 1119-1129.

Cox, D.T., Shin, S., 2003. Laboratory measurements of void fraction and turbulence in the bore region of surf zone waves. Journal of Engineering Mechanics 129(10), 1197-1205.

Deane, G.B., 1997. Sound generation and air entrainment by breaking waves in the surf zone. Journal of the Acoustical Society of America 102(5), 2671–2689.

Deane, G.B., Stokes, M.D., 2002. Scale dependence of bubble creation mechanisms in breaking waves. Nature, 418, 839-844.

Deen, N.G., Westerweel, J., Delnoij, E., 2002. Two-phase PIV in bubbly flows: status and trends. Chemical Engineering & Technology 25, 97-101.

Dehaeck, S., Van Beeck, J.P.A.J., Riethmuller, M.L., 2005. Extended glare point velocimetry and sizing for bubbly flows. Experiments in Fluids 39, 407-419.

Drazen, D.A., Melville W.K., 2009. Turbulence and mixing in unsteady breaking surface waves. Journal of Fluid Mechanics 628, 85-119.

Dyott, R.B., 1978. The fibre-optic Doppler anemometer. Microwaves, Optics and Acoustics 2, 13-18.

Fan, C.H., Longtin, J.P., 2000. Laser-based measurement of liquid temperature or concentration at a solid-liquid interface. Experimental Thermal and Fluid Science 23, 1-9.

Fischer, H.B., List, E.J., Koh, R.C.Y., Imberger, J., Brooks N.H., 1979. Mixing in Inland

and Coastal Waters. Academic Press, San Diego.

Govender, K., 1999. Velocity, vorticity and turbulence measurements in the surf zone. Ph.D. dissertation, University of Natal, Durban.

Govender, K., Alport, M.J., Mocke, G.P., Michallet H., 2002a. Video measurements of fluid velocities and water levels in breaking wave. Physica Scripta T97, 152-159.

Govender, K., Mocke, G.P., Alport, M.J., 2002b. Video-imaged surf zone wave and roller structures and flow fields. Journal of Geophysical Research 107(3072), X1-X21.

Govender, K., Mocke, G.P., Alport, M.J., 2004. Dissipation of isotropic turbulence and length-scale measurements through the wave roller in laboratory spilling waves. Journal of Geophysical Research 109, C08018-1-8.

Guet, S., Fortunati, R.V., Mudde, R.F., Ooms, G., 2003. Bubble velocity and size measurement with a four-point optical fiber probe. Particle & Particle Systems Characterization 20, 219-230.

Herbert, P.M., Gauthier, T.A., Briens, C.L., Bergougnou, M.A., 1994. Application of fiber optic reflection probes to the measurement of local particle velocity and concentration in gas-solid flow. Powder Technology 80, 243-252.

Hoque, A., Aoki, S.-I., 2005. Distributions of void fraction under breaking waves in the surf zone. Ocean Engineering 32, 1829-1840.

Huang, Z.-C., Hsiao, S.-C., Hwung, H.-H., Chang, K.-A., 2009. Turbulence and energy dissipations of surf zone spilling breakers. Coastal Engineering 56, 733-746.

Jansen, P.C.M., 1986. Laboratory observations of the kinematics in the aerated region of breaking waves. Coastal Engineering 9, 453–477.

Juliá, J.E., Harteveld, W.K., Mudde, R.F., Van den Akker, H.E.A., 2005. On the accuracy of the void fraction measurements using optical probes in bubbly flows. Review of Scientific Instruments 76, 35103-1-15.

Kashima, H., Mori, N., Kakuno, S., 2006. Air bubble measurements of the surf zone breaking waves by bubble tracking velocimetry. In: Proceedings of the 30th International Conference on Coastal Engineering, San Diego, CA, 934-945.

Kawaguchi, T., Akasaka, Y., Maeda, M., 2002. Size measurements of droplets and bubbles by advanced interferometric laser imaging technique. Measurement Science and Technology 13, 308-316.

Kiambi, S.L., Duquenne, A.M., Bascoul, A., Delmas, H., 2001. Measurements of local interfacial area: application of bi-optical fibre technique. Chemical Engineering Sciences 56, 6447-6453.

Kimmoun, O., Branger, H., 2007. A particle image velocimetry investigation on laboratory surf-zone breaking waves over a sloping beach. Journal of Fluid Mechanics 588, 353-397.

Krishna, V., Fan, C.H., Longtin, J.P., 2000. Real-time precision concentration measurement for flowing liquid solutions. Review of Scientific Instruments 71, 3864-3868.

Lamarre, E., Melville, W.K., 1991. Air entrainment and dissipation in breaking waves. Nature 351, 469-471.

Lamarre, E., Melville, W.K., 1992. Instrumentation for the measurement of void-fraction in breaking waves: laboratory and field results. IEEE Journal of Oceanic Engineering

17, 204–215.

Lamarre, E., Melville, W.K., 1994. Void-fraction measurements and sound-speed fields in bubble plumes generated by breaking waves. Journal of the Acoustical Society of America 95(3), 1317–1328

Lim, H.-J., Chang, K.-A., Su, C.B., Chen, C.-Y., 2008. Bubble velocity, diameter, and void fraction measurements in a multiphase flow using fiber optic reflectometer. Review of Scientific Instruments 79, 125105-1-11.

Lin, J., Brown, C.W., 1993a. Spectroscopic measurement of NaCl and seawater salinity in the near IR region of 680-1230 nm. Applied Spectroscopy 47, 239-241.

Lin, J., Brown, C.W., 1993b. Near-IR fibre-optic for electrolytes in aqueous solution. Analytical Chemistry 65, 287-292.

Lin, P., Liu, P.-F., 1998a. A numerical study of breaking waves in the surf zone. Journal of Fluid Mechanics 359, 239-264.

Lin, P., Liu, P.-F., 1998b. Turbulence transport, vorticity dynamics, and solute mixing under plunging breaking waves in surf zone. Journal of Geophysical Research 103, 15677-15694.

Lindken, R., Gui, L., Merzkirch, W., 1999. Velocity measurements in multiphase flow by means of particle image velocimetry. Chemical Engineering & Technology 22, 202-206.

Longo, S., 2003. Turbulence under spilling breakers using discrete wavelets. Experiments in Fluids 34, 181-191.

Luther, S., Rensen, J., Guet, S., 2004. Bubble aspect ratio and velocity measurement

using a four-point fiber-optical probe. Experiments in Fluids 36, 326-333.

Lynett, P.J., 2006. Wave breaking velocity effects in depth-integrated models. Coastal Engineering 53, 425-333.

Meggitt, B.T., Boyle, W.J.O., Grattan, K.T.V., Palmer, A.W., Ning, Y.N., 1990. Fibre optic anemometry using an optical delay cavity technique. In: Proceedings of SPIE, London, UK.

Melville, W.K., Veron, F., White, C.J., 2002. The velocity field under breaking waves: coherent structures and turbulence. Journal of Fluid Mechanics 454, 203-233.

Murzyn, F., Mouaze, D., Chaplin, J.R., 2005. Optical fibre probe measurements of bubbly flow in hydraulic jump. International Journal of Multiphase Flow 31, 141-154.

Nadaoka, K., Hino, M., Koyano, Y., 1989. Structure of the turbulent flow field under breaking waves in the surf zone. Journal of Fluid Mechanics 204, 359-387.

Ning, Y.N., Grattan, K.T.V., Palmer, A.W., 1992. Fibre-optic interferometric systems using low-coherence light sources. Sensors and Actuators 30, 181-192.

Nishihara, H., Matsumoto, K., Koyama, J., 1984. Use of a laser diode and an optical fiber for a compact laser-Doppler velocimeter. Optics Letters 9, 62-64.

Peregrine, D.H., 1983. Breaking waves on beaches, Annual Review of Fluid Mechanics 15, 149-178.

Perlin, M., He, J., Bernal, L.P., 1996. An experimental study of deep water plunging breakers. Physics of Fluids 8, 2365-2374.

Raffel, M., Willert, C., Kompenbans, J., 2001. Particle Image Velocimetry: A Practical Guide, Springer-Verlag, Göttingen, Germany.

Rensen, J., Roig, V., 2001. Experimental study of the unsteady structure of a confined bubble plume. International Journal of Multiphase Flow 27, 1431-1449.

Rinne, A., Loth, R., 1996. Development of local two-phase flow parameters for vertical bubbly flow in a pipe with sudden expansion. Experimental Thermal and Fluid Science 13, 152-166.

Rojas, G., Loewen, M.R., 2007. Fiber-optic probe measurements of void fraction and bubble size distributions beneath breaking waves. Experiments in Fluids 43, 895-906.

Ryu, Y., Chang, K.-A., Lim, H.-J., 2005. Use of bubble image velocimetry for measurement of plunging wave impinging on structure and associated greenwater. Measurement Science and Technology 16, 1945-1953.

Schaffer, H.A., Madsen, P.A., Deigaard, R., 1993. A Boussinesq model for waves breaking in shallow water. Coastal Engineering 20, 185-202.

Seol, D.-G., Bhaumik, T., Bergmann, C., Socolofsky, A., 2007. Particle image velocimetry measurements of the mean flow characteristics in a bubble plume. Journal of Engineering Mechanics 133, 665-676.

Shin, S., Cox, D.T., 2006. Laboratory observations of inner surf zone and swash zone hydrodynamics on a steep slope. Continental Shelf Research 26, 561-573.

Skyner, D.J., 1996. A comparison of numerical predictions and experimental measurements of the internal kinetics of a deep-water plunging wave. Journal of Fluid Mechanics 315, 51-64.

Skyner, D.J., Gray, C., Greated, C.A., 1990. A comparison of the time-stepping numerical predictions with whole-field flow measurement in breaking waves. In:

Water Wave Kinematics, ed. Torum, A. and Gudmestad, O. T., Kluwer Academic Publishers, Boston, 491-508.

Stansby, P.K., Feng, T., 2005. Kinematics and depth-intergrated terms in surf zone waves from laboratory measurement. Journal of Fluid Mechanics 529, 279-310.

Ting, F.C.K., Kirby, J.T., 1994. Observation of undertow and turbulence in a laboratory surf zone. Coastal Engineering 24, 51-80.

Ting, F.C.K., Kirby, J.T., 1995. Dynamics of surf-zone turbulence in a strong plunging breaker. Coastal Engineering 24, 177-204.

Ting, F.C.K., Kirby, J.T., 1996. Dynamics of surf-zone turbulence in a spilling breaker. Coastal Engineering 27, 131-160.

Vagle, S., Farmer, D.M., 1998. A comparison of four methods for bubble size and void fraction measurements. IEEE Journal of Oceanic Engineering 23(3), 211–222.

Watanabe, Y., Saeki, H., 1999. Three-dimensional large eddy simulation of breaking waves. Coastal Engineering 41, 281-301.

Watanabe, Y., Saeki, H., Hosking, R.J., 2005. Three-dimensional vortex structures under breaking waves. Journal of Fluid Mechanics 545, 291-328.

Wedin, R., Davoust, L., Cartellier, A., Dahlkild, A., 2000. A mono-modal fiber-optices velocimeter for electrochemically generated bubbles. In: Proceedings of 10th International Symposium on Applications of Laser Techniques to Fluid Dynamics, July 10-13, Lisbon, Portugal, 202-206.

Wilson, T.A., Reed W.F., 1993. Low cost, interferometric differential refractometer. American Journal of Physics 61, 1046-1048

Woodruff, S.D., Yeung, B.S., 1982. Double-beam Fabry-Perot interferometer as a refractive index detector in liquid chromatography. Analytical Chemistry 54, 2124-2125.

Yunus, W.M.M., 1992. Temperature dependence of refractive-index and absorption of NaCl, MgCl2, and Na2SO4 solution as major component in natural seawater. Applied Optics 31, 2963-2964.

APPENDIX A

ADDITIONAL FIGURES FROM BIV ANALYSIS

Additional figures obtained from the BIV measurements are provided in this Appendix. The time difference between figures is 0.05 s and description for each figure is summarized in Table A.1.

Table A.1

Description of figures (BIV)

Figure Number	Description
Fig. A.1	Mean Velocity Map ($\sqrt{U^2+W^2}$)
Fig. A.2	Normalized Horizontal Velocity (U/C)
Fig. A.3	Normalized Vertical Velocity (W/C)
Fig. A.4	Normalized Mean Vorticity (Ω_H/C)
Fig. A.5	Normalized Mean Kinetic Energy (κ/C^2)
Fig. A.6	Normalized Turbulent Kinetic Energy (k/C^2)
Fig. A.7	Normalized Horizontal Turbulence Intensity ($\sqrt{u'^2}/C$)
Fig. A.8	Normalized Vertical Turbulence Intensity ($\sqrt{w'^2}/C$)
Fig. A.9	Normalized Reynolds Stress ($-u'w'/C^2$)
Fig. A.10	Normalized Turbulent Kinetic Energy Transport by U (kU/C^3)
Fig. A.11	Normalized Turbulent Kinetic Energy Transport by W (kW/C^3)
Fig. A.12	Mean Void Ratio Before Calibration (α)
Fig. A.13	Relative Velocity ($U-C, W$)
Fig. A.14	Normalized Horizontal Local Acceleration ($\frac{\partial U}{\partial t}\Big/g$)
Fig. A.15	Normalized Vertical Local Acceleration ($\frac{\partial W}{\partial t}\Big/g$)
Fig. A.16	Normalized Horizontal Convective Acceleration ($\left(U\frac{\partial U}{\partial x}+W\frac{\partial U}{\partial z}\right)\Big/g$)
Fig. A.17	Normalized Vertical Convective Acceleration ($\left(U\frac{\partial W}{\partial x}+W\frac{\partial W}{\partial z}\right)\Big/g$)
Fig. A.18	Normalized Horizontal Total Acceleration ($\left(\frac{\partial U}{\partial t}+U\frac{\partial U}{\partial x}+W\frac{\partial U}{\partial z}\right)\Big/g$)
Fig. A.19	Normalized Vertical Total Acceleration ($\left(\frac{\partial W}{\partial t}+U\frac{\partial W}{\partial x}+W\frac{\partial W}{\partial z}\right)\Big/g$)

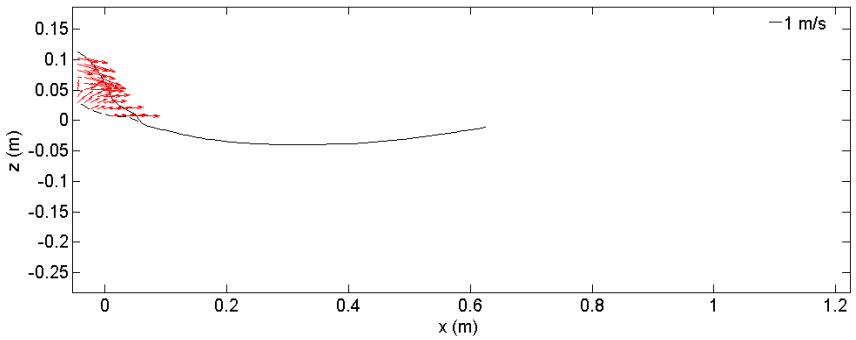

(a) $t = 0.01$ s

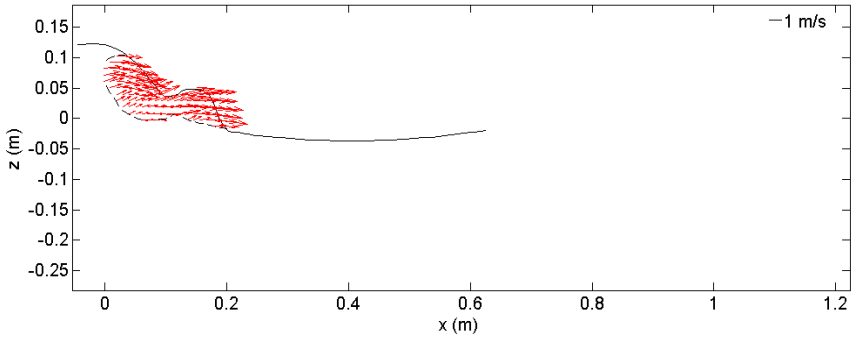

(b) $t = 0.06$ s

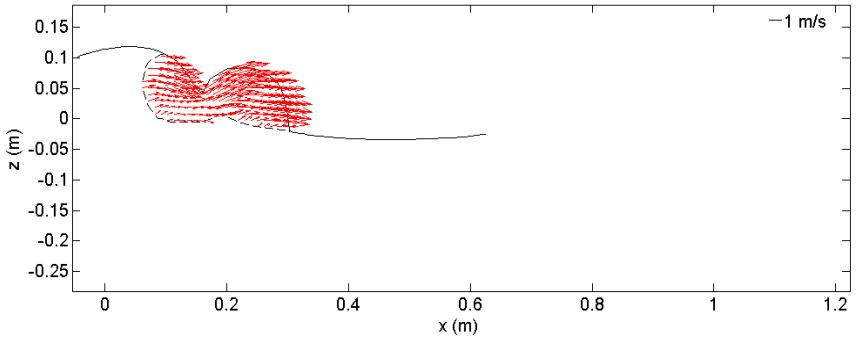

(c) $t = 0.11$ s

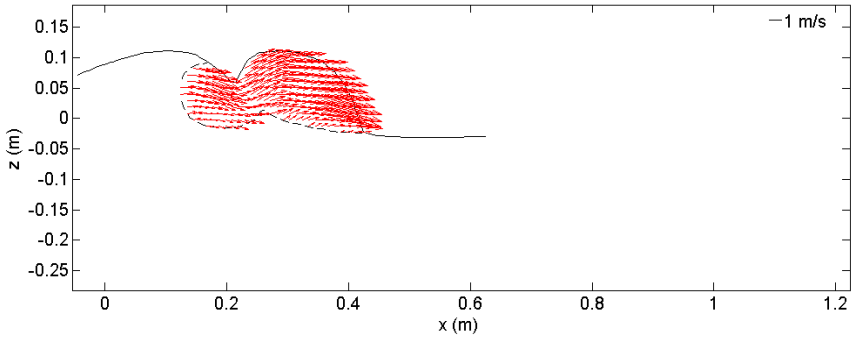

(d) $t = 0.16$ s

Fig. A.1 Velocity.

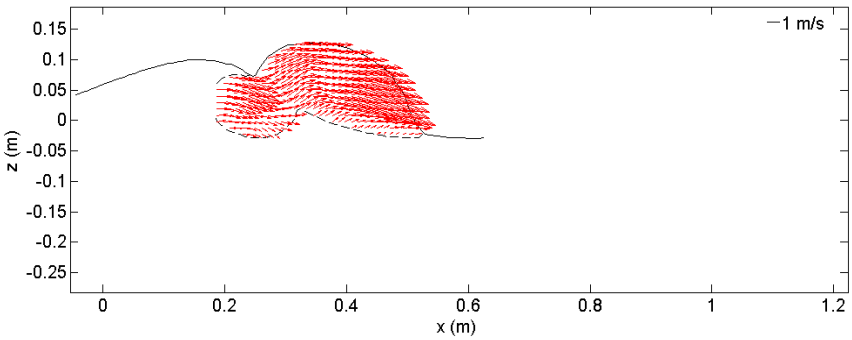

(e) $t = 0.21$ s

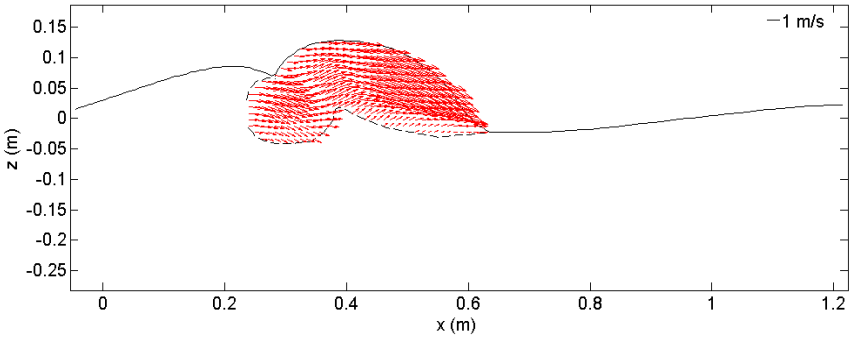

(f) $t = 0.26$ s

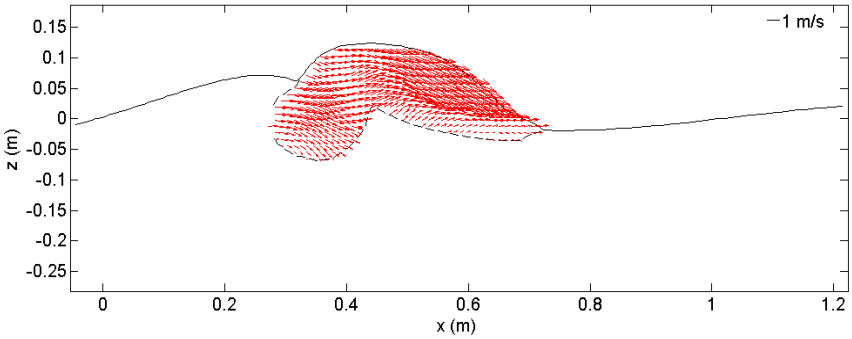

(g) $t = 0.31$ s

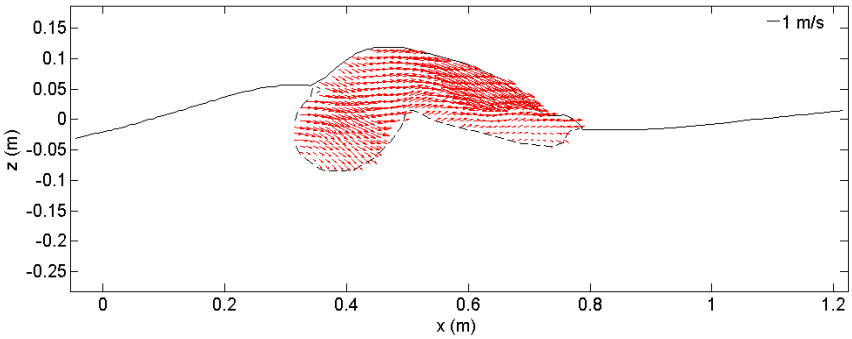

(h) $t = 0.36$ s

Fig. A.1 (Continued).

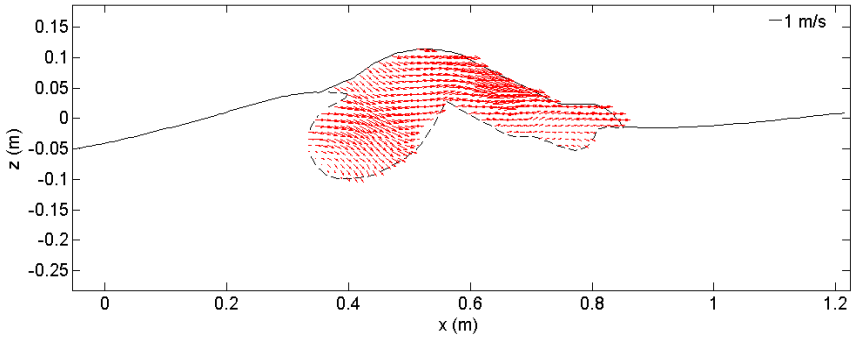

(i) $t = 0.41$ s

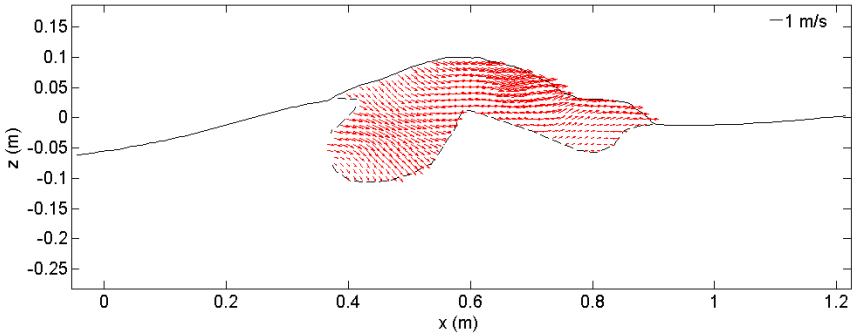

(j) $t = 0.46$ s

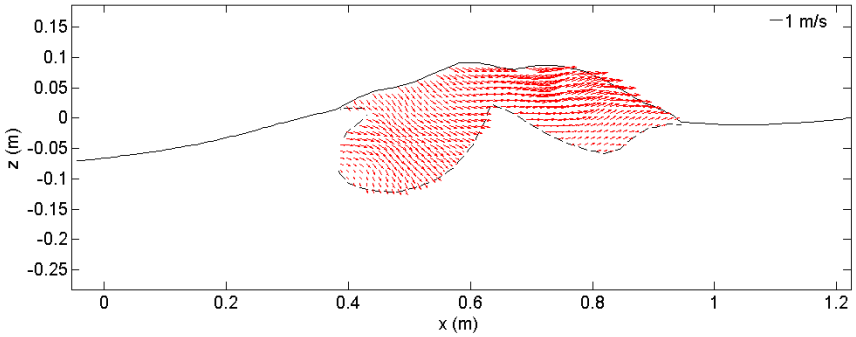

(k) $t = 0.51$ s

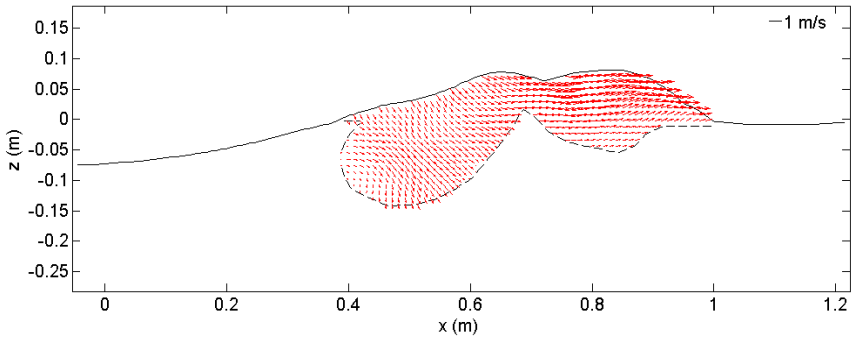

(l) $t = 0.56$ s

Fig. A.1 (Continued).

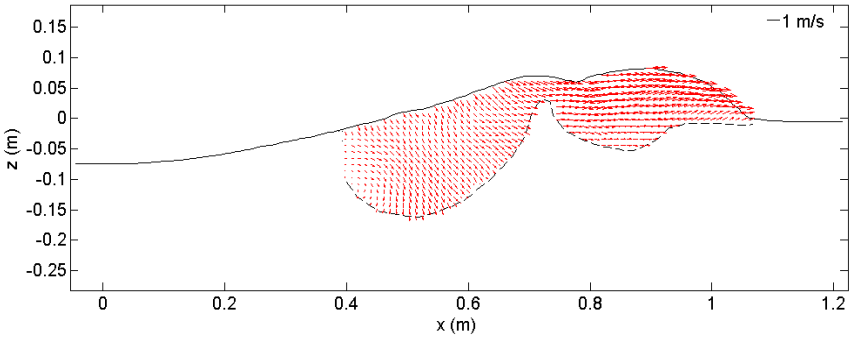

(m) $t = 0.61$ s

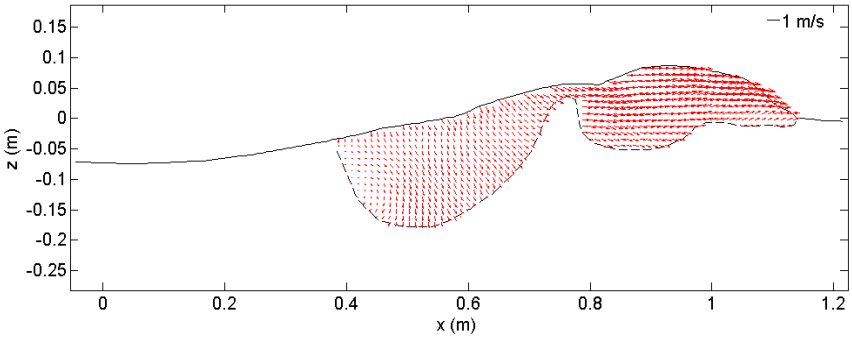

(n) $t = 0.66$ s

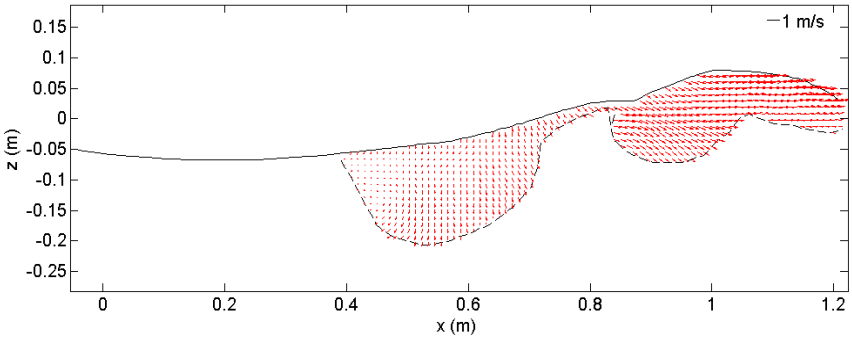

(o) $t = 0.71$ s

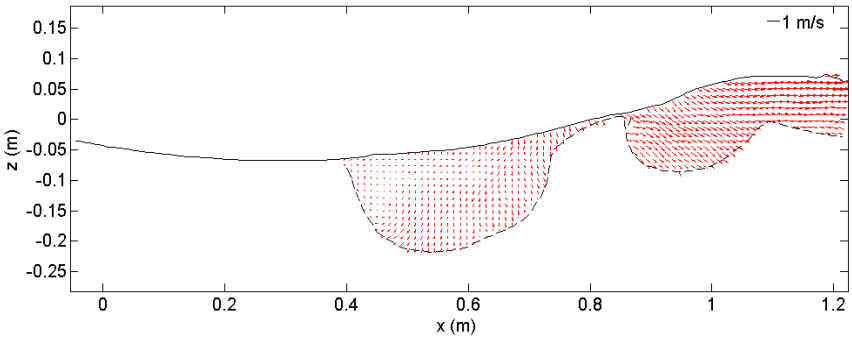

(p) $t = 0.76$ s

Fig. A.1 (Continued).

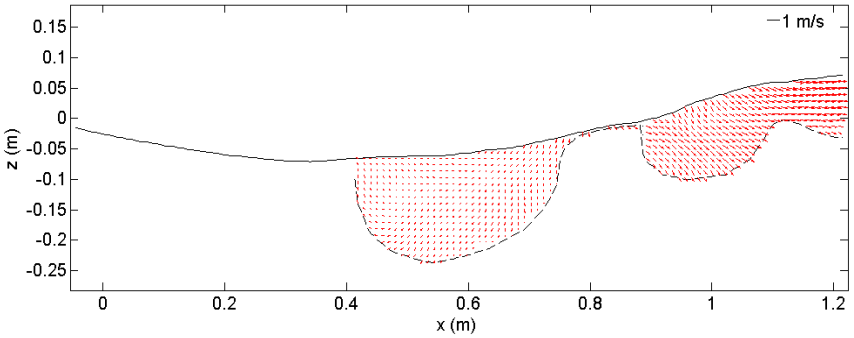

(q) $t = 0.81$ s

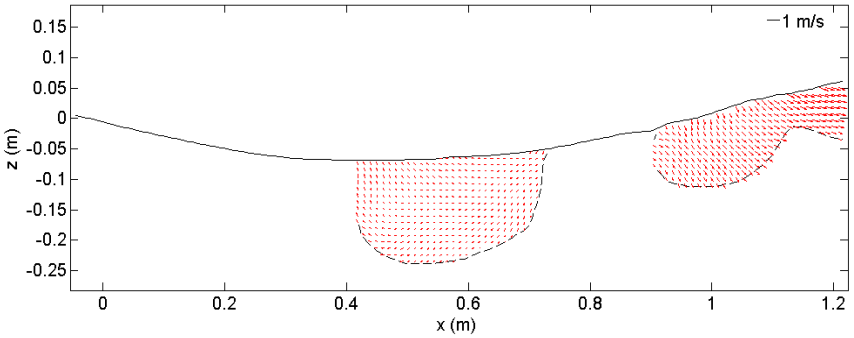

(r) $t = 0.86$ s

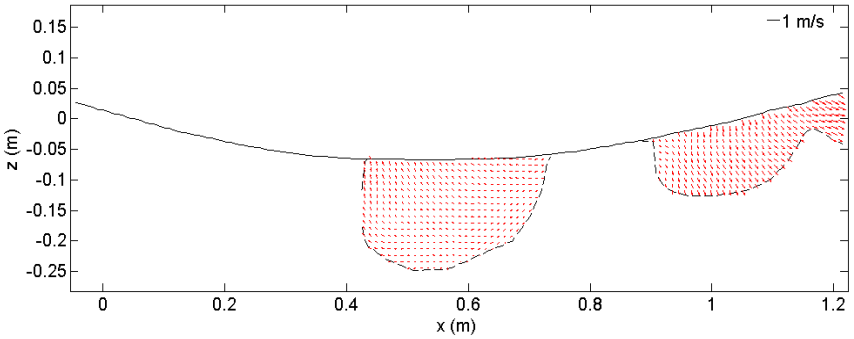

(s) $t = 0.91$ s

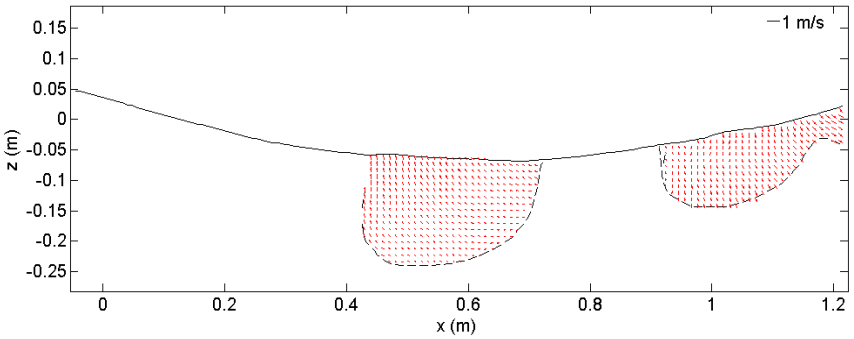

(t) $t = 0.96$ s

Fig. A.1 (Continued).

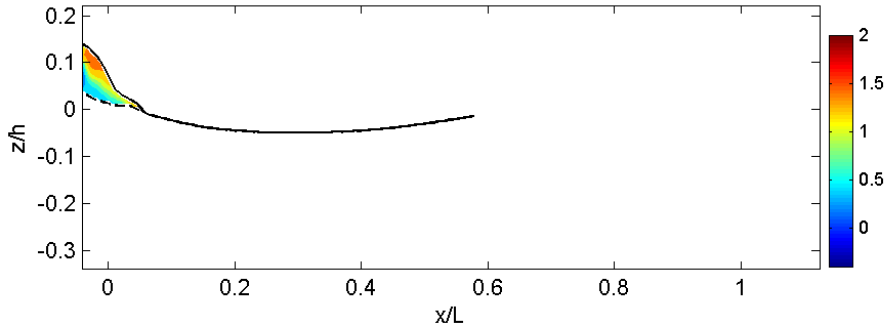

(a) $t = 0.01$ s

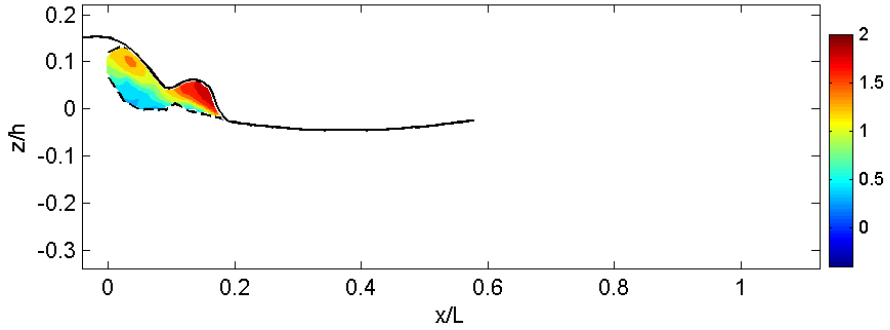

(b) $t = 0.06$ s

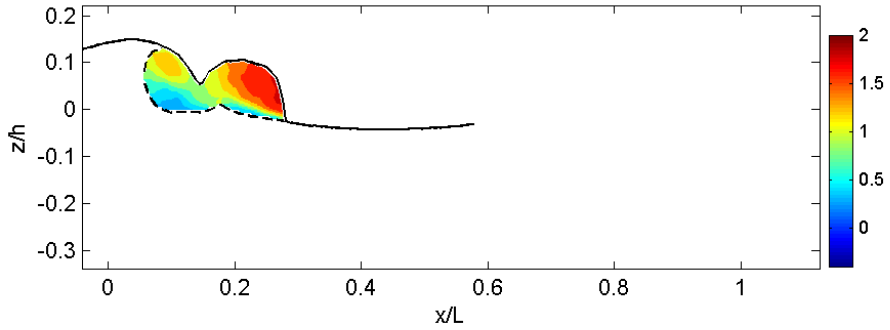

(c) $t = 0.11$ s

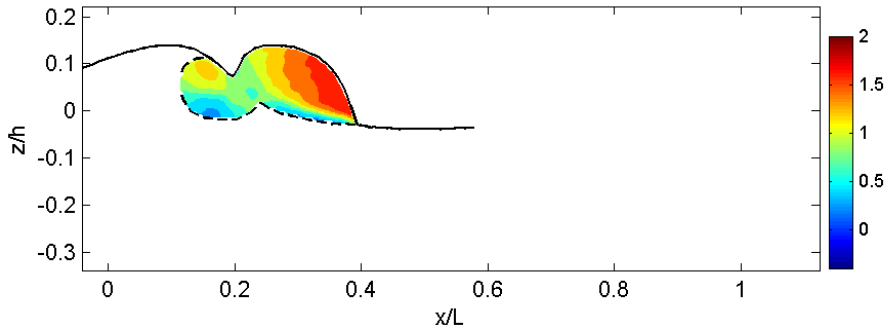

(d) $t = 0.16$ s

Fig. A.2 Normalized horizontal velocity, *U*/*C*.

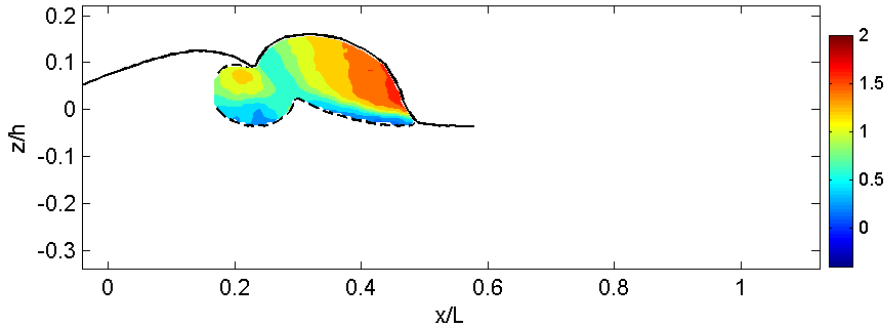

(e) t = 0.21 s

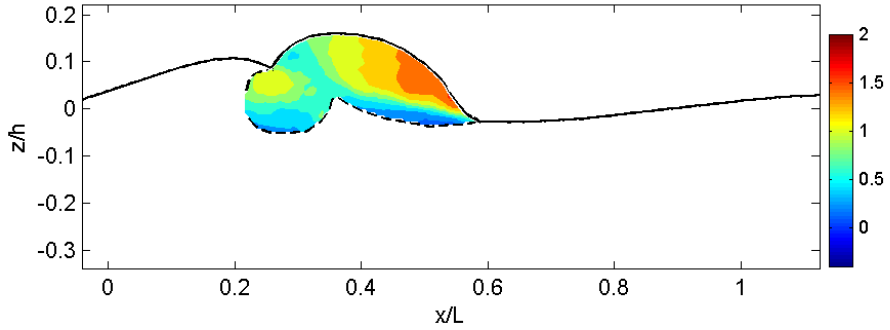

(f) t = 0.26 s

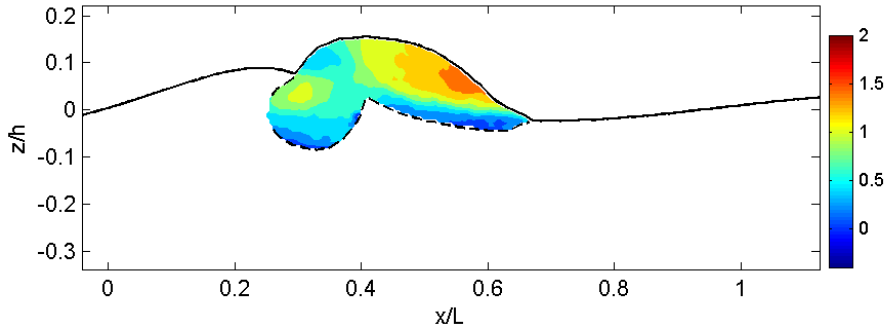

(g) t = 0.31 s

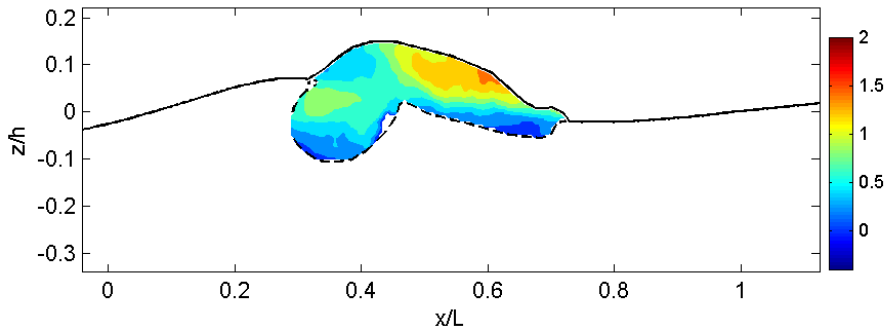

(h) t = 0.36 s

Fig. A.2 (Continued).

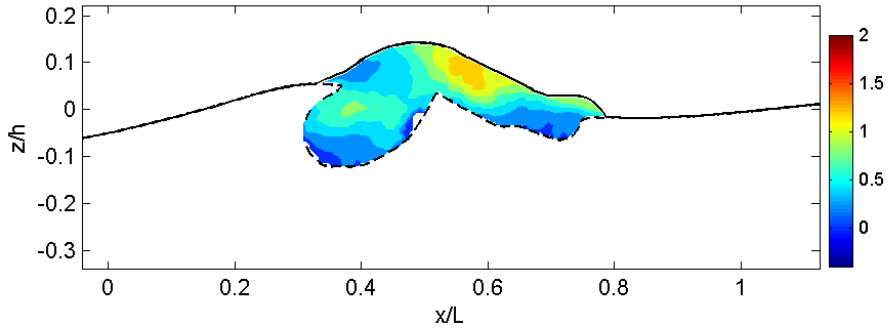

(i) $t = 0.41$ s

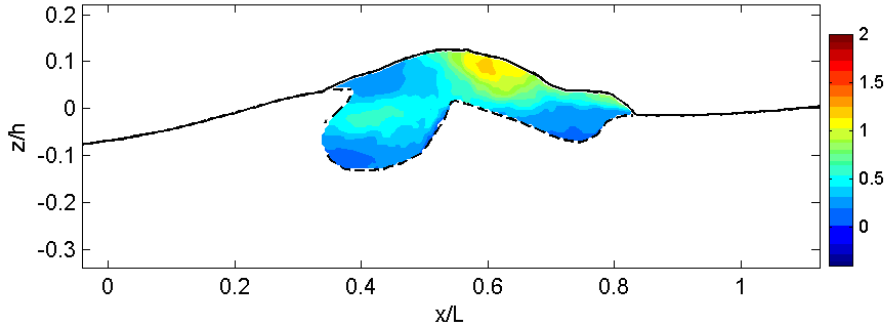

(j) $t = 0.46$ s

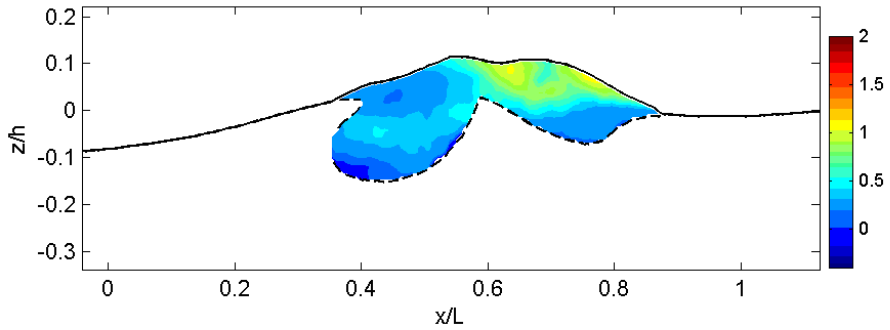

(k) $t = 0.51$ s

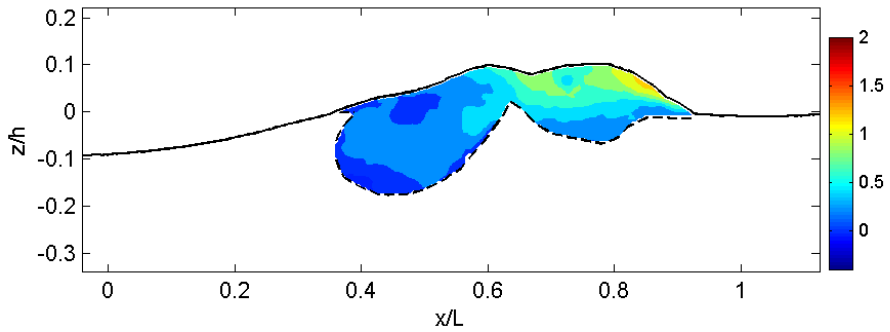

(l) $t = 0.56$ s

Fig. A.2 (Continued).

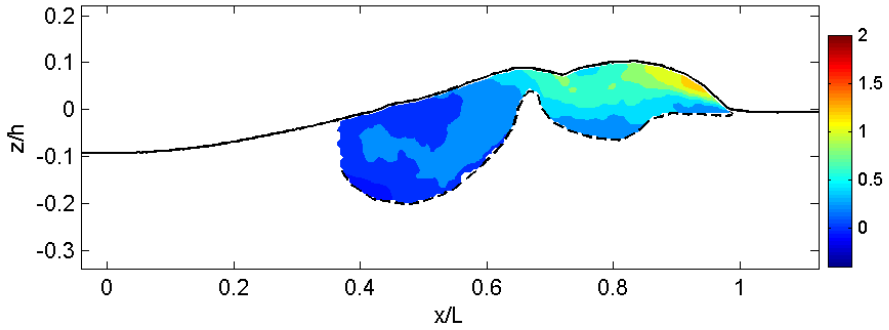

(m) $t = 0.61$ s

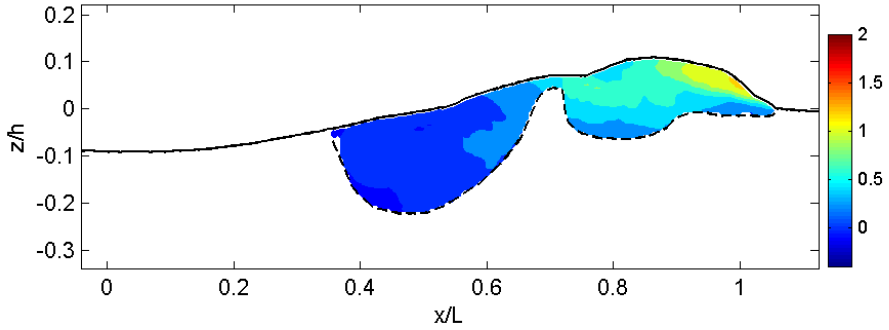

(n) $t = 0.66$ s

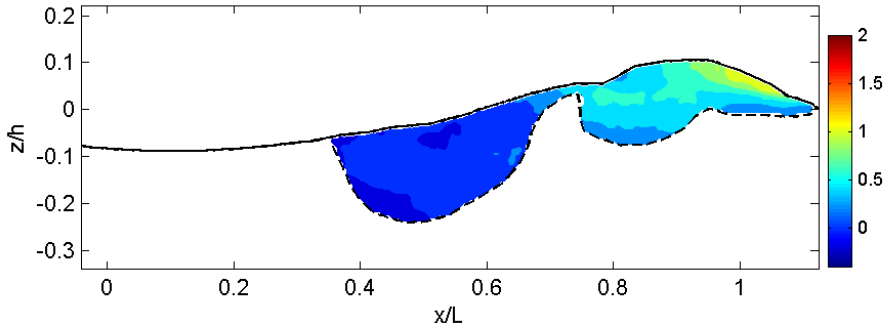

(o) $t = 0.71$ s

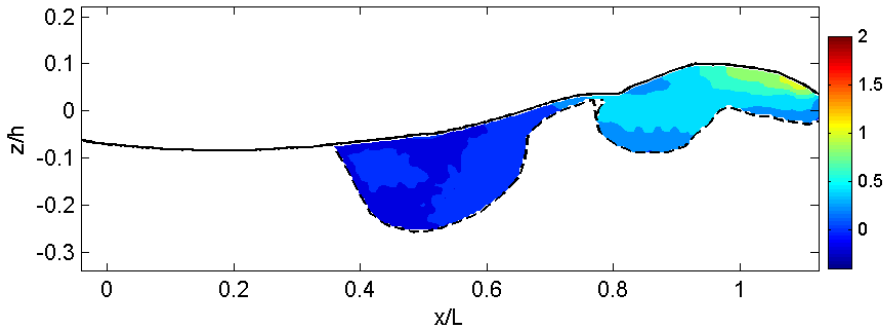

(p) $t = 0.76$ s

Fig. A.2 (Continued).

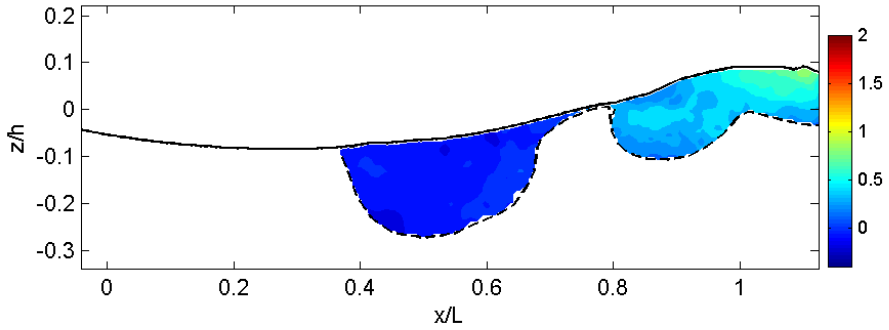

(q) t = 0.81 s

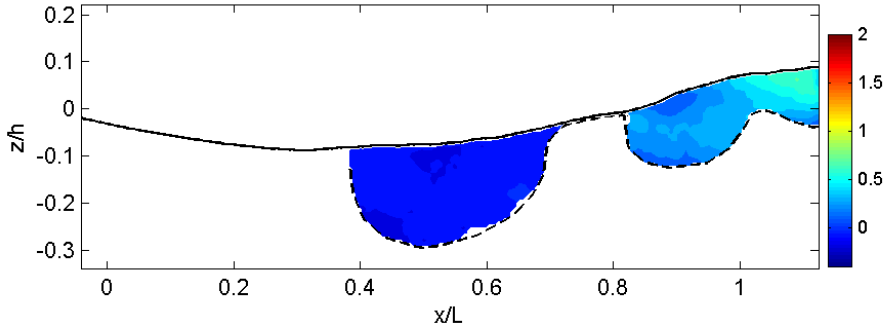

(r) t = 0.86 s

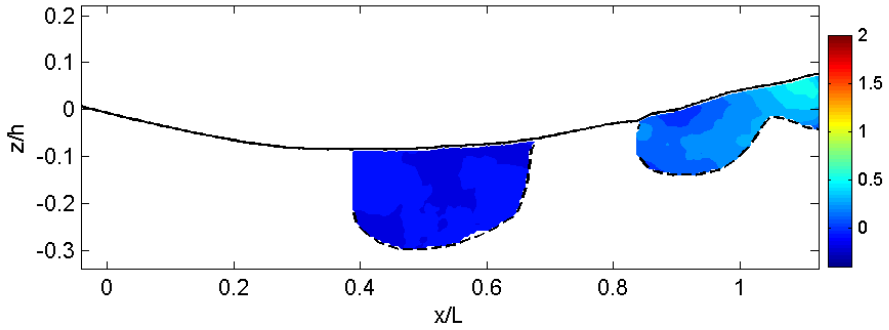

(s) t = 0.91 s

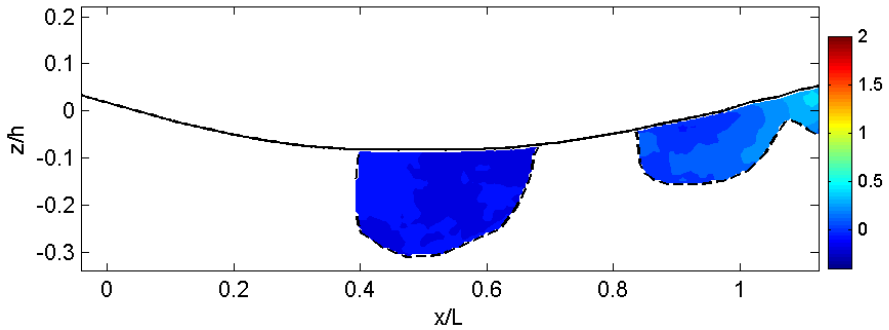

(t) = 0.96 s

Fig. A.2 (Continued).

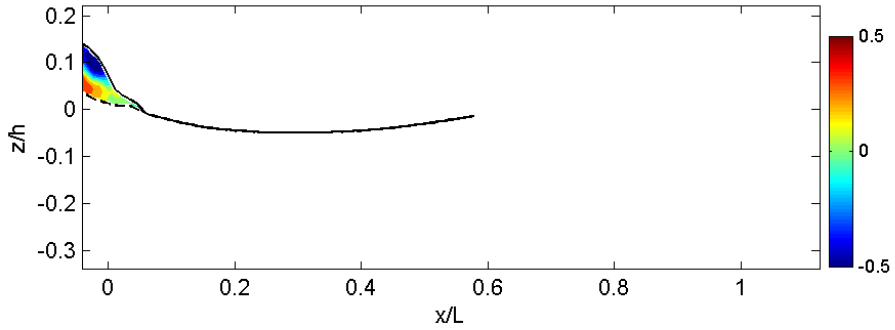

(a) $t = 0.01$ s

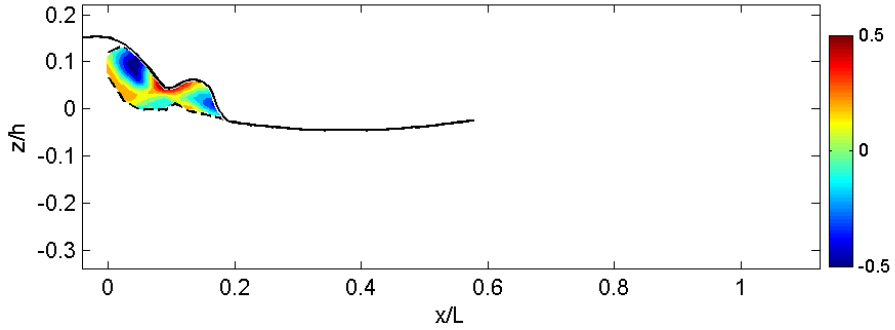

(b) $t = 0.06$ s

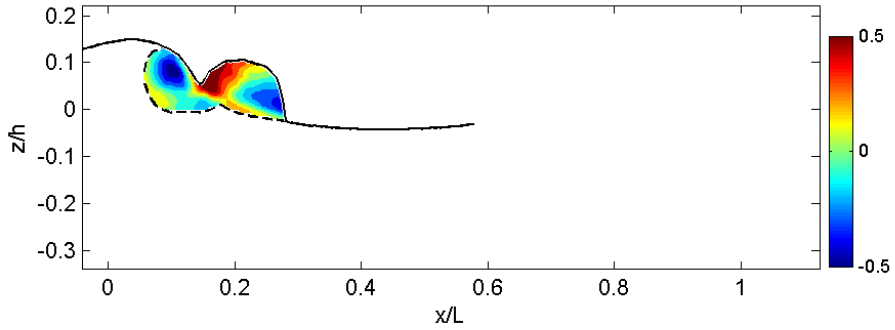

(c) $t = 0.11$ s

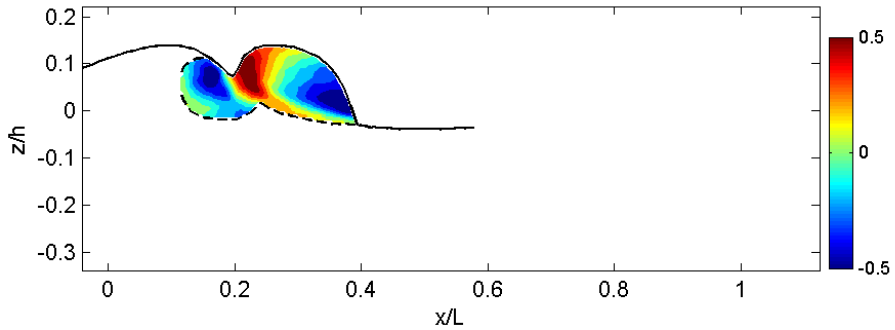

(d) $t = 0.16$ s

Fig. A.3 Normalized vertical velocity, *W/C*.

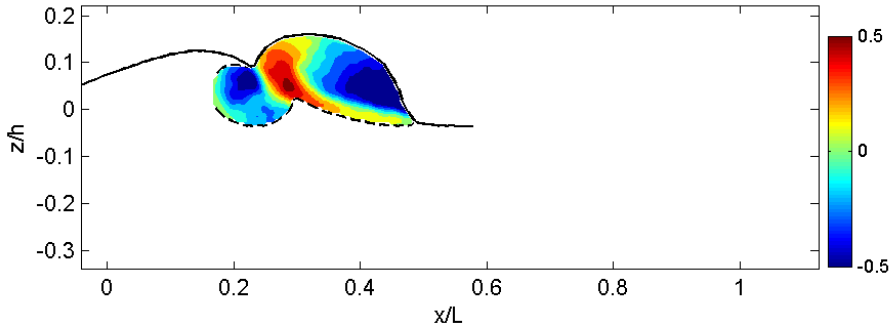

(e) $t = 0.21$ s

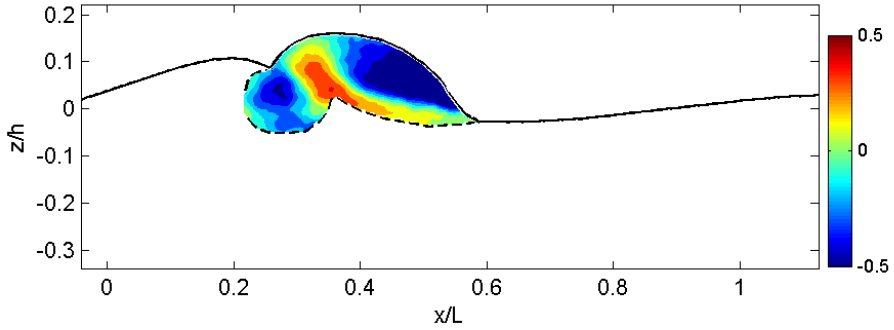

(f) $t = 0.26$ s

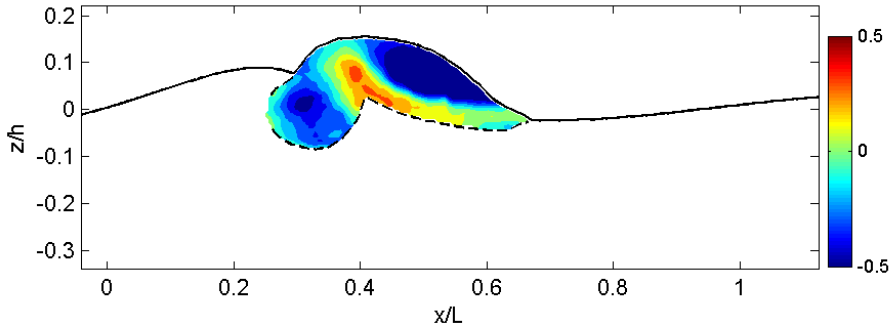

(g) $t = 0.31$ s

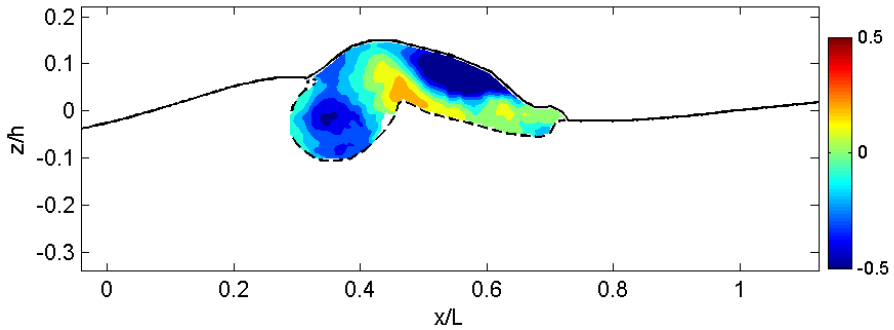

(h) $t = 0.36$ s

Fig. A.3 (Continued).

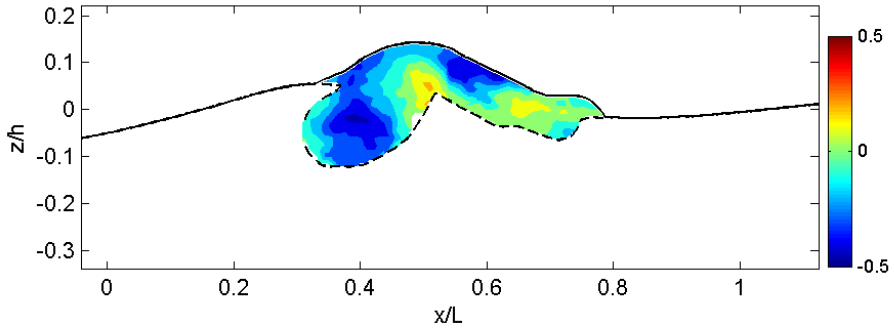

(i) $t = 0.41$ s

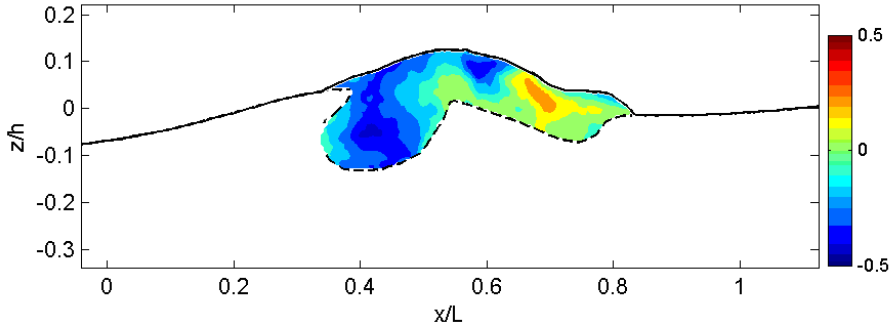

(j) $t = 0.46$ s

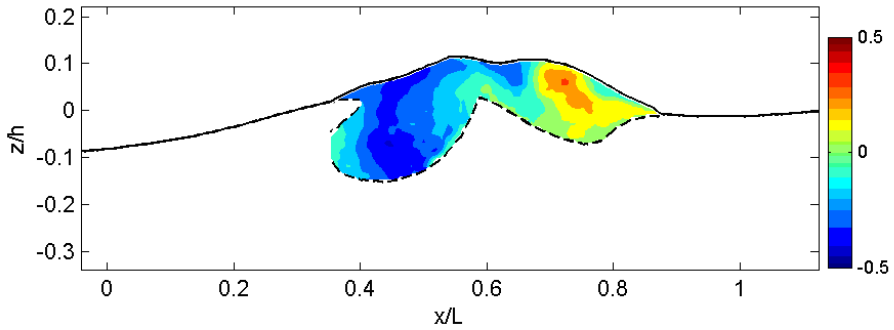

(k) $t = 0.51$ s

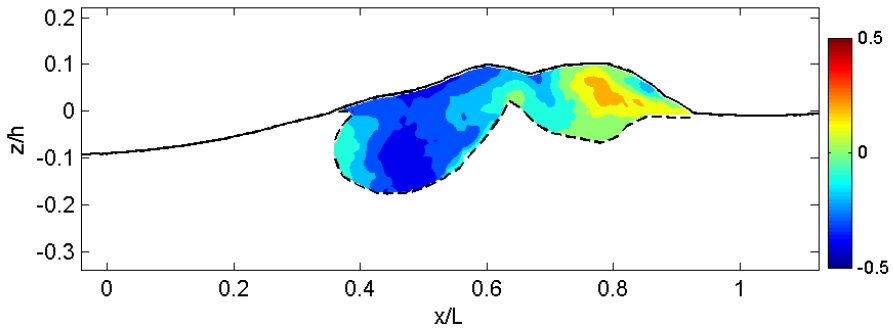

(l) $t = 0.56$ s

Fig. A.3 (Continued).

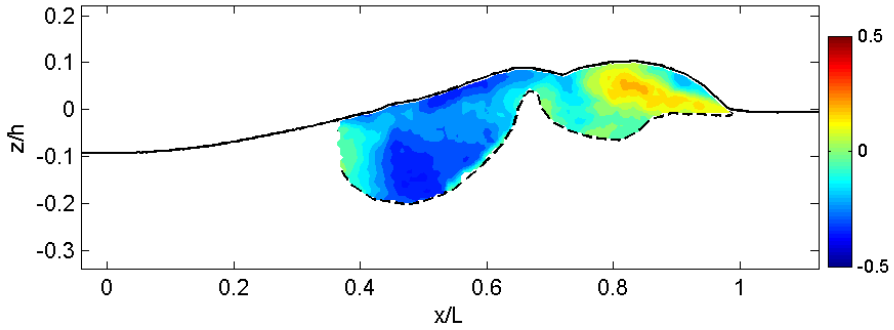

(m) $t = 0.61$ s

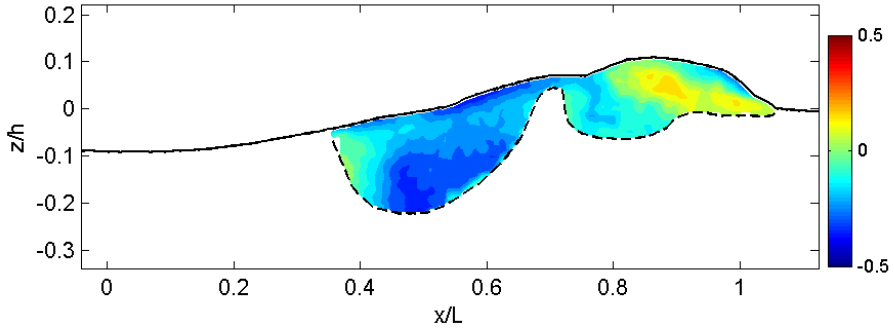

(n) $t = 0.66$ s

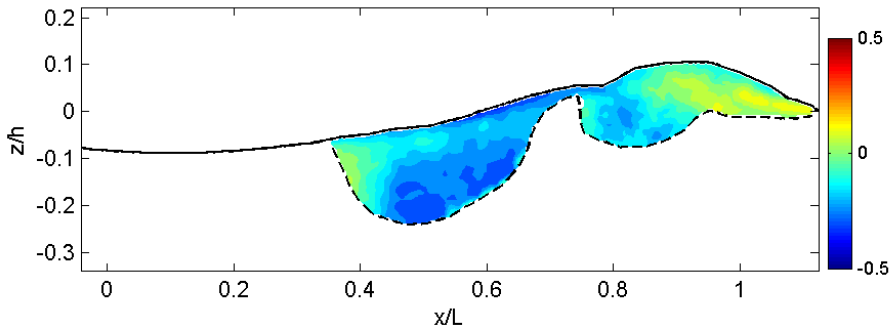

(o) $t = 0.71$ s

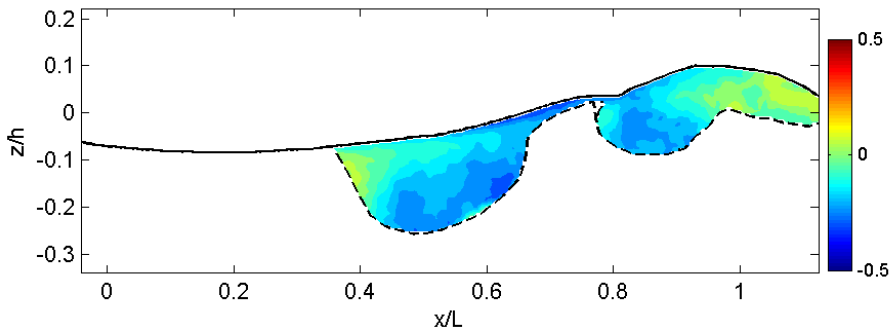

(p) $t = 0.76$ s

Fig. A.3 (Continued).

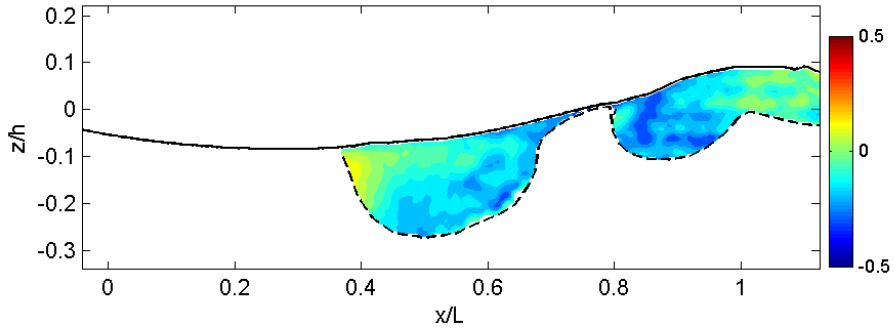

(q) t = 0.81 s

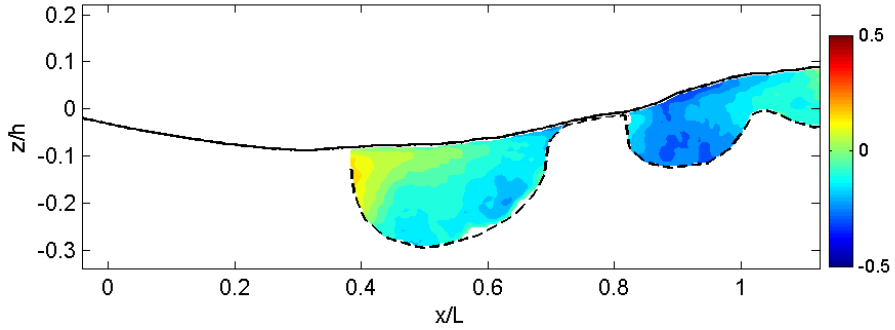

(r) t = 0.86 s

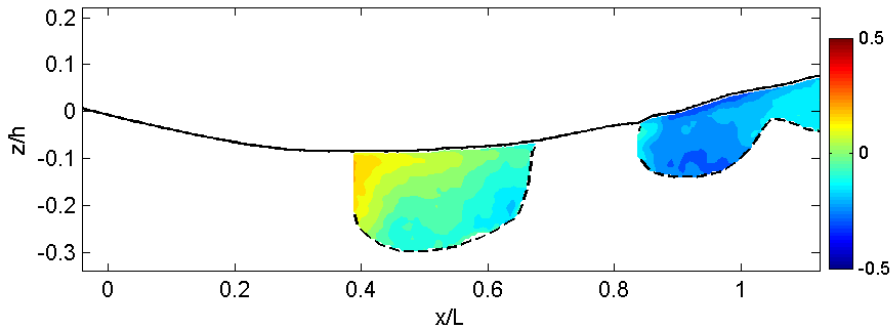

(s) t = 0.91 s

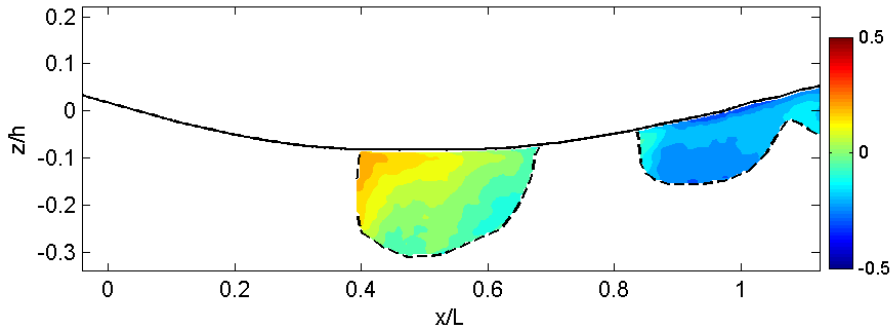

(t) = 0.96 s

Fig. A.3 (Continued).

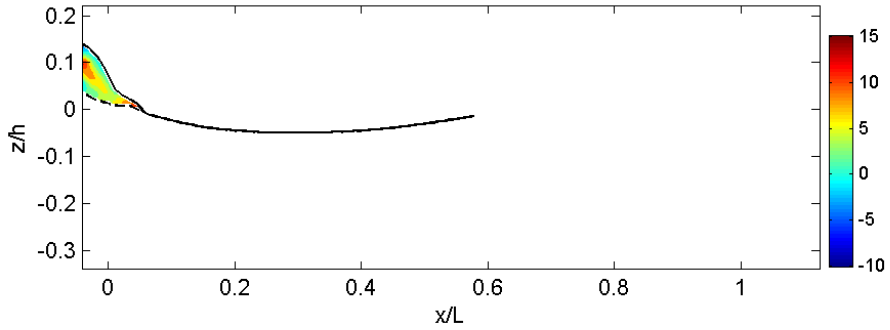

(a) $t = 0.01$ s

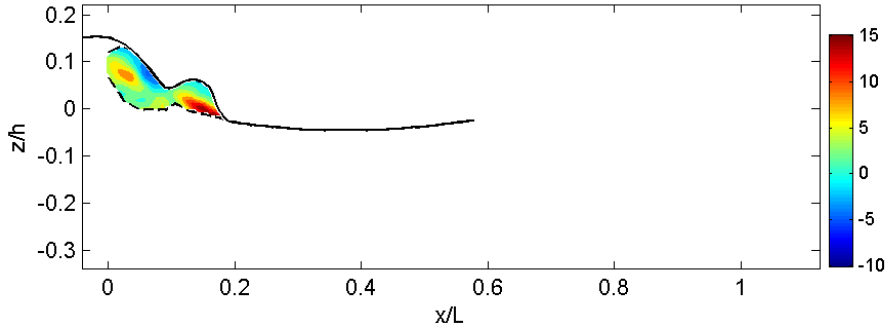

(b) $t = 0.06$ s

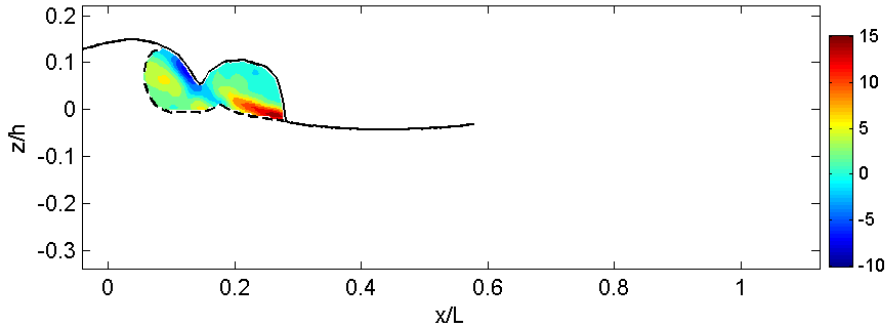

(c) $t = 0.11$ s

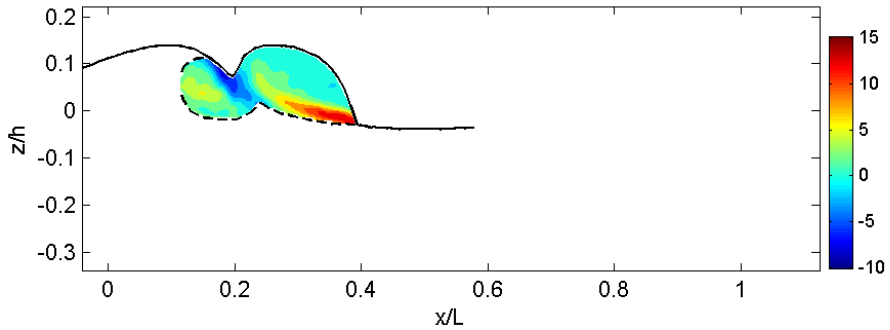

(d) $t = 0.16$ s

Fig. A.4 Normalized Vorticity, $\Omega H/C$.

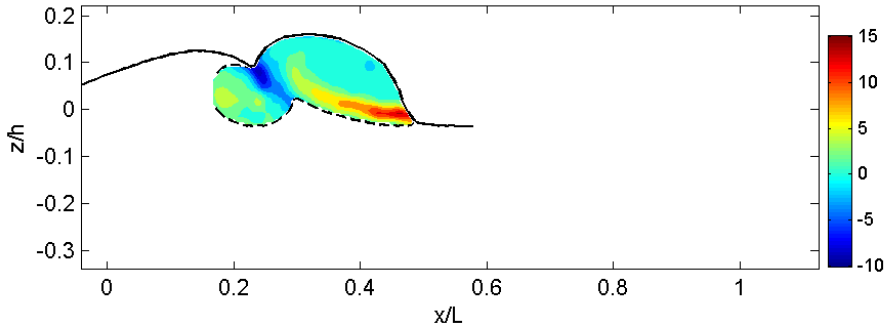

(e) t = 0.21 s

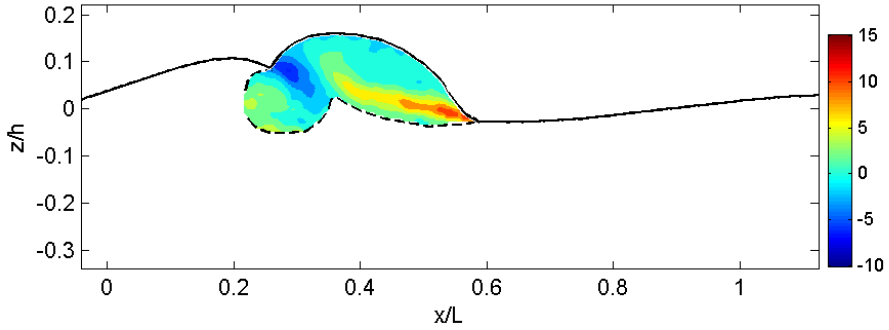

(f) t = 0.26 s

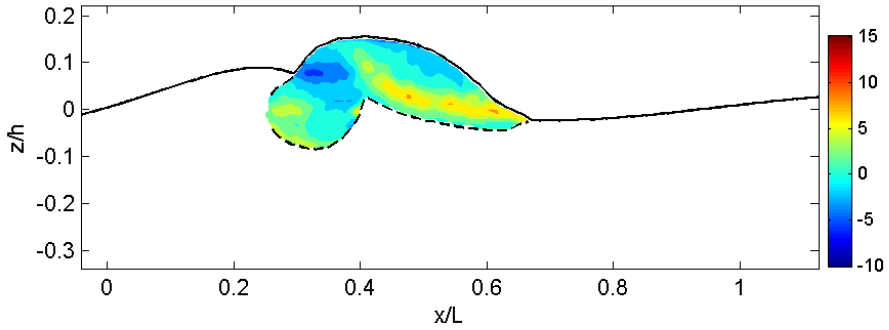

(g) t = 0.31 s

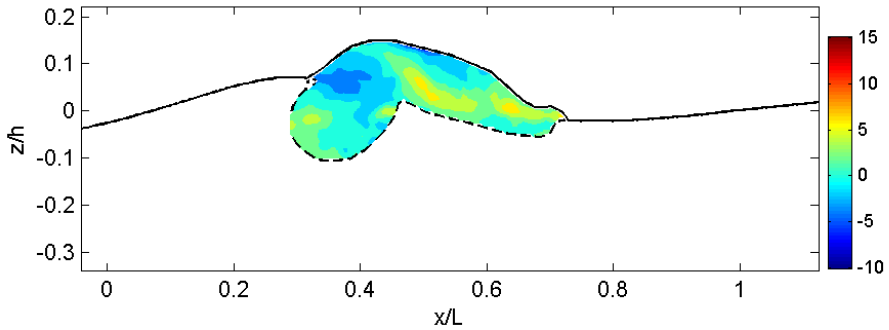

(h) t = 0.36 s

Fig. A.4 (Continued).

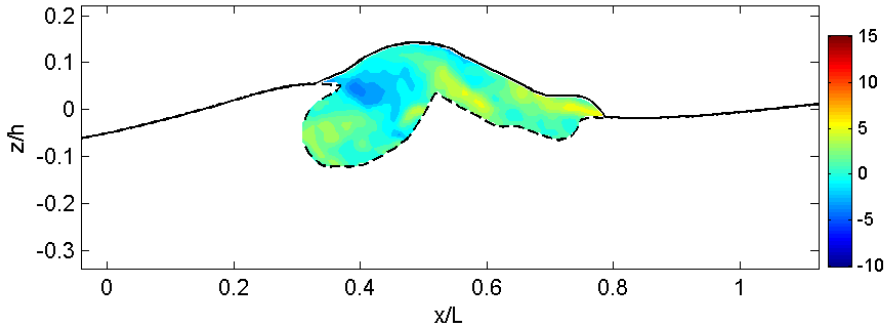

(i) $t = 0.41$ s

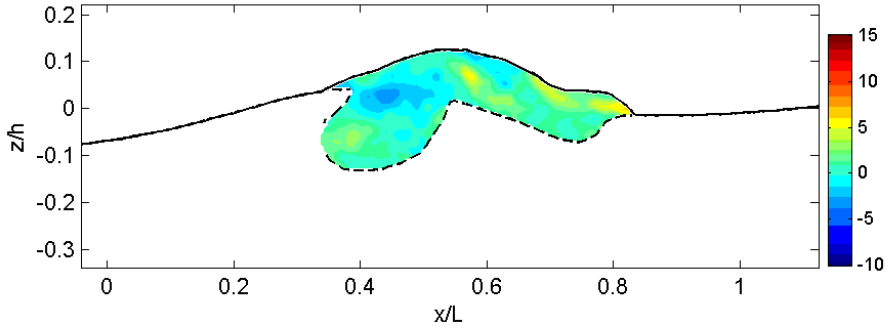

(j) $t = 0.46$ s

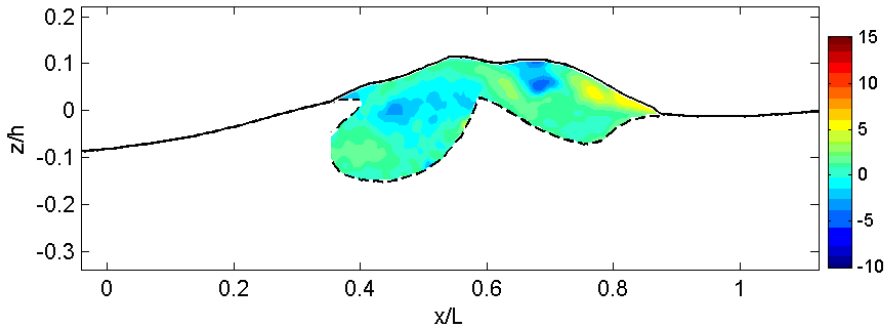

(k) $t = 0.51$ s

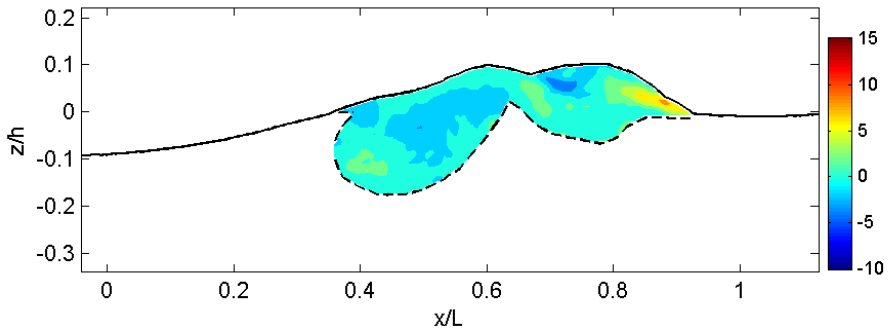

(l) $t = 0.56$ s

Fig. A.4 (Continued).

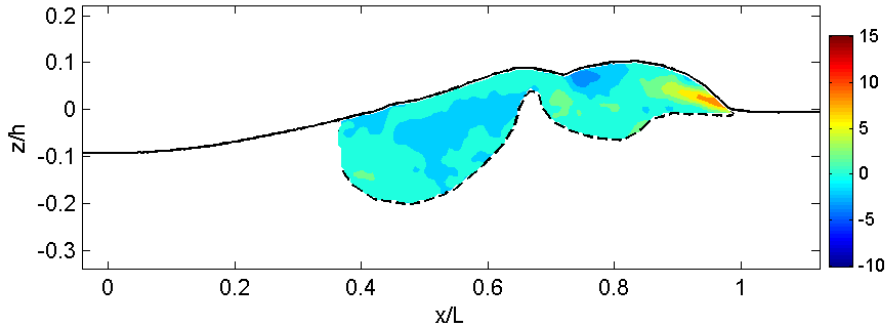

(m) $t = 0.61$ s

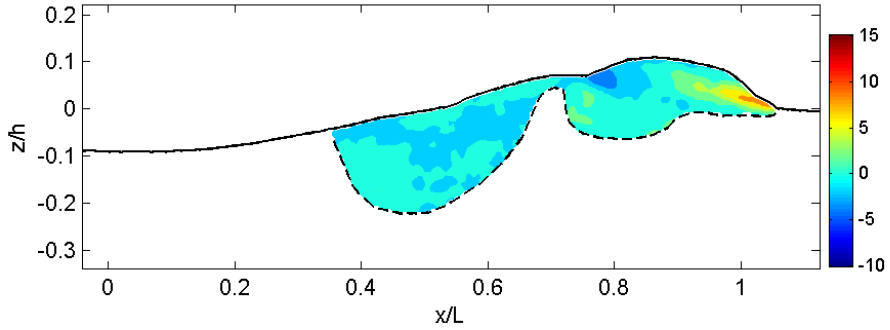

(n) $t = 0.66$ s

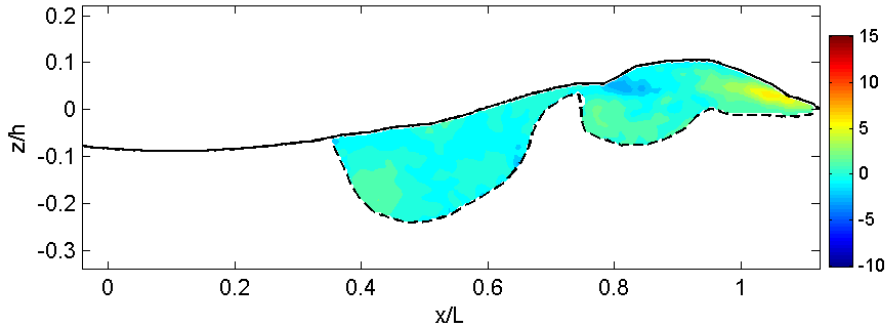

(o) $t = 0.71$ s

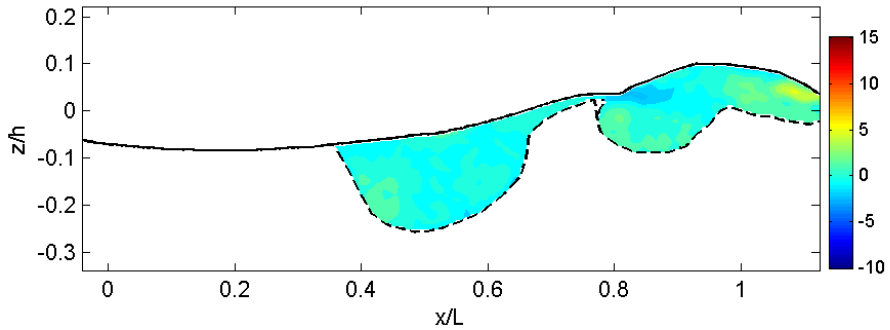

(p) $t = 0.76$ s

Fig. A.5 (Continued).

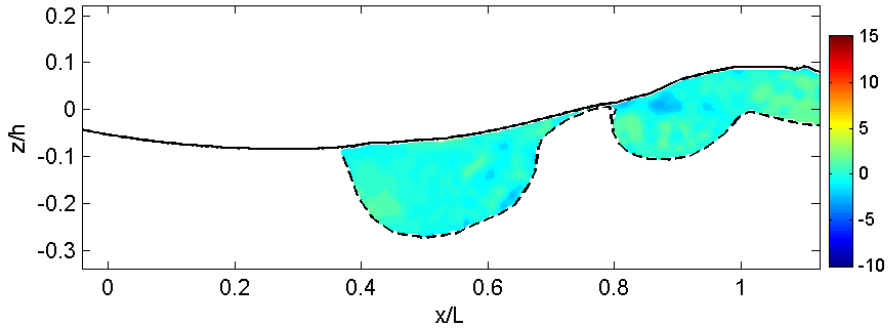

(q) t = 0.81 s

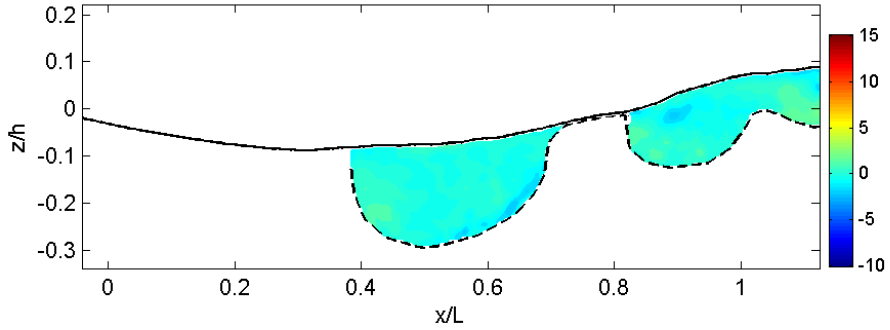

(r) t = 0.86 s

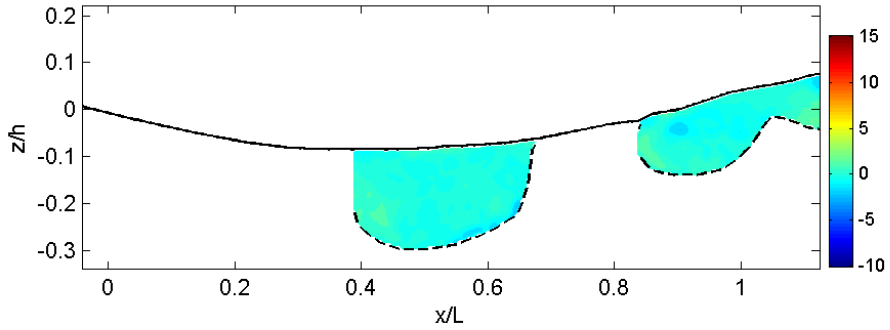

(s) t = 0.91 s

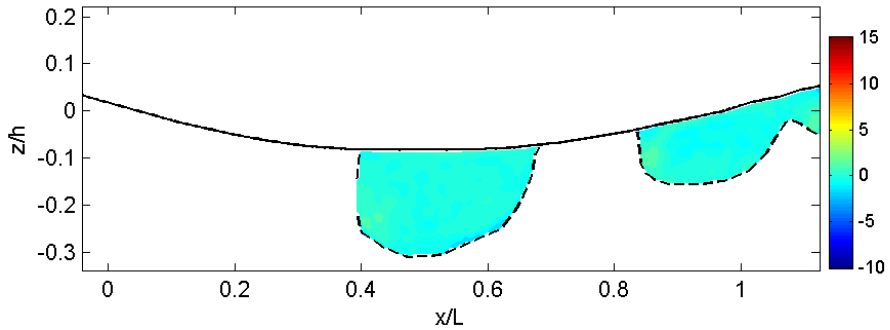

(t) = 0.96 s

Fig. A.5 (Continued).

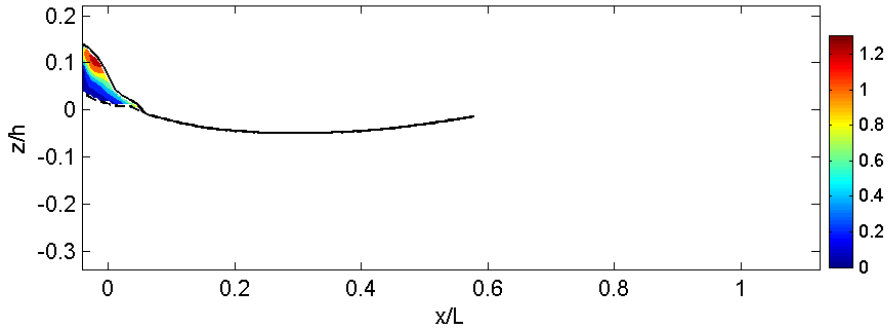

(a) t = 0.01 s

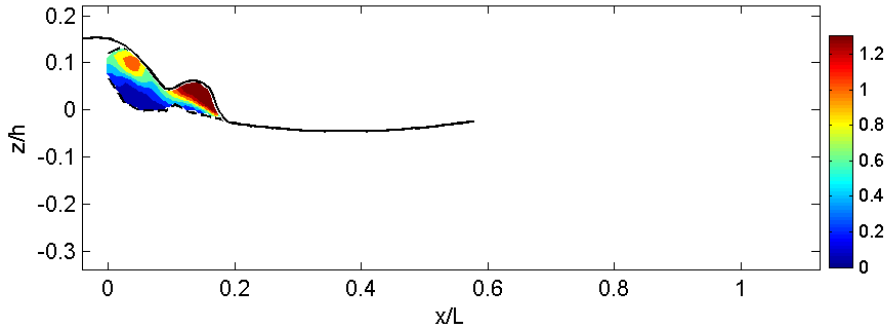

(b) t = 0.06 s

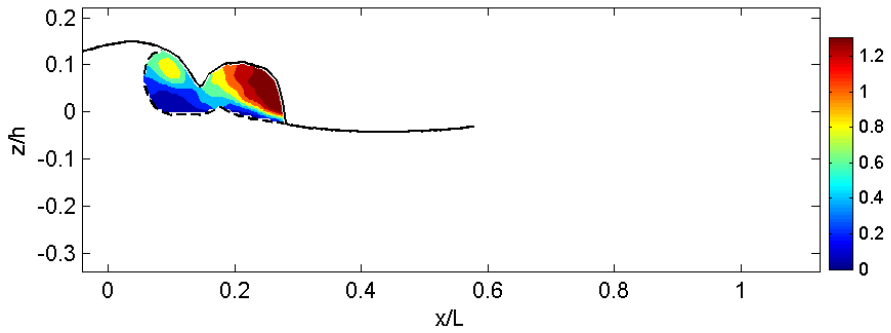

(c) t = 0.11 s

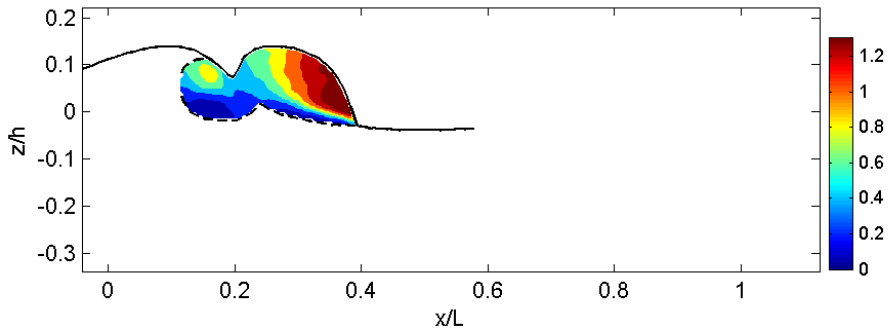

(d) t = 0.16 s

Fig. A.5 Normalized mean kinetic energy, K/C^2 .

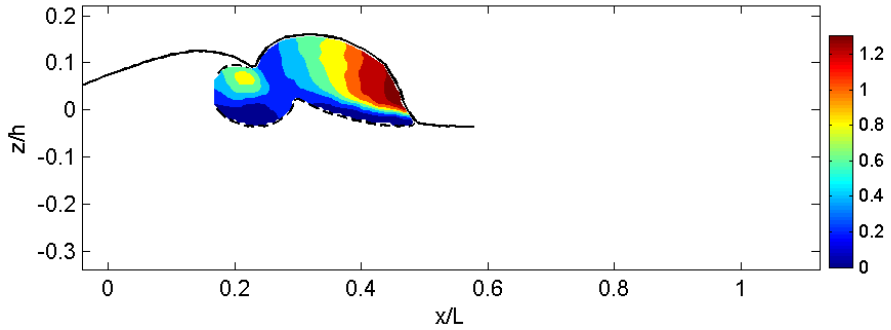

(e) t = 0.21 s

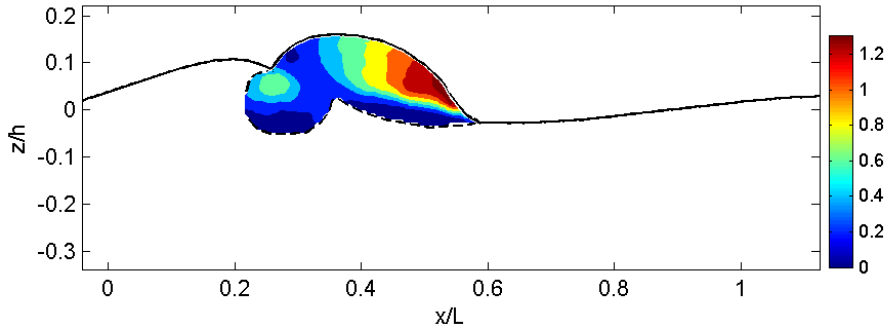

(f) t = 0.26 s

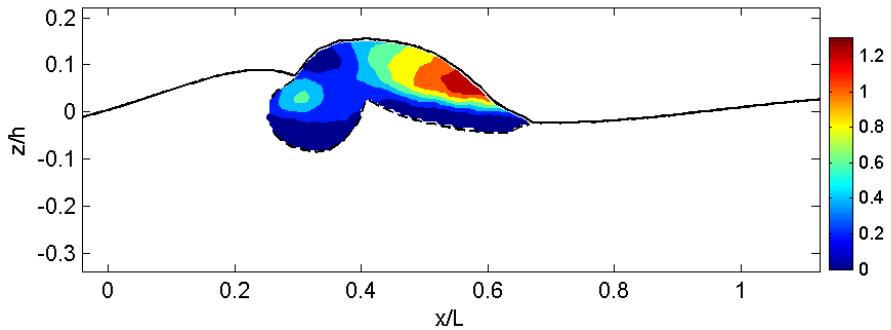

(g) t = 0.31 s

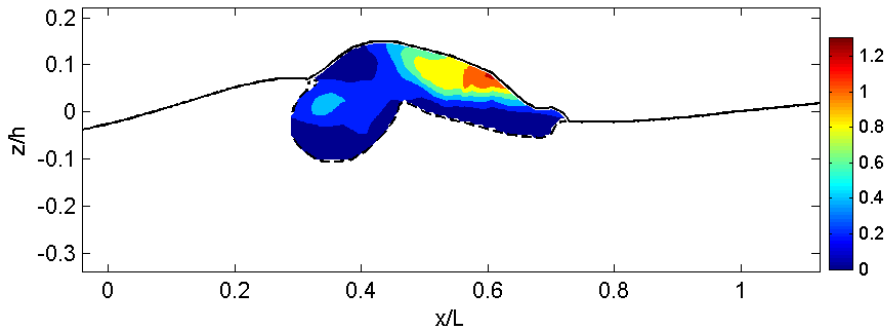

(h) t = 0.36 s

Fig. A.5 (Continued).

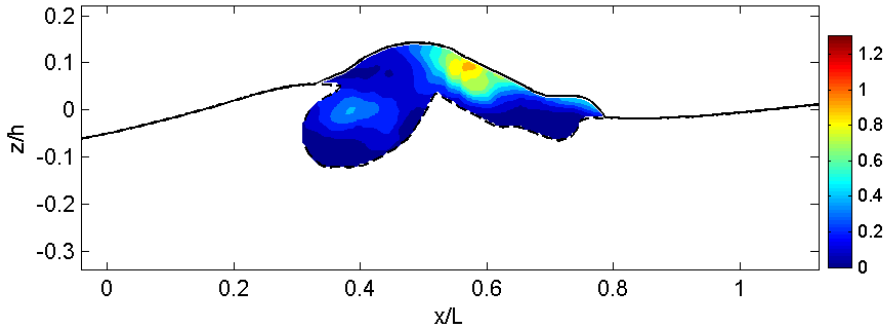

(i) $t = 0.41$ s

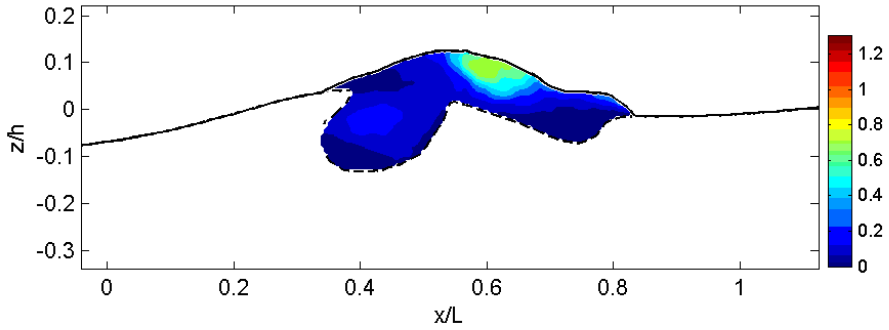

(j) $t = 0.46$ s

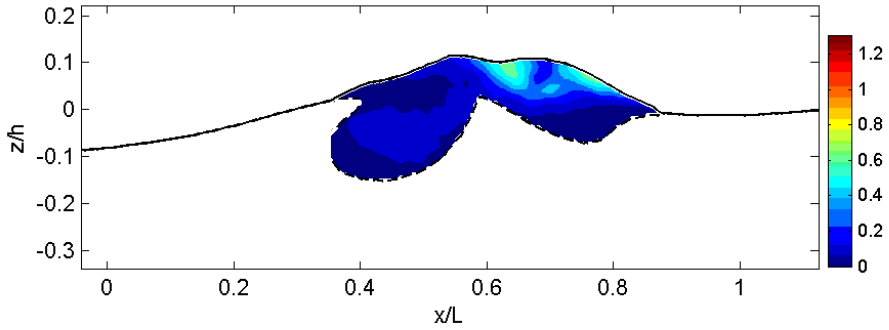

(k) $t = 0.51$ s

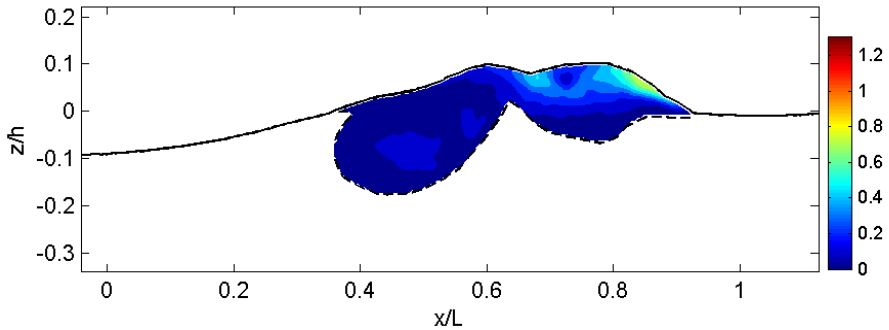

(l) $t = 0.56$ s

Fig. A.5 (Continued).

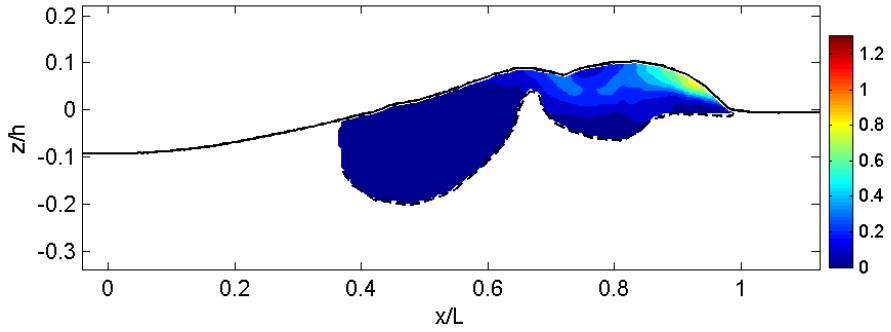

(m) $t = 0.61$ s

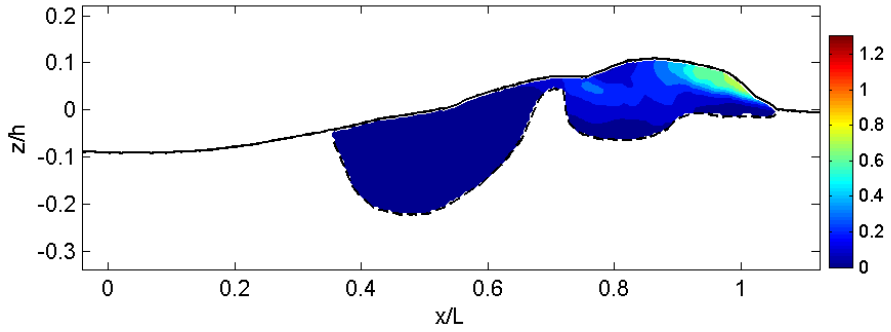

(n) $t = 0.66$ s

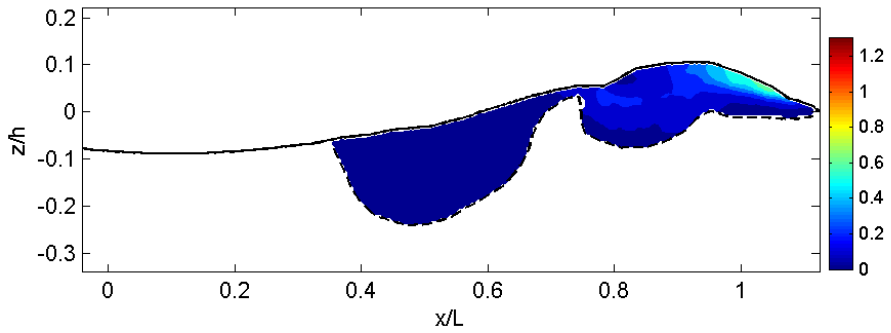

(o) $t = 0.71$ s

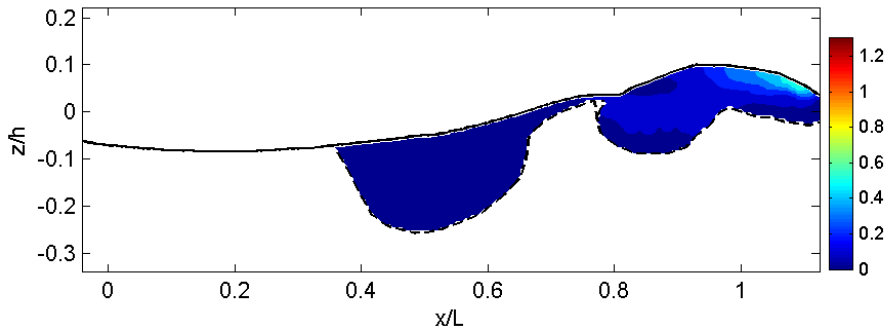

(p) $t = 0.76$ s

Fig. A.5 (Continued).

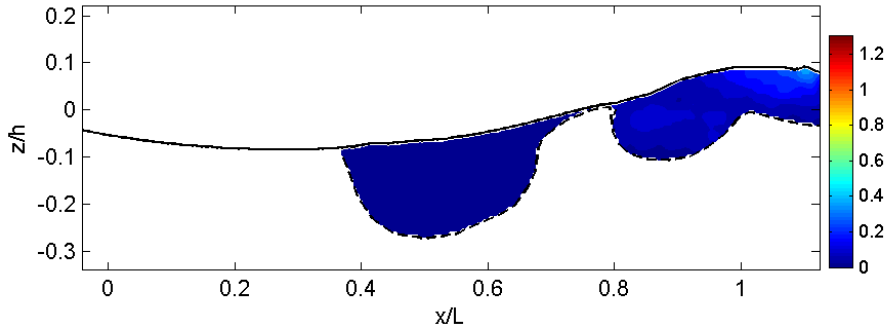

(q) t = 0.81 s

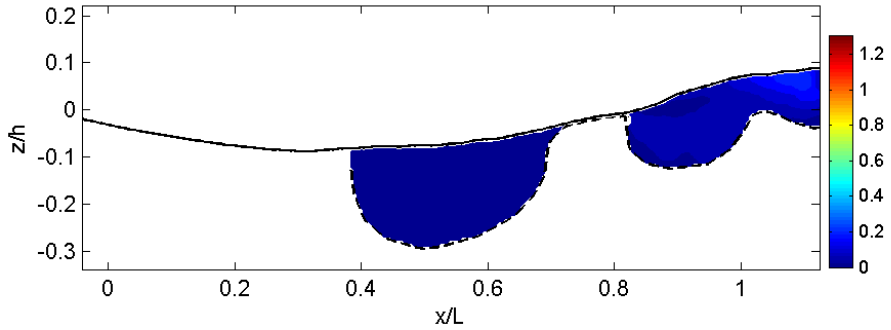

(r) t = 0.86 s

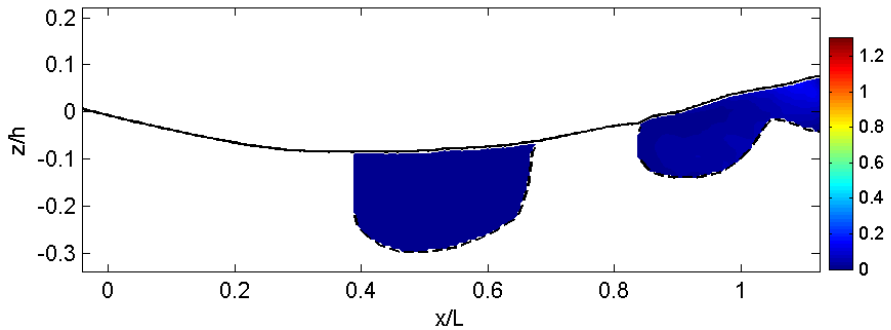

(s) t = 0.91 s

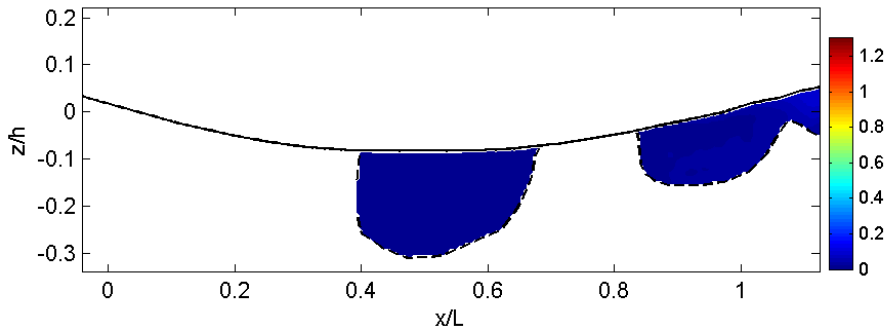

(t) = 0.96 s

Fig. A.5 (Continued).

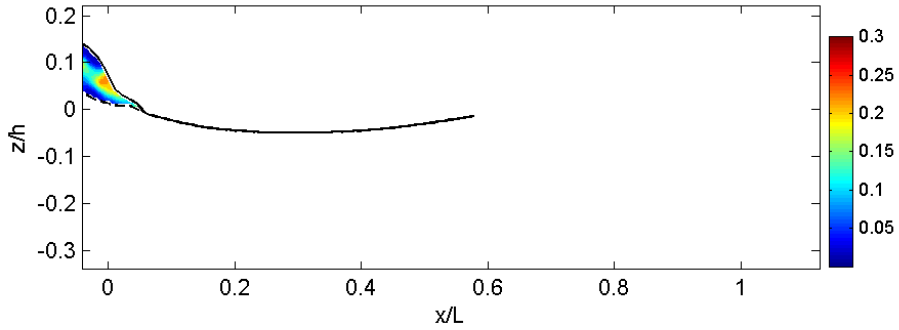

(a) $t = 0.01$ s

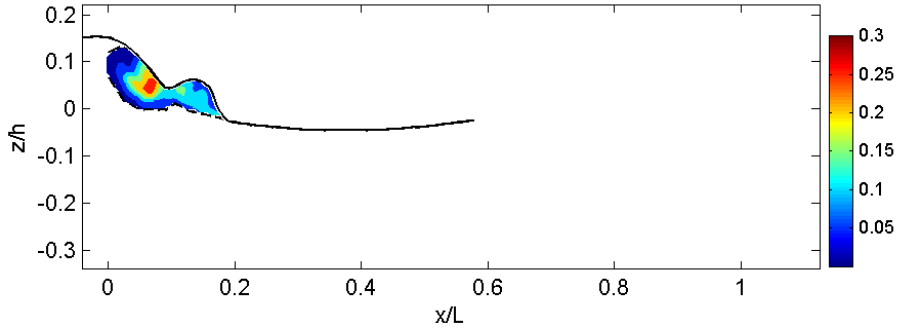

(b) $t = 0.06$ s

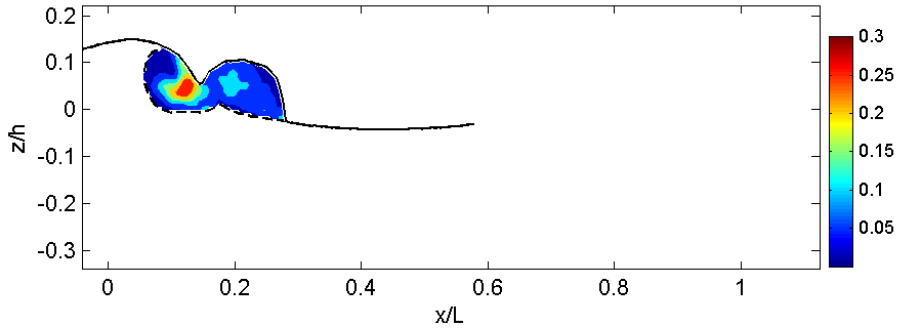

(c) $t = 0.11$ s

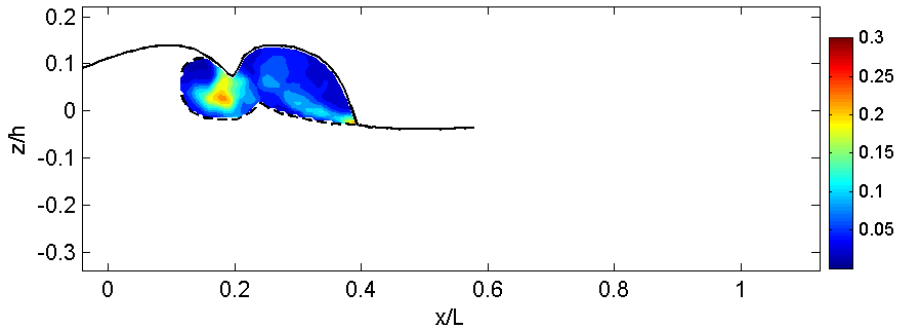

(d) $t = 0.16$ s

Fig. A.6 Normalized turbulent kinetic energy, k/C^2.

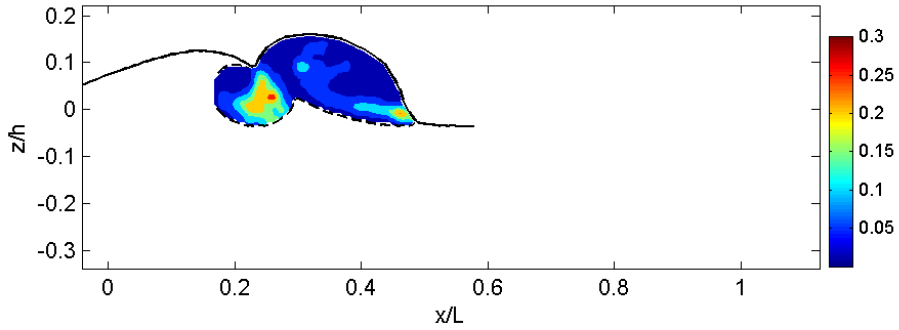

(e) $t = 0.21$ s

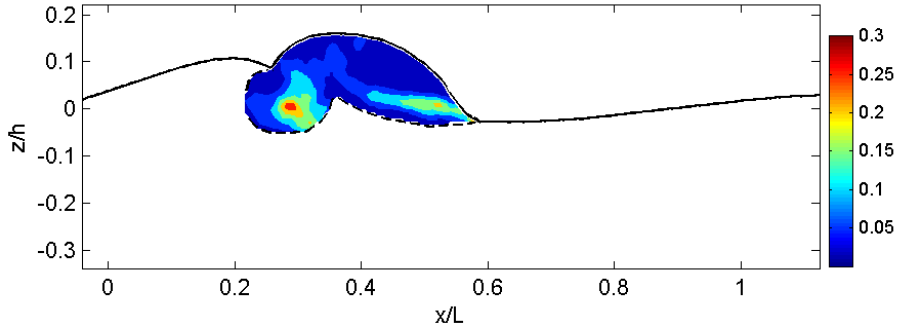

(f) $t = 0.26$ s

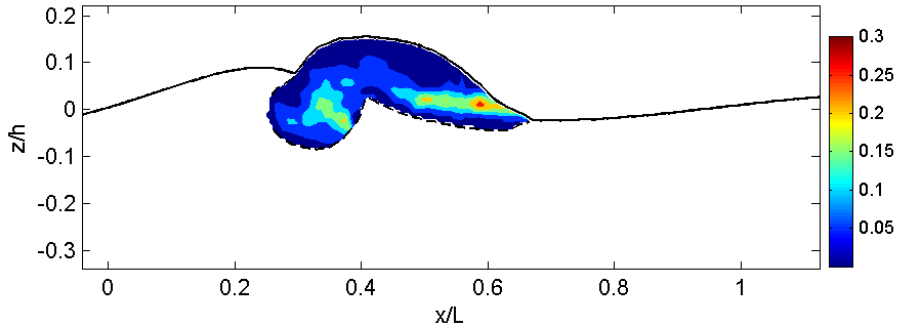

(g) $t = 0.31$ s

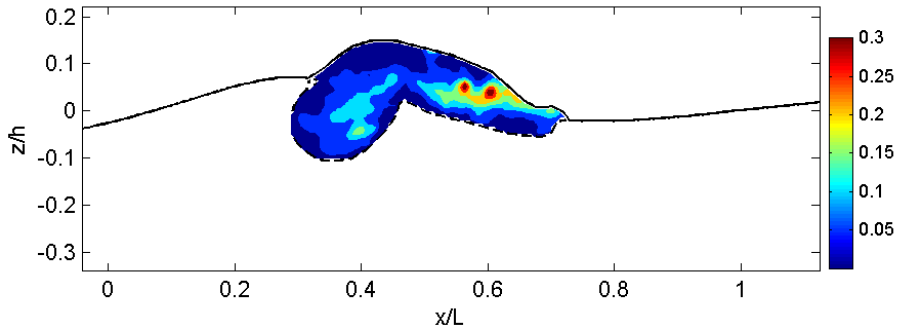

(h) $t = 0.36$ s

Fig. A.6 (Continued).

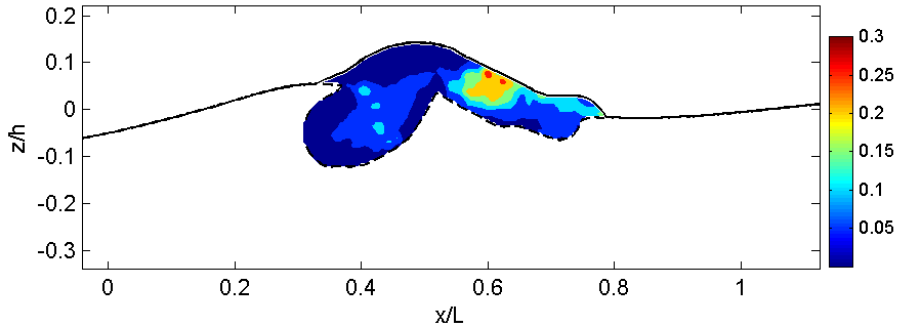

(i) $t = 0.41$ s

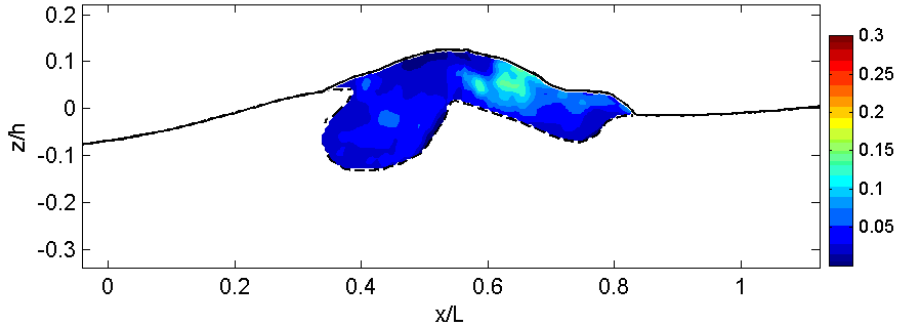

(j) $t = 0.46$ s

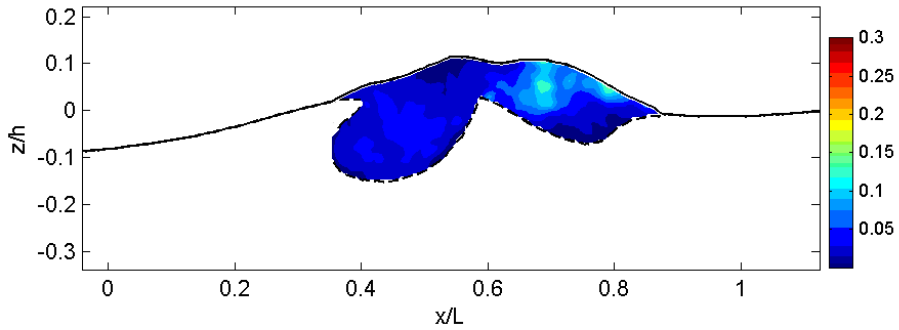

(k) $t = 0.51$ s

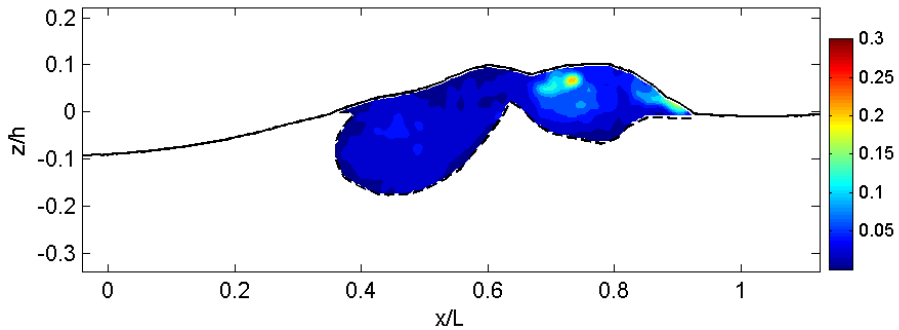

(l) $t = 0.56$ s

Fig. A.6 (Continued).

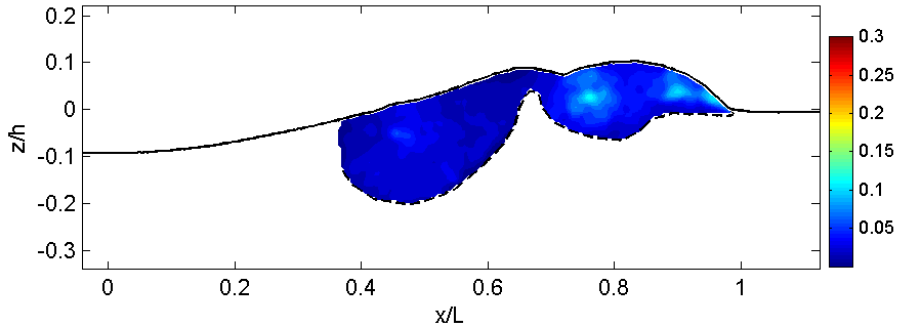

(m) $t = 0.61$ s

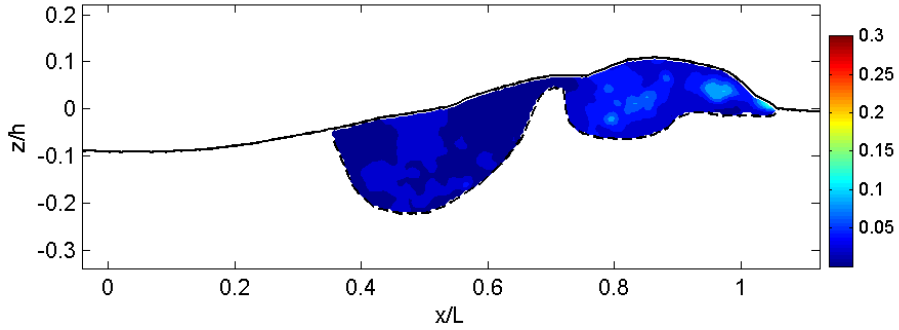

(n) $t = 0.66$ s

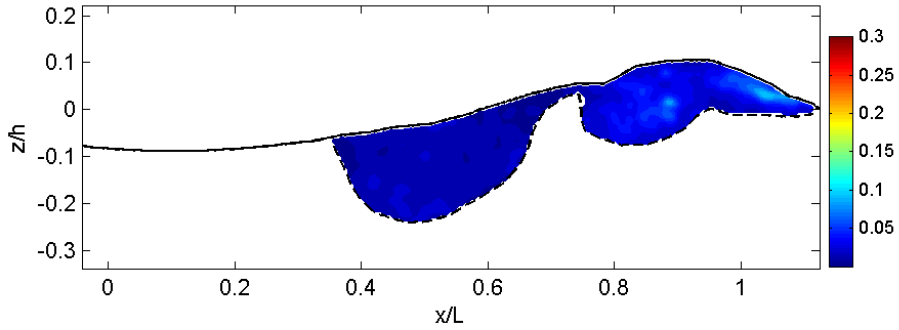

(o) $t = 0.71$ s

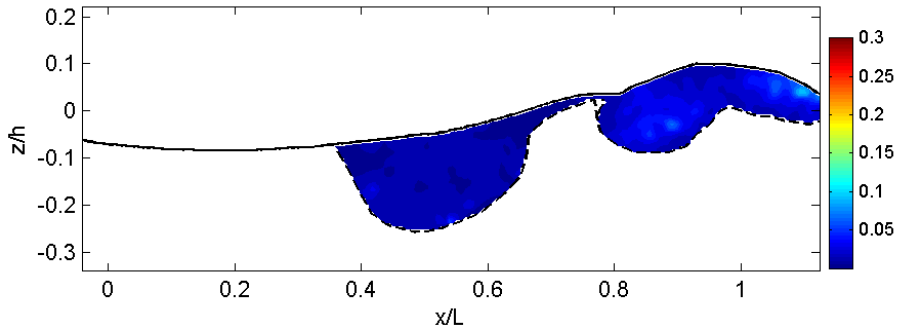

(p) $t = 0.76$ s

Fig. A.6 (Continued).

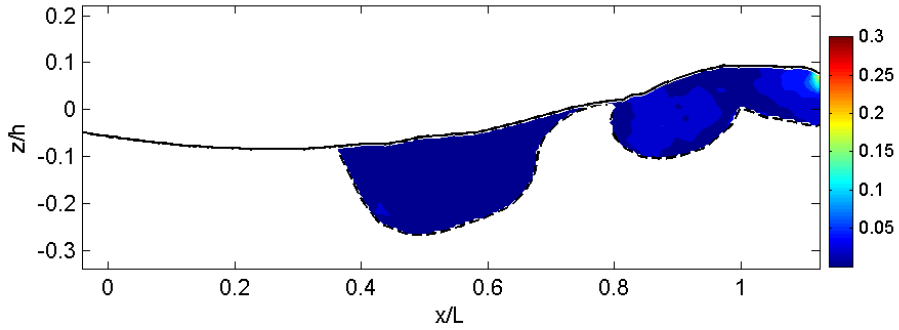

(q) t = 0.81 s

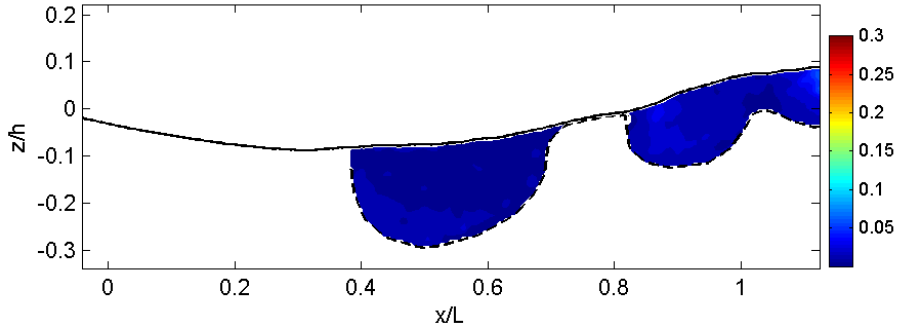

(r) t = 0.86 s

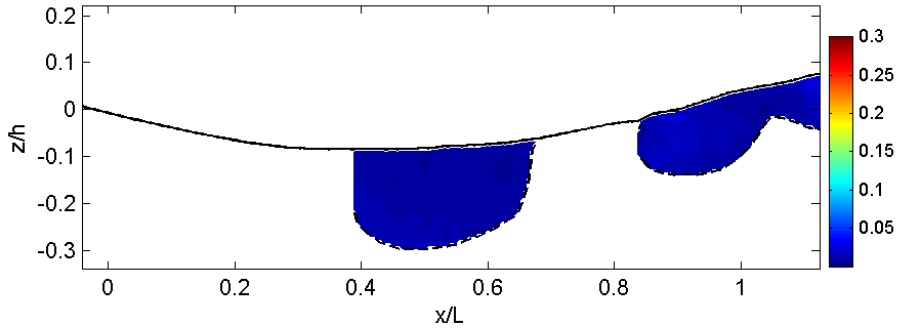

(s) t = 0.91 s

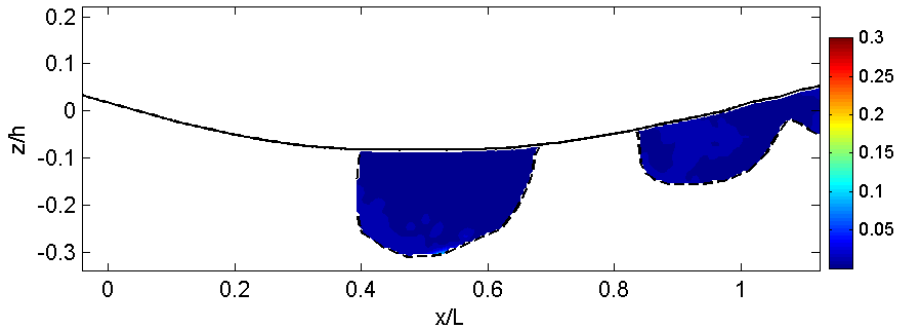

(t) = 0.96 s

Fig. A.6 (Continued).

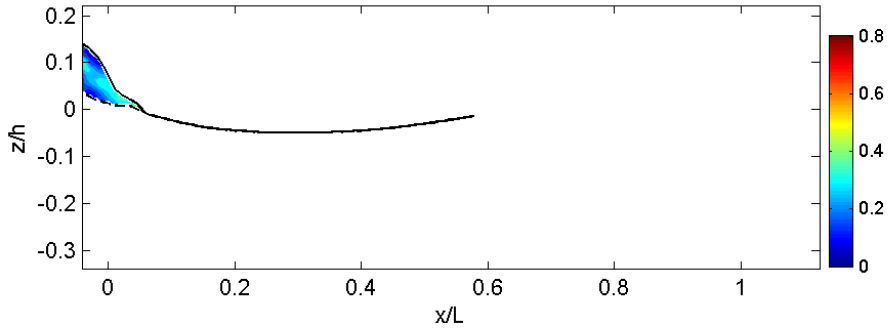

(a) t = 0.01 s

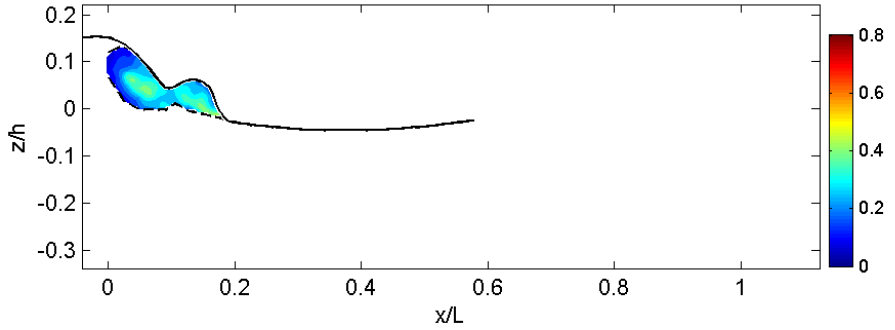

(b) t = 0.06 s

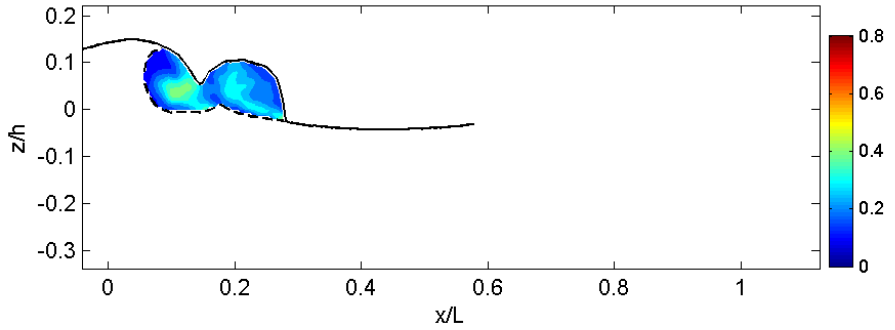

(c) t = 0.11 s

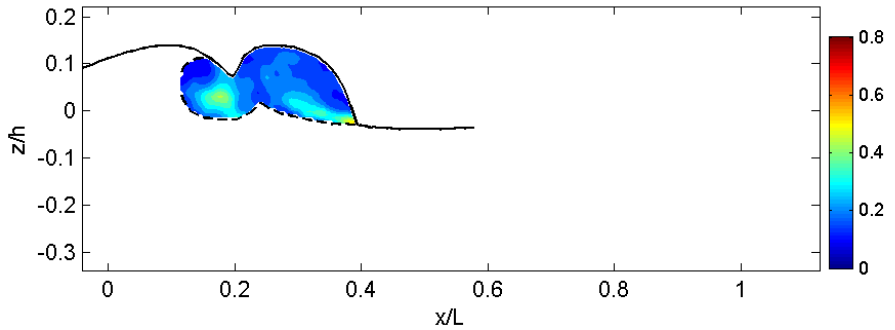

(d) t = 0.16 s

Fig. A.7 Normalized horizontal turbulence intensity, $\sqrt{u'^2}/C$.

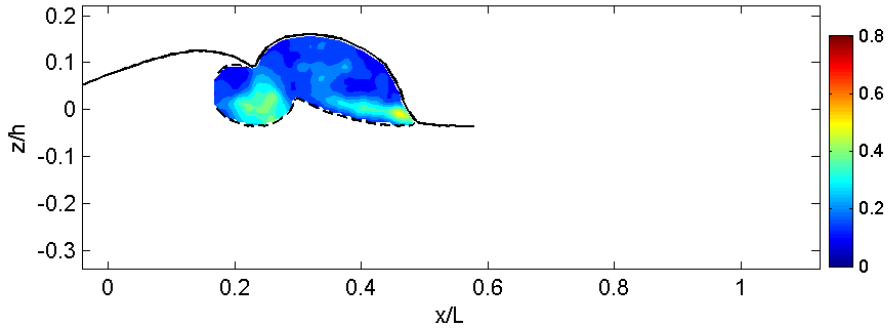

(e) t = 0.21 s

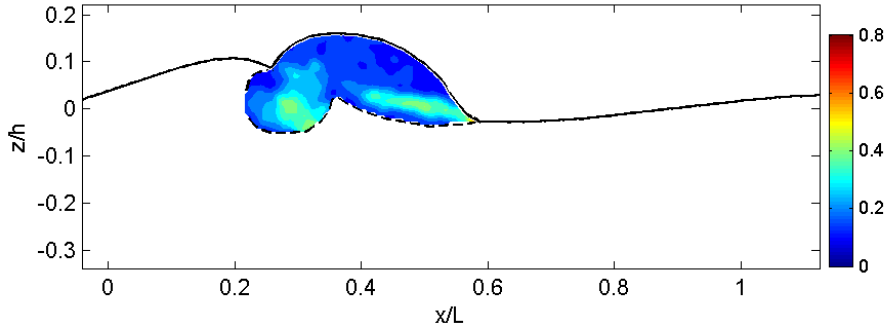

(f) t = 0.26 s

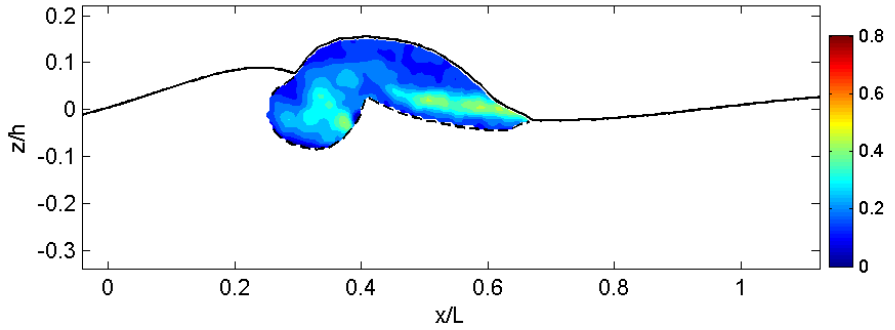

(g) t = 0.31 s

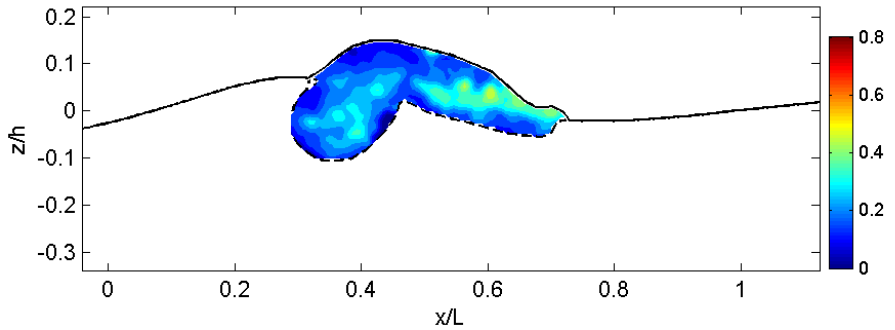

(h) t = 0.36 s

Fig. A.7 (Continued).

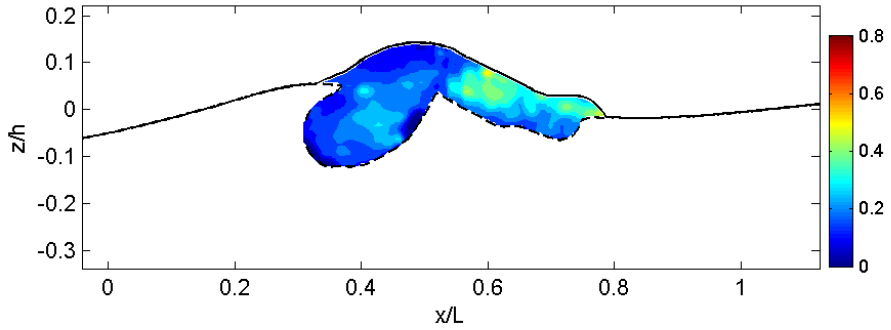

(i) $t = 0.41$ s

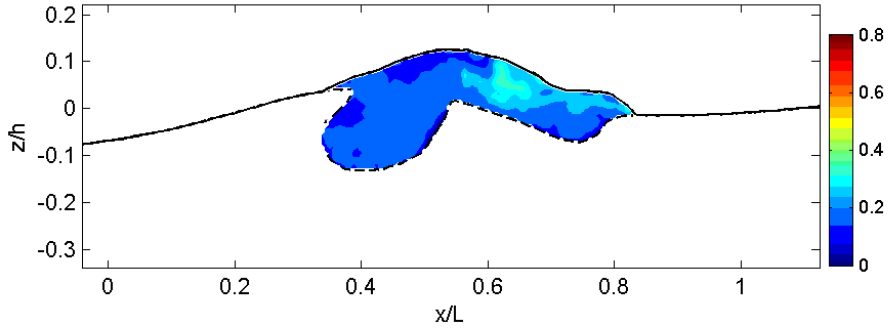

(j) $t = 0.46$ s

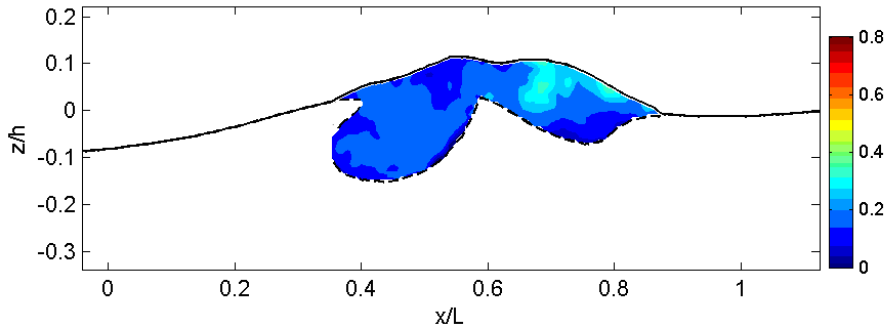

(k) $t = 0.51$ s

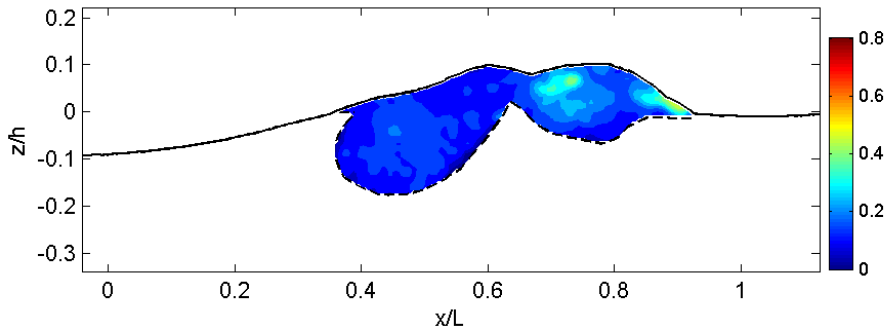

(l) $t = 0.56$ s

Fig. A.7 (Continued).

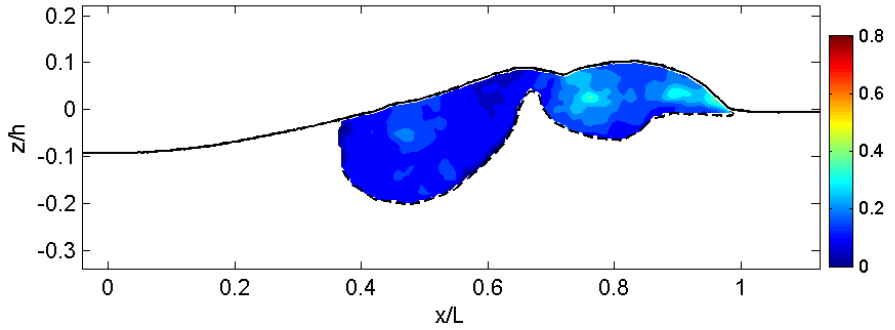

(m) $t = 0.61$ s

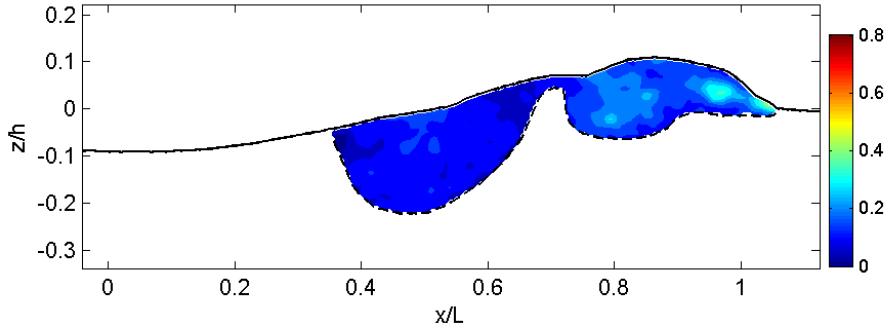

(n) $t = 0.66$ s

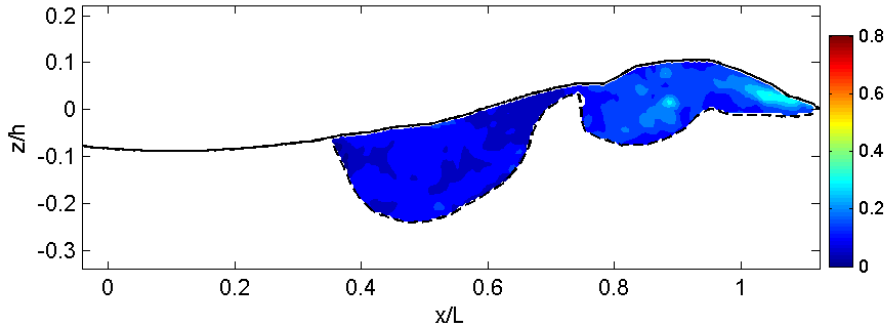

(o) $t = 0.71$ s

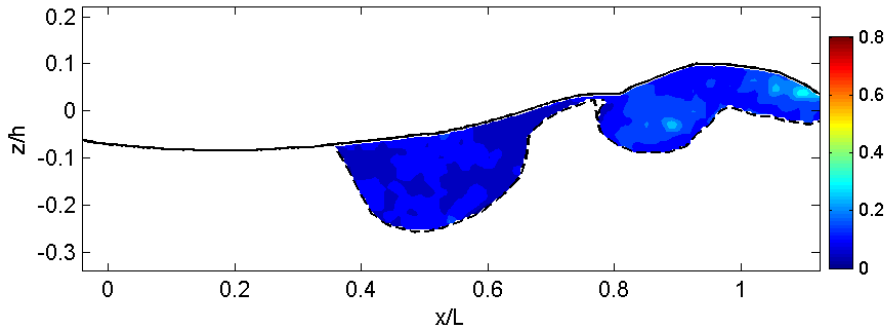

(p) $t = 0.76$ s

Fig. A.7 (Continued).

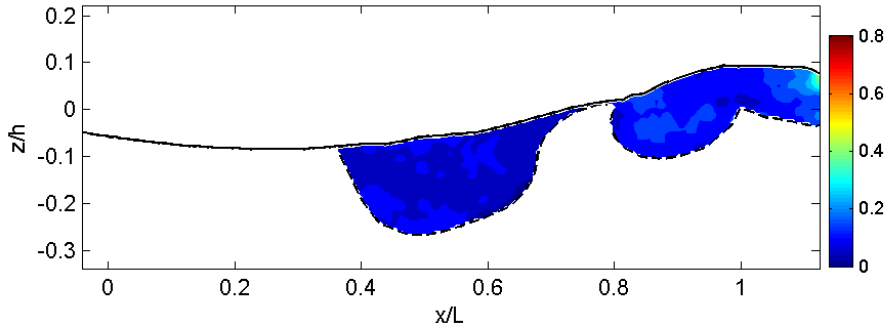

(q) t = 0.81 s

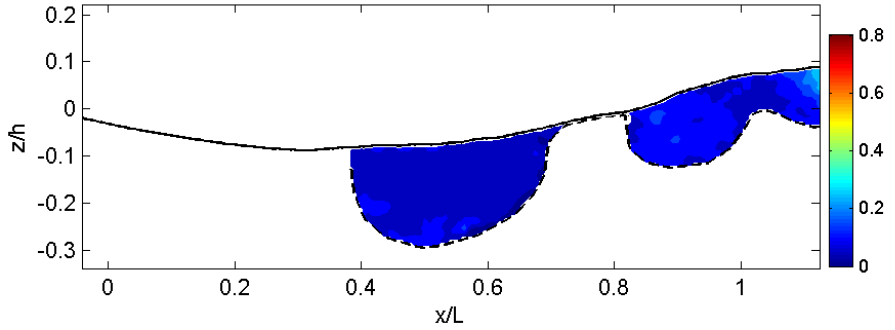

(r) t = 0.86 s

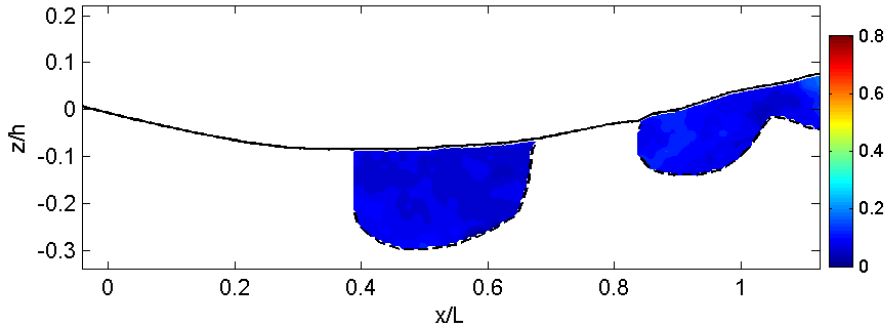

(s) t = 0.91 s

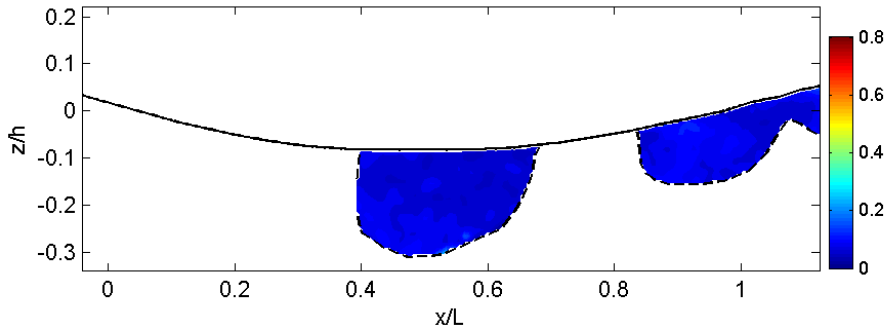

(t) = 0.96 s

Fig. A.7 (Continued).

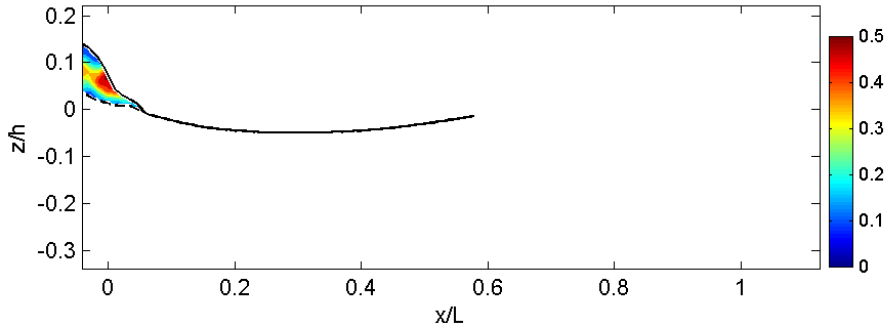

(a) t = 0.01 s

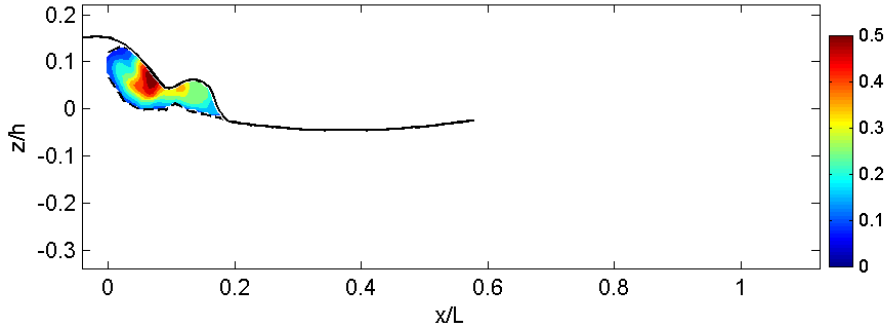

(b) t = 0.06 s

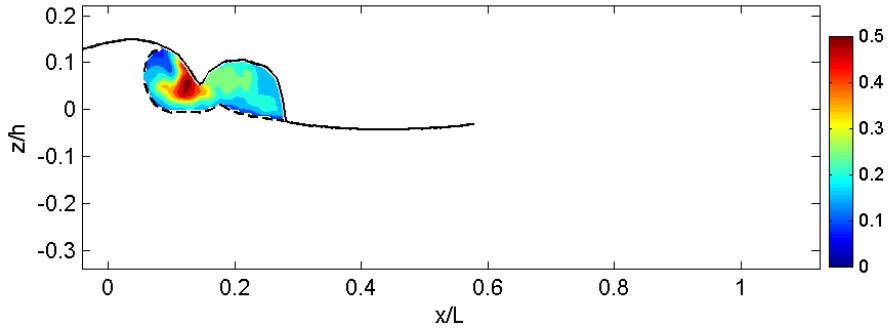

(c) t = 0.11 s

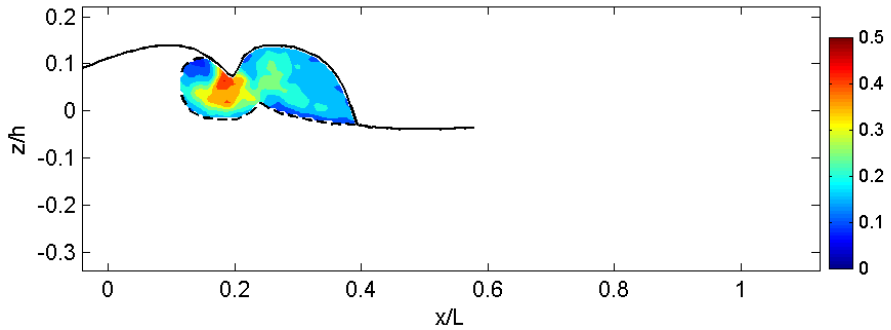

(d) t = 0.16 s

Fig. A.8 Normalized vertical turbulence intensity, $\sqrt{w'^2}/C$.

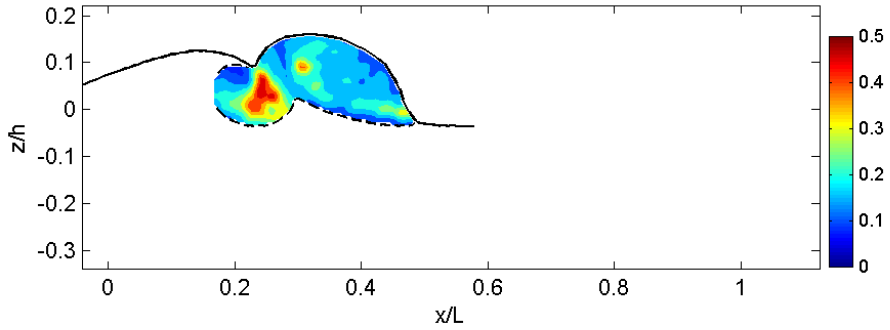

(e) t = 0.21 s

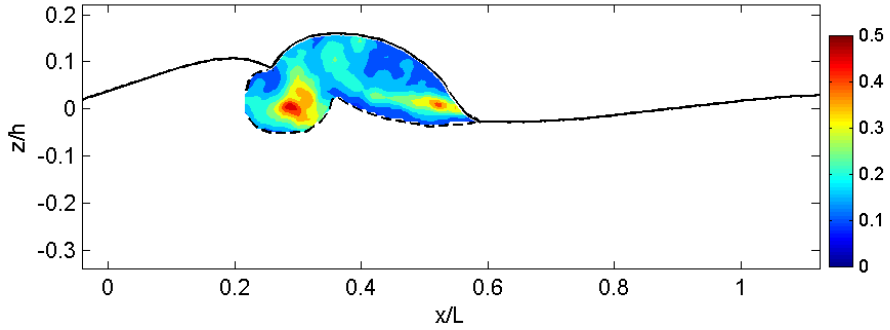

(f) t = 0.26 s

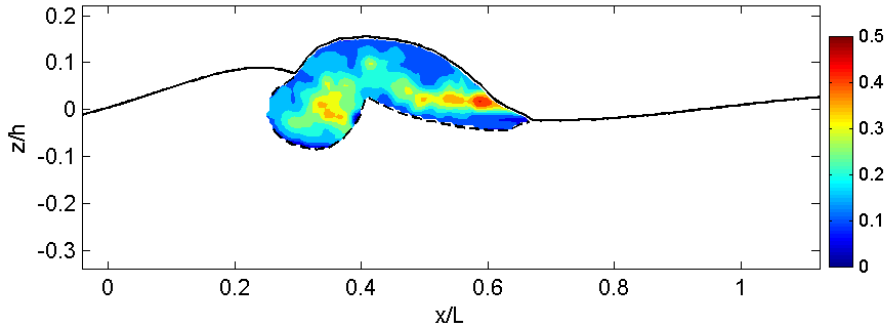

(g) t = 0.31 s

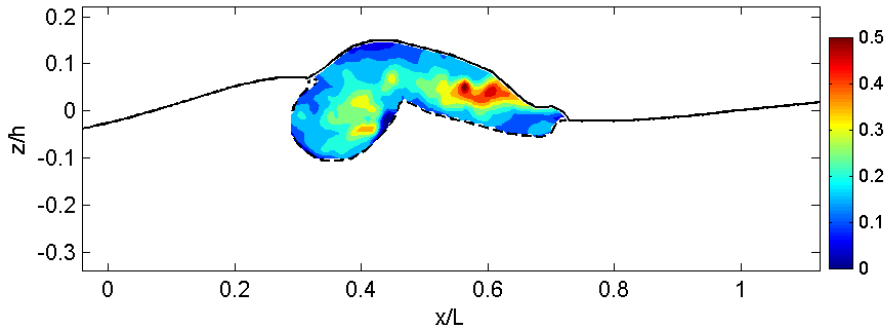

(h) t = 0.36 s

Fig. A.8 (Continued).

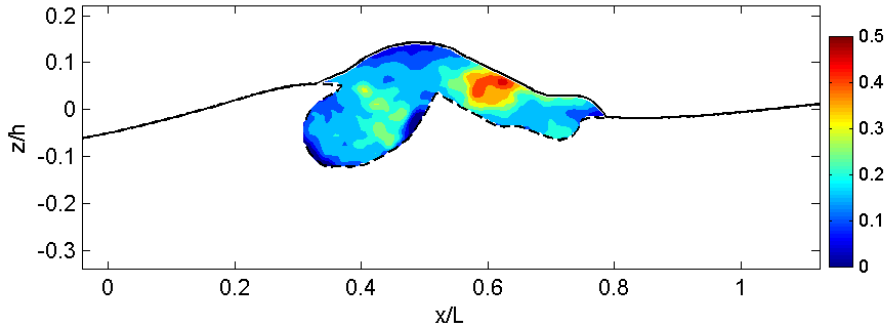

(i) $t = 0.41$ s

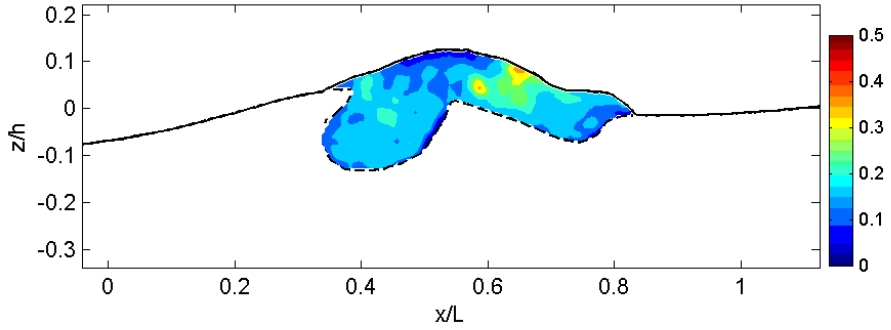

(j) $t = 0.46$ s

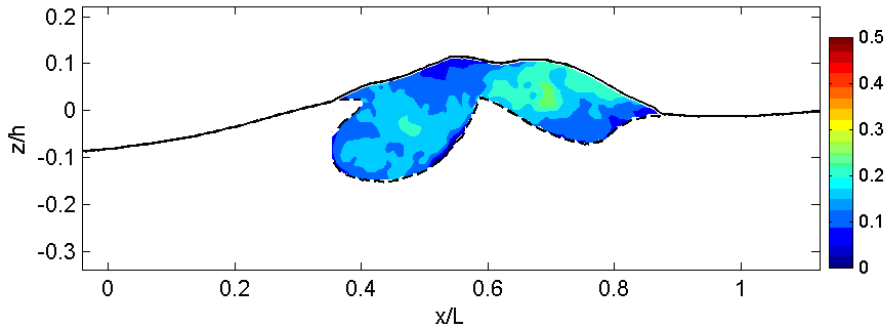

(k) $t = 0.51$ s

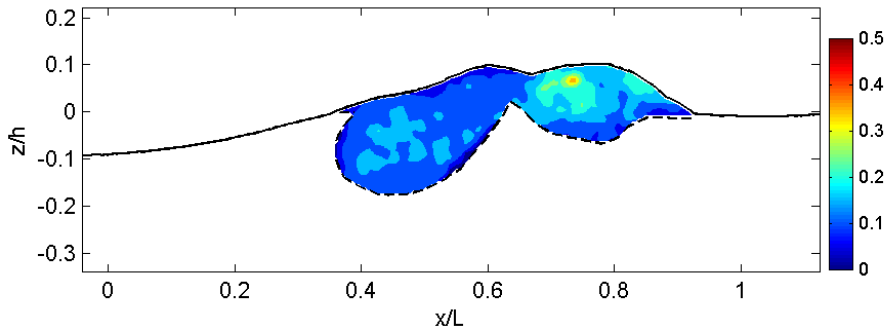

(l) $t = 0.56$ s

Fig. A.8 (Continued).

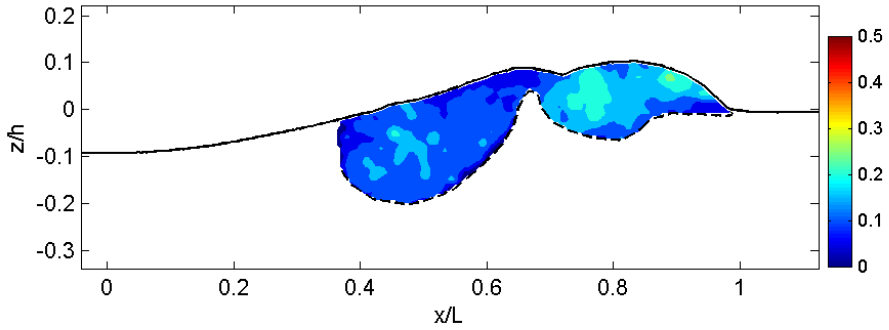

(m) $t = 0.61$ s

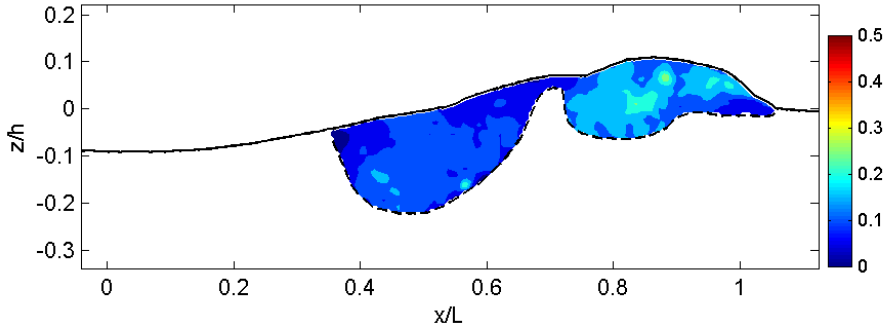

(n) $t = 0.66$ s

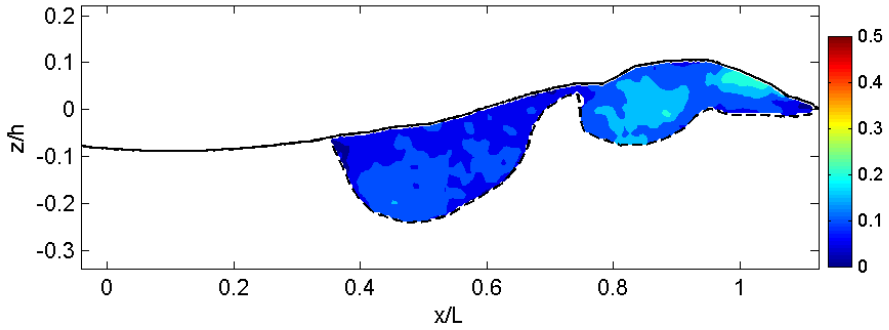

(o) $t = 0.71$ s

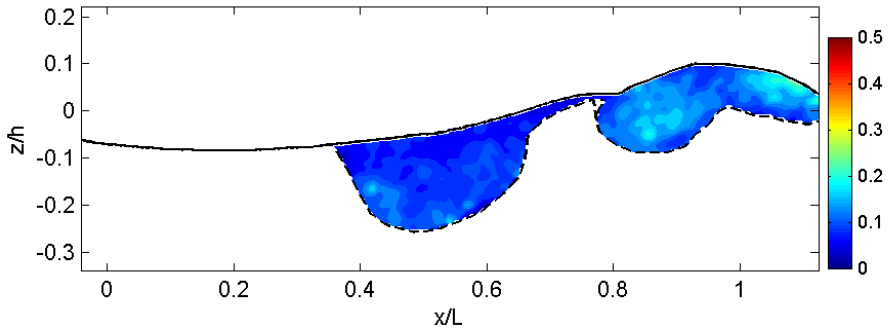

(p) $t = 0.76$ s

Fig. A.8 (Continued).

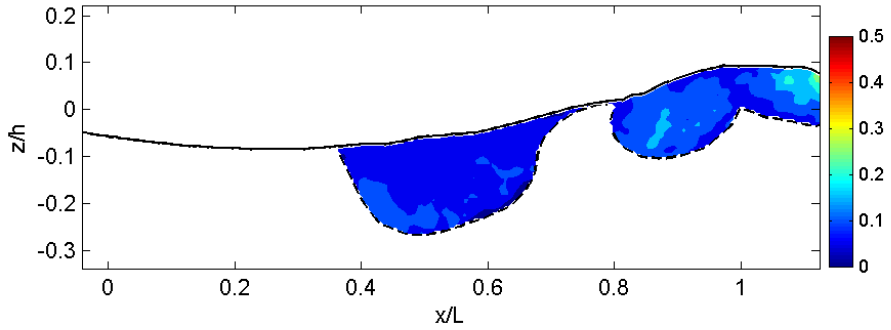

(q) t = 0.81 s

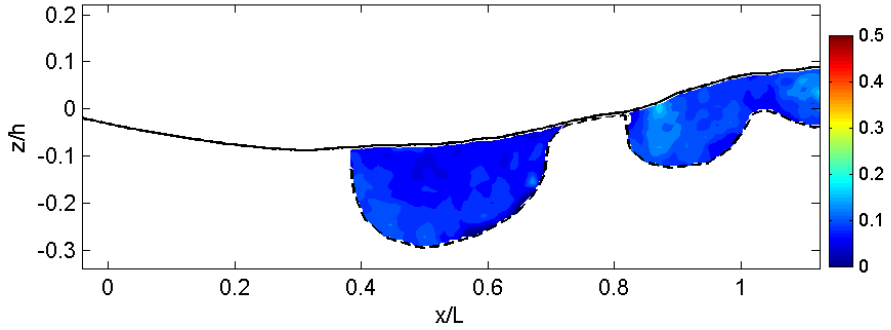

(r) t = 0.86 s

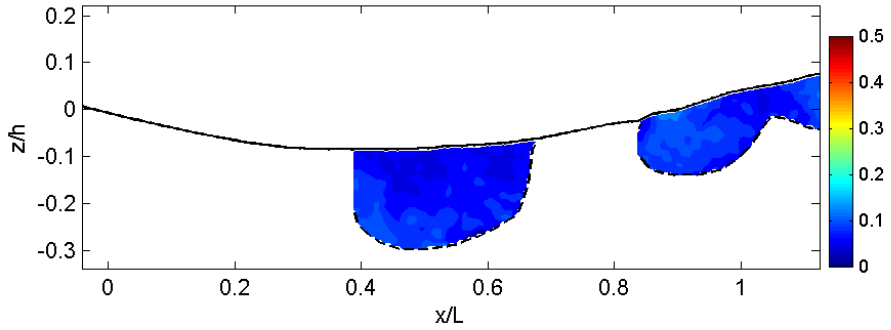

(s) t = 0.91 s

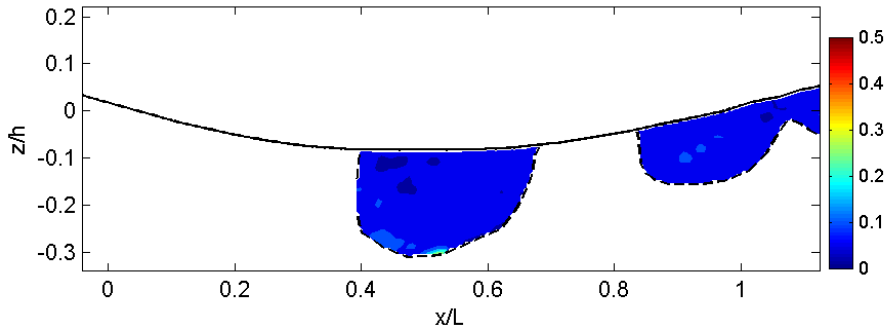

(t) = 0.96 s

Fig. A.8 (Continued).

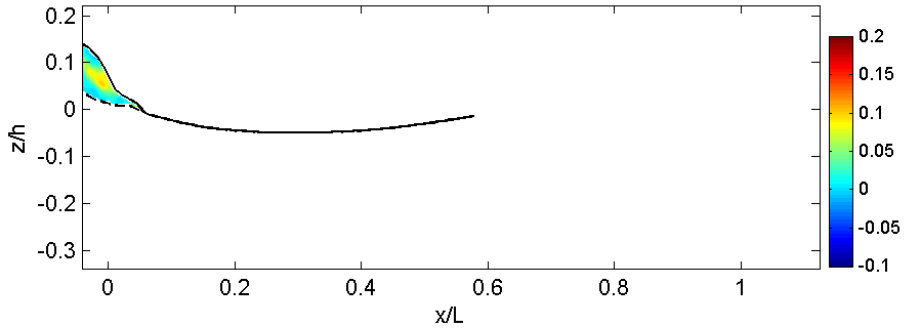

(a) $t = 0.01$ s

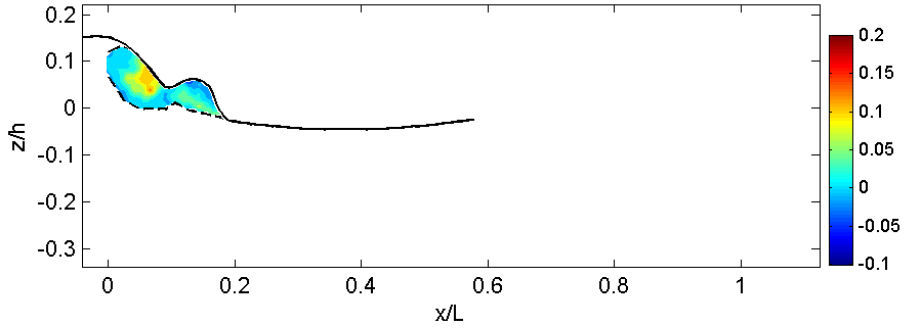

(b) $t = 0.06$ s

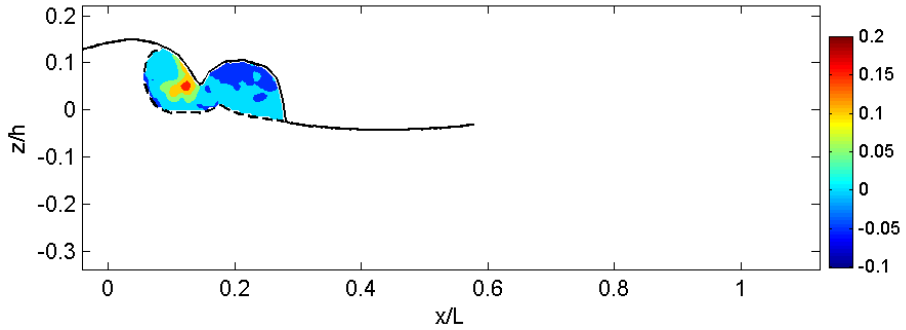

(c) $t = 0.11$ s

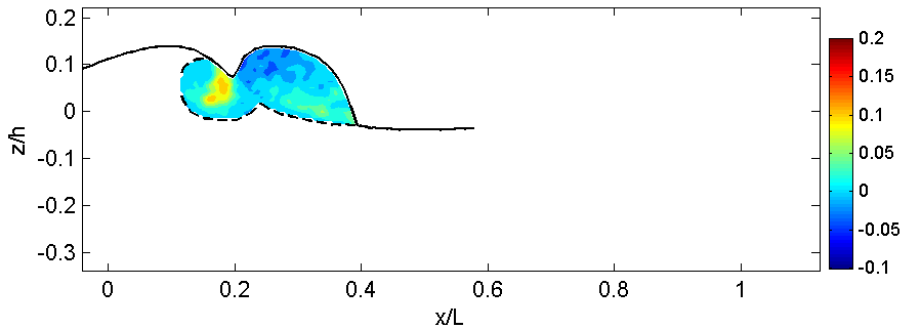

(d) $t = 0.16$ s

Fig. A.9 Normalized Reynolds stress, $-u'w'/C^2$.

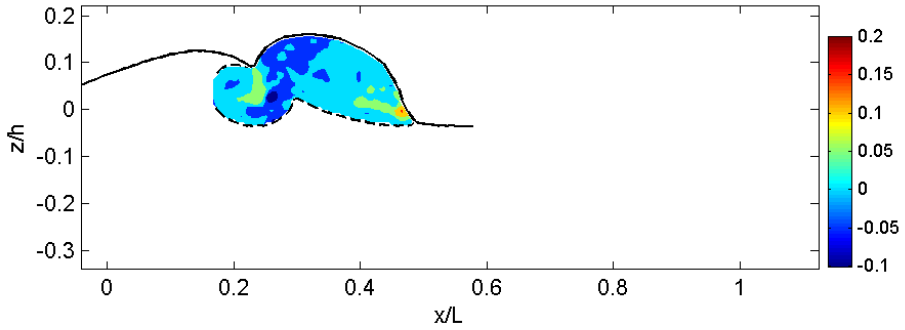

(e) $t = 0.21$ s

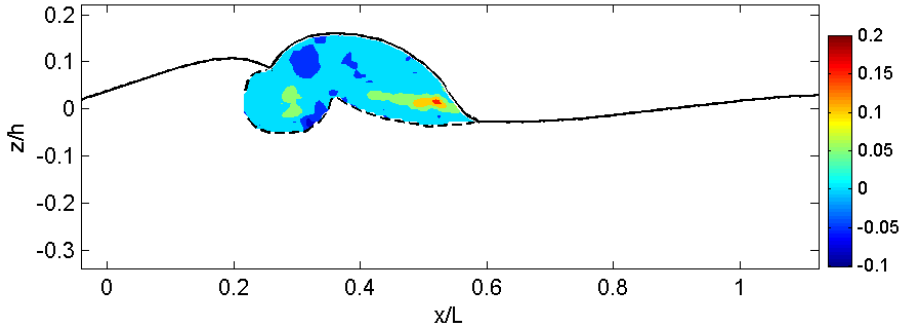

(f) $t = 0.26$ s

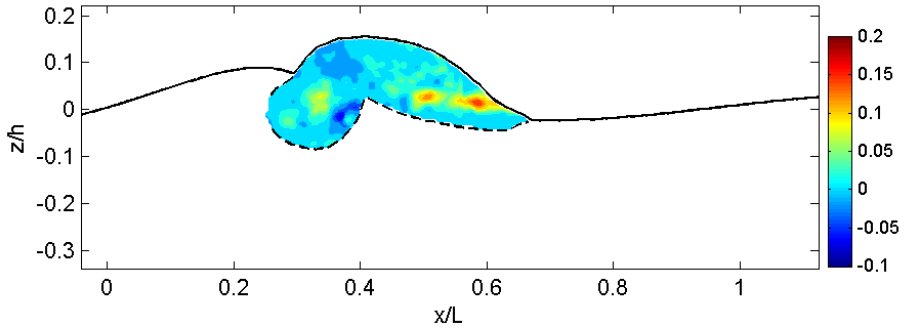

(g) $t = 0.31$ s

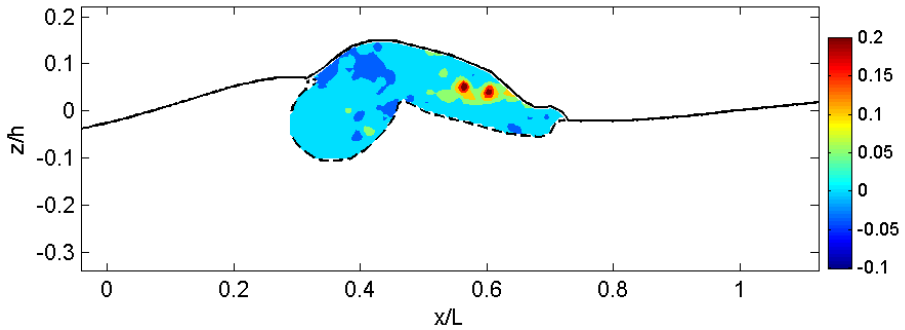

(h) $t = 0.36$ s

Fig. A.9 (Continued).

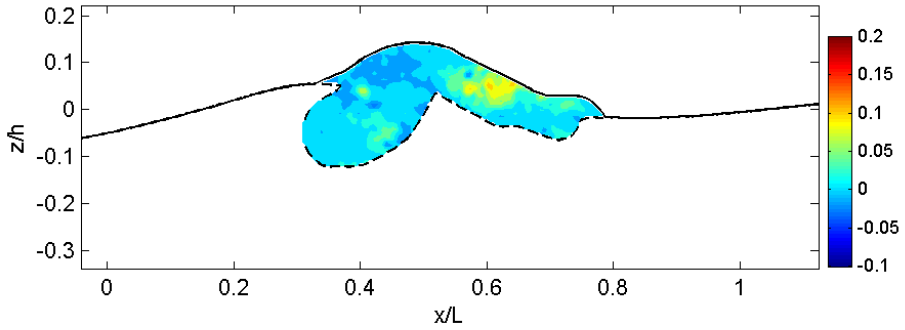

(i) $t = 0.41$ s

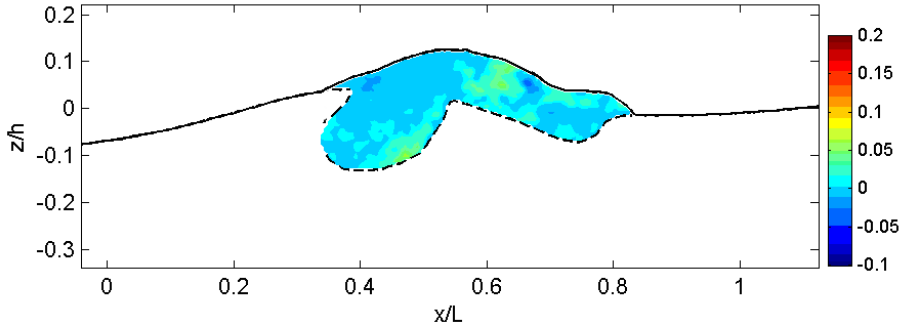

(j) $t = 0.46$ s

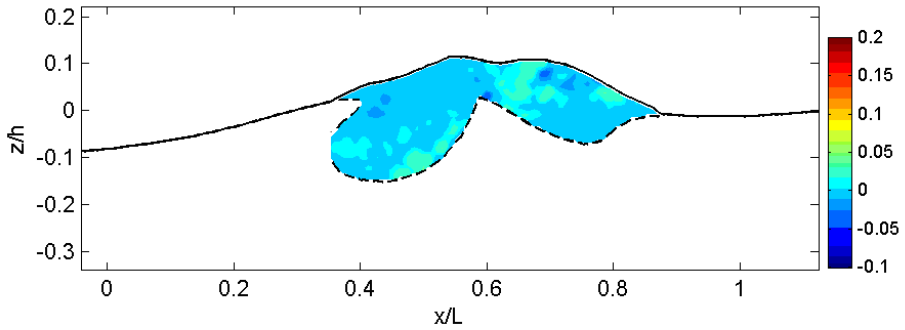

(k) $t = 0.51$ s

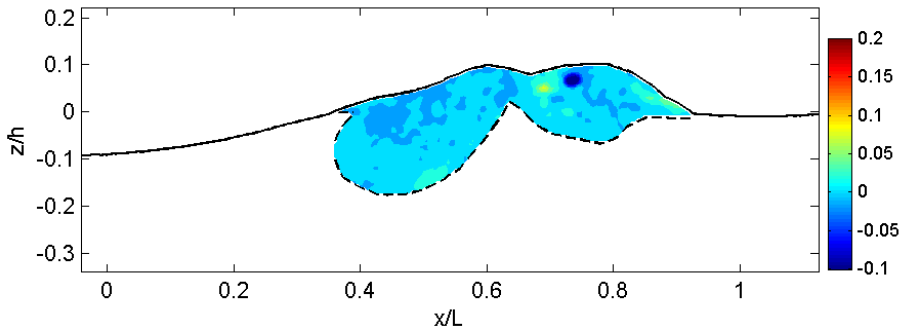

(l) $t = 0.56$ s

Fig. A.9 (Continued).

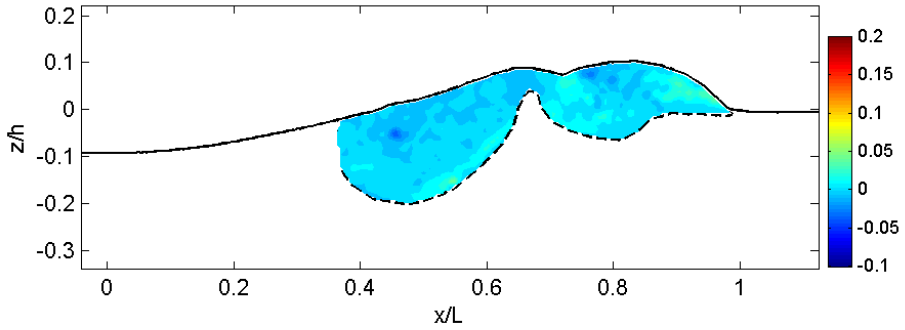

(m) $t = 0.61$ s

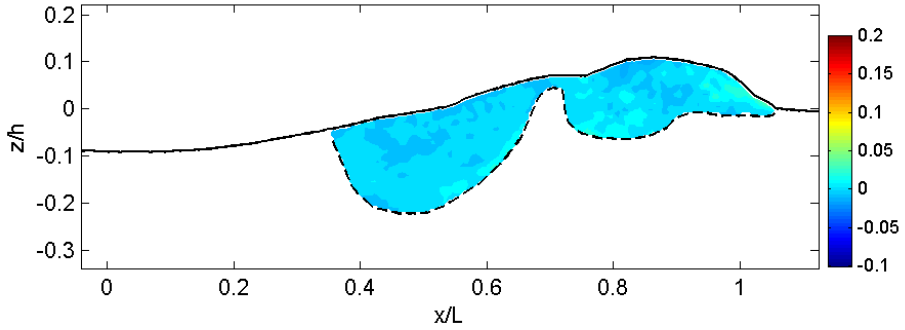

(n) $t = 0.66$ s

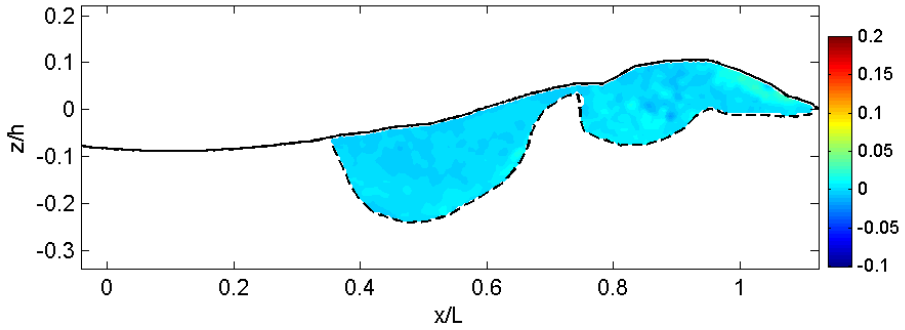

(o) $t = 0.71$ s

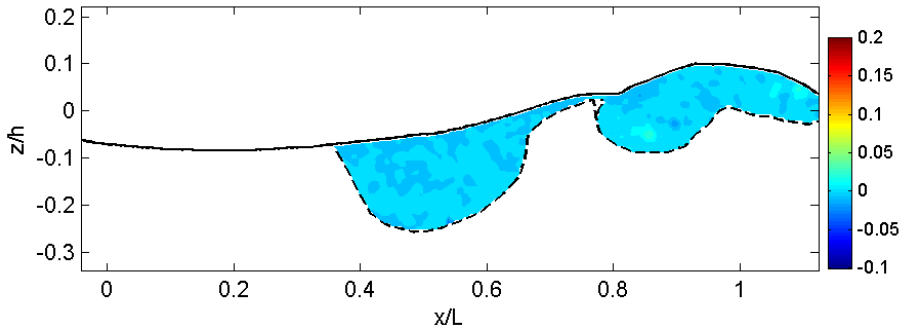

(p) $t = 0.76$ s

Fig. A.9 (Continued).

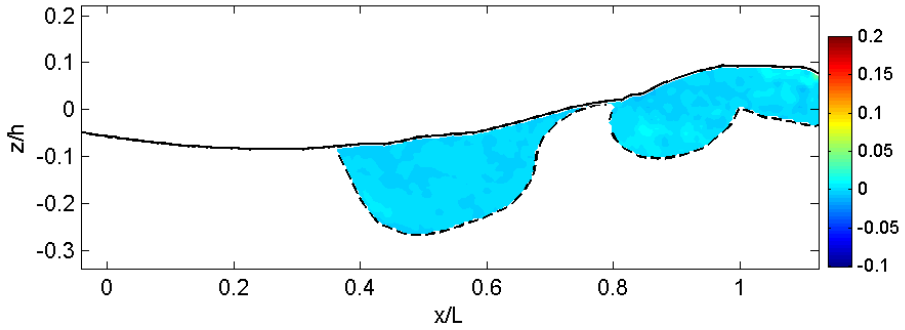

(q) $t = 0.81$ s

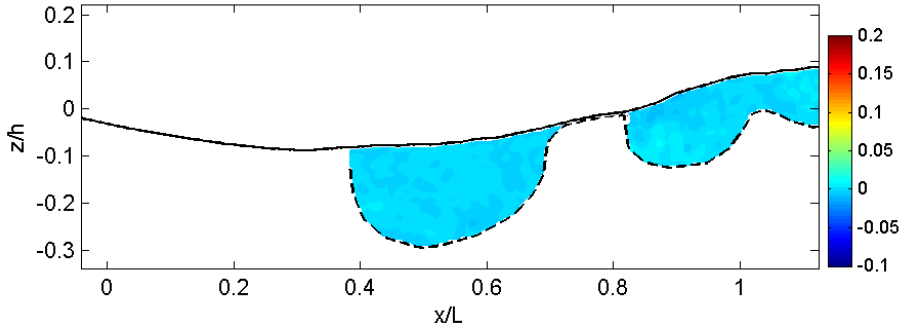

(r) $t = 0.86$ s

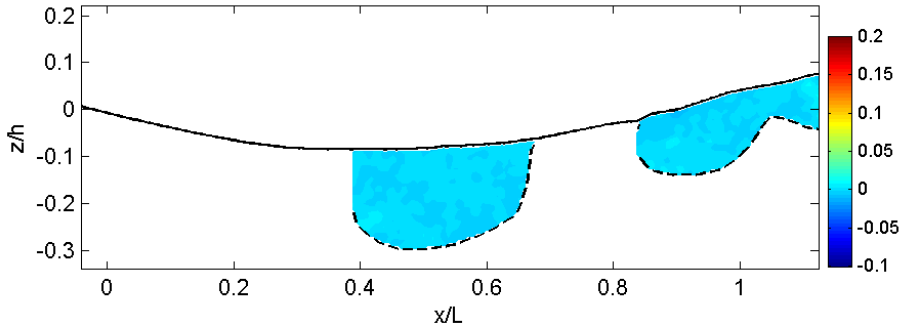

(s) $t = 0.91$ s

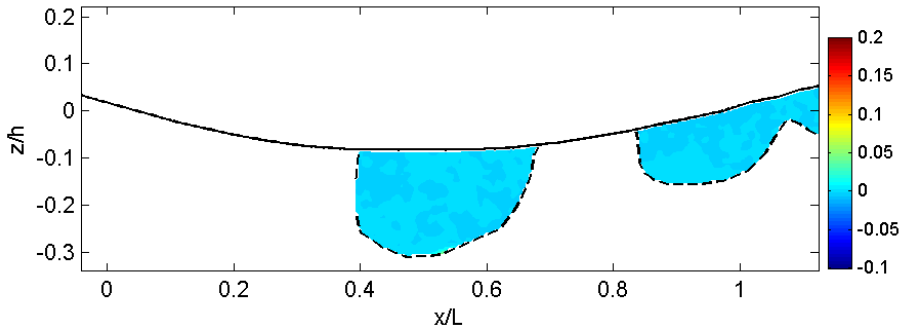

(t) $t = 0.96$ s

Fig. A.9 (Continued).

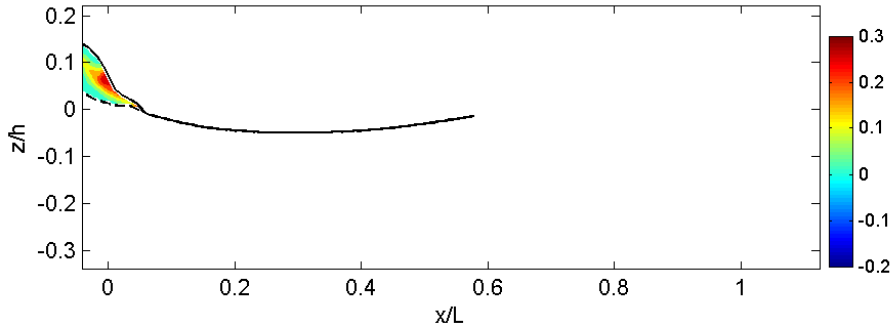

(a) $t = 0.01$ s

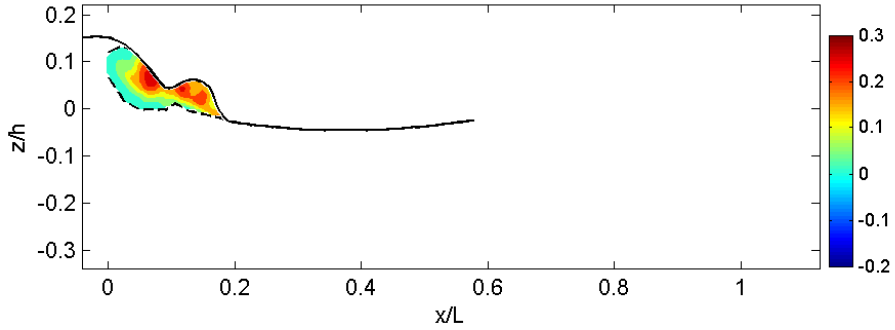

(b) $t = 0.06$ s

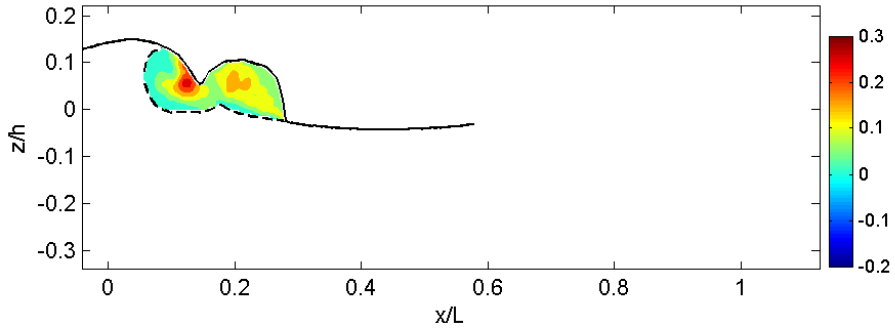

(c) $t = 0.11$ s

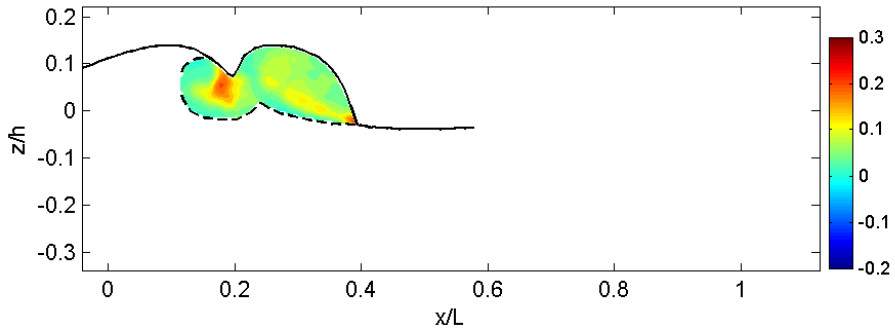

(d) $t = 0.16$ s

Fig. A.10 kU/C^3.

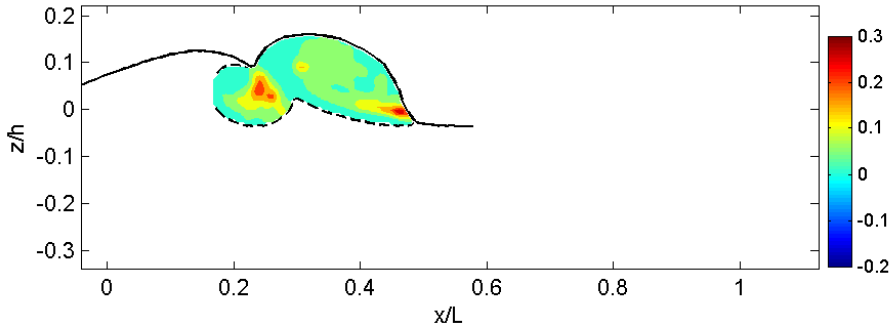

(e) t = 0.21 s

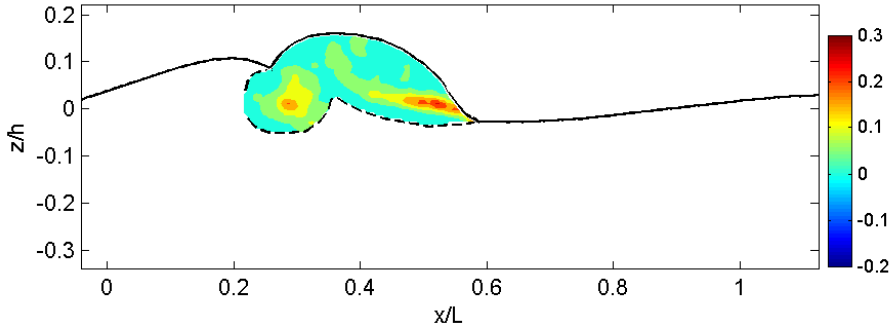

(f) t = 0.26 s

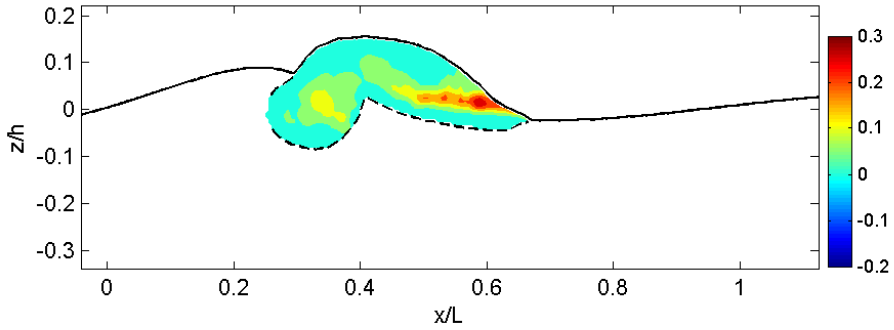

(g) t = 0.31 s

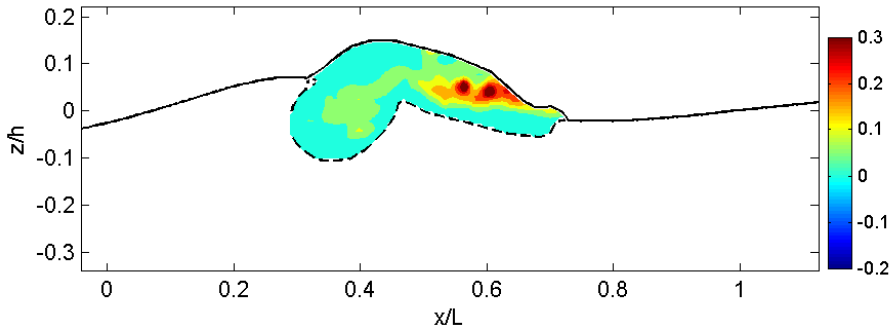

(h) t = 0.36 s

Fig. A.10 (Continued).

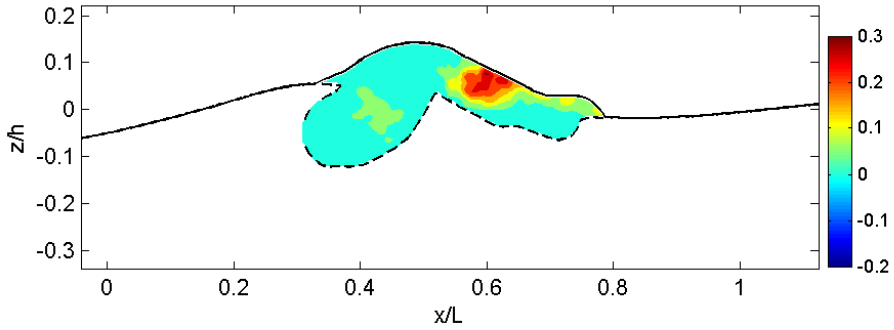

(i) $t = 0.41$ s

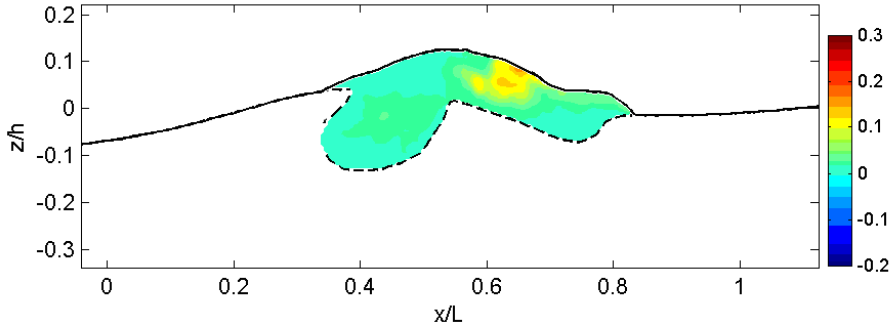

(j) $t = 0.46$ s

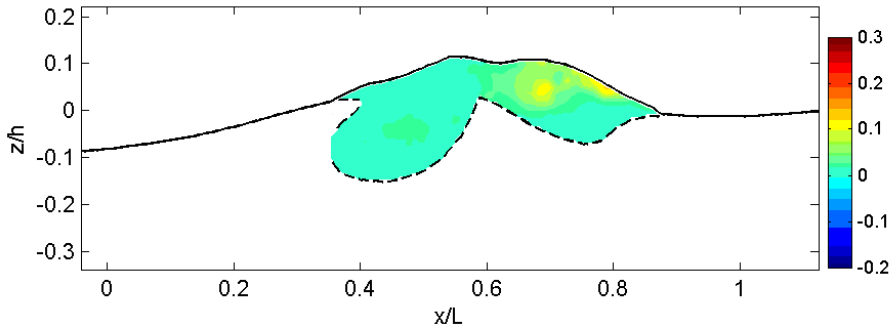

(k) $t = 0.51$ s

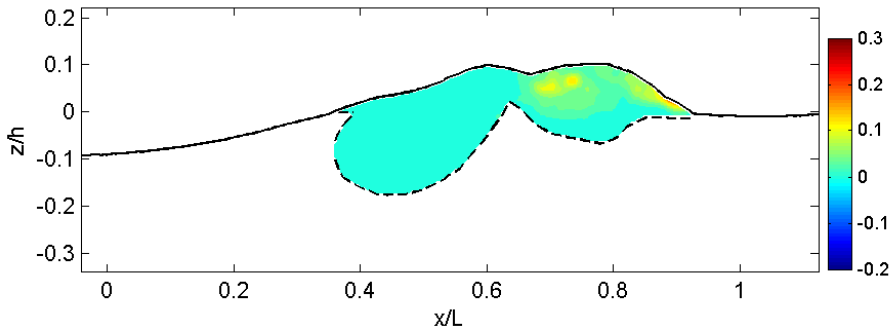

(l) $t = 0.56$ s

Fig. A.10 (Continued).

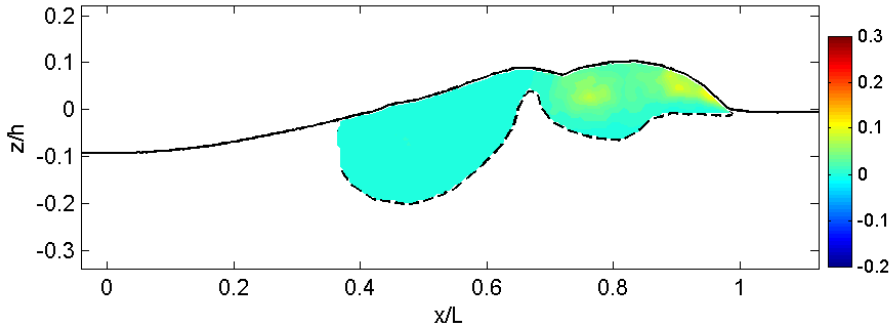

(m) $t = 0.61$ s

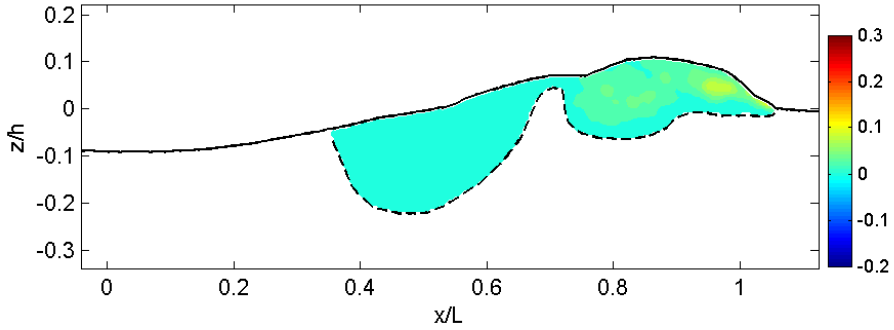

(n) $t = 0.66$ s

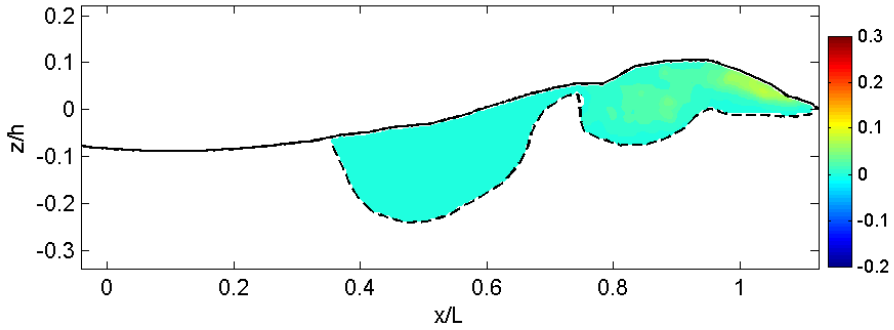

(o) $t = 0.71$ s

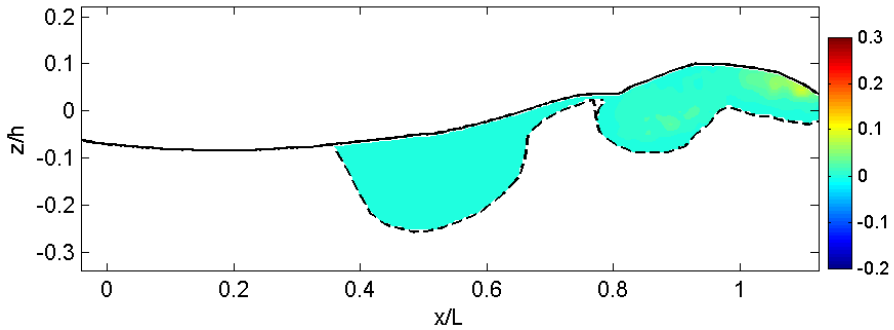

(p) $t = 0.76$ s

Fig. A.10 (Continued).

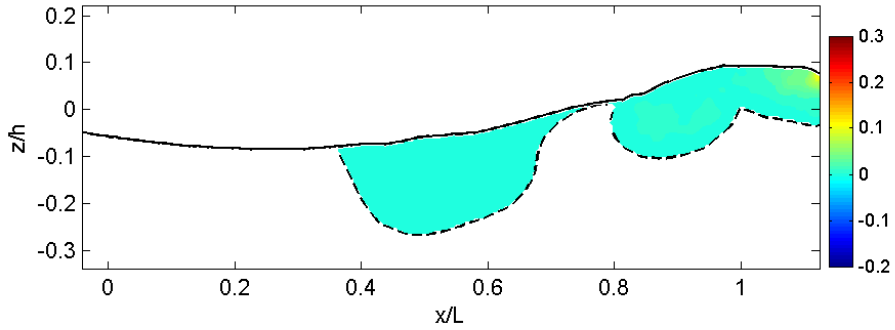

(q) $t = 0.81$ s

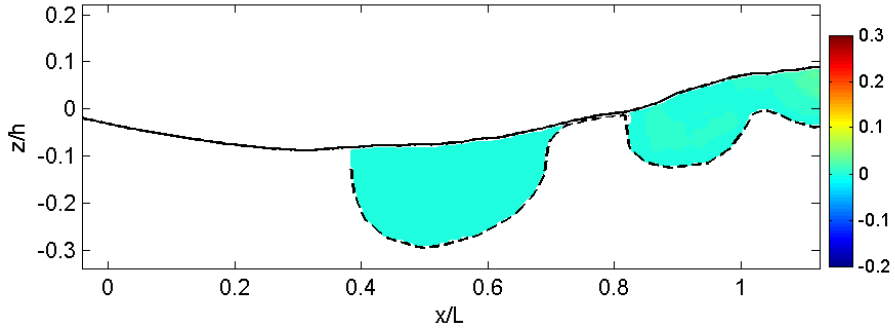

(r) $t = 0.86$ s

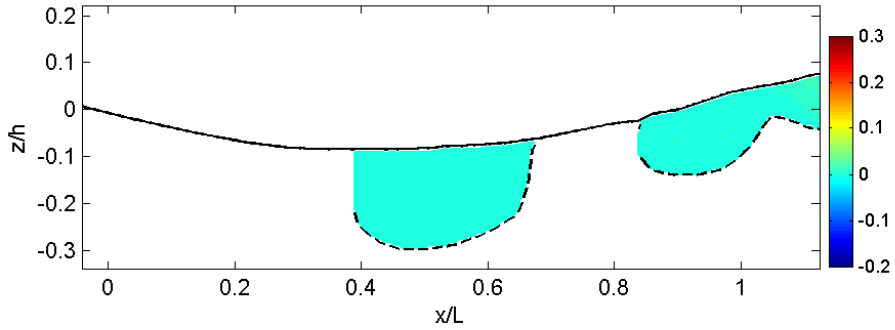

(s) $t = 0.91$ s

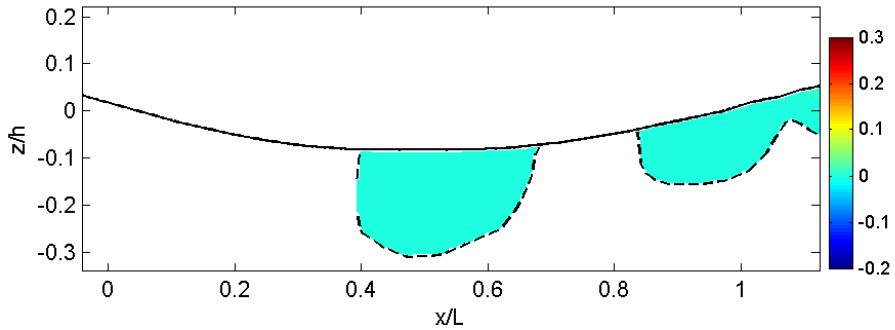

(t) $t = 0.96$ s

Fig. A.10 (Continued).

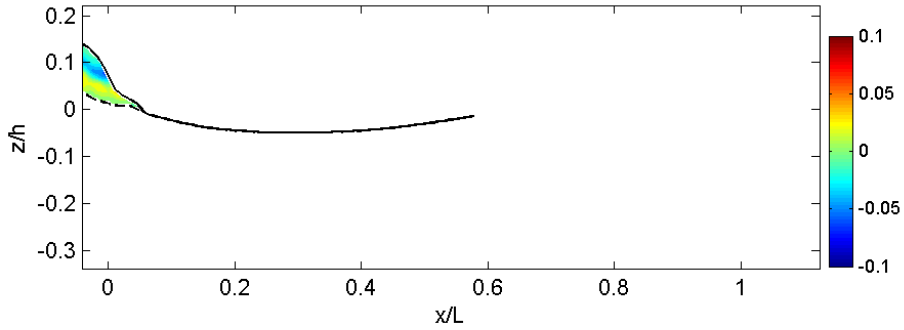

(a) $t = 0.01$ s

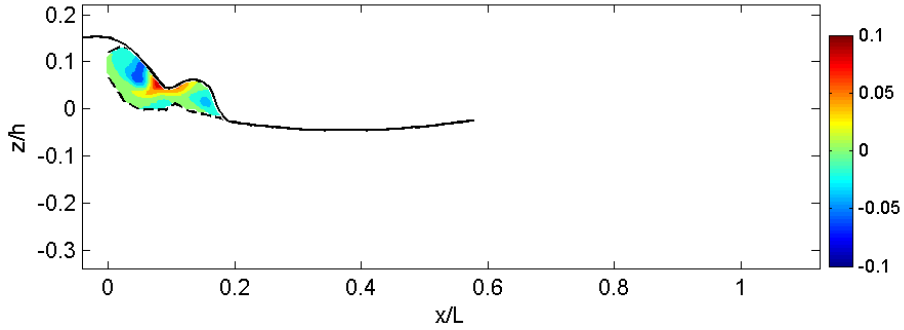

(b) $t = 0.06$ s

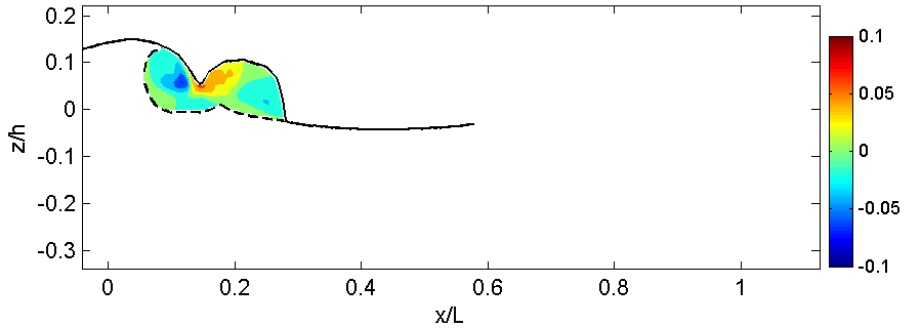

(c) $t = 0.11$ s

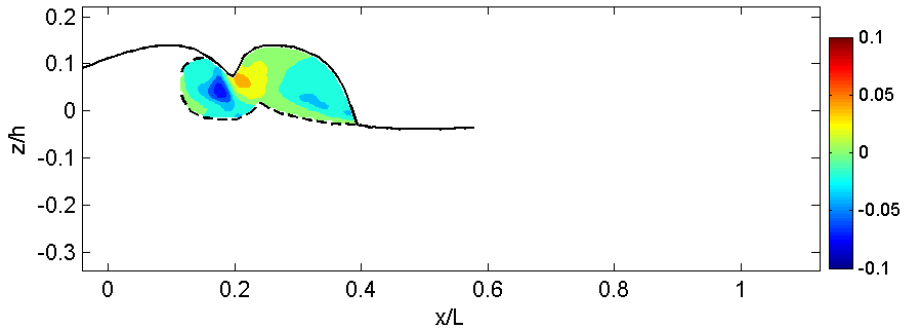

(d) $t = 0.16$ s

Fig. A.11 kW/C^3.

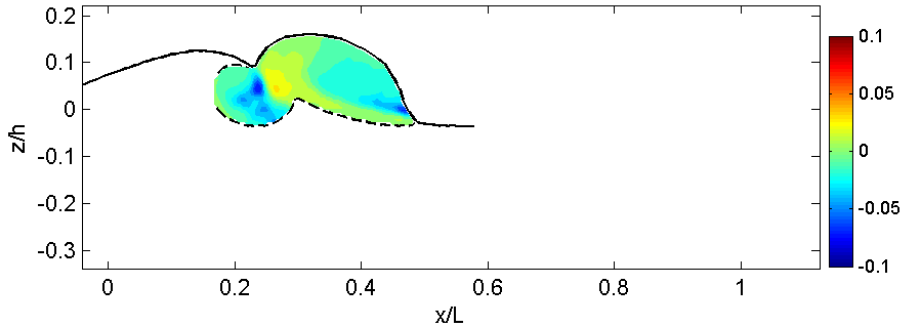

(e) t = 0.21 s

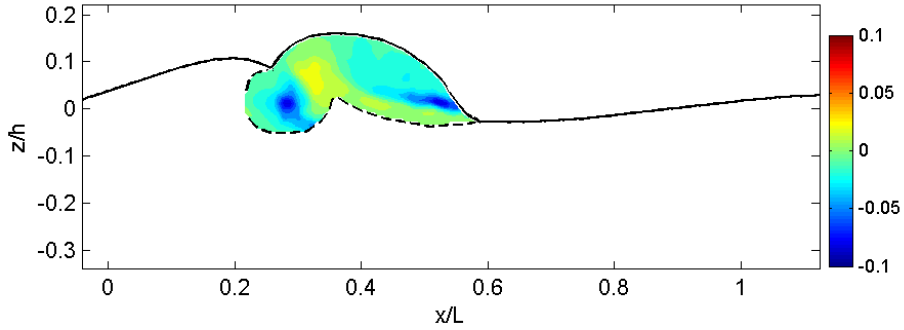

(f) t = 0.26 s

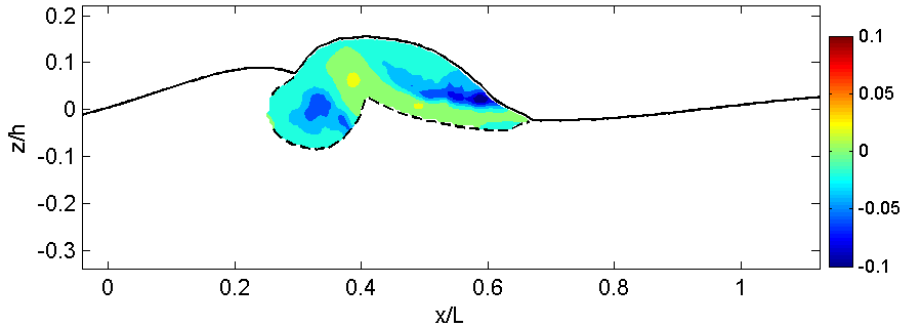

(g) t = 0.31 s

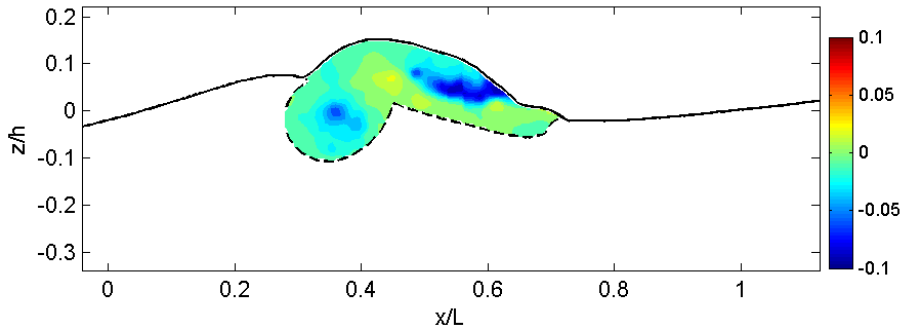

(h) t = 0.36 s

Fig. A.11 (Continued).

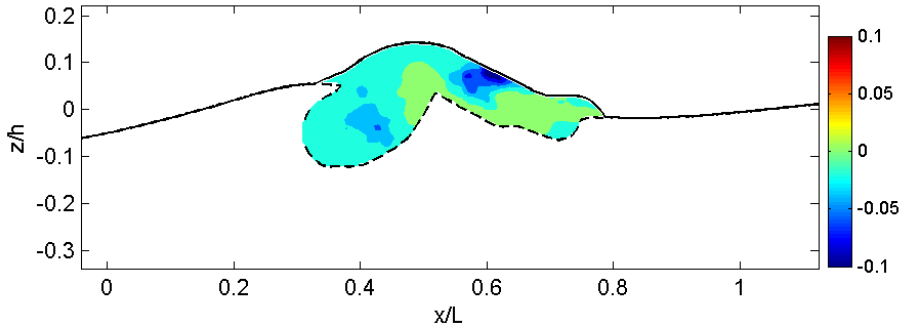

(i) $t = 0.41$ s

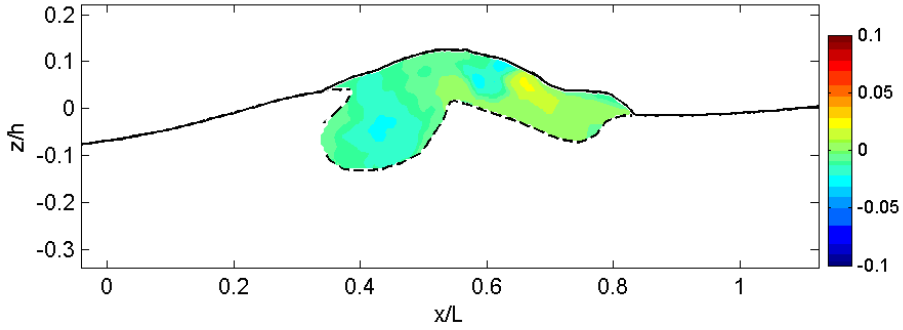

(j) $t = 0.46$ s

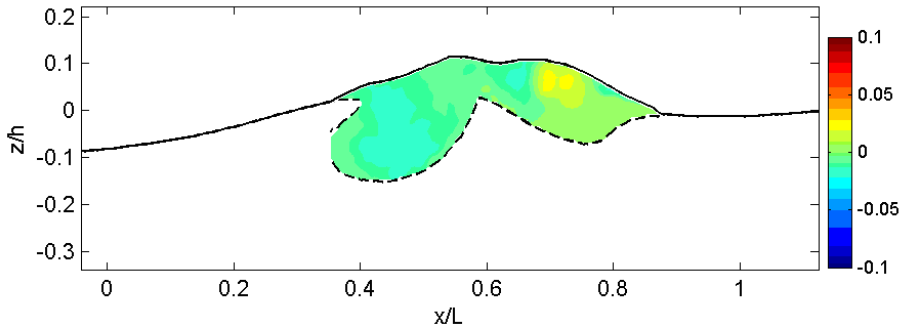

(k) $t = 0.51$ s

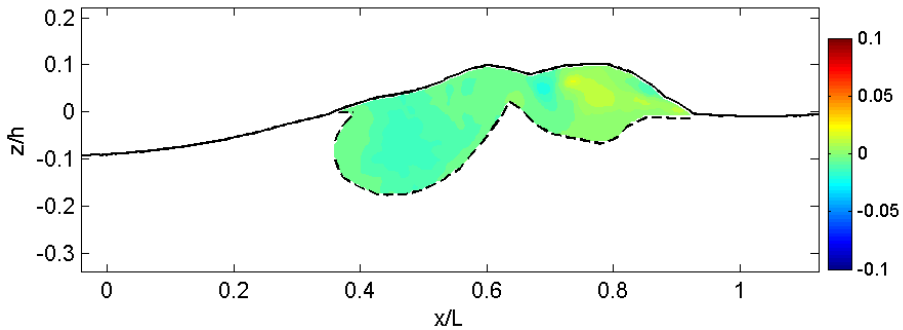

(l) $t = 0.56$ s

Fig. A.11 (Continued).

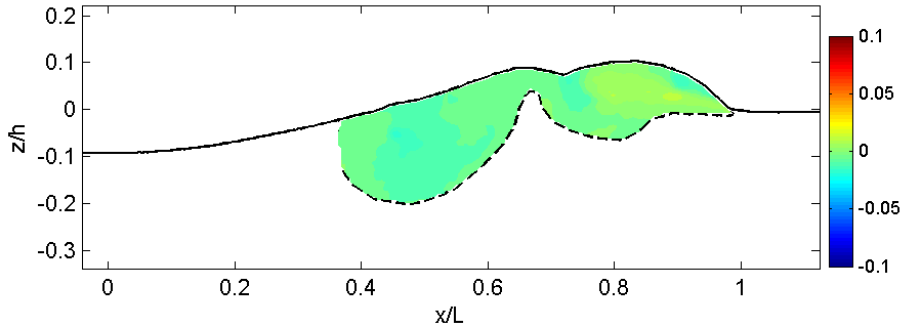

(m) $t = 0.61$ s

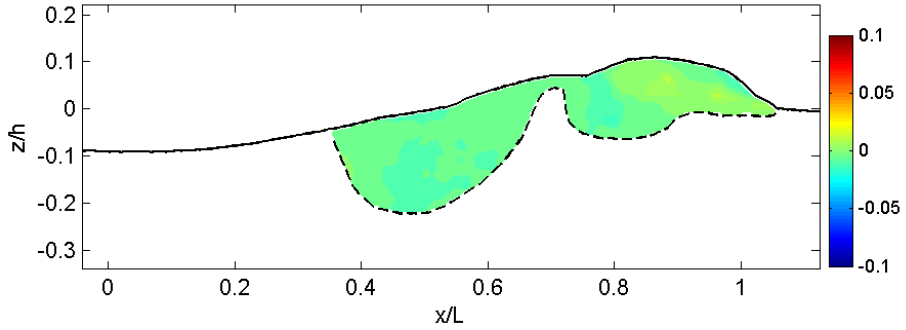

(n) $t = 0.66$ s

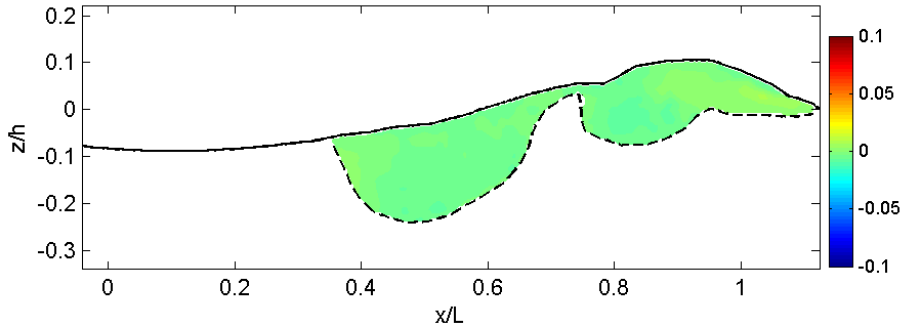

(o) $t = 0.71$ s

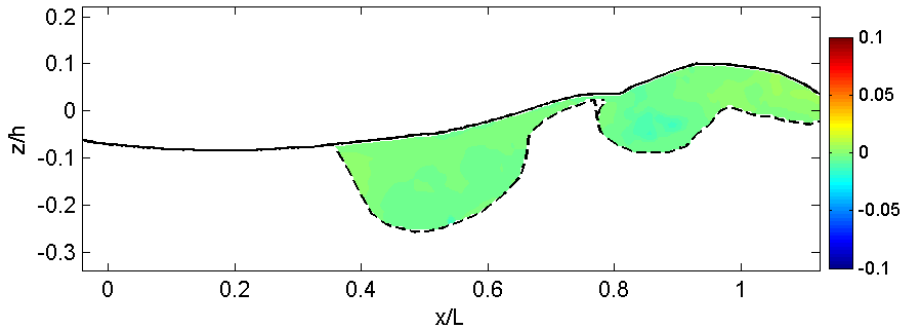

(p) $t = 0.76$ s

Fig. A.11 (Continued).

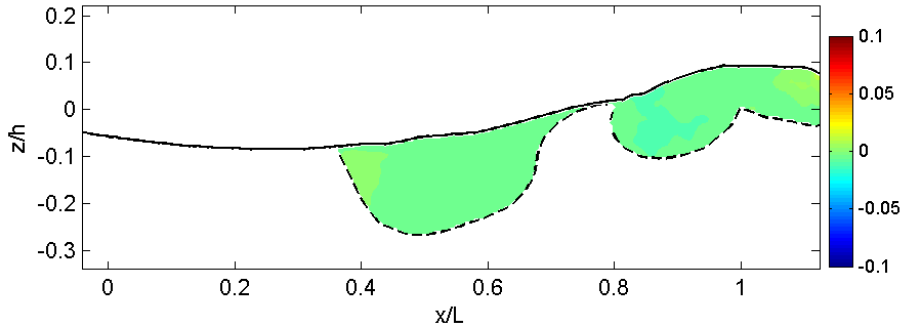

(q) $t = 0.81$ s

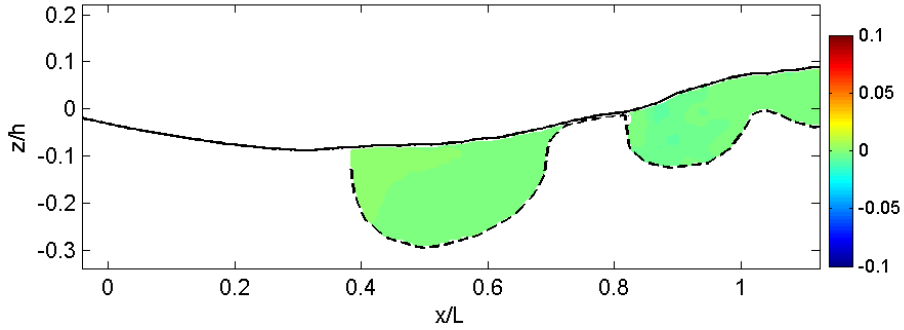

(r) $t = 0.86$ s

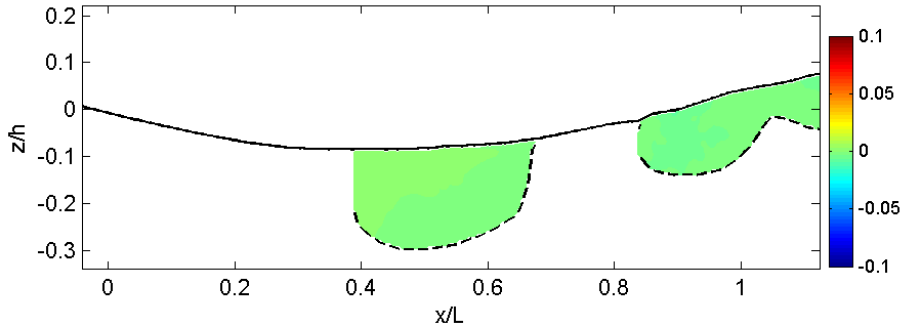

(s) $t = 0.91$ s

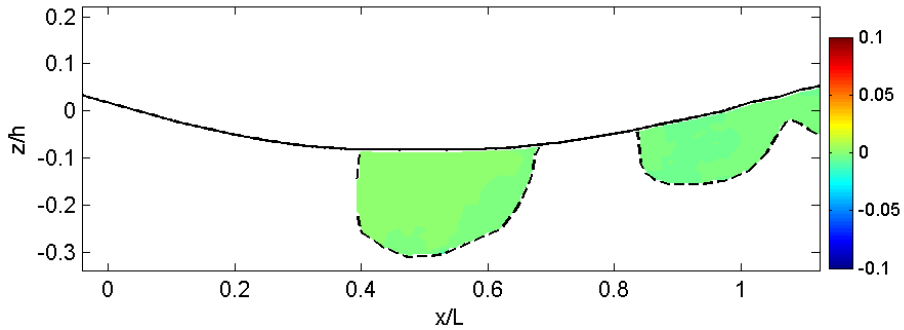

(t) $t = 0.96$ s

Fig. A.11 (Continued).

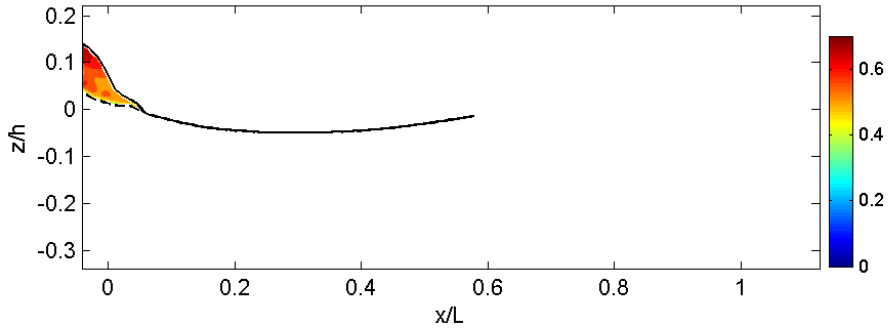

(a) t = 0.01 s

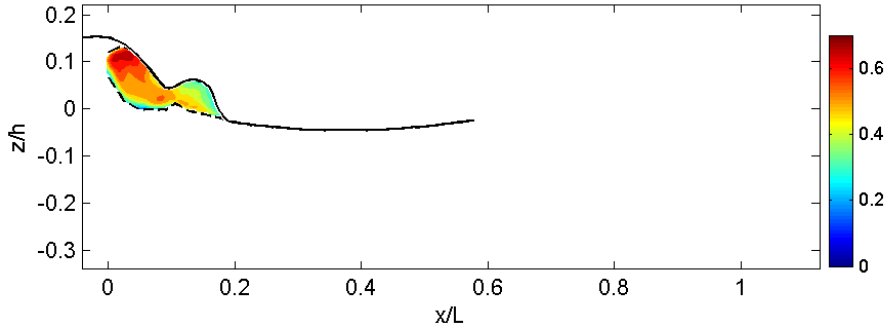

(b) t = 0.06 s

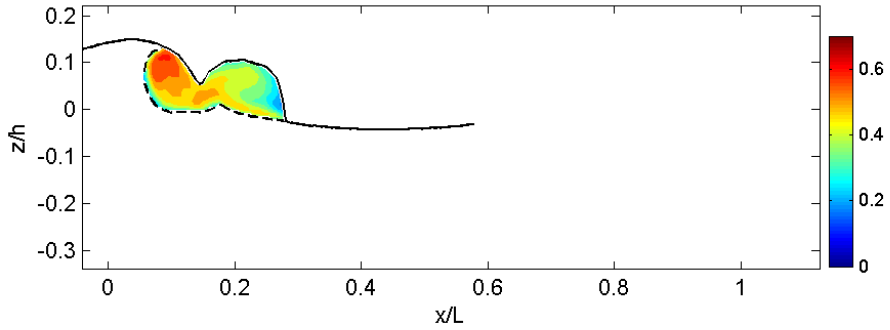

(c) t = 0.11 s

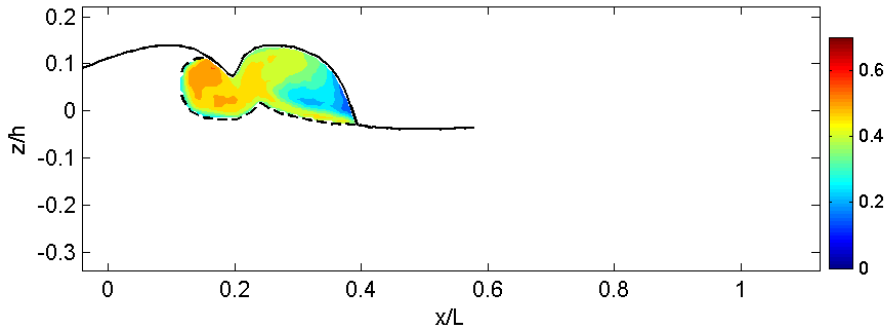

(d) t = 0.16 s

Fig. A.12 Void ratio, *α*.

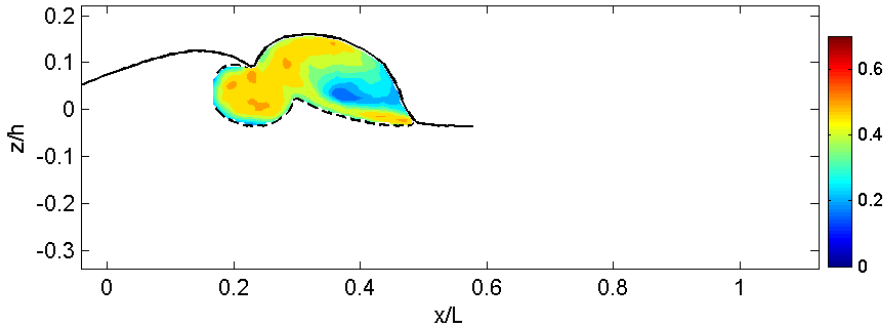

(e) t = 0.21 s

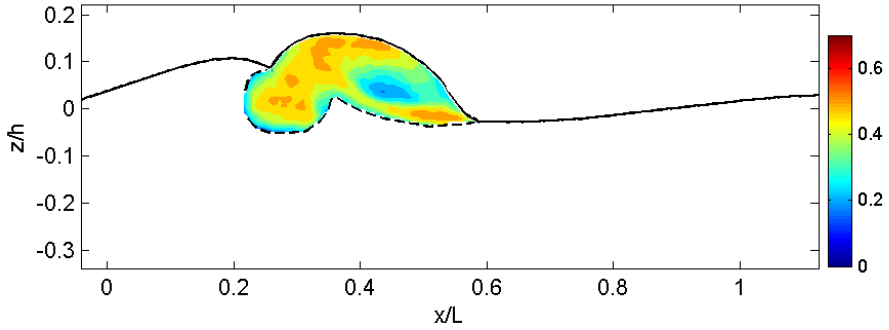

(f) t = 0.26 s

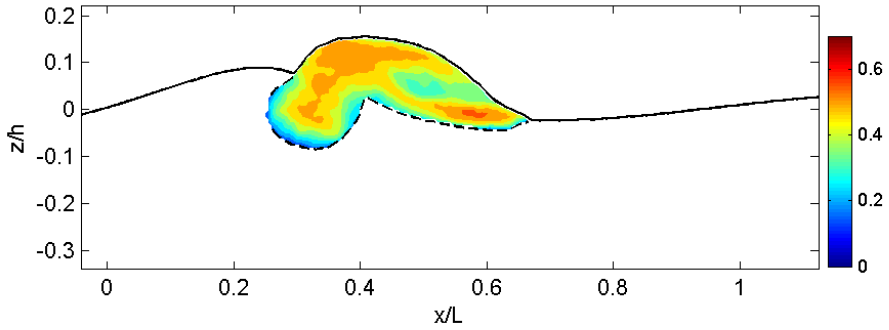

(g) t = 0.31 s

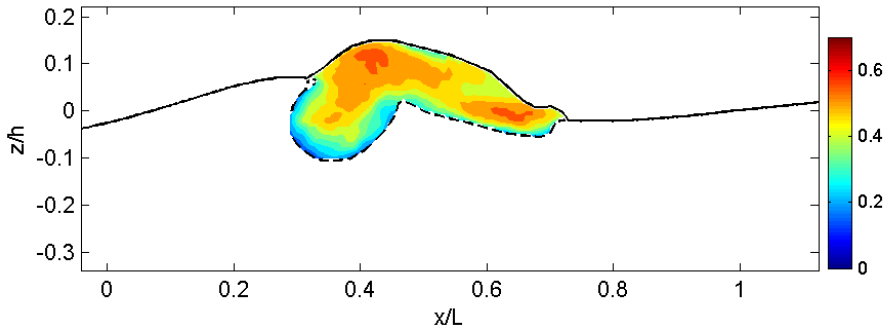

(h) t = 0.36 s

Fig. A.12 (Continued).

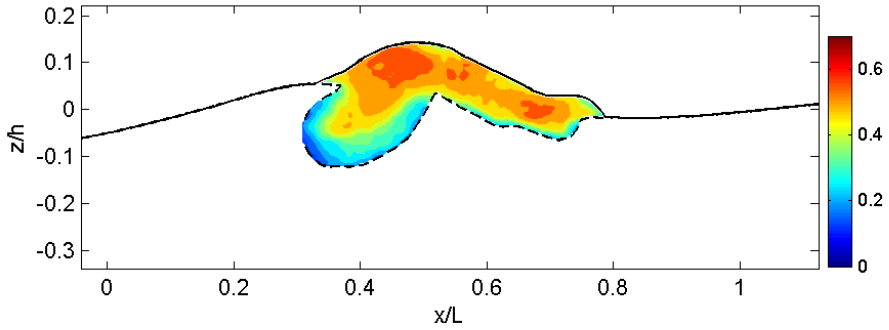

(i) $t = 0.41$ s

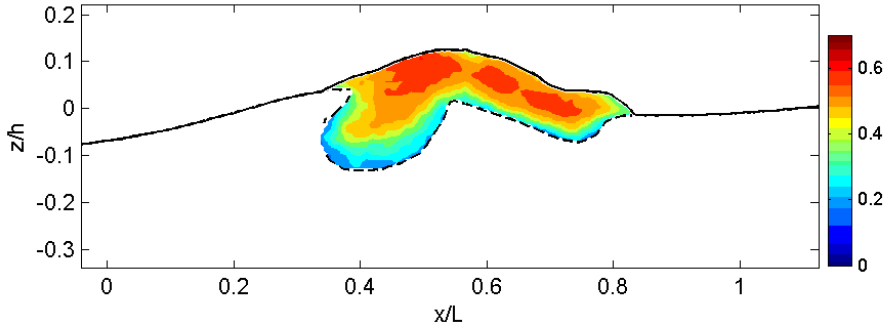

(j) $t = 0.46$ s

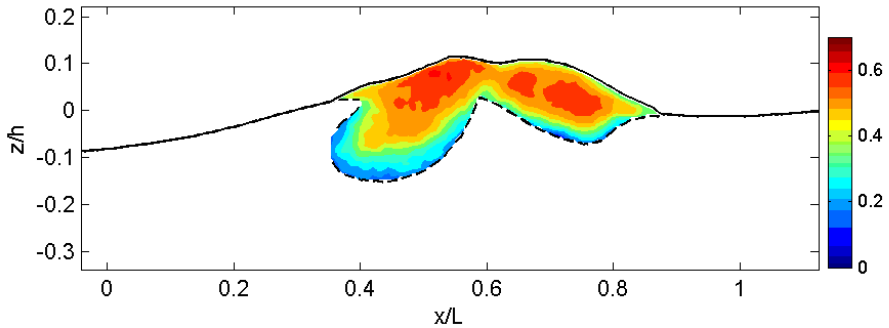

(k) $t = 0.51$ s

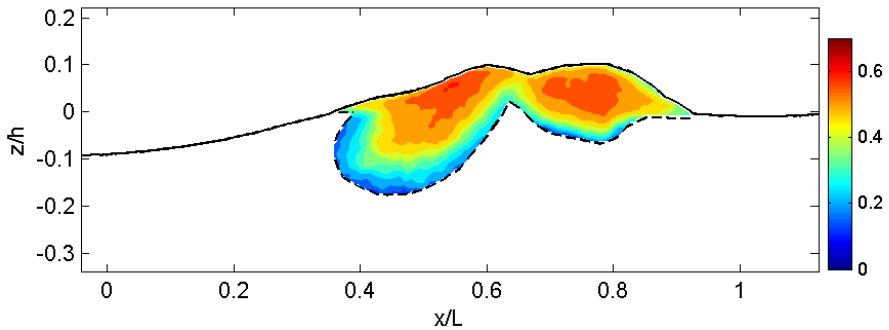

(l) $t = 0.56$ s

Fig. A.12 (Continued).

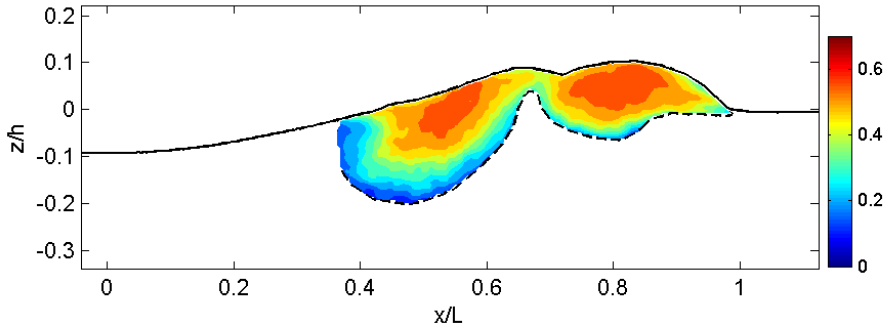

(m) $t = 0.61$ s

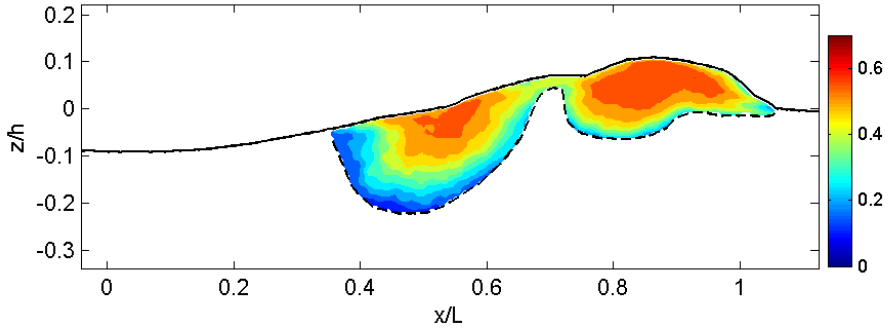

(n) $t = 0.66$ s

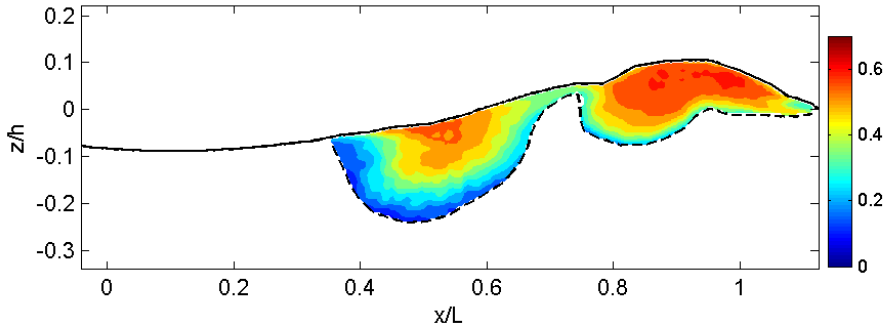

(o) $t = 0.71$ s

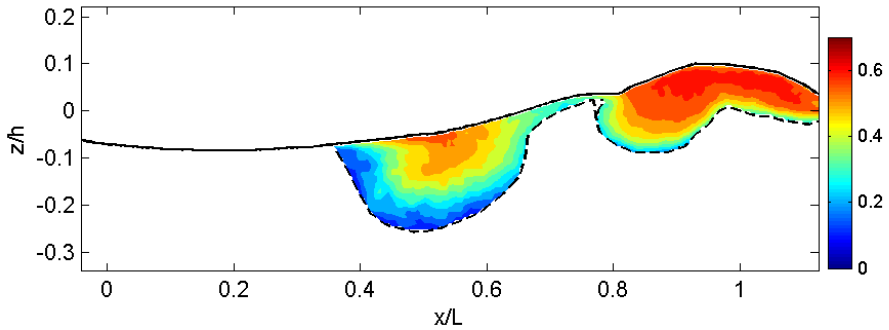

(p) $t = 0.76$ s

Fig. A.12 (Continued).

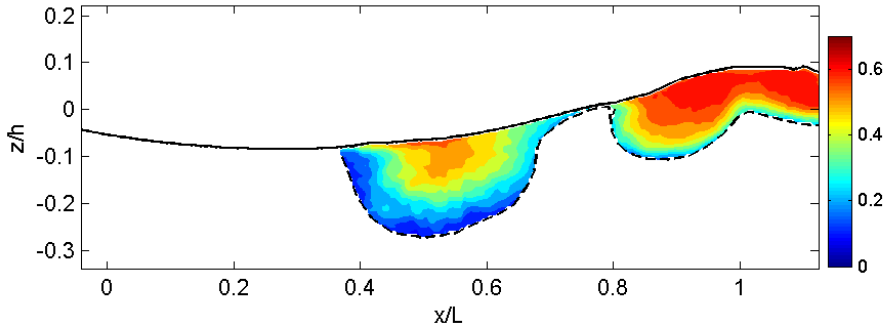

(q) t = 0.81 s

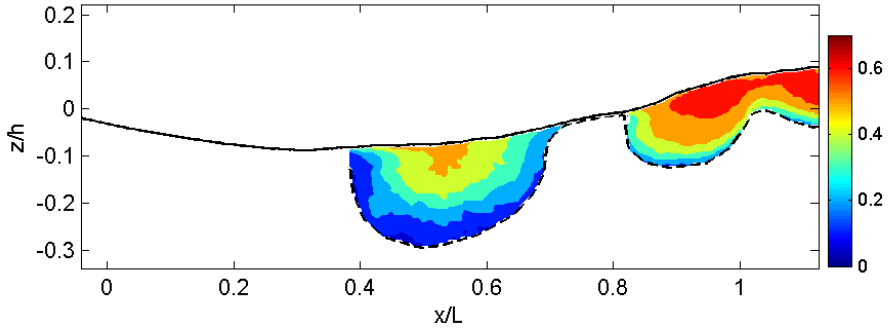

(r) t = 0.86 s

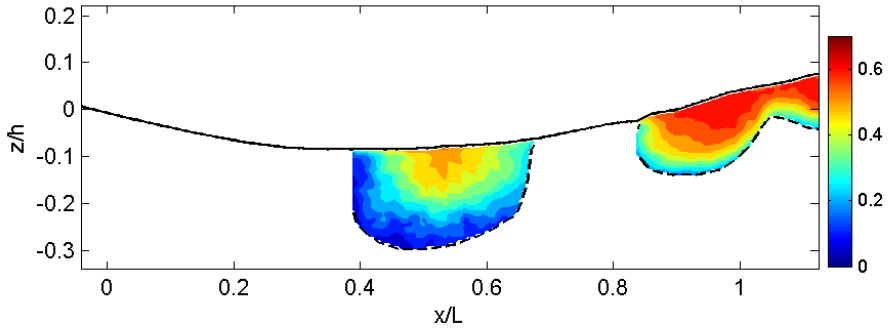

(s) t = 0.91 s

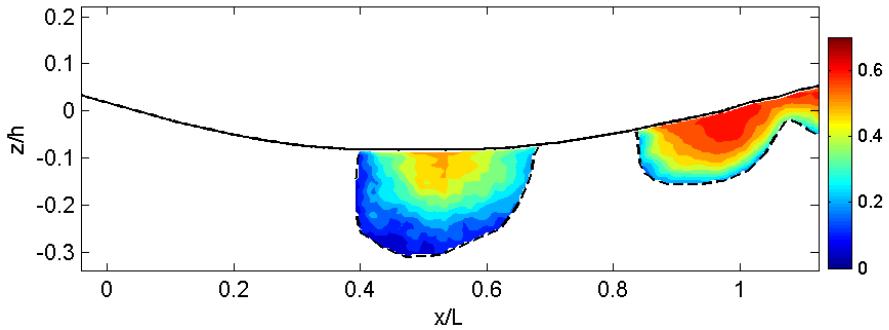

(t) t = 0.96 s

Fig. A.12 (Continued).

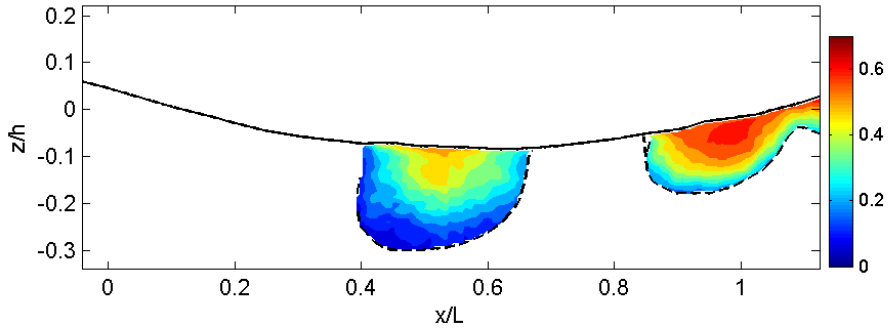

(u) t = 1.01 s

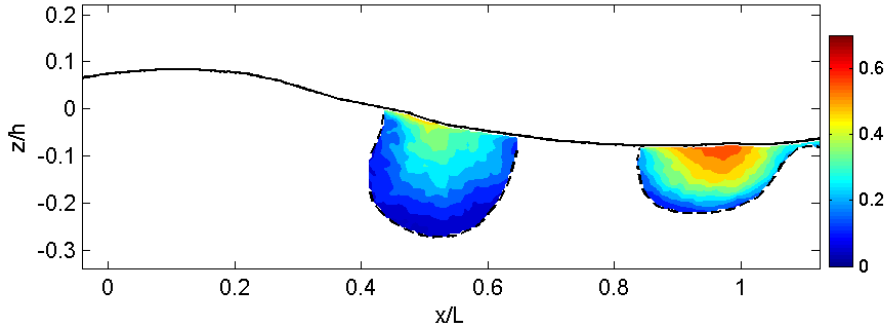

(v) t = 1.21 s

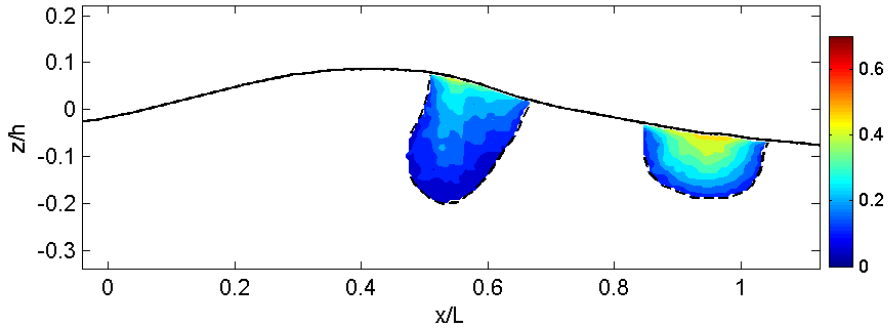

(w) t = 1.41 s

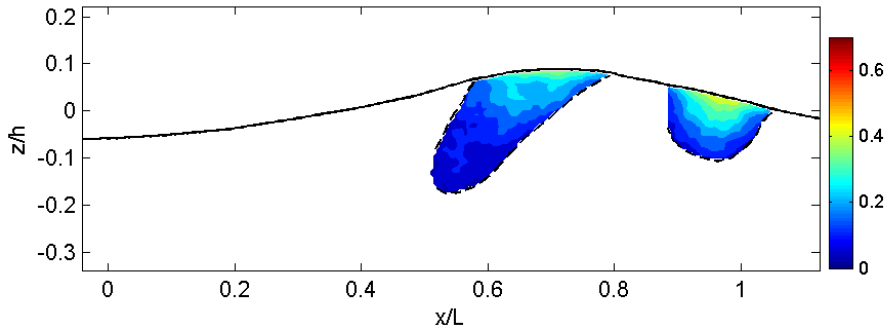

(x) t = 1.61 s

Fig. A.12 (Continued).

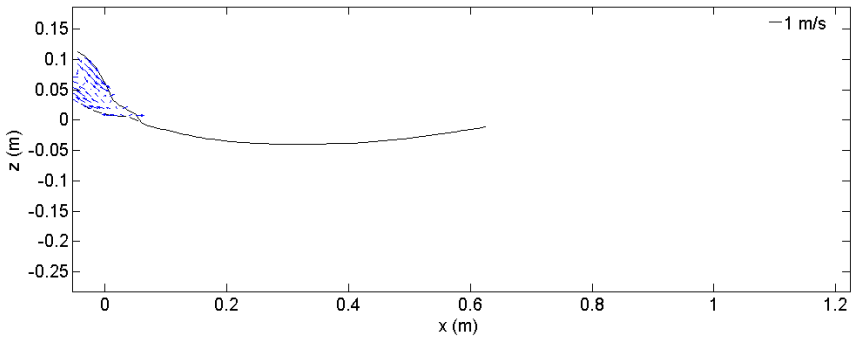

(a) $t = 0.01$ s

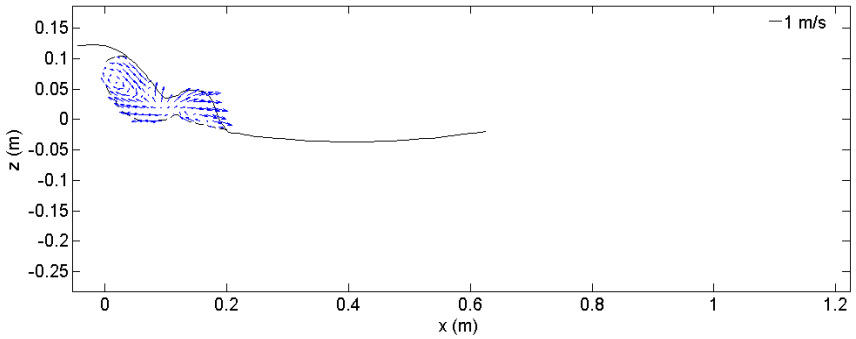

(b) $t = 0.06$ s

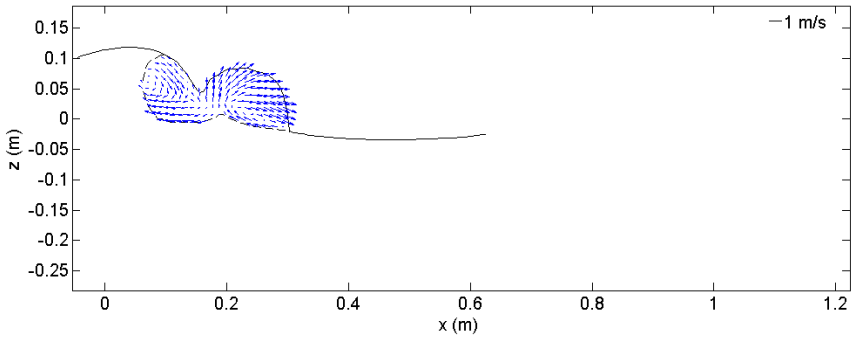

(c) $t = 0.11$ s

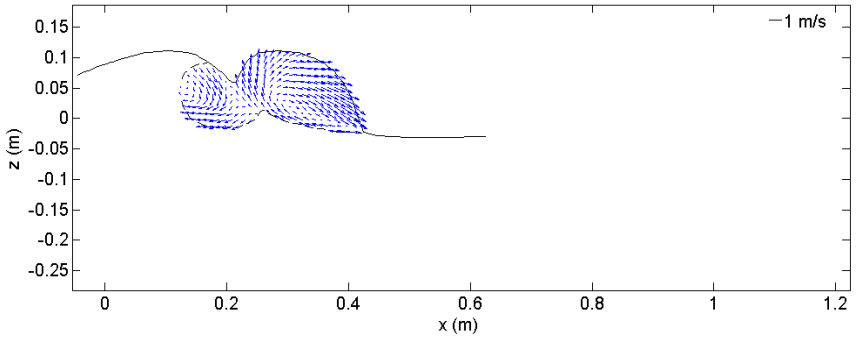

(d) $t = 0.16$ s

Fig. A.13 Relative Velocity, $\sqrt{(U-C)^2+W^2}$.

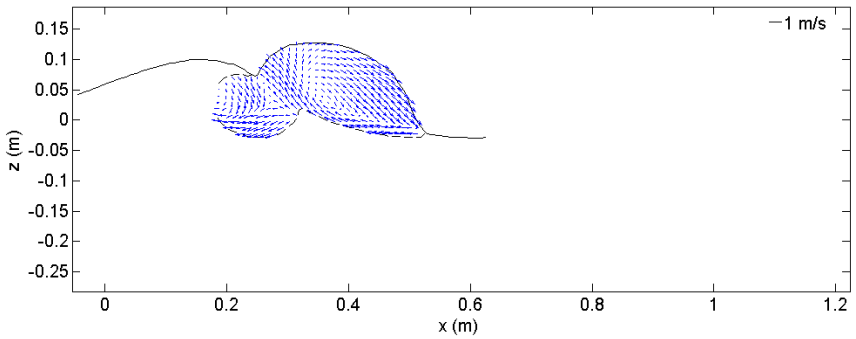

(e) $t = 0.21$ s

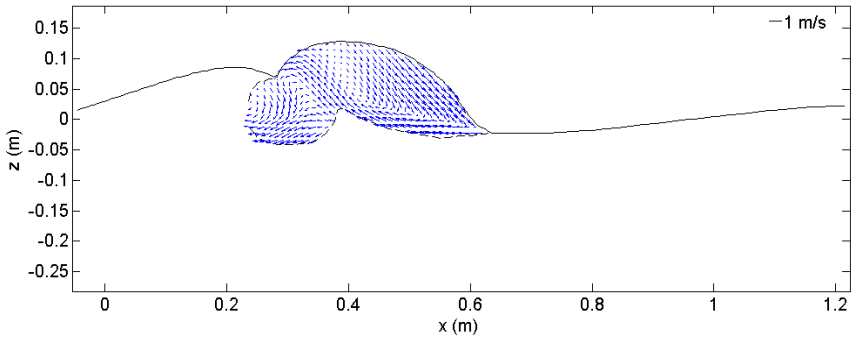

(f) $t = 0.26$ s

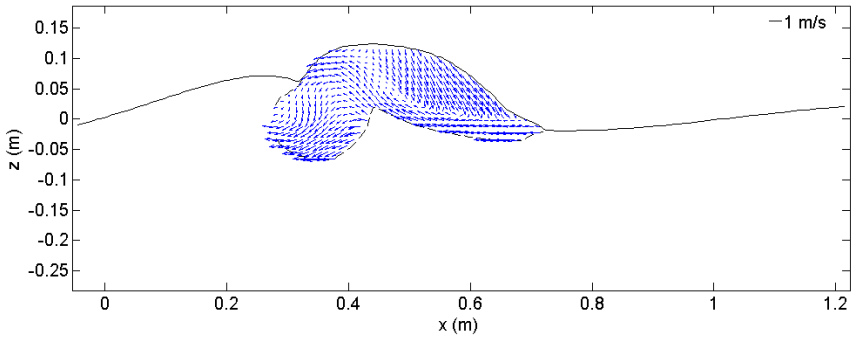

(g) $t = 0.31$ s

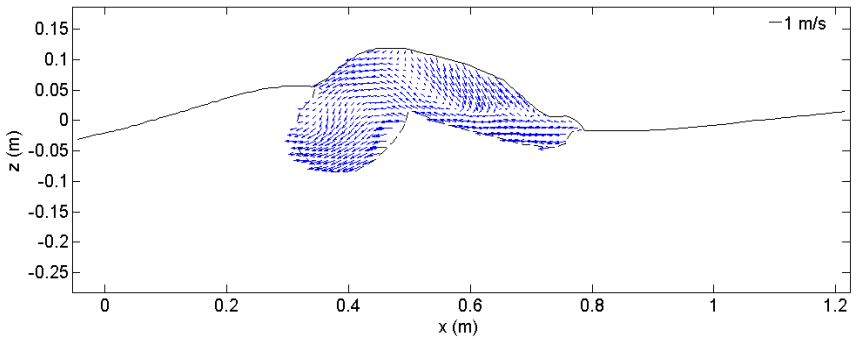

(h) $t = 0.36$ s

Fig. A.13 (Continued).

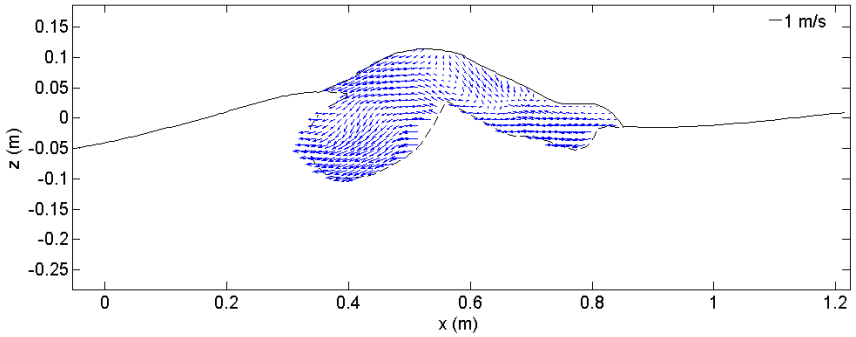

(i) $t = 0.41$ s

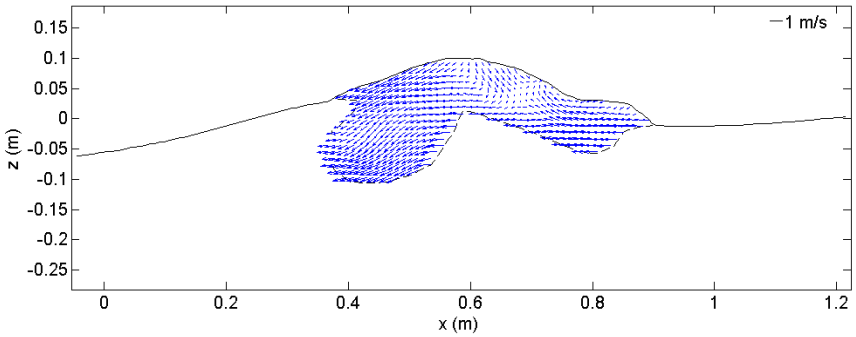

(j) $t = 0.46$ s

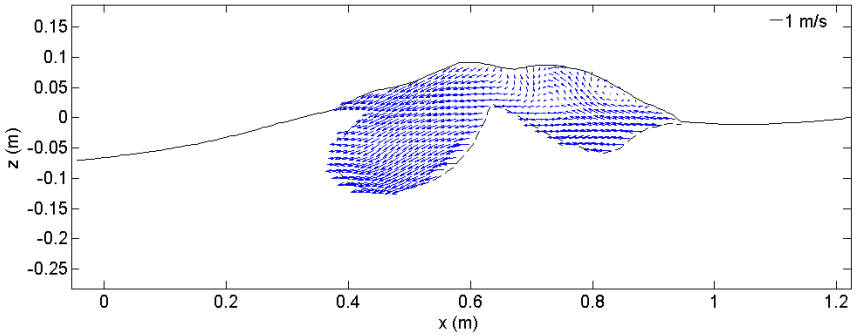

(k) $t = 0.51$ s

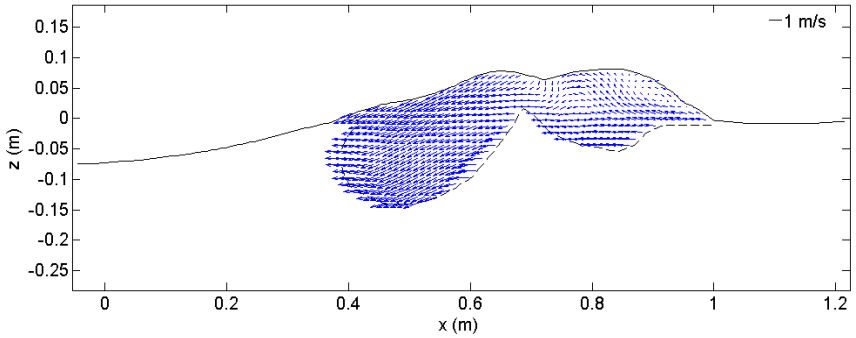

(l) $t = 0.56$ s

Fig. A.13 (Continued).

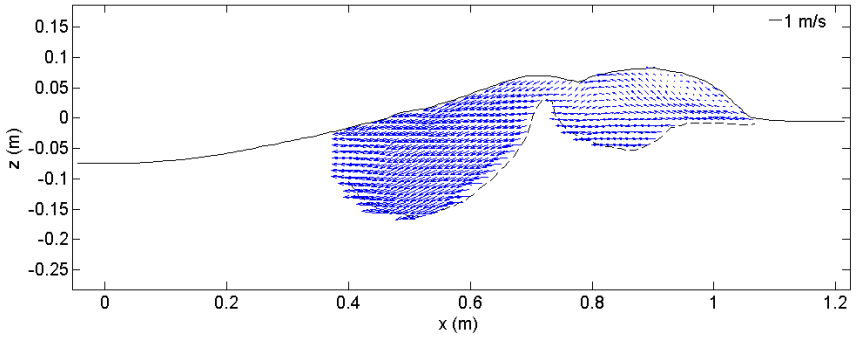

(m) $t = 0.61$ s

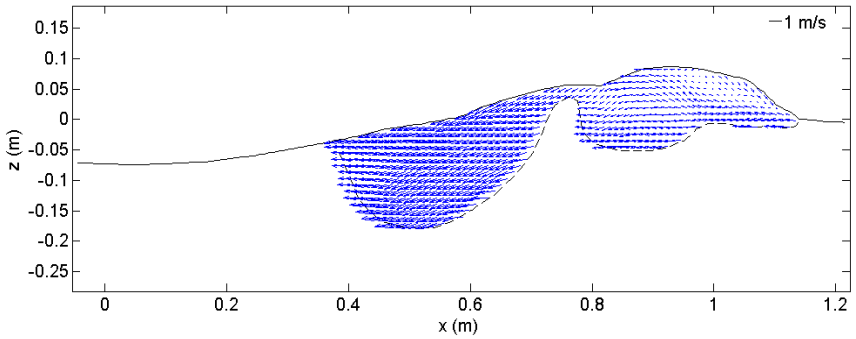

(n) $t = 0.66$ s

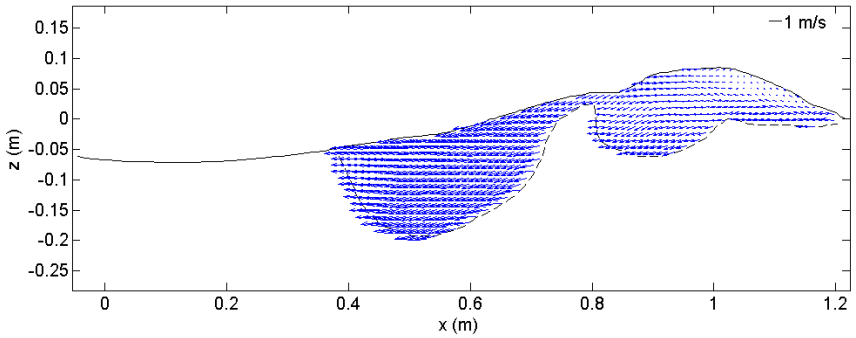

(o) $t = 0.71$ s

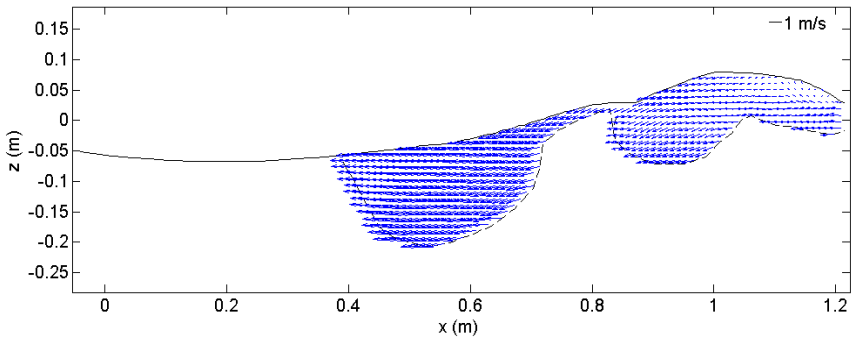

(p) $t = 0.76$ s

Fig. A.13 (Continued).

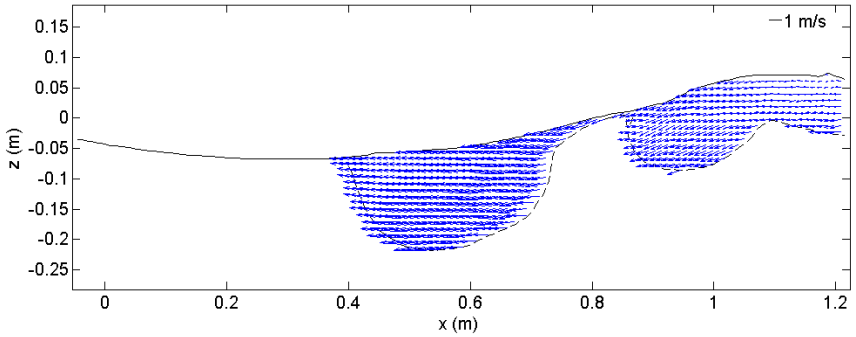

(q) $t = 0.81$ s

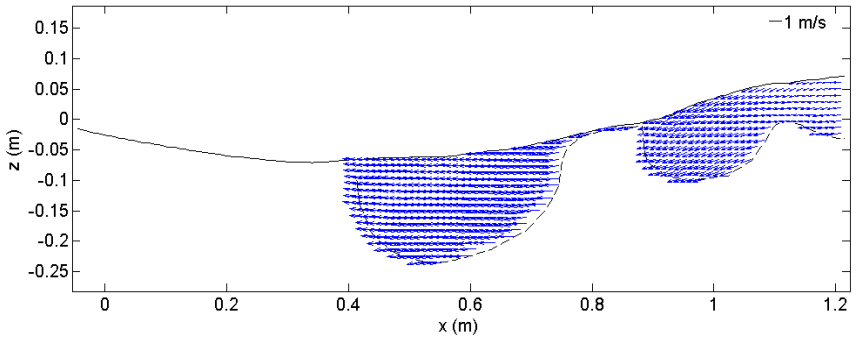

(r) $t = 0.86$ s

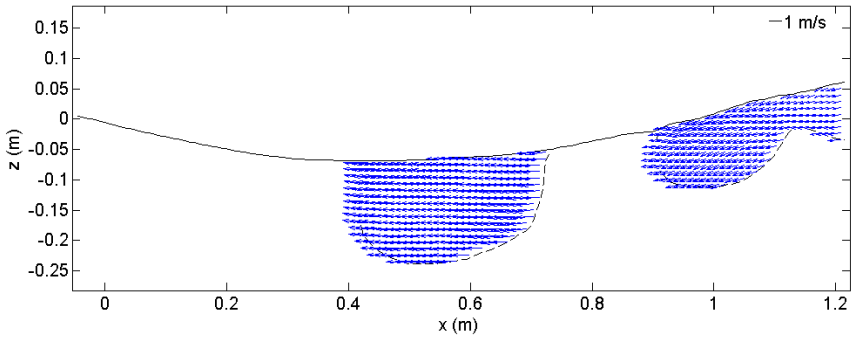

(s) $t = 0.91$ s

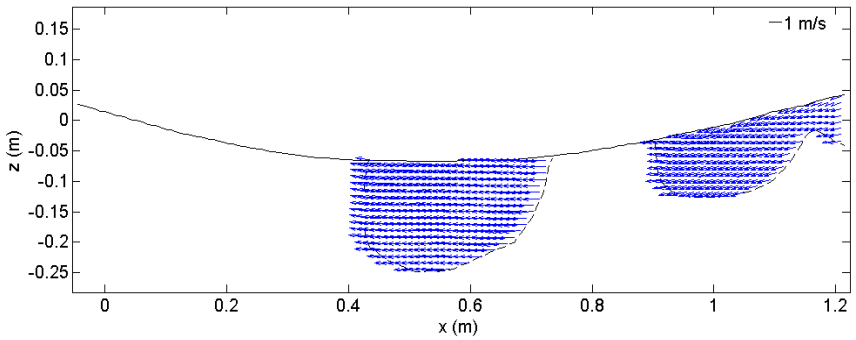

(t) $t = 0.96$ s

Fig. A.13 (Continued).

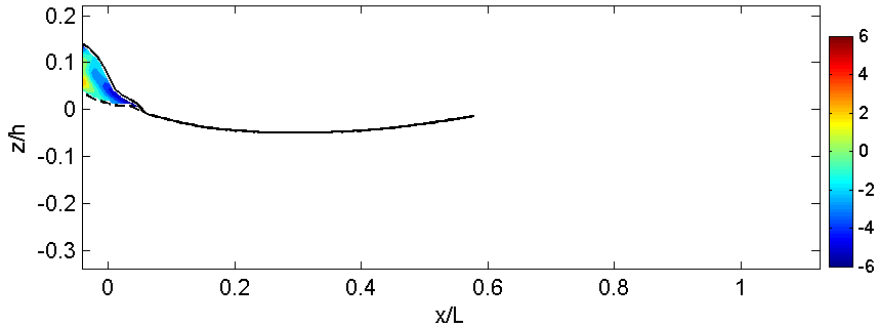

(a) t = 0.01 s

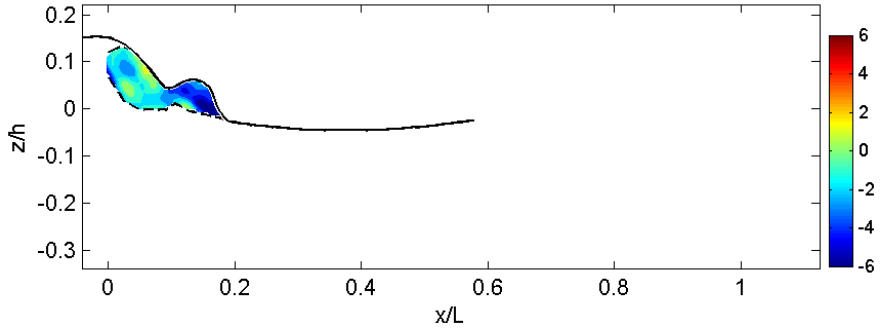

(b) t = 0.06 s

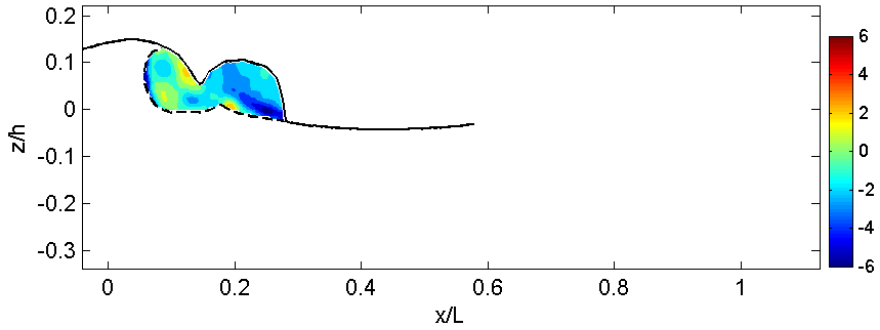

(c) t = 0.11 s

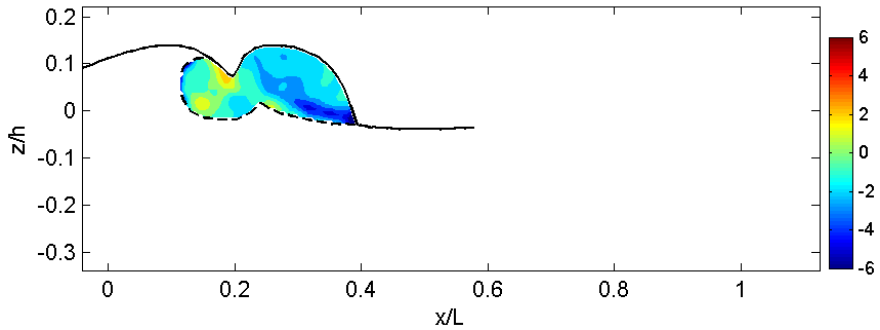

(d) t = 0.16 s

Fig. A.14 Normalized horizontal local acceleration, $\frac{\partial U}{\partial t}\Big/ g$.

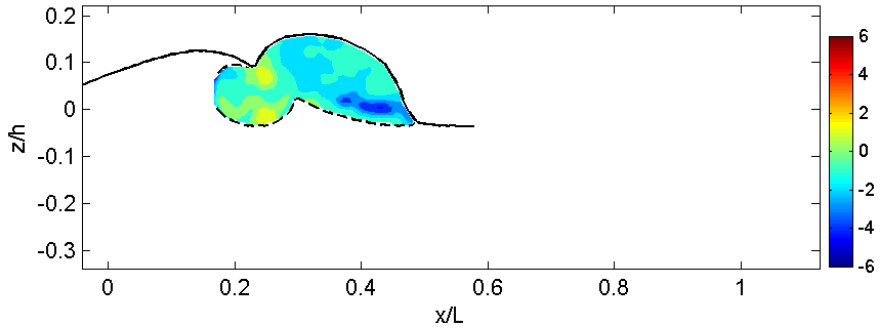

(e) t = 0.21 s

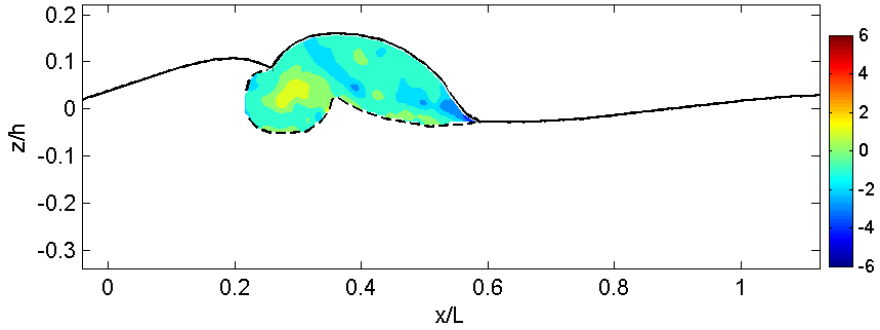

(f) t = 0.26 s

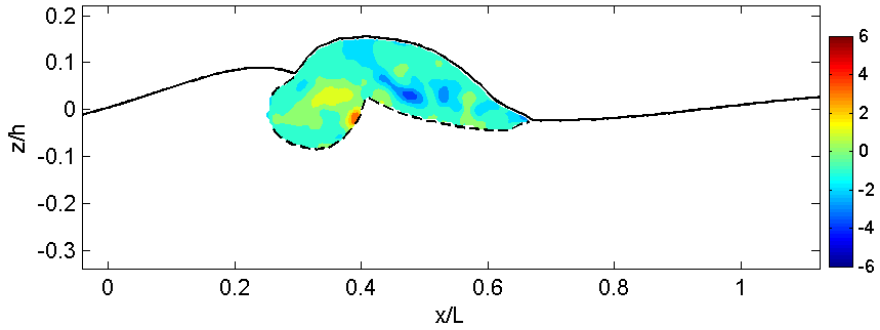

(g) t = 0.31 s

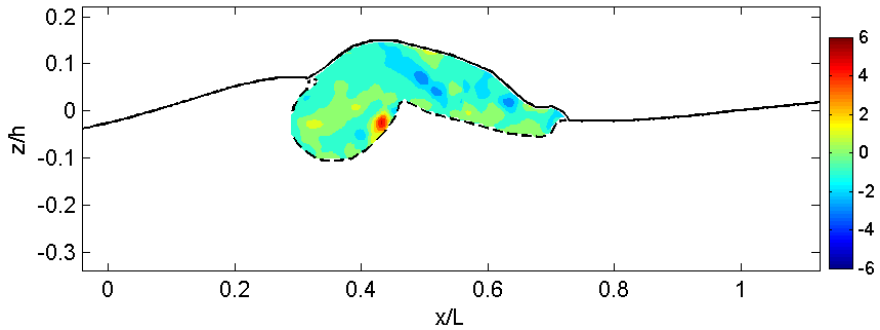

(h) t = 0.36 s

Fig. A.14 (Continued).

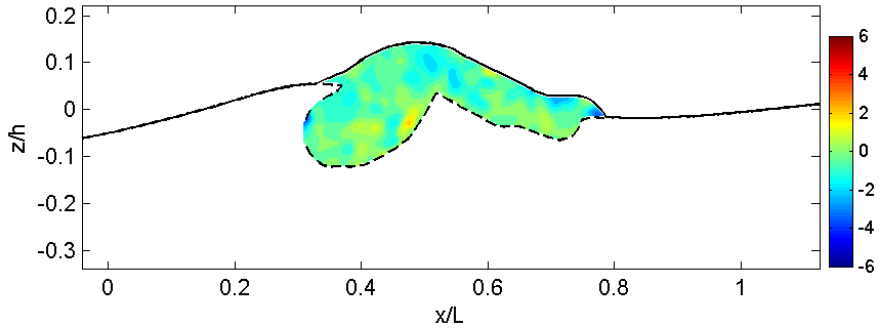

(i) $t = 0.41$ s

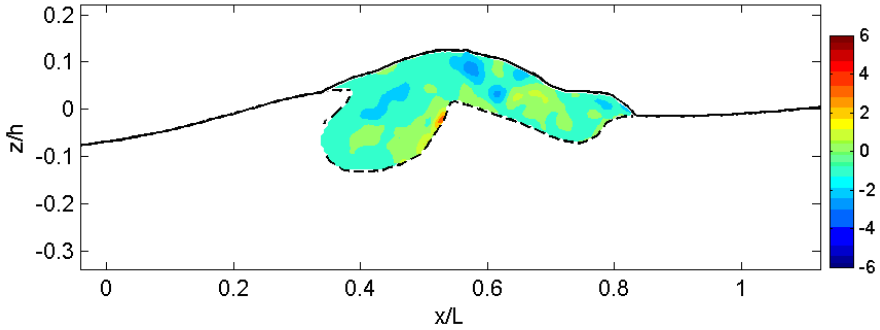

(j) $t = 0.46$ s

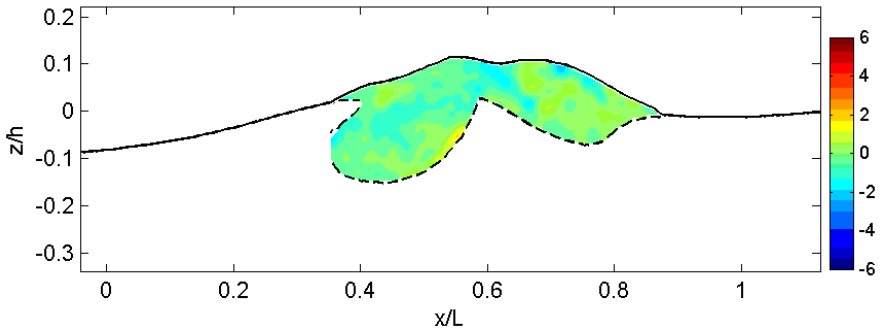

(k) $t = 0.51$ s

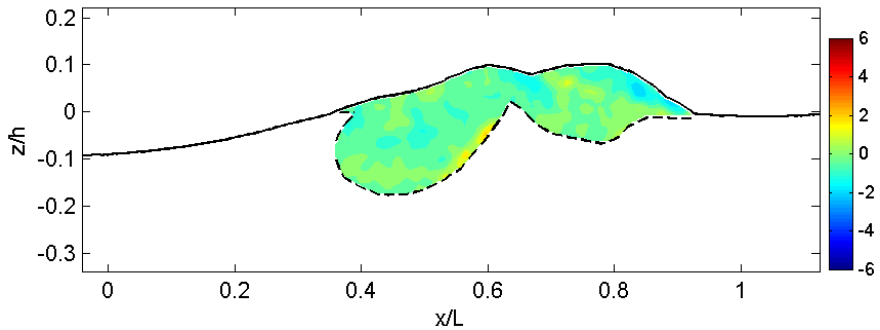

(l) $t = 0.56$ s

Fig. A.14 (Continued).

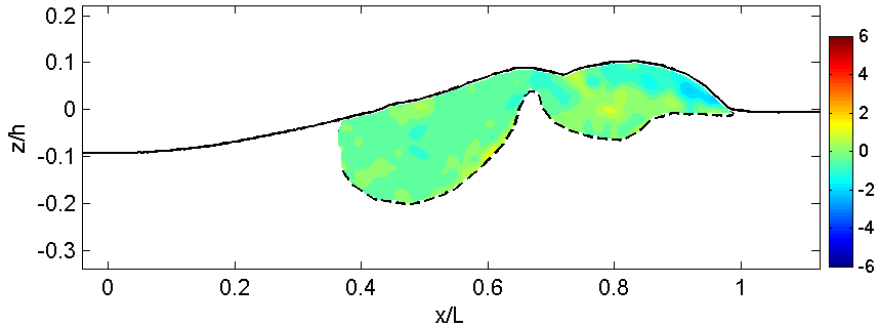

(m) $t = 0.61$ s

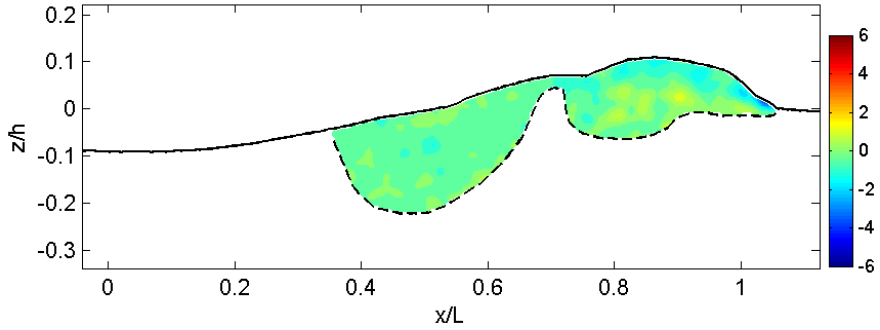

(n) $t = 0.66$ s

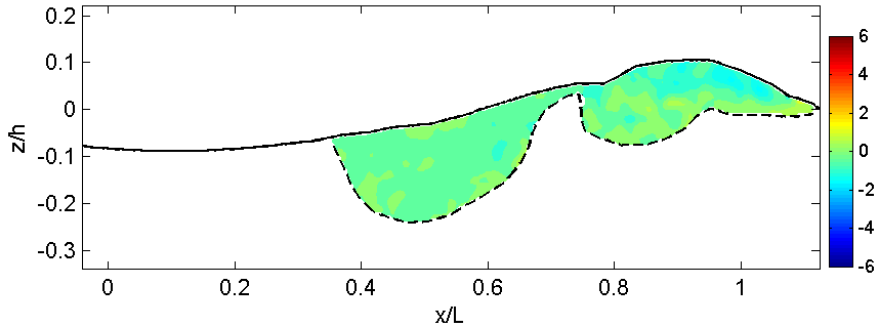

(o) $t = 0.71$ s

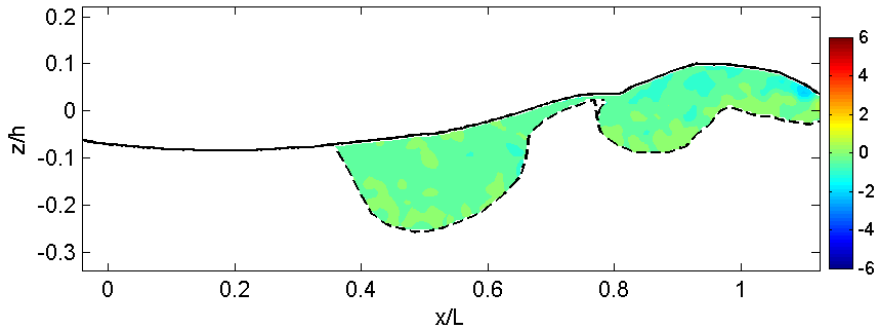

(p) $t = 0.76$ s

Fig. A.14 (Continued).

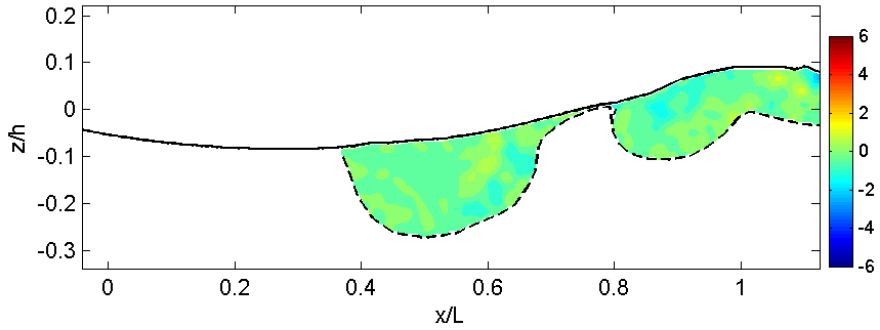

(q) $t = 0.81$ s

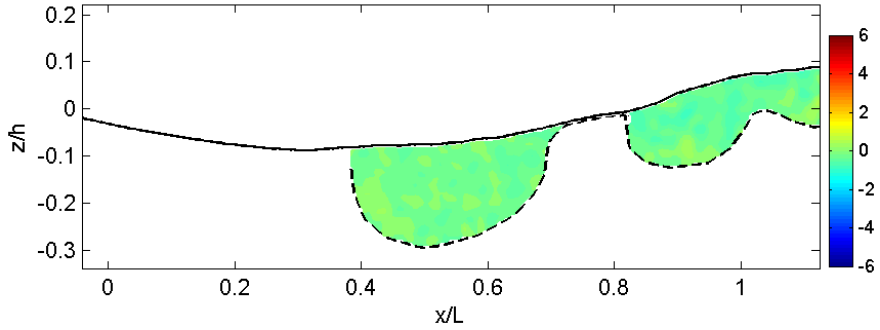

(r) $t = 0.86$ s

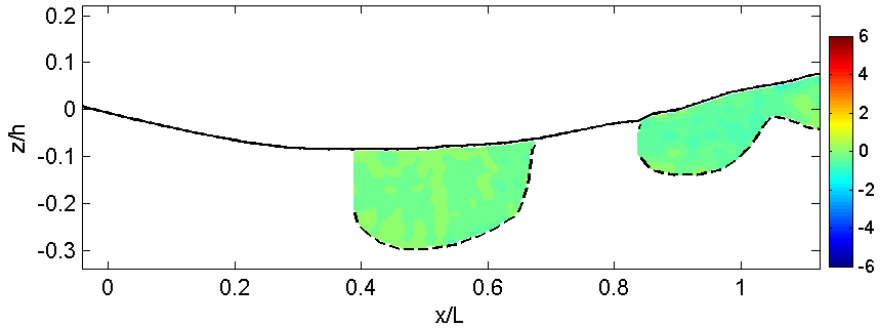

(s) $t = 0.91$ s

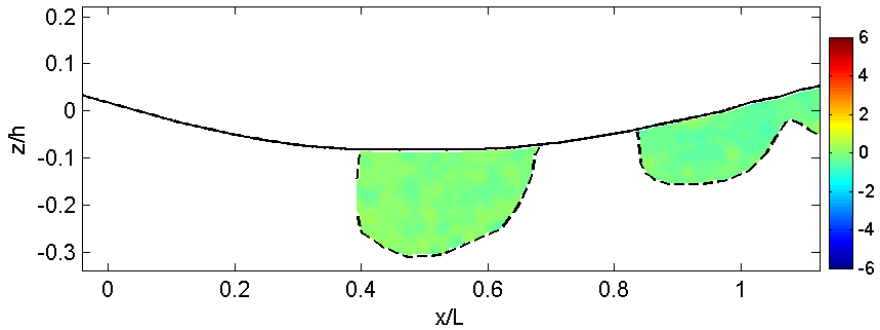

(t) $t = 0.96$ s

Fig. A.14 (Continued).

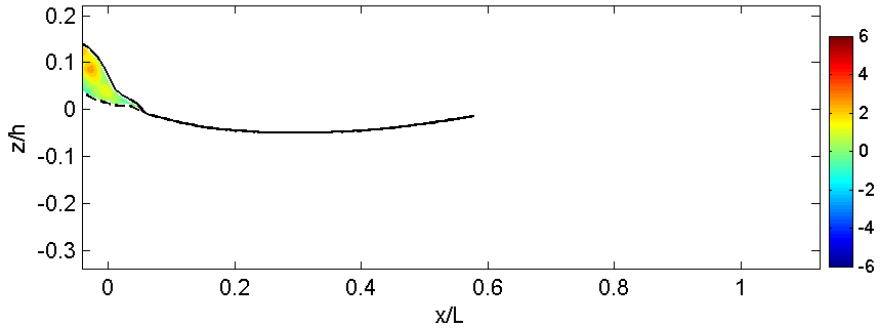

(a) t = 0.01 s

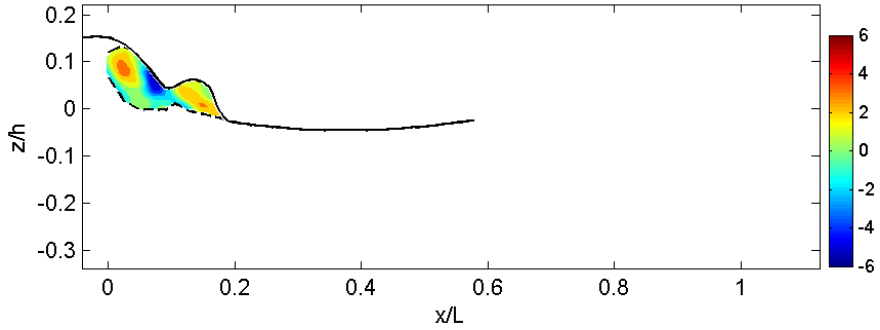

(b) t = 0.06 s

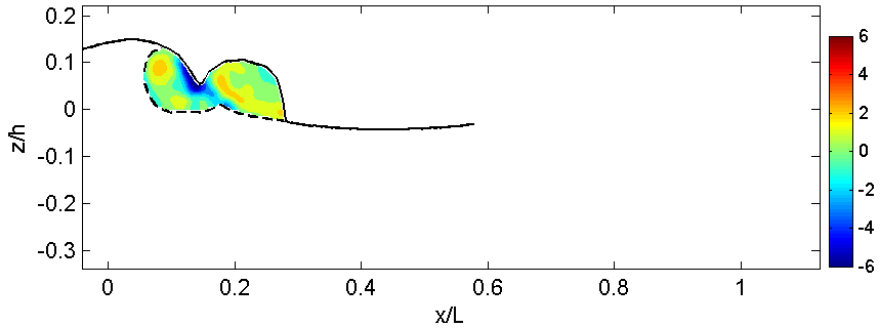

(c) t = 0.11 s

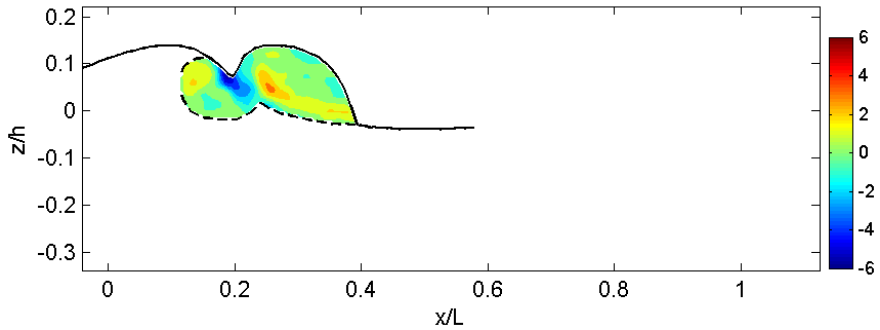

(d) t = 0.16 s

Fig. A.15 Normalized vertical local acceleration, $\frac{\partial W}{\partial t}\Big/ g$.

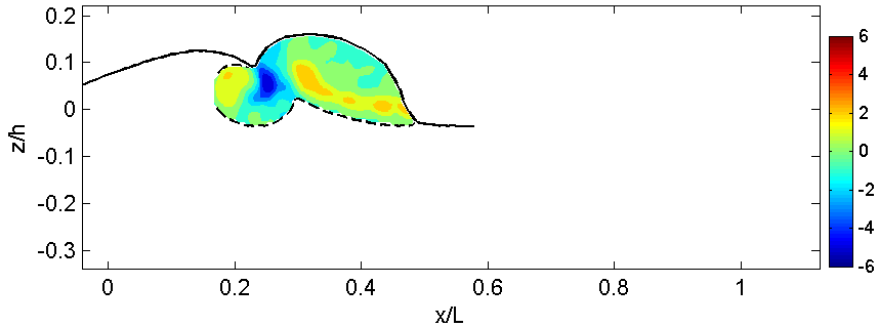

(e) t = 0.21 s

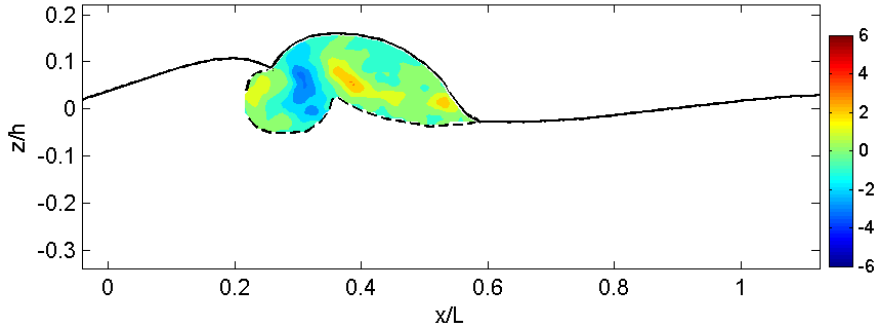

(f) t = 0.26 s

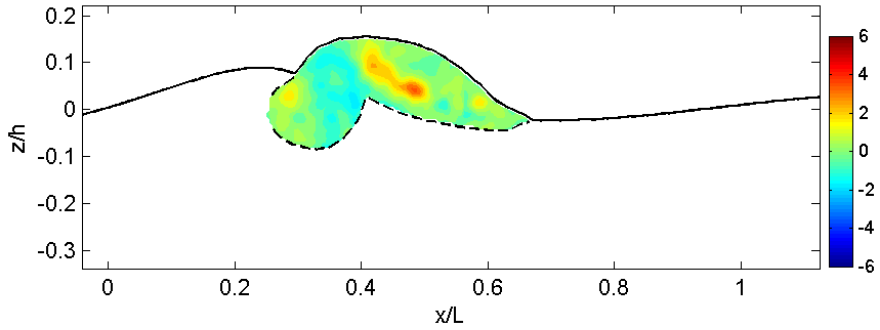

(g) t = 0.31 s

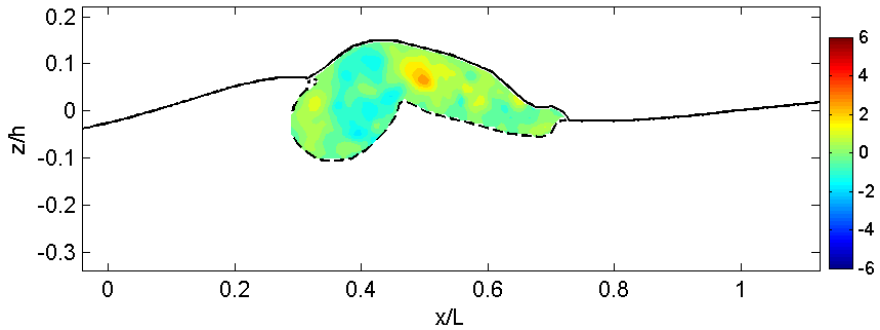

(h) t = 0.36 s

Fig. A.15 (Continued).

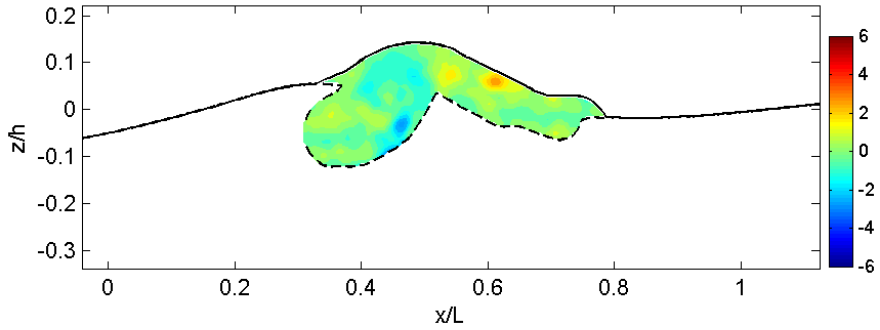

(i) $t = 0.41$ s

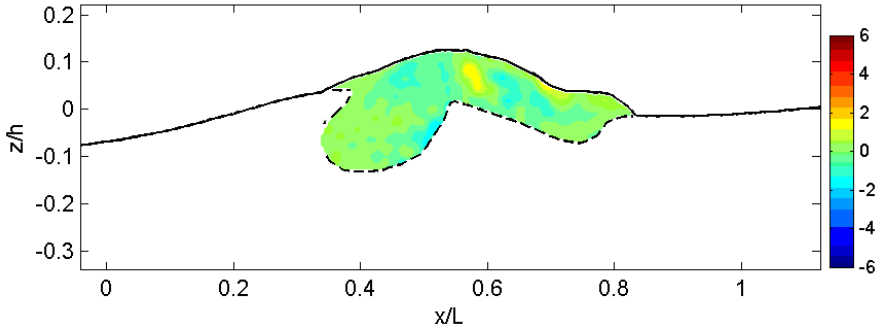

(j) $t = 0.46$ s

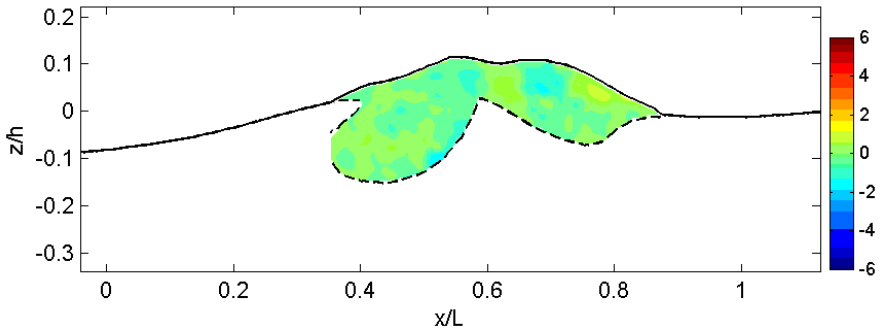

(k) $t = 0.51$ s

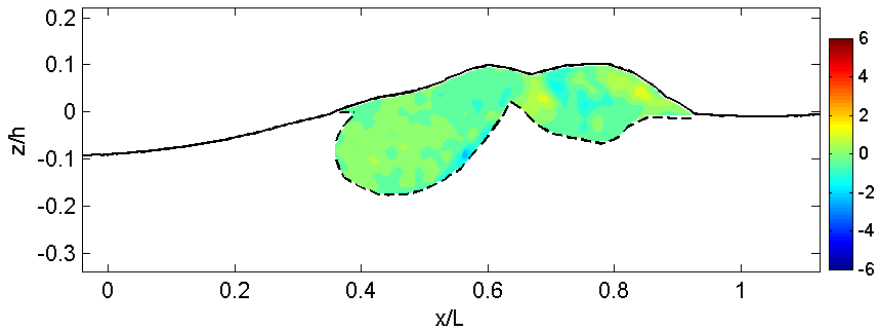

(l) $t = 0.56$ s

Fig. A.15 (Continued).

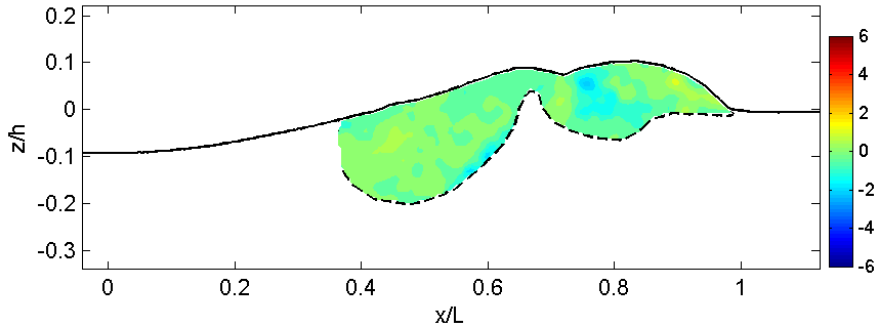

(m) $t = 0.61$ s

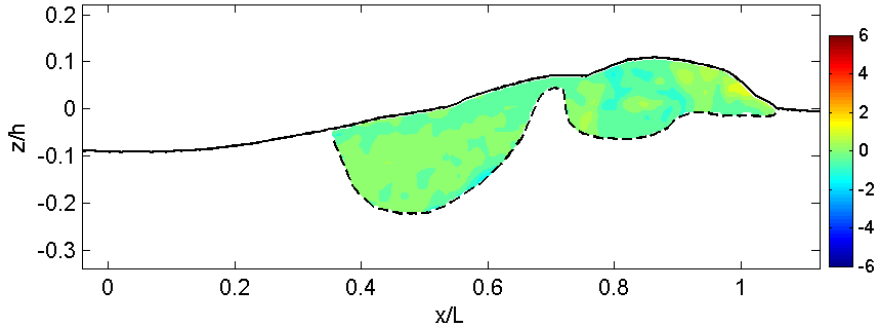

(n) $t = 0.66$ s

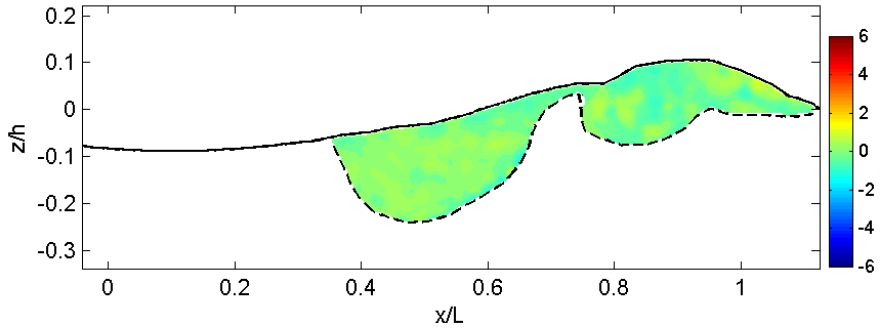

(o) $t = 0.71$ s

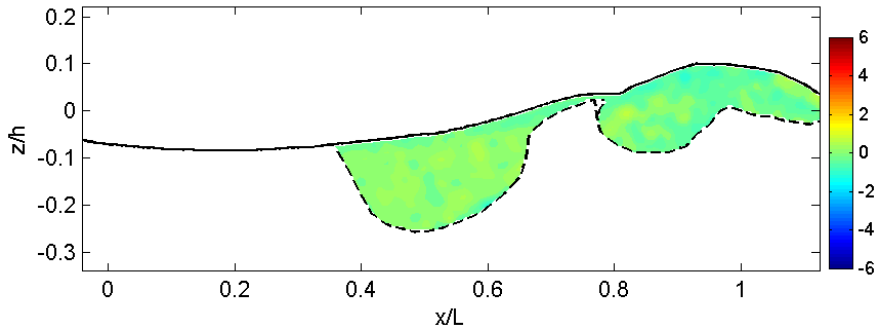

(p) $t = 0.76$ s

Fig. A.15 (Continued).

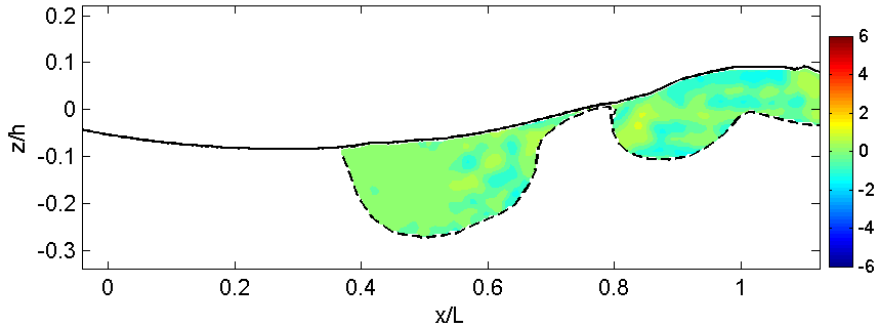

(q) $t = 0.81$ s

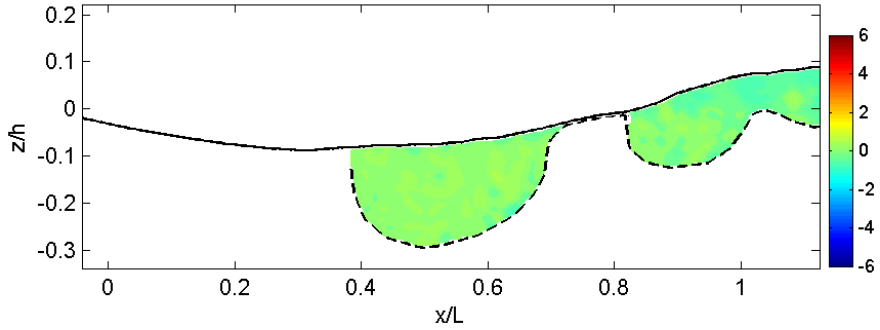

(r) $t = 0.86$ s

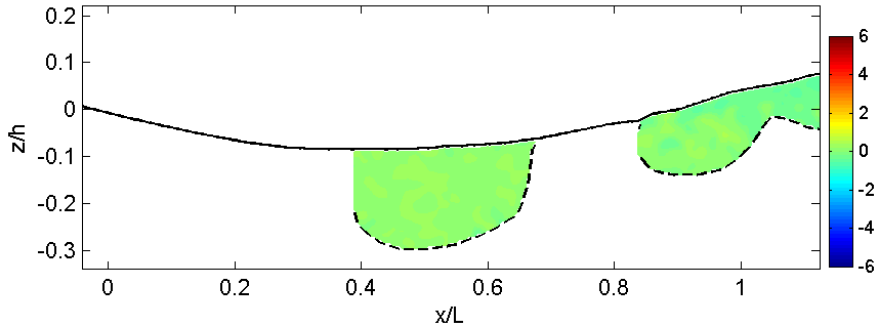

(s) $t = 0.91$ s

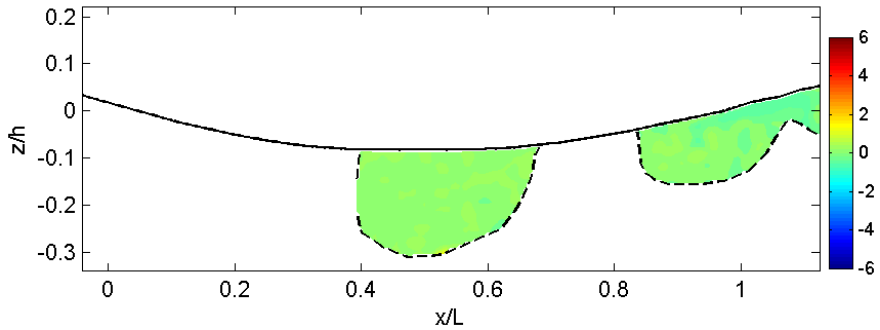

(t) $t = 0.96$ s

Fig. A.15 (Continued).

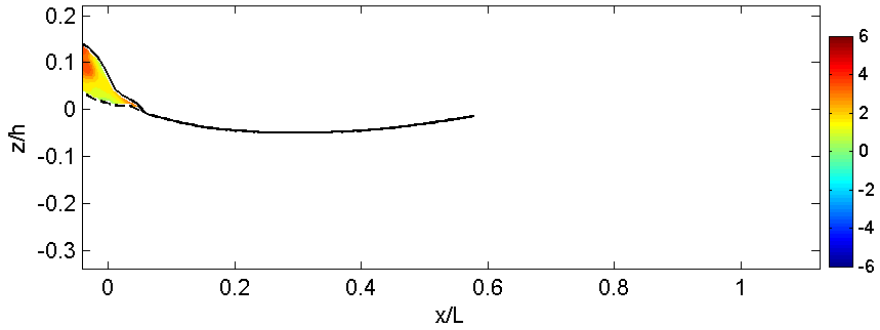

(a) t = 0.01 s

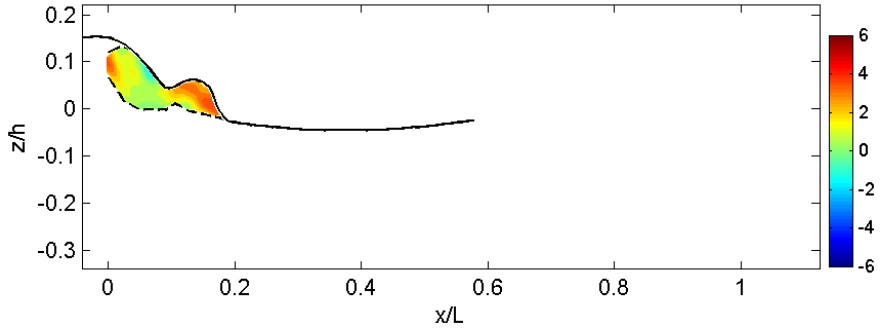

(b) t = 0.06 s

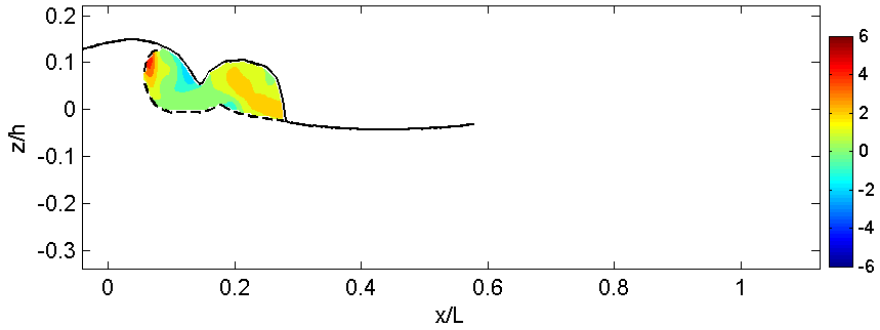

(c) t = 0.11 s

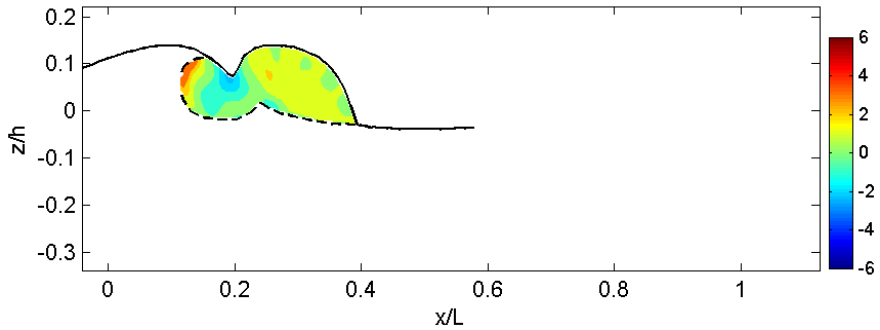

(d) t = 0.16 s

Fig. A.16 Normalized horizontal convective acceleration, $\left(U\frac{\partial U}{\partial x}+W\frac{\partial U}{\partial z}\right)\Big/g$ **.**

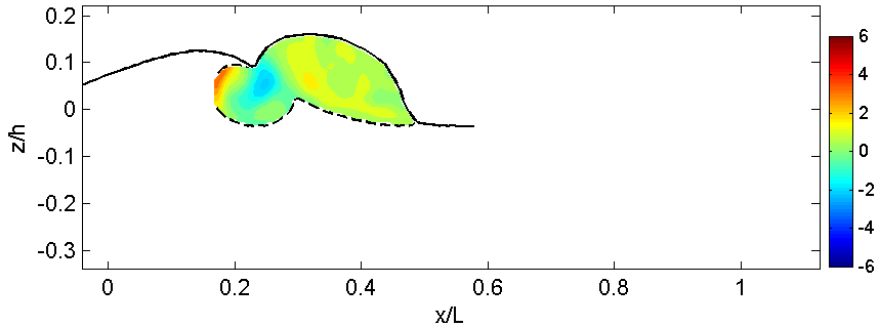

(e) t = 0.21 s

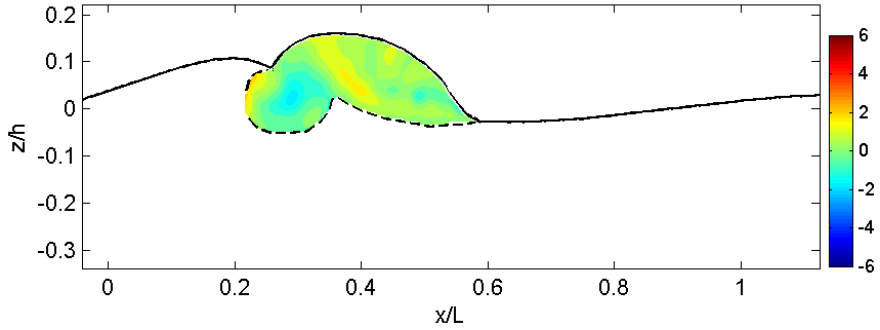

(f) t = 0.26 s

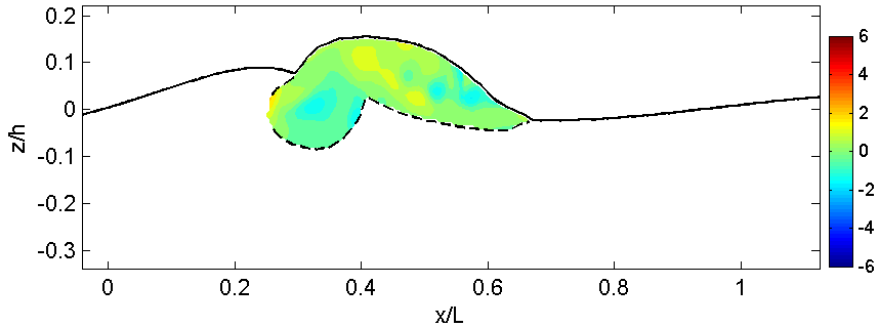

(g) t = 0.31 s

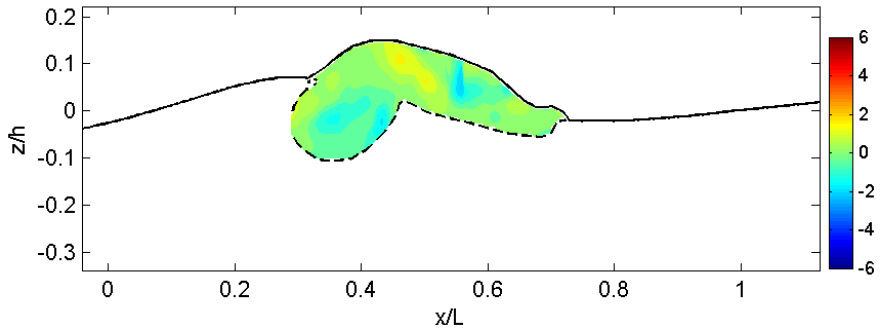

(h) t = 0.36 s

Fig. A.16 (Continued).

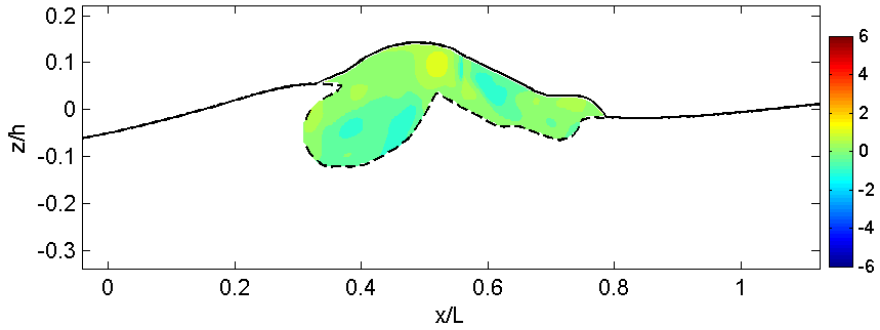

(i) $t = 0.41$ s

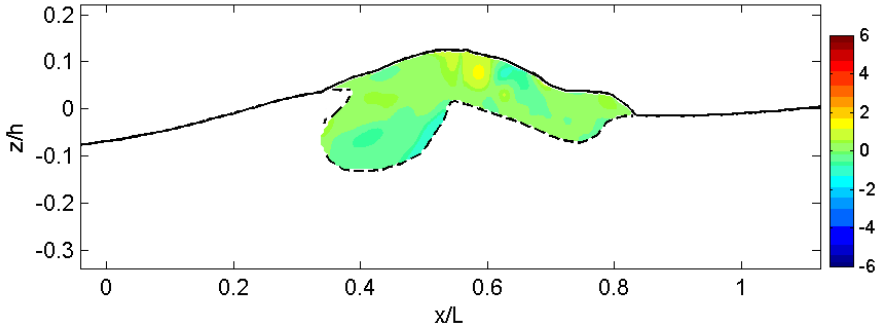

(j) $t = 0.46$ s

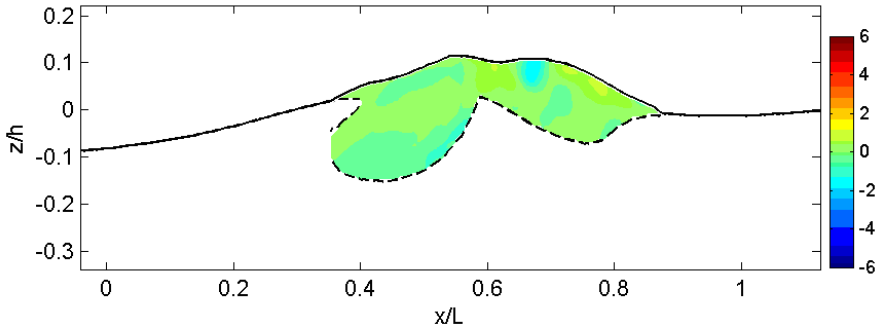

(k) $t = 0.51$ s

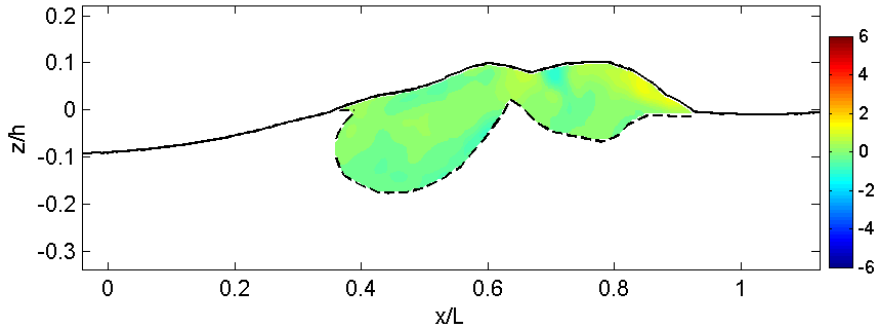

(l) $t = 0.56$ s

Fig. A.16 (Continued).

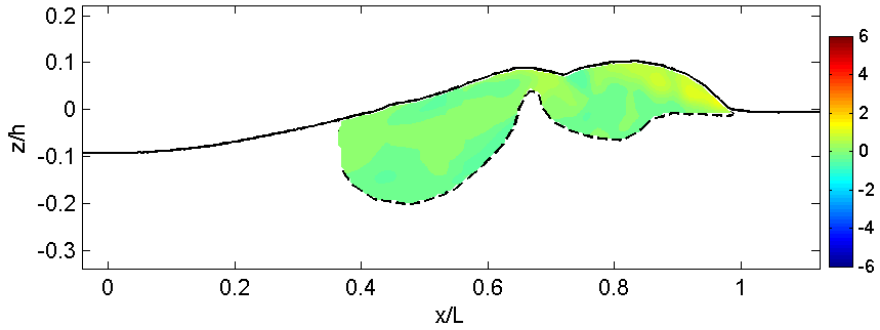

(m) $t = 0.61$ s

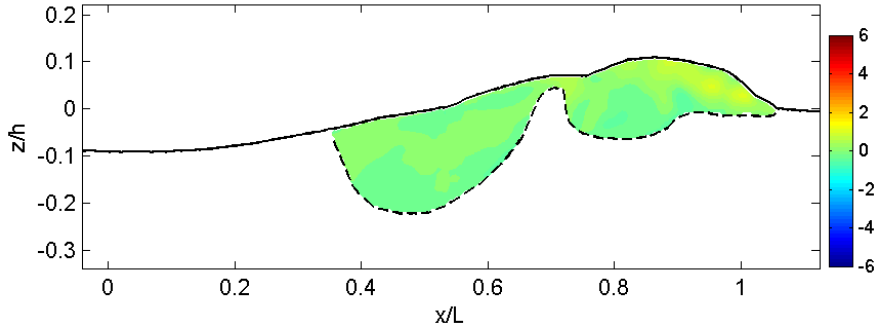

(n) $t = 0.66$ s

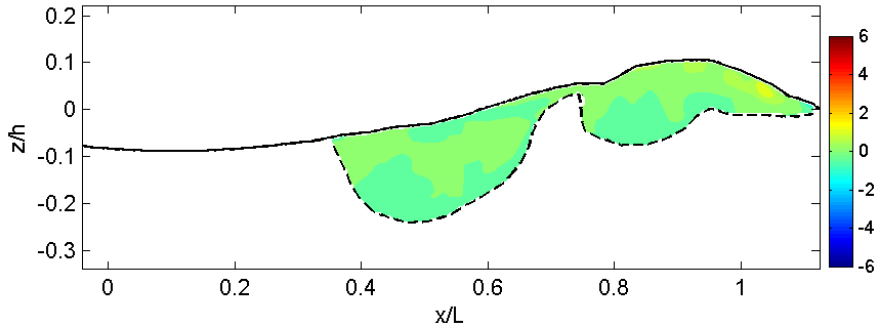

(o) $t = 0.71$ s

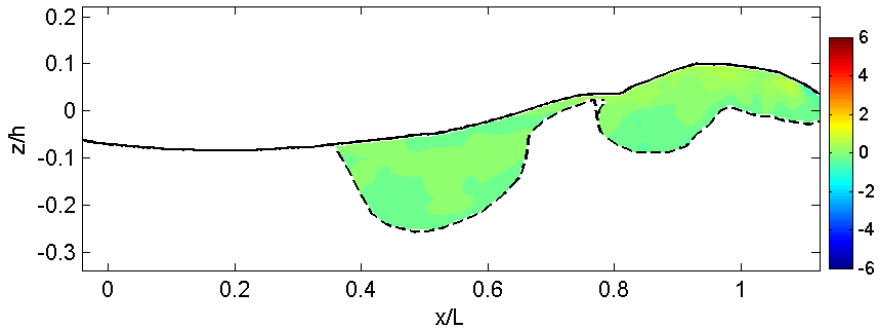

(p) $t = 0.76$ s

Fig. A.16 (Continued).

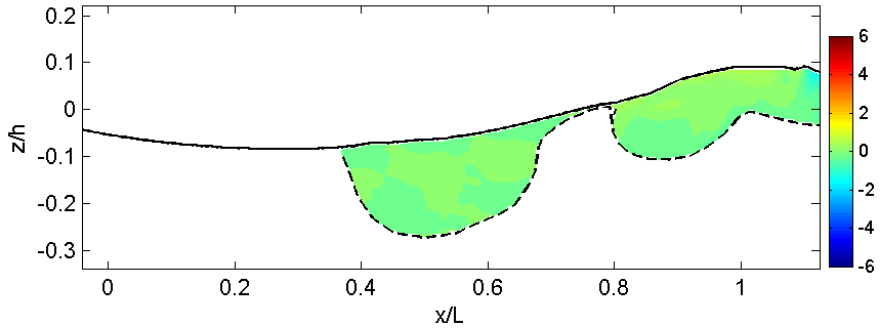

(q) $t = 0.81$ s

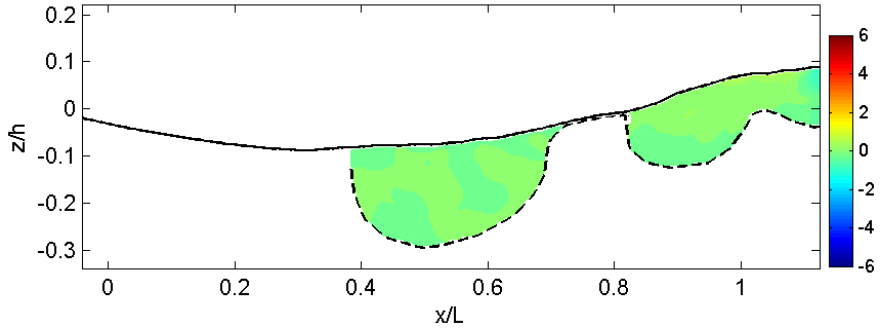

(r) $t = 0.86$ s

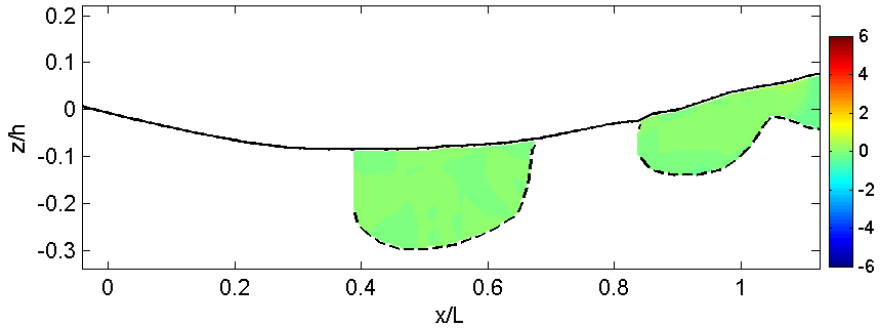

(s) $t = 0.91$ s

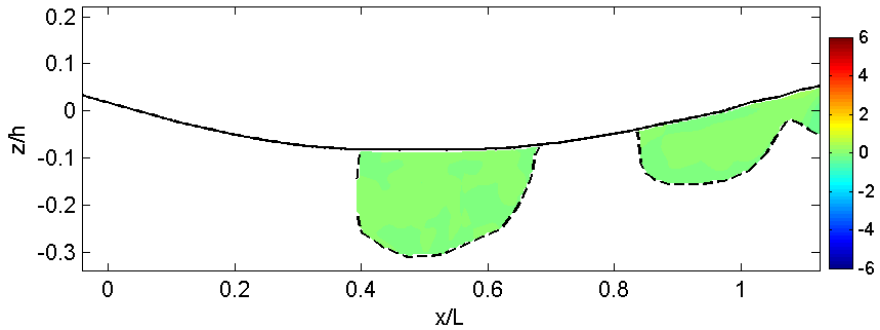

(t) $t = 0.96$ s

Fig. A.16 (Continued).

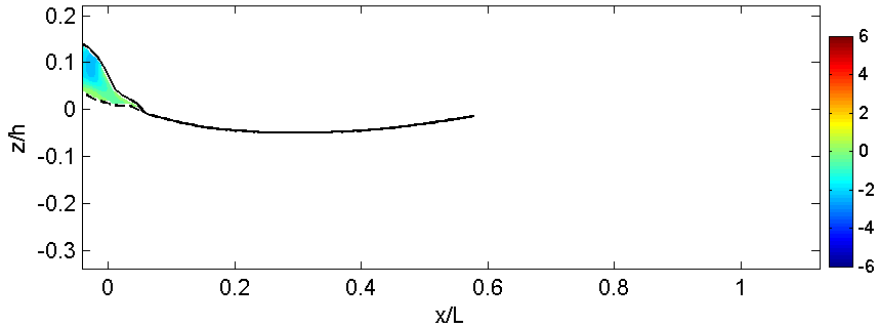

(a) t = 0.01 s

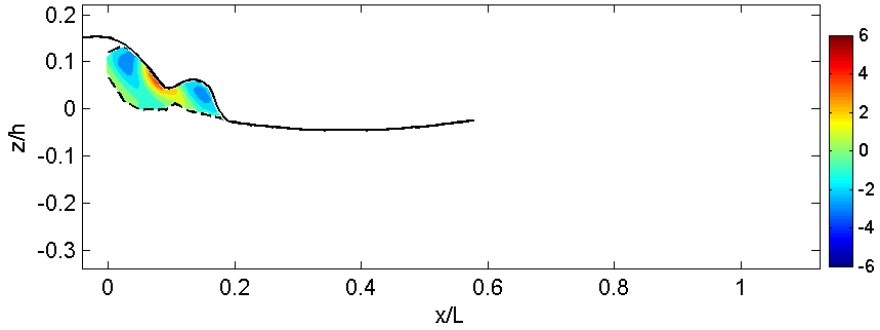

(b) t = 0.06 s

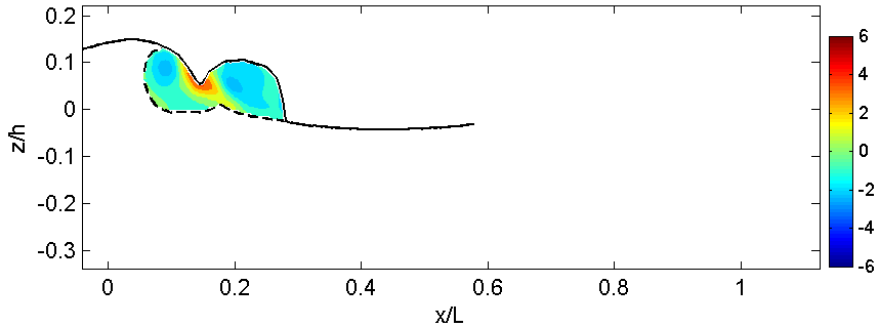

(c) t = 0.11 s

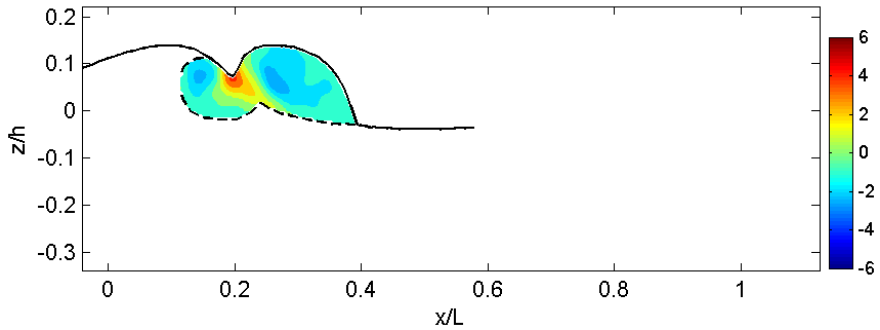

(d) t = 0.16 s

Fig. A.17 Normalized vertical convective acceleration, $\left(U\frac{\partial W}{\partial x}+W\frac{\partial W}{\partial z}\right)\Big/g$ **.**

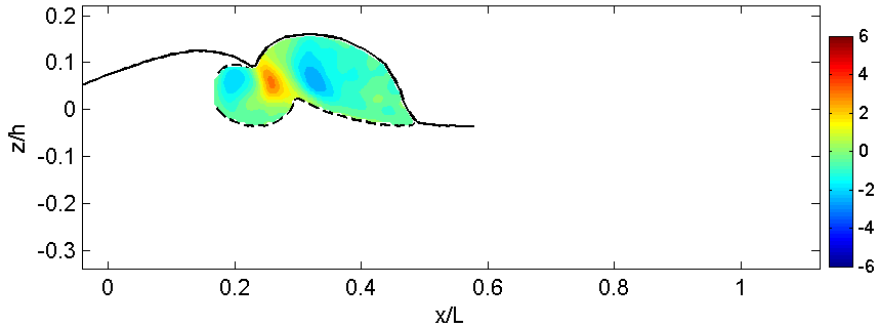

(e) t = 0.21 s

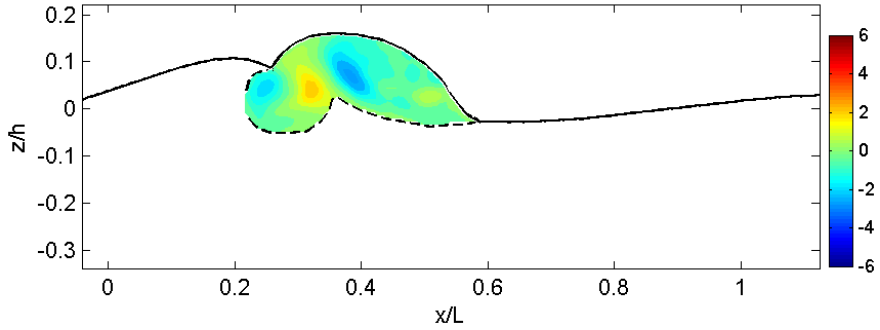

(f) t = 0.26 s

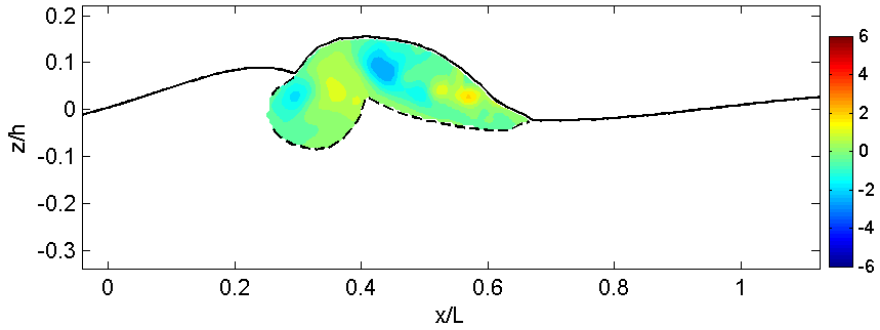

(g) t = 0.31 s

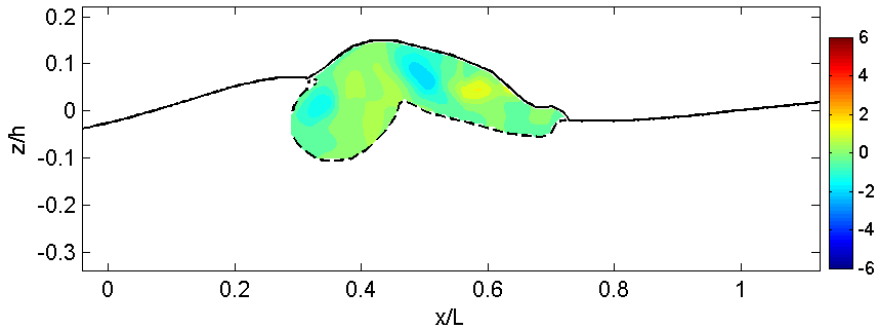

(h) t = 0.36 s

Fig. A.17 (Continued).

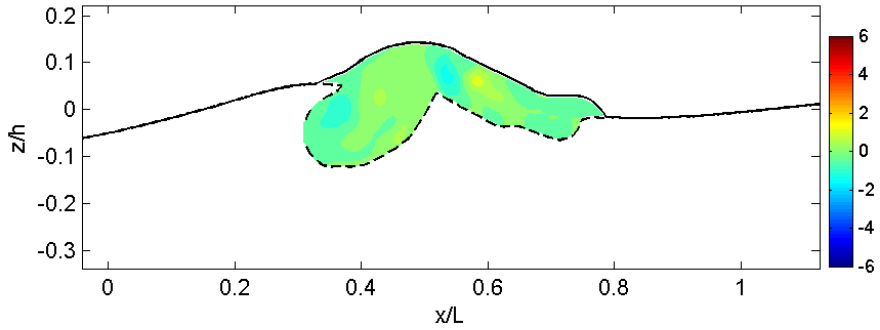

(i) $t = 0.41$ s

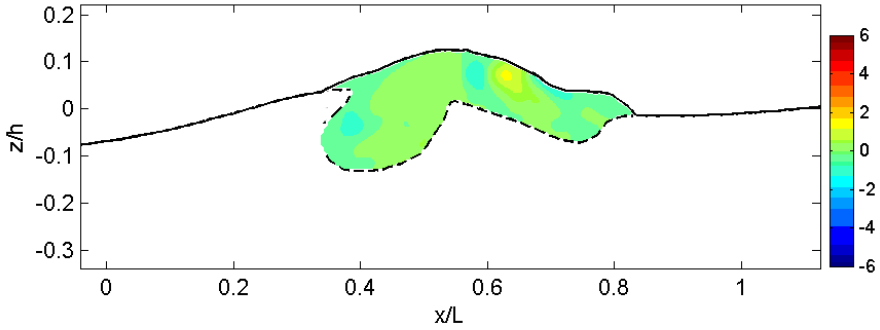

(j) $t = 0.46$ s

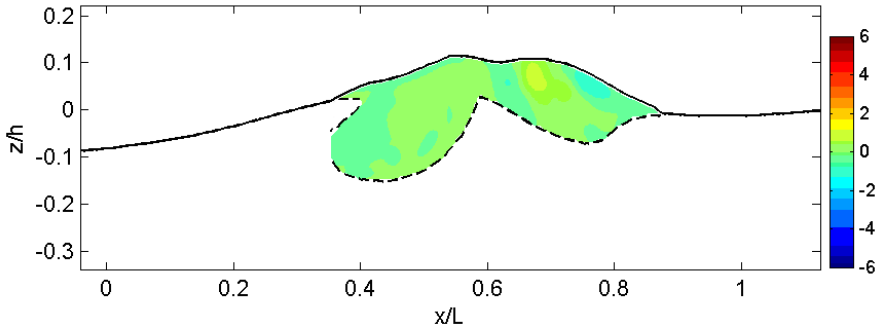

(k) $t = 0.51$ s

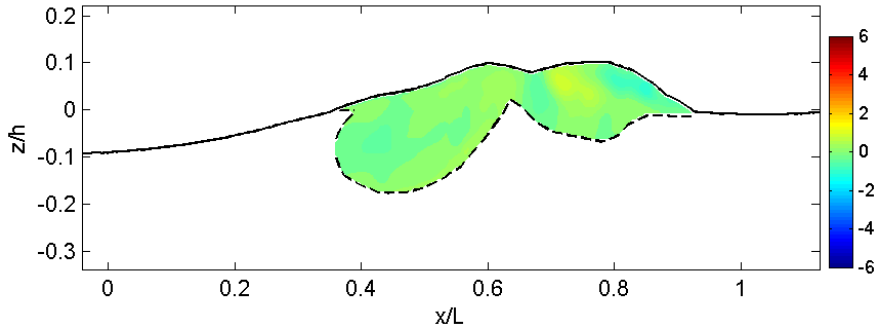

(l) $t = 0.56$ s

Fig. A.17 (Continued).

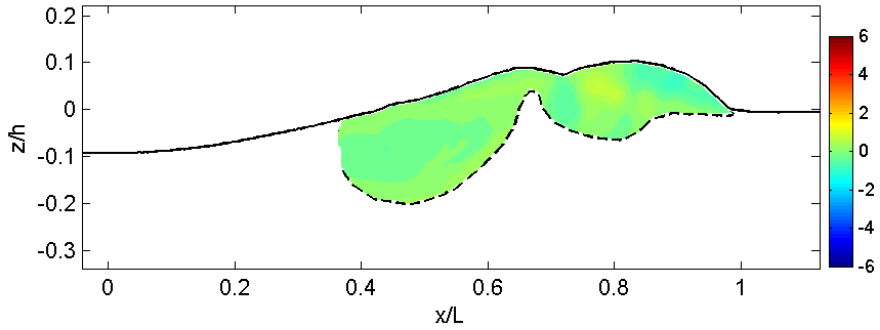

(m) $t = 0.61$ s

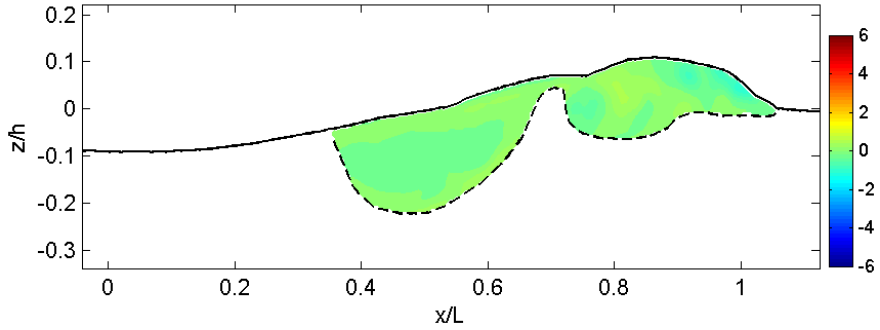

(n) $t = 0.66$ s

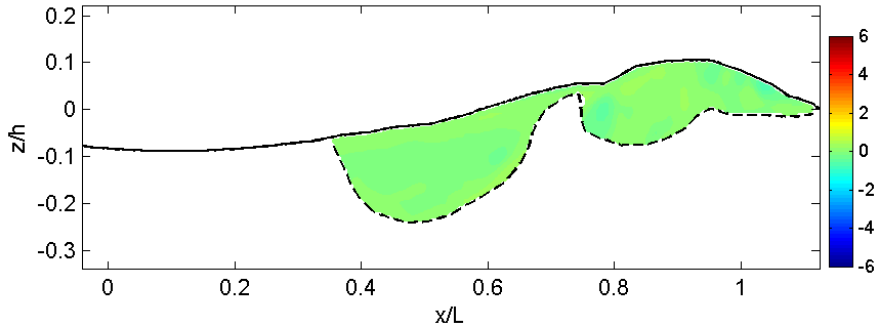

(o) $t = 0.71$ s

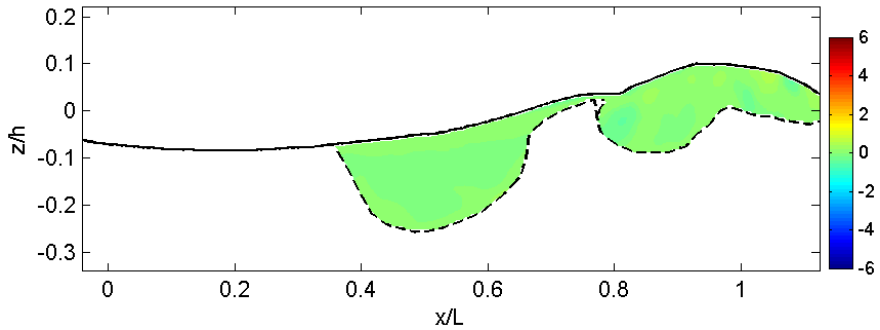

(p) $t = 0.76$ s

Fig. A.17 (Continued).

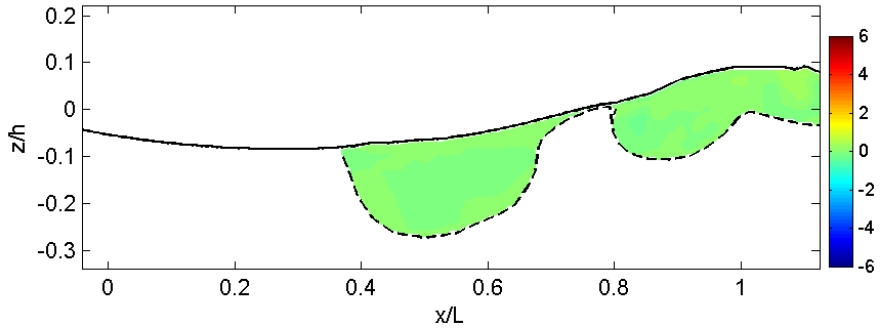

(q) $t = 0.81$ s

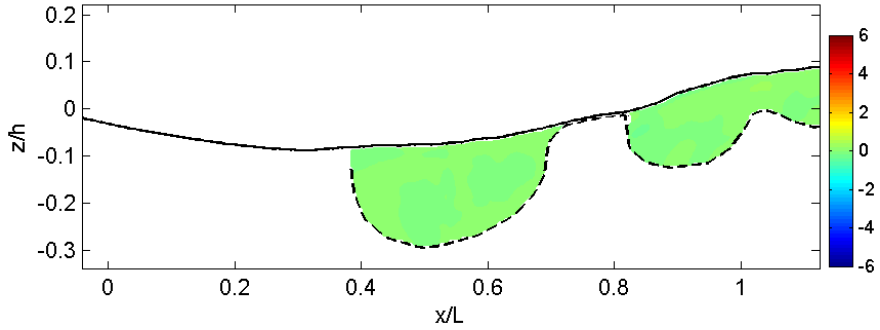

(r) $t = 0.86$ s

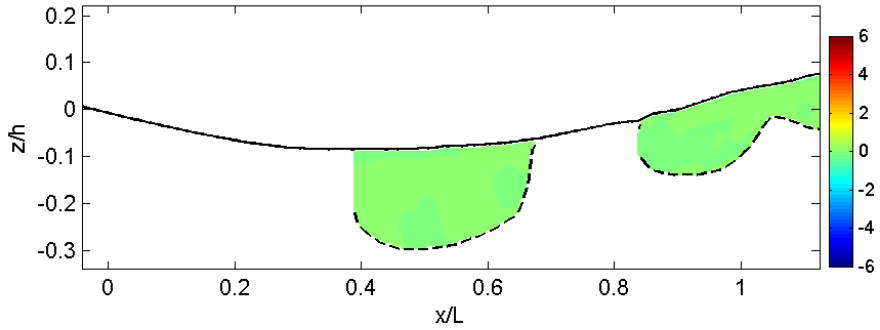

(s) $t = 0.91$ s

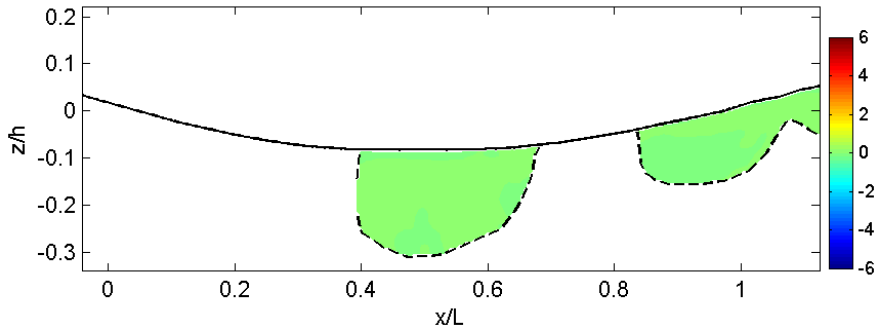

(t) $t = 0.96$ s

Fig. A.17 (Continued).

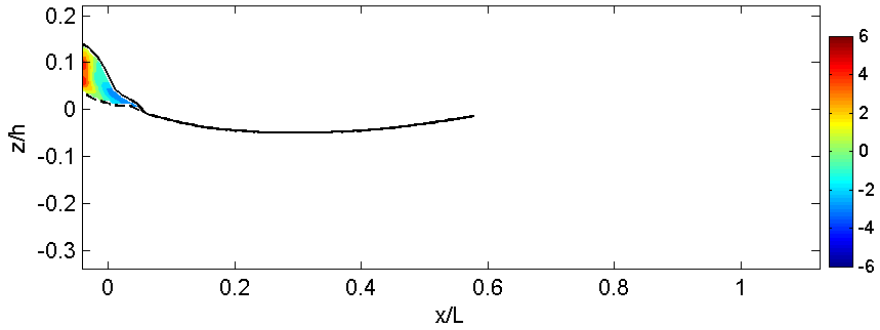

(a) t = 0.01 s

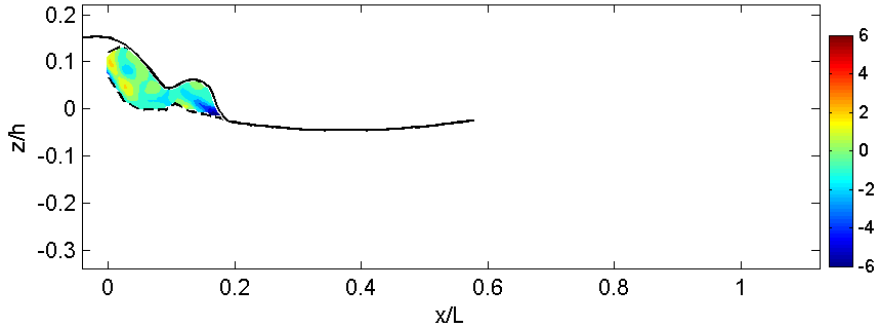

(b) t = 0.06 s

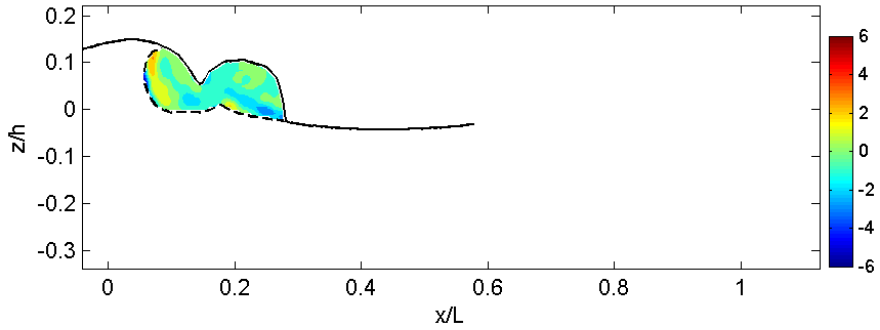

(c) t = 0.11 s

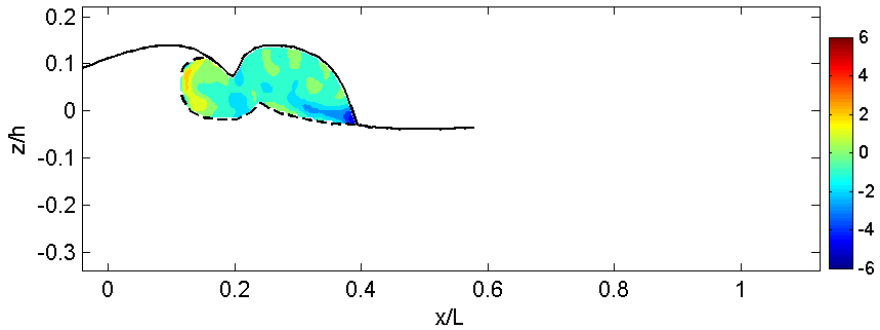

(d) t = 0.16 s

Fig. A.18 Normalized horizontal total acceleration, $\left(\frac{\partial U}{\partial t}+U\frac{\partial U}{\partial x}+W\frac{\partial U}{\partial z}\right)\Big/g$ **.**

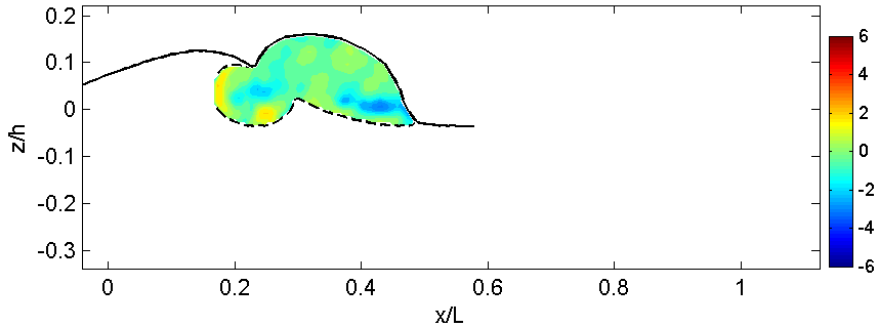

(e) t = 0.21 s

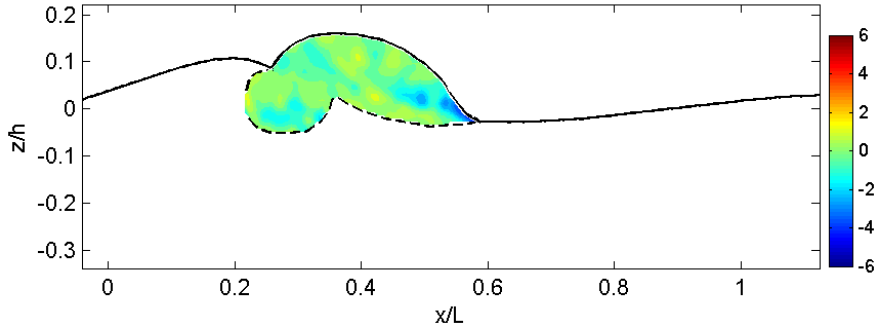

(f) t = 0.26 s

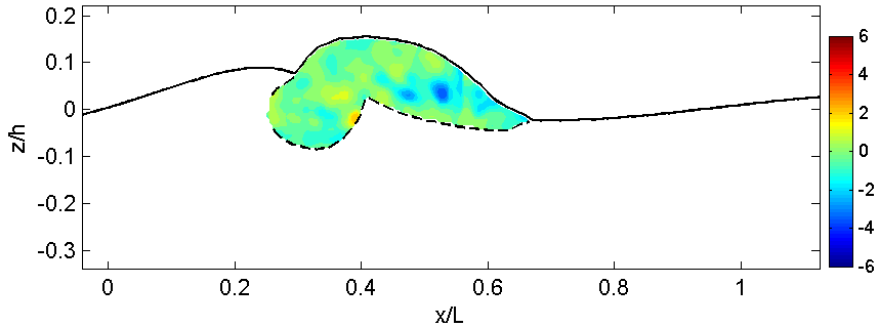

(g) t = 0.31 s

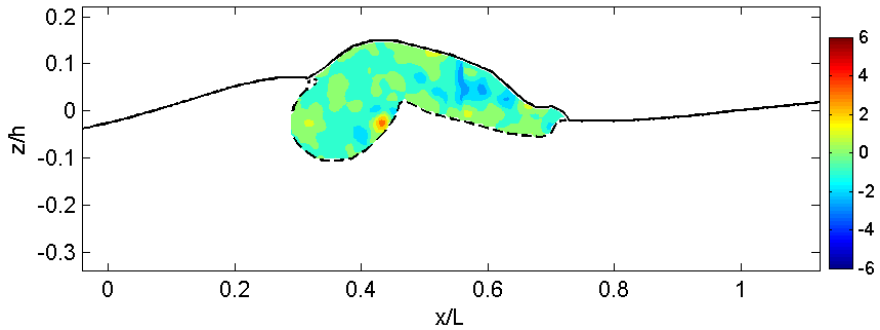

(h) t = 0.36 s

Fig. A.18 (Continued).

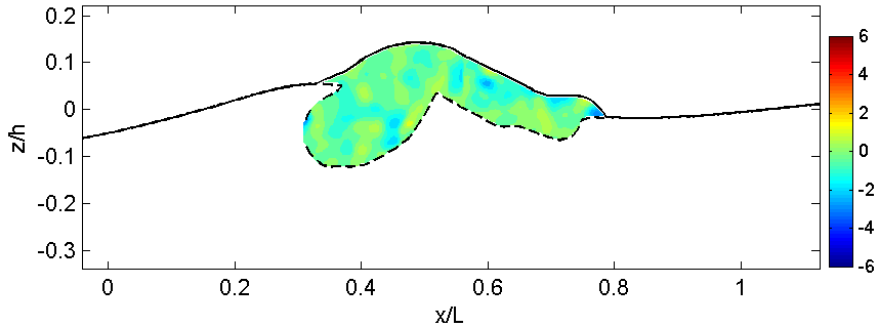

(i) $t = 0.41$ s

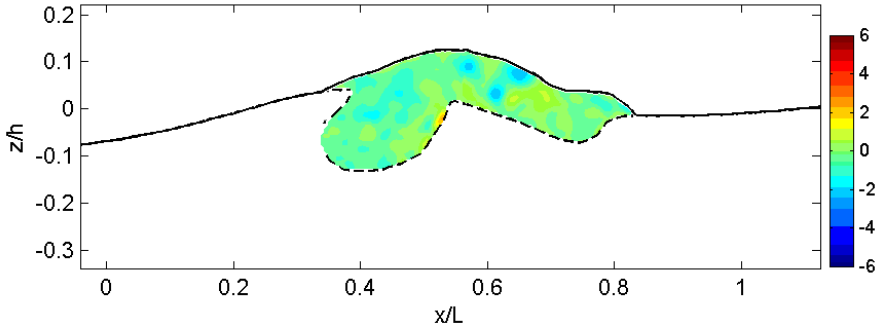

(j) $t = 0.46$ s

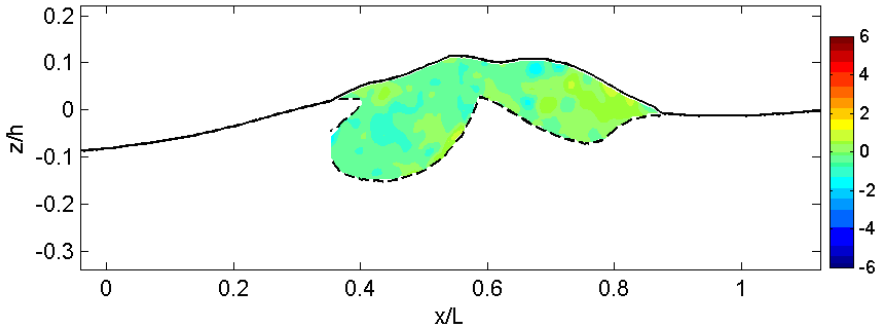

(k) $t = 0.51$ s

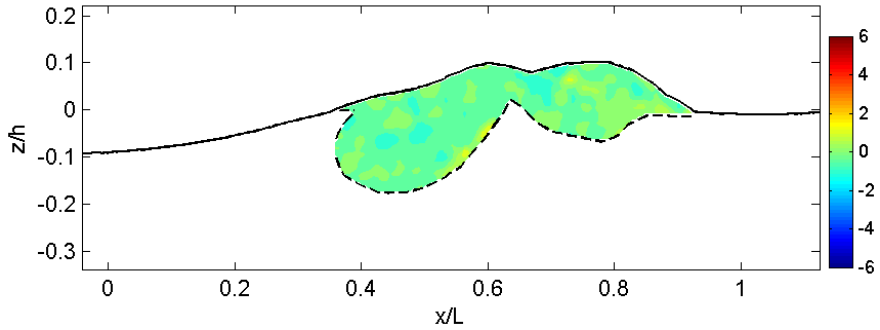

(l) $t = 0.56$ s

Fig. A.18 (Continued).

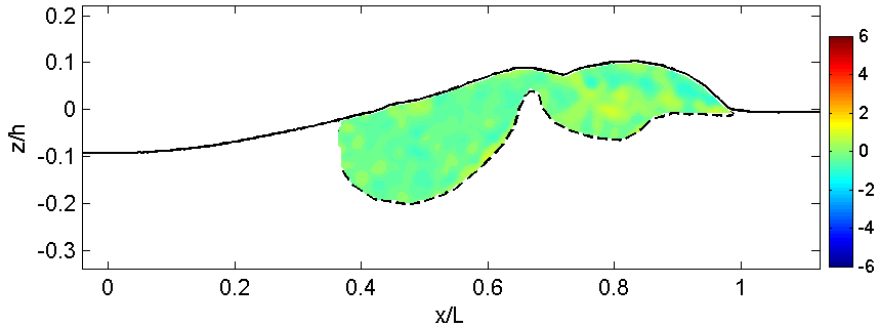

(m) $t = 0.61$ s

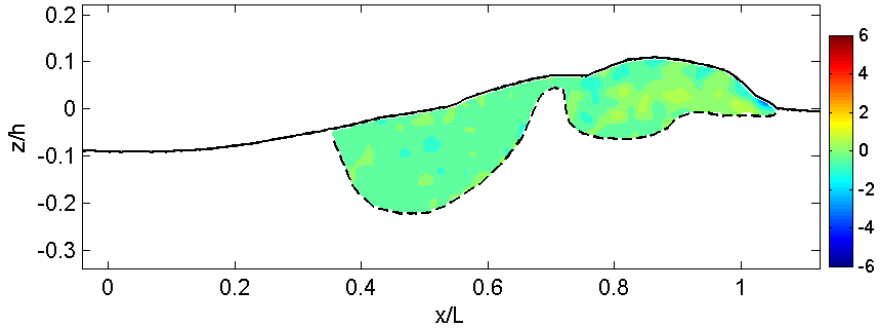

(n) $t = 0.66$ s

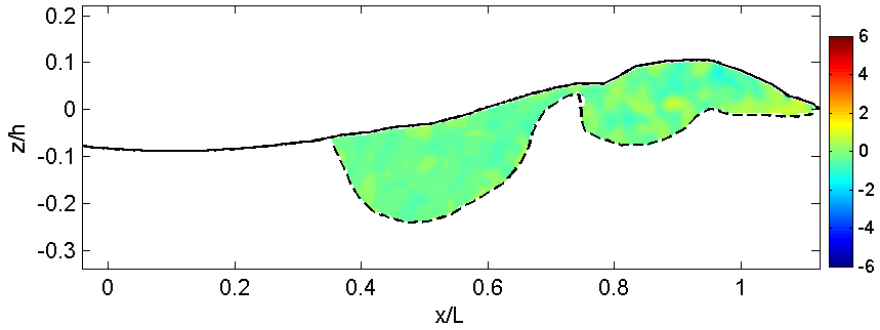

(o) $t = 0.71$ s

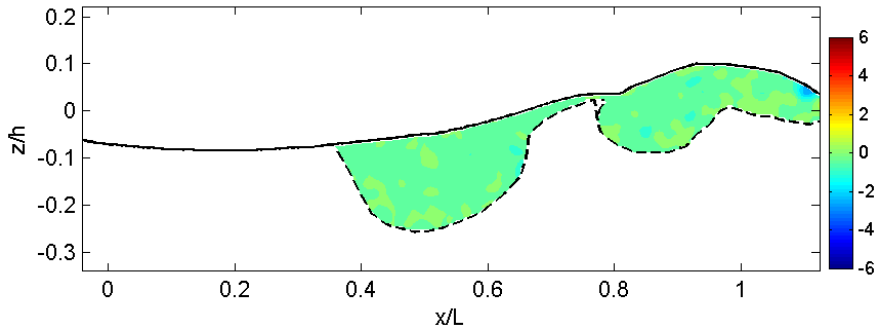

(p) $t = 0.76$ s

Fig. A.18 (Continued).

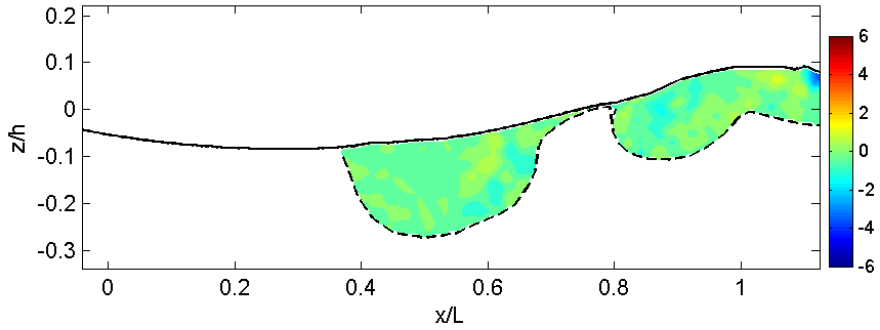

(q) $t = 0.81$ s

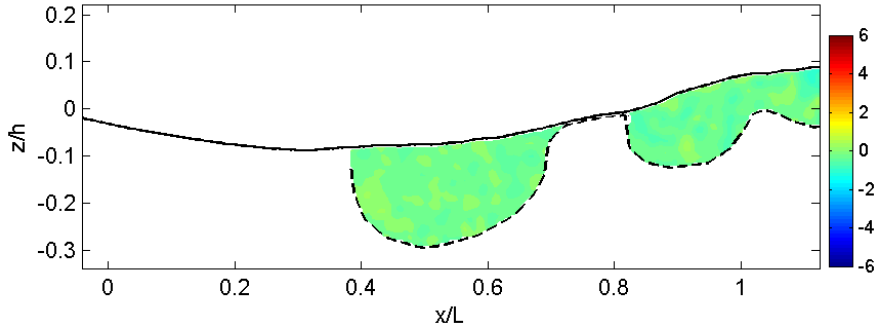

(r) $t = 0.86$ s

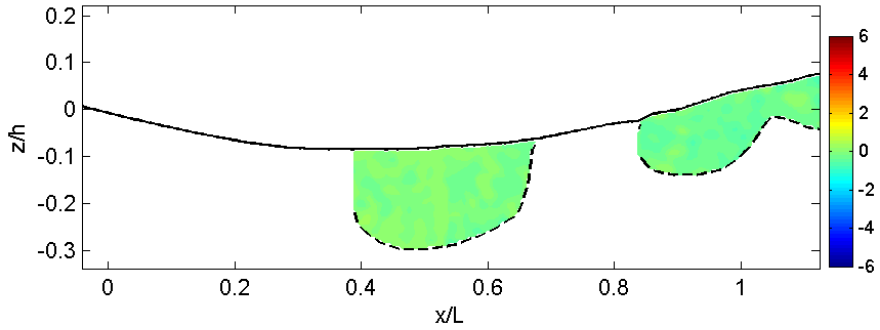

(s) $t = 0.91$ s

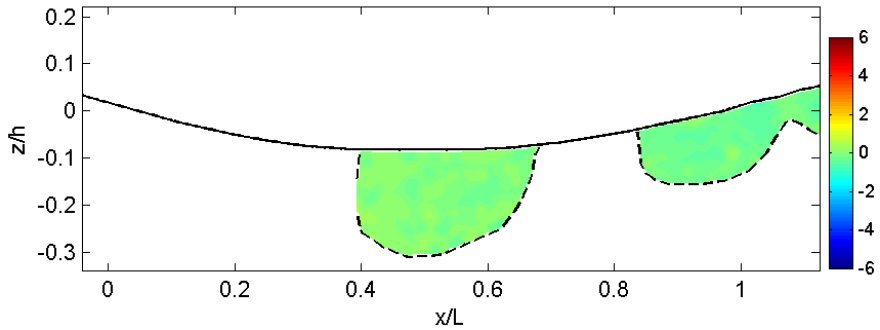

(t) $t = 0.96$ s

Fig. A.18 (Continued).

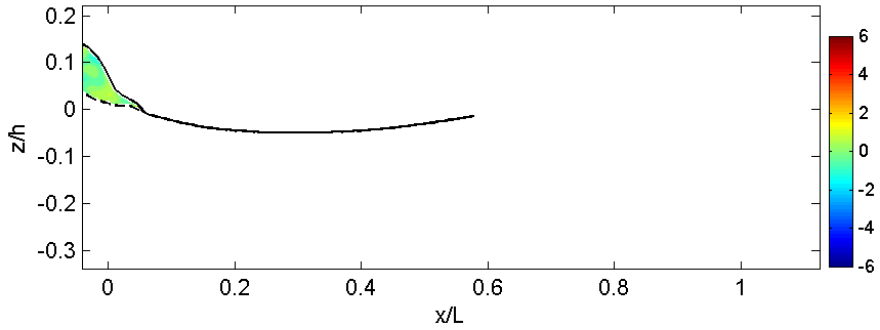

(a) t = 0.01 s

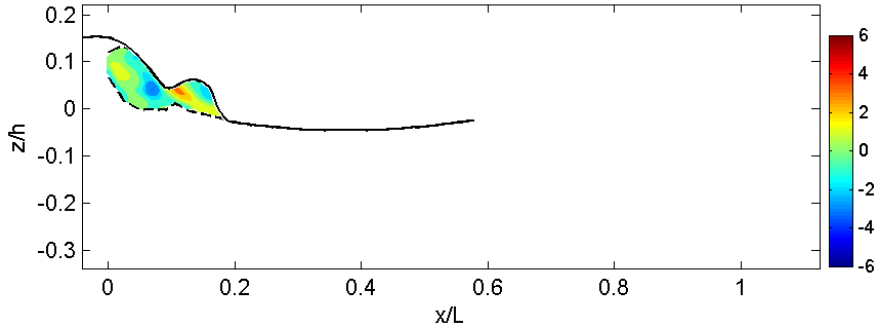

(b) t = 0.06 s

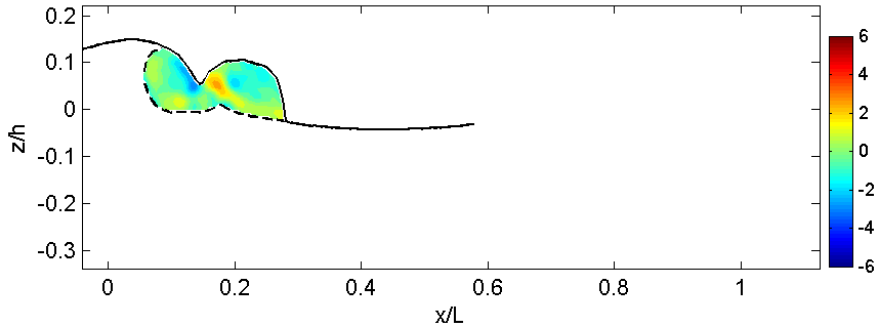

(c) t = 0.11 s

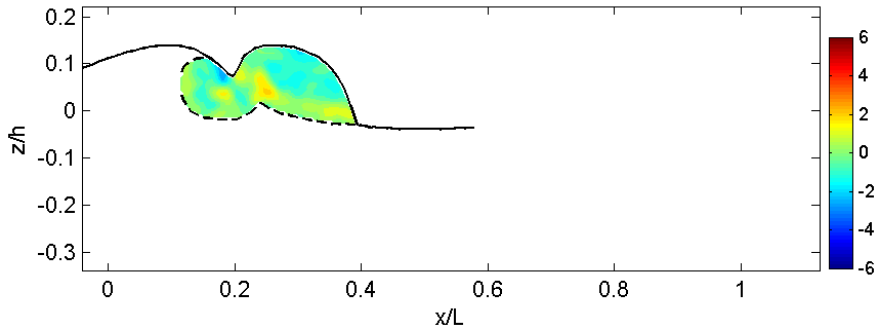

(d) t = 0.16 s

Fig. A.19 Normalized vertical total acceleration, $\left(\frac{\partial W}{\partial t}+U\frac{\partial W}{\partial x}+W\frac{\partial W}{\partial z}\right)\Big/g$ **.**

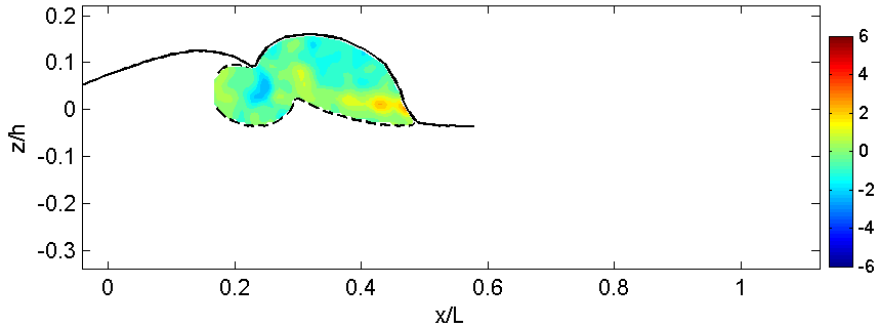

(e) t = 0.21 s

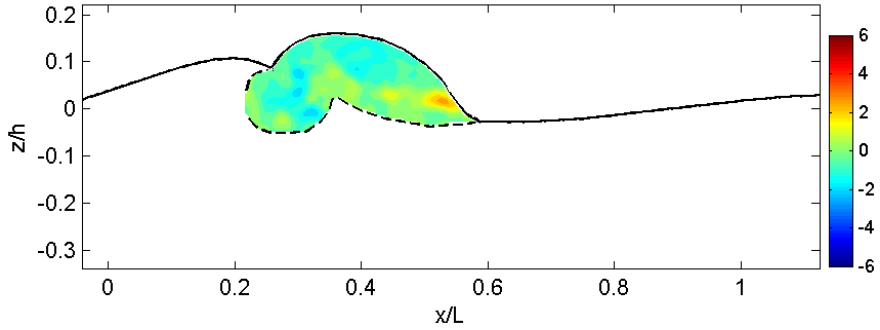

(f) t = 0.26 s

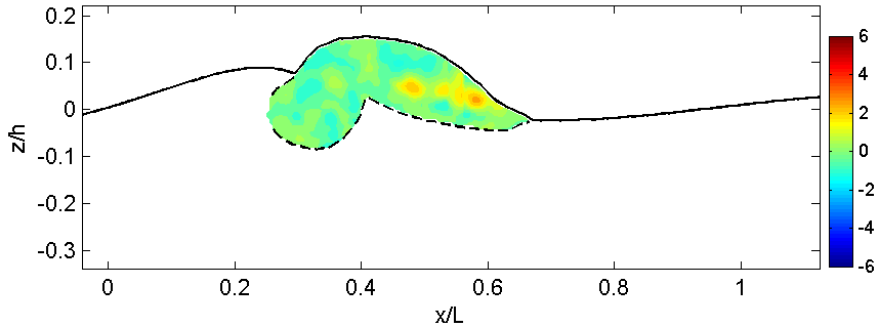

(g) t = 0.31 s

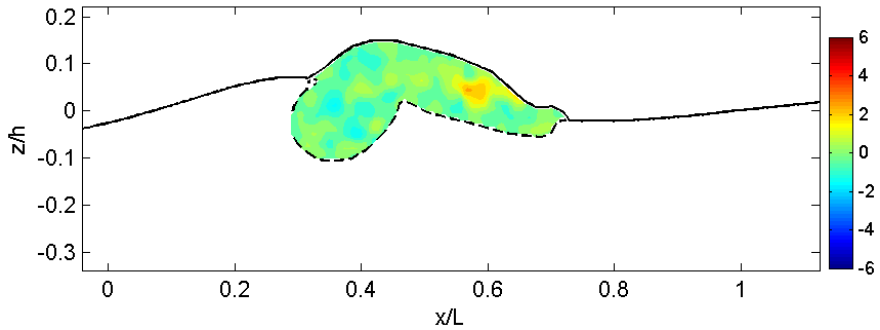

(h) t = 0.36 s

Fig. A.19 (Continued).

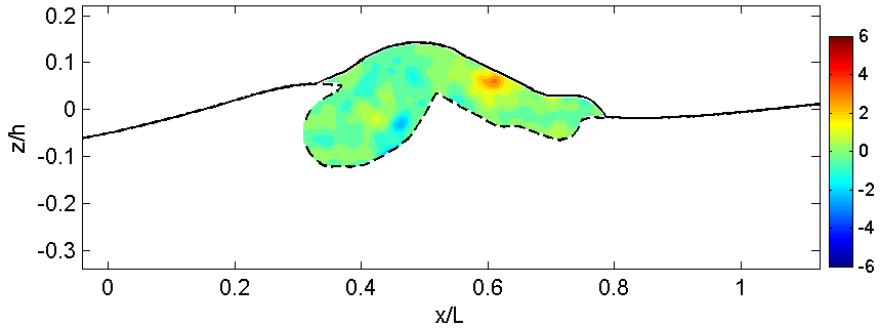

(i) $t = 0.41$ s

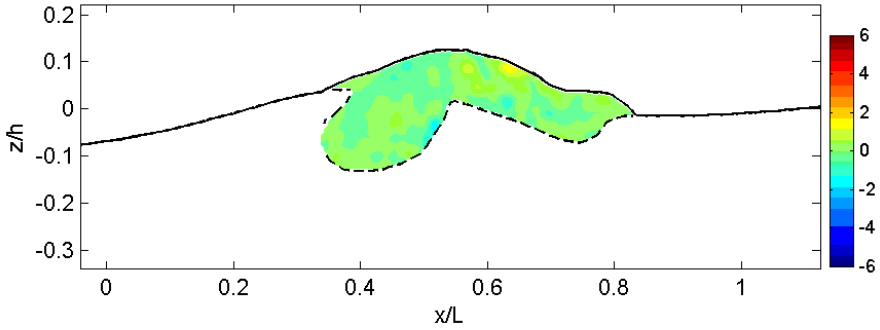

(j) $t = 0.46$ s

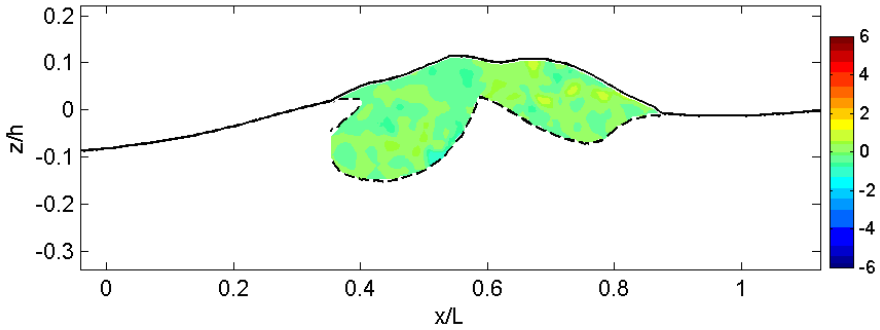

(k) $t = 0.51$ s

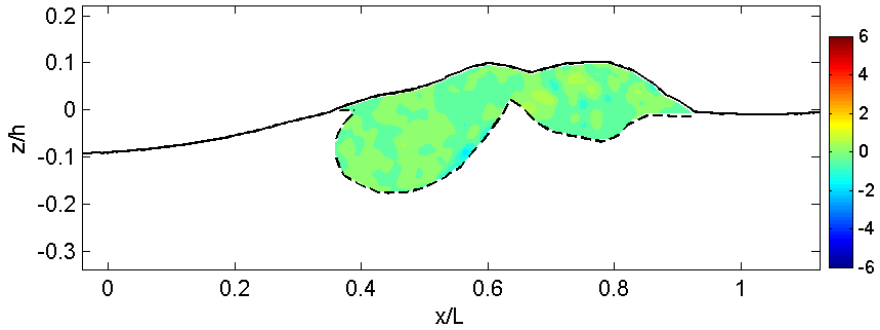

(l) $t = 0.56$ s

Fig. A.19 (Continued).

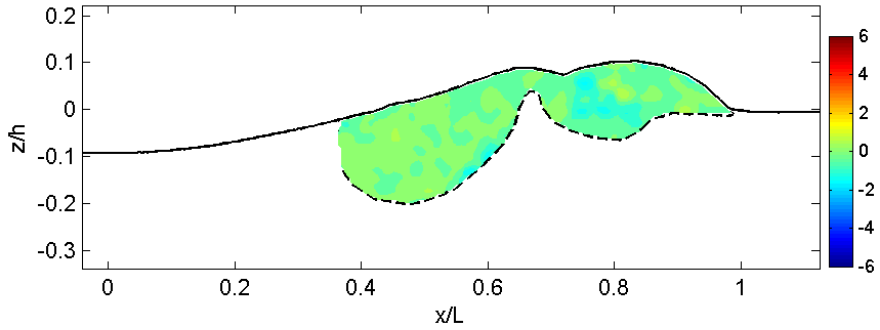

(m) $t = 0.61$ s

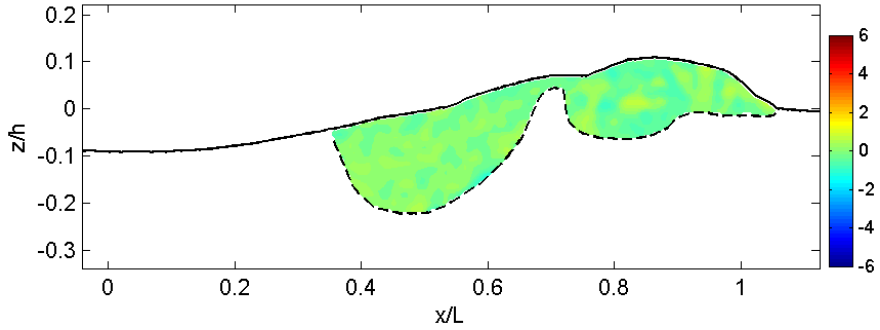

(n) $t = 0.66$ s

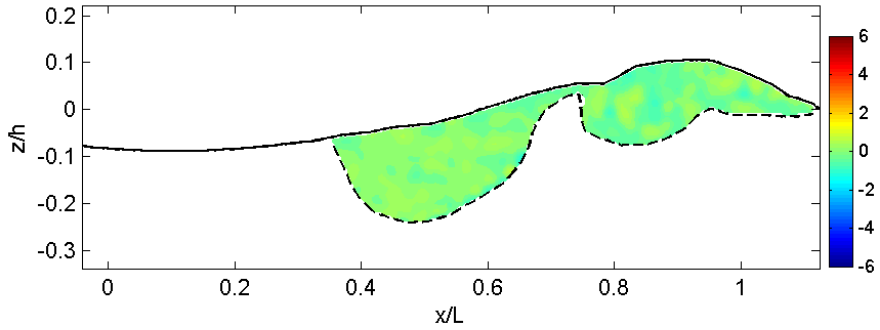

(o) $t = 0.71$ s

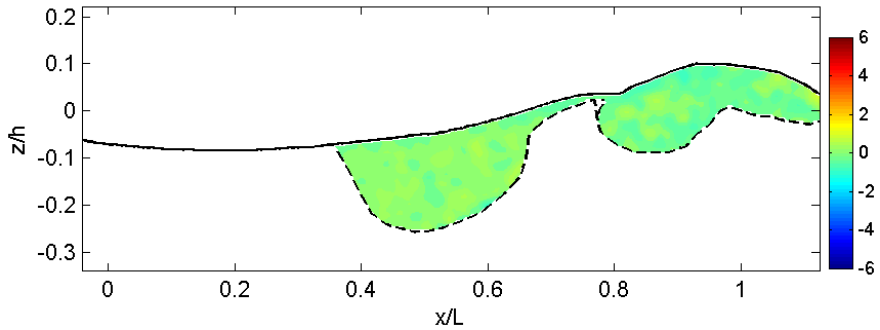

(p) $t = 0.76$ s

Fig. A.19 (Continued).

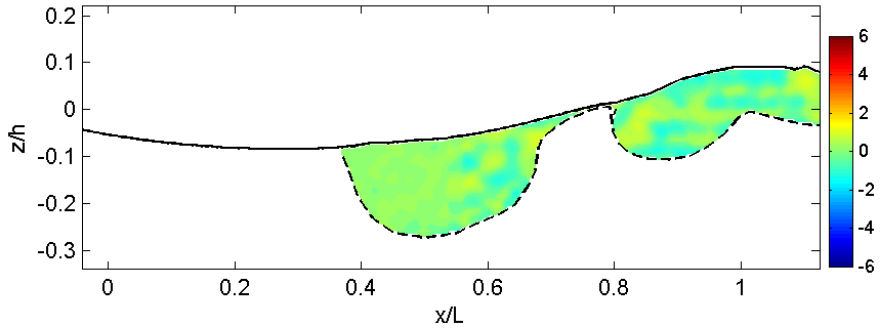

(q) $t = 0.81$ s

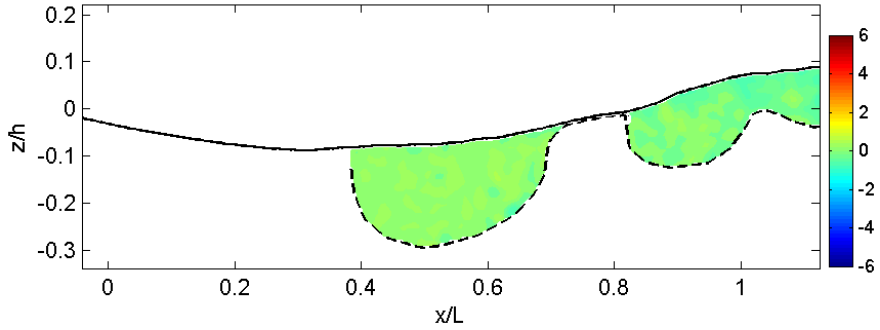

(r) $t = 0.86$ s

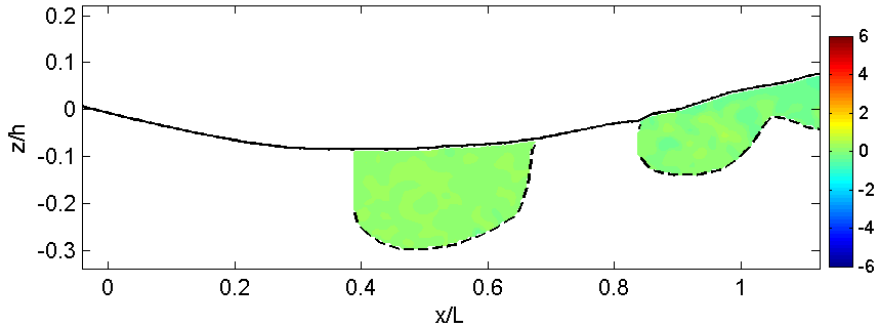

(s) $t = 0.91$ s

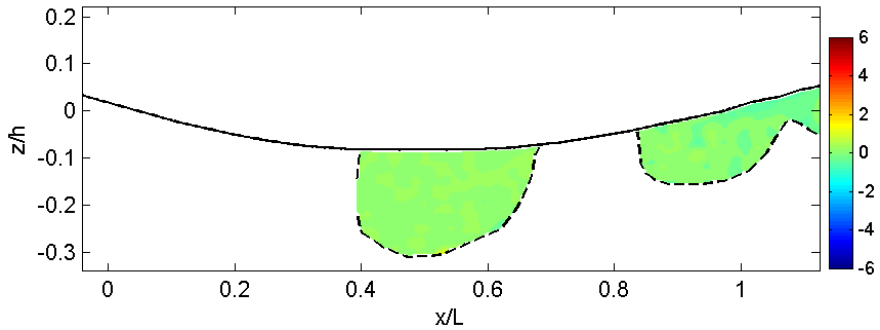

(t) $t = 0.96$ s

Fig. A.19 (Continued).

APPENDIX B

ADDITIONAL FIGURES FROM PIV ANALYSIS

Additional figures obtained from the PIV measurements are provided in this Appendix. The time difference between figures is 0.05 s and description for each figure is summarized in Table B.1.

Table B.1

Description of figures (PIV)

Figure Number	Description
Fig. B.1	Mean Velocity Map ($\sqrt{U^2+W^2}$)
Fig. B.2	Normalized Horizontal Velocity (U/C)
Fig. B.3	Normalized Vertical Velocity (W/C)
Fig. B.4	Normalized Mean Vorticity (Ω_H/C)
Fig. B.5	Normalized Mean Kinetic Energy (κ/C^2)
Fig. B.6	Normalized Turbulent Kinetic Energy (k/C^2)
Fig. B.7	Normalized Horizontal Turbulence Intensity ($\sqrt{u'^2}/C$)
Fig. B.8	Normalized Vertical Turbulence Intensity ($\sqrt{w'^2}/C$)
Fig. B.9	Normalized Reynolds Stress ($-u'w'/C^2$)
Fig. B.10	Normalized Turbulent Kinetic Energy Transport by U (kU/C^3)
Fig. B.11	Normalized Turbulent Kinetic Energy Transport by W (kW/C^3)
Fig. B.12	Normalized Horizontal Convective Acceleration ($\left(U\frac{\partial U}{\partial x}+W\frac{\partial U}{\partial z}\right)/g$)
Fig. B.13	Normalized Vertical Convective Acceleration ($\left(U\frac{\partial W}{\partial x}+W\frac{\partial W}{\partial z}\right)/g$)
Fig. B.14	Normalized Horizontal Local Acceleration ($\frac{\partial U}{\partial t}/g$)
Fig. B.15	Normalized Vertical Local Acceleration ($\frac{\partial W}{\partial t}/g$)
Fig. B.16	Normalized Horizontal Total Acceleration ($\left(\frac{\partial U}{\partial t}+U\frac{\partial U}{\partial x}+W\frac{\partial U}{\partial z}\right)/g$)
Fig. B.17	Normalized Vertical Total Acceleration ($\left(\frac{\partial W}{\partial t}+U\frac{\partial W}{\partial x}+W\frac{\partial W}{\partial z}\right)/g$)
Fig. B.18	Relative Velocity ($U-C, W$)

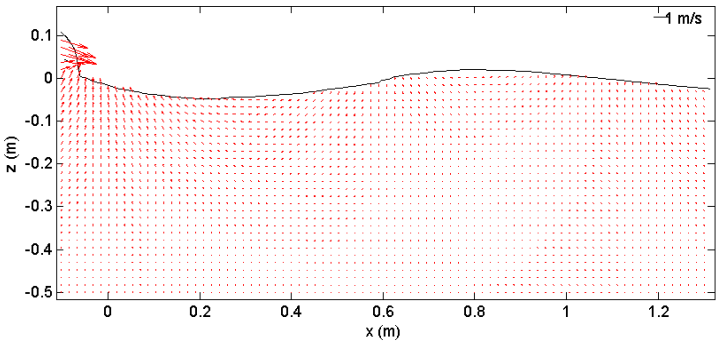

(a) t = -0.04 s

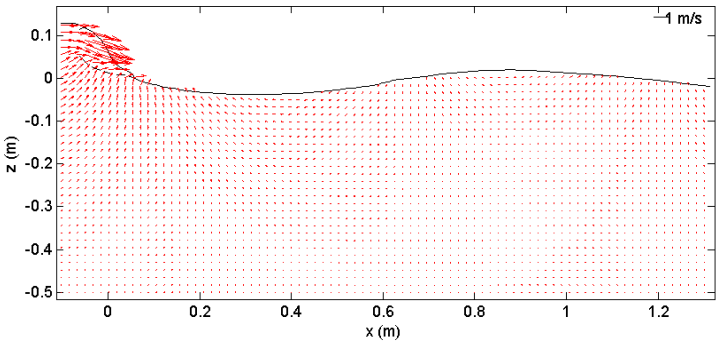

(b) t = 0.01 s

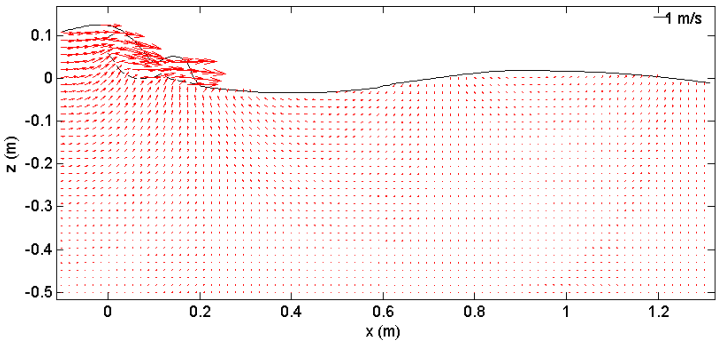

(c) t = 0.06 s

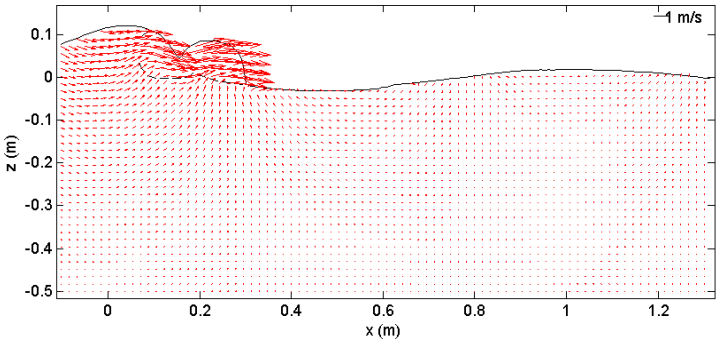

(d) t = 0.11 s

Fig. B.1 Velocity.

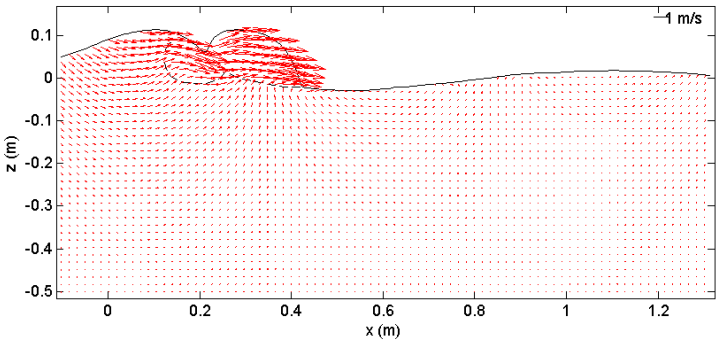

(e) $t = 0.16$ s

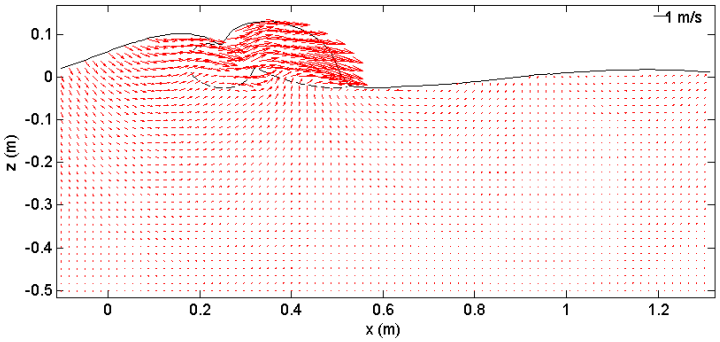

(f) $t = 0.21$ s

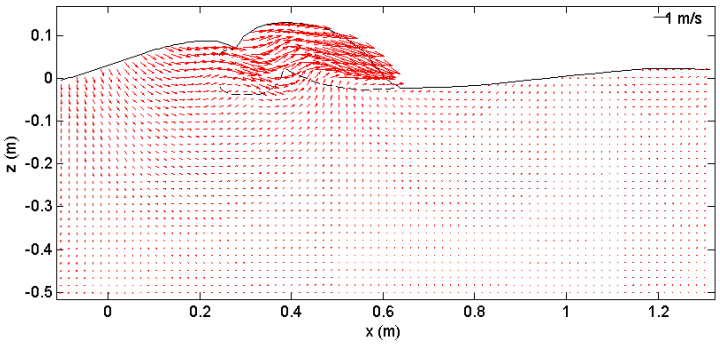

(g) $t = 0.26$ s

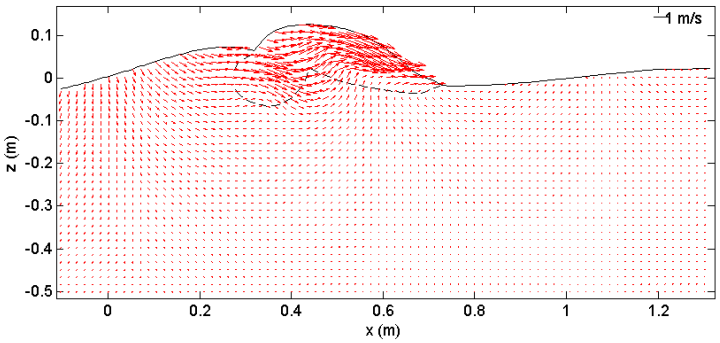

(h) $t = 0.31$ s

Fig. B.1 (Continued).

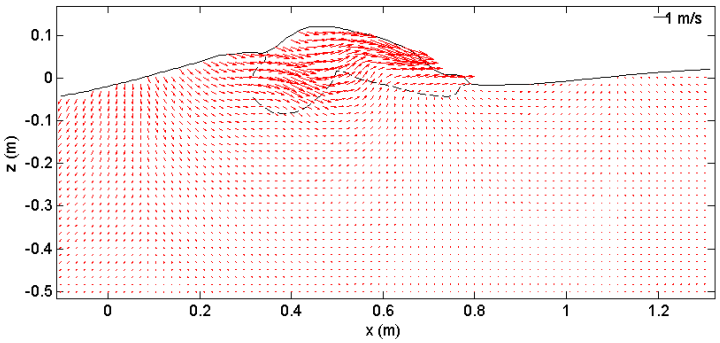

(i) $t = 0.36$ s

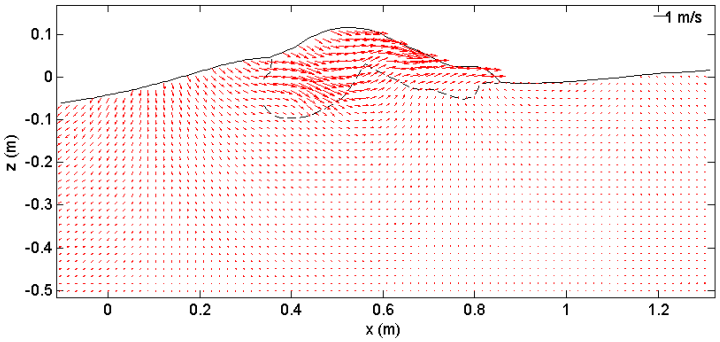

(j) $t = 0.41$ s

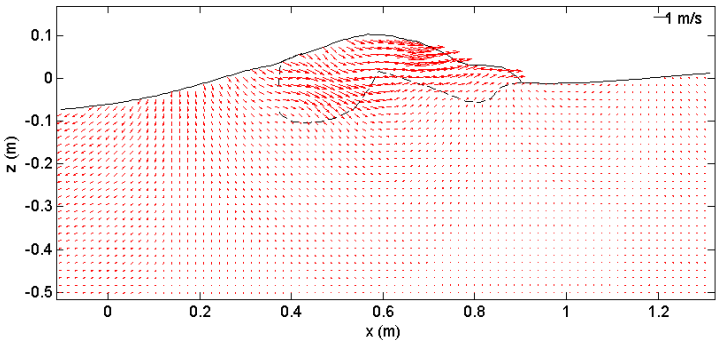

(k) $t = 0.46$ s

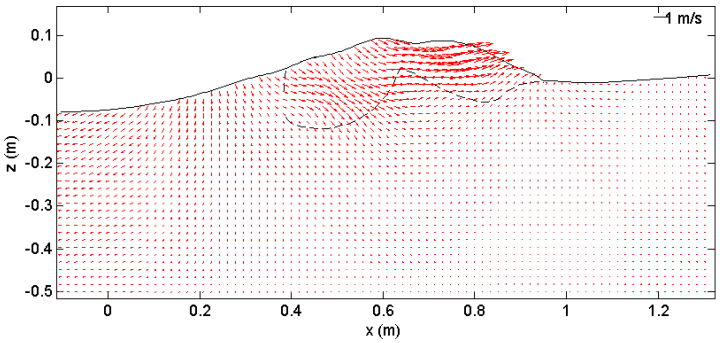

(l) $t = 0.51$ s

Fig. B.1 (Continued).

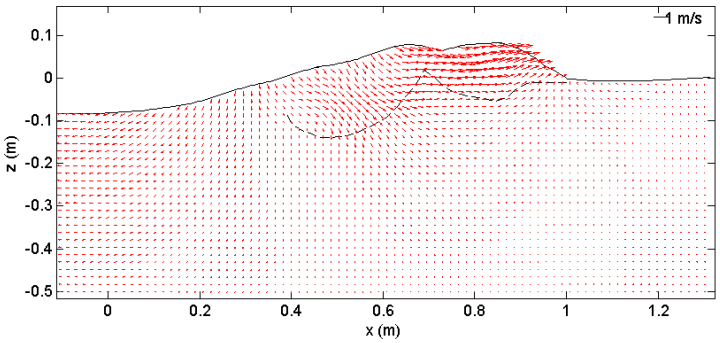

(m) t = 0.56 s

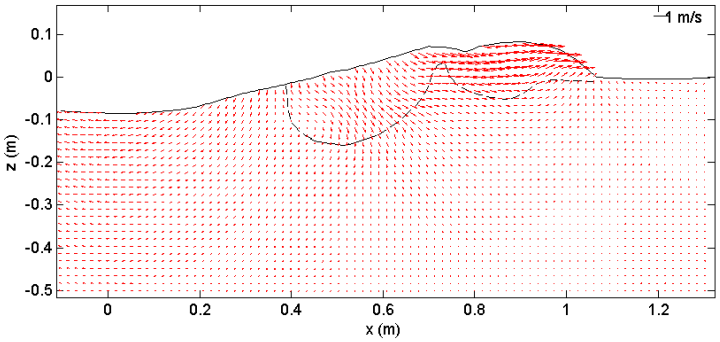

(n) t = 0.61 s

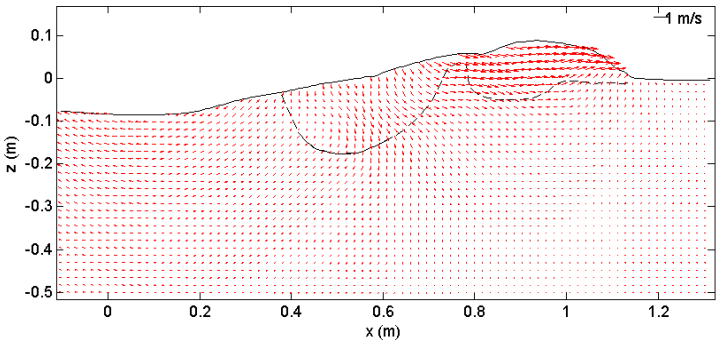

(o) t = 0.66 s

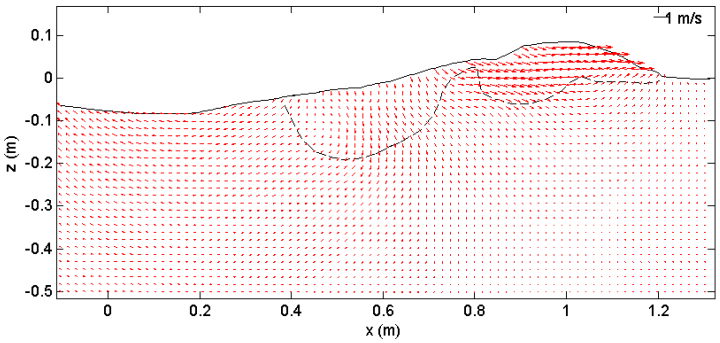

(p) t = 0.71 s

Fig. B.1 (Continued).

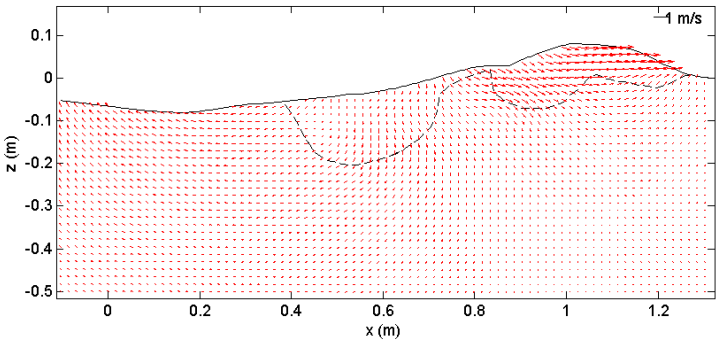

(q) t = 0.76 s

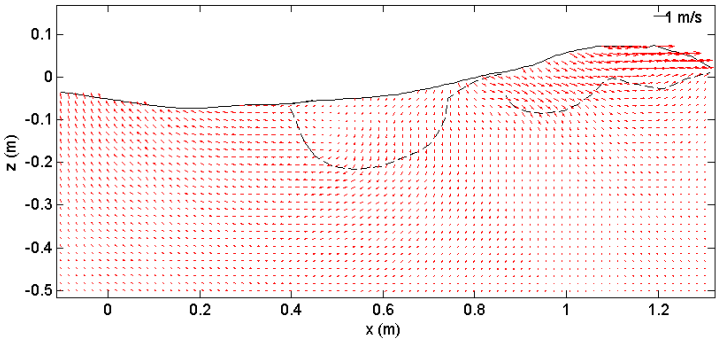

(r) t = 0.81 s

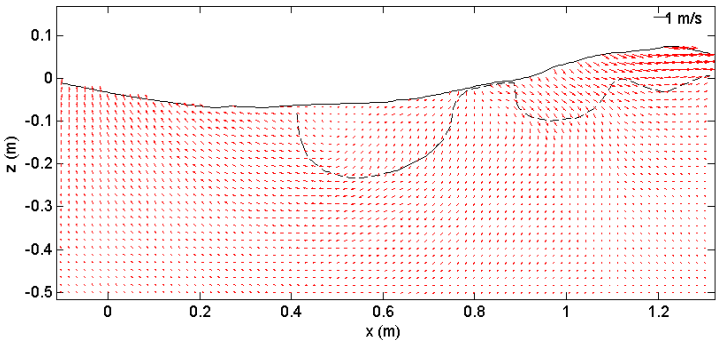

(s) t = 0.86 s

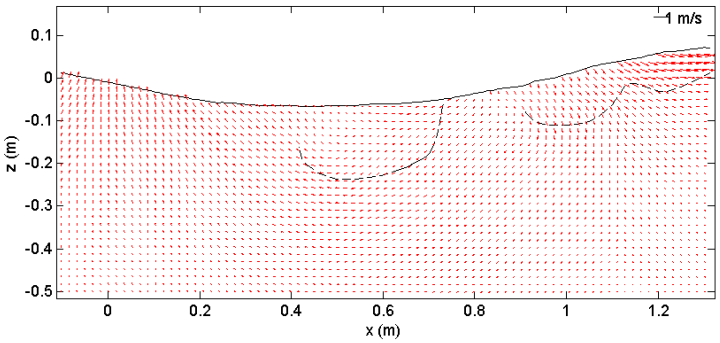

(t) t = 0.91 s

Fig. B.1 (Continued).

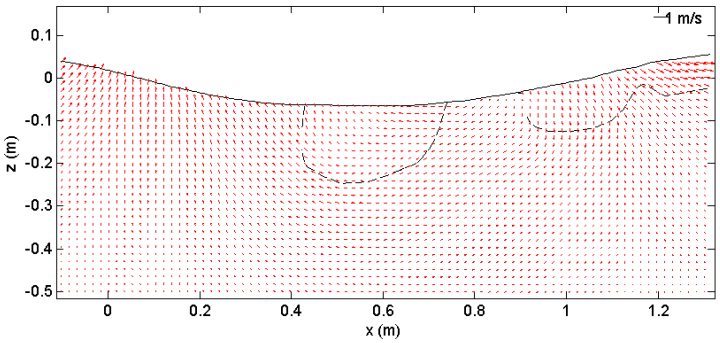

(u) t = 0.96 s

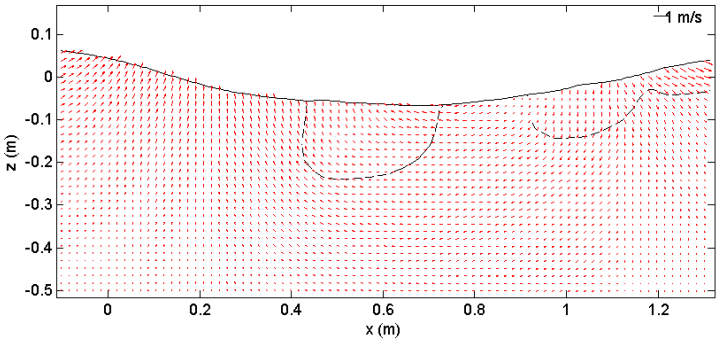

(v) t = 1.01 s

Fig. B.1 (Continued).

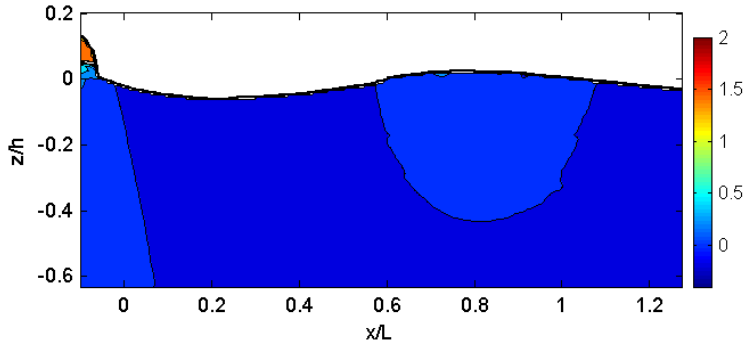

(a) t = -0.04 s

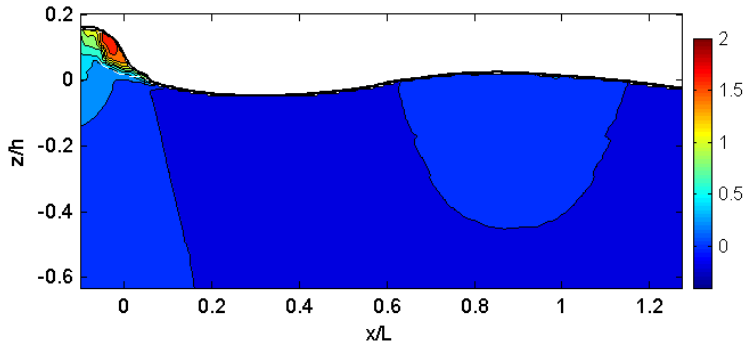

(b) t = 0.01 s

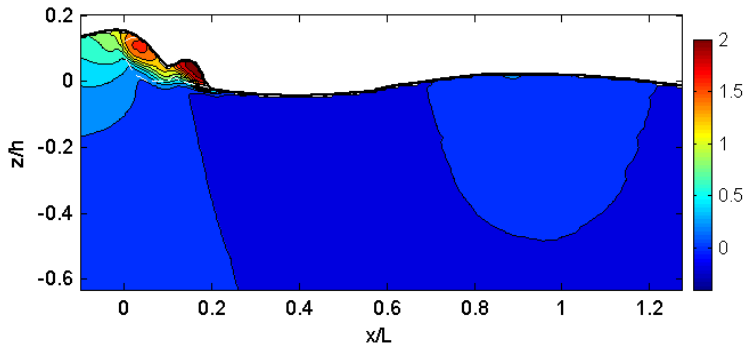

(c) t = 0.06 s

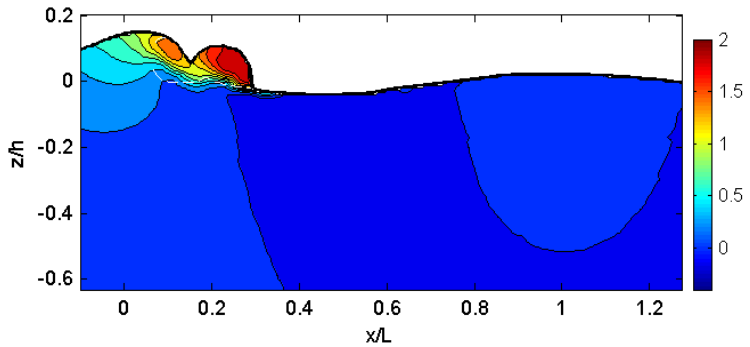

(d) t = 0.11 s

Fig. B.2 Normalized horizontal velocity, *U*/*C*.

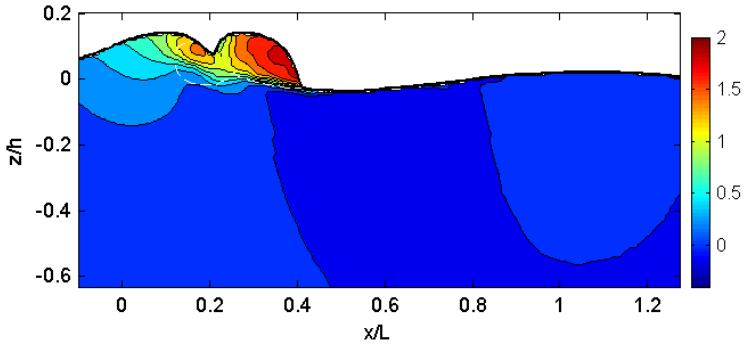

(e) $t = 0.16$ s

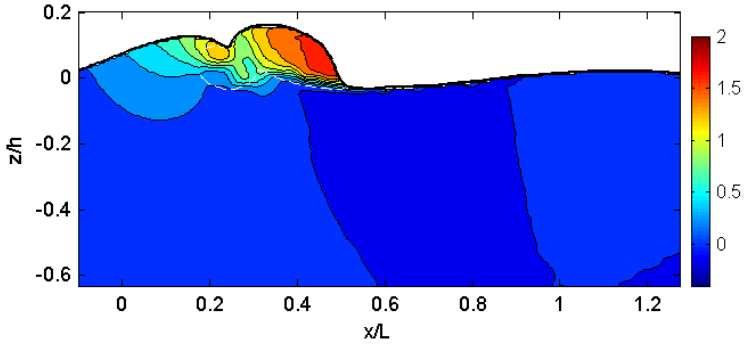

(f) $t = 0.21$ s

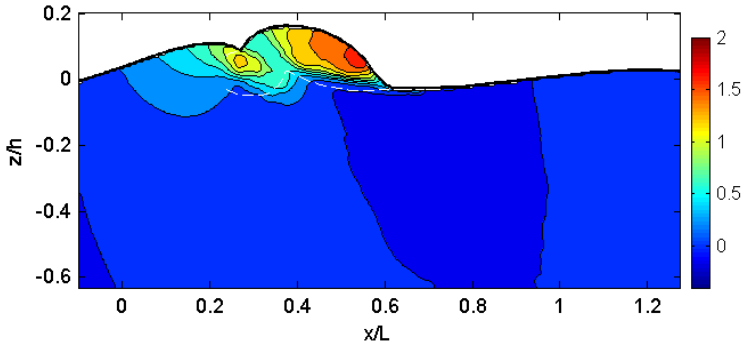

(g) $t = 0.26$ s

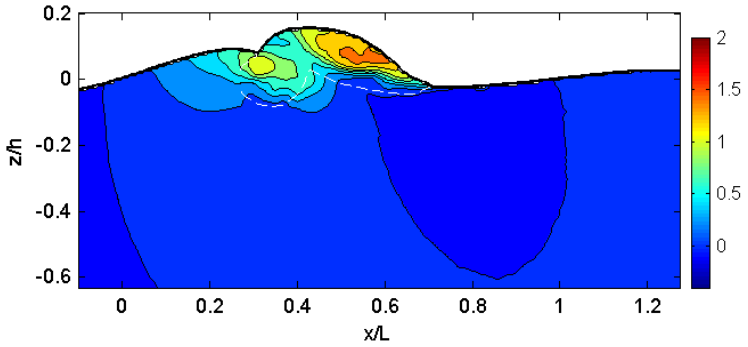

(h) $t = 0.31$ s

Fig. B.2 (Continued).

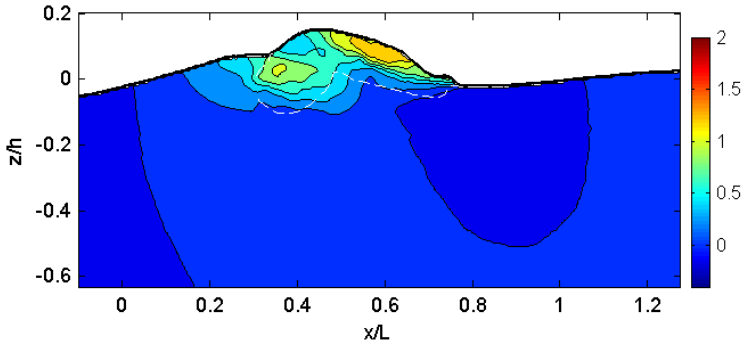

(i) $t = 0.36$ s

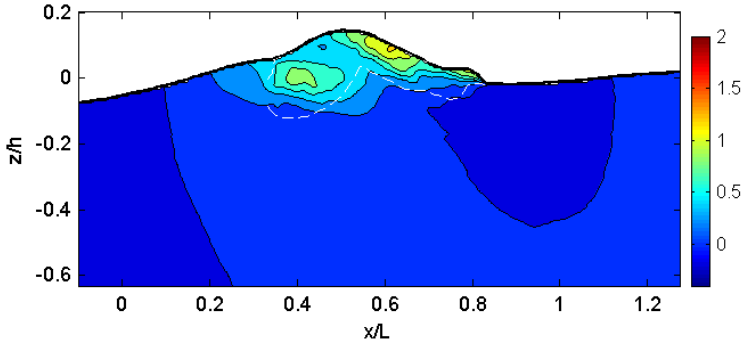

(j) $t = 0.41$ s

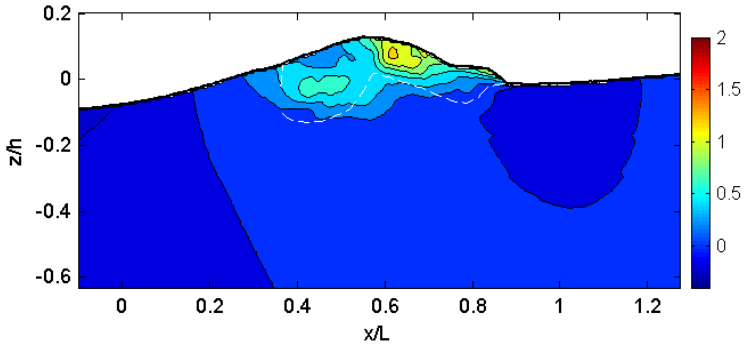

(k) $t = 0.46$ s

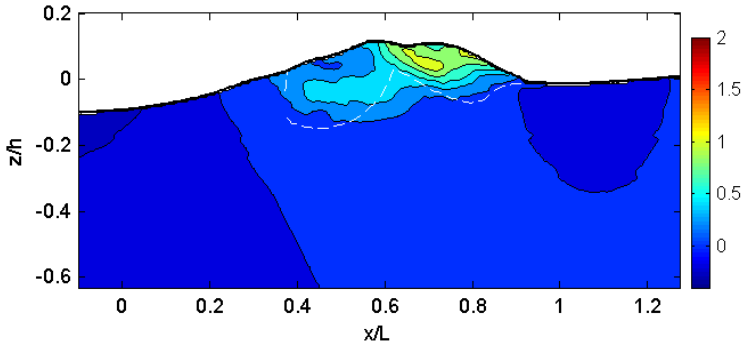

(l) $t = 0.51$ s

Fig. B.2 (Continued).

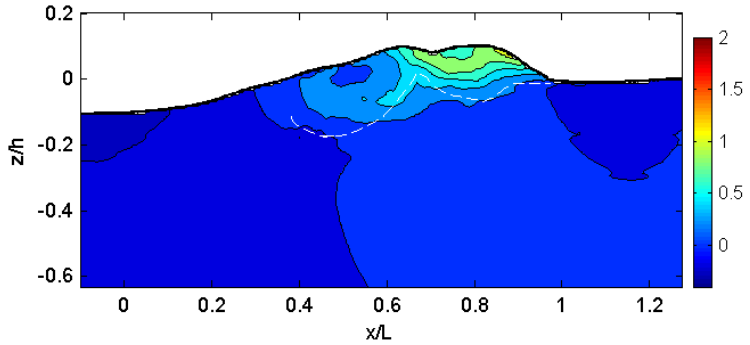

(m) $t = 0.56$ s

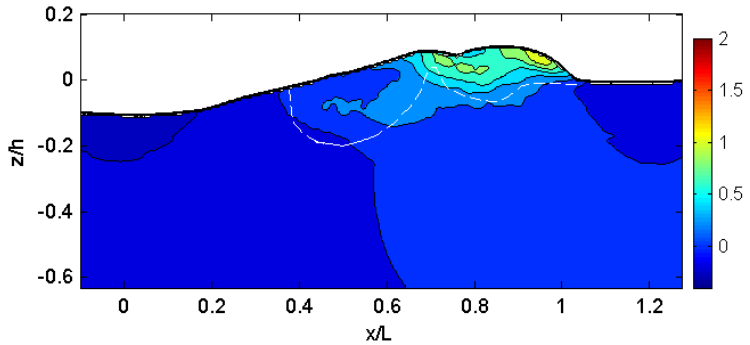

(n) $t = 0.61$ s

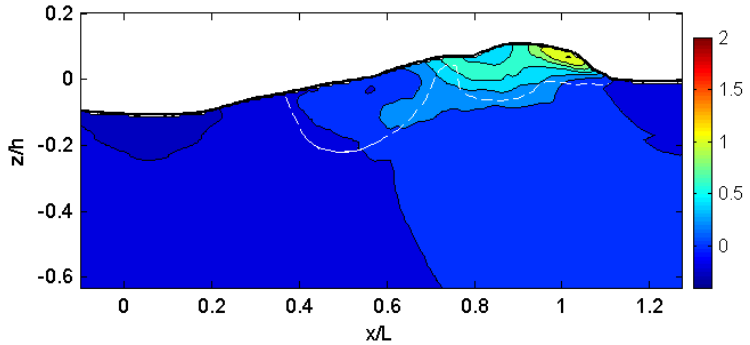

(o) $t = 0.66$ s

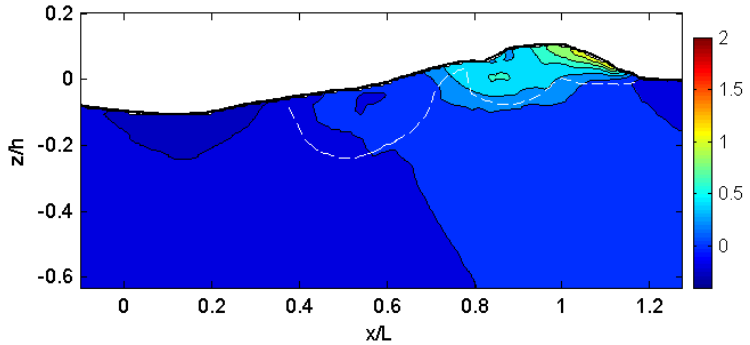

(p) $t = 0.71$ s

Fig. B.2 (Continued).

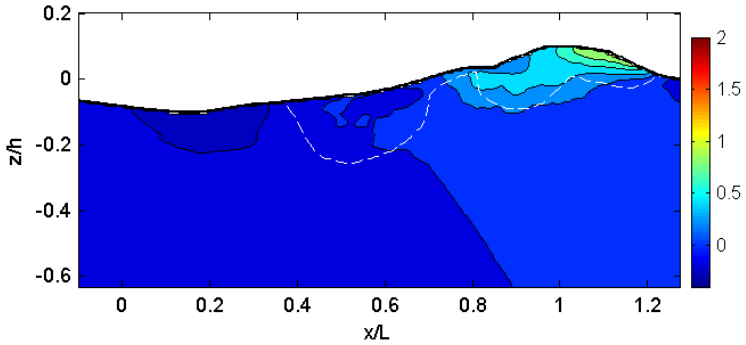

(q) t = 0.76 s

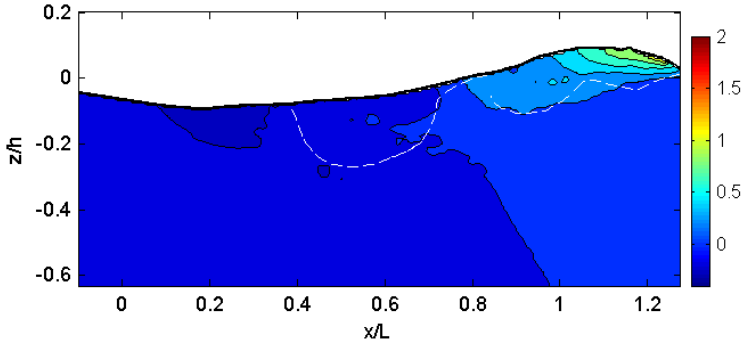

(r) t = 0.81 s

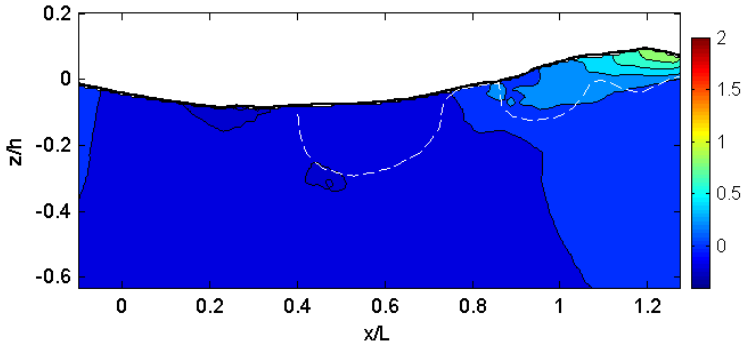

(s) t = 0.86 s

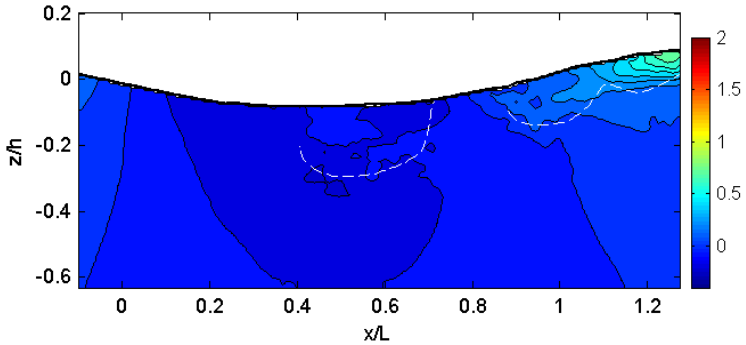

(t) t = 0.91 s

Fig. B.2 (Continued).

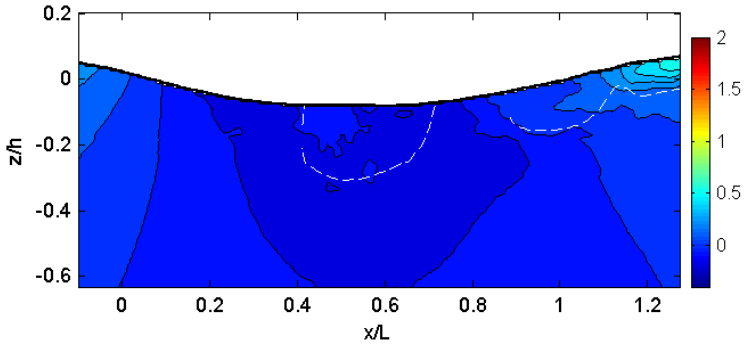

(u) t = 0.96 s

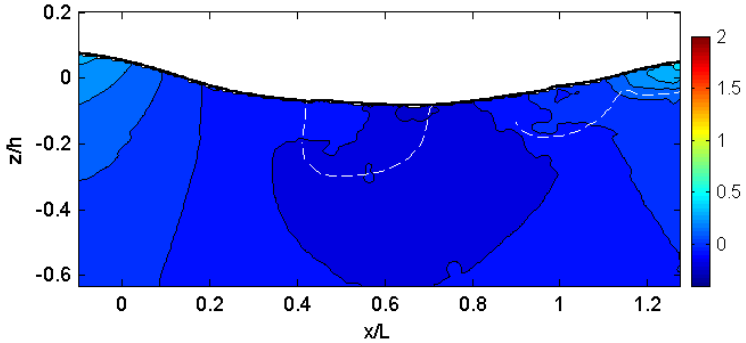

(v) t = 1.01 s

Fig. B.2 (Continued).

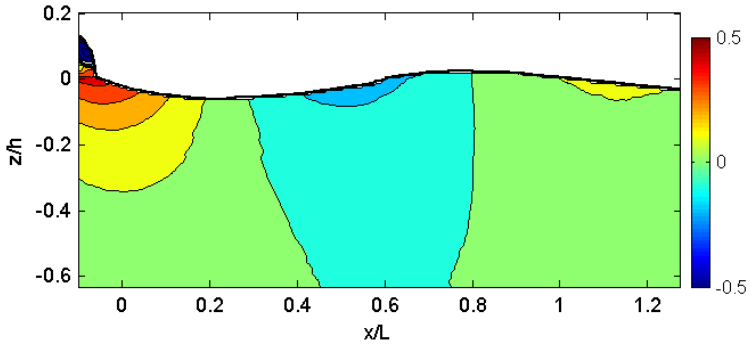

(a) t = -0.04 s

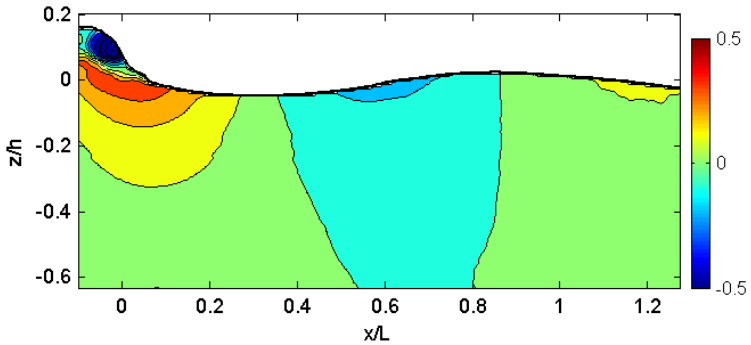

(b) t = 0.01 s

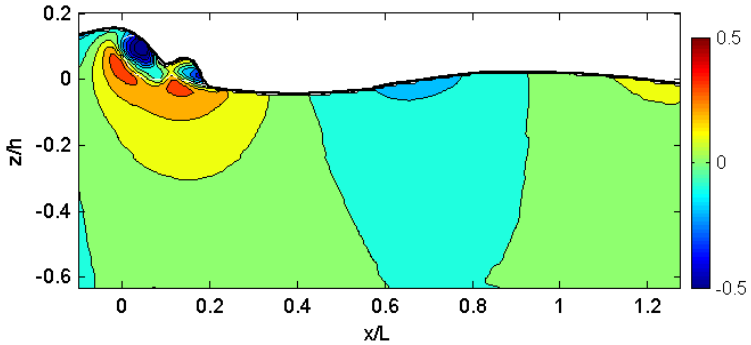

(c) t = 0.06 s

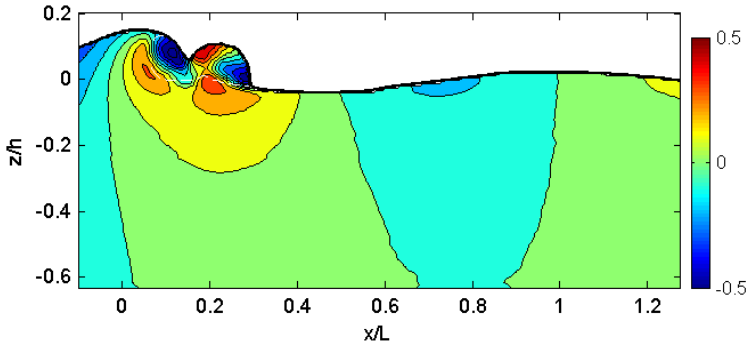

(d) t = 0.11 s

Fig. B.3 Normalized vertical velocity, *W/C*.

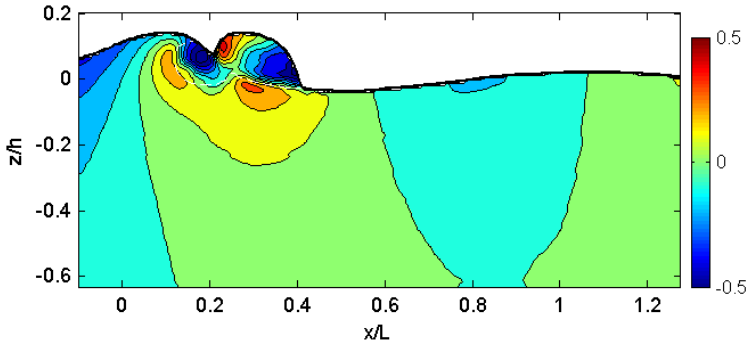

(e) $t = 0.16$ s

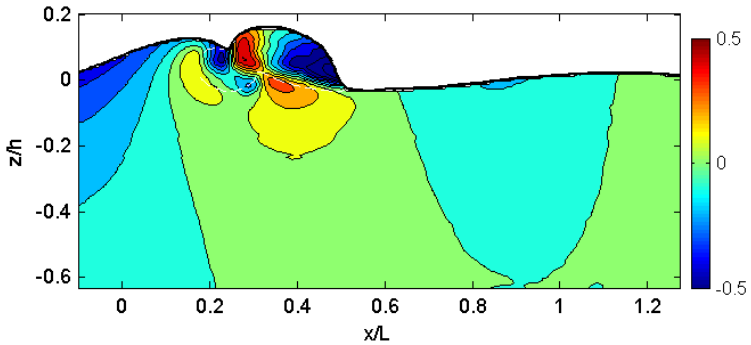

(f) $t = 0.21$ s

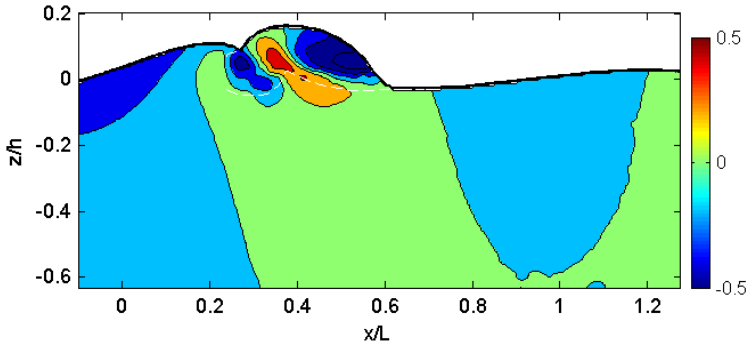

(g) $t = 0.26$ s

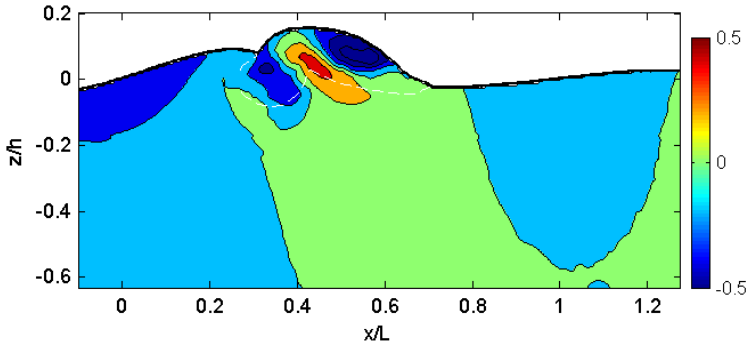

(h) $t = 0.31$ s

Fig. B.3 (Continued).

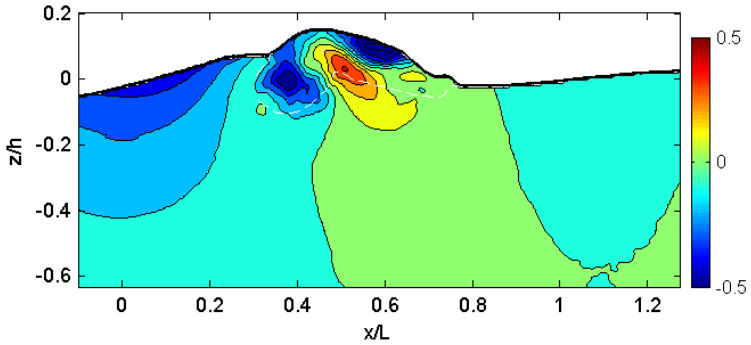

(i) $t = 0.36$ s

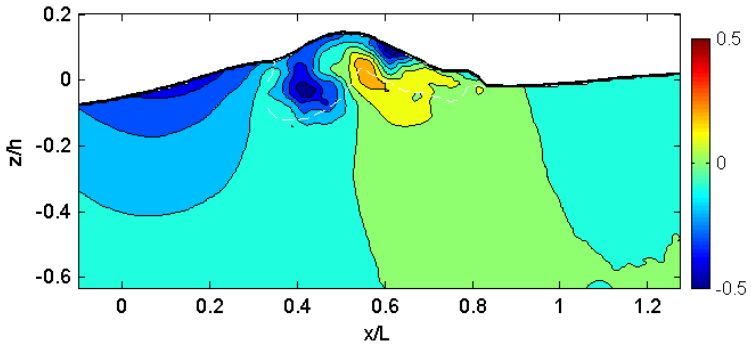

(j) $t = 0.41$ s

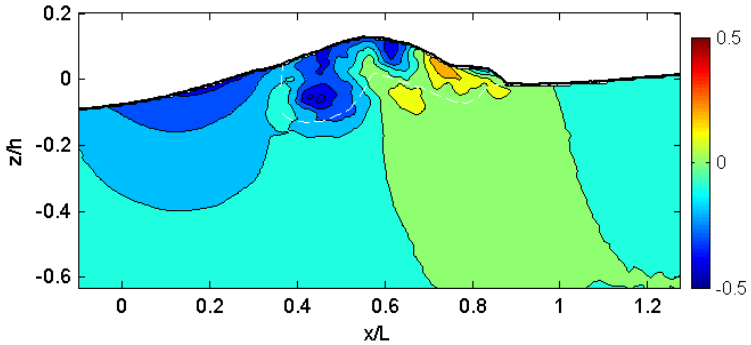

(k) $t = 0.46$ s

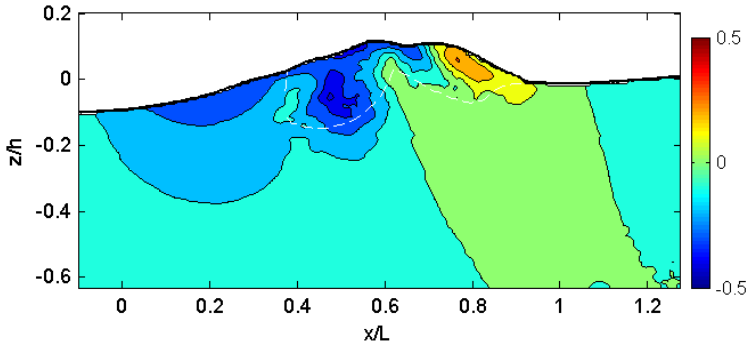

(l) $t = 0.51$ s

Fig. B.3 (Continued).

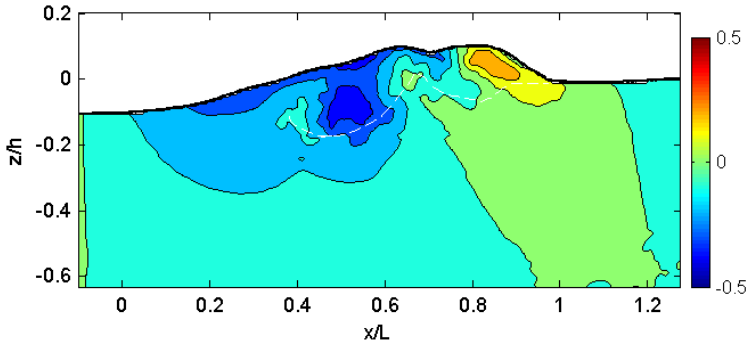

(m) $t = 0.56$ s

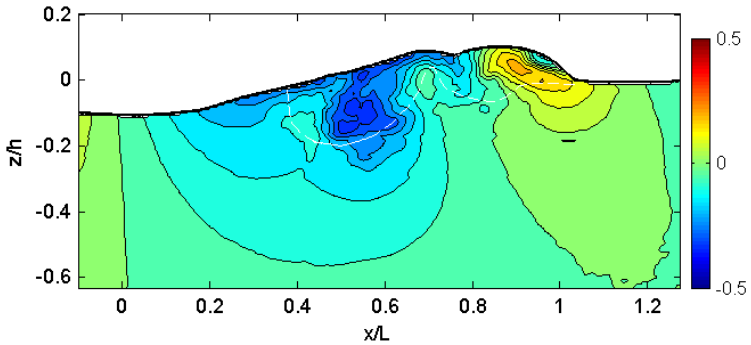

(n) $t = 0.61$ s

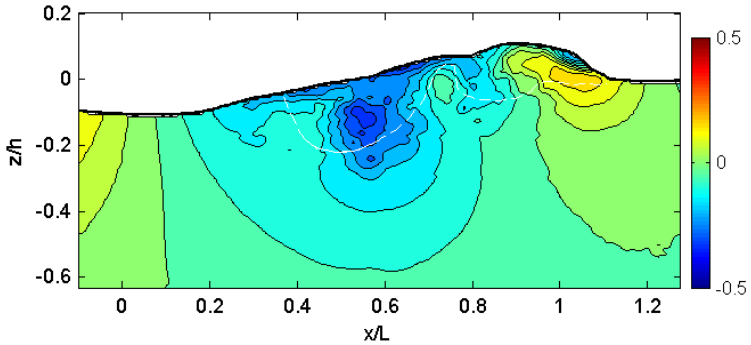

(o) $t = 0.66$ s

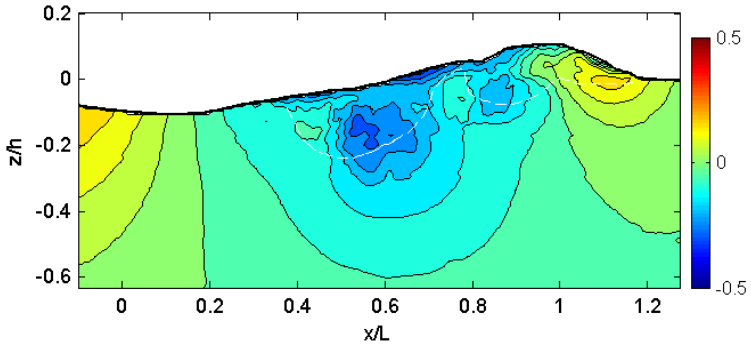

(p) $t = 0.71$ s

Fig. B.3 (Continued).

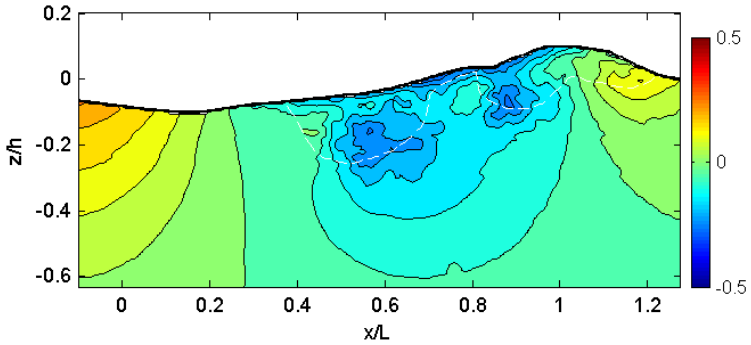

(q) t = 0.76 s

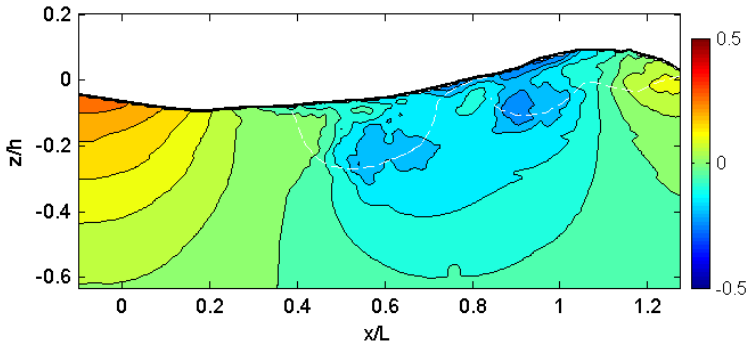

(r) t = 0.81 s

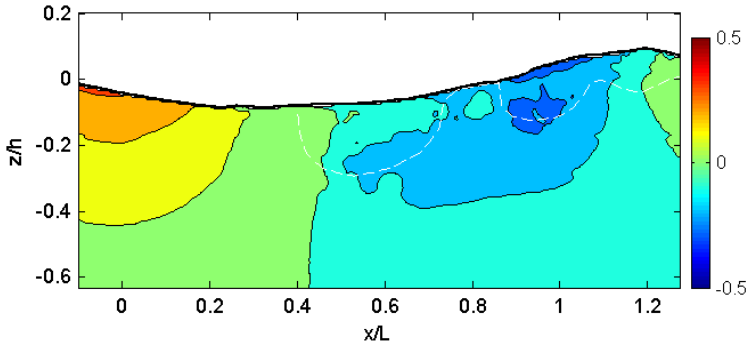

(s) t = 0.86 s

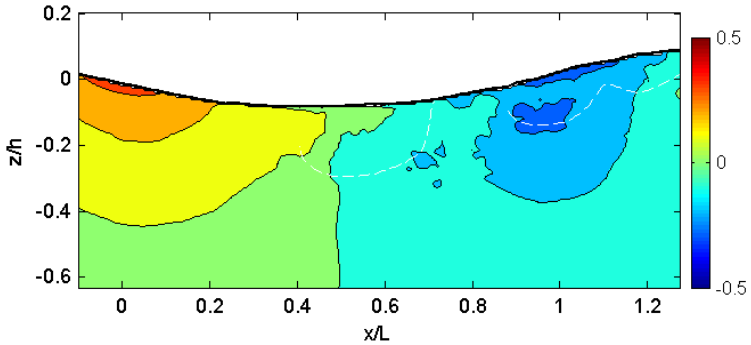

(t) t = 0.91 s

Fig. B.3 (Continued).

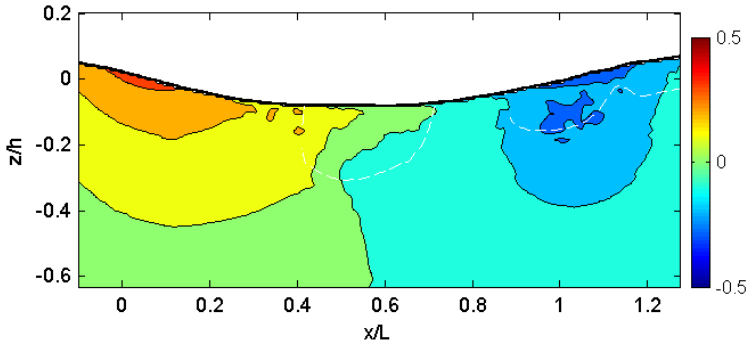

(u) t = 0.96 s

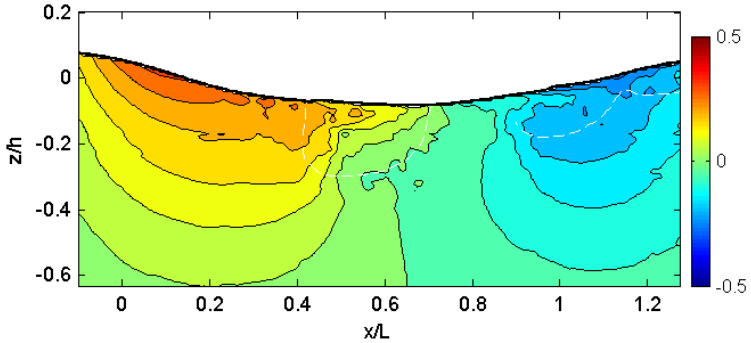

(v) t = 1.01 s

Fig. B.3 (Continued).

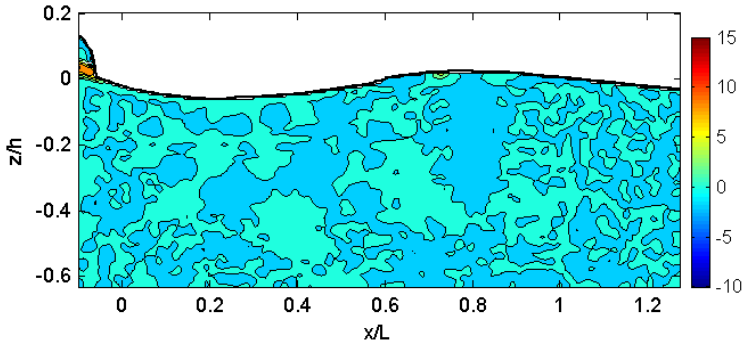

(a) t = -0.04 s

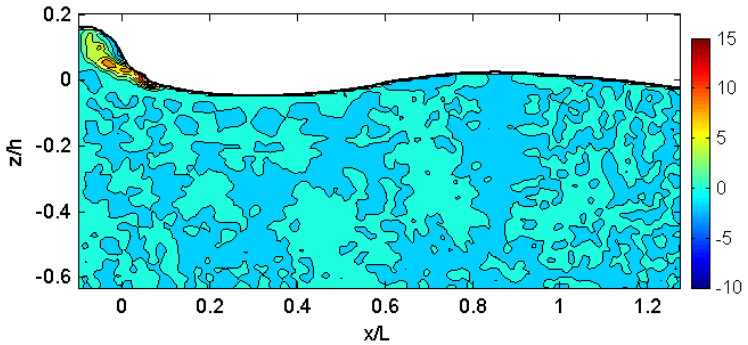

(b) t = 0.01 s

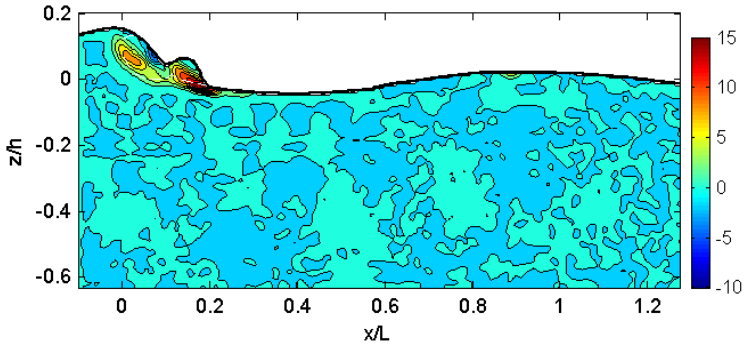

(c) t = 0.06 s

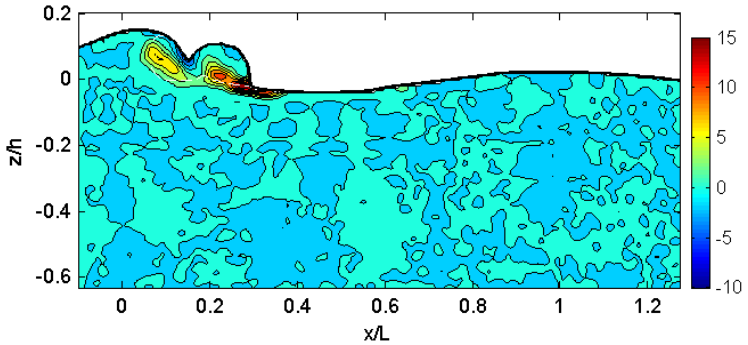

(d) t = 0.11 s

Fig. B.4 Normalized mean vorticity, $\Omega H/C$.

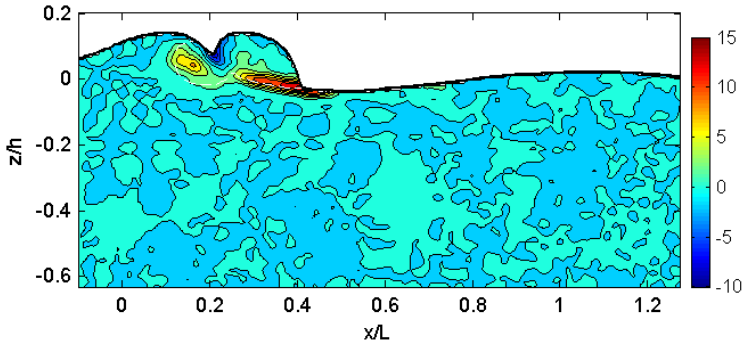

(e) $t = 0.16$ s

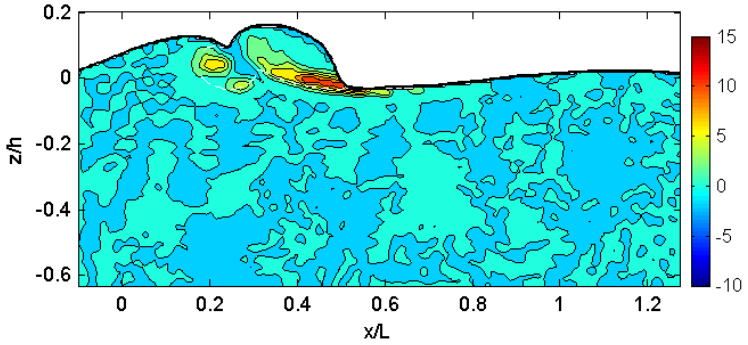

(f) $t = 0.21$ s

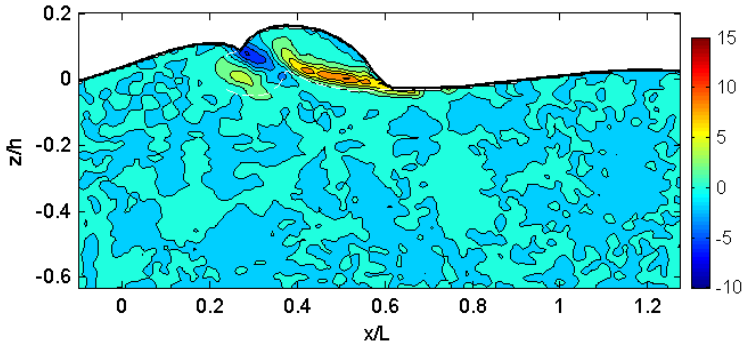

(g) $t = 0.26$ s

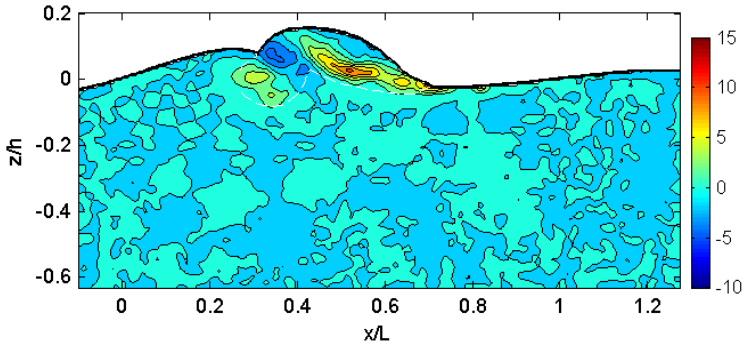

(h) $t = 0.31$ s

Fig. B.4 (Continued).

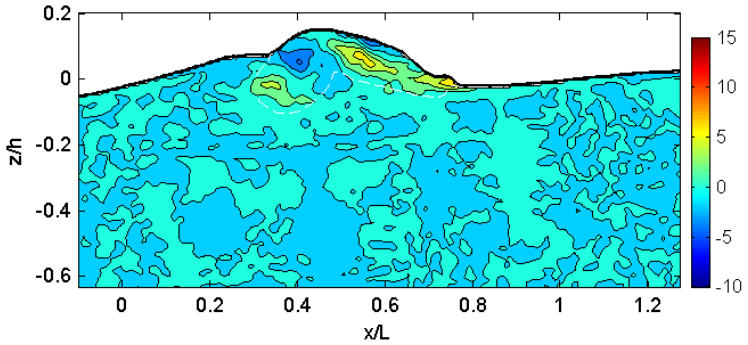

(i) $t = 0.36$ s

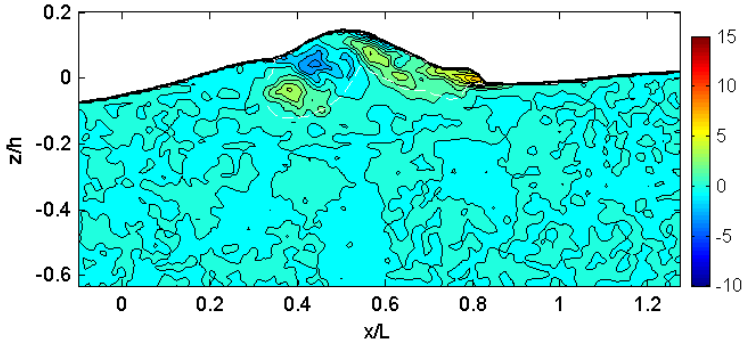

(j) $t = 0.41$ s

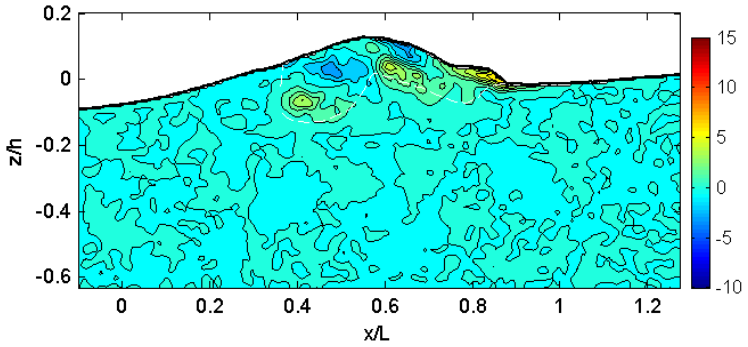

(k) $t = 0.46$ s

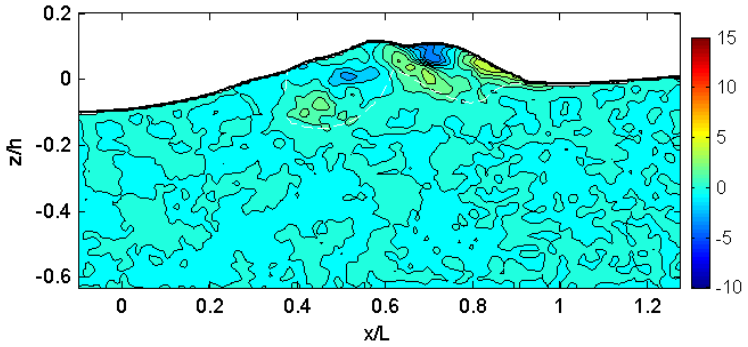

(l) $t = 0.51$ s

Fig. B.4 (Continued).

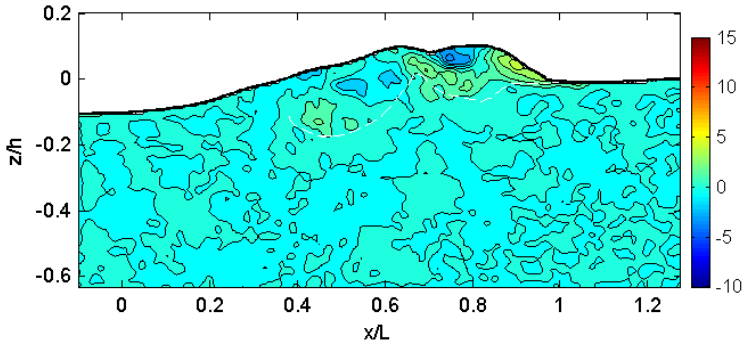

(m) $t = 0.56$ s

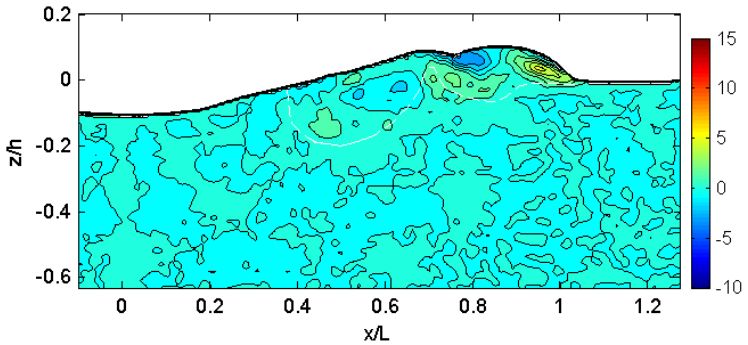

(n) $t = 0.61$ s

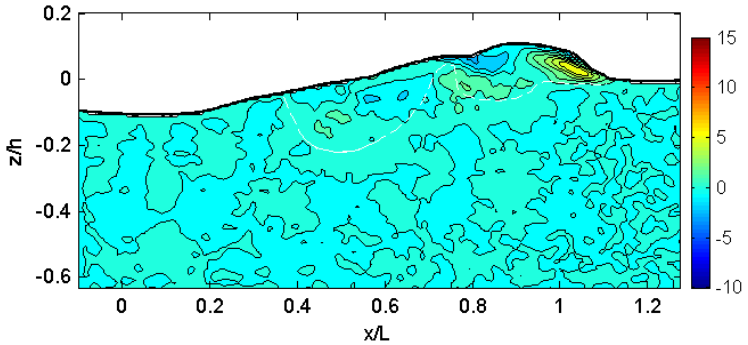

(o) $t = 0.66$ s

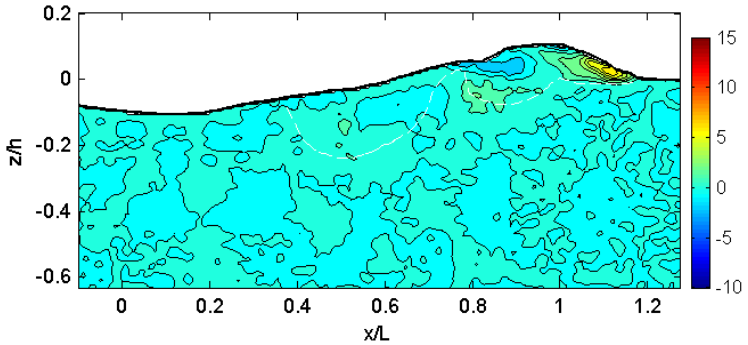

(p) $t = 0.71$ s

Fig. B.4 (Continued).

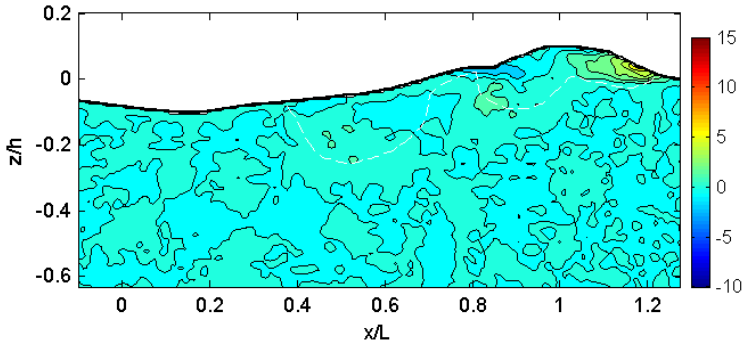

(q) $t = 0.76$ s

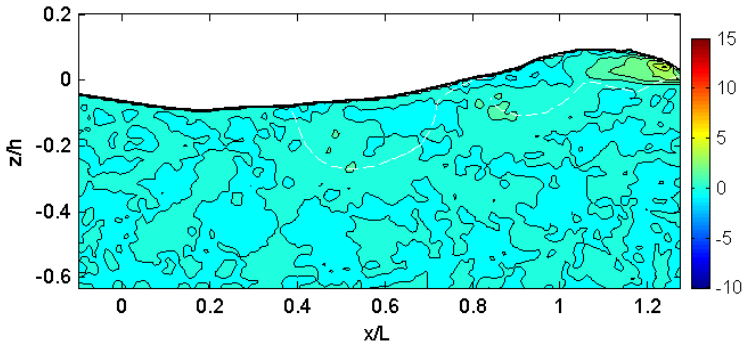

(r) $t = 0.81$ s

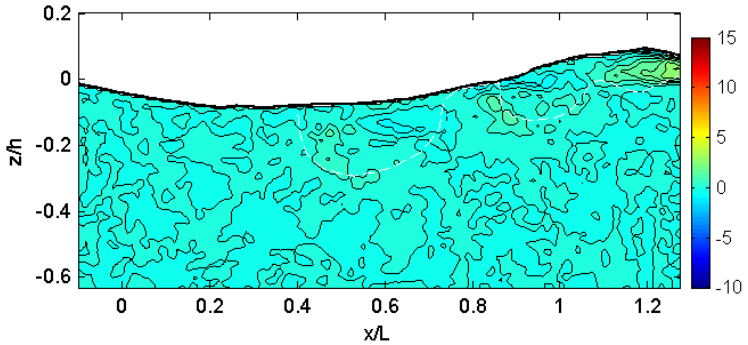

(s) $t = 0.86$ s

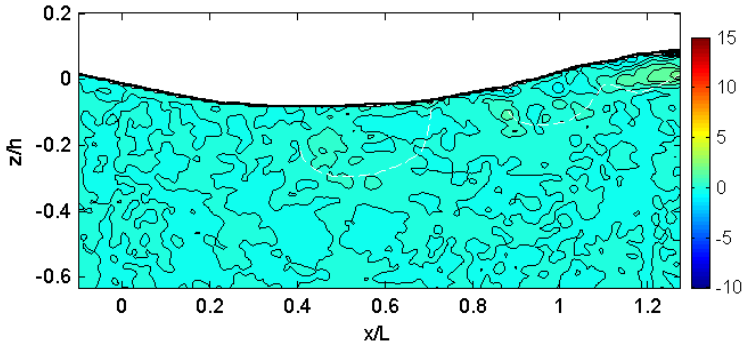

(t) $t = 0.91$ s

Fig. B.4 (Continued).

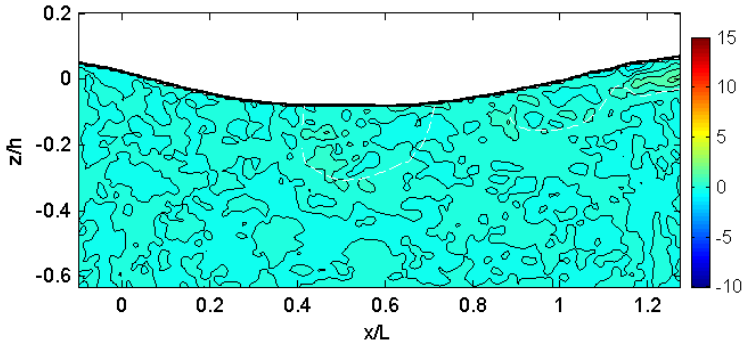

(u) $t = 0.96$ s

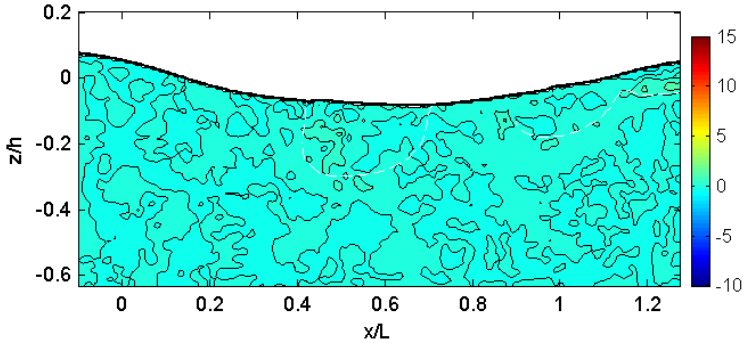

(v) $t = 1.01$ s

Fig. B.4 (Continued).

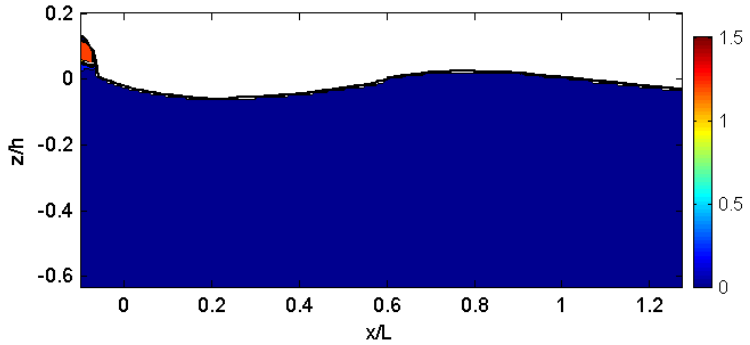

(a) t = -0.04 s

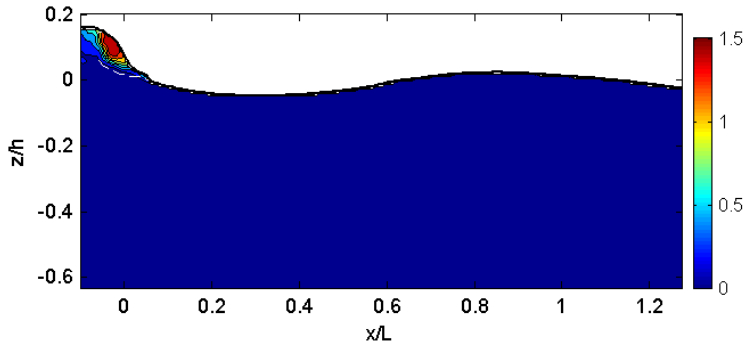

(b) t = 0.01 s

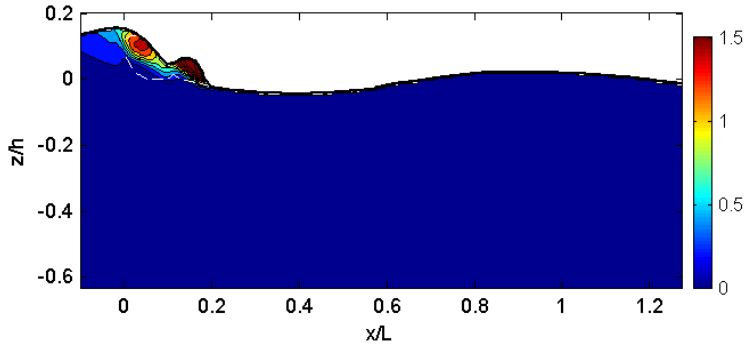

(c) t = 0.06 s

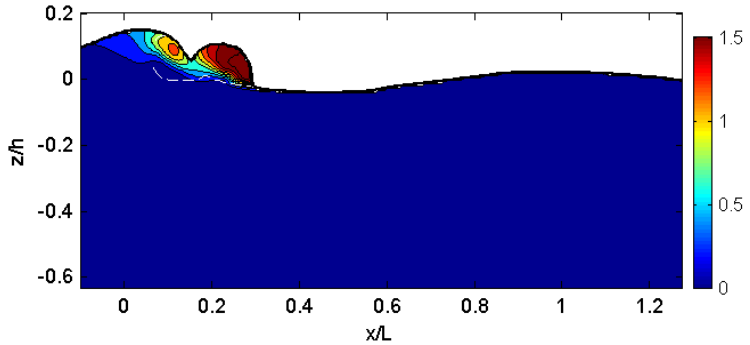

(d) t = 0.11 s

Fig. B.5 Normalized mean kinetic energy, κ/c^2 .

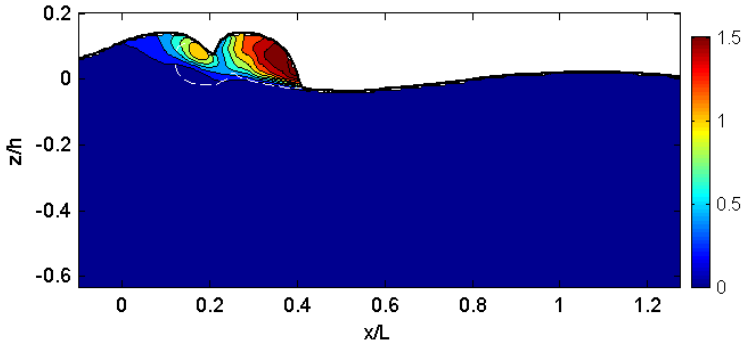

(e) $t = 0.16$ s

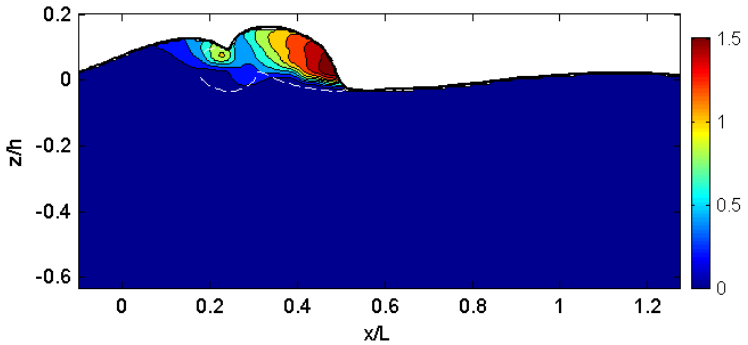

(f) $t = 0.21$ s

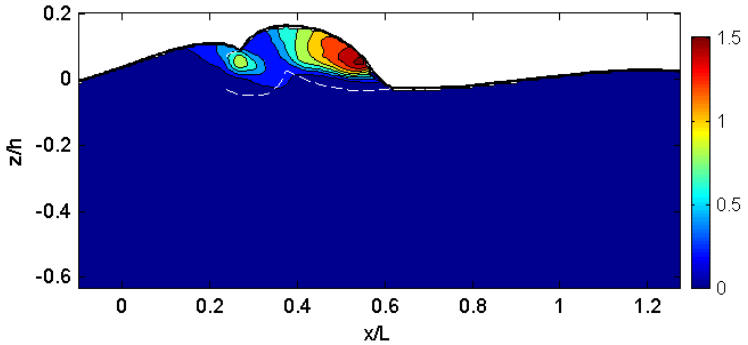

(g) $t = 0.26$ s

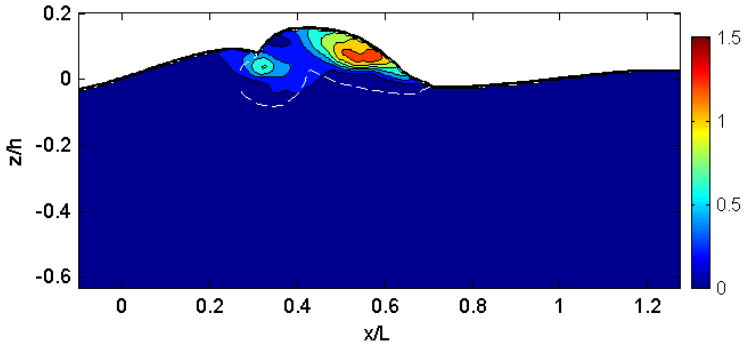

(h) $t = 0.31$ s

Fig. B.5 (Continued).

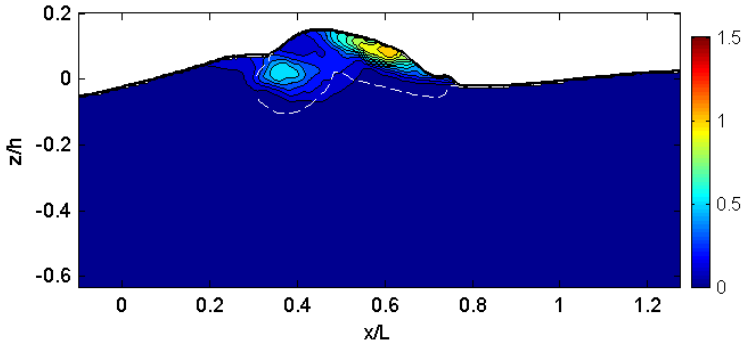

(i) $t = 0.36$ s

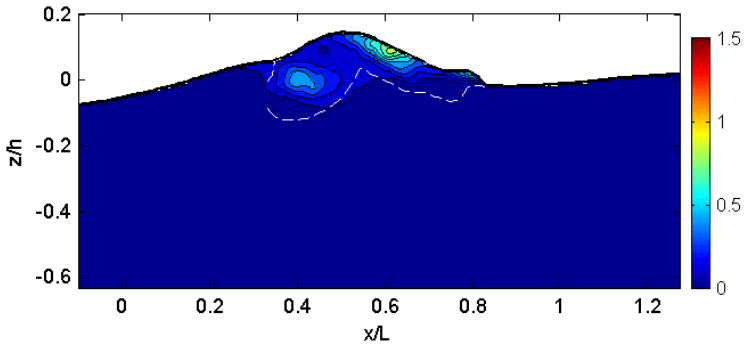

(j) $t = 0.41$ s

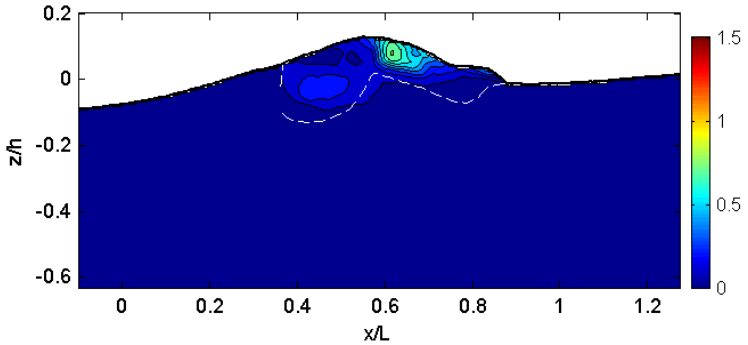

(k) $t = 0.46$ s

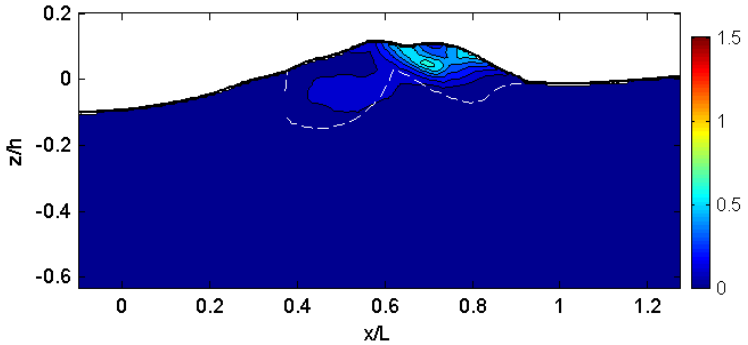

(l) $t = 0.51$ s

Fig. B.5 (Continued).

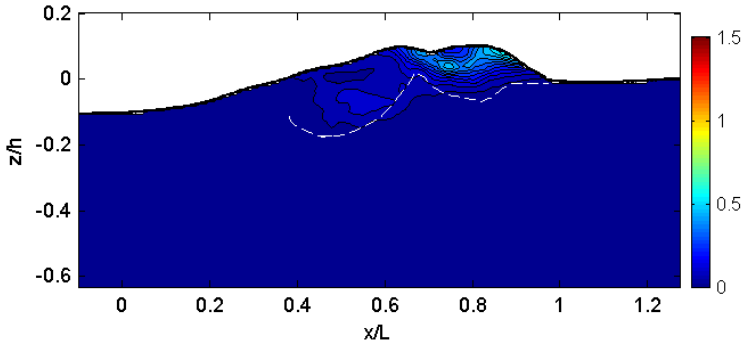

(m) $t = 0.56$ s

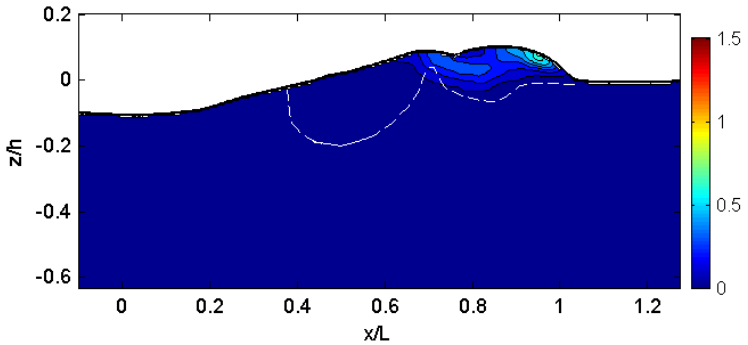

(n) $t = 0.61$ s

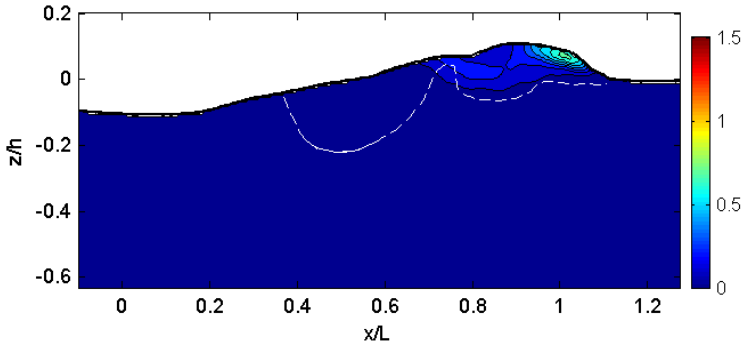

(o) $t = 0.66$ s

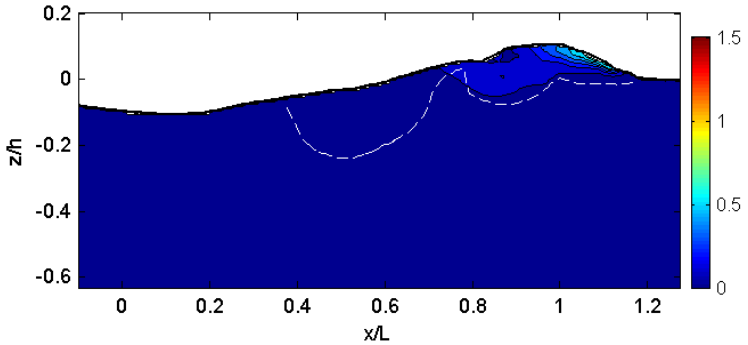

(p) $t = 0.71$ s

Fig. B.5 (Continued).

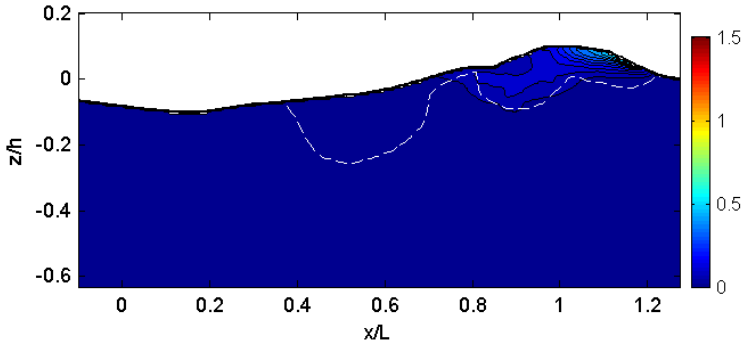

(q) $t = 0.76$ s

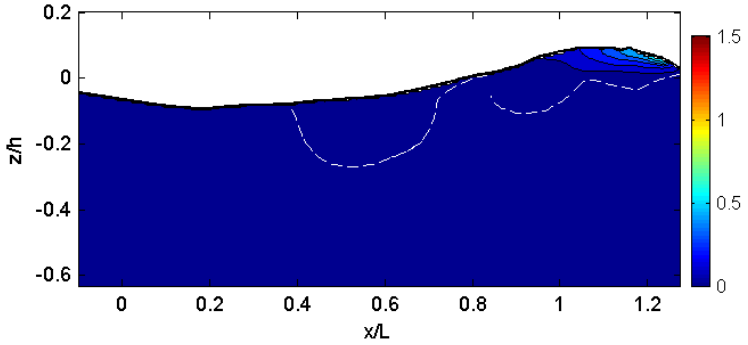

(r) $t = 0.81$ s

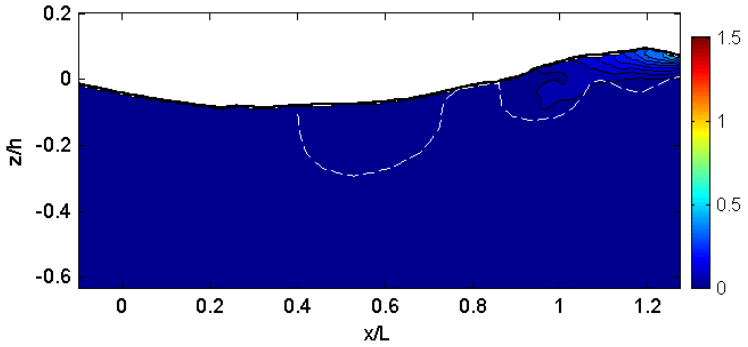

(s) $t = 0.86$ s

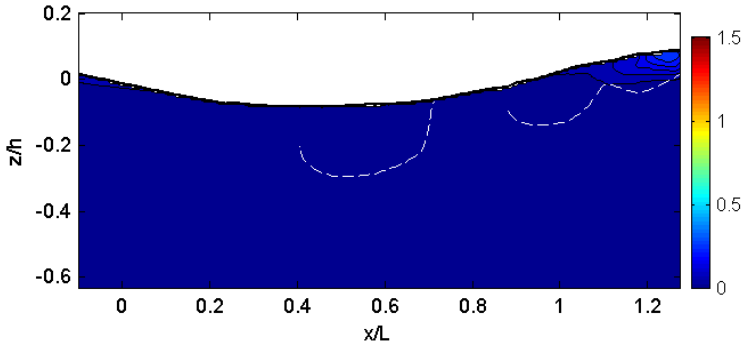

(t) $t = 0.91$ s

Fig. B.5 (Continued).

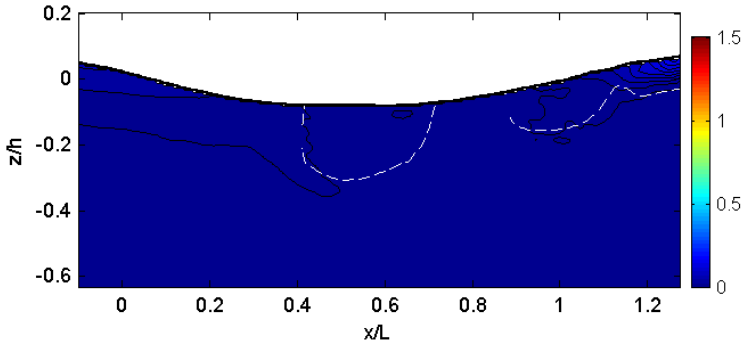

(u) t = 0.96 s

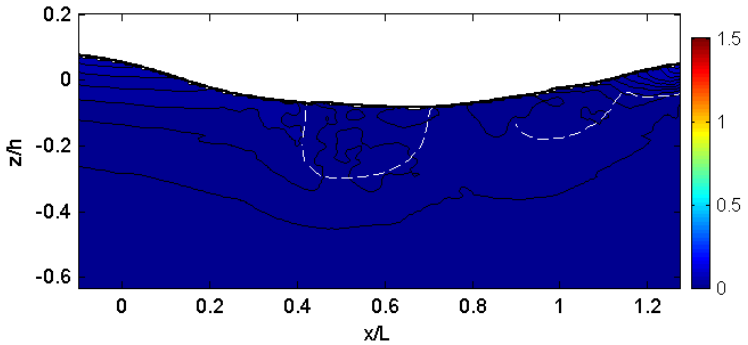

(v) t = 1.01 s

Fig. B.5 (Continued).

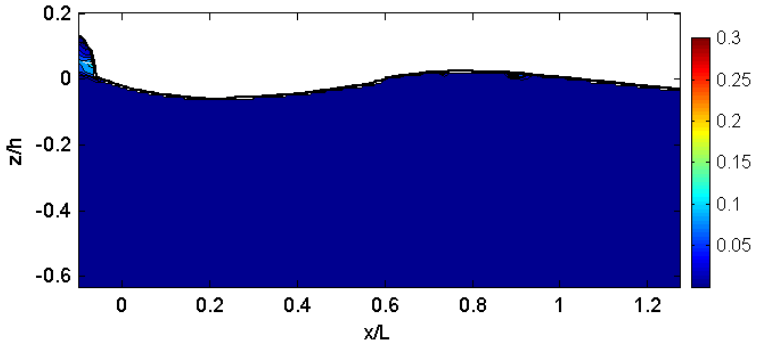

(a) t = -0.04 s

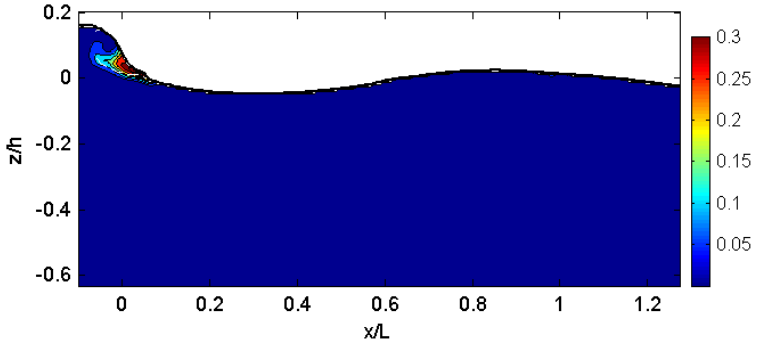

(b) t = 0.01 s

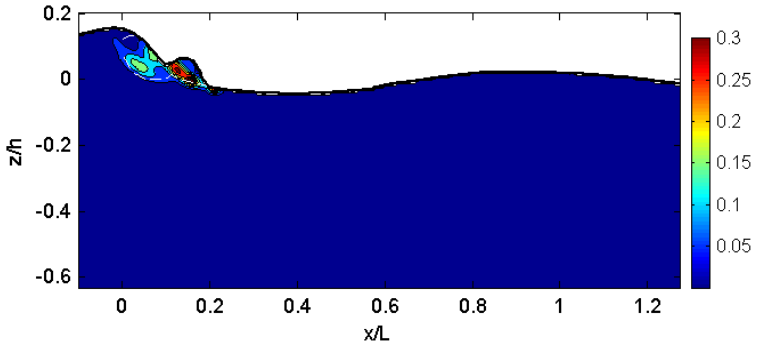

(c) t = 0.06 s

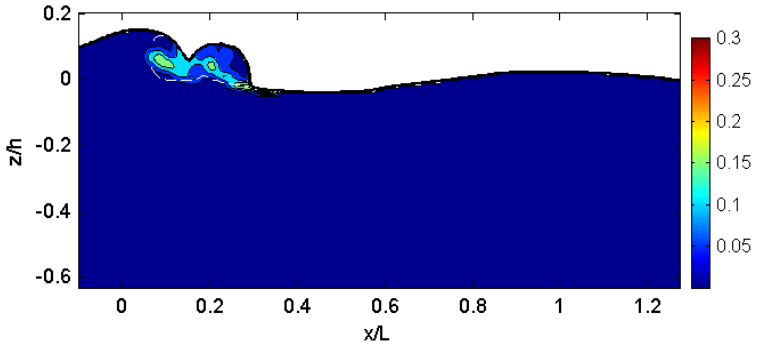

(d) t = 0.11 s

Fig. B.6 Normalized turbulent kinetic energy, k/C^2 .

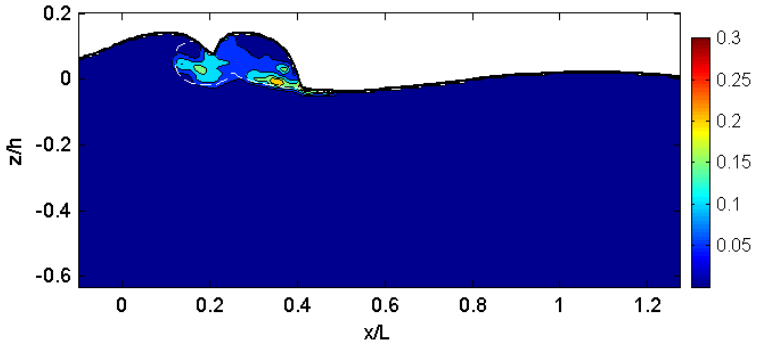

(e) $t = 0.16$ s

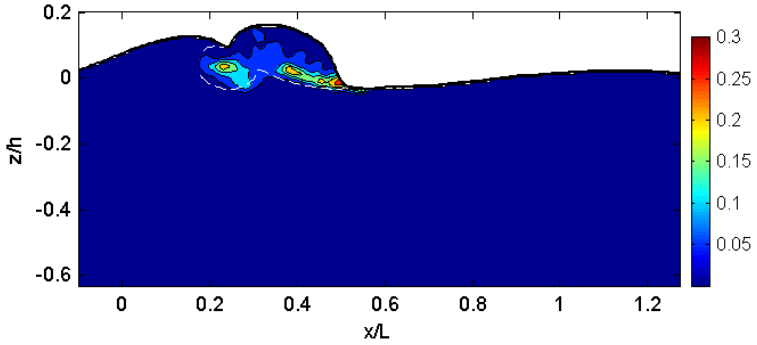

(f) $t = 0.21$ s

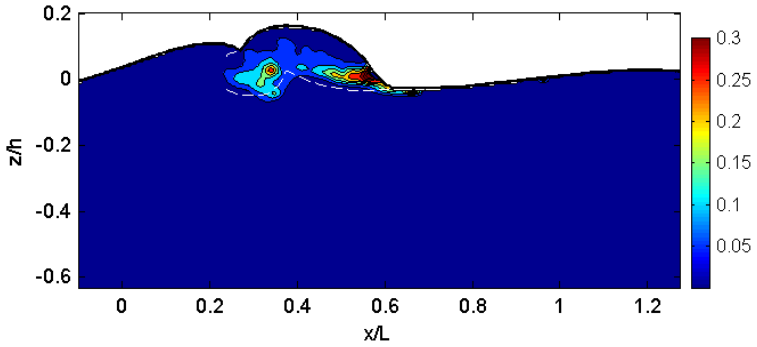

(g) $t = 0.26$ s

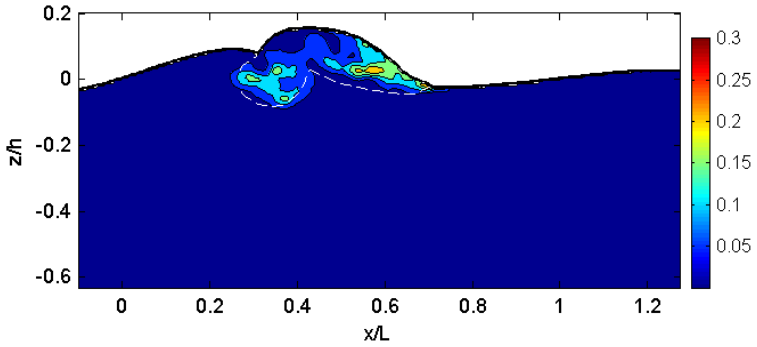

(h) $t = 0.31$ s

Fig. B.6 (Continued).

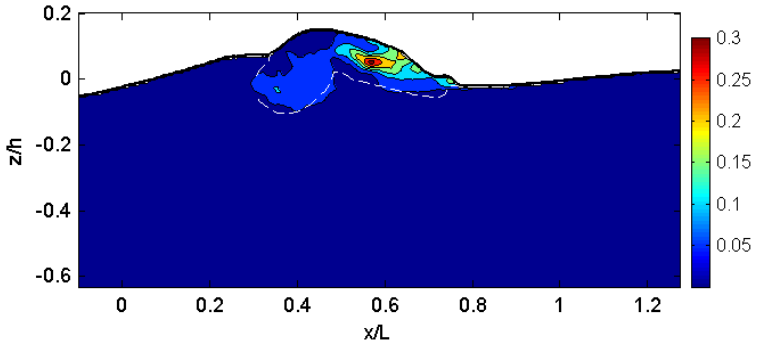

(i) $t = 0.36$ s

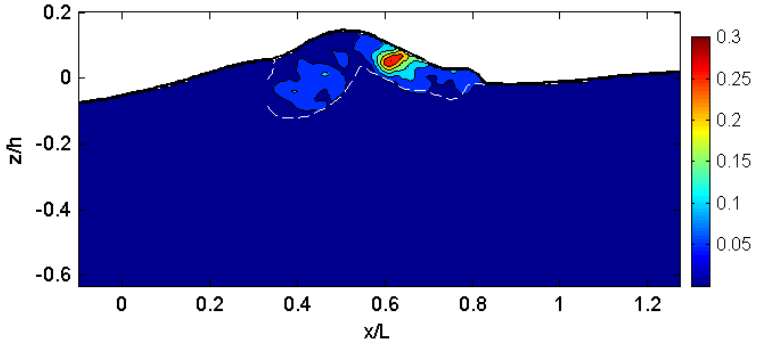

(j) $t = 0.41$ s

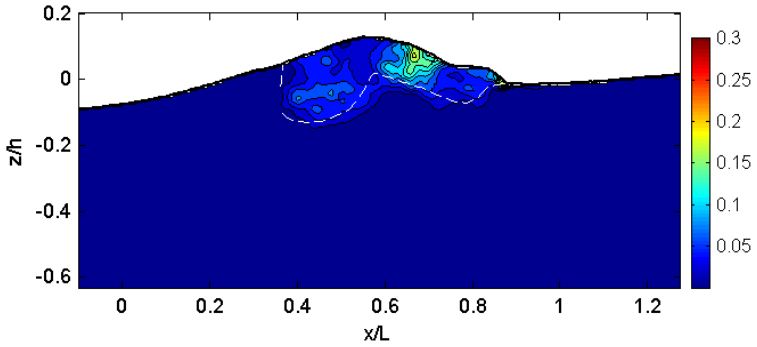

(k) $t = 0.46$ s

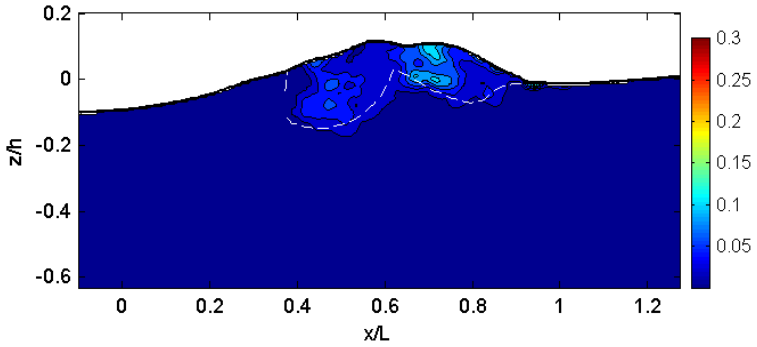

(l) $t = 0.51$ s

Fig. B.6 (Continued).

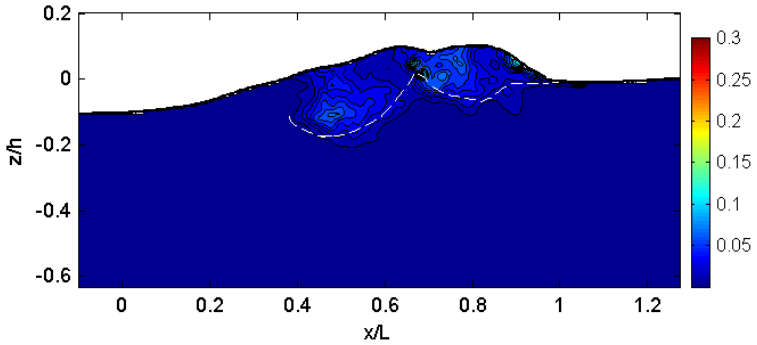

(m) $t = 0.56$ s

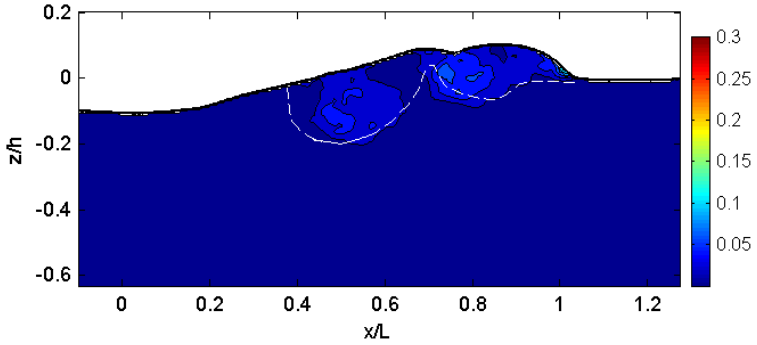

(n) $t = 0.61$ s

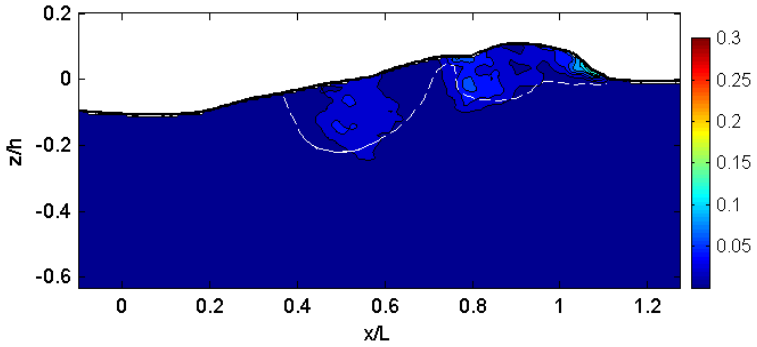

(o) $t = 0.66$ s

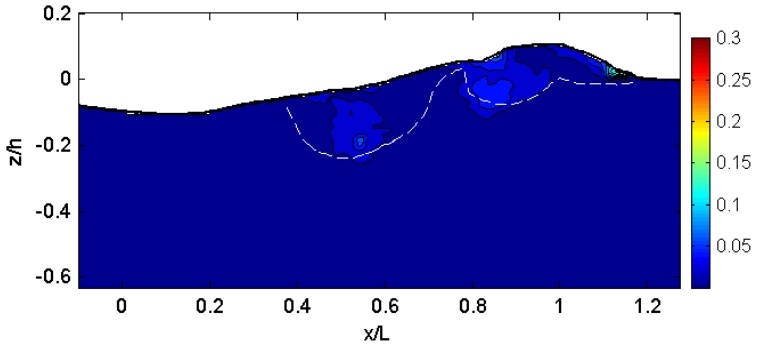

(p) $t = 0.71$ s

Fig. B.6 (Continued).

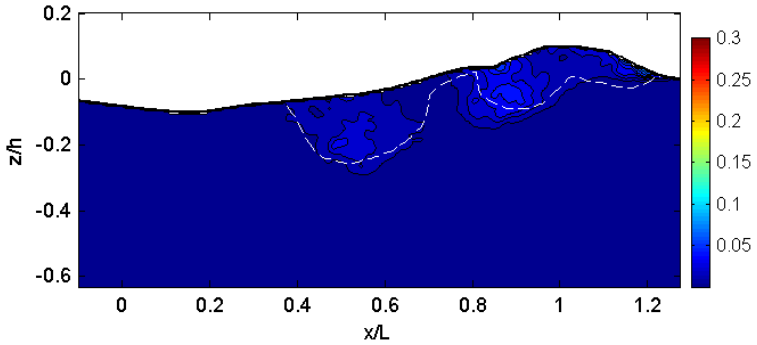

(q) t = 0.76 s

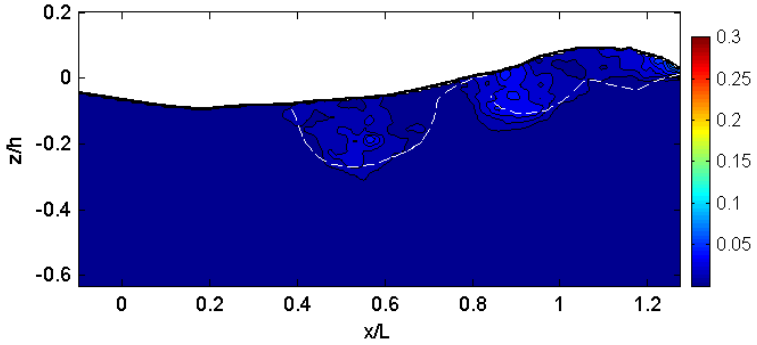

(r) t = 0.81 s

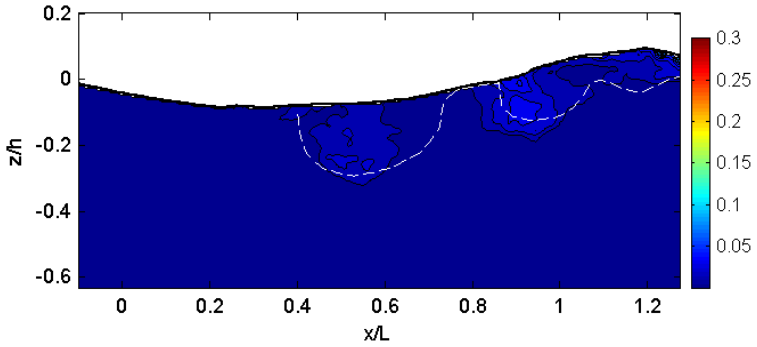

(s) t = 0.86 s

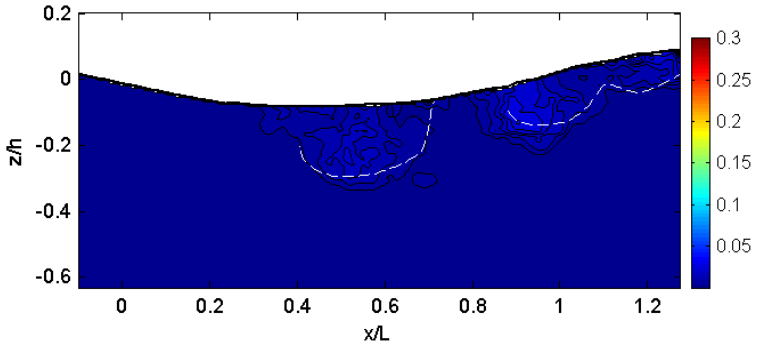

(t) t = 0.91 s

Fig. B.6 (Continued).

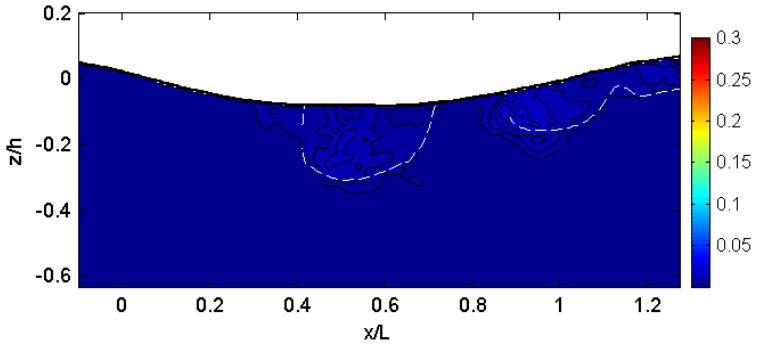

(u) t = 0.96 s

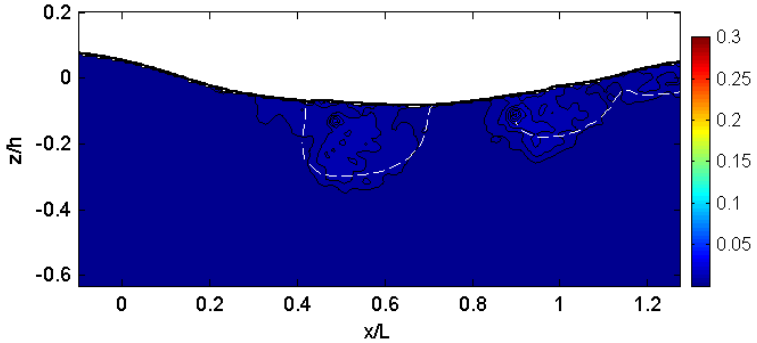

(v) t = 1.01 s

Fig. B.6 (Continued).

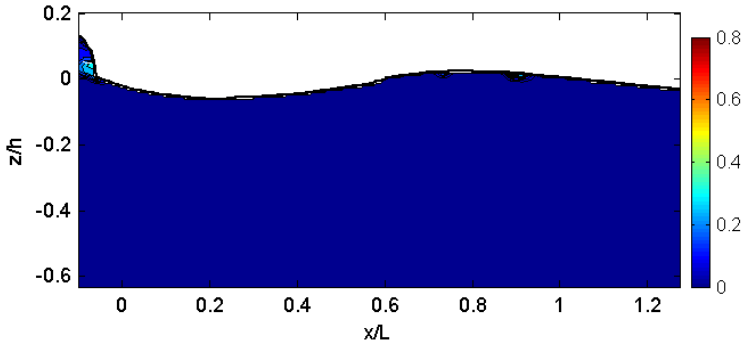

(a) t = -0.04 s

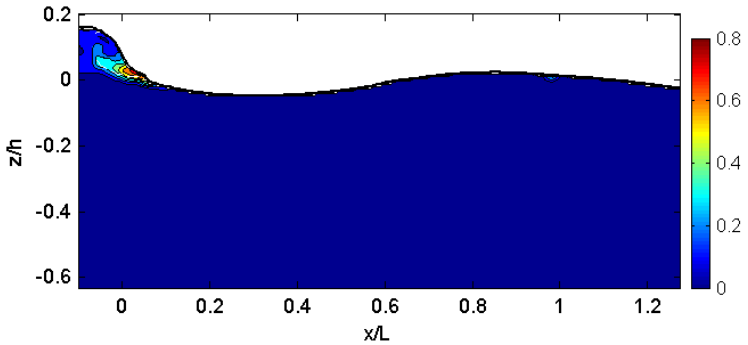

(b) t = 0.01 s

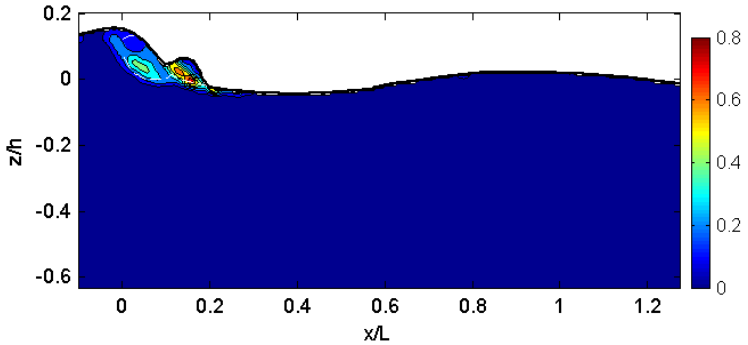

(c) t = 0.06 s

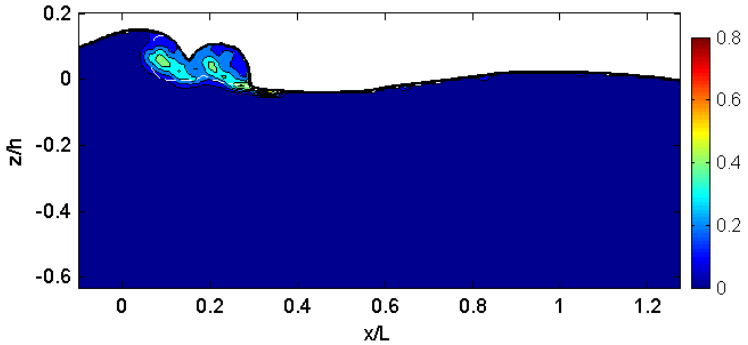

(d) t = 0.11 s

Fig. B.7 Normalized horizontal turbulent intensity, $\sqrt{u^2}/c$.

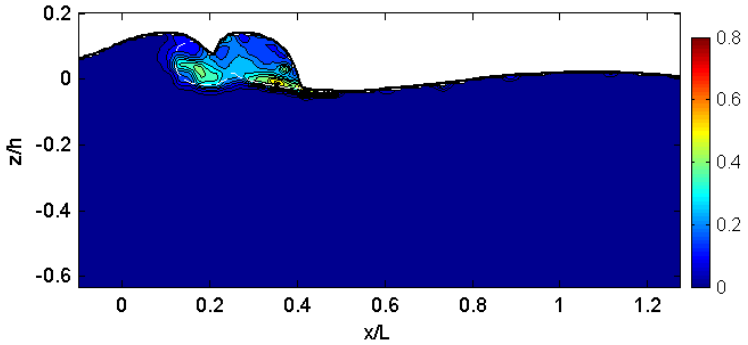

(e) $t = 0.16$ s

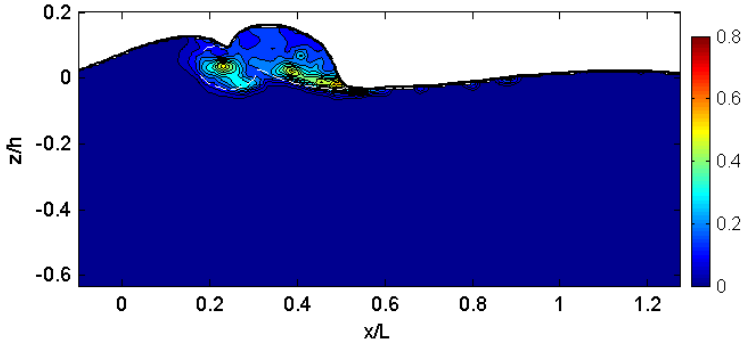

(f) $t = 0.21$ s

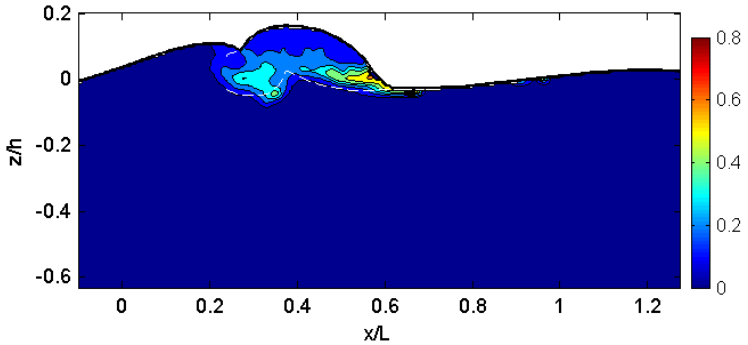

(g) $t = 0.26$ s

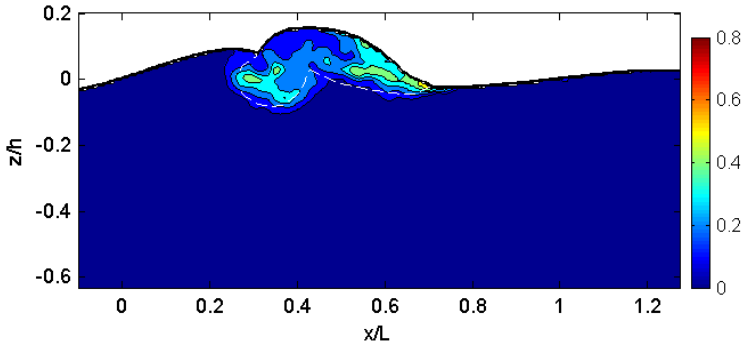

(h) $t = 0.31$ s

Fig. B.7 (Continued).

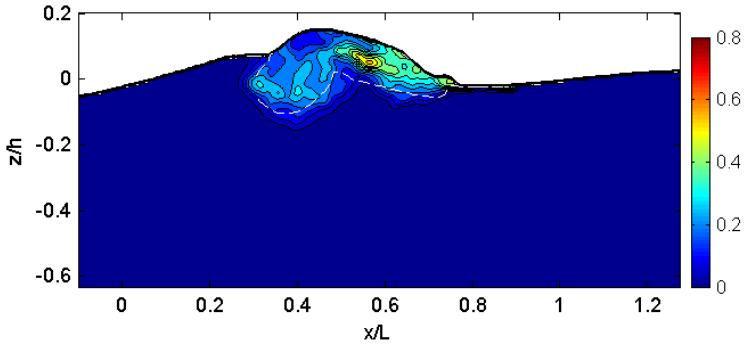

(i) $t = 0.36$ s

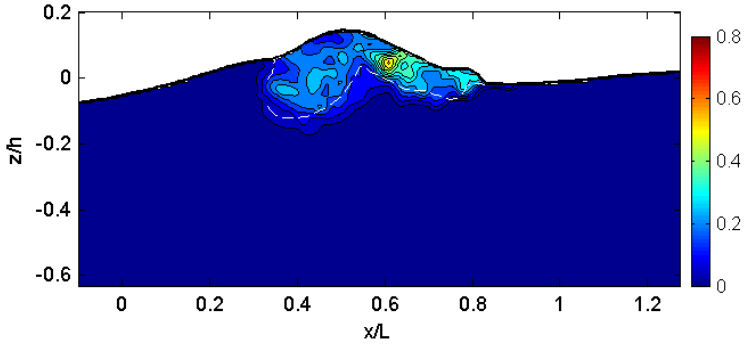

(j) $t = 0.41$ s

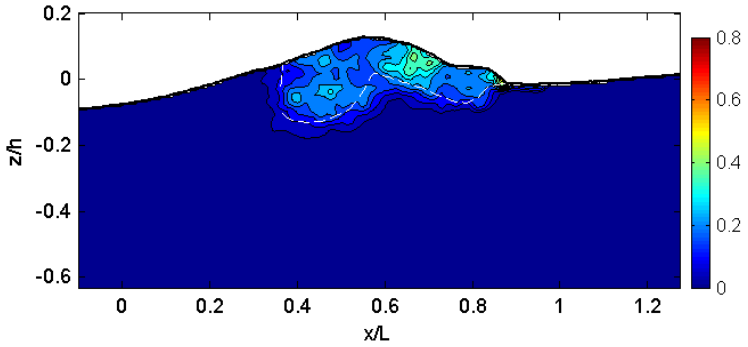

(k) $t = 0.46$ s

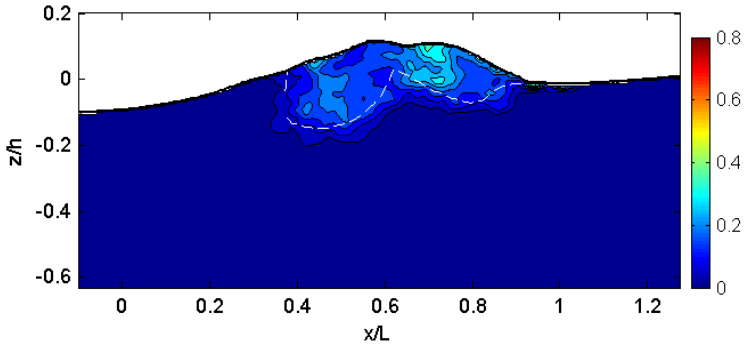

(l) $t = 0.51$ s

Fig. B.7 (Continued).

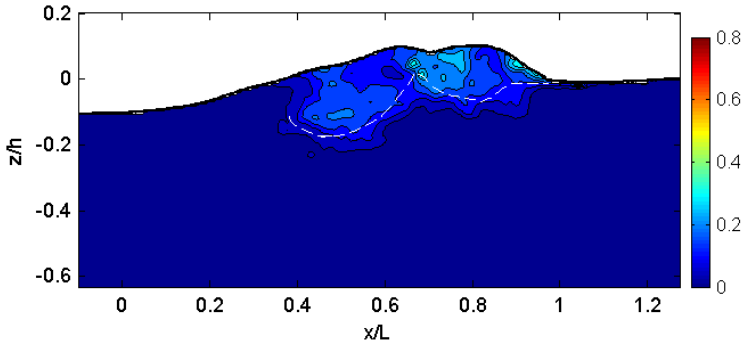

(m) $t = 0.56$ s

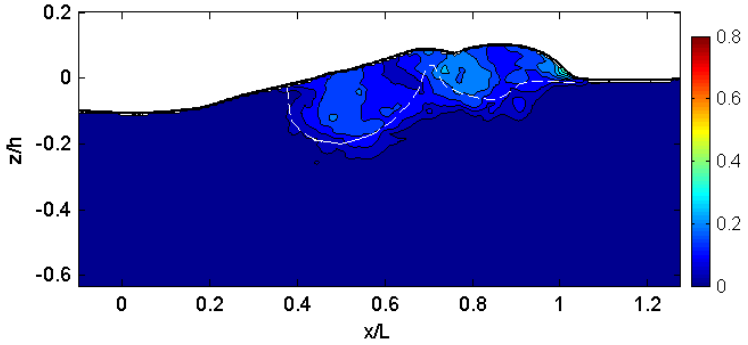

(n) $t = 0.61$ s

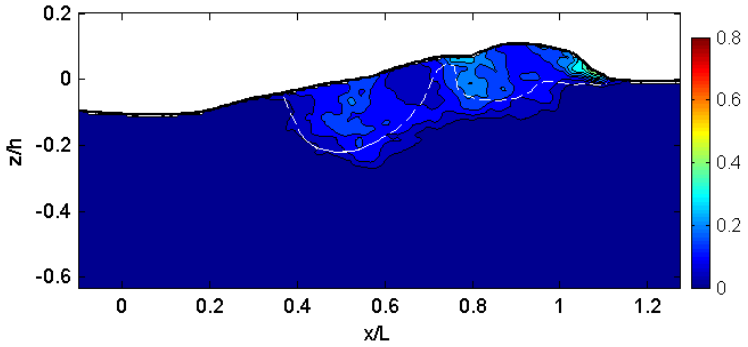

(o) $t = 0.66$ s

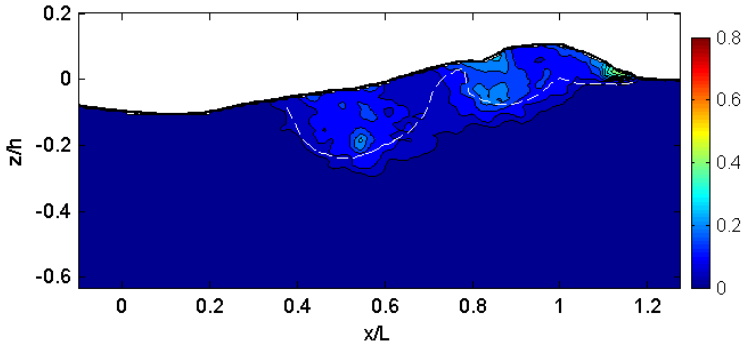

(p) $t = 0.71$ s

Fig. B.7 (Continued).

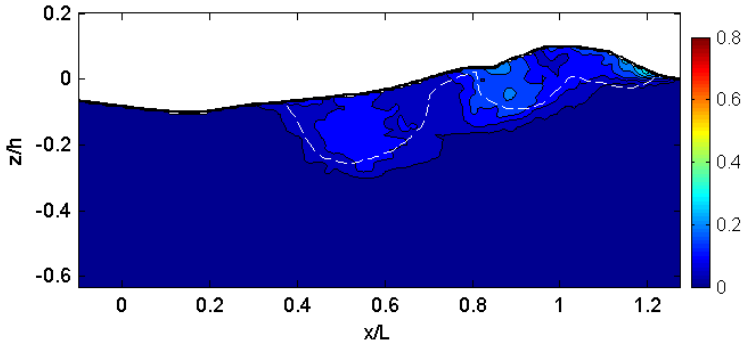

(q) t = 0.76 s

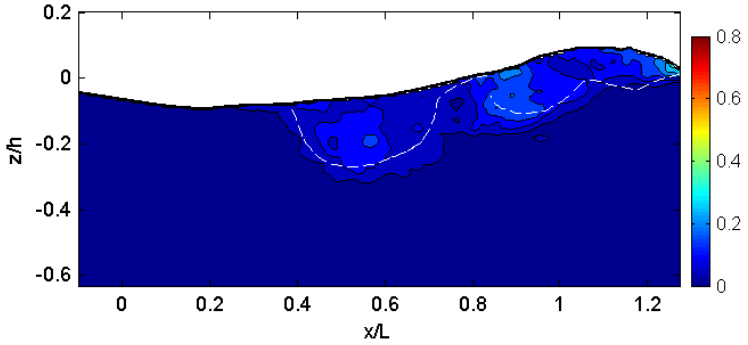

(r) t = 0.81 s

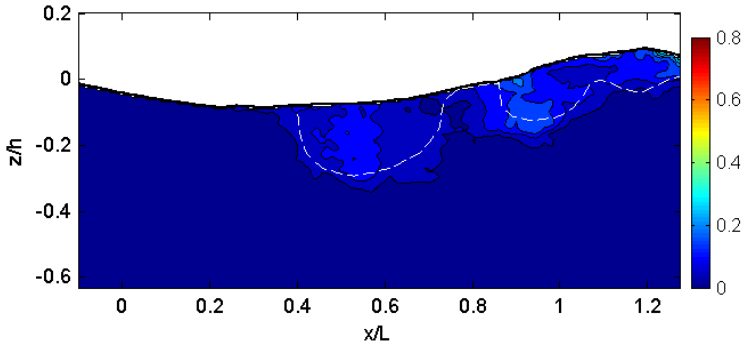

(s) t = 0.86 s

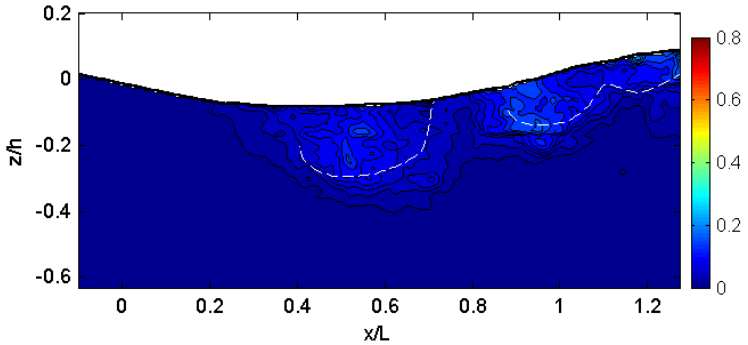

(t) t = 0.91 s

Fig. B.7 (Continued).

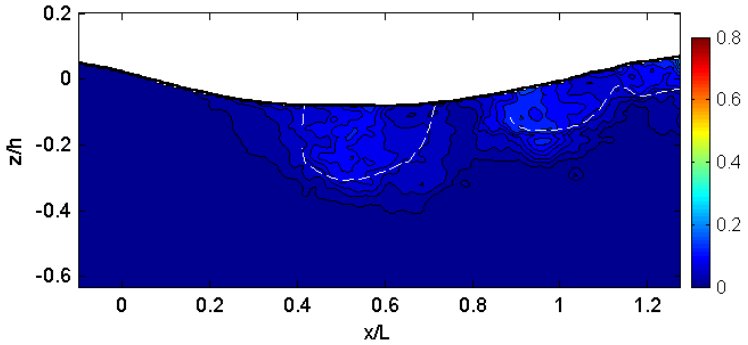

(u) t = 0.96 s

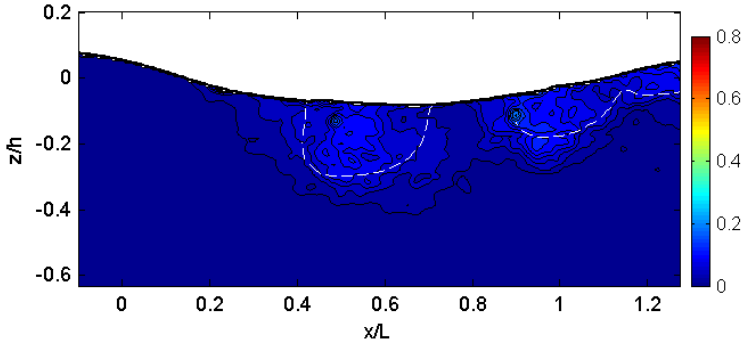

(v) t = 1.01 s

Fig. B.7 (Continued).

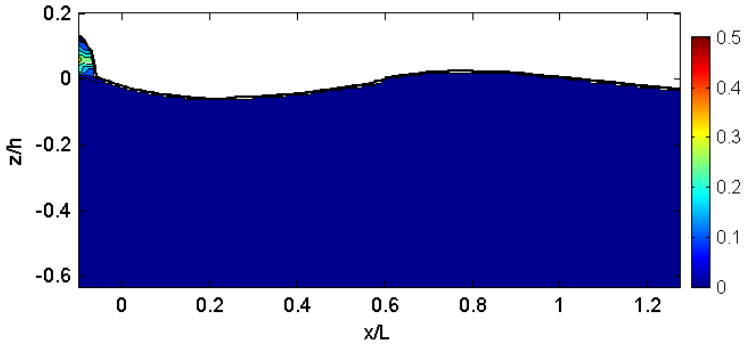

(a) t = -0.04 s

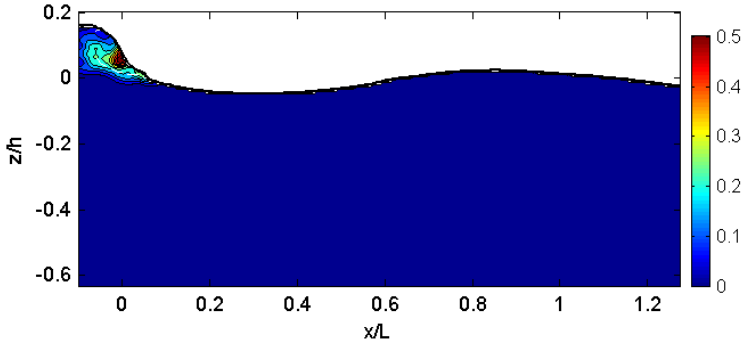

(b) t = 0.01 s

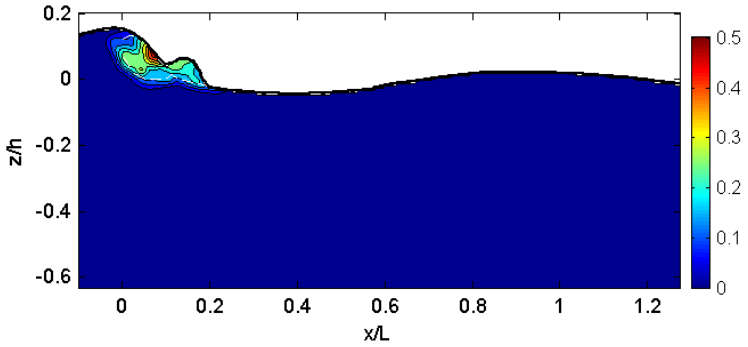

(c) t = 0.06 s

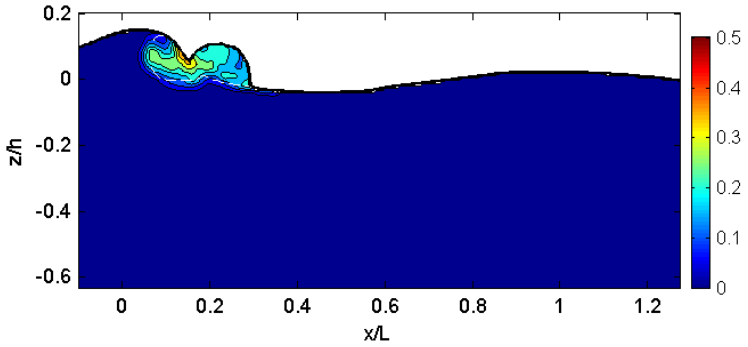

(d) t = 0.11 s

Fig. B.8 Normalized vertical turbulence intensity, $\sqrt{w'^2}/c$.

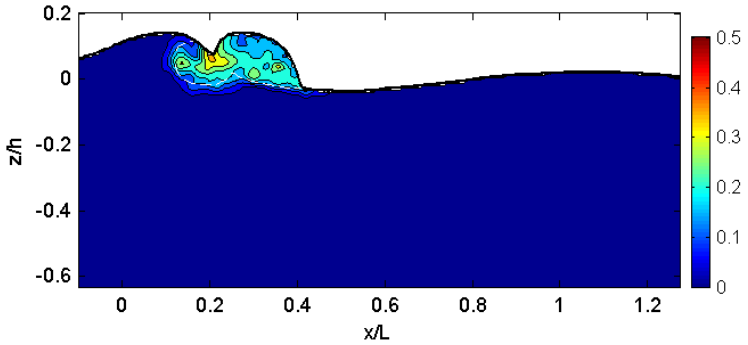

(e) $t = 0.16$ s

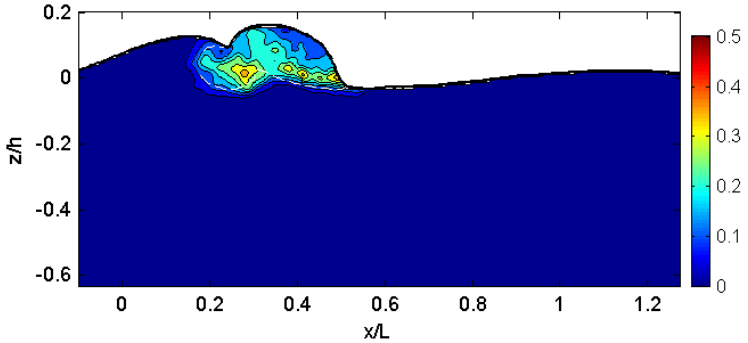

(f) $t = 0.21$ s

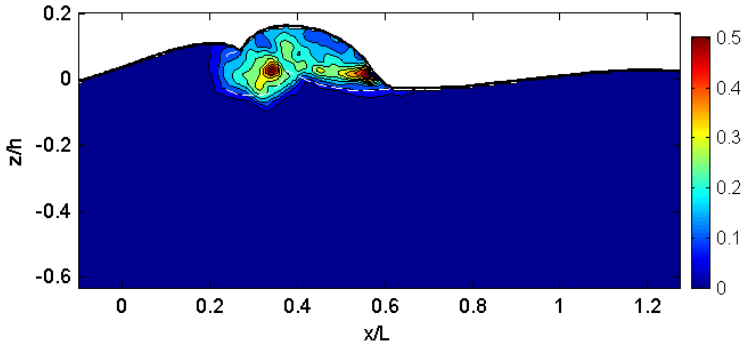

(g) $t = 0.26$ s

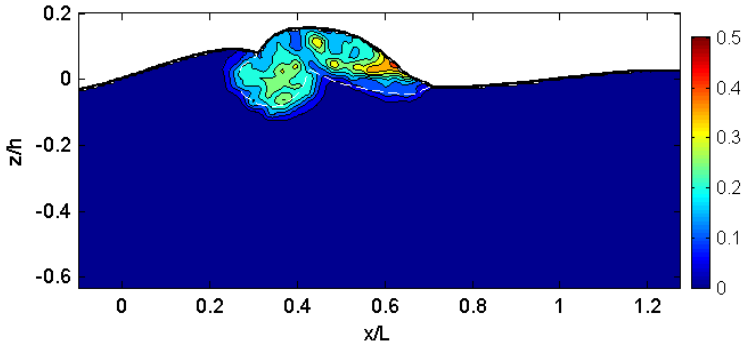

(h) $t = 0.31$ s

Fig. B.8 (Continued).

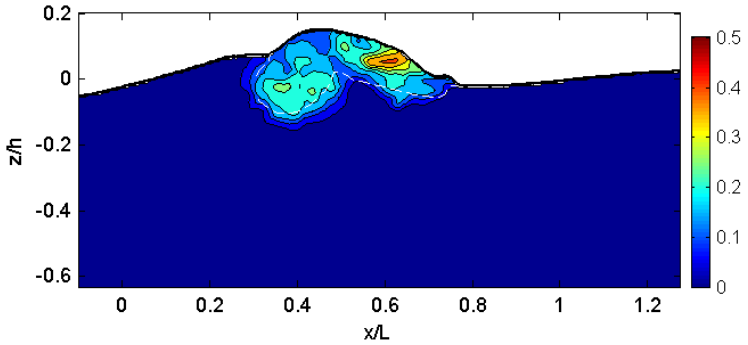

(i) $t = 0.36$ s

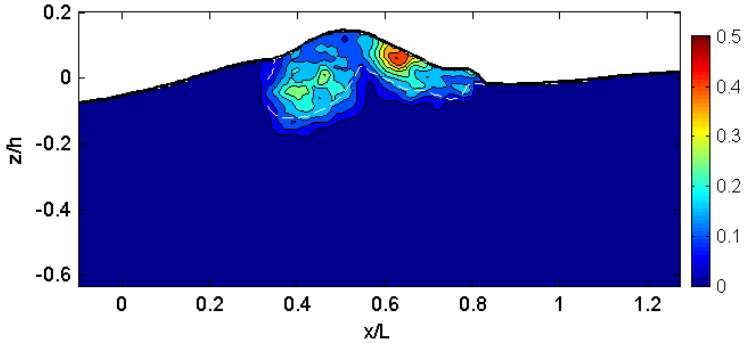

(j) $t = 0.41$ s

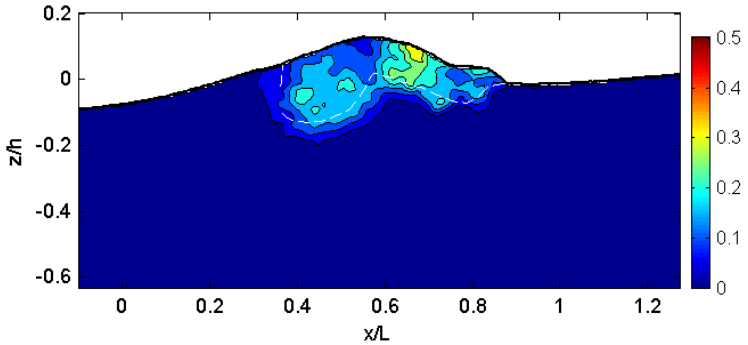

(k) $t = 0.46$ s

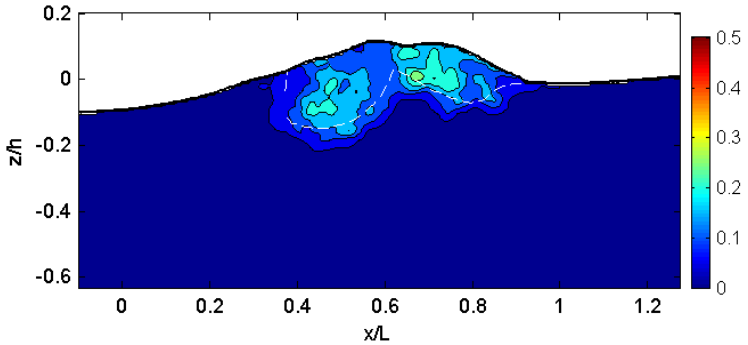

(l) $t = 0.51$ s

Fig. B.8 (Continued).

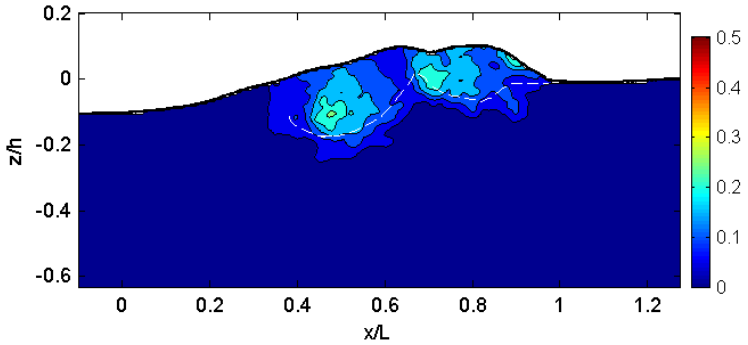

(m) $t = 0.56$ s

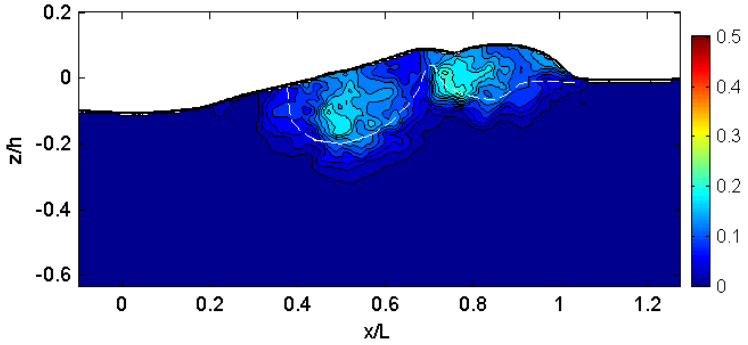

(n) $t = 0.61$ s

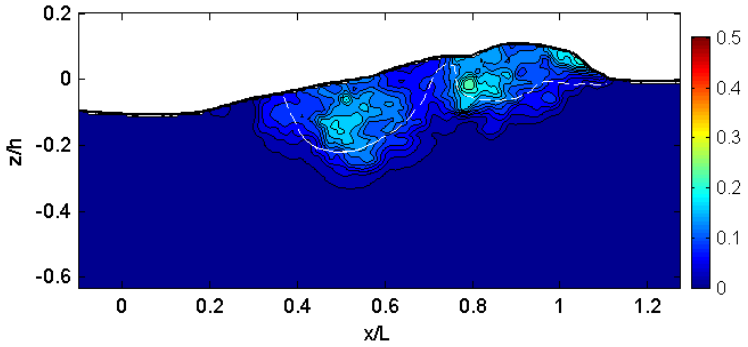

(o) $t = 0.66$ s

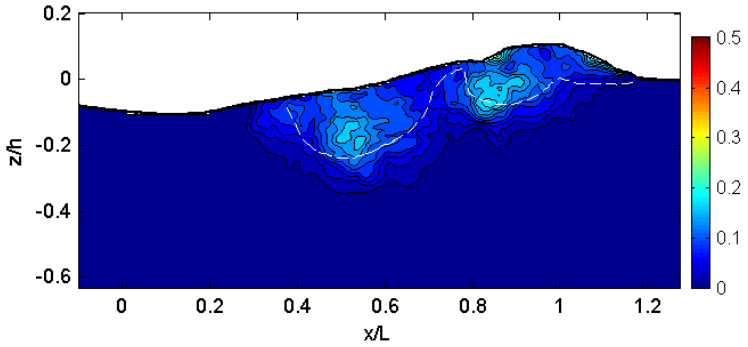

(p) $t = 0.71$ s

Fig. B.8 (Continued).

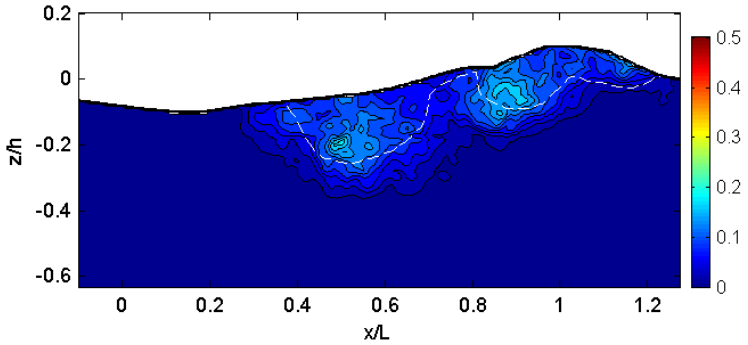

(q) t = 0.76 s

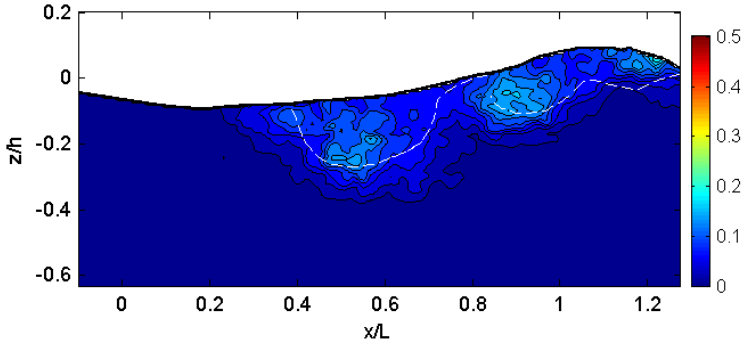

(r) t = 0.81 s

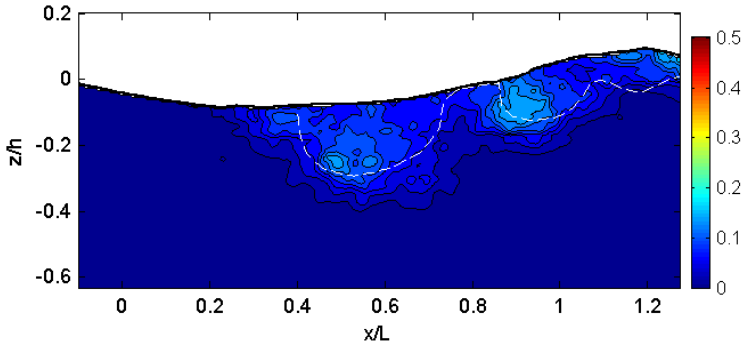

(s) t = 0.86 s

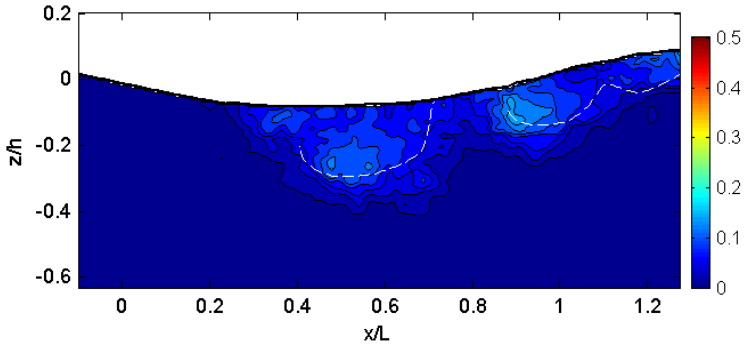

(t) t = 0.91 s

Fig. B.8 (Continued).

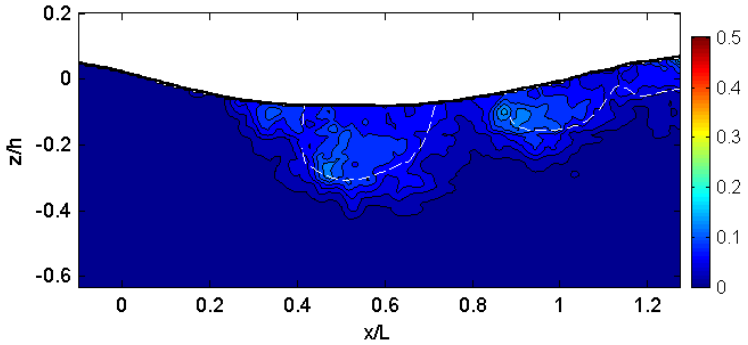

(u) t = 0.96 s

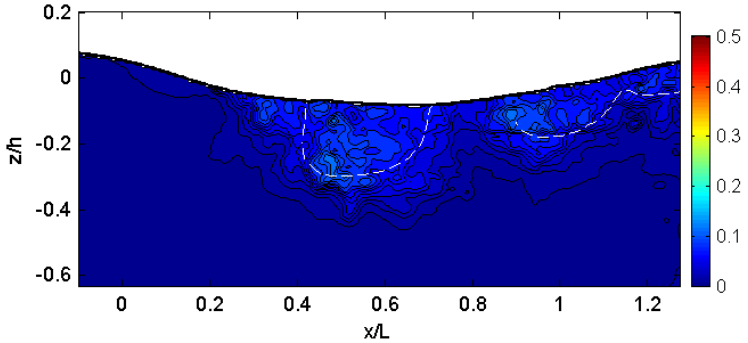

(v) t = 1.01 s

Fig. B.8 (Continued).

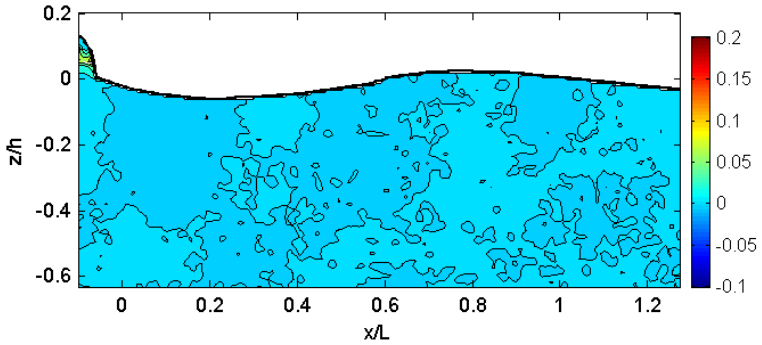

(a) t = -0.04 s

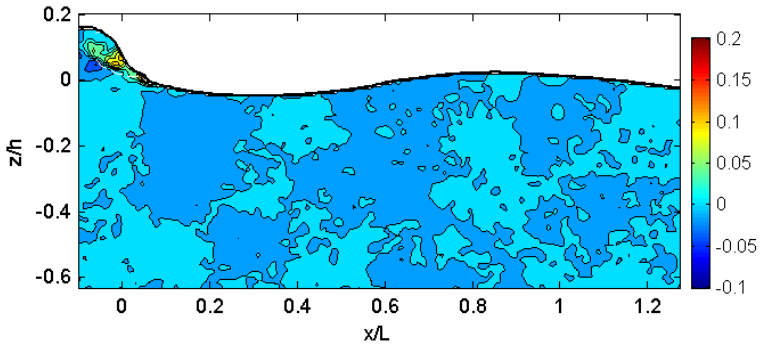

(b) t = 0.01 s

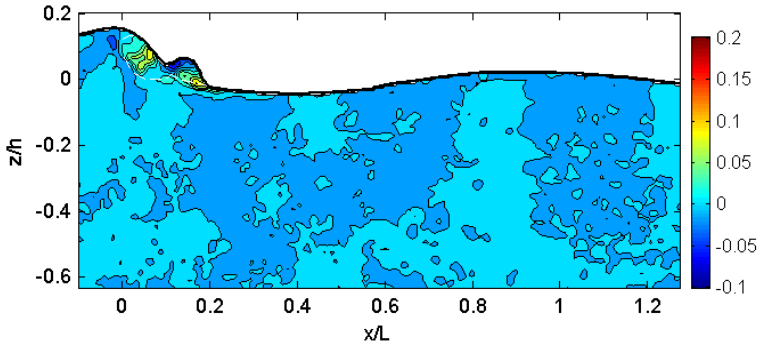

(c) t = 0.06 s

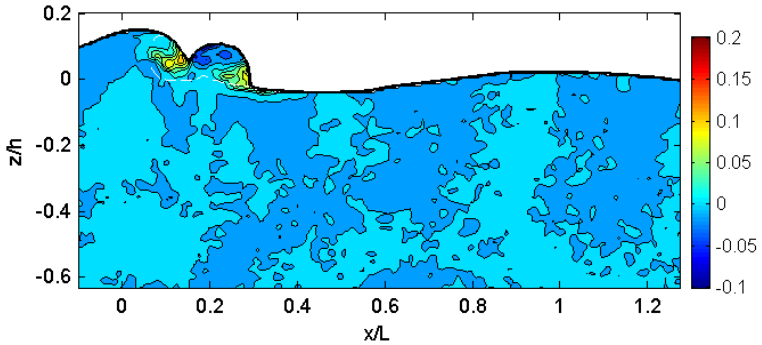

(d) t = 0.11 s

Fig. B.9 Normalized Reynolds stress, $-\overline{u'w'}/C^2$.

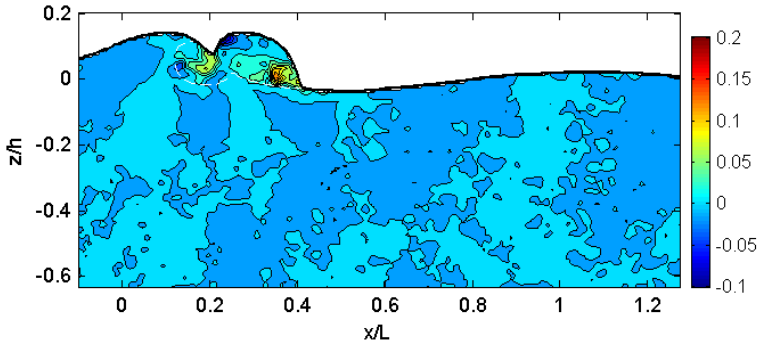

(e) $t = 0.16$ s

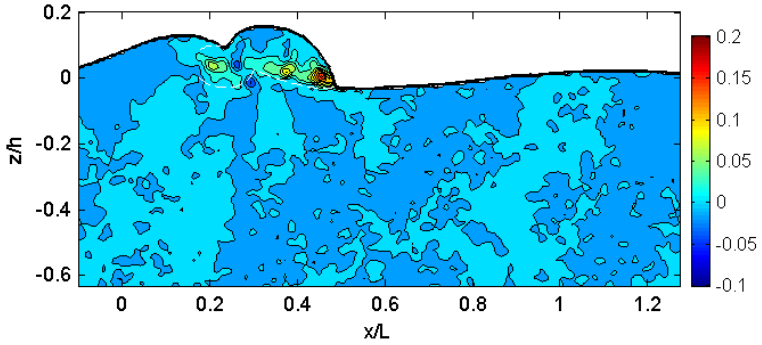

(f) $t = 0.21$ s

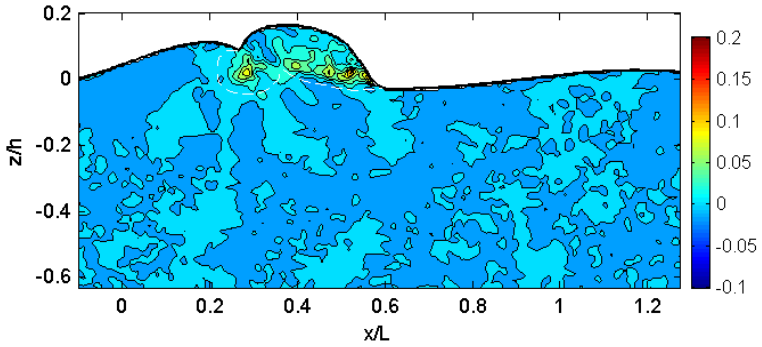

(g) $t = 0.26$ s

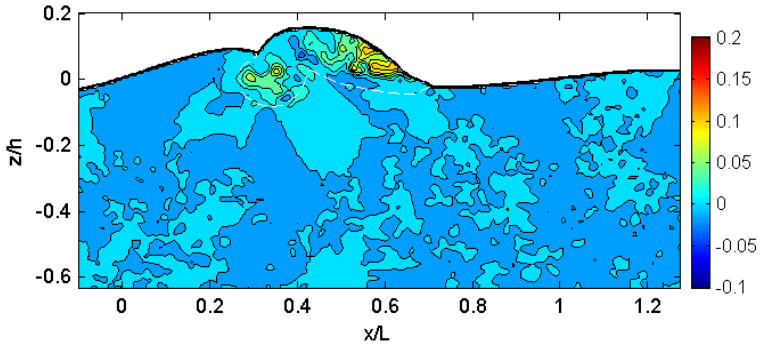

(h) $t = 0.31$ s

Fig. B.9 (Continued).

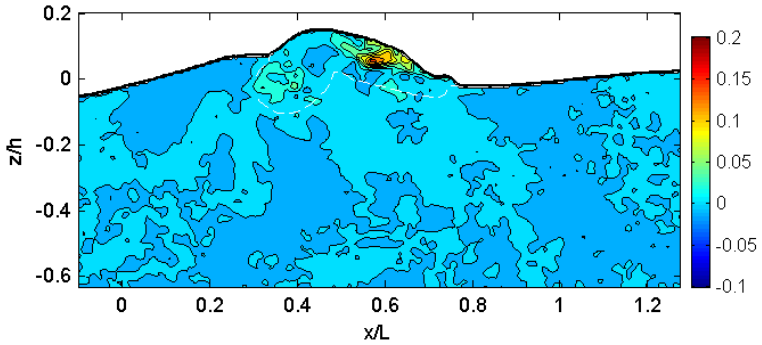

(i) $t = 0.36$ s

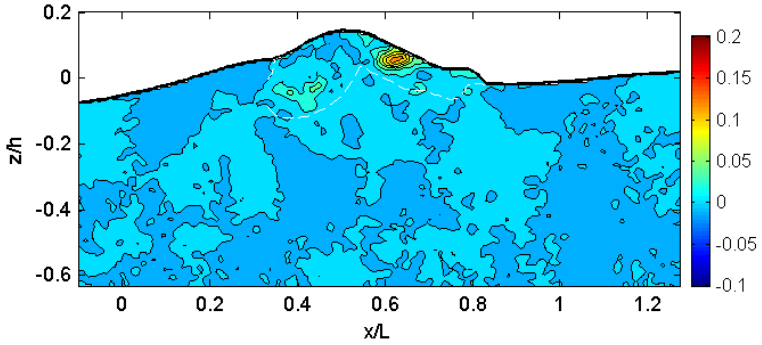

(j) $t = 0.41$ s

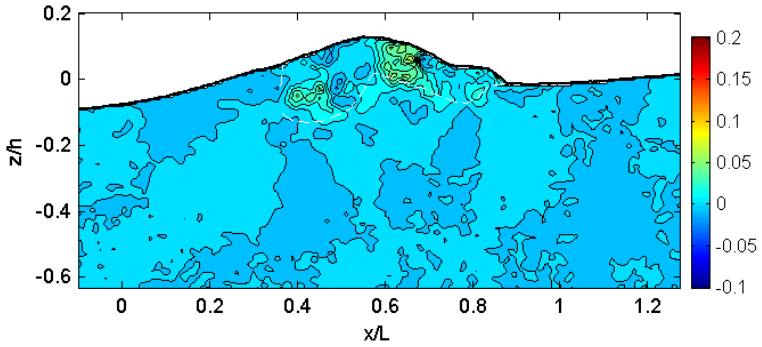

(k) $t = 0.46$ s

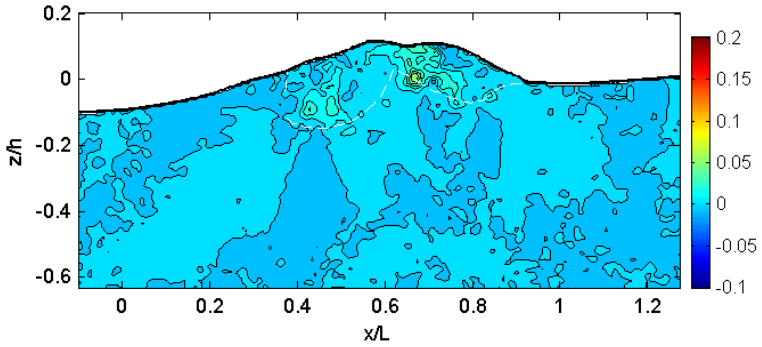

(l) $t = 0.51$ s

Fig. B.9 (Continued).

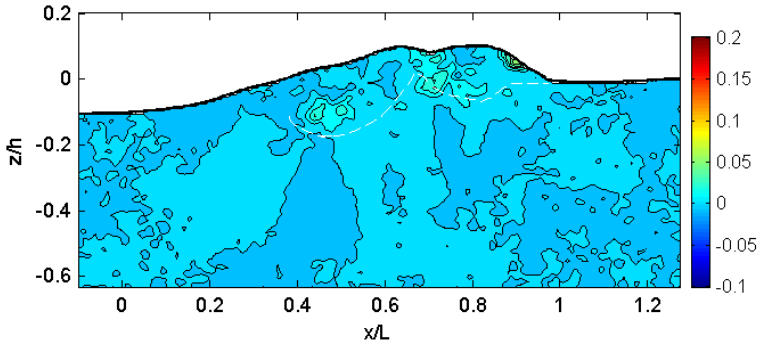

(m) $t = 0.56$ s

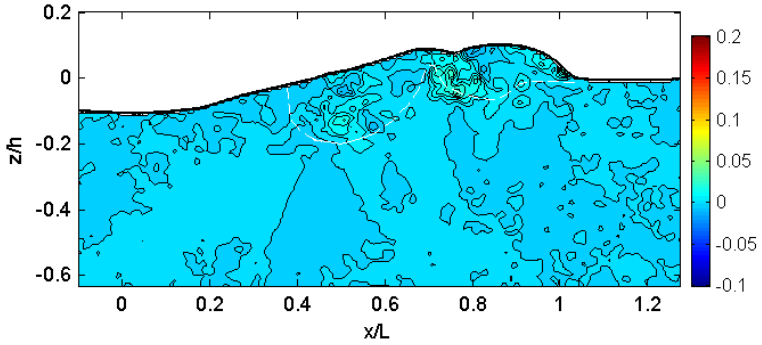

(n) $t = 0.61$ s

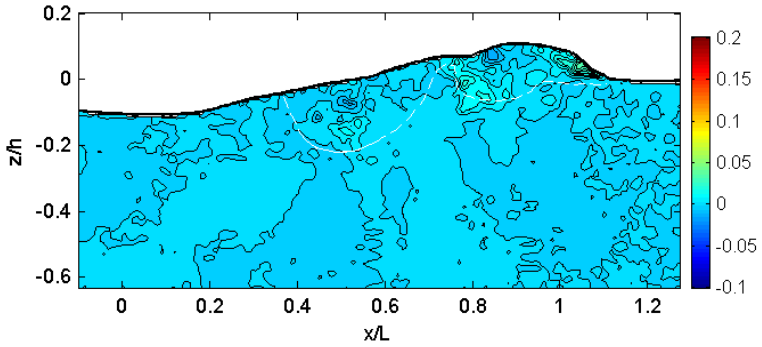

(o) $t = 0.66$ s

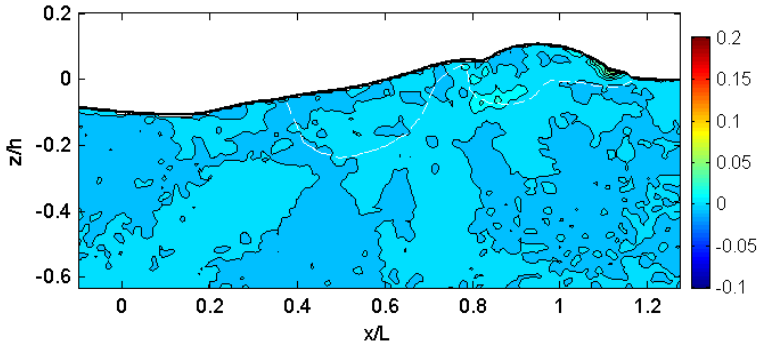

(p) $t = 0.71$ s

Fig. B.9 (Continued).

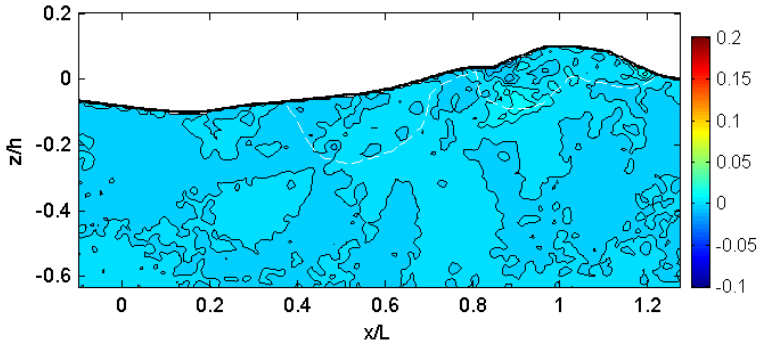

(q) t = 0.76 s

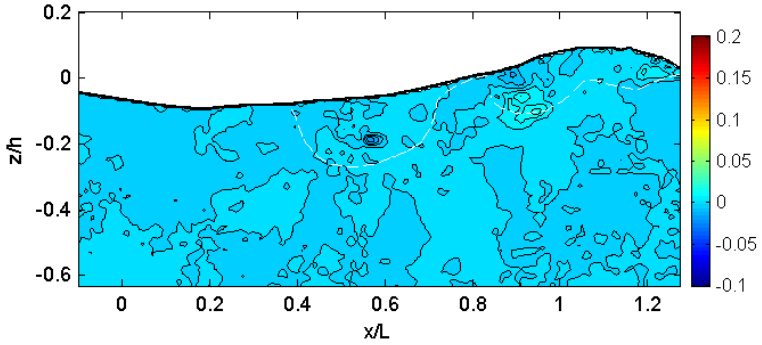

(r) t = 0.81 s

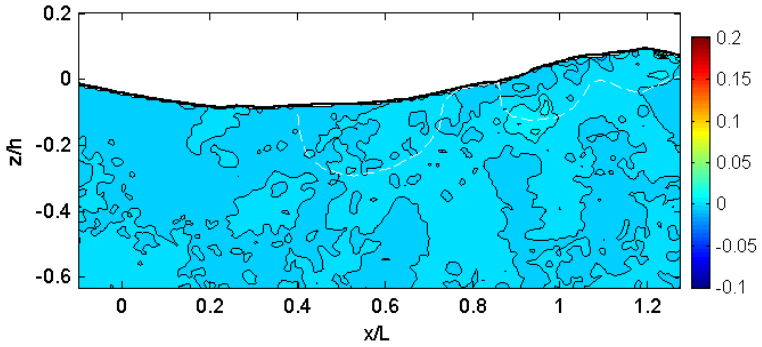

(s) t = 0.86 s

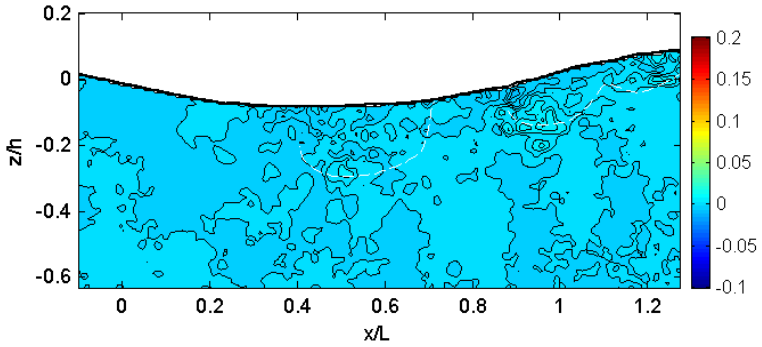

(t) t = 0.91 s

Fig. B.9 (Continued).

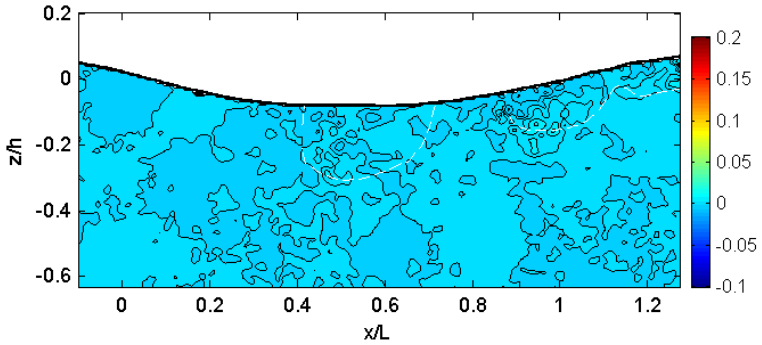

(u) t = 0.96 s

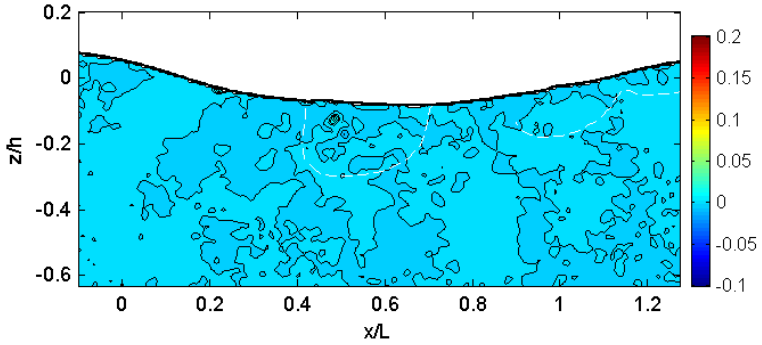

(v) t = 1.01 s

Fig. B.9 (Continued).

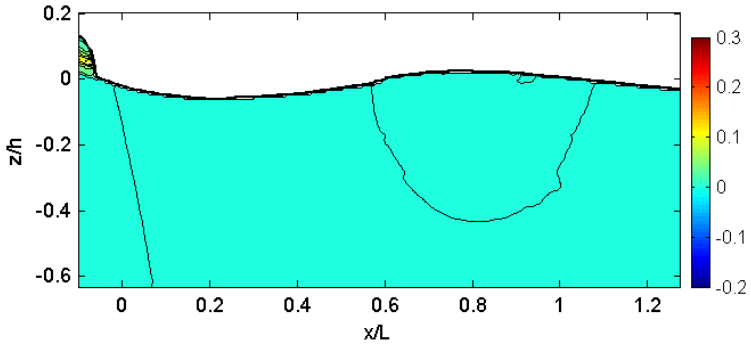

(a) t = -0.04 s

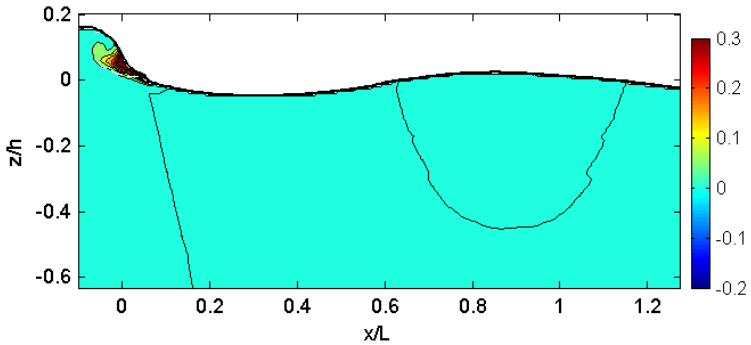

(b) t = 0.01 s

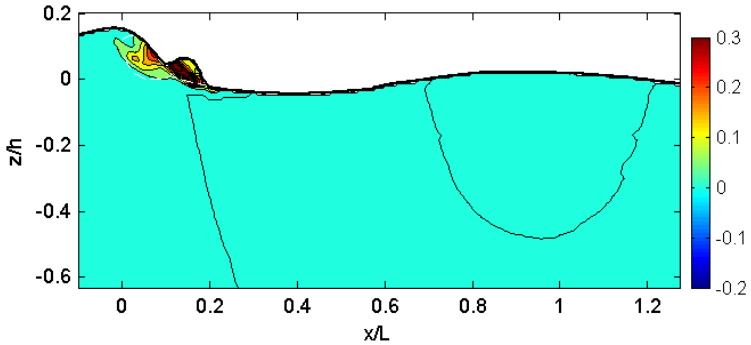

(c) t = 0.06 s

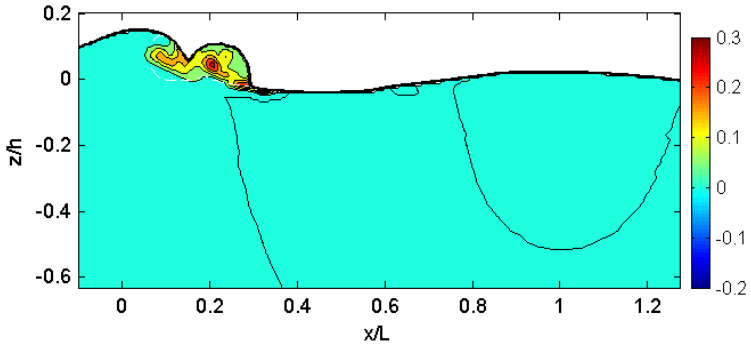

(d) t = 0.11 s

Fig. B.10 Normalized turbulent kinetic energy transport by U, kU/c^3 .

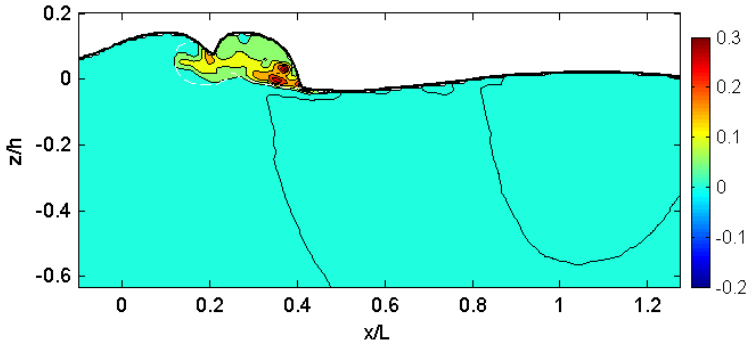

(e) $t = 0.16$ s

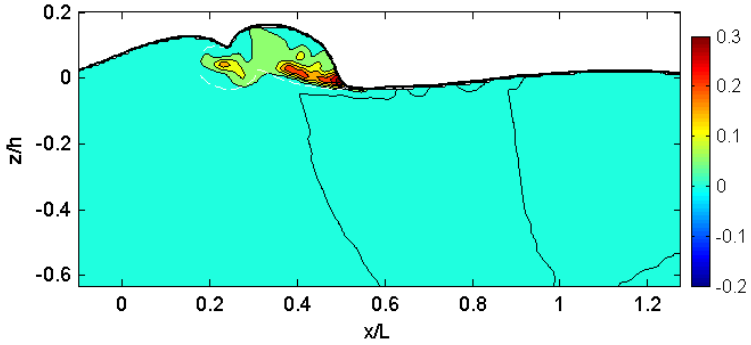

(f) $t = 0.21$ s

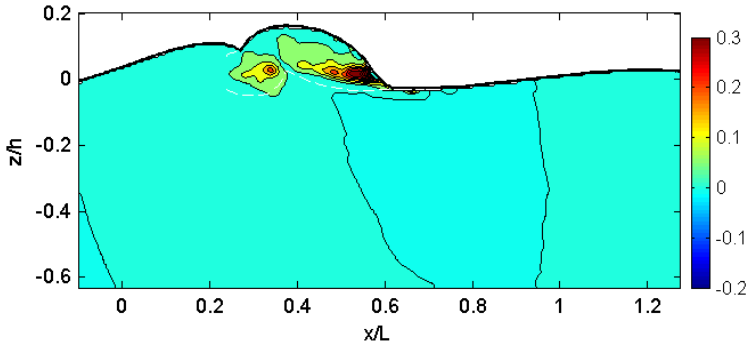

(g) $t = 0.26$ s

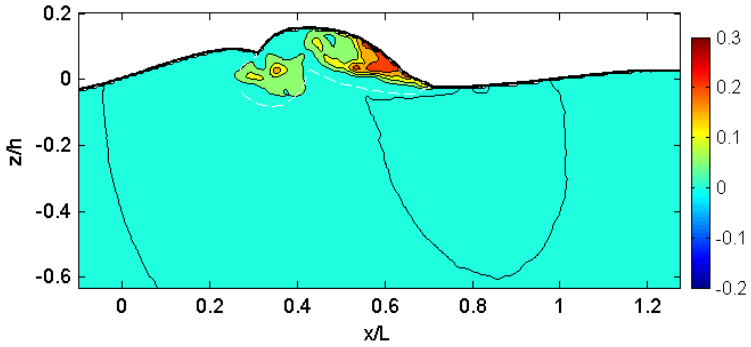

(h) $t = 0.31$ s

Fig. B.10 (Continued).

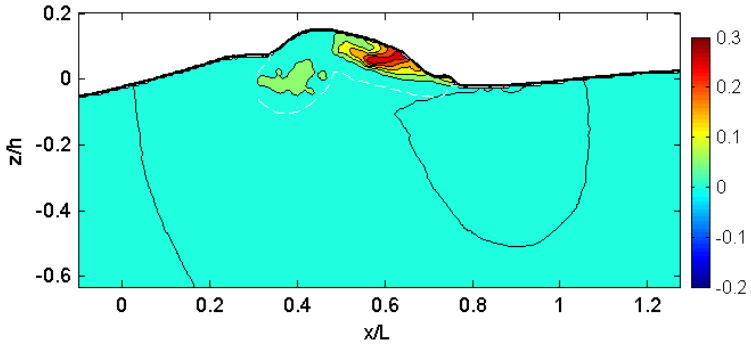

(i) $t = 0.36$ s

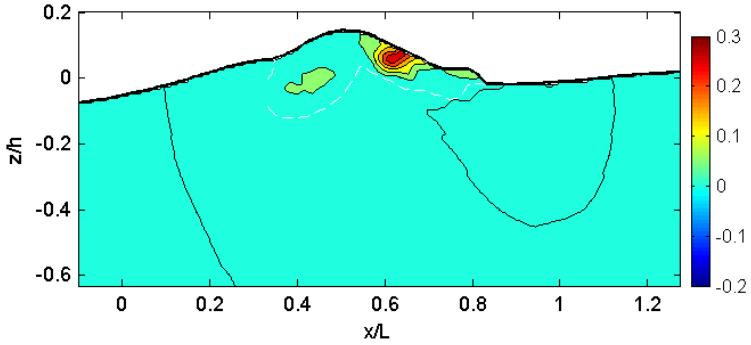

(j) $t = 0.41$ s

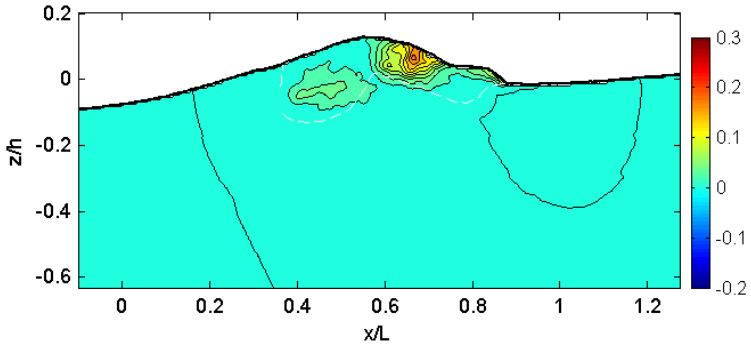

(k) $t = 0.46$ s

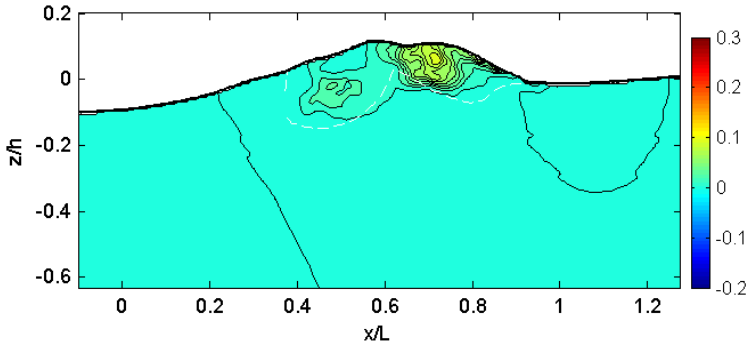

(l) $t = 0.51$ s

Fig. B.10 (Continued).

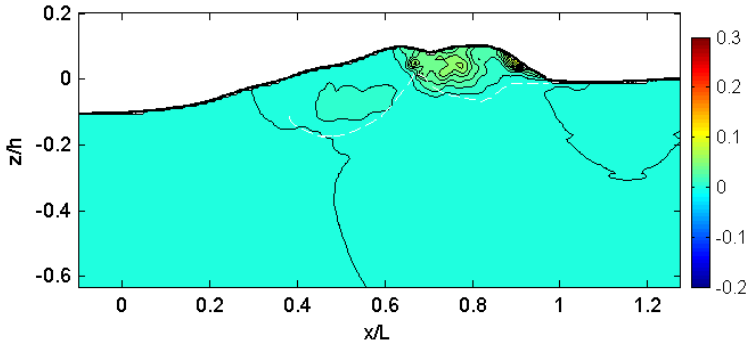

(m) $t = 0.56$ s

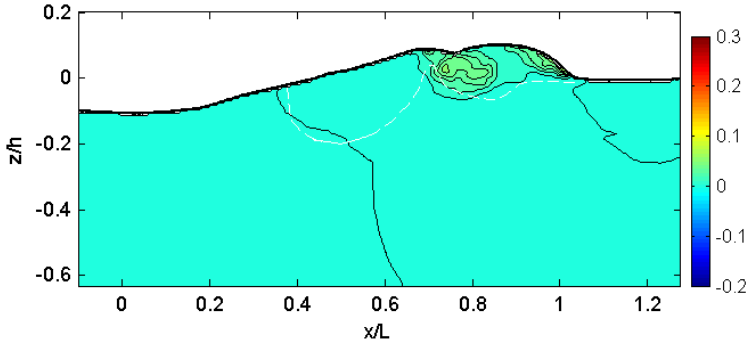

(n) $t = 0.61$ s

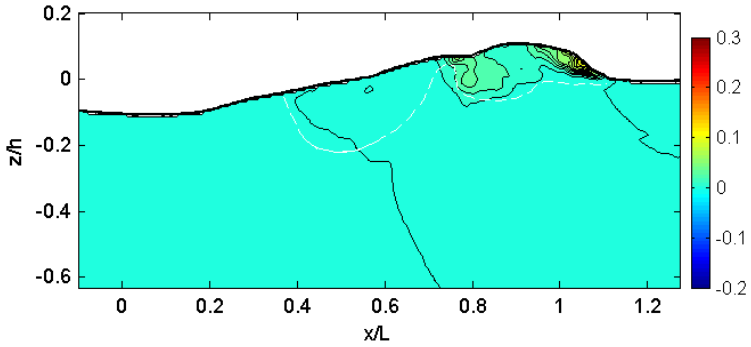

(o) $t = 0.66$ s

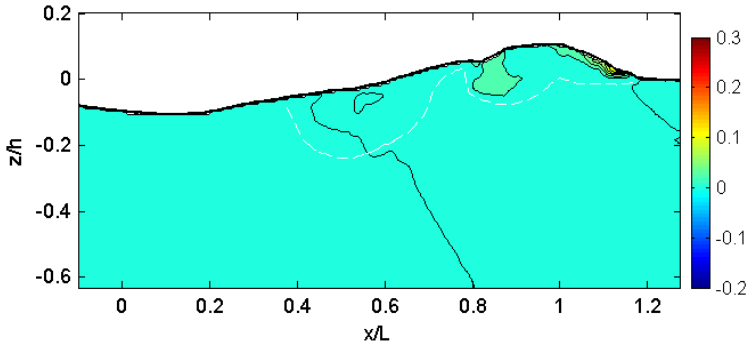

(p) $t = 0.71$ s

Fig. B.10 (Continued).

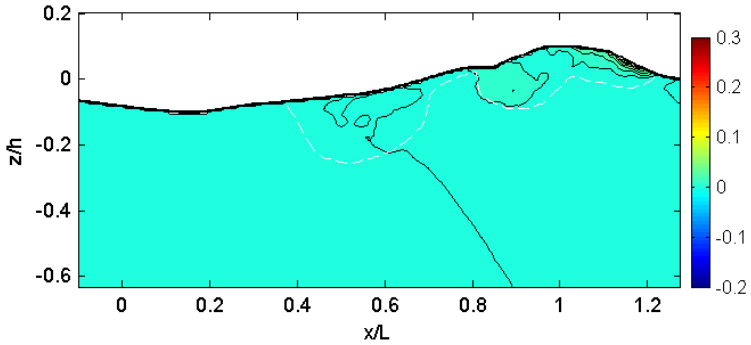

(q) $t = 0.76$ s

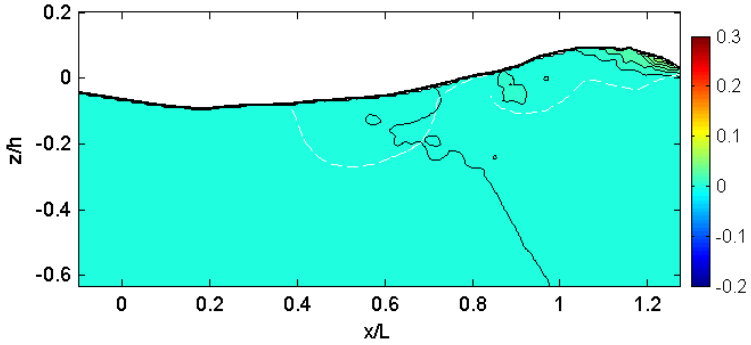

(r) $t = 0.81$ s

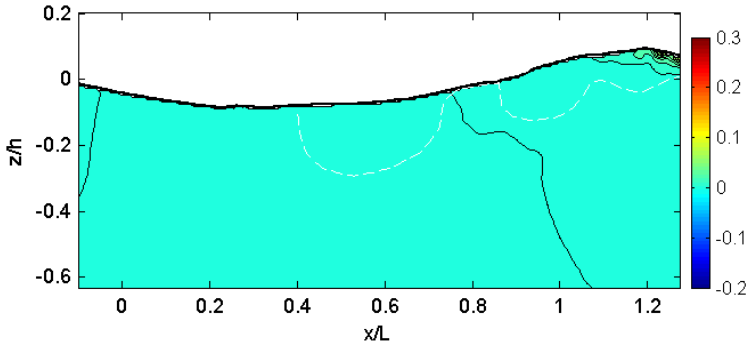

(s) $t = 0.86$ s

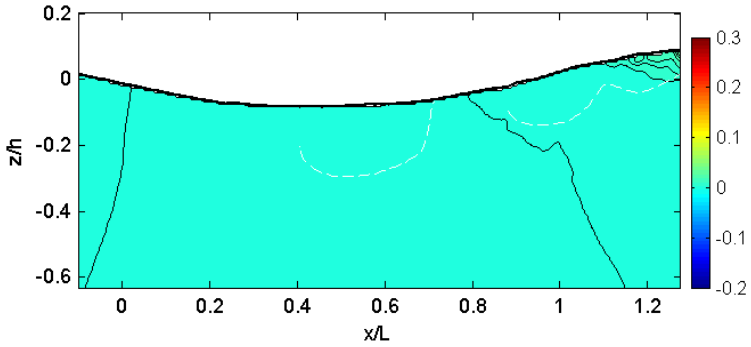

(t) $t = 0.91$ s

Fig. B.10 (Continued).

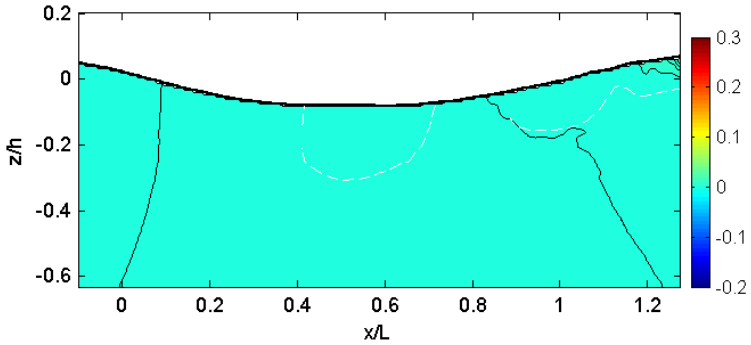

(u) t = 0.96 s

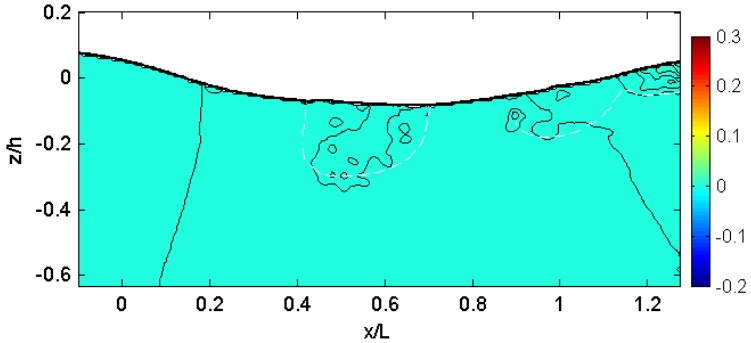

(v) t = 1.01 s

Fig. B.10 (Continued).

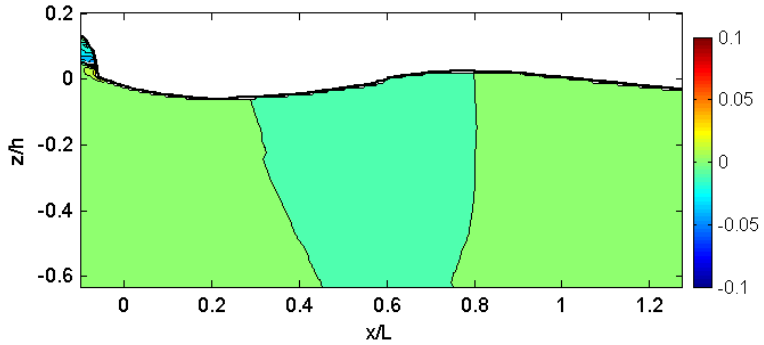

(a) t = -0.04 s

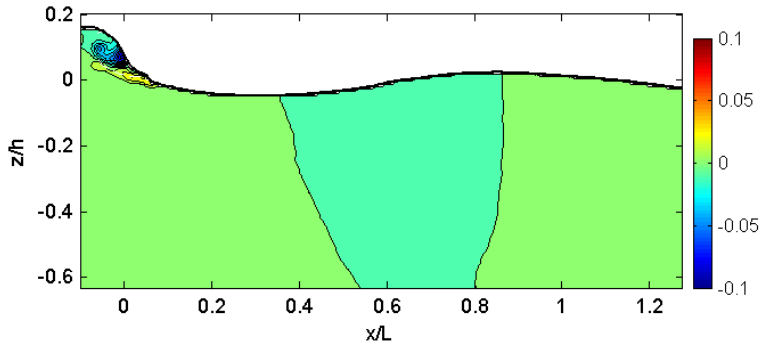

(b) t = 0.01 s

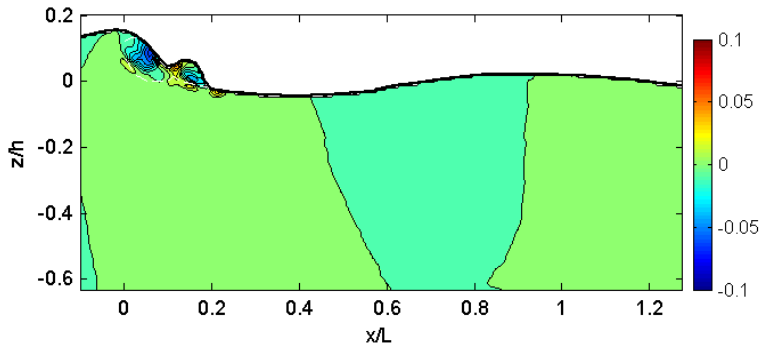

(c) t = 0.06 s

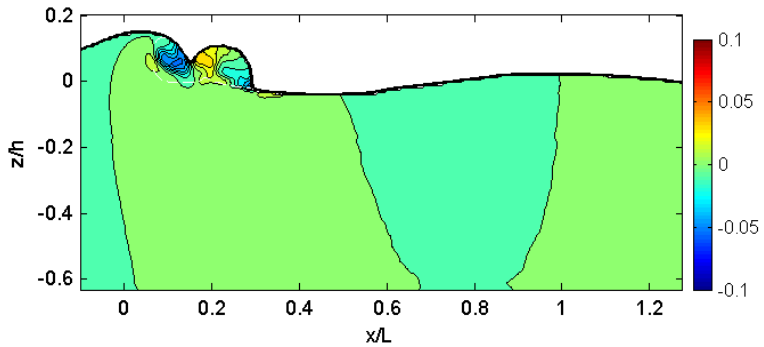

(d) t = 0.11 s

Fig. B.11 Normalized turbulent kinetic energy transport by W, kW/C^3 .

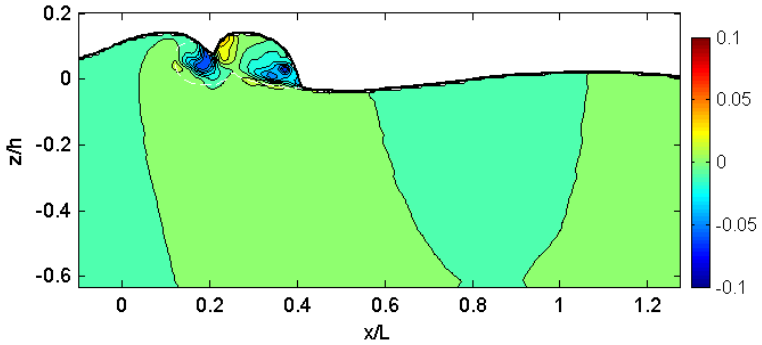

(e) $t = 0.16$ s

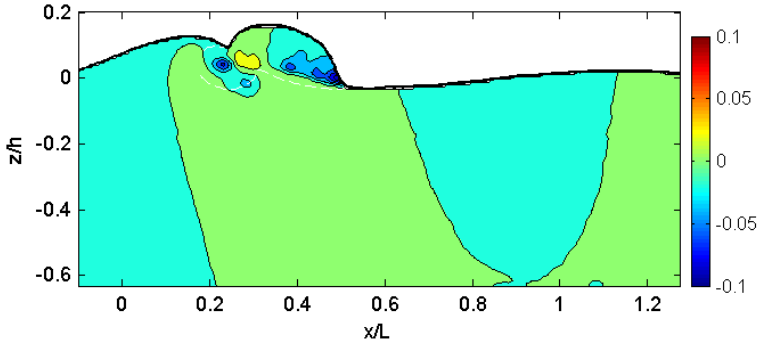

(f) $t = 0.21$ s

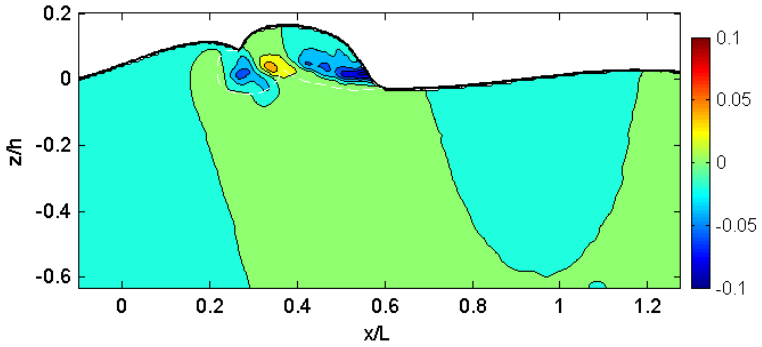

(g) $t = 0.26$ s

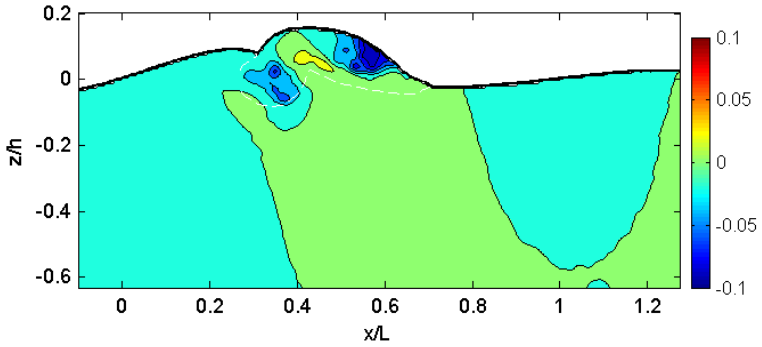

(h) $t = 0.31$ s

Fig. B.11 (Continued).

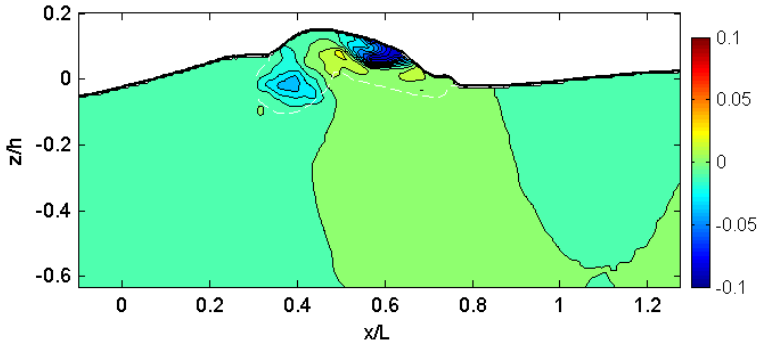

(i) $t = 0.36$ s

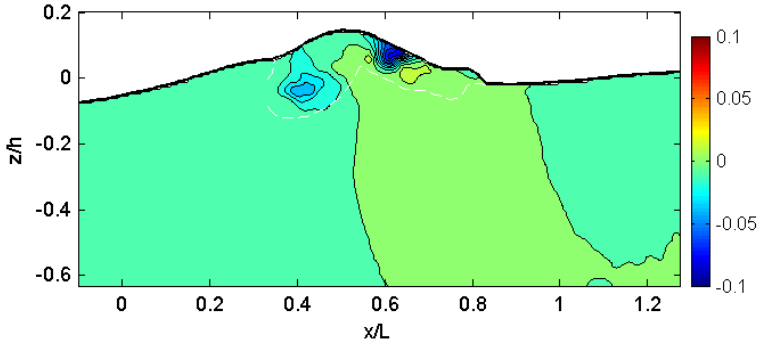

(j) $t = 0.41$ s

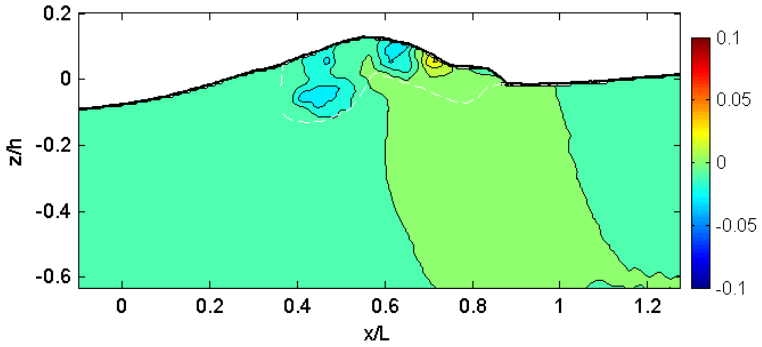

(k) $t = 0.46$ s

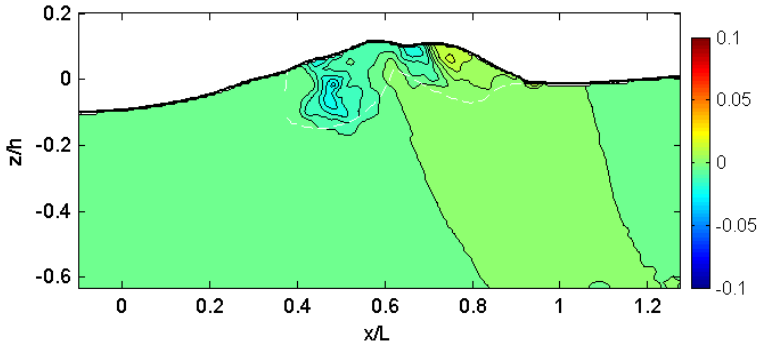

(l) $t = 0.51$ s

Fig. B.11 (Continued).

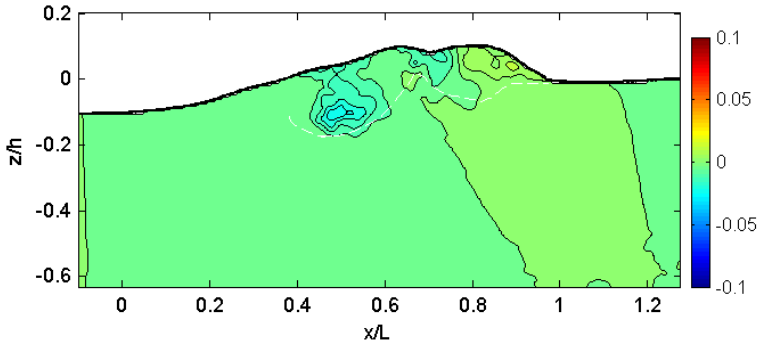

(m) $t = 0.56$ s

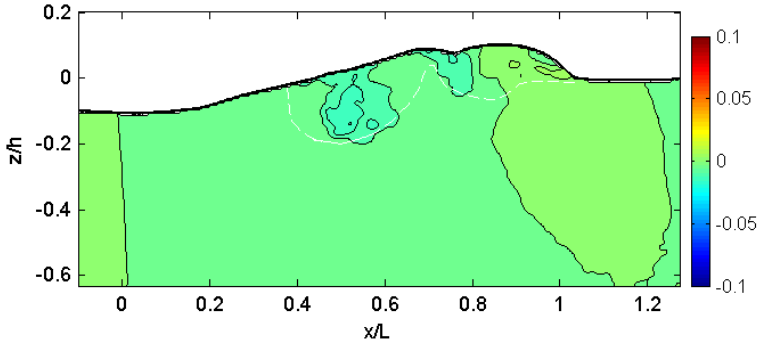

(n) $t = 0.61$ s

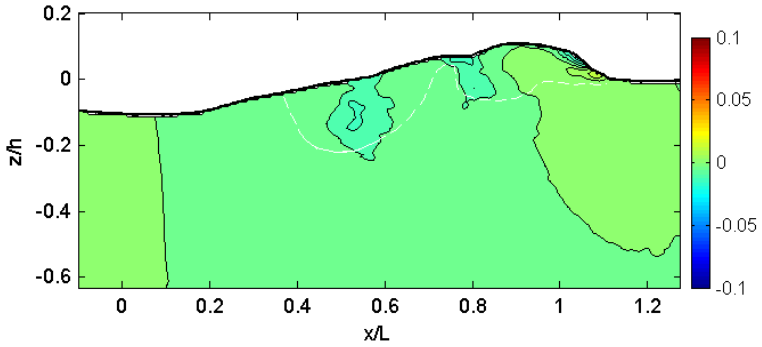

(o) $t = 0.66$ s

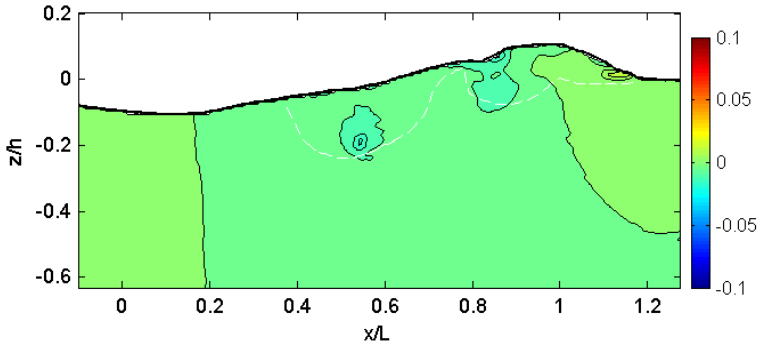

(p) $t = 0.71$ s

Fig. B.11 (Continued).

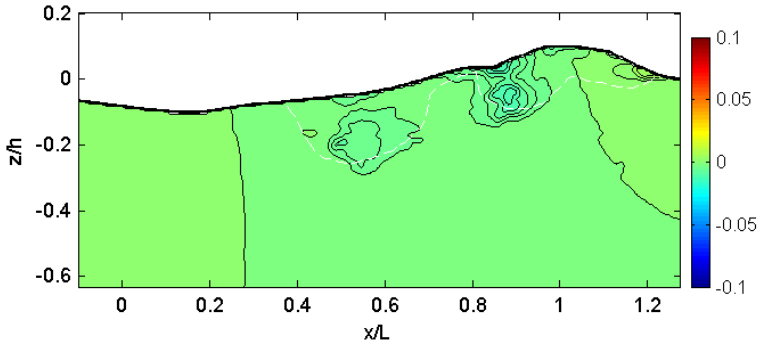

(q) $t = 0.76$ s

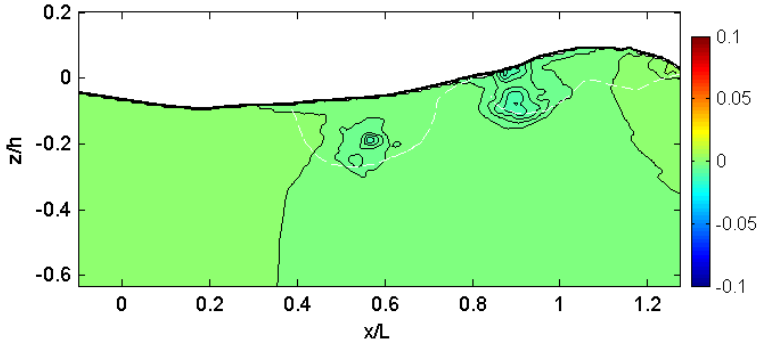

(r) $t = 0.81$ s

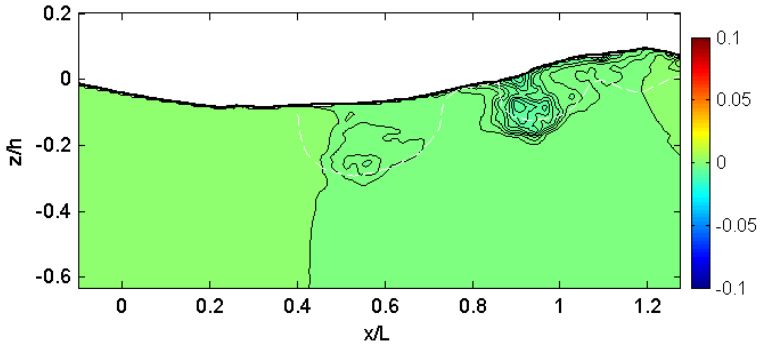

(s) $t = 0.86$ s

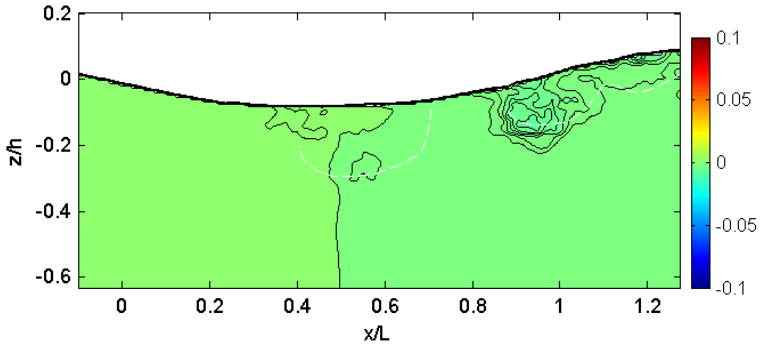

(t) $t = 0.91$ s

Fig. B.11 (Continued).

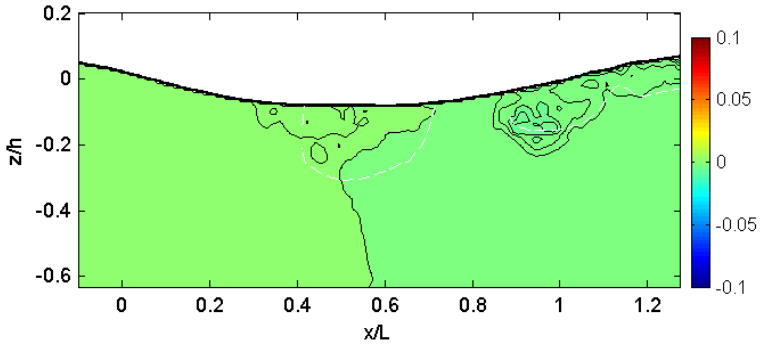

(u) t = 0.96 s

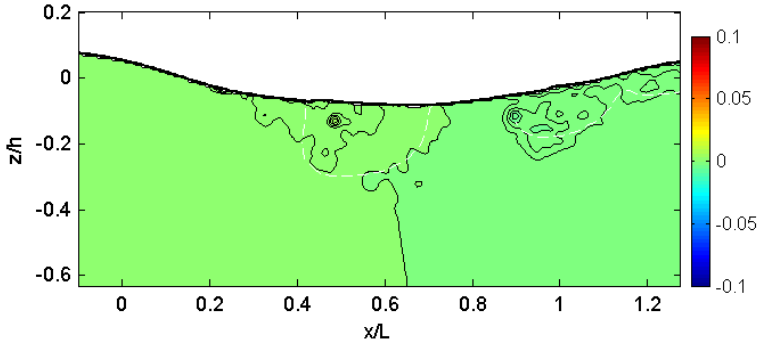

(v) t = 1.01 s

Fig. B.11 (Continued).

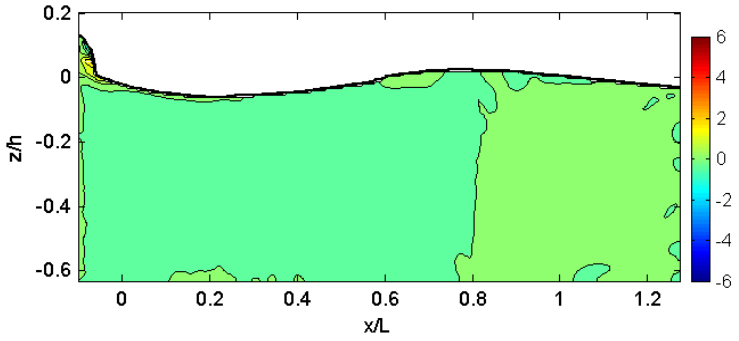

(a) t = -0.04 s

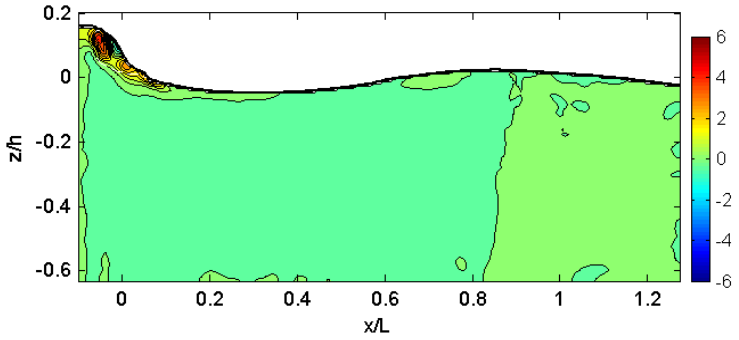

(b) t = 0.01 s

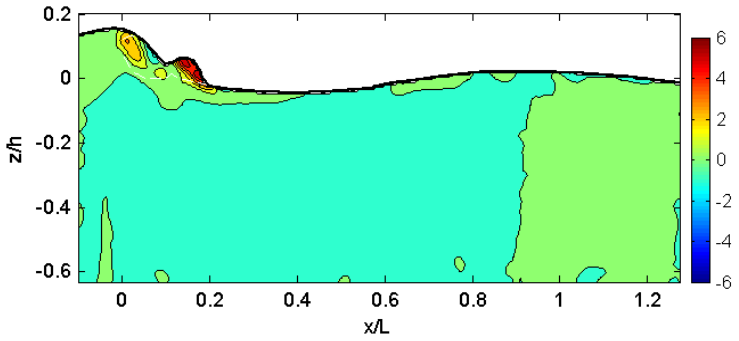

(c) t = 0.06 s

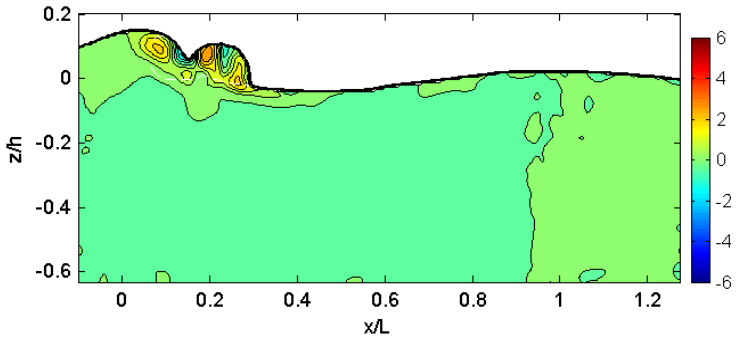

(d) t = 0.11 s

Fig. B.12 Normalized horizontal convective acceleration, $\left(U\frac{\partial U}{\partial x}+W\frac{\partial U}{\partial z}\right)\Big/g$ **.**

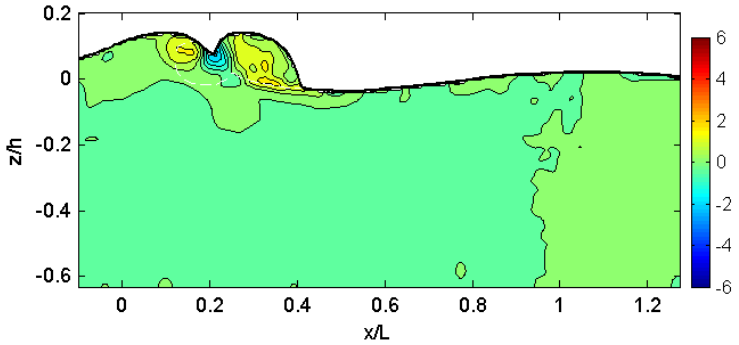

(e) $t = 0.16$ s

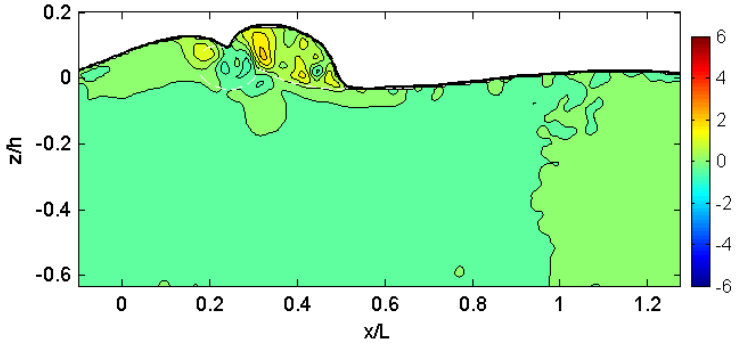

(f) $t = 0.21$ s

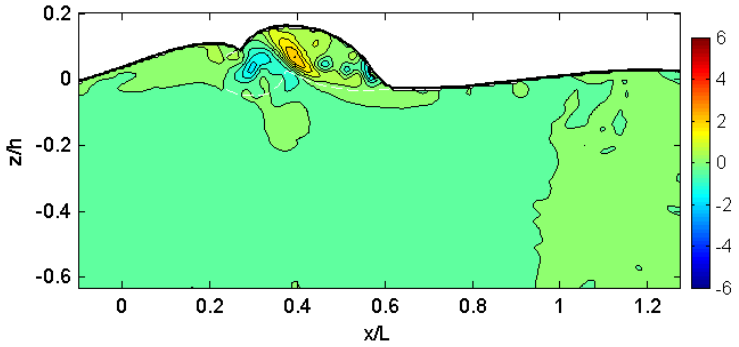

(g) $t = 0.26$ s

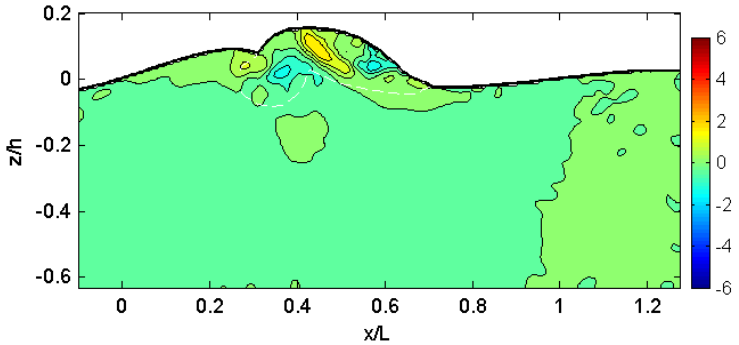

(h) $t = 0.31$ s

Fig. B.12 (Continued).

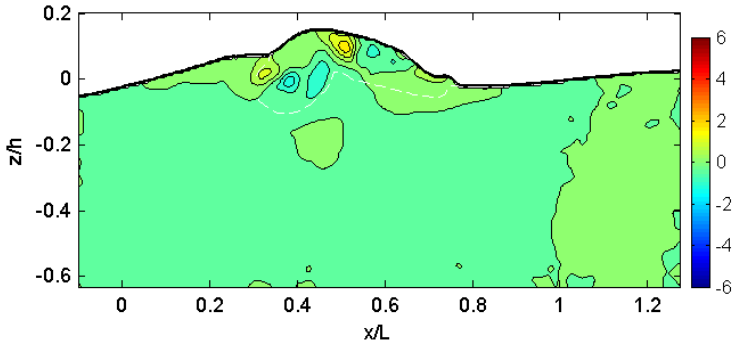

(i) $t = 0.36$ s

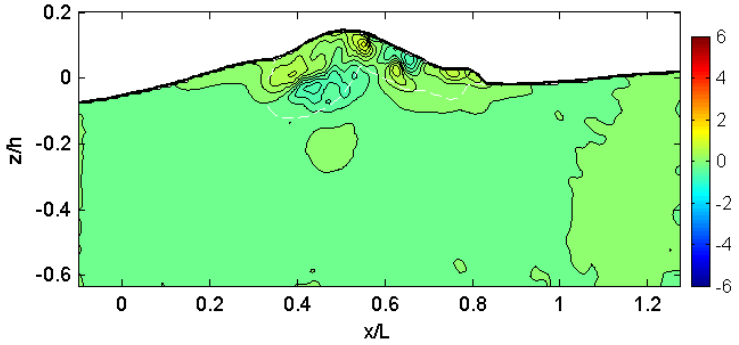

(j) $t = 0.41$ s

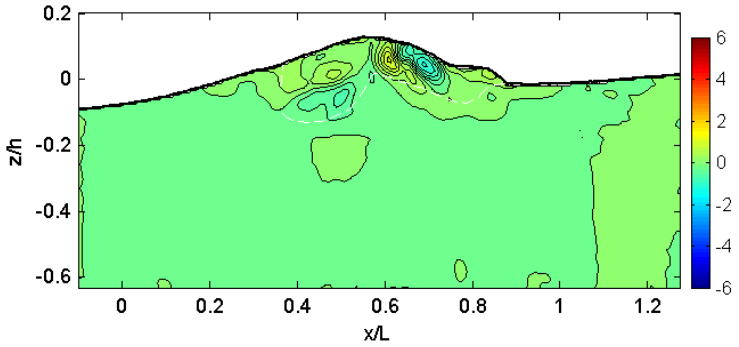

(k) $t = 0.46$ s

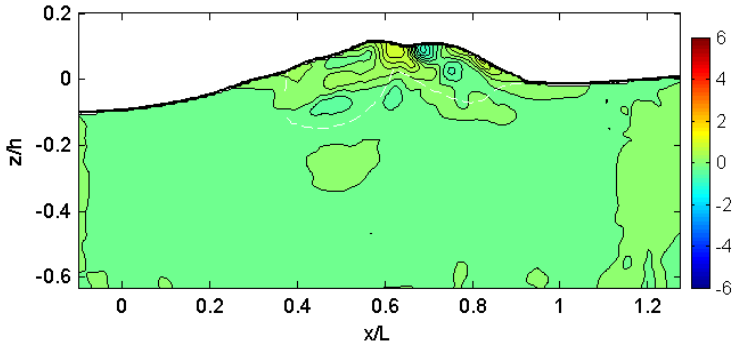

(l) $t = 0.51$ s

Fig. B.12 (Continued).

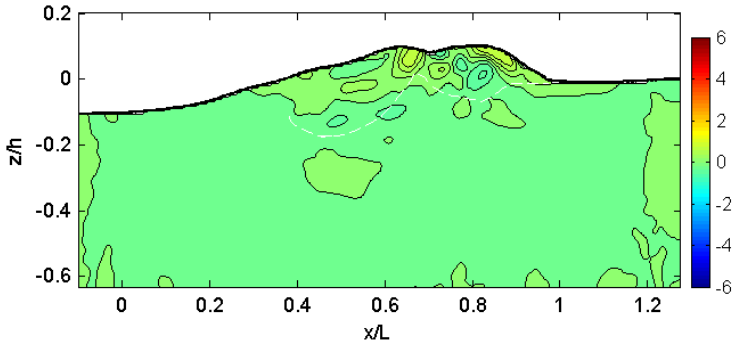

(m) $t = 0.56$ s

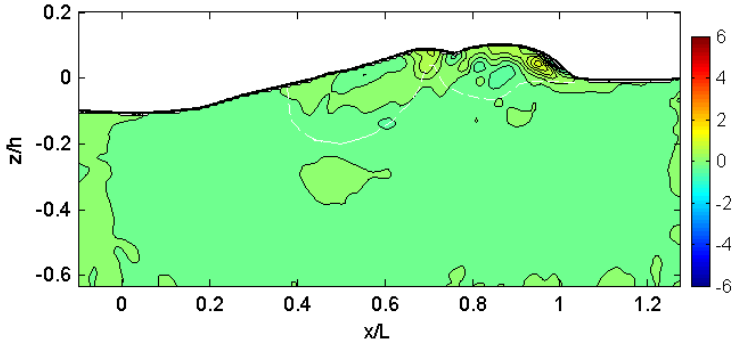

(n) $t = 0.61$ s

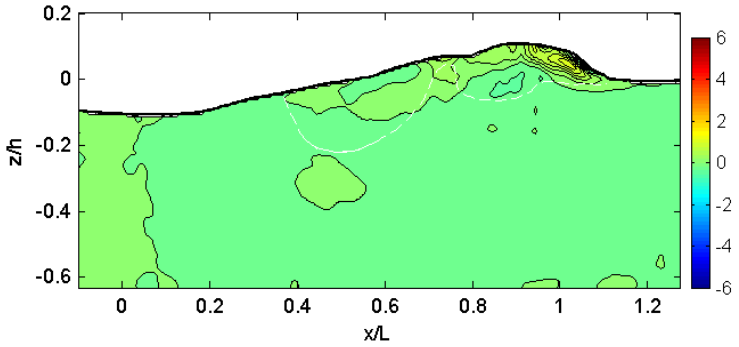

(o) $t = 0.66$ s

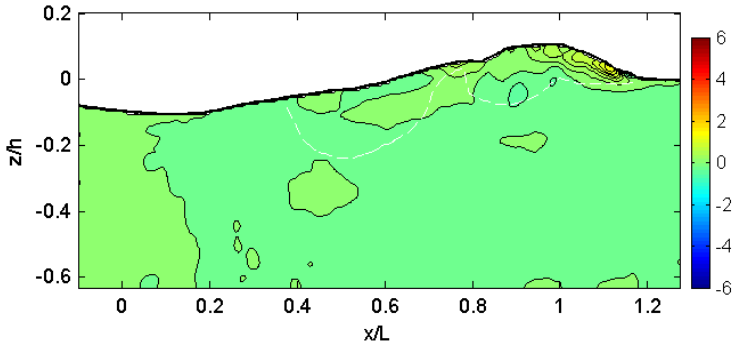

(p) $t = 0.71$ s

Fig. B.12 (Continued).

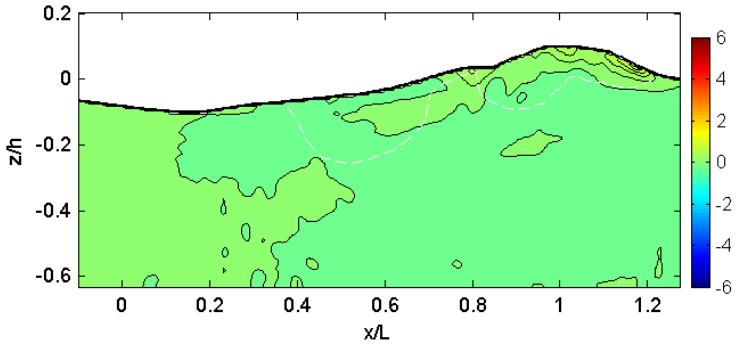

(q) t = 0.76 s

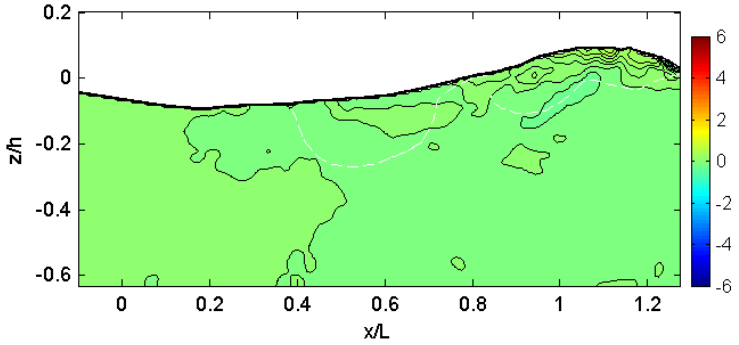

(r) t = 0.81 s

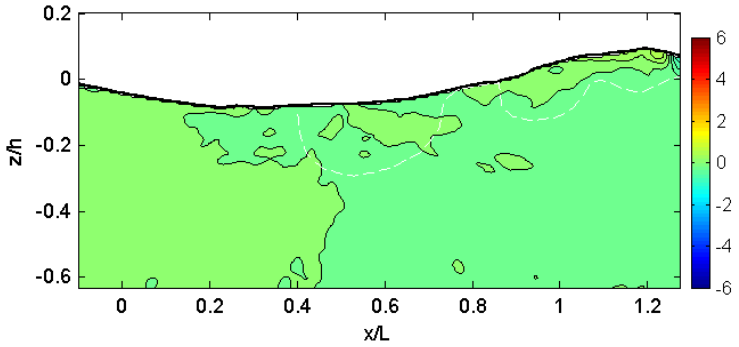

(s) t = 0.86 s

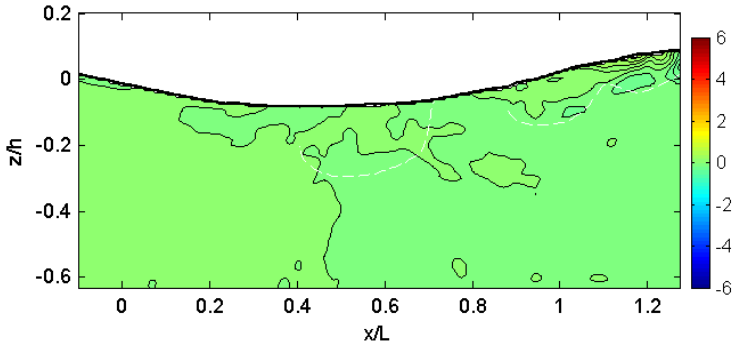

(t) t = 0.91 s

Fig. B.12 (Continued).

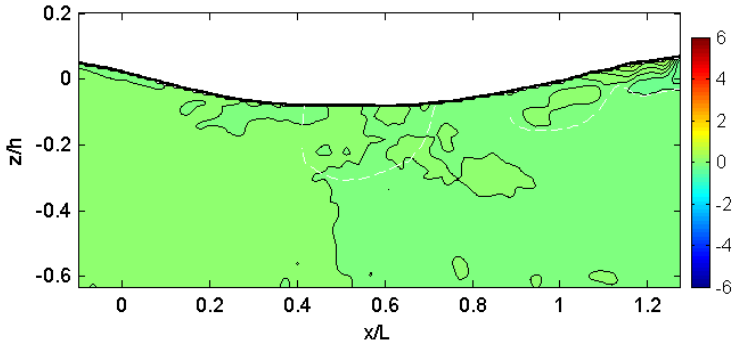

(u) t = 0.96 s

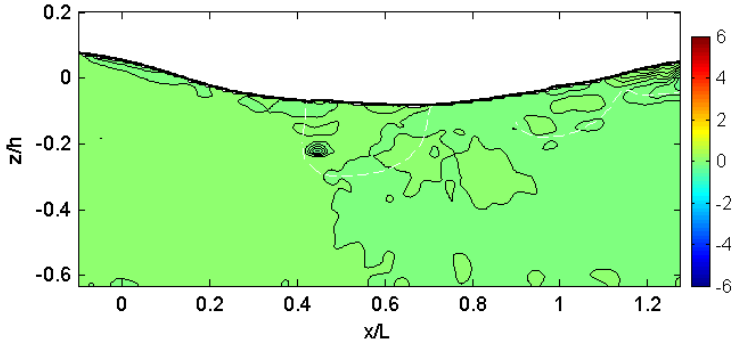

(v) t = 1.01 s

Fig. B.12 (Continued).

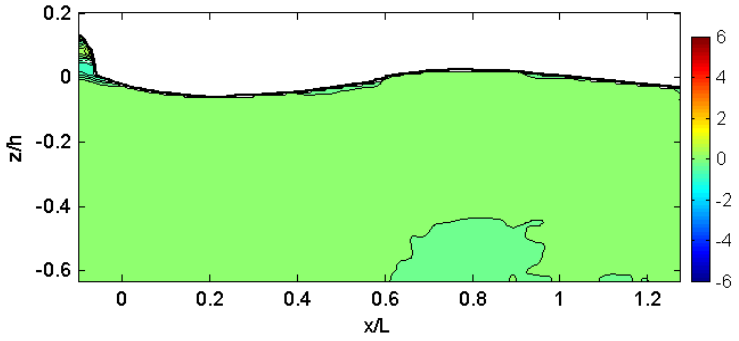

(a) t = -0.04 s

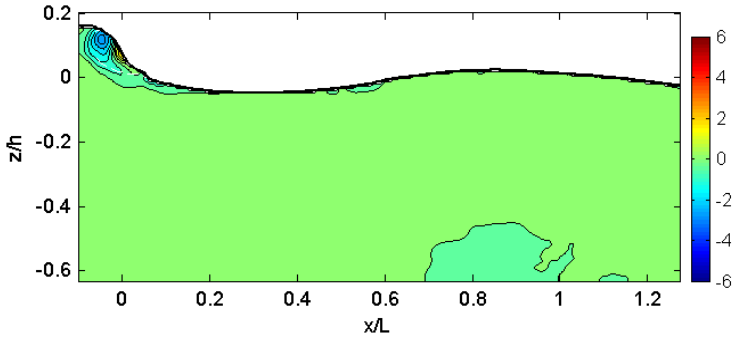

(b) t = 0.01 s

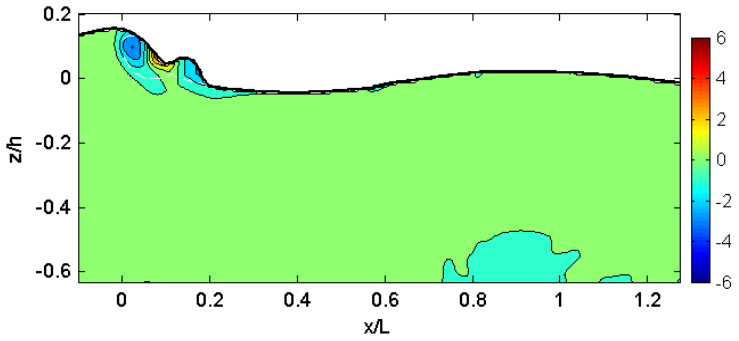

(c) t = 0.06 s

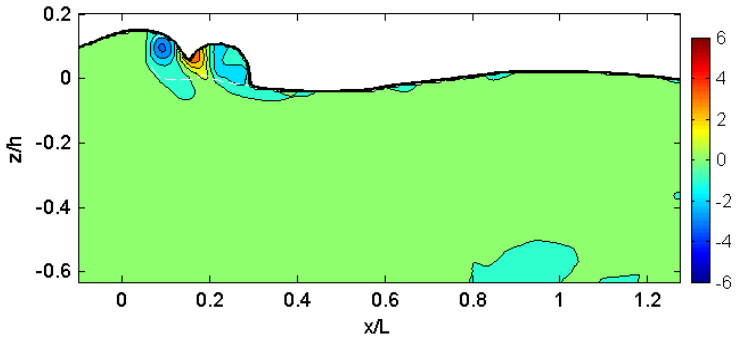

(d) t = 0.11 s

Fig. B.13 Normalized vertical convective acceleration, $\left(U\frac{\partial W}{\partial x}+W\frac{\partial W}{\partial z}\right)\Big/g$ **.**

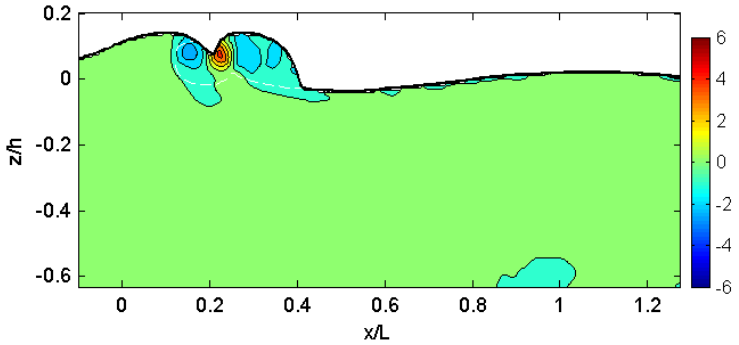

(e) $t = 0.16$ s

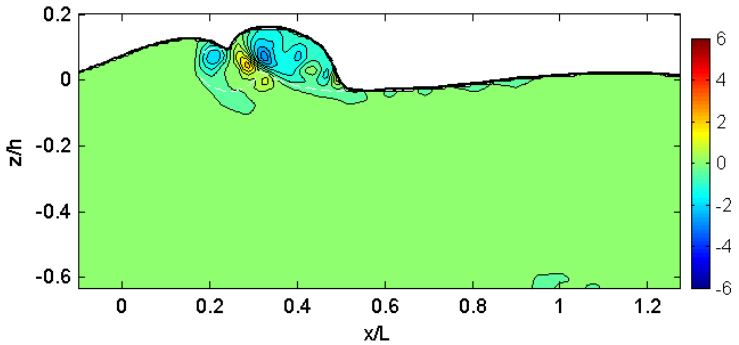

(f) $t = 0.21$ s

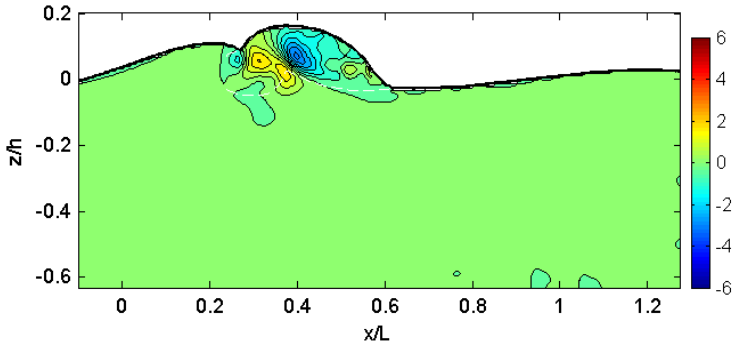

(g) $t = 0.26$ s

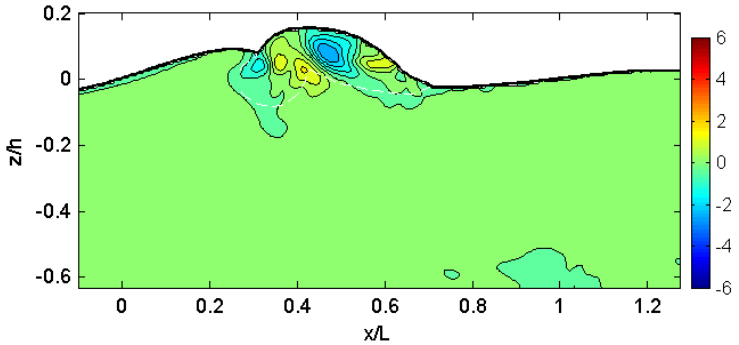

(h) $t = 0.31$ s

Fig. B.13 (Continued).

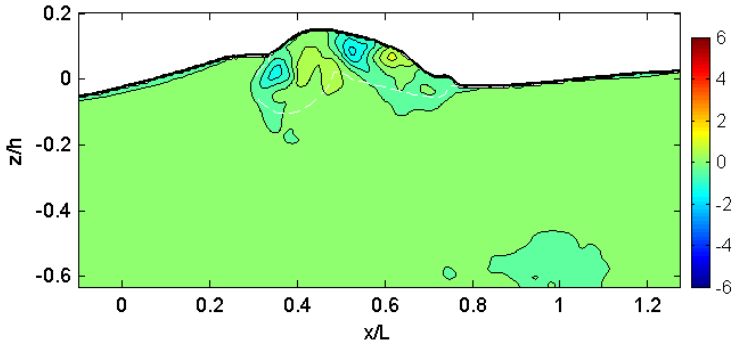

(i) $t = 0.36$ s

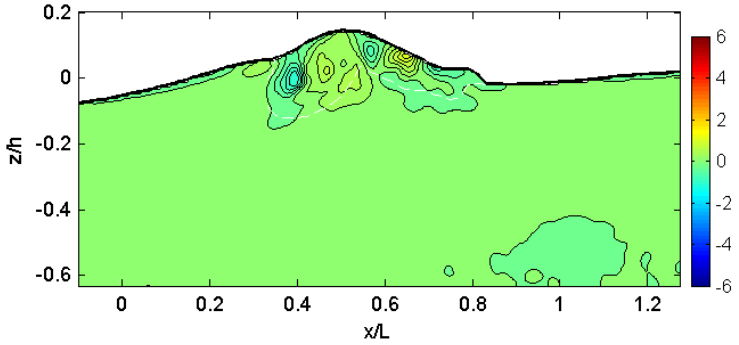

(j) $t = 0.41$ s

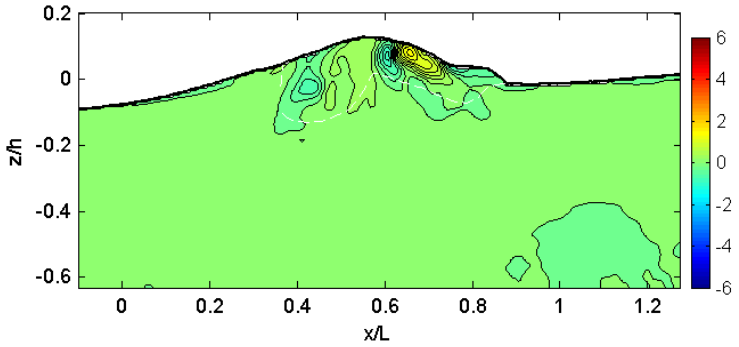

(k) $t = 0.46$ s

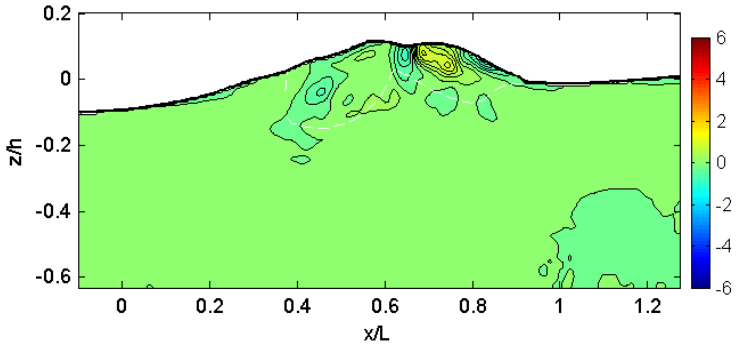

(l) $t = 0.51$ s

Fig. B.13 (Continued).

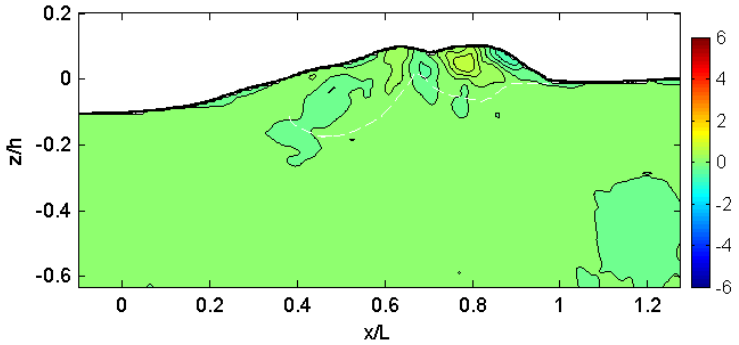

(m) $t = 0.56$ s

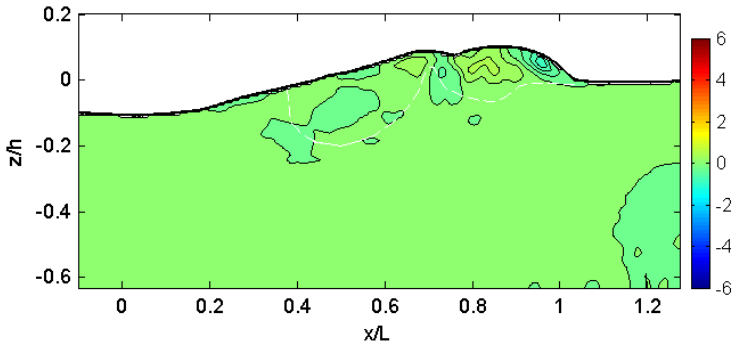

(n) $t = 0.61$ s

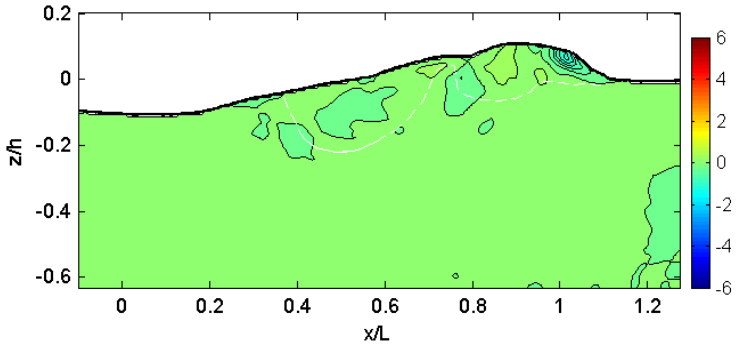

(o) $t = 0.66$ s

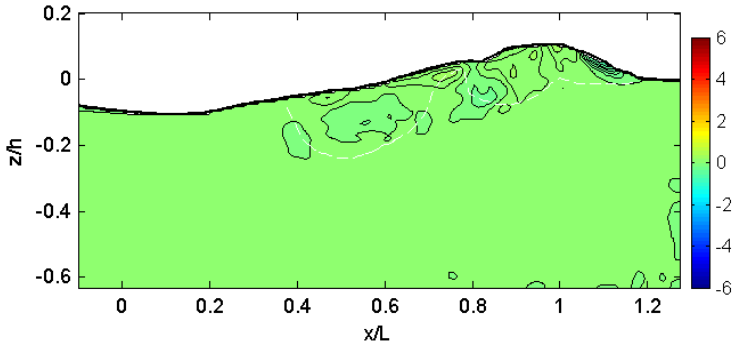

(p) $t = 0.71$ s

Fig. B.13 (Continued).

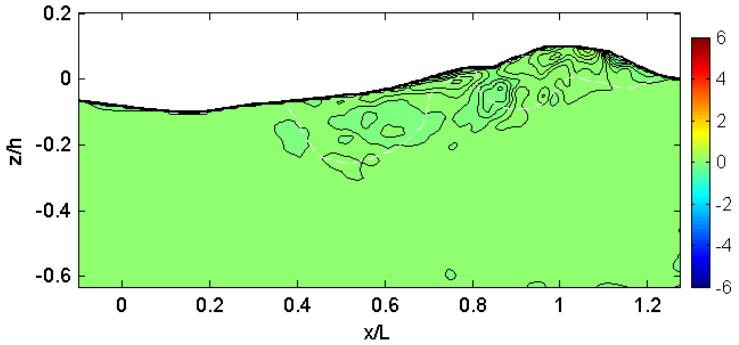

(q) $t = 0.76$ s

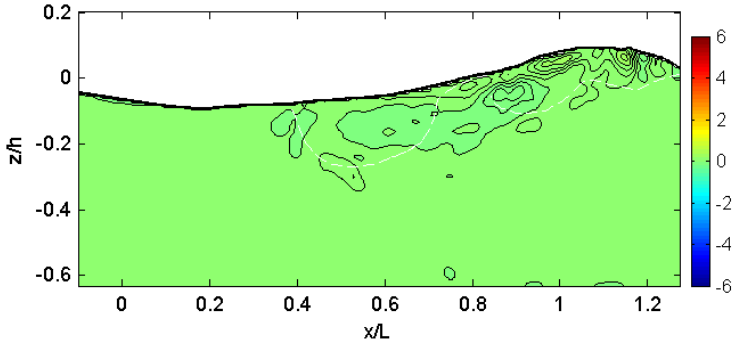

(r) $t = 0.81$ s

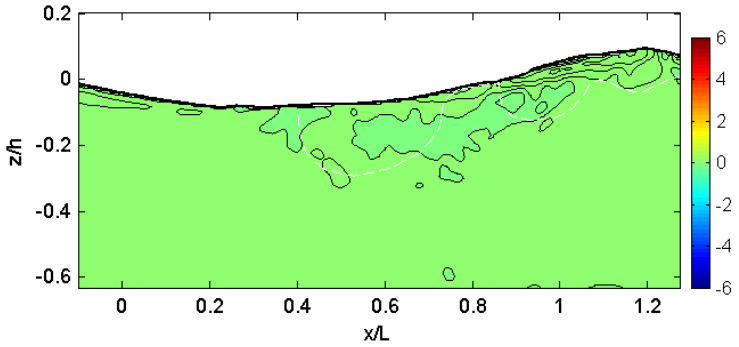

(s) $t = 0.86$ s

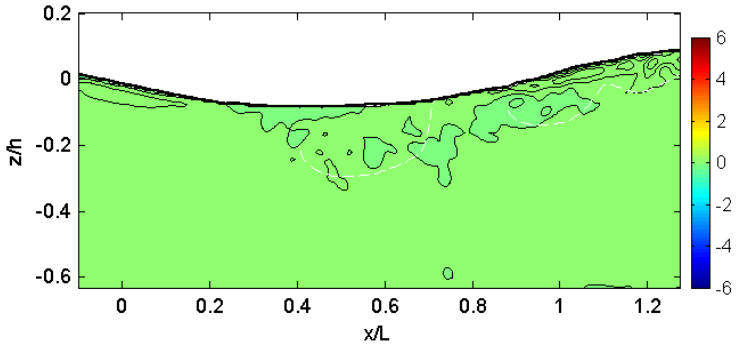

(t) $t = 0.91$ s

Fig. B.13 (Continued).

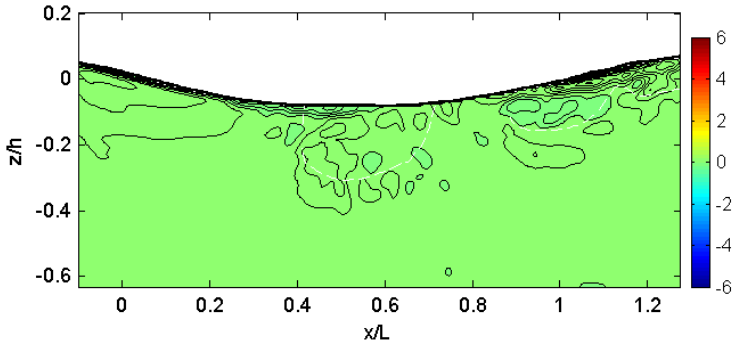

(u) t = 0.96 s

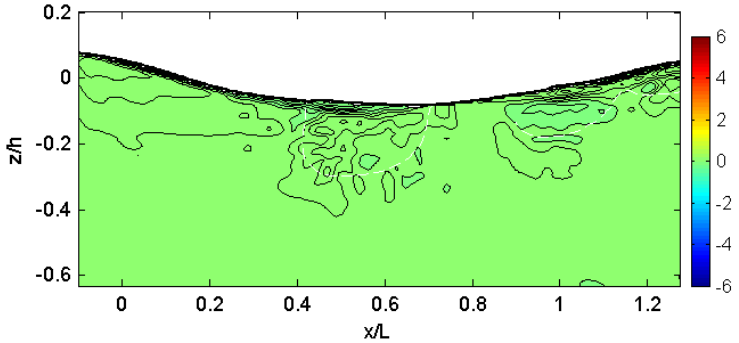

(v) t = 1.01 s

Fig. B.13 (Continued).

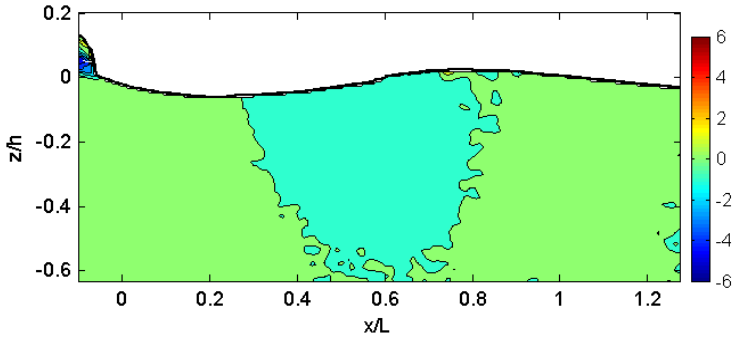

(a) t = -0.04 s

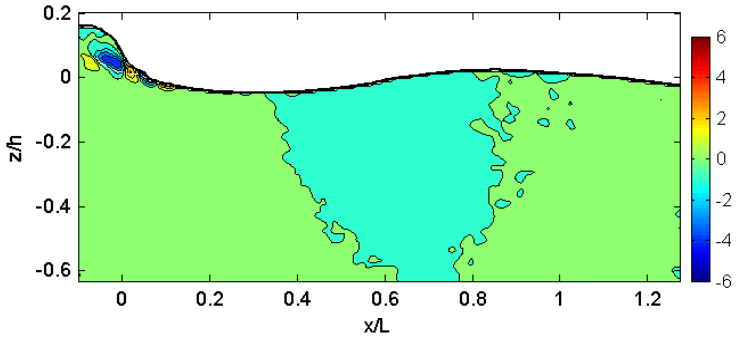

(b) t = 0.01 s

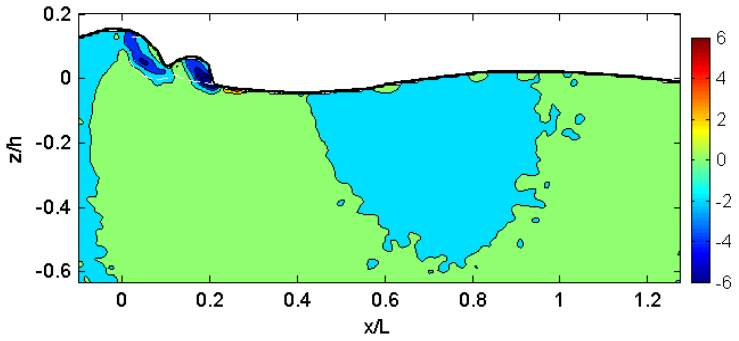

(c) t = 0.06 s

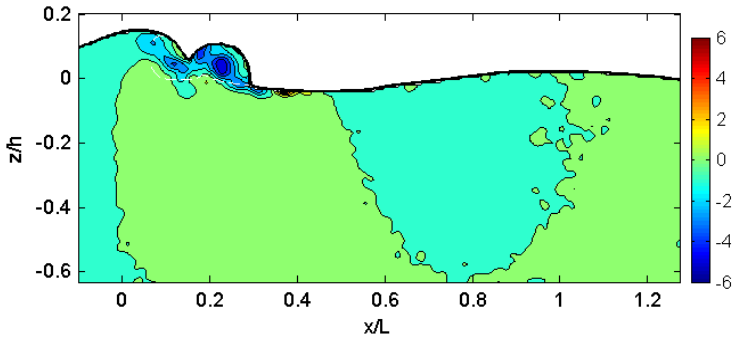

(d) t = 0.11 s

Fig. B.14 Normalized horizontal local acceleration, $\frac{\partial U}{\partial t}\Big/ g$.

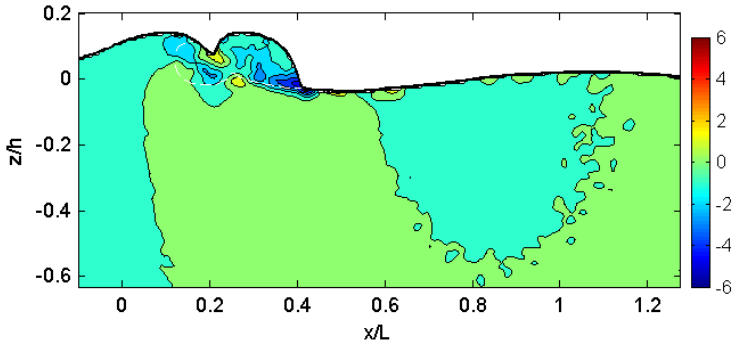

(e) $t = 0.16$ s

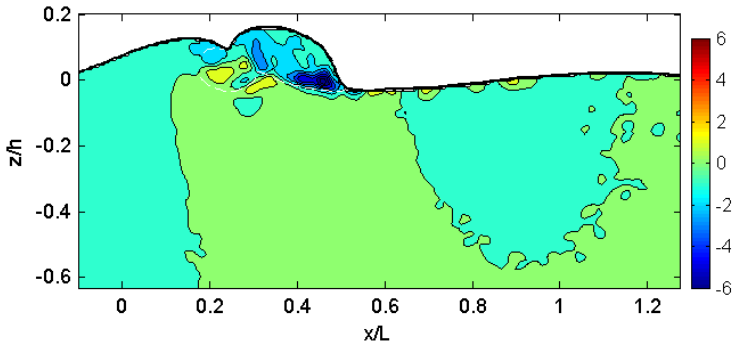

(f) $t = 0.21$ s

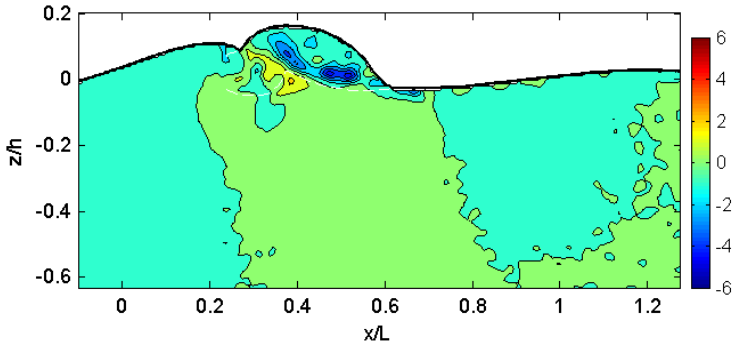

(g) $t = 0.26$ s

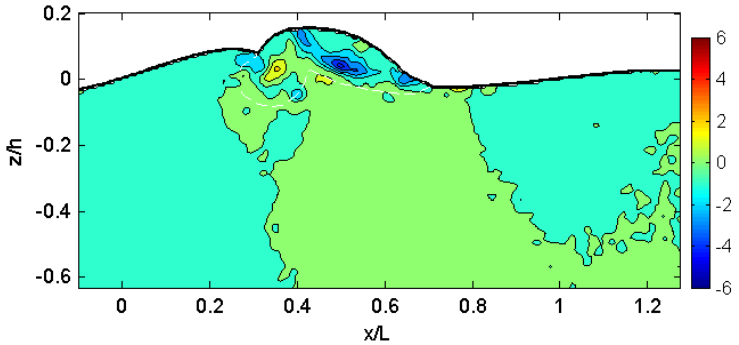

(h) $t = 0.31$ s

Fig. B.14 (Continued).

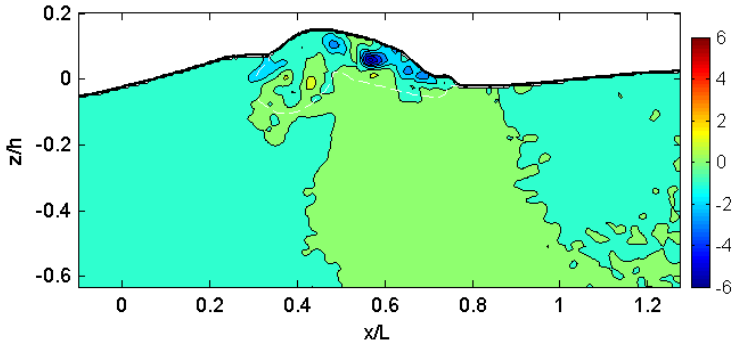

(i) $t = 0.36$ s

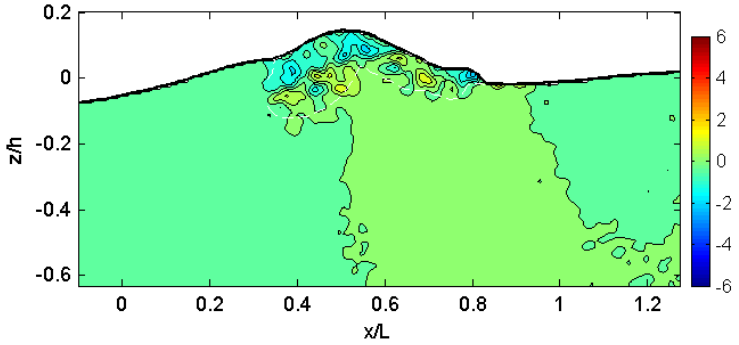

(j) $t = 0.41$ s

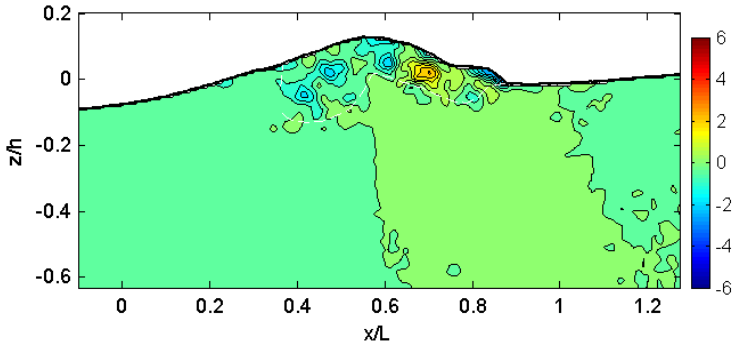

(k) $t = 0.46$ s

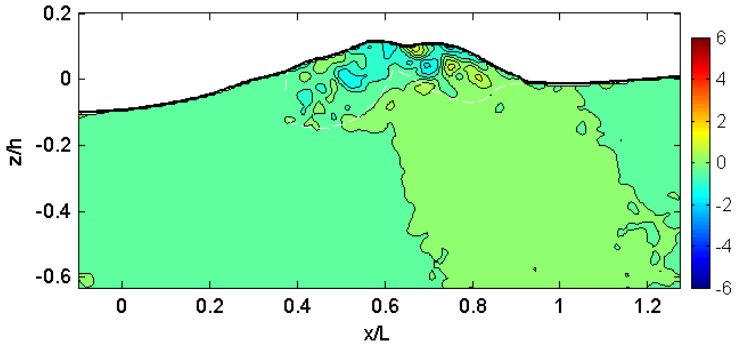

(l) $t = 0.51$ s

Fig. B.14 (Continued).

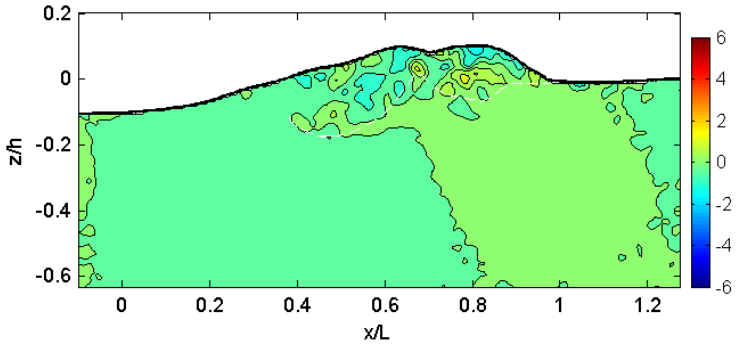

(m) t = 0.56 s

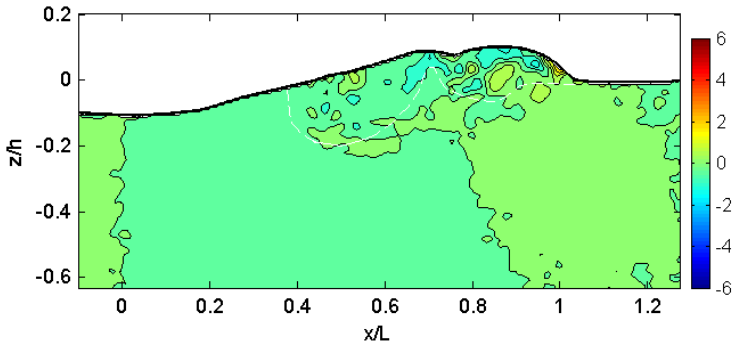

(n) t = 0.61 s

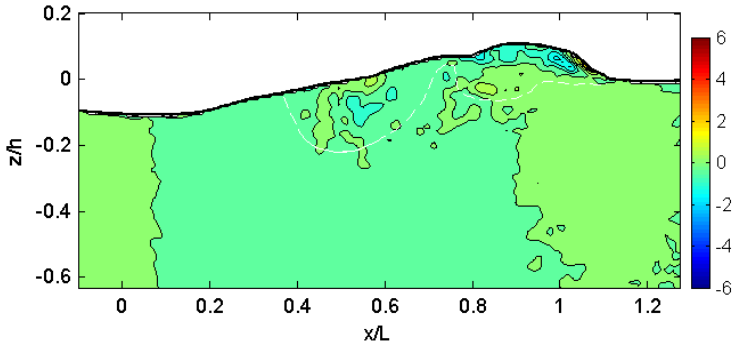

(o) t = 0.66 s

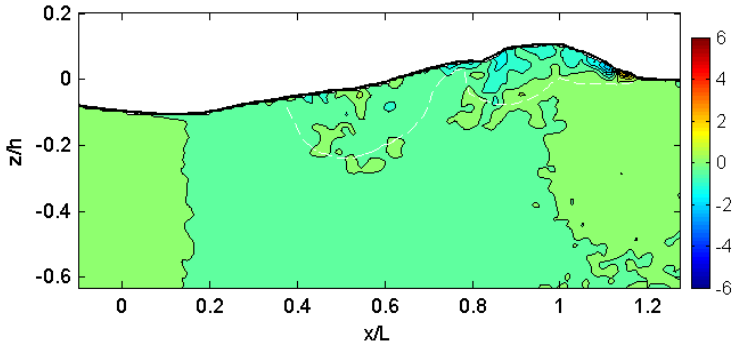

(p) t = 0.71 s

Fig. B.14 (Continued).

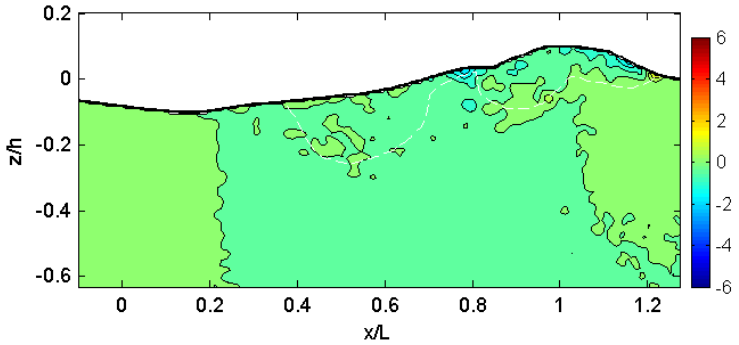

(q) $t = 0.76$ s

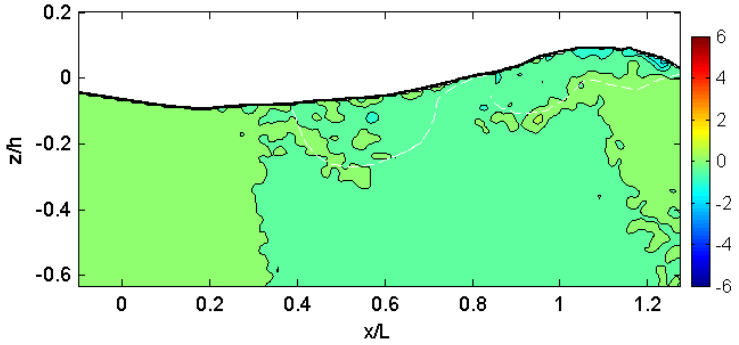

(r) $t = 0.81$ s

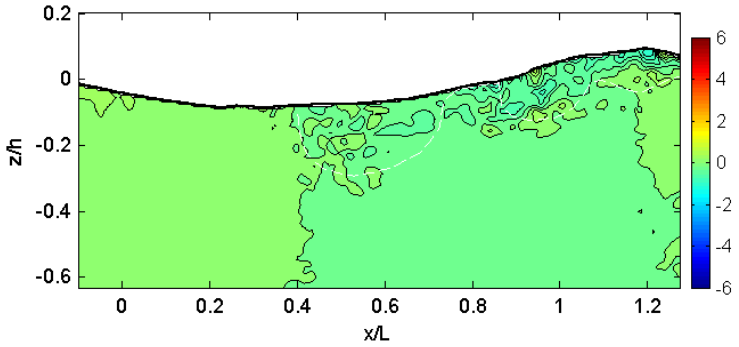

(s) $t = 0.86$ s

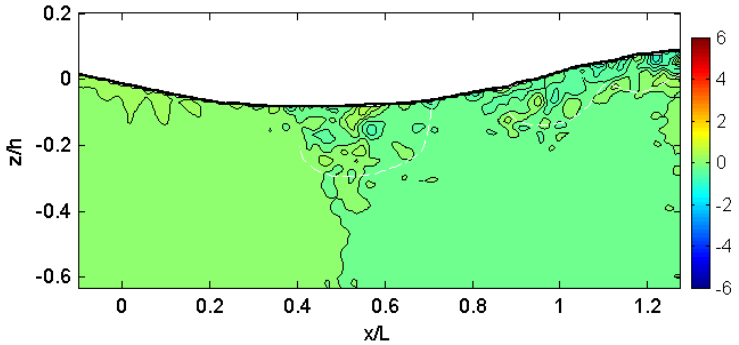

(t) $t = 0.91$ s

Fig. B.14 (Continued).

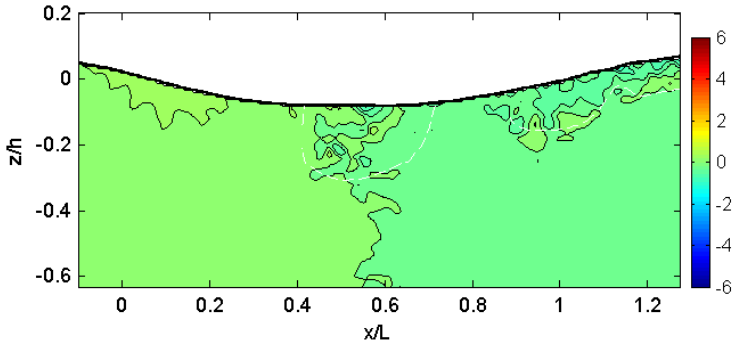

(u) t = 0.96 s

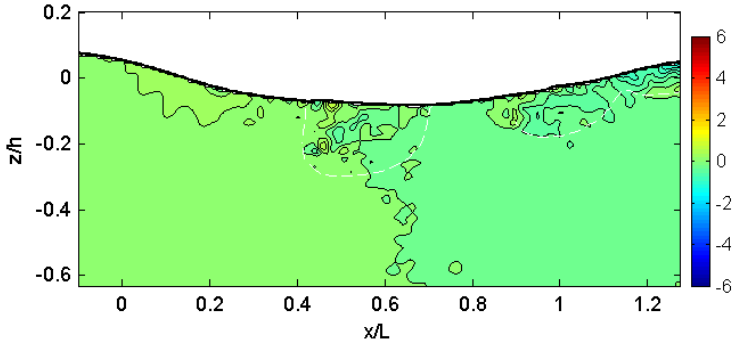

(v) t = 1.01 s

Fig. B.14 (Continued).

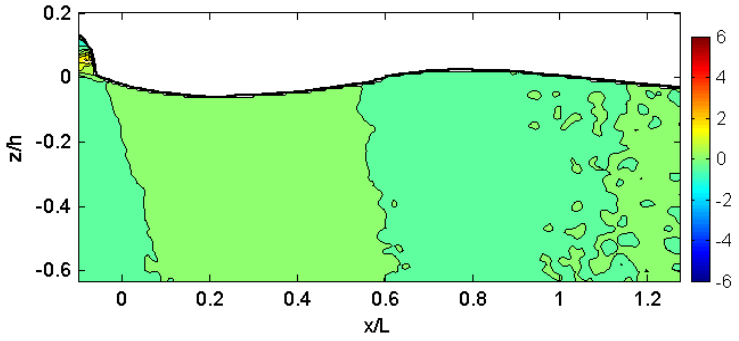

(a) t = -0.04 s

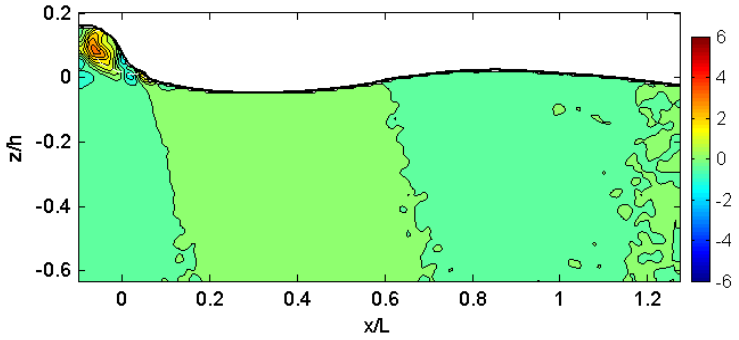

(b) t = 0.01 s

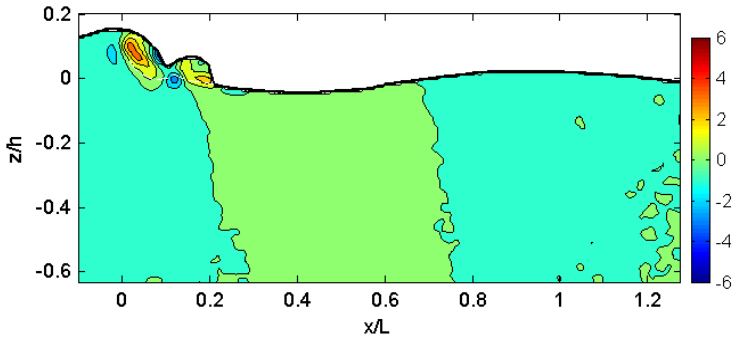

(c) t = 0.06 s

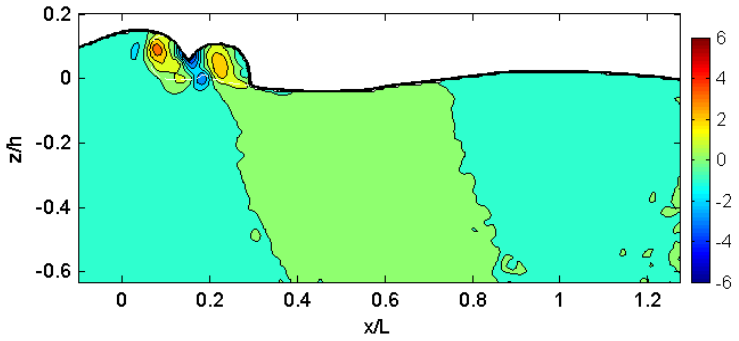

(d) t = 0.11 s

Fig. B.15 Normalized vertical local acceleration, $\frac{\partial W}{\partial t}\Big/ g$.

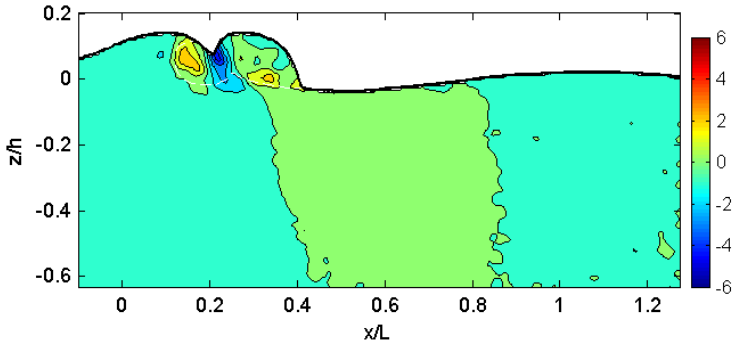

(e) $t = 0.16$ s

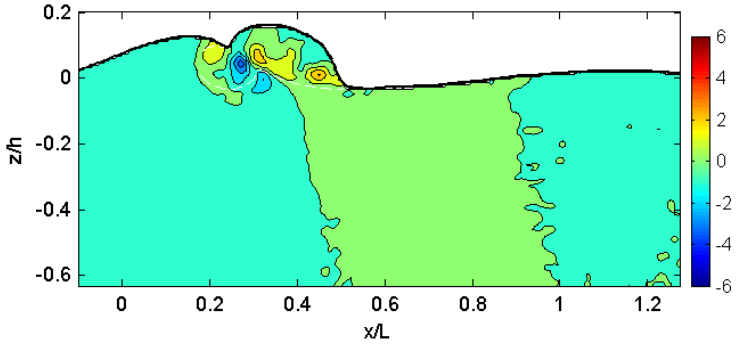

(f) $t = 0.21$ s

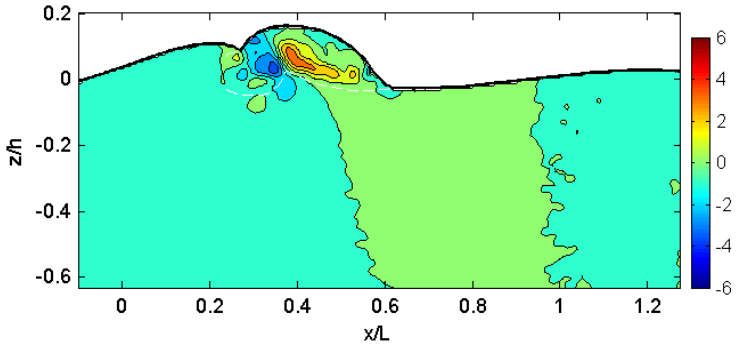

(g) $t = 0.26$ s

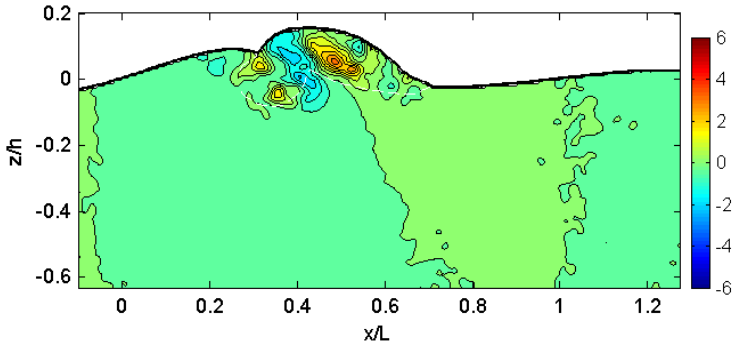

(h) $t = 0.31$ s

Fig. B.15 (Continued).

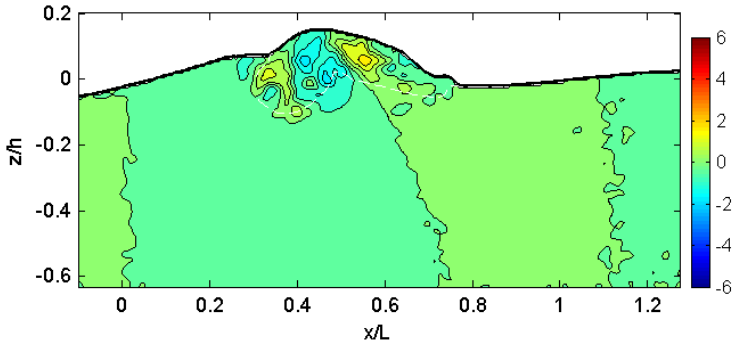

(i) $t = 0.36$ s

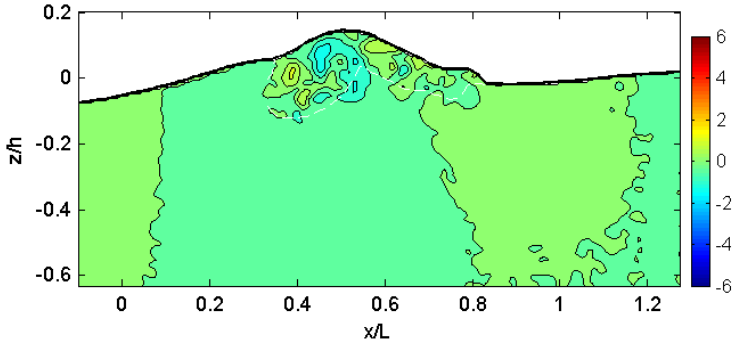

(j) $t = 0.41$ s

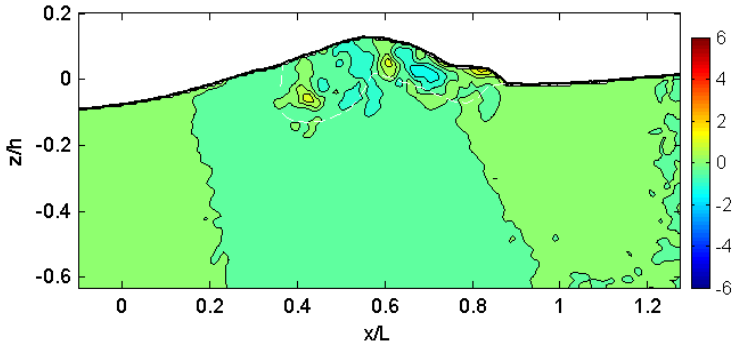

(k) $t = 0.46$ s

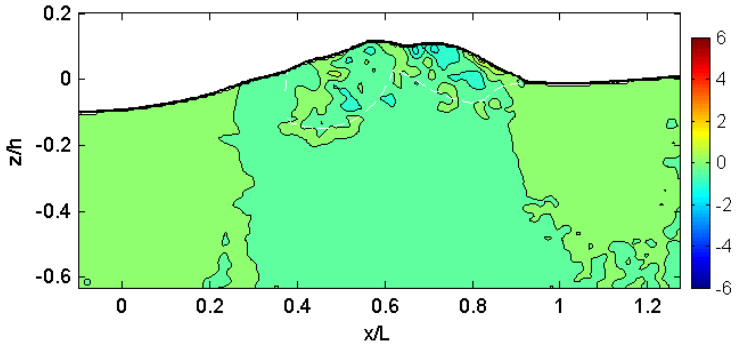

(l) $t = 0.51$ s

Fig. B.15 (Continued).

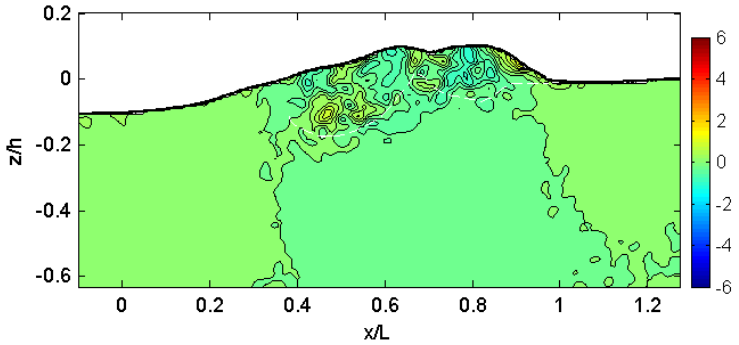

(m) $t = 0.56$ s

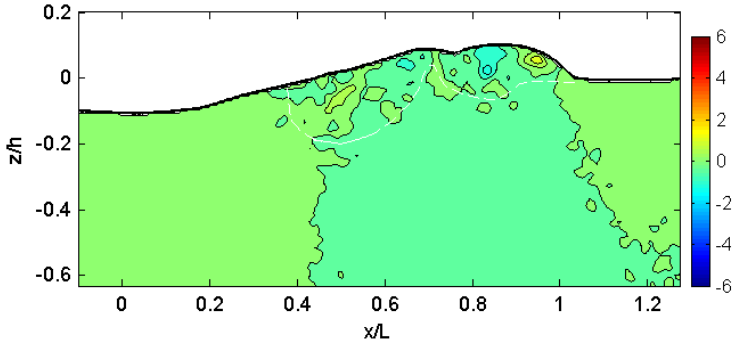

(n) $t = 0.61$ s

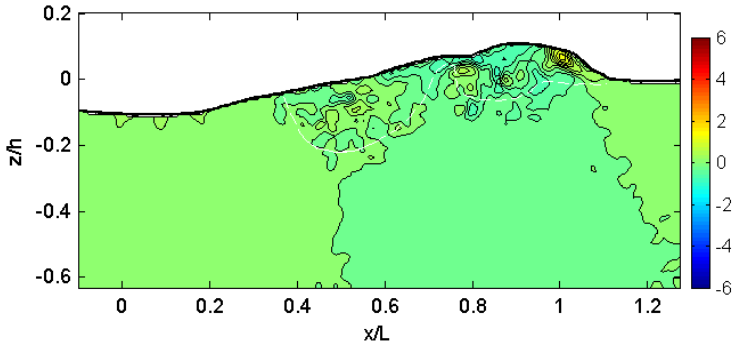

(o) $t = 0.66$ s

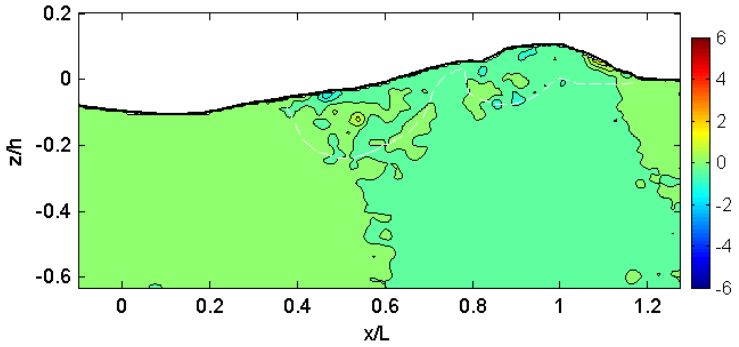

(p) $t = 0.71$ s

Fig. B.15 (Continued).

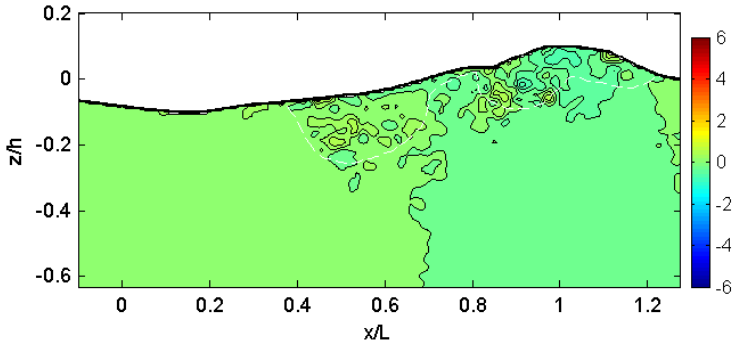

(q) t = 0.76 s

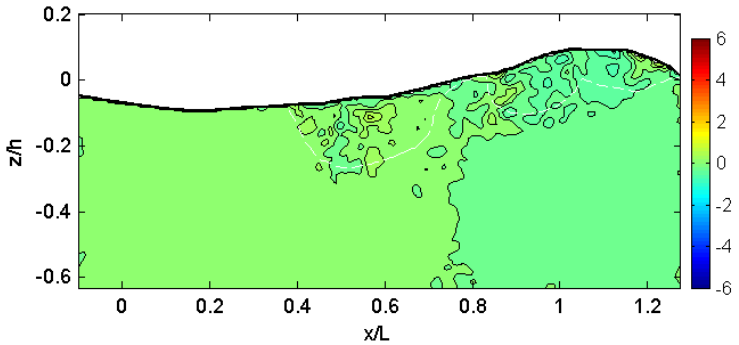

(r) t = 0.81 s

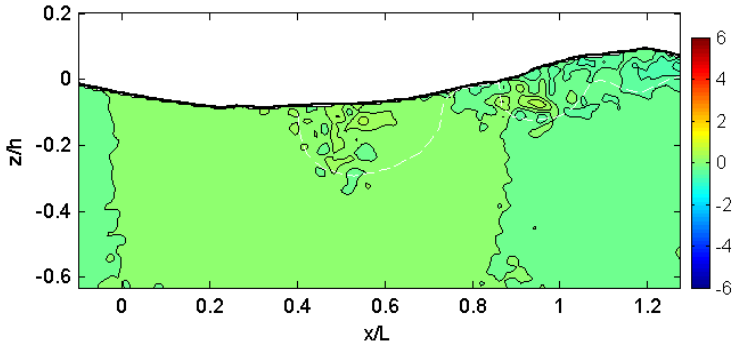

(s) t = 0.86 s

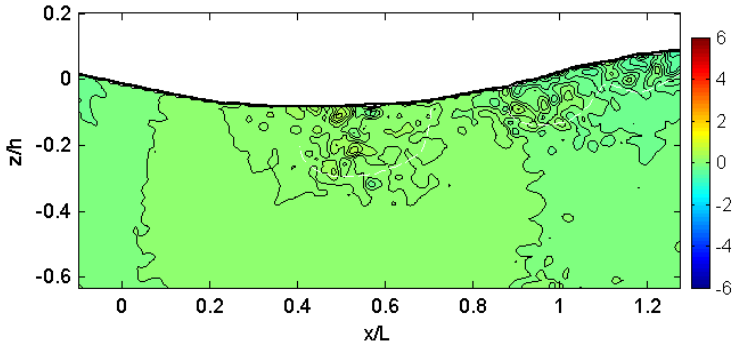

(t) t = 0.91 s

Fig. B.15 (Continued).

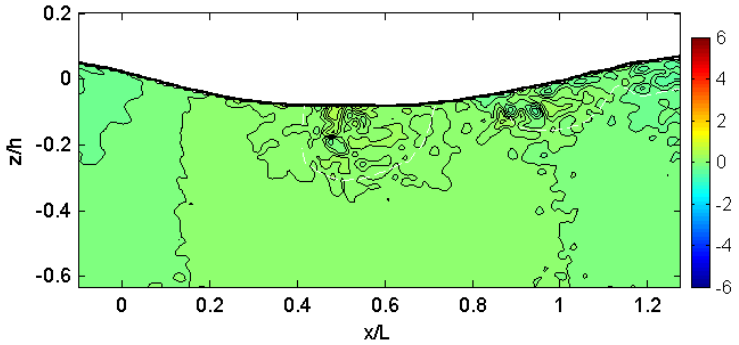

(u) t = 0.96 s

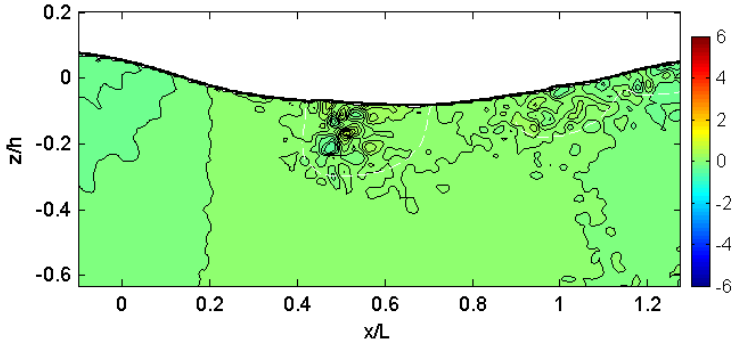

(v) t = 1.01 s

Fig. B.15 (Continued).

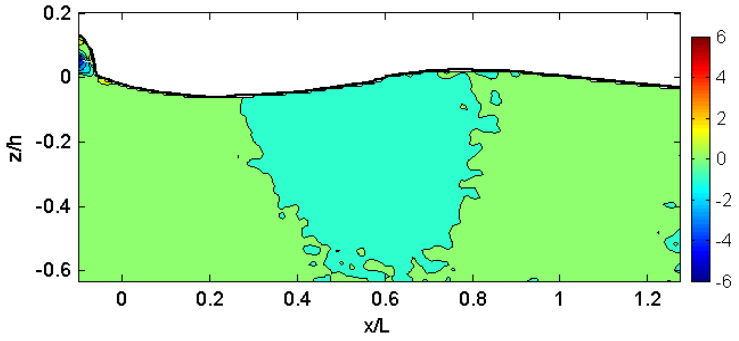

(a) t = -0.04 s

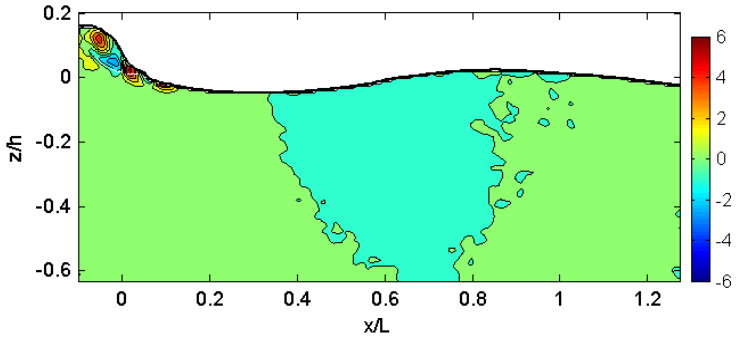

(b) t = 0.01 s

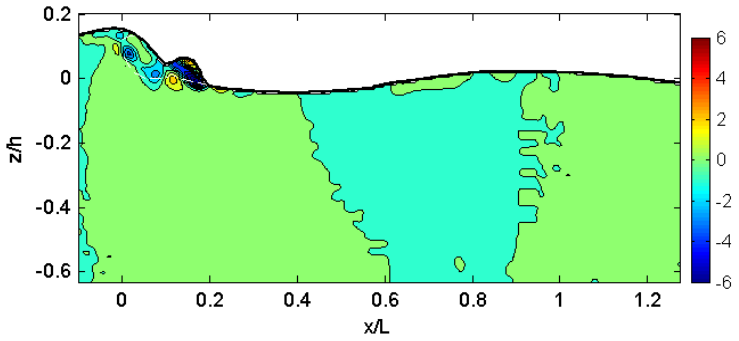

(c) t = 0.06 s

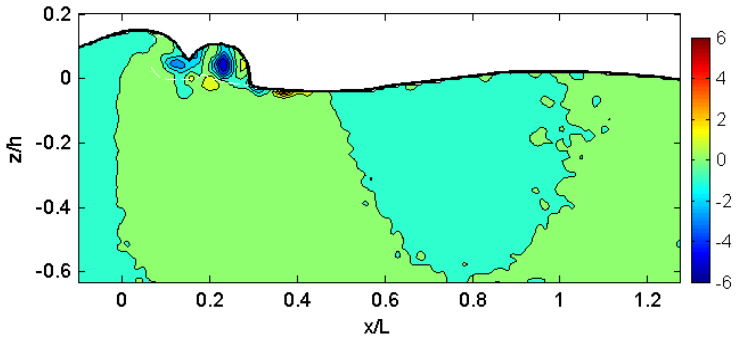

(d) t = 0.11 s

Fig. B.16 Normalized horizontal total acceleration, $\left(\frac{\partial U}{\partial t}+U\frac{\partial U}{\partial x}+W\frac{\partial U}{\partial z}\right)\Big/g$ **.**

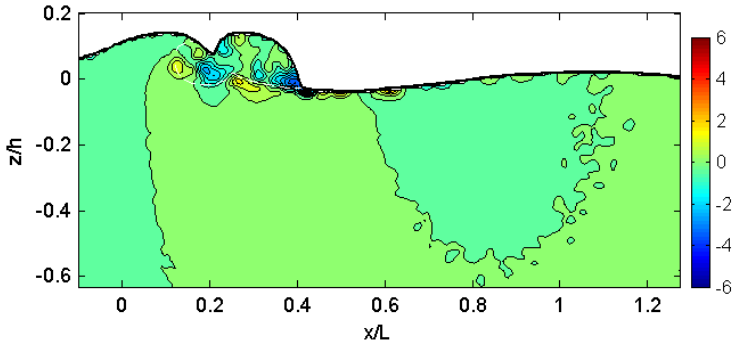

(e) $t = 0.16$ s

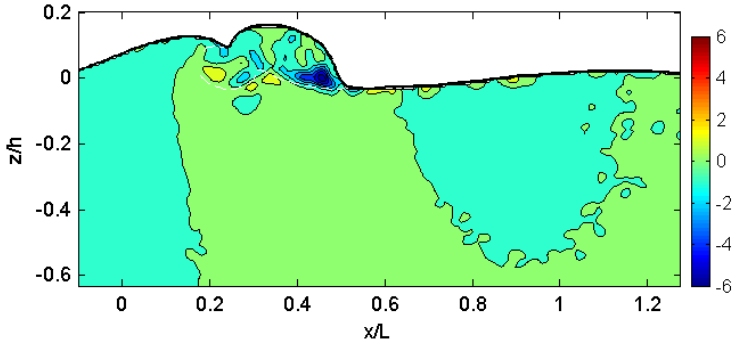

(f) $t = 0.21$ s

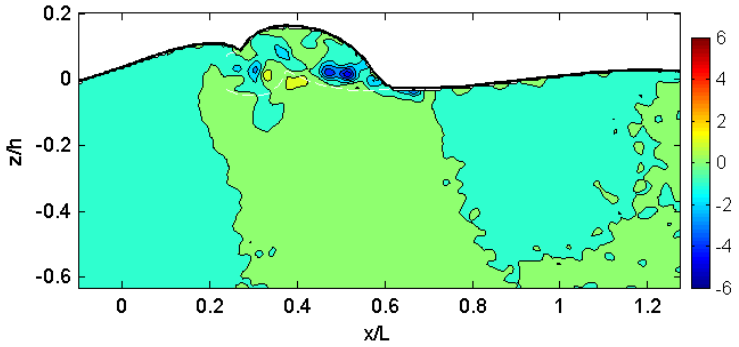

(g) $t = 0.26$ s

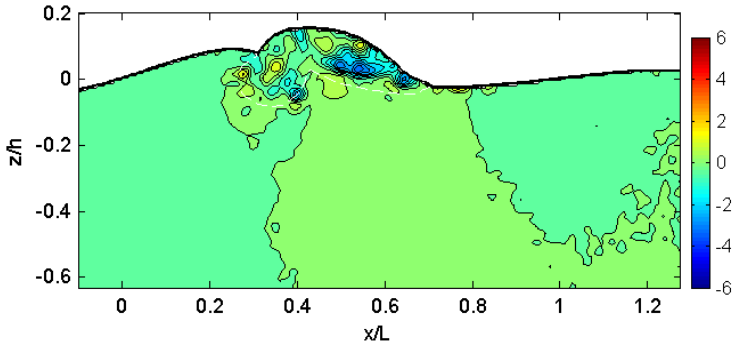

(h) $t = 0.31$ s

Fig. B.16 (Continued).

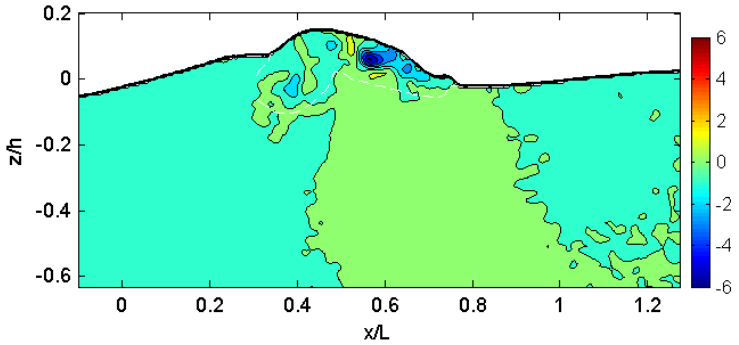

(i) $t = 0.36$ s

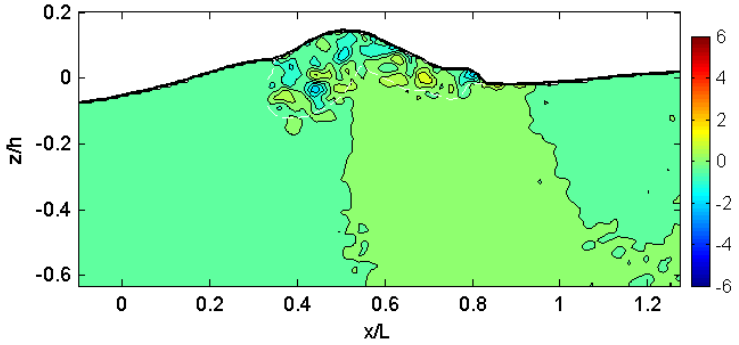

(j) $t = 0.41$ s

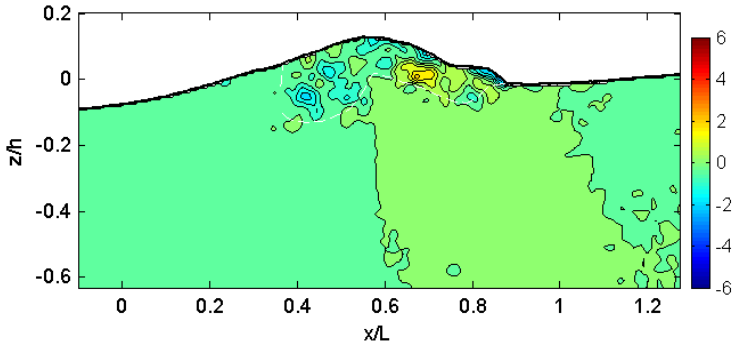

(k) $t = 0.46$ s

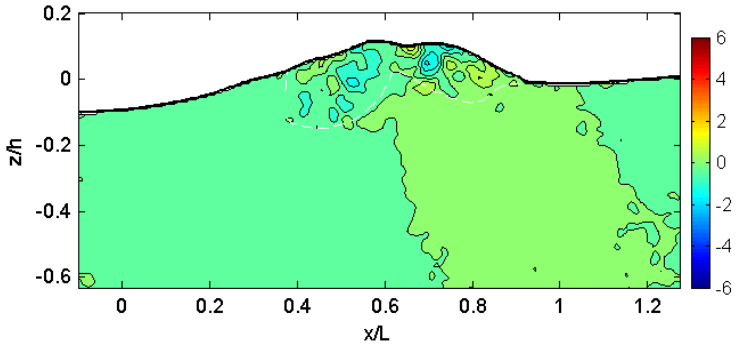

(l) $t = 0.51$ s

Fig. B.16 (Continued).

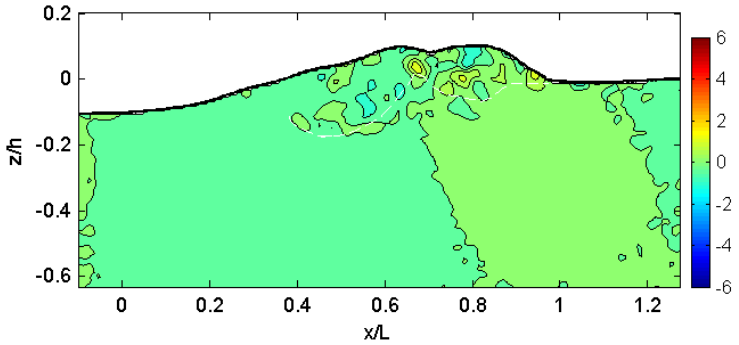

(m) $t = 0.56$ s

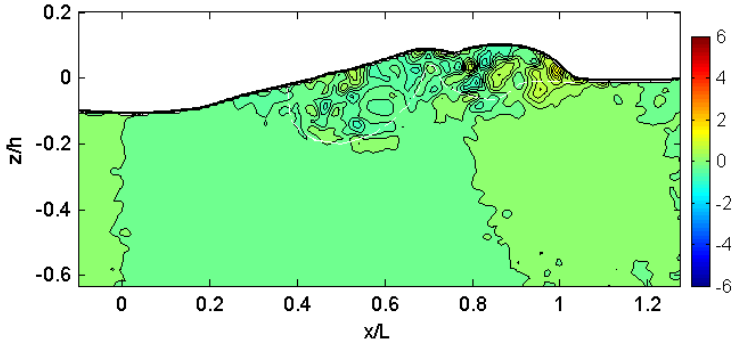

(n) $t = 0.61$ s

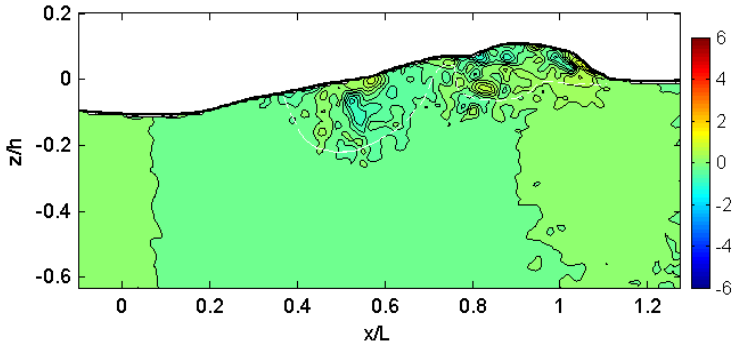

(o) $t = 0.66$ s

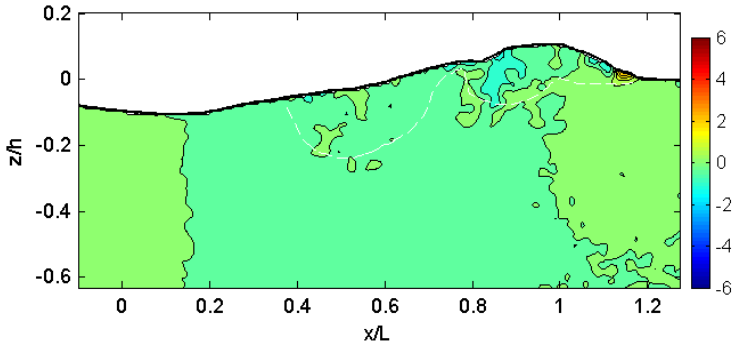

(p) $t = 0.71$ s

Fig. B.16 (Continued).

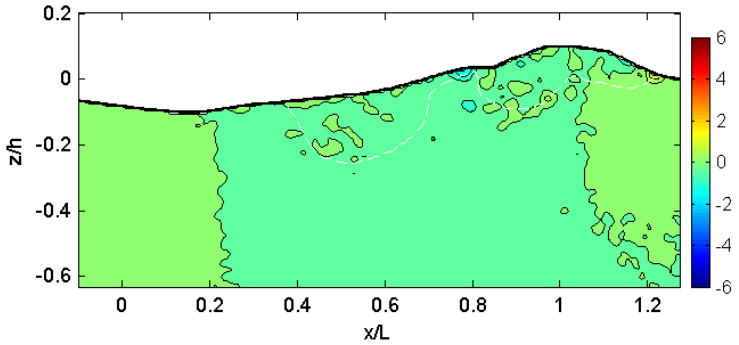

(q) t = 0.76 s

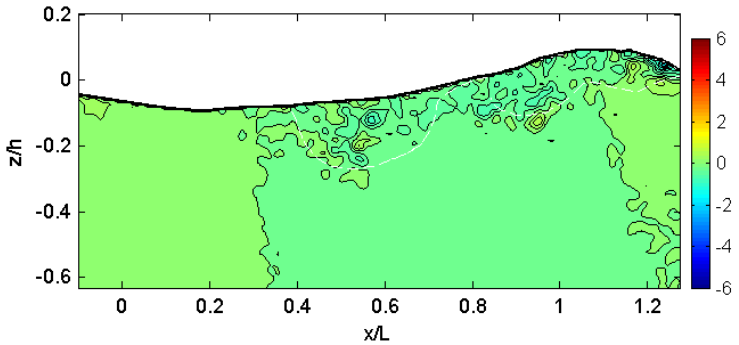

(r) t = 0.81 s

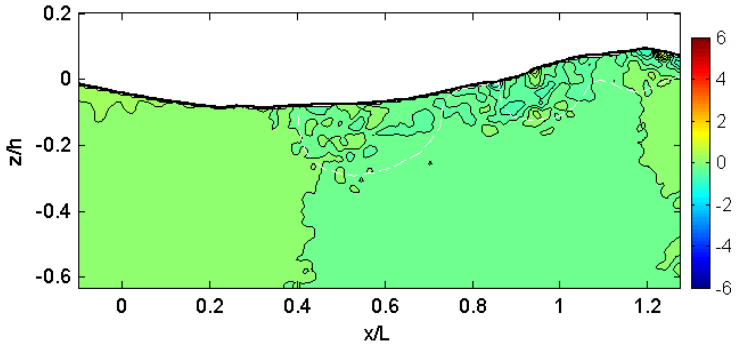

(s) t = 0.86 s

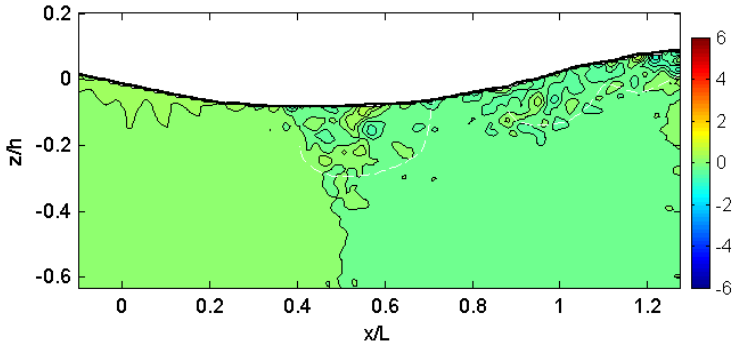

(t) t = 0.91 s

Fig. B.16 (Continued).

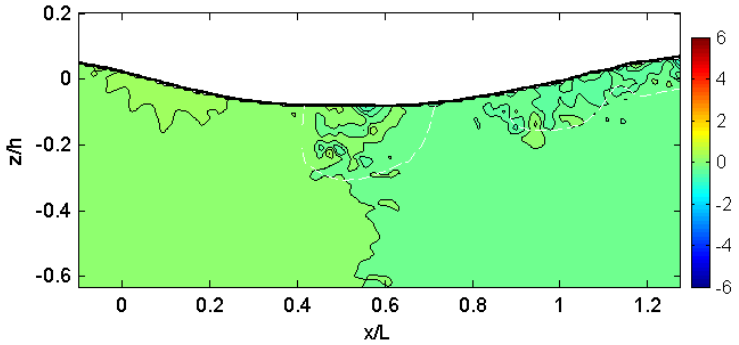

(u) t = 0.96 s

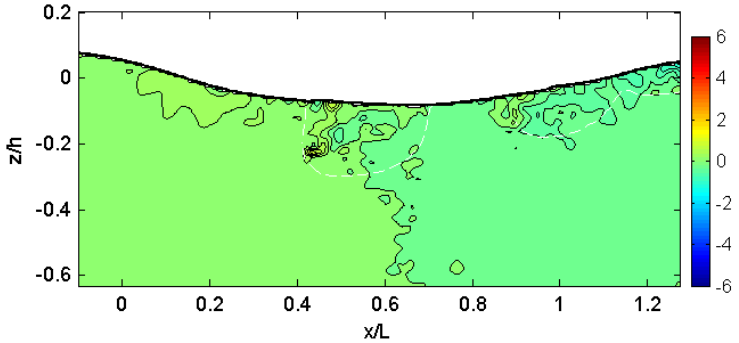

(v) t = 1.01 s

Fig. B.16 (Continued).

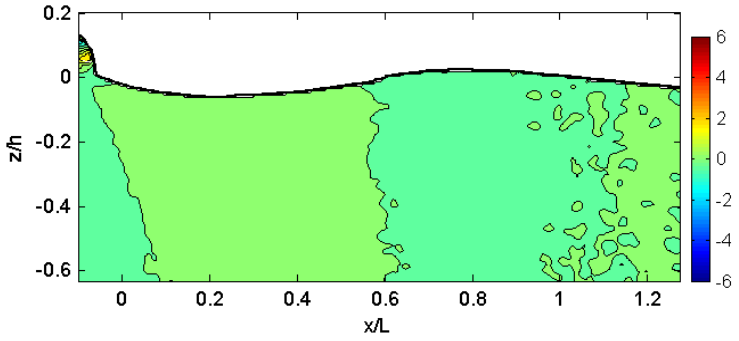

(a) t = -0.04 s

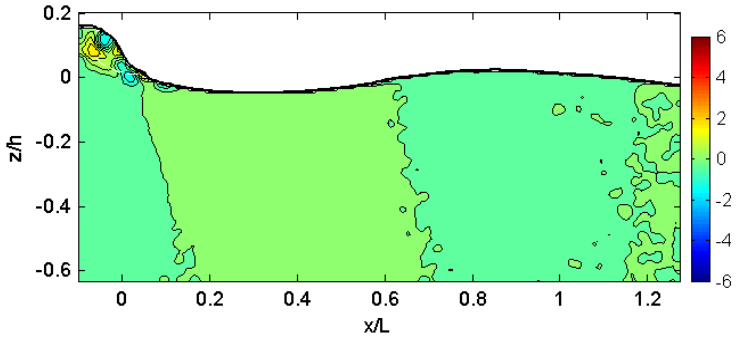

(b) t = 0.01 s

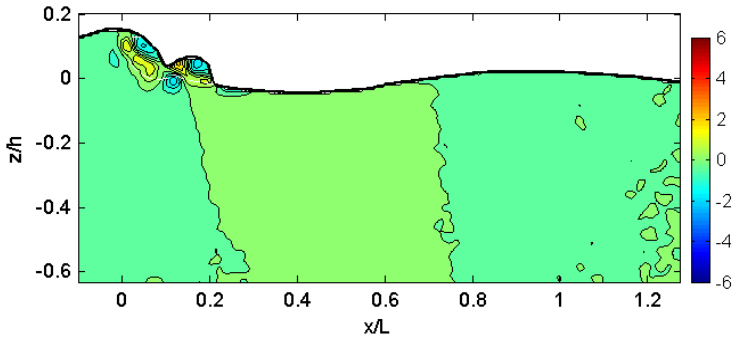

(c) t = 0.06 s

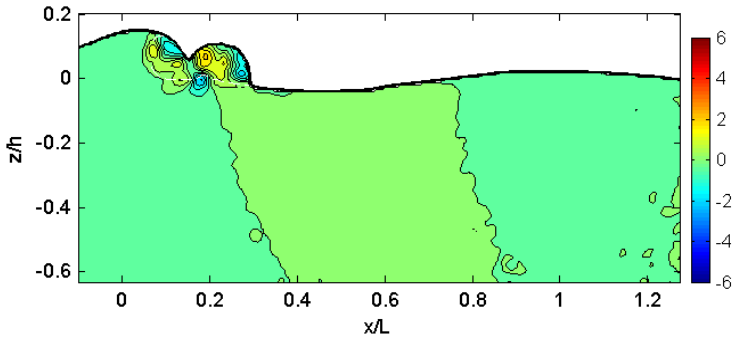

(d) t = 0.11 s

Fig. B.17 Normalized vertical total acceleration, $\left(\frac{\partial W}{\partial t}+U\frac{\partial W}{\partial x}+W\frac{\partial W}{\partial z}\right)\Big/ g$ **.**

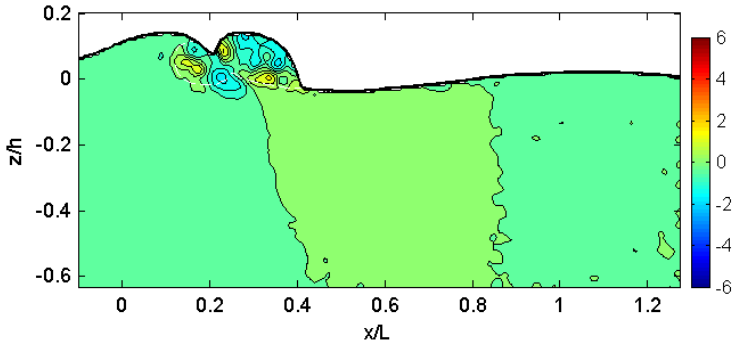

(e) $t = 0.16$ s

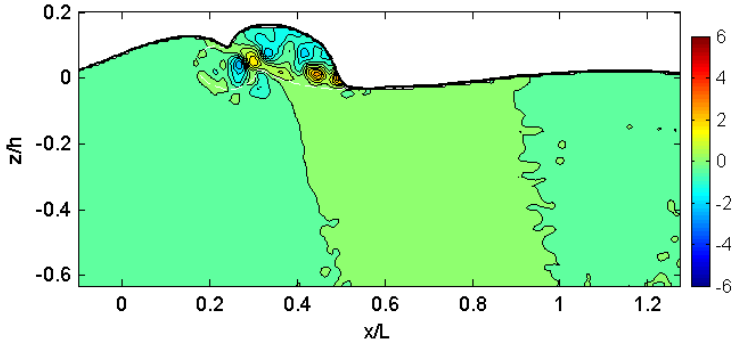

(f) $t = 0.21$ s

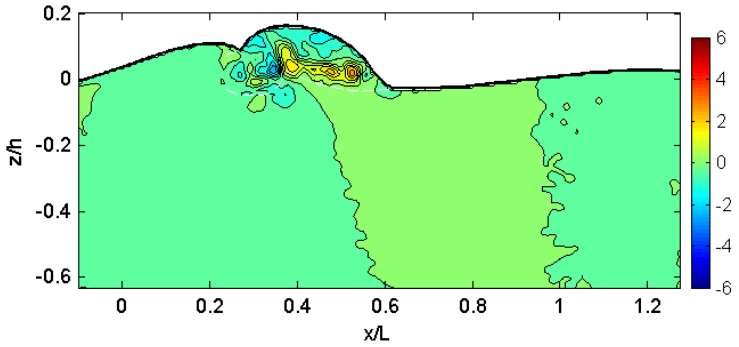

(g) $t = 0.26$ s

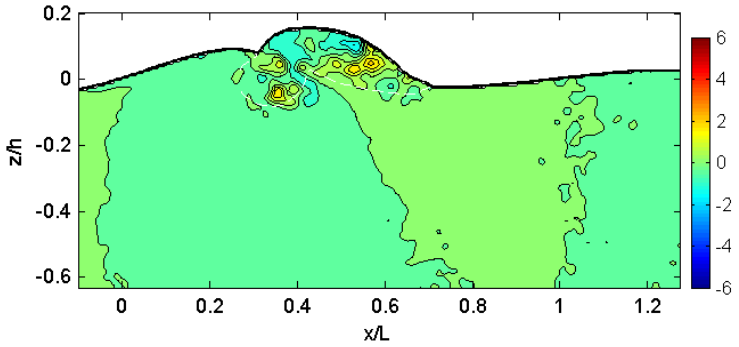

(h) $t = 0.31$ s

Fig. B.17 (Continued).

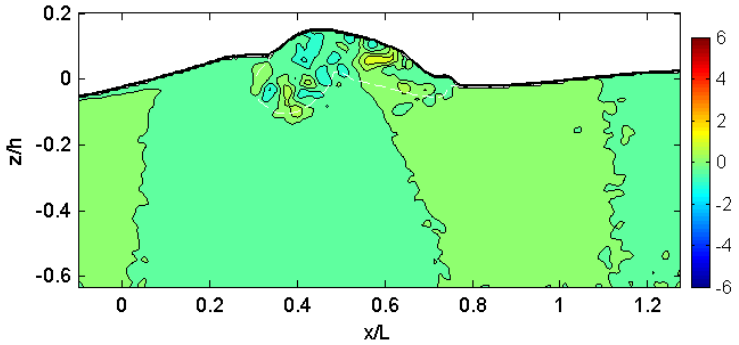

(i) $t = 0.36$ s

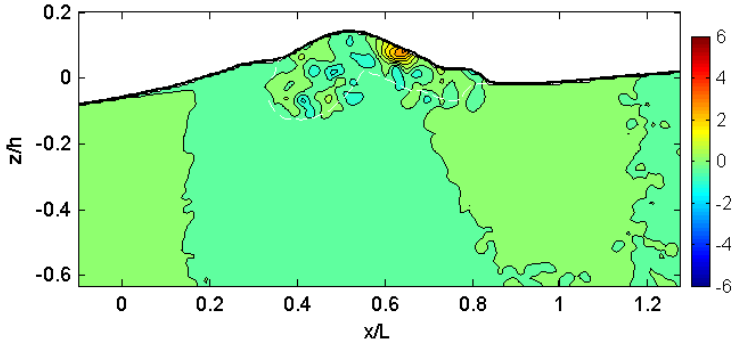

(j) $t = 0.41$ s

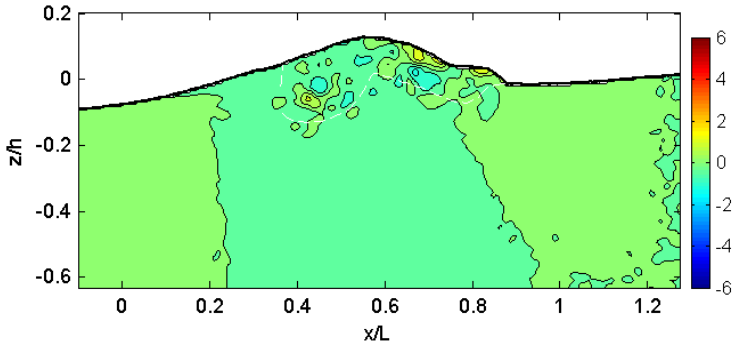

(k) $t = 0.46$ s

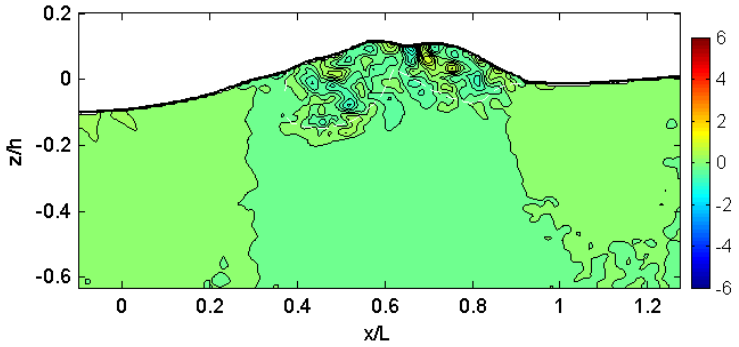

(l) $t = 0.51$ s

Fig. B.17 (Continued).

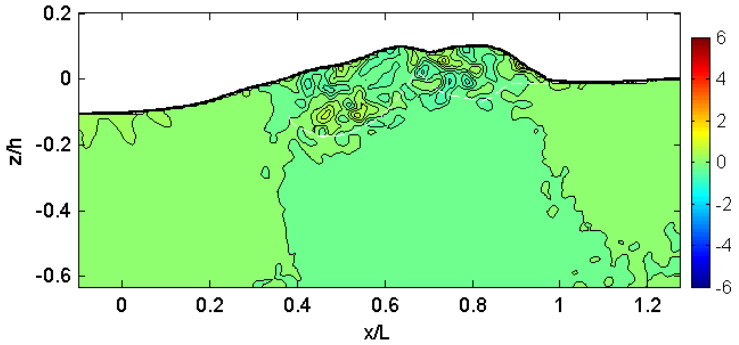

(m) t = 0.56 s

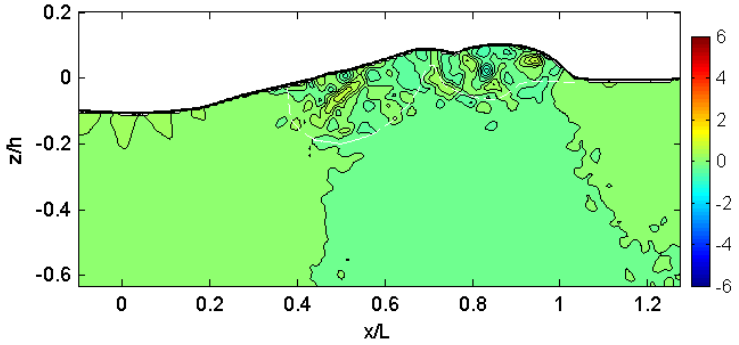

(n) t = 0.61 s

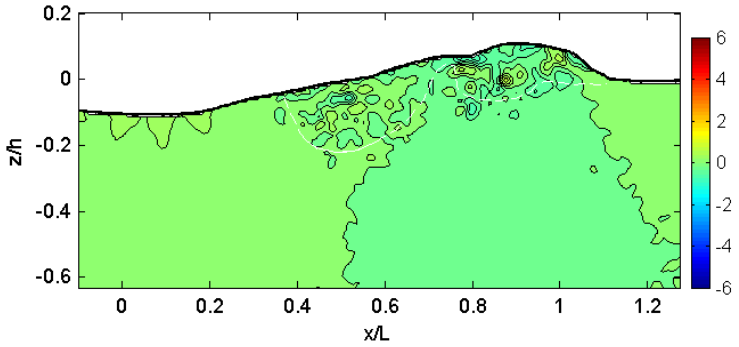

(o) t = 0.66 s

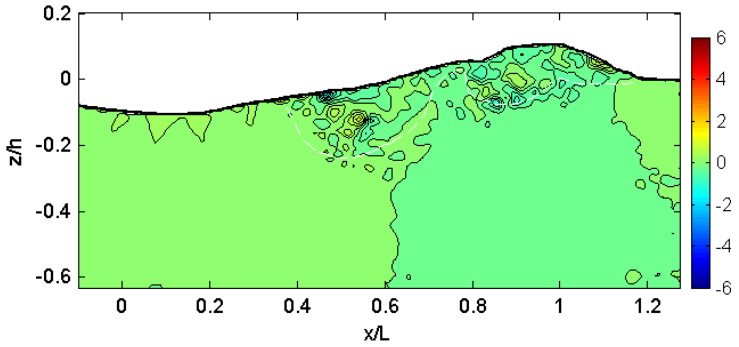

(p) t = 0.71 s

Fig. B.17 (Continued).

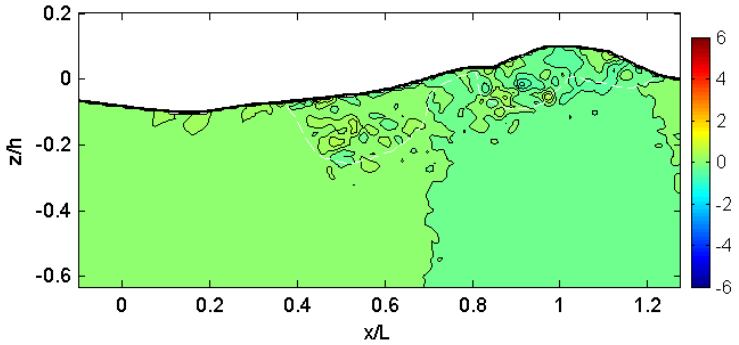

(q) t = 0.76 s

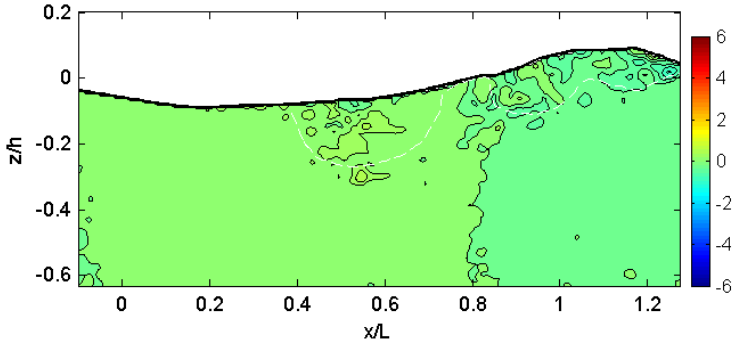

(r) t = 0.81 s

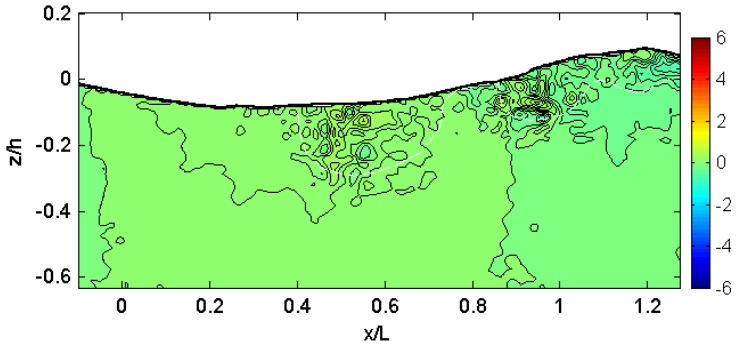

(s) t = 0.86 s

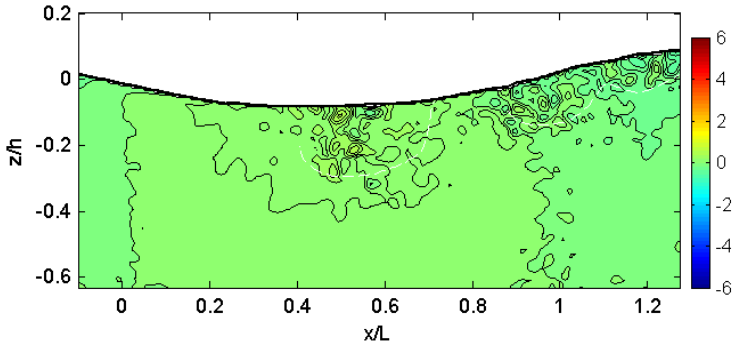

(t) t = 0.91 s

Fig. B.17 (Continued).

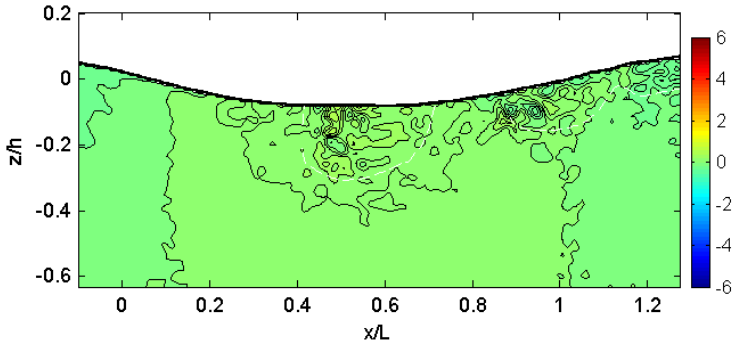

(u) t = 0.96 s

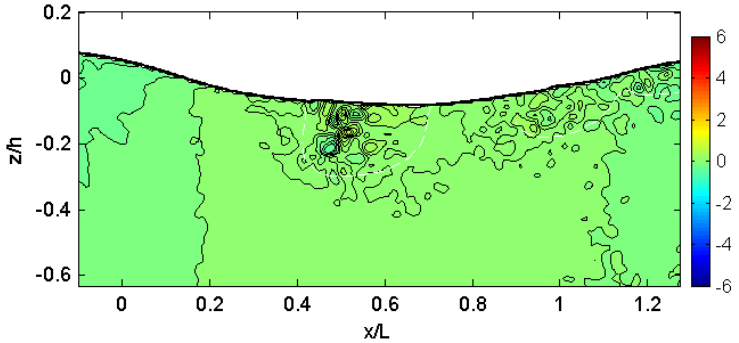

(v) t = 1.01 s

Fig. B.17 (Continued).

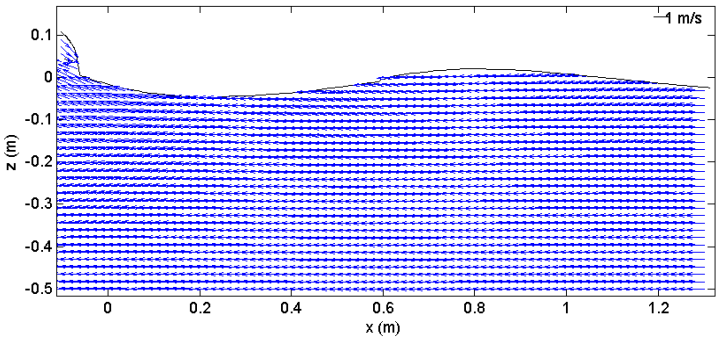

(a) t = -0.04 s

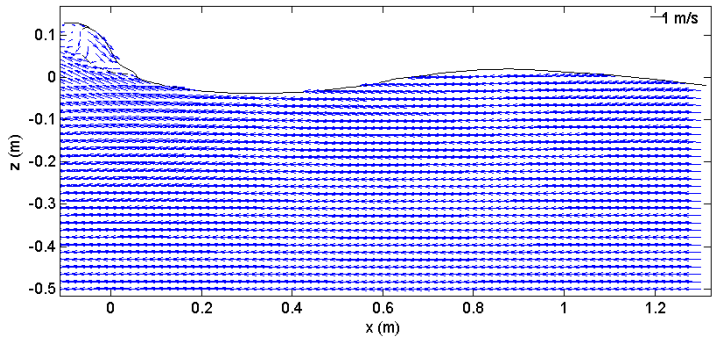

(b) t = 0.01 s

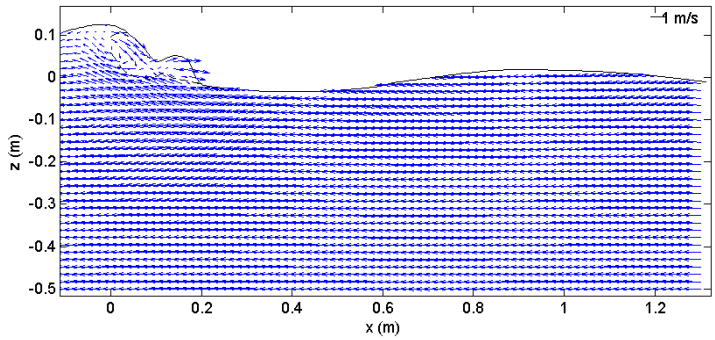

(c) t = 0.06 s

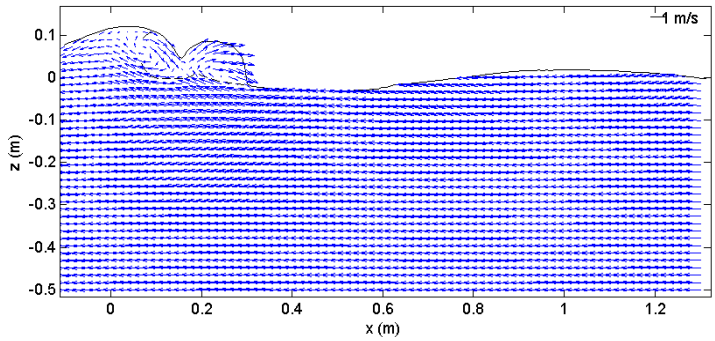

(d) t = 0.11 s

Fig. B.18 Relative velocity, $U - C, W$.

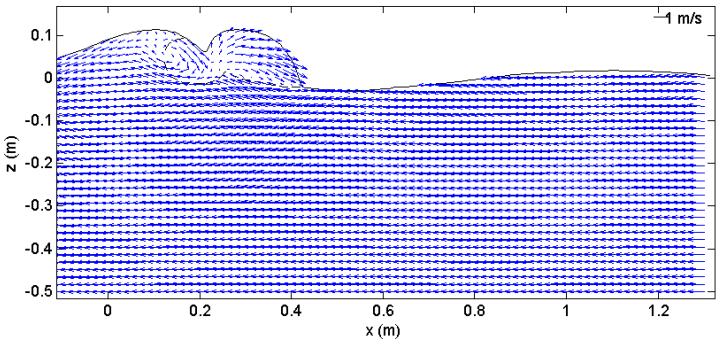

(e) $t = 0.16$ s

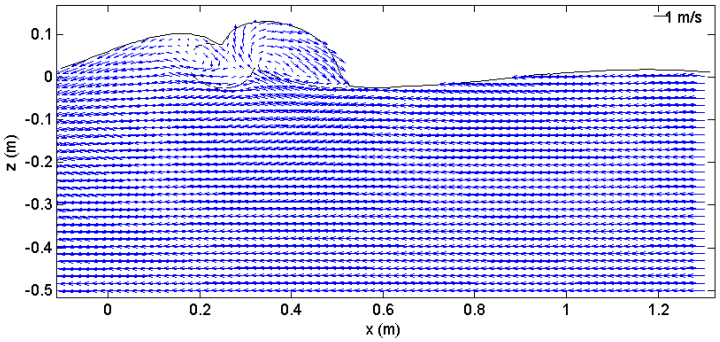

(f) $t = 0.21$ s

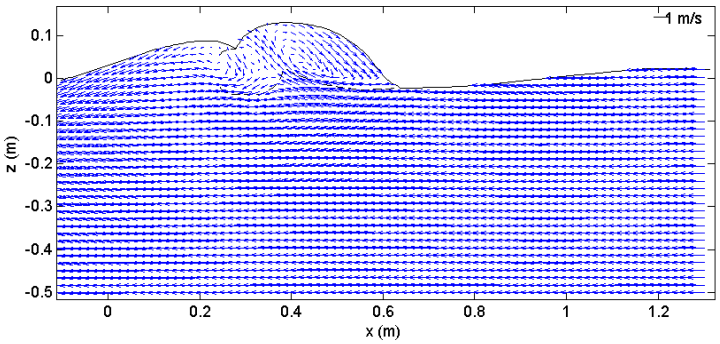

(g) $t = 0.26$ s

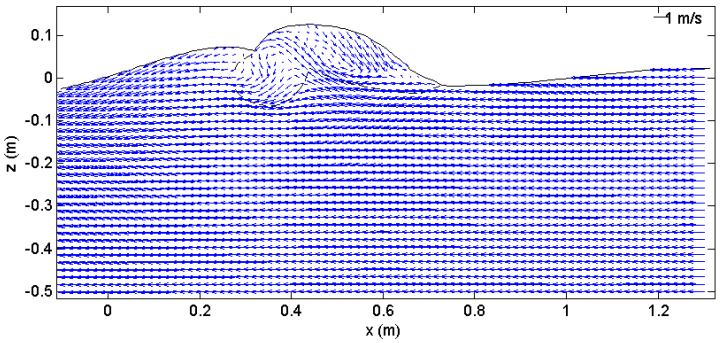

(h) $t = 0.31$ s

Fig. B.18 (Continued).

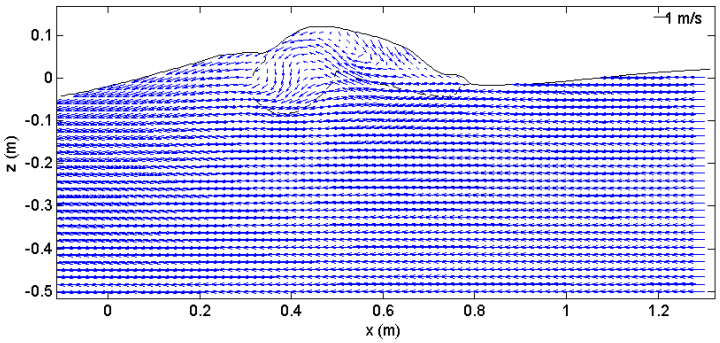

(i) $t = 0.36$ s

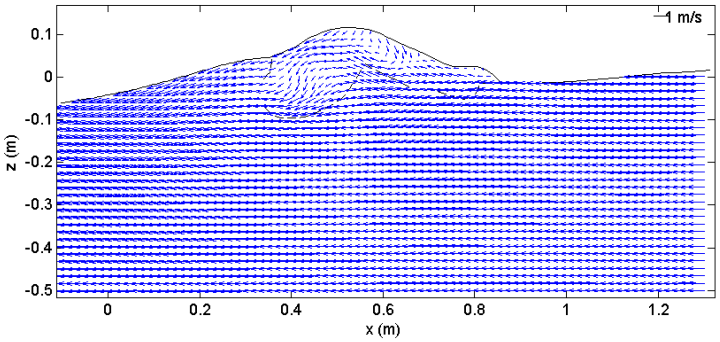

(j) $t = 0.41$ s

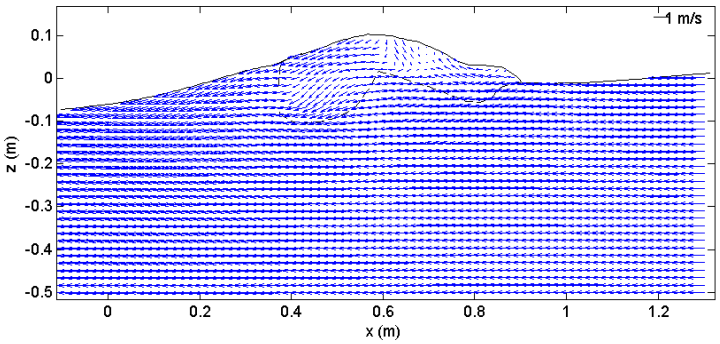

(k) $t = 0.46$ s

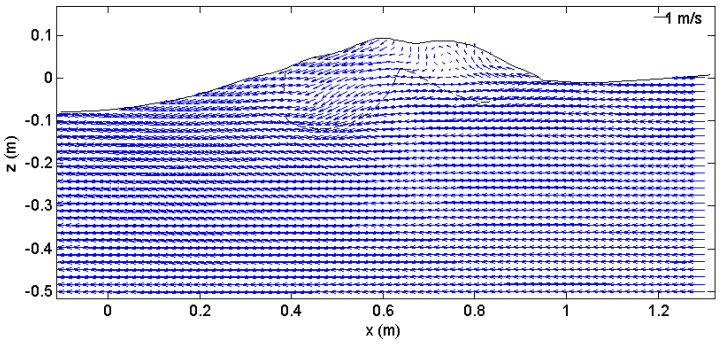

(l) $t = 0.51$ s

Fig. B.18 (Continued).

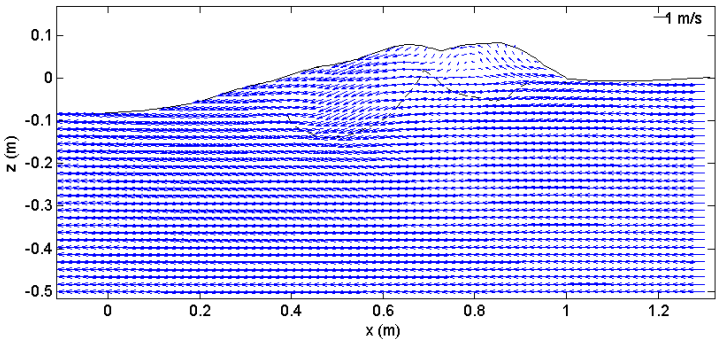

(m) $t = 0.56$ s

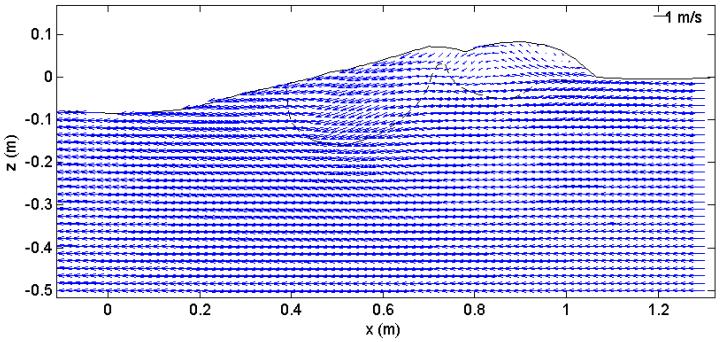

(n) $t = 0.61$ s

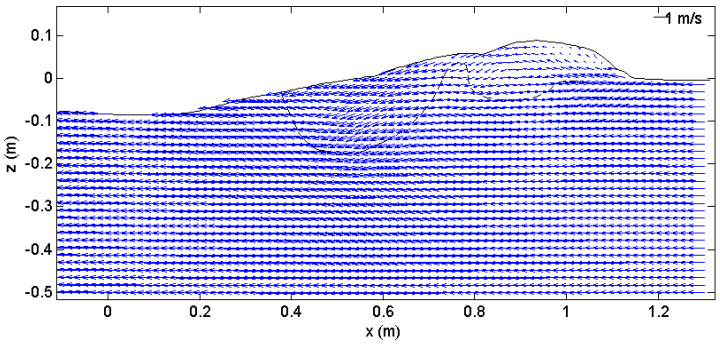

(o) $t = 0.66$ s

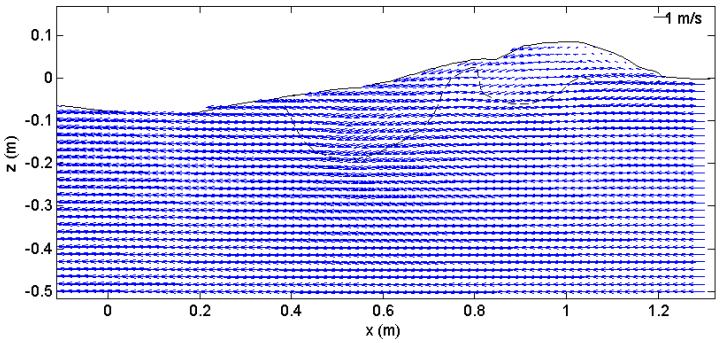

(p) $t = 0.71$ s

Fig. B.18 (Continued).

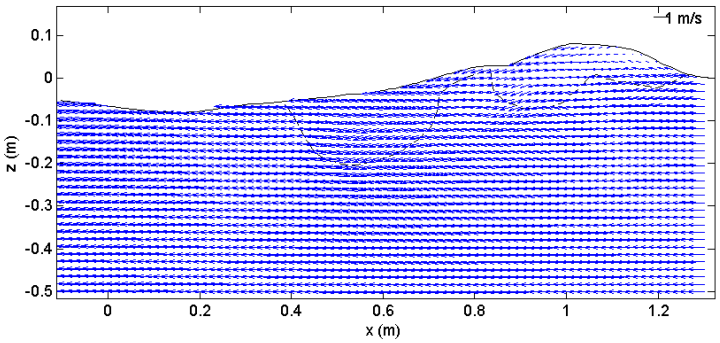

(q) $t = 0.76$ s

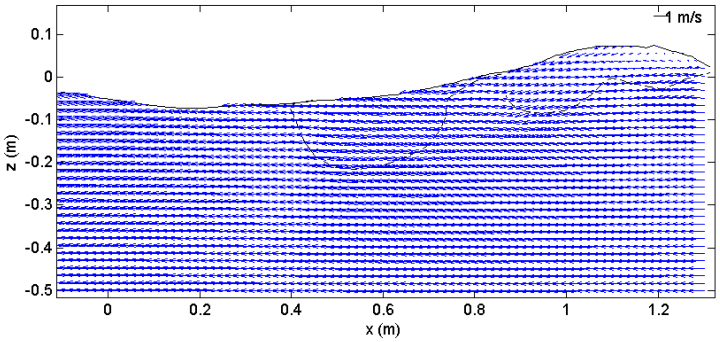

(r) $t = 0.81$ s

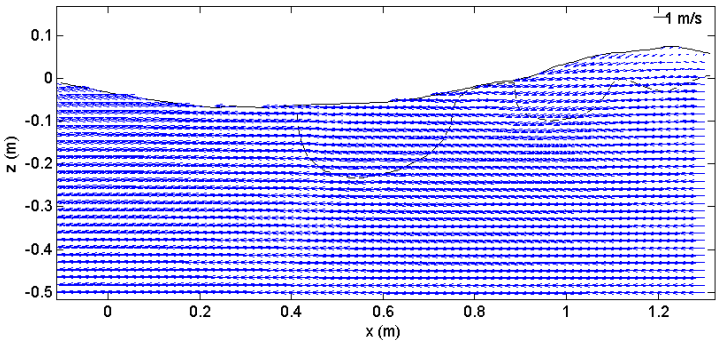

(s) $t = 0.86$ s

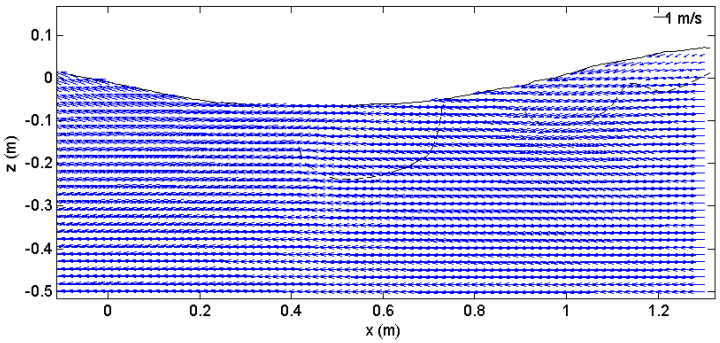

(t) $t = 0.91$ s

Fig. B.18 (Continued).

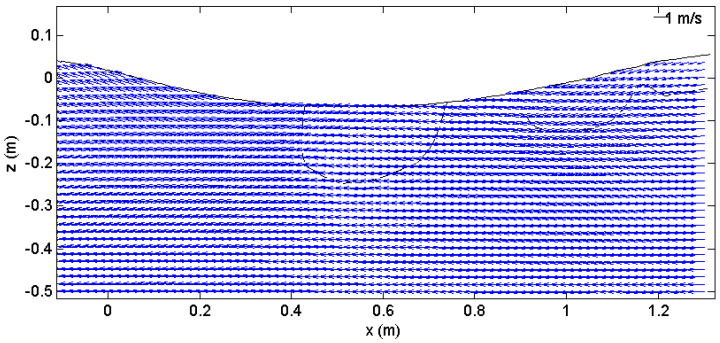

(u) t = 0.96 s

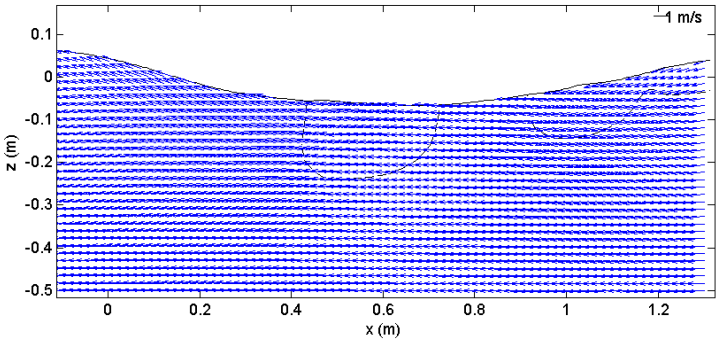

(v) t = 1.01 s

Fig. B.18 (Continued).

VITA

Name: Ho Joon Lim

Address: Ocean Engineering Program
Department of Civil Engineering, Texas A&M University
3136 TAMU, College Station, TX 77843-3136

Email Address: limhojoon@hotmail.com

Education: B.S., Naval Architecture and Ocean Engineering,
Inha University, 1997

M.S., Naval Architecture and Ocean Engineering,
Inha University, 1999

Ph.D., Ocean Engineering,
Texas A&M University, 2010